The circumstellar medium of massive stars

Habilitationsschrift (kumulativ)

Mathematisch-Naturwissenschaftliche Fakultät
der
Universität Potsdam

von
Dr. Dominique M.-A. Meyer
aus
Straßburg, Frankreich

Potsdam, 2023

1. Gutachter: Prof. Martin Pohl
2. Gutachter: Prof. Niccolo Bucciantini
3. Gutachter: Prof. Anna Bartkiewicz

Tag der Habilitation: 25, Oktober 2023
Erscheinungsjahr: 2023

Acknowledgements

This thesis has been prepared and written in astroparticle physics group of the Institute of Physics at the University of Potsdam, led by Prof. M. Pohl. I am very grateful to him to have permitted me to continue my research on the circumstellar medium of high-mass stars and to extend it to the world of cosmic rays physics, while introducing me to the subtleties of academic teaching and to the art of supervising students.

My immediate thank goes to Prof. L. Oskinova, met again on the rivers of Strasbourg, for her invitation in Potsdam, where we later performed together numerical simulations of Wolf-Rayet nebulae. I express a profound gratitude towards Dr. K. Egberts from the astroparticle physics group of the University of Potsdam, for many inspiring help, starry discussions and loud supportive moments, to I. Tietgen for warm presence in the corridors of the Institut für Physik und Astronomie at Universität Potsdam, and to Dr. B. Kliem for his physics books and for having been a very friendly office colleague. Schön war die Zeit mit euch.

The part of this thesis devoted to the circumstellar medium of young massive stars benefited from the advice and the passion for both young stars and numerical fluid dynamics of the very regretted Prof. Wilhelm Kley. The success of this research on massive star formation is more than largely due to Dr. Eduard Vorobyov from Vienna University. It has been a privilege to receive invaluable help from him and a chance to collaborate. I look for the future together.

Advances on the the surroundings of evolving runaway massive stars have been possible thanks to Dr. K. Scherer from the University of Bochum. Similarly, this research profited invaluable advice from the irreplaceable founder of numerical nebular studies Prof. A. Raga at the University of Mexico.

My research on core-collapse supernova remnants would not have been possible without the technical help of Prof. A. Mignone from the University of Torino and of MSc. Mykola Petrov from the Max Planck Supercomputer in Garching. The explosive advice on supernovae remnants of Prof. P. Velazquez and his group at the Universidad Nacional de Mexico have ignited and greatly contributed to the results presented in this thesis. Finally, I am grateful to Dr. Zakaria Meliani from the Observatory of Paris, for opening me the magnificent door of pulsar wind nebulae.

I thank the member of this Habilitation reviewers and commitee (Prof. N. Bucciantini from Florence, Prof. A. Bartkiewicz from Torun, Prof. M. Pohl, Prof. L. Oskinova, Prof. C. Pfrommer, Dr.-Habil A. Schwope, Prof. E. Eibl, Prof. F. Krüger, Prof. Z. Nokoloski) for their time throughout the entire, long examination process, as well as A. Brockhaus and Prof. P. Richter for their administrative supports.

Final acknowledgements go to my relatives, whose constant presence made this path in science possible.

Foreword

Massive stars are infrequent, seminal and generate strong feedback such as wind and radiation forming superbubbles around stellar clusters. Throughout their feedback, such high-mass stars act as driving engines in the cycle of matter in galaxies by enriching the interstellar medium with heavy chemical elements and driving turbulence regulating future star-forming processes. The so-called circumstellar medium, or region of the interstellar medium which evolution is ruled by stellar feedback, is a fantastic laboratory to learn about the formation of high-mass objects, constrain their internal evolution, understand the ISM magneto-hydrodynamics properties and progress on the comprehension of cosmic-ray acceleration and non-thermal emission mechanisms. This habilitation thesis investigates the large variety of scales and physical mechanisms involved in the surroundings of massive stars, successively shaping as au-large discs to parsec-scale bubbles or bow shocks and finally to remnant nebulae which can be observed. The detailed description of the complex physics at work inside and outside massive stars requires synergy between high-performances computing, plasma and astroparticle physics, as well as the latest developments in observational astronomy.

The first part of this thesis deals with the formation mechanisms of individual massive stars. It reveal that high-mass stellar objects form as a scaled-up version of solar-star formation and obey the picture of the burst mode of accretion in star formation. During their infant formation phase, large circumstellar accretion discs form and fragment by gravitational instability before gaseous clumps inward-migrate down to the stellar surface, eruptively adding mass to the protostar. This governs their entire internal structure and early evolution in the Hertzsprung-Russell diagram. This work predicted that the disc clumps should be observables by millimeter interferometric observations, which has been verified experimentally since that time.

The second part of this thesis investigates the evolution of the circumstellar medium of elder massive stars. It is shown that accounting for the magnetic fields of the interstellar medium is necessary in order to understand the stability and emission properties of the astrospheres of fast-moving main-sequence and red supergiant stars. Particularly, stellar evolution is invoked in order to propose that Betelgeuse's bar is of interstellar nature. Last, it explores and quantifies the formation mechanisms of rings and bipolar nebulae around Wolf-Rayet stars.

The third part of this thesis is devoted to the core-collapse supernova remnants left after the explosive death of massive stars. It demonstrates that the middle-term evolution, the morphology of the remnant nebulae, the mixing of the several kind of materials at work in those core-collapse supernovae remnants as well as the cosmic-rays-related mechanisms happening therein such as non-thermal synchrotron and inverse Compton emission, are a function of the history of their defunct massive progenitors. It is controlled by the past stellar wind feedback evolution coupled to the local magneto-hydrodynamical conditions the interstellar medium. Last, this work reveals that the influencing role of the past of massive stars continues to the final pulsar wind nebula phase of some core-collapse supernova remnant.

This cumulative thesis, which chapters are constituted of my post-doctoral dissertation, leading-author refereed publications to be found as Appendices, show that information on the final fate of massive stars is already included on the very initial condition of the medium they form in. Hence, the detailed and global understanding of the functioning of massive stars requires the detailed and complete knowledge of their entire past evolution history. It is an enterprise of intrinsical interdisciplinary nature, only possible at the cost of concatenating together results from the research fields of star formation, stellar evolution and cosmic-rays physics.

Contents

CHAPTER 1

Introduction

This chapters introduces the global context of the research constituting this cumulative habilitation. It presents the interstellar medium of Galaxies, the evolution of massive stars as well as the close surroundings of massive stars, their circumstellar medium.

1.1 Stars and the interstellar medium

The observable Universe is composed of myriads galaxies, self-gravitating ensemble made, from the baryonic point of view, of gas and dust. Galaxies can reveal multiple shapes, from elliptic to spiral, and have typical diameters of the order of 1−100 kpc. Our galaxy, the Milky Way, is a flat disc-like object with a central bulge from which several spiral arms extend to the outer region of this system. It is principally made of stars, separated by the so-called tenuous *interstellar medium* (ISM), see Lequeux (2005); Kwok (2007).

The ISM is a multi-phase plasma made, which, in addition to be magnetised, turbulent, chemically complex and dusty, is constituted of three cold, warm and hot components. In the ISM, stars form, evolve and die, release their feedback that drives the cycle of interstellar matter taken, which understanding it an entire field of research (McKee, 1995). The cold ($T_{\rm ISM} \sim 10^2$ K) phase of the ISM is the dense ($n_{\rm ISM} \sim 10^2\,{\rm cm}^{-3}$), neutral, molecular region located near the galactic plane of the Milky Way in which star formation occurs. It is in thermal equilibrium with a second, warm ($T_{\rm ISM} \sim 10^4$ K) phase of the ISM that is also neutral but of higher number density ($n_{\rm ISM} \sim 1\,{\rm cm}^{-3}$). This is typically where the surrounding gas heated by the radiation of massive stars belong (Field, Goldsmith & Habing, 1969). A third, hot ($T_{\rm ISM} \sim 10^6$ K) and diluted ($n_{\rm ISM} \sim 0.01\,{\rm cm}^{-3}$) phase, generated by the explosive death of some stars, induce an additional component to the ISM (McKee & Ostriker, 1977; McKee, 1995). Hence, stars do not only sit in the ISM, but are living part of it as they form out of its cold mass and by release in it warm and hot processed stellar material.

Stars are smaller-scale gravitationally bound systems of gas which collapsed under its own gravity throughout a process of *star formation* in dense molecular clouds of the cold phase of the ISM (McKee & Ostriker, 2007). Although the complete, detailed characterisation of stellar objects requires the knowledge of several parameters such as their radius $R_\star$, effective surface temperature $T_{\rm eff}$, photospheric luminosity $L_\star$, equatorial rotation velocity $v_\star$, surface gravity g, chemical com-

position, etc., the main quantity distinguishing stars is their mass $M_\star$ at the very end of the star formation process, or zero-age main-sequence (ZAMS) time. The study of the evolution of stars from its early life to the end of their live is called *stellar evolution* (Maeder, 2009). The distribution of star in a given star-forming region of galaxies observed so-far with high-resolution facilities obey a universal law known as the *initial mass function* (IMF) which is a decreasing piece-wise function of stellar occurrences N as as function of $\log(M_\star)$, see Kroupa (2001). In other words, many light stars form, while heavy stars are rare, and, one defines *massive stars* as the $\sim 1\%$ of all stellar objects with $M_\star \geq 8\,\mathrm{M}_\odot$. The evolution of massive stars is of prime importance in the understanding of the ISM and of the internal functioning of galaxies (van Buren, 1993; Vink, 2006).

1.2 Massive stars and their evolution

Massive stars can only form out of the fragmentation of turbulent giant molecular clouds (Kenyon et al., 1990; Tasker & Tan, 2009; Tasker, 2011) into rotating cores of mass $M_\mathrm{c} \gg M_\star \geq 8\,\mathrm{M}_\odot$, which subsequently experience gravitational collapse (Shu, 1977; Evans, 1999; Shu, 1992; Bergin & Tafalla, 2007; Elmegreen, 2007) that lead to the formation of large star-forming regions (Gordon et al., 2017) which distribution of stars, including high-mass stellar objects, is given by the IMF. These systems engender stellar clusters (Geyer, 2002; Oh & Kroupa, 2018) once the stars reach their ZAMS, and the ionizing as well as the outflow feedback of massive stars governs the evolution of the clusters, both stopping star formation in their host giant molecular cloud by dismissing the molecular material and driving away the turbulence that will regulate the formation of the next generation of stars. The understanding of their early formation phase is necessary to study in detail the manner they will live and die, simultaneously affecting the evolution of the ISM. Therefore, massive stars are preponderant ingredients in the functioning of galaxies like our Milky Way, the neighbouring small and large Magellanic clouds as well as other galaxies (Lahén et al., 2020b,a).

High-mass stars live fast and die young. Their evolution is by far quicker than the other numerous solar-like stars. Depending on rotation (Brott et al., 2011a,b), metallicity (Maeder & Meynet, 2000; Szécsi et al., 2022a) and multiplicity (Sana, 2012), massive stars evolve from a long main-sequence phase, by undergoing several evolutionary phases, characterised by changing surface and wind properties which alternate hot, fast-wind with cold, slow-wind phases (Langer, 2012). They typically spend much of their time ($\sim 10\,\mathrm{Myr}$) on a main-sequence phase, expelling diluted winds at mass-loss rates of $\dot{M} \sim 10^{-11}$–$10^{-7}\,\mathrm{M}_\odot\,\mathrm{yr}^{-1}$ and with wind speed of the order of $v_\mathrm{w} \sim 1000\,\mathrm{km\,s}^{-1}$ with an OB spectral type corresponding to surface temperatures $T_\mathrm{eff} \approx 20000$–$40000\,\mathrm{K}$ (Vink, de Koter & Lamers, 2000; Brott et al., 2011b; Ekström, 2012). Then, they evolve to the short (~ 0.1–$2\,\mathrm{Myr}$) red supergiant phase which is characterised by inflated radii $R_\star \sim 1000\,_\odot$ as well as $\dot{M} \sim 10^{-6}$–$10^{-5}\,\mathrm{M}_\odot\,\mathrm{yr}^{-1}$, $v_\mathrm{w} \sim 50\,\mathrm{km\,s}^{-1}$, $T_\mathrm{eff} \approx 5000\mathrm{K}$ for an observed M spectral type (Levesque, 2010; Davies, 2017). Further evolution is poorly understood, although more massive stars seem to end their life as red supergiants. The most massive ones ($M_\star \geq 30$–$35\,\mathrm{M}_\odot$) can further evolve to the additional, short (~ 1–$10\,\mathrm{kyr}$) Wolf-Rayet phase, characterised by very powerful $\dot{M} \sim 10^{-6}$–$10^{-4}\,\mathrm{M}_\odot\,\mathrm{yr}^{-1}$ fast $v_\mathrm{w} \sim 1000$–$5000\,\mathrm{km\,s}^{-1}$ winds expelled from these small $R_\star \sim 5\,_\odot$, hot $T_\mathrm{eff} \approx 50000\mathrm{K}$ stars. It subdivided into 3 classes, i.e. WN, WC, WO depending on the dominant element (N, C or O) present at their surface and ruling their emission profiles (Underhill, 1968; Hamann, 1992; Crowther, 2007).

More exotic evolutionary paths for the fate of massive stars exist (Groh et al., 2014), and, the heavier their mass, the higher the probability for such stars to undergo unusual stages like luminous blue variable (or blue supergiant) eruptions such as those of the famous star η Carina (Langer, García-Segura & Mac Low, 1999; Smith, 2014). Finally, high-mass stars die as a core-collapse supernova potentially leaving behind a compact object such as a neutron star (Woosley & Weaver, 1986; Weiler & Sramek, 1988; Smartt, 2009; Eldridge, Langer & Tout, 2011), or in the case of very massive objects, generate long γ-ray bursts (Yoon & Langer, 2005; Woosley & Bloom, 2006) or directly collapse as a black hole (Woosley, Heger & Weaver, 2002).

Massive stars, via their feedback, hence play a driving role in the cycle of material of galaxies. From their birth in the cold phase of the ISM, their evolution is responsible for the production of its warm phase, while high-mass stars death generate its hot phase.

1.3 The circumstellar medium of massive stars

The circumstellar medium of massive stars is the subset of the ISM which evolution is rules by the feedback of these high-mass stellar objects. Each massive star possesses a surrounding sphere of influence produced by the interaction of its stellar wind and radiation with the local ambient ISM. The morphology, magneto-dynamical, thermodynamical and emission properties of the circumstellar medium of massive stars are function of the both the stellar feedback properties and the surrounding ISM characteristics. Their study permit to learn about the ambient medium properties, to constrain evolution and to understand the thermal and non-thermal emission of the nebulae around massive stars. Typically:

The circumstellar medium of young massive stars was unobserved until modern inteferometric facilities could finally see deep inside the cold molecular clouds in which massive protostars form (Johnston et al., 2020a). The presented numerical simulations of the surroundings of young massive stellar objects are prior to that time and constitute partly today verified predictions for the formation of massive protostars (Meyer et al., 2017b, 2018, 2019b; Meyer, Haemmerlé & Vorobyov, 2019; Meyer et al., 2019a, 2021c). They show that, as low-mass stars do, the collapsing molecular material lands onto a centrifugally-balanced accretion disc which fragments. Some disc clumps inward-migrate to the protostellar surface, inducing accretion-driven outbursts while some clumps can form nascent low-mass stars into the disc. These models showed that high-mass stars formation is a scaled-up version of their low-mass counterpart.

The circumstellar medium of evolved massive stars shapes when the strong stellar wind of early-type OB stars blowing on the onset of the ZAMS interacts with the ambient medium, creating wind bubble, or series of concentric circular shocks separating stellar wind and ISM material (Weaver et al., 1977). Those mainly infrared-observed wind bubbles turn into bow shocks in the case of the 20−30% of massive stars moving fast through the ISM (Wilkin, 1996). When evolving, either to the red supergiant or eventually to the Wolf-Rayet phase, the properties of wind bubbles and stellar wind bow shocks change accordingly, producing a variety of arc-like and bilateral nebulae of diverse morphologies. The presented numerical magneto-hydrodynamical models and associated synthetic observables (Meyer et al., 2016, 2017a, 2021a, 2020; Meyer, 2021) of the circumstellar medium of evolved massive stars such as Betelgeuse, IRC-10414 and NGC6886 are efficient tools in the understanding of the study of the stellar evolution of massive stars.

The circumstellar medium of dying massive stars Most massive stars eventually explose as core-collapse supernova and generate blastwave inside of their pre-shaped circumstellar medium.

The shock wave produced by the explosion interacts with the surrounding environment, made of wind and ISM gas, and, by a game of wave reflections, produce a hot asymmetric supernova remnant (Meyer, Petrov & Pohl, 2020; Meyer et al., 2021b; **?**; **?**; **?**). Their shapes are numerous and can adopt many morphologies such as bilateral and rectangular shapes that emit both thermally and non-thermally. Last the pulsar wind nebulae eventually released into of those peculiar supernova remnants also report asymmetries function on the past circumstellar medium of the progenitor star.

The evolution of the surroundings of massive stars mirror that of their driving, central stellar properties, and, consequently, understanding it provides insights into the evolution of massive stars, together with a manner to constrain the properties of the the local ambient medium in which nebulae lay. The final goal of this research field devoted to the study of the circumstellar medium of massive stars is, on the basis of the single observation of one of their nebulae, to identify the entire physical characteristics of the star. This permits to constrain its evolution and to reconstruct that of its neighbouring region in the ISM, as well as to predict their future, both from the thermal and non-thermal point of view.

1.4 The role of numerical simulations

Massive stars, which are infrequent, seminal and generate ionized superbubbles around stellar clusters (Langer, 2012). They gain eruptively their mass, and throughout their life, their strong winds and explosive death enrich the ISM, drive away turbulence regulating future star formation and produce cosmic rays. The large variety of scales and physical mechanisms involved therein reflects in their observed circumstellar medium, successively shaping as au-large discs (Johnston et al., 2020a) to pc-scale bubbles (Weaver et al., 1977) or bow shocks (van Buren & McCray, 1988a) and finally to remnant nebulae (Green & Stephenson, 2003).

Multi-physics numerical simulations only can probe these extreme environments, unfolding the complex morphologies of the circumstellar structures accompanying the life of massive stars. However, despite of significant progresses in numerical computing and the accumulation of high-resolution observations at different wavelengths, our knowledge of the the close surroundings of massive stars is still deficient and further progresses require numerical efforts that are enterprises of intrinsical interdisciplinary nature. Indeed, the detailed description of the complex physics at work in both inside and outside massive stars requires synergy between high-performances computing, plasma and astroparticle physics, as well as the latest developments in multi-messenger astronomy, both from the thermal and the non-thermal point of view.

This cumulative habilitation is articulated to the surroundings of the three above described characteristic phases of the evolution of high-mass stars. The following chapters are constituted of a summary of my first-author refereed publications written since the completion of my doctoral studies, presented here in the context of the current state-of-art.

CHAPTER 2

Massive star formation

This chapter investigates the formation mechanisms of young massive stellar objects. It is based on a series of papers devoted to radiation-hyudrodynamics simulations of the circumstellar medium of massive protostars (Meyer et al., 2017b, 2018, 2019b; Meyer, Haemmerlé & Vorobyov, 2019; Meyer et al., 2019a, 2021c), see Appendix. These studies have shown that the so-called burst mode of accretion picture for low-mass star formation applies to forming high-mass stars.

2.1 The secret formation of massive stars

How looks young massive stars ? Such question has no answer since decades because of the high opacity of the large, cold molecular clouds which they are born in (Zinnecker & Yorke, 2007). As motivations for the study of surroundings of young high-mass stars, let remember that since most fast-wind-blowing main-sequence massive stars display close companions (Vanbeveren, 1991; Chini et al., 2012; Mahy et al., 2013) which affect their evolution in the temperature-luminosity (or Hertzsprung–Russel) diagram (Dessart, Langer & Petrovic, 2003; Petrović, 2004; Sana, 2012). Hence, it has been long believed that massive binarity forms in the surroundings of young pre-ZAMS stellar objects, by analogy with planets in gravitationally-instable accretion discs around solar-like stars (Bonnell & Bate, 2005; Johnston et al., 2011).

A growing number of observational facts concerning either collapsing high-mass pre-stellar cores (Beuther et al., 2015), accretion flows (Keto & Wood, 2006), jets from young high-mass stars (Cunningham, Moeckel & Bally, 2009; Purser et al., 2016), or other phenomenons linked to circumstellar discs and the physics of accretion have been monitored, such as ionised gas in H II regions regions released into cavities produced by protostellar bipolar outflows (Cesaroni et al., 1999) or even pseudo-disc circumstellar structures resembling (Cesaroni et al., 2006; Beuther, Linz & Henning, 2012). The updates of the Atacama Large (sub-)Millimeter Array (ALMA) interferometric facility permitted for the first time to demonstrate the existence of a Keplerian structure in the vicinity of the massive protostars star AFL-4176 (Johnston et al., 2015), G11.920.61 MM1 (Ilee et al., 2016) and IRAS172163801 (Kraus et al., 2017). Those observational discoveries gave more and more credits to the consideration of massive star formation as a scaled-up version of low-mass star formation.

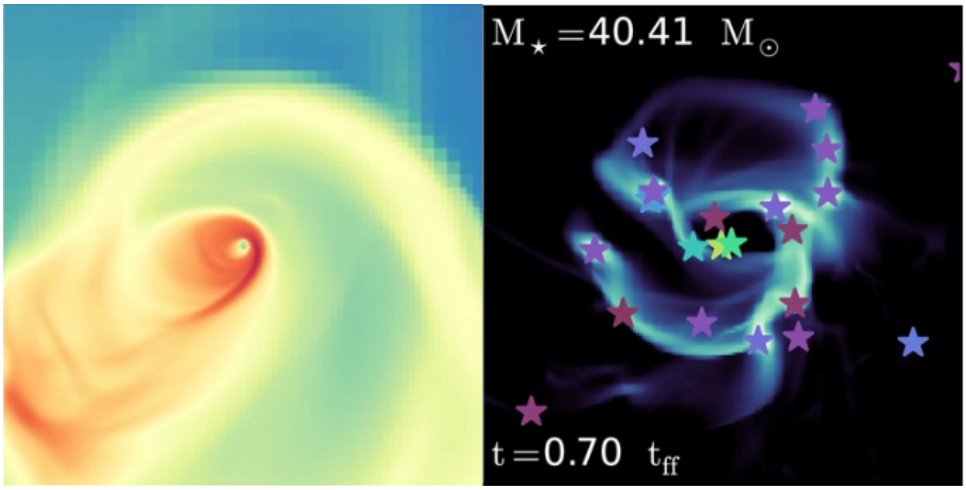

Figure 2.1: The fragmenting accretion disc paradigm as is 2016. Not only the accretion discs of young massive stars remained a theoretical prediction which had not yet been observed, but their stability properties were under debate: 3D MHD gravito-radiation-hydrodynamical simulation of molecular cloud collapse did not predict secondary star formation in them (see disc midplace density field in the left panel), while some others did it too efficiently (see disc midplace density field in the right panel). Models used grid-based codes with adaptative-mash refinment and artificial sink particles algorithm to track star formation into the disc. From Klassen et al. (2016); Rosen et al. (2016).

This observational context of the formation of massive protostars was accompanied by a numerical crisis, provided by contradicting results of similar models performed with different numerical codes. The typical initial conditions for the gravito-radiation-hydrodynamical modelling young high-mass stars consist in a molecular core of mass $100\,M_\odot$, radius $R_c = 0.1$ pc that is solid-body-rotating by a ratio of kinetic-to-gravitational energies $\beta \sim$ a few which free-fall collapses under its own mass. However, if all models predicted the formation of an accretion disc around the massive protostar, its stability properties greatly differ according to the used code, see Fig. 2.1. Some simulations produced stable disc (Klassen et al., 2016), challenging the existence of binary companions to massive stars, while some others predicted the formation of multiple massive systems (Rosen et al., 2016). This is the paradigm in which the following series of papers had been started (Meyer et al., 2017b, 2018, 2019b; Meyer, Haemmerlé & Vorobyov, 2019; Meyer et al., 2019a, 2021c).

2.2 The burst mode of accretion in massive star formation

2.2.1 Disc formation and fragmentation

My study Meyer et al. (2017b) brought novelties in the field of massive stars formation by the higher-spatial resolution reached in the inner region of the accretion disc. Indeed, precent works used 3D Cartesian mesh-refined grids allowing to globally model disc+outflows systems up to a given spatial resolution $\Delta >$ a few au, too coarse to capture secondary gravitational collapse in the discs. This required the injection of artificial Lagrangian *sink particles* mimicing secondary star

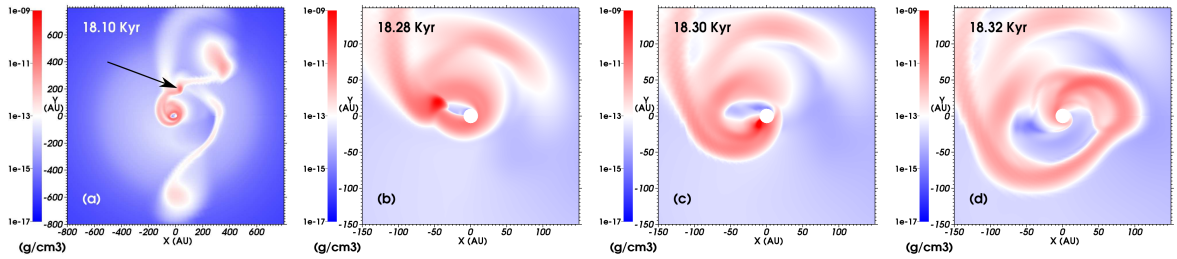

Figure 2.2: Density field (in g cm3) in the midplane of an accretion disc modelled in spherical coordinate with the PLUTO code and including self-gravity, radiation-hydrodynamics and stellar irradiation. Panel (a) shows the entire fragmenting disc around the time of the first outburst, where a clump forms inside of a spiral arm about 200 au away from the protostar. Panel (b,c and d) plot zooms revealing the migration and subsequent accretion of some of the clump material at different time instance. From Meyer et al. (2017b).

formation in the discs and injected when grid zone verified a given set of criteria, e.g. based on gas density, temperature or velocity (Federrath et al., 2010; Myers et al., 2013; Machida, Inutsuka & Matsumoto, 2014; Rosen et al., 2017). However, the manner sink particles were implemented led to contradictory results (Fig. 2.1). The spherical grid of the magneto-hydrodynamical code PLUTO (Mignone et al., 2007, 2012; Kolb et al., 2013), together with its radial logarithmically-expanding grid permitted to reach $\Delta <$ au spatial resolution in the inner disc region, to resolve the Jeans length (the cloud scale where gravity counterbalances its thermal energy, provoking a gravitational collapse) and to self-consistently capture its fragmentation (Fig. 2.2a). This had a number of immediate consequences which were explored in series of papers.

First of all, the fragmentation of inner accretion discs around massive protostars revealed the gaseous clumps dynamics, especially when, by torque exchange, some circumstellar clump episodically detach from the disc and inward-migrate from their host spiral arm to the protostellar surface. This provokes a sudden increase of the disc-star mass transfer, or protostellar accretion rate, by several orders of magnitude. The protostellar total luminosity evolves accordingly and the young high-mass star undergoes an accretion-driven outburt, a so far observed feature of low-mass stars formation, which most vivid manifestation is known as FU-Orionis bursts, and a theoretical prediction for the youth of supermassive stars. This study proposes that high-mass stars experiences the same kind of pre-ZAMS outbursts, and that the luminous flares from forming high-mass stars region () might be an observational consequence of the fragmentation of circumstellar accretion discs of massive protostars (Meyer et al., 2017b).

Secondly, the mechanism of accretion-driven outbursts has been found to happen many times in the youth of a given massive protostar. Each time a clump is accreted, it experiences a distortion while inward-migrating, the stretched tail of the clump being swung-away to the outer disc region, perturbing its dynamics, rearranging its organisation and lowering the disc degree of fragmentation. Hence, the process of disc fragmentation, clump migration and accretion-driven outbursts repetitively regulates itself through the pre-ZAMS circumstellar evolution of massive protostars. Changing the spin of the molecular pre-stellar core and/or it initial radial velocity profile in order to simulate more realistic collapsing clouds produce qualitatively similar results (Meyer et al., 2018). Moreover, all fragments in the models verified the semi-analytical criteria characterizing the fragmentation of self-gravitating discs, such as the Toomre, Gammie and Hill rules (Toomre, 1963; Gammie, 1996; Rogers & Wadsley, 2012).

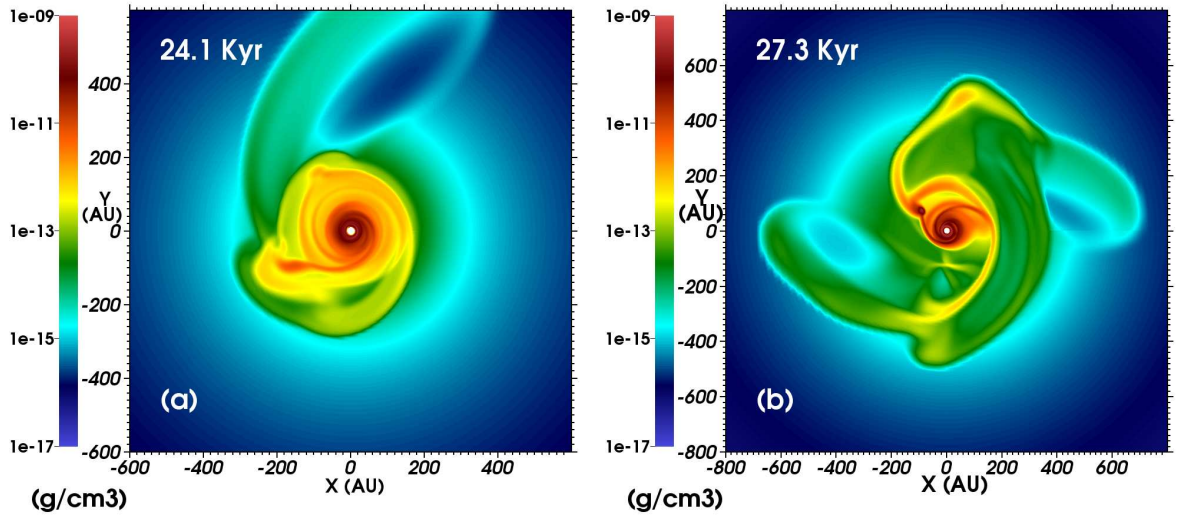

Figure 2.3: Density fields time evolution (in g cm3) of a fragmenting accretion disc around a massive protostar. From Meyer et al. (2018).

Third, the fate of the gaseous clumps is twofold. As above discussed, they can migrate onto the protostellar surface and induce accretion-driven bursts, while affecting the overall disc morphology. Nevertheless a careful look at the properties of the core of some migrating clumps show that they can keep on experience further gravitational contraction while approaching the central protostar. The evolution of such clump in the temperature-density diagram is plotted in Fig. 2.6 and highlight that the core heats and collapses up to entering the region of molecular hydrogen dissociation and thus acquiring the properties of a nascent low-mass star. The last Keplerian orbit of such disc fragments is compatible with the radii of close low-mass binaries observed in the vicinity of evolved massive stars (Vanbeveren, 1991). The formation of close/spectroscopic binaries to massive protostars and the generation of accretion-driven outbursts can happen together, the core of the clump material being responsible for the companion and its diffuse envelope falling on the protostellar surface, provoking a burst. Consequently, both phenomenons can happen simultaneously, the burst being the observable of close binary formation.

Fourth, the accretion rate history onto massive stars is an informative mine onto the live of protostars. An example of the variability of the disc-to-star mass transfer on a massive young stellar object is plotted in Fig. 2.5a. After an initial free-fall gravitational collapse, the envelope molecular material lands onto a centrifugally-balanced disc from which the protostar gets its mass as accretion variability is at work. The protostar enters the high-mass regime before first bursts and later gains it mass by step-like increase, corresponding to the accretion of heavy gaseous clumps (Fig. 2.5a). Its Lightcurve is made of a background photospheric luminosity interspersed by luminosity peaks (Fig. 2.5b). The simulation philosophy, based on high-resolution gravito-radiation-hydrodynamical models, permitted great advances on the circumstellar medium of massive stars. It has, however, a caveat: as the grid resolution effort is devoted to the disc, the protostellar feedback that dissipates the clouds when the young high-mass stars reach its ZAMS is not taken into account. In other words, such simulations do not yet allow to estimate when the star will become an adult object and have to be stopped.

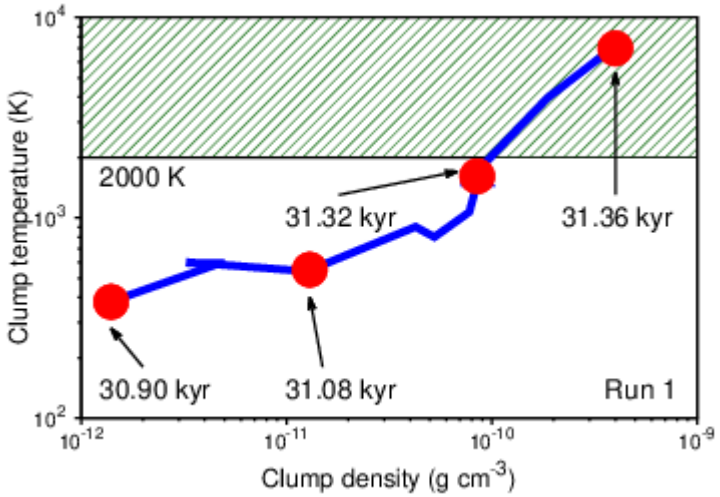

Figure 2.4: Evolution in the temperature-density diagram of a gaseous circumstellar medium migrating-inward into an accretion disc around a massive protostar. Some of the clump material are responsible for an outburst experienced by the young massive stellar object, however, while migrating, it core heats and contract up to entering the region of molecular hydrogen dissociation and acquiring the properties of a nascent low-mass star. The model shows that massive protostars have fragmenting discs, that disc clumps can form low-mass companions, migrate close to its surface generating (i) accretion outbursts and (ii) spectroscopic binary systems. From Meyer et al. (2017b).

2.2.2 Burst occurrence and spectroscopic excursions of massive protostars

The study of each individual accretion-driven outbursts from young massive stars falls under signal analysis considerations. Once a background, burstsless average luminosity of the protostar $L_{\rm bck}$ is defined, one can measure for each flare by how much $L_{\rm tot}$ and M raises before returning to the quiscent phase of accretion. This allows us to separate spurious increase of M produced by bounary effects and to classify physical bursts as a $i-$ mag burst if its total protostellar luminosity is such that $2.5^{i}L_{\rm bck} \leq L_{\rm tot} \leq 2.5^{i+1}L_{\rm bck}$, with 1-mag bursts being the mildest ones, and 4-mag bursts FU-Orionis outbursts. The models reveal that bursts do not happen solely, by rather in series of consecutive flares in which faint outbursts are much more common than bright ones because low-$\dot{M}$ variability generated by the accretion of overdensities in spiral arms is more common than low-$\dot{M}$ variability induced by the inward-migration of detached circumstellar clumps. Very interestingly, the occurence of bursts with high magnitude increases as the protostar, approaching the ZAMS, becomes more massive and is surrounded by a fragmented disc of complex structure (Fig. 2.6) and protostars gain up to half of their mass witinth the $\approx 2\%$ of their pre-ZAMS time spent in the burst mode of accretion Meyer et al. (2019b).

In order to study the burst properties in the detail, the burst duration-accreted mass diagram has been introduced in Meyer et al. (2019b), see also Fig. 2.7. Such figure is suitable to see the temporal and mass distribution of a collection of accretion-driven outbursts, while informing on their magnitude, peak luminosity and on the occurrence of burst happening within a given time period and/or permitting the protostar to acquire a given mass quantity. It is a pawerful tool in the exploitation of data from, e.g. large parameter studies and to compare models with obser-

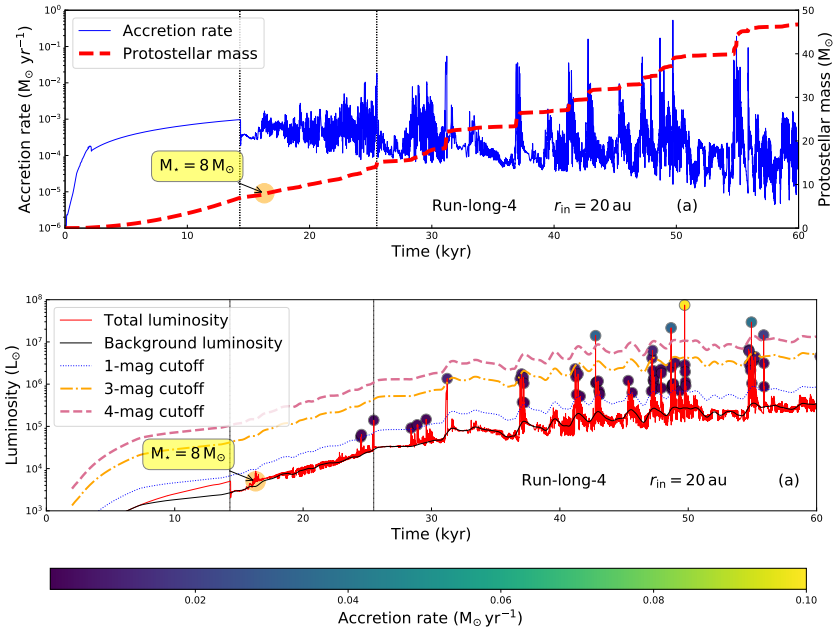

Figure 2.5: Variable disc-star mass transfer, or accretion rate onto a massive protostar formed from the collapse of a 100 $M_\odot$ molecular cloud sold-body-rotating kinetic-to-gravitational ratio $\beta = 4\%$, together with its mass evolution, shown as a function of time (in kyr), panel (a). The corresponding lightcurve of the protostar is plotted in (panel b), with background luminosity (black), curves highlighting luminosities larger than 2.5, 6.3 and 39.0 times the background luminosity (respectively called 1-, 2- and 4-mag cut-offs). The accretion bursts undergone by the protostar are plotted with filled circles, which colour gives the peak accretion associated to each bursts. From Meyer et al. (2019b).

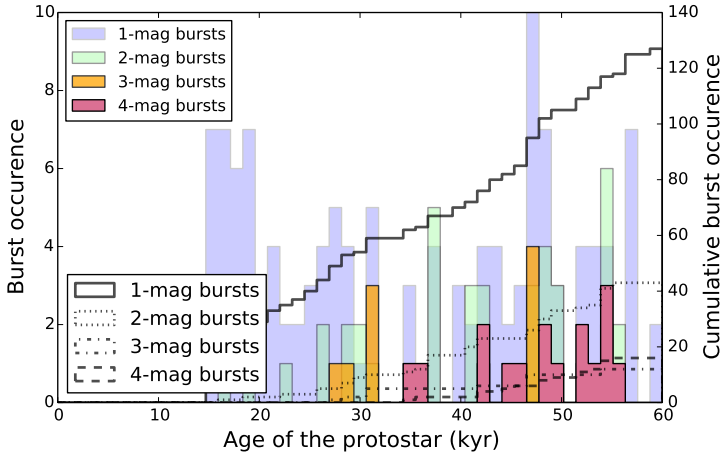

Figure 2.6: Histogram displaying the occurence of accretion-driven outbursts over the pre-main-sequence evolutionary phase of a young massive object. Bursts are classified as a function of the difference with the pre-burst protostellar luminosty. Fainter bursts are more common than bright bursts, which appear at later time in evolution of the protostar. From Meyer et al. (2019b).

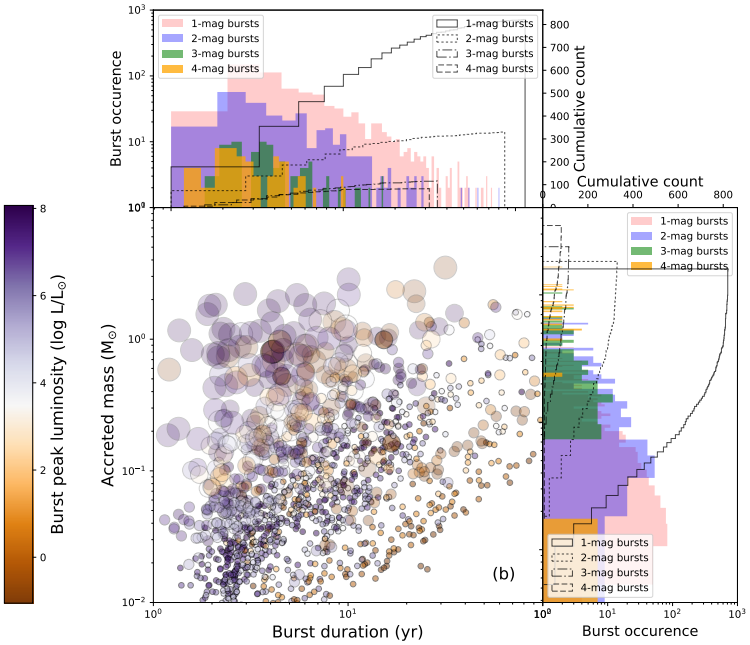

Figure 2.7: Distribution of the accretion-driven bursts of a collection of models for massive protostars represented in the accreted mass-burst duration plane. Each individual bursts are coloured as a function of their peak luminosity. The marginal histograms show the burst occurrence versus the duration of the bursts, peak luminosity, and mass accreted by the protostar during each individual bursts. From Meyer et al. (2021c).

vations (Meyer et al., 2021c). Because of the turbulent charater of fragmented discs developing gravitational instability, its bursts activity turned not to be directly a funtion of the initial properties of the molecular cloud in which the massive protostar formed. The accretion bursts of same magnitude and/or peak luminosity distribute along diagonals, see dots from bottom left to upper right in Fig. 2.7. This trends indicates that the mass accreted by the star is rather constant throughout a single burst, hence when the duration of the bursts increase, the corresponding mass gained by the protostar increases linearly, producing the parallal distribution of the bursts in the duration-mass plane.

It is well-known fact that sudden and strong increase of the accretion rate onto massive protostars ($\approx 10^{-2}$–10^{-1}) generate a diminishing of the entropy inside of the star accompanied by an increase of the entropy at the stellar surface, inducing the production an upper convective layer which makes the star to swell (Hosokawa & Omukai, 2009; Haemmerlé et al., 2016). Since its radius increases and its luminosity decreases, the massive protostar undergoes an excursion to the red, cool regions of the Hertzsprung-Russell diagram (Fig. 2.8). When the accretion rate decreases as the protostar comes back to the quiescent phase of accretion, it returns to the evolutionary track corresponding of that of a non-bursting pre-ZAMS high-mass object. This excursive phenomenon repeats itself each time young massive stars experiences a strong, 3-magnitude or 4-magnitude outburst (Meyer, Haemmerlé & Vorobyov, 2019).

Consequently, the entire evolution of all protostellar surface quantities are affected by the episodic accretion of dense disc clumps. Note that is it not the amount of accreted mass which matters, but rather the rate at which it is transferred from the disc to the star. The evolution of the protostellar

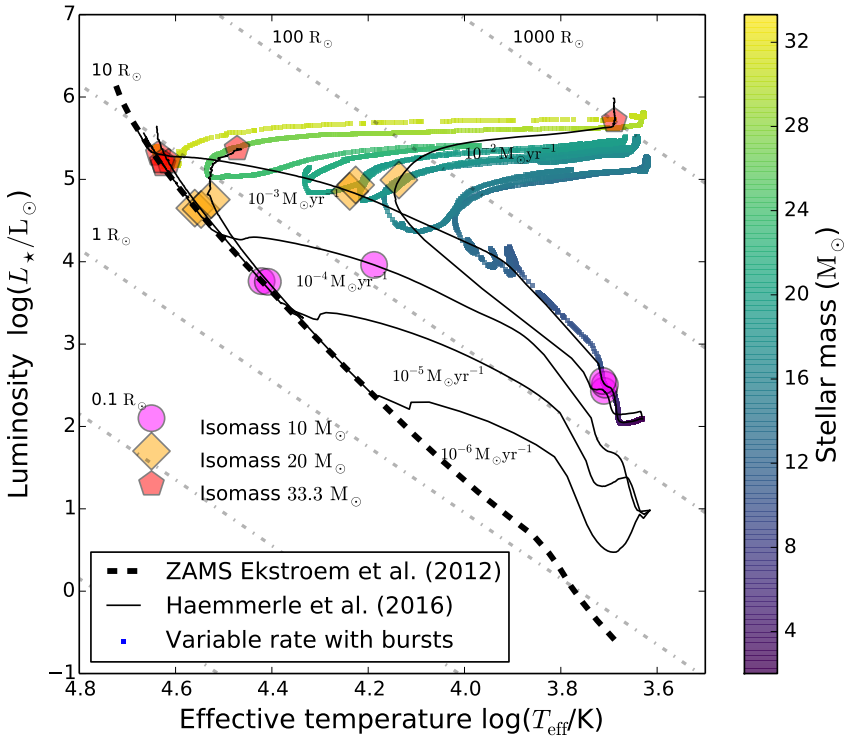

Figure 2.8: Effects of an episodic accretion rate onto the spectroscopic evolution of a young massive star. The evolutionary tracks without disc accretion rate of Haemmerlé et al. (2016) show the evolution of massive protostars from their seed embryo to the zero-age main-sequence track of Ekström (2012). The track with episodic mass transfert onto the protostar is coloured as a function of the mass of the young star (in $M_\odot$). Coloured symbols are isomasses, diagonal lines are isoradii. From Meyer, Haemmerlé & Vorobyov (2019).

radius presents, at the time of the bursts, sudden peaks up to $\approx 1000\,R_\odot$, while the temperature time evolution exhibits antagonist variations down to ~ 5000 K. Since a massive star, at the first order, is a black body emitter, one can estimate the number of photons $S_\star$ released by the photosphere with energies above the UV ionising threshold. It globally increases as a function of time because the growing protostar is hotter as it gets close to the ZAMS, except at the moment of the strongest accretion bursts, when $S_\star$ episodically drops down.

The variations of the ionizing photon flux of massive protostars has observational consequences, because, by analogy with low-mass star formation, it should be is channelled into the bipolar cavity developing normal to the plane of accretion discs. Such ionizing feedback has been observed when outflowing the obscure parent molecular clouds of the high-mass protostars (Cesaroni et al., 1999). Its variability indicates that the photo flux should decrease during the spectroscopic excursions towards the red part of the Hertzsprung-Russell diagram, intermittently switching-off/in the photon flux feeding the H II region of the massive protostar each time the accretion process of a circumstellar clump responsible for a strong burst.

The newly discovered behaviour of young massive protostars within the burst mode of accretion in massive star formation raised the question of its validity in the context of the many parameters describing collapsing molecular clouds. A parameter study has been conducted in order to answer

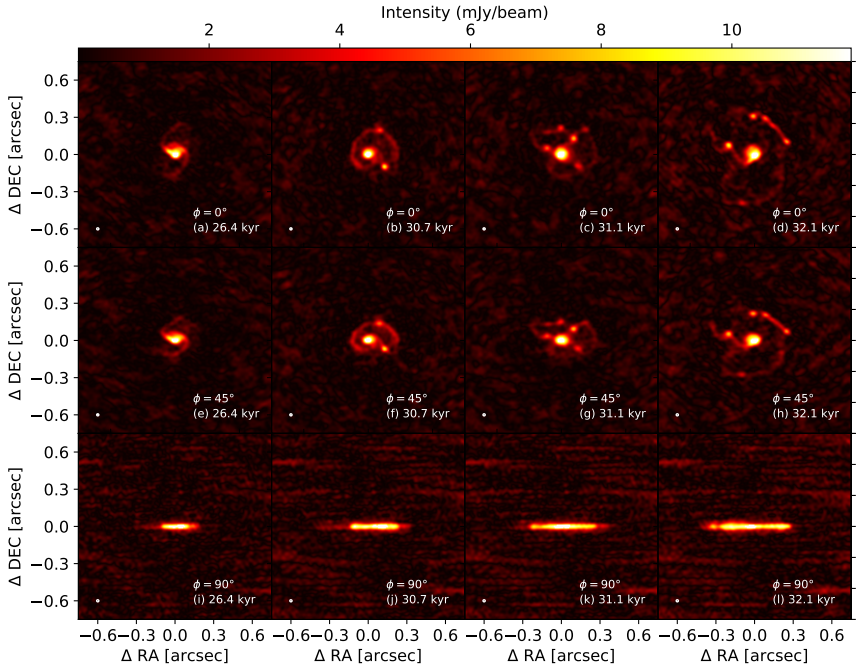

Figure 2.9: Predictions for the (1.2 mm observation of fragmented circumstellar discs around young massive stars, for different time instances of the disc evolution and according to several viewing angles. The calculations are performed for the cycle 10 interferometer, using its broadest antenna disposition C43 during 10 minutes of exposure time, assuming a distance to the source of 2 kpc. From Meyer et al. (2019a).

this question, exploring both the mass of the collapsing clouds (M_c = 60−200 $M_\odot$) and the ratio of rotational-to-gravitational energies (β = 0.005−0.33), see Meyer et al. (2021c). This study confirmed the results obtained in the precedent papers of this series, on the basis of a few selected simulation models. Interestingly, it is found that no corner of te parameter sutdy produced stable discs, i.e. circumstellar environment to massive stars that are not affected by gravitational instability and which do not display accretion bursts. This is a therefore a major difference between the formation of solar-like and massive stars, as the existence of discs without planets exist. Furthermore, an inspection of the time interval between consecutive bursts indicates a bimodal distribution, with a short duration ($\sim$ 1−10 yr) component from the faint quick bursts and a bright long peak component (at $\sim 10^3$−10^4 yr).

The formation of massive stars is far from being a achieved field of research. Particularly, many physical processes have to be included into numerical models, and the spatial resolution of the simulations must be further increased to better capture the internal functioning of circumstellar discs of young high-mass stars. This challenges the current capacity of modern supercomputers. A firsts along this direction is the inclusion of the disc gravitational backaction onto the growing massive star, or stellar wobbling, in high-resolution models (Meyer et al., 2022b). This has the quantitative effect to slightly delay disc fragmentation by readjusting the position of the protostar as soon as gravitational instability begins to be efficient.

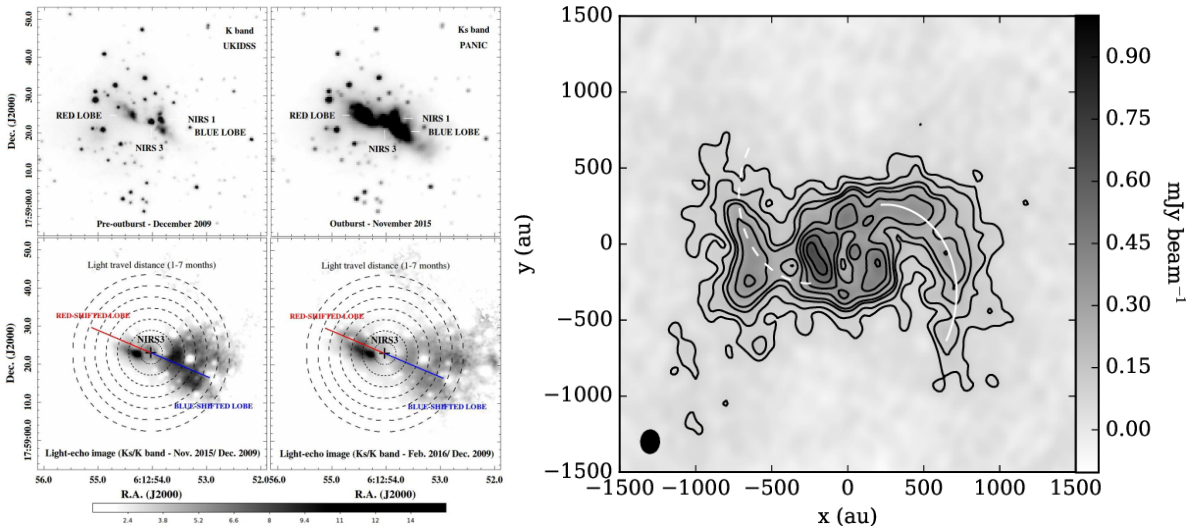

Figure 2.10: Two verified predictions of the burst mode of accretion in massive star formation. Left: optical image of the region surrounding the massive young stellar object S255IR-NIRS3 which experienced a disc-mediated outburst. Right: 1.3 mm ALMA image of the fragmented accretion disc around the massive protostar AFGL-4179. From Caratti o Garatti et al. (2017); Johnston et al. (2020a).

2.2.3 Can the surroundings of massive protostars be observed ?

The last step of or investigation of the circumstellar medium of massive protostars is to test the observability of the disc fragments. Since it was known that pseudo-disc, perhaps Keplerian structures, can be seen around massive young stellar objects (Johnston et al., 2015; Ilee et al., 2016; Kraus et al., 2017), it is legitimate to questions whether the disc sub-structures that are predicted in Meyer et al. (2017b, 2018) might be seen by means of modern facilities such as the *ALMA* interferometer, providing thus observational proofs of the predictions of the burst of accretion in massive star formation. To this end, a post-processing procedure made of successive radiative transfer calculations against dust opacity completed with synthetic imaging for the *ALMA* telescope similar to that of Krumholz, Klein & McKee (2007); Harries, Douglas & Ali (2017) for massive stars and to that of Vorobyov, Zakhozhay & Dunham (2013); Seifried et al. (2016); Dong et al. (2016) for low-mass stars is performed.

In Meyer et al. (2019a), the disc models of Meyer et al. (2018) are imported into the RADMC-3D code (Dullemond, 2012) where dust density and temperature fields are reconstructed. The protostellar surface properties such as the radius $R_\star$, effective temperature $T_{\rm eff}$ and luminosity $L_\star$ are obtained by feeding the stellar evolution code GENEVA (Eggenberger et al., 2008) by the accretion rate history onto the protostellar model of Fig. 2.3. This provides the time-dependent evolution of the quantities necessary to model the photon packages ray-traced from the protostellar surface towards the accretion disc. We make use of the Laor & Draine (1993) dust mixture based on Si crystals when irradiating the disc with millions of photon packages by assuming that the protostar is a black body of temperature $T_{\rm eff}$ and 1.2 mm emission maps are produced by projecting of the disc emitted flux. The distance between the protostar and the observer is taken to be of the order of 1.0 kpc, which is in accordance with the distance to the closest massive star-forming regions such as Orion. The images are further treated with the Common Astronomy Software

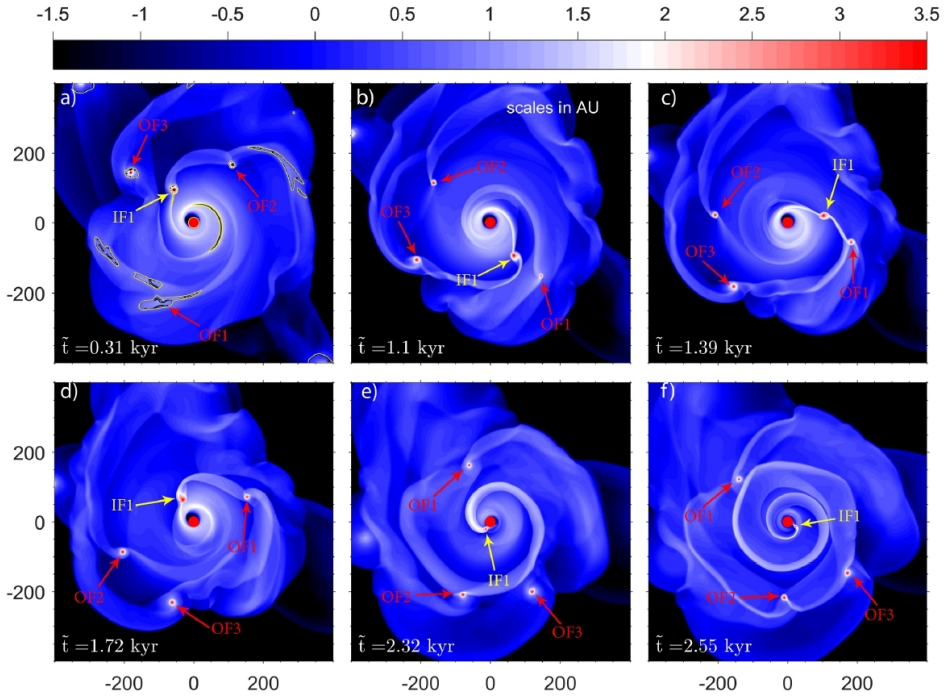

Figure 2.11: Similarities between low- and high-mass star formation, both of them unified within the burst mode of accretion picture, the low-mass nascent companions in discs around massive protostars being the equivalent of the planets in discs around low-mass stars. From Vorobyov & Pavlyuchenkov (2017).

Applications CASA software (McMullin et al., 2007) to calculate synthetic fluxes of the accretion disc models as they would be if observed by *ALMA* at band 6 (1.2 mm or equivalently 249.827 Ghz with channelwidth 50.0 Mhz) using the 43 12-metres large antennae with configuration C43 of maximal extension, i.e. reaching the highest possible resolution.

Fig. 2.9 display synthetic *ALMA* images of the accretion disc model of Fig. 2.3, shown for different viewing angles with respect to the plane of the sky after a 10 min exposition time. It shows that the spiral arms and clumpy fragments of the disc subject to efficient gravitational instabilities can be seen in the ALMA projected emission signatures as being brighter than the disc structure. In other words, the dense spiral arms and gaseous clumps, that episodically inward-migrate to the innermost part of the accretion disc should be observable. The clumps which have further contracted and are on the way to low-mass star formation, are either the precursors of close/spectroscopic binary companions to the central protostar or will induce accretion driven outbursts should be seen. The models show that the finest substrucures of accretion discs around young massive stars can be observed regardless of the inclinaision of the discs with respect to the plane of sky, even in the inner region ≥ 500 au from the irradiating protostar when it has reached 20 $M_{\odot}$. The large extended accretion discs around to massive protostars about to complete their early formation phase and to enter the ZAMS are more prone to be detected than that of much younger protostars. Moreover, they had more time to develop more clumps. Particularly, Meyer et al. (2019a) shows that spiral arms and disc clumps can be inferred in the context of the bursting young high-mass stars S255IR-NIRS3 (Zinchenko et al., 2015; Caratti o Garatti et al., 2017) and NGC 6334I-MM1 (Hunter et al., 2017), see Section 2.3.

2.3 Observational verifications

The theoretical modelling of the surroundings of massive protostars which revealed the compatibility of the high-mass region of star formation with the burst mode picture coincidently came together with high spatial resolution and monitoring observations. These data provided a breakthrough in the current knowledge of that time regarding the youth of massive stars, and, interestingly, confirmed the numerical predictions of Meyer et al. (2017b, 2018) and following studies. This started with the monitoring of a disc-mediated burst from the massive young stellar object S255IR-NIRS3 (Caratti o Garatti et al., 2017), soon followed by the direct imaging of substructures in the accretion disc surrounding the proto-O star AFGL-4179 (Hunter et al., 2017). In the coming years, many other young massive sources revealed either pre-main-sequence outbursts or clumpy surrounding discs. The associated building statistics of bursting massive protostars goes in the direction of validating the burst mode picture for star formation as an accepted model in the understanding of how high stars gain their mass reach their main-sequence.

The extraordinary outburst time-dependently observed from the 20 $M_\odot$ massive protostar S255IR-NIRS3, with an estimated beginning of the burst time around mid-June 2015 and a monitoring of the flare infrared light echo scattered by the dust present in the cavities carved by the protostellar outflow between November 2015 and February 2016, see Fig. 2.10. Using 2009 archival data, an near infrared (1.65−2.16 μm) increase of observed flux from both the central object and the surrounding cavity the with respect to the pre-burst, quiescent phase of accretion has been estimated to $\approx$ 3.5 mag and $\approx$ 2.5 mag, respectively. This was accompanied with an increase of several other quantities, such as the stellar mass, the accretion rate, the total luminosity of the protostar and the luminosity of emission lines, by several orders of magnitude. This burst was the first of that kind ever observed and it made young massive star formation entering the world of the accretion-driven outbursts like those monitored from low-mass stars (Postel et al., 2019). The recoding of accretion bursts from young high-mass stars continued during the past few years, together with that of directly-observed accretion discs from high-mass stars. Particularly, S255IR-NIRS3 turned to be surrounded by a structured disc, which is fully in accordance with the burst mode of accretion picture for high-mass stars (Zinchenko et al., 2015). S255IR-NIRS3 was associated to a 6.7 GHz methanol maser presented in Fujisawa et al. (2015); Szymczak et al. (2018a,b), which is a well-known tracer of high-mass star forming region (Reid et al., 2009), see also (Szymczak et al., 2018a; Hunter et al., 2019). Is has been followed by that of G358-MM1 (Burns et al., 2020) NGC6334I-MM1 Hunter et al. (2017); Brogan et al. (2018); MacLeod et al. (2018).

More protostellar jets, believed to be ejected perpendicularly from an accretion disc have been found and studied (Caratti o Garatti et al., 2015; Burns et al., 2017; Burns, 2018; Reiter et al., 2017; Purser et al., 2018; Samal et al., 2018; Boley et al., 2019; Zinchenko et al., 2019; Goddi et al., 2020; Purser et al., 2021) Over the same time period, a increasing number of discs-like objects and/or convering accretion flow observed by interferometric measures were published (Forgan et al., 2016; Chen et al., 2017; Ginsburg et al., 2018; Maud et al., 2018; Beuther et al., 2018; Sanna et al., 2019; Ahmadi, Kuiper & Beuther, 2019; Bosco et al., 2019). Accretion discs have been reported G11.92-0.61 MM1 (Ilee et al., 2016), as well as Keplerian, fragmented discs around G11.920.61 MM 1 (Ilee et al., 2018), AFGL 4176 mm1 (Johnston et al., 2020b), G17.64+0.16 (Maud et al., 2018, 2019), G353.273+0.641 (Motogi et al., 2019). All these elements plead in favour of the burst mode of accretion adequately depicting the circumstellar medium of massive protostars.

2.4 Towards the unification of star-forming processes

The series of events characterising the formation of high-mass stars, triggering each other from the free-fall collapse of molecular clouds, the formation of accretion discs, its fragementation, the migrationg of clumps both generating obsrevable companions to the central star and incucing accretion-driven outbursts, themselves responsbile for spectroscopic excursions towards the red part of the Hertzsprung-Russell diagram are not a peculiarity of the massive regime of star formation. The burst mode of accretion in star firmation has been developed and advanced in the past two decades in the context of low-mass star formation (Vorobyov & Basu, 2005, 2006; Vorobyov, 2010). It permitted to use the variable accretion onto young protostars (Vorobyov, 2009) as a solution to the so-called luminosity problem, or the huge bursts such as FU-Orioni outbursts emitted from some young stars and screening entire star-forming regions (Dunham & Vorobyov, 2012). Interestingly, young low-mass stars in the burst mode of accretion also experience pre-main-sequence spectroscopic excursions in the Hertzsprung-Russell diagram (Elbakyan et al., 2019) and the disc clumps formed by gravitational instability (Vorobyov, Zakhozhay & Dunham, 2013) produce planets orbiting in discs (Vorobyov & Basu, 2010; Vorobyov, 2013). This has been confirmed by independent codes (Stamatellos & Whitworth, 2009a,b; Stamatellos et al., 2011; Stamatellos, Whitworth & Hubber, 2011)

Similarly, young stars at low-metallicity and primordial protostars also theoretically gain their mass via the burst mode of accretion (Vorobyov, DeSouza & Basu, 2013). Again, the fragmenting behavious of circumstellar discs around primordial young supermassive stars has been modelled by means of many different numerical frameworks (Greif et al., 2012; Schleicher et al., 2016). This similarities between star-forming mechanisms in the low-, high- and supermassive- mass regimes, all together obeying a common set of a few principles depicted by the burst mode of accretion picture of star formation, suggest the universality of star formation processes.

Summary on the circumstellar medium of young massive stars. I showed that the formation mechanisms of young massive stars are strongly similar to that of low-mass stellar objects, and, particularly, that the so-called burst mode of accretion in star formation applies. The variability of the accretion flow of present-day forming massive stars can be accompanied by strong increase of the disc-to-star mass transfert. It generates accretion-driven luminous outbursts induced by the episodic accretion of gaseous clumps formed in fragmented accretion disc by gravitational instability, constituting high-mass equivalent to the FU-Orionis bursts of young low-mass stars. It provides an explanation to the outbursts of the massive young stellar object S255IRNIRS3. The clumps migrating down to the protostellar surface can acquiring the characteristics of a nascent low-mass companion with final Keplerian orbit compatible with that of observed close massive protobinary systems, made of both high-mass and a low-mass components. Both processes, i.e. close massive binary formation and accretion bursts, can happen simultaneously, outbursts being the tracer of close massive binary formation. The models show that young massive stars spend a few percent of their early lifetime bursting, but that they can acquire up to half of their mass via bursts, which serialy follow one another, fainter bursts being much more more common than brighter flares. Strongly bursting young massive stars experience rapid excursions towards the red, cold part of the Hertzsprung–Russell diagram, before becoming bright again during the next phase of quiescent disc-star accretion. During such event, their HII region blinks intermittently, testifying the the presence of a fragmenting circumstellar accretion disc around the protostar. Radiative transfer and synthetic images calculations of discs predicted that spiral arms and clumps could

be seen by the Atacama Large Millimeter/submillimeter Array (ALMA), which has been verified since then. A parameter study exploring the initial masses star's parent moledular clouds and its rotational-to-gravitational energies ratio reveal that no stable discs are produced, which is the sole major difference found so far between low-mass star formation mechanisms.

CHAPTER 3

Evolved massive stars nebulae

This chapter explores the organisation and evolution of the surroundings of evolved massive stars which have ceased their early formation phase and already acquired their zero-age main-sequence mass. It mostly concentrate on the fraction of massive stars moving supersonically through the ISM, or runaway stars, as their circumstellar stellar wind bubble is shape as characteristics bow shocks (Meyer et al., 2016, 2017a, 2021a, 2020; Meyer, 2021), see Appendix. These studies reveal the importance of magnetic fields in the shaping and the optical/infrared emission of stellar wind bow shocks around runaway main-sequence OB stars. Models have been successuly applied to the runaway red supergiants IRC-10414 and Betelgeuse. Finally, the formation of rings and bipolar nebulae of both static and runaway Wolf-Rayet stars is considered within the pecular evolution of such stars.

3.1 Bow shocks of runaway massive stars

There are three mechanisms able to accelerate massive stars up to supersonic bulk velocities, namely, (i) the dynamical ejection of high-mass stellar objects out of their native cluster by means of multiple-body interaction (Hoogerwerf, de Bruijne & de Zeeuw, 2000), (ii) the explosion of supernovae in massive binary systems which transmits a kick to the high-mass component (Hoogerwerf, de Bruijne & de Zeeuw, 2000) and (iii) the accidental encountering of more than two stars in the ISM (Gvaramadze & Gualandris, 2011). About 20−30% of all massive OB-type stars are so-called runaway or exiled objects, and sail away into the ISM of the Milky Way (Blaauw, 1961; Gies, 1987) and of neighbouring galaxies (Banerjee, Kroupa & Oh, 2012; Gebrehiwot & Tesklehaimanot, 2021). Their reconstructed trajectories inform on the location of their parent cluster or of the explosion of their companion's final supernova (Conlon et al., 1990; de Wit et al., 2005).

The interaction of the strong stellar wind of early-type massive stars with their ambient medium generate a stellar wind bubble (Weaver et al., 1977). This is the theoretical circumstellar structure of massive stars, made of two inner/outer shocks bracketing a discontinuity between the hot wind and the cold ISM, respectively. In the case of runaway stars, wind bubbles are transformed into stellar wind bow shocks (Baranov, Krasnobaev & Onishchenko, 1975; Wilkin, 1996).

A about 4−10% of all OB stars are runaway objects which also display a visible stellar wind bow

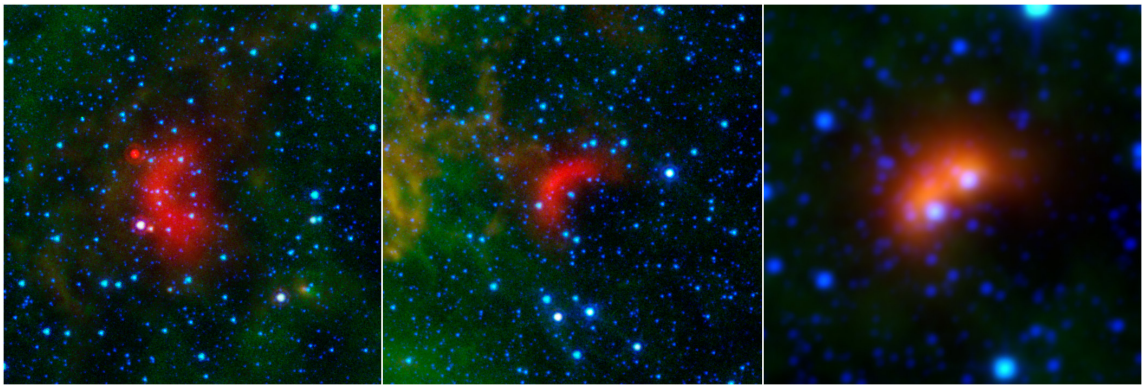

Figure 3.1: Near-infrared stellar wind bow shocks of 8−30 $M_\odot$ OB-type runaway massive stars. Red color is dust emission, blue are stars. Credits: NASA's Jet Propulsion Laboratory, Spitzer Space Telescope and WISE missions for NASA.

shock (Huthoff & Kaper, 2002). Originally serendipitously remarked, such as the optical distorted wind bubbles around fast-moving high-mass stars such as ζ Ophiuchi (Gull & Sofia, 1979), a growing statistics of bow shocks has built, leading to the establishment of catalogues compiling hundreds of them (Peri et al., 2012; Peri, Benaglia & Isequilla, 2015; Kobulnicky et al., 2016, 2017). Because of the all-sky surveys carried out in the years 1980-1990's, most bow shocks of massive have been found in mining, i.e. near-infrared *NASA/IRAS*, *NASA/Spitzer* and optical *AAO/UKST SuperCOSMOS H*α, data from (van Buren & McCray, 1988b; van Buren, Noriega-Crespo & Dgani, 1995; Noriega-Crespo, van Buren & Dgani, 1997; Parker et al., 2005), see Fig. 3.1. Nevertheless, dedicated archive searches and original observations revealed that stellar wind bow shocks emit throughout the entire electromagnetic spectrum (Kaper et al., 1997), including non-thermal emission (López-Santiago et al., 2012; Toalá et al., 2016; De Becker et al., 2017).

The runaway nature of some massive stars is independent on their stellar evolution and it does not stop the inevitable time-dependent changes of their surface properties. Hence, some evolved massive stars such as red or blue supergiant stars display a stellar wind bow shock, which is a unique laboratory for the study of the supergiant wind properties (Noriega-Crespo et al., 1997; Decin et al., 2012; Decin, 2012; Katushkina et al., 2018). Interestingly, no Wolf-Rayet star display stellar wind bow shocks (see Section 3.2.1). The high occurrence of these circumstellar nebulae spurred the interest of the scientific community developing hydrodynamical computer models and the modelling of bubbles and bow shocks of massive stars led to a still-growing literature (Comerón & Kaper, 1998; Dwarkadas, 2005, 2007; van Marle et al., 2011; van Marle, Decin & Meliani, 2014; van Marle, Meliani & Marcowith, 2015a).

The interest of studying stellar wind bow shocks lies in the explicit dependence of their morphology on both the stellar surface properties (mass-loss rate, wind velocity) and the properties of the ambient medium (density, velocity). Reproducing bow shock nebulae with numerical simulations and comparing them with real observations is a powerful method which permits to constrain stellar evolution as well as understanding the ISM without relying on any assumptions other than the distance to the object. The catalogues of bow shock nebulae around OB stars call generic studies devoted to their formation, internal and emission properties, with as ultimate goal the identification of the driving star's properties on the sole knowledge of its bow shock observation.

3.1.1 Bow shocks around main-sequence OB-type stars

First of all, the main question regarding stellar wind bow shocks from massive stars concerns their differences between those of low-mass stars, such as around the Sun, which has been studied in great details throughout the second half of the XX$^{\text{th}}$ century. The heliosphere indeed provides a laboratory for experimental investigations of the surroundings of our Sun, e.g. by means of space-crafts like *Voyager*, see Herbst et al. (2022) and references therein. Our knowledge of the internal functioning of bow shocks from high-mass stars is therefore largely based on the assumptions that they are scaled-up versions of the Sun's astrosphere. Which layer emits bright in the near-infrared and produce the observations of Fig. 3.1 ? Why some massive runaway stars do not have an observed bow shock ? Are these circumstellar structures also subject to cosmic-ray modulation ?

Dedicated theoretical studies of fast-moving massive stars astropheres started with the works of Comerón & Kaper (1998). It has led to the well-accepted depiction for stellar wind bow shock sketched in Fig. 3.2, that is a distortion of the classical picture for stellar wind bubbles around static massive stars of Weaver et al. (1977). A bow shocks is then essentially an inner hot diluted region of wind material embedding the freely-expanding stellar wind and surrounded by an additional dense cold layer of ISM gas. This work has been continued in Meyer et al. (2014c) who included the time-dependence of the wind properties in the models. However, observations revealing pathological objects Gull & Sofia (1979) suggest that the truth is by far different, the complexity of real bow shocks might reach that of the heliosphere. Hence, despite of considerable advances in the two last decades, the field associated to the question of low-/high-mass astrospheres is still in its infancy.

To make a dent in this field, a parameter study exploring the appearance and global properties of OB stars' bow shocks has been performed in Meyer et al. (2016). It consisted in concentrating on $M_\star = 20\text{–}40\,\mathrm{M}_\odot$ stars moving with velocities $v_\star = 20\text{–}70\,\mathrm{km\,s^{-1}}$ in media of density $n_{\mathrm{ISM}} = 0.01\text{–}10\,\mathrm{cm^{-3}}$. The physics included into these series of simulations is that of this time's state-of-art, i.e. optically-thin heating/cooling together with thermal conduction. Several quantities were measured for each simulation model, the most important of them being reported in Fig. 3.3. It has been found that (i) the aspect ratio of bow shocks, defined as the ratio of distance between the star and the wind/ISM discontinuity measured along and normal to the direction of motion of the star is in agreement with the analytic predictions of Wilkin (1996) for stable bow shocks and deviates from it for unstable bow shocks. This is a simple, observation-based alternative to the stability analysis for growth modes in bow shocks of Dgani, van Buren & Noriega-Crespo (1996a,b), see top left panel of Fig. 3.3.

Moreover, this shows that (ii) bow shocks of slow, light ($\leq 20\,M_\odot$) stars moving slowly ($v_\star \sim 20\,\mathrm{km\,s^{-1}}$) in rather diluted environments $n_{\mathrm{ISM}} \leq 0.1\,\mathrm{cm^{-3}}$ should not generate bow shock nebulae bright enough to be observed optically, explaining the existence of runaway massive stars without seen bow shocks, see bottom left panel of Fig. 3.3. Similarly, (iii) the same relatively light stars slowly-moving in diluted medium can produce bow shocks which near infrared emission are much smaller than that of the driving star which might screen them, see top right panel of Fig. 3.3. This provides a second explanation for the absence of stellar wind bow shocks around some runaway stars, based on the scattering of starlight on ISM dust trapped into the nebula. Last, by applying the criterion derived in Meyer et al. (2015) for the generation of asymmetric supernova remnants by runaway core-collapse progenitors, it is found that (iv) the heavy ($\leq 40\,M_\odot$), slowly-moving stars ($v_\star \sim 20\,\mathrm{km\,s^{-1}}$) into a rather dense medium ($n_{\mathrm{ISM}} \sim 10\,\mathrm{cm^{-3}}$) are more prone to induce non-spherical remnants, see bottom right panel of Fig. 3.3.

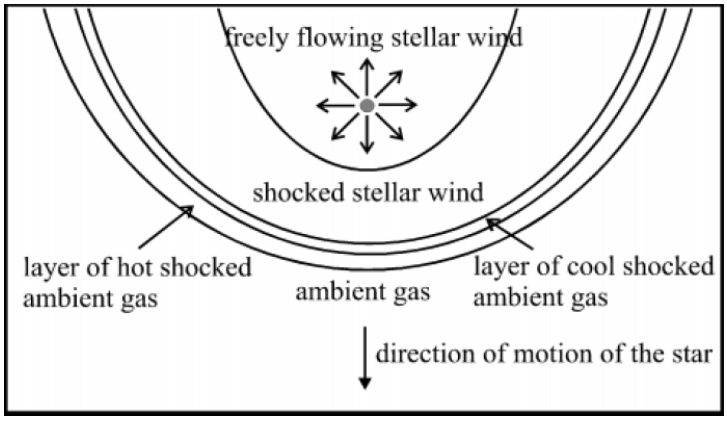

Figure 3.2: Sketches of a stellar wind bow shock around a massive runaway star (right). From Kaper et al. (1997).

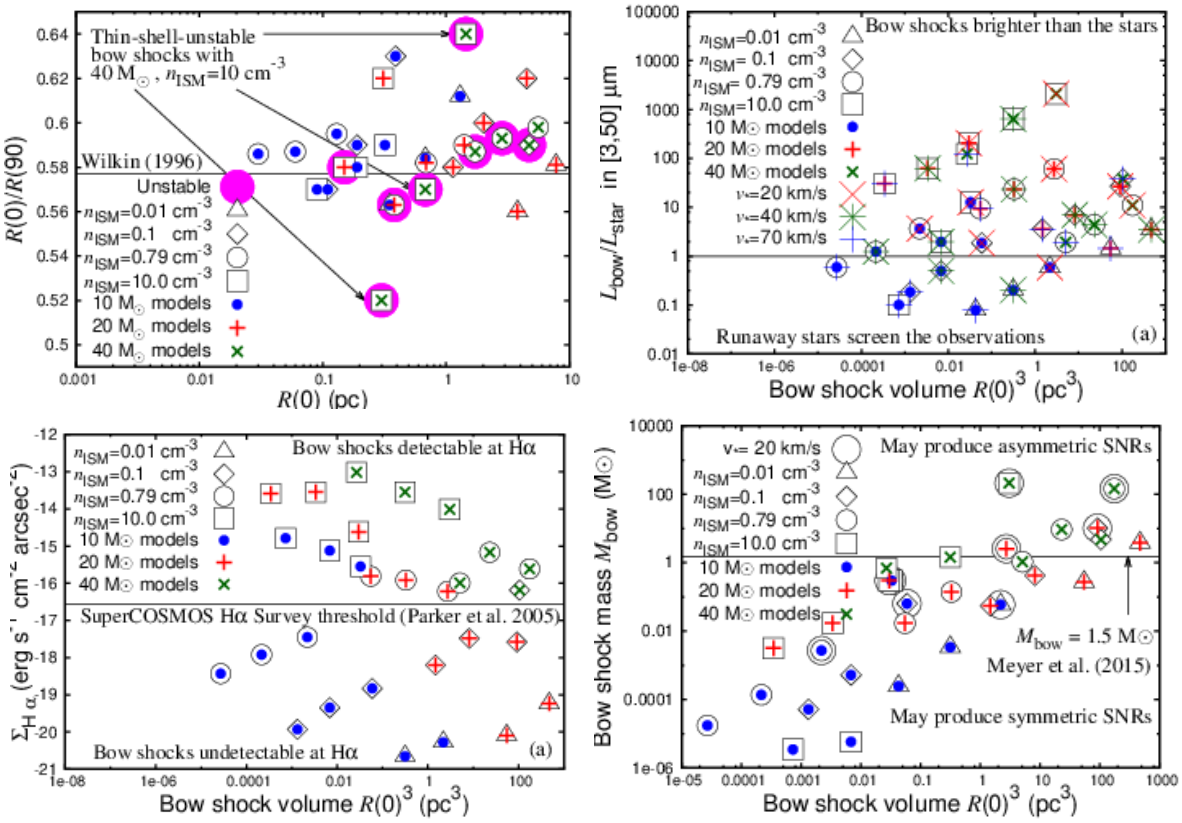

Figure 3.3: Properties of stellar wind bow shocks around OB runaway stars, modelled as moving in media $0.01-10\,\mathrm{cm}^{-3}$ with velocities $20-70\,\mathrm{km\,s}^{-1}$. The figures show the aspect ratio as a function of stand-off distance (top left), bow shock-star infrared ratio as a function of bow shock volume (top right), optical Hα surface brightness as a function of bow shock volume (bottom left), bow shock mass as a function of bow shock volume (bottom right). From Meyer et al. (2016).

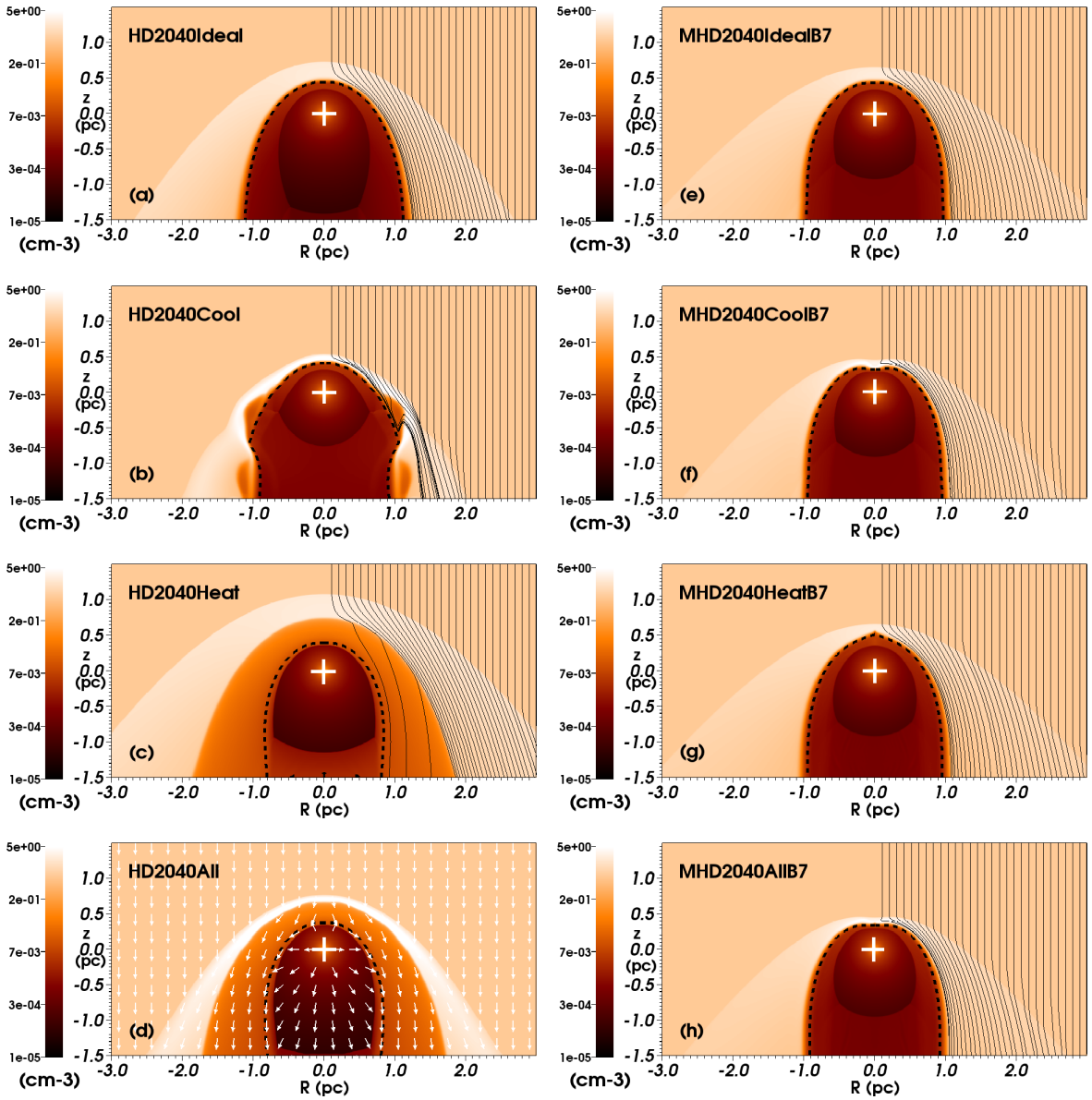

Figure 3.4: Effects of the included physics on models of stellar wind bow shocks around a runaway OB star. The plots display the gas number density (in cm^{-3}), for a $40\,M_\odot$ star moving with velocity $40\,km\,s^{-1}$ in a medium of magnetic field $7\,\mu G$. The left part of the models indicate the ISM magnetic fieldlines, the dotted black line is the wind/ISM contact discontinuity and the white arrows highlight the gas velocity direction. It shown models of the same star moving in the same medium at the same velocity, but considered without (left column) and with (right column) ISM magnetic field, adiabatically (a,b), with optically-thin radiative cooling/heating (c,d), thermal conduction (e,f), with cooling/heating and heating conduction (g,h). From Meyer et al. (2017a).

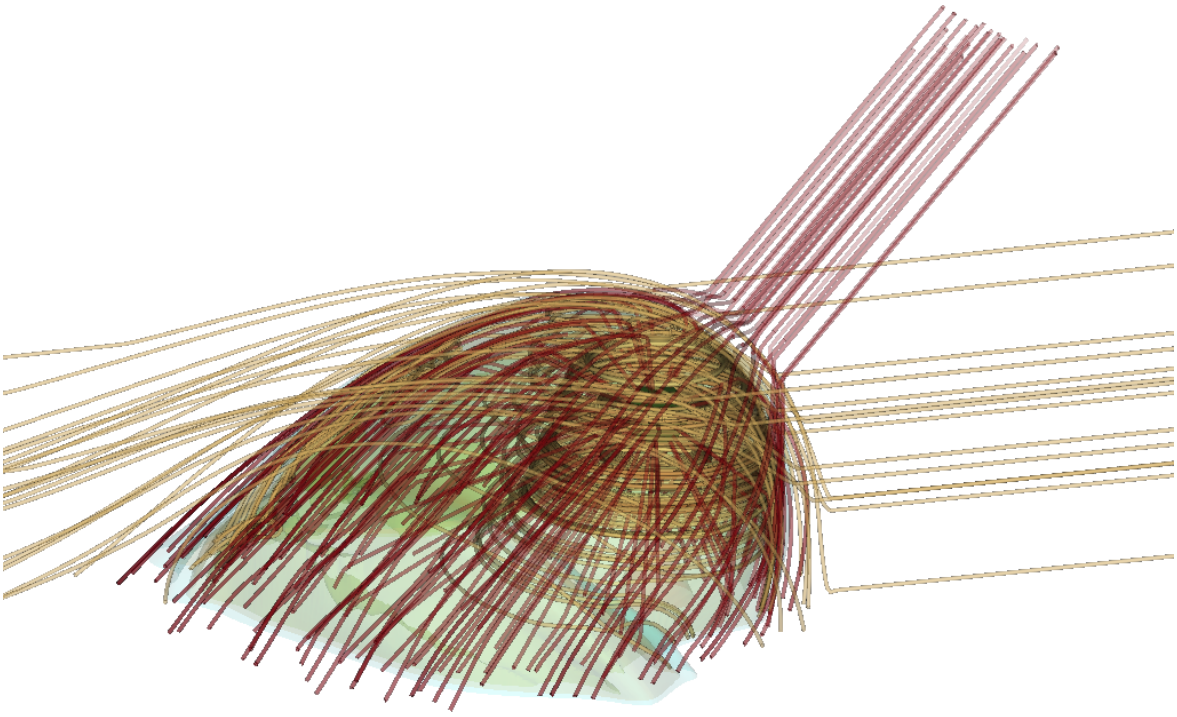

Figure 3.5: Rendering of a 3D MHD model of the bow shock around a runaway red supergiant star, moving into an uniform ISM which local magnetic field direction make an angle of 45° with that of the stellar motion. Coloured surfaces highlihght are number density isocontours and lines show the gas velocity stream (yellow) and magnetic field (red). From Meyer et al. (2021a).

Apart from the identification of runaway massive stars properties from their bow shocks, the main interrogation concerns the detailed internal organization of these nebulae. By which physical processes are bow shocks shaped is a problem that must be tackled numerically. In Comerón & Kaper (1998); Meyer et al. (2014c) it is shown that the heat transfers at work between the inner hot and outer cold layers of the bow shocks induce an efficient mixing of material and internal energy, leading to the penetration of dusty ISM gas into the hot region. Since it is a well-known that magnetic fields affect the direction of thermal transfers (Balsara, Tilley & Howk, 2008), a magneto-hydrodynamical modelling of OB stars nebulae with anisotropic heat transfers became necessary. In Meyer et al. (2017a) a selected number of bow shocks of runaway OB stars in the Galactic plane of the Milky Way has been modelled, adding ISM magnetic fields providing anisotropy to heat conduction. The effects of the included physics on such nebula is illustrated in Fig. 3.4.

As optically-thin radiative cooling strongly influences circumstellar wind nebulae (van Marle & Keppens, 2010), ambient magnetic fields have a governing role on their morphology and emission properties. It compressed the gas by providing an additional pressure in the rest frame of the moving star, and therefore make bow shocks smaller. The field lines penetrating the external layers of the nebula inhibits heat conduction, change the wind/ISM discontinuity and modify the volume of the gas occupied by the ISM dust responsible for the infrared emission, which turn to be slightly fainter Meyer et al. (2017a).

3.1.2 Bow shocks around red supergiant stars

After the exhaustion of Hydrogen fuel in the stellar core of main-sequence massive stars, their evolution continues and induce dramatic variations of the wind properties. As a high-mass star enters its red supergiant phase, the mass-loss rate increases and the wind velocity becomes slower, while the surface temperature decreases, respectively (Brott et al., 2011b). In the evolving star is in supersonic motion through the ISM, its astropshere produce by wind-ISM interaction changes accordingly and a new born bow shock of different structure forms. Its inner region of shocked wind is therefore denser than the outer layer, the whole astrophere is now filled with dust wind plus ISM dust and develops non-linear thin-shell instabilities (Vishniac, 1994; Blondin & Koerwer, 1998; Meyer et al., 2014c). Nevertheless, if the astropsheres of MK-type red supergiant stars are numerous (Hansen & Blanco, 1973; Cox et al., 2012b; Messineo & Brown, 2019), those associated with a runaway motion are rather rare. Four Galactic runaway red supergiant are known so far, i.e. Betelgeuse (Noriega-Crespo et al., 1997), IRC-10414 (Gvaramadze et al., 2014), μ Cep (Cox et al., 2012b; Montargès et al., 2019) and HD 137071 (Comerón & Figueras, 2020) and an extragalactic hypervelocity is escaping from the M31 (Evans & Massey, 2015).

Betelgeuse (αOri) is an historical red supergiant which has an infrared-discovered of complex astrophere made of a bow shock and an enigmatic bar above it (Noriega-Crespo et al., 1997). Its closed bow shock is young as the star recently entered the red supergiant phase (Mohamed, Mackey & Langer, 2012), includes an inner neutral shell generated by an external ionizing radiation field (Mackey et al., 2014) and might just have finished a blue loop (Mackey et al., 2012). However, the smooth appearance of Betelgeuse bow shocks as well as its multiple-arced astrophere challenges the clumpiness and instabilities predicted by means of both Eulerian and Langragian simulations (Mohamed, Mackey & Langer, 2012; Meyer et al., 2014c). Performing the first 3D MHD and radiative transfer calculations for the surroundings of red supergiants, Meyer et al. (2021a) demonstrates that the ambient medium magnetic field can smooth the astropshere of Betelgeuse and that its bar can be explained as the edge of an other interstellar structure, such as a giant nearby H II region, seen as projection (Fig. 3.6).

IRC-10414 is a M-type, possibly pulsating red supergiant star which revealed first a maser-detected outflow (Imai, Deguchi & Miyoshi, 1999; Maeda et al., 2008), before it has been shown it is an evolved high-mass runaway object surrounded by a smooth, optical arc-like astropshere (Gvaramadze et al., 2014). Further work on IRC-10414's nebula demonstrated that its circumstellar medium is a stellar wind bow shock (Meyer et al., 2014a). 3D MHD simulations of the bow shock of IRC-10414 shown including an ISM magnetic field that is not parallel to the direction of motion of the star by more than 5°, permits to generate stable bow shock for a wider range of stellar wind parameters than that constrained on the basis of ionising considerations, revealing that the mass-loss rates of red supergiant stars can be smaller than that predicted by stellar evolution models (Brott et al., 2011a; Ekström, 2012; Szécsi et al., 2022b). Furthermore, the production of a bow shock fitting observations of the surroundings of IRC-10414 (bottom panel of Fig. 3.6) required constant wind parameters, suggesting that this star is in a rather steady state of its evolution.

The new results provided by the 3D MHD modelling of the astropsheres of runaway red supergiant stars (Meyer et al., 2021a), as well as other high-mass stellar objects such as the blue supergiant Vela-X1 and κ-Cas (Gvaramadze et al., 2018; Katushkina et al., 2018; Baalmann et al., 2020, 2021), open a door to more realistic investigations of the surroundings of evolved stars. This should come together with the inclusion of additional physical processes into the simulations such as the creation/destruction of dust and/or non-ideal magneto-hydrodynamical effects.

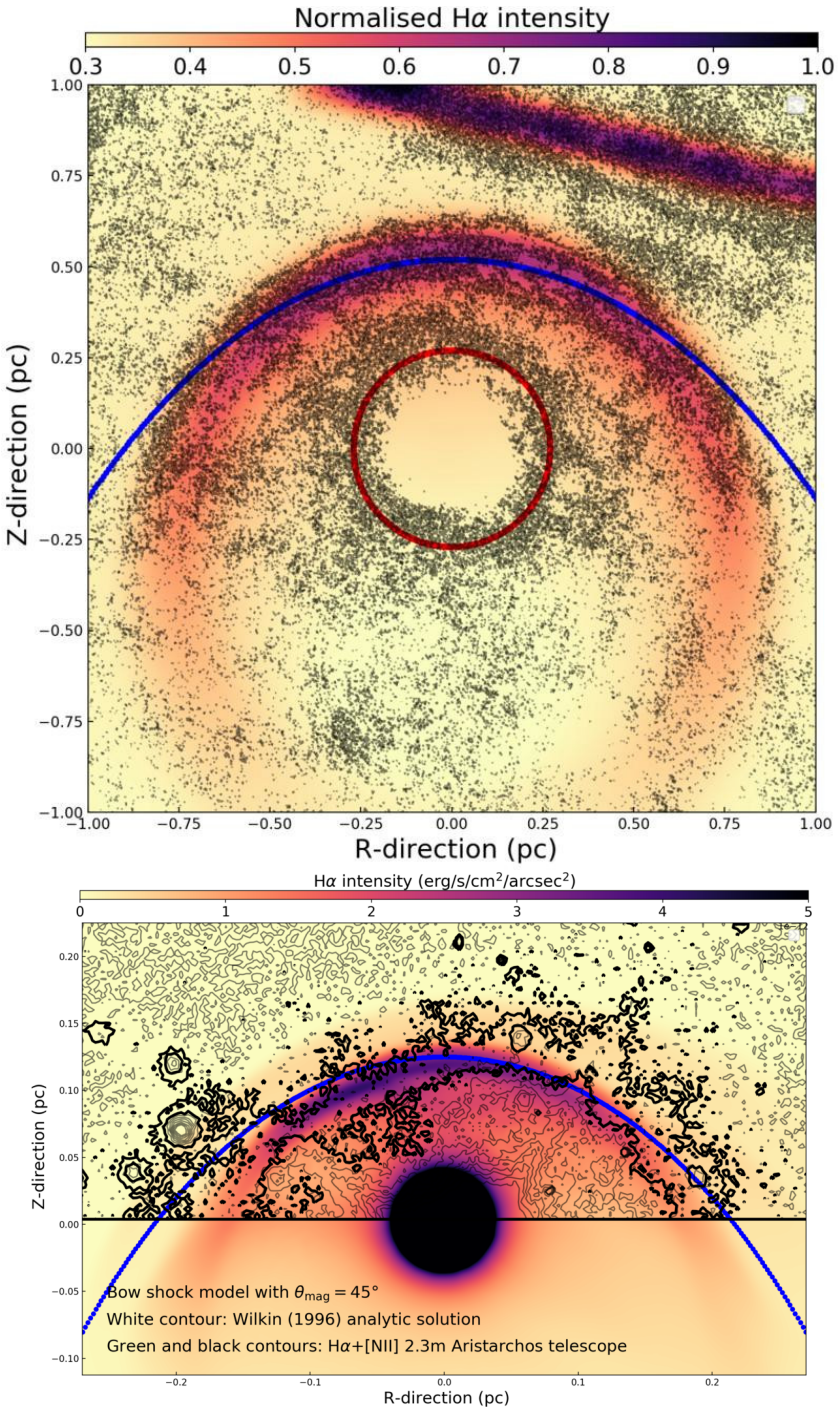

Figure 3.6: 3D MHD model/observations comparison for the runaway supergiant stars Betelgeuse (top) and IRC-10414 (bottom). Colours are synthetic Hα surface brightness (in erg cm^2 s^1 arcsec^2) calculated from the models with the RAMDC-3D code (Dullemond, 2012), the blue line represents Wilkin (1996)'s analytic solution, black contours are observational data from the space-borne telescope HERSCHEL (infrared 170μm, top) and from the 2.3m Aristarchos telescope (Meyer et al., 2014b) (at Hα+[N II], bottom) see (Decin et al., 2012). In top figure, the red circle is the inner H II region of Betelgeuse (Mackey et al., 2014) and the bar structure it bar (Noriega-Crespo et al., 1997). From Meyer et al. (2021a).

3.2 Nebulae of evolved Wolf-Rayet stars

If sufficiently massive ($\geq 30\,M_\odot$), some stars further continue their evolution beyond the red supergiant phase and enter the so-called Wolf-Rayet part of their life, although alternative channels have been proposed to explain their formation (Crowther, 2007; Langer, 2012). Their principal characteristics is the enriched strong stellar wind they blow, expelling material containing C, N and O at terminal velocities reaching 3000-5000 km s^{-1}. Their important mass-loss rates is of the order of $\approx 10^{-5}\,M_\odot\,yr^{-1}$ while their radius remains a few times that of the Sun (Hamann, Gräfener & Liermann, 2006a; Bestenlehner, Gräfener & Vink, 2014; Sander, Hamann & Todt, 2012). The number of Wolf-Rayet stars in the Milky Way is small ($\sim$ 250), see van der Hucht (2001, 2006), and, their location far above the Galactic plane is a revelator of their runaway nature (Moffat et al., 1998; Munoz et al., 2017; Toalá et al., 2018). Such rare evolved massive stars must by consequence greatly modify their surroundings, and, in their turn, also generate nebulae of characteristics reflecting the unusual wind properties of Wolf-Rayet stars.

Observations of Wolf-Rayet stars mostly concentrated on the peculiar properties of their enriched winds, which allowed huge progresses in the field of radiative transfer (Schmutz, Hamann & Wessolowski, 1989; Hamann & Koesterke, 1998; Hamann, Gräfener & Liermann, 2006b). The observational study of their circumstellar medium started with the optical compilatory work of Chu (1981); Chu & Treffers (1981a,b); Chu et al. (1982); Chu, Treffers & Kwitter (1983), who attempted to classify Wolf-Rayet nebulae on the basis of their shape, depending on their driving star and proposed morphological evolutionary sequences. The arrival of all-sky infrared surveys in the years 1980-1990's started providing dust scattered light counterparts to Wolf-Rayet nebulae (Menzies & Wolstencroft, 1990; Marston, 1991; Shylaja & Anandarao, 1993; Flagey et al., 2011; Jiménez-Hernández, Arthur & Toalá, 2020), and thus insights of the mixing of dusty material from previous supergiant evolutionary phases, with dust-free clumpy Wolf-Rayet stellar winds (Oskinova, Feldmeier & Kretschmar, 2012).

Numerical simulations of the surroundings of Wolf-Rayet stars started as soon as the computing facilities permitted to tackle problems which comprehension relies on two-dimensional hydrodynamics. Although not particularly numerous, these models had a very important impact on the current knowledge of massive stars and their evolution. Several studies have demonstrated that the wind-wind collisions between Wolf-Rayet material and that of other evolved wind such as that of a red or blue supergiant lead to non-linear instabilities happens inside of the main-sequence bubble of the massive star, such as those observed around WR 136 and its nebula NGC6886 (Garcia-Segura, Mac Low & Langer, 1996; Garcia-Segura, Langer & Mac Low, 1996; Dwarkadas, 2007; Toalá & Arthur, 2011; van Marle & Keppens, 2012). In other words, no ISM material is involved in the shaping of Wolf-Rayet nebulae. Besides, the role of stellar rotation onto the size and properties of Wolf-Rayet shells is shown in Georgy et al. (2013) and the connections of Wolf-Rayet nebula with supernovae and γ-ray bursts are investigated in van Marle, Langer & García-Segura (2005).

This large variety of Wolf-Rayet nebulae is therefore an unexplored playground for numerical astrophysics. In this habilitation, two particular kind of iconic but poorly understood type of possible morphologies for the circumstellar medium of Wolf-Rayet stars are explored. First, the missing Wolf-Rayet bow shock problem is considered, in connection with the ring nebulae observed around the fastest Galactic Wolf-Rayet stars. Secondly, the formation of bipolar Wolf-Rayet nebulae such as NGC6886 is investigated by mean of the first multi-dimensional magneto-hydrodynamical models for Wolf-Rayet nebulae.

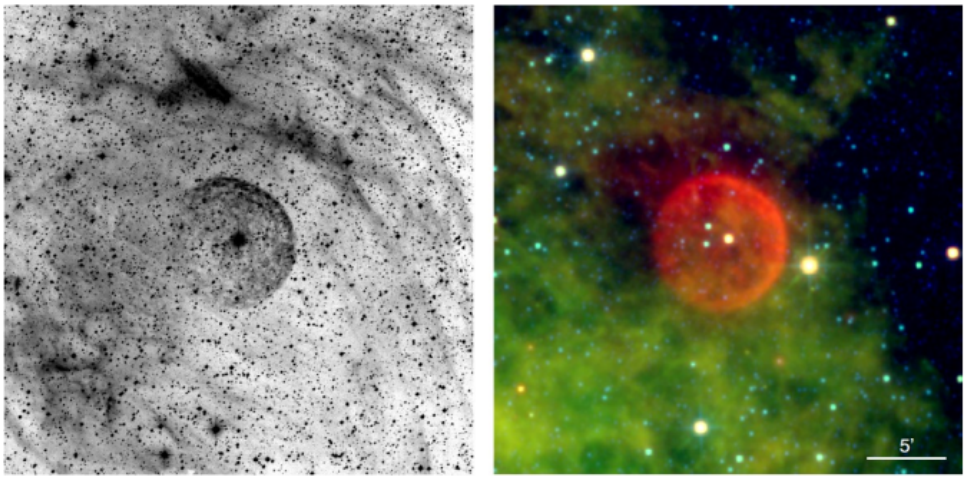

Figure 3.7: Super COSMOS Sky Survey (Parker et al., 2005) optical Hα and WISE (Wright et al., 2010) infrared image at $4.6, 12, 22\mu$m image of the nebula surrounding the runaway Wolf-Rayet star WR16. From Toalá & Guerrero (2013).

3.2.1 The missing Wolf-Rayet bow shock problem

The numerical simulations for the circumstellar medium of a runaway Wolf-Rayet-evolving star of Brighenti & D'Ercole (1995b,a) indicate that its motion brings the star out of his own main-sequence bow shock. Hence, the Wolf-Rayet wind interacts directly with the ISM, producing specific, dense and unstable bow shocks van Marle, Langer & García-Segura (2005, 2007). However, such strong bow shock have not been detected, and the fastest-moving galactic Wolf-Rayet stars display circular ring-like nebulae (Fig. 3.7) which seem to be co-moving with their driving star, see Gvaramadze et al. (2010); Gvaramadze, Kniazev & Fabrika (2010) and reference therein. Since these circumstellar structures are produced by the strongest-winded and quickest massive stars, such absence of bow shocks challenges the picture of Brighenti & D'Ercole (1995a); Wilkin (1996). The solution proposed by Meyer et al. (2020) relies exclusively on the past history of the Wolf-Rayet star, which, according to the current state-of-art of stellar evolution modeling, differ greatly from those adopted 25 years ago by Brighenti & D'Ercole (1995a).

In the magneto-hydrodynamical models of Meyer et al. (2020), it is found that as soon as the stellar wind history is complex and violent enough (see left-hand panel of Fig. 3.8), i.e. the star being massive $M_\star$ = 35-60) enough (Groh et al., 2014), a huge main-sequence stellar wind bubble ($\approx$ 30-60 pc) forms. Whatever evolution channel undergoes the star between the main-sequence and Wolf-Rayet phases will remain embedded into it, leading to complex wind-wind collisions of evolved, potentially dusty materials. As long as the new-born Wolf-Rayet stellar wind has not yet reached the termination shock of the main-sequence bubble, the material it sweeps-up shapes as an infrared-bright expanding ring (right-hand panel of Fig. 3.8). This effect is magnified if the star moves into the low-density medium of the high Galactic latitudes, as in the cases of the runaway Wolf-Rayet star WR 124 and its surrounding nebulae structure M1-67 (van der Sluys & Lamers, 2003).

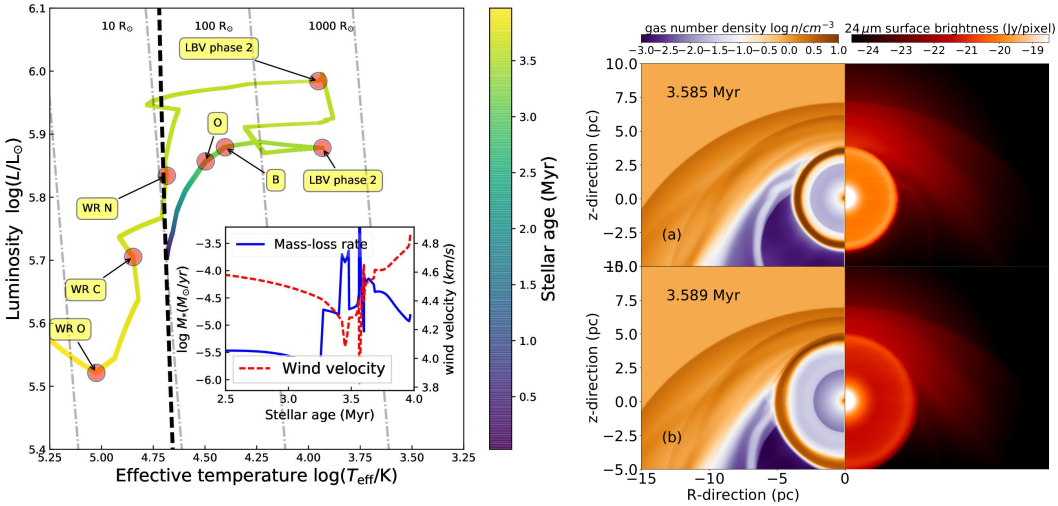

Figure 3.8: Left: Complex evolutionary path of a very massive star of zero-age main-sequence mass 60 $M_\odot$ (Groh et al., 2014), with, as inset, the evolution of both the mass-loss rate and the wind velocity for the post-main-sequence phases. Right: Number density and 24 μm near-infrared emission maps of the bow shock of a 60 $M_\odot$ star moving with velocity 100 km s^1 in an uniform ambient medium of number density 0.79 cm^3. The fast Wolf-Rayet wind–slow blue supergiant wind interaction induces a ring nebula around the current runaway Wolf-Rayet star appearing to be co-moving with the star, and which is surrounded by series of filamentary arcs in the main-sequence bow shock, see optical Hα surroundings of WR 16 in fig. 1 of Toalá & Guerrero (2013). From Meyer et al. (2020).

3.2.2 Bilateral Wolf-Rayet nebulae

An other class of Wolf-Rayet nebulae is the so-called bilateral ones, which archetype is NGC6886, developing around the star WR 136 and which morphology is usually associated with asymmetric stellar wind. However, observations of Wolf-Rayet wind revealed their relative sphericity, implying that the assymetries of NGC6886 originate from the pre-Wolf-Rayet circumstellar medium. The hydrodynamical model of Brighenti & D'Ercole (1997) assumed that the asymmetries are produced by an equatorially-launched red supergiant wind, which has not been observed so far Vlemmings, van Langevelde & Diamond (2005); Kervella et al. (2018). Learning from the shaping of the asymmetric nebula of the luminous blue variable η Carina Langer, García-Segura & Mac Low (1999); González et al. (2004, 2010); González (2018), the study of **?** presents the first magneto-hydrodynamical simulation of the environment of a rotating blue supergiant star that undergoes a phase transition towards the Wolf-Rayet phase.

Bilaterality in Wolf-Rayet nebulae is closely and firmly connected to the evolution of rotating massive stars. The changes in the pole-to-equator density ratio of the pre-Wolf-Rayet wind are the governing factor in its asymmetric expansion, leading to the formation of oblate circumstellar nebula (Fig. 3.10). Radiative transfer claculations against dust opacity of the magneto-hydrodynamical models show that their projected 24 μm emission can appear as oblate, bipolar, ellipsoidal or ring structures, depending on the adopted viewing angle. The stellar magnetic field turns not to play a significant role in the shaping of Wolf-Rayet nebula, as it remains dynamically unimportant throughout the symmetric-asymmetric wind collision, although it is a key ingredient in the acceleration of particles in massive stars nebulae Ohm, Hinton & Domainko (2010); Prajapati et al.

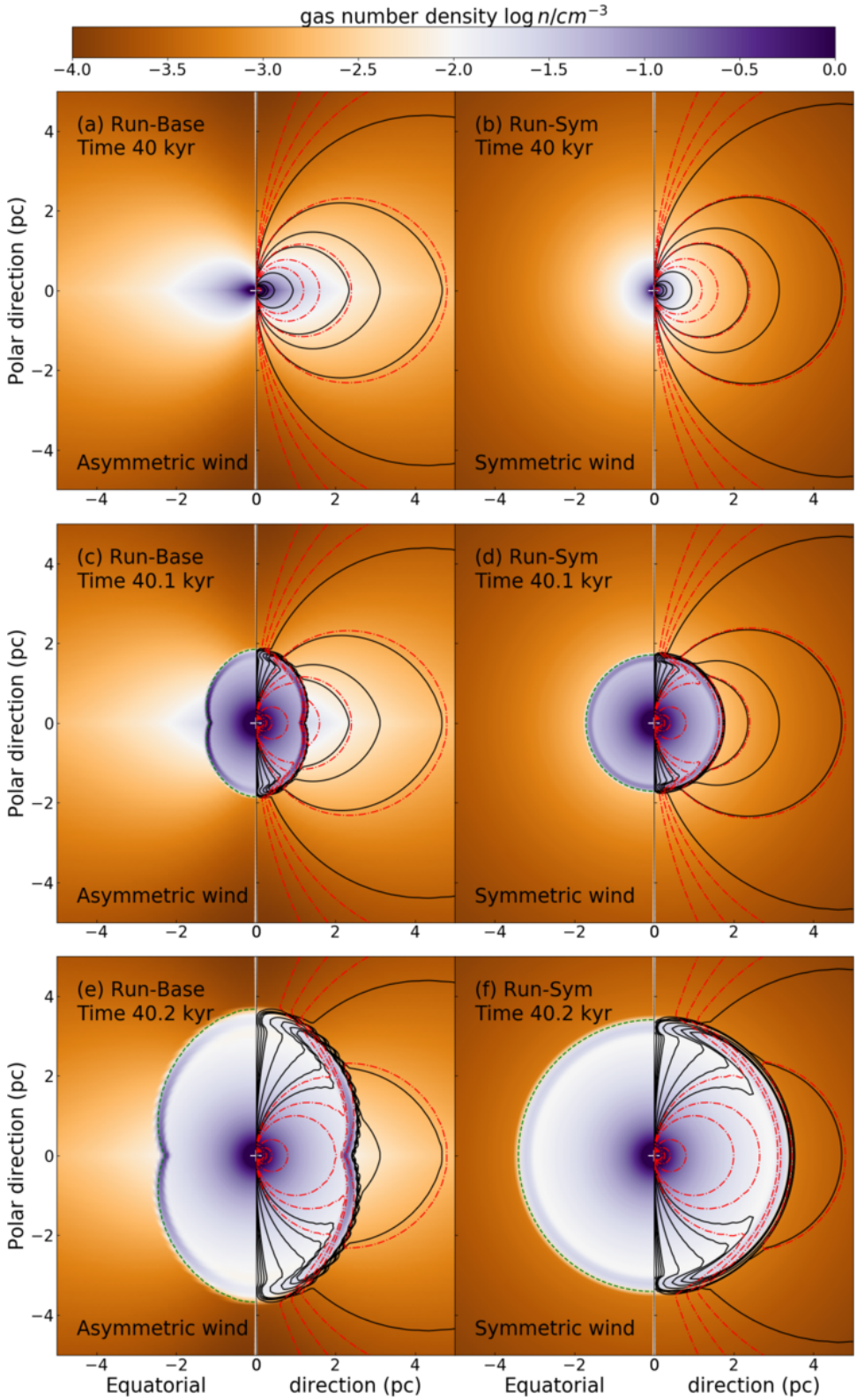

Figure 3.9: Number density field in 2.5D MHD simulations of forming Wolf-Rayet nebulae which blue supergiant stellar wind is either asymmetric (left) or symmetric (right). The position of the star is mark by a white cross, the dashed green line highlihts the tangential discontinuity of the wind-wind interface in the nebula, the solid black and dashed–dotted red contours show toroidal magnetic field B_ϕ and vecloty field component isovalues v_ϕ, respectively. From Meyer (2021).

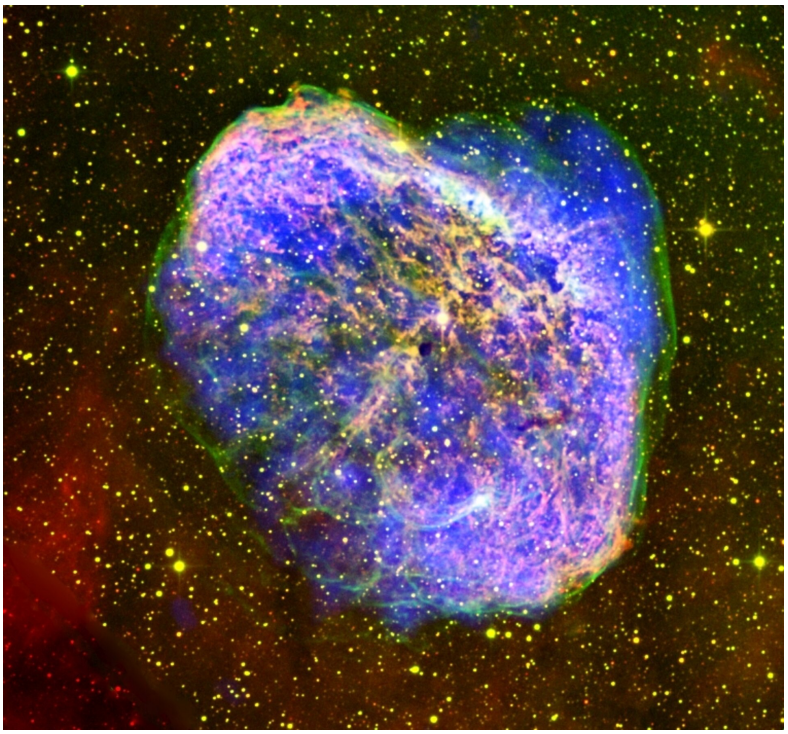

Figure 3.10: The veil nebula or NGC6886 around the Wolf-Rayet star WR136. Credits: ESA.

(2019).

Summary on the circumstellar medium of evolved massive stars. Stellar wind bow shocks are the distorted bubbles forming around the 20 to 30% of massive stars which move fast through the interstellar medium (ISM). The internal structure and organisation of stellar wind bow shocks around OB star is very sensitive to the cooling, heating and to the ISM magnetic field which makes their Hα optical/infrared emission fainter by about 1–2 orders of magnitude. Bow shock nebulae should be preferentially observed in the infrared waveband where they emit bright and their spectral energy distribution is the approparite tool to study them as it is independent of the temporary effects of unstable bow shocks. Brightest optical/infrared bow shocks around OB stars are generated by most massive stars ($\geq 20\,M_\odot$) moving in dense ISM, where they might be much brighter than the central star itself. After the massive star evolve to the red supergiant phase, its bow shock is easily smoothed and stabilised by the ambient magnetised flow. Projection effects produce complex astrospheric morphologies such as the astrospheres of IRC-10414 and Betelgeuse (αOri). Results propse that IRC-10414 is in a steady state of its evolution and advance the interstelar origin of Betelgeuse's bar. Last, once some massive stars reach the Wolf–Rayet phase, their strong wind can induce huge, diluted bow shocks too faint to be observed. Inside of them, wind-wind collision induce spherical shells seeming to be co-moving with the runaway star, as observed around WR71, WR124 and WR148. Such wind-wind collision also happens if the star is at rest, and, depending on the asymmetries in the pre-Wolf-Rayet wind, the nebulae can appear as oblate, bipolar, ellipsoidal, or ring structures. The geometry of Wolf-Rayet nebulae reflect its recent past stellar evolution and bipolar nebulae such as NGC 6888 can only form within the red supergiant scenario by multiple/merged massive stellar systems, or within the single blue supergiant scenario.

CHAPTER 4

Core-collapse supernova remnants

This chapter is devoted to the study of core-collapse supernova remnants generated by both static and fast-moving massive stars. It is based on a series of papers presenting magneto-hydrodynamical simulations of supernova remnants (Meyer, Petrov & Pohl, 2020; Meyer et al., 2021b, 2022a; Meyer & Meliani, 2022), see Appendix. It shows that the comprehension of supernova remnants is a complex enterprise which has to take into account the detailed past evolution history of the progenitor, the presence of the ISM magnetic fields, the mixing of materials at work therein. All these elements reflect in their thermal and non-thermal emission, and numerical models have been applied to Puppis A. Last, it is shown that the eventual pulsar wind nebula of some core-collapse supernova remnants also mirrors the past history of the defunct progenitor, and that the stellar wind history must be taken into account when deciphering the complex morphologies of pulsar wind nebulae.

4.1 Asymmetric morphologies

According to their initial masses, high-mass stars can finish their life either by a catastrophic explosion or by directly collapsing as a black hole. Core-collapse supernova remnants are the nebulae leftovers of defunct massive stars which ended their life via the explosive channel (Woosley & Weaver, 1986). These structures constitute the hot phase of the ISM (McKee & Ostriker, 1977; McKee, 1995) and take the shape of complex, heterogeneous gaseous nebulae that evolve over timescales of about several kyrs. The explosion takes place in the stellar core and its shock wave asymmetrically propagates inside of the dying star up to the moment of the so-called shock breakout when it goes through the former stellar surface and expands into the last stellar wind (Gabler, Wongwathanarat & Janka, 2021). As the supernova blastwave travels away from the center of the explosion, it successively encounters the circumstellar structures generated by the progenitor's stellar wind-ISM interaction history. Both shells expelled several $\sim 100\,\mathrm{yr}$ before the explosion (Orlando et al., 2016) and the larger-scale circumstellar medium such as stellar wind bubbles (Weaver et al., 1977) will influence the propagation of the supernova blastwave. The morphology of supernova remnants, and consequently their emission properties, are therefore a convolution of the exposion geometry, the stellar wind properties and the local conditions of the ambient medium.

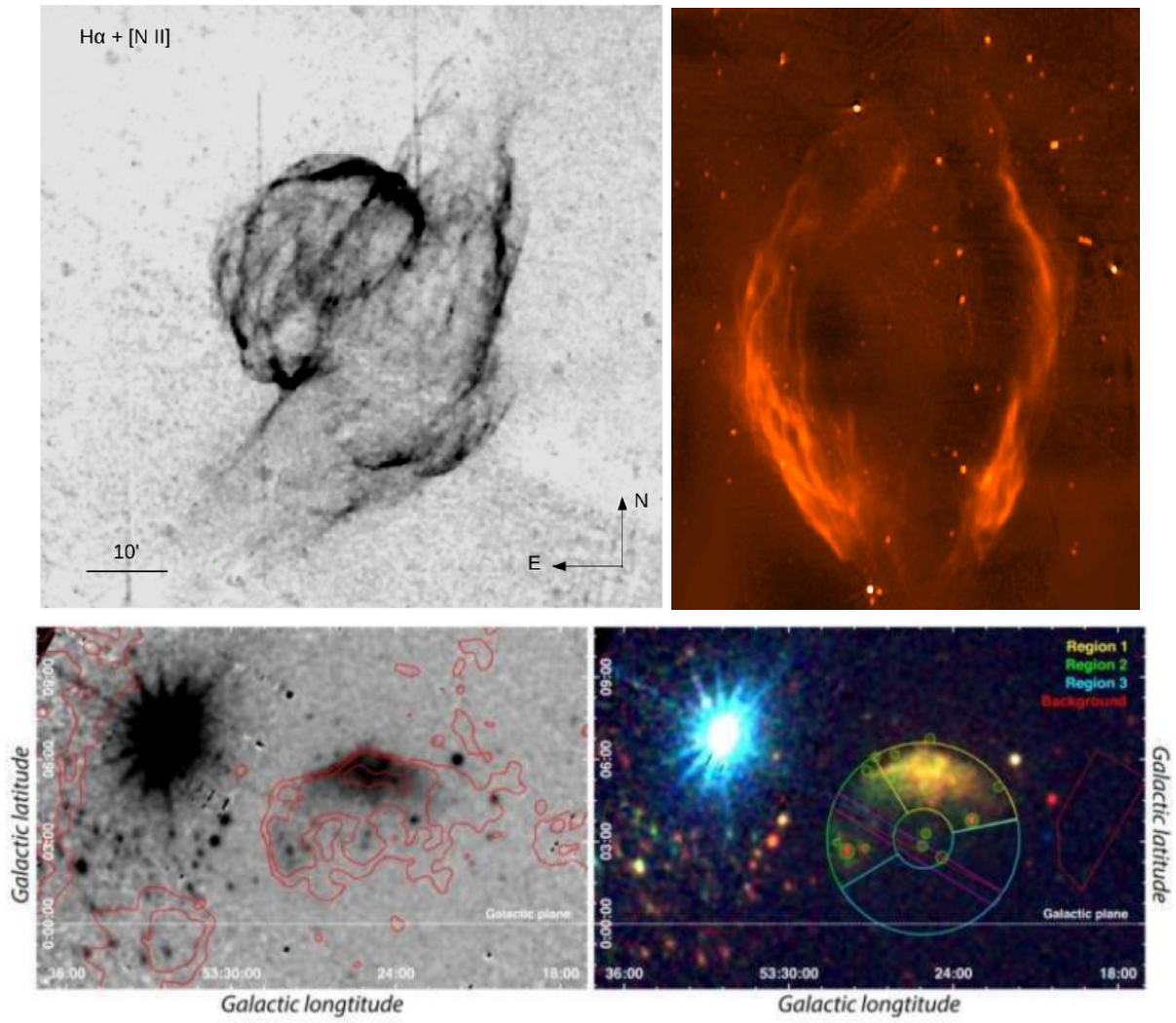

Figure 4.1: Asymmetric core-collapse supernova remnants. Top: optical Hα+[NII] image of the supernova remnant VRO 42.05.01, suspected to have been produced by a runaway progenitor (Boumis, 2019). Bottom left: 1.4 GHz view of the bilateral radio supernova remnant G296.5+10.0 done with the Australia Telescope Compact Array. It displays magnetized red supergiant stellar wind in which a magnetized neutron star is (Harvey-Smith et al., 2010). Bottom right: half-radio shell of the supernova remnant G53.41+0.0, plotted in the 0.8−4.0 keV (left) and 0.8−1.5 keV (red, right), 1.5−2.5 keV (green, right), 2.5−4.0 keV (blue, right) energy band (Domček et al., 2022).

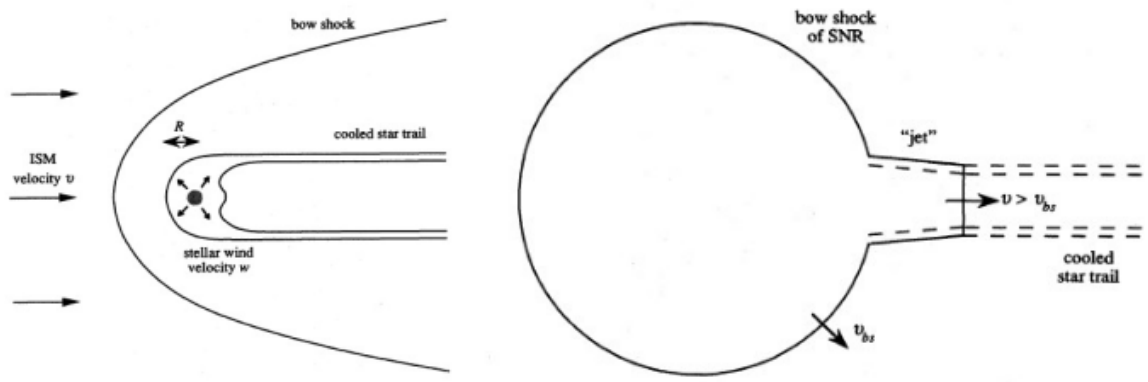

Figure 4.2: Sketch of the effect of a dense stellar wind bow shock of a dying runaway massive star onto the asymmetric expansion of the blastwave of a core collapse supernova. From Cox, Gull & Green (1991).

Middle-age core-collapse supernova remnants ($\geq$ 5000 yr) gather both a growing number of available high-resolution, multi-wavelength observations, together with a lack of numerical simulations devoted to that particular problem. Those supernova shock wave of these supernova remnants have long time terminated its freely-expanding phase and the shock wave is either already strongly interacting with its progenitor's circumstellar environment or has gone through it and expands into the unperturbed ISM. Moreover, observations reveal that most elder supernova remnants have very asymmetric morphology deviating from the classical spherial-symmetry solution of Chevalier & Liang (1989). Puzzingly, no typical shape seems to govern the Galactic population of remnants from defunct high-mass stars, and each individual object displays an irregular shape (Fig. 4.1). The huge parameter space of the problem makes their understanding pathologic and no typical formation scenario arise so far from their study.

Since about a third of all massive stars in the Milky Way are not at rest but animated with a supersonic bulk motion through the ISM, their stellar evolution happens inside of their surrounding stellar wind bow shock. Hence, once the star explode, the supernova shock wave will interact with the bow shock along the direction of motion of the progenitor star, while it will chanelled into the tail of low-density stellar wind in the opposite direction, respectively. This scenario naturally produces asymmetric supernova remnants (Fig. 4.2). Although this is certainly not the unique mechanism at work which governs the shaping of aged core-collapse supernova remnants, it is a preponderant ingredient to take in account, at least in the case of remnants from runaway ancestors such as isolated objects, e.g. away from star formation regions or above the Galactic plane.

Conversely, the peculiar circumstellar medium of static massive stars (van Marle, Meliani & Marcowith, 2015b) should equivalently affect the propagation of supernova shock waves, and this can only be explored by means of numerical simulations. Indeed, only in some very particular cases can the ISM be considered as an uniform, neutral, laminar medium of constant temperatures, and, this habilitation begins the exploration of that promising research avenue. Finally, the ultimate evolutionary step of the massive stars is the generation of a neutron star out of the defunct stellar progenitor material. The rotation properties of that compact object induce a so-called pulsar wind nebula by swepting-up the supernova ejecta over pc-scale distances. Over the past decades, the thorough study of the Crab nebula taugh us such plerionic supernova remnants are important non-thermal emiters.

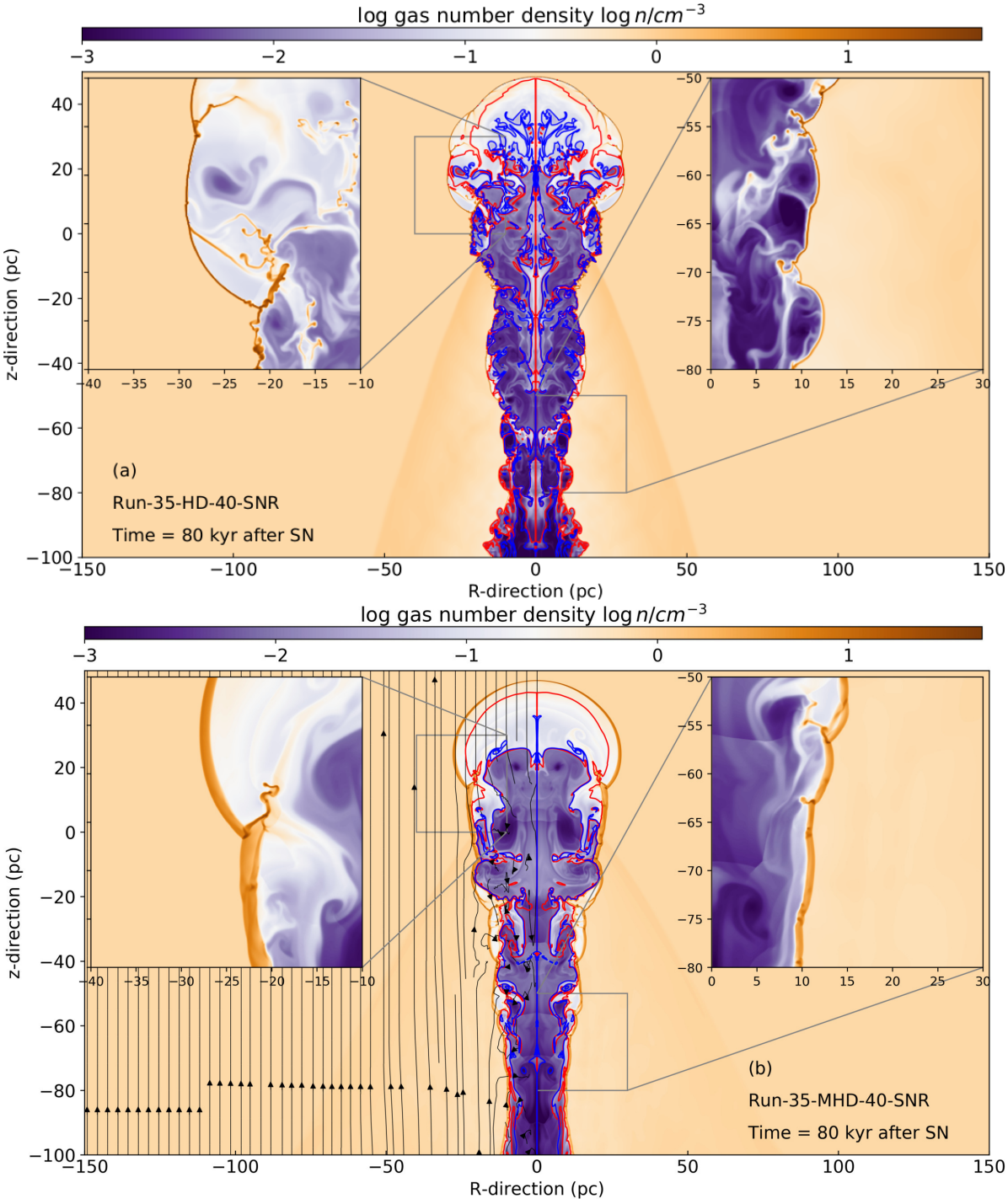

Figure 4.3: Number density in a hydrodynamical (top) and magneto-hydrodynamical (bottom) model of a supernova remnant generated by a 35 $M_\odot$ moving with velocity 20 km s^{-1} in an ambient medium. The ISM magnetic field is set parallal to the vertical direction and insets boxes show the dynamic filamentary structures forming at the ejecta-wind-ISM interactions (left) and the walls of the cavity (right). Temperature isocontours are in red and the location of the supernova ejecta by 10% in number density are in blue. The progenitor is a non-rotating massive star from the GENEVA library (Ekström, 2012). From Meyer et al. (2021b).

4.2 Non-thermal emission

The presence of a stellar wind bow shock in the shaping of asymmetric supernova remnants has already been investigated in the peculiar case of Kepler, which binary progenitor had a component responsible for the circusmtellar medium, and an other for the explosion (Chiotellis, Schure & Vink, 2012). The present work extends this model to the high-mass regime of supernova progenitor in supersonic motion through the magnetised ISM, building upon the hydrodynamical models for runaway dying massive stars in Meyer et al. (2015).

It is found in Meyer et al. (2021b) that the magnetisation of the ISM in which fast-moving stars run are a game-changer regarding to the morphologies and properties of their shock/emission (Fig. 4.4). Because of the damping of turbulence, the magneto-hydrodynamical shocks properties in the pre-supernova cirucmstellar medium are modified in the sense that its density jump is reduced. Simiarly, the discontinuity between stellar wind and ISM material is greatly stabilised, and this makes the mixing of materials (enriched stellar wind, ejecta and ISM) within the part of the interior of the remnant where the shock wave is reverberated. This work reveals the role of the ISM magnetic field in core-collapse supernova remnants onto the acceleration processes of cosmic rays therein.

The magneto-hydrodynamical models of supernova remnants are used as initial conditions for radiative transfert calculations for non-thermal radio emission, using the RADMC-3D code (Dullemond, 2012). The emission maps (Fig. 4.4) can be directly compared with observations of non-thermal radio supernova remnants available in the litterature. Particularly, it is found that the bright bipolar morphologies produced by the remnants when the angle between the plane of the sky and the plane of the object is relatively small ($\leq 30°$) are very similar to G296.5+10.0 (Harvey-Smith et al., 2010). This supernova remnant is made of magnetised red supergiant wind and hosts a neutron star in it. The simulations of Meyer et al. (2021b) permit to propose that it is a 6 kyr remnant of a 20 $M_\odot$ star moving with velocity $v_\star \approx 20\,\mathrm{km\,s^{-1}}$. Simulations with a heavier 35 $M_\odot$ progenitor display shapes similar to the shell-type remnant CTB 109, for an age of 14 kyr derived by Katsuda et al. (2018). We predict that CTB 109 should be surrounded by red supergiant material around which is a Wolf–Rayet ring interacting with the supernova shock wave (Kothes & Foster, 2012; Castro et al., 2012). In both the cases of G296.5+10.0 and CTB 109, the work of Meyer et al. (2021b) reveal the probable runaway nature of their progenitor star.

4.3 Mixing of materials

The two-dimensional numerical models of the series of works initiated by Meyer, Petrov & Pohl (2020) include a series of passive scalar tracers permitting to easily distinguish the three gases constituting a supernova remnant (wind, ejecta, ISM) and to time-dependently follow their advection inside of it. The two-dimensional nature of the models allows to reach a rather high spatial resolution, that could not be afforded in full three-dimensional calculations, as well as to explore the parameter space of the problem. The exploitation of chemistry in middle-age supernova remnants models is a so-far rather unexplored research avenue which merits more efforts and attention. On the long-term, this will permit to associate observed distributions of material in supernova remnants to the identity of its supernova progenitor, such asymmetric its zero-age main-sequence, rotation properties, chemistry and space motion.

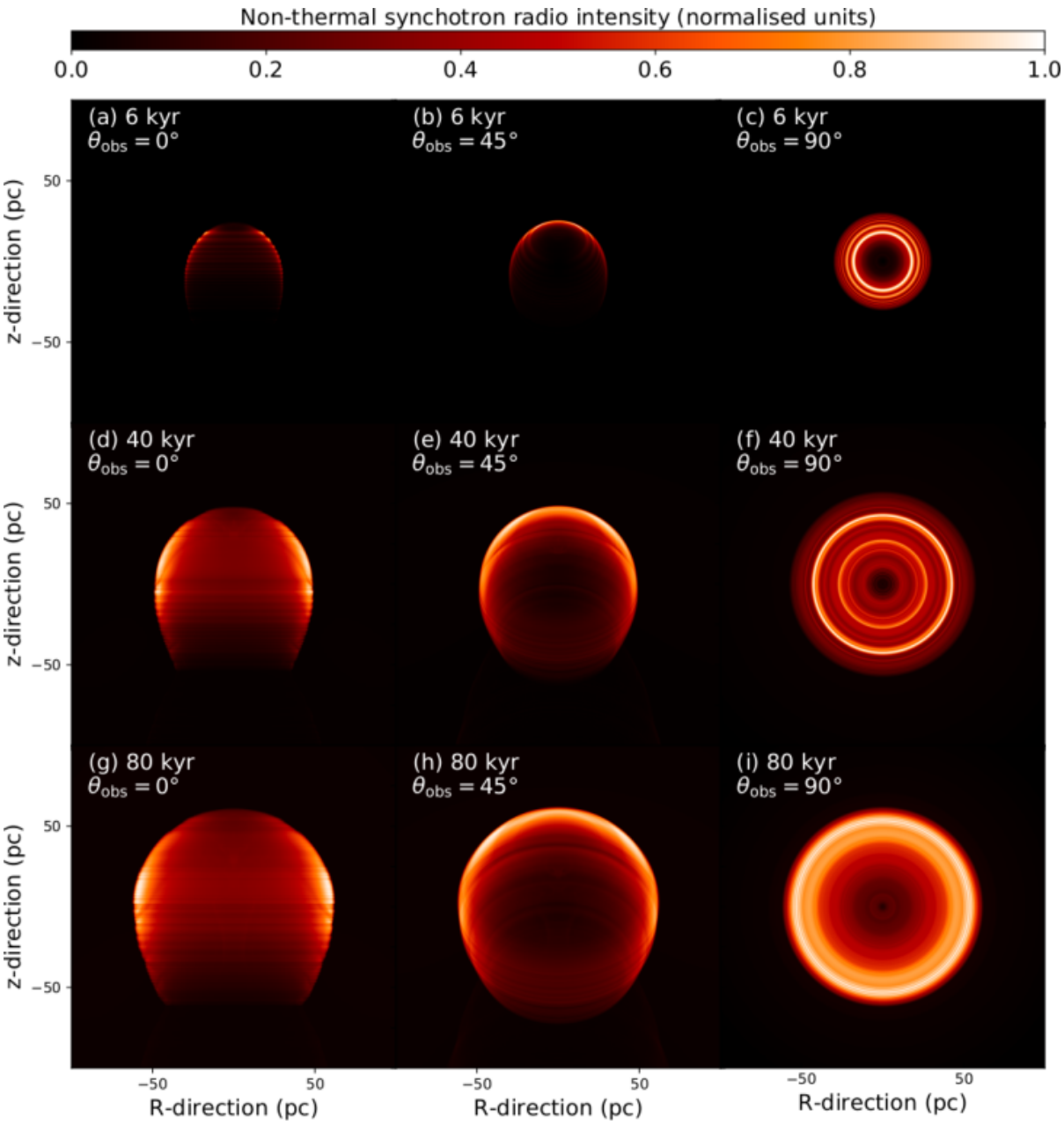

Figure 4.4: Normalized maps of radio synchrotron intensity of supernova remnants with progenitor speed $v_\star = 20\,\mathrm{km\,s^{-1}}$ at times 6 kyr (top), 40 kyr (middle), and 80 kyr (bottom) after the supernova explosion, respectively. The viewing angle between the equatorial plane and the line of sight is $\theta_{obs} = 0°$ (left), $\theta_{obs} = 45°$ (middle), and $\theta_{obs} = 90°$ (right). From Meyer et al. (2021b).

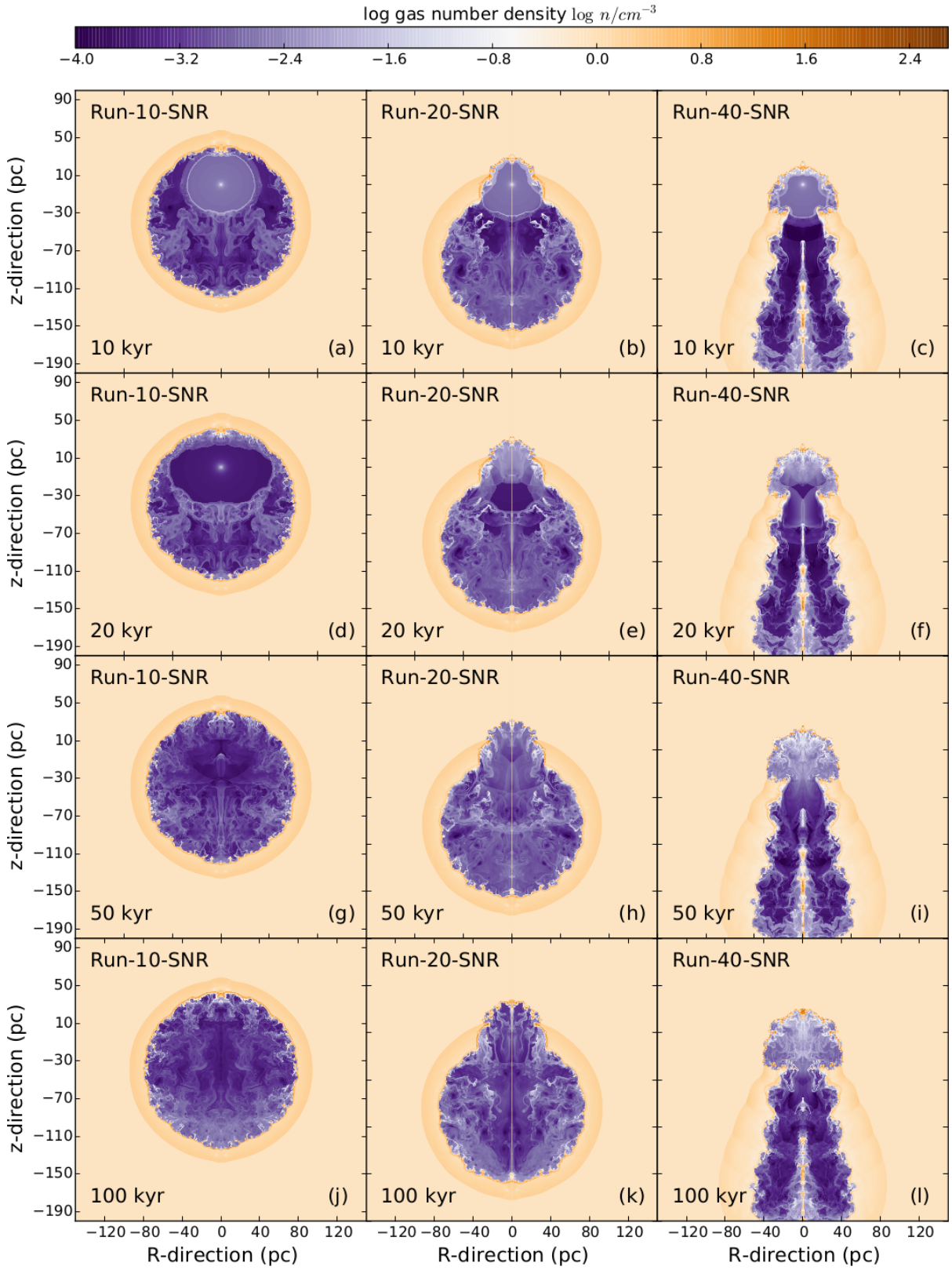

Figure 4.5: Series of number density field in simulation models of supernova remnants of a 60 $M_\odot$ star moving with velocity 0 km^{-1} (left), 20 km^{-1} (center) and 40 km^{-1} (right). From Meyer, Petrov & Pohl (2020).

The differential expansion of the supernova shock wave generates an asymmetric remnant. The inner region around the location of the explosion host an important mixing of materials when the forward shock of the blastwave reverberates against the stellar wind bow shock. The study of Meyer et al. (2021b) highlights the role of the ISM magnetic field in reducing the mixing of supernova ejecta in the inner region close to the center of the explosion, in both models with $v_\star = 20\,\mathrm{km\,s^{-1}}$ (Fig. 4.3) and $v_\star = 40\,\mathrm{km\,s^{-1}}$, respectively. The blue contours of Figs. 4.3 represent the region with a 10% also mirror the past history of the defunct progenitor, and that the stellar wind history must be taken into account in the comprehension of pulsar wind (). also mirror the past history of the defunct progenitor, and that, the stellar wind history also mirror the past history of the defunct progenitor, and that the stellar wind history must be taken into account in the comprehension of pulsar wind nebulae. also mirror the past history of the defunct progenitor, and that the stellar wind history Must be taken into account in the comprehension of pulsar wind nebulae. also mirror the past history of the defunct progenitor, and that the stellar wind history must be taken into account in the comprehension of pulsar wind nebulae.

In the context of the rarest, very massive ($\geq 60\,\mathrm{M_\odot}$) stars, two distinct regimes must be separated: on the one hand the case with a walkaway star, not moving supersonically through the ISM, but still sufficiently fast to generate a supernova remnant drastically different from that of a static star, while the situtation of a runaway stellar object generating a stellar wind bow shock, see the work of Meyer, Petrov & Pohl (2020). In the situation of a $v_\star \leq 20\,\mathrm{km\,s^{-1}}$, the short stellar life (less than 5 Myr) the star remains inside of the stellar wind bubble produced during the main-sequence phase of its evolution (left-hand column of Fig. 4.5). On the contrary, if the star moves fast enough, it can leave its elongated wind bubble, propagate directly into the unperturbed ISM where its stellar wind develops a bow shock (right-hand column of Fig. 4.5). The morphology of the wake left behind the moving object constraining the expantion of the supernova blastwave in the direction opposite of that of the progenitor's motion, it is posible to associate a given time after the explosion to a typical distribution of the ejecta. Slow-motioned very massive stars induce ejecta fields made of a mushroom of shock wave interacting with the direction of stellar motion that overhangs the region of ejecta spreading into the wind bubble (Fig. 4.6). Ejecta of fast moving stars fill jet-like region of up to $\simeq$ 100-pc large appearing as a trail of enriched material propagating away from the location of the explosion, see Appendix XIII.

4.4 Rectangular core-collapse supernova remnants

The large-scale magnetisation of the ISM of the Milky Way takes the form of organised field lines that are enrolled along its spiral arms (Beck, 2009). The work of van Marle, Meliani & Marcowith (2015b) dem Meyer, Petrov & Pohl (2020). onstrated that this native magnetisation of the ISM is sufficient to profoundly affect the developement of stellar wind bubbles around massive stars. Their constact discontinuity and the region of unshocked stellar wind adopts an elongated morphology along the direction of the local magnetic field, although the stellar wind keeps on being blown isotropically. This is emphasised by the high magnetisation of the dense molecular clouds. Motivated by the existence of squared planetary nebulae produced by evolved winds into magnetically-collimated circumstellar environments of low-mass stars (Heiligman, 1980; García-Segura et al., 1999), the morphological aspects of core-collapse supernova remnants generated by static massive stars in magnetised ISM.

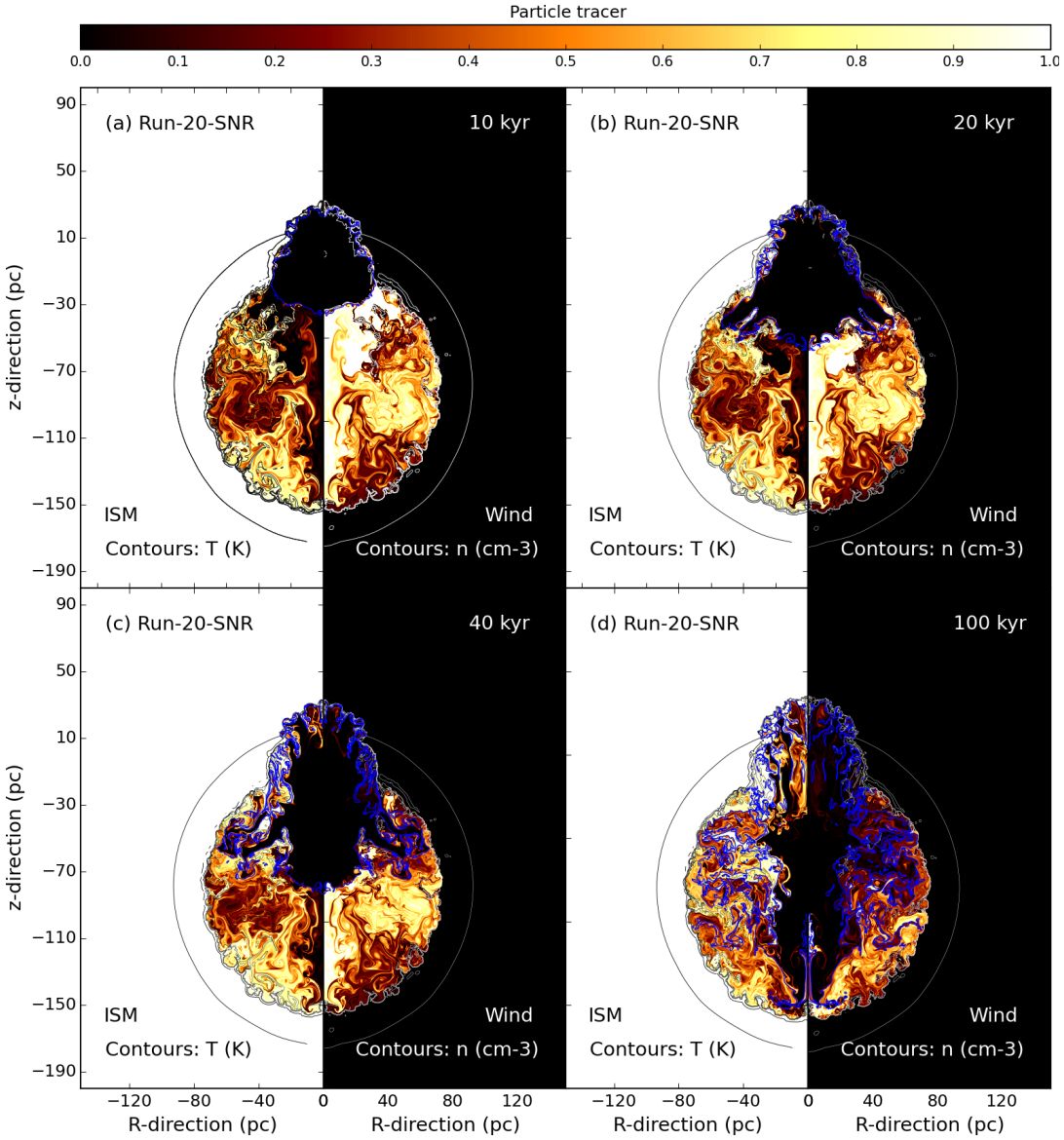

Figure 4.6: Illustration of the mixing of materials at work in the core-collapse supernova remnant of a runaway massive star. The plots show the proportion of IS Meyer, Petrov & Pohl (2020). M material (left part of the panels) and stellar wind (right part of the panels), respectively. Black contours indicate the temperature, white contours stands for gas number density and blue contours are the location of supernova ejecta by an amount of 10% in number density. From Meyer, Petrov & Pohl (2020).

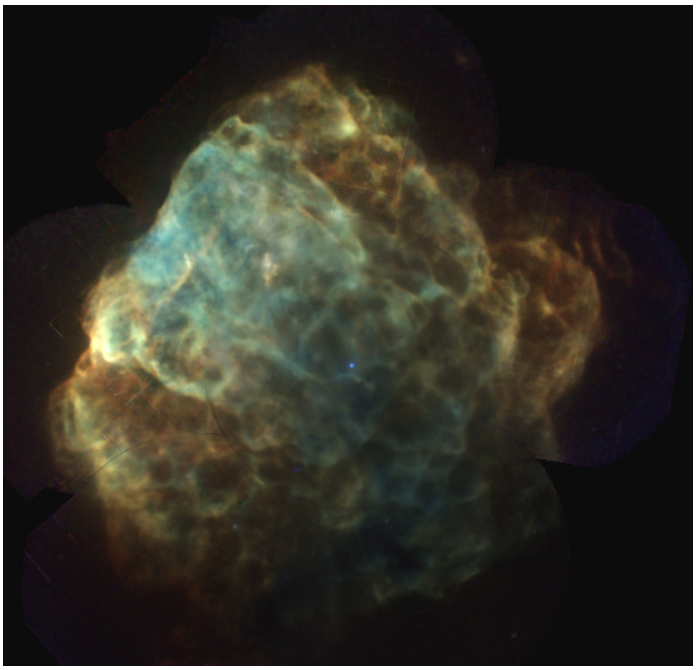

Figure 4.7: Mosaic image in the X-ray waveband of the rectagular core-collapse supernova remnant Puppis A, made of XMM-Newton and Chandra data. From Dubner et al. (2013). The differential expantion of the supernova shock wave generates an asymmetric remnant.

The 2.5D magnetohydrodynamical simulations of a supernova explosion in the circumstellar environment of a $20 M_{\odot}$ in the warm phase of a magnetised ISM in Meyer et al. (2022a) show that when it reaches its middle age (15–20 kyr), the remnant adopts a tubular shape that results from the interaction between the isotropic supernova ejecta and the anisotropic, magnetized, shocked stellar progenitor bubble into which the supernova blast wave expands. Such morphology of the supernova shock wave, when reverberated onto the walls of the elongated stellar wind cavity, shapes as a cylinder that is also aligned with the direction of the local magnetic field, and which, by projection, appears as a rectangle. This mechanism is responsible for both the production of thermal (X-rays, optical) and non-thermal (radio synchrotron, inverse Compton) projected emission transciently resembling the square appearance of the core-collapse supernova remnant Puppis A. The rectangular morphology of the remnant disappears at later times, when the reverberated shock wave reaches the location of the explosion.

4.5 Plerions

Once the supernova explosion occurs, a rotating, high-magnetised neutron star is often left at the location of the explosion and it develops a powerful leptonic so-called pulsar wind releasing kinetic luminosity that can reach $\dot{E} \sim 10^{39}\,\mathrm{erg\,s^{-1}}$ inside of the ejecta. Because of numerical and physical difficulties associated with the circumstellar medium modelling, the simulations of pulsar wind nebulae are mainly performed in classical hydrodynamics of moving pulsars inside supernova ejecta (Blondin, Chevalier & Frierson, 2001; van der Swaluw et al., 2001, 2003; van der Swaluw, 2003; Temim et al., 2015; Slane et al., 2018; **?**). However, these works did not account for all the

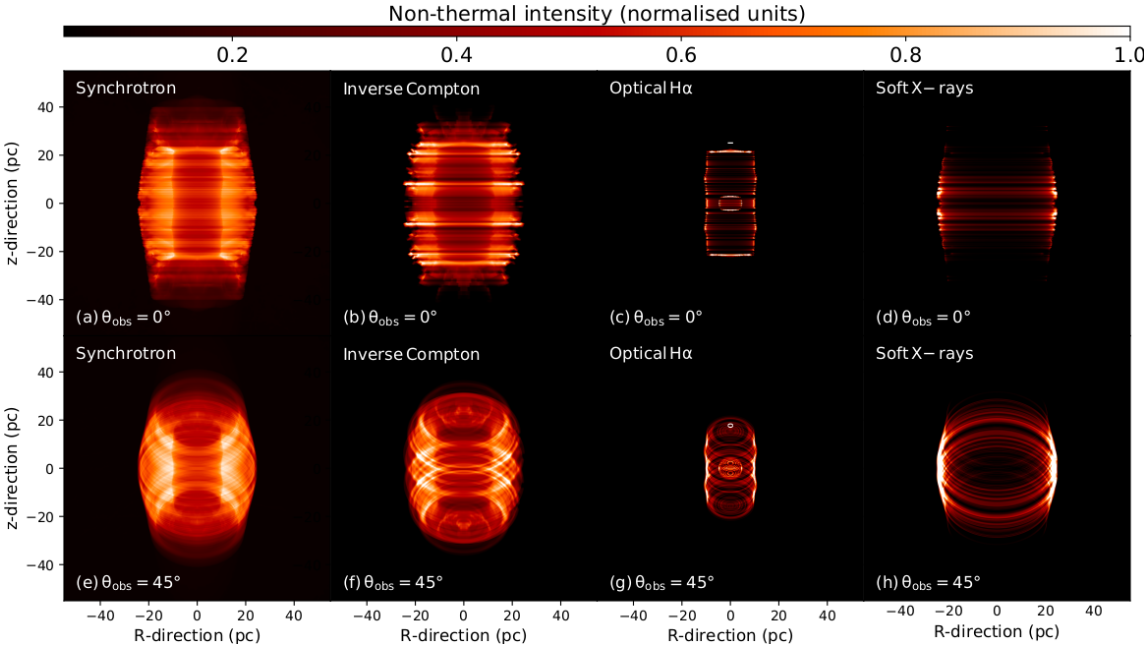

Figure 4.8: Normalized non-thermal radio synchrotron (a,e), inverse Compton (b,f), thermal optical Hα (c,g) and thermal X-rays (d,h) emission maps of a rectangular core-collapse supernova remnant model qualitatively resembling Puppis A. The remnants are observed with viewing angles of $\theta_{\rm obs} = 0°$ (top) and $\theta_{\rm obs} = 45°$ (bottom). The 35 $M_\odot$ Wolf-Rayet-evolving progenitor star is static and placed in a uniform, magnetized ambient medium at time 17.5 kyr after the explosion. From Meyer et al. (2022a).

evolutionary phases of the stellar progenitor of the pulsar.

For pulsars from massive runaway stars, their winds mainly expand in core-collapse supernova remnant constituted of supernova ejecta and circumstellar materials. Thus, shocks and instabilities, as well as the overall pulsar wind morphology, will be affected by these structures. Since remnants are strongly affected by the distribution of the circumstellar medium, the pulsar wind nebulae and the properties of the various shocks therein should be, in turn, a function of their surroundings. Particularly, the $\sim$ 30% of massive stars moving through the circumstellar medium release large amount of red-supergiant material as dense asymmetric stellar-wind bow shocks (Cox et al., 2012a; Henney & Arthur, 2019a,b,c; Meyer, Petrov & Pohl, 2020; Herbst et al., 2022), which this should not be omitted in the modelling of their pulsar wind nebulae.

The study of Meyer & Meliani (2022) shows, in the particular context of a 20 $M_\odot$ fast-moving red-supergiant star in the Galactic plane, that the wind-blown bubble of a core-collapse supernova progenitor has a governing impact on the morphology of its subsequent pulsar wind nebulae. As early as 2.5 kyr, the distribution of the contact discontinuity between a magnetized pulsar wind and the supernova ejecta adopts an oblong shape as a result of the anisotropic ejecta distribution. Since core-collapse supernova remnants are shaped according to their circumstellar medium, pulsar wind nebulae similarly take their morphology as a direct consequence of their progenitor's stellar evolution history. Because a significant fraction of massive stars are runaway objects, our findings imply that the stellar-wind history should not be neglected in the understanding of pulsar wind nebulae and that the circumstellar-induced asymmetries should account for up to 10 – 25% per cent of all individual pulsar wind nebulae.

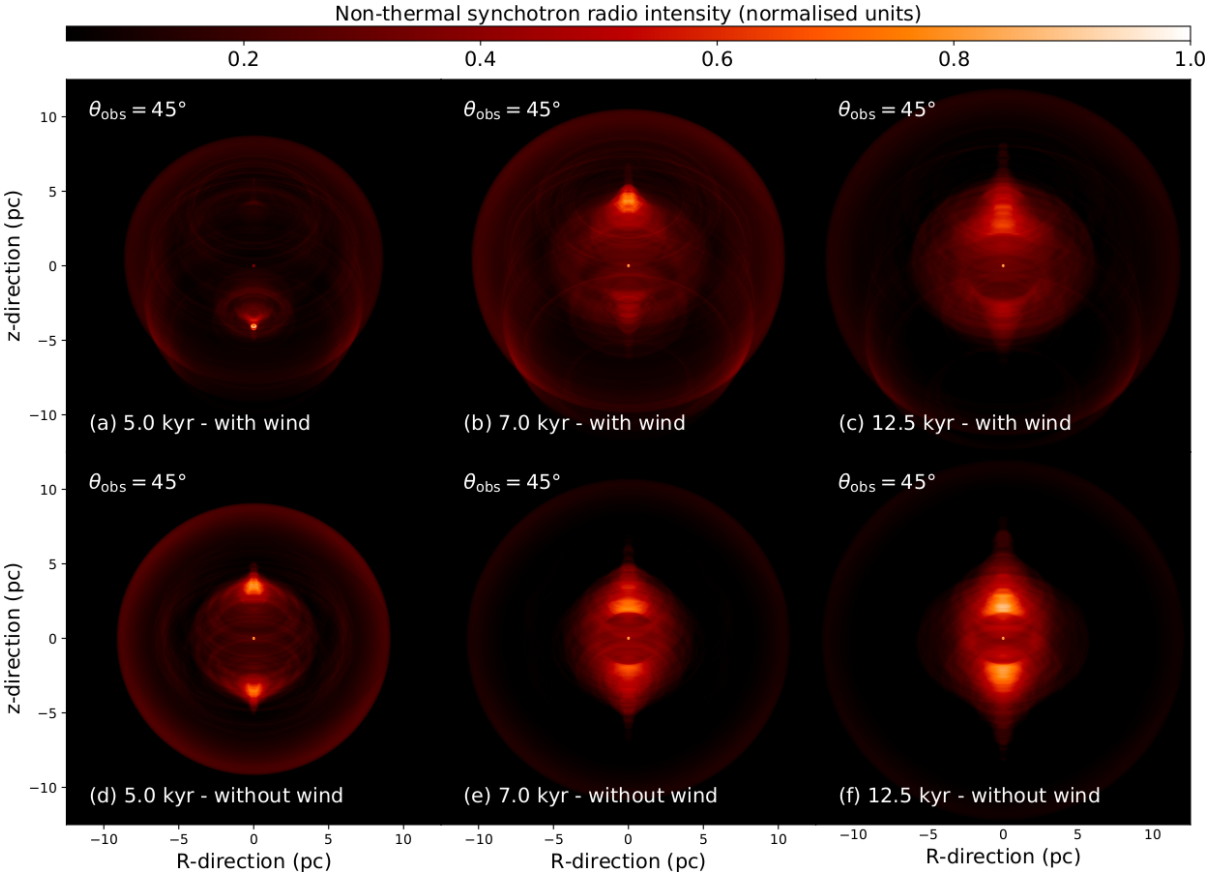

Figure 4.9: Effects of the pre-supernova circumstellar medium onto the devopment of the subsequent pulsar wind nebula. Non-thermal synchrotron emission maps of the pulsar wind nebulae simulated with (top) and without (bottom) the stellar wind of the supernova progenitor. The figures are shown for several time instances for a viewing angle of $\theta_{\rm obs} = 45°$. From Meyer & Meliani (2022).

We generate predictive images for our asymmetric pulsar wind nebulae from a runaway massive star. The pulsar wind is at first not visible in the region facing the progenitor's direction of motion, where the supernova shock wave interacting with the wind bubble dominates (Figs 4.9a, d). Once the pulsar polar jet grows and penetrates the dense region of stellar wind and ejecta, it becomes brighter than that in the cavity (Figs 4.9b, c). This projected up–down surface brightness asymmetry increases with time, as the front jet starts to interact with the shocked supernova material and the jet on the other side continues to propagate in the rarefied medium of the stellar-wind cavity. Our results show that the effects of the progenitor's stellar wind impacts the global morphology of pulsar wind nebulae and consequently influ- ences the properties of the shocks therein. This should significantly modify the injection and acceleration physics of the relativistic particle population, which, in turn, is responsible for the non-thermal emission properties of pulsar wind nebulae.

Summary on the circumstellar medium of dead massive stars. The morphology of the supernova remnant from Wolf-Rayet-evolving runaway massive stars are largely governed by the circumstellar medium of the defunct progenitor star. A mild 7 μG ambient magnetic field can stabilizes the large-scale pre-supernova circumstellar medium in which the supernova ejecta are released, reducing the mixing efficiency of ejecta, wind and ISM materials. Non-thermal radio emission of the remnants has characteristic features reflecting the asymmetry of exiled core-collapse supernova remnants such as G296.5+10.0, CTB109 or and Kes 17. If the star is at rest, an organised ISM magnetic field produce elongation of the wind bubble. Due to reflections and projection effects, the subsequent supernova remnant adopts a tubular shape which can appear as a rectangular object like Puppis A, as some bipolar and elliptical planetary nebula do in the low-mass regime of stellar evolution. The small fraction of stars with masses 60–70 $M_\odot$ are predicted to undergo a very complex and brutal evolution before dying as a core-collapse supernova. Their circumstellar medium shapes as 100 pc-scale wind nebula that can be pierced by star when fast-moving in the Galactic plane, off-centering the location of the supernova explosion inside of their bow shock nebula. The extended, filamentary wind cavity in which chemically enriched supernova ejecta expand, mix efficiently wind and ISM materials and tracer of the runaway nature of the very massive progenitors. Ultimately, supernova remnants might host a fast-rotating magnetised neutron star which leptonic wind produce a pulsar wind nebula. The morphology of the pulsar wind nebulae are in their turn strongly constrained by the distribution of stellar wind released by the dead massive ancestor, and they display up-down asymmetric non-thermal synchrotron emission.

CHAPTER 5

Conclusion and perspectives

The main results of the research devoted to the surroundings of massive stars presented in this thesis can be summarized via the three paragraphs below.

On the formation of young massive stars. The manner young massive stars form and gain their mass resembles by many aspects that of their low-mass siblings and the common picture describing them is the burst mode of accretion in star formation. Their accretino discs fragments, and gaseous disc fragments inward-migrate towards the protostar, generating series of luminous outbursts. Clumps can turn into generate binary companions, of various possible orbits, such that of close massive protobinaries. Dics clumps and nascent stars can be observed with the ALMA interferometer. Massive protostars in the burst mode of accretion episodically experience excursions in the red part of the Hertzsprung-Russell diagram, which provoke the intermettency of their ionized H II region. The burst mode of accretion is massive star formation provides an explanation to the outbursts of the massive young stellar object S255IRNIRS3.

On wind nebulae of evolved massive stars. Stellar wind bow shocks of OB stars are very sensitive to magnetic fields which makes their Hα optical/infrared emission fainter. The brightests optical/infrared bow shock nebulae emit more than theridirving star, and they are produced when most massive stars moving in a dense ISM Magentised bow shocks of red supergiant stars are smooth and stable, however these astrospheres can appear complex due to projection effects. It is proposed that IRC-10414 is in a steady state of its evolution and Betelgeuse's bar is of interstelar origin. Bow shock of Wolf–Rayet stars exist and host bright rings generated by wind-wind collision seeming to be co-moving with it, such around WR71, WR124 and WR148. Bipolar Wolf-Rayet nebulae such as NGC 6888 witness a complex past stellar evolution, involving multiple/merged systems or blue supergiant scenario ancestors.

On the supernova remnants of dead massive stars. The supernova remnants of runaway massive stars have asymmetric non-thermal radio morphologies such as those of G296.5+10.0, CTB109 or and Kes 17, determined by the stellar motion and the wind history of the defunct progenitor star. Magnetic fields stabilise the circumstellar medium in which supernova ejecta are released, reducing the materials mixing efficiency therein. Massive stars at rest explode in elondated wind bubbles indcing tubular remnants which can appear as a rectangular object like Puppis A, as some bipolar and elliptical planetary nebula do in the low-mass regime of stellar evolution. Most massive runaway stars (60–70 $M_\odot$) undergo complex evolutionary paths and produce huge wind bubbles ($\sim$ 100 pc) in which off-centered supernova explosion happen, enriching cavities with ejecta efficiently mixing with wind and ISM materials. Last, the morphology and emission of pulsar wind nebulae hosted by some core-collapse supernova remnants are in their turn, strongly constrained by the asymmetries in the progenitor's circumstellar medium.

Future prespectives in terms of research on the circumstellar medium of massive stars are numerous. Publicly-available numerical codes permitting to simulate the dynamics and emission of astrophysical plasma and the growing amount of accessible computing resources, make the predictive modelling of nebulae around high-mass stars much more attainable than during the past decades.

High spatial resolution as well as the inclusion of additional physical processes (chemistry, cosmic-rays, non-ideal magnetohydrodynamical processes, turbulence, complex emission mechanisms) is now about to hand, allowing us to carry on large parameter studies and various applications to specific astrophysical objects. This will converge towards the production of multidisciplinary studies investigating the transitions between the young, evolved and defunct regimes of the lives of massive stars. Such work are higly desirable and will greatly improve our understanding of the coupled evolution of such stars together with their circumstellar nebulae.

CHAPTER 6

Bibliography

Ahmadi A., Kuiper R., Beuther H., 2019, A&A, 632, A50

Baalmann L. R., Scherer K., Fichtner H., Kleimann J., Bomans D. J., Weis K., 2020, A&A, 634, A67

Baalmann L. R., Scherer K., Kleimann J., Fichtner H., Bomans D. J., Weis K., 2021, A&A, 650, A36

Balsara D. S., Tilley D. A., Howk J. C., 2008, MNRAS, 386, 627

Banerjee S., Kroupa P., Oh S., 2012, ApJ, 746, 15

Baranov V. B., Krasnobaev K. V., Onishchenko O. G., 1975, Soviet Astronomy Letters, 1, 81

Beck R., 2009, Astrophysics and Space Sciences Transactions, 5, 43

Bergin E. A., Tafalla M., 2007, ARA&A, 45, 339

Bestenlehner J. M., Gräfener G., Vink J. S. e. a., 2014, A&A, 570, A38

Beuther H., Linz H., Henning T., 2012, A&A, 543, A88

Beuther H., Ragan S. E., Johnston K., Henning T., Hacar A., Kainulainen J. T., 2015, A&A, 584, A67

Beuther H. et al., 2018, A&A, 614, A64

Blaauw A., 1961, Bull. Astron. Inst. Netherlands, 15, 265

Blondin J. M., Chevalier R. A., Frierson D. M., 2001, ApJ, 563, 806

Blondin J. M., Koerwer J. F., 1998, New Ast., 3, 571

Boley P. A. et al., 2019, arXiv e-prints, arXiv:1912.08510

Bonnell I. A., Bate M. R., 2005, MNRAS, 362, 915

Bosco F., Beuther H., Ahmadi A., Mottram J. C., Kuiper R., Linz H., Maud e. a., 2019, A&A, 629, A10

Boumis P., 2019, in Supernova Remnants: An Odyssey in Space after Stellar Death II, p. 13

Brighenti F., D'Ercole A., 1995a, MNRAS, 277, 53

Brighenti F., D'Ercole A., 1995b, MNRAS, 273, 443

Brighenti F., D'Ercole A., 1997, MNRAS, 285, 387

Brogan C. L. et al., 2018, ApJ, 866, 87

Brott I. et al., 2011a, A&A, 530, A115

Brott I. et al., 2011b, A&A, 530, A116

Burns R. A., 2018, in IAU Symposium, Vol. 336, Astrophysical Masers: Unlocking the Mysteries of the Universe, Tarchi A., Reid M. J., Castangia P., eds., pp. 263–266

Burns R. A. et al., 2017, MNRAS, 467, 2367

Burns R. A., Sugiyama K., Hirota T., Kim K.-T., Sobolev A. M., Stecklum B., MacLeod G. C., Yonekura Y. e. a., 2020, Nature Astronomy, 4, 506

Caratti o Garatti A. et al., 2017, Nature Physics, 13, 276

Caratti o Garatti A., Stecklum B., Linz H., Garcia Lopez R., Sanna A., 2015, A&A, 573, A82

Castro D., Slane P., Ellison D. C., Patnaude D. J., 2012, ApJ, 756, 88

Cesaroni R., Felli M., Jenness T., Neri R., Olmi L., Robberto M., Testi L., Walmsley C. M., 1999, A&A, 345, 949

Cesaroni R., Galli D., Lodato G., Walmsley M., Zhang Q., 2006, Nature, 444, 703

Chen X., Ren Z., Zhang Q., Shen Z., Qiu K., 2017, ApJ, 835, 227

Chevalier R. A., Liang E. P., 1989, ApJ, 344, 332

Chini R., Hoffmeister V. H., Nasseri A., Stahl O., Zinnecker H., 2012, MNRAS, 424, 1925

Chiotellis A., Schure K. M., Vink J., 2012, A&A, 537, A139

Chu Y. H., 1981, ApJ, 249, 195

Chu Y. H., Gull T. R., Treffers R. R., Kwitter K. B., Troland T. H., 1982, ApJ, 254, 562

Chu Y. H., Treffers R. R., 1981a, ApJ, 249, 586

Chu Y. H., Treffers R. R., 1981b, ApJ, 250, 615

Chu Y. H., Treffers R. R., Kwitter K. B., 1983, ApJS, 53, 937

Comerón F., Figueras F., 2020, A&A, 638, A90

Comerón F., Kaper L., 1998, A&A, 338, 273

Conlon E. S., Dufton P. L., Keenan F. P., Leonard P. J. T., 1990, A&A, 236, 357

Cox C. I., Gull S. F., Green D. A., 1991, MNRAS, 250, 750

Cox N. L. J., Kerschbaum F., van Marle A.-J., Decin L., Ladjal D., Mayer A., 2012a, A&A, 537, A35

Cox N. L. J., Kerschbaum F., van Marle A. J., Decin L., Ladjal D., Mayer A., 2012b, A&A, 543, C1

Crowther P. A., 2007, ARA&A, 45, 177

Cunningham N. J., Moeckel N., Bally J., 2009, ApJ, 692, 943

Davies B., 2017, Philosophical Transactions of the Royal Society of London Series A, 375, 20160270

De Becker M., del Valle M. V., Romero G. E., Peri C. S., Benaglia P., 2017, MNRAS, 471, 4452

de Wit W. J., Testi L., Palla F., Zinnecker H., 2005, A&A, 437, 247

Decin L. et al., 2012, A&A, 548, A113

Decin L., 2012, Advances in Space Research, 50, 843

Dessart L., Langer N., Petrovic J., 2003, A&A, 404, 991

Dgani R., van Buren D., Noriega-Crespo A., 1996a, ApJ, 461, 927

Dgani R., van Buren D., Noriega-Crespo A., 1996b, ApJ, 461, 372

Domček V., Vink J., Zhou P., Sun L., Driessen L., 2022, A&A, 659, A63

Dong R., Vorobyov E., Pavlyuchenkov Y., Chiang E., Liu H. B., 2016, ApJ, 823, 141

Dubner G., Loiseau N., Rodríguez-Pascual P., Smith M. J. S., Giacani E., Castelletti G., 2013, A&A, 555, A9

Dullemond C. P., 2012, RADMC-3D: A multi-purpose radiative transfer tool. Astrophysics Source Code Library

Dunham M. M., Vorobyov E. I., 2012, ApJ, 747, 52

Dwarkadas V. V., 2005, ApJ, 630, 892

Dwarkadas V. V., 2007, ApJ, 667, 226

Eggenberger P., Meynet G., Maeder A., Hirschi R., Charbonnel C., Talon S., Ekström S., 2008, Ap&SS, 316, 43

Ekström S. e. a., 2012, A&A, 537, A146

Elbakyan V. G., Vorobyov E. I., Rab C., Meyer D. M.-A., Güdel M., Hosokawa T., Yorke H., 2019, MNRAS, 484, 146

Eldridge J. J., Langer N., Tout C. A., 2011, MNRAS, 414, 3501

Elmegreen B. G., 2007, ApJ, 668, 1064

Evans K. A., Massey P., 2015, AJ, 150, 149

Evans, II N. J., 1999, ARA&A, 37, 311

Federrath C., Banerjee R., Clark P. C., Klessen R. S., 2010, ApJ, 713, 269

Field G. B., Goldsmith D. W., Habing H. J., 1969, ApJ, 155, L149

Flagey N., Noriega-Crespo A., Billot N., Carey S. J., 2011, ApJ, 741, 4

Forgan D. H., Ilee J. D., Cyganowski C. J., Brogan C. L., Hunter T. R., 2016, MNRAS, 463, 957

Fujisawa K., Yonekura Y., Sugiyama K., Horiuchi H., Hayashi T., Hachisuka K., Matsumoto N., Niinuma K., 2015, The Astronomer's Telegram, 8286

Gabler M., Wongwathanarat A., Janka H.-T., 2021, MNRAS, 502, 3264

Gammie C. F., 1996, ApJ, 462, 725

Garcia-Segura G., Langer N., Mac Low M.-M., 1996, A&A, 316, 133

García-Segura G., Langer N., Różyczka M., Franco J., 1999, ApJ, 517, 767

Garcia-Segura G., Mac Low M.-M., Langer N., 1996, A&A, 305, 229

Gebrehiwot Y. M., Teklehaimanot B. T., 2021, New Ast., 82, 101455

Georgy C., Walder R., Folini D., Bykov A., Marcowith A., Favre J. M., 2013, A&A, 559, A69

Geyer M. P., 2002, PhD thesis, Ruprecht-Karls University of Heidelberg, Germany

Gies D. R., 1987, ApJS, 64, 545

Ginsburg A., Bally J., Goddi C., Plambeck R., Wright M., 2018, ApJ, 860, 119

Goddi C., Ginsburg A., Maud L. T., Zhang Q., Zapata L. A., 2020, ApJ, 905, 25

González R. F., 2018, A&A, 609, A69

González R. F., de Gouveia Dal Pino E. M., Raga A. C., Velázquez P. F., 2004, ApJ, 616, 976

González R. F., Villa A. M., Gómez G. C., de Gouveia Dal Pino E. M., Raga A. C., Cantó J., Velázquez P. F., de La Fuente E., 2010, MNRAS, 402, 1141

Gordon M. S., Jones T. J., Gehrz R. D., Helton L. A., 2017, ApJ, 834, 122

Green D. A., Stephenson F. R., 2003, in Lecture Notes in Physics, Berlin Springer Verlag, Vol. 598, Supernovae and Gamma-Ray Bursters, Weiler K., ed., pp. 7–19

Greif T. H., Bromm V., Clark P. C., Glover S. C. O., Smith R. J., Klessen R. S., Yoshida N., Springel V., 2012, MNRAS, 424, 399

Groh J. H., Meynet G., Ekström S., Georgy C., 2014, A&A, 564, A30

Gull T. R., Sofia S., 1979, ApJ, 230, 782

Gvaramadze V. V., Alexashov D. B., Katushkina O. A., Kniazev A. Y., 2018, MNRAS, 474, 4421

Gvaramadze V. V., Gualandris A., 2011, MNRAS, 410, 304

Gvaramadze V. V., Kniazev A. Y., Fabrika S., 2010, MNRAS, 405, 1047

Gvaramadze V. V., Kniazev A. Y., Hamann W. R., Berdnikov L. N., Fabrika S., Valeev A. F., 2010, MNRAS, 403, 760

Gvaramadze V. V., Menten K. M., Kniazev A. Y., Langer N., Mackey J., Kraus A., Meyer D. M.-A., Kamiński T., 2014, MNRAS, 437, 843

Haemmerlé L., Eggenberger P., Meynet G., Maeder A., Charbonnel C., 2016, A&A, 585, A65

Hamann W. R., 1992, in The Atmospheres of Early-Type Stars, Heber U., Jeffery C. S., eds., Vol. 401, p. 87

Hamann W. R., Gräfener G., Liermann A., 2006a, A&A, 457, 1015

Hamann W. R., Gräfener G., Liermann A., 2006b, A&A, 457, 1015

Hamann W. R., Koesterke L., 1998, A&A, 335, 1003

Hansen O. L., Blanco V. M., 1973, AJ, 78, 669

Harries T. J., Douglas T. A., Ali A., 2017, MNRAS, 471, 4111

Harvey-Smith L., Gaensler B. M., Kothes R., Townsend R., Heald G. H., Ng C. Y., Green A. J., 2010, ApJ, 712, 1157

Heiligman G. M., 1980, MNRAS, 191, 761

Henney W. J., Arthur S. J., 2019a, MNRAS, 486, 3423

Henney W. J., Arthur S. J., 2019b, MNRAS, 486, 4423

Henney W. J., Arthur S. J., 2019c, MNRAS, 489, 2142

Herbst K. et al., 2022, Space Sci. Rev., 218, 29

Hoogerwerf R., de Bruijne J. H. J., de Zeeuw P. T., 2000, ApJ, 544, L133

Hosokawa T., Omukai K., 2009, ApJ, 691, 823

Hunter T. et al., 2019, BAAS, 51, 13

Hunter T. R. et al., 2017, ApJ, 837, L29

Huthoff F., Kaper L., 2002, A&A, 383, 999

Ilee J. D., Cyganowski C. J., Brogan C. L., Hunter T. R., Forgan D. H., Haworth T. J., Clarke C. J., Harries T. J., 2018, ApJ, 869, L24

Ilee J. D., Cyganowski C. J., Nazari P., Hunter T. R., Brogan C. L., Forgan D. H., Zhang Q., 2016, MNRAS, 462, 4386

Imai H., Deguchi S., Miyoshi M., 1999, PASJ, 51, 587

Jiménez-Hernández P., Arthur S. J., Toalá J. A., 2020, MNRAS, 497, 4128

Johnston K. G. et al., 2020a, A&A, 634, L11

Johnston K. G. et al., 2020b, A&A, 634, L11

Johnston K. G., Keto E., Robitaille T. P., Wood K., 2011, MNRAS, 415, 2953

Johnston K. G. et al., 2015, ApJ, 813, L19

Kaper L., van Loon J. T., Augusteijn T., Goudfrooij P., Patat F., Waters L. B. F. M., Zijlstra A. A., 1997, ApJ, 475, L37

Katsuda S., Takiwaki T., Tominaga N., Moriya T. J., Nakamura K., 2018, ApJ, 863, 127

Katushkina O. A., Alexashov D. B., Gvaramadze V. V., Izmodenov V. V., 2018, MNRAS, 473, 1576

Kenyon S. J., Hartmann L. W., Strom K. M., Strom S. E., 1990, AJ, 99, 869

Kervella P. et al., 2018, A&A, 609, A67

Keto E., Wood K., 2006, ApJ, 637, 850

Klassen M., Pudritz R. E., Kuiper R., Peters T., Banerjee R., 2016, ApJ, 823, 28

Kobulnicky H. A. et al., 2016, ApJS, 227, 18

Kobulnicky H. A., Schurhammer D. P., Baldwin D. J., Chick W. T., Dixon D. M., Lee D., Povich M. S., 2017, AJ, 154, 201

Kolb S. M., Stute M., Kley W., Mignone A., 2013, A&A, 559, A80

Kothes R., Foster T., 2012, ApJ, 746, L4

Kraus S. et al., 2017, ApJ, 848, L11

Kroupa P., 2001, MNRAS, 322, 231

Krumholz M. R., Klein R. I., McKee C. F., 2007, ApJ, 665, 478

Kwok S., 2007, Physics and Chemistry of the Interstellar Medium

Lahén N., Naab T., Johansson P. H., Elmegreen B., Hu C.-Y., Walch S., 2020a, ApJ, 904, 71

Lahén N., Naab T., Johansson P. H., Elmegreen B., Hu C.-Y., Walch S., Steinwandel U. P., Moster B. P., 2020b, ApJ, 891, 2

Langer N., 2012, ARA&A, 50, 107

Langer N., García-Segura G., Mac Low M.-M., 1999, ApJ, 520, L49

Laor A., Draine B. T., 1993, ApJ, 402, 441

Lequeux J., 2005, The Interstellar Medium

Levesque E. M., 2010, , 54, 1

López-Santiago J. et al., 2012, ApJ, 757, L6

Machida M. N., Inutsuka S.-i., Matsumoto T., 2014, MNRAS, 438, 2278

Mackey J., Mohamed S., Gvaramadze V. V., Kotak R., Langer N., Meyer D. M.-A., Moriya T. J., Neilson H. R., 2014, Nature, 512, 282

Mackey J., Mohamed S., Neilson H. R., Langer N., Meyer D. M.-A., 2012, ApJ, 751, L10

MacLeod G. C. et al., 2018, MNRAS, 478, 1077

Maeda T. et al., 2008, PASJ, 60, 1057

Maeder A., 2009, Physics, Formation and Evolution of Rotating Stars, springer-verlag edn. Astronomy and Astrophysics Library

Maeder A., Meynet G., 2000, ARA&A, 38, 143

Mahy L., Rauw G., De Becker M., Eenens P., Flores C. A., 2013, A&A, 550, A27

Marston A. P., 1991, ApJ, 366, 181

Maud L. T., Cesaroni R., Kumar M. S. N., Rivilla V. M., Ginsburg A., Klaassen P. D., Harsono D. e. a., 2019, A&A, 627, L6

Maud L. T. et al., 2018, A&A, 620, A31

McKee C. F., 1995, in Astronomical Society of the Pacific Conference Series, Vol. 80, The Physics of the Interstellar Medium and Intergalactic Medium, Ferrara A., McKee C. F., Heiles C., Shapiro P. R., eds., p. 292

McKee C. F., Ostriker E. C., 2007, ARA&A, 45, 565

McKee C. F., Ostriker J. P., 1977, ApJ, 218, 148

McMullin J. P., Waters B., Schiebel D., Young W., Golap K., 2007, in Astronomical Society of the Pacific Conference Series, Vol. 376, Astronomical Data Analysis Software and Systems XVI, Shaw R. A., Hill F., Bell D. J., eds., p. 127

Menzies J. W., Wolstencroft R. D., 1990, MNRAS, 247, 177

Messineo M., Brown A. G. A., 2019, AJ, 158, 20

Meyer D. M. A., 2021, MNRAS, 507, 4697

Meyer D. M.-A., Gvaramadze V. V., Langer N., Mackey J., Boumis P., Mohamed S., 2014a, MNRAS, 439, L41

Meyer D. M.-A., Gvaramadze V. V., Langer N., Mackey J., Boumis P., Mohamed S., 2014b, MNRAS, 439, L41

Meyer D. M. A., Haemmerlé L., Vorobyov E. I., 2019, MNRAS, 484, 2482

Meyer D. M. A., Kreplin A., Kraus S., Vorobyov E. I., Haemmerle L., Eislöffel J., 2019a, MNRAS, 487, 4473

Meyer D. M.-A., Kuiper R., Kley W., Johnston K. G., Vorobyov E., 2018, MNRAS, 473, 3615

Meyer D. M.-A., Langer N., Mackey J., Velázquez P. F., Gusdorf A., 2015, MNRAS, 450, 3080

Meyer D. M.-A., Mackey J., Langer N., Gvaramadze V. V., Mignone A., Izzard R. G., Kaper L., 2014c, MNRAS, 444, 2754

Meyer D. M. A., Meliani Z., 2022, MNRAS, 515, L29

Meyer D. M. A., Mignone A., Kuiper R., Raga A. C., Kley W., 2017a, MNRAS, 464, 3229

Meyer D. M. A., Mignone A., Petrov M., Scherer K., Velázquez P. F., Boumis P., 2021a, MNRAS, 506, 5170

Meyer D. M. A., Oskinova L. M., Pohl M., Petrov M., 2020, MNRAS, 496, 3906

Meyer D. M. A., Petrov M., Pohl M., 2020, MNRAS, 493, 3548

Meyer D. M. A., Pohl M., Petrov M., Oskinova L., 2021b, MNRAS, 502, 5340

Meyer D. M.-A., van Marle A.-J., Kuiper R., Kley W., 2016, MNRAS, 459, 1146

Meyer D. M. A. et al., 2022a, MNRAS, 515, 594

Meyer D. M. A., Vorobyov E. I., Elbakyan V. G., Eislöffel J., Sobolev A. M., Stöhr M., 2021c, MNRAS, 500, 4448

Meyer D. M. A., Vorobyov E. I., Elbakyan V. G., Kraus S., Liu S. Y., Nayakshin S., Sobolev A. M., 2022b, MNRAS

Meyer D. M.-A., Vorobyov E. I., Elbakyan V. G., Stecklum B., Eislöffel J., Sobolev A. M., 2019b, MNRAS, 482, 5459

Meyer D. M.-A., Vorobyov E. I., Kuiper R., Kley W., 2017b, MNRAS, 464, L90

Mignone A., Bodo G., Massaglia S., Matsakos T., Tesileanu O., Zanni C., Ferrari A., 2007, ApJS, 170, 228

Mignone A., Zanni C., Tzeferacos P., van Straalen B., Colella P., Bodo G., 2012, ApJS, 198, 7

Moffat A. F. J., Marchenko S. V., Seggewiss W., van der Hucht et al. K. A. e. a., 1998, A&A, 331, 949

Mohamed S., Mackey J., Langer N., 2012, A&A, 541, A1

Montargès M. et al., 2019, MNRAS, 485, 2417

Motogi K., Hirota T., Machida M. N., Yonekura Y., Honma M., Takakuwa S., Matsushita S., 2019, ApJ, 877, L25

Munoz M., Moffat A. F. J., Hill G. M., Shenar T., Richardson N. D., Pablo H., St-Louis N., Ramiaramanantsoa T., 2017, MNRAS, 467, 3105

Myers A. T., McKee C. F., Cunningham A. J., Klein R. I., Krumholz M. R., 2013, ApJ, 766, 97

Noriega-Crespo A., van Buren D., Cao Y., Dgani R., 1997, AJ, 114, 837

Noriega-Crespo A., van Buren D., Dgani R., 1997, AJ, 113, 780

Oh S., Kroupa P., 2018, MNRAS, 481, 153

Ohm S., Hinton J. A., Domainko W., 2010, ApJ, 718, L161

Orlando S., Miceli M., Pumo M. L., Bocchino F., 2016, ApJ, 822, 22

Oskinova L. M., Feldmeier A., Kretschmar P., 2012, MNRAS, 421, 2820

Parker Q. A., Phillipps S., Pierce M. J., Hartley M., Hambly N. C., Read M. A., MacGillivray, 2005, MNRAS, 362, 689

Peri C. S., Benaglia P., Brookes D. P., Stevens I. R., Isequilla N. L., 2012, A&A, 538, A108

Peri C. S., Benaglia P., Isequilla N. L., 2015, A&A, 578, A45

Petrović J., 2004, PhD thesis, Utrecht University

Postel A., Audard M., Vorobyov E., Dionatos O., Rab C., Güdel M., 2019, A&A, 631, A30

Prajapati P., Tej A., del Palacio S., Benaglia P., CH I.-C., Vig S., Mandal S., Kanti Ghosh S., 2019, ApJ, 884, L49

Purser S. J. D., Lumsden S. L., Hoare M. G., Cunningham N., 2018, MNRAS, 475, 2

Purser S. J. D., Lumsden S. L., Hoare M. G., Kurtz S., 2021, MNRAS, 504, 338

Purser S. J. D. et al., 2016, MNRAS, 460, 1039

Reid M. J. et al., 2009, ApJ, 700, 137

Reiter M., Kiminki M. M., Smith N., Bally J., 2017, MNRAS, 470, 4671

Rogers P. D., Wadsley J., 2012, MNRAS, 423, 1896

Rosen A. L., Krumholz M. R., McKee C. F., Klein R. I., 2016, MNRAS, 463, 2553

Rosen A. L., Krumholz M. R., Oishi J. S., Lee A. T., Klein R. I., 2017, Journal of Computational Physics, 330, 924

Samal M. R., Chen W. P., Takami M., Jose J., Froebrich D., 2018, MNRAS, 477, 4577

Sana H. e. a., 2012, Science, 337, 444

Sander A., Hamann W. R., Todt H., 2012, A&A, 540, A144

Sanna A. et al., 2019, A&A, 623, A77

Schleicher D. R. G., Bovino S., Latif M. A., Ferrara A., Grassi T., 2016, A&A, 585, A11

Schmutz W., Hamann W. R., Wessolowski U., 1989, A&A, 210, 236

Seifried D., Sánchez-Monge Á., Walch S., Banerjee R., 2016, MNRAS

Shu F. H., 1977, ApJ, 214, 488

Shu F. H., 1992, Journal of the British Astronomical Association, 102, 230

Shylaja B. S., Anandarao B. G., 1993, Ap&SS, 205, 283

Slane P. et al., 2018, ApJ, 865, 86

Smartt S. J., 2009, ARA&A, 47, 63

Smith N., 2014, ARA&A, 52, 487

Stamatellos D., Maury A., Whitworth A., André P., 2011, MNRAS, 413, 1787

Stamatellos D., Whitworth A. P., 2009a, MNRAS, 392, 413

Stamatellos D., Whitworth A. P., 2009b, MNRAS, 400, 1563

Stamatellos D., Whitworth A. P., Hubber D. A., 2011, ApJ, 730, 32

Szécsi D., Agrawal P., Wünsch R., Langer N., 2022a, A&A, 658, A125

Szécsi D., Agrawal P., Wünsch R., Langer N., 2022b, A&A, 658, A125

Szymczak M., Olech M., Sarniak R., Wolak P., Bartkiewicz A., 2018a, MNRAS, 474, 219

Szymczak M., Olech M., Wolak P., Gérard E., Bartkiewicz A., 2018b, A&A, 617, A80

Tasker E. J., 2011, ApJ, 730, 11

Tasker E. J., Tan J. C., 2009, ApJ, 700, 358

Temim T., Slane P., Kolb C., Blondin J., Hughes J. P., Bucciantini N., 2015, ApJ, 808, 100

Toalá J. A., Arthur S. J., 2011, ApJ, 737, 100

Toalá J. A., Guerrero M. A., 2013, A&A, 559, A52

Toalá J. A., Oskinova L. M., González-Galán A., Guerrero M. A., Ignace R., Pohl M., 2016, ApJ, 821, 79

Toalá J. A., Oskinova L. M., Hamann W. R., Ignace R. e. a., 2018, ApJ, 869, L11

Toomre A., 1963, ApJ, 138, 385

Underhill A. B., 1968, ARA&A, 6, 39

van Buren D., 1993, in Astronomical Society of the Pacific Conference Series, Vol. 35, Massive Stars: Their Lives in the Interstellar Medium, Cassinelli J. P., Churchwell E. B., eds., p. 315

van Buren D., McCray R., 1988a, ApJ, 329, L93

van Buren D., McCray R., 1988b, ApJ, 329, L93

van Buren D., Noriega-Crespo A., Dgani R., 1995, AJ, 110, 2914

van der Hucht K. A., 2001, VizieR Online Data Catalog, III/215

van der Hucht K. A., 2006, A&A, 458, 453

van der Sluys M. V., Lamers H. J. G. L. M., 2003, A&A, 398, 181

van der Swaluw E., 2003, A&A, 404, 939

van der Swaluw E., Achterberg A., Gallant Y. A., Downes T. P., Keppens R., 2003, A&A, 397, 913

van der Swaluw E., Achterberg A., Gallant Y. A., Tóth G., 2001, A&A, 380, 309

van Marle A. J., Decin L., Meliani Z., 2014, A&A, 561, A152

van Marle A. J., Keppens R., 2010, ArXiv e-prints

van Marle A. J., Keppens R., 2012, A&A, 547, A3

van Marle A. J., Langer N., García-Segura G., 2005, A&A, 444, 837

van Marle A. J., Langer N., García-Segura G., 2007, A&A, 469, 941

van Marle A. J., Meliani Z., Keppens R., Decin L., 2011, ApJ, 734, L26

van Marle A. J., Meliani Z., Marcowith A., 2015a, A&A, 584, A49

van Marle A. J., Meliani Z., Marcowith A., 2015b, A&A, 584, A49

Vanbeveren D., 1991, Space Sci. Rev., 56, 249

Vink J. S., 2006, in Astronomical Society of the Pacific Conference Series, Vol. 353, Stellar Evolution at Low Metallicity: Mass Loss, Explosions, Cosmology, Lamers H. J. G. L. M., Langer N., Nugis T., Annuk K., eds., p. 113

Vink J. S., de Koter A., Lamers H. J. G. L. M., 2000, A&A, 362, 295

Vishniac E. T., 1994, ApJ, 428, 186

Vlemmings W. H. T., van Langevelde H. J., Diamond P. J., 2005, A&A, 434, 1029

Vorobyov E. I., 2009, ApJ, 704, 715

Vorobyov E. I., 2010, ApJ, 723, 1294

Vorobyov E. I., 2013, A&A, 552, A129

Vorobyov E. I., Basu S., 2005, ApJ, 633, L137

Vorobyov E. I., Basu S., 2006, ApJ, 650, 956

Vorobyov E. I., Basu S., 2010, ApJ, 714, L133

Vorobyov E. I., DeSouza A. L., Basu S., 2013, ApJ, 768, 131

Vorobyov E. I., Pavlyuchenkov Y. N., 2017, A&A, 606, A5

Vorobyov E. I., Zakhozhay O. V., Dunham M. M., 2013, MNRAS, 433, 3256

Weaver R., McCray R., Castor J., Shapiro P., Moore R., 1977, ApJ, 218, 377

Weiler K. W., Sramek R. A., 1988, ARA&A, 26, 295

Wilkin F. P., 1996, ApJ, 459, L31

Woosley S. E., Bloom J. S., 2006, ARA&A, 44, 507

Woosley S. E., Heger A., Weaver T. A., 2002, Reviews of Modern Physics, 74, 1015

Woosley S. E., Weaver T. A., 1986, ARA&A, 24, 205

Wright E. L. et al., 2010, AJ, 140, 1868

Yoon S.-C., Langer N., 2005, A&A, 443, 643

Zinchenko I. et al., 2015, ApJ, 810, 10

Zinchenko I. I., Liu S.-Y., Su Y.-N., Wang K.-S., Wang Y., 2019, arXiv e-prints, arXiv:1911.11447

Zinnecker H., Yorke H. W., 2007, ARA&A, 45, 481

CHAPTER 7

Appendix

The appendices of this thesis are constituted of my post-doctoral leading-author refereed publications.

Massive star formation

Paper I: On the existence of accretion-driven outbursts in massive star formation,
Meyer D. M.-A., Voroboyov E., Kuiper R., W. Kley,
MNRAS: Letters, Vol. 464, Issue 1, p.L90-L94; arXiv:1609.03402, 2017; doi:10.1093/mnrasl/slw187

Paper II: Forming spectroscopic massive proto-binaries by disk fragmentation,
Meyer D. M.-A., Kuiper R., Kley W., Voroboyov E., Johnston K.
MNRAS, Vol. 473, Issue 3, p.3615-3637, 2018; arXiv:1710.01162; doi:10.1093/mnras/stx2551

Paper III: Burst occurrence in young massive stellar objects,
Meyer D. M.-A., Voroboyov E., V. Elbaykan, Stecklum B., Eisloeffel J., Sobolev A.
MNRAS, Vol. 482, Issue 4, p.5459-5476, 2019; arXiv:1811.00574; doi:10.1093/mnras/sty2980

Paper IV: On the excursions of massive protostars in the Hertzsprung-Russell diagram,
Meyer D. M.-A., Haemmerle L., Vorobyov E.
MNRAS, Vol. 484, Issue 2, p.2482-2498, 2019; arXiv:1812.10762; doi:10.1093/mnras/sty3527

Paper V: An ALMA view of nascent massive multiple systems formed by gravitational instability,
Meyer D. M.-A., Kreplin A., Kraus S., Voroboyov E., Haemmerle L., Eisloeffel J.
MNRAS, Vol. 487, Issue 4, p.4473-4491, 2019; arXiv:1906.02015; doi:10.1093/mnras/stz1585

Paper VI: Parameter study for the burst mode of accretion in massive star formation,
Meyer D. M.-A., Voroboyov E., Elbaykan V., Eisloeffel J., Sobolev A., Stoehr M.
MNRAS, Vol. 500, Issue 4, pp.4448-4468, 2021; arXiv:2011.05017; doi:10.1093/mnras/staa3528

Paper VII: The burst mode of accretion in massive star formation with stellar inertia,
Meyer D. M.-A., Vorobyov E. I., Elbakyan V., Kraus S., Liu S.-Y., Nayakshin S., Sobolev A. M.
Accepted to MNRAS 2022, arXiv:2210.09662
https://academic.oup.com/mnras/advance-article/doi/10.1093/mnras/stac2956/6761717

Evolved massive stars nebulae

Paper VIII: On the observability of bow shocks of Galactic runaway OB stars,
Meyer D. M.-A., van Marle A.-J., R. Kuiper, W. Kley,
MNRAS, Vol. 459, Issue 2, p.1146-1158, 2016; arXiv:1603.04755; doi:10.1093/mnras/stw651

Paper IX: Bow shocks of hot massive stars in a magnetized medium,
Meyer D. M.-A., Mignone A., Kuiper R., Raga A., W. Kley,
MNRAS, Vol. 464, Issue 3, p.3229-3248, 2017; arXiv:1610.00543; doi:10.1093/mnras/stw2537

Paper X: 3D MHD astrospheres: applications to IRC-10414 and Betelgeuse,
Meyer D. M.-A., Mignone A., Petrov M., Scherer K., Velazquez P. F., Boumis P.
MNRAS, Vol. 506, Issue 4, pp.5170-5189, 2021; arXiv:2107.05513; doi:10.1093/mnras/stab2026

Paper XI: On the ring nebulae around runaway Wolf-Rayet stars,
Meyer D. M.-A., Oskinova L., Pohl M., Petrov M.
MNRAS, Vol. 496, Issue 3, pp.3906-3911, 2020; arXiv:2006.06027; doi:10.1093/mnras/staa1700

Paper XII: On the bipolarity of Wolf-Rayet nebulae,
Meyer D. M.-A.
MNRAS, Vol. 507, Issue 4, pp.4697-4714, 2021; arXiv:2108.09273; doi:10.1093/mnras/stab2426

Core-collapse supernova remnants

Paper XIII: Wind nebulae and supernova remnants of very massive stars,
Meyer D. M.-A., Petrov M., Pohl M.
MNRAS, Vol. 493, Issue 3, p.3548-3564, 2020; arXiv:2002.08268; doi:10.1093/mnras/staa554

Paper XIV: Non-thermal radio supernova remnants of exiled Wolf-Rayet stars,
Meyer D. M.-A., Pohl M., Petrov M., Oskinova L.
MNRAS, Vol. 502, Issue 4, pp.5340-5355, 2021; arXiv:2102.06000; doi:10.1093/mnras/stab452

Paper XV: Rectangular core-collapse supernova remnants: application to Puppis A,
Meyer D. M.-A., Velazquez P. F., Petruk O., Chiotellis A., Pohl M., Camps-Farina A., Petrov M., Reynoso E. M., Toledo-Roy J. C., Schneiter E. M., Castellanos-Ramirez A., Esquivel A.
MNRAS 2022, Volume 515, Issue 1, pp.594-605, arXiv:2206.14495; doi:10.1093/mnras/stac1832

Paper XVI: Pulsar wind nebulae of runaway massive stars,
Meyer D. M.-A., Meliani, Z.
MNRAS Letters 2022, Volume 515, Issue 1, pp.L29-L33, arXiv:2206.03916; doi:10.1093/mnrasl/slac062

Massive star formation

Monthly Notices
of the
ROYAL ASTRONOMICAL SOCIETY

MNRAS **464,** L90–L94 (2017)
Advance Access publication 2016 September 15

doi:10.1093/mnrasl/slw187

On the existence of accretion-driven bursts in massive star formation

D. M.-A. Meyer,[1]★ E. I. Vorobyov,[2,3] R. Kuiper[1] and W. Kley[1]

[1]*Institut für Astronomie und Astrophysik, Universität Tübingen, Auf der Morgenstelle 10, D-72076 Tübingen, Germany*
[2]*Department of Astrophysics, The University of Vienna, Vienna A-1180, Austria*
[3]*Research Institute of Physics, Southern Federal University, Stachki 194, Rostov-on-Don 344090, Russia*

Accepted 2016 September 13. Received 2016 September 10; in original form 2016 June 21

ABSTRACT

Accretion-driven luminosity outbursts are a vivid manifestation of variable mass accretion on to protostars. They are known as the so-called FU Orionis phenomenon in the context of low-mass protostars. More recently, this process has been found in models of primordial star formation. Using numerical radiation hydrodynamics simulations, we stress that present-day forming massive stars also experience variable accretion and show that this process is accompanied by luminous outbursts induced by the episodic accretion of gaseous clumps falling from the circumstellar disc on to the protostar. Consequently, the process of accretion-induced luminous flares is also conceivable in the high-mass regime of star formation and we propose to regard this phenomenon as a general mechanism that can affect protostars regardless of their mass and/or the chemical properties of the parent environment in which they form. In addition to the commonness of accretion-driven outbursts in the star formation machinery, we conjecture that luminous flares from regions hosting forming high-mass stars may be an observational implication of the fragmentation of their accretion discs.

Key words: stars: flare – stars: massive.

1 INTRODUCTION

Stars form in reservoirs of gas and dust, which collapse under their own gravity. However, a significant fraction of pre-stellar gas, thanks to the conservation of the gas net angular momentum, lands on to a centrifugally balanced circumstellar disc rather than falling directly on to the forming protostar. The manner in which matter accretes from the disc on to the star is still poorly understood and, notably, early spherical collapse models (Larson 1969; Shu 1977) that neglect the disc formation phase cannot explain the variety of mass accretion rates observed in present-day star-forming regions (Vorobyov 2009). In particular, these models yield accretion luminosities that are factors of 10−100 greater than the mean luminosity measured for nearby star-forming regions.

This so-called luminosity problem (Kenyon et al. 1990) can be solved if the accretion history on to the protostar is not smooth or quasi-constant, as predicted by spherical collapse models, but highly time-variable, as it naturally occurs in self-consistent models that follow the transition from clouds to protostellar discs (Dunham & Vorobyov 2012). In these models, protostars spend most of their time in the quiescent phase with low rate of accretion, which is interspersed with short but intense accretion bursts (see Vorobyov & Basu 2006, 2010; Machida, Inutsuka & Matsumoto 2011; Zhu et al. 2012; Vorobyov & Basu 2015). Spectacular examples of these burst systems are a special class of young stars called FU Orionis objects, which display outbursts of a factor of hundreds in luminosity which last several decades to hundreds of years. Such flares are thought to be due to drastic increases in the mass accretion rate of such young stars (Kley & Lin 1996).

Until recently, it was thought that FU-Orionis-type accretion and luminosity bursts were constrained to occur in the solar mass regime of present-day star formation (Audard et al. 2014). However, recent numerical hydrodynamics simulations of primordial disc formation around the first very massive stars have also revealed the presence of accretion bursts caused by disc gravitational fragmentation followed by rapid migration of the fragments on to the protostar (Stacy, Greif & Bromm 2010; Greif et al. 2012; Smith et al. 2012; Vorobyov, DeSouza & Basu 2013; Hosokawa et al. 2016). These studies have revealed highly variable protostellar accretion with multiple bursts, exceeding in numbers their present-day counterparts (DeSouza & Basu 2015). The same process of bursts driven by disc fragmentation operates around primordial supermassive stars, relaxing the ultraviolet photon output and enabling the stellar growth to the limit where general relativistic instability results in the formation of supermassive black holes (Sakurai et al. 2016).

Consequently, the emerging question is, how universal is variable accretion with episodic bursts in star formation and whether it can be associated with a unique physical mechanism? Time variability of accretion on to present-day massive stars at the early phase of their formation is a known process (Krumholz, Klein & McKee 2007; Peters et al. 2010; Kuiper et al. 2011; Klassen et al. 2016). Those

★ E-mail: dominique.meyer@uni-tuebingen.de

studies interpret this phenomenon as a natural consequence of the three-dimensional nature of their self-gravitating numerical simulations, while Kuiper & Yorke (2013) explains it by the interplay between mass accretion, stellar evolution, and radiative feedback. They report how asymmetries can develop in self-gravitating discs and generate an azimuthal anisotropy in the accretion flow on to the protostars. One can particularly notice that in addition to its variable character, it is interspersed with several accretion peaks (see fig. 4 of Klassen et al. 2016). In the above-cited references, the sharp increases of the accretion rate are generated in simulations assuming different pre-stellar core masses, ratio of kinetic by gravitational energy β, assuming either a *rigidly* rotating cloud or a turbulent pre-stellar core.

The study of a maser outflow in the high-mass star-forming region W75N equally conjectures that 'short-lived outflows in massive protostars are probably related to episodic increases in the accretion rates, as observed in low-mass star formation' (Carrasco-González et al. 2015). Additionally, a luminosity outburst of the massive ($\approx$20 $M_\odot$) young star S255IR-NIRS3 was reported in Fujisawa et al. (2015) by means of 6.7 GHz methanol maser emission. This emission line has been discovered by Menten (1991) and constitutes today a well-known tracer of high-mass star-forming regions (see Bartkiewicz, Szymczak & van Langevelde 2016, and references therein). Recent observation of the same object show brightness variations that resemble strongly FU-Orionis-type outbursts (Stecklum et al. 2016).

Motivated by the above listed numerical studies and observational arguments, we continue to investigate the burst phenomenon in the high-mass regime of star formation. We follow existing models showing accretion spikes in high-mass star formation, further analyse their nature in the context of the star–disc evolution, and conjecture on possible observational implications. This study is organized as follows. In Section 2, we review the methods that we utilize to carry out our high-resolution self-gravity radiation-hydrodynamical simulation of the formation and evolution of a disc surrounding a growing present-day massive protostar generated by the collapse of a *non-rigidly* rotating pre-stellar core. Our outcomes are presented and discussed in Section 3. Particularly, our model also generates such outbursts and we show that they are caused by the rapid migration of disc fragments on to the protostar. Finally, we conclude on their significances in Section 4.

2 NUMERICAL SIMULATION

We perform a 3D numerical radiation hydrodynamics simulation with the PLUTO code (Mignone et al. 2007, 2012) that has been augmented with several physics modules for (i) self-gravity of the gas and (ii) a careful treatment of the protostellar irradiation feedback (Kuiper et al. 2010a; Kuiper & Klessen 2013). Our model has been carried out using a spherical coordinate system (r, θ, ϕ) mapped with a grid of size $[r_{\rm min}, r_{\rm max}] \times [0, \pi/2] \times [0, 2\pi]$ that is made of $128 \times 21 \times 128$ cells, respectively. The grid resolution expands logarithmically in the radial direction, scales as $\cos(\theta)$ in the polar direction, is uniform in the azimuthal direction and assumes mid-plane symmetry about $\theta = \pi/2$, such that it allows us to reach sub-au spatial resolution in the inner region of the disc. The dynamics of the collapse and the accretion flow is calculated in the frame of reference of the fixed protostar that is considered to be evolving inside a static, semipermeable sink cell of initial mass $\approx 10^{-3}$ $M_\odot$ with a radius $r_{\rm min} = 10$ au such that the mass flux through it represents the protostellar accretion rate $\dot{M}$ on to the stellar surface. The creation of other sink cells is not allowed. As described in Kuiper et al. (2010b), we utilize $\dot{M}$ to self-consistently update the stellar mass and interpolate the pre-calculated protostellar evolutionary tracks of Hosokawa & Omukai (2009) to use them as boundary conditions for the radiation transport module.

We follow the gravitational collapse of an $M_{\rm c} = 100\,M_\odot$ pre-stellar core of outer radius $r_{\rm max} = 0.1$ pc. The radiation is regulated using the dust opacity prescription of Laor & Draine (1993) while the constant gas opacity is taken to be $\kappa_{\rm g} = 0.01$ cm^2 g^{-1}. This hybrid radiation transport method allows us to carefully treat disc thermodynamics and to generate the dust sublimation front in massive protostellar accretion discs (cf. Vaidya, Fendt & Beuther 2009). Our pre-stellar core has the canonical radial density distribution $\rho(r) \propto r^{-3/2}$. We do not consider a rigidly rotating core but impose a radial angular momentum distribution $\Omega(R) \propto R^{-3/4}$ with $R = r\sin(\theta)$ the cylindrical radius. We impose a ratio of rotational to gravitational energy $\beta = 4$ per cent, its initial temperature is uniformly taken to $T_{\rm g} = 10$ K and we set its pressure assuming that the gas is at solar metallicity and obeys an ideal equation of state. The dust temperature $T_{\rm d}$ is considered as equal to the gas temperature $T_{\rm g} = T_{\rm d}$. The collapse of the core and the evolution of the accretion disc is followed during 30 kyr.

3 RESULTS

3.1 Episodic accretion of dense gaseous clumps

The mid-plane density field from the simulation (in g cm^{-3}) is shown in Fig. 1 at different evolutionary times (in kyr). While panel (a) represents an overview of the whole disc region (where material orbits the star with approximately Keplerian velocity), panels (b)–(d) are zooms focusing on the inner region of the disc. The first snapshot (a) shows the circumstellar medium of the protostar at a time 18.10 kyr. In addition to the gas that is being accreted in the innermost 50 au of the disc, it develops inhomogeneities by gravitational instability that take the form of spiral arms terminated by dense blobs of gas orbiting at radii 450–800 au from the protostar. One of those Truelove-resolved arms ($\lambda/\Delta \sim$ 6–8, where λ is the Jeans length and Δ is the grid cell size; see Truelove et al. 1998) experiences a local increase in density and develops an overdense clump of circumstellar material at a radial distance of $\approx$200 au to the central star. This is how fragmentation occurs at those radii ($\geq$150 au) predicted by the analytic study of Kratter & Matzner (2006), despite the fact that only marginal fragmentation for discs like the one around our $\approx$4.5 $M_\odot$ protostar is foreseen (see also Fig. 3b).

By means of angular momentum transfer to the closest spiral arm, the clump migrates towards the protostar. At the onset of migration (Fig. 1a), the closest distance to which the clump can fall, assuming angular momentum conservation, is $\sim$2000 $R_\odot$, and it decreases to $\sim$260 $R_\odot$ (Fig. 1b) before to become comparable to the stellar radius of $\sim$90 $R_\odot$ shortly before entering the sink cell. This value is certainly an upper limit because the angular momentum of the clump decreases during its inward migration thanks to the gravitational interaction with the closest spiral arm (the gravitational torque acting on the clump is negative), as was shown in application to low-mass star formation by Vorobyov & Basu (2006). As a consequence, we expect the clump to fall directly on to the star. However, if the gas temperature in the clump interior exceeds 2000 K, the clump will further contract owing to dissociation of molecular hydrogen. In this case, not captured by our numerical simulations due to limited numerical resolution, its

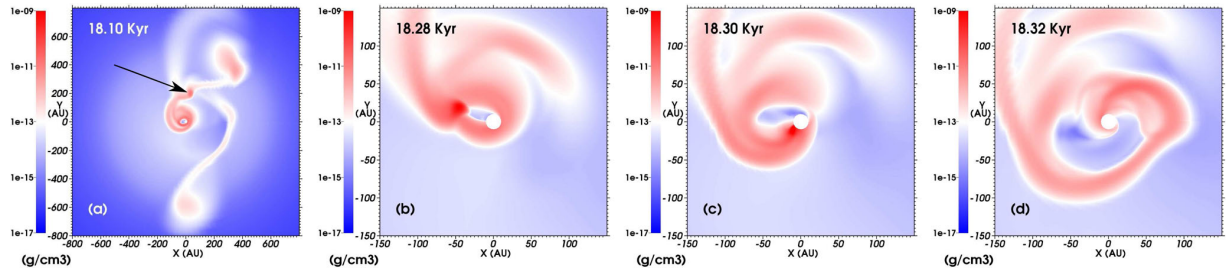

Figure 1. Mid-plane density in the centre of the computational domain around the time of the first outburst. (a) The region within 800 au when a clump forms in a spiral arm ∼200 au away from the protostar, at a time 18.10 kyr. Panel (b and c) display zooms to illustrate the migration and accretion of a part of the clump at times 18.28, 18.30, and 18.32 kyr, respectively. The density is plotted in g cm^{-3} on a logarithmic scale and the size of the panels is in au.

subsequent evolution will depend on the amount of rotational energy in the clump. By extrapolation of the clump properties formed in discs around solar-mass stars showing that about half of the clumps are rotationally supported (see Vorobyov 2016), we expect that part of the clump material will retain in the form of a disc/envelope around the newly formed protostar. This material can still be lost on to the central protostar via the Roche lobe creating an accretion burst though of lesser amplitude, as was shown in Nayakshin & Lodato (2012). Furthermore, high-resolution studies of low-mass and primordial star formation showed that further fragmentation may happen within in the innermost disc regions occupied by our sink cell, likely triggered by already existing outer fragments or efficient H_2 cooling and collisionally induced emission (see Greif et al. 2012; Meru 2015). If fragmentation in the inner disc occurs also in the case of high-mass star formation, this may provoke the formation of a pattern of very small clumps which complex mutual gravitational interactions can make them merging together, orbiting on to the protostar or being dynamically ejected away. This would modify the physics of accretion and the accretion luminosity of the protostar, however, heavy clumps migrating very rapidly will still fall directly on to the stellar surface. To follow this process in detail, however, a much smaller (than 10 au) sink cell and, as a consequence, much longer integration times are needed. We leave this investigation for a subsequent study.

At time 18.28 kyr, the clump is at about 60 au from the protostar (Fig. 1b) and its density reaches $\geq 10^{-9}$ g cm^{-3}. The self-gravitating clump adopts a slightly elongated shape due to the gravitational influence of the massive protostar. At time 18.30 kyr (Fig. 1c), the stretched clump starts wrapping around the sink cell. A part of its material is accreted on to the protostar, and, consequently, it affects the star's accretion luminosity $L_{\rm acc} \propto GM_\star \dot{M}/R_\star$ (see Section 3.2). When the clump starts migrating towards the star its radius is 20 au. As the clump approaches the sink cell, its mass has decreased to $\simeq$0.7 M$_\odot$ and its Hill radius decreases from approximately 35 au to $\lesssim$10 au, causing the clump to lose part of its mass in the diffuse outer envelope. Finally, about 0.55 M$_\odot$ is accreted through the sink cell. After time 18.32 kyr (Fig. 1d), the structure of the density field around the sink cell is that of a spiral of unaccreted dense gas material.

This scenario is episodic in the disc evolution and repeats itself at a time about 21.00 kyr when another clump is similarly accreted. The time interval between recurrent accretion bursts can be determined as the time needed to replenish the disc material lost during the last accretion event $t_{\rm repl} = M_{\rm cl}/\dot{M}_{\rm infall}$, where $M_{\rm cl}$ is the clump mass and $\dot{M}_{\rm infall}$ the mass infall rate on to the disc from the collapsing envelope (see Section 3.2). For $M_{\rm cl} \sim 0.55\,{\rm M}_\odot$ and $\dot{M}_{\rm infall} = (2\text{–}3) \times 10^{-4}\,{\rm M}_\odot$ yr^{-1}, typical values for the time of the bursts, the characteristic time of recurrent outbursts is $t_{\rm repl} \approx$ 2–2.5 kyr. If $t_{\rm repl}$ is regarded as the time required to increase the disc mass to the limit when the disc fragments, i.e. as the fragmentation time-scale, then the clump migration time-scale is much shorter than the fragmentation time-scale $t_{\rm repl}$. This is indeed evident from Fig. 1.

3.2 Accretion-induced strong outbursts

The accretion rate $\dot{M}$ on to the protostar exhibits rapid variations after the disc formation at about 4 kyr (see Fig. 2a). Comparing $\dot{M}$ measured at $r_{\rm min} = 10$ au with the smooth infall rate $\dot{M}_{\rm infall}$ from the envelope on to the disc measured at $r = 3000$ au, it becomes evident that the oscillations of $\dot{M}$ from about 10^{-6} to about 10^{-3} M$_\odot$ yr^{-1} are caused by the disc gravitational instability when filaments and spiral arms of different density and length converge towards the protostar. This correlation between the strength of disc gravitational instability and the protostellar accretion variability is well known in low-mass star formation (Dunham & Vorobyov 2012; Vorobyov & Basu 2015). The envelope, on the other hand, has a smooth density and velocity structure, and its infall rate that gradually increases with time for the initial free-fall time of the mass reservoir. Note also that the self-similar solution for the singular isothermal sphere (Shu 1977) computed as the mean isothermal infall rate at $r = 3000$ au, underestimates the accretion on to the protostar by about an order of magnitude (Fig. 2a), as previously noticed in the context of low-mass and high-mass star formation, see Vorobyov (2009) and Banerjee & Pudritz (2007), respectively.

At times 18.29 and 21.30 kyr the accretion of parts of the heaviest clumps occurs. The total luminosity of the protostar, i.e. the sum of its photospheric luminosity $L_\star$ and its accretion luminosity $L_{\rm acc}$ rises simultaneously (see Fig. 2b). The first luminosity outburst is particularly strong reaching in magnitude 5×10^5 L$_\odot$. The second burst is notably weaker because the radius of the protostar has greatly increased after the first one. These accretion and luminosity outbursts are a direct consequence of the accretion of in-spiralling clumps that fall on to the protostar because of the loss of angular momentum that has been exchanged with other structures of the disc such as spiral arms, filaments, and arcs. In Fig. 3, we present various disc and stellar properties around the time of the first burst. The accretion rate exhibits a rapid increase from $\dot{M} \sim 10^{-3}\,{\rm M}_\odot$ yr^{-1} to $\dot{M} \approx 10^{-1}\,{\rm M}_\odot$ yr^{-1} over a time interval of $\approx$10 yr, while the protostar experiences a flare reaching $\geq 5 \times 10^5$ L$_\odot$ (Fig. 3a). As the protostar accretes the clump, its mass increases while the disc mass decreases by the amount of mass of the accreted clump. This results in a remarkable step-like decrease of the disc-to-star mass ratio (see Fig. 3b), making the disc temporarily stable to gravitational fragmentation. It takes a few several kyr for the disc to accrete additional mass from the collapsing envelope and produce another

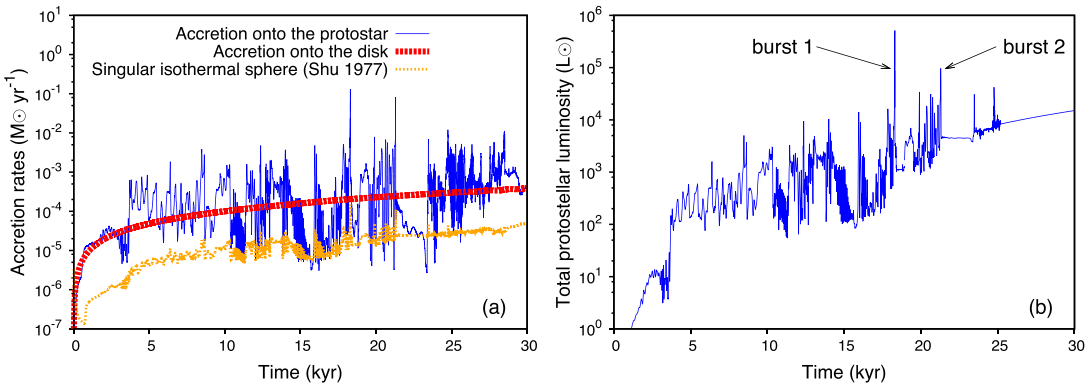

Figure 2. Left: accretion rate on to the protostar and mass infall rate on to the disc (in $M_\odot$ yr^{-1}). Right: total luminosity of the protostar (in $L_\odot$).

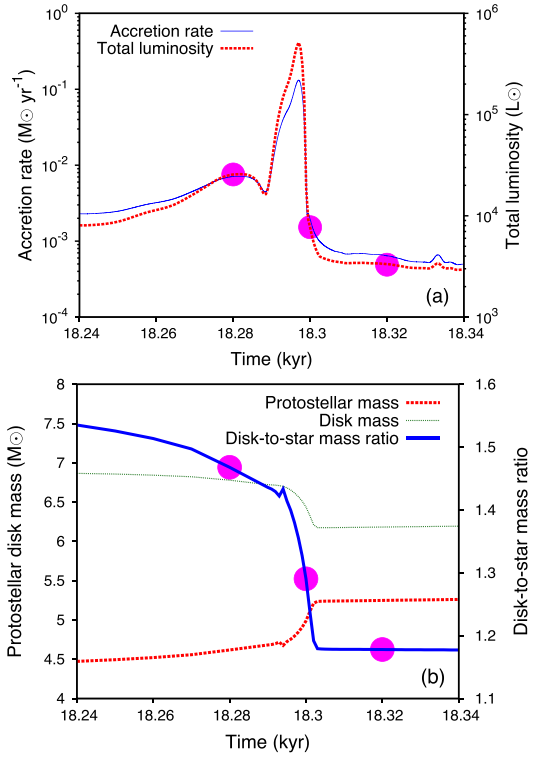

Figure 3. Upper panel: as in Fig. 2 during the time interval corresponding to the first accretion-induced outburst. Bottom panel: protostellar mass ($M_\odot$) and disc-to-star mass. The magenta dots mark the times of the zooms in Fig. 1(b)–(d).

similar fragmentation episode. This phenomenon repeats for as long as there is enough material in the envelope to replenish the disc mass, as was previously found for low-mass (Vorobyov 2010) and primordial star formation (Vorobyov et al. 2013; Hosokawa et al. 2016).

4 DISCUSSION AND CONCLUSION

We have confirmed the presence of strong peaks in the variable accretion history of high-mass protostars, already present in the literature for a wide range of initial conditions of the pre-stellar core. All models have a standard initial density distribution $\propto r^{-3/2}$ that is assumed in the absence of corresponding observations, except $\propto r^{-2}$ in Kuiper et al. (2011) and Kuiper & Yorke (2013). All rotating models preceding our study assumed cores in solid-body rotation. Radiation-hydrodynamics (with and without turbulence) and magnetohydrodynamics simulations include, with initial conditions in terms of of M_c and β-ratio, 100–200 $M_\odot$ without rotation (Krumholz et al. 2007), 100 $M_\odot$ with 2 per cent (Krumholz et al. 2009), 120 $M_\odot$ with a few per cent (Kuiper et al. 2011) 1000 $M_\odot$ with 5 per cent (Peters et al. 2010), 100 $M_\odot$ with 0.04–20 per cent (Seifried et al. 2011), and 100; 200 $M_\odot$ with 10.5; 5.3 per cent (Klassen et al. 2016), respectively, while we use 100 $M_\odot$ with 4 per cent. Our higher spatial resolution in the inner disc allows us to explicitly capture the fall of forming circumstellar clumps rather than modelling overdense filaments in the disc that wrap on to the star. It enables to study this process, well known in the low-mass and primordial regime of star formation as the so-called episodic accretion-driven outbursts, which we conclude to be also present in the high-mass regime of contemporary star formation. To confirm this result, we have performed preliminary simulations varying the initial rotation curves of the pre-stellar core. In the subsequent studies, numerical simulations with a smaller sink cell are needed to determine more in detail the final fate of the accreted clumps. However, we expect that the protostellar accretion history remains quantitatively similar in models with sink radii varied by a factor of 2, as was earlier shown for low-mass star formation (see Vorobyov & Basu 2015, and references therein).

We obtain the protostellar accretion history which is highly time-variable and shows sudden accretion spikes, as was found in several previous models of massive star-forming pre-stellar cores and interpreted as caused by azimuthal asymmetries in the accretion flow. The higher spatial resolution of our model reveals that, in addition to variable accretion indeed caused by the asymmetric character of its disc, the growing massive protostar can accrete material of gaseous clumps formed in spiral arms owing to disc gravitational fragmentation, which rapidly migrate towards the protostar and induce luminous protostellar outbursts. A similar rapid migration of dense clumps is present in gravitationally unstable discs around solar-mass stars, in primordial discs around the first stars and when high-mass planets form (Baruteau, Meru & Paardekooper 2011; Vorobyov 2013). Our work indicates that this also applies to the high-mass regime of star formation, which implies a change in the paradigm which, to the best of our knowledge, considered episodic accretion-induced protostellar outbursts as inherent to low-mass and

primordial star formation only. Our study shows that it concerns star formation in general, for a wide range of the physical properties such as the initial mass, β-ratio, angular momentum distribution or chemical composition of the parent environment in which stars form.

It supports the consideration of star formation as a process ruled by a common set of mechanisms leading to circumprotostellar structures similarly organized, but scaled-up with respect to each other as a function of the initial properties of their parental pre-stellar cores, as observationally suggested (Shepherd & Churchwell 1996; Fuente et al. 2001; Testi 2003; Keto & Zhang 2010; Johnston et al. 2015). Finally, we propose to consider flares from high-mass protostellar objects as a possible tracer of the fragmentation of their accretion discs. This may apply to the young star S255IR-NIRS3 that has recently been associated with a 6.7 GHz methanol maser outburst (Fujisawa et al. 2015; Stecklum et al. 2016), but also to the other regions of high-mass star formation from which originated similar flares (Menten 1991) and which are showing evidences of accretion flow associated with massive protostars, see e.g. in W3(OH) (Hirsch et al. 2012), W51 (Keto & Klaassen 2008; Zapata et al. 2009), and W75 (Carrasco-González et al. 2015).

ACKNOWLEDGEMENTS

We thank the anonymous reviewer for his valuable comments which improved the quality of the paper. This study was conducted within the Emmy Noether research group on 'Accretion Flows and Feedback in Realistic Models of Massive Star Formation' funded by the German Research Foundation under grant no. KU 2849/3-1. EIV acknowledges support from the Austrian Science Fund (FWF) under research grant I2549-N27 and RFBR grant 14-02-00719.

REFERENCES

Audard M. et al., 2014, Protostars and Planets VI. Univ. Arizona Press, Tucson, AZ, p. 387
Banerjee R., Pudritz R. E., 2007, ApJ, 660, 479
Bartkiewicz A., Szymczak M., van Langevelde H. J., 2016, A&A, 587, A104
Baruteau C., Meru F., Paardekooper S.-J., 2011, MNRAS, 416, 1971
Carrasco-González C. et al., 2015, Science, 348, 114
DeSouza A. L., Basu S., 2015, MNRAS, 450, 295
Dunham M. M., Vorobyov E. I., 2012, ApJ, 747, 52
Fuente A., Neri R., Martín-Pintado J., Bachiller R., Rodríguez-Franco A., Palla F., 2001, A&A, 366, 873
Fujisawa K., Yonekura Y., Sugiyama K., Horiuchi H., Hayashi T., Hachisuka K., Matsumoto N., Niinuma K., 2015, Astron. Telegram, 8286
Greif T. H., Bromm V., Clark P. C., Glover S. C. O., Smith R. J., Klessen R. S., Yoshida N., Springel V., 2012, MNRAS, 424, 399
Hirsch L. et al., 2012, ApJ, 757, 113
Hosokawa T., Omukai K., 2009, ApJ, 691, 823
Hosokawa T., Hirano S., Kuiper R., Yorke H. W., Omukai K., Yoshida N., 2016, ApJ, 824, 119
Johnston K. G. et al., 2015, ApJ, 813, L19
Kenyon S. J., Hartmann L. W., Strom K. M., Strom S. E., 1990, AJ, 99, 869
Keto E., Klaassen P., 2008, ApJ, 678, L109
Keto E., Zhang Q., 2010, MNRAS, 406, 102
Klassen M., Pudritz R. E., Kuiper R., Peters T., Banerjee R., 2016, ApJ, 823, 28
Kley W., Lin D. N. C., 1996, ApJ, 461, 933
Kratter K. M., Matzner C. D., 2006, MNRAS, 373, 1563
Krumholz M. R., Klein R. I., McKee C. F., 2007, ApJ, 656, 959
Krumholz M. R., Klein R. I., McKee C. F., Offner S. S. R., Cunningham A. J., 2009, Science, 323, 754
Kuiper R., Klessen R. S., 2013, A&A, 555, A7
Kuiper R., Yorke H. W., 2013, ApJ, 772, 61
Kuiper R., Klahr H., Dullemond C., Kley W., Henning T., 2010a, A&A, 511, A81
Kuiper R., Klahr H., Beuther H., Henning T., 2010b, ApJ, 722, 1556
Kuiper R., Klahr H., Beuther H., Henning T., 2011, ApJ, 732, 20
Laor A., Draine B. T., 1993, ApJ, 402, 441
Larson R. B., 1969, MNRAS, 145, 271
Machida M. N., Inutsuka S.-I., Matsumoto T., 2011, ApJ, 729, 42
Menten K. M., 1991, ApJ, 380, L75
Meru F., 2015, MNRAS, 454, 2529
Mignone A., Bodo G., Massaglia S., Matsakos T., Tesileanu O., Zanni C., Ferrari A., 2007, ApJS, 170, 228
Mignone A., Zanni C., Tzeferacos P., van Straalen B., Colella P., Bodo G., 2012, ApJS, 198, 7
Nayakshin S., Lodato G., 2012, MNRAS, 426, 70
Peters T., Banerjee R., Klessen R. S., Mac Low M.-M., Galván-Madrid R., Keto E. R., 2010, ApJ, 711, 1017
Sakurai Y., Vorobyov E. I., Hosokawa T., Yoshida N., Omukai K., Yorke H. W., 2016, MNRAS, 459, 1137
Seifried D., Banerjee R., Klessen R. S., Duffin D., Pudritz R. E., 2011, MNRAS, 417, 1054
Shepherd D. S., Churchwell E., 1996, ApJ, 472, 225
Shu F. H., 1977, ApJ, 214, 488
Smith R. J., Hosokawa T., Omukai K., Glover S. C. O., Klessen R. S., 2012, MNRAS, 424, 457
Stacy A., Greif T. H., Bromm V., 2010, MNRAS, 403, 45
Stecklum B., Caratti o Garatti A., Cardenas M. C., Greiner J., Kruehler T., Klose S., Eisloeffel J., 2016, Astron. Telegram, 8732
Testi L., 2003, in De Buizer J. M., van der Bliek N. S., eds, ASP Conf. Ser. Vol. 287, Galactic Star Formation Across the Stellar Mass Spectrum. Astron. Soc. Pac., San Francisco, p. 163
Truelove J. K., Klein R. I., McKee C. F., Holliman II J. H., Howell L. H., Greenough J. A., Woods D. T., 1998, ApJ, 495, 821
Vaidya B., Fendt C., Beuther H., 2009, ApJ, 702, 567
Vorobyov E. I., 2009, ApJ, 704, 715
Vorobyov E. I., 2010, ApJ, 723, 1294
Vorobyov E. I., 2013, A&A, 552, A129
Vorobyov E. I., 2016, A&A, 590, A115
Vorobyov E. I., Basu S., 2006, ApJ, 650, 956
Vorobyov E. I., Basu S., 2010, ApJ, 714, L133
Vorobyov E. I., Basu S., 2015, ApJ, 805, 115
Vorobyov E. I., DeSouza A. L., Basu S., 2013, ApJ, 768, 131
Zapata L. A., Ho P. T. P., Schilke P., Rodríguez L. F., Menten K., Palau A., Garrod R. T., 2009, ApJ, 698, 1422
Zhu Z., Hartmann L., Nelson R. P., Gammie C. F., 2012, ApJ, 746, 110

This paper has been typeset from a TEX/LATEX file prepared by the author.

Monthly Notices
of the
ROYAL ASTRONOMICAL SOCIETY

MNRAS **473,** 3615–3637 (2018) doi:10.1093/mnras/stx2551
Advance Access publication 2017 October 2

Forming spectroscopic massive protobinaries by disc fragmentation

D. M.-A. Meyer,[1]★ R. Kuiper,[1] W. Kley,[1] K. G. Johnston[2] and E. Vorobyov[3,4,5]

[1]*Institut für Astronomie und Astrophysik, Universität Tübingen, Auf der Morgenstelle 10, D-72076 Tübingen, Germany*
[2]*School of Physics and Astronomy, E.C. Stoner Building, The University of Leeds, Leeds LS2 9JT, UK*
[3]*Institute of Fluid Mechanics and Heat Transfer, TU Wien, Vienna A-1060, Austria*
[4]*Department of Astrophysics, The University of Vienna, Vienna, A-1180, Austria*
[5]*Research Institute of Physics, Southern Federal University, Stachki 194, Rostov-on-Don, 344090, Russia*

Accepted 2017 September 26. Received 2017 September 26; in original form 2017 March 13

ABSTRACT

The surroundings of massive protostars constitute an accretion disc which has numerically been shown to be subject to fragmentation and responsible for luminous accretion-driven outbursts. Moreover, it is suspected to produce close binary companions which will later strongly influence the star's future evolution in the Hertzsprung–Russel diagram. We present three-dimensional gravitation-radiation-hydrodynamic numerical simulations of 100 $M_\odot$ pre-stellar cores. We find that accretion discs of young massive stars violently fragment without preventing the (highly variable) accretion of gaseous clumps on to the protostars. While acquiring the characteristics of a nascent low-mass companion, some disc fragments migrate on to the central massive protostar with dynamical properties showing that its final Keplerian orbit is close enough to constitute a close massive protobinary system, having a young high- and a low-mass components. We conclude on the viability of the disc fragmentation channel for the formation of such short-period binaries, and that both processes – close massive binary formation and accretion bursts – may happen at the same time. FU-Orionis-type bursts, such as observed in the young high-mass star S255IR−NIRS3, may not only indicate ongoing disc fragmentation, but also be considered as a tracer for the formation of close massive binaries – progenitors of the subsequent massive spectroscopic binaries – once the high-mass component of the system will enter the main-sequence phase of its evolution. Finally, we investigate the *Atacama Large (sub-)Millimeter Array* observability of the disc fragments.

Key words: accretion, accretion discs – methods: numerical – stars: massive – stars: protostars.

1 INTRODUCTION

Massive star formation is a process happening in large, cold and opaque molecular clouds (Zinnecker & Yorke 2007; Langer 2012) but its repercussions upon the functioning of the interstellar medium are huge (Vink 2006, 2012). Understanding the formation of these high-mass stars in detail would allow us to predict – given a set of initial properties of the parent molecular cloud in which these stars form – their final fate, e.g. as core-collapse supernovae or gamma-ray bursts (Woosley, Heger & Weaver 2002). It has been shown that most of the massive stars experience (close) multiplicity even during their early main-sequence phase (Vanbeveren 1991; Chini et al. 2012; Mahy et al. 2013), which in turn strongly impacts their future evolutionary path in the Hertzsprung–Russel diagram (Dessart, Langer & Petrovic 2003; Petrović 2004; Sana et al. 2012). Additionally, while rapidly leaving their pre-main-sequence tracks, high accretion rates of circumstellar material $\sim 10^{-3}$ $M_\odot$ yr^{-1} can already affect the evolution of massive protostars before entering the main-sequence phase (Hosokawa & Omukai 2009; Haemmerlé et al. 2016, 2017).

Close massive binaries are believed to have formed in the surroundings of pre-main-sequence massive stars, by analogy with low-mass star formation (Bonnell & Bate 1994). Consequently, the detailed study of the protocircumstellar medium of young high-mass stars is a preponderant step towards a complete stellar evolution of massive stars. Amongst the several formation scenarios of massive binaries that have been proposed, the direct formation of low-mass companion(s) from the fragmentation of the accretion disc of a still growing massive protostar is one of the most natural (Cesaroni et al. 2006). It consists in assuming that high-mass star formation is a scaled-up version of the formation of low-mass stellar systems (Fuente et al. 2001; Testi 2003) and the formation of companions to massive stars might be seen as a scaled up version of gas giant planet formation via gravitational instability. This is strengthened by more and more unambiguous observations of collapsing high-mass pre-stellar cores (Beuther et al. 2015), jets (Purser et al. 2016) and accretion flows at their centre (Keto & Wood 2006). Several

★ E-mail: dominique.meyer@uni-tuebingen.de

circumstellar mechanisms associated with disc accretion have been observed, such as ionized HII regions channelled into cavities shaped by bipolar outflows (Cesaroni et al. 2010).

Direct imaging of discs are only beginning to be resolvable by modern facilities (Beuther, Linz & Henning 2012). Particularly, the *Atacama Large (sub-)Millimeter Array (ALMA)* recently revealed the existence of a Keplerian accretion disc around the forming O-type star AFL 4176 (Johnston et al. 2015) and in the surroundings of the young early massive star G11.92−0.61 MM1 (Ilee et al. 2016). More recently, observations of the high-mass proto-binary IRAS17216−3801 in Kraus et al. (2017) revealed together the circumstellar accretion discs of each massive components of a system similar to the numerical model of Krumholz et al. (2009a), themselves surrounded by a circumbinary disc.

The physics of collapsing gaseous clouds has been extensively studied (Evans 1999; Bergin & Tafalla 2007; McKee & Ostriker 2007, and references therein), and angular momentum conservation may lead to the formation of an accretion disc. Many mechanisms have been proposed to explain angular momentum transport in accretion discs around low-mass stars such as baroclinic instabilities (Klahr & Bodenheimer 2003; Klahr 2004), convective instabilities (Lin, Papaloizou & Kley 1993), magnetorotational instabilities (Ruden & Pollack 1991; Hawley & Balbus 1992; Flaig et al. 2012) and vertical shear instabilities (Nelson, Gressel & Umurhan 2013; Stoll & Kley 2014). None the less, gravitational torques arising from the innermost to the outer part of self-gravitational discs is the most efficient momentum transport phenomenon in discs around high-mass stars (Kuiper et al. 2011). After the gravitational collapse of pre-stellar cores, spiral arms developing in accretion discs may become unstable and experience local gravitational collapse leading to the formation of dense gaseous clumps – progenitors of massive giant planets, brown dwarfs or stellar companions (Stamatellos & Whitworth 2009a; Vorobyov 2013; Boss 2017). The migration of disc substructures (clumps and spiral arcs) on to their central protostar is responsible for violent accretion-driven outbursts broadly studied in the low-mass (Vorobyov 2010), the high-mass (Meyer et al. 2017) and the primordial (Vorobyov 2013; Hosokawa et al. 2016) regimes of star formation.

The surroundings of young stars has been investigated with sophisticated numerical models including appropriate physical processes such as the presence of the cloud magnetic fields (Banerjee, Pudritz & Holmes 2004; Banerjee & Pudritz 2006; Commerçon et al. 2010; Fendt 2011; Fendt & Sheikhnezami 2013; Machida & Hosokawa 2013; Seifried et al. 2013; Stepanovs, Fendt & Sheikhnezami 2014; Seifried et al. 2015) or (external) stellar radiation feedback (Yorke & Welz 1996; Richling & Yorke 1997; Kessel, Yorke & Richling 1998; Richling & Yorke 1998, 2000). However, only a small number of studies tackled the problem of star formation in its high-mass regime (Bonnell, Bate & Zinnecker 1998; Yorke & Sonnhalter 2002; Banerjee & Pudritz 2007; Krumholz, Klein & McKee 2007b; Kuiper et al. 2010; Peters et al. 2010; Commerçon, Hennebelle & Henning 2011; Kuiper et al. 2011; Seifried et al. 2011, 2012; Kuiper, Yorke & Turner 2015; Harries 2015; Kuiper, Turner & Yorke 2016; Klassen et al. 2016; Harries, Douglas & Ali 2017). The outcomes of those studies have been post-processed with radiative transfer methods in order to obtain synthetic observations, e.g. as seen from the *ALMA* telescope (Krumholz, Klein & McKee 2007a; Seifried et al. 2017). In addition to different spatial resolution that limits the proper capture of local gravitational collapse in a disc, those studies devoted to massive star formation differ by (i) the level of realism taken into account in order to model the protostellar feedback, (ii) the spatial resolution allowed by the scheme and (iii) the criteria applied to consider a dense region of the disc as a fragment, e.g. introducing sink particles (see Federrath et al. 2010, for a description of such technique).

The characterization of the fragmentation of self-gravitating discs is not a trivial task and several criteria necessary but not sufficient have been derived so far. The coupling of *N*-body solvers to hydrodynamical codes via the introduction of sink particles alleviate the computation of longer time-scales, because subgrid models save computing time since they do not have to resolve the smallest scales (Federrath et al. 2010). However, the required conditions of their creation throughout a simulation is subject to debate and may lead to artificial fragmentation which can, for instance, affects their host spiral arm dynamics. The two main of those criteria are the so-called Toomre and Gammie criteria and they compare the local effects of gravitational instability (Toomre 1963) and cooling (Gammie 1996) against the combined effects of the disc thermodynamics with the gas rotation shear, respectively. A large literature confronts these criteria with numerical simulations of protostellar and low-mass self-gravitating discs and highlights their sensitivity to initial conditions, viscosity, resolution and numerics (Stamatellos & Whitworth 2009b; Forgan et al. 2011; Lodato & Clarke 2011; Meru & Bate 2011; Forgan & Rice 2012; Rice, Forgan & Armitage 2012; Paardekooper 2012; Rice et al. 2014; Tsukamoto et al. 2015). Interestingly, in Klassen et al. (2016), numerical simulations of massive protostellar discs that fulfill those criteria may not necessarily form fragments, while this apparent stability is consistent with the so-called Hill criterion (Rogers & Wadsley 2012).

The consistency of an FU-Orionis-like scenario producing strong accretion outbursts by fast migration of disc debris has just been shown for massive star formation (Meyer et al. 2017) and is in accordance with the outflows observed in the young massive stellar system S255IR−SMA1 (Burns et al. 2016; Caratti o Garatti et al. 2017) and NGC6334I−MM1 (Hunter et al. 2017). In this study, we extend our numerical investigation of the stability of self-gravitating accretion discs around massive protostars and its connection to the accretion-driven flares as well as multiplicity. While the scientific literature already covered the question of the gravitational collapse of massive ($\geq$30 $M_\odot$) pre-stellar cores generating a massive protostar surrounded by a growing accretion disc, those studies generally assumed a simplified treatment of the protostellar feedback, i.e. within the FLD approximation (Krumholz et al. 2007b, 2009a) or suffer from a lack of resolution (Kuiper et al. 2011), especially in the region close to the star (Krumholz et al. 2007b, 2009a; Rosen et al. 2016; Klassen et al. 2016). The studies above presented evidence for (i) multiplicity in the high-mass regime by generating large-separation low-mass companions in spiral arms of massive protostellar accretion discs (Krumholz et al. 2007b; Rosen et al. 2016), (ii) massive binaries made of two high-mass protostars (Krumholz et al. 2009a), (iii) close massive binaries of two high-mass components (Bonnell & Bate 1994), while (iv) Klassen et al. (2016) does not conclude on the formation of stars around young massive protostellar objects. Nevertheless, no satisfactory theoretical models have yet explained the existence of small-separation/short-period low-mass companions to young high-mass stars. This is an important question because such systems are believed to evolve towards so-called spectroscopic (massive) binary systems, i.e. a particular class of close massive binaries made of an O-type star surrounded by one or more closely separated low-mass companions (see Mahy et al. 2013; Kobulnicky et al. 2014).

The goal of this study consists in testing the disc fragmentation scenario for the formation of those short-period massive binaries

made of a proto-O star and (at least) a close low-mass companion, using high-resolution hydrodynamical simulations of the gravitational collapse of rotating pre-stellar cores. We perform three-dimensional numerical simulations including self-gravity, radiative transport and a mid-plane-symmetric spherical computational domain centred at a sink cell in which a protostar is assumed to form and evolve. The young star acquires mass by disc accretion, as in many current studies devoted to disc fragmentation around low-mass and primordial protostars (Vorobyov & Basu 2007; Vorobyov et al. 2013; Vorobyov & Basu 2015; Hosokawa et al. 2016). Our highly resolved models neglect the internal turbulence and magnetization of the collapsing pre-stellar cores but allow a sub-au spatial resolution close to the protostar which is higher than in any models previously published so far. We find that all our modelled discs show clear sign of instability, fragment and generate a series of sudden increase of the accretion rate caused by fragments migrating towards the central protostar. Interestingly, some of those migrating clumps have interior thermodynamic properties indicating that they may be secondary pre-stellar embryos, and, therefore, we conclude on the viability of disc fragmentation as a channel for the formation of close low-mass companions to forming massive stars.

Our study is organized as follows. We begin in Section 2 with introducing the reader to our numerical setup. In Section 3, we describe our particular initial conditions in terms of density and angular frequency distribution of the collapsing pre-stellar cores that we consider. Their evolution, the formation of accretion discs and their subsequent fragmentation are qualitatively described in Section 4. In Section 5, we investigate the physical and numerical processes at work in this study, i.e. the role of the central protostellar irradiation and the effects of the spatial resolution in the simulations, while we further test our outcomes for accretion disc against various criteria for disc stability in Section 6. In Section 7, we detail the fate of the disc debris and investigate their properties as forming low-mass stars and further discuss our findings in the context of the formation of close massive binary systems. In Section 8, we compare our results to previous theoretical and observational studies. Finally, we give our conclusions in Section 9.

2 METHOD

In the following paragraphs, we introduce the reader to the method used to perform our numerical simulations. Our simulations model the collapse of a pre-stellar core forming around a self-gravitating accretion disc that evolves as being irradiated by the time-dependent luminosity of the central protostar. We detail the various assumptions and prescriptions used to model the microphysical processes of the gas and the dust of the pre-stellar core, describe the manner we treat the protostellar feedback on to the disc and we present the computational grid and the numerical scheme utilized in this study.

2.1 Governing equations

As other studies devoted to star formation, we work at the interplay between gas dynamics, gravity and radiation transport. The hydrodynamics is described by the equations of fluid dynamics for compressible gas that consist of the relations for mass,

$$\frac{\partial \rho}{\partial t} + \nabla \cdot (\rho \boldsymbol{v}) = 0, \tag{1}$$

momentum,

$$\frac{\partial \rho \boldsymbol{v}}{\partial t} + \nabla \cdot (\rho \boldsymbol{v} \otimes \boldsymbol{v}) + \nabla p = \boldsymbol{f}, \tag{2}$$

and total energy conservation,

$$\frac{\partial E}{\partial t} + \nabla \cdot ((E + p)\boldsymbol{v}) = \boldsymbol{v} \cdot \boldsymbol{f} \tag{3}$$

where ρ, $\boldsymbol{v}$ and p are the Eulerian variables, i.e. the mass density, the vector velocity and the gas pressure, respectively. The gas assumes an ideal equation of state $p = (\gamma - 1)E_{\rm int}$ where $\gamma = 5/3$ is the constant adiabatic index. The variable $E_{\rm int}$ is the internal energy of the medium such that,

$$E = E_{\rm int} + \frac{1}{2}\rho \boldsymbol{v}^2, \tag{4}$$

represents the total energy of the plasma.

The radiation transport scheme is taken from Kuiper et al. (2010). In equations (2) and (3) the quantity,

$$\boldsymbol{f} = -\rho \nabla \Phi_{\rm tot} - \frac{\rho \kappa_{\rm R}(T_\star)}{c}\boldsymbol{F}_\star - \frac{\rho \kappa_{\rm R}(T)}{c}\boldsymbol{F}, \tag{5}$$

is the force density vector with $\Phi_{\rm tot}$ total gravitational potential, $\kappa_{\rm R}$ the Rossland opacity, c the speed of light, $\boldsymbol{F}$ the radiation flux and $\boldsymbol{F}_\star$ the stellar radiation flux. The equations of radiation transport govern the time evolution of the radiation energy density $E_{\rm R}$,

$$\frac{\partial E_{\rm R}}{\partial t} + f_{\rm c} \nabla \cdot (\boldsymbol{F} + \boldsymbol{F}_\star) = 0, \tag{6}$$

where $f_{\rm c} = 1/(c_{\rm v}\rho/4aT^3 + 1)$ with $c_{\rm v}$ the specific heat capacity and a the radiation constant. We solve equation (6) in the flux-limited diffusion (FLD) approximation, where $\boldsymbol{F} = -D\nabla E_{\rm R}$. The diffusion constant is $D = \lambda c/\rho\kappa_{\rm R}$ where λ is the flux limiter and $\kappa_{\rm R}$ is the mean Rossland opacity. The relation,

$$\frac{\boldsymbol{F}_\star(r)}{\boldsymbol{F}_\star(R_\star)} = \left(\frac{R_\star}{r}\right)^2 {\rm e}^{-\tau(r)}, \tag{7}$$

reports the decrease of the flux during the ray tracing of the stellar incident radiation with the stellar radius $R_\star$ and $\tau(r) = \kappa_{\rm P}(T_\star)\rho(r)$ being the optical depth of the medium. The total opacity takes into account both the gas and the dust attenuation of the radiation, i.e. $\kappa_{\rm P} = \kappa_{\rm P}^{\rm g} + \kappa_{\rm P}^{\rm d}$, where $\kappa_{\rm P}^{\rm g}$ and $\kappa_{\rm P}^{\rm d}$ are the gas and dust opacities, respectively. To this end, we use constant gas opacity of $\kappa_{\rm P}^{\rm g} = 0.01\,{\rm cm}^2\,{\rm g}^{-1}$ and utilize the tabulated dust opacity of Laor & Draine (1993). Gas and dust temperature are calculated assuming the equilibrium between the dust temperature and the total radiation field,

$$aT^4 = E_{\rm R} + \frac{\kappa_{\rm P}(T_\star)}{\kappa_{\rm P}(T)}\frac{|\boldsymbol{F}_\star|}{c}. \tag{8}$$

We employed the time-dependent treatment of the dust for photo-evaporation and sublimation described in Kuiper et al. (2011) and used in subsequent works (Hosokawa et al. 2016). At every time-step and in each cells of the mesh, the dust temperature that is obtained solving equation (8) is compared with the local evaporation temperature of the dust grains $T_{\rm evap}$. It is initially determined in Pollack et al. (1994) and has been reformulated in Isella & Natta (2005) as the power-law expression $T_{\rm evap} = g\rho^\beta$ where $g = 2000\,{\rm K}$ and $\beta = 0.0195$. It permits to adjust the local dust-to-gas mass ratio by taken into account the evaporation ($T > T_{\rm evap}$) and the sublimation ($T < T_{\rm evap}$) of the dust grains component of our mixture treated as a single fluid. It particularly applies to the hot regions of the computational domain such as in the innermost part of the disc, see Kuiper et al. (2010).

The stellar luminosity represents the total irradiation, i.e. the sum of the photospheric luminosity $L_\star$ plus the accretion luminosity $L_{\rm acc} \propto M_\star \dot{M}/R_\star$ of the central protostar. This quantity is mainly a

function of the stellar radius $R_\star$, the effective temperature $T_{\rm eff}$ and the accretion rate $\dot{M}$ that are interpolated from the pre-main-sequence stellar evolutionary models assuming high accretion of Hosokawa & Omukai (2009). The tracks allow us to time-dependently adapt the protostellar luminosity as a function of the accretion history on to the forming massive star.

The gravity of the gas is taken into account calculating the total gravitational potential felt by a volume element of the gas,

$$\Phi_{\rm tot} = \Phi_\star + \Phi_{\rm sg}, \tag{9}$$

where $\Phi_\star = -GM_\star/r$, with $M_\star$ the protostellar mass and G the universal gravity constant. The self-gravity of the gas $\Phi_{\rm sg}$ is described by the Poisson equation,

$$\boldsymbol{\Delta}\,\Phi_{\rm sg} = 4\pi G\rho, \tag{10}$$

that we solve separately. This allows the simulation to tend towards a solution which reports both the accretion phenomena on to the central protostar but also the gravitational interactions that disc substructures share with each other. No additional artificial shear viscosity is injected into the system, via e.g. an α-prescription of Shakura & Sunyaev (1973), since three-dimensional models produce self-consistently gravitational torques accounting for efficient angular momentum transport (Kuiper et al. 2011; Hosokawa et al. 2016).

2.2 Grid, boundary conditions and numerical scheme

We perform our three-dimensional numerical simulations using a static, non-uniform grid mapped on to a spherical coordinate system (r, θ, ϕ). Assuming mid-plane symmetry of the computational domain with respect to $\theta = \pi/2$, the grid size is $[r_{\rm in}, r_{\rm max}] \times [0, \pi/2] \times [0, 2\pi]$ along the radial, polar and azimuthal directions, respectively. The grid is made of $128 \times 21 \times 128$ cells so that we use squared cells in inner region of the mid-plane. The mesh is logarithmically stretched in the radial direction, i.e. their size radially increases as $r(10^f - 1)$ with $f = \log(r_{\rm max}/r_{\rm in})$, and it expands as $\cos(\theta)$ in the polar direction (Ormel, Shi & Kuiper 2015) whereas it is uniform along the azimuthal direction. This grid choice allows us to save computing time in reducing the total number of cells while having both a high spatial resolution of up to $\Delta r < 1$au in the inner region of the mid-plane. Particularly, the grid resolution is at below 10 au in the $\approx$500 au region of the domain. The inner boundary in $r_{\rm in} = 10$ au, whereas the outer one is $R_{\rm c} = 0.1$ pc. Outflow conditions are assigned at both boundaries of the radial directions so that we can on-the-fly estimate, e.g. $\dot{M}$ as the mass of the material crossing $r_{\rm in}$.

We solve the above described equations using the PLUTO code (Mignone et al. 2007, 2012) that has been augmented with several modules for self-gravity, radiation transport and stellar evolution that are described in Kuiper et al. (2010, 2011) and Kuiper & Yorke (2013b). The distinctive feature of this method consists in carefully treating the stellar radiation, first ray tracing the photons from the stellar atmosphere to the disc and then mimicking their propagation into the disc by FLD (see also Kuiper et al. 2012; Kuiper & Klessen 2013). This algorithm has shown the existence of a dust-free front in the massive stars' surroundings (Kuiper et al. 2010) and this has been strengthened by semi-analytical calculations (Vaidya et al. 2011).

Our method uses a Godunov-type solver made of a shock-capturing Riemann solver embedded in a conservative finite-volume scheme. We use the HLLC solver for fluid dynamics that is ruled by the Courant–Friedrich–Levy parameter set to $C_{\rm cfl} = 0.1$ (Run 3, see Section 3) and to higher initial values ($C_{\rm cfl} = 0.2-0.3$) for the other runs. Furthermore, we use the minmod flux limiter and the WENO3 interpolation scheme with the third-order Runge–Kutta (RK3) time integrator. Additionally, we use the FARGO (Fast Advection in Rotating Gaseous Objects) method (Masset 2000) which permits larger time-steps than if exclusively controlled by a strict application of the Courant–Friedrich–Levy rule. FARGO has been designed to be utilized in the context of problems with a background orbital motion like our simulations and it is available in PLUTO (Mignone et al. 2012). Therefore, our overall scheme is third order in space and time. To reduce the huge computing time of such calculations, the radiation transport is performed within the grey approximation. The self-gravity of the gas is calculated up to reaching $\boldsymbol{\Delta}\,\Phi_{\rm sg}/\Phi_{\rm sg} \leq 10^{-5}$ as in Kuiper et al. (2011). Finally, note that the seed perturbations for the non-axisymmetric modes are numerical (cf. Kuiper et al. 2011; Hosokawa et al. 2016).

3 INITIAL CONDITIONS

In this section, we present the initial internal structure of the pre-stellar core of our numerical calculations. We first describe the gas density and velocity distribution laws that we consider, before presenting our models and their respective initial characteristics.

3.1 Gas density distribution

We consider a rotating pre-stellar core that has a radial mass density distribution $\rho(r)$ represented by the following standard power law,

$$\rho(r) = K_\rho r^{\beta_\rho}, \tag{11}$$

where K_ρ is a function of the core size and mass and where β_ρ is a negative exponent characterizing the steepness of the density profile, respectively. The total mass of the pre-stellar core that is included between the origin of the computational domain and its outermost boundary $r_{\rm max}$ is $M_{\rm c} = M(r = r_{\rm max})$ where,

$$M(r) = M_{\rm c}\left(\frac{r}{R_{\rm c}}\right)^{\beta_\rho+3}, \tag{12}$$

and one can therefore determine the constant K_ρ. The density distribution of the pre-stellar core is,

$$\rho(r) = \frac{(\beta_\rho+3)}{4\pi}\frac{M_{\rm c}}{R_{\rm c}^{\beta_\rho+3}} r^{\beta_\rho}, \tag{13}$$

with r the distance to the central protostar.

3.2 Gas velocity distribution

Similarly, an angular momentum distribution is initially imposed in the pre-stellar core via a particular choice in the initial velocity field in the ϕ direction. The angular velocity profile is given by,

$$\Omega(R) = \Omega_0\left(\frac{R}{r_0}\right)^{\beta_\Omega}, \tag{14}$$

where $R = r\sin(\theta)$ is the cylindrical radius and where β_Ω is an exponent that describes the profile such that $\beta_\Omega = 0$ corresponds to a core in solid-body rotation. The parameter Ω_0 normalizes the distribution and depends on the ratio of kinetic energy with respect to the gravitational energy $\beta = E_{\rm rot}/E_{\rm grav}$ that initially characterizes the system. Considering both density and momentum profiles in

Table 1. Initial conditions. Quantity β_Ω is the slope of the angular velocity index of the pre-stellar core. Simulations are run until $t_{\rm end}$ (in kyr).

Models	Angular frequency index β_Ω	$t_{\rm end}$ (kyr)	Motivation
Run 1	0.0	50.0	Solid-body rotation (cf. run M100 in Klassen et al. 2016)
Run 1-noIrr	0.0	45.0	cf. Run 1, without protostellar irradiation
Run 1-LR	0.0	40.0	cf. Run 1, with a coarser spatial resolution
Run 1-HR	0.0	32.1	cf. Run 1, with a finer spatial resolution
Run 2	−0.35	40.0	Intermediate initial angular velocity radial distribution
Run 3	−0.75	35.0	Steep initial angular velocity radial distribution (see Meyer et al. 2017)

equations (11) and (14), the gravitational energy of the pre-stellar cloud is,

$$E_{\rm grav} = \frac{\beta_\rho + 3}{2\beta_\rho + 5}\frac{GM_{\rm c}^2}{R_{\rm c}}, \quad (15)$$

whereas its rotational kinetic energy is,

$$E_{\rm rot} = \frac{(\beta_\rho + 3)}{(\beta_\rho + 2\beta_\Omega + 5)}\frac{\Omega_0^2 M_{\rm c} R_{\rm c}^{2(\beta_\Omega+1)}}{4r_0^{2\beta_\Omega}}\int_0^\pi {\rm d}\theta\,\sin(\theta)^{3+2\beta_\Omega}, \quad (16)$$

which must be integrated numerically. Finally, one can, for a given molecular cloud characterized by a choice of $M_{\rm c}$, β_ρ and β_Ω and fixing the desired ratio β, find the corresponding Ω_0.

3.3 Models presentation

The momentum distribution is initially implemented into the code via the ϕ component of the velocity $v_\phi(R) = R\Omega(R)$, while the other components of the velocity field are $v_{\rm r} = v_\theta = 0$. We assume that the percentage of kinetic energy with respect to the gravitational energy is $\beta = 4$ per cent for all three models. Additionally, we assume that the dust is coupled to the gas with a gas-to-dust mass ratio of 100. The thermal pressure is set to $p = R\rho T_{\rm c}/\mu$ with R the ideal gas constant, μ the mean molecular weight and $T_{\rm c} = 10$ K the temperature of the pre-stellar core. The dust temperature $T_{\rm d}$ is considered as equal to the gas temperature $T_{\rm g} = T_{\rm d} = T_{\rm c}$. We run three simulations (our Table 1) initially setting the density distribution $\beta_\rho = -3/2$ that is a typical value for a collapsing pre-stellar core that generates a present-day massive protostar (van der Tak et al. 2000; Mueller et al. 2002). The difference between simulations concern the initial angular velocity distribution of the pre-stellar cloud, which is $\beta_\Omega = 0$ (Run 1, cf. Klassen et al. 2016), $\beta_\Omega = -0.35$ (Run 2) and $\beta_\Omega = -3/4$ (Run 3). Run 3 is the same simulation as in Meyer et al. (2017), but with a longer run-time. Our simulations explore the parameter space in terms of initial angular frequency distribution $\Omega(R)$ at fixed $M_{\rm c}$, $R_{\rm c}$, $T_{\rm c}$, β and β_ρ. Additionally, we perform three other models with the same initial conditions as Run 1, but without protostellar irradiation (Run 1-noIrr), with a lower spatial resolution using a grid of 64 × 11 × 64 cells (Run 1-LR) and with a higher spatial resolution using a grid of 256 × 41 × 256 cells (Run 1-HR) (see Section 5).

4 ACCRETION DISC FRAGMENTATION

In this section, we analyse the properties of the collapsing pre-stellar cores. We follow the evolution of the density fields in the simulations and discuss their differences before describing the fragmentation of the accretion discs. For each model, we look at the accretion rate on to the protostar and its feedback to the disc as accretion-driven outbursts.

4.1 Accretion disc fragmentation and protostar evolution

In Figs 1–3, we plot the mid-plane density field (in g cm^{-3}) from our models Run 1, 2 and 3 at six different representative evolutionary times (in kyr) elapsed since the beginning of the simulations. The figures show the inner region of ≈ few (k)au around the protostar, while the computational domain is much more extended ($R_{\rm c}$ = 0.1pc). Every figure corresponds to times after the formation of the disc at times 11.5, 7.2 and 3.7 kyr for our models Run 1, 2 and 3, respectively, once pre-stellar core material orbits the protostar with approximately Keplerian velocity. Despite of the fact that the overall evolution of the discs is globally similar, sensitive morphological differences appear. The accretion discs develop spiral arms under the effects of gravitational instability and the discs adopt the typical filamentary structure of self-gravitating systems under the effects of rotation (Lodato 2007).

The discs are rather compact if $\beta_\Omega = 0$ (Run 1) and more extended if the initial angular velocity distribution is steeper, because it favours the fast growth of large spiral arms, e.g. if $\beta_\Omega = -0.75$ (Run 3). All discs strongly fragment by developing inhomogeneous regions in their spiral arms, however, discrepancies arise with the distribution of those circumstellar clumps, as seen in Figs 1–3. While orbiting the protostar in their host spiral arm, the clumps can migrate to larger radii or rapidly move inwards under the effects of gravitational torques, before disappearing into the sink cell. Note that the overdensity at ≈200 au from the sink cell in the spiral arm of Fig. 3(d) is subject to a rapid migration on to protostar that is described in detail in Meyer et al. (2017). This scenario of falling clumps repeats itself throughout the integration time of all models. Particularly, this mechanism is responsible for the variable accretion on to the protostar and it governs its mass evolution (see section 7.1).

Fig. 5 plots time evolution of the mass of the protostars (in $M_\odot$, thick dotted red line). We measure the mass of the discs (in $M_\odot$, thin dotted yellow line) and the disc-to-star mass ratio (thin solid blue line) in our simulations Run 1 (a), Run 2 (b) and Run 3 (c) by considering the material in a cylinder of radius 1500 au and height 500 au centred at the origin and perpendicular to the disc, as suggested by Klassen et al. (2016). Such a cylinder contains the discs throughout their evolution (see Fig. 4). The vertical dotted black line marks the time of the onset of the disc formation. The mass of our protostars monotonically increases as a function of time with a slope corresponding to accretion rate of circumstellar material. The periods of smooth mass increase, e.g. at times between 11.5 and 26.5 kyr (Fig. 5a) is produced by the baseline (but variable) accretion rate generated when non-fragmenting portions of spiral arms wrap and vanish into the sink cell (Fig. 1a). This dominates the mass accretion at the time of disc formation and during the early disc fragmentation. At later times, the stellar mass evolution experiences sudden increases of up to a few solar masses, e.g. at times 27.6, 35.1 or 41.0 kyr, which marks the accretion of clumps.

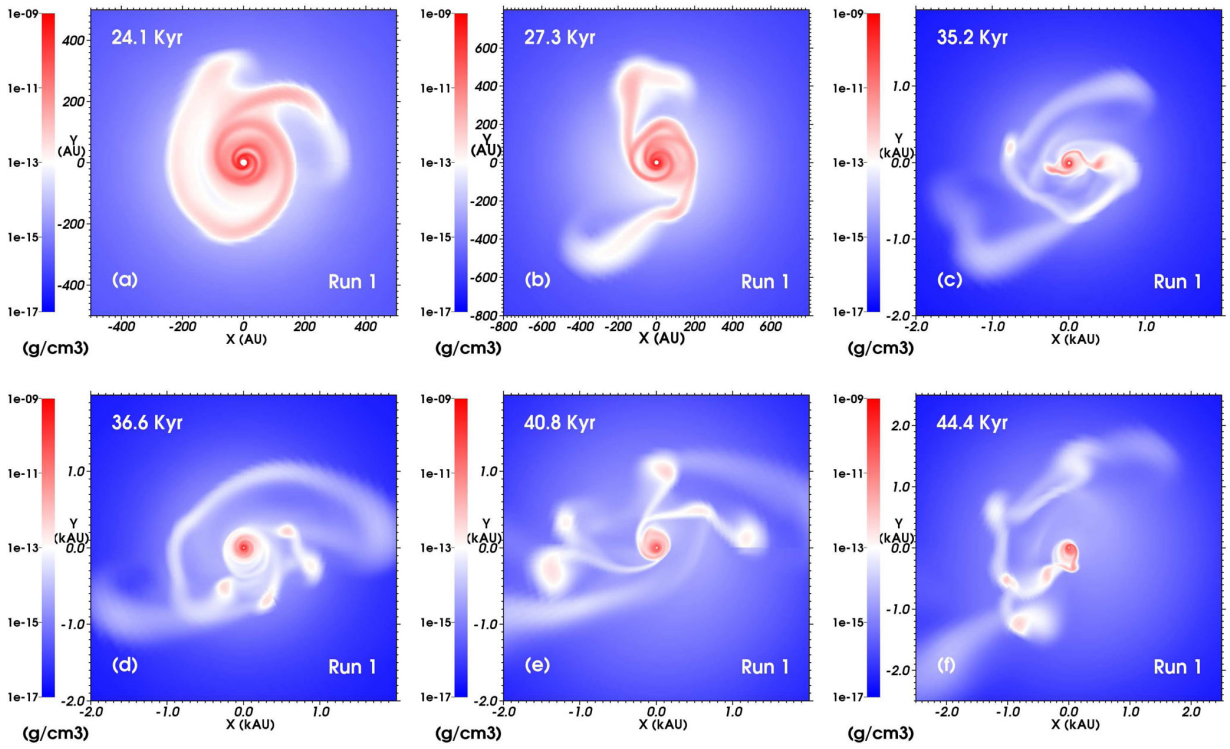

Figure 1. Mid-plane density (in g cm^{-3}) of the accretion disc generated in Run 1, showed at different characteristic times of its evolution (in kyr). The density is plotted on a logarithmic scale and the size of the panels is in au (top left and middle panel) or kau (elsewhere).

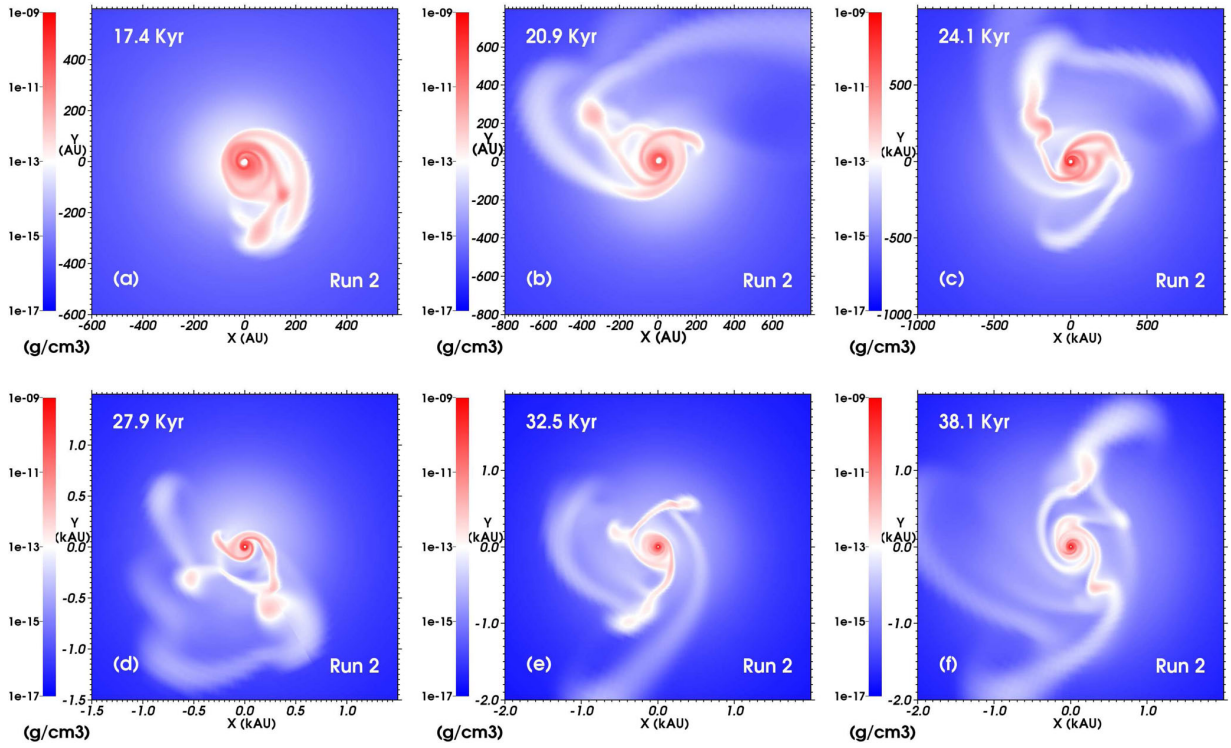

Figure 2. Similar to Fig. 1 for Run 2.

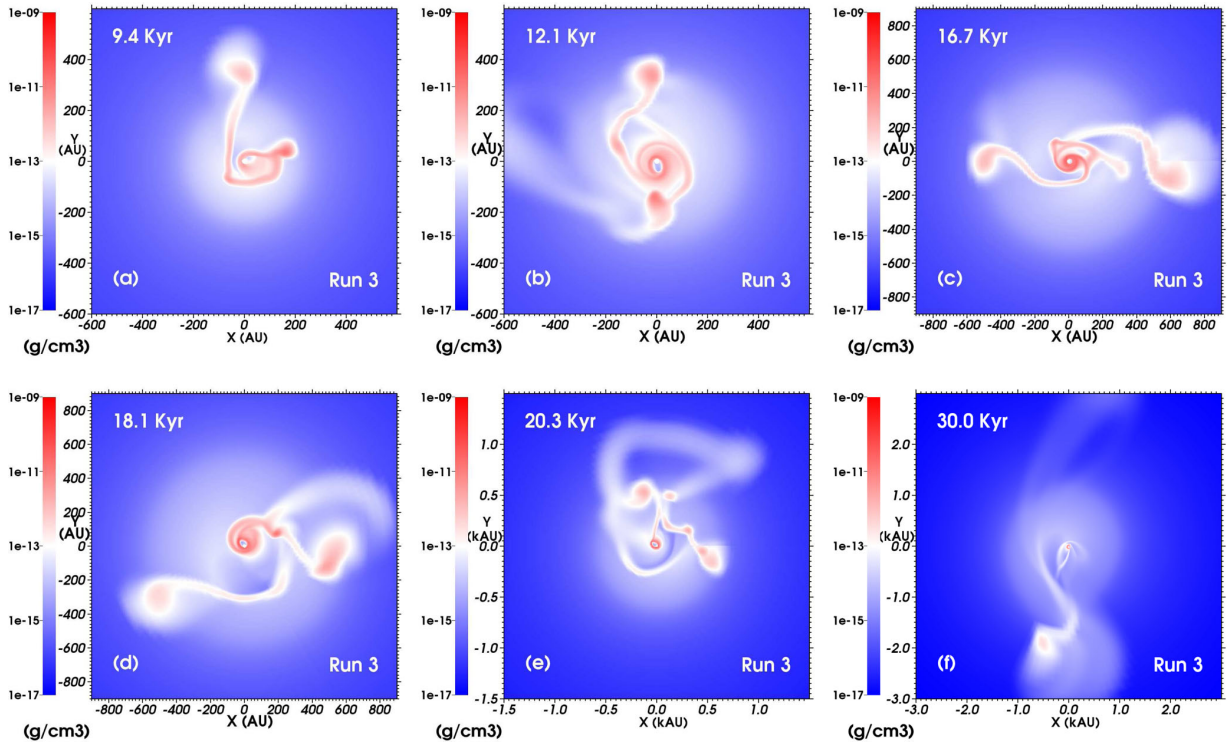

Figure 3. Similar to Fig. 1 for Run 3.

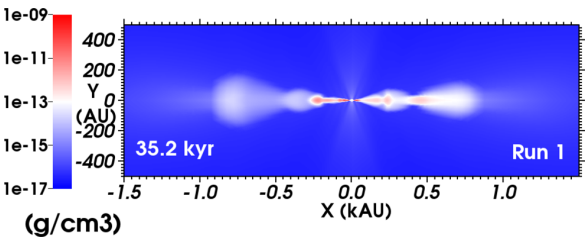

Figure 4. Vertical density structure (in g cm^{-3}) of the accretion disc generated in Run 1 at a time 35.2 kyr and shown with $\phi = 0$. The density is plotted on a logarithmic scale and the size of the figure is in (k)au.

As our model with solid-body rotation forms a disc that is smaller in size, it produces more fragments, which in turn generate a larger number of step-like jumps in the protostellar mass history (Fig. 5a) than the other runs (Figs 5b and c). The computational cost of our simulations increases as a function of the steepness in the initial velocity distribution, which is the only parameter differentiating Runs 1−3. Consequently, we can have long integration times for the model with solid-body rotation and form a 35 $M_\odot$ protostar while the other stars reach only 25 and 18 $M_\odot$, respectively. The disc mass evolves accordingly, with sudden decreases when a clump leaves the disc to fall on to the protostar (see Section 4.2). The disc-to-star mass evolution reports the simultaneous increases of the protostellar and disc mass. Importantly, the disc fragmentation does not prevent accretion on to the protostar.

4.2 Variable accretion on to the protostar

Fig. 6 displays the accretion properties of the systems. The figure shows the accretion rate (in $M_\odot$ yr^{-1}, from the envelope on to the disc measured at $r = 3000$ au (cf. Meyer et al. 2017), thick dotted red line) and the accretion rate on to the protostar (in $M_\odot$ yr^{-1}, thin solid blue line) in our Run 1 (a), Run 2 (b) and Run 3 (c). As a result of disc formation and its subsequent fragmentation, mass accretion on to the protostar is highly variable. The variety of lengths and sizes of the filaments and gaseous clumps accreted by the protostar generates the variability of $\dot{M}$. This has already been found in several previous numerical studies, e.g. devoted to low-mass star formation (Vorobyov & Basu 2007; Machida, Inutsuka & Matsumoto 2011; Vorobyov & Basu 2015), and in the context of primordial star formation (Vorobyov et al. 2013). When a dense circumstellar clump falls on to the protostar, violent accretion spikes happen thanks to the mechanism depicted in Meyer et al. (2017). All models have such remarkable accretion peaks, with increases of the accretion rate up to about a few 10^{-1} $M_\odot$ yr^{-1} over a time interval of ≈20 yr. The time interval separating the accretion spikes corresponds to a temporary damping of the oscillations of the accretion rate induced by the leftover of the clumps which are gravitationally swung away (Meyer et al. 2017). The frequency of the occurrence of accretion bursts is about $M_{\rm cl}/\dot{M}_{\rm d} \approx 2 - 0.5$ kyr with $M_{\rm cl} \approx 0.5 -$ few $M_\odot$ the typical mass of a circumstellar clumps and $\dot{M}_{\rm d}$ being the mass infall rate on to the disc.

4.3 Protostellar luminosity and accretion-driven outbursts

Fig. 7 shows the evolution of the photospheric luminosity $L_\star$ (dotted red line) and the total luminosity $L_{\rm tot} = L_\star + L_{\rm acc}$ (solid blue line) where $L_{\rm acc} = GM_\star\dot{M}/2R_\star$ is the accretion luminosity of the

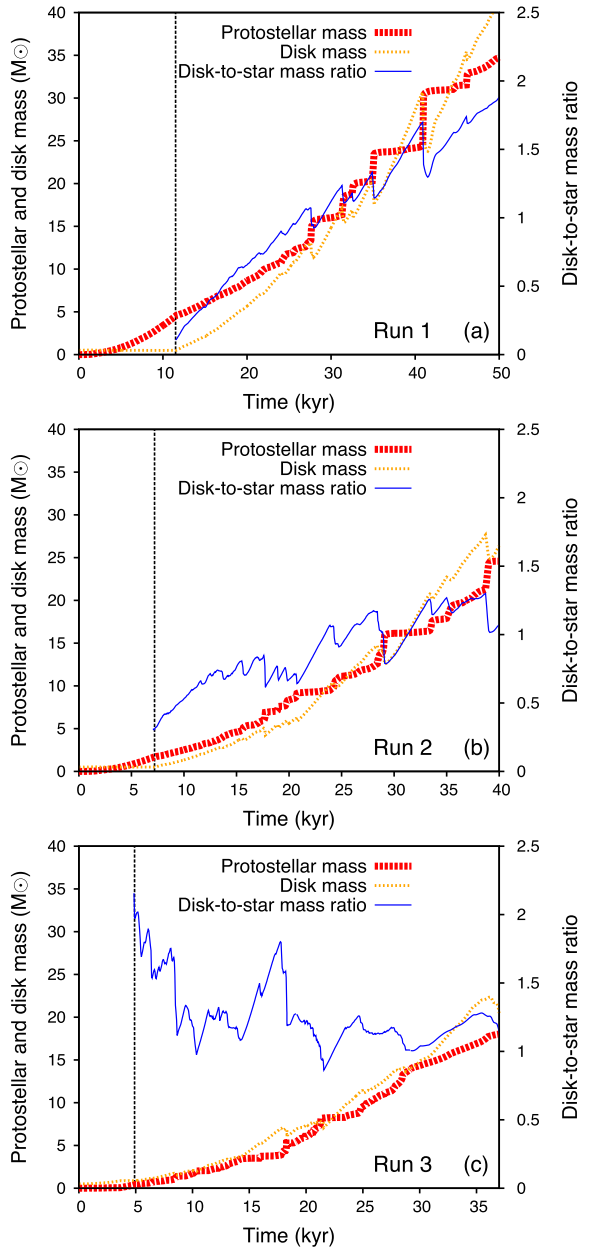

Figure 5. Protostellar mass, disc mass and disc-to-star mass ratio evolving with time. Vertical lines mark the end of the free-fall collapse and the onset of the disc formation.

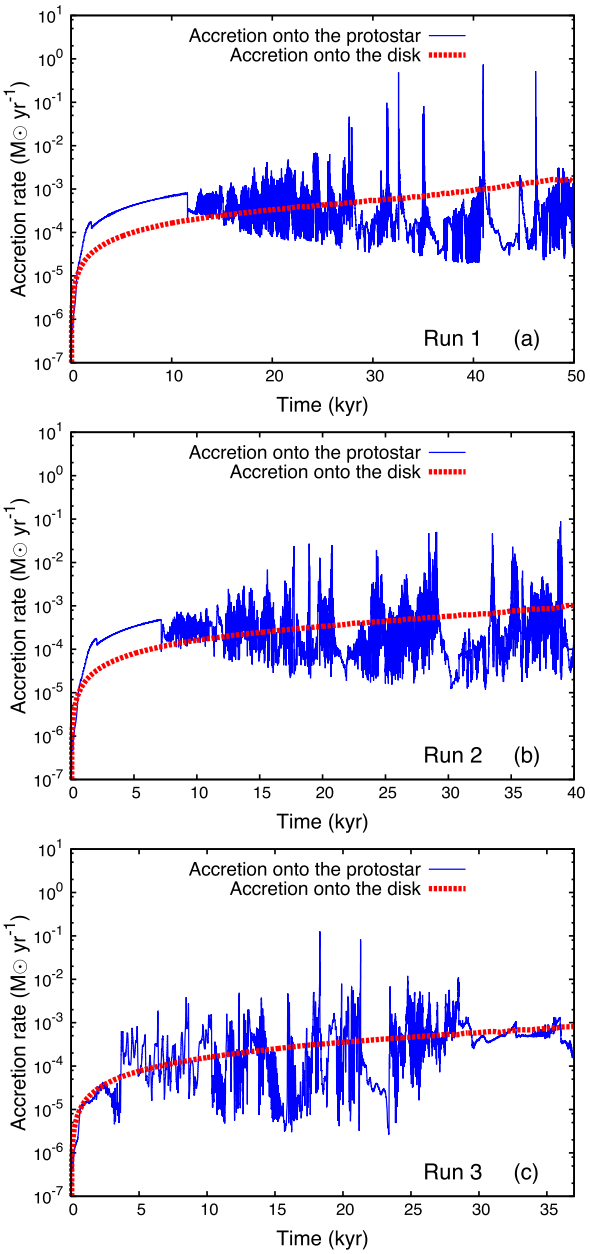

Figure 6. Accretion rates on to the protostar-disc systems.

protostar (in $L_{\odot}$) throughout our simulations Run 1 (a), Run 2 (b) and Run 3 (c). To each strong increase of the accretion rate corresponds a rise of the bolometric luminosity of the protostar that is clearly above the mean stellar luminosity. The intensity of those accretion-driven outbursts is also influenced by the protostellar radius, i.e. a bloated protostar decreases the intensity of accretion-driven outburst, since $L_{\rm acc} \propto 1/R_{\star}$ (Hosokawa & Omukai 2009). This explains why the relative intensity of the flares (governed by the accretion luminosity at times $\geq$ 25–30 kyr) does not correspond to the relative strength of the associated accretion peaks, see e.g. the forest of peaks in Figs 6(a) and 7(a) at times $\geq$ 30 kyr, respectively.

The bloating of the young star has not finished, i.e. much longer integration times of the system, ideally up to the zero-age main-sequence time, is necessary in order to produce detailed statistics of accretion-driven outbursts as a function of the initial conditions of our models.

Interestingly, Run 3 does not have further accretion peaks after times $\geq$ 28 kyr, at least for the integration times that we consider. This model generates our more extended disc of radius $\approx$4 kau, which develops structures resembling a second accretion disc bridged by a gaseous filament. By second disc, we mean that the circumstellar clump concerned, while rotating, migrates to radii larger than $\approx$2 kau and begins accreting from the primary disc but

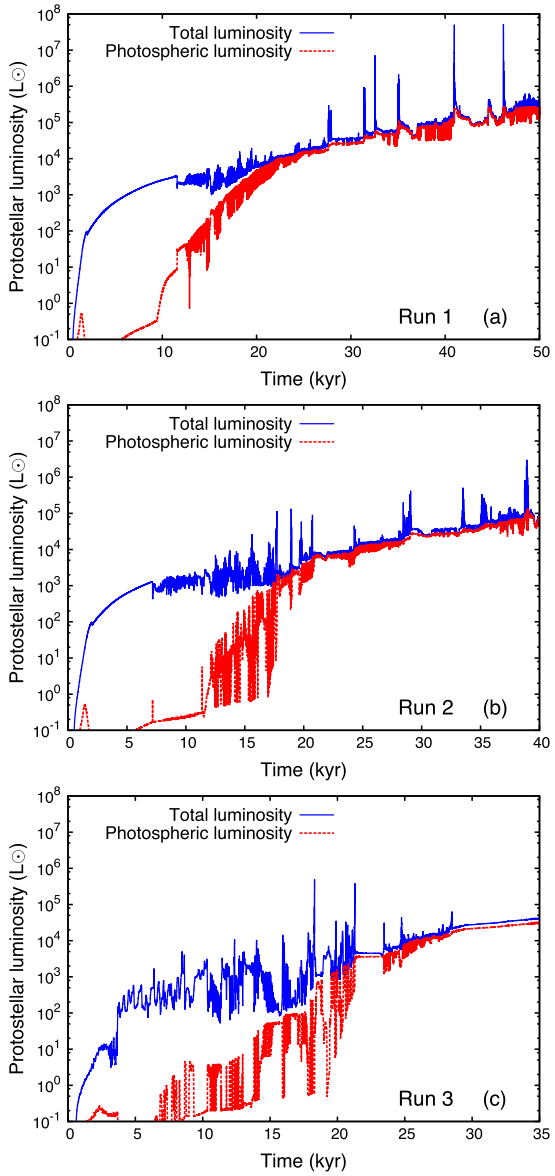

Figure 7. Bolometric protostellar luminosities (blue solid lines) and photospheric emission of our protostars (dotted red lines). The light curves report the changes in the accretion rates of Fig. 6.

also from the still collapsing pre-stellar core material, such that the clump forms its own accretion disc (not properly resolved by our logarithmic grid at this distance from the primary protostar), see also simulations of Offner et al. (2010) and Kratter et al. (2010). The mid-plane density field suggests that it may be due to the formation of a massive binary star of separation ≈2 kau (Fig. 3f), however, our logarithmically expanding grid in the radial direction does not resolve the Jeans length at such large radii from the central protostar and, consequently, it does not allow us to conclude on this with more certitude. Our series of models show that the phenomenon of accretion-driven outbursts is a general feature of the parameter space in terms of initial angular velocity distribution. It stresses the very close similarities existing between the variability of forming massive stars and the other regimes of star formation, see the extended literature about the formation of low-mass stars (Vorobyov & Basu 2010, 2015) and primordial stars (Stacy, Greif & Bromm 2010; Greif et al. 2011, 2012; Hosokawa et al. 2016; Sakurai et al. 2016). Further work will provide us with more statistics on luminous accretion-driven outbursts to be compared with the FU-Orionis-like outburst of S255IR (Burns et al. 2016; Caratti o Garatti et al. 2017).

5 PHYSICAL AND NUMERICAL EFFECTS

The role of the incident protostellar radiation and effects of the spatial resolution on the fragmentation of an accretion disc formed around a young high-mass star are examined in this section.

5.1 Effects of protostellar irradiation

Fig. 8 compares the accretion rate history (a) and the protostellar mass evolution (b) of two models with $\beta_\Omega = 0$. Run 1 considers the protostellar radiation feedback in addition to the radiation transport in the accretion disc (thin blue solid line), while Run 1-noIrr ignores the protostellar irradiation (thick dotted red line). The mean accretion rate on to the central growing star is similar in both cases, with a mean value of about 10^{-4}–$10^{-3}\,M_\odot\,yr^{-1}$ and lowest values of $\approx 5\times10^{-5}$–$5\times10^{-4}\,M_\odot\,yr^{-1}$. The absence/presence of stellar feedback does not prevent regular accretion spikes in the mass accretion rate from developing (Fig. 8a). In the non-irradiated case, the accretion bursts are more numerous, appear sooner and are of higher mean intensity than their irradiated counterparts, although no remarkable spikes reaching intensities of more than a few $10^{-1}\,M_\odot\,yr^{-1}$ happen, as in Run 1.

This indicates an earlier but more violent fragmentation of the disc of Run 1-noIrr as compared to the irradiated disc of Run 1. Once fragmentation is triggered (at times larger than 30 kyr), the variable accretion rate reaches values slightly higher than in the non-irradiated case. However, once the first accretion-driven outbursts take place, both stellar mass histories are very analogous for times $\leq$ 18 kyr (Fig. 8b), with differences arising later. Indeed, despite of this similar qualitative stellar mass evolution ending with the formation of a star of mass $> 30\,M_\odot$ at times ≥ 45 kyr, Run 1-noIrr globally reports a higher number of step-like increases of $M_\star$. They correspond to the accretion of a larger number of dense circumstellar clumps. One can notice that the migrating gaseous clumps are of smaller individual mass in Run 1-noIrr, leading to less intense accretion spikes compare to those of Run 1 (Fig. 8a). This is consistent with the disc being of lower temperature, having smaller Jeans length and thus lower mass clumps.

Fig. 9 shows two snapshots of the mid-plane density field of Run 1-noIrr, at times 24.1 and 27.3 kyr. The figures correspond to times before (a) and after (b) the initial fragmentation of the disc in Run 1 (Figs 1a and b). This time interval brackets the formation of the first fragment in the simulation of the accretion disc with irradiation (Run 1). When stellar feedback is considered, the disc is still stable at time a 24.1 kyr (Fig. 1a) while in the case without incident protostellar radiation it has already multiple distinct spiral arms (Fig. 9a) in which develop overdense regions (Fig. 9b) that are responsible for the formation of (migrating) circumstellar clumps, producing the accretion-driven bursts in Fig. 8(b). Earlier disc fragmentation happens since the close surroundings of the non-irradiated disc are colder and therefore fragment faster. Our comparison models illustrate the role of the direct protostellar heating in the stabilization of self-gravitating accretion discs around young high-mass stars.

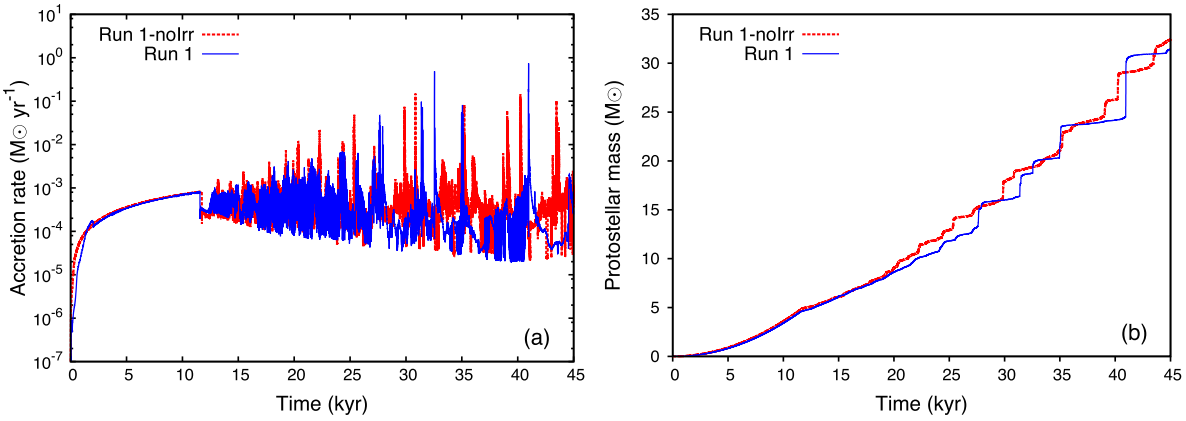

Figure 8. Comparison between (a) the accretion rate and the (b) mass evolution of a model considered with (Run 1) and without irradiation (Run 1-noIrr).

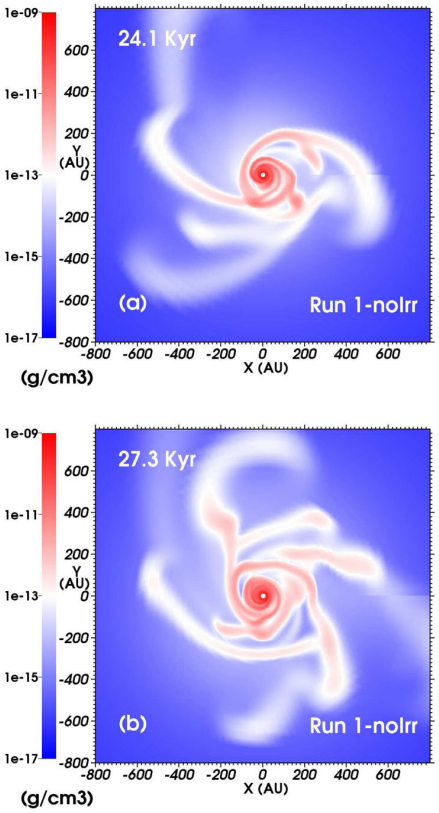

Figure 9. Mid-plane density field of the model with initial solid-body rotation ($\beta_\Omega = 0$) modelled without protostellar irradiation (Run 1-noIrr).

5.2 Effect of resolution

Fig. 10 plots the mid-plane density field in Run 1-LR (left), Run 1 (middle) and Run 1-HR (right) at times 24.1 (top panels), 27.3 kyr (cf. Run 1 in Figs 1a and b), and at times at times $>$ 30 kyr (bottom panels), when the fragmentation process is already triggered. In all three models, the disc at a time of 24.1 kyr has the shape of twisted spiral of distance about 350–400 au from the protostar (Figs 10a–c). The innermost part of the disc is more resolved in Run 1 than in Run 1-LR and has numerous thin arms spiraling around the sink cell (Fig. 10b), while Run 1-HR has just exhibited the first formation signs of denser substructure in its outer arm (Fig. 10c). At time 27.3 kyr, one can see that extended spiral arms have already grown. The lowest resolution model (Run 1-LR) does not show traces of undergoing substructure formation (Fig. 10d), while Run 1 has portions of spirals arms including the curved, denser sections (Fig. 10e). Since the only difference between all models is the grid resolution, one can directly estimate the effect the spatial resolution has on disc fragmentation. The highest resolution model evolves similarly, except that the first fragment forms and migrates sooner (Fig. 10f). At times $>$ 30 kyr, the patterns show either spiral arms (Fig. 10g), or fragments in the case of the most-resolved model (Fig. 10i). The bottom line of panels illustrates the effects of spatial resolution on the random development of the disc structures once the fragmentation process begins. Using the finest grid resolution to date, we point the prime importance for the treatment of the close stellar environment for reliability of numerical disc fragmentation studies. This was expected from comparison with disc fragmentation studies in the low-mass star formation regime where the irradiation is negligible, see e.g. Lichtenberg & Schleicher (2015), but also from models in the context of primordial star formation, in which stellar feedback is efficiently at work, see Greif et al. (2011), Vorobyov, DeSouza & Basu (2013), Machida & Nakamura (2015) and fig. 3 of Hosokawa et al. (2016) for a resolution study.

Fig. 11 is similar to Fig. 8 for models Run 1 and Run 1-HR, which are our two most resolved models having an initial rigidly rotating pre-stellar core ($\beta_\Omega = 0$). One can notice the good agreement between their accretion rate histories (Fig. 11a). Especially, the first remarkable accretion spike happens similarly at the times of $\approx$22 kyr showing that the solution has converged up to the formation, fall and accretion of the first gaseous clumps. Further discs evolution logically differs in the sense that a higher resolution reveals the typical stochastic and fractal behaviour of fragmenting disc. The number of accretion-driven events slightly increases with the disc resolution because more clumps are formed, i.e. Run 1-HR has 3 separated spikes reaching $\geq 10^{-2}\,M_\odot\,yr^{-1}$, while Run 1 has only a twin one of the same intensity (Fig. 11c). The accreted mass per unit time is similar in both models and the mass evolution of the central protostar converges up to $\approx$ 22 kyr, the time of the first clump migration. At times $<$ 30 kyr, the mean mass of a gaseous

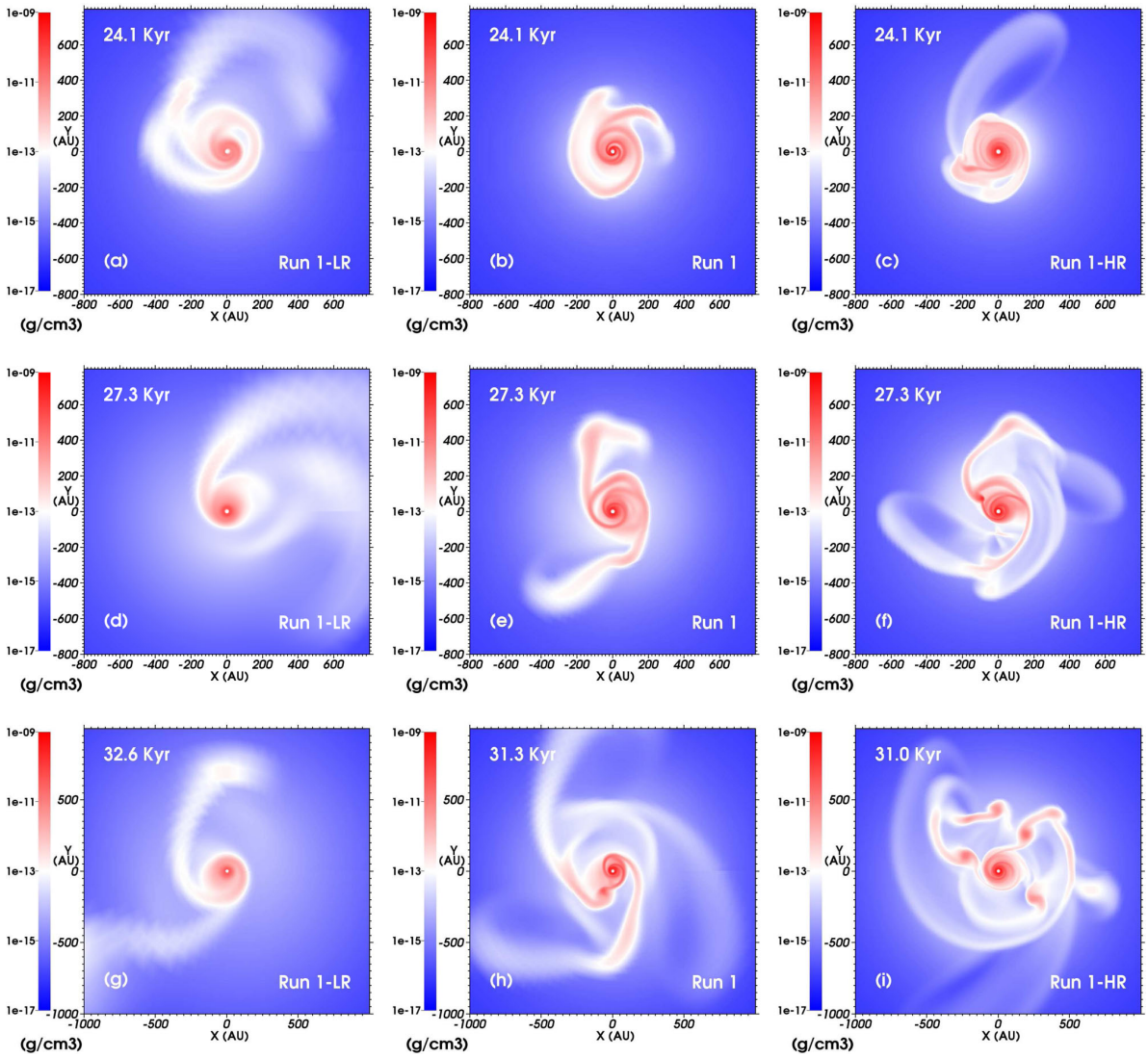

Figure 10. Density fields of models with initial solid-body rotation, considered with different spatial resolution (Run 1-LR, Run 1 and Run 1-HR).

clump is smaller in Run 1-HR because more numerous but lighter fragments form in the disc, and large accretion events are replaced by the successive accretion of lighter fragments for a roughly equal total mass, see for example at times ≈ 26–29 kyr (Fig. 11b).

We have performed a resolution study by increasing the resolution of our models up to the highest spatial resolution to date. The above presented elements show that our solutions are sufficient to extract the parameters required for our analyses and conclusions in terms of accretion variability, inner disc fragmentation and migrating gaseous clumps.

5.3 Jeans length resolution

This paragraph investigates our discs with respect of the Truelove criterion (Truelove et al. 1998), which stipulates that the local Jeans length must be resolved by at least four grid cells. The so-called Jeans number is defined by,

$$n_{\rm J} = \frac{\Delta}{\lambda_{\rm J}}, \tag{17}$$

where,

$$\lambda_{\rm J} = \left(\frac{\pi c_{\rm s}^2}{G\rho}\right)^{1/2}, \tag{18}$$

is the Jeans length and Δ is the grid cell size. Therefore, the Truelove criterion reads,

$$\frac{1}{n_{\rm J}} = \frac{\lambda_{\rm J}}{\Delta} \geq 4, \tag{19}$$

and the clump-forming regions of the disc must satisfy this relation. Figs 12(a)–(c) shows the minimal disc mid-plane inverse Jeans number $1/n_{\rm j}$, estimated from different simulation snapshots and plotted as a function of the radial direction for the inner 1000 au

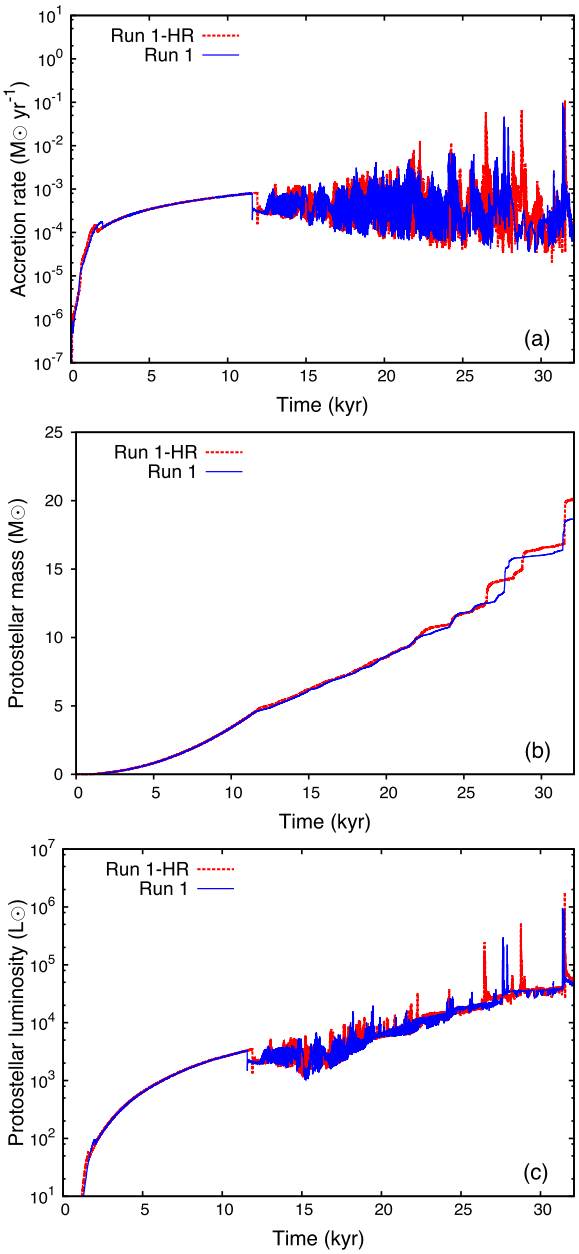

Figure 11. Comparison between the (a) accretion rate, (b) the mass evolution and (c) the luminosity of a model with several grid resolutions.

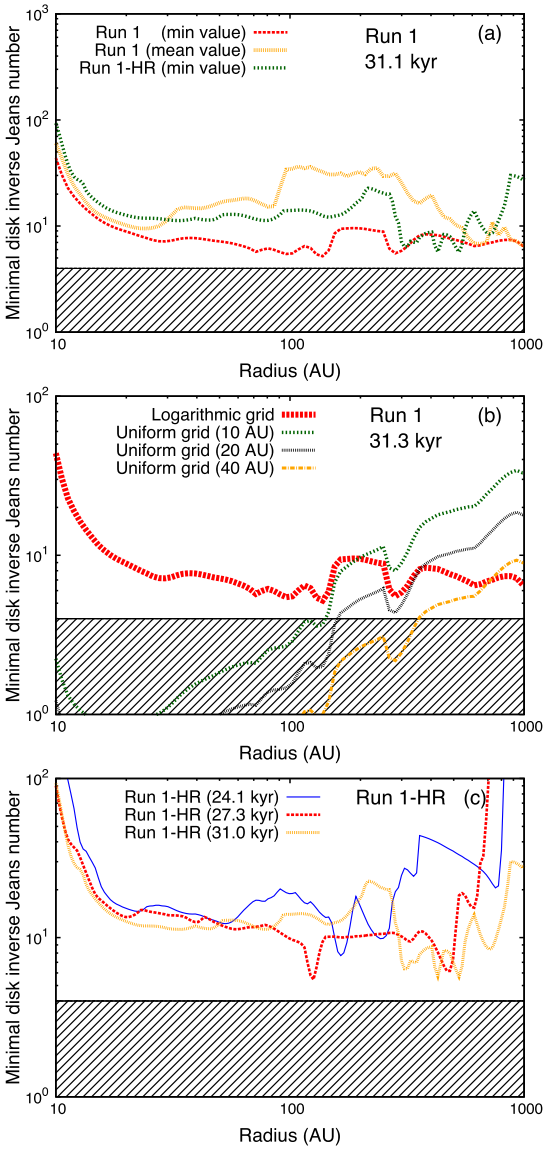

Figure 12. Minimal inverse Jeans number in the disc mid-plane as a function of radius. It is plotted for the resolution study involving (a) our initially solid-body rotating simulations, (b) our disc in Run 1 as considered with different grids and resolutions and (c) for our run 1-HR. Truelove-unresolved regions are hatched.

which is the typical size of our discs. The hatched region in the figures indicates values $1/n_{\rm J} < 4$, where the Truelove criterion is violated. Run 1 is fully resolved in the inner 1000 au of the disc (red thick dotted line). The minimal inverse Jeans number exhibits variations corresponding to the presence of the dense spiral arms hosting circumstellar clumps (local minimum) and the underdense regions between the spiral arms (local maximum). Note that the mean value of the azimuthally averaged inverse Jeans number is much larger (thick solid orange line). High-resolution simulation Run 1-HR is our best Truelove-resolved model (green thick dashed line). This criterion is a minimal requirement to consider simulations of self-gravitating discs are numerically reliable. It does not consist of a strict convergence rule, as illustrated by the density pattern differences of the Truelove-resolved models Run 1 and Run 1-HR.

Fig. 12(b) is similar to Fig. 12(a) but for Run 1, assuming different grid types and resolutions. The thick dotted red line assumes the logarithmic simulation grid, while the other lines considers minimal inverse Jeans lengths calculated with our disc mid-plane density field together with uniform grids of resolution $\Delta = 10$–40 au, corresponding to the resolution typically reached by codes with Cartesian grids for this kind of simulations. The logarithmic grid is better than any considered uniform grid up to radii of about 150–200 au, which is similar to the inner disc size after simulation times of ≈23–30 kyr, depending on the models. Particularly, the resolution $\Delta = 40$ au is not able to reach our disc resolution up to radii of ≈ 600–800 au.

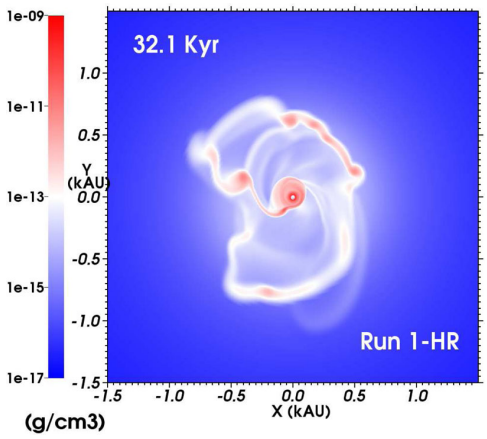

Figure 13. Mid-plane density field of at the end of Run 1-HR.

This mean that substructures of the disc in Run 1 cannot be reproduced with such a grid size, as the onset of clump formation and migration happens in spiral arms at a typical distance of a few hundreds au from the central protostar (see Meyer et al. 2017). This resolution dependence of the numerical capture of accretion-driven outbursts phenomenon explains why it could not be captured by mesh-refinement codes with a Cartesian grid since their maximum disc resolution of 10 au is so far coarser in the inner disc than in our simulations (see e.g. Krumholz et al. 2007b; Klassen et al. 2016; Rosen et al. 2016). Fig. 12(c) is similar to Fig. 12(b), but for Run 1-HR at different times of its evolution, corresponding to the snapshots in Figs 10(c), (f) and (j). Throughout the whole simulation time, this model is well Truelove-resolved ($1/n_{\rm j} \geq 10$), even when clumps start flourishing at the outskirt of the disc ($1/n_{\rm j} \geq 4$–6, see Fig. 13). The necessary resolution of the Jeans number in the clump cores is achieved partly because they evolve in the disc mid-plane, see Figs 12(a)–(c). In all our simulations, we generally find values of $\lambda_{\rm J}/\Delta \sim 6$–8, see details relative to the first migrating clump of Run 3 in Meyer et al. (2017).

The equatorial symmetry of our setup forces the clump to develop and evolve within the mid-plane. While this prevents clumps from potentially scattering to high disc latitudes. Indeed, clumps are therefore resolved at all radii with the smallest grid cells permitted by the used cosine-like grid along the polar direction. The disc scaleheight in the clump-forming regions is $H \approx 10$ au and can increase with r up to $H \approx 100$ au in the outer disc region. The choice of an expanding grid resolution $\Delta(r)$ allows us to resolve the disc scaleheight $H(r) \gg \Delta(r)$ and at the same time to reduce the number of cells and the computing time of the simulations. The Hill radii of the clumps, i.e. the surrounding regions that is gravitationally influenced by their mass, is $R_{\rm H} \approx 64$–96 au for a clump mass of $M_{\rm cl} \approx 1.0\,{\rm M}_{\odot}$ located at $r \approx 200$–300 au from a star of $M_{\star} \approx 10\,{\rm M}_{\odot}$, whereas the grid resolution is of $\Delta \simeq$ a few au at that radius in our Runs 1–3 (and a factor of 2 smaller in Run 1-HR). The Hill radius goes as $R_{\rm H} \approx r(M_{\rm cl}/3M_{\star})^{1/3}$ and therefore increases at larger radii, which compensates the linear loss of resolution of the logarithmically expanding grid compared to the inner part of the disc. As the protostar grows, $M_{\star}$ increases and assuming $M_{\star} \approx 30\,{\rm M}_{\odot}$ we find $R_{\rm H} \approx 45$–67 au, which is still correctly resolved. As the clump falls in, it loses mass but the grid resolution increases; leading to similar conclusions as above. What is new in this study is not the included microphysical processes, but the high spatial resolution allowed by the method in the innermost part of the accretion disc. We resolve the stellar surroundings better than any simulation before and explore the initial perturbations of the disc together with their effects on its subsequent overall instability.

6 HOW TO CHARACTERIZE DISC INSTABILITY?

Simulations with lower spatial resolution than used in our study often made use of sink particles to generate nascent stars in the accretion disc. Forming those sink particles underlines the assumption of disc fragmentation at this location, however, different simulation codes also apply different criteria, from density thresholds (Krumholz et al. 2007b) to the onset of local isotropic gravitational collapse (Federrath et al. 2010). Our different method, without sink particles, allows us to pronounce on the reliability of analytic criteria for disc fragmentation, by computing them for our resolved discs models and directly compare if they result in disc fragmentation. Therefore, we test the protostellar discs with respect to several criteria for the fragmentation of self-gravitating discs, i.e. the so-called Toomre, Gammie and Hill criteria. Particularly, we discuss whether those criteria are consistent with our results, and if they are necessary and/or sufficient to determine the unstable character of the discs, in the spirit of the analysis carried out in Klassen et al. (2016).

6.1 Toomre criterion

The so-called Toomre parameter measures the unstable character of a self-gravitating disc by comparing the effects of the gravity (Toomre 1963) against the combined effects of the disc thermodynamics, i.e. the gas thermal pressure, together with the rotational shear induced by the Keplerian motion of the gas, providing a stabilizing force to the system. A region of a gaseous disc is Toomre-unstable (or Q-unstable) if the dimensionless quantity,

$$Q = \frac{\kappa c_{\rm s}}{\pi G \Sigma} \leq Q_{\rm crit}, \tag{20}$$

where $c_{\rm s}$ is the sound speed of the gas, Σ the column mass density of the disc and κ the local epicyclic frequency. The aforementioned Toomre criterion was derived in the thin-disc limit for polytropic and axisymmteric discs, for which case $Q_{\rm crit} = 1$. In more realistic situations, the exact value of the critical Toomre parameter $Q_{\rm crit}$ depends somewhat on the disc thickness, rotation curve and thermodynamics. Numerous numerical studies indicate that circumstellar discs become unstable to the growth of a spiral structure if Q becomes less than $Q_{\rm crit}$ =1.5–2.0 (e.g. Durisen et al. 2007). When the local Q-parameter becomes smaller than 1.0, spiral arms may fragment to form compact gaseous clumps. This criterion is a necessary condition with respect to gravitational fragmentation, however, recent studies updated condition equation (20) to $Q < 0.6$, see the study of protoplanetary discs of Takahashi, Tsukamoto & Inutsuka (2016).

The middle column of panels of Fig. 14 plots the Q-analysis of the disc in our Run 1 at several characteristic time-scales of its evolution. The colour scale indicates whether the disc is prone to fragment ($Q \leq 1$, red), marginally unstable to fragmentation ($Q \simeq 1$, white) or stable to fragmentation ($Q > 1$, blue). Figs 14(e)–(h) show that the Toomre criterion is satisfied by the denser regions of the spiral arms and by the circumstellar clumps in the accretion disc. The surface of the disc mid-plane which is prone to

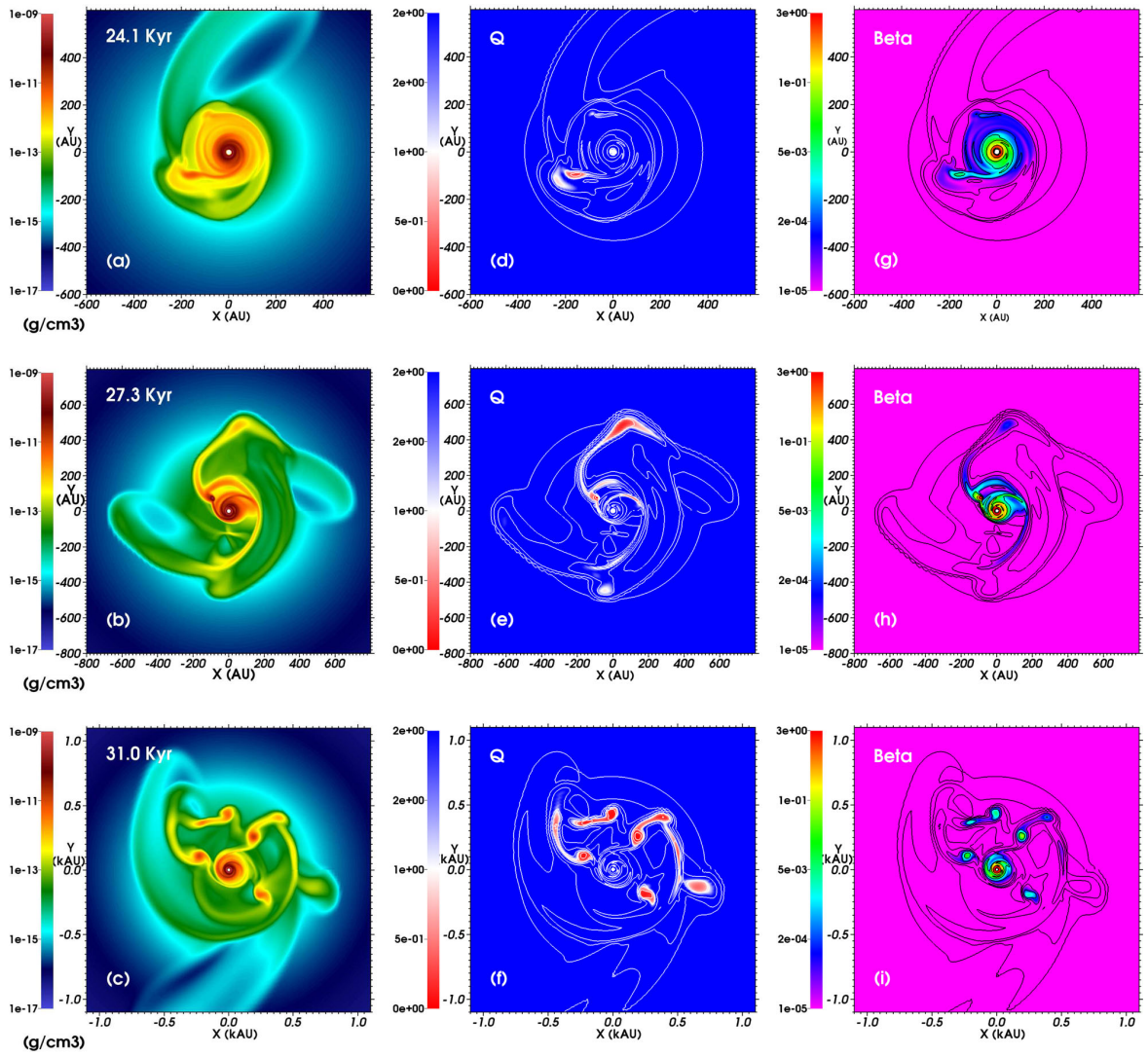

Figure 14. Density fields of Run 1-HR (left, as in Figs 1a–c) together with corresponding Toomre Q-maps (middle) and Gammie β-maps (right).

fragmentation increases as a function of time, as the circumstellar medium of the protostar loses axisymmetry (Figs 14e and h). As noted in Klassen et al. (2016), the disc's growing tendency to Q-instability comes along with an increase of the accretion variability. The ejection of the leftover of the first accreted clump, producing the first accretion-driven outburst, provokes the formation of a dense filament propagating outwards as described in figs 1(b)–(d) of Meyer et al. (2017), which in its turn favours the generation of thin but extended spiral arms, enhancing the disc's instability and susceptibility to experience further fragmentation events. The more violent the disc fragmentation, the lower the value of the associated local Q-parameter.

At time 24.1 kyr, the most Toomre-unstable clump located at a radius ≈100 au from the protostar has $Q \approx 0.25$–0.4 (Fig. 14d). This value is typical of the spiral arm in the discs which develop throughout our simulations. Q-values of ≈2.6–3.2 in the inner region of the disc (≤100 au) indicate stability, except for some very thin (but still marginally Toomre-stable with $Q \approx 1.7$) twisted spiral located at radii of ≈55 au. At a time of 27.3 kyr, unstable spiral arms in the disc with $Q = 0.8$–0.86 are noticeable, see for example the thin spiral arm at x = −200 au and y = 300 au in Fig. 14(e). The other regions of the disc which are fragmenting into blobs have characteristics such that $Q = 0.8$–1.2. The snapshot in Fig. 14(f) draws similar conclusions with multiple Q-unstable clumps of $Q \leq 0.4$ linked to each other by spiral arms which central regions can also be locally unstable ($Q \leq 0.4$–0.5), however, most part of those arms are such that $Q = 0.8$–1.35. Therefore, our results are consistent with the update of the Toomre criterion reported in Takahashi et al. (2016), i.e. the only necessary condition for disc instability is $Q < 0.6$, as already confirmed in the context of the stable discs shown in Klassen et al. (2016).

6.2 Gammie criterion

In the right-hand column of panels of Fig. 14, we show maps of the so-called Gammie criterion. It locally compares the effects of

the gas cooling with the hydrodynamics, i.e. the heating of the gas pressure due to the shear due to the disc rotation (Gammie 1996), and reads,

$$t_{\rm cool}\Omega \leq \beta \approx 3\text{–}5, \tag{21}$$

where the local cooling time-scale $t_{\rm cool}$ depends on the disc thermodynamics. We compute it as,

$$t_{\rm cool} = \frac{E_{\rm int}}{F}, \tag{22}$$

with $E_{\rm int}$ the internal energy in a disc column (Klassen et al. 2016) and F the radiation flux leaving the disc surface. Our protostars are surrounded by discs that are not irradiated so that they adopt the vertical isothermal structure described in Rafikov (2009), and their mid-plane temperature still is governed by the pressure work of the spiral arms and the radiation flux leaving the disc can be estimated as $F = \sigma T^4/f(\tau)$ measured at the disc surface, where σ is the Stefan–Boltzman constant and $f(\tau) = \tau + 1/\tau$ is a function of the optical depth which interpolates between the optically thin ($\tau < 1$, outer part) and the optically thick ($\tau > 1$, inner part) regimes of the discs (Rafikov 2007, 2009). The figure's colour coding illustrates where the disc is β-stable ($t_{\rm cool}\Omega \geq 3$–5, red) or β-unstable ($t_{\rm cool}\Omega < 3$–5, other colours). This criterion has been numerically derived for self-gravitating discs around low-mass stars and it is subject to numerous discussions regarding the critical value of β, which has been shown to be resolution-dependent (Meru & Bate 2011, 2012) and equation-of-state-dependent (Rice, Lodato & Armitage 2005; Clarke, Harper-Clark & Lodato 2007). Therefore, the existence of a universal β-value remains unclear (Lodato & Clarke 2011; Rice et al. 2012, 2014). The Gammie criterion can also be derived from the requirement that the local cooling time $t_{\rm cool}$ be shorter than the fastest growth time of gravitational instability $t_{\rm grav} = 2\pi/(\Omega\sqrt{1-Q^2})$ (Shu 1992), so that the local density enhancements can get rid of excess heat generated during gravitational contraction. In this case,

$$t_{\rm cool}\Omega \leq \frac{2\pi}{\sqrt{1-Q^2}}. \tag{23}$$

This form of the Gammie criterion explains the recent results of Boss (2017) arguing that disc fragmentation can take place at higher values of β given lower Q-values.

Figs 14(g)–(i) show that our discs satisfy the Gammie criterion for instability, including the hot regions of spiral arms and gaseous clumps which are more β-stable than the interarm region, but nevertheless largely β-unstable. At the beginning of our simulations, the disc is mostly Gammie unstable, testifying a rapid and efficient cooling of the gas, except in the very inner dense region of radius $\leq$20–80 au, close to the protostar, see Figs 14(g) and (h) and Klassen et al. (2016). Throughout the simulations, the spiral arms have a typical value of $t_{\rm cool}\Omega = 0.01$–$0.005$ (Figs 14h and i) and even lower values ($t_{\rm cool}\Omega \ll 0.005$) in the interarm regions of the disc mid-plane, which means that the cooling time-scale of the gas is shorter than the orbital period. Considering the both Toomre- and Gammie-unstable parts of the discs, we find that only the very innermost part of the disc does not satisfy the two criteria ($Q > 1$ and $t_{\rm cool}\Omega \leq 3$–5). Our results therefore agree with the analysis of the stable accretion discs around massive stars of Klassen et al. (2016) who found a low β-value in their (clumpless) discs and concluded on (i) their capacity of undergoing future fragmentation and (ii) the non-sufficiency of the Gammie criterion to distinguish fragmenting from non-fragmenting regions of accretion discs around young massive stars. Note that our simulations are also in accordance with the predictions of fig. 1 of Rafikov (2009), which concludes on the inevitable existence of a regime of disc fragmentation, located in regions at large distances from the central object in accretion discs with high accretion rates like ours, with $\dot{M} \geq 10^{-4}$–$10^{-3}\,{\rm M}_\odot\,{\rm yr}^{-1}$ and $\Omega \simeq 10^{-11}$–$10^{-10}\,{\rm s}^{-1}$. Section 8.2 further discusses the usefulness of a Gammie criterion for discs around young massive stars.

6.3 Hill criterion

The so-called Hill criterion compares the effects of the self-gravity of a spiral arm with respect to the shear produced by the stellar tidal forces (Rogers & Wadsley 2012). It has been derived in the context planet embryos in protostellar discs by examining its local sphere of influence, i.e. the capacity of segment of spiral arm to further accrete planetesimals and it has been applied with success in the context of the circumstellar medium of massive protostars (Klassen et al. 2016). A segment of a spiral arm of a given thickness l is Hill-unstable if,

$$\frac{l}{2R_{\rm Hill}} < 1, \tag{24}$$

where,

$$R_{\rm Hill} \approx \sqrt[3]{\frac{G\Sigma l^2}{3\Omega^2}} \tag{25}$$

is the Hill radius. The circumstellar gas that is not within twice the Hill radius of the fragment has its evolution governed by the gravity of the central protostar (Rogers & Wadsley 2012). Note that their work considered an isolated disc that was not further accreting from its pre-stellar core. This criterion turned to be more general than the Toomre and Gammie criteria because it was consistent with the apparent stability of Q- and β-unstable discs (Klassen et al. 2016). We calculate the Hill number of a selected number of cross-sections of spiral arms in our Run 1-HR. The blobby arm of Fig. 14(a) gives $l = 40$ au, $\Sigma \approx 4.19 \times 10^3\,{\rm g\,cm}^{-2}$ and $\Omega = 3.0 \times 10^{-10}\,{\rm s}^{-1}$, respectively, which makes $R_{\rm Hill} \approx 48$ au and $l/2R_{\rm Hill} \approx 0.41 < 1$. We repeat this analysis with the northern arm of Fig. 14(b), the southern arm of Fig. 14(b), the western arm of Fig. 14(c) and the eastern arm of Fig. 14(c). With the values of $l = 29, 14, 42, 39$ au, $\Sigma \approx 3.47 \times 10^2, 2.09 \times 10^2, 1.57 \times 10^2, 3.5 \times 10^2\,{\rm g\,cm}^{-2}$ and $\Omega = 2.3 \times 10^{-10}, 2.7 \times 10^{-10}, 8.05 \times 10^{-11}, 5.01 \times 10^{-11}\,{\rm s}^{-1}$, respectively, and therefore $R_{\rm Hill} \approx 20.1, 9.43, 54.8, 49.6$ au and $l/2R_{\rm Hill} \approx 0.70, 0.74, 0.38$ and $0.39 < 1$, respectively. Those numbers are in accordance with the unstable appearance of our discs and identical analysis at different times give similar results. We conclude that the Hill criterion is a reliable tool to predict the stability of self-gravitating discs around young massive stars.

7 SPECTROSCOPIC MASSIVE BINARIES FORMATION BY DISC FRAGMENTATION

Massive binaries are fundamental in the understanding of high-mass stellar evolution (Sana et al. 2012). The case of a massive protobinary made of two young high-mass stars has been predicted (Krumholz et al. 2009a) and observed (Kraus et al. 2017). However, the formation scenario of massive binaries made of a high-mass component and a close low-mass component is so-far unexplained, although it is suspected to be closely correlated to the hierarchical multiple systems of protostars formed by disc fragmentation (Krumholz et al. 2007b; Rosen et al. 2016). This study explores such hypothesis in the context of the observed spectroscopic massive binaries (Mahy et al. 2013), a particular case of close massive binaries

made of an O star with a short-period, low-mass companion which we explain by showing that disc fragmentation is a viable road for the formation of proto-O star with a short-period, low-mass companion. This section details that our simulations are consistent with the disc fragmentation channel of close/spectroscopic massive proto-binaries formation that evolve towards close/spectroscopic massive binaries once the most massive component enters the main-sequence phase of its evolution. Finally, we connect it with the phenomenon of accretion-driven outbursts in the high-mass regime of star formation.

7.1 Accretion-driven outbursts from young massive stars

Using the same numerical method as in this study, we demonstrated in Meyer et al. (2017) that disc fragmentation around young high-mass star is followed by the formation of circumstellar clumps prone to migrate and fall on to the central protostar. We previously interpreted those observable as a tracer of disc fragmentation and postulated that the recent burst from the young high-mass star S255IR−SMA1 (Caratti o Garatti et al. 2017) could be caused by the accretion of a circumstellar clump on to the protostellar surface. However, the fate of the clumps once they crossed the inner 10 au was not calculated within our method and our conclusions are interpreted (i) by analogy with other studies on FU-Orionis(-like) ourbursts from young stars and (ii) calculating the centrifugal radius of one of those circumstellar clumps. We have drawn the conclusion that accretion-driven outbursts are a general feature of massive star formation, already well known in low-mass star formation as the FU-Orionis phenomenon (Smith et al. 2012; Vorobyov & Basu 2015) and in primordial star formation (Hosokawa et al. 2016).

This study extends the work of Meyer et al. (2017) to different angular velocity distributions of initial collapsing pre-stellar cores. Our set of simulations includes the case of a core in solid-body rotation that has recently been associated, with the help of several fragmentation criteria, as possessing all characteristics required for disc fragmentation, despite the clear lack of fragments captured in the hydrodynamical model (see Klassen et al. 2016, and discussion on sink-particle algorithms in Section 8.3). Differences between simulations of Klassen et al. (2016) and our models mainly lies in that we avoid using subgrid models (sink particles, see Section 8.3) and a higher spatial resolution than previously allowed by mesh-refinement codes in the close environment of the young high-mass protostar. Our models show fragmenting accretion discs whose evolution results in a pattern of clumps and filaments. This allows us to stress similarities between our results and simulations devoted to low-mass and primordial star formations. The remaining open questions consist in knowing more in detail the number of circumstellar clumps formed in massive discs and the exact subset of them migrating down to the central protostar. Other explanations of the formation of circumstellar clumps are plausible, such as the gravitational attraction of gaseous clumps formed within the pre-stellar core or by fragmentation of a neighbouring accretion disc, e.g. during the formation of two massive binaries, and subsequently ejected away by the gravitational sling effect (Vorobyov 2016). In this paper, we continue the interpretation of the clumps' fate. They can lose their envelope and produce accretion-driven events once the material reaches the stellar surface, however, if the clump continues to collapse and does not fall directly to the protostar, it will end up as a close, low-mass companion. An example of a clump having such properties is detailed below.

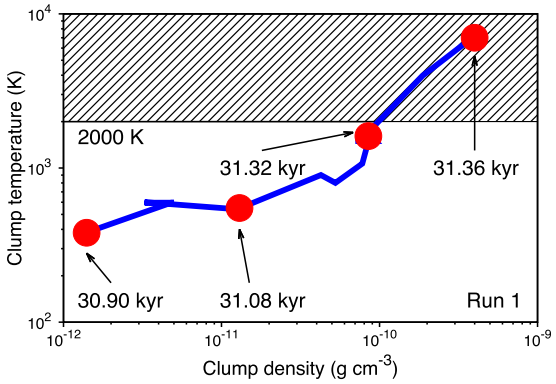

Figure 15. Temperature–density evolution of the circumstellar clump responsible for the first outburst of our Run 1, showing the characteristics of a gaseous blob on the path to low-mass star formation. The hatched region fall under dissociation, not included in our simulations.

7.2 Forming close/spectroscopic massive binaries by clump migration

Fig. 15 shows the evolution of the densest grid cell of the clump responsible for the burst happening in Run 1 at 31.4 kyr. We follow its evolution between the times 30.9 and 31.4 kyr. At 31.32 kyr, the core of the clump reaches a density of $\rho \approx 8.6 \times 10^{-11}$ g cm^{-3} and $T \approx 1724$ K. About 24 yr later, those numbers are $\rho \approx 4.13 \times 10^{-10}$ g cm^{-3} and a temperature $T \approx 4638 \gg 2000$ K because no dissociation is included into our equation of state. This is sufficient to consider this clump as to be on its path to star formation, indicating that our simulations are consistent with the formation scenario of a massive binary by disc fragmentation. The central protostar is therefore in an embryonic binary system of a current separation of 10 au and below when the hot disc fragment disappear into the sink cell, which is much smaller than found in previous calculations (a few 100–1000 au, see Krumholz et al. 2007b).

Furthermore, given the clump's properties and assuming angular momentum conservation, we estimate at a time 31.36 kyr its centrifugal radius, i.e. the Keplerian orbit at which it falls (see analysis in Meyer et al. 2017). The clump of $M_c \approx 1.2\,M_\odot$ is located at a radius of $r = 38$ au from the protostar, has an azimuthal velocity of $v_\phi \approx 1.8 \times 10^6$ cm s^{-1} and the protostellar mass is $M_\star \approx 16.36\,M_\odot$ with a disc mass in the region ≤ 38 au of $M_d \approx 3.16\,M_\odot$. We find that, in the mid-plane, $R_c = (r v_\phi)^2/(G(M_\star + M_d)) \approx 27.01$ au, and 20 yr later at a time 31.38 kyr, we find $R_c \approx 4.64$ au $\approx 996\,R_\odot \gg R_\star \approx 100$–$10\,R_\odot$. Under our assumptions, it shows that this clump does not directly land on to the protostar as in Meyer et al. (2017). The value of R_c calculated just before the clump enters the sink cell corresponds to a Keplerian period of $P \approx 842$ d which is of the order to the period range observed in some massive binaries (Kobulnicky et al. 2014). As discussed in Meyer et al. (2017), this value of R_c is an upper limit because of the clump's angular momentum loss during its inward migration. Therefore, the corresponding system will be tighter and result in a so-called short-period binary ($P \sim$ 10–100d). This naturally evolves towards a massive spectroscopic binary ($P \sim$ 1–10d) (Kobulnicky et al. 2014), when the central protostar leaves the pre-main-sequence phase and becomes an O-type star.

7.3 Accretion-driven outbursts from high-mass star-forming regions as tracer of close/spectroscopic massive binary formation

Since envelope and core of the clumps may separate during the infall due to tidal stripping, both phenomenon – accretion-driven outbursts and close binary formation – may happen together, and the bursts would be, in this case, a tracer of close/spectroscopic binary formation. A follow-up study will statistically investigate the properties of the accretion spikes in our simulations, as in Vorobyov & Basu (2015). Although, our study demonstrates its consistency within our assumptions, we nevertheless cannot give the definitive proof that close binaries can form by the disc fragmentation in the surroundings of the protostar, since the migration of circumstellar clumps can only be followed up to $r_{\rm in} = 10\,{\rm au} \gg {\rm R}_\star$. Discriminating the fate of the clumps between close binaries and accretion-driven outbursts is difficult since it requires multiscale simulations resolving at the same time the disc fragmentation at $\sim$100 au and the fall of clumps down to $\sim 1000\,{\rm R}_\odot$ for a close/spectroscopic binary, and/or eventually to $\sim 100\,{\rm R}_\odot$ for an accretion burst. Such simulations are far beyond the scope of this work.

8 DISCUSSION

This section is devoted to a general discussion of our results. We review the limitation of our setup, especially in terms of microphysical processes that we may include into future studies in order to tend towards a more realistic description of the surroundings of massive protostars. We briefly compare our results with previous studies, compare them with results obtained with sink-particle methods and we discuss what could influence the fragmentation of our accretion discs. Finally, we predict what our results would look like when observed.

8.1 Limitation of the model

Despite of reaching sub-au resolution within the inner region of the accretion discs, our simulations still suffer from a lack of spatial resolution. Increasing the grid resolution would allow us to calculate in more detail, e.g. the internal physics of the migrating circumstellar clumps. This problem equally affects codes with static grids or with mesh-refinement techniques such as FLASH (Banerjee & Pudritz 2007), ORION (Krumholz et al. 2007b) or RAMSES (Commerçon et al. 2010). Although chosen in accordance with current numerical studies on disc fragmentation in star formation, several other assumptions of our method could be subject to further improvements. In addition to the treatment of the radiation itself, it mainly concerns:

(i) The utilized prescription to estimate the accretion luminosity. In Meyer et al. (2017), the accretion luminosity is assumed to be a fraction $f = 1$ of the gravitational potential energy of the material crossing the inner boundary. This fraction is finally converted into stellar radiation instead of being absorbed and mixed to the stellar interiors. Motivated by observations, Offner et al. (2009) constrained this value to $f = 3/4$, that, in our case, will make our accretion spikes less intense. This will change our estimate of the increase in accretion luminosity during the bursts and make our results even more consistent with the observations of Caratti o Garatti et al. (2017), strengthening their interpretation as a manifestation of the burst mode of massive star formation. Complex star–disc interaction simulations calculating in detail the accretion and penetration of disc material into the interior of the protostar in the vein of Kley & Lin (1996) are required to determine f more accurately.

(ii) The initial shape of the pre-stellar core and/or the choice of perturbation seeds for the gravitational instability. We initialize the simulation with spherically symmetric pre-stellar cores, however, observations have revealed their non-isotropic, filamentary shapes. Particularly, the study on massive star formation of Banerjee, Pudritz & Anderson (2006) uses initial conditions taken as a turbulent core structure extracted from a previously calculated cluster-forming clump. The considered symmetry breaking of the gravitational collapse in our case is numerical (cf. Hosokawa et al. 2016), while many studies initially sparse the density field of the pre-stellar core with a particular seed mode ($m = 2$, see Banerjee & Pudritz 2007) that is azimuthally imposed on the top of the density profile.

(iii) The stellar motion. The gravitational influence of the disc on to the star is neglected in our setup in which the star is static. The effect of the disc inertia on to the protostar becomes important when discs develop heavy and/or extended spiral arms displacing the barycentre of the star/disc system at radii larger than the size of the sink cell, which in its turn influences the stellar motion. This is intrinsically taken into account in simulations utilizing moving sink particles as representations of forming stars and it will be included in future studies with the method described in Hosokawa et al. (2016) and Regály & Vorobyov (2017). This is a well-known inconvenience of simulations of accretion discs with static central object. Also note that numerical simulations with grid-refinement methods do not strictly conserve angular momentum and suffer from grid-alignment effects. However, since the models of Klassen et al. (2016) do not fragment to the same degree as ours, we conclude that the preponderant issue for disc fragmentation is spatial resolution. Including the stellar motion should make the discs have net angular momentum that is lower than in the case without stellar motion. The disc will be of smaller radius and them less prone to fragmentation. However, this effect can easily be counterbalanced by a mild increase of the initial rotation rate in the parental cloud, as shown in Regály & Vorobyov (2017).

(iv) Simulation time. The numerical cost of simulations of massive stars like ours is huge and currently obliges investigations to be restricted to the early formation phase. However, since long-term evolution simulation of low-mass star formation (Matsumoto, Machida & Inutsuka 2017) highlighted that, under some circumstances, discs modify their shape and orientation, one can wonder whether totally new disc morphologies will arise around more evolved young high-mass stars.

(v) Missing physical mechanisms. Apart from covering the parameter space which is still far from being fully explored in terms of initial pre-stellar core mass $M_{\rm c}$, size $R_{\rm c}$ and ratio of kinetic per gravitational energy β, neglected microphysical processes may also change our results. Particularly, the ionization feedback of the protostar filling the bipolar outflows which develops perpendicular to the discs and giving birth to bipolar H II regions that can be observed (Campbell 1984), may experience intermittency (Tanaka et al. 2017) as in primordial star formation (see Hosokawa et al. 2016). Thus, the inclusion of the magnetization of the pre-stellar core is also necessary to tend towards a global picture of star formation because it influences at the same time the jet morphology (Pudritz et al. 2007; Frank et al. 2014) and the fragmentation of accretion discs (Hennebelle et al. 2016; Fontani et al. 2016), see Section 8.4.

(vi) The mid-plane-symmetric nature of our simulations. This can be improved by considering the full three-dimensional

evolution of the protostellar disc. We force the disc to develop symmetrically with respect to the plane normal to the rotation axis, see Fig. 4. Full '4π' models would allow us to take into account the vertical bending of the disc visible, for example in fig. 13 of Krumholz et al. (2007b). Note also, that, if our simulations with static stars do not allow us to appreciate the effects of the disc wobbling, models with Cartesian grids cannot qualitatively pronounce on the absence of stellar motion on the disc dynamics. For all those reasons, the assumptions of mid-plane symmetry of our simulations are reasonable and our method does not overestimate fragmentation from this point of view. What causes disc bending modes and how that can affect disc fragmentation deserves a separate focused study.

(vii) The size of the sink cell. Indeed, our method neglects the fate of the clumps once they cross the innermost boundary of 10 au (see also Meyer et al. 2017), which has so far not been modelled up to the boundary layer of the disc. The presence in the close environment of protostars of more (smaller) clumps in chaotic and mutual interaction would change the geometry of the accretion flow on to the protostar, that are influenced by complex radiation processes, such as the line-ablation mechanisms acting in the surroundings of O/Be stars (Kee, Owocki & Sundqvist 2016). However, studies devoted to low-mass star formation demonstrated that while about half of the clumps are gravitationally supported and remain in the disc, the falling clumps may be ejected from the disc or further fragment within the innermost disc regions (Greif et al. 2012; Meru 2015; Vorobyov 2016). This may be enhanced by H_2 cooling and collisional emission, not treated in our simulations.

However, such improvements would only be possible at the cost of even more computationally intensive simulations requiring higher spatial resolution and huge memory resources. Particularly, this will give us access to the probable chaotic behaviour of the circumstellar clumps in the inner region of the disc (see discussion in Meyer et al. 2017).

8.2 General discussion

The study of low-mass star formation has led to a large literature on its theory, but the three-dimensional modelling of the birth of high-mass stars is still a relatively recent field of research. A few works only tackled the problem and their differences principally lie in the way to treat the stellar feedback and/or in the choice of pre-stellar core initial configuration. Most simulations assume a density distribution $\rho(r) \propto r^{-3/2}$, but models such as in Kuiper et al. (2011) and Kuiper & Yorke (2013a) additionally consider $\rho(r) \propto r^{-2}$. The other fundamental parameter of the pre-stellar core is its initial velocity field. While some studies considered non-rotating pre-stellar environments in which turbulence was initially driven (Krumholz et al. 2007b), non-solid body rotating pre-stellar cores have begun to be investigated in Meyer et al. (2017) with $\Omega(R) \propto R^{-0.75}$ and our work continues this with $\Omega(R) \propto R^{-0.35}$. The initial mass of pre-stellar cores is typically taken to $M_c \approx 100\,M_\odot$ and the ratio of rotational-to-gravitational energy to $\beta \approx$ few per cent as in our study, but models have been calculated with $M_c = 1000\,M_\odot$ (Peters et al. 2010) and $\beta \geq 10$ per cent (Seifried et al. 2011; Klassen et al. 2016). A more detailed review of the initial conditions of the pre-stellar cores in terms of M_c and β-ratio can be found in Meyer et al. (2017).

The manner of treatment of radiation feedback differs greatly from study to study. Pre-calculated cooling curves are less accurate, but allow the coverage of large parameter spaces (Banerjee & Pudritz 2007; Seifried et al. 2011), e.g. including the magnetization of turbulent pre-stellar cores (Seifried et al. 2013), whereas radiation transport algorithms taking into account the physics of dust are able to self-consistently model the dust sublimation front (Kuiper et al. 2010). Our method is a modification of the PLUTO code (Mignone et al. 2007, 2012) described in Kuiper et al. (2010, 2011). Recently, a similar scheme has been implemented into the FLASH and ORION codes, using a mesh-refinement grid (Klassen et al. 2014; Rosen et al. 2017). In that sense, our study has the advantage to have a highly resolved grid in the inner parts of the disc together with a radiative transfer solver more accurate than a simple cooling law, but it has the disadvantage not to properly resolve clumps potentially forming at larger radii. Although the frequency-dependent ray-tracing method has been successfully benchmarked with respect to our utilized grey solver (Kuiper & Klessen 2013), its requirement in terms of numerical resources was too high. However, radiation transport methods making use of a frequency-dependent ray-tracing solver have been developed and used in the context of three-dimensional massive star formation simulations (Kuiper et al. 2011; Rosen et al. 2016). Particularly, the effects of the interplay between such radiation transport methods and grid resolution on the modelling of (Rayleigh–Taylor unstable) bipolar outflows from massive stars is largely discussed in Kuiper et al. (2012), Rosen et al. (2016) and Harries et al. (2017).

Another similarity between our simulations and recent studies is their consistency with respect to analytical criteria predicting disc fragmentation. Numerical solutions of the surroundings of high-mass protostars is typically compared to the Toomre, Gammie and Hill criteria. As for other kind of self-gravitating discs, the Toomre criterion characterize well fragmenting regions ($Q \leq 0.6$, see Takahashi et al. 2016; Klassen et al. 2016), whereas the Gammie analysis alone is in most regions fulfilled and therefore not sufficient to discriminate between fragmenting and non-fragmenting scenario, e.g. at the early stage of the disc formation. Additionally, accordance between numerical simulations and the Hill analytic prediction were found. It applies to our unstable models as it did in the disc simulations of Klassen et al. (2016) that are stable to fragmentation, but unstable to development of spiral modes. Consequently, this criterion is the most reliable tool so far to characterize the stability of spiral arms in discs from young stars.

Fragmentation as a response of accretion discs against gravitational instability has been widely investigated analytically and numerically in different astrophysical contexts. Particularly, the study of Kratter & Matzner (2006) considers the antagonistic effects of both angular momentum transport, leading discs to fragmentation and viscous heating tending to stabilize them. Under those assumptions which 'underestimate the prevalence of disc fragmentation', they found that discs around high-mass stars ($\geq 10\,M_\odot$) are prone to fragmentation and that this probability increases with $M_\star$. Our Run 1 with solid-body rotation is consistent with such prediction since the disc fragments at a time $\approx$30 kyr when the protostar has reached $\approx 17\,M_\odot$, see Figs 1c and 5a). However, our disc models initially deviating from rigid rotation fragment before the protostar reaches such mass, e.g. at a time $\approx$30 kyr when the central protostar is only $\approx 7\,M_\odot$ (Run 2, see Figs 2b and 5b). Finally, we recall that the episodic feedback of secondary objects have been shown to play a role in further enhancing disc fragmentation shortly after accretion-driven outbursts (Mercer & Stamatellos 2017). This process may apply to our discs around massive protostars and further enhance their fragmentation (see Section 8.3).

8.3 Self-consistent versus sink-particle simulations

The sink-particle approach consists in coupling a discrete *N*-body-like method to a continuous resolution of the hydrodynamics equations in a grid-based code. Therefore, it is a violation of the self-consistent treatment of the different physical processes at work in the computational domain. Such approach is nevertheless unavoidable, since low-mass stars such as brown dwarfs or solar-type stars appear as point-mass objects, once they undergo second collapse from first hydrostatic cores down to stellar densities. All the subtlety lies in (i) applying sufficiently strong sink-creation criteria in order to avoid fictitious particle formation leading to overestimating the number of stars and (ii) introducing them as late as possible during the secondary gravitational collapse, ideally when the grid size is of the order of the radius of the new-born star, not to artificially influence the local protostellar disc dynamics. Indeed, introducing sinks modifies the gas dynamics, itself a function of the resolution of the simulation at the moment of the particle creation.

Criteria allowing codes to generate sinks greatly vary between numerical schemes and simulations. A too sophisticated but very realistic particle-creation algorithm will rarefy secondary star formation, leading to the conclusion of disc stability, despite of a Q- and β-unstable disc (Klassen et al. 2016), whereas a simplified one will produce overnumerous and unphysical star formation. Indeed, Rosen et al. (2016) notes that 'multiplicity results are sensitive to the physics included, radiative transfer treatment used, and sink creation and merging criteria employed'. Moreover, choosing a (set of) criteria(on) for sink-particle creation is equivalent to a preference for particular star formation laws, still largely under debate. Particularly, Machida, Inutsuka & Matsumoto (2014) showed with non-turbulent, (non-)ideal magnetohydrodynamics simulations of rotating Bonnor−Ebert spheres of initial mass ranging from 1.0 to 100 $M_\odot$, how sensitive disc solutions around low-and high-mass stars can be as a function of both the accretion radius of sink particles and the density threshold constituting their principal creation condition (see also discussion in Padoan & Nordlund 2011). They concluded on the necessity of sink accretion radius $\leq$1.0 au and a sink particle density threshold $\geq 10^{13} \simeq 10^{-11}$ g cm^{-3}. The properties of the companion core in Fig. 15 is consistent with this assertion, however, one can clearly see that our clump becomes a star when its core is denser than 10^{-10} g cm^{-3}, revealing (at least in this case) the insufficiency of the criterion of Machida et al. (2014) since our gaseous clump is not yet hot enough to be considered as a secondary star. Perhaps a more reliable criterion for sink-particle creation could be the temperature of the clump's core? Also pointed by Hennebelle et al. (2011), the 'use of sinks may alter significantly the evolution of the calculations in particular in the presence of magnetic field', which is an additional drawback of numerical models like in Myers et al. (2013, 2014).

Our method gets rid of those caveats since the local collapse is self-consistently captured in the density and temperature fields. We justify the use of a spherical coordinate system by our scientific goal, which is to understand the formation of spectroscopic companions to massive OB stars, by exploring star formation and migration in the inner part of the disc. The main caveat of our disc dynamics is therefore the lack of spatial resolution in their outer region. However, as discussed in Section 5, this is acceptable since the migrating clumps develop in the inner and intermediate regions of the protostellar disc. Our alternative method to simulations with Cartesian grids and sink particles self-consistently produce discs fragmenting into clumps hot enough to verify the condition of secondary star formation, which is a confirmation of the discovery of multiplicity in the massive protostellar context in Krumholz et al. (2007b). With both methods, the number of companions forming in the disc decreases with the consideration of the pre-stellar core's magnetization (Machida et al. 2014; Commerçon et al. 2011), see also Section 8.4. No formation of twin massive binaries (Krumholz et al. 2009a) is observed directly in our models, although Run 3 shows the formation of a massive disc-like clump (Fig. 3).

In case of models with 'smart' particles possessing their own feedback, high numerical resolution is needed to resolve the accretion discs around the formed secondary stars, in which the complex flow induces accretion rate variability and makes the feedback of the secondary stars episodic by the mechanisms largely described in Vorobyov & Basu (2010) and Bae et al. (2014). This will subsequently affect the results by further favouring violent fragmentation of the discs (see Mercer & Stamatellos 2017). Even more realistic sink particles should take into account jet-launching mechanisms perturbing the disc dynamics by creating disc cavities or outflows, and/or, in the case of, e.g. intermediate-mass secondary star formation (Reiter et al. 2017). Located beyond the dust sublimation radius, their H II region will intermittently release ionized gas into the radiation-shielded part of the central protostar's disc and enrich it with momentum and energy, perturbing its internal thermodynamics.

8.4 What can we expect on disc fragmentation by improving on the limitations of the models?

With the help of a grid more resolved in the stellar close environment than ever before, Meyer et al. (2017) revealed the fragmenting character of circumstellar discs. Since our models showed the clump-forming nature of discs around massive stars, one may ask, whether additional physical effects, not resolved in our simulations may arise and change the global picture of our solutions? As an example, increasing the spatial resolution in low-mass star formation simulations enhanced the possibility of circumstellar clumps to be ejected out of their host accretion disc (Vorobyov 2016). High-resolution studies in the context of low-mass and primordial star formation have also shown that further fragmentation may take place in the very innermost disc regions modelled by our static sink cell. Those phenomenons are provoked by migrating falling fragments or by H_2 cooling and/or by collisionally induced emission, see Stacy et al. (2010) and Greif et al. (2012) but also Meru (2015), however, they did not suppress physical conclusions that were previously drawn in their respective context. Therefore, the same may apply in the massive protostellar context.

Higher resolution simulations may highlight other detailed features in the fragmentation dynamics such as very inner accretion disc fragmentation occurs during massive star formation. This will therefore result in a pattern of very small gaseous clumps that can merge together, orbit on to the central protostar or be dynamically ejected away by gravitational sling, revealing amongst other clump–clump interactions as those discussed in detail in Zhu et al. (2012). Although this would change the geometry of the accretion and affect the detailed variability of the protostellar luminosity, the trajectory heavy clumps such ours that migrate fast, hosting the birth of a secondary star, will not be greatly perturbed. They will either fall directly on to the stellar surface (accretion burst), orbit around it (close binary formation) or lose their envelope while reaching a Keplerian orbit around the central protostar (close binary formation accompanied by accretion-driven event). One should also keep in mind that such criticisms are also valid regardless the used coordinate system, the grid refinement criteria and/or the utilized

sink-particle creation algorithms. Cartesian simulations of massive star formation like in, e.g. Krumholz et al. (2007b) or Klassen et al. (2016), but allowing more grid refinement levels and/or comparing different sink-particle algorithms are therefore highly desirable.

The above discussion refers to the aggravation of fragmentation once it has been triggered in the core, however, some physical processes can directly influence the fragmentation by modifying the disc temperature. Two other processes can indeed, under some circumstances, directly control whether fragmentation itself occurs, namely the presence of magnetic fields and/or the initial turbulence of the pre-stellar core. Often neglected for the sake of simplicity, the magnetization of the gravitationally collapsing structures can modify the disc dynamics. This has been reported at different length-scales, spanning from giant molecular clouds to low-mass star-producing cores (Commerçon et al. 2010; Tomida et al. 2010). The effects of the pre-stellar core magnetic properties on delaying, promoting, or preventing disc fragmentation, together with a description of the variety of the forming different low-mass binaries systems are discussed in Tomida, Okuzumi & Machida (2015). Particularly, the interplay between the magnetic breaking of the infalling gas and the radiative feedback of the protostar can inhibit the initial fragmentation processes of collapsing pre-stellar cores. Note that this applies to the regime of a strong magnetic field strength (Commerçon et al. 2011) under which our results do not fall as we neglect magnetization.

These magnetized models in the study of Commerçon et al. (2011) propose a channel to generate isolated O stars. However, it also underlines that two secondary fragments 'associated with a relatively high Jeans mass reservoir' form, and consequently one could expect 'this early fragmented system [to] give rise to a close massive binary system'. Such conclusions were beforehand only drawn by Lagrangian particles simulations of Bonnell & Bate (2005) and by the hydrodynamical disc fragmentation model of Krumholz et al. (2009b). Although using two totally different methods, they both demonstrate the possibility of producing twin massive binaries by pre-stellar core gravitational collapse followed by disc fragmentation, under the assumption of a neglected magnetization of the gas. Finally, note that since star-forming regions are dense, the non-ideal character of magneto-hydrodynamical processes such as Ohmic dissipation, Hall effect and ambipolar diffusion can, as an additional effect, influence the gas dynamics. Their significance on the physics of interstellar filaments (Ntormousi et al. 2016) and on low-mass star formation (Masson et al. 2012; Tomida et al. 2015; Masson et al. 2016; Marchand et al. 2016) implies that they, no doubt, should impact high-mass star formation as well.

Turbulence is another key ingredient in the theoretical determination of star formation rates (Hennebelle & Chabrier 2011). In the case of the gravitational collapse of a single, isolated pre-stellar cloud, turbulence modifies the gravitational collapse itself but also directly affects its magnetization. Particularly, it has been suggested that the so-called magnetic breaking catastrophe is a natural consequence of the overidealized initial conditions of low-mass star formation simulations, and that native pre-stellar turbulence naturally leads to Keplerian disc formation (Seifried et al. 2012), although the work of Wurster, Price & Bate (2016) brings a non-ideal but non-turbulent solution to this problem. Additionally, turbulence strongly influences the pre-stellar core magnetic field coherence (Seifried et al. 2015). The study of Rosen et al. (2016) includes simulations with stellar radiation and turbulent initial conditions which evolve towards complete disorganization of the disc-bubble system in the protostellar surroundings. As Keplerian discs (Johnston et al. 2015) and clear disc-outflow structures (Zinchenko et al. 2015) have been observed around young high-mass stars, those models indicate that other feedback processes stabilizing the pressure-driven radiative bubble such as outflow launching mechanisms (Kuiper et al. 2015, 2016) must be at work efficiently during the formation of massive stars. Since sub-au-resolved, three-dimensional gravitation-radiation-magnetohydrodynamic, turbulent simulations of high-mass star formation have not been conducted yet, the question is therefore to know by how much fragmentation in the context of our pre-stellar cores would be affected if considered with both (non-ideal) magnetization and turbulence. Those questions will be addressed in a subsequent study.

8.5 Prediction of observed emission

Although observational evidences for bipolar H II regions (Franco-Hernández & Rodríguez 2004) and accretion flows (Keto & Wood 2006) around young high-mass stars became more numerous over the past years, the direct imaging of their accretion discs was until recently under debate (Beuther et al. 2012), mostly because of the high opacity of the parent environment in which they form and large distances to these objects (Zinnecker & Yorke 2007). Recent observations from the *ALMA* interferometer suggested the presence of a Keplerian accretion disc in the surroundings of the early O-type star AFGL 4176 (Johnston et al. 2015). Similar techniques revealed the presence of a clumpy gaseous disc-like structure around the young high-mass stellar object of the S255IR area (Zinchenko et al. 2015) which is associated with an FU Orionis-like outburst (Burns et al. 2016; Caratti o Garatti et al. 2017). An equivalent discovery around the young early massive star G11.92−0.61 MM1 has been reported using the velocity gradient of compact molecular line emission oriented perpendicularly to a bipolar molecular outflow in Ilee et al. (2016) and the number of young massive candidates surrounded by a self-gravitating disc increases (Forgan et al. 2016). Several ongoing observational campaigns currently aim at detecting signs of disc fragmentation, e.g. with the *ALMA* facility (Cesaroni et al. 2017).

To appreciate our results in the context of observations, we perform a dust continuum radiative transfer calculation with the code RADMC-3D[1] (Dullemond 2012) using a Laor & Draine (1993) dust mixture based of silicates crystals with density and temperature distributions are directly imported from our simulations. Fig. 16 shows a synthetic 1.2 mm dust continuum emission of our Run 1 at a time ≈40 kyr, viewed under an inclination angle of 30°. The protostellar mass is ≈25 $M_\odot$ which corresponds to AFGL 4176's constrained mass, however, the disc mass is ≈30 $M_\odot$ which is larger than the 12 $M_\odot$ used to fit the properties of AFGL 4176. The radius of the disc of ≈2 kau is consistent with the observations. We assumed the protostar to be a blackbody source of effective temperature directly given by the stellar evolution routine of the simulation $T_{\rm eff} \approx 37\,500$ K and of bolometric luminosity $L \approx 85\,500\,L_\odot$ from which photon packages are ray-traced through the accretion disc. The calculations are further post-processed with the SIMOBSERVE and CLEAN tasks of the *Common Astronomy Software Applications*[2] (McMullin et al. 2007) to produce synthetic *ALMA* observations of our disc as if located at the coordinates of AFGL 4176. Telescope parameters are chosen to be the configuration 4.9 for Cycle 4 *ALMA* observations, with a bandwidth of 1.8 GHz with ≈3 h of integration time. The central frequency of the combined continuum emission is

[1] http://www.ita.uni-heidelberg.de/dullemond/software/radmc-3d/
[2] https://casa.nrao.edu/

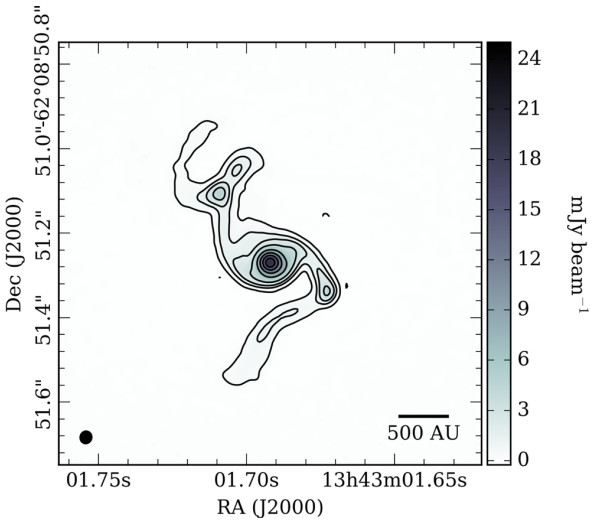

Figure 16. Dust continuum *ALMA* prediction of our Run 1 in the context of the young high-mass stars AFGL 4176 (Johnston et al. 2015). We consider a snapshot from the model at a time 40.0 kyr, when the protostar has reached 24.5 $M_\odot$. The overall disc and its brightest circumstellar clumps have a radius 2 and ≈0.6–1.0 kau from the protostar, respectively. Image intensity is in mJy beam^{-1}.

249.827 GHz (1.2 mm) and imaging was carried out using Briggs weighting with a robust parameter of 0.5. Under those assumptions and parameters, our *ALMA* rendering of Run 1 that is shown in Fig. 16 has observable emission. It presents the typical structure of an accretion disc around with spiral arms and clumpy substructures in it. A more detailed analysis of the molecular surroundings of this model, including line emission, is left for future work (Johnston et al., in preparation).

9 CONCLUSION

We have run three-dimensional gravito-radiation-hydro simulations of the collapse of 100 $M_\odot$ pre-stellar cores rotating with a kinetic-to-gravitational energy ratio of $\beta = 4$ per cent and with different initial conditions in terms of initial angular momentum distribution, in the context of a non-magnetized disc generated by an initially non-turbulent pre-stellar core. We perform the simulations during at least ≈35 kyr to generate protostars of ≈18–35 $M_\odot$. Our state-of-the-art treatment of the stellar radiation feedback, together with the sub-au spatial resolution of the inner region of the accretion disc allow us to realistically follow the evolution of the circumstellar medium of the early high-mass stars. We have investigated the stabilizing role of the direct stellar irradiation and performed a resolution study, ensuring that disc gravitational fragmentation accounts for the central protostellar feedback and/or artificially triggered. All our models have accretion discs whose spiral arms fragments by gravitational instability into a pattern of gaseous clumps, while continuously feeding the central protostars at highly variable accretion rates of $\sim 10^{-4}$–10^{-3} $M_\odot$ yr^{-1}. As in the other regimes of star formation (see Smith et al. 2012; Vorobyov et al. 2013; Vorobyov & Basu 2015, and references therein), those circumstellar clumps episodically generate luminous accretion-driven outbursts when migrating down on to the protostar. Our study shows that the mechanism introduced in Meyer et al. (2017) also happens for the different rotation profiles investigated herein.

Particularly, those flares are similar to the FU-Orionis-like episodic accretion-driven outbursts observed in the young high-mass stellar system S255IR−SMA1 (Burns et al. 2016; Caratti o Garatti et al. 2017). Some gaseous clumps migrate to the close surroundings (≤10 au) of the central protostar while simultaneously experiencing an increase of their central density and temperature that can reach up to $\approx 10^{-8}$ g cm^{-3} and ≥2000 K, respectively. The clumps are sufficiently massive (≃0.5–a few $M_\odot$) and their core is hot and dense enough to be considered as being on the path to the second gravitational collapse down to stellar densities. We show that such nascent companions can fast migrate down to the central protostar, constituting a massive binary system, made of a massive component plus a low-mass companion in close Keplerian orbit around it. We conclude on the viability of the disc fragmentation channel to explain the formation of close massive protobinaries made of a young high-mass component and at least a low-mass companion, which are the progenitors of the future post-main-sequence spectroscopic massive binaries (see also Sana et al. 2012; Mahy et al. 2013; Kobulnicky et al. 2014, for an observational study of close-orbit, O-star-involving massive binary statistics). We underline that disc fragmentation, high variations of the protostellar accretion rate, episodic accretion-driven outbursts and close binary formation are tightly correlated mechanisms, and we predict that both phenomenons can happen together. Consequently, luminous outbursts from young massive stars are the signature of the presence of its surrounding accretion disc, a tracer of the migration of circumstellar disc fragments but may also be at the same time a signature of the formation of close companions that will become the spectroscopic companions of a future O-type star.

We test our accretion discs against several semi-analytical criteria characterizing the fragmentation of self-gravitating discs. We find that our discs are consistent with the so-called Toomre, Gammie and Hill criteria, which is consistent with the analysis presented in Klassen et al. (2016), which we can summarize as follows: the Gammie criterion is fulfilled by our discs while the Toomre criterion alone allows us to discriminate fragmenting from non-fragmenting accretion discs ($Q \leq 0.6$, see Takahashi et al. 2016). The Hill criterion, even applied to the early formation phase of our discs, predicts their subsequent evolution with respect to fragmentation. Radiative transfer calculations against dust opacity in the context of the Keplerian disc surrounding the young high-mass star AFGL-4176 (Johnston et al. 2015) indicate that clumps in our disc models are detectable with *ALMA*. Such disc fragments should be searched with modern facilities such as *ALMA* or the future *European Extremely Large Telescope* within high-mass star formation regions from which strong maser emission or evidence of accretion flows have been recorded, e.g. W51 (Keto & Klaassen 2008; Zapata et al. 2009) and W75 (Carrasco-González et al. 2015).

This work highlights the need for highly spatially resolved simulations of massive star formation simulations as an additional issue to numerical methods and physical processes. It further stresses the challenging character of numerical studies devoted to the surrounding of young hot stars, as well as the similarities between massive star formation mechanisms (accretion variability and disc fragmentation) with the other (low- and primordial-) mass regimes of star formation. Our work, showing a possible pathway for the formation of spectroscopic massive binaries, will be continued and expanded to obtain a deeper understanding of the circumstellar medium of young massive stars and the implications for massive stellar evolution. Follow-up studies will investigate the effects of several physical processes which we have so far neglected, such as the inertia of the protostar, its ionizing feedback or the

magnetization of the pre-stellar core. This should allow us to pronounce more in detail the effects of disc fragmentation around early protostars as a function of the initial properties of their pre-stellar cores.

ACKNOWLEDGEMENTS

The authors thank the anonymous referee for their useful advice and suggestions which greatly improved the manuscript. DMAM and EV thank B. Stecklum for his invitation at Thüringer Landessternwarte Tautenburg. This study was conducted within the Emmy Noether research group on 'Accretion Flows and Feedback in Realistic Models of Massive Star Formation' funded by the German Research Foundation under grant no. KU 2849/3-1. EV acknowledges support from the Austrian Science Fund (FWF) under research grant I2549-N27. The authors gratefully acknowledge the computing time provided on the bwGrid cluster Tübingen. and on the ForHLR I cluster at the Steinbuch Center for Computing Karlsruhe. This research has made use of Astropy, a community-developed core PYTHON package for Astronomy (Astropy Collaboration 2013) and of SAOImage DS9.

REFERENCES

Astropy Collaboration, 2013, A&A, 558, A33
Bae J., Hartmann L., Zhu Z., Nelson R. P., 2014, ApJ, 795, 61
Banerjee R., Pudritz R. E., 2006, ApJ, 641, 949
Banerjee R., Pudritz R. E., 2007, ApJ, 660, 479
Banerjee R., Pudritz R. E., Holmes L., 2004, MNRAS, 355, 248
Banerjee R., Pudritz R. E., Anderson D. W., 2006, MNRAS, 373, 1091
Bergin E. A., Tafalla M., 2007, ARA&A, 45, 339
Beuther H., Linz H., Henning T., 2012, A&A, 543, A88
Beuther H., Ragan S. E., Johnston K., Henning T., Hacar A., Kainulainen J. T., 2015, A&A, 584, A67
Bonnell I. A., Bate M. R., 1994, MNRAS, 271
Bonnell I. A., Bate M. R., 2005, MNRAS, 362, 915
Bonnell I. A., Bate M. R., Zinnecker H., 1998, MNRAS, 298, 93
Boss A. P., 2017, ApJ, 836, 53
Burns R. A., Handa T., Nagayama T., Sunada K., Omodaka T., 2016, MNRAS, 460, 283
Campbell B., 1984, ApJ, 282, L27
Caratti o Garatti A. et al., 2017, Nature Phys., 13, 276
Carrasco-González C. et al., 2015, Science, 348, 114
Cesaroni R., Galli D., Lodato G., Walmsley M., Zhang Q., 2006, Nature, 444, 703
Cesaroni R., Hofner P., Araya E., Kurtz S., 2010, A&A, 509, A50
Cesaroni R. et al., 2017, A&A, 602, A59
Chini R., Hoffmeister V. H., Nasseri A., Stahl O., Zinnecker H., 2012, MNRAS, 424, 1925
Clarke C. J., Harper-Clark E., Lodato G., 2007, MNRAS, 381, 1543
Commerçon B., Hennebelle P., Audit E., Chabrier G., Teyssier R., 2010, A&A, 510, L3
Commerçon B., Hennebelle P., Henning T., 2011, ApJ, 742, L9
Dessart L., Langer N., Petrovic J., 2003, A&A, 404, 991
Dullemond C. P., 2012, Astrophysics and Space Science Library, RADMC-3D: A Multi-Purpose Radiative Transfer Tool. Springer-Verlag, Berlin
Durisen R. H., Boss A. P., Mayer L., Nelson A. F., Quinn T., Rice W. K. M., 2007, in Reipurth B., Jewitt D., Keil K., eds, Protostars and Planets V. Univ. Arizona Press, Tucson, AZ, p. 607
Evans N. J., II, 1999, ARA&A, 37, 311
Federrath C., Banerjee R., Clark P. C., Klessen R. S., 2010, ApJ, 713, 269
Fendt C., 2011, ApJ, 737, 43
Fendt C., Sheikhnezami S., 2013, ApJ, 774, 12
Flaig M., Ruoff P., Kley W., Kissmann R., 2012, MNRAS, 420, 2419
Fontani F. et al., 2016, A&A, 593, L14
Forgan D., Rice K., 2012, MNRAS, 420, 299
Forgan D., Rice K., Cossins P., Lodato G., 2011, MNRAS, 410, 994
Forgan D. H., Ilee J. D., Cyganowski C. J., Brogan C. L., Hunter T. R., 2016, MNRAS, 463, 957
Franco-Hernández R., Rodríguez L. F., 2004, ApJ, 604, L105
Frank A. et al., 2014, in Beuther H., Klessen R.S., Dullemond C.P., Henning Th., eds., Protostars and Planets VI. Univ. Arizona Press, Tucson, AZ, p. 451
Fuente A., Neri R., Martín-Pintado J., Bachiller R., Rodríguez-Franco A., Palla F., 2001, A&A, 366, 873
Gammie C. F., 1996, ApJ, 462, 725
Greif T. H., Springel V., White S. D. M., Glover S. C. O., Clark P. C., Smith R. J., Klessen R. S., Bromm V., 2011, ApJ, 737, 75
Greif T. H., Bromm V., Clark P. C., Glover S. C. O., Smith R. J., Klessen R. S., Yoshida N., Springel V., 2012, MNRAS, 424, 399
Haemmerlé L., Eggenberger P., Meynet G., Maeder A., Charbonnel C., 2016, A&A, 585, A65
Haemmerlé L., Eggenberger P., Meynet G., Maeder A., Charbonnel C., Klessen R. S., 2017, A&A, 602, A17
Harries T. J., 2015, MNRAS, 448, 3156
Harries T. J., Douglas T. A., Ali A., 2017, MNRAS, 471, 4111
Hawley J. F., Balbus S. A., 1992, ApJ, 400, 595
Hennebelle P., Chabrier G., 2011, ApJ, 743, L29
Hennebelle P., Commerçon B., Joos M., Klessen R. S., Krumholz M., Tan J. C., Teyssier R., 2011, A&A, 528, A72
Hennebelle P., Commerçon B., Chabrier G., Marchand P., 2016, ApJ, 830, L8
Hosokawa T., Omukai K., 2009, ApJ, 691, 823
Hosokawa T., Hirano S., Kuiper R., Yorke H. W., Omukai K., Yoshida N., 2016, ApJ, 824, 119
Hunter T. R. et al., 2017, SMA Newsletter, 24, 2
Ilee J. D., Cyganowski C. J., Nazari P., Hunter T. R., Brogan C. L., Forgan D. H., Zhang Q., 2016, MNRAS, 462, 4386
Isella A., Natta A., 2005, A&A, 438, 899
Johnston K. G. et al., 2015, ApJ, 813, L19
Kee N. D., Owocki S., Sundqvist J. O., 2016, MNRAS, 458, 2323
Kessel O., Yorke H. W., Richling S., 1998, A&A, 337, 832
Keto E., Klaassen P., 2008, ApJ, 678, L109
Keto E., Wood K., 2006, ApJ, 637, 850
Klahr H., 2004, ApJ, 606, 1070
Klahr H. H., Bodenheimer P., 2003, ApJ, 582, 869
Klassen M., Kuiper R., Pudritz R. E., Peters T., Banerjee R., Buntemeyer L., 2014, ApJ, 797, 4
Klassen M., Pudritz R. E., Kuiper R., Peters T., Banerjee R., 2016, ApJ, 823, 28
Kley W., Lin D. N. C., 1996, ApJ, 461, 933
Kobulnicky H. A. et al., 2014, ApJS, 213, 34
Kratter K. M., Matzner C. D., 2006, MNRAS, 373, 1563
Kratter K. M., Matzner C. D., Krumholz M. R., Klein R. I., 2010, ApJ, 708, 1585
Kraus S. et al., 2017, ApJ, 835, L5
Krumholz M. R., Klein R. I., McKee C. F., 2007a, ApJ, 665, 478
Krumholz M. R., Klein R. I., McKee C. F., 2007b, ApJ, 656, 959
Krumholz M. R., Klein R. I., McKee C. F., Offner S. S. R., Cunningham A. J., 2009a, Science, 323, 754
Krumholz M. R., Klein R. I., McKee C. F., Offner S. S. R., Cunningham A. J., 2009b, Science, 323, 754
Kuiper R., Klessen R. S., 2013, A&A, 555, A7
Kuiper R., Yorke H. W., 2013a, ApJ, 763, 104
Kuiper R., Yorke H. W., 2013b, ApJ, 772, 61
Kuiper R., Klahr H., Dullemond C., Kley W., Henning T., 2010, A&A, 511, A81
Kuiper R., Klahr H., Beuther H., Henning T., 2010, ApJ, 722, 1556
Kuiper R., Klahr H., Beuther H., Henning T., 2011, ApJ, 732, 20
Kuiper R., Klahr H., Beuther H., Henning T., 2012, A&A, 537, A122
Kuiper R., Yorke H. W., Turner N. J., 2015, ApJ, 800, 86
Kuiper R., Turner N. J., Yorke H. W., 2016, ApJ, 832, 40
Langer N., 2012, ARA&A, 50, 107
Laor A., Draine B. T., 1993, ApJ, 402, 441
Lichtenberg T., Schleicher D. R. G., 2015, A&A, 579, A32
Lin D. N. C., Papaloizou J. C. B., Kley W., 1993, ApJ, 416, 689

Lodato G., 2007, Nuovo Cimento Riv. Ser., 30, 293
Lodato G., Clarke C. J., 2011, MNRAS, 413, 2735
Machida M. N., Hosokawa T., 2013, MNRAS, 431, 1719
Machida M. N., Nakamura T., 2015, MNRAS, 448, 1405
Machida M. N., Inutsuka S.-i., Matsumoto T., 2011, ApJ, 729, 42
Machida M. N., Inutsuka S.-i., Matsumoto T., 2014, MNRAS, 438, 2278
Mahy L., Rauw G., De Becker M., Eenens P., Flores C. A., 2013, A&A, 550, A27
Marchand P., Masson J., Chabrier G., Hennebelle P., Commerçon B., Vaytet N., 2016, A&A, 592, A18
Masset F., 2000, A&AS, 141, 165
Masson J., Teyssier R., Mulet-Marquis C., Hennebelle P., Chabrier G., 2012, ApJS, 201, 24
Masson J., Chabrier G., Hennebelle P., Vaytet N., Commerçon B., 2016, A&A, 587, A32
Matsumoto T., Machida M. N., Inutsuka S.-i., 2017, ApJ, 839, 69
McKee C. F., Ostriker E. C., 2007, ARA&A, 45, 565
McMullin J. P., Waters B., Schiebel D., Young W., Golap K., 2007, in Shaw R. A., Hill F., Bell D. J., eds, ASP Conf. Ser., Vol. 376, Astronomical Data Analysis Software and Systems XVI, CASA Architecture and Applications. Astron. Soc. Pac., San Francisco, p. 127
Mercer A., Stamatellos D., 2017, MNRAS, 465, 2
Meru F., 2015, MNRAS, 454, 2529
Meru F., Bate M. R., 2011, MNRAS, 411, L1
Meru F., Bate M. R., 2012, MNRAS, 427, 2022
Meyer D. M.-A., Vorobyov E. I., Kuiper R., Kley W., 2017, MNRAS, 464, L90
Mignone A., Bodo G., Massaglia S., Matsakos T., Tesileanu O., Zanni C., Ferrari A., 2007, ApJS, 170, 228
Mignone A., Zanni C., Tzeferacos P., van Straalen B., Colella P., Bodo G., 2012, ApJS, 198, 7
Mueller K. E., Shirley Y. L., Evans N. J., II, Jacobson H. R., 2002, ApJS, 143, 469
Myers A. T., McKee C. F., Cunningham A. J., Klein R. I., Krumholz M. R., 2013, ApJ, 766, 97
Myers A. T., Klein R. I., Krumholz M. R., McKee C. F., 2014, MNRAS, 439, 3420
Nelson R. P., Gressel O., Umurhan O. M., 2013, MNRAS, 435, 2610
Ntormousi E., Hennebelle P., André P., Masson J., 2016, A&A, 589, A24
Offner S. S. R., Klein R. I., McKee C. F., Krumholz M. R., 2009, ApJ, 703, 131
Offner S. S. R., Kratter K. M., Matzner C. D., Krumholz M. R., Klein R. I., 2010, ApJ, 725, 1485
Ormel C. W., Shi J.-M., Kuiper R., 2015, MNRAS, 447, 3512
Paardekooper S.-J., 2012, MNRAS, 421, 3286
Padoan P., Nordlund Å., 2011, ApJ, 730, 40
Peters T., Banerjee R., Klessen R. S., Mac Low M.-M., Galván-Madrid R., Keto E. R., 2010, ApJ, 711, 1017
Petrović J., 2004, PhD thesis, Utrecht University
Pollack J. B., Hollenbach D., Beckwith S., Simonelli D. P., Roush T., Fong W., 1994, ApJ, 421, 615
Pudritz R. E., Ouyed R., Fendt C., Brandenburg A., 2007, in Reipurth B., Jewitt D., Keil K., eds, Protostars and Planets V. Univ. Arizona Press, Tucson, AZ, pp. 277–294.
Purser S. J. D. et al., 2016, MNRAS, 460, 1039
Rafikov R. R., 2007, ApJ, 662, 642
Rafikov R. R., 2009, ApJ, 704, 281
Regály Z., Vorobyov E., 2017, A&A, 601, A24
Reiter M., Kiminki M. M., Smith N., Bally J., 2017, MNRAS, 470, 4671
Rice W. K. M., Lodato G., Armitage P. J., 2005, MNRAS, 364, L56
Rice W. K. M., Forgan D. H., Armitage P. J., 2012, MNRAS, 420, 1640
Rice W. K. M., Paardekooper S.-J., Forgan D. H., Armitage P. J., 2014, MNRAS, 438, 1593
Richling S., Yorke H. W., 1997, A&A, 327, 317
Richling S., Yorke H. W., 1998, A&A, 340, 508
Richling S., Yorke H. W., 2000, ApJ, 539, 258
Rogers P. D., Wadsley J., 2012, MNRAS, 423, 1896
Rosen A. L., Krumholz M. R., McKee C. F., Klein R. I., 2016, MNRAS, 463, 2553
Rosen A. L., Krumholz M. R., Oishi J. S., Lee A. T., Klein R. I., 2017, J. Comput. Phys., 330, 924
Ruden S. P., Pollack J. B., 1991, ApJ, 375, 740
Sakurai Y., Vorobyov E. I., Hosokawa T., Yoshida N., Omukai K., Yorke H. W., 2016, MNRAS, 459, 1137
Sana H. et al., 2012, Science, 337, 444
Seifried D., Banerjee R., Klessen R. S., Duffin D., Pudritz R. E., 2011, MNRAS, 417, 1054
Seifried D., Pudritz R. E., Banerjee R., Duffin D., Klessen R. S., 2012, MNRAS, 422, 347
Seifried D., Banerjee R., Pudritz R. E., Klessen R. S., 2012, MNRAS, 423, L40
Seifried D., Banerjee R., Pudritz R. E., Klessen R. S., 2013, MNRAS, 432, 3320
Seifried D., Banerjee R., Pudritz R. E., Klessen R. S., 2015, MNRAS, 446, 2776
Seifried D., Sánchez-Monge Á., Walch S., Banerjee R., 2017, MNRAS, 459, 1892
Shakura N. I., Sunyaev R. A., 1973, A&A, 24, 337
Shu F. H., 1992, J. Br. Astron. Assoc., 102, 230
Smith R. J., Hosokawa T., Omukai K., Glover S. C. O., Klessen R. S., 2012, MNRAS, 424, 457
Stacy A., Greif T. H., Bromm V., 2010, MNRAS, 403, 45
Stamatellos D., Whitworth A. P., 2009a, MNRAS, 392, 413
Stamatellos D., Whitworth A. P., 2009b, MNRAS, 400, 1563
Stepanovs D., Fendt C., Sheikhnezami S., 2014, ApJ, 796, 29
Stoll M. H. R., Kley W., 2014, A&A, 572, A77
Takahashi S. Z., Tsukamoto Y., Inutsuka S., 2016, MNRAS, 458, 3597
Tanaka K. E. I., Tan J. C., Staff J. E., Zhang Y., 2017, ApJ, 835, 32
Testi L., 2003, in De Buizer J. M., van der Bliek N. S., eds, ASP Conf. Ser., Vol. 287, Galactic Star Formation Across the Stellar Mass Spectrum, Intermediate Mass Stars (Invited Review). Astron. Soc. Pac., San Francisco, p. 163
Tomida K., Tomisaka K., Matsumoto T., Ohsuga K., Machida M. N., Saigo K., 2010, ApJ, 714, L58
Tomida K., Okuzumi S., Machida M. N., 2015, ApJ, 801, 117
Toomre A., 1963, ApJ, 138, 385
Truelove J. K., Klein R. I., McKee C. F., Holliman J. H., II, Howell L. H., Greenough J. A., Woods D. T., 1998, ApJ, 495, 821
Tsukamoto Y., Takahashi S. Z., Machida M. N., Inutsuka S., 2015, MNRAS, 446, 1175
Vaidya B., Fendt C., Beuther H., Porth O., 2011, ApJ, 742, 56
van der Tak F. F. S., van Dishoeck E. F., Evans N. J., II, Blake G. A., 2000, ApJ, 537, 283
Vanbeveren D., 1991, Space Sci. Rev., 56, 249
Vink J. S., 2006, in Lamers H. J. G. L. M., Langer N., Nugis T., Annuk K., eds, ASP Conf. Ser., Vol. 353, Stellar Evolution at Low Metallicity: Mass Loss, Explosions, Cosmology, Massive Star Feedback – From the First Stars to the Present. Astron. Soc. Pac., San Francisco, p. 113
Vink J., 2012, A&AR, 20, 49
Vorobyov E. I., 2010, ApJ, 723, 1294
Vorobyov E. I., 2013, A&A, 552, A129
Vorobyov E. I., 2016, A&A, 590, A115
Vorobyov E. I., Basu S., 2007, MNRAS, 381, 1009
Vorobyov E. I., Basu S., 2010, ApJ, 719, 1896
Vorobyov E. I., Basu S., 2015, ApJ, 805, 115
Vorobyov E. I., Baraffe I., Harries T., Chabrier G., 2013, A&A, 557, A35
Vorobyov E. I., DeSouza A. L., Basu S., 2013, ApJ, 768, 131
Woosley S. E., Heger A., Weaver T. A., 2002, Rev. Mod. Phys., 74, 1015
Wurster J., Price D. J., Bate M. R., 2016, MNRAS, 457, 1037
Yorke H. W., Sonnhalter C., 2002, ApJ, 569, 846
Yorke H. W., Welz A., 1996, A&A, 315, 555
Zapata L. A., Ho P. T. P., Schilke P., Rodríguez L. F., Menten K., Palau A., Garrod R. T., 2009, ApJ, 698, 1422
Zhu Z., Hartmann L., Nelson R. P., Gammie C. F., 2012, ApJ, 746, 110
Zinchenko I. et al., 2015, ApJ, 810, 10
Zinnecker H., Yorke H. W., 2007, ARA&A, 45, 481

This paper has been typeset from a TEX/LATEX file prepared by the author.

Monthly Notices
of the
ROYAL ASTRONOMICAL SOCIETY

MNRAS **482,** 5459–5476 (2019) doi:10.1093/mnras/sty2980

Burst occurrence in young massive stellar objects

D. M.-A. Meyer,[1★] E. I. Vorobyov,[2,3] V. G. Elbakyan,[3] B. Stecklum,[4] J. Eislöffel[4] and A. M. Sobolev[5]

[1]*Astrophysics Group, School of Physics and Astronomy, University of Exeter, Exeter EX4 4QL*
[2]*Department of Astrophysics, The University of Vienna, Vienna A-1180, Austria*
[3]*Research Institute of Physics, Southern Federal University, Stachki 194, Rostov-on-Don 344090, Russia*
[4]*Thüringer Landessternwarte Tautenburg, Sternwarte 5, D-07778 Tautenburg, Germany*
[5]*Astronomical Observatory, Institute for Natural Sciences and Mathematics, Ural Federal University, Ekaterinburg 620000, Russia*

Accepted 2018 October 30. Received 2018 October 30; in original form 2018 May 23

ABSTRACT

Episodic accretion-driven outbursts are an extreme manifestation of accretion variability. It has been proposed that the development of gravitational instabilities in the proto-circumstellar medium of massive young stellar objects (MYSOs) can lead to such luminous bursts, when clumps of fragmented accretion discs migrate on to the star. We simulate the early evolution of MYSOs formed by the gravitational collapse of rotating 100-$M_\odot$ pre-stellar cores and analyse the characteristics of the bursts that accompany their strongly time-variable protostellar light curve episodically. We predict that MYSOs spend $\approx 10^3$ yr ($\approx$1.7 per cent) of their modelled early 60 kyr experiencing eruptive phases, during which the peak luminosity exceeds the quiescent pre-burst values by factors from 2.5 to more than 40. Throughout these short time periods, they can acquire a substantial fraction (up to $\approx$50 per cent) of their zero-age main-sequence mass. Our findings show that fainter bursts are more common than brighter ones. We discuss our results in the context of the known bursting MYSOs, e.g. NGC 6334I-MM1 and S255IR-NIRS3, and propose that these monitored bursts are part of a long-time ongoing series of eruptions, which might, in the future, be followed by other luminous flares.

Key words: methods: numerical – stars: flare – stars: massive.

1 INTRODUCTION

Massive stars, i.e. stellar objects heavier than 8 $M_\odot$, are well-established in their preponderant role in the cycle of matter of the interstellar medium of galaxies (Langer 2012). Throughout successive stellar evolutionary phases, from the (post-)main sequence (Meyer et al. 2014) to the supernova phase (Meyer et al. 2015), massive stars are mainly responsible for enriching their surroundings chemically and driving turbulence, which further regulates local star formation. Gravitational interactions and/or mass exchange with close companions modify their internal structures and play an important role in the recent, realistic picture of massive star evolution (Sana et al. 2012; Schneider et al. 2015). Furthermore, observations of massive young stellar objects (MYSOs, i.e. protostars heavier than 8 $M_\odot$ and having a bolometric luminosity $L_{\rm bol} \geq 5 \times 10^3\,L_\odot$) demonstrated that binarity can already exist during the early formation phase of high-mass stellar objects; see also Chini et al. (2012), Mahy et al. (2013) and Kraus et al. (2017). Hence, the subsequent main-sequence evolution of MYSOs in the Hertzsprung–Russell diagram is a function of mechanisms that have already been at work since the initial stage of their formation phase. The evolution of massive stars starts well before the onset of their main-sequence phase, at a formation epoch that has been shown to be highly sensitive to mass accretion from the protocircumstellar medium (Hosokawa & Omukai 2009; Haemmerlé & Peters 2016; Haemmerlé et al. 2016, 2017).

Our knowledge of the formation of proto-O stars is driven mainly by observations. Fuente et al. (2001), Testi (2003) and Cesaroni et al. (2006) noticed that massive star formation resembles any other low-mass star formation process. Indeed, the surroundings of proto-O stars revealed the presence of converging accretion flows (Keto & Wood 2006), jets (Caratti o Garatti et al. 2015; Burns et al. 2017; Burns 2018; Purser et al. 2018; Samal et al. 2018), bipolar radiation-driven bubbles filled by ionizing radiation (Cesaroni et al. 2010; Purser et al. 2016) and collimated pulsed precessing jets (e.g. in Cepheus A: see Cunningham, Moeckel & Bally 2009; Reiter et al. 2017). Numerically, global simulations of monolithic gravitational collapse of isolated pre-stellar cores predicted the formation of dense accretion discs (Krumholz, Klein & McKee 2007); however, such models still clearly suffer from a lack of spatial resolution. Despite advances in supercomputing, it is difficult to resolve the central disc fully, from the outer infalling pre-stellar core material to the stellar surface, including substructures, such as dense

★ E-mail: dmameyer.astro@gmail.com

portions of spiral arms and eventually dense gaseous clumps developing with the arms. This is mainly due to the fact that their complex thermodynamic structure makes the so-called thin-disc approach less realistic than in the context of e.g. low-mass star formation, and obliges researchers to tackle the problem with three-dimensional models (Bonnell, Bate & Zinnecker 1998; Yorke & Sonnhalter 2002; Peters et al. 2010; Seifried et al. 2011; Harries 2015; Klassen et al. 2016; Harries, Douglas & Ali 2017). Therefore, parameter studies are numerically not conceivable and this justifies analytic treatments of the problem (Tanaka, Tan & Zhang 2017). High-resolution, self-consistent simulations focusing on the early evolution of MYSOs revealed the existence of accretion-driven outbursts in the context of young massive stars, caused by gravitational fragmentation of dense spiral arms followed by migration of gaseous clumps on to the forming star (Meyer et al. 2017). Furthermore, some gaseous clumps can collapse before reaching the star, initiating secondary (low-mass) star formation and forming spectroscopic protobinaries by direct disc fragmentation (Meyer et al. 2018). These findings orient further investigations on the evolution of massive protostars to their inner proto-circumstellar medium, where mass accretion on to MYSOs occurs.

This is our current picture of the formation of massive stars: theoretical models and available observational data indicate that it is nothing but a scaled-up version of low-mass star formation, retouched by corrections accounting for extreme photospheric conditions via radiation feedback (Richling & Yorke 1997; Rosen et al. 2017) and its coupling to magnetic fields (Seifried et al. 2011). However, the opaque environment in which they form still keeps direct disc observation of deeply embedded proto-O-type stars out of reach of modern instrumentation, although good candidates have been identified (Johnston et al. 2015; Forgan et al. 2016; Ilee et al. 2016; Cesaroni et al. 2017). A more systematic campaign with Atacama Large Milimeter/submilimeter Array (ALMA) failed in finding evidence of fragmented disc structures within a radius of 1000 au from young protostars (Beuther et al. 2017), though they were predicted numerically (Meyer et al. 2018).

While a growing number of Keplerian discs around MYSOs have been detected directly (Johnston et al. 2015; Forgan et al. 2016; Ilee et al. 2016), some of them including signs of substructures potentially linked to gravitational instability (Ginsburg et al. 2018), the fragmentation scenario proposes an explanation that bridges the gap between strong variability in the light curve of MYSOs (an observable) and a precursor mechanism – disc fragmentation at ∼100 au from the growing protostar. It is a vivid manifestation of the effectiveness of gravitational non-linear instabilities in the radiatively cooled protostellar surroundings (Gammie 1996) of newborn hot stars, which is regulated by the mechanical heating of dense spiral arms (Rogers & Wadsley 2012). Accretion bursts caused by disc fragmentation followed by inward migration of dense clumps on to the star have the advantage of being well understood in the context of young low-mass stars (Vorobyov & Basu 2005, 2015; Machida & Matsumoto 2011; Nayakshin & Lodato 2012; Zhao et al. 2018). In the high-mass context, bursts constitute a formidable insight into the recent past of the circumprotostellar medium, allowing us to probe the inner disc regions, which are not yet directly observable. Coincidently, such disc-mediated bursts have recently been observed, e.g. from the MYSOs S255IR NIRS 3 (Fujisawa et al. 2015; Stecklum et al. 2016; Caratti o Garatti et al. 2017) and NGC 6334I-MM1 (Hunter et al. 2017).

This work aims at studying the properties and occurrence of accretion-driven outbursts from massive stars. We perform three-dimensional gravito–radiation–hydrodynamical simulations of collapsing 100-$M_\odot$ rotating pre-stellar cores to model the long-term evolution of gravitationally unstable accretion discs around MYSOs. We extract from those simulations both the highly variable accretion-rate histories and luminosity curves interspersed with episodic bursts. The bursts are generated by the accretion of dense material from spiral arms in the disc and/or by the inward migration of fragments as described in Meyer et al. (2018). This picture is well-supported by observations of the spiral filament that is feeding the candidate disc around the young massive stellar object MM1-Main (Maud et al. 2017) and of a young stellar object fed by a gaseous clump in the double-cored system G350.69-0.49 (Chen et al. 2017). We separate the bursts of our modelled MYSOs using the method developed in the context of FU Orionis bursts (Vorobyov & Basu 2015; Vorobyov et al. 2018). The intensity and duration of individual bursts are analysed and compared with each other. We evaluate their occurrence during the early pre-main-sequence phase of stellar evolution and estimate the amount of time our MYSOs spend experiencing accretion bursts.

This study is organized as follows. In Section 2, we review the methods and initial conditions that we used to perform numerical hydrodynamical simulations of the circumstellar medium of our massive protostars. The total internal luminosities of young massive protostars obtained, exhibiting violent luminous spikes, are analysed in order to study the burst occurence throughout the life of their early pre-main-sequence stars. The evolution of accretion rate on to the MYSOs and analysis of their luminosity histories and their occurence are presented in Section 3, and we investigate the effects of stellar inertia on burst activity in Section 4. In Section 5, we detail the different types of accretion bursts happening throughout the early formation phase of MYSOs, investigate the effects of the burst phenomenon on the growth of young massive protostars and discuss our results further in the context of observations. Finally, we conclude in Section 6.

2 METHODS

In this section, we provide a concise description of the gravito–radiation–hydrodynamical simulations utilized to derive the mass transport rate on to our forming high-mass stars and summarize briefly the subsequent analysis method of their total luminosity history.

2.1 Numerical model

Numerical simulations are performed using a midplane-symmetric computational domain, which we initialize with a 100-$M_\odot$ solid-body-rotating pre-stellar core of uniform temperature $T_c = 10$ K and of an initially spherically symmetric density distribution, profiled as $\rho(r) \propto r^{\beta_\rho}$, with $\beta_\rho = -3/2$ and r the radial coordinate. Its inner radius r_{in} constitutes a semi-permeable sink cell fixed on to the origin of the domain and its outer radius, assigned to outflow boundary conditions, is located at $R_c = 0.1$ pc. The grid mesh maps the domain $[r_{in}, R_c] \times [0, \pi/2] \times [0, 2\pi]$, composed of $N_r = 138 \times N_\theta = 21 \times N_\phi = 138$ grid zones minimum. It expands logarithmically along the radial direction r, goes as a cosine in the polar direction θ and is uniformly spaced along the azimuthal direction ϕ. Such a grid intrinsically saves computing resources, while resolving the inner region of the midplane at high spatial resolution with a reduced total number of grid zones. We follow the gravitational collapse of the pre-stellar core and the early formation and evolution of the subsequent circumstellar accretion disc that surrounds the protostar. We calculate the material loss $\dot{M}$ through the

Table 1. Initial characteristics of our 100-$M_\odot$ solid-body-rotating pre-stellar cores. The table gives the inner sink-cell radius r_{in}, the ratio of rotational-to-gravitational energy β, final simulation time t_{end} and indicates whether stellar inertia is included in the models.

Models	r_{in} (au)	β (%)	t_{end} (kyr)	Wobbling
Run-long-4$^{(a)}$	20	4	60	no
Run-long-5$^{(a)}$	20	5	60	no
Run-long-10$^{(a)}$	20	10	60	no
Run1-hr$^{(b)}$	10	4	32	no
Run-without$^{(a)}$	12	4	40	no
Run-with$^{(a)}$	12	4	40	yes

Note. (*a*) this work, (*b*) Meyer et al. (2018).

sink cell directly as being the accretion rate on to the protostar, the properties of which (e.g. stellar radius and photospheric luminosity) are updated in time-dependent fashion using the pre-calculated protostellar evolutionary tracks of Hosokawa & Omukai (2009). Hence, our estimate of the protostellar radius is in accordance with the calculations of Hosokawa & Omukai (2009), as in Meyer et al. (2017, 2018). The different models are therefore characterized by the radius of the sink-cell r_{in} and the spin of the pre-stellar core, which is parametrized by its ratio of rotational-by-gravitational energy β. Two additional simulations are performed in order to test the validity of our assumption, consisting of neglecting the stellar inertia (Regály & Vorobyov 2017; Hirano et al. 2017). The comparison is effectuated in our Section 4. We use a slightly larger sink-cell radius ($r_{in} = 20$ au) than in our pilot study (see Meyer et al. 2017), which allows us to reach longer integration times t_{end} without dealing with dramatic time-step restrictions in the innermost grid zones. Such models, the characteristics of which are summarized in Table 1, permit us to obtain a large burst population, which is more suitable for our study.

We solve the equations of gravito–radiation–hydrodynamics with the PLUTO code[1] (Mignone et al. 2007, 2012). Direct protostellar irradiation feedback and radiation transport in the accretion disc are taken into account within the grey approximation with the scheme of Kolb et al. (2013)[2] adapted in the fashion of Meyer et al. (2018). This twofold algorithm ray-traces photon packages from the protostellar surface and diffuses their propagation into the disc in flux-limited fashion. Although other sophisticated methods have been developed for non-uniform Cartesian coordinate systems (Klassen et al. 2016; Rosen et al. 2017), it allows us to treat both the inner heating and the outer cooling of our irradiated discs accurately (Vaidya et al. 2011). Equivalent radiation–hydrodynamics methods have also been presented in e.g. Commerçon et al. (2011), Flock et al. (2013) and Bitsch et al. (2014). The opacity description, as well as the estimate of the local dust properties, is similar to that in Meyer et al. (2018), where gas and dust temperature are calculated assuming equilibrium between the silicate grain temperature and the total radiation field. We model stellar gravity by calculating the total gravitational potential of the central protostar and include the self-gravity of the gas[3] with the method of Black & Bodenheimer (1975) by solving the Poisson equation using the PETSC library.[4] As in the other articles of this series, we neglect turbulent viscosity by assuming that the most efficient angular momentum transport mechanism consists of the gravitational torque generated once a self-gravitating disc has formed after collapse (see also Hosokawa et al. 2016). We refer the reader interested further in the numerical method to Meyer et al. (2018).

[1] http://plutocode.ph.unito.it/
[2] http://www.tat.physik.uni-tuebingen.de/pluto/pluto_radiation/
[3] https://shirano.as.utexas.edu/SV.html
[4] https://www.mcs.anl.gov/petsc/

2.2 Internal luminosities of accreting protostars

The internal luminosity history of our accreting young stars is calculated as the sum of their photospheric luminosity $L_\star$, interpolated from the protostellar tracks of Hosokawa & Omukai (2009), plus the accretion luminosity $L_{acc} = GM_\star\dot{M}/2R_\star$, where G is the universal gravitational constant, $M_\star$ is the stellar mass, $\dot{M}$ is the accretion rate on to the protostar and $R_\star$ is the protostellar radius, respectively. Using pre-calculated tracks is a good compromise between the direct (but computationally costly) coupling of the gravito–radiation–hydrodynamics simulations to a stellar evolution code, which updates the stellar properties in real time by solving the stellar structure, and the simple treatment of $L_\star$ as a function of the stellar effective temperature. We analyse the total luminosity histories using four models, namely runs Run-long-4 per cent, Run-long-5 per cent and Run-long-10 per cent plus the model Run1-hr of Meyer et al. (2018). While Run-long-4 per cent, Run-long-5 per cent and Run-long-10 per cent form a homogeneous ensemble of simulations that assume similar grid resolution and sink-cell radius, model Run1-hr differs in its smaller sink-cell radius and higher grid resolution (see Table 1). The main limitation of such simulations, in addition to spatial resolution, is the radius of the inner sink cell, which should be as small as possible. The maximum radius of our sink cell is 20 au, which is smaller than in some other studies (up to 50 au, see in Hosokawa et al. 2016). Smaller sinks are very expensive computationally, due to strong limitations imposed by the Courant time-step condition. We note that the numerical convergence of runs with a grid resolution such as ours was demonstrated in section 5 of Meyer et al. (2018). Our overall goal consists of identifying the accretion bursts, numbers, characteristics and occurrence, in order to determine the time that young massive stars spend bursting during their early formation phase and the mass they accrete while experiencing those luminous events.

We use the statistical method developed in the context of accreting low-mass protostars in Vorobyov & Basu (2015) and Vorobyov et al. (2018). It aims at discriminating between the background secular variability, accounting for anisotropies in the accretion flow generated by the presence of enrolled spiral arms, and the various luminosity bursts generated by the accretion of dense gaseous clumps. It can be summarized as follows. A background luminosity L_{bg} is calculated by filtering out all accretion-driven events such that a smooth function of time is obtained. The quantity L_{bg} is taken as being $L_{acc} + L_\star$ if the instantaneous accretion rate $\dot{M}(t)$ is smaller than $\dot{M}_{crit} = 5 \times 10^{-4}\,M_\odot\,yr^{-1}$ and $L_{acc} \times \dot{M}_{crit}/\dot{M}(t) + L_\star$ otherwise, which has the effect of filtering out all strong accretion bursts from the stellar internal luminosity. We then derive the intensities and durations of so-called 1-mag, 2-mag, 3-mag and 4-mag accretion-driven outbursts. In particular, by the 1-mag outburst we mean all outbursts with luminosity greater than 2.5 times the background luminosity (1-mag cut-off), but lower than 2.5^2 times the background luminosity (2-mag cut-off). The 2-, 3- and 4-mag bursts are defined accordingly, with the exception of the 4-mag bursts having no upper limit (Table 2). The filtering method additionally ensures that (i) the accretion-driven burst duration is short enough that slow increases and decreases of the total internal stellar luminosity are not mistaken as outbursts and (ii) low-intensity kinks of less than 1 mag present in the light curves are also not interpreted

Table 2. Summary of burst characteristics. $N_{\rm bst}$ is the number of bursts at a given magnitude cut-off. $L_{\rm max}/L_{\rm min}/L_{\rm mean}$ are the maximum, minimum and mean burst luminosities, respectively. Similarly, $\dot{M}_{\rm max}/\dot{M}_{\rm min}/\dot{M}_{\rm mean}$ are the maximum, minimum and mean accretion rates through the central sink cell and $t_{\rm bst}^{\rm max}/t_{\rm bst}^{\rm min}/t_{\rm bst}^{\rm mean}$ are the maximum, minimum and mean burst duration, while $t_{\rm bst}^{\rm tot}$ is the integrated burst duration time throughout the star's life.

Model	$N_{\rm bst}$	$L_{\rm max}/L_{\rm min}/L_{\rm mean}$ (10^5 L$_\odot$ yr^{-1})	$\dot{M}_{\rm max}/\dot{M}_{\rm min}/\dot{M}_{\rm mean}$ (M$_\odot$ yr^{-1})	$t_{\rm bst}^{\rm max}/t_{\rm bst}^{\rm min}/t_{\rm bst}^{\rm mean}$ (yr)	$t_{\rm bst}^{\rm tot}$ (yr)
			1-mag cut-off		
Run-long-4%	34	14.7 / 0.56 / 7.39	0.018 / 0.003 / 0.007	39 / 5 / 14	471
Run-long-5%	21	15.1 / 0.067 / 4.4	0.019 / 0.001 / 0.008	88 / 9 / 26	553
Run-long-10%	49	13.1 / 0.054 / 3.78	0.023 / 5.13 $\times$ 10^{-4} / 0.006	94 / 5 / 16	790
Run-hr	24	2.9 / 0.06 / 0.54	0.029 / 0.001 / 0.008	100 / 5 / 51	1231
Total all models	**128**	**15.1 / 0.054 / 4.03**	**0.029 / 5.13 $\times$ 10^{-4} / 0.007**	**100 / 5 / 27**	**761**
			–		
Run-without	9	4.31 / 0.11 / 1.49	0.0177 / 0.0022 / 0.0081	107 / 9 / 38	340
Run-with	6	3.60 / 0.123 / 1.19	0.0262 / 0.0024 / 0.0131	66 / 9 / 29	173
			2-mag cut-off		
Run-long-4%	22	45.6 / 10.5 / 25.7	0.036 / 0.012 / 0.022	55 / 3 / 13	285
Run-long-5%	6	35.7 / 6.4 / 15.3	0.049 / 0.010 / 0.027	17 / 6 / 12	69
Run-long-10%	13	28 / 0.15 / 7.65	0.049 / 0.003 / 0.021	74 / 6 / 20	264
Run-hr	3	4.26 / 1.59 / 2.76	0.059 / 0.035 / 0.050	61 / 30 /44	131
Total all models	**44**	**45.6 / 0.15 / 12.9**	**0.059 / 0.003 / 0.03**	**74 / 3 / 22**	**187**
			–		
Run-without	5	8.05 / 1.90 / 4.64	0.0479 / 0.0241 / 0.0343	34 / 5 / 18	88
Run-with	5	9.80 / 1.57 / 4.12	0.0567 / 0.0175 / 0.0397	33 / 7 / 21	105
			3-mag cut-off		
Run-long-4%	5	65.7 / 13.5 / 48.8	0.054 / 0.035 / 0.044	29 / 4 / 12	60
Run-long-5%	2	37.4 / 4.99 / 21.2	0.062 / 0.045 / 0.053	35 / 8 / 22	43
Run-long-10%	3	38.5 / 9.24 / 23.2	0.071 / 0.038 / 0.056	8 / 3 / 6	17
Run-hr	2	17.9 / 5.28 / 11.6	0.111 / 0.069 / 0.090	51 / 50 / 51	101
Total all models	**12**	**65.7 / 4.99 / 26.2**	**0.111 / 0.035 / 0.061**	**51 / 3 / 23**	**55**
			–		
Run-without	2	12.2 / 8.55 / 10.4	0.105 / 0.083 / 0.094	6 / 4 / 5	10
Run-with	2	17.8 / 16.2 / 17.0	0.121 / 0.059 / 0.0895	11 / 7 / 9	18
			4-mag cut-off		
Run-long-4%	5	745 / 140.5 / 308	0.524 / 0.093 / 0.226	9 / 2 / 5	27
Run-long-5%	8	644.3 / 37.5 / 221.3	0.438 / 0.080 / 0.215	10 / 2 / 4	32
Run-long-10%	4	432.4 / 100 / 261.9	0.925 / 0.101 / 0.424	7 / 2 / 4	14
Run-hr	–	–	–	–	–
Total all models	**17**	**745 / 37.5 / 263.7**	**0.925 / 0.080 / 0.288**	**10 / 2 / 4**	**24**
			–		
Run-without	–	–	–	–	–
Run-with	1	51.2 / 51.2 / 51.2	0.16 / 0.16 / 0.16	4 / 4 / 4	4

as accretion outbursts, because they may be produced by boundary effects. Fig. 1 illustrates the burst filtering method on a series of successive accretion peaks, for which their prominence (luminous intensity with respect to $L_{\rm bg}$) and duration (width at half-maximal prominence) are plotted. Statistical quantities such as variance and standard deviations of the collection of selected bursts are finally derived (Table 3). We refer the reader interested in further details about the burst analysis method to Vorobyov & Basu (2015) and Vorobyov et al. (2018).

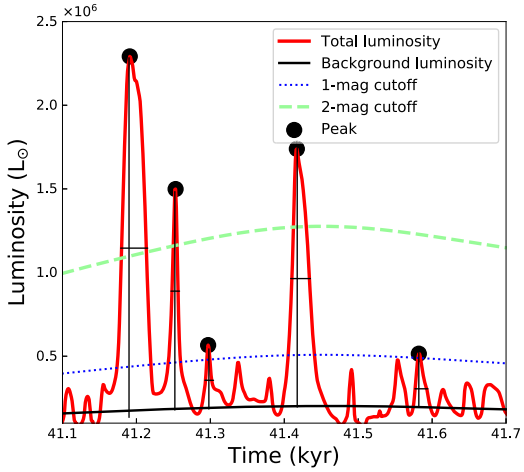

Figure 1. Illustration of the burst filtering method on a series of peaks. For each burst, the prominence and duration at half maximum are indicated.

3 EPISODIC ACCRETION-DRIVEN BURSTS

In this section, we present the accretion-rate histories of our set of simulations and describe their corresponding protostellar luminosities. We then analyse the burst characteristics in order to extract their properties, such as duration and occurence.

3.1 Accretion-rate histories

Fig. 2 shows the evolution of accretion rate (in M$_\odot$ yr^{-1}) on to our protostars, formed out of pre-stellar cores with initial rotational-to-gravitational energy ratios $\beta = 4$ per cent (Run-long-4, panel a),

Table 3. Mass (in $M_\odot$) and proportion (in %) of final protostellar mass accreted as a function of the protostellar brightness at the moment of accretion.

Models	$M_\star$	$L_{tot} \sim L_{bg}$	1-mag	2-mag	3-mag	4-mag
			Accreted mass (in $M_\odot$)			
Run-long-4%	47.33	25.06	5.28	10.04	2.59	4.36
Run-long-5%	41.57	21.48	5.48	4.97	5.20	4.44
Run-long-10%	34.15	19.35	6.39	3.66	0.93	3.82
Run-hr	20.07	15.25	1.13	1.88	1.74	0.07
Mean ($r_{in} = 20$ au)	**41.02**	**21.96**	**5.72**	**6.22**	**2.91**	**4.21**
			–			
Run-without	24.76	18.64	3.01	2.46	0.63	0.00
Run-with	24.35	15.46	3.76	3.63	1.19	0.29
			Proportion of final protostellar mass (in %)			
Run-long-4%	100	52.94	11.17	21.21	5.47	9.21
Run-long-5%	100	51.66	13.18	11.95	12.51	10.70
Run-long-10%	100	56.65	18.70	10.73	2.74	11.18
Run-hr	100	75.97	5.60	9.36	8.70	0.37
Mean ($r_{in} = 20$ au)	**100**	**53.75**	**14.35**	**14.63**	**6.91**	**10.36**
			–			
Run-without	100	75.30	12.19	9.93	2.55	0.00
Run-with	100	63.49	15.45	14.94	4.89	1.21

5 per cent (Run-long-5, panel b), 10 per cent (Run-long-10, panel c) and Run1-hr (panel d). The effects of accretion on protostar growth are illustrated explicitly in the figure by plotting the evolution of protostellar mass (thick dotted red line, in $M_\odot$) over the accretion-rate histories (thin solid blue lines). Additionally, an orange dot marks the time instance when the young star becomes a massive object ($M_\star \geq 8\,M_\odot$). The dotted black vertical lines separate different sequences of the young star's life, characterized by distinct accretion regimes. The first vertical line corresponds to the onset of disc formation, when the free-fall of the envelope material on to the star ceases and the star starts gaining its mass via accretion from the circumstellar disc. The second vertical line marks the beginning of the first sudden increase of accretion rate, which is associated with a $\geq$2 mag burst (see Section 3.2). These two vertical lines highlight distinct protostellar mass accretion regimes corresponding to several different accretion phases.

First, the collapse of the parent pre-stellar core generates an infall of material through the sink cell, producing the initial increase in mass flux through the inner boundary. During the initial $\approx$2 Myr, the mass accretion rate increases from $\approx 10^{-6}$ to $\approx 10^{-4}\,M_\odot\,yr^{-1}$ and a further increase of the collapsing gas radial velocity happens over the next $\approx$ 10 kyr, increasing $\dot{M}$ from $\approx 10^{-4}$ to slightly less than $\approx 10^{-3}\,M_\odot\,yr^{-1}$. The latter value is the typical rate at which MYSOs are predicted to accrete (Hosokawa & Omukai 2009). The time instance of disc formation is a function of the initial spin of the pre-stellar core; see also Meyer et al. (2018). When the disc forms (first vertical line of Fig. 2a–d), moderate variability appears immediately in the accretion flow, as a result of anisotropies in the density and velocity fields close to the MYSOs. The values of $\dot{M}(t)$ evolve such that the variation amplitude gradually augments up to spanning over almost 2 orders of magnitude, from $\approx 10^{-4}$ to $\approx 10^{-2}\,M_\odot\,yr^{-1}$ (Fig. 2b). A slight change in the slope of the mass evolution is associated with the beginning of this second, variable-accretion phase. All our protostars become heavier than 8 $M_\odot$ and therefore enter the massive regime of stellar masses in this phase (see orange dot). Although the increase in stellar mass is still smooth (thick dotted red line), step-like augmentations due to the fast accretion of dense material by the sink cell happen, e.g. at times $\approx$23 kyr in model Run-long-5 and $\approx$24 kyr in model Run-1-hr (thick red dotted line of Fig. 2b,d), when the protostellar mass has reached $\approx 10\,M_\odot$. Those accretion spikes grow in number and intensity as a function of time, because the discs surrounding the MYSOs, while growing in size, develop complex morphologies by adopting the filamentary structure of self-gravitational rotating discs. A more detailed description of the early disc structure evolution of massive irradiated self-gravitating discs can be found in Meyer et al. (2018).

The variation in amplitude of the accretion rate continues to increase during about 10−15 kyr after disc formation, until the MYSOs enter the next evolution phase, marked by the second dotted vertical line. For each model, such events are highlighted in Fig. 2 with the second vertical line. Without stopping baseline accretion (at the average rate of $\approx 10^{-3}\,M_\odot\,yr^{-1}$), this evolution phase is regularly interspersed with strong accretion spikes, which generate luminosity outbursts via the mechanism highlighted in Meyer et al. (2017). The essence of this mechanism is gravitational fragmentation of the disc's spiral arms, which extend up to radii $\approx$100−1000 au, followed by inward migration and infall of gaseous clumps on the protostar. At this stage, the mass of the protostar grows, essentially due to those strong accretion events, and the mass gained by accretion during the quiescent phase is negligible (see also discussion in Section 5.3). The difference in the spike occurrence is only a function of the initial gravitational-to-kinetic energy β (our Table 1), as it is the sole parameter by which models Run-long-4, Run-long-5 and Run-long-10 differ (Fig. 2a–c). At $t_{end} = 60$ kyr, the MYSOs have masses of about $\approx$47, $\approx$42 and $\approx$34 $M_\odot$, respectively. Their growth should continue up to exhaustion of disc's envelope mass reservoir. When the envelope no longer fuels the star–disc system, both infall rate on to the disc and accretion rate on to the protostar should gradually decrease and stop (not modelled in our simulations), as happens in the context of low-mass star formation (Vorobyov 2010; Vorobyov et al. 2017).

3.2 Protostellar luminosities

Fig. 3 plots the total, bolometric luminosity of the MYSO evolution (photospheric plus accretion luminosity, in $L_\odot$) as a function of time (in kyr) of our protostars generated by the collapse of pre-stellar cores of initial kinetic-to-gravitational energy ratio $\beta = 4$ per cent (Run-long-4, panel a), 5 per cent (Run-long-5, panel b), 10 per cent (Run-long-10, panel c) and Run1-hr (panel d). The thin dotted red

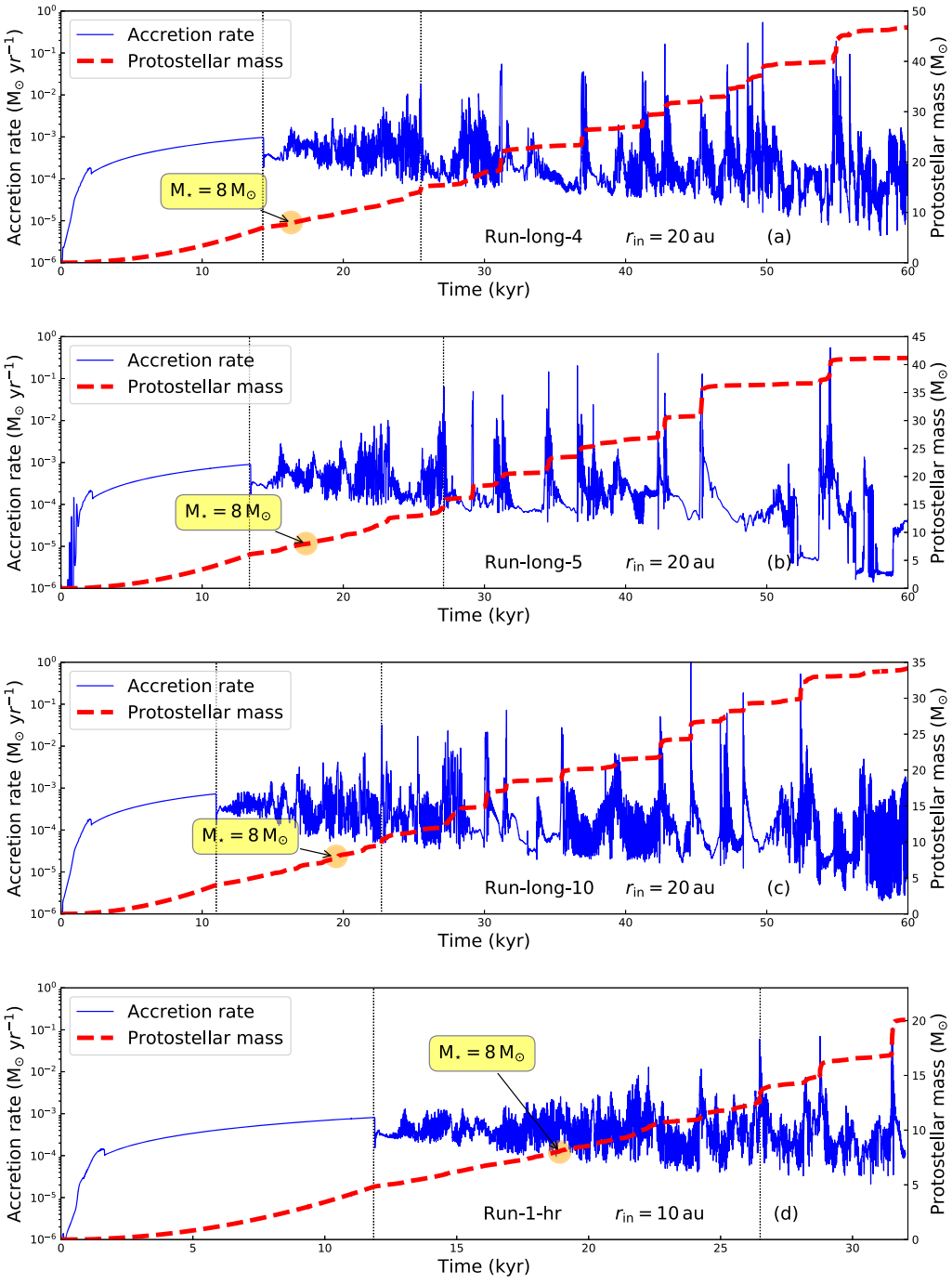

Figure 2. Mass accretion rate (thin solid line, in $M_\odot\,yr^{-1}$) and protostellar mass evolution (thick dashed line, in $M_\odot$) in our simulations of 100-$M_\odot$ solid-body-rotating pre-stellar cores with β of (a) 4 per cent, (b)5 per cent, (c) 10 per cent and (d) Run1-hr.

line represents the total luminosity, the black solid line corresponds to the background luminosity L_{bg}, while the dotted thin blue line, dashed dotted orange line and dashed violet lines show the limits of the 1-, 3- and 4-mag cut-offs with respect to L_{bg}. The overplotted dots are the peak accretion rates for the burst, the peak luminosity of which is at least 2.5 times brighter than the quiescent pre-flare protostellar luminosity. Shown in the 0.01–0.1 $M_\odot$ range, their colour corresponds to the peak's accretion rate (in $M_\odot\,yr^{-1}$). As in Fig. 2, the orange dot indicates the time instance when the star becomes a massive object ($M_\star \geq 8\ M_\odot$) and the dotted black vertical lines sep-

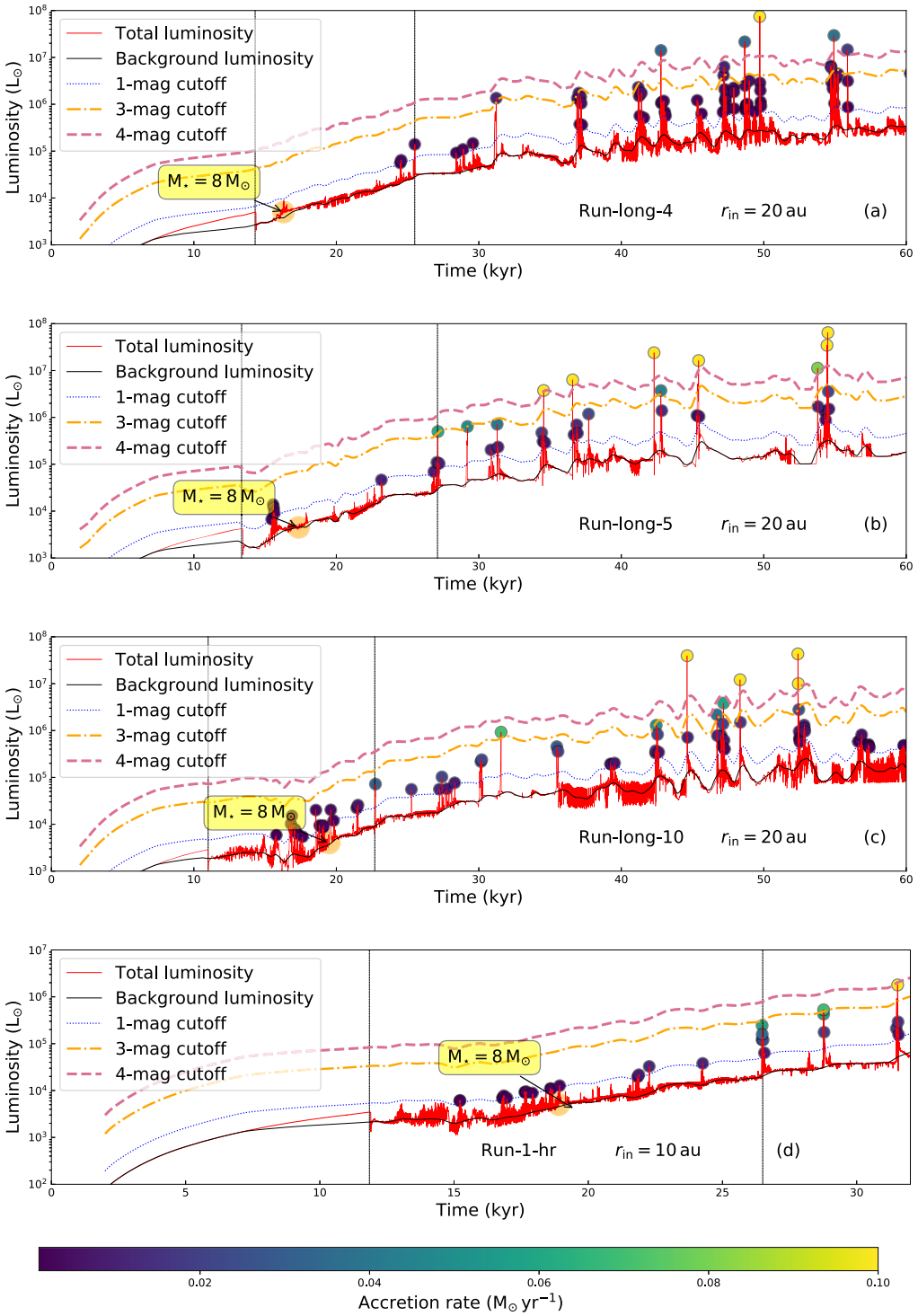

Figure 3. Total luminosity (thin solid red line, in $L_\odot$) as a function of time (in kyr) of our models with β of (a) 4 per cent, (b) 5 per cent, (c) 10 per cent and (d) Run1-hr. The panels show the background luminosity (thin solid black line) and the dotted lines indicate luminosity greater than 2.5, ≈6.3 and ≈39.0 times the background luminosity (1-, 2- and 4-mag cut-off), respectively. The colour bar indicates the accretion rate for the filled circles.

arate the mass regimes described above: the onset of disc formation and the beginning of the spiked accretion phase.

The initial free-fall gravitational collapse of pre-stellar cores corresponds to a luminosity phase $< 10^3\,L_\odot$ which lasts ≈10 kyr. As demonstrated in fig. 7 of Meyer et al. (2018), the protostars still have negligible accretion luminosity: because of still relatively small stellar mass and/or large stellar radius, their luminosity is governed by their photospheric component $L_{\rm bol} \approx L_\star \leq 10^4\,L_\odot$ (Fig. 3a–d). Stellar objects in such a phase are likely not observable, as they are not bright enough to produce photons able to escape their opaque embedded host cores. Once the circumstellar disc forms (first black vertical line), the luminosity adopts a time-dependent behaviour, which reflects the protostellar accretion-rate history (Fig. 2a). All our models exhibit a spectrum of burst magnitudes from 1-mag bursts to 4-mag bursts, except for model Run-1-hr, which lacks the 4-mag bursts (perhaps due to shorter simulation times, ≈35 kyr, compared with other models). However, the total number of bursts and number of bursts of a certain magnitude vary from model to model.

Indeed, a finer grid resolution resolves the Jeans length better. That, in its turn, allows us to treat the disc gravitational instabilities more realistically and reveals smaller disc fragments, a subset of which of will end up migrating on to the protostar and generating (milder intensity) bursts. As an example, our model Run-long-4 has a single 1-mag burst (Fig. 3a), whereas our model Run-1-hr exhibits nine of them over roughly the same time interval (between the two vertical black lines, see Fig. 3d). A more thorough discussion of the resolution dependence of numerical investigations on disc fragmentation can be found in Meyer et al. (2018). Similarly, bursts are more frequent at higher β ratio, e.g. Run-long-4 has a single 1-mag burst, but Run-long-10 has more than a dozen (Fig. 3a,c). This illustrates the effects of the initial conditions on the disc dynamics. We also notice that, in the case of our fast-rotating models, bursts develop earlier in time, e.g. models Run-long-10 and Run-long-4 have their first 1-mag burst at time ≈15 kyr and ≈26 kyr, respectively.

After the first strong ($\geq$ 2-mag) burst, variations in the total protostellar luminosity gradually increase, as the accretion luminosity overwhelms the photospheric contribution to the total luminosity. This is tied to the rising complexity of the disc pattern: the multiple spiral arms and gaseous clumps forming in the disc experience a chaotic motion and interact violently by formation, destruction, merging and migration in the star's surroundings (Meyer et al. 2018). The number of bursts per unit time consequently increases after ≈30 kyr and the protostellar light curve is shaped as a forest of accretion-driven peaks. The burst intensity is not a monotonic function of time, as high-intensity bursts (e.g. 3- and 4-mag) can be interspersed with lower intensity ones (e.g. 1- and 2-mag) or quiescent burstless phases. Bursts often appear grouped as a collection of different magnitude bursts over a rather small time interval, see e.g. our model Run-long-4 at times 45−50 kyr.

Note that accretion-driven bursts can appear either isolated or clustered. Single bursts are provoked by the infall of a gaseous clump that is detached from its parent spiral arm and experiences a migration towards the central MYSO; see the mechanism described in Meyer et al. (2017). They correspond to the accretion of a relatively large amount of compact circumstellar material over rather short time-scales (∼10 yr), which produces a unique high-luminosity burst. The rapid successive accretion of several migrating clumps from different parent arms, the merging of clumps into inhomogeneous gaseous structures or even the migration of clumps that separate an inner portion of spiral arms into two segments makes the accretion pattern more complex and can produce different a type of light curve exhibiting lower-intensity, clustered bursts, in a manner consistent with the description of Vorobyov & Basu (2015) for low-mass star formation.

3.3 Burst characteristics

We summarize the analysis of our population of accretion-driven bursts in our Table 2. For each of the four models, it reports the number of bursts with specific magnitude (1, 2, 3 and 4 mag) and also the total number of bursts. It also indicates the maximum, minimum and mean values of the burst luminosity ($L_{\rm max}$, $L_{\rm min}$, $L_{\rm mean}$, in $10^5\,L_\odot\,{\rm yr}^{-1}$), the maximum, minimum and mean values of the burst peak accretion rate through the sink cell ($\dot{M}_{\rm max}$, $\dot{M}_{\rm min}$, $\dot{M}_{\rm mean}$, in $M_\odot\,{\rm yr}^{-1}$) and the maximum, minimum and mean values of the burst duration ($t_{\rm bst}^{\rm max}$, $t_{\rm bst}^{\rm min}$, $t_{\rm bst}^{\rm mean}$, in yr), respectively. Finally, it provides the integrated duration of bursts $t_{\rm bst}$ (in yr), i.e. the time that the protostar in each model spends in the burst phase during the initial 60 kyr of evolution. For each cut-off magnitude, the bold line reports the averaged values of those quantities.

The number of low-intensity accretion-driven bursts is much higher than that of high-intensity bursts, e.g. the integrated number of 1-mag bursts in our set of models is $N_{\rm bst} = 128$, while it is $N_{\rm bst} = 44$ and $N_{\rm bst} = 12$ for 2- and 4-mag bursts, respectively. This is because low-rate accretion variability, provoked by accretion of dense portions of spiral arms, is more frequent than the high-rate variability caused by the infalling gaseous clumps. Our simulations with $\beta = 4$ per cent and 10 per cent have more 1-, 2- and 3-mag bursts than our simulations with $\beta = 5$ per cent; however, the opposite trend is seen for the 4-mag bursts. Thus, our results do not support an interpretation of the simplistic picture of discs exhibiting an efficiency of gravitational instability directly proportional to the initial spin of the pre-stellar core and gradually increasing with β. The peak luminosities of 1-mag bursts range from $L_{\rm min} = 0.054 \times 10^5\,L_\odot$ to $L_{\rm max} = 15.1 \times 10^5\,L_\odot$, whereas they vary by two and one order of magnitude for our 2- and 3-mag bursts, exhibiting $L_{\rm min} = 0.15 \times 10^5$ and $4.99 \times 10^5\,L_\odot$, to reach $L_{\rm max} = 45.6 \times 10^5$ and $65.7 \times 10^5\,L_\odot$, respectively. Therefore, some 1-mag bursts can be more luminous (in bolometric luminosity) than some 2- or 3-mag bursts, depending on the corresponding pre-burst background stellar luminosity. The model Run-1-hr does not have 4-mag bursts because, due to time-step restrictions, we could not run it for longer integration times.

Figs 4–6 show several correlation plots of the various burst characteristics of a homogeneous subset of three of our models ($r_{\rm in} = 20$ au). Fig. 4 displays the burst peak luminosity $L_{\rm burst}$ (in $L_\odot$) as a function of the burst duration $t_{\rm bst}$, with a colour coding giving information about the accreted mass per burst (see panel (a), in $M_\odot$), and the peak accretion rate $\dot{M}$ (in $M_\odot\,{\rm yr}^{-1}$) as a function of the burst duration $t_{\rm bst}$, with a colour coding giving information about the accreted mass per burst (see panel (b), in $M_\odot$). On each plot, the symbols and their sizes are functions of the burst magnitude (smallest symbols for 1-mag bursts and largest symbols for 4-mag bursts) and specify the models to which each burst belongs (circles for our Run-long-4 per cent, squares for Run-long-5 per cent and triangles for Run-long-10 per cent). The overplotted line is a fit of all bursts together.

Fig. 4(a) and (b) shows that 4-mag bursts have $L_{\rm tot} > 3 \times 10^6\,L_\odot$ and a duration time < 10 yr, while 1-mag bursts are located in the region with $L_{\rm tot} < 3 \times 10^6\,L_\odot$ and > 4 yr. The same distribution appears regardless of the model conditions. The overplotted line fitting the burst population highlights this general trend − luminous bursts are shorter in duration, even if our bursts show diversity in

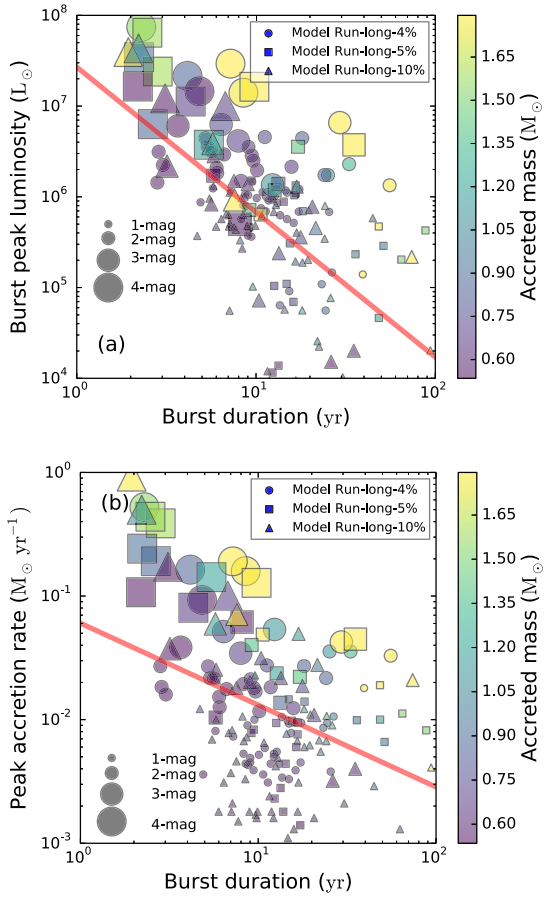

Figure 4. Correlation between (a) burst duration versus peak luminosity and (b) burst duration versus peak accretion rate for each individual burst, with colours representing the mass accreted by the protostar during the bursts.

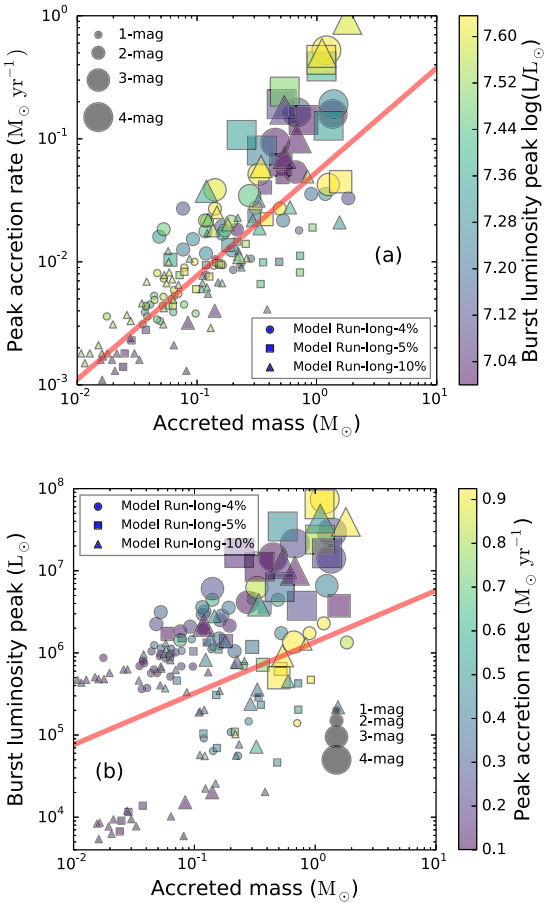

Figure 5. Correlation between (a) accreted mass versus peak accretion rate and (b) accreted mass versus peak luminosity for each individual burst, with colours representing (a) peak luminosity and (b) peak accretion rate, respectively.

the form of scatter in bolometric luminosity spanning over several orders of magnitude at a given burst duration. Therefore, the burst peak luminosity (Fig. 4a) and maximal accretion rate (Fig. 4b) decrease globally with the burst duration (thick red lines in Fig. 4). The more efficient mass-accreting bursts are mostly 3 and 4 mag, short-lived and some high-luminosity events or long-lived 1-mag bursts (see colour scale of Fig. 4a). Such bursts are typically associated with the largest peak accretion rates, located in the short-duration and high-luminosity region of the figure (Fig. 4b). This statistical discrepancy between the global correlation between peak accretion mass and peak accretion rate is already visible in our Table 2 and illustrates the variety of burst durations produced for a given increase of MYSO bolometric luminosity with respect to the pre-burst luminosity.

Fig. 5(a) shows the accreted mass (in $M_\odot$ as a function of the burst peak accretion rate (in $M_\odot\,yr^{-1}$) and Fig. 5(b) plots the accreted mass as a function of the the burst peak luminosity (in $L_\odot$), respectively. Additionally, the colour coding indicates (a) the burst peak luminosity and (b) the peak accretion rate during bursts. Our models reveal a good correlation between the peak accretion rate and the accreted mass of their bursts (see thick red line). Fig. 5(a) is a consequence of the typical Gaussian-like shape of the accretion profiles, the integral of which as a function of time (i.e. the accreted

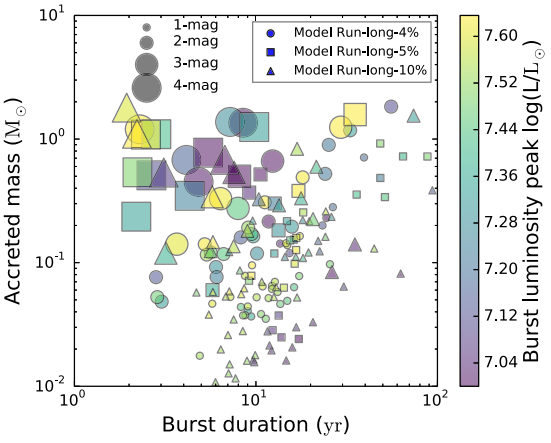

Figure 6. Correlation between burst duration and accreted mass for each individual burst, with colours representing the burst peak luminosity.

mass) is proportional to the peak accretion rate, whereas Fig. 5(b) is a natural outcome of the prescription used to estimate $L_{\rm acc} \propto \dot{M}$, low-luminosity deviations appearing because of occasional, rapid fluctuations of the stellar radius (Hosokawa & Omukai 2009). Finally, Fig. 6 plots the burst duration (in yr) as a function of the accreted mass during the corresponding burst (in $M_\odot$), with colour coding giving information about the burst luminosity (in $L_\odot$). This figure clearly illustrates our model predictions regarding luminosity bursts in MYSOs: more luminous bursts (3 and 4 mag) accrete more mass than their less luminous counterparts (1 and 2 mag), although the former are shorter in duration than the latter. Accordingly, the different burst populations do not overlap in the figure and organize in different, adjacent regions (Fig. 6b).

4 THE EFFECT OF STELLAR MOTION

The role of stellar motion on the disc dynamics and burst properties is examined in this section. We first introduce the mechanism responsible for stellar motion and its implementation in our code and then compare two simulations of equivalent initial conditions and included physics, but considered without and with stellar wobbling.

4.1 Stellar inertia and its implementation in the PLUTO code

When hydrodynamical simulations of circumstellar discs are run using a curvilinear coordinate system, the sink cell representing the star and its direct surroundings is attached to the origin of the computational domain. The natural response of the star to changes in the mass distribution of its circumstellar disc, when the disc barycentre does not coincide with the origin of the domain, is therefore neglected. Taking stellar motion into account may become important when the initial axisymmetry of the rigidly rotating pre-stellar core is broken by the development of dense spiral arms and heavy gaseous clumps in the disc and their gravitational pull on the star is not mutually cancelled. This mechanism was first revealed in the analytical study on eccentric gravitational instabilities in discs around low-mass protostars of Adams, Ruden & Shu (1989). It is intrinsically taken into account in Lagragian simulations such as the smooth hydrodynamical models (SPH) of e.g. Bonnell & Bate (1994), Rice, Lodato & Armitage (2005), Meru & Bate (2010) and Lodato & Clarke (2011), as well as in simulations performed with three-dimensional Cartesian codes; see e.g. Krumholz et al. (2007), Kratter et al. (2010), Commerçon, Hennebelle & Henning (2011), Klassen et al. (2016) and Rosen et al. (2016). Regály & Vorobyov (2017) and Vorobyov & Elbakyan (2018) studied the effect of stellar wobbling on disc evolution and migration of gaseous clumps and protoplanets using grid-based codes in polar coordinates. They found that stellar motion may affect the migration speeds of gaseous clumps and protoplanets in the disc notably, but the final disc masses and sizes and also disc propensity to fragment were affected to a lesser extent. Since high-mass protostars are surrounded by massive discs (Johnston et al. 2015; Forgan et al. 2016; Ilee et al. 2016; Cesaroni et al. 2017) in which heavy substructures (gaseous clumps, low-mass companions and/or asymmetric spiral arms) can form by fragmentation in the disc (Meyer et al. 2018), the question is therefore how much those asymmetries may affect the total gravitational potential of the protostar–disc system during the rather short pre-main-sequence phase (∼kyr); see Section 4.2.

Our implementation of stellar motion into the PLUTO code for a spherical coordinate system consists of calculating the resultant gravitational force applied by the disc to the star using Cartesian projections and is inspired by Hirano et al. (2017). The gravitational force applied by the massive disc to the growing protostar is

$$\delta \boldsymbol{F}_{\rm disc/\star} = -G \frac{\delta M_{\rm disc}(r) M_\star}{r^2} \boldsymbol{e}_r, \tag{1}$$

where $\delta M_{\rm disc}(r)$ is the mass of a grid zone located in the disc, r is the distance from the cell considered to the central protostar and $\boldsymbol{e}_r$ is the unit vector in the radial direction. The projection of the force $\boldsymbol{F}_{\rm disc/\star}$ on to the Cartesian directions $(\boldsymbol{e}_x, \boldsymbol{e}_y, \boldsymbol{e}_z)$ is

$$\delta F^x_{\rm disc/\star} = \delta \boldsymbol{F}^x_{\rm disc/\star} \cdot \boldsymbol{e}_x = \delta |\boldsymbol{F}_{\rm disc/\star}| \cos(\phi) \sin(\theta), \tag{2}$$

$$\delta F^y_{\rm disc/\star} = \delta \boldsymbol{F}^y_{\rm disc/\star} \cdot \boldsymbol{e}_y = \delta |\boldsymbol{F}_{\rm disc/\star}| \sin(\phi) \sin(\theta), \tag{3}$$

$$\delta F^z_{\rm disc/\star} = \delta \boldsymbol{F}^z_{\rm disc/\star} \cdot \boldsymbol{e}_z = \delta |\boldsymbol{F}_{\rm disc/\star}| \cos(\theta), \tag{4}$$

where ϕ and θ represent the azimuthal and polar angles, respectively. We integrate the Cartesian components of the gravitational backaction of the circumstellar disc on to the protostar. Therefore, the Cartesian components of the total force $\boldsymbol{F}_{\rm disc/\star}$ read

$$F^x_{\rm disc/\star} = \int_{\rm disc} \delta F^x_{\rm disc/\star}, \tag{5}$$

$$F^y_{\rm disc/\star} = \int_{\rm disc} \delta F^y_{\rm disc/\star}, \tag{6}$$

$$F^z_{\rm disc/\star} = \int_{\rm disc} \delta F^z_{\rm disc/\star}, \tag{7}$$

where the disc is evaluated as the gas that lies within the innermost envelope located at radii ≤ 3000 au of the computational domain (Meyer et al. 2018). Finally, we recover

$$\boldsymbol{F}_{\rm disc/\star} = \sqrt{{F^x_{\rm disc/\star}}^2 + {F^y_{\rm disc/\star}}^2 + {F^z_{\rm disc/\star}}^2}\, \boldsymbol{e}_r, \tag{8}$$

which is the total force exerted by the disc on the star. In our midplane-symmetric picture,

$$F^z_{\rm disc/\star} = 0 \tag{9}$$

and $\boldsymbol{F}_{\rm disc/\star}$ reduces to

$$\boldsymbol{F}_{\rm disc/\star} = \sqrt{{F^x_{\rm disc/\star}}^2 + {F^y_{\rm disc/\star}}^2}\, \boldsymbol{e}_r. \tag{10}$$

As we keep the protostar fixed at the origin of the computational domain, the effective force that we apply to each grid cell is

$$\boldsymbol{F}_{\rm wobbling} = \boldsymbol{F}_{\star/\rm disc} = -\boldsymbol{F}_{\rm disc/\star}, \tag{11}$$

which has the effect of translating the disc solution around the star by the opposite vector of the force exerted by the disc on it. The effect of the wobbling force is finally introduced as an additional acceleration term,

$$\boldsymbol{g}' = \frac{\boldsymbol{F}_{\rm wobbling}}{M_\star}, \tag{12}$$

in the gravity solver of the PLUTO code. In spherical coordinates, the different components of $\boldsymbol{g}'$ read

$$g'_r = \frac{1}{M_\star} \Big[F^x_{\rm disc/\star} \sin(\theta) \cos(\phi) + F^y_{\rm disc/\star} \sin(\theta) \sin(\phi) + F^z_{\rm disc/\star} \cos(\theta) \Big], \tag{13}$$

$$\boldsymbol{g}'_{\phi} = \frac{1}{M_{\star}}\Big[F^{x}_{\mathrm{disc}/\star}\cos(\theta)\cos(\phi) + F^{y}_{\mathrm{disc}/\star}\cos(\theta)\sin(\phi) - F^{z}_{\mathrm{disc}/\star}\sin(\theta)\Big], \tag{14}$$

$$\boldsymbol{g}'_{\theta} = \frac{1}{M_{\star}}\Big[-F^{x}_{\mathrm{disc}/\star}\sin(\phi) + F^{y}_{\mathrm{disc}/\star}\cos(\phi)\Big], \tag{15}$$

respectively. As described by Regály & Vorobyov (2017), this method induces boundary effects at the outer extremities of the computational domain, when the stellar motion is so pronounced that the corresponding translation of the whole solution by $\boldsymbol{F}_{\mathrm{wobbling}}$ gradually provokes cavities that open at the outer edges of the pre-stellar core. This is an issue meriting future numerical investigations and code development; however, it does not affect our comparison tests, because we run simulations with high-mass cores that collapse faster (∼40 kyr) than in the context of solar-mass pre-stellar cores. In the section below, we compare two simulations of gravitational collapse and disc formation of similar initial conditions but considered with and without stellar motion.

4.2 Effects of stellar wobbling on mass accretion

To compare the effects of stellar motion on the accretion disc and protostellar properties, we carry out two additional simulations initialized with a 100-$M_{\odot}$ pre-stellar core, rigidly rotating with $\beta = 4$ per cent and having a sink cell with a radius of $r_{\mathrm{in}} = 12$ au. We use a small sink-cell radius in order to follow the clump migration at radii $\leq$ 20 au. This, however, reduces the time step of the simulations and the time-scale over which we can perform the model runs (see Run-1-hr). Hydrodynamics and radiation transport are treated as in the other runs of this study (see Table 1). We additionally include the effects of stellar motion in one run (Run-with), whereas the other simulation neglects it (Run-without). Fig. 7(a) shows the evolution of the accretion rate on to the protostar (in $M_{\odot}\ \mathrm{yr}^{-1}$) in our comparison simulations as a function of time (in yr). The figure distinguishes between the models without (red solid line) and with (blue dashed line) stellar wobbling. The mass of the protostar is also plotted for the runs without (thick dotted black line) and with (thick solid black line) wobbling. As the initial conditions are similar, the time of free-fall collapse is the same in both runs (≈ 12 kyr) and moderate accretion variability on to the MYSOs develops in the accretion flow similarly after the onset of the disc formation phase. In both cases (without and with stellar motion), the accretion rate is interspersed with episodic accretion spikes arising in addition to the baseline accretion rate of a few $\times 10^{-4}\ M_{\odot}\ \mathrm{yr}^{-1}$. This demonstrates that the stellar motion does not prevent the production of accretion-driven outbursts through the disc-fragmentation-based mechanism described in Meyer et al. (2017, 2018) and also has little effect on the final mass of the MYSOs (≈25 $M_{\odot}$).

The thin red lines in Fig. 7(b) and (c) show the total luminosity of the MYSOs, i.e. the sum of the photospheric and accretion luminosity (in $L_{\odot}$) as a function of time (in kyr) of both comparison models. In addition, the black solid lines show the background luminosity L_{bg}, while the dotted thin blue line, dashed dotted orange line and dashed violet lines show the limits of the 1-, 3- and 4-mag cut-offs with respect to L_{bg}, respectively. The overplotted dots represent the peak accretion rates for each individual burst, the peak luminosity of which is at least 2.5 times brighter than the quiescent pre-flare luminosity, and they are coloured as a function of the peak accretion rate, shown in the 0.001–0.1 $M_{\odot}\ \mathrm{yr}^{-1}$ range. As in our other models, the time evolution of the luminosity is a direct function of the mass accretion rate (Fig. 7a). In both comparison models (without and with wobbling), variations in luminosity begin at $t \approx 12$ kyr, when the accretion luminosity ceases to be negligible compared with the photospheric luminosity. The protostellar accretion-rate history then affects the total luminosity of the protostars further by producing variations of increasing intensity in their light curves, according to the mechanism described above in this work and in Meyer et al. (2017). Moreover, we recover the initial development of mild accretion-driven bursts with a peak accretion rate $\leq 10^{-3}\ M_{\odot}\ \mathrm{yr}^{-1}$ at ≈17 kyr (1-, 2-mag bursts) that precede stronger flares with a peak accretion rate $\geq 10^{-1}\ M_{\odot}\ \mathrm{yr}^{-1}$ at times $\geq$ 29 yr (3,4-mag bursts). We report in Table 2 the burst statistics and properties (peak luminosity, peak accretion rate, duration).

The similitude between the two comparison models goes beyond a simple general, qualitative aspect of their accretion-rate histories and luminosity curves, but it also concerns the properties of the bursts themselves. The number of bursts is similar in both models. For example, we obtain the same number of bursts for the 2- and 3-mag flares and find only a slight difference for the 1-mag bursts (nine in comparison with six flares when wobbling is included). We also note the presence of a 4-mag burst in the model with stellar wobbling. In both cases, the bursts have durations of the same order of magnitude, with $t_{\mathrm{bst}}^{\mathrm{mean}} = 38$ yr (without) and 29 yr (with), $t_{\mathrm{bst}}^{\mathrm{mean}} = 18$ yr (without) and 21 yr (with) and $t_{\mathrm{bst}}^{\mathrm{mean}} = 5$ yr (without) and 9 yr (with) for the 1-, 2- and 3-mag bursts, respectively. Additionally, one can note that the total time the model with stellar wobbling spends in the burst phase (300 yr, representing ≈0.75 per cent of the modelled 40 kyr) is slightly shorter than that without wobbling (438 yr, representing ≈1.1 per cent of the modelled 40 kyr), while the accretion mass is larger (see below). The mean luminosity and mean peak accretion rates of the two models are equivalent. For example, for the 2-mag bursts, $L_{\mathrm{mean}} \approx 4.64 \times 10^{5}$ and $\dot{M}_{\mathrm{mean}} \approx 0.0343\ M_{\odot}\ \mathrm{yr}^{-1}$ in the model without stellar wobbling and $L_{\mathrm{mean}} \approx 4.12 \times 10^{5}\ L_{\odot}\ \mathrm{yr}^{-1}$ and $\dot{M}_{\mathrm{mean}} \approx 0.0397\ M_{\odot}\ \mathrm{yr}^{-1}$ in the model with stellar wobbling. Moreover, both models exhibit bursts happening either isolated or in clusters, which strengthens the similitude between the two comparison simulations.

More importantly, the analysis of the fractions of final mass accreted as a function of the protostellar luminosity (Table 3) shows that the disc response to stellar motion does not affect our conclusions dramatically in terms of the accreted mass throughout the eruptive episodes. In both comparison models, the star accretes ≈24 $M_{\odot}$ over 40 kyr and gains 18.64 $M_{\odot}$ (≈75 per cent) and 15.46 $M_{\odot}$ (≈63 per cent) of its final mass when $L_{\mathrm{tot}} \simeq L_{\mathrm{bg}}$, which is in accordance with what was found in our model Run-1-hr that was modelled over a similar time-scale (35 kyr). Our results show that the model with stellar wobbling accretes more mass through bursts, compared with the simulation without wobbling, especially during the 2- and 3-mag bursts, for which the accreted mass is doubled compared with the model without wobbling. Interestingly, our model with wobbling exhibits a 4-mag burst, while the model without stellar wobbling does not (at least during the first 40 kyr), as our simulation Run-long-4 with $\beta = 4$ per cent but $r_{\mathrm{in}} = 20$ au has its first 4-mag burst at ≈43 kyr). This mean that our models with stellar motion form massive clumps earlier in the evolution than the models without wobbling. We conclude that the burst characteristics are only weakly sensitive to stellar motion.

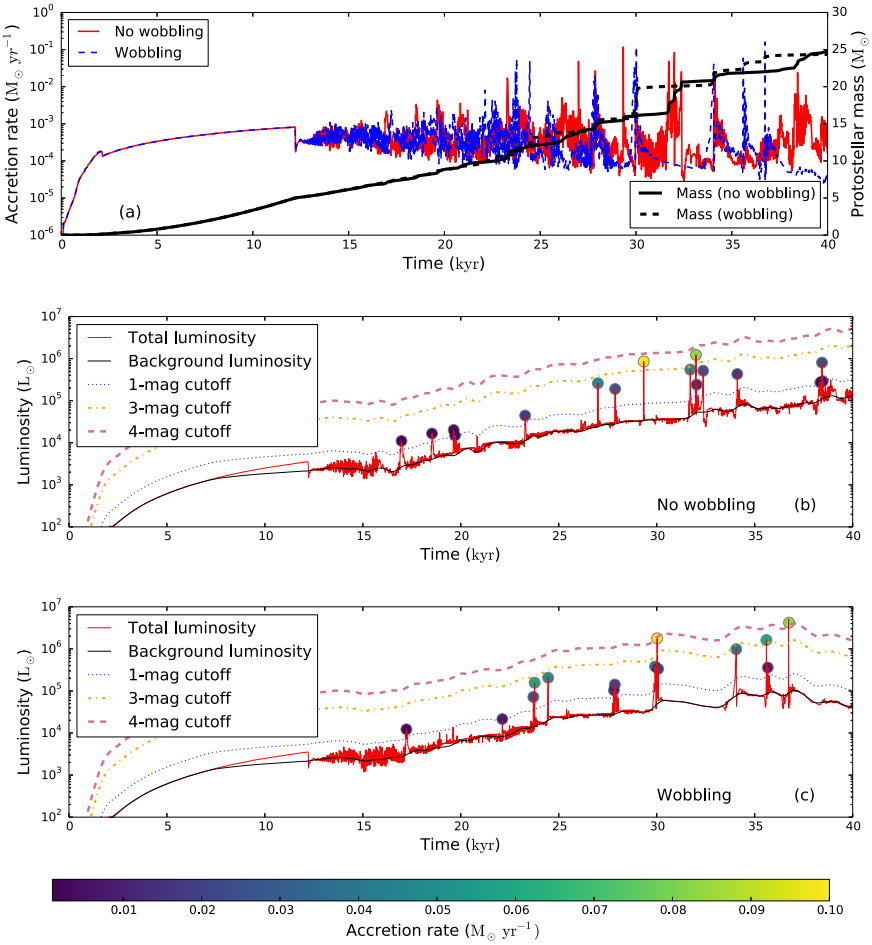

Figure 7. Comparison of mass accretion rates and luminosities in our comparison model ($\beta = 4$ per cent and $r_{\rm in} = 12$ au) with and without stellar wobbling. Panel (a) shows the mass accretion rate (thin lines, in $M_\odot$ yr^{-1}) and protostellar masses (thick lines, in $M_\odot$) in our simulations without (solid lines) and with (dashed lines) stellar wobbling. Panels (b) and (c) present the total luminosities (thin red solid lines, in kyr), background luminosities (thin solid black lines) and luminosity cut-offs (the dotted and dashed lines) for the model without stellar wobbling (middle panel) and with stellar wobbling (bottom panel). The colour bar indicates the accretion rate for the filled circles in panels (b) and (c).

5 DISCUSSION

In this section, we present the limitation and caveats of our model, estimate the burst occurence during the early protostellar formation phase and discuss the connection between bursts and protostellar mass growth. Furthermore, we review our knowledge of observations of several monitored bursts of massive protostars.

5.1 Model limitation

The assumptions of our models are globally similar to those of Meyer et al. (2017), where we describe several improvements that could be added to our model. These improvements include making the initial conditions more realistic and improving the grid geometry/resolution. Indeed, our parent pre-stellar cores are assumed to be initially spherically symmetric, while high-mass stars also form in filamentary structures (see e.g. Banerjee, Pudritz & Anderson 2006). The midplane symmetry imposed in our simulations could be improved in favour of full three-dimensional protostellar disc models. Moreover, although the logarithmically expanding grid in the radial direction permits fulfilment of the Truelove criterion (Truelove et al. 1998), which warrants the correct treatment of self-gravity within the disc, a full convergence of the entire disc structure is not reached (if possible at all) and higher resolution models would allow us to investigate the clump trajectories in the very inner disc. Nevertheless, we show in Meyer et al. (2018) that our accretion-rate histories converge qualitatively as the numerical resolution is increased.

As an improvement compared with the previous works in this series, the longer integration times of our simulations up to 60 kyr follow the disc evolution, the aftermath of gravitational instabilities and/or clump migration in the protostellar light curves better. Even longer runs should be conceived, e.g. in order to determinate the zero-age main sequence of MYSOs and see whether the discs modify their morphology and/or orientation, as around evolved low-mass protostars (Matsumoto, Machida & Inutsuka 2017). Additionally, the huge parameter space should be explored within a large grid of simulations. One should nevertheless keep in mind that such improvements will make the simulations more computationally intensive, which at the moment is not affordable and

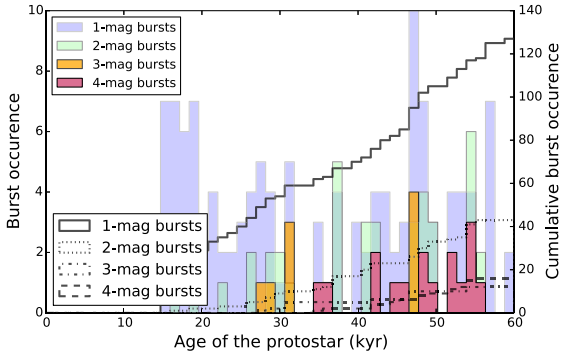

Figure 8. Burst occurence as a function of the age of the protostar.

remains out of reach of modern supercomputing capabilities. Apart from the above-mentioned caveats, the sink cell size may affect our results. A smaller size of the sink cell allows us to follow the clump migration, internal evolution and probable stretching and fragmentation further. Using a smaller sink cell decreases the time step of the simulations dramatically, which in turn makes them even more costly. A more thorough discussion of our model limitations can be found in Meyer et al. (2018).

5.2 Burst occurence

Fig. 8 plots the burst occurrence as a function of the age of the protostar. More specifically, the histograms report the number of bursts per time interval for different burst magnitudes (1, 2, 3 and 4 mag). The lines show the cumulative burst occurrence for different burst magnitudes as a function of protostellar age. The colour coding is similar to that in Figs 4–6. As indicated in Table 2, our MYSO burst incidence is 128, 44, 12 and 17 for 1- (solid line), 2- (dotted line), 3- (dashed dotted line) and 4-mag bursts (dashed line), respectively. Initially, the bursts are mostly 1-mag bursts up to ≈30 yr, although run-long-5 already has some 3-mag bursts at a time ≈27 kyr (Fig. 2b) and run-long-10 shows 2-mag bursts at time ≈20 kyr (Fig. 2c). As the protostars evolve towards the main-sequence phase, the burst activity increases strongly, with an accumulation of 3- and 4-mag bursts starting from ≈40 kyr, when our protostars experience a period of rapid and violent eruption (Fig. 2a), during which the probability of observing such a phenomenon is higher.

Fig. 9 presents the number of bursts and the cumulative number of bursts as a function of (a) the burst duration, (b) accreted mass per burst, (c) burst peak luminosity and (d) burst accretion rate. The burst duration remains within the 2–100 yr limits, with a moderate dependence on the initial pre-stellar core spin, as a result of the convergence of our simulations. A higher-resolution model run-hr has about twice as many bursts as run-long-4, despite similar initial conditions, since the former resolves better and follows further the second collapse of migrating clumps, because of its smaller sink-cell radius $r_{\rm in}$. As the higher magnitude bursts are caused by more massive and compact clumps, these bursts are evidently shorter in time ($t_{\rm bst}^{\rm mean} \approx 4$ yr) than lower magnitude ones ($t_{\rm bst}^{\rm mean} \approx 27$ yr), which are caused by more diffuse and extended clumps. The stronger the bursts, the shorter their duration and therefore the less probable it is to observe such events in MYSOs, which raises the question of their possible observability. Our lower amplitude burst (1 and 2 mag) characteristics are nevertheless in rather good agreement with observations of bursts from massive protostars (Section 5.4).

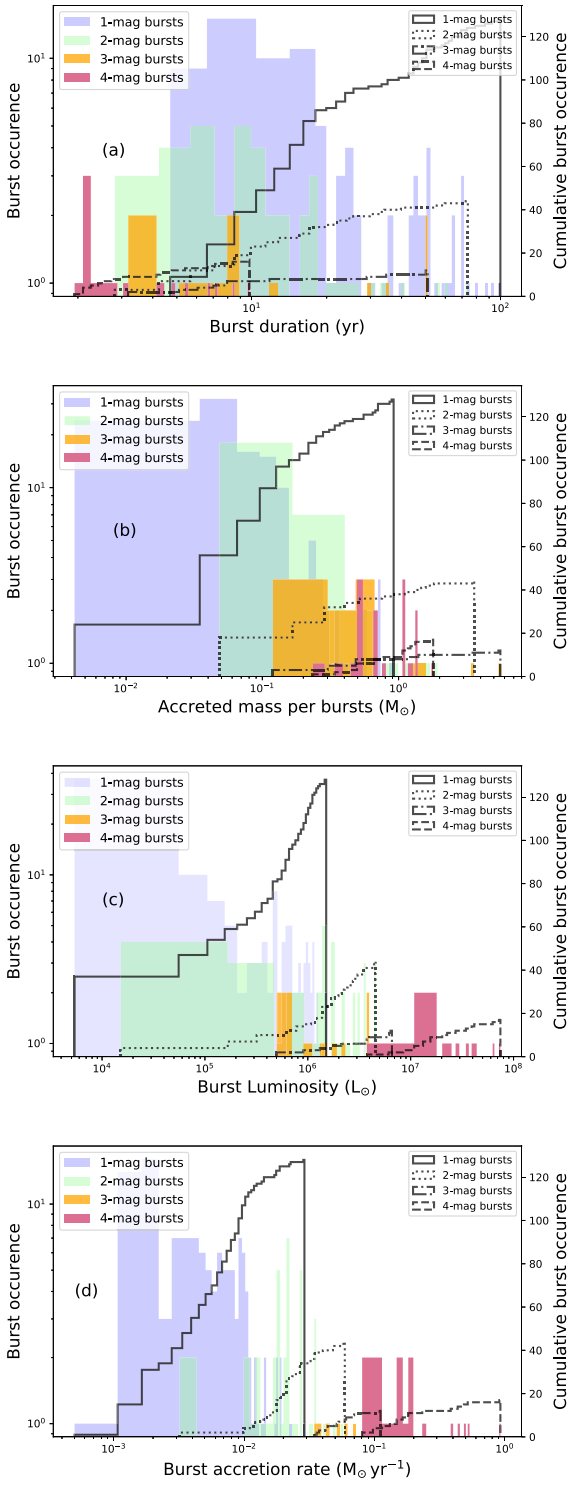

Figure 9. Burst occurence as a function of (a) burst duration, (b) accreted mass per burst, (c) burst peak luminosity and (d) burst peak accretion rate.

The accreted mass spans a range from a few Jupiter masses to a few solar masses and the accreted mass during the outburst of S255IR NIRS 3 lies in this range of values (Caratti o Garatti et al. 2017). This distribution of accreted masses reflects the apparent variety of disc fragments, e.g. collapsing clumps or overdense portion of spiral arms formed via disc gravitational instability and fragmentation and migrated in the inner disc region. The strongest accretion events may be associated with the formation of low-mass companions to the central MYSOs. In Meyer et al. (2018), within the so-called disc fragmentation scenario for the formation of close/spectroscopic binaries around proto-OB stars, we showed the formation possibility of such objects, when migrating massive clumps may both lose their diffuse envelope and contract further into their centre to form a secondary low-mass protostellar core. Such an event would then produce a companion and a strong (4-mag) burst from a single infalling dense clump. Since we do not consider this effect in the current study, the actual bursts may be of slightly lower amplitude than our model predicts. Interestingly, the number of 4-mag bursts predicted in our model (from 5–8) is consistent with the occurrence of close binaries around OB stars (Chini et al. 2012; Mahy et al. 2013; Kobulnicky et al. 2014).

The burst luminosity distribution clearly shows that 1- and 2-mag bursts are by far the more frequent (Fig. 9c), with a luminosity peak $\approx 10^5$–$10^6\,\mathrm{L}_\odot$. Other bursts of higher luminosity are not as common as their fainter counterparts and, if some 3-mag bursts can reach luminosity peaks $\geq 10^6\,\mathrm{L}_\odot$, only 4-mag bursts can reach luminosities $\geq 10^7\,\mathrm{L}_\odot$. As was stated above, these strong bursts might simultaneously be associated with the formation of binaries and thus may be of slightly fainter intensity. Consequently, and given their rareness, one should not expect to observe bursts from MYSOs more luminous than $\sim 10^7\,\mathrm{L}_\odot$, if at all. The last histogram (Fig. 9d) plots the burst peak accretion rate distribution. It underlines the correlation between $L_{\rm max}$ and $\dot{M}_{\rm max}$, already depicted in Fig. 5(b): the stronger the burst, the higher the peak accretion rate of circumstellar material. Most bursts peak at $\simeq 10^2\,\mathrm{M}_\odot\,\mathrm{yr}^{-1}$, while only a minor fraction of them exceed $\simeq 10^{-1}\,\mathrm{M}_\odot\,\mathrm{yr}^{-1}$.

5.3 Protostellar mass growth by episodic accretion

Fig. 10 plots the mass evolution of the protostar (in $\mathrm{M}_\odot$) in our run-long-4 model as a function of time (in yr). The figure distinguishes between the total accreted mass of the protostar (thick solid red line) and the mass accreted when the protostar is in the quiescent phase (thin solid black line), experiencing 1- (thin dotted blue line), 2- (thin dashed green line), 3- (solid orange line) and 4-mag (thin dotted dashed purple line) bursts. During free-fall gravitational collapse and up to the end of the smooth accretion phase, the protostar grows exclusively by quiescent accretion driven by gravitational torques that are generated by anisotropies in the inner disc flow. In this case, variations in stellar brightness remain smaller than 1-mag, i.e. increase by a maximal factor of $\approx$2.5 compared with $L_{\rm bg}$. When a young star enters the high-mass regime ($\geq 8\,\mathrm{M}_\odot$, orange circle), no clear bursts have yet happened, although accretion bursts start to occur in the models with a higher β (Fig. 3). During the burst phase of accretion, more and more mass is accreted, while the protostar experiences $\geq$ 2-mag bursts. As was already discussed in our Table 2, the higher the burst intensity, the later bursts appear and the rarer they are, testified by the decreasing number of step-like escalations of the mass histories at times ≥ 35 kyr. The figure also depicts the larger proportion of 1- and 2-mag bursts compared with the less frequent 3- and 4-mag ones. All our models have similar behaviour.

In Table 3, we summarize the stellar accreted in the quiescent PHASE and during bursts (for bursts of different magnitude) and express the results in terms of mass and percentage of the final protostellar mass, respectively. Our model run-long-4 accretes $\approx 25.06\,\mathrm{M}_\odot$ in the quiescent phase and $\approx 5.28\,\mathrm{M}_\odot$, $\approx 10.04\,\mathrm{M}_\odot$, $\approx 2.59\,\mathrm{M}_\odot$ and $\approx 4.36\,\mathrm{M}_\odot$ while experiencing 1- to 4-mag bursts, respectively. By performing an average of the different values over our models with $r_{\rm in} = 20$ au, we find that protostars gain, during their early 60 kyr, about 5.72, 6.22, 2.91 and $4.21\,\mathrm{M}_\odot$ while experiencing 1-, 2-, 3- and 4-mag bursts, respectively. In other words, a fraction of $\approx$53.75 per cent of the final mass is gained by quiescent accretion (when $L_{\rm tot} \simeq L_{\rm bg}$), while about 14.35, 14.63, 6.91 and 10.36 per cent of the final mass is accreted during 1- to 4-mag accretion-driven events. Over the first 60 kyr of their life, as a direct consequence of the rareness of the strongest flares, the total time that MYSOs spend in 1-mag bursts (≈ 1.27 per cent of $t_{\rm end}$) is longer than the cumulative time of all higher intensity bursts (≈ 0.43 per cent of $t_{\rm end}$), which implies a very rare observation probability. The total burst time $\approx$1027 yr is ≈ 1.7 per cent of 60 kyr, but it permits the accretion of a significant fraction of about half ($\approx$46.25 per cent) of their final mass, which demonstrates the importance and non-negligibility of accretion bursts in understanding the early evolution and mass growth of MYSOs.

5.4 Comparison with observations

The discovery and analysis of episodic bursts from massive protostars is hampered by various circumstances. According to the initial stellar mass function, these objects are much rarer than their low-mass counterparts and thus, on average, more distant. Their protostellar evolution occurs at a much higher pace compared with low-mass young stellar objects, so they remain deeply embedded during most of this evolutionary period. This renders the discovery of burst-induced photometric variability impossible at optical and difficult at infrared wavelengths, in contrast to smaller-mass YSOs (Scholz, Froebrich & Wood 2013). Since the most massive young stars dominate the emission of embedded clusters, attempts were made to trace their variability in scattered light (Stecklum et al. 2017). A remedy comes from the frequent association of high-mass young stellar objects with masers. In particular, methanol Class II masers are a reliable signpost of massive star formation (Breen et al. 2013). These masers arise from molecules that are released from the ice mantles of grains to the gas phase by heating of the dust that surrounds the massive protostar. The maser excitation can be collisional, e.g. in shocks of bipolar outflows, or due to radiative pumping, as in the case of 6.7-GHz Class II methanol masers (Sobolev, Cragg & Godfrey 1997). Thus, the temporary increase in luminosity due to an accretion burst may cause flares of radiatively pumped masers. However, other circumstances affect the maser strength as well. In fact, many of these masers show pronounced variability, which can even be periodic (Goedhart, Gaylard & van der Walt 2003). The non-linear maser response in the non-saturated regime makes it difficult to judge the increase of mid-IR radiation. Nevertheless, to some extent, the variability of Class II methanol masers may be considered to reflect luminosity variations of MYSOs (Szymczak et al. 2018). Indeed, recent observations confirmed this view for two objects, described in the following.

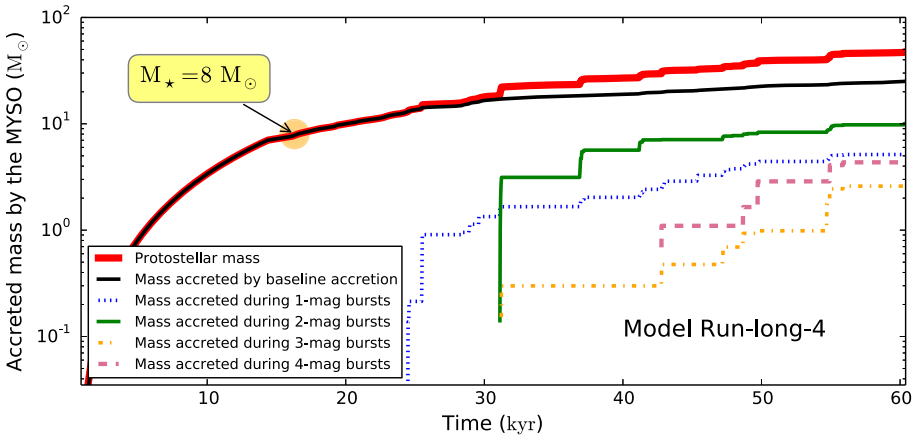

Figure 10. Protostellar mass growth as a function of the star's total luminosity.

The first evidence for bursts from massive protostars was gained from the case of V723 Carinae (Tapia, Roth & Persi 2015b,a), a $\sim$10 $M_\odot$ MYSO with a post-burst luminosity of 4×10^3 $L_\odot$. It was fainter than $K_s \simeq 16.6$ in 1993 and found to be three magnitudes brighter in 2003 (Tapia et al. 2006). The object reached its maximum K_s brightness of 12.9 in 2004 February and shows erratic variability of up to $\Delta K_s = 2$ since then. Its infrared colours resemble those of Class I objects and indicate the presence of very substantial extinction. Because of the sparse pre-burst IR photometry, no conclusion on the luminosity increase during the burst could be drawn. At the time of its discovery, V723 Carinae was the most luminous, most massive, most deeply embedded, and possibly youngest eruptive young variable.

This situation changed in 2015 when a flare of the 6.7-GHz methanol maser in the S255-IR star forming region was announced (Fujisawa et al. 2015). Immediate near-infrared (NIR) follow-up imaging disclosed that NIRS3, a $\sim$20 $M_\odot$ MYSO representing the most luminous member of the embedded cluster, brightened by $\Delta K_s = 2.5$ compared with the latest archival data from 2009 (Stecklum et al. 2016). A thorough investigation of the NIRS3 burst was possible thanks to observational advancement since the V723 Carinae event and the availability of spectroscopic as well as photometric pre-burst data. Major results include the discovery of spectral features typical for young low-mass eruptive variables, however three orders of magnitude stronger, the discovery of the light echo from the burst, which allows us to reconstruct its history, and an increase of the bolometric luminosity from $(2.9\pm^{1}_{0.7}) \times 10^4$ $L_\odot$ to $(1.6\pm^{0.4}_{0.3}) \times 10^5$ $L_\odot$, which points to an accretion rate of $(5 \pm 2) \times 10^{-3}$ $M_\odot$ yr^{-1} (Caratti o Garatti et al. 2017). The burst was accompanied by a spatial rearrangement of 6.7-GHz methanol masers (Moscadelli et al. 2017) at subluminal speed (Stecklum et al. 2018), as well as enhanced outflow activity traced by an increase of the radio continuum emission, delayed by about one year (Cesaroni et al. 2018).

Notably, there is evidence from the distribution of molecules around NIRS3 that its nearest vicinity may be considerably inhomogeneous (Zinchenko et al. 2015, 2017) and may be subject to gravitational instability. Various authors reported about four bursts from NIRS3, including the recent one, within the last $\sim$7000 years (Wang et al. 2011; Zinchenko et al. 2015; Burns et al. 2016). The arrangement of bow shocks in the outflows in this region seems to support multiple outbursts (Zinchenko et al. 2015), although the most recent ALMA data show that the situation is complicated and the youngest of the bow shocks is produced by another source in the region, SMA2 (Zinchenko et al. 2018).

This seems to indicate that the 2015 burst is part of a series of eruptive events and, probably, more are to come in the future. Such a remark can be applied to the other observed bursts from MYSOs and, more generally, by analogy with low-mass star formation, we propose that episodic bursts from massive protostars are produced in groups of successive flares of different, possibly decreasing, magnitude. Some properties of the burst of S255-IR derived in Caratti o Garatti et al. (2017) are consistent with our results. Its luminosity increased by a factor 3.6–5.1, making it a 2-mag burst, which are amongst the most common bursts we predict. Its accretion rate of $(5 \pm 2) \times 10^{-3}$ $M_\odot$ yr^{-1} fits the lower limit of accretion rates that we predict for 2-mag bursts (3×10^{-3} $M_\odot$ yr^{-1}). Note that this observed accretion rate has been estimated using a canonical value for the protostellar radius, which corresponds to the standard radius of a massive star of the mass of NIRS3 at the zero-age main-sequence time. As indicated in Caratti o Garatti et al. (2017), the accretion rate would be larger if one assumed that the protostar is bloating. Indeed, if the radius is larger, more mass has to be accreted to produce a similar burst energy. One should also keep in mind that our model accretion rates were derived neglecting the formation of close (spectroscopic) companions to the MYSOs, which have been shown to be consistent with the disc fragmentation and accretion-driven burst scenario in the context of massive protostars (Meyer et al. 2018). Hence, the observed accretion rate, which corresponds well to our minimal predictions, is probably a lower bound to its real value and our predictions may be slightly overestimated.

While the observed and model burst durations remain within the same order of magnitude, a difference seems to be present nevertheless. The value of 1.5 yr (Caratti o Garatti et al. 2017) is shorter than the lower limit of our predictions of 3.0 yr for that kind of 2-mag burst (our Table 2). However, very recent results obtained by monitoring the maser emission associated with NIRS3 solve this discrepancy. The radio observations of Szymczak et al. (2018) show that the methanol maser flare of S255IR had already started in 2014 February, i.e. before the estimated date of Caratti o Garatti et al. (2017). This difference is due primarily to their simplified initial analysis of the light echo, which neglected multiple scattering. Therefore, the estimated burst duration of 1.5 yr represents a lower bound. The radio observations point to an effective burst length of

the order of ≈2.0 yr, which brings the burst of S255-IR closer to our minimal prediction of 3.0 yr.

By coincidence, another MYSO accretion event was detected at about the same time as NIRS3 was bursting. However, the burst from NGC 6334I-MM1 could be observed at mm/submm wavelengths only (Hunter et al. 2017). From the quadruple rise of the dust continuum emission, a sustained luminosity surge by a factor of 70 ± 20 was derived. It suggests that the burst from NGC 6334IMM1 was a major one, possibly lasting longer than that from NIRS3, which ceased after ∼2.0 yr. This conjecture is also supported by the duration of the flare in different maser transitions, which lasts longer than 3 years (MacLeod et al. 2018). Similarly to NIRS3, this event was also accompanied by strong flares of 6.7-GHz methanol and other maser transitions of various molecules, including new components that emerged due to the burst (Hunter et al. 2018; MacLeod et al. 2018). High-resolution ALMA and Very Large Array (VLA) data revealed the presence of an outflow with a dynamic age of about 170 yr, which suggests that there was another recent accretion burst. A decrease in the water maser emission around MM1 also suggests the presence of high infrared radiation density in this region (Brogan et al. 2018). The analysis of the maser data provides evidence that there were two earlier maser flares, which hints at the recurrent nature of the flares in this object (MacLeod et al. 2018).

6 CONCLUSION

In this study, we have explored numerically the mass accretion history of a series of massive protostars formed during the gravitational collapse of 100-$M_\odot$ pre-stellar clouds. Our three-dimensional gravito–radiation–hydrodynamics simulations follow the formation and early (60 kyr) evolution of gravitationally unstable circumstellar discs that surround young protostars, in the spirit of Meyer et al. (2017, 2018). Massive fragments that form in the outer disc through gravitational fragmentation regularly generate sudden increases of the accretion rate when migrating towards the protostar and produce violent accretion-driven luminosity bursts accompanying the background variability of the protostellar light curves. We analysed the characteristics, properties and occurrence of those bursts. All our MYSOs have accretion-rate histories exhibiting a gradual increase in accretion-rate variability, from a smooth, burstless accretion phase during the initial gravitational collapse, through a variable accretion phase with $\dot{M}$ varying around the canonical value of $10^{-3}\,M_\odot\,yr^{-1}$ (Hosokawa & Omukai 2009) in the early 10 kyr of disc evolution, and finally to a violent accretion phase with multiple luminous bursts. We classified the bursts in terms of their peak luminosity. More specifically, we defined 1-, 2-, 3- and 4-mag luminosity bursts as those having peak luminosity factors 2.512, $2.512^2 \approx 6.3$, $2.512^3 \approx 15.9$ and $2.512^4 \approx 39$ higher than the luminosity in the quiescent phase. Interestingly, the inclusion of stellar motion in the simulation slightly accelerates the fragmentation of the disc and the development of strong bursts during the early phase (≤ 40 kyr) of its evolution. However, the absence/presence in the numerical set-up of the effects of stellar motion neither strongly affected nor dramatically modified the burst occurrence and the main burst characteristics.

The main prediction of this study is the scaling between burst magnitude and flare duration: the more intense (3 and 4 mag) the burst, the rarer its occurrence and the shorter ($\simeq$ yr) its duration and hence the associated observation probability. The burst occurrence increases as a function of protostellar age, at least within the computed time limit of 60 kyr. The same is true for the peak stellar luminosity during the burst. Very luminous (3- and 4-mag) outbursts are generated at later times ($\geq$ 40 kyr), i.e. they are less frequent than fainter flares associated with moderate accretion events. Our analysis demonstrates that the most luminous bursts accrete at higher rates and over smaller time-scales than fainter and longer ones. While our MYSOs exhibit a few dozen 1-mag bursts over their early pre-main-sequence phase, only about 4–8 violent 4-mag bursts develop over the pre-main-sequence phase. Their occurrence is consistent with the number of close/spectrosopic companions to MYSOs (Mahy et al. 2013; Kobulnicky et al. 2014), with which such violent events may be simultaneously associated (Meyer et al. 2018). We note that our limited number of simulations does not yet exhibit clear trends in terms of burst properties and/or occurrence as a function of the initial properties (rigidly rotating cores with kinetic-to-gravitational energy ratios $\beta \approx 4$–10 per cent), although bursts tend to appear slightly sooner as β increases. More numerical investigations, such as a parameter study exploring the pre-stellar core internal structure and providing us with more statistics, are required to address this question.

Although the total time our protostars spend in the burst phase represents only a small fraction (≈ 1.7 per cent) of their early formation phase, the mass accreted during the bursts constitutes a significant fraction (up to 50 per cent) of their final mass. The strongest, 4-mag bursts account for ≈0.1 per cent of the early 60 kyr pre-main-sequence life of MYSOs. While they are not frequent, we should nevertheless expect modern observation facilities to record signatures of more and more similar bursts in the years to come. Finally, we discuss our results in the light of our knowledge of observations of flares from MYSOs, i.e. the flare of the 10-$M_\odot$ massive Class I eruptive variable V723 Carinae (Tapia et al. 2006), the disc-mediated burst observed from the young massive stellar object S255IR NIRS 3 (Caratti o Garatti et al. 2017) and the eruption in the massive protostellar system NGC 6334I-MM1 (Hunter et al. 2017). According to our study, we suggest that the burst activity of S255IR NIRS 3 and NGC 6334I-MM1 may have just started and might evolve further as a series of flares. This conjecture is supported by the observational data, which hint at the possible recurrent nature of flares in these sources. Our study constitutes a step towards an understanding of the burst phenomenon in the high-mass star context and further work, as well as obtaining more observational data, is necessary to compare our theoretical predictions accurately with measures and understand the mechanisms of bursts from young high-mass stars properly.

ACKNOWLEDGEMENTS

The authors thank the anonymous referee for useful advice and suggestions, which greatly improved the manuscript. DM-AM thanks T. Hosokawa for kindly sharing his pre-main-sequence stellar evolutionary tracks and for discussions on stellar motion and W. Kley for his expertise in radiation hydrodynamics with the PLUTO code. EIV and AMS acknowledge support from Russian Science Foundation grant 18-12-00193.

REFERENCES

Adams F. C., Ruden S. P., Shu F. H., 1989, ApJ, 347, 959
Banerjee R., Pudritz R. E., Anderson D. W., 2006, MNRAS, 373, 1091
Beuther H., Walsh A. J., Johnston K. G., Henning T., Kuiper R., Longmore S. N., Walmsley C. M., 2017, A&A, 603, A10
Bitsch B., Morbidelli A., Lega E., Crida A., 2014, A&A, 564, A135
Black D. C., Bodenheimer P., 1975, ApJ, 199, 619
Bonnell I. A., Bate M. R., 1994, MNRAS, 271, 999

Bonnell I. A., Bate M. R., Zinnecker H., 1998, MNRAS, 298, 93
Breen S. L., Ellingsen S. P., Contreras Y., Green J. A., Caswell J. L., Stevens J. B., Dawson J. R., Voronkov M. A., 2013, MNRAS, 435, 524
Brogan C. L. et al., 2018, ApJ, 866, 87
Burns R. A., 2018, in Tarchi A., Reid M. J., Castangia P., eds, IAU Symp. Vol. 336, Astrophysical Masers: Unlocking the Mysteries of the Universe. Cambridge Univ. Press, Cambridge,p. 263
Burns R. A., Handa T., Nagayama T., Sunada K., Omodaka T., 2016, MNRAS, 460, 283
Burns R. A. et al., 2017, MNRAS, 467, 2367
Caratti o Garatti A., Stecklum B., Linz H., Garcia Lopez R., Sanna A., 2015, A&A, 573, A82
Caratti o Garatti A. et al., 2017, Nature Physics, 13, 276
Cesaroni R., Galli D., Lodato G., Walmsley M., Zhang Q., 2006, Nature, 444, 703
Cesaroni R., Hofner P., Araya E., Kurtz S., 2010, A&A, 509, A50
Cesaroni R., Sánchez-Monge Á., Beltrán M. T., Johnston K. G., Maud L. T., Moscadelli L., Mottram J. C., 2017, A&A, 602, A59
Cesaroni R. et al., 2018, A&A, 612, A103
Chen X., Ren Z., Zhang Q., Shen Z., Qiu K., 2017, ApJ, 835, 227
Chini R., Hoffmeister V. H., Nasseri A., Stahl O., Zinnecker H., 2012, MNRAS, 424, 1925
Commerçon B., Teyssier R., Audit E., Hennebelle P., Chabrier G., 2011, A&A, 529, A35
Commerçon B., Hennebelle P., Henning T., 2011, ApJ, 742, L9
Cunningham N. J., Moeckel N., Bally J., 2009, ApJ, 692, 943
Flock M., Fromang S., González M., Commerçon B., 2013, A&A, 560, A43
Forgan D. H., Ilee J. D., Cyganowski C. J., Brogan C. L., Hunter T. R., 2016, MNRAS, 463, 957
Fuente A., Neri R., Martín-Pintado J., Bachiller R., Rodríguez-Franco A., Palla F., 2001, A&A, 366, 873
Fujisawa K., Yonekura Y., Sugiyama K., Horiuchi H., Hayashi T., Hachisuka K., Matsumoto N., Niinuma K., 2015, The Astronomer's Telegram, 8286
Gammie C. F., 1996, ApJ, 462, 725
Ginsburg A., Bally J., Goddi C., Plambeck R., Wright M., 2018, ApJ, 860, 119
Goedhart S., Gaylard M. J., van der Walt D. J., 2003, MNRAS, 339, L33
Haemmerlé L., Peters T., 2016, MNRAS, 458, 3299
Haemmerlé L., Eggenberger P., Meynet G., Maeder A., Charbonnel C., 2016, A&A, 585, A65
Haemmerlé L., Eggenberger P., Meynet G., Maeder A., Charbonnel C., Klessen R. S., 2017, A&A, 602, A17
Harries T. J., 2015, MNRAS, 448, 3156
Harries T. J., Douglas T. A., Ali A., 2017, MNRAS, 471, 4111
Hirano S., Hosokawa T., Yoshida N., Kuiper R., 2017, Science, 357, 1375
Hosokawa T., Omukai K., 2009, ApJ, 691, 823
Hosokawa T., Hirano S., Kuiper R., Yorke H. W., Omukai K., Yoshida N., 2016, ApJ, 824, 119
Hunter T. R. et al., 2017, ApJ, 837, L29
Hunter T. R. et al., 2018, ApJ, 854, 170
Ilee J. D., Cyganowski C. J., Nazari P., Hunter T. R., Brogan C. L., Forgan D. H., Zhang Q., 2016, MNRAS, 462, 4386
Johnston K. G. et al., 2015, ApJ, 813, L19
Keto E., Wood K., 2006, ApJ, 637, 850
Klassen M., Pudritz R. E., Kuiper R., Peters T., Banerjee R., 2016, ApJ, 823, 28
Kobulnicky H. A. et al., 2014, ApJS, 213, 34
Kolb S. M., Stute M., Kley W., Mignone A., 2013, A&A, 559, A80
Kratter K. M., Matzner C. D., Krumholz M. R., Klein R. I., 2010, ApJ, 708, 1585
Kraus S. et al., 2017, ApJ, 835, L5
Krumholz M. R., Klein R. I., McKee C. F., 2007, ApJ, 656, 959
Langer N., 2012, ARA&A, 50, 107
Lodato G., Clarke C. J., 2011, MNRAS, 413, 2735
Machida M. N., Matsumoto T., 2011, MNRAS, 413, 2767
MacLeod G. C. et al., 2018, MNRAS, 478, 1077
Mahy L., Rauw G., De Becker M., Eenens P., Flores C. A., 2013, A&A, 550, A27
Matsumoto T., Machida M. N., Inutsuka S.-i., 2017, ApJ, 839, 69
Maud L. T., Hoare M. G., Galván-Madrid R., Zhang Q., de Wit W. J., Keto E., Johnston K. G., Pineda J. E., 2017, MNRAS, 467, L120
Meru F., Bate M. R., 2010, MNRAS, 406, 2279
Meyer D. M.-A., Mackey J., Langer N., Gvaramadze V. V., Mignone A., Izzard R. G., Kaper L., 2014, MNRAS, 444, 2754
Meyer D. M.-A., Langer N., Mackey J., Velázquez P. F., Gusdorf A., 2015, MNRAS, 450, 3080
Meyer D. M.-A., Vorobyov E. I., Kuiper R., Kley W., 2017, MNRAS, 464, L90
Meyer D. M.-A., Kuiper R., Kley W., Johnston K. G., Vorobyov E., 2018, MNRAS, 473, 3615
Mignone A., Bodo G., Massaglia S., Matsakos T., Tesileanu O., Zanni C., Ferrari A., 2007, ApJS, 170, 228
Mignone A., Zanni C., Tzeferacos P., van Straalen B., Colella P., Bodo G., 2012, ApJS, 198, 7
Moscadelli L. et al., 2017, A&A, 600, L8
Nayakshin S., Lodato G., 2012, MNRAS, 426, 70
Peters T., Banerjee R., Klessen R. S., Mac Low M.-M., Galván-Madrid R., Keto E. R., 2010, ApJ, 711, 1017
Purser S. J. D. et al., 2016, MNRAS, 460, 1039
Purser S. J. D., Lumsden S. L., Hoare M. G., Cunningham N., 2018, MNRAS, 475, 2
Regály Z., Vorobyov E., 2017, A&A, 601, A24
Reiter M., Kiminki M. M., Smith N., Bally J., 2017, MNRAS, 470, 4671
Rice W. K. M., Lodato G., Armitage P. J., 2005, MNRAS, 364, L56
Richling S., Yorke H. W., 1997, A&A, 327, 317
Rogers P. D., Wadsley J., 2012, MNRAS, 423, 1896
Rosen A. L., Krumholz M. R., McKee C. F., Klein R. I., 2016, MNRAS, 463, 2553
Rosen A. L., Krumholz M. R., Oishi J. S., Lee A. T., Klein R. I., 2017, Journal of Computational Physics, 330, 924
Samal M. R., Chen W. P., Takami M., Jose J., Froebrich D., 2018, MNRAS, 477, 4577
Sana H. et al., 2012, Science, 337, 444
Schneider F. R. N., Izzard R. G., Langer N., de Mink S. E., 2015, ApJ, 805, 20
Scholz A., Froebrich D., Wood K., 2013, MNRAS, 430, 2910
Seifried D., Banerjee R., Klessen R. S., Duffin D., Pudritz R. E., 2011, MNRAS, 417, 1054
Sobolev A. M., Cragg D. M., Godfrey P. D., 1997, A&A, 324, 211
Stecklum B., Caratti o Garatti A., Cardenas M. C., Greiner J., Kruehler T., Klose S., Eisloeffel J., 2016, The Astronomer's Telegram, 8732
Stecklum B., Heese S., Wolf S., Garatti A. C. o., Ibanez J. M., Linz H., 2017, preprint (arXiv:e-prints)
Stecklum B., Caratti o Garatti A., Hodapp K., Linz H., Moscadelli L., Sanna A., 2018, in Tarchi A., Reid M. J., Castangia P., eds, IAU Symp. Vol. 336, Astrophysical Masers: Unlocking the Mysteries of the Universe. Cambridge Univ. Press, Cambridge
Szymczak M., Olech M., Wolak P., Gérard E., Bartkiewicz A., 2018, A&A, 617, A80
Szymczak M., Olech M., Sarniak R., Wolak P., Bartkiewicz A., 2018, MNRAS, 474, 219
Tanaka K. E. I., Tan J. C., Zhang Y., 2017, ApJ, 835, 32
Tapia M., Persi P., Bohigas J., Roth M., Gómez M., 2006, MNRAS, 367, 513
Tapia M., Roth M., Persi P., 2015a, MNRAS, 448, 1402
Tapia M., Roth M., Persi P., 2015b, MNRAS, 446, 4088
Testi L., 2003, in De Buizer J. M., van der Bliek N. S., eds, ASP Conf. Ser. Vol. 287, In Galactic Star Formation Across the Stellar Mass Spectrum. Astron. Soc. Pac., San Francisco, p. 63
Truelove J. K., Klein R. I., McKee C. F., Holliman J. H., II, Howell L. H., Greenough J. A., Woods D. T., 1998, ApJ, 495, 821
Vaidya B., Fendt C., Beuther H., Porth O., 2011, ApJ, 742, 56
Vorobyov E. I., 2010, ApJ, 713, 1059
Vorobyov E. I., Basu S., 2005, ApJ, 633, L137
Vorobyov E. I., Basu S., 2015, ApJ, 805, 115
Vorobyov E. I., Elbakyan V. G., 2018, A&A, 618, A7

Vorobyov E. I., Elbakyan V., Hosokawa T., Sakurai Y., Guedel M., Yorke H., 2017, A&A, 605, A77
Vorobyov E. I., Elbakyan V. G., Plunkett A. L., Dunham M. M., Audard M., Guedel M., Dionatos O., 2018, A&A, 613, A18
Wang Y. et al., 2011, A&A, 527, A32
Yorke H. W., Sonnhalter C., 2002, ApJ, 569, 846
Zhao B., Caselli P., Li Z.-Y., Krasnopolsky R., 2018, MNRAS, 473, 4868
Zinchenko I. et al., 2015, ApJ, 810, 10
Zinchenko I., Liu S.-Y., Su Y.-N., Sobolev A. M., 2017, A&A, 606, L6
Zinchenko I., Liu S.-Y., Su Y.-N., Zemlyanukha P., 2018, in Cunningham M., Millar T., Aikawa Y., eds, IAU Symp. Vol. 332, Astrochemistry VII: Through the Cosmos from Galaxies to Planets. Cambridge Univ. Press, Cambridge, p. 270

This paper has been typeset from a TEX/LATEX file prepared by the author.

Monthly Notices
of the
ROYAL ASTRONOMICAL SOCIETY

MNRAS **484,** 2482–2498 (2019)
Advance Access publication 2019 January 10

doi:10.1093/mnras/sty3527

On the episodic excursions of massive protostars in the Hertzsprung–Russell diagram

D. M.-A. Meyer [1]★, L. Haemmerlé,[2] and E. I. Vorobyov[3,4]

[1]*Astrophysics Group, School of Physics and Astronomy, University of Exeter, Exeter EX4 4QL, UK*
[2]*Observatoire de Genève, Université de Genève, chemin des Maillettes 51, CH-1290 Sauverny, Switzerland*
[3]*Research Institute of Physics, Southern Federal University, Stachki 194, Rostov-on-Don 344090, Russia*
[4]*Department of Astrophysics, The University of Vienna, Vienna A-1180, Austria*

Accepted 2018 December 27. Received 2018 December 19; in original form 2018 August 27

ABSTRACT

Massive protostars grow and evolve under the effect of rapid accretion of circumstellar gas and dust, falling at high rates ($\geq 10^{-4}-10^{-3}\,M_{\odot}\,yr^{-1}$). This mass infall has been shown, both numerically and observationally, to be episodically interspersed by accretion of dense gaseous clumps migrating through the circumstellar disc to the protostellar surface, causing sudden accretion and luminous bursts. Using numerical gravitoradiation-hydrodynamics and stellar evolution calculations, we demonstrate that, in addition to the known bloating of massive protostars, variable episodic accretion further influences their evolutionary tracks of massive young stellar objects (MYSOs). For each accretion-driven flare, they experience rapid excursions towards more luminous, but colder regions of the Hertzsprung–Russell diagram. During these excursions, which can occur up to the end of the pre-main-sequence evolution, the photosphere of massive protostars can episodically release much less energetic photons and MYSOs surreptitiously adopt the same spectral type as evolved massive (supergiants) stars. Each of these evolutionary loop brings the young high-mass stars close to the forbidden Hayashi region and might make their surrounding H II regions occasionally fainter, before they recover their quiescent, pre-burst surface properties. We interpret such cold, intermittent pre-main-sequence stellar evolutionary excursions, and the dipping variability of H II regions as the signature of the presence of a fragmenting circumstellar accretion disc surrounding the MYSOs. We conjecture that this mechanism might equivalently affect young stars in the intermediate-mass regime.

Key words: methods: numerical – stars: circumstellar matter – stars: evolution – stars: flares.

1 INTRODUCTION

Gravitationally collapsing pre-stellar cores give birth to new young stars, which grow by mass accretion of surrounding molecular material. The rates at which protostars gain mass have been shown to exhibit such a diversity that the initial picture of isotropic collapse (Larson 1969; Shu 1977) fails to explain the observed spread in accretion rates (Vorobyov 2009). Meanwhile, variations of the protostellar accretion rate can induce enormous changes in protostellar luminosity, the most extreme manifestations of which are the so-called FO-Orionis and the very low-luminosity objects (Vorobyov et al. 2017). Numerical simulations have demonstrated that this is possible, thanks to the presence of a self-gravitating circumstellar accretion disc prone to gravitational fragmentation (Vorobyov & Basu 2005, 2010, 2015; Machida & Matsumoto 2011; Nayakshin & Lodato 2012; Vorobyov & Elbakyan 2018; Zhao et al. 2018)

The disc fragmentation scenario equivalently applies to star formation in the high-mass regime. Numerical simulations predicted the formation of accretion discs around massive young stellar objects (MYSOs; Bonnell, Bate & Zinnecker 1998; Yorke & Sonnhalter 2002; Peters et al. 2010; Seifried et al. 2011), together with additional structures such as bipolar cavities filled with ionizing radiation generated by the UV feedback of the protostars (Harries 2015; Klassen et al. 2016; Harries, Douglas & Ali 2017). Accretion variability is a direct consequence of asymmetries in the accretion flow (Seifried et al. 2011) and of the coupling between the prostellar radiation feedback and its surrounding disc (Peters et al. 2010). Such variability is a generic feature of massive star formation in the sense that it is neither stopped by the radiation pressure in the bipolar H II regions (Peters et al. 2010) nor by disc fragmentation (Meyer et al. 2018b). Other studies on massive star formation also reported

★ E-mail: dmameyer.astro@gmail.com

time-variabilities of the disc-to-star mass transfer rate (Krumholz et al. 2009; Rosen et al. 2016). In addition, self-gravitating discs around high-mass stars are subject to efficient gravitational instabilities, generating heavy spiral arms in which dense gaseous clumps form, eventually leading to the formation of multiple hierarchical systems (Krumholz, Klein & McKee 2007; Peters et al. 2010). These circumstellar clumps can either rapidly migrate on to the stellar surface, trigger increases of the protostellar accretion rate that aggravate the variability (Meyer et al. 2018b) and produce luminous bursts (Meyer et al. 2017) or evolve to secondary low-mass stars, which finally end up as low-mass spectroscopic companions to the MYSOs (Meyer et al. 2018b). Accretion bursts are a feature of the formation of young massive stellar objects that seem common to most massive protostars as it does not depend on the initial properties of their parent pre-stellar core (Meyer et al. 2018a). Moreover, although these eruptive phases represent a small fraction ($\sim$ per cent) of their early formation time, MYSOs can acquire a substantial fraction of their zero-age-main-sequence (ZAMS) mass via these flaring episods (Meyer et al. 2018a).

From the point of view of observations, (variable) accretion flows (Keto & Wood 2006; Stecklum et al. 2017) and ionized, pulsed, collimated structures (Cunningham, Moeckel & Bally 2009; Cesaroni et al. 2010; Caratti o Garatti et al. 2015; Purser et al. 2016; Burns et al. 2017; Reiter et al. 2017; Burns et al. 2018; Purser et al. 2018; Samal et al. 2018) underlined the scaled-up character of massive star formation with respect to low-mass stars (see also Fuente et al. 2001; Testi 2003; Cesaroni et al. 2006; Stecklum et al. 2018). A growing number of observations of (Keplerian) discs around MYSOs have been reported (Johnston et al. 2015; Forgan et al. 2016; Ilee et al. 2016; Ginsburg et al. 2018), together with evidences of a spiral filament feeding the candidate disc MM1-Main (Maud et al. 2017) and an infalling gaseous clump in the double-cored system G350.69–0.49 (Chen et al. 2017). Interestingly, a recent Atacama Large (sub-)Millimeter Arrays (*ALMA*) view of the massive young object G023.01–00.41 exhibited a clear disc–jet association (Sanna et al. 2018). In addition, some objects revealed the presence of high-mass protobinary systems within a circumbinary disc (Kraus et al. 2017). Finally, several MYSOs experienced multiwavelengths flares (Moscadelli et al. 2017; Cesaroni et al. 2018) in a fashion of the predictions of Meyer et al. (2017), among which are the accretion-bursts of S255IR NIRS 3 (Fujisawa et al. 2015; Stecklum et al. 2016; Caratti o Garatti et al. 2016) and from NGC 6334I-MM1 (Hunter et al. 2017) experienced accretion-driven outbursts.

Early stellar evolution calculations demonstrated the dominant influence of accretion on the internal stellar structure prior to the ZAMS phase (Palla & Stahler 1991). The formation of a radiative barrier that turns the fully convective stellar embryo into a stable radiative core and an outer convective shell that causes the star to swell has been shown in the context of young intermediate-mass stars for a wide range of different constant accretion rates (Palla & Stahler 1992, 1993; Beech & Mitalas 1994; Bernasconi & Maeder 1996; Bernasconi 1996). A monotonically increasing accretion rate yields similar results (Behrend & Maeder 2001). Calculations with high-rate mass accretion exceeding $10^{-3}\,\mathrm{M_\odot\,yr^{-1}}$ equivalently showed that disc-accreting young massive stellar objects have their pre-main-sequence evolution governed by the accretion of circumstellar material, see Bernasconi & Maeder (1996), Norberg & Maeder (2000), Behrend & Maeder (2001), Hosokawa & Omukai (2009), Hosokawa, Yorke & Omukai (2010). These models reported a rapid swelling of the protostars up to radii $\sim$1000 $\mathrm{R_\odot}$ produced by the so-called luminosity wave (Larson 1972), an internal redistribution of entropy following the abrupt decrease of the opacity in the protostellar interior. Interestingly, for the constant accretion rates $\geq 10^{-2}\,\mathrm{M_\odot\,yr^{-1}}$, the protostars evolve to the red part of the Hertzsprung–Russell diagram (Hosokawa et al. 2010; Haemmerlé et al. 2016). The authors postulate therein that the H II region generated by those stars can then disappear as their protostellar radius bloats, ultimately leading to lower luminosity young massive stellar objects. Simultaneous hydrodynamical and stellar evolution calculations revealed that variable-accreting MYSOs can experience a unique loop to the red before recovering their bluer characteristics and reach the ZAMS (Kuiper & Yorke 2013). However, those 2.5-dimensional axisymmetric simulations do not account for disc fragmentation physics and its influence on the protostellar variability (Meyer et al. 2017) and the corresponding rates were burstsless. More complex theoretical studies tackled the problem of the impact of various feedback mechanisms of MYSOs on to star formation efficiency, however, without considering their accretion variability (Tanaka et al. 2018).

Motivated by the above arguments, we aim at investigating the effects of the repetitive accretion events responsible for luminous bursts on the evolution of pre-main-sequence young massive stellar objects. With the help of three-dimensional gravitoradiation-hydrodynamics models of collapsing rotating massive pre-stellar cores, we first simulate the formation and evolution of fragmenting circumstellar accretion discs from which protostars gain mass (Meyer et al. 2018b). From the disc models, we extract variable accretion rate histories, interspersed by episodic accretion bursts caused by dense gaseous clumps that form in spiral arms and rapidly migrate on to the protostars (Meyer et al. 2017). Finally, we calculate stellar evolution models with the Geneva stellar evolutionary code (Eggenberger et al. 2008; Haemmerlé 2014) fed by our accretion rate histories. Using the method developed in the context of constant-accreting MYSOs (Haemmerlé et al. 2016, 2017) and accretion flows on to large-scale H II regions (Haemmerlé & Peters 2016), we calculate the changes in the internal structure and the surface properties of MYSOs experiencing bursts.

In this paper, we investigate the effects of variable accretion on the evolution of MYSOs. We perform numerical gravitoradiation-hydrodynamics simulations and stellar evolution calculations of pre-main-sequence accreting massive stellar objects to explore the effects of strong accretion bursts on to their internal as well as their surface properties and evolutionary path in the Hertzsprung–Russell diagram. This study is organized as follows. In Section 2, we review the methods utilized to perform (i) gravitoradiation-hydrodynamical simulations of the monolithic collapse of present-day rotating pre-stellar cores, from which we extract accretion rate histories, and (ii) stellar evolutionary calculations of MYSOs which accrete from their circumstellar discs at pre-calculated time-variable rates. Our results are presented in Section 3, the effects of the initial conditions on the stellar excursions are investigated in Section 4, and our findings further discussed in Section 5. Particularly, we highlight that strong outbursts provoke rapid excursions towards colder regions of the Herztsprung–Russel diagram, which typically is not associated with such hot and young stellar objects. Finally, we discuss our results and conclude in Section 6.

2 MODELLING

In the following paragraphs, we introduce the reader to the method employed to carry out our gravitoradiation-hydrodynamical simulations of high-mass star formation, from which we extract time-dependent protostellar accretion rate histories. Furthermore, we detail how the outputs of the hydrodynamical models are

subsequently used as boundary conditions for stellar evolution calculations.

2.1 Hydrodynamical simulations

Our three-dimensional mid-plane-symmetric hydrodynamical simulations are initialized with a rigidly rotating spherically symmetric, pre-stellar core of density distribution $\rho(r) \propto r^{\beta_\rho}$, with $\beta_\rho = -3/2$ (Butler & Tan 2012; Butler, Tan & Kainulainen 2014) and r is the radial coordinate. The inner edge of the core is made of a semi-permeable sink cell centred on to the origin of the computational domain and the outer edge of the core, at $R_c = 0.1$ pc, is assigned to the outflow boundary conditions. We map the domain $[r_{in}, R_c] \times [0, \pi/2] \times [0, 2\pi]$ with a mesh of $N_r = 128 \times N_\theta = 11 \times N_\phi = 128$ grid zones, logarithmically expanding along the r-direction, as a cosine in the polar θ-direction, and uniformly spaced along the azimuthal ϕ-direction. As in Meyer et al. (2018a), we use a size of the sink cell of 20 au, which is larger than that of the first paper of this series (Meyer et al. 2017) in order to reach longer integration times t_{end}, while avoiding very restrictive Courant–Friedrich–Levy conditions on the time-step within the direct protostellar surroundings. We simulate the gravitational collapse of several pre-stellar cores with different initial masses M_c. Each core forms a central protostar and a massive circumstellar disc. The accretion rate from the disc on to the protostar is computed as the rate of mass transport $\dot{M}$ through the sink cell. The pre-stellar core temperature is uniformly set to $T_c = 10$ K and its rotational-by-gravitational energy ratio is set to a typical value of $\beta = 4$ per cent (Meyer et al. 2017). The models are run until the mass of the central star $M_\star$ becomes equal to one-third that of the initial mass core M_c. The characteristics of our models are summarized in Table 1.

To solve the evolution of the above described physical system, we numerically integrate the equations of gravitoradiation-hydrodynamics with the PLUTO code[1] (Mignone et al. 2007, 2012). Our method takes into account the direct irradiation of the protostar and radiation transport in the accretion disc within the grey approximation using the scheme of Kolb et al. (2013)[2] adapted following the prescriptions of Meyer et al. (2018b), see also equivalent radiation-hydrodynamics methods implementations in e.g. Commerçon et al. (2011), Flock et al. (2013), and Bitsch et al. (2014). The photospheric photons are first ray-traced from the stellar atmosphere and propagate by flux-limited diffusion into the circumstellar disc. Such method permits to treat the disc thermodynamics accurately, with its central heating together with the outer cooling of the discs, as predicted by Vaidya et al. (2011). Opacities and calculation of the dust properties are as in Meyer et al. (2018b), i.e. estimated by assuming that disc silicate grains are in equilibrium with the total radiation field. The gravitational force includes the gravity of the growing young massive star and the self-gravity of the gas, the latter computed using the prescriptions of Black & Bodenheimer (1975) and the implementation method inspired by Hirano et al. (2017)[3] by time-dependently solving the Poisson equation with the help of the PETSC library.[4] We assume that the angular momentum transport in the disc is essentially produced by the spiral arms in the discs and we therefore do not include additional turbulent α-viscosity (Meyer et al. 2018b).

[1] http://plutocode.ph.unito.it/
[2] http://www.tat.physik.uni-tuebingen.de/~pluto/pluto_radiation/
[3] https://shirano.as.utexas.edu/SV.html
[4] https://www.mcs.anl.gov/petsc/

2.2 Stellar evolution calculations

We used our accretion rate histories to compute the evolutionary tracks of our MYSOs in the Hertzsprung–Russel diagram. The one-dimensional stellar evolution calculations were performed with the hydrostatic GENEVA code, the original version of which (Eggenberger et al. 2008) has recently been updated for disc accretion physics in the context of pre-main-sequence massive protostars (Haemmerlé 2014). The code was tested in the context of constant-accreting MYSOs (see details relative to the numerical scheme and the implementation method in Haemmerlé et al. 2016) and showed full consistency with the original results on high-constant-rate accreting MYSOs of Hosokawa et al. (2010). Accretion is treated within the so-called *cold disc accretion* scenario (Palla & Stahler 1992), which assumes that the inner disc region is geometrically thin when the accreted material reached the stellar surface. Hence, we follow the mass growth of the hydrostatic core (i.e. the protostar), without considering a spherical envelope during the accretion phase (Palla & Stahler 1992). Subsequent theoretical and numerical works demonstrated that such assumption is fully reasonable (Vaidya et al. 2011; Meyer et al. 2018b). Any entropy excess is radiated away in direction perpendicular to the disc and it is channeled into the radiatively driven outflow associated with young massive stars (Harries et al. 2017). The circumstellar material is advected inside the protostar assuming that its thermal properties are similar to those of the surface layer of the MYSOs.

Since we assume that most of the energy produced by the accretion shock (not modelled in the calculations) is radiated away before it reaches the protostellar surface, no additional entropy from the liberation of gravitational energy is added to the surface of the star. Such an assumption is the lower limit on the entropy attained by the star during the accretion process, while the upper limit is the so-called spherical (or hot) accretion scenario, scenario, in which a fraction of accretion entropy is added to the star, see the sketch in fig. 1 of Hosokawa et al. (2010). We choose the cold scenario as it has recently been used in the context of accreting H II regions (Haemmerlé & Peters 2016). Calculations of the stellar structure are performed with the Henyey method within the Lagrangian formulation (Haemmerlé 2014) at solar metallicity ($Z = 0.014$) using the abundances of Asplund, Grevesse & Sauval (2005) and Cunha, Hubeny & Lanz (2006) and the deuterium mass fractions of Norberg & Maeder (2000) and Behrend & Maeder (2001). The simulations make use of the Schwarzschild criterion for convection, overshooting is considered and they are initialized with fully convective stellar embryo because they are the most difficult models to bloat (Haemmerlé et al. 2016; Haemmerlé & Peters 2016). Hence, our method threats the stellar swelling most conservatively, avoiding any artificial effects that can lead to excessive swelling. To facilitate the stellar evolution calculations, we average the accretion rate histories over a time period of 10 yr. This excludes the smallest variabilities. However, one can justify such an assumption as we know that high accretion rates ($\geq 10^{-2}\,M_\odot\,yr^{-1}$) responsible for protostellar bloating are exclusively reached during the strongest and longest accretion bursts (Meyer et al. 2017, 2018b).

3 RESULTS

This section presents the accretion rate histories of our MYSOs and investigates the effects of the accretion of dense gaseous clumps on the structure and evolutionary path of high-mass protostars in the Hertzsprung–Russell diagram.

Table 1. Characteristics of our models, with initial pre-stellar core mass M_c, final protostellar age t_{end}, final stellar mass $M_\star$, details of their corresponding accretion rate histories, and of the initial conditions of the stellar evolution calculations.

Models	M_c ($M_\odot$)	t_{end} (kyr)	$M_\star$ ($M_\odot$)	Accretion rate	Method
Run-100-hydro	100	50.0	33.3	Episodic	Full hydrodynamical simulation with variable rate
Run-100-constant	100	50.0	33.3	Constant	Hydrodynamical simulation (collapse) + constant analytic rate (disc)
Run-100-smoothed	100	50.0	33.3	Smoothed	Hydrodynamical simulation (collapse) + smoothed burst-free rate (disc)
Run-100-compact	100	50.0	33.3	Episodic	As Run-100-hydro, with more compact initial conditions
Run-60-hydro	60	65.2	20.0	Episodic	Full hydrodynamical simulation with variable rate

3.1 Accretion rate histories

Fig. 1 shows the accretion rate histories on to the MYSOs forming during the gravitational collapse of 100 $M_\odot$ (a) and 60 $M_\odot$ (b) pre-stellar cores, respectively. The accretion rates (in $M_\odot\,yr^{-1}$) are plotted as a function of time (in kyr), from the beginning of the collapse to the end of the simulation when $M_\star = M_c/3$. The thin black vertical line marks the onset of disc formation when the free-collapsing material of the envelope begins to land on a centrifugally balanced circumstellar disc instead of keeping on directly falling on to the protostellar surface. From this time instance on, the protostar starts gaining mass via accretion from the disc. The thick, solid lines represent the accretion rate on to the young high-mass stars while the dashed lines are the corresponding protostellar masses (in $M_\odot$). Furthermore, we indicate by the orange circles the time instance when the MYSOs enter the high-mass regime ($M_\star > 8\,M_\odot$). We run two distinct hydrodynamical simulation with $M_c = 100\,M_\odot$ (model Run-100-hydro) and with $M_c = 60\,M_\odot$ (model Run-60-hydro), and in order to particularly investigate the effects of the accretion spikes on the protostellar evolution, we construct additional accretion rate histories by modifying the accretion rate of our model Run-100-hydro (our Table 1), by keeping constant the final mass of ≈33.3 $M_\odot$ and either (i) imposing a constant rate once the disc has formed (model Run-100-constant, see black lines of Fig. 1a) or (ii) filtering out the accretion spikes (model Run-100-smoothed, see red lines of Fig. 1a) with a method similar to that described in Vorobyov & Basu (2015).

The free-fall collapse of the molecular pre-stellar core produces an initial infall of material through the sink cell increasing the accretion rate during the first ≈12–15 kyr, up to reaching the canonical value of $\approx 10^{-3}\,M_\odot\,yr^{-1}$ at which MYSOs are predicted to accrete (Hosokawa & Omukai 2009). Once the disc has formed (see vertical thin line of Fig. 1), variability immediately develops in the accretion flow as a direct consequence of important anisotropies in the protostellar surroundings (Meyer et al. 2018b). The variations amplitude in the accretion rate continues increasing up to being interspersed by violent accretion spikes becoming more numerous and more intense as a function of time. They are regularly generated by the rapid migration of massive disc fragments forming in its outer region by gravitational fragmentation and falling on to the protostellar surface, provoking sudden increases of the accretion rate. Those dense gaseous clumps detached from spiral arms developing in the self-gravitational discs are responsible for violent accretion-driven luminosity bursts (Meyer et al. 2017). Such mechanism is connected to the formation of spectroscopic binary companions to the protostars, as long as the clumps sufficiently contract in the core and heat up beyond the dissociation temperature of molecular hydrogen (Meyer et al. 2018b). The protostellar mass evolution reflects the accretion history from the disc in the sense that to each strong accretion events ($\dot{M} \geq 10^{-1}\,M_\odot\,yr^{-1}$) corresponds a step-like increase of the stellar mass (Meyer et al. 2017). The integration time of model Run-60-hydro is longer (≈50 kyr) than that of Run-100-hydro (≈65.2 kyr) because we perform the simulations up to the time instance when $M_\star = M_c/3$. This is longer in the case of the lower mass pre-stellar core ($M_c = 60\,M_\odot$) since the mass infall on to the disc is intrinsically smaller.

3.2 Stellar structure evolution

Fig. 2 plots the evolution of the stellar structure of our protostars as a function of the stellar age for our models with $M_c = 100\,M_\odot$, distinguishing from different accretion histories. The figure indicates, in addition to the temporal variations in photospheric radius, the convective (blue) and radiative (orange) regions of the protostar, respectively. The protostars are initially fully convective (blue regions) with an internal temperature profile too cold to ignite Deuterium burning. As its centre heats up by gravitational contraction, a radiative core forms and grows in mass while rapidly expanding towards the stellar surface once the Deuterium fuel is out. The accreting stars further evolve once energetic photons are released out of the radiative core and propagate upwards to be absorbed by the still cold and convective envelope. During the gradual diminishing of the convective envelope thickness (when the protostars of our Run-100-hydro is ≈10 $M_\odot$, see Fig. 2a) concludes the phase transition from radiative to convective stellar interior. As the protostellar mass increases, the so-called luminosity wave mechanism takes place (Larson 1972). We illustrate in Fig. 3 the development of the luminosity wave of the growing protostar in our model Run-100-hydro. A maximum in the luminosity profile forms (Fig. 3a) and moves outwards until it reaches the stellar surface and adopts a strictly monotonically increasing shape, i.e. the luminosity gradient is positive everywhere (Fig. 3c). The energy equation of the stellar structure reads as

$$\frac{\mathrm{d}L_\star(r)}{\mathrm{d}M_\star(r)} = -T_{\rm eff}\frac{\mathrm{d}s_\star}{\mathrm{d}t}, \quad (1)$$

where $L_\star(r)$, $M_\star(r)$, $T_{\rm eff,}$ and $s_\star$ are the internal luminosity, mass, temperature, and specific entropy radial profiles. It implies that interior to the luminosity peak (at $r < R_c$) the entropy of the star decreases with time, i.e.

$$\frac{\mathrm{d}L_\star(r)}{\mathrm{d}M_\star(r)} > 0 \Rightarrow \frac{\mathrm{d}s_\star}{\mathrm{d}t} < 0 \text{ if } r < R_c, \quad (2)$$

while exterior to the luminosity peak (at $r > R_c$) the entropy of the star increases with time, i.e.

$$\frac{\mathrm{d}L_\star(r)}{\mathrm{d}M_\star(r)} < 0 \Rightarrow \frac{\mathrm{d}s_\star}{\mathrm{d}t} > 0 \text{ if } r > R_c. \quad (3)$$

Therefore, the entropy of the surface layers ($r > R_c$) increases as they absorb energy triggering the stellar bloating, whereas when the $L(r)$ peak reaches the stellar surface at $r = R_\star$ all the layers lose entropy and the protostar contracts. Each time a violent accretion event with an accretion peak of $\approx 10^{-2}$–$10^{-1}\,M_\odot\,yr^{-1}$ deposits mass to the star, another luminosity maximum sets in the interior (Fig. 3b)

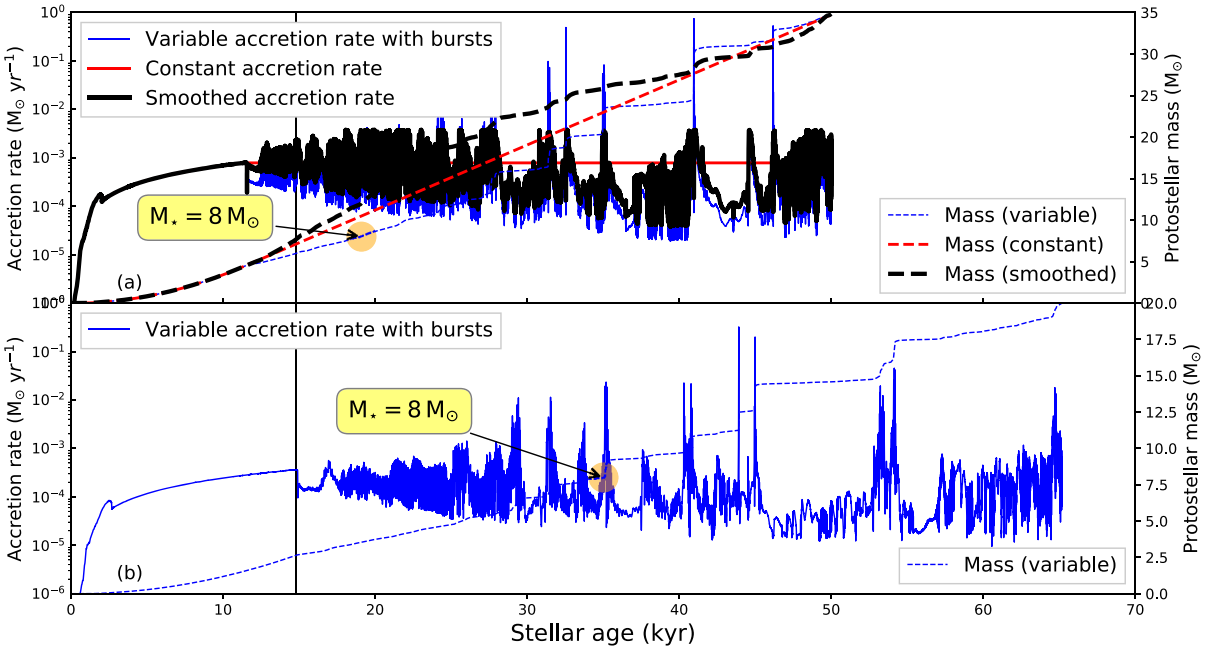

Figure 1. Accretion rate and protostellar mass evolution in our models with a pre-stellar core mass of 100 $M_\odot$ (a) and 60 $M_\odot$ (b), respectively.

and the luminosity wave forms again in the upper layers of the protostar (Fig. 3d), provoking a new swelling episod. Our model with $M_c = 60\,M_\odot$ gives similar results.

Fig. 4 presents two characteristic time-scales, which are usually used to describe the evolution of accreting protostars, and reports their time evolution next to the accretion rate history and the protostellar mass evolution. More specifically, the figure plots the so-called accretion time-scale

$$t_{\rm acc} = \frac{M_\star}{\dot{M}}, \tag{4}$$

representing the characteristic time-scale of mass growth of the accreting star (thin dashed red lines), and the Kelvin–Helmholtz time-scale

$$t_{\rm KH} = \frac{G M_\star^2}{R_\star L_\star}, \tag{5}$$

related to the entropy loss through radiation (thick solid blue lines). The protostar begins accreting at a variable rate once the disc forms (thick red lines), with $t_{\rm acc} < t_{\rm KH}$ at times when their evolution is only governed by disc accretion instead of mass infall from the pre-stellar core. During the gravitational collapse and the early disc evolution, the protostars evolve by gaining entropy by advection, with negligible radiative loss ($t_{\rm acc} < t_{\rm KH}$, see Figs 4b and d). Note that our model Run-100-hydro is already a MYSOs when the first burst happens, whereas our model Run-60-hydro experiences its first swelling as an intermediate-mass star (thin solid line of Figs 4a and c). Once the photospheric luminosity has grown enough, the energy loss governs the protostellar evolution ($t_{\rm acc} > t_{\rm KH}$ because $t_{\rm KH} \propto 1/R_\star L_\star$ throughout the bursts) and $L_{\rm acc} < L_\star$, which means that $L_{\rm acc}$ can be neglected (see Section 3.4). Interestingly, the protostars experience episods with $t_{\rm KH}/t_{\rm acc} > 1$ at the same time instance of the swelling. The MYSOs intermittently see their evolution ruled by mass accretion (the bloating) before recovering a more classical evolution governed by energy losses (the unswelling). This repeats each time an accretion burst happens. Therefore, each accretion-driven burst corresponds to a swelling episod of the MYSOs followed by a redistribution of the internal entropy restoring the internal thermal equilibrium.

3.3 Evolution of the surface properties of the MYSOs

In Fig. 5, we show the evolution of the protostellar iternal photospheric luminosity (a), radius (b), and effective temperature (c) as a function of the stellar age of our MYSOs. The figure distinguishes between the variable-accreting models with a 100 $M_\odot$ pre-stellar core (thin solid blue lines) and with a 60 $M_\odot$ pre-stellar core (thick dashed red line), respectively. We assume that the MYSOs are blackbodies, therefore, the photospheric luminosity is estimated as

$$L_\star = 4\pi R_\star^2 \sigma T_{\rm eff}^4, \tag{6}$$

where σ is the Stefan–Boltzman constant. The stellar surface properties does not evolve much during the free-fall gravitational collapse on to the MYSOs and the early phase of the disc formation, at times ≤ 20 kyr. Only a moderate and monotonical increase of the stellar radius and corresponding photospheric luminosity occurs, as the deuterieum burning maintains the central temperature nearly constant (Fig. 5a). When the variations of the accretion rate substantially increase in response to the growing strength of gravitational instability and fragmentation in the circumstellar disc, the protostar grows faster, and, after the first luminosity wave, its surface becomes radiative so that any episodic deposit of mass on it generates an augmentation of the effective temperature and the surface luminosity. With one important exception, the time evolution of stellar surface properties is similar to what was found in the context of calculations carried out with a constant accretion rate – the photospheric luminosity (Fig. 5a) and effective temperature (Fig. 5c) generally increase, while the stellar radius decreases (Fig. 5b) for as long as the star remains in the quiescent accretion

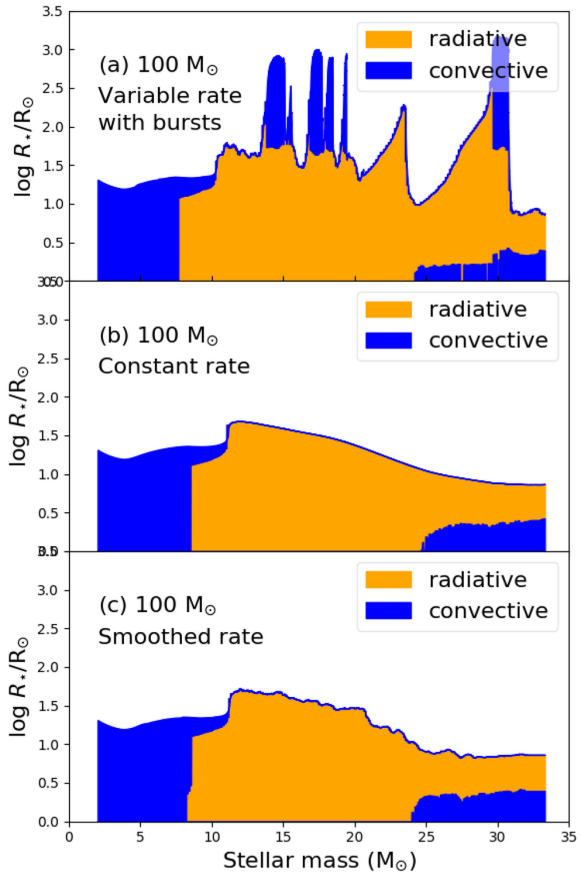

Figure 2. Kippenhahn diagram of MYSOs generated with an initial 100 $M_\odot$ pre-stellar core. It shows the evolution of the internal stellar structure as a function of time. The blue and orange regions denote the convective and radiative parts of the protostar, respectively.

phase. However, this monotonic behaviour is interspersed with brief excursion events associated with violent accretion bursts, during which the MYSOs adopt opposite photospheric properties by becoming bigger and cooler. Such a behaviour of $R_\star$ and $T_{\rm eff}$ is a direct consequence of the changes in the internal structure of the MYSOs, which is sensitive to the accretion rate. In the next section, we demonstrate how the variable accretion rate with episodic bursts can affect the evolutionary path of MYSOs in the Hertzsprung–Russell diagram.

3.4 Pre-main-sequence excursions in the Hertzsprung–Russell diagram

Fig. 6 shows the evolutionary tracks of our MYSOs in the Hertzsprung–Russell diagram. More specifically, the evolution of the central star in the model with a 100 $M_\odot$ pre-stellar core was calculated using a variable (thin blue line), constant (thick dashed red line), and smoothed (thick black line) accretion rates and are plotted in panel (a) together with the ZAMS track of Ekström et al. (2012). The tracks of the central stars in the models with different pre-stellar core masses of 60 and 100 $M_\odot$ are shown in panel (b). In this case, only the variable accretion rate was considered. Grey solid lines are isoradii. From the definition of $t_{\rm KH}$ and $t_{\rm acc}$ (Hosokawa & Omukai 2009; Hosokawa et al. 2010) it can be shown that

$$\frac{t_{\rm KH}}{t_{\rm acc}} \propto \frac{L_{\rm acc}}{L_\star}, \tag{7}$$

with the accretion luminosity $L_{\rm acc} \propto G\dot{M}M_\star/R_\star$, where G is the gravitational constant. The initial stages of the stellar evolution calculations are similar as we assume identical accretion rates during the free-fall collapse. Differences occur at the onset of the disc formation. In Fig. 6(a), we directly see that the final stellar mass at the end of the main accretion phase is not the key quantity that governs the evolutionary tracks of high-mass protostars in the Hertzsprung–Russell diagram. Despite all models are calculated up to reaching a similar stellar mass of 33.3 $M_\odot$, their track are qualitatively different. Furthermore, the track of the Run-100-smoothed model with a smoothed accretion rate (but retaining small-amplitude variations) is globally similar to the track of the Run-100-constant model, which assumes a constant accretion rate. The small-amplitude variations in the accretion rate only induce tiny deviations from the constant accretion track. The model with accretion spikes strongly deviates from the constant accretion track. Strong accretion bursts generate short but important changes in the pre-main-sequence evolutionary track of the MYSOs in the form of evolutionary loops to the red part of the Hertzsprung–Russell diagram. These excursions repeat themselves as more and more accretion spikes occur. We find similar behaviour for our model with a pre-stellar core mass of 60 $M_\odot$ (Fig. 6b).

4 EFFECT OF THE INITIAL CONDITIONS ON THE STELLAR EVOLUTIONARY TRACKS OF MYSOS

This section explores the effects of different initial conditions of the protostellar seed in the evolution calculations on stellar structures, the various protostellar properties and on the pre-ZAMS evolutionary track of the MYSOs in the Hertzsprung–Russell diagram.

4.1 Stellar structures

The seed core taken as a stellar embryo to initialize the stellar evolution calculations is a parameter which both depends on the properties of the pre-stellar core (Vaytet & Haugbølle 2017; Bhandare et al. 2018) and influences the stellar evolution calculations (Haemmerlé & Peters 2016). In order to investigate the effects of the bursts on the evolutionary tracks as a function of the initial seeds, we carry out a comparison study between two cases using our accretion rate derived from the hydrodynamical simulation with an initial 100 $M_\odot$ pre-stellar core with variable accretion rates (Run-100-hydro and Run-100-compact), see our Table 2. The model Run-100-hydro is initialized with a convective core of 2 $M_\odot$ of radius 20.4 $R_\odot$, temperature 4270 K, and luminosity 123 $L_\odot$, while the model Run-100-compact is started as a fully radiative star of 2 $M_\odot$ with radius 2.9 $R_\odot$, temperature 5960 K, and luminosity 9.7 $L_\odot$, respectively. They principally differ by the internal entropy profiles, i.e. the initial convective model Run-100-hydro exhibits a flat entropy profile towards the protostellar surface, whereas the initial radiative model Run-100-compact has a positive entropy gradient. Therefore, Run-100-hydro is adiabatically convective and is larger than Run-100-compact by about an order of magnitude. Details about these protostellar seeds are given in Haemmerlé & Peters (2016). Particularly, the authors stressed therein that the convective and radiative protostellar embryos have properties similar to models of $M_\star = 2\,M_\odot$ built by hot and cold accretion, respectively, while

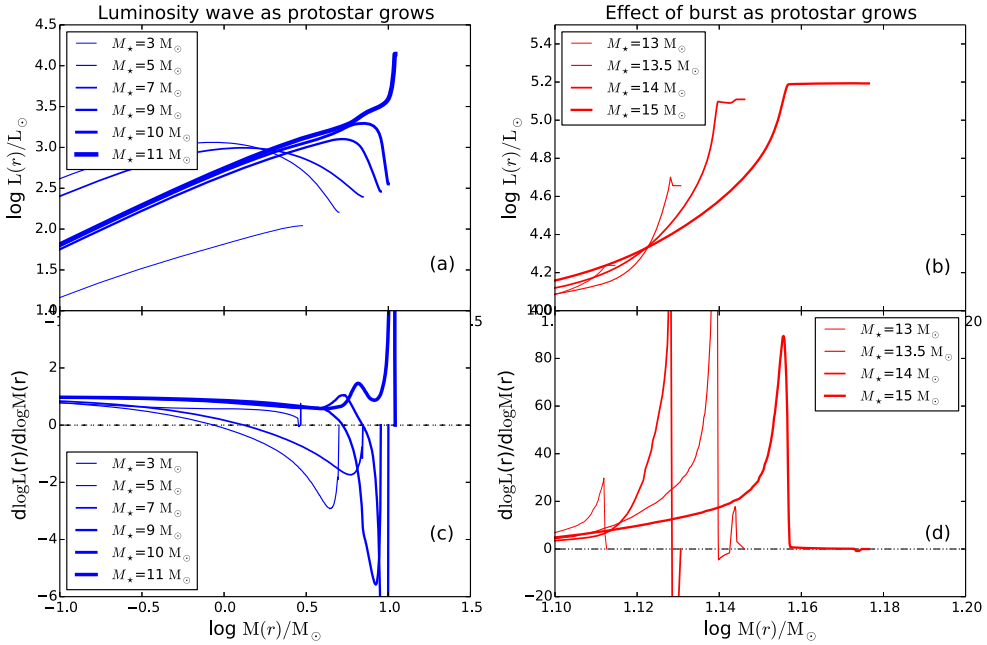

Figure 3. Internal luminosity profiles (top panels) and gradient of luminosity profiles (bottom panels) in our massive protostellar model Run-100-hydro. The panels illustrate the development of the luminosity wave (left-hand panels) and the effect of a burst (right-hand panels) on to the structure of a growing MYSO.

the geometry of the accretion is cold for both cases throughout the stellar evolution calculations. Our comparison models therefore investigate the effects of the early accretion geometry on the evolution of the MYSOs.

Fig. 7 reports the Kippenhahn diagram two MYSOs calculated with the same episodic accretion rate history but different initial conditions (Table 2). Despite of differences in the evolution of the outer radius of the protostar, notable swelling episods of the MYSO appear at the time instances corresponding to the accretion bursts. Although differences are visible, especially (i) during the clustered bursts at 15–20 $M_\odot$ in the model Run-100-hydro (a) which results in a single inflation of $R_\star$ in Run-100-compact (b), and (ii) in the burst at $\sim$22.5 $M_\odot$ that is more pronounced in the initially convective case (b), the major outbursts nevertheless generate similar effects regardless of the initial conditions of the calculations. Once the protostar reaches $\sim$10 $M_\odot$, both simulated MYSOs are structured with a convective layer that inflates under the effects of the entropy deposition by accretion of gaseous circumstellar clumps and a radiative interior which progressively develops a convective core once the protostar is heavy and hot enough for H-burning at $\sim$25 $M_\odot$. The development of a luminosity wave in the outer layer of the MYSO each time a burst happens is similar as above pictured in the context of an initially radiative protostellar embryo (Fig. 3). Note that the radiative model is numerically more difficult to calculate, and it has been simulated over a slightly smaller time interval. Both initial conditions produce similar effects on the evolution of the radius of MYSOs as a response of the accretion of circumstellar gaseous clumps.

4.2 Surface properties and excursions in the Hertzsprung–Russel diagram

Fig. 8 plots the evolution of the stellar surface luminosity $L_\star$ (panel a, in $L_\odot$), the stellar radius $R_\star$ (panel b, in $R_\odot$), and the effective temperature $T_{\rm eff}$ (panel c, in K) as a function of time (in kyr) of our $M_c = 100\,M_\odot$ collapsing pre-stellar cores that are considered with large, convective (thin solid blue line) and compact, radiative (thick dotted red line) initial conditions, respectively. The only difference in the calculations is the past evolution of the stellar embryo of 2 $M_\odot$ which is mimiced by the initial conditions of the models (Table 2). Accretion on to the radiative embryo produces an immediate swelling ($>100\,R_\odot$) as a response of the deposition of entropy by cold accretion (Fig. 8b), which also diminishes the surface temperature (Fig. 8c) and increases the surface luminosity (Fig. 8a). These differences between the surface properties of the MYSOs persist up to $\approx$20–25 kyr, when the series of accretion-driven outbursts begins. As illustrated in Fig. 7, the effects of the accretion spikes on to the protostellar properties are qualitatively similar: the most important luminosity rises and falls coincide with each other as a function of time and their respective offsets are due to slightly shifted values of $R_\star$ and $T_{\rm eff}$. Note that the initial compact model has a more pronounced swelling during the series of moderate bursts at $\approx$20–25 kyr (Fig. 8b). Once the strong accretion events on to the MYSO have started, the initial convective model has baseline values of $R_\star$ and $T_{\rm eff}$ more compact and hotter than that of the initial radiative calculation (see thick red dotted lines of Fig. 8a–c).

Fig. 9 shows the evolutionary tracks in the Hertzsprung–Russell diagram of the models Run-100-hydro (thin solid blue line) and Run-100-compact (thick dotted red line), respectively. The grey dotted solid lines are isoradii and the thick black dashed line is the ZAMS track of Ekström et al. (2012). It underlines the initial differences between the two models, especially the rapid swelling of the compact model by $\sim$2 orders of magnitude accompanied by a decrease of its temperature and an increase of its luminosity, respectively. It also further illustrates that the early bursts are more pronounced in the compact case than it the convective case. The protostellar radius of the initially radiative Run-100-compact (thick

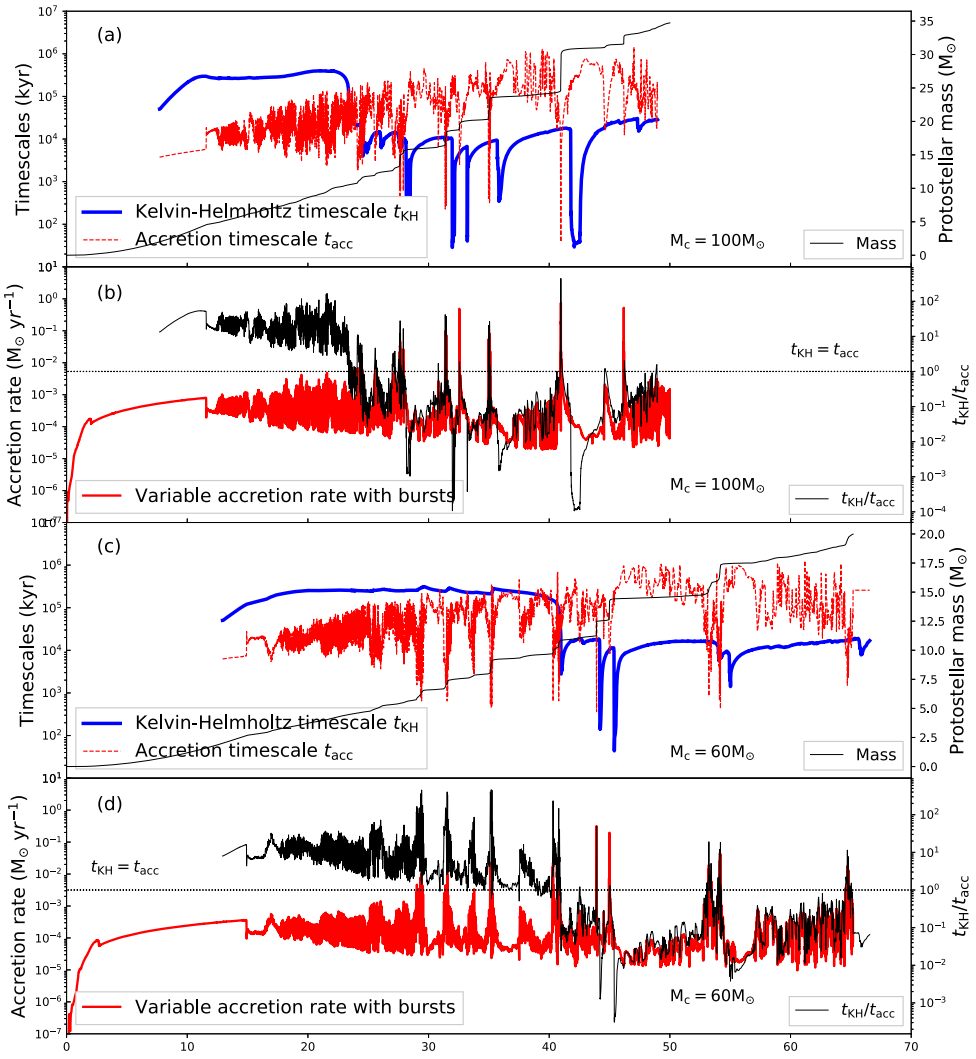

Figure 4. Characteristic time-scales of our bursting protostars accreting at variable accretion rates and generated from an initial 100 $M_\odot$ (a, b) and 60 $M_\odot$ (c, d) pre-stellar core, respectively. Panels (a) and (c) plot the Kelvin–Helmholtz time-scale t_{KH} (thick solid blue line, in kyr), the accretion time-scale t_{acc} (thin dotted red line, in kyr), and the protostellar mass (thin solid black line, in $M_\odot$). Panels (b) and (d) show the accretion rate on to the protostars (thick solid red line, in $M_\odot$ yr^{-1}), the ratio t_{KH}/t_{acc} (thin solid black line), and the thin dotted black line corresponds to $t_{KH}/t_{acc} = 1$.

dotted red line) is larger than that of the initially convective model Run-100-hydro in the quiescent phases (Fig. 8b), therefore, its evolutionary track is closer to the 100 $R_\odot$ isoradius. This difference diminishes as a function of time and the two tracks overlap each other in the quiescent phase after the third excursion which almost reach the 1000 $R_\odot$ isoradius occurs. Finally, let notice that in both cases, the tracks cross the 1000 $R_\odot$ isoradius throughout the strongest swelling episods and reach the Hayashi limit. In the initial convective case, when the peak of the excursions happens, the track of the MYSO slightly follows vertically the Hayashi track before it recovers the values of $R_\star$ and $L_\star$ corresponding to the quiescent accretion phase. Although the properties of the first Larson core depend on the intrinsic pre-stellar core characteristics (Vaytet & Haugbølle 2017; Bhandare et al. 2018), our suite of comparison simulations shows that the mechanism triggering the excursions of MYSOs in the Hertzsprung–Russell diagram is independent of their initial conditions. This shows that, under our assumptions, the accretion geometry induces little qualitative differences on the evolution of the surface properties of episodically accreting MYSOs.

5 DISCUSSION

In this section, we present the limitation of our method, compare our outcomes to those of other studies assuming burst-free disc accretion histories and extrapolate the findings of our study to the formation of intermediate-mass stars, and we discuss the observable implications of our results. Finally, we review alternative explanations for FU-Orionis-like bursts from young stars.

5.1 Model caveats

The limitations of our method are two-fold. First, the numerical hydrodynamics simulations of disc formation are subject to caveats

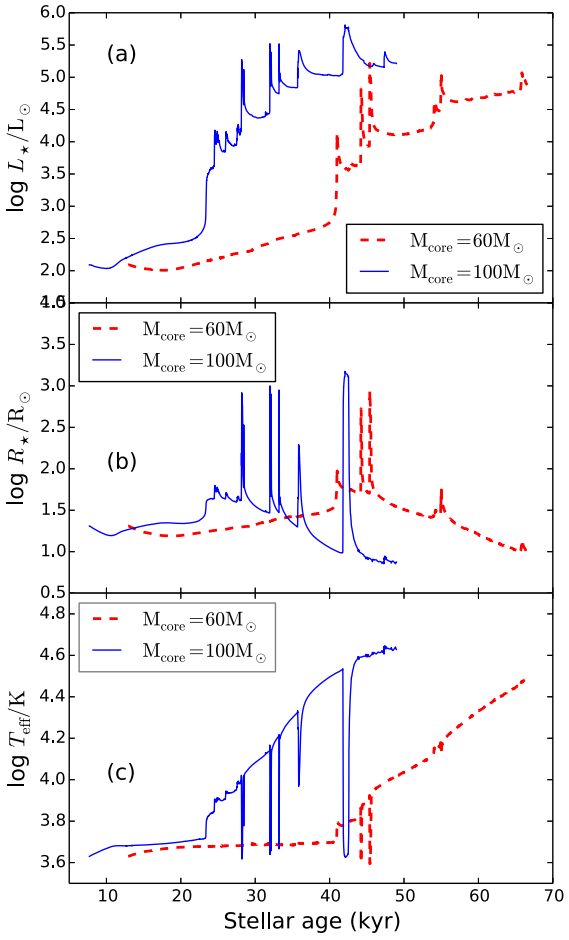

Figure 5. Evolution as a function of time (in kyr) of the stellar surface luminosity (a), stellar radius (b), and effective temperature (c) of our MYSOs experiencing variable disc accretion interspersed by bursts. The panels distinguish between the models assuming an initial 60 $M_\odot$ (thick dotted red line) and 100 $M_\odot$ (thin solid blue line) pre-stellar core, respectively.

which merit future improvements, whereas the stellar calculations are also subject to assumptions potentially calling follow-up betterments. In addition to the well-known limitation of disc fragmentation simulations given by the logarithmically expanding radial grid (Meyer et al. 2018b), the sink cell radius, which strongly influences the time-step of the simulations, is kept to a value making the simulations affordable from the point of view of their numerical cost. Decreasing the inner hole would allow us to better follow the migration of the gaseous clumps responsible for the accretion-driven bursts, and therefore make our accretion histories more accurate. However, the value used in this paper is kept to a decent value ($r_{\rm in}$ = 20 au) that is still smaller than that of other studies on disc fragmentation, see e.g. the supermassive protostellar models of Hosokawa et al. (2016).

For the sake of completeness, future improvements should equivalently include the initial non-sphericity and differential rotation of the parent pre-stellar cores (see, e.g. Banerjee, Pudritz & Anderson 2006) and take into account stellar motion in response to the gravitational force of the disc, as massive disc sub-structures can shift notably the centre of mass of the system from coordinate centre where the protostar resides (Regály & Vorobyov 2017). Nevertheless, despite the fact that the effects of the stellar inertia on the behaviour of accretion discs have been analytically shown to play a role on the development of asymmetries in their structures (Adams, Ruden & Shu 1989), recent numerical simulations demonstrated that wobbling neither prevents disc fragmentation nor reduces the bursts intensities in the early formation phase of young high-mass stars (Meyer et al. 2018a). A set of comparison simulations with and without wobbling is shown in the Fig. 7 of their section 4 and its illustrates that high-magnitudes accretion-driven outbursts develop similarly within the same time-scale after the onset of the disc formation which followed the free-fall gravitational collapse. Only the time instance and perhaps the long-term occurrence of the excursions of MYSOs in the Hertzsprung–Russell diagram would change if a moving sink-cell is used in the hydrodynamical simulations. Our assumptions related to the hydrodynamical simulations are discussed in great detail in Meyer et al. (2017).

The manner our stellar evolution calculations treat the accretion of circumstellar material can also be improved. Although the so-called cold accretion scenario is a well-established method to include the accretion of disc material on to the stellar surface (see Hosokawa & Omukai 2009, and references therein), it is the lower limit in terms of for the accretion of entropy (Hosokawa et al. 2010). Despite of the fact that high-resolution observations recently demonstrated the disc-plus-jet structure surrounding MYSOs, the exact topology of the accretion flow within a few tens of stellar radii from the protostellar surface is unknown and may differ from accretion in the mid-plane, for example via the formation of accretion columns (Romanova et al. 2012). The deviations of the accretion geometry from the cold accretion scenario can be explored within the so-called hot accretion scenario or by hybridizing the cold and hot accretion scenarios (Vorobyov et al. 2017). Haemmerlé & Peters (2016) showed how the stellar bloating can significantly change as a function of the early accretion geometry, regardless of the accretion rate. However, this concerned smaller accretion rates than ours and our calculations are performed with the initial convective model (CV) of Haemmerlé & Peters (2016), with a larger initial radius than that of the radiative models (RD) for spherical accretion, for which the bloating of the radius is less pronounced.

Our study make use of the methods developed in Haemmerlé et al. (2016) and Haemmerlé & Peters (2016). These works showed that (i) when a massive protostar accretes at very high constant rates ($\geq 10^{-2}\,M_\odot\,{\rm yr}^{-1}$), its corresponding evolutionary track derives towards the red part of the Hertzsprung–Russell diagram (Haemmerlé et al. 2016), and (ii) that variabilities in the accretion rate on to H II regions around massive protostar taken from large-scale hydrodynamical simulations (see Peters et al. 2010) produce luminosity changes reflecting that of the fluctuating accretion rates (Haemmerlé & Peters 2016). Since we focus on the accretion in the vicinity of massive protostars, the accretion rates histories measured from small-scale hydrodynamical simulations (Meyer et al. 2017, 2018b) are more realistic and we investigate how massive protostellar structures reacts under the effect of such accretion variability. We show that high episodic accretion rates ($\geq 10^{-2}-10^{-1}\,M_\odot\,{\rm yr}^{-1}$) produce repetitive excursions in the Hertzsprung–Russell diagram. It was not the case in Hosokawa & Omukai (2009) and Hosokawa et al. (2010) because their accretion rates were constant and weaker than that ours (up to $10^{-3}\,M_\odot\,{\rm yr}^{-1}$). Indeed, the entropy accreted is higher than for cold accretion, hence, the radius will be larger according to the homology relations,

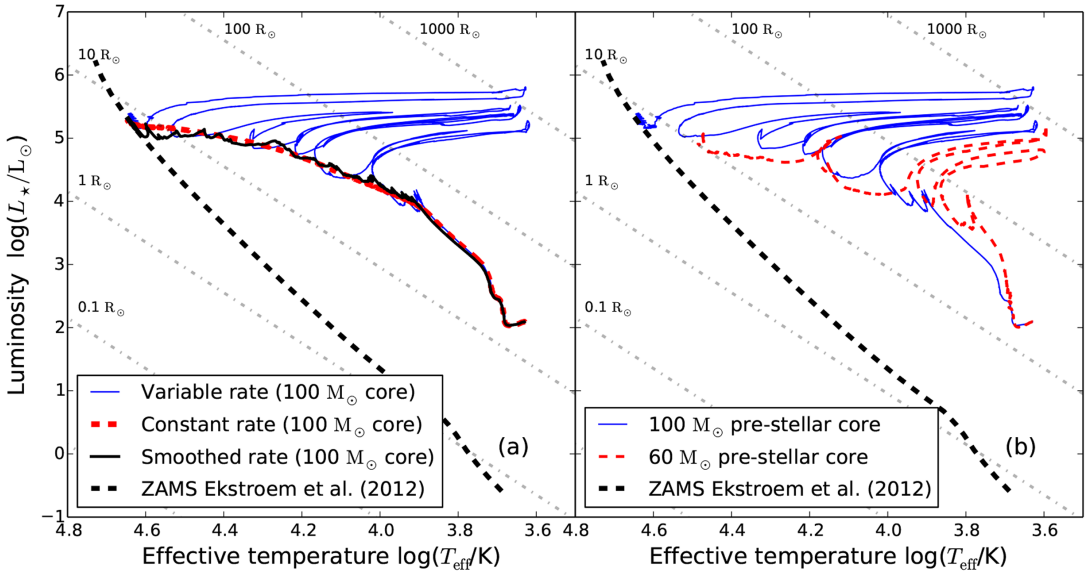

Figure 6. Hertzsprung–Russell diagram of our proto-stellar models with a similar pre-stellar core mass of 100 $M_\odot$, but experiencing different initial accretion rate histories (a) and evolutionary tracks with pre-stellar cores of different initial masses of 60 and 100 $M_\odot$, respectively (b). Grey dotted solid lines are isoradius and the thick black dashed line is the ZAMS track of Ekström et al. (2012).

Table 2. Characteristics of the 2 $M_\odot$ protostellar seeds used in our comparison simulations of our models with 100 $M_\odot$ core and episodic accretion.

Models	$R_\star$ ($R_\odot$)	$L_\star$ ($L_\odot$)	$T_{\rm eff}$ (K)	Initial conditions
Run-100-hydro	20.4	123	4270	Convective embryo with large initial radius mimicing spherical, then disc accretion[a]
Run-100-compact	2.9	9.7	5960	Radiative embryo with small initial radius mimicing continuous disc accretion[a]

[a]See section 2.3 of Haemmerlé & Peters (2016).

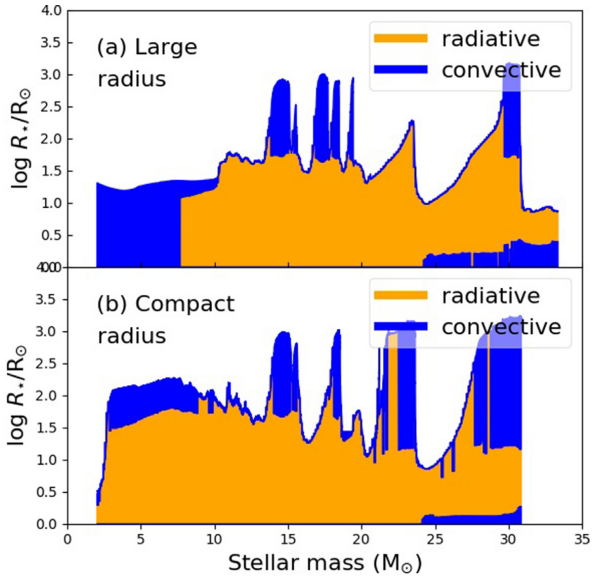

Figure 7. As Fig. 2 for our of MYSOs generated with an initial 100 $M_\odot$ pre-stellar core, variable accretion rates, large (a) and compact (b) initial protostellar radius.

as confirmed for constant rates in Hosokawa & Omukai (2009); Hosokawa et al. (2010), and, since the tracks already reached the Hayashi limit, substantial differences in the maximal values of the prostellar radius should not be expected.

One can nevertheless wonder whether the mean protostellar radius of the MYOS may be affected by hybrid/hot accretion geometries, by making the protostars slightly colder during the phases of quiescent accretion and consequently diminishing the amplitudes of the excursions, as shown in the context of low-mass star formation (Hosokawa, Offner & Krumholz 2011). However, the incidence of massive magnetic OB stars is small (Fossati et al. 2015, 2016) and pre-main-sequence massive stars do have strong surface radiation field because of their high effective temperatures (Hosokawa & Omukai 2009; Hosokawa et al. 2010). Therefore, quiescent accretion processes in most MYSOs should happen via boundary layer mechanisms at the equatorial plane, as investigated by radiation-hydrodynamics simulations (Kee, Owocki & Kuiper 2018). The assumption of cold accretion is therefore appropriate for this first study on the effects of strong, episodic accretion variability on the stellar evolutionary tracks of pre-ZAMS massive protostars.

5.2 Comparison with other works assuming constant disc accretion rates

Our work extends previous studies on the modifications brought by disc mass accretion on to the evolutionary path of young massive stars in the Hertzsprung–Russell diagram. We perform the most

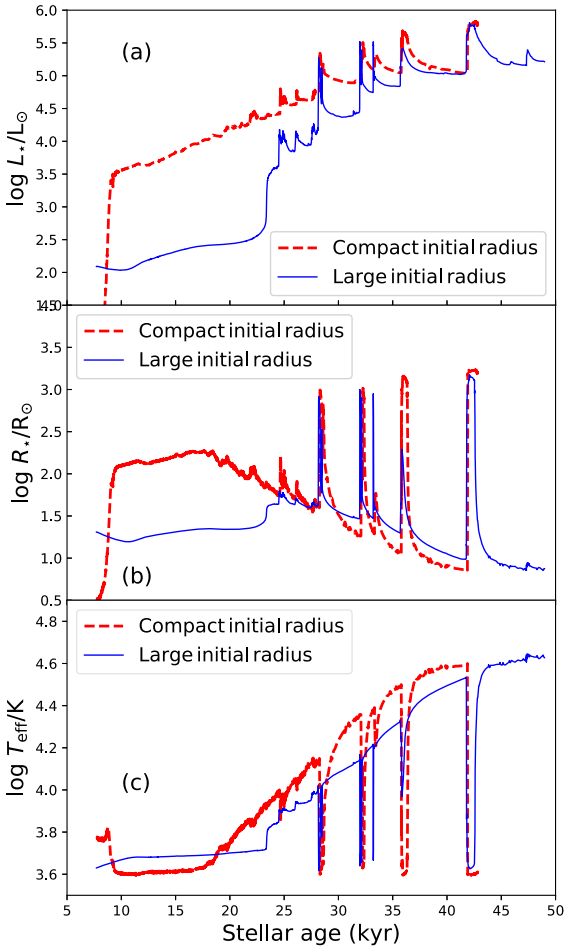

Figure 8. As Fig. 5 with the evolution as a function of time (in kyr) of the stellar surface luminosity (a), stellar radius (b), and effective temperature (c) of our $M_c = 100\,M_\odot$ collapsing pre-stellar cores, considered with different initial radii of the protostellar embryo in the stellar evolution calculations, respectively.

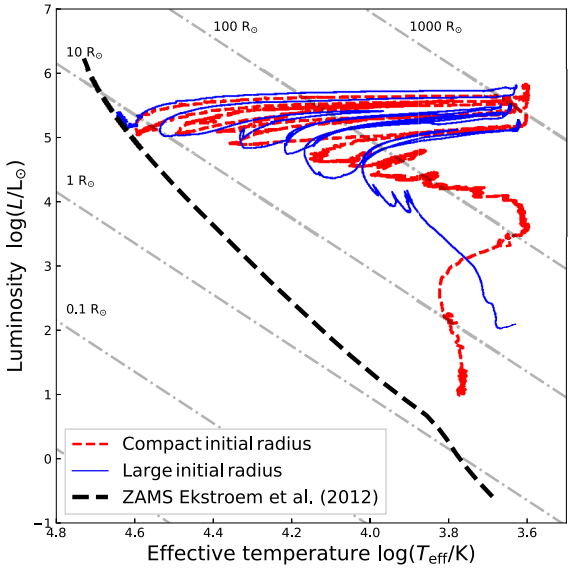

Figure 9. As Fig. 6 with the evolutionary tracks of our models of $M_c = 100\,M_\odot$ collapsing pre-stellar cores and episodic accretion rates on to the protostar, considered with different initial conditions of the stellar embryo, respectively.

spatially resolved numerical simulations of the inner accretion disc around MYSOs that have revealed self-consistent fragmentation of the irradiated circumstellar disc into spiral arms interspersed with dense gaseous clumps, whose migration on to the protostar induces strong variability and bursts in the accretion rate histories. These variabilities in the accretion rate evolution account for the specifics of the inner disc physics that was information that were not passed to the protostars in previous works on the evolution of massive protostars. Indeed, constant accretion rate is considered in early studies (Palla & Stahler 1992, 1993; Beech & Mitalas 1994; Bernasconi & Maeder 1996; Bernasconi 1996) and in more recent works (Hosokawa & Omukai 2009; Hosokawa et al. 2010, 2016). The latter found that rapid strong accretion produces a strong swelling of the protostars, which bloat so that their radii reach $\simeq 100\,R_\odot$. This bloating results in inducing a reduction of the effective temperature so that the H II region reestablishes only when the star contracts again and comes back to the bluer part of the Hertzsprung–Russell diagram (Haemmerlé & Peters 2016). Variabilities produced by the initial gravitational collapse of the host pre-stellar core in which the star grows and by the effect of outflows launched perpendicularly to the disc have been explored with stellar calculations based on the 2.5-dimensional axisymmetric gravitoradiation-hydrodynamics models, leading to a single excursion to the redder region of the Hertzsprung–Russell diagram (Kuiper & Yorke 2013).

Our study investigates the effects of strong accretion-driven bursts predicted to happen in the context of massive protostars (Meyer et al. 2017). We show that the swelling of the MYSOs, occasionally going to the cold part of the Hertzsprung–Russell diagram (Kuiper & Yorke 2013), can be generalized in a wider context, as a successive series of evolutionary loops to the red region of the Hertzsprung–Russell diagram, before the protostars converge to the ZAMS. Fig. 10 compares our models with the tracks of Haemmerlé et al. (2016) by plotting our evolutionary tracks with a colour coding informing on the stellar mass (in $M_\odot$). In general, our MYSOs follow the track of a massive protostar accreting at a constant rate of $10^{-3}\,M_\odot\,{\rm yr}^{-1}$ (Haemmerlé et al. 2016), but, in addition, our tracks exhibit excursions to the red part of the Hertzsprung–Russell diagram caused by repetitive accretion bursts that modify their surface properties. Our tracks are therefore consistent in terms of final mass and location on the ZAMS (Ekström et al. 2012), modulo the excursions which deviate from the constant-accretion solutions. Particularly, we recover the non-monotonous evolution of the radius and effective temperature of two-dimensional present-day models of disc-accreting MYSOs noted by Kuiper & Yorke (2013), but reveal their episodic nature together with the intermittency of their ionized flux, as it is known to exist in the context of primordial supermassive protostars gaining mass from a fragmented disc (Hosokawa et al. 2016).

5.3 Observational implications

Fig. 11 compares the excursions of our protostars in the Hertzsprung–Russell diagram with observational data of various high-mass stars. The figure clearly illustrates that the properties

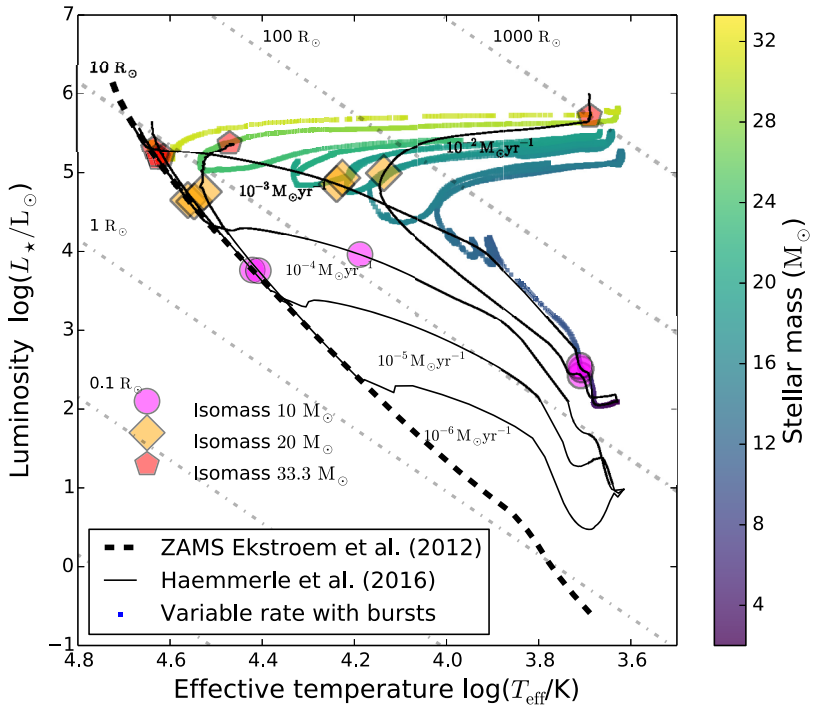

Figure 10. Comparison between our massive protostar with $M_c = 100\,M_\odot$ experiencing variable accretion (thick coloured line) and the evolutionary tracks for massive protostars accreting with constant rates (thin black lines) of Haemmerlé et al. (2016). The colour coding of the track indicates the stellar mass (in $M_\odot$) and the coloured dots are isomasses, respectively. Grey dotted solid lines are isoradius and the thick black dashed line is the ZAMS track of Ekström et al. (2012).

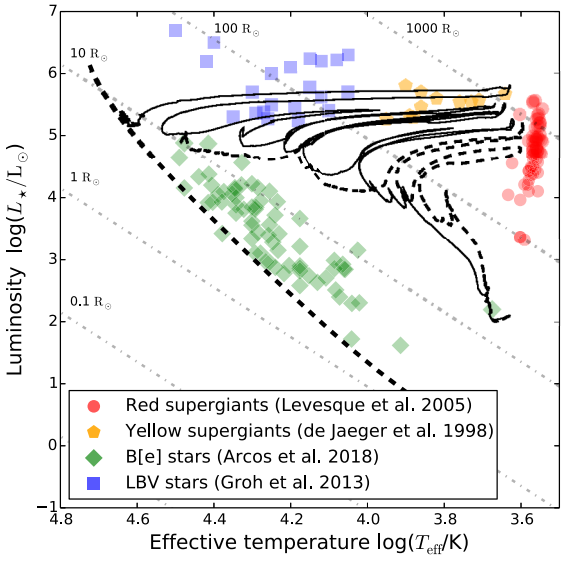

Figure 11. Comparison between our evolutionary tracks with variable accretion rates of $M_c = 60\,M_\odot$ (thick dashed black line) and $M_c = 100\,M_\odot$ (thin solid black line) collapsing pre-stellar cores, respectively, and observational data. Grey dotted-dashed lines are isoradius and the thick black dashed line is the ZAMS track of Ekström et al. (2012).

of young massive stars during the bursts may be similar to those of evolved, supergiant massive stars with high-luminosity, large radii, and cold-effective temperature. One can note that the model with $M_c = 60\,M_\odot$ (dashed black line) has surface characteristics at the peak of the burst that are similar to the characteristics of a red supergiant (Levesque et al. 2005). On the other hand, the $M_c = 60\,M_\odot$n model has surface characteristics similar to Be stars (Arcos et al. 2018) when converging to the ZAMS in the post burst phase. At the same time, the model with a more massive pre-stellar core ($M_c = 100\,M_\odot$) crosses the luminous blue variables (LBV) region (Groh et al. 2013) attains the characteristics a yellow supergiant (YSG) star at the peak of the burst (de Jager 1998). To avoid confusion with evolved massive stars, one should use unique spectral signature of young massive protostars, such as infrared excess and line emission typically associated with accretion discs.

Most important observational implication of our results is the intermittent character of the H II regions associated with massive protostars accreting from a fragmented circumstellar disc. We estimate its impact on the ionization feedback with the stellar properties obtained from our stellar evolution calculations by computing the number of UV-ionizing photons per unit time $S_\star$ as the integral of the blackbody spectrum above the ionizing energy threshold (Haemmerlé & Peters 2016), i.e.

$$S_\star = 4\pi R_\star^2 \int_{h\nu > 13.6\,\mathrm{eV}} \frac{F_\nu}{h\nu} d\nu, \tag{8}$$

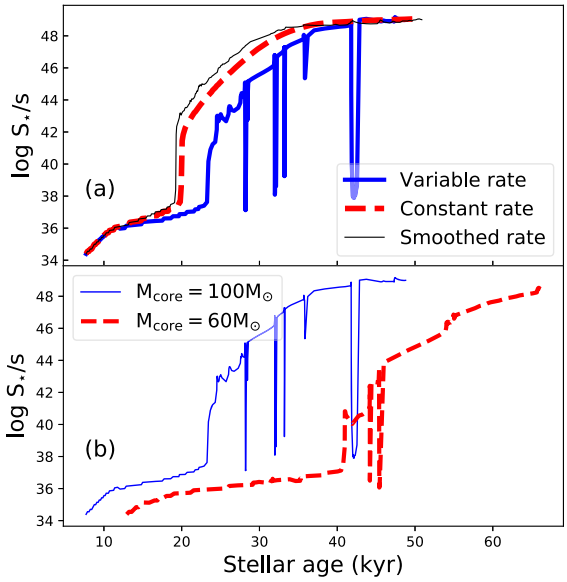

Figure 12. Evolution of the number of surface ionizing photons $S_\star$ per second produced by our young massive stars as a function of the protostellar age, for our models with an initial 100 $M_\odot$ assuming different accretion histories (a) and generated by different initial pre-stellar core masses but experiencing variable accretion rate (b).

with,

$$F_\nu = \frac{2\pi(h\nu)^3}{c^2h^2}\frac{1}{e^{\frac{h\nu}{k_B T_{\rm eff}}}-1}, \quad (9)$$

where h, ν, c, and k_B are the Planck constant, photon frequency, speed of light, and Boltzman constant, respectively. We report its evolution during the pre-main-sequence phase for our protostellar models in Fig. 12. The number of photons gradually increases up to the time instance of the disc formation at 10–20 kyr (Fig. 12a) after the beginning of the gravitational collapse. The accretion variability breaks the strict monotonic time-evolution of $S_\star$ at ≈25 kyr (Run-100-hydro with variable accretion, thick blue line of Fig. 12a) and at the time of each burst (equivalently each spectroscopic excursions), $S_\star$ sharply decreases by up to ≈8–9 orders of magnitude, inducing dippering in the variability of the H II regions of MYSOs. Such a phenomenon is only a consequence of the bursts, as our models with constant and smoothed accretion histories do not exhibit sharp decreases in $S_\star$ (thin solid black and thick dotted lines of Fig. 12a). A similar behaviour is found for our model Run-60-hydro (12b). The H II regions become fainter, which makes them much more difficult to detect on time-scales corresponding to those of the bursts. Fig. 13 further highlights the correlation between evolution of the protostellar radius and number of ionizing photons released by the protostellar surface $S_\star$ as a function of the growing mass of the MYSOs. The time interval corresponding to the bloating phases is of the order of the collisional recombination time-scale in the plasma (∼100 yr) derived for the intermittent H II regions around supermassive stars in Hosokawa et al. (2016).

5.4 Implication for intermediate-mass star formation

Both theoretical and observational works have recently highlighted a possible similarity between the star-forming processes in different mass regimes. First evidence came form the direct observation of H II regions piercing opaque pre-stellar clouds in high-mass star-forming regions (Fuente et al. 2001; Testi 2003; Cesaroni et al. 2010). Then, the observation of accretion flow (Keto & Wood 2006) and Keplerian disc structure surrounding protostars of various mass (Johnston et al. 2015; Forgan et al. 2016; Ilee et al. 2016; Ginsburg et al. 2018) strengthened that picture. The numerical proof of disc fragmentation around MYSOs and triggering of FU-Orionis-like events supported the scaled-up character of high-mass star formation with respect to that of low-mass and primordial stars (Vorobyov & Basu 2015; Hosokawa et al. 2016; Meyer et al. 2017). Moreover, the intermittent character of H II regions from young primordial stars has been demonstrated with the help of gravitoradiation-hydrodynamics models of the same kind as ours Hosokawa et al. (2016). By coupling the outcomes of the hydrodynamical results to stellar evolution calculations, they derive the intermittent properties of the UV feedback that is channelled through the radiation-driven cavity perpendicular to the accretion disc of young supermassive stars.

Our results extends such phenomenon to young massive stars, and we speculate that similar mechanisms may be at work in the intermediate-mass systems as they equivalently generate ionizing photons (Haemmerlé & Peters 2016) and form accretion discs and jets (Kessel, Yorke & Richling 1998; Fuente et al. 2001; Torrelles et al. 2014; Reiter et al. 2017). Young intermediate-mass stars indeed have all necessary prerequisites, i.e. circumstellar disc and H II regions (Fontani et al. 2012; Lumsden et al. 2012; Menu et al. 2015; Zakhozhay et al. 2018), to experience disc fragmentation and accretion variability. They may episodically produce FU-Orionis-type bursts which will subsequently make the UV feedback that fills their radiation-driven bubbles intermittent. Such a prediction is supported by various observational results, including amongst others the variability of the eruptive intermediate-mass stellar object IRAS 18507 + 0121 (Nikoghosyan, Azatyan & Khachatryan 2017) and the ionized outflow of the intermediate-mass stellar object IRAS 05373 + 2349 Very Large Array 2 (Brown et al. 2016). Additionally, we interpret the spectroscopic excursions of massive protostars in the Hertzsprung–Russell diagram triggered by FU-Orionis bursts as a direct consequence of the inward migration of a gaseous clump in their fragmented accretion discs on to the stellar surface, and, consequently, consider the intermittency of their H II regions as a possible signature of disc gravitational fragmentation.

5.5 Alternative explanations for bursting young stellar objects

ALMA views of bursting objects such as protostars with EXor revealed that their accretion discs seem not to be Toomre-instable, which suggests that outbursts should be triggered by mechanisms different than gravitational instabilities followed by inward migration of clumps in the disc (Cieza et al. 2018). Although the massive accretion discs of MYSOs implies that the fragmentation scenario is likely to happen (Kratter & Matzner 2006; Kratter & Lodato 2016), various other mechanisms have indeed been proposed to explain luminosity rises from young low-mass stellar objects, particularly in the low-mass regime of star formation. The work of Cieza et al. (2018) lists the principal alternatives for the generation of bursts without the classical picture of migrating disc gaseous clumps, i.e. (i) coupling between magnetorotational and gravitational instabilities, (ii) thermal-viscous instability, (iii) instabilities induced by planets or companions, and (iv) the infall clumpiness mechanism.

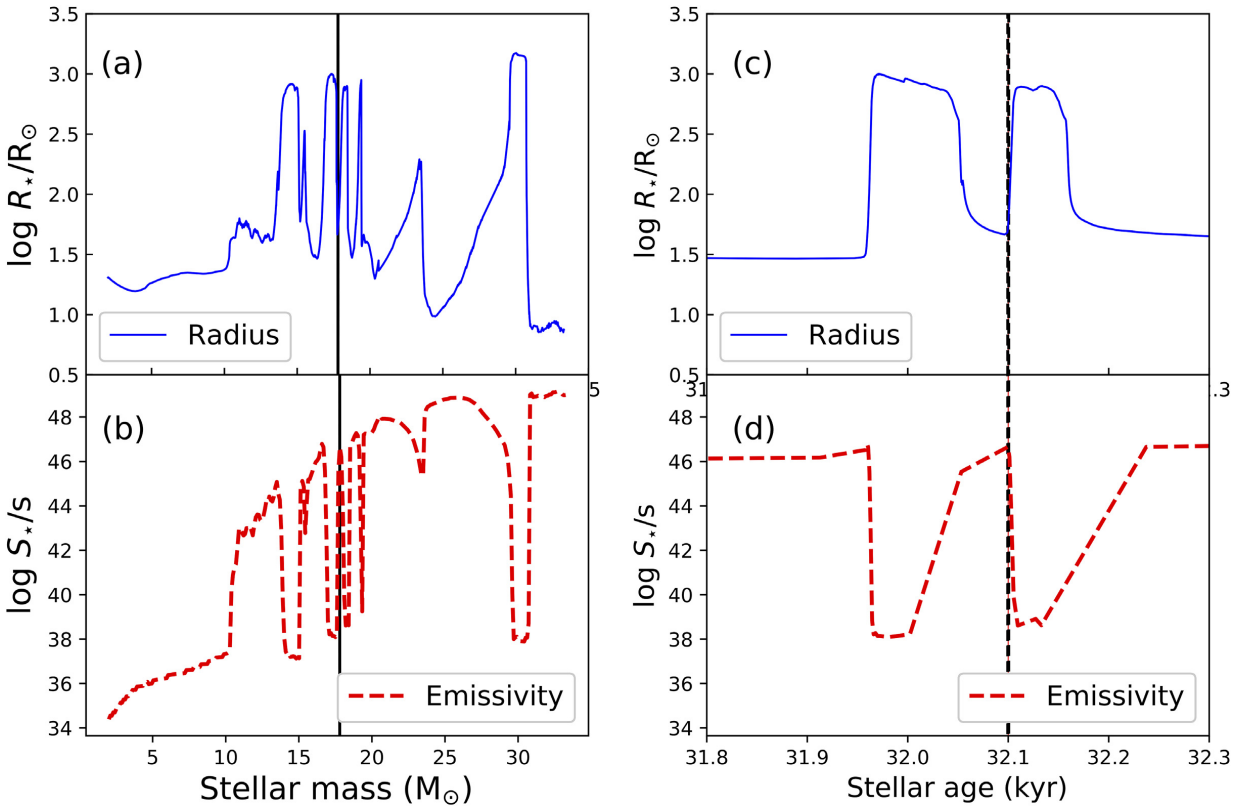

Figure 13. Correlation between the evolution of the protostellar radius and the number of surface UV ionizing photons $S_\star$ in our model Run-100-hydro. The protostellar radius and the emissivity is shown as a function of the mass of the MYSO (a, b) and as a function of the stellar age for two of its main bursts-producing excursions in the Herztsprung–Russel diagram (c, d). The vertical thick dashed black line marks the beginning of a bloating episod of the protostar. A similar figure illustrating the intermittency of the H II region of supermassive protostars can be found in Hosokawa et al. (2016).

Although these mechanisms are very different, they all consist in providing a manner to suddenly/episodically increase the accretion rate on to young stars. First, a cyclic magnetohydrodynamical instability in the inner ∼1 au of protoplanetary discs is proposed in Armitage, Livio & Pringle (2001). It is further demonstrated in Zhu, Hartmann & Gammie (2009) that the magnetorotational instability or the gravitational instability alone cannot be responsible for the radial mass transport over the overall disc and produce high fluctuations of the accretion rate on young protostars that is required for FU-Orionis bursts. However, these two instabilities can couple together in the innermost au of the disc and induce accretion variabilities compatible with the observed infrared spectra of FU-Orionis objects (Zhu et al. 2009). Secondly, a thermal ionization instability at the inner region of accretion discs around low-mass protostars has been proposed to explain episodic increases of the disc–star mass transfers associated with luminous flashes from ionized gas. This model has successfully been compared to the major observational characteristics of FU-Orionis objects (Clarke, Lin & Pringle 1990; Bell & Lin 1994; Bell et al. 1995). Additionally, the thermal viscous ionization instability scenario has been extended to a wider mechanism, which assumes that it naturally develops away from the disc edge by the presence of an embedded planet (Lodato & Clarke 2004). Similarly, instable mass transfers in a binary system modelled with Lagrangian methods gave accretion rate and luminosity rises consistent with that of FU-Orionis protostars (Bonnell & Bastien 1992). Last, the infall clumpiness scenario consists in assuming than the dense material which falls on to the young stars is directly formed by gas from converging, clumpy filamentary flows in the collapsing turbulent molecular clouds in which stellar clusters form (Padoan, Haugbølle & Nordlund 2014). Such gravitoturbulent, large-scale models do not resolve small-scale structures as accretion discs and spot the forming stars with sink particles (Federrath et al. 2010), however, it gives results consistent with the disc fragmentation scenario (Vorobyov & Basu 2005, 2015).

These alternative mechanisms can all explain the production of flares from young stellar objects, with or without the presence of an accretion disc around them, and they potentially can be applied to the high-mass regime of star formation. The strong ionization feedback of MYSOs (Vaidya et al. 2011), the efficient gravitational instability in their surrounding discs (Meyer et al. 2018b), and the possible therein magnetorotational instability (Kratter, Matzner & Krumholz 2008) make the model of Armitage et al. (2001) and Zhu et al. (2009) applicable in the context of massive protostars. The thermal viscous ionization instability scenario is conceivable in objects such as the high-mass proto-binary IRAS17216–3801 (Kraus

et al. 2017) and the infall clumpiness scenario applicable to regions such as the massive collapsing and high-mass star-forming filament IRDC 18223 (Beuther et al. 2015).

6 CONCLUSION

Our study explores for the first time the effects of a strongly variable protostellar accretion rate history, including strong accretion-driven luminosity bursts (Meyer et al. 2017), on the internal structure and evolutionary path of pre-main-sequence, MYSOs. We model growing massive protostars by performing three-dimensional gravitoradiation-hydrodynamics simulations of the formation and evolution of their circumstellar discs, unstable to gravitational instability, from which the protostars gain mass (Meyer et al. 2018b). Direct stellar irradiation feedback and appropriate disc thermodynamics are taken into account, in addition to a sub-astronomical unit spatial resolution of the inner region of the self-gravitating circumstellar discs. Gaseous clumps produced in the fragmented discs episodically migrate towards the protostar and produce brief, but violent increases of the accretion rate on to the MYSOs, subsequently responsible for luminous outbursts via the mechanism described in Meyer et al. (2017). We post-process our accretion rate histories by using them as inputs when feeding a stellar evolutionary code including the physics of pre-main-sequence disc accretion at high rates ($\geq 10^{-3}\,\mathrm{M_\odot\,yr^{-1}}$) within the so-called *cold accretion* formalism (Hosokawa & Omukai 2009; Hosokawa et al. 2010; Haemmerlé et al. 2016, 2017). The internal and surface stellar properties are self-consistently calculated, together with the evolutionary track of the protostars in the Hertzsprung–Russell. Our models differ by the initial mass of the collapsing pre-stellar cores, taken to be 60 and 100 $\mathrm{M_\odot}$, respectively.

The protostars are initially fully convective and highly opaque, but soon develop a radiative core. At the outer boundary of the radiative core the internal luminosity peaks and moves outwards to the surface as a luminosity wave following the decrease of the internal opacity (Larson 1972). At the moment of the strong increase of the accretion rate ($\geq 10^{-2}\,\mathrm{M_\odot\,yr^{-1}}$), the MYSOs bloat as a consequence of the redistribution of entropy, thus reestablishing the internal thermal equilibrium. The photospheric luminosity first sharply augments as a response of the increase of the accretion rate, before gradually decreasing up to recovering its quiescent, pre-burst value. In addition to the swelling of the stellar radius that accompanies the burst, the effective temperature decreases during the bursts. This found decrease in the effective temperature is in stark contrast to what was found for low-mass stars (Vorobyov et al. 2017). In the latter case, the effective temperature increases and the protostars migrate to the left portion of the Hertzsprung–Russell diagram. Our models recover the principal feature of the protostars accreting at rates $\geq 10^{-2}\,\mathrm{M_\odot\,yr^{-1}}$ extensively studied in Hosokawa et al. (2010) and Haemmerlé et al. (2016), i.e. their evolutionary track reach the forbidden Hayashi region. The decrease of the accretion rate which follows each accretion spike brings back the evolutionary track of our massive protostars to the standard ZAMS (Ekström et al. 2012), as previously calculated in the models of Kuiper & Yorke (2013). Importantly, this phenomenon is qualitatively independent of the choice of the initial stellar radius considered in the stellar evolution calculations. Our simulations with accretion histories derived from three-dimensional simulations show that this mechanism is repetitive. Consequently, while gradually gaining mass, the protostellar radius episodically swells and the MYSOs experience multiple pre-main-sequence spectroscopic excursions towards the colder regions of the Hertzsprung–Russell diagram. Each additional evolutionary loop to the red corresponds to an ongoing accretion burst inducing intermittent changes in the surface entropy of the protostar.

Our work demonstrates that the successive excursions of massive protostars in the Herztsprung–Russel are only possible during strong accretion bursts, and that mild disc-induced variability is insufficient to trigger them. Accretion bursts make MYSOs appear colder and much fainter than during their quiescent accretion phase, eventually crossing the luminous blue variable and yellow supergiant sectors of the Hertzsprung–Russell diagram to reach the red supergiants region, particularly if the initial pre-stellar core mass is sufficiently large ($\geq 100\,\mathrm{M_\odot}$). To each high-magnitude accretion burst (Meyer et al. 2018b) corresponds an excursion assuming that none of them produce a close/spectroscopic binary companion to the massive protostar (Chini et al. 2012; Mahy et al. 2013). The changes in the stellar structure cause a decrease the effective temperature while increasing the stellar radius, which greatly affects number of ionizing UV photons released by the MYSOs and induces intermittencies in their surrounding H II region, as was previously noticed in the context of primordial stars (Hosokawa et al. 2016). The present study highlights the scaled-up character of star-forming processes, as models for the evolution of brown dwarfs and low-mass stars also revealed excursions in the Herztsprung–Rusell as a response to strong variable disc accretion (Baraffe, Chabrier & Gallardo 2009; Baraffe et al. 2017; Vorobyov et al. 2017). Finally, we conjecture that such mechanism should equivalently affect star formation in the intermediate-mass regime and constitute a typical feature of hot, UV-feedback producing young stars.

ACKNOWLEDGEMENTS

The authors thank the anonymous referee for useful advice and suggestions that greatly improved the manuscript. DM-AM thanks N. Castro-Ramirez for kindly sharing his knowledge on observational data and B. Stecklum for insightful remarks. This work was sponsored by the Swiss National Science Foundation (project number 200020–172505). EIV acknowledges support from the Russian Ministry of Education and Science grant 3.5602.2017.

REFERENCES

Adams F. C., Ruden S. P., Shu F. H., 1989, ApJ, 347, 959
Arcos C., Kanaan S., Chávez J., Vanzi L., Araya I., Curé M., 2018, MNRAS, 474, 5287
Armitage P. J., Livio M., Pringle J. E., 2001, MNRAS, 324, 705
Asplund M., Grevesse N., Sauval A. J., 2005, in Barnes T. G., III, Bash F. N., eds, ASP Conf. Ser. Vol. 336, Cosmic Abundances as Records of Stellar Evolution and Nucleosynthesis. The Solar Chemical Composition. Astron. Soc. Pac., San Francisco, p. 25
Banerjee R., Pudritz R. E., Anderson D. W., 2006, MNRAS, 373, 1091
Baraffe I., Chabrier G., Gallardo J., 2009, ApJ, 702, L27
Baraffe I., Elbakyan V. G., Vorobyov E. I., Chabrier G., 2017, A&A, 597, A19
Beech M., Mitalas R., 1994, ApJS, 95, 517
Behrend R., Maeder A., 2001, A&A, 373, 190
Bell K. R., Lin D. N. C., 1994, ApJ, 427, 987
Bell K. R., Lin D. N. C., Hartmann L. W., Kenyon S. J., 1995, ApJ, 444, 376
Bernasconi P. A., 1996, A&AS, 120, 57
Bernasconi P. A., Maeder A., 1996, A&A, 307, 829
Beuther H., Ragan S. E., Johnston K., Henning T., Hacar A., Kainulainen J. T., 2015, A&A, 584, A67
Bhandare A., Kuiper R., Henning T., Fendt C., Marleau G.-D., Kölligan A., 2018, A&A, 618, A95

Bitsch B., Morbidelli A., Lega E., Crida A., 2014, A&A, 564, A135
Black D. C., Bodenheimer P., 1975, ApJ, 199, 619
Bonnell I., Bastien P., 1992, ApJ, 401, L31
Bonnell I. A., Bate M. R., Zinnecker H., 1998, MNRAS, 298, 93
Brown G. M., Johnston K. G., Hoare M. G., Lumsden S. L., 2016, MNRAS, 463, 2839
Burns R. A. et al., 2017, MNRAS, 467, 2367
Burns R. A. et al., 2018, preprint (arXiv:e-prints:1812.09454)
Butler M. J., Tan J. C., 2012, ApJ, 754, 5
Butler M. J., Tan J. C., Kainulainen J., 2014, ApJ, 782, L30
Caratti o Garatti A. et al., 2016, Nature Physics, Nature Publishing Group, p. 1745
Caratti o Garatti A., Stecklum B., Linz H., Garcia Lopez R., Sanna A., 2015, A&A, 573, A82
Cesaroni R. et al., 2018, A&A, 612, A103
Cesaroni R., Galli D., Lodato G., Walmsley M., Zhang Q., 2006, Nature, 444, 703
Cesaroni R., Hofner P., Araya E., Kurtz S., 2010, A&A, 509, A50
Chen X., Ren Z., Zhang Q., Shen Z., Qiu K., 2017, ApJ, 835, 227
Chini R., Hoffmeister V. H., Nasseri A., Stahl O., Zinnecker H., 2012, MNRAS, 424, 1925
Cieza L. A. et al., 2018, MNRAS, 474, 4347
Clarke C. J., Lin D. N. C., Pringle J. E., 1990, MNRAS, 242, 439
Commerçon B., Teyssier R., Audit E., Hennebelle P., Chabrier G., 2011, A&A, 529, A35
Cunha K., Hubeny I., Lanz T., 2006, ApJ, 647, L143
Cunningham N. J., Moeckel N., Bally J., 2009, ApJ, 692, 943
de Jager C., 1998, A&A Rev., 8, 145
Eggenberger P., Meynet G., Maeder A., Hirschi R., Charbonnel C., Talon S., Ekström S., 2008, Ap&SS, 316, 43
Ekström S. et al., 2012, A&A, 537, A146
Federrath C., Banerjee R., Clark P. C., Klessen R. S., 2010, ApJ, 713, 269
Flock M., Fromang S., González M., Commerçon B., 2013, A&A, 560, A43
Fontani F., Palau A., Busquet G., Isella A., Estalella R., Sanchez-Monge Á., Caselli P., Zhang Q., 2012, MNRAS, 423, 1691
Forgan D. H., Ilee J. D., Cyganowski C. J., Brogan C. L., Hunter T. R., 2016, MNRAS, 463, 957
Fossati L. et al., 2015, A&A, 582, A45
Fossati L. et al., 2016, A&A, 592, A84
Fuente A., Neri R., Martín-Pintado J., Bachiller R., Rodríguez-Franco A., Palla F., 2001, A&A, 366, 873
Fujisawa K., Yonekura Y., Sugiyama K., Horiuchi H., Hayashi T., Hachisuka K., Matsumoto N., Niinuma K., 2015, Astron. Tel., 8286
Ginsburg A., Bally J., Goddi C., Plambeck R., Wright M., 2018, ApJ, 860, 119
Groh J. H., Meynet G., Georgy C., Ekström S., 2013, A&A, 558, A131
Haemmerlé L., 2014, PhD thesis, University of Geneva
Haemmerlé L., Peters T., 2016, MNRAS, 458, 3299
Haemmerlé L., Eggenberger P., Meynet G., Maeder A., Charbonnel C., 2016, A&A, 585, A65
Haemmerlé L., Eggenberger P., Meynet G., Maeder A., Charbonnel C., Klessen R. S., 2017, A&A, 602, A17
Harries T. J., 2015, MNRAS, 448, 3156
Harries T. J., Douglas T. A., Ali A., 2017, MNRAS, 471, 4111
Hirano S., Hosokawa T., Yoshida N., Kuiper R., 2017, Science, 357, 1375
Hosokawa T., Omukai K., 2009, ApJ, 691, 823
Hosokawa T., Yorke H. W., Omukai K., 2010, ApJ, 721, 478
Hosokawa T., Offner S. S. R., Krumholz M. R., 2011, ApJ, 738, 140
Hosokawa T., Hirano S., Kuiper R., Yorke H. W., Omukai K., Yoshida N., 2016, ApJ, 824, 119
Hunter T. R. et al., 2017, ApJ, 837, L29
Ilee J. D., Cyganowski C. J., Nazari P., Hunter T. R., Brogan C. L., Forgan D. H., Zhang Q., 2016, MNRAS, 462, 4386
Johnston K. G. et al., 2015, ApJ, 813, L19
Kee N. D., Owocki S., Kuiper R., 2018, MNRAS, 479, 4633
Kessel O., Yorke H. W., Richling S., 1998, A&A, 337, 832
Keto E., Wood K., 2006, ApJ, 637, 850
Klassen M., Pudritz R. E., Kuiper R., Peters T., Banerjee R., 2016, ApJ, 823, 28
Kolb S. M., Stute M., Kley W., Mignone A., 2013, A&A, 559, A80
Kratter K., Lodato G., 2016, ARA&A, 54, 271
Kratter K. M., Matzner C. D., 2006, MNRAS, 373, 1563
Kratter K. M., Matzner C. D., Krumholz M. R., 2008, ApJ, 681, 375
Kraus S. et al., 2017, ApJ, 835, L5
Krumholz M. R., Klein R. I., McKee C. F., 2007, ApJ, 656, 959
Krumholz M. R., Klein R. I., McKee C. F., Offner S. S. R., Cunningham A. J., 2009, Science, 323, 754
Kuiper R., Yorke H. W., 2013, ApJ, 772, 61
Larson R. B., 1969, MNRAS, 145, 271
Larson R. B., 1972, MNRAS, 157, 121
Levesque E. M., Massey P., Olsen K. A. G., Plez B., Josselin E., Maeder A., Meynet G., 2005, ApJ, 628, 973
Lodato G., Clarke C. J., 2004, MNRAS, 353, 841
Lumsden S. L., Wheelwright H. E., Hoare M. G., Oudmaijer R. D., Drew J. E., 2012, MNRAS, 424, 1088
Machida M. N., Matsumoto T., 2011, MNRAS, 413, 2767
Mahy L., Rauw G., De Becker M., Eenens P., Flores C. A., 2013, A&A, 550, A27
Maud L. T., Hoare M. G., Galván-Madrid R., Zhang Q., de Wit W. J., Keto E., Johnston K. G., Pineda J. E., 2017, MNRAS, 467, L120
Menu J., van Boekel R., Henning T., Leinert C., Waelkens C., Waters L. B. F. M., 2015, A&A, 581, A107
Meyer D. M.-A., Vorobyov E. I., Kuiper R., Kley W., 2017, MNRAS, 464, L90
Meyer D. M.-A., Vorobyov E. I., Elbakyan V. G., Stecklum B., Eislöffel J., Sobolev A. M., 2018a, MNRAS, 482, 5459
Meyer D. M.-A., Kuiper R., Kley W., Johnston K. G., Vorobyov E., 2018b, MNRAS, 473, 3615
Mignone A., Bodo G., Massaglia S., Matsakos T., Tesileanu O., Zanni C., Ferrari A., 2007, ApJS, 170, 228
Mignone A., Zanni C., Tzeferacos P., van Straalen B., Colella P., Bodo G., 2012, ApJS, 198, 7
Moscadelli L. et al., 2017, A&A, 600, L8
Nayakshin S., Lodato G., 2012, MNRAS, 426, 70
Nikoghosyan E. H., Azatyan N. M., Khachatryan K. G., 2017, A&A, 603, A26
Norberg P., Maeder A., 2000, A&A, 359, 1025
Padoan P., Haugbølle T., Nordlund Å., 2014, ApJ, 797, 32
Palla F., Stahler S. W., 1991, ApJ, 375, 288
Palla F., Stahler S. W., 1992, ApJ, 392, 667
Palla F., Stahler S. W., 1993, ApJ, 418, 414
Peters T., Banerjee R., Klessen R. S., Mac Low M.-M., Galván-Madrid R., Keto E. R., 2010, ApJ, 711, 1017
Peters T., Klessen R. S., Mac Low M.-M., Banerjee R., 2010, ApJ, 725, 134
Purser S. J. D. et al., 2016, MNRAS, 460, 1039
Purser S. J. D., Lumsden S. L., Hoare M. G., Cunningham N., 2018, MNRAS, 475, 2
Regály Z., Vorobyov E., 2017, A&A, 601, A24
Reiter M., Kiminki M. M., Smith N., Bally J., 2017, MNRAS, 470, 4671
Romanova M. M., Ustyugova G. V., Koldoba A. V., Lovelace R. V. E., 2012, MNRAS, 421, 63
Rosen A. L., Krumholz M. R., McKee C. F., Klein R. I., 2016, MNRAS, 463, 2553
Samal M. R., Chen W.-P., Takami M., Jose J., Froebrich D., 2018, MNRAS, 477, 4577
Sanna A. et al., 2018, preprint (arXiv:e-prints:1805.09842)
Seifried D., Banerjee R., Klessen R. S., Duffin D., Pudritz R. E., 2011, MNRAS, 417, 1054
Shu F. H., 1977, ApJ, 214, 488
Stecklum B., Caratti o Garatti A., Cardenas M. C., Greiner J., Kruehler T., Klose S., Eisloeffel J., 2016, Astron. Tel., 8732
Stecklum B., Heese S., Wolf S., Garatti A. C. o., Ibanez J. M., Linz H., 2017, preprint (arXiv:e-prints:1712.01451)

Stecklum B., Caratti o Garatti A., Hodapp K., Linz H., Moscadelli L., Sanna A., 2018, in Tarchi A., Reid M. J., Castangia P., eds, Proc. IAU Symp. Vol. 336, Astrophysical Masers: Unlocking the Mysteries of the Universe. International Astronomical Union, p. 37
Tanaka K. E. I., Tan J. C., Zhang Y., Hosokawa T., 2018, ApJ, 861, 68
Testi L., 2003, in De Buizer J. M., van der Bliek N. S., eds, ASP Conf. Ser. Vol. 287, Galactic Star Formation Across the Stellar Mass Spectrum. Intermediate Mass Stars (Invited Review), Astron. Soc. Pac., San Francisco,p. 163
Torrelles J. M. et al., 2014, MNRAS, 442, 148
Vaidya B., Fendt C., Beuther H., Porth O., 2011, ApJ, 742, 56
Vaytet N., Haugbølle T., 2017, A&A, 598, A116
Vorobyov E. I., 2009, ApJ, 704, 715
Vorobyov E. I., Basu S., 2005, ApJ, 633, L137
Vorobyov E. I., Basu S., 2010, ApJ, 719, 1896
Vorobyov E. I., Basu S., 2015, ApJ, 805, 115
Vorobyov E. I., Elbakyan V., 2018, A&A, 618, A7
Vorobyov E. I., Elbakyan V., Dunham M. M., Guedel M., 2017, A&A, 600, A36
Vorobyov E. I., Elbakyan V., Hosokawa T., Sakurai Y., Guedel M., Yorke H., 2017, A&A, 605, A77
Yorke H. W., Sonnhalter C., 2002, ApJ, 569, 846
Zakhozhay O. V., Miroshnichenko A. S., Kuratov K. S., Zakhozhay V. A., Khokhlov S. A., Zharikov S. V., Manset N., 2018, MNRAS, 477, 977
Zhao B., Caselli P., Li Z.-Y., Krasnopolsky R., 2018, MNRAS, 473, 4868
Zhu Z., Hartmann L., Gammie C., McKinney J. C., 2009, ApJ, 701, 620
Zhu Z., Hartmann L., Gammie C., 2009, ApJ, 694, 1045

This paper has been typeset from a TEX/LATEX file prepared by the author.

Monthly Notices
of the
ROYAL ASTRONOMICAL SOCIETY

MNRAS **487,** 4473–4491 (2019)
Advance Access publication 2019 June 10

doi:10.1093/mnras/stz1585

On the ALMA observability of nascent massive multiple systems formed by gravitational instability

D. M.-A. Meyer [1,2]★ A. Kreplin,[2] S. Kraus,[2] E. I. Vorobyov,[3,4] L. Haemmerle[5] and J. Eislöffel[6]

[1]*Astrophysics Group, School of Physics and Astronomy, University of Exeter, Exeter EX4 4QL, UK*
[2]*Institute of Physics and Astronomy, University of Potsdam, D-14476, Potsdam, Germany*
[3]*Research Institute of Physics, Southern Federal University, Stachki 194, Rostov-on-Don, 344090, Russia*
[4]*Department of Astrophysics, The University of Vienna, Vienna, A-1180, Austria*
[5]*Observatoire de Genéve, Université de Genéve, chemin des Maillettes 51, CH-1290 Sauverny, Switzerland*
[6]*Thüringer Landessternwarte Tautenburg, Sternwarte 5, D-07778 Tautenburg, Germany*

Accepted 2019 June 5. Received 2019 June 5; in original form 2019 March 20

ABSTRACT

Massive young stellar objects (MYSOs) form during the collapse of high-mass pre-stellar cores, where infalling molecular material is accreted through a centrifugally balanced accretion disc that is subject to efficient gravitational instabilities. In the resulting fragmented accretion disc of the MYSO, gaseous clumps and low-mass stellar companions can form, which will influence the future evolution of massive protostars in the Hertzsprung–Russell diagram. We perform dust continuum radiative transfer calculations and compute synthetic images of disc structures modelled by the gravito-radiation-hydrodynamics simulation of a forming MYSO, in order to investigate the *Atacama Large Millimeter/submillimeter Array* (ALMA) observability of circumstellar gaseous clumps and forming multiple systems. Both spiral arms and gaseous clumps located at $\simeq$ a few 100 au from the protostar can be resolved by interferometric ALMA Cycle 7 C43-8 and C43-10 observations at band 6 (1.2 mm), using a maximal 0.015 aracsec beam angular resolution and at least 10–30 min exposure time for sources at distances of 1–2 kpc. Our study shows that substructures are observable regardless of their viewing geometry or can be inferred in the case of an edge-viewed disc. The observation probability of the clumps increases with the gradually increasing efficiency of gravitational instability at work as the disc evolves. As a consequence, large discs around MYSOs close to the zero-age-main-sequence line exhibit more substructures than at the end of the gravitational collapse. Our results motivate further observational campaigns devoted to the close surroundings of the massive protostars S255IR-NIRS3 and NGC 6334I-MM1, whose recent outbursts are a probable signature of disc fragmentation and accretion variability.

Key words: radiative transfer – methods: numerical – stars: circumstellar matter.

1 INTRODUCTION

Multiplicity is an indissociable characteristic of massive star evolution. Observational studies of OB stars indicate that multiplicity is an intrinsic feature, which strongly influences the evolution of massive stars in the Hertzsprung–Russell diagram (Sana et al. 2012). A wide dispersion of the semimajor axis in hierarchical massive stellar systems, which span a range from a small fraction of au for close/spectroscopic companions (Chini et al. 2012; Mahy et al. 2013; Kobulnicky et al. 2014) to up to a few 100 au in the context of massive proto-binaries (Kraus et al. 2017), asks the puzzling question of their formation channel. This must be prior to the launching of the strong stellar winds at the zero-age-main-sequence (ZAMS), which dissipate the disc and therefore limit the companion formation time-scale (Vink, de Koter & Lamers 2000). On the one hand, investigations of the gravitational capture scenario of stellar systems with *N*-body simulations failed in explaining this high occurence of the small separations observed in spectroscopic companions to massive stars (Fujii & Portegies Zwart 2011). On the other hand, the disc fragmentation approach by means of multidimensional hydrodynamics simulations coupled to Lagrangian sink particles that spot secondary star formation in self-gravitating accretion discs suffers from the dramatic qualitative

★ E-mail: dmameyer.astro@gmail.com

algorithm-dependence of the results (Klassen et al. 2016). Therefore, understanding the early formation mechanism of hierarchical multiple systems around massive stars by confronting numerical models to observations is of prime interests in the study of the pre-ZAMS (Zinnecker & Yorke 2007) but also the pre-supernovae evolution of massive stars (Langer 2012).

State-of-the-art numerical models of the formation of MYSOs predicted the existence of an accretion disc connected with bipolar cavities filled by ionized stellar wind and outflow material (Seifried et al. 2011; Harries 2015; Harries, Douglas & Ali 2017). The recent gravito-radiation-hydrodynamical simulations of the formation of massive protostars in Meyer et al. (2017) and Meyer et al. (2018) showed that it is possible to obtain self-consistent solutions for multiplicity in the high-mass regime of star formation without using artificial sink particles, as long as the spatial resolution of the inner disc region is sufficiently high. Those high-resolution simulations of $\simeq$100 $M_\odot$ collapsing pre-stellar cores also demonstrate that even irradiated, massive, self-gravitating accretion discs around massive young objects are subject to gravitational fragmentation and generate dense spiral arms in which gaseous clumps form. These clumps can contract further and reach the molecular hydrogen dissociation temperature while migrating inward on to the central forming massive object. The migrating clump can experience a second collapse and become low-mass stars, progenitors of the future companions and/or close (spectroscopic) companions to the massive stars.

The series of studies of Meyer et al. (2017) and Meyer et al. (2018) provides a self-consistent picture unifying disc fragmentation and binary formation in the context of massive young stellar objects (MYSOs). The model also predicts that a fraction of the migrating gaseous clump material can directly fall on to the protostellar surface and produce accretion-driven outbursts as monitored in the MYSOs S255IR-NIRS3 and NGC 6334I-MM1. In this picture, accretion bursts are a signature of the presence of a self-gravitating disc in which efficient gravitational instability occurs. The bursts happen in a series of multiple eruptions, whose intensity scales with the quantity of accreted material (Meyer et al. 2019). These episodic events generate modifications in the internal protostellar structure leading to excursions in the Hertzsprung–Russel diagram (Meyer, Haemmerlé & Vorobyov 2019). Note that this burst mode of massive star formation has an scaled-up equivalent in the low-mass regime, as outlined in a series of papers of Vorobyov & Basu (2010), Vorobyov, DeSouza & Basu (2013), Dong et al. (2016), and Elbakyan et al. (2019), as well as in the primordial mass regime of star formation (see Greif et al. 2012 and Vorobyov et al. 2013). The remaining question is, therefore, whether such self-gravitating effects can be directly observed and what we can learn from the disc density structure about the high-mass star formation process.

Searching for the direct observational signatures of clumpy structures in massive star-forming regions is a very active field, as modern facilities are now able to probe the highly-opaque pre-stellar cores in which MYSOs grow. The last decade saw the report of observations of variabilities in the accretion flow on to massive protostars (Keto & Wood 2006; Stecklum et al. 2017) and in the pulsed bipolar outflows that release ionized gas (Cunningham, Moeckel & Bally 2009; Cesaroni et al. 2010; Caratti o Garatti et al. 2015; Purser et al. 2016; Burns et al. 2017; Reiter et al. 2017; Burns 2018; Purser et al. 2018; Samal et al. 2018), together with proofs of disc–jet associations such as G023.01–00.41 (Sanna et al. 2018). Direct observation of Keplerian discs around MYSOs (Johnston et al. 2015; Forgan et al. 2016; Ilee et al. 2016; Ginsburg et al. 2018; Maud et al. 2018) and evidence of filamentary spirals feeding the candidate disc W33A MM1-Main (Maud et al. 2017) and of infalling clumps in the systems G350.69–0.49 (Chen et al. 2017) and G11.92–0.61 MM1 (Ilee et al. 2018) revealed the existence of substructures in discs that are similar to those modelled in Meyer et al. (2018). Furthermore, the investigations for molecular emission from collapsing clouds and from the close surroundings of high-mass protostars confirm the possibility of fragmentation and the presence of inhomogeneities in their discs (Ahmadi et al. 2018; Beuther et al. 2019), without excluding the possibility of magnetic self-regulation of the inner disc fragmentation (Beuther et al. 2018) as predicted by analytic and numerical studies (Hennebelle et al. 2016).

This study aims at testing the observability of the overdensities and various substructures such as spiral arms and gaseous clumps that are predicted by Meyer et al. (2017) and Meyer et al. (2018). We adopt the standard approach of radiative transfer calculations against dust opacities, performed on the basis of the accretion disc density and temperature fields from numerical simulations of Meyer et al. (2018) and further post-processed in order to obtain synthetic interferometric *Atacama Large Millimeter/submillimeter Array* (ALMA) band 6 (1.2 mm) images. This corresponds to the typical waveband at which the surroundings of MYSOs are observed, as it offers a good compromise between high spatial resolution and phase calibration problems occurring at longer interferometric baselines. This approach has been adopted to predict the observability of gravitational instabilities in discs around low-mass stars (Vorobyov, Zakhozhay & Dunham 2013; Dong et al. 2016; Seifried et al. 2016). Only very few similar studies have been conducted in the context of high-mass stars, either using artificial sink particles as tracers of multiplicity in the disc (Krumholz, Klein & McKee 2007) or on the basis of simplistic, analytic disc models (Jankovic et al. 2019). Our synthetic images predict what disc morphologies should be observable with ALMA and constitute prognostications that are directly comparable with future high angular resolution observations campaigns.

Our work is organized as follows. In Section 2, we review the methods used to perform numerical hydrodynamical simulations, radiation transfer calculations and to compute synthetic images of the fragmented circumstellar medium of a massive protostar. In Section 3, we present our results as a series of synthetic images of accretion discs one should expect to observe with ALMA in the surroundings of forming MYSOs. We consider several viewing angles of the objects with respect to the plane of the sky. Our synthetic images are further discussed in Section 4. Finally, we provide our conclusions in Section 5.

2 METHOD

In the following paragraphs, we remind the reader about the numerical methods used to carry out our hydrodynamics disc models. The structure and accretion properties of the discs are extracted from the simulation of the collapse of a solid-body-rotating pre-stellar core that produces a central, single MYSO (Meyer et al. 2018). The accretion history on to the MYSO is used to feed a stellar evolution code, in order to self-consistently derive its protostellar surface properties. Then, we present the radiation transfer methods utilized to produce dust continuum millimeter images of the discs, by post-processing the density and temperature fields of the hydrodynamical circumstellar disc model. Finally, we review our method for retrieving synthetic ALMA images, allowing us to transform the radiation transfer calculations into realistic

ALMA synthetic observations and to discuss the observability of the clumps in the disc as a function of, e.g. the protostellar formation phases.

2.1 Hydrodynamical simulations

This study focuses on the high-resolution gravito-radiation-hydrodynamics simulation Run-1-hr of Meyer et al. (2018). It is a numerical model of the gravitational collapse of a $100\,M_\odot$ solid-body-rotating cold pre-stellar core of uniform initial temperature $T_c = 10\,K$ and of density distribution $\rho(r) \propto r^{-3/2}$, with r the radial coordinate. The initial ratio of kinetic-by-gravitational energy of the pre-stellar core was set to $\beta = 4$ per cent. The spherical midplane-symmetric computational domain on to which the run has been performed has an inner radius $r_{in} = 10\,au$ and an outer radius $R_c = 0.1\,pc$, respectively. A grid maps the domain $[r_{in}, R_c] \times [0, \pi/2] \times [0, 2\pi]$ with $N_r = 256 \times N_\phi = 41 \times N_\theta = 256$ grid cells, expanding logarithmically along the radial direction r, going as a cosine in the polar direction ϕ and uniformly spaced along the azimuthal direction θ. The inner hole is a semipermeable sink cell attached on to the origin of the domain whereas outflow boundary conditions are assigned to the outer radius. Therefore, the material $\dot{M}$ that is lost through the sink cell allows us to calculate the accretion rate on to the protostar, while the protostellar properties such as its stellar radius and its photospheric luminosity are time-dependently estimated using the pre-calculated protostellar evolutionary tracks of Hosokawa & Omukai (2009). Because of time-step restrictions due to the high resolution of the grid, we computed the collapse of the core together with the initial formation phase of the circumstellar disc of the protostar up to $t_{end} = 32.1\,kyr$.

We integrate the system by solving the equations of gravito-radiation-hydrodynamics with the PLUTO code[1] (Mignone et al. 2007, 2012), which has been modified to account for (i) the protostellar feedback and (ii) the self-gravity of the gas. The direct proto-stellar irradiation feedback of the central star as well as the inner disc radiative transport are taken into account using the grey approximation that has been adapted from the publicly available scheme of Kolb et al. (2013); see the method section of Meyer et al. (2018). This twofold algorithm intelligently ray-traces photon packages from the protostellar atmosphere and then diffuses their energy by flux-limited propagation into the accretion disc. However, this scheme allows us to accurately treat both the inner heating and the outer cooling of the irradiated disc surrounding our MYSO (Vaidya et al. 2011). We use a constant gas opacity of $0.01\,cm^2\,g^{-1}$ and the tabulated dust opacities of Laor & Draine (1993) in order to account for the attenuation of the radiation field. Gas and dust temperatures are calculated assuming the equilibrium between the temperature of the silicate dust grains and the total protostellar irradiation and disc radiation fields. Any turbulent viscosity is neglected in the computational domain and we assume that the most efficient mechanism for angular momentum transport are the gravitational torques generated in the self-gravitating accretion disc that surrounds the protostar. The gravity of the central star is taken into account by calculating its total gravitational potential and our simulations include the self-gravity of the circumstellar gas by directly solving the Poisson equation. Finally, we refer the reader who is interested in further details about the numerical method to Meyer et al. (2018).

[1] http://plutocode.ph.unito.it/

2.2 Stellar evolution calculations

The modelled accretion rate history is used as initial conditions to compute the evolutionary tracks in the Hertzsprung–Russel diagram of the corresponding episodically accreting massive protostar, following the method of Meyer et al. (2019). To this end, a one-dimensional stellar evolution calculation is carried out with the hydrostatic GENEC (i.e. GENEVA code) code (Eggenberger et al. 2008), which was updated with respect to disc accretion physics for the study of pre-main-sequence high-mass stars (Haemmerlé 2014; Haemmerlé et al. 2016). The accretion mechanism is therein treated within the so-called cold disc accretion approximation (Palla & Stahler 1992). The inner disc region is assumed to be geometrically thin as the accreted material falls on to the surface of the protostar and the implementation of Haemmerlé (2014) showed full consistency with the original results of Hosokawa, Yorke & Omukai (2010). Any entropy excess is immediately radiated away and the circumstellar material is advected inside the protostar, i.e. the simulation considers that the thermal properties of the inner edge of the disc are similar to those of the suface layer of the MYSOs. This approach is the lower limit on the entropy attained by the protostar throughout the accretion mechanism, the upper limit being the so-called spherical (or hot) accretion scenario (Hosokawa et al. 2010). The calculation of the stellar structure is performed with the Henyey method, using the Lagrangian formulation (Haemmerlé 2014) at solar metallicity ($Z = 0.014$) and making use of the abundances of Asplund, Grevesse & Sauval (2005) and Cunha, Hubeny & Lanz (2006), together with the deuterium mass fractions described in the studies of Norberg & Maeder (2000) and Behrend & Maeder (2001). The stellar structure calculation is started with a fully convective stellar embryo (Haemmerlé & Peters 2016) and make use of overshooting and of the Schwarzschild criterion in the treatment of the internal stellar convection. The outcomes of the calculation are evolution of $L_\odot$, $R_\star$, and T_{eff} as a function of time.

2.3 Radiative transfer calculations

A series of characteristic simulation snapshots is selected from the simulation Run-1-hr of Meyer et al. (2018) and they are post-processed by performing radiative transfer calculations against dust opacity with the code RADMC-3D[2] (Dullemond 2012). We make use of the Laor & Draine (1993) dust mixture based on silicates crystals. Hence, our simulated emission is calculated with the same dust opacity that was used in the gravito-radiation-hydrodynamical simulations. In our approach, RADMC-3D directly uses dust density and temperature fields imported from the PLUTO outputs and we do not perform any Monte Carlo simulation prior to the image building; see comparison of both methods in Section 4.1. The interface between the PLUTO and RADMC-3D codes is an interpolation between the above-described non-uniform mesh of PLUTO and the uniform spherically symmetric grid of RADMC-3D, which reconstructs the full three-dimensional structure of the disc taking into account the midplane-symmetry of the hydrodynamical models. The protostar is located at the origin of both grids and the RADMC-3D calculations is then effectuated concentrating on to the inner 1000–3000 au regions of the disc, such that the corresponding map has 2000×2000 cells along the horizontal and vertical directions of the sky plane, respectively.

The accretion discs are irradiated by packages of 5×10^6 photons ray-traced from the protostellar atmosphere of radius r_{in} to the outer

[2] http://www.ita.uni-heidelberg.de/dullemond/software/radmc-3d/

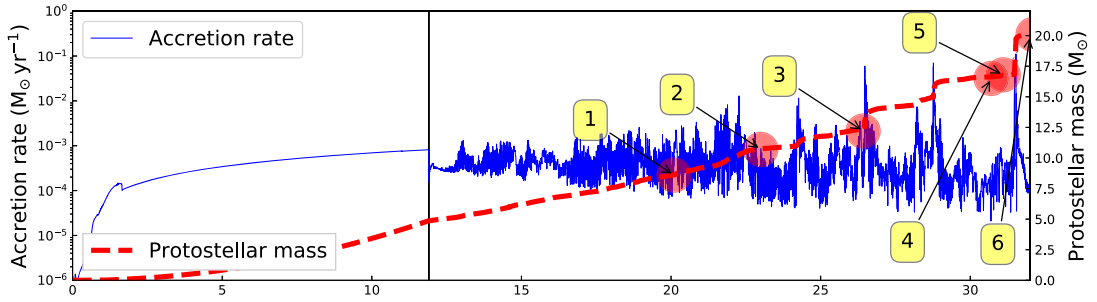

Figure 1. Protostellar accretion rate (thin solid blue line, in $M_\odot$ yr^{-1}) and protostellar mass (thick dashed line, in $M_\odot$) of model Run-1-hr in Meyer et al. (2018). The labelled red dot represents the six selected simulation snapshots for this study and the thin vertical line is the time instance of the disc formation.

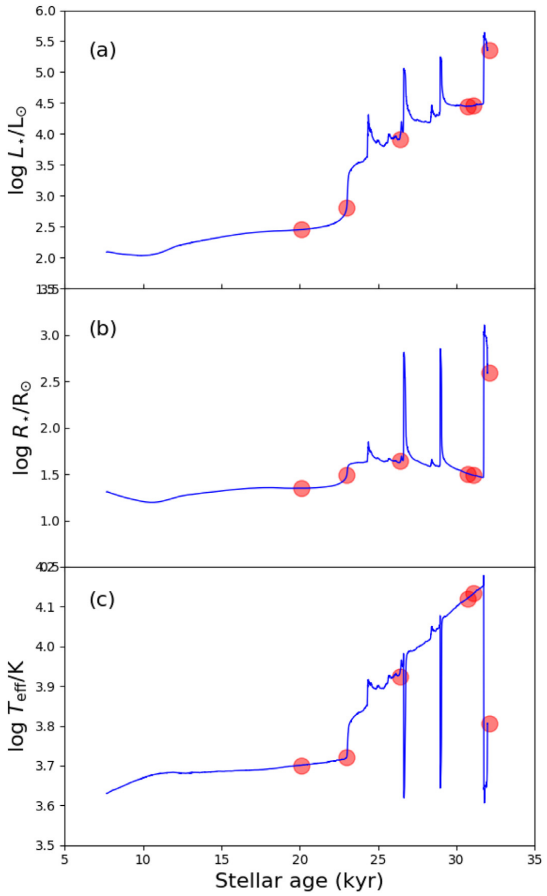

Figure 2. Evolution as a function of time (in kyr) of the stellar surface luminosity (a), stellar radius (b), and effective temperature (c) of our MYSOs experiencing variable disc accretion, episodically interspersed by strong accretion events responsible for luminous bursts. The protostellar properties of the different disc models are marked with red dots.

disc region, at a radius of a few 1000 au. The protostar is assumed to be a blackbody radiator of effective temperature $T_{\rm eff}$, bolometric luminosity $L_\star$, and stellar radius $R_\star$ with values taken from the outcomes of the stellar evolution calculation at the time of the selected snapshots. The radiative transfer calculations are performed within the anisotropic scattering approximation using the Henyey–Greenstein formula. For each of the selected simulation snapshots, we build 1.2 mm emission maps by projecting the emitted flux. This is the typical waveband at which observation campaigns for the study of accretion discs around MYSOs are currently conducted (see e.g. Maud et al. (2018), as this waveband offers a good compromise between high angular resolution and atmosphere phase stability. The distance between the source and the observer is set to 1.0 kpc, that is of the order of the distance to the closest massive star-forming regions such as Orion (0.41 kpc), Cep A (0.70 kpc), and VY CMa (1.14 kpc), see table 4 in Reid et al. (2009), as the angular resolution reached by ALMA when observing them is the highest possible. Additionally, we also investigate the observability of disc substructures for MYSOs located at a distance of 2.0 kpc which corresponds to further afield star-forming regions such as W3(OH); see Section 3.5. For each of the six selected simulation shapshots, we use the possibility of RADMC-3D to compute 1.2 mm synthetic images for three different system inclination angles, namely face-on ($\phi = 0^\circ$), intermediate inclination ($\phi = 45^\circ$), and edge-on ($\phi = 90^\circ$). The disc models and their emission properties are presented in detail in Section 3.

2.4 Synthetic observables

We further post-process the RADMC-3D radiation transfer calculations with the Common Astronomy Software Applications CASA[3] (McMullin et al. 2007) in order to obtain synthetic fluxes of the disc models as they would look like if seen by ALMA observations. The successive technical updates and enhancements of ALMA are labelled as 'Cycles' and to each of them corresponds a call for proposals followed by a series of observations. For each cycle, ALMA operates at different wavebands (the 'bands'). The one of interest in our study is band 6, corresponding to 1.2 mm (Brown, Wild & Cunningham 2004; Wootten & Thompson 2009). Observations are performed with a given spatial configuration of all the antennas constituting the ALMA interferometer. The more compact the configuration the larger the beam size probing the sky, while the more extended the antennas configuration the better the spatial resolution in the observed images. The antennas are available in two categories, distinguishable by the diameter of their parabola, i.e. 7 m and 12 m, respectively. The maximum number of 12 m-antenna that can be used simultaneously is 43. We are interested in the 12 m antenna arrays because these 43 antennas can be spread over a wider surface on the Llano de Chajnantor plateau, offering a larger maximal separation between two antennas (the maximum baseline) and hence a smaller beam size to probe the internal

[3] https://casa.nrao.edu/

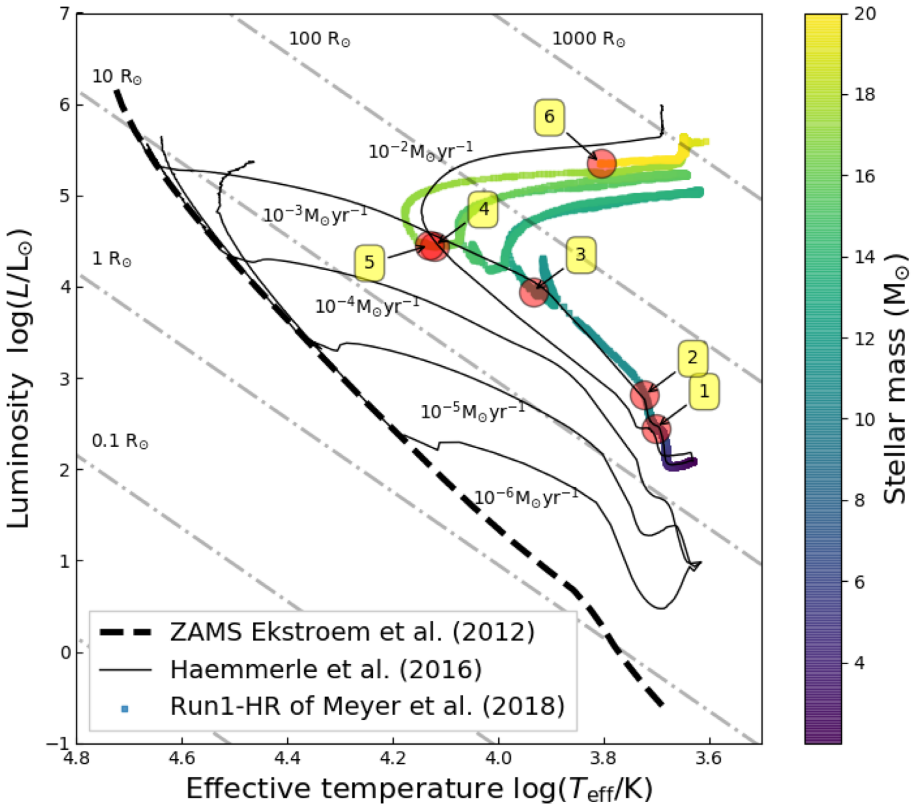

Figure 3. Comparison between the massive protostar in Run-1-hr (thick coloured line) of Meyer et al. (2018) and the evolutionary tracks for massive protostars accreting with constant rates (thin black lines) of Haemmerlé et al. (2016). The colour coding of our simulated track indicates the stellar mass (in $M_\odot$). Grey dashed-dotted lines are isoradius and the thick black dashed line is the zero-age-main-sequence (ZAMS) track of Ekström et al. (2012). The numbered red dots are the selected simulation snapshots from Meyer et al. (2018) that we consider in this study.

Table 1. Accretion disc models selected from Meyer et al. (2018). The table gives the simulation time (in kyr), protostellar mass (in $M_\odot$), the total protostellar luminosity, the protostellar radius and a brief description of the disc structure for each of the considered disc models.

Model	t (kyr)	$M_\star$ ($M_\odot$)	$L_\star$ ($L_\odot$)	$R_\star$ ($R_\odot$)	$T_{\rm eff}$ (K)	Description
1	20.1	8.6	283.0	22.3	5020.0	Young, stable disc
2	23.0	10.7	650.0	30.6	5275.0	Stable disc with first gravitational perturbation
3	26.4	12.1	8359.0	43.6	8374.0	Disc with spiral arms and migrating gaseous clump
4	30.7	16.6	27 973.0	32.0	13 210.0	Disc with multiple ring-like spiral arms hosting clumps
5	31.1	16.7	28 625.0	30.6	13 586.0	Strongly fragmenting disc with multiple clumps
6	32.1	20.0	226 454.0	389.0	6393.0	Extended strongly fragmented disc with filamentary spiral arms and clumps

structure of our accretion discs. The ALMA Cycle 7 offers ten 12 m antenna array configurations, labelled from 1 (most compact) to 10 (most extended). We perform synthetic images at two of the most extended configurations (8 and 10) of the 43 different 12 m-antenna, also called configurations C43-8 and C43-10. We therefore model images of our discs as ALMA Cycle 7 configuration 8 and 10 observations at band 6 (1.2 mm), respectively.

The RADMC-3D to CASA interface is effectuated via the RADMC3DPY python package available with the current distribution of RADMC-3D. It allows the user to directly output the radiative transfer calculations as standard FITS files, which header can be read by the CASA software. We make use the SIMALMA task of CASA with a central frequency of the combined continuum emission of 249.827 Ghz (1.2 mm, ALMA band 6) and a channelwidth of 50.0 Mhz. The different used long-baseline configurations result in angular resolutions of 0.029 arcsec (antenna configuration 8 with maximal baseline of 8.5 km) and 0.015″ (antenna configuration 10 with maximal baseline of 16.2 km), respectively. The observation integration time is chosen to be 600 s (10 min) of exposition time, as longer durations do not provide better images (see Section 4). The precipitable water vapor (pwv) parameter is chosen to be 0.5 mm, which represent the amount of pwv at the Llano de Chajnantor plateau in the Chilean Andes during 25 per cent of the time during which the ALMA is operated.

3 RESULTS

In this section, we begin by presenting the samples of the hydrodynamical simulation that we post-process to obtain synthetic 1.2 mm interferometric images of dust continuum emission. Then,

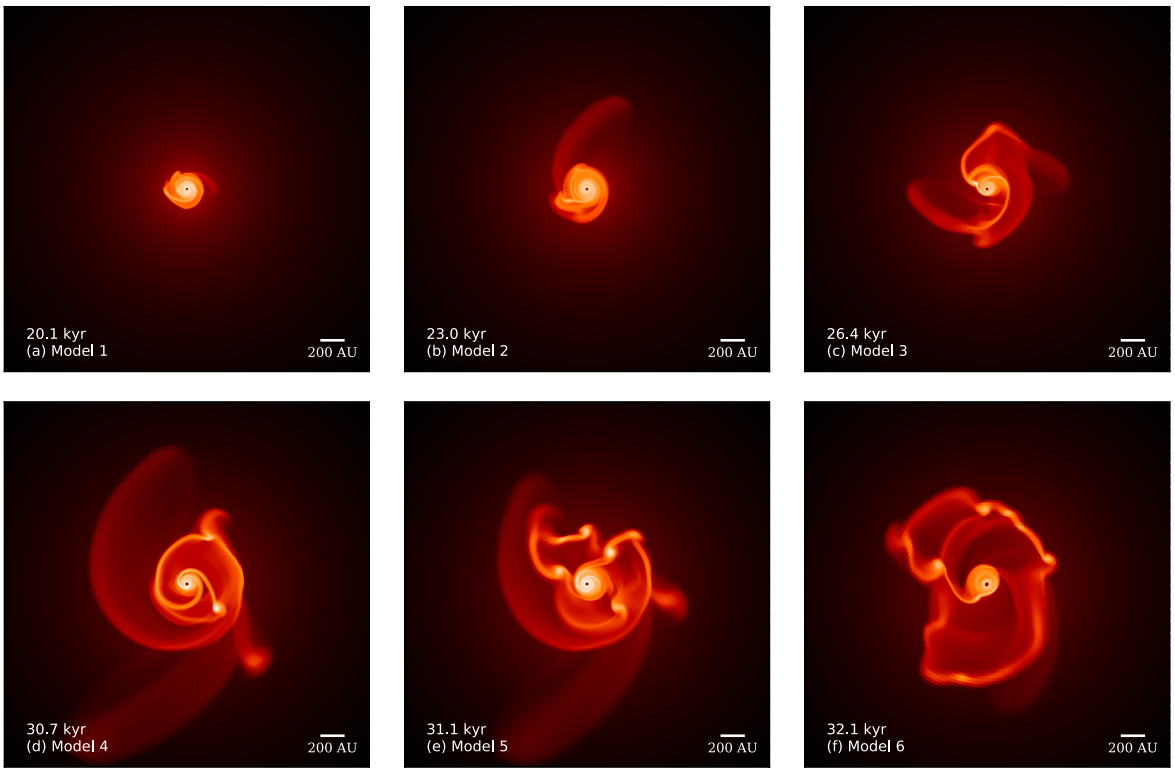

Figure 4. Rendering of the dust-rich, infrared-emitting regions in the structure of our accretion discs. The figures show the growing disc for different selected time instances throughout the hydrodynamical simulation and no inclination angle is assumed. Each image is plotted on the logarithmic scale, the most diluted part of the discs are in black colour, and the densest disc regions are in white colour, respectively.

we discuss the time effects due to the disc evolution and the effects of the disc inclination angle with respect to the plane of sky.

3.1 Hydrodynamical model and stellar properties

The simulation model Run1-hr of Meyer et al. (2018) begins with the gravitational collapse of 100 $M_\odot$ of pre-stellar rotating molecular material on to the stellar embryo. At the end of the free-fall collapse phase, the infalling material ends on a centrifugally-balanced disc, from which the gas is subsequently transferred to the growing protostar. Fig. 1 plots the accretion rate history on to the central massive protostar (solid blue line, in $M_\odot\,yr^{-1}$) together with the evolution of the protostellar mass (dashed red line, in $M_\odot$) that is calculated as the integrated disc-to-star mass transfer rate through the sink cell. The vertical thin black line indicates the onset of disc formation, when the free-fall collapse of the envelope material on to the protostar stops and the star begins to gain its mass exclusively via accretion from its surrounding disc. After the initial infall of material, the collapse of the parent pre-stellar core material generates an initial increase of the mass flux through the inner boundary at a time ≈2 kyr. The accretion rate then reaches the standard value predicted for MYSOs of $10^{-3}\,M_\odot\,yr^{-1}$ (Hosokawa & Omukai 2009) up to the onset of the disc formation happening at ≈12 kyr. Variabilities in the accretion flow begin right after the disc formation and the accretion rate history exhibit numerous peaks of growing intensity as the MYSO becomes heavier. This is not caused by different inner boundary conditions, but simply reflects the time-dependent azimuthal anisotropies induced in the accretion flow by the disc evolution. The efficient gravitational instabilities produce complex substructures in the disc, such as overdense spiral arms in which gaseous clumps of various morphologies form at radii of ∼100 au and inward-migrate down to the central protostar. This produces luminosity outbursts via the mechanism revealed in Meyer et al. (2017) for massive stars. These outbursts are responsible for step-like increases in the stellar mass evolution (see thick dotted red line) due to the fast accretion of dense circumstellar material inside the sink cell. A more detailed description of the evolution of circumstellar discs around young massive stars irradiating their self-gravitating discs can be found in our precedent study (Meyer et al. 2018). In Fig. 1, several magenta dots mark the time instances of the chosen simulation snapshots considered in this study. Note that the young star becomes, by definition, a massive object when $M_\star = 8\,M_\odot$. Hence, our selected disc models are all in the high-mass regime.

Fig. 2 plots the stellar surface properties obtained by post-processing the accretion rate history displayed in Fig. 1 with the GENEC evolution code, with the evolution of the protostellar iternal photospheric luminosity (a), radius (b), and effective temperature (c) as a function of the stellar age of the MYSO. No notable variations happen up to the end of the free-fall collapse and during the early phase of the disc formation at times ≈20 kyr. A slight monotonical increase of the photospheric luminosity $L_\star$ and of the protostellar radius $R_\star$ happens as the deuterieum burning keeps the core temperature almost constant. When the evolution of the accretion rate

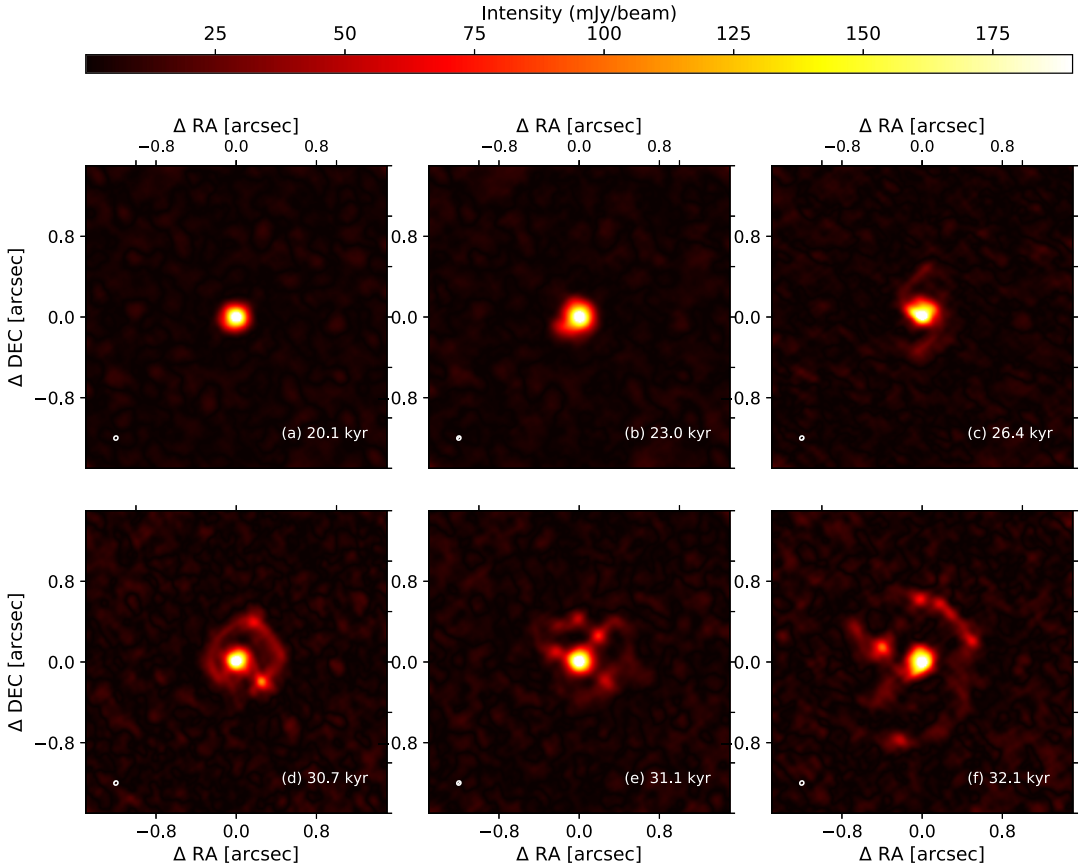

Figure 5. ALMA C43-8 images simulated images at band 6 (1.2 mm) of the accretion disc growing around our protostar, assuming an antenna configuration 8 and 10 min exposure time. The images are shown for the face-on viewing angle. The beam size is 0.029 arcsec and it is given in the lower left corner of each panel. The source distance is assumed to be 1 kpc.

exhibits sudden variations in response to the accretion of gaseous circumstellar clumps formed in the fragmented accretion disc, it generates changes in the internal structure resulting in the bloating of the protostellar radius (Haemmerlé et al. 2016). At this stage, the entropy of the external layers is high and any episodic deposit of mass on it consequently induces an augmentation of $T_{\rm eff}$ and $L_\star$, as described in Meyer et al. (2019). During each strong accretion burst, the MYSOs episodically experiences changes in the photospheric properties by becoming bigger and cooler. Fig. 3 shows the evolutionary track of our MYSO in the Hertzsprung–Russell diagram and compares it with the pre-ZAMS tracks calculated with constant accretion rates (thin solid black lines) of Haemmerlé et al. (2016) and with the ZAMS track (thick dashed black line) of Ekström et al. (2012). The grey solid lines are isoradii. As detailed in Meyer et al. (2019), each strong accretion event reaching rates $\geq 10^{-2}\,{\rm M}_\odot\,{\rm yr}^{-1}$ induces important rapid changes in the pre-main-sequence evolutionary track of the MYSOs. Following an internal redistribution of entropy in the upper layer of the stellar structure, $R_\star$ increases. Successive evolutionary loops toward the red part of the Hertzsprung-Russell diagram occur during these bloating periods. The protostellar properties, required for the radiative transfer calculations, are reported for the six selected simulation snapshots in our Table 1.

3.2 Emission maps at 1.2 mm

Fig. 4 plots the projected 1.2 mm emission maps of our models 1–6. The emission intensity is normalised, the black colour representing the faintest pixels and the white one the brightest ones, respectively. The white bar in the bottom right corner of each figure indicates the physical size of each images. The top series of panels represent the young disc at times 20.1 yr (Fig. 4a), 23.0 yr (Fig. 4b), and 26.4 yr (Fig. 4c) after the beginning of the simulation, respectively. These snapshots correspond to time instances before the MYSO experiences its first accretion-driven burst. The disc model 1 in Fig. 4(a) is a circular and stable disc that does no show any noticeable sign of either fragmentation by gravitational instability or substructures in it. This shape persists up to at least 23.0 yr (model 2; Fig. 4b). During this time interval, the protostellar mass evolves from 8.6, $\rm M_\odot$ to 10.7 $\rm M_\odot$, but its circumstellar medium fails in developing a clear spiral structure, although a faint trailing structure begins to appear at radii $\geq$200–600 au. The brightest region is the inner 50 au of the disc. Our model 3 (Fig. 4b) starts exhibiting a two-arms pattern extending up to radii $\sim$400 au from the MYSO. Moreover, a dense gaseous clump formed in the spiral arm inward-migrates and fast-moves on to the protostar. The clump keeps on contracting during its migration and its core increases in density and temperature, constituting the maximal-emitting region

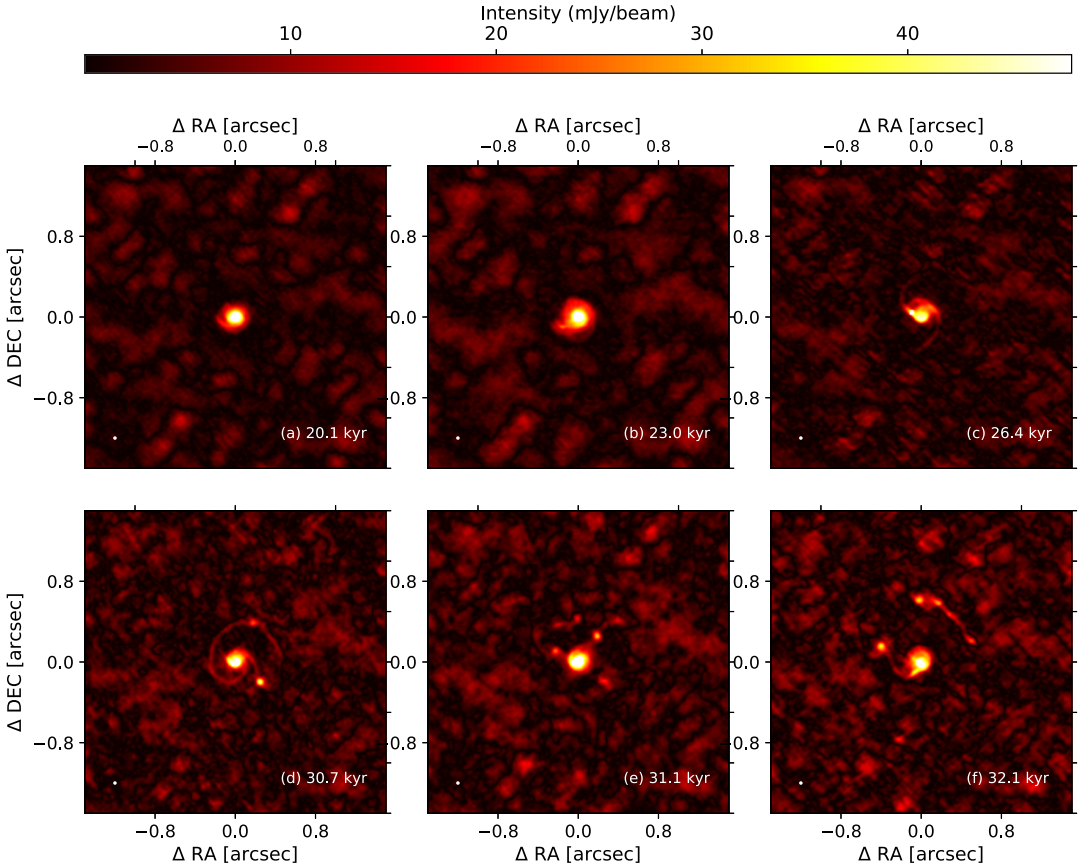

Figure 6. ALMA C43-10 images simulated images at band 6 (1.2 mm) of the accretion disc growing around our protostar, assuming an antenna configuration 10 and 10 min exposure time. The images are shown for the face-on viewing angle. The beam size is 0.015 arcsec and it is given in the lower left corner of each panel. The source distance is assumed to be 1 kpc.

of the disc. The successive, rapid accretion of several migrating clumps from different parent arms, the merging of clumps into inhomogeneous gaseous structures or even the migration of clumps that separate an inner portion of spiral arms into two segments make the accretion pattern more and more complex and strengthen the accretion variability (Fig. 1).

The bottom series of panels of Fig. 4 shows emission maps of our disc models 4–6, corresponding to the young disc at times 30.7 yr (Fig. 4c), 31.1 yr (Fig. 4e), and 32.1 yr (Fig. 4f), respectively. The disc model 4 (Fig. 4d) has the typical morphology of the circumstellar medium of a protostellar disc undergoing efficient gravitational instability. In addition to clear enrolled spiral arms starting close to the star and fading away at $\geq$600-800 au, several gaseous clumps have formed inside the spiral arms, at distances $\geq$200–400 au from the protostar. The spiral arms and clumps appear very prominently in the images, with a higher integrated surface brightness than the homogenous parts of the disc. The disc model 5 (Fig. 4e) is more complex than the rather standard ring-like clump-hosting structure of model 4. Its strongly fragmented disc experiences a complex dynamics in which multiple Toomre-instable gaseous clumps (Meyer et al. 2018) exert torques with each other, with the neighbouring spiral arms and with the central MYSO of 16.7 $M_\odot$, respectively. Finally, the disc model 6 (Fig. 4f) exhibits an extended, strongly fragmented disc with a filamentary spiral arm hosting several bright gaseous clumps. This morphological configuration of the disc substructures is typical of the time following an accretion-driven burst, when the tail of a migrating clump is swung away and pushes the circumstellar material to the larger radii as described in Meyer et al. (2017). The subsequently forming dense ring is the location of the formation of new clumps, whose integrated surface brightness can be similar to that of the inner disc.

3.3 Observability of evolving discs around growing protostars

Figs 5 and 6 show emission maps of our disc models as seen by ALMA if located at a distance of 1 kpc from the observer and monitored with antenna configuration 8 and 10, respectively. Both figures show 1.2 mm simulated images of the selected snapshots at times 20.1 kyr (a), 23.0 kyr (b), 26.4 kyr (c), 30.7 kyr (d), 31.1 kyr (e), and 32.1 kyr (f), respectively. The images assume a face-on viewing geometry. On each panel the beam size is given in the bottom left panel. The map scale is in units of arcsec and the surface brightness intensity is in mJy beam^{-1}. The synthetic images of stable disc model 1 exhibit a bright circular shape for both antenna configuration 8 (Fig. 5a) and the most extended configuration 10 (Fig. 6a). The same is the case for our disc model 2 (23.0 kyr), as the current beam resolution of ALMA is not able to spatially resolve the early forming

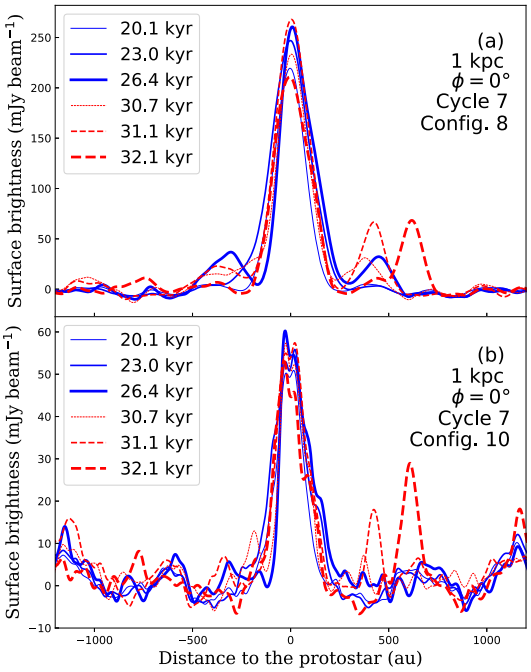

Figure 7. Cross-sections taken in our ALMA C43-8 (a) and C43-10 (b) images simulated images with 10 min exposure time at band 6 (1.2 mm) of our accretion discs. The cuts are taken through images with face-on viewing angle and the source distance is 1 kpc. The cuts are taken along the vertical direction through the origin of the images.

overdensities in its principal spiral arm (Figs 5b and 6b). The 1.2 mm signature of the effects of gravitational instability begins to appear at time 26.4 kyr with the antenna configuration 10 (Fig. 6c), when the protostar has reached 12.1 $M_\odot$ and a series of twin spiral arms in which a detached migrating clump falls on to the protostar. The images at time 30.7 kyr clearly reveal the fragmenting characteristic of our disc, i.e. a self-gravitating spiral arm that includes a few bright gaseous clumps (Fig. 5d) potentially on the way to low-mass star formation (Meyer et al. 2018). The accretion disc and its substructures can be resolved with the ALMA antenna configuration 8. A more extended antenna configuration (configuration 10) yields similar results (see Fig. 6d). At time $\geq$ 31.1 kyr the synthetic observations of models 5 and 6 reveal a nascent multiple, hierarchical massive system with clumps and filamentary structures organized around a hot, young massive star of mass 16.7 $M_\odot$ (Figs 5e and f) and 20.0 $M_\odot$ (Figs 6e and f), respectively.

Shown in Fig. 7 are cross-sections extracted from the ALMA cycle 6 maps with antenna configuration 8 (Fig. 5) and antenna configuration 10 (Fig. 6), respectively. The figures compare the emission intensity at times 20.1 kyr (thin solid blue line), 23.0 kyr (solid blue line), 26.4 kyr (thick solid blue line), 30.7 kyr (thin dashed red line), 31.1 kyr (dashed red line), and 32.1 kyr (thick dashed red line). These profiles assume a face-on viewing geometry ($\phi = 0^\circ$). The source distance is 1 kpc and the cuts are taken along the vertical direction through the re of the synthetic images. The shape of the cross-sections (solid blue lines) corresponding to Fig. 5 further illustrates that the surface brightness of our modelled accretion disc does not exhibit signs of substructured circumstellar disc at times $\leq$23.0 kyr, when the protostar is $\leq$10.7 $M_\odot$, although the intensity cut extracted from the image at 26.4 kyr (thick solid blue line) has two additional bright emission peaks corresponding to the two spiral arms. The slightly negative fluxes in some places in the interarm region of the discs result from the noise of the substracted background thermal emission arising from the incomplete u–v coverage in the simulated observations. The cuts taken in the models 4–6 clearly highlight the presence of a dense ring-like spiral arm that surrounds the MYSO and that produces intensity peaks of $\approx$75 mJy beam^{-1} above the background of $\approx$10 mJy beam^{-1}. The emission cuts in Fig. 7(b) have a higher spatial resolution but a lower sensitivity than those of Fig. 7(a), i.e. the intensity differences between the close stellar surroundings and the arms/clumps in the disc are less pronounced (see also Fig. 14). For example, the northern ring of model 6 (32.1 kyr) peaks at $\approx$50 and $\approx$30 mJy beam^{-1}, which represents about 25 per cent and 60 per cent of the disc central emission, respectively. The images in Figs 5(a)–(f) are complementary to those of Figs 6(a)–(f) in the observation and analysis of the discs, and observations of the circumstellar medium of a high-mass star should be performed with several antenna configurations of ALMA for a given waveband.

3.4 Effect of the inclination angle

Figs 8 and 9 show synthetic ALMA cycle 6 (1.2 mm) images of our disc models. In the figure, each row represents an inclination, and each column a time, and the images are calculated for the ALMA C43-8 configuration, assuming a distance to the source of 1 kpc. The beam size is given in the lower left corner of each panel. Again, the map scale is in units of arcsec and the surface brightness intensity is in mJy beam^{-1}. For $\phi = 45^\circ$, the emission maps do not exhibit important changes in the disc shapes, except that their projected size is squeezed by a factor cos (π/4) along the direction normal of the disc plane (the vertical direction of the maps). This is consistent with the studies on discs from low-mass stars of Dong et al. (2016), which demonstrated that moderate inclination angles with respect to the plane of sky have little incidence in the disc emission maps compared to that with $\phi = 0^\circ$. In the case of edge-on accretion discs, the antenna configuration 8 does not allow the observer to clearly distinguish clumpy structures in the accretion discs, even if they can be inferred from the meridional emission profile, e.g. at time 32.1 kyr (Fig. 8l). Similar trends in the morphological signatures of the accretion discs happen with a higher resolution of the beam, when the antenna configuration is more extended (Fig. 9).

Fig. 10 compares cross-sections taken from our simulated ALMA cycle 6 (1.2 mm) images, with antenna configuration 8 (compact, coarser resolution) and 10 (extended, higher resolution). The source distance is 1 kpc and all cuts are taken along the horizontal direction through the location of the star. The first panel of Fig. 10(a) illustrates the main difference between face-on and edge-viewed accretion discs during the early phase, at times $\leq$ 26.4 kyr. While the face-on disc ($\phi = 0^\circ$) has first an emission profile that does not exhibit clear substructures, its edge view ($\phi = 90^\circ$) indicates the presence of its large, developing spiral arm. At later time and by projection, it gives the disc a symmetric morphology but not a uniform surface brightness with respect to its axis of rotation.

Similar conclusions are drawn with the antenna configuration 10 (Fig. 10c). The disc projected intensity deceases as a function of the inclination, as other circumstellar structures around more evolved massive stars do (Meyer et al. 2016). The time evolution of the surface brightnesses of the edge-viewed accretion discs is as follows: the intensity peaks on the projection plane at the location of the star. The emission signature gradually increases

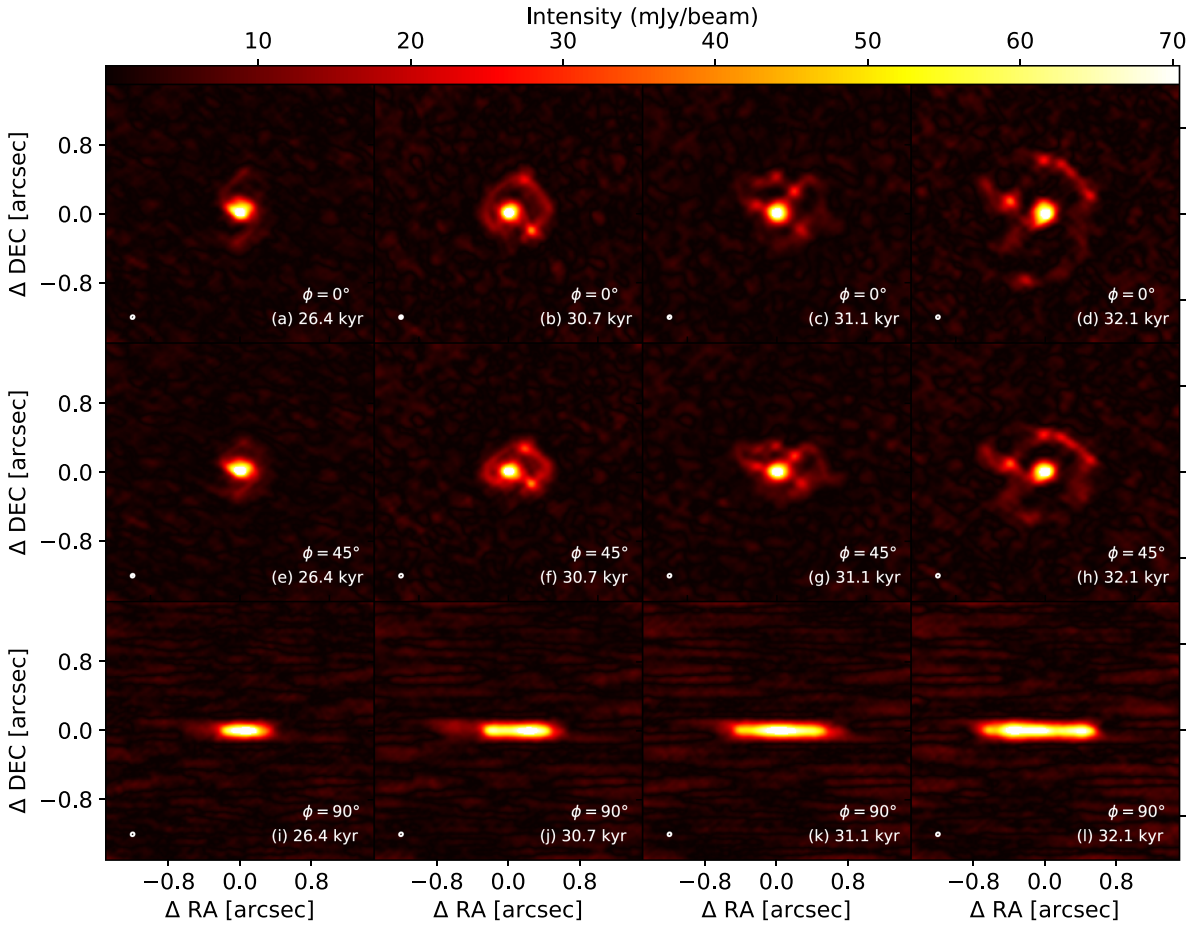

Figure 8. ALMA C43-8 images simulated images at band 6 (1.2 mm) of the accretion disc growing around our protostar at times 26.4 kyr (left), 30.7 kyr (middle left), 31.1 kyr (middle right), and 32.1 kyr (right), assuming 10 min exposure time. The images are shown with a viewing angle of 0° (top), 45° (middle), and 90° (bottom) with respect to the plane of sky. The beam size is 0.029 arcsec and it is given in the lower left corner of each panel. The source distance is assumed to be 1 kpc.

in size as the disc grows, by accumulating molecular gas from the surrounding infalling envelope, up to reaching a radius of ≃800–1000 au (thick red curves of Figs 10b and d). As a result of the antenna configuration 10 and smaller beam size, the meridional cuts through the disc reveal more details in the projected disc emission. Interestingly, some intensity peaks such as at time 30.7 kyr (thin black-dotted dashed line of Fig. 10d) reveal the presence of a couple of aligned clumps, while the other snapshots do not. Polarization measurements in the near-infrared waveband may be useful to further investigate this phenomenon.

3.5 Effect of the distance of the source

Although the Earth's closest high-mass star-forming regions are located at distances ≤1 kpc (Reid et al. 2009), numerous giant molecular regions with massive protostars are more distant. We check the observability of the substructures in our accretion disc models assuming a distance of ≤2 kpc. The radiative transfer methods and the computations of synthetic images are identical as above described for sources located at 1 kpc, the only difference being the exposure time that we derive to be 30 min (Section 4.2).

Fig. 11 shows synthetic ALMA cycle 6 (1.2 mm) images of our disc models. In the figure, each row represents an inclination, and each column a time, and the images are calculated for the ALMA C43-10 configuration, assuming a distance to the source of 2 kpc. The beam size is given in the lower left corner of each panel. Again, the map scale is in units of arcsec and the surface brightness intensity is in mJy beam^{-1}. In accretion discs located at 2 kpc rather than at 1 kpc, it is more difficult to observe clearly detached clumps for young discs such at times ≤26.4 kyr whatever their viewing geometry is (Figs 11a, e, and i). Synthetic images of later time instances (>26.4 kyr) lead to similar conclusions regarding the possible observability of clumps and spiral arms as those derived on the basis of the synthetic images computed assuming a distance of 1 kpc. In the case of edge-on discs, inferring clumps is somewhat less evident (Figs 11i–k), even though the far West clump developing at time 32.1 kyr can be distinguished from the rest of the circumstellar structure in Fig. 11. We conclude that the outcomes of gravitational instabilities in accretion discs around MYSOs can be detected with ALMA, with observations performed during the Cycle 7 observational run and using its most extended available antenna configuration.

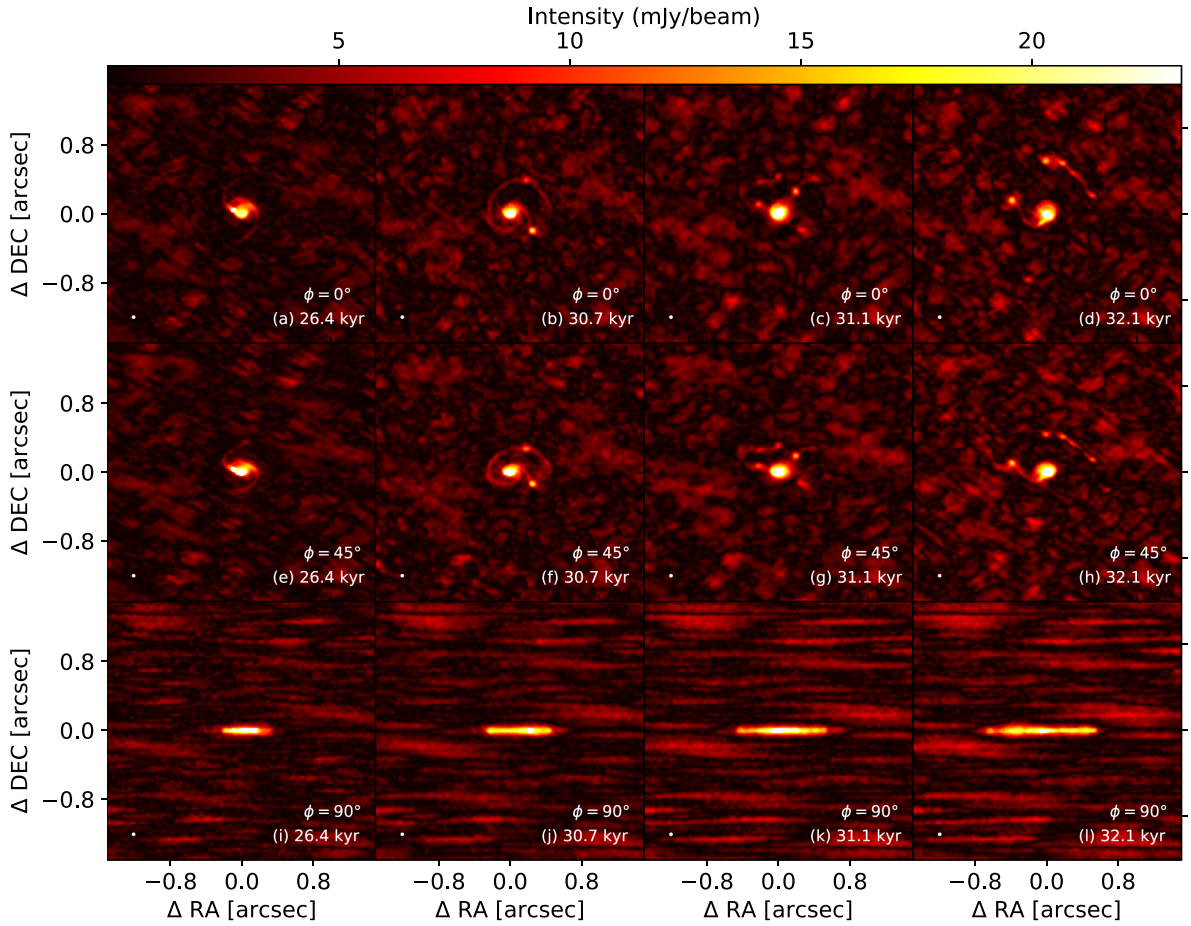

Figure 9. ALMA C43-10 images simulated images at band 6 (1.2 mm) of the accretion disc growing around our protostar at times 26.4 kyr (left), 30.7 kyr (middle left), 31.1 kyr (middle right), and 32.1 kyr (right), assuming 10 min exposure time. The images are shown with a viewing angle of 0° (top), 45° (middle), and 90° (bottom) with respect to the plane of sky. The beam size is 0.015 arcsec and it is given in the lower left corner of each panel. The source distance is assumed to be 1 kpc.

4 DISCUSSION

This last section is devoted to the discussion of our synthetic observations of fragmenting circumstellar discs around MYSOs. We first review the limitations and caveats of our methods, investigate how the effects of the integration time of the interferometric observations and of the ALMA facility beam resolution can affect the detection of substructures in the disc. We briefly compare our results with precedent studies and we discuss future prospects for observing gravitational instability and disc fragmentation around MYSOs. Finally, we discuss our results in the context of high-mass protostellar disc-hosting candidates.

4.1 Limitations of the model

Our models of synthetic images are affected by two kinds of caveats: on the one hand the numerical hydrodynamics simulations of our forming accretion discs are intrinsically subject to limitations justifying future improvements, on the other hand the radiation transfer methods that we use in this study might, in their turn, be improved as well. The principal limitation of our models comes from the restrictions on the hydrodynamical time-step, controlled by the standard Courant–Friedrichs–Levy parameter (Mignone et al. 2007, 2012). It decreases proportionally to the smallest grid size of the grid mapping the computational domain, and, therefore gets smaller as the spatial resolution augments. The sink cell radius also influences the speed of the time-marching algorithm in our simulations. It should be as small as possible since we study the accretion of inward-migrating disc fragments by the protostellar surroundings. In this study, we adopt the smallest value ($r_{\rm in} = 10$ au) where the simulations are still computationally affordable, which is still smaller than in recent works on disc fragmentation. Nevertheless, the most critical point of the disc simulations in spherical coordinate systems remains the effect of the inertia of the central star to the disc dynamics, which is neglected when the high-mass protostar is fixed at the origin of the computational domain; see also discussion in Meyer et al. (2019). The stellar motion in response to the gravitational force of the disc has been shown not only to reduce the strength of gravitational instability (but not shutting it down completely) in the low-mass regime of star formation but also to introduce unpleasant boundary effects (Regály & Vorobyov 2017), as it displaces the barycenter of the star–disc system from the origin of the domain. This is in accordance with the analytic study of Adams, Ruden & Shu (1989) that pointed out the role

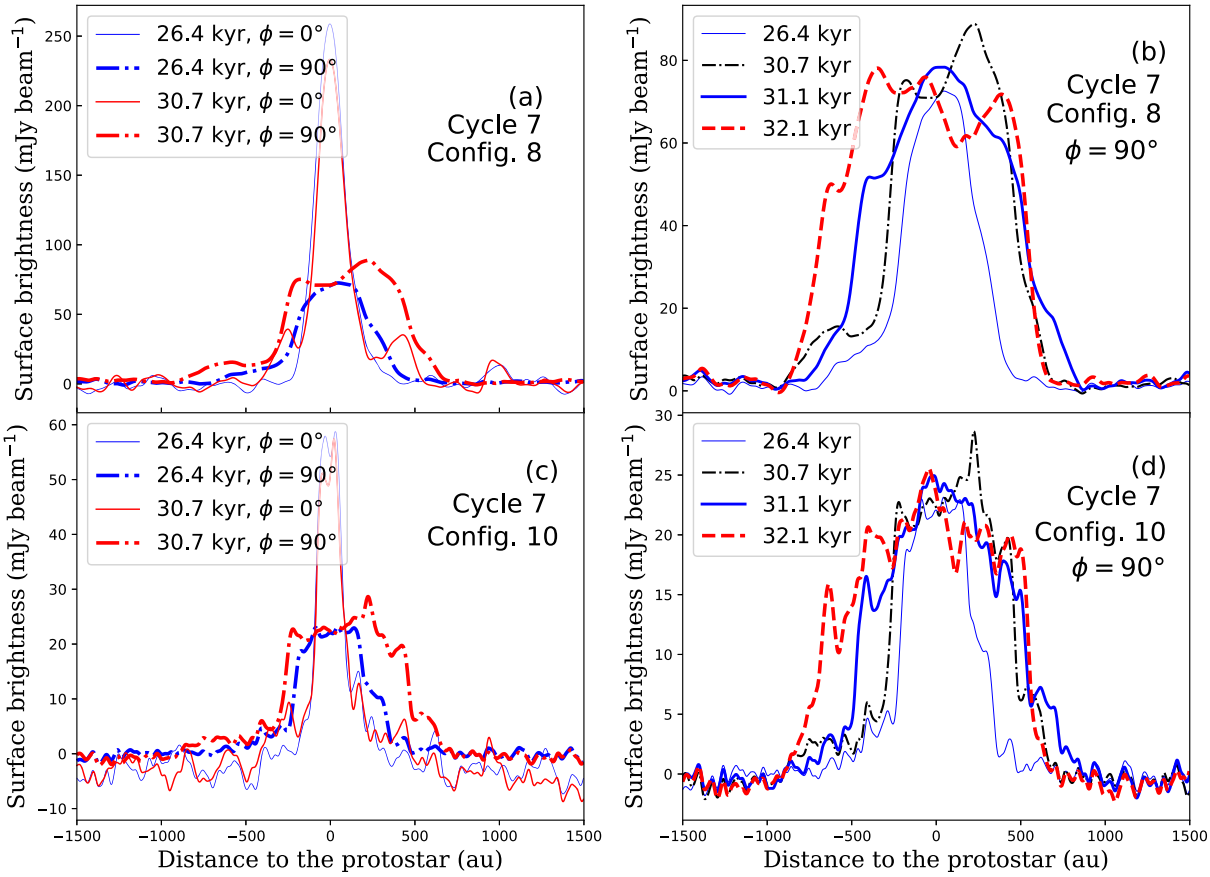

Figure 10. Comparison between the cross-sections taken in our simulated ALMA images simulated at band 6 (1.2 mm) and assuming antenna configurations 8 (C43-8 observations) and 10 (C43-10 observations), respectively. Left-hand panels compare the surface brightnesses of the discs at times 20.1 kyr and 23.0 kyr considered with viewing angles of $\phi = 0^{\circ}$ and $\phi = 90^{\circ}$, respectively. Right-hand panels compare the surface brightnesses of the discs at times 26.4 kyr, to 30.7 kyr (blue) considered with viewing angles of $\phi = 0^{\circ}$ and $\phi = 90^{\circ}$, respectively. The source distance is 1 kpc. The cut are taken in East–West direction through the origin of the images.

of stellar inertia in the development of asymmetries in discs. The study of Meyer et al. (2019) demonstrated that the disc inertial force does not entirely stabilise discs or shuts off the burst phases of the protostellar growth, in accordance with results of Regály & Vorobyov (2017). The assumptions in our numerical simulations of the disc structures are presented and discussed in detail in Meyer et al. (2018, 2019).

The dust temperature is a key parameter governing the brightness of the accretion discs. Fig. 12 compares simulated ALMA cycle 6 (1.2 mm) images with an antenna configuration 10 of a stable (left) and a fragmented (right) disc model, where the radiation transfer calculations are performed with different methods to compute the dust temperature fields: either by Monte Carlo in the RADMC-3D code (top panels) or using the dust temperatures from the hydrodynamics simulations (bottom panels). The images are shown for face-on viewing angle ($\phi = 0^{\circ}$). The beam size is indicated in the lower left corner of each panel and the source distance is 1 kpc. It appears that the synthetic ALMA images of the stable model at time 20.1 kyr do not exhibit strong differences if modelled on the basis of either of a Monte Carlo method or using the temperature fields imported from the hydrodynamical simulations (left-hand panels of Fig. 12). Nevertheless, differences are observed with respect to the observability of the clumps of fragmented discs (right-hand panels of Fig. 12). Such changes in the simulated images are due to the fact that the hydrodynamical temperature field results in a self-consistent simulation, including the treatment of the mechanical pdV work from gravity forces in the disc, i.e. the internal thermodynamics of the clumps are taken into account. The cores of these clumps experience an internal gravitational collapse (Meyer et al. 2018), while a Monte Carlo calculation of the temperature fields is less realistic as it simply ray-traces photon packages through the clumps without accounting for their thermal properties. This results in brighter 1.2 mm clumps in the spiral arms of the fragmented discs (bottom right-hand panel of Fig. 12), and, consequently, in a higher brightness and better observability at the considered sub-millimetre wavelength. This effect was also reported in Dong et al. (2016) in the context of fragmented discs around low-mass protostars.

Fig. 13 compares several of the cross-sections taken through our simulated ALMA cycle 6 (1.2 mm) antenna configuration 10 images displayed in Fig. 12. Two disc models are compared: a first one corresponding to a time 20.1 kyr when the disc is stable (blue lines) and another one at time 30.7 kyr when the disc fragments (red), in which the dust temperature is estimated by Monte Carlo simulations (thin solid lines) and by thermal equilibrium (thick dashed lines).

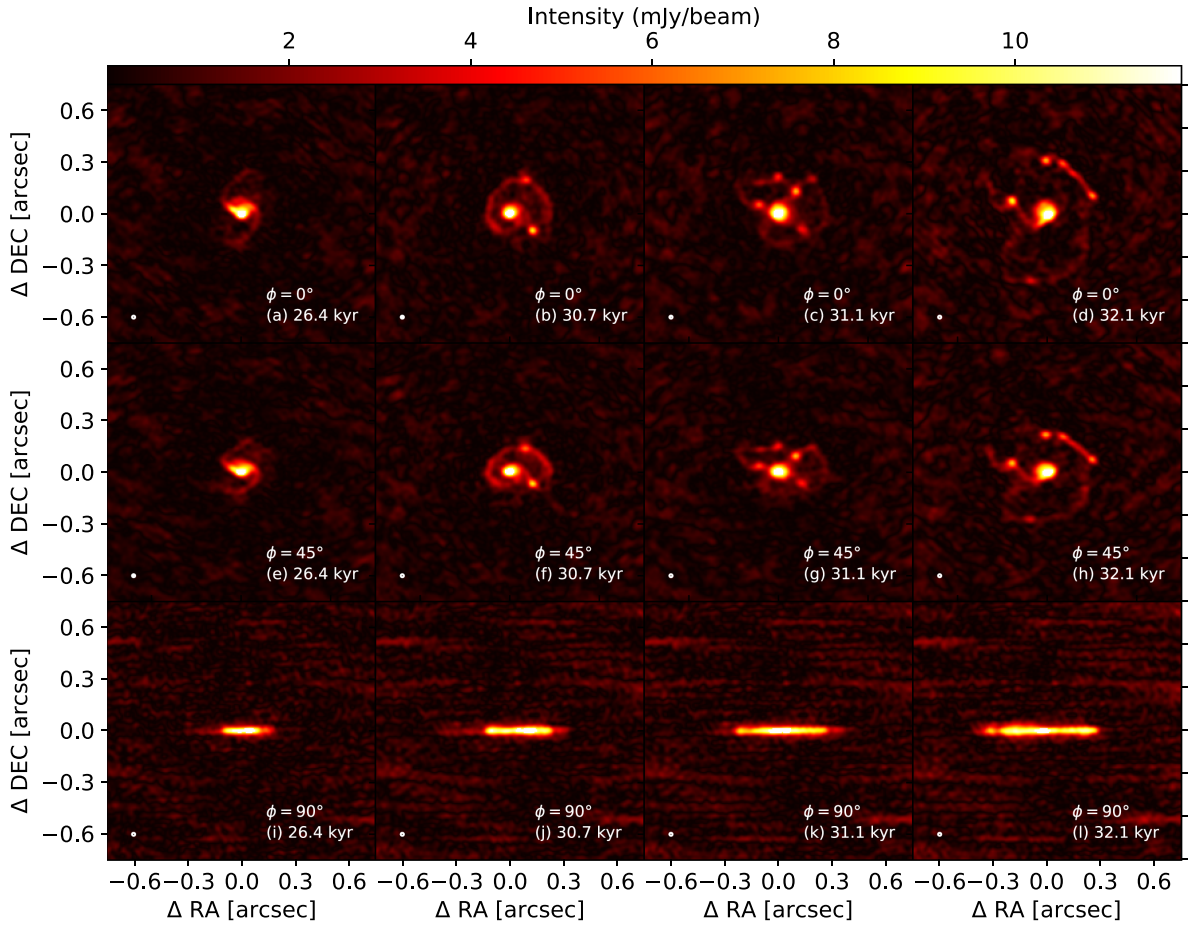

Figure 11. Similar to Fig. 9, but for a distance to the source of 2 kpc. It displays ALMA Cycle 7 band 6 (1.2 mm) images simulated with an antenna configuration 10 (C43-10 images). The beam size is 0.015 arcsec and it is given in the lower left corner of each panel. Note that the angular scales are different than for the models with a distance to the source of 1 kpc (see Fig. 9).

It further highlights the differences between the two methods for the determination of the disc dust temperature. One can see that the simulated images performed with two consecutive Monte Carlo ray-tracings (RADMC-3D) are slightly fainter in intensity than that carried out on the basis of PLUTO temperatures, e.g. the central part of the RADMC-3D image peaks at $\approx$35 mJy beam^{-1} while the PLUTO peaks at $\approx$50 mJy beam^{-1}, respectively. As another example, the peaks intensities in the clumps calculated with RADMC-3D and PLUTO temperatures are $\approx$10 and $\approx$14 mJy beam^{-1}, respectively, which is slightly more noticeable than at the location of the central high-mass protostar. Our simulations with RADMC-3D tend to underestimate the surface brightness in the synthetic images. As a conclusion, we stress the need for the use of self-consistently determined temperatures for the modelling of emission maps of accretion discs of massive protostars.

4.2 Effect of integration time and angular resolution

Fig. 14 compares the effects of the antenna configuration and of the integration time on the simulated images of our fragmented accretion disc at time 30.7 kyr. The top panels are simulated with the most compact antenna configuration (cycle 6.6) and lower panels are simulated with the most extended configuration (cycle 6.10), respectively. The integration time is 600 s (left) and 1800 s (right). All images are shown assuming a face-on viewing angle of the discs. The beam size is indicated in the lower left corner of each panel and the source is located at 1 kpc. The series of tests highlights that the more extended the antenna configuration, i.e. the smaller the beam scanning a region of the sky, the better visible are the substructures inside the protostellar disc. If the images performed with 600 s of integration time and an antenna configuration 6 do not reveal clumps in the disc, those with antenna configuration $\geq$7 do. The latter show both the distinct features of two clumps that are brighter than the background, and it equivalently reveals the main spiral arm of the disc. Note that the best available beam resolution (bottom panels) even shows the asymmetric character of some clumps. The two series of panels comparing the ALMA integration time of 600 s (right) and 1800 s (left) indicate that the more extended the antenna configuration, the faster the convergence of the solution in terms of exposure time. Indeed, the more compact antenna configuration 6 (top series of panel) shows that the image modeled with 1800 s reveals a clump above the protostar that is not visible with only 600 s integration time, while the other images with the antenna configuration $\geq$7 do not exhibit such differences, i.e. the beam resolution

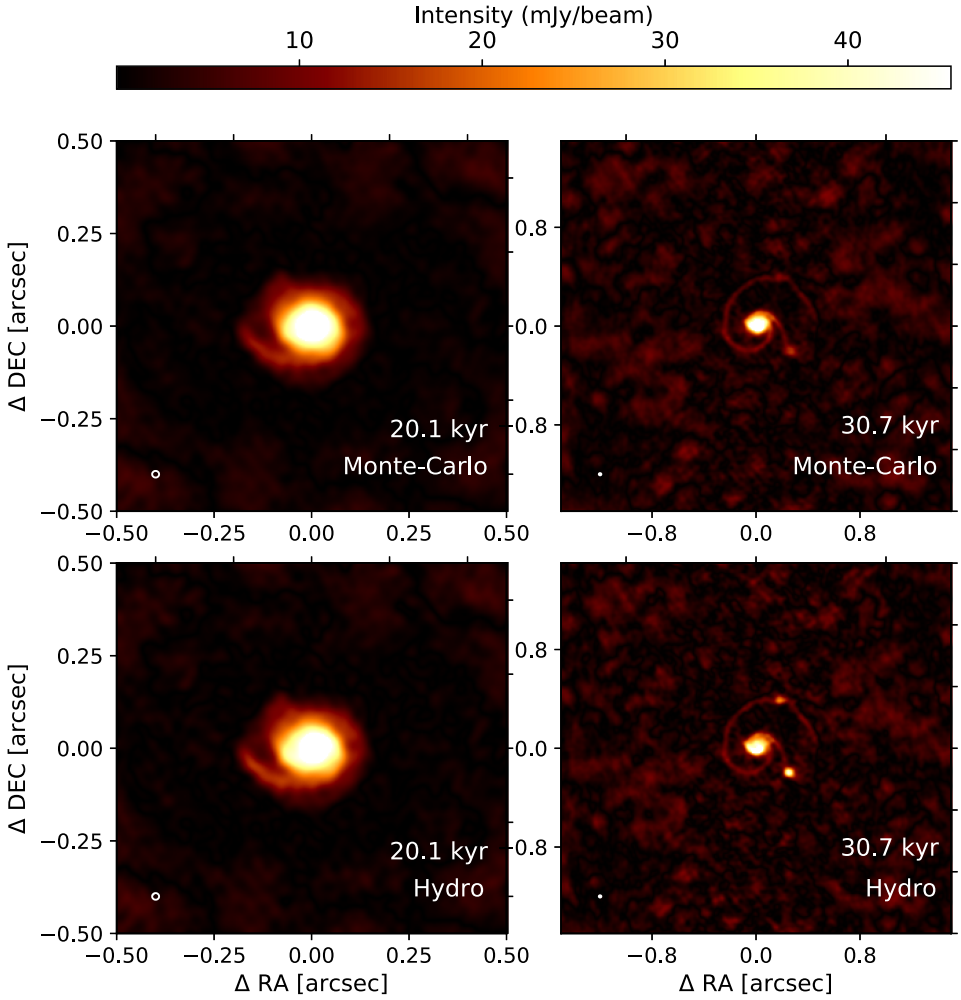

Figure 12. Comparison between simulated ALMA Cycle 7 band 6 (1.2 mm) images with antenna configuration 10 of stable (left) and fragmented (right) disc models, respectively. Differences lie in the dust temperature field calculation method, either by the Monte Carlo simulation (top) or by importing the dust temperatures from the hydrodynamics simulations (bottom). The images are shown for face-on viewing geometry. The beam size is indicated in the lower left corner of each panel and the source distance is located at 1 kpc.

is more important than the integration time. Similarly, we derive a reasonable exposure time to observe sources located at 2 kpc to be 30 min.

4.3 Comparison with other studies

A couple of previous works have performed synthetic imaging of both analytic and self-consistent hydrodynamical simulations of forming massive stars at the disc scale ($\leq$1000 au); see Krumholz et al. (2007), Harries et al. (2017), Meyer et al. (2018), and Jankovic et al. (2019). First, the paper of Krumholz et al. (2007) investigated synthetic ALMA and NOEMA images of disc structures forming from collapsing turbulent pre-stellar cores located at $\leq$2 kpc, in which secondary star formation is tracked with the use of Lagrangian sink particles whose caveats are discussed in Meyer et al. (2018). Our models therefore provide more accurate density and temperature disc structures, as the gaseous clumps and secondary low-mass stars are self-consistently produced and their internal thermodynamics is intrinsically taken into account. Secondly, Harries et al. (2017) carried out state-of-the-art gravito-radiation-chemo-hydrodynamical simulations and checked the disc spiral arm observability with simulated 1 mm ALMA interferometric observations. This study includes the most accurate treatment of the radiative protostellar feedback to-date; however, its disc models neither strongly fragment nor produce the formation of clumps because of a lack of spatial resolution.

In the earlier studies of this series devoted to the burst mode of massive star formation, Meyer et al. (2018) showed that spiral arms can be observed in continuum and molecular emission for a fragmenting disc located at a distance and with an inclination corresponding to the disc around the MYSO AFGL-4176 (Johnston et al. 2015). Last, the work of Jankovic et al. (2019) predicts the observability of spiral arms and clumps in discs around massive stars by computing images of analytic disc structures. They predict their observability up to a distance $\leq$5 kpc for arbitrary inclinations by direct imaging discs with $\phi \leq 50^{\circ}$ and/or by their kinematic

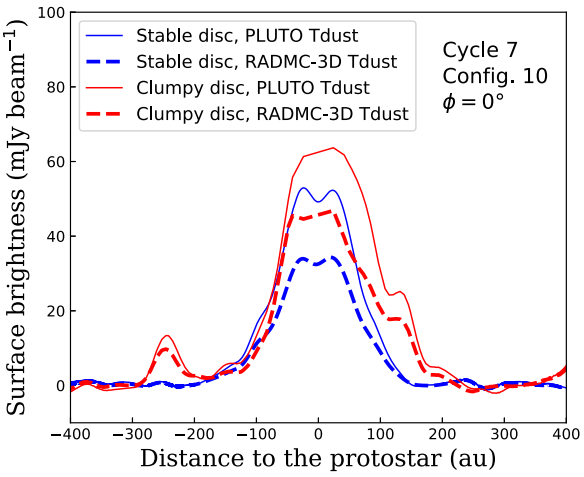

Figure 13. Comparison between the cross-sections of simulated ALMA Cycle 7 band 6 (1.2 mm) antenna configuration 10 images of our snapshots 1 (stable disc model, blue) and 4 (fragmented disc model, red), in which the dust temperature is either estimated using a radiative transfer calculation with the RADMC-3D code (thick dashed lines) or estimated on-the-fly with the hydrodynamical PLUTO code and taking into account compressional heating (thin solid lines). Note that the left and right series of images are not plotted on the same physical size, respectively. The source distance is located at 1 kpc.

signature. Our results show that clumps can, under some circumstances, be directly imaged or at least inferred for edge-viewed discs. These studies highlight the possible observation of circumstellar discs around young massive stars. Our work allows for the first time to obtain self-consistent solution from the hydrodynamical, stellar evolution, and radiative transfer point of view, which permits qualitative predictions relative to the emission properties of disc substructures.

4.4 Prospect for observing disc fragmentation around MYSOs: the cases of S255IR-NIRS3 and NGC 6334I-MM1

In this sub-section, we discuss the prospects for the potential observability of signatures of gravitational instabilities in the surroundings of outbursting sources. We focus on the two high-mass protostars for which potentially accretion-driven bursts have been observed, namely S255IR-NIRS3 (Caratti o Garatti et al. 2017) and NGC 6334I-MM1 (Hunter et al. 2017). Note that a third burst from a MYSO, V723 Car, has been reported in Tapia, Roth & Persi (2015), however, its discovery in archival data did not permit further monitoring of it. S255IR-NIRS3 is the very first massive protostar observed experiencing a disc-mediated burst and it is therefore a natural target to investigate the possible presence of other clumps in its disc. NGC 6334I-MM1 is the second known bursting MYSO and it exhibited a successive quadruple temporal variation in the dust continuum emission that suggests that this eruptive event is stronger in intensity than that of S255IR-NIRS3. This makes NGC 6334I-MM1 the second most obvious candidate to chase for substructures in its close surroundings. A summary of the recent research concerning these two MYSOs is given in section 5.4 of Meyer et al. (2019). The predictions for their circumstellar medium are performed following the comparison method utilized for the proto-O-type star AFGL 4176 in Meyer et al. (2018). We select a simulation snapshot of our hydrodynamical model at a

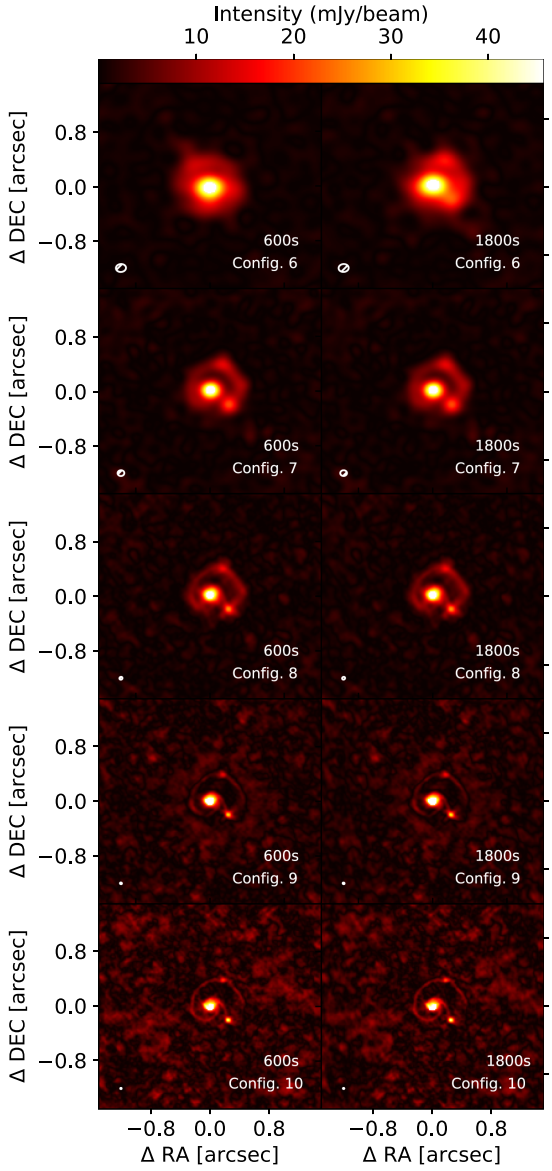

Figure 14. Effects of the antenna configuration and integration time on the simulated images of our fragmented accretion disc at time 30.7 kyr. Upper panels are the most compact antenna configuration (Cycle 7 band 6 with antenna configuration 6) and lower panels the most extended (Cycle 7 band 6 with antenna configuration 10), respectively. The integration time is 600 s (left) and 1800 s (right). The images are shown assuming face-on viewing geometry. The beam size is indicated in the lower left corner of each panel and the source distance is located at 1 kpc.

time corresponding to the estimated masses of the MYSOs and run radiative transfer calculations as above described, with RADMC3D and CASA. The dust continuum models are run using the values for $L_\star$, $R_\star$, and $T_{\rm eff}$ either constrained by observations or derived from our stellar evolution calculation, and we account for the position of the MYSO on the sky, its distance to the observer, and, when possible, the inclination angle of the disc with respect to the plane of sky.

Table 2. Adopted properties of the bursting MYSOs S255IR-NIRS3 (Caratti o Garatti et al. 2017) and (b) NGC 6334I-MM1 (Hunter et al. 2017).

Name	$M_\star$ ($M_\odot$)	$L_\star$ ($L_\odot$)	$R_\star$ ($R_\odot$)	$T_{\rm eff}$ (K)	d (kpc)	ϕ	References
S255IR-NIRS3	20	2.9×10^4	10	23 800[a]	1.8	80°	Caratti o Garatti et al. (2017), Meyer et al. (2019)
NGC 6334I-MM1	20	1.5×10^5[a]	350	6100	1.3	ϕ[b]	Forgan et al. (2016), Hunter et al. (2017)

Note. [a]Derived assuming that the MYSO just experienced a strong accretion burst as in Fig. 2, and [b]Undetermined.

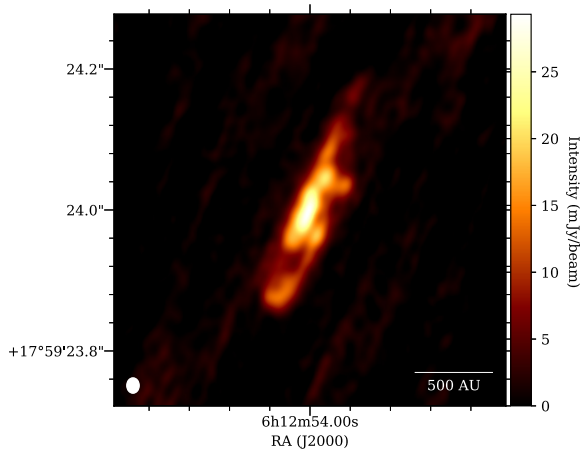

Figure 15. Dust continuum ALMA Cycle 7 C43-10 at band 6 (1.2 mm) predictions for the observability of disc substructures in the context of the bursting young high-mass star S255IR-NIRS3 (Caratti o Garatti et al. 2017).

We adopt the stellar parameters of S255IR-NIRS3 and NGC 6334I-MM1 summarized in the studies of Caratti o Garatti et al. (2017), Eislöffel & Davis (1995), Bøgelund et al. (2018), and Hunter et al. (2017). For S255IR-NIRS3, we consider that it has recovered the pre-burst quiescent value of $L_\star$, although our stellar evolution calculation predicts a rather slow post-burst luminosity decay lasting $\simeq 10^2$ yr (see our Fig. 2 and Meyer et al. 2019). Our choice to adopt protostellar parameters fainter than that of Run-1-hr is justified because we have classified the flare of S255IR-NIRS3 to be a modest 2-mag burst in Meyer et al. (2019), which cannot be responsible for long-lasting spectral excursions in the Hertzsprung–Russell diagram as experienced by the MYSO of Run-1-hr (see also Meyer et al. 2019). Concerning NGC 6334I-MM1, which experienced a strong burst, one has to keep in mind that the values of $R_\star$ in Forgan et al. (2016) do not account for the burst-induced protostellar bloating. However, the values of $T_{\rm eff}$ are fully consistent with our stellar evolution calculation. We correct this discrepancy by assuming a larger value of the protostellar radius, taken from Run-1-hr, which in its turn also affects $L_\star$. Hence, the only unknown is the inclination angle ϕ of the possible disc of NGC 6334I-MM1 with respect to the plane of sky. The various parameters of these two MYSOs are summarized in Table 2 and our results are shown in Figs 15 and 16.

The Cycle 7 band 6 synthetic observation of S255IR-NIRS3 is plotted in Fig. 15. The disc position angle is chosen to match the direction of the two lobes inside which material is expelled during the burst in Caratti o Garatti et al. (2017). It is interesting to see that a few clumps in the disc can still be observed despite the almost edge-on view of the disc around S255IR-NIRS3. The Cycle 7 band 6 synthetic observation of NGC 6334I-MM1 is shown in Fig. 16. As the inclination of its disc is not known, we assumed several angles ($\phi = 0°$, 30°, and 90°). We conclude for all the considered angles ϕ that substructures can easily be observed in the disc and its surroundings. Hence, these two targets are good candidates for further exploration of substructures in their circumstellar discs. Our results also permit to speculate that NGC 6334I-MM1 might be recovering its quiescent, luminous ground state after a spectral excursion in the red part of the Hertzsprung–Russell. Consequently, this object is also a candidate to test our prediction regarding the intermittency of the H II region surrounding outbursting MYSOs that was predicted in Meyer et al. (2019).

One should keep in mind that the two MYSOs that we selected to study the observability of their (possibly substructured) accretion discs are the two MYSOs that had a known burst. This was intentional, as the burst mode picture of star formation predicts a direct correspondance between the occurrence and properties of the burst with the effects of gravitational instability in those discs (Meyer et al. 2017). However, all MYSOs may have an accretion disc and the absence of observed bursts in most of them can simply be interpreted as them being in a quiescent phase of accretion, not as the absence of discs or even not as the absence of fragments in their discs. Indeed, the numerical models for bursting massive protostars of Meyer et al. (2019) indicate that MYSOs spend < 2 per cent of their early 60 kyr being in the eruptive state. Consequently, the other young massive stars with candidate discs might also be worth observing with future high-resolution ALMA campaigns. Possible targets are listed in the observational studies reporting the Red MSW Source survey of Galactic hot massive protostars (Lumsden et al. 2013). The closest ones, located at ≈ 1.4 pc, are G076.3829–00.6210 (S106) and G080.9383–00.1268 (IRAS 20376+4109) while a few others are at a distance of ≈ 2.0 pc. For instance, G015.0357–00.6795 (M17), the W3IRS objects, G192.5843–00.0417 (G192.58) might deserve particular attention for the observer observational astronomical concentrating on multi-epoch VLBI (very long baseline interferometry) observations of maser emission.

Last, we should also mention that there is a growing suspicion of correlations between the maser emission from MYSOs and their recent accretion activity, as maser flares originating from the surroundings of massive protostars continue to be monitored (Burns et al. 2016, 2017; MacLeod et al. 2018). This promising research avenue might investigate, amongst others, if maser variability is an outcome of episodic accretion. Such results would be of great interest not only in the understanding of massive star formation mechanisms but also a huge leap forward in the validity of the burst mode picture of star formation.

5 CONCLUSIONS

This work explores the observability of a fragmenting accretion disc surrounding MYSOs, as modelled in Meyer et al. (2017, 2018), using the ALMA interferometer. Such discs are subject to efficient gravitational instabilities, generating the formation of dense spiral arms and gaseous clumps, which episodically inward-migrate to the

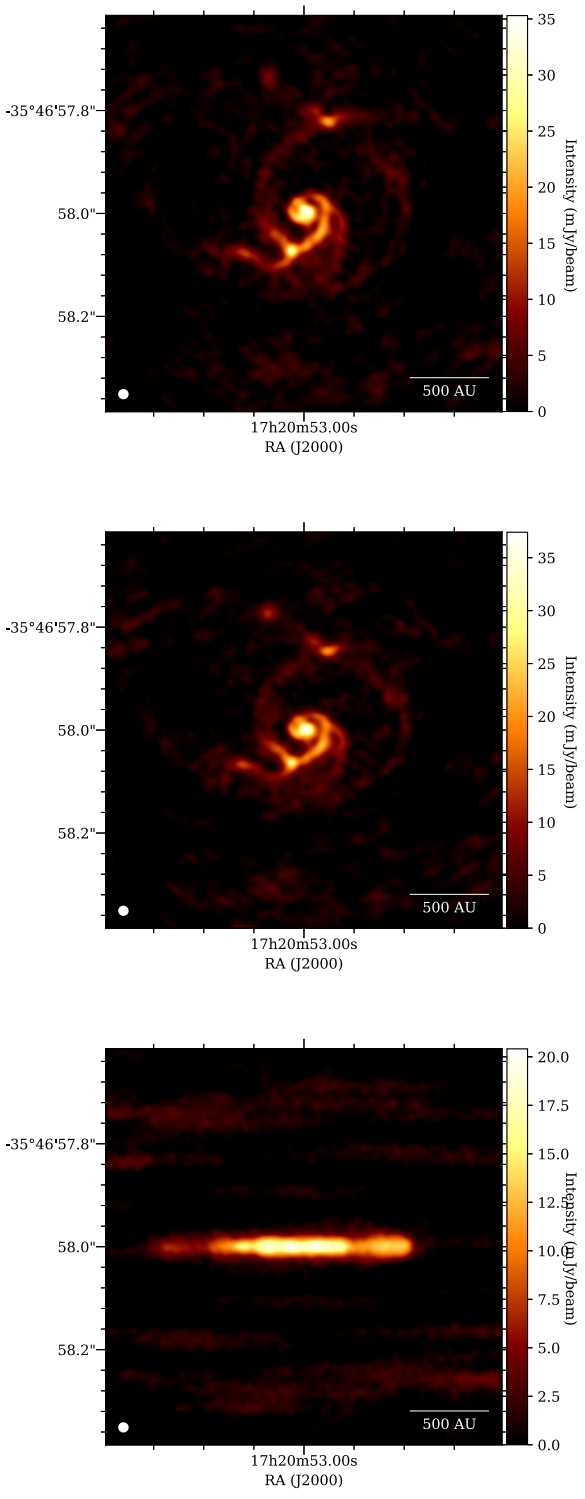

Figure 16. Dust continuum ALMA Cycle 7 C43-10 at band 6 (1.2 mm) predictions for the observability of disc substructures in the context of the bursting young high-mass star NGC 6334I-MM1 (Hunter et al. 2017). The viewing angle of the disc, not constrained by observations, is hereby assumed to be 0° (top), 30° (middle), and 90° (bottom), respectively.

inner disc region. Some of them further contract up to become the precursors of close/spectroscopic binary companions to the central protostar (Meyer et al. 2018) and/or (simultaneously) provoke accretion driven outbursts of various intensities (Meyer et al. 2019). Representative simulation snapshots exhibiting the characteristic formation and evolutionary stages of the disc are selected from model run-1-hr of Meyer et al. (2018), which results from the gravitational collapse of a 100 $M_\odot$ molecular pre-stellar core. We performed stellar evolution and radiative transfer calculations to produce ALMA at band 6 (1.2 mm) emission maps of the discs and obtain synthetic images. These images are then used to investigate the observability of spiral arms and clumpy fragments. In addition to the disc evolution, we explore how its inclination angle with respect to the plane of sky affects the 1.2 mm projected emission signatures. We also look at the effects of various ALMA beam resolutions and/or antenna configurations to predict the best facility configuration and the ages of accretion discs from MYSOs that are the easiest ones to observe.

Our results demonstrate that not only the spiral arms developing in the disc by gravitational instability, but also the gaseous clumps can be observed, as their internal density and temperature make them much brighter than the disc itself. For sources located at a distance of 1.0 kpc, 10 min exposition time with a 0.015 arcsec beam resolution permits to clearly distinguish those nascent stars and reveal the multiplicity in the environment of young massive protostars. We predict that in the millimeter waveband (band 6), an antenna configuration 8 (corresponding to a beam resolution of 0.029 arcsec) is necessary to reach a beam resolution required to identify the disc substructures with a rather short 10 min exposure time. However, only antenna configuration 10 (corresponding to a beam resolution of 0.015 arcsec) might allow us to distinguish the finest disc substructures. Interestingly, our ALMA images also revealed clumps in inclined discs and they can be inferred for edge-on accretion discs, as long as these fragments develop at radii $\geq$600 au from the protostar, i.e. they are not fully screened by the irradiation of the central massive protostar. In our models, this corresponds to discs older than $\approx$26.7 kyr after the onset of the gravitational collapse, when the MYSO has already reached a mass of $\approx$16 $M_\odot$. Hence, good candidates for hunting disc substructures are MYSOs of $\simeq$20 $M_\odot$. Our conclusions regarding the observability of substructures in our disc models are valid up to distances of 2 kpc, using a 0.015 arcsec beam resolution with the ALMA Cycle 7 antenna configuration 10 and at least 30 min exposure time.

The detection probability of the structures increases as the disc grows, i.e. accretion discs around protostars close to the ZAMS are more extended, and host more clumps in the outer region of the disc that is not screened by the MYSO irradiation. Infalling clumps in the inner few 10 − 100 au of the disc might not be observable and the probability to directly associate a clump with a burst is rather small. Last, our study emphasizes the necessity to perform simulated images of discs around massive stars by accounting for the gaseous clumps thermodynamics by using temperatures self-consistently determined during the hydrodynamics simulations instead of dust temperature fields obtained using steady-state radiative transfer models that neglect *pdV* work. In addition to demonstrating the possible direct imaging of nascent multiple massive protostellar systems with ALMA, we also highlight that gaseous clumps and spiral overdensities can clearly be observed/inferred at distances corresponding to the bursting massive protostars S255IR-NIRS3 (Caratti o Garatti et al. 2017) and NGC 6334I-MM1 (Hunter et al. 2017). Those objects might deserve particular future attention from the

point of view of high-resolution observations (Zinchenko et al. 2015). Similarly, the Earth's closest sources, at ≈1.4 − 2.0 pc, of the Red MSW Source survey of Galactic hot massive protostars (Lumsden et al. 2013) also constitute valuable potential targets. As the models for fragmented discs of Meyer et al. (2017, 2018) predict a pre-main-sequence outburst of massive protostars to be the direct outcome of rapidly inward-migrating clumps, we suggest observers to consider their respective circumstellar discs as priority targets to search for the substructures that can be signatures of fragmentation by gravitational instability in their accretion disc.

ACKNOWLEDGEMENTS

The authors thank the referee for her/his valuable comments that improved the quality of the manuscript. D. M.-A. Meyer acknowledges B. Magnelli from the German ALMA Regional Center (ARC) Node at the Argelander-Institut für Astronomie of the University of Bonn for his help, and C. Dullemond for his advices in using the RADMC-3D code. D. M.-A. Meyer also thanks Dr. Z. Regály from Konkoly Observatory for his advices in using the CASA software and Dr. K. G. Johnston for kindly sharing her explanations with the MATPLOTLIB PYTHON package. S. Kraus and A. Kreplin acknowledge support from an ERC Starting Grant (Grant Agreement No. 639889), an STFC Rutherford Fellowship (ST/J004030/1) and an STFC Rutherford Grant (ST/K003445/1). E. I. Vorobyov acknowledges support from the Russian Science Foundation grant 18-12-00193. This work was sponsored by the Swiss National Science Foundation (project number 200020-172505).

REFERENCES

Adams F. C., Ruden S. P., Shu F. H., 1989, ApJ, 347, 959
Ahmadi A. et al., 2018, A&A, 618, A46
Asplund M., Grevesse N., Sauval A. J., 2005, in Barnes T. G., III, Bash F. N., eds, ASP Conf. Ser. Vol. 346, Cosmic Abundances as Records of Stellar Evolution and Nucleosynthesis, The Solar Chemical Composition. Astron. Soc. Pac., San Francisco, p. 25
Behrend R., Maeder A., 2001, A&A, 373, 190
Beuther H. et al., 2018, A&A, 614, A64
Beuther H. et al., 2019, A&A, 621, A122
Brown R. L., Wild W., Cunningham C., 2004, Adv. Space Res., 34, 555
Burns R. A. et al., 2017, MNRAS, 467, 2367
Burns R. A., 2018, in Tarchi A., Reid M. J., Castangia P., eds, Proc. IAU Symp. 336, Astrophysical Masers: Unlocking the Mysteries of the Universe, Water Masers in Bowshocks: Addressing the Radiation Pressure Problem of Massive Star Formation. Kluwer, Dordrecht, p. 263
Burns R. A., Handa T., Nagayama T., Sunada K., Omodaka T., 2016, MNRAS, 460, 283
Bøgelund E. G. et al., 2018, A&A, 615, A88
Caratti o Garatti A. et al., 2017, Nat. Phys., 13, 276
Caratti o Garatti A., Stecklum B., Linz H., Garcia Lopez R., Sanna A., 2015, A&A, 573, A82
Cesaroni R., Hofner P., Araya E., Kurtz S., 2010, A&A, 509, A50
Chen X., Ren Z., Zhang Q., Shen Z., Qiu K., 2017, ApJ, 835, 227
Chini R., Hoffmeister V. H., Nasseri A., Stahl O., Zinnecker H., 2012, MNRAS, 424, 1925
Cunha K., Hubeny I., Lanz T., 2006, ApJ, 647, L143
Cunningham N. J., Moeckel N., Bally J., 2009, ApJ, 692, 943
Dong R., Vorobyov E., Pavlyuchenkov Y., Chiang E., Liu H. B., 2016, ApJ, 823, 141
Dullemond C. P., 2012, RADMC-3D: A Multi-purpose Radiative Transfer Tool, Astrophysics Source Code Library, record ascl:1108.016
Eggenberger P., Meynet G., Maeder A., Hirschi R., Charbonnel C., Talon S., Ekström S., 2008, Ap&SS, 316, 43
Eislöffel J., Davis C. J., 1995, Ap&SS, 233, 59
Ekström S. et al., 2012, A&A, 537, A146
Elbakyan V. G., Vorobyov E. I., Rab C., Meyer D. M.-A., Güdel M., Hosokawa T., Yorke H., 2019, MNRAS, 484, 146
Forgan D. H., Ilee J. D., Cyganowski C. J., Brogan C. L., Hunter T. R., 2016, MNRAS, 463, 957
Fujii M. S., Portegies Zwart S., 2011, Science, 334, 1380
Ginsburg A., Bally J., Goddi C., Plambeck R., Wright M., 2018, ApJ, 860, 119
Greif T. H., Bromm V., Clark P. C., Glover S. C. O., Smith R. J., Klessen R. S., Yoshida N., Springel V., 2012, MNRAS, 424, 399
Haemmerlé L., 2014, PhD thesis, Univ. Geneva
Haemmerlé L., Peters T., 2016, MNRAS, 458, 3299
Haemmerlé L., Eggenberger P., Meynet G., Maeder A., Charbonnel C., 2016, A&A, 585, A65
Harries T. J., 2015, MNRAS, 448, 3156
Harries T. J., Douglas T. A., Ali A., 2017, MNRAS, 471, 4111
Hennebelle P., Commerçon B., Chabrier G., Marchand P., 2016, ApJ, 830, L8
Hosokawa T., Omukai K., 2009, ApJ, 691, 823
Hosokawa T., Yorke H. W., Omukai K., 2010, ApJ, 721, 478
Hunter T. R. et al., 2017, ApJ, 837, L29
Ilee J. D., Cyganowski C. J., Nazari P., Hunter T. R., Brogan C. L., Forgan D. H., Zhang Q., 2016, MNRAS, 462, 4386
Ilee J. D., Cyganowski C. J., Brogan C. L., Hunter T. R., Forgan D. H., Haworth T. J., Clarke C. J., Harries T. J., 2018, ApJ, 869, L24
Jankovic M. R. et al., 2019, MNRAS, 482, 4673
Johnston K. G. et al., 2015, ApJ, 813, L19
Keto E., Wood K., 2006, ApJ, 637, 850
Klassen M., Pudritz R. E., Kuiper R., Peters T., Banerjee R., 2016, ApJ, 823, 28
Kobulnicky H. A. et al., 2014, ApJS, 213, 34
Kolb S. M., Stute M., Kley W., Mignone A., 2013, A&A, 559, A80
Kraus S. et al., 2017, ApJ, 835, L5
Krumholz M. R., Klein R. I., McKee C. F., 2007, ApJ, 665, 478
Langer N., 2012, ARA&A, 50, 107
Laor A., Draine B. T., 1993, ApJ, 402, 441
Lumsden S. L., Hoare M. G., Urquhart J. S., Oudmaijer R. D., Davies B., Mottram J. C., Cooper H. D. B., Moore T. J. T., 2013, ApJS, 208, 11
MacLeod G. C. et al., 2018, MNRAS, 478, 1077
Mahy L., Rauw G., De Becker M., Eenens P., Flores C. A., 2013, A&A, 550, A27
Maud L. T. et al., 2018, A&A, 620, A31
Maud L. T., Hoare M. G., Galván-Madrid R., Zhang Q., de Wit W. J., Keto E., Johnston K. G., Pineda J. E., 2017, MNRAS, 467, L120
McMullin J. P., Waters B., Schiebel D., Young W., Golap K., 2007, in Shaw R. A., Hill F., Bell D. J., eds, ASP Conf. Ser. Vol. 376, Astronomical Data Analysis Software and Systems XVI, CASA Architecture and Applications. Astron. Soc. Pac., San Francisco, p. 127
Meyer D. M.-A., van Marle A.-J., Kuiper R., Kley W., 2016, MNRAS, 459, 1146
Meyer D. M.-A., Vorobyov E. I., Kuiper R., Kley W., 2017, MNRAS, 464, L90
Meyer D. M.-A., Kuiper R., Kley W., Johnston K. G., Vorobyov E., 2018, MNRAS, 473, 3615
Meyer D. M.-A., Vorobyov E. I., Elbakyan V. G., Stecklum B., Eislöffel J., Sobolev A. M., 2019, MNRAS, 482, 5459
Meyer D. M.-A., Haemmerlé L., Vorobyov E. I., 2019, MNRAS, 484, 2482
Mignone A., Bodo G., Massaglia S., Matsakos T., Tesileanu O., Zanni C., Ferrari A., 2007, ApJS, 170, 228
Mignone A., Zanni C., Tzeferacos P., van Straalen B., Colella P., Bodo G., 2012, ApJS, 198, 7
Norberg P., Maeder A., 2000, A&A, 359, 1025
Palla F., Stahler S. W., 1992, ApJ, 392, 667
Purser S. J. D. et al., 2016, MNRAS, 460, 1039
Purser S. J. D., Lumsden S. L., Hoare M. G., Cunningham N., 2018, MNRAS, 475, 2
Regály Z., Vorobyov E., 2017, A&A, 601, A24

Reid M. J. et al., 2009, ApJ, 700, 137
Reiter M., Kiminki M. M., Smith N., Bally J., 2017, MNRAS, 470, 4671
Samal M. R., Chen W. P., Takami M., Jose J., Froebrich D., 2018, MNRAS, 477, 4577
Sana H. et al., 2012, Science, 337, 444
Sanna A. et al., 2019, A&A, 623, A77
Seifried D., Banerjee R., Klessen R. S., Duffin D., Pudritz R. E., 2011, MNRAS, 417, 1054
Seifried D., Sánchez-Monge Á., Walch S., Banerjee R., 2016, MNRAS, 459, 1892
Stecklum B., Heese S., Wolf S., Garatti A. C. o., Ibanez J. M., Linz H., 2017, preprint (arXiv:1712.01451)
Tapia M., Roth M., Persi P., 2015, MNRAS, 446, 4088
Vaidya B., Fendt C., Beuther H., Porth O., 2011, ApJ, 742, 56
Vink J. S., de Koter A., Lamers H. J. G. L. M., 2000, A&A, 362, 295
Vorobyov E. I., Basu S., 2010, ApJ, 719, 1896
Vorobyov E. I., DeSouza A. L., Basu S., 2013, ApJ, 768, 131
Vorobyov E. I., Zakhozhay O. V., Dunham M. M., 2013, MNRAS, 433, 3256
Wootten A., Thompson A. R., 2009, IEEE Proc. 97, 1463
Zinchenko I. et al., 2015, ApJ, 810, 10
Zinnecker H., Yorke H. W., 2007, ARA&A, 45, 481

This paper has been typeset from a TEX/LATEX file prepared by the author.

Monthly Notices
of the
ROYAL ASTRONOMICAL SOCIETY

MNRAS **500,** 4448–4468 (2021)
Advance Access publication 2020 November 17

doi:10.1093/mnras/staa3528

Parameter study for the burst mode of accretion in massive star formation

D. M.-A. Meyer [1]★ E. I. Vorobyov,[2,3] V. G. Elbakyan [4] J. Eislöffel,[5] A. M. Sobolev [6] and M. Stöhr[7,8]

[1]*Institut für Physik und Astronomie, Universität Potsdam, Karl-Liebknecht-Strasse 24/25, D-14476 Potsdam, Germany*
[2]*Department of Astrophysics, The University of Vienna, A-1180 Vienna, Austria*
[3]*Institute of Astronomy, Russian Academy of Sciences, Pyatnitskaya str. 48, Moscow 119017 , Russia*
[4]*School of Physics and Astronomy, University of Leicester, Leicester, LE1 7RH, United-Kingdom*
[5]*Thüringer Landessternwarte Tautenburg, Sternwarte 5, D-07778 Tautenburg, Germany*
[6]*Ural Federal University, 51 Lenin Str., 620051 Ekaterinburg, Russia*
[7]*VSC Research Center, TU Wien, Operngasse 11, A-1040 Vienna, Austria*
[8]*BOKU-IT, University of Natural Resources and Life Sciences, Peter-Jordan-Strasse 82, A-1190 Vienna, Austria*

Accepted 2020 November 9. Received 2020 October 28; in original form 2020 June 6

ABSTRACT

It is now a widely held view that, in their formation and early evolution, stars build up mass in bursts. The burst mode of star formation scenario proposes that the stars grow in mass via episodic accretion of fragments migrating from their gravitationally unstable circumstellar discs, and it naturally explains the existence of observed pre-main-sequence bursts from high-mass protostars. We present a parameter study of hydrodynamical models of massive young stellar objects (MYSOs) that explores the initial masses of the collapsing clouds ($M_{\rm c} = 60$–$200\,{\rm M}_{\odot}$) and ratio of rotational-to-gravitational energies ($\beta = 0.005$–0.33). An increase in $M_{\rm c}$ and/or β produces protostellar accretion discs that are more prone to develop gravitational instability and to experience bursts. We find that all MYSOs have bursts even if their pre-stellar core is such that $\beta \leq 0.01$. Within our assumptions, the lack of stable discs is therefore a major difference between low- and high-mass star formation mechanisms. All our disc masses and disc-to-star mass ratios $M_{\rm d}/M_{\star} > 1$ scale as a power law with the stellar mass. Our results confirm that massive protostars accrete about $40 - 60$ per cent of their mass in the burst mode. The distribution of time periods between two consecutive bursts is bimodal: there is a short duration ($\sim 1 - 10$ yr) peak corresponding to the short, faintest bursts and a long-duration peak (at $\sim 10^3 - 10^4$yr) corresponding to the long, FU-Orionis-type bursts appearing in later disc evolution, i.e. around 30 kyr after disc formation. We discuss this bimodality in the context of the structure of massive protostellar jets as potential signatures of accretion burst history.

Key words: methods: numerical – stars: evolution – stars: circumstellar matter – stars: flare.

1 INTRODUCTION

Stars are born in collapsing pre-stellar cores, made of cold molecular material. Although the early, classical picture for star formation concluded that young stellar objects gain their mass by constant mass accretion via spherical accretion (Larson 1969; Shu 1977), the free-falling gas landing on to an accretion disc rather than interacting with the protostellar surface. This continual mass loading sustains the disc in a gravitationally unstable state, which is characterized by highly variable accretion rates, in agreement with those monitored by observations of low-mass star-forming regions (Vorobyov 2009). Among many disc-based models developed to describe the way stars gain their mass, the burst mode of accretion is a picture developed in the context of the formation of low-mass stars (Vorobyov & Basu 2006, 2010, 2015). This depiction of star formation processes includes the gravitational collapse of a parent cloud, followed by the establishment and fragmentation of a gravitationally unstable circumstellar accretion disc, and the inward migration of gas clumps towards the star. The inward-migrating clumps trigger an increase of the accretion rate and generate accretion-driven luminosity outbursts as they are tidally destroyed in the vicinity of the star. It was successfully applied to solve the so-called 'luminosity problem', stating that young protostars are on average less luminous than expected from simple spherical collapse calculations (Offner & McKee 2011; Dunham & Vorobyov 2012; Padoan, Haugbølle & Nordlund 2014), showed consistencies with observations of FU-Orionis flares (Vorobyov & Basu 2015), and demonstrated agreement with the knot spacing in protostellar jets (Vorobyov et al. 2018). The clump-infall-triggered mechanism of accretion bursts in low-mass stars was confirmed and further elaborated in three-dimensional (magneto)-hydrodynamical simulations (Zhao et al. 2018) and in semi-analytic studies (Nayakshin & Lodato 2012). These results and the observational discovery of a luminous flare from the massive young stellar object (MYSO) S255IR-NIRS3, triggered by a sudden increase of its accretion rate, raised the question of the existence of a scaling relationship between the forming mechanisms of low- and high-mass stellar objects, respectively.

Observations of the circumstellar medium of proto-OB stars have accumulated, increasing our knowledge of the formation of massive stellar objects. In particular, the works of Fuente et al. (2001), Testi (2003), and Cesaroni et al. (2006) revealed that the mecha-

★ E-mail: dmameyer.astro@gmail.com

nisms involved in the formation of massive stars are characterized by the presence of certain features such as converging accretion flows (Keto & Wood 2006) and jets (Cunningham, Moeckel & Bally 2009; Caratti o Garatti et al. 2015; Burns et al. 2017; Reiter et al. 2017; Burns 2018; Purser et al. 2018; Samal et al. 2018; Boley et al. 2019; Zinchenko et al. 2019). Differences lie in the fact that young massive stars exhibit lobed bubbles of ionized gas (Cesaroni et al. 2010; Purser et al. 2016). At the same time, a growing number of (Keplerian) disc-like structures has been reported in interferometric observations (Johnston et al. 2015; Forgan et al. 2016; Ilee et al. 2016; Ahmadi et al. 2018; Ginsburg et al. 2018; Maud et al. 2018; Beuther et al. 2019; Sanna et al. 2019), some of them revealing the presence of substructures in it such as MM1-Main (Maud et al. 2017), the massive double-core proto-system G350.69-0.49 (Chen et al. 2017), the protomassive object G11.920.61 MM 1 (Ilee et al. 2018), the AFGL 4176 mm1 (Johnston et al. 2019), the O-type (proto-)star G17.64 + 0.16 (Maud et al. 2019), and G353.273 + 0.641 (Motogi et al. 2019), suggesting similar qualitative formation mechanisms to those in the low-mass regime of star formation (Bosco et al. 2019), see also Wurster & Bate (2019b) and Wurster & Bate (2019a). Most recent high-angular ALMA observations in the region S255IR-SMA1 show a clear consistency between the predictions of the burst mode of accretion in high-mass star formation and the properties of the accretion flow of the circumstellar medium of S255IR-NIRS3 (Liu et al. 2020).

These observations have been supported by 3D hydrodynamics and radiative transfer calculations, predicting how accretion discs surrounding young high-mass stars form (Bonnell, Bate & Zinnecker 1998; Yorke & Sonnhalter 2002; Krumholz, Klein & McKee 2007; Peters et al. 2010; Seifried et al. 2011; Harries 2015; Klassen et al. 2016; Harries, Douglas & Ali 2017; Rosen et al. 2019; Ahmadi, Kuiper & Beuther 2019; Añez-López et al. 2020). Multiplicity, as an indissociable characteristic of massive star formation, suggests that disc fragmentation can play a crucial role in the formation of the (spectroscopic) companions observed in most systems involving OB stars (Chini et al. 2012; Mahy et al. 2013; Kobulnicky et al. 2014; Kraus et al. 2017). Young massive stars are also sites of strongly variable maser emission, see, in particular, strong maser flares of the MYSOs NGC 6334 I, S255IRNIRS3, and G358.93-0.03 associated with accretion bursts (MacLeod et al. 2018; Szymczak et al. 2018; Burns et al. 2020). It is now established that the methanol emission traces accretion discs around MYSOs (Sanna et al. 2017, and references therein) while water maser emission traces well outflows from these objects (Brogan et al. 2018, and references therein). New maser species and a growing number of Class II CH3OH maser lines are discovered from massive star-forming regions (Brogan et al. 2018; Breen et al. 2019; MacLeod et al. 2019; Chen et al. 2020b). Lastly, it is worth mentioning the evidence of non-thermal synchrotron emission from the outflows reported in a number of MYSOs (Carrasco-González et al. 2010; Obonyo et al. 2019) and probable detection of the synchrotron emission from accretion disc (Shchekinov & Sobolev 2004). It is now established that water maser emission traces well protostellar outflows (Hunter 2019) and a growing number of Class II CH_3OH maser lines are discovered from massive star-forming regions. Lastly, it is worth mentioning that the evidence for non-thermal synchrotron radiation from an outflow originating from an MYSO has been reported in Obonyo et al. (2019).

The radiation–hydrodynamics simulations of Meyer et al. (2017) discovered the burst mode of accretion in the formation of massive stars. The bursts are triggered by the accretion of fast-moving circumstellar gaseous clumps, which migrate inwards from the gravitationally fragmenting spiral arms towards the star. Moreover, we showed that some fragments have internal thermodynamical properties (e.g. temperature $> 2000 - 3000$ K) consistent with the onset of molecular hydrogen dissociation and run-away collapse, showing the disc fragmentation channel to be a viable route for making high-mass spectroscopic protobinaries (Meyer et al. 2018). The setups developed for the burst mode in accretion by Meyer et al. (2017) and Meyer et al. (2018) have been further elegantly used in André Oliva & Kuiper (2020). We then calculated that MYSOs spend only (≤ 2 per cent) in the bursting phase, while they can therethrough accrete up to 50 per cent of their final mass (Meyer et al. 2019a). The episodic increase of the mass transfers on to the surface of the protostar induces bloating of its radius, provoking quick excursions towards redder region of the temperature–luminosity diagram. This process is accompanied by intermittency of the photon fluxes, which fill and irradiate the bipolar outflow as an H II region (Meyer, Haemmerlé & Vorobyov 2019b). Lastly, we have performed synthetic images of the accretion discs around our massive protostars and predicted their ALMA signature (Meyer et al. 2019c; Jankovic et al. 2019). However, given to the computationally expensive aspect of massive star formation calculations, such results were so far obtained on a limited number of star–disc models, which raises the question of the effects of the pre-stellar core properties used as initial conditions in numerical simulations.

This paper performs a parameter study for the burst mode of accretion in the context of forming high-mass stars. Using methods developed in Meyer et al. (2017), we investigate here the effects of the mass of the core, together with its rotational-to-gravitational energy ratio, on the accretion history and protostellar mass evolution. For each model, we analyse (i) the disc properties developing around the protostars and (ii) the accretion-driven burst properties, using the method presented in Meyer et al. (2019a). If such a parameter study is original for high-mass stars, similar works exist for low-mass stars Vorobyov (2011a). Our results show that, in opposite to low-mass star formation, all models exhibit highly variable accretion rate histories and that their associated light curves are interspersed with episodic bursts, i.e. no young massive stars appear to be burstsless. Particularly, we discuss our findings within observations of massive protostars, which exhibited accretion variability and/or (probable signs of) disc fragmentation, such as S255IR-NIRS3 and NGC 6334I-MM1. We further consider our results in connection with the morphology and temporal domain of protostellar jets of some massive protostars.

In Section 2, we introduce our numerical methods and specify which parameter space is explored in this paper. We detail the properties of our simulated accretion discs in Section 3 and analyse the burst properties for our whole sample of MYSOs in Section 4. Our outcomes are discussed in Section 5 and we conclude in Section 6.

2 METHOD

We hereby present our numerical methods and initial conditions used to perform our gravito-radiation-hydrodynamics disc models, from which we extract accretion discs masses and time-dependent protostellar accretion rate histories.

2.1 Governing equations

The hydrodynamics of the gas obeys the conservation of mass,

$$\frac{\partial \rho}{\partial t} + \nabla \cdot (\rho \boldsymbol{v}) = 0, \quad (1)$$

the conservation of momentum

$$\frac{\partial \rho \boldsymbol{v}}{\partial t} + \nabla \cdot (\rho \boldsymbol{v} \otimes \boldsymbol{v}) + \nabla p = \boldsymbol{f}, \tag{2}$$

and the conservation of energy

$$\frac{\partial E}{\partial t} + \nabla \cdot ((E + p)\boldsymbol{v}) = \boldsymbol{v} \cdot \boldsymbol{f}, \tag{3}$$

with the fluid density ρ, velocity $\boldsymbol{v}$, and thermal pressure p. The latter is defined as

$$p = (\gamma - 1)E_{\rm int}, \tag{4}$$

with the adiabatic index $\gamma = 5/3$. In equation (4), $E_{\rm int}$ stands for the gas internal energy, and the total energy is written as

$$E = E_{\rm int} + \rho \frac{1}{2}\boldsymbol{v}^2. \tag{5}$$

Our model considers the total gravitational potential

$$\Phi_{\rm tot} = \Phi_\star + \Phi_{\rm sg}, \tag{6}$$

where the stellar contribution reads

$$\Phi_\star = -G\frac{M_\star}{r}, \tag{7}$$

with $M_\star$ being the protostellar mass and G the universal constant of gravity. Self-gravity is found by numerically solving for the Poisson equation

$$\boldsymbol{\Delta}\Phi_{\rm sg} = 4\pi G\rho. \tag{8}$$

Our setup does not include artificial shear viscosity (Hosokawa et al. 2016).

The source term function $\boldsymbol{f}$ in equations (2) and (3) is the force density vector. It reads

$$\boldsymbol{f} = -\rho\nabla\Phi_{\rm tot} - \lambda\nabla E_{\rm R} - \nabla \cdot \left(\frac{\boldsymbol{F}_\star}{c}\right)\boldsymbol{e}_{\rm r}, \tag{9}$$

where λ represents the flux limiter, $E_{\rm R}$ the thermal radiation energy density, $\boldsymbol{e}_{\rm r}$ the radial unit vector, $\boldsymbol{F}_\star$ the stellar radiation flux, and c the speed of light. The equation of radiation transport,

$$\frac{\partial}{\partial t}\left(\frac{E_{\rm R}}{f_{\rm c}}\right) + \nabla \cdot \boldsymbol{F} = -\nabla \cdot \boldsymbol{F}_\star, \tag{10}$$

governs the thermal radiation energy density $E_{\rm R}$ with

$$f_{\rm c} = \frac{1}{\frac{c_{\rm v}\rho}{4aT^3} + 1}, \tag{11}$$

where a is the radiation constant and $c_{\rm v}$ the specific heat capacity. We solve it within the so-called flux-limited diffusion formalism, i.e.

$$\boldsymbol{F} = -D\nabla E_{\rm R} \tag{12}$$

stands for the radiation flux with the diffusion constant,

$$D = \frac{\lambda c}{\rho\kappa_{\rm R}}, \tag{13}$$

with the average Rosseland opacity $\kappa_{\rm R}$. Therefore,

$$\frac{\boldsymbol{F}_\star(r)}{\boldsymbol{F}_\star(R_\star)} = \left(\frac{R_\star}{r}\right)^2 e^{-\tau(r)} \tag{14}$$

accounts for diminishing the incident stellar radiation flux as it penetrates through the circumstellar medium.

The quantity $R_\star$ denotes the radius of the MYSO and the optical depth of the medium is

$$\tau(r) = \int_{r_{\rm in}}^{r} G(r')dr', \tag{15}$$

while the total opacity includes radiation attenuation by dust and gas, with in the inner boundary of the grid in the radial direction (see below). The function $G(r)$ reads,

$$G(r) = \kappa_{\rm g}\rho_{\rm g}(r) + \kappa_{\rm d}(r)\rho_{\rm d}(r), \tag{16}$$

where the quantities $\kappa_{\rm d}$ and $\kappa_{\rm g}$ are the opacities of the dust and gas components of the disc material, respectively. The gas-to-dust mass ratio is initially set to 100, the gas opacity is taken to a constant value $\kappa_{\rm g} = 0.01\ {\rm cm^2\ g^{-1}}$, while the opacity of the dust comes from Laor & Draine (1993). Therefore,

$$aT^4 = E_{\rm R} + \frac{\kappa(r)}{\kappa_{\rm P}(T)}\frac{|\boldsymbol{F}_\star|}{c}, \tag{17}$$

with

$$\kappa(r) = \kappa_{\rm g}(r) + \kappa_{\rm d}(r), \tag{18}$$

using $\kappa_{\rm P}$, the Planck opacity. Lastly, the stellar flux $\boldsymbol{F}_\star(R_\star)$ through the sink cell is the total irradiation, constituted by $L_\star$, the photospheric luminosity, and the accretion luminosity of the MYSO. The values of the effective temperature $T_{\rm eff}$ and stellar radius $R_\star$ are taken from the stellar evolutionary tracks of Hosokawa & Omukai (2009).

2.2 Numerical scheme, initial conditions, and parameter space

The 3D models are carried out in spherical coordinates (r, θ, ϕ) with a static grid. Under the simplifying assumption of the mid-plane symmetry, the size of the grid is $[r_{\rm in}, r_{\rm max}] \times [0, \pi/2] \times [0, 2\pi]$ along the different radial, polar, and azimuthal directions. It is constructed of $128 \times 21 \times 128$ grid zones, while the mesh expands along r as a logarithm, along θ as a cosine, and is kept uniform along ϕ. The inner and outer boundaries are $r_{\rm in} = 10$ AU and $r_{\rm max} = R_{\rm c} = 0.1$ pc, where $R_{\rm c}$ stands for the core radius, respectively. Outflow conditions are assigned at both boundaries of the radial directions r so that we can measure the accretion rate on to the protostar $\dot{M}$ as the mass of the gas crossing $r_{\rm in}$. The set of above described equations are solved using a second order in space and time numerical scheme with the PLUTO code (Mignone et al. 2007, 2012), including stellar evolution, radiation transport, and self-gravity (Meyer et al. 2017, 2018). Our scheme treats the protostellar radiation by which the photons propagate from the atmosphere of the MYSO to the accretion disc and their subsequent propagation into the disc by flux-limited diffusion performed in the grey approximation. Finally, our multidimensional scheme is solved making use of the Strang operator splitting available in the PLUTO code, which permits to calculate fluxes such as radiation fluxes as a series of independent one-dimensional problems.

We initialize our models with a spinning molecular core characterized by the density profile,

$$\rho(r) = K_\rho r^{\beta_\rho}, \tag{19}$$

with K_ρ being a constant and where β_ρ is negative. The core mass that is embedded inside a given radius r is

$$M(r) = M_{\rm c}\left(\frac{r}{R_{\rm c}}\right)^{\beta_\rho+3}, \tag{20}$$

and it determines the quantity K_ρ. Hence, one can find the density profile,

$$\rho(r) = \frac{(\beta_\rho + 3)}{4\pi}\frac{M_{\rm c}}{R_{\rm c}^{\beta_\rho+3}}r^{\beta_\rho}, \tag{21}$$

where r is the radial coordinate. The angular momentum distribution is

$$\Omega(R) = \Omega_0\left(\frac{R}{r_0}\right)^{\beta_\Omega}, \tag{22}$$

with

$$R = r\sin(\theta) \tag{23}$$

the so-called cylindrical radius and Ω_0 a normalization constant. It is a function of the ratio of kinetic-to-gravitational energy,

$$\beta = \frac{E_{\rm rot}}{E_{\rm grav}}, \tag{24}$$

which fixes the initial rotation properties of the system. Finally, the cloud total gravitational energy reads

$$E_{\rm grav} = \frac{\beta_\rho + 3}{2\beta_\rho + 5}\frac{GM_{\rm c}^2}{R_{\rm c}}, \tag{25}$$

whereas its rotational kinetic energy is,

$$E_{\rm rot} = \frac{(\beta_\rho + 3)}{4(\beta_\rho + 2\beta_\Omega + 5)}\frac{\Omega_0^2 M_{\rm c} r_0^{-2\beta_\Omega}}{R_{\rm c}^{-2(\beta_\Omega+1)}}\int_0^\pi d\theta\,\sin(\theta)^{3+2\beta_\Omega}, \tag{26}$$

which must be solved prior to the numerical simulations to find Ω_0. We initially set the molecular core with $\beta = 4$ per cent. The radial profile for the distribution reads,

$$v_\phi(R) = R\Omega(R), \tag{27}$$

but $v_{\rm r} = 0$ and $v_\theta = 0$. The system's thermal pressure is

$$p = \frac{R\rho T_{\rm c}}{\mu}, \tag{28}$$

where μ is the mean molecular weight, R is the ideal gas constant, and where $T_{\rm c} = 10\,{\rm K}$ is the core temperature. We initialize the simulations by setting

$$T_{\rm d} = T_{\rm g} = T_{\rm c}, \tag{29}$$

and we do not distinguish between gas and dust temperature throughout the simulation.

The gas and dust temperatures are obtained by solving equation (17) where $E_{\rm R}$ is calculated from equation (10).

We run a series of simulations exploring the effects of the mass $M_{\rm c}$ and the initial ratio β of the pre-stellar core. Instead of running the simulations up to the complete collapse of all the core material, we implicitly account for stellar feedback and its role in stopping accretion. Estimating when a protostar reaches the ZAMS is complicated; however, our stellar evolution calculations in Meyer et al. (2019b) concluded that a $100\,{\rm M}_\odot$ cloud with $\beta = 4$ per cent produces a protostar reaching the ZAMS (zero-age main sequence) ≈ 50 kyr after the beginning of the collapse, when $M_{\rm c}/3 \approx 33.3\,{\rm M}_\odot$ of the core has been accreted. This is the criterion we applied as an educated guess to terminate the simulations for the line of increasing $M_{\rm c}$. Otherwise, the mass loading from the infalling core would continue to replenish the disc with material during the entire collapse phase if the simulation had been allowed to continue. It would thus sustain strong gravitational instability and fragmentation and hence the production of bursts which qualitative properties would remain unchanged with respect to the present study. We summarize our models in Table 1.

3 DISCS PROPERTIES

This section investigates the protostellar mass evolution, the mass of the accretion disc, and the ratio of the disc-to-star masses in our simulations for the formation of young massive stellar objects. We discuss these quantities for the different initial conditions of our models (masses and spins of parent pre-stellar cores).

Table 1. Initial characteristics of the solid-body-rotating pre-stellar cores in our grid of simulations. The table gives the mass of the molecular pre-stellar core $M_{\rm c}$, the ratio of rotational-to-gravitational energy β (in %), the final simulation time $t_{\rm end}$, and the final stellar mass $M_\star(t_{\rm end})$ of each model, respectively.

Models	$M_{\rm c}$ ($\rm M_\odot$)	β (%)	$t_{\rm end}$ (kyr)	$M_\star(t_{\rm end})$
Run − 60 − 4%[a]	60	4	65.2	20.0
Run − 80 − 4%	80	4	53.6	26.6
Run − 100 − 4%[a]	100	4	47.6	33.3
Run − 120 − 4%	120	4	44.3	40.0
Run − 140 − 4%	140	4	41.0	46.6
Run − 160 − 4%	160	4	39.0	53.3
Run − 180 − 4%	180	4	36.5	60.0
Run − 200 − 4%	200	4	33.7	66.6
Run − 60 − 0.1%	60	0.1	60.0	41.6
Run − 60 − 0.3%	60	0.3	60.0	31.6
Run − 60 − 0.5%	60	0.5	60.0	29.9
Run − 60 − 1%	60	1	60.0	13.7
Run − 100 − 2%	100	2	60.0	51.6
Run − 100 − 5%[b]	100	5	60.0	41.5
Run − 100 − 6%	100	6	60.0	39.3
Run − 100 − 8%	100	8	60.0	34.0
Run − 100 − 10%[b]	100	10	60.0	34.1
Run − 100 − 12%	100	12	60.0	33.8
Run − 100 − 14%	100	14	60.0	29.5
Run − 100 − 16%	100	16	60.0	29.6
Run − 100 − 18%	100	18	60.0	22.2
Run − 100 − 20%	100	20	60.0	25.0
Run − 100 − 25%	100	25	60.0	19.8
Run − 100 − 33%	100	33	60.0	27.4

[a]Meyer et al. (2018) and Meyer et al. (2019b). [b]Meyer et al. (2019a).

3.1 Gravitational collapse and disc fragmentation

Fig. 1 reports the collection of accretion rate histories on to the MYSOs that we obtained in this parameter study. The accretion rates (thin blue line, in $\rm M_\odot\,yr^{-1}$) are displayed starting from the early simulation time, when the gravitational collapse is initiated, up to the moment we stop the simulations, i.e. as soon as the protostellar mass has reached $M_\star = M_{\rm c}/3$ for the runs with changing $M_{\rm c}$ and to 60 kyr for the runs with changing β, respectively. The rates with different pre-stellar core mass are in Figs 1(a)–(h) and the rates with changing β are displayed in Figs 1 (i)–(t). In the rest of this paper, we will refer to these series of simulations as the 'line of increasing $M_{\rm c}$' and the 'line of increasing β', respectively; see also Vorobyov (2010) and Vorobyov (2011b). The last series of models with $M_{\rm c} = 60\,{\rm M}_\odot$ and $\beta \leq 1$ per cent explores the effect of lower initial spin of the core on to the formation of high-mass stars (Figs 1 u–x).

After the very initial rise of $\dot{M}$ during the free-fall collapse of the parent molecular core, the protostar ceases accreting envelope material as the gas lands on a centrifugally balanced disc, while it starts acquiring its mass by accretion of disc material (Fig. 1). The accretion rate shows variability once the disc has formed since it mirrors the anisotropies of the accretion flow (Meyer et al. 2018). They are caused by the development of dense spiral arms and clumps in the disc produced by efficient gravitational fragmentation. These variations in the accretion rate continue after the disc formation and they are interspersed by violent accretion spikes of increasing occurrence as the disc growths (Meyer et al. 2019a). These strong bursts are repeatedly produced by the quick inward migration of dense fragments in the disc, themselves formed by gravitational fragmentation and generating accretion-driven outbursts (Meyer et al. 2017).

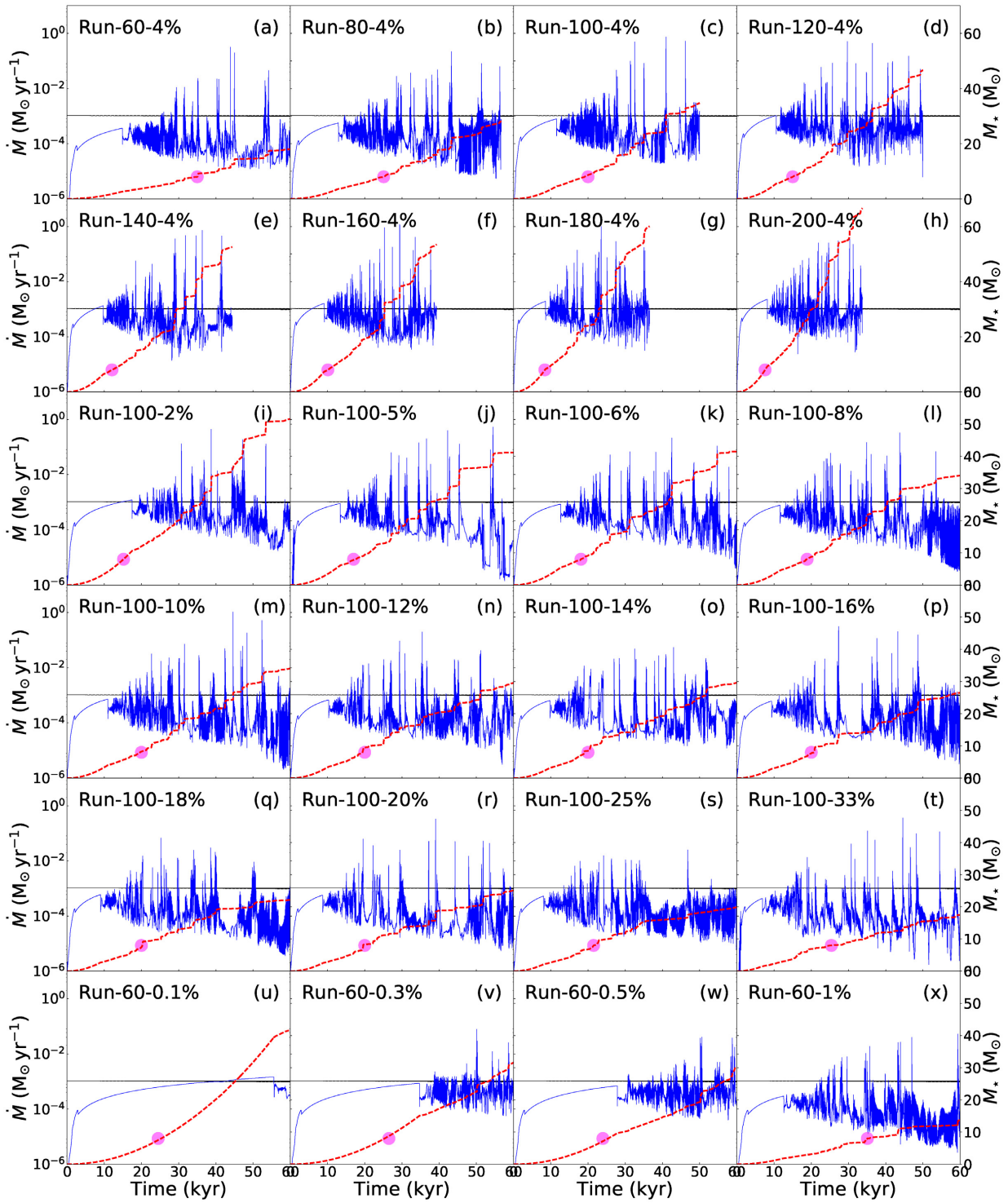

Figure 1. Accretion rate histories $\dot{M}(t)$ in our parameter study. For each 20 models, the figure shows the accretion rate (in $\mathrm{M}_\odot\ \mathrm{yr}^{-1}$, thin blue line) and the time evolution of the stellar mass $M_\star(t)$ (thick dotted red line, in $\mathrm{M}_\odot$). The thin horizontal black line indicates a rate of $\dot{M} = 10^{-3}\,\mathrm{M}_\odot\ \mathrm{yr}^{-1}$, and the magenta dot marks times where the protostar enters the high-mass regime ($M_\star = 8\,\mathrm{M}_\odot$).

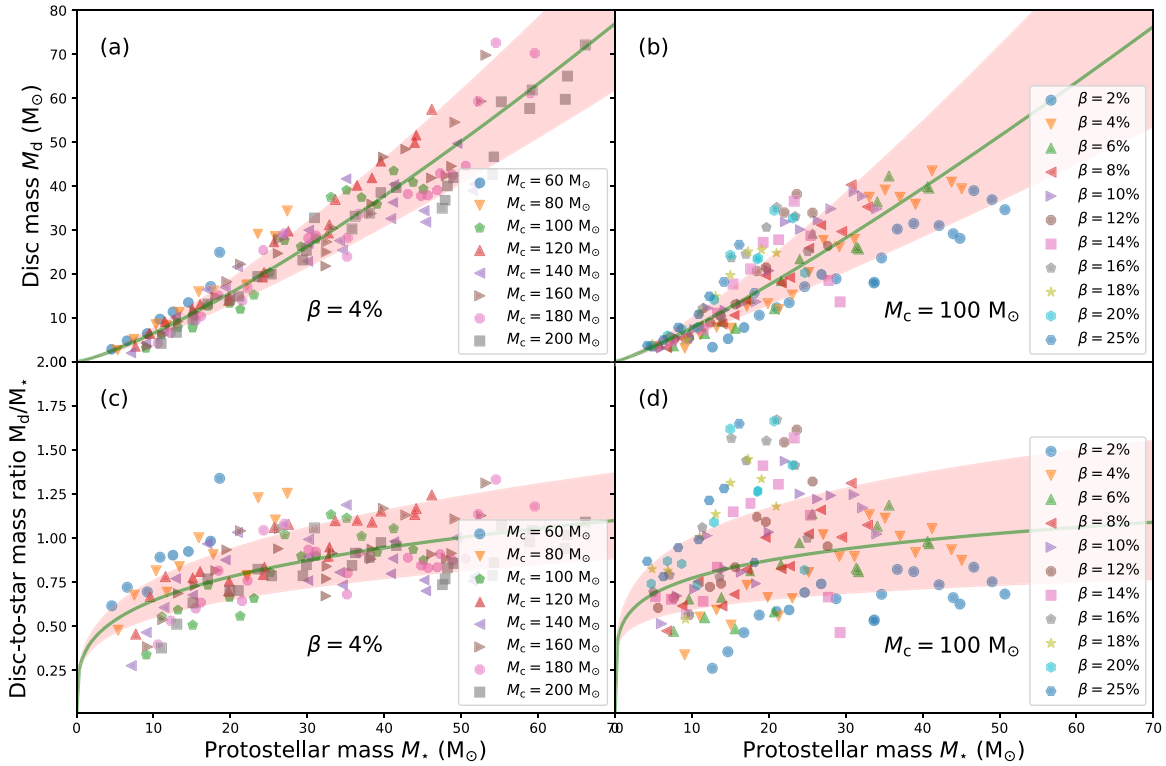

Figure 2. Disc masses $M_\star$ (in $M_\odot$, top panels) and ratio of the disc-to-star masses $M_d/M_\star$ (bottom panels) shown according to the protostellar mass $M_\star$ (in $M_\odot$) for all models with changing core mass M_c (left panels) and for all models with changing β-ratio (right panels). The green lines show the power-law fits, respectively, and the red zone represents the errors to the fits.

The Toomre parameter estimates the disc gravitational instability by evaluating the respective effects of gas self-gravity versus that of stabilizing disc thermal pressure and rotational shear induced by Keplerian rotation (Toomre 1963). Hence, the condition for Toomre instability is,

$$Q = \frac{\kappa c_s}{\pi G \Sigma} \leq Q_{\rm crit}, \tag{30}$$

where c_s is the sound speed of the gas, Σ the column mass density of the disc, and κ the local epicyclic frequency (Durisen et al. 2007). Fragmentation of spiral arms into compact gaseous clumps may develop if $Q_{\rm crit} \leq 1$, although recent studies derived $Q_{\rm crit} < 0.6$; see the study of Meyer et al. (2018). Q-unstable discs are made of dense regions representing spiral arms, which are more prone to fragmentation (Klassen et al. 2016).

The exact nature of disc fragmentation is nevertheless a problem of which complexity cannot be reduced to the sole Toomre criterion. Let us review other criteria for the sake of completeness. The comparison between the local effects of disc thermodynamics regarding the rotation-induced shear is known as the co-called Gammie criterion that reads (Meyer et al. 2018)

$$\beta = t_{\rm cool}\Omega_K \leq \frac{2\pi}{\sqrt{1-Q^2}}, \tag{31}$$

with the Keplerian frequency,

$$\Omega_K = \sqrt{\frac{GM_\star}{r^3}}, \tag{32}$$

with $t_{\rm cool}$ the local cooling time-scale (Gammie 2001). In the precedent papers of this series, we have shown that this criterion is satisfied in the warm spiral arms location as well as in the blobs; however, it is not sufficient to characterize fragmentation as the interarm regions were β-unstable (Meyer et al. 2018). Note that the Gammie criterion is approximate and exclusively applies to axisymmetric accretion discs. The last criterion based on the Hill radius measures the capability of spiral arm segments to locally keep on gaining mass to eventually fragment by confronting the consequences of self-gravity versus the stellar tidal forces engendering shears in the disc (Rogers & Wadsley 2012). A spiral arm of local cross-section l is therefore subject to instability if,

$$\frac{l}{2R_{\rm Hill}} < 1, \tag{33}$$

with $R_{\rm Hill}$ the so-called the Hill radius. Material lying more than 2 $R_{\rm Hill}$ of a given region fragment will not feel the gravity of the local dense region but will have its evolution governed by the overall disc dynamics. For discs around high-mass stars, the Hill-radius-based criterion of Rogers & Wadsley (2012) has been shown to be more consistent with numerical simulations (Meyer et al. 2018).

3.2 Disc and masses of the MYSOs

Top panels of Fig. 2 show the masses M_d of the disc (in $M_\odot$) versus the protostellar mass $M_\star$ (in $M_\odot$) regarding the line of increasing pre-stellar core mass ($\beta = 4$ per cent, panel a) and for the line of

increasing β-ratio ($M_c = 100\,M_\odot$, panel b). For each model, the stellar mass is calculated as being a proportion of the gas mass leaving the computational domain per unit time through the inner region of the accretion disc, i.e.

$$M_\star(t) = \int_0^t \dot{M}(t')dt', \tag{34}$$

where t denotes the time at which the protostellar mass $M_\star = M_\star(t)$ is calculated. Similarly, the disc mass $M_d(t)$ is estimated for each output of the simulation, following the method used in Klassen et al. (2016). The disc mass in the figure is sampled starting from the end of the gravitational collapse and each data point is represented by a symbol and the colour coding distinguishes the models with $M_c = 60$-$200\,M_\odot$ (Fig. 2a) and with $\beta = 2$-25 per cent (Fig. 2b), respectively. Each coloured symbol therefore corresponds to a MYSO produced out of a distinct pre-stellar core, characterized by both a specific mass and spin. The overplotted solid green lines are fits using a power law of the model data, respectively.

The data distribution in Fig. 2 suggests a correlation between M_d and $M_\star$. We performed the least-squares regressions (solid green) and found the following relations,

$$\left(M_{d,\beta=4\text{ per cent}}\right) = 10^{-0.46\pm0.042}\left(M_{\star,\beta=4\text{ per cent}}^{1.27\pm0.029}\right), \tag{35}$$

and

$$\left(M_{d,\frac{M_c}{M_\odot}=100}\right) = 10^{-0.29\pm0.063}\left(M_{\star,\frac{M_c}{M_\odot}=100}^{1.17\pm0.049}\right), \tag{36}$$

where the subscripts β and M_c stand for the lines of increasing spin pre-stellar core and spin, respectively. The time sampling of the disc mass history to construct Fig. 2(a) may also influence the data distribution in the M_d–$M_\star$ plane which, in its turn, makes the finding of a best fit somehow uneasy. However, the power-law fits (solid green line) match fairly well except for $M_c \gg 60\,M_\odot$, meaning that the slope of $\approx$1.27 is relatively good (see equation 35). In our example, the data for high-mass protostars are not as dispersed as those in Vorobyov (2011b) because all the considered models have the same gravitational-to-kinetic ratio $\beta = 4$ per cent. One can immediately see that the models with the heavier pre-stellar cores $M_c \geq 100\,M_\odot$ are slightly offset with respect to the fit, and that the slope of the overall fit might weaken if more models with higher pre-stellar cores $M_c \gg 200\,M_\odot$ will be considered.

In Fig. 2(b), we show the M_d–$M_\star$ plane for the line of increasing β. It reveals more scattering of the data compared that for the line of increasing M_c, meaning that the effect of the core spin on the mass of the disc is more important than that of the core mass. As found by Vorobyov (2011b), faster-rotating, lower mass cores tend to form heavier discs, which results in scattering in the disc mass distribution. In our case, this happens in the 10–30 $M_\odot$ range. The fit might weaken if simulation models with smaller β-ratio are added. Models with initial rotational properties such that $\beta \gg 25$ per cent, populating the upper part of the figure, are rather unrealistic, despite the fact that such models for massive star formation have been produced (Klassen et al. 2016). The models that produce high scattering above the fit are also the models in which the burst activity is weakened, indicating a smaller fragmentation probability of the accretion discs in them; see Tables 2–3.

3.3 Disc-to-star mass ratio

Bottom panels of Fig. 2 show the ratio of the disc-to-star masses, defined as

$$\xi = \frac{M_d}{M_*}, \tag{37}$$

with M_d (in $M_\odot$) the above discussed disc mass and $M_\star$ (in $M_\odot$) the protostellar mass, respectively, for both the line of increasing pre-stellar core mass ($\beta = 4$ per cent, panel c) and for the line of increasing β-ratio ($M_c = 100\,M_\odot$, panel d). The disc mass evolution is sampled starting from the end of the gravitational collapse and each model is represented by a different symbol and colour coding, which helps to distinguish the simulations with $M_c = 60$–$200\,M_\odot$ (Fig. 2c) and with $\beta = 2$-25 per cent (Fig. 2d), respectively. Each coloured symbol therefore represents a single protostar, which has formed out of a distinct pre-stellar core characterized with particular initial conditions of M_c and β-ratios that scan our parameter space for MYSOs. The solid green line is a fit of the model data.

The data distribution in Fig. 2 equivalently suggests a correlation between M_d and $M_\star$. We performed first least-squares fits (solid green lines) and found that

$$\left(\xi_{d,\beta=4\text{ per cent}}\right) = 10^{-0.46\pm0.042}\left(\xi_{\star,\beta=4\text{ per cent}}^{0.27\pm0.029}\right), \tag{38}$$

and

$$\left(M_{d,\frac{M_c}{M_\odot}=100}\right) = 10^{-0.29\pm0.063}\left(M_{\star,\frac{M_c}{M_\odot}=100}^{0.17\pm0.049}\right), \tag{39}$$

where the subscripts β and M_c stand for the lines of increasing spin pre-stellar core and spin, respectively. Fig. 2(c) plots the ξ–$M_\star$ correlation for the line of increasing M_c. The power-law fits agree well except in the range of $M_\star \leq 15\,M_\odot$. The models with lower M_c populate the figure's upper left part, above the fits, while the models with higher M_c are located in the lower part of the figure, where more statistics might exist. No model seems to have $\xi < 0.25$ and all of them have $\xi > 0.5$ as long as the protostellar mass has reached $M_\star \approx 15\,M_\odot$. This can be explained by the substantial mass gained by the discs around protostars, which already entered the high-mass region, while the efficiency of mass transport via gravitational torques in their surrounding accretion discs is not strong enough to compete with the mass inflowing from the still collapsing molecular envelope. Young fragmenting discs with $\xi < 0.25$ should therefore be very unusual along both the lines of increasing M_c and β (Fig. 2d).

The distribution of ξ for the line of increasing β is obviously more scattered than that of the line of increasing M_c as a consequence of the dispersion of the M_c distribution (see Fig. 2) and the fit of the data deviates a lot for $M_\star \leq 30\,M_\odot$. Slowly spinning pre-stellar cores will produce lighter accretion discs and therefore populate the $\xi < 0.5$ region of the figure, while fast-rotating core with high β-ratio will tend to populate the upper left region of the figure in which $\xi > 1.0$, respectively. The increase of ξ is the direct consequence of changes in the mass transport governing mechanism in circumstellar discs. When the disc forms after the cloud collapse, ξ is rather low but it quickly increases as in the disc interior no physical process can yet cope with the infalling envelope. However, when the disc gains sufficient mass for gravitational instability to occur, the resulting torques stimulate protostellar accretion and the mass begins to grow, thus decelerating the initial increase in ξ. As soon as inward migration of dense and heavy clumps is triggered, accompanied by accretion bursts, the disc mass is reduced by an equivalent amount of the clump mass gained by the protostar and ξ decreases, typically in the $M_\star \geq 30\,M_\odot$ mass range. Again, this indicates that the variations of

Table 2. Summary of burst characteristics along the line of increasing β. $N_{\rm bst}$ is the number of bursts at a given magnitude cutoff. $L_{\rm max}/L_{\rm min}/L_{\rm mean}$ are the maximum, minimum, and mean burst luminosities, respectively. Similarly, $\dot{M}_{\rm max}/\dot{M}_{\rm min}/\dot{M}_{\rm mean}$ are the maximum, minimum, and mean accretion rates through the central sink cell and $t_{\rm bst}^{\rm max}/t_{\rm bst}^{\rm min}/t_{\rm bst}^{\rm mean}$ are the maximum, minimum, and mean bursts duration, while $t_{\rm bst}^{\rm tot}$ is the integrated bursts duration time throughout the star's live.

Model	$N_{\rm bst}$	$L_{\rm max}/L_{\rm min}/L_{\rm mean}$ (10^5 L$_\odot$)	$\dot{M}_{\rm max}/\dot{M}_{\rm min}/\dot{M}_{\rm mean}$ (M$_\odot$ yr^{-1})	$t_{\rm bst}^{\rm max}/t_{\rm bst}^{\rm min}/t_{\rm bst}^{\rm mean}$ (yr)	$t_{\rm bst}^{\rm tot}$ (yr)
		1-mag cutoff			
Run-100-2%	38	21.12 / 1.855 / 10.75	0.0194 / 0.0033 / 0.0076	81 / 5 / 16	626
Run-100-4%	33	21.43 / 0.558 / 7.91	0.0180 / 0.0031 / 0.0068	39 / 5 / 13	444
Run-100-5%	21	15.09 / 0.067 / 4.44	0.0190 / 0.0014 / 0.0083	88 / 9 / 26	553
Run-100-6%	36	18.69 / 0.149 / 5.77	0.0222 / 0.0023 / 0.0094	73 / 3 / 22	807
Run-100-8%	29	9.60 / 0.057 / 3.28	0.0301 / 0.0012 / 0.0082	53 / 5 / 15	449
Run-100-10%	44	13.07 / 0.063 / 3.83	0.0228 / 0.0013 / 0.0060	94 / 5 / 16	705
Run-100-12%	30	6.19 / 0.057 / 1.84	0.0198 / 0.0012 / 0.0094	110 / 4 / 26	789
Run-100-14%	30	10.73 / 0.052 / 3.04	0.0216 / 0.0012 / 0.0081	114 / 6 / 27	806
Run-100-16%	30	4.99 / 0.035 / 1.16	0.0209 / 0.0007 / 0.0073	76 / 7 / 28	829
Run-100-18%	26	2.54 / 0.037 / 0.64	0.0160 / 0.0008 / 0.0054	97 / 6 / 31	794
Run-100-20%	7	3.02 / 0.064 / 1.54	0.0241 / 0.0016 / 0.0087	78 / 5 / 27	188
Run-100-25%	21	0.83 / 0.043 / 0.21	0.0148 / 0.0012 / 0.0048	89 / 5 / 41	855
Run-100-33%	6	0.34 / 0.036 / 0.12	0.0116 / 0.0012 / 0.0035	79 / 12 / 39	234
Total all models	27	21.43 / 0.035 / 3.42	0.0301 / 0.0007 / 0.0072	114 / 3 / 25	622
		2-mag cutoff			
Run-100-2%	13	50.44 / 17.752 / 26.67	0.0337 / 0.0127 / 0.0197	40 / 3 / 11	139
Run-100-4%	22	45.60 / 10.495 / 26.62	0.0356 / 0.0117 / 0.0226	56 / 3 / 13	277
Run-100-5%	6	35.66 / 6.385 / 15.34	0.0488 / 0.0104 / 0.0265	17 / 6 / 11	69
Run-100-6%	8	35.15 / 4.124 / 23.22	0.0519 / 0.0150 / 0.0307	14 / 6 / 9	73
Run-100-8%	11	22.62 / 0.221 / 6.81	0.0603 / 0.0044 / 0.0322	44 / 4 / 12	127
Run-100-10%	11	27.96 / 0.201 / 8.32	0.0494 / 0.0040 / 0.0236	74 / 6 / 20	217
Run-100-12%	8	23.31 / 0.146 / 5.18	0.0422 / 0.0031 / 0.0155	78 / 8 / 35	281
Run-100-14%	10	12.68 / 0.144 / 3.48	0.0478 / 0.0033 / 0.0191	80 / 5 / 30	305
Run-100-16%	7	4.25 / 0.211 / 1.10	0.0330 / 0.0042 / 0.0145	60 / 4 / 31	217
Run-100-18%	9	3.38 / 0.188 / 1.24	0.0669 / 0.0037 / 0.0196	87 / 6 / 36	320
Run-100-20%	7	7.63 / 0.129 / 1.75	0.0482 / 0.0035 / 0.0166	81 / 10 / 37	262
Run-100-25%	6	2.99 / 0.150 / 0.68	0.0250 / 0.0038 / 0.0082	91 / 16 / 36	216
Run-100-33%	10	1.84 / 0.116 / 0.46	0.0566 / 0.0031 / 0.0117	68 / 9 / 35	351
Total all models	4	50.44 / 0.116 / 9.30	0.0669 / 0.0031 / 0.0200	91 / 3 / 24	220
		3-mag cutoff			
Run-100-2%	4	117.38 / 30.481 / 68.54	0.1303 / 0.0386 / 0.0711	14 / 5 / 9	37
Run-100-4%	4	65.74 / 13.512 / 50.64	0.0537 / 0.0385 / 0.0466	29 / 4 / 13	52
Run-100-5%	2	37.41 / 4.992 / 21.20	0.0616 / 0.0448 / 0.0532	35 / 8 / 22	43
Run-100-6%	3	44.86 / 11.743 / 26.04	0.0663 / 0.0636 / 0.0651	16 / 6 / 11	32
Run-100-8%	3	70.36 / 40.645 / 52.45	0.0683 / 0.0371 / 0.0558	8 / 3 / 6	18
Run-100-10%	3	38.50 / 9.240 / 23.18	0.0708 / 0.0375 / 0.0559	8 / 3 / 6	17
Run-100-12%	2	6.63 / 0.575 / 3.60	0.0902 / 0.0124 / 0.0513	25 / 10/ 18	35
Run-100-14%	1	12.23 / 12.234 / 12.23	0.0525 / 0.0525 / 0.0525	4 / 4 / 4	4
Run-100-16%	1	10.07 / 10.068 / 10.07	0.1148 / 0.1148 / 0.1148	5 / 5 / 5	5
Run-100-18%	–	–	–	–	–
Run-100-20%	4	15.17 / 0.384 / 7.72	0.0511 / 0.0083 / 0.0345	23 / 4 / 12	46
Run-100-25%	1	0.42 / 0.415 / 0.42	0.0097 / 0.0097 / 0.0097	17 /17 / 17	17
Run-100-33%	5	9.83 / 0.620 / 4.09	0.1124 / 0.0132 / 0.0738	21 / 3 / 7	35
Total all models	3	117.38 / 0.384 / 24.18	0.1303 / 0.0083 / 0.0570	35 / 3 / 11	28
		4-mag cutoff			
Run-100-2%	4	456.50 / 167.523 / 277.06	0.4224 / 0.1057 / 0.2104	22 / 4 / 11	44
Run-100-4%	5	745.03 / 140.465 / 307.95	0.5235 / 0.0929 / 0.2260	9 / 2 / 5	27
Run-100-5%	8	644.26 / 37.481 / 221.32	0.4384 / 0.0804 / 0.2146	10 / 2 / 4	32
Run-100-6%	2	190.73 / 166.192 / 178.46	0.2117 / 0.1108 / 0.1612	32 / 2 / 18	37
Run-100-8%	2	195.60 / 30.315 / 112.96	0.3164 / 0.1457 / 0.2311	6 / 3 / 4	9
Run-100-10%	4	432.37 / 100.012 / 261.88	0.9294 / 0.1007 / 0.4241	7 / 2 / 3	14
Run-100-12%	1	24.54 / 24.540 / 24.54	0.1966 / 0.1966 / 0.1966	4 / 4 / 4	4
Run-100-14%	–	–	–	–	–
Run-100-16%	3	42.30 / 12.521 / 28.73	0.2903 / 0.1527 / 0.2155	5 / 3 / 4	11
Run-100-18%	–	–	–	–	–
Run-100-20%	2	40.11 / 2.822 / 21.47	0.3285 / 0.0600 / 0.1942	10 / 4 / 7	13
Run-100-25%	–	–	–	–	–
Run-100-33%	1	12.92 / 12.920 / 12.92	0.3145 / 0.3145 / 0.3145	2 / 2 / 2	2
Total all models	3	745.03 / 2.822 / 144.74	0.9294 / 0.0600 / 0.2388	32 / 2 / 6	19

Table 3. Same as Table 2 for the models with $M_c = 60\,M_\odot$ and $\beta \leq 1$.

Model	N_{bst}	$L_{max}/L_{min}/L_{mean}$ (10^5 L$_\odot$)	$\dot{M}_{max}/\dot{M}_{min}/\dot{M}_{mean}$ (M$_\odot$ yr^{-1})	$t_{bst}^{max}/t_{bst}^{min}/t_{bst}^{mean}$ (yr)	t_{bst}^{tot} (yr)
		1-mag cutoff			
Run-60-0.1%	–	–	–	–	–
Run-60-0.5%	4	11.88 / 5.32 / 7.83	0.0121 / 0.0063 / 0.0100	45 / 7 / 19	77
Run-60-0.8%	10	0.70 / 0.03 / 0.15	0.0265 / 0.0011 / 0.0048	109 / 6 / 59	594
Run-60-1%	8	15.55 / 2.11 / 8.18	0.0173 / 0.0065 / 0.0100	56 / 9 / 19	152
All models	7	15.55 / 0.03 / 5.39	0.0265 / 0.0011 / 0.0083	109 / 6 / 32	274
		2-mag cutoff			
Run-60-0.1%	–	–	–	–	–
Run-60-0.5%	2	23.41 / 11.02 / 17.21	0.0290 / 0.0255 / 0.0272	20 / 12 / 16	32
Run-60-0.8%	10	2.32 / 0.10 / 0.56	0.0495 / 0.0027 / 0.0154	79 / 4 / 34	336
Run-60-1%	4	25.52 / 5.80 / 14.74	0.0406 / 0.0222 / 0.0311	49 / 9 / 21	86
All models	4	25.52 / 0.10 / 10.84	0.0495 / 0.0027 / 0.0246	79 / 4 / 24	151
		3-mag cutoff			
Run-60-0.1%	–	–	–	–	–
Run-60-0.5%	–	–	–	–	–
Run-60-0.8%	4	0.88 / 0.33 / 0.52	0.0187 / 0.0074 / 0.0111	25 / 6 / 17	70
Run-60-1%	–	–	–	–	–
All models	4	0.88 / 0.33 / 0.52	0.0187 / 0.0074 / 0.0111	25 / 6 / 17	70

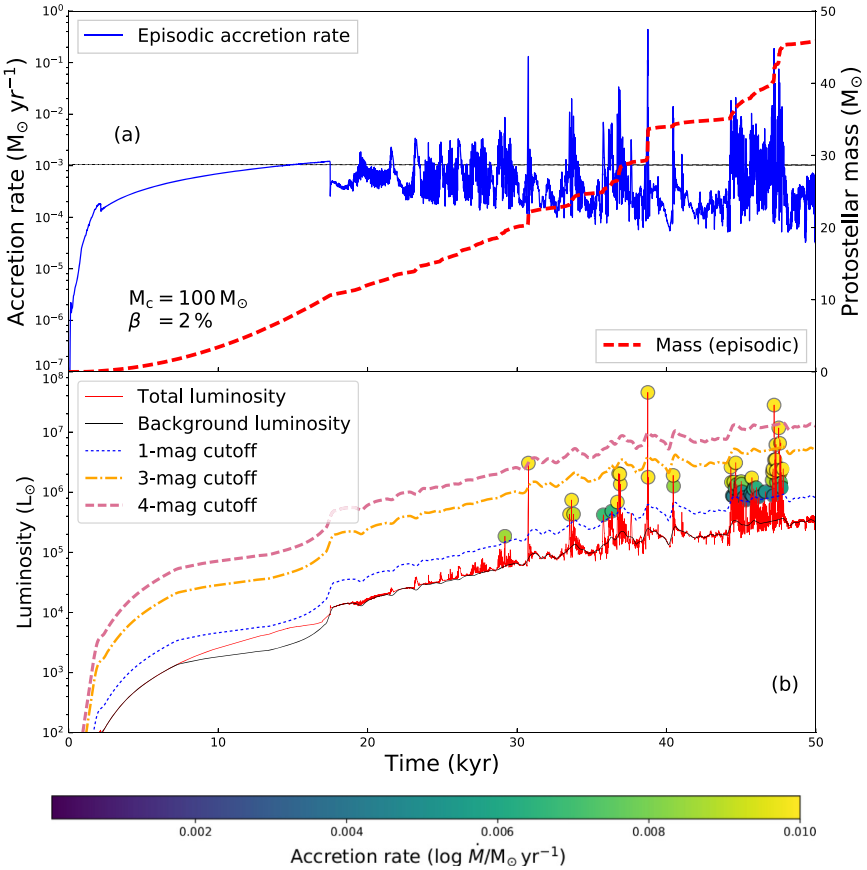

Figure 3. Top: Evolution of the accretion rate (in M$_\odot$ yr^{-1}, thin solid line) and evolution of the mass of the protostar (in M$_\odot$, thick dashed line) in our simulation Run-100-2 per cent. The thin horizontal black line marks a rate $\dot{M} = 10^{-3}$ M$_\odot$ yr^{-1} and the magenta dot marks when the protostar enters the high-mass regime ($M_\star = 8\,M_\odot$). Bottom: Total luminosity (thin solid red line, in L$_\odot$) of the same model (b), background luminosity (thin solid black line), and cutoff magnitudes for the 1-mag (2.5 times the background luminosity) to the 4-mag ($2.5^4 \approx 39$ times the background luminosity) accretion bursts, respectively.

β-ratio in the initial conditions have a stronger effect on ξ than the variations of the core mass M_c.

4 BURSTS PROPERTIES

We perform an analysis of the accretion-driven bursts contained in the light curves of our MYSOs. The burst properties are investigated according to their parent core properties, and we determine how stars gain their mass, either by quiescent accretion or by accretion-driven bursts.

4.1 Protostellar luminosities

We extract from each disc simulation the protostellar light curves and the properties of the corresponding accretion bursts. The total luminosity of the protostars,

$$L_{\rm tot} = L_\star + L_{\rm acc}, \tag{40}$$

is calculated being the luminosity $L_\star$ of the protostellar photosphere taken from Hosokawa & Omukai (2009), plus the accretion luminosity,

$$L_{\rm acc} = f G \frac{M_\star \dot{M}}{R_\star}, \tag{41}$$

where $M_\star$ is the mass of the MYSOs, G is the universal gravitational constant, $\dot{M}$ denotes the protostellar mass accretion rate from the disc, and $R_\star$ is the protostellar radius. In equation (41), the coefficient $f = 3/4$ stands for the proportion of mass that is considered as being accreted by the star as compared to that going in a protostellar jet/outflow (Meyer et al. 2019a). Fig. 3 illustrates how the mass transport from the accretion disc to the protostellar surface affects the variations of the light curve.

We analyse the accretion bursts together with their occurrence and characteristics throughout the modelled stellar lifetime. The method separates the background secular variability, which accounts for spiral-arms-induced anisotropies formed in the disc, from the episodic accretion events caused by infalling dense gaseous clumps. We first define $L_{\rm bg}$, the so-called background luminosity, which is calculated by filtering out all accretion bursts. It reads

$$L_{\rm bg}(t) = \begin{cases} \left\langle L_\star(t) + L_{\rm acc}(t) \right\rangle & \text{if } \dot{M} \leq \dot{M}_{\rm crit} \\ \left\langle L_\star(t) + \delta L_{\rm acc}(t) \right\rangle & \text{if } \dot{M} > \dot{M}_{\rm crit}\ , \end{cases} \tag{42}$$

where

$$\delta = \frac{\dot{M}_{\rm crit}}{\dot{M}}, \tag{43}$$

and with $\dot{M}_{\rm crit} = 5 \times 10^{-4}\,{\rm M}_\odot\,{\rm yr}^{-1}$, which replaces strong accretion bursts from $L_{\rm acc}$. The time averaging in equation (42) is 1000 yr. We then derive the properties for the so-called i-mag bursts with $1 \leq {\rm i} \leq 4$, where an i-mag outburst is a burst with $L_{\rm acc} \geq 2.5^{\rm i} L_{\rm bg}$ (Meyer et al. 2019a). Our algorithm selecting the bursts makes sure that very mild luminosity variations smaller than 1 mag, potentially originating from boundary effects, are not qualified as physical accretion bursts and that the duration of the bursts is sufficiently short and that any secular variations of $L_{\rm tot}$ are not confused with an outburst. All bursts and their properties are displayed as appendix in our Tables 2–3, respectively.

4.2 Bursts properties

In Fig. 4, we display the correlation between the maximum luminosity of the accretion bursts (in $L_\odot$) versus the burst duration (in yr) (top panels) and the bursts peak accretion rate (in $M_\odot\,yr^{-1}$) versus the burst duration (in yr) (bottom panels), where the colour coding representing the pre-stellar core mass M_c (in $M_\odot$) (top panels) and its corresponding β-ratio (in per cent) (bottom panels), respectively. The panels display the data for the line of increasing core mass M_c (left-hand panels) and the line of increasing β ratio (right-hand panels), respectively. The numbers and detailed properties of those burst are reported in the tables in the appendix.

The meaning of this figure is described in great details in Meyer et al. (2019a). Fig. 4(a) shows that along the line of increasing M_c, the burst peak luminosity augments with M_c. The burst magnitude augments as a function of the burst luminosity, except for the 4-mag bursts that are more dispersed in the figure (Table 4). Fig. 4(b) illustrates that the most luminous flares are typically short-duration 3-mag and 4-mag bursts. These bright outbursts are generally shorter and more luminous in models with lower β-ratio than in models with higher β. The effect of the increase of pre-stellar core M_c results in a concentration of the bursts in the small duration-high luminosity part of the diagram, except for the 1-mag bursts, which do not accrete much mass (Fig. 4a). The effect of the increase of pre-stellar β-ratio results in the shift of the burst distribution to the region of longer bursts (Fig. 4b). Fig. 4(c) indicates that the 1-mag and 2-mag bursts accrete less mass by bursts than the 3-mag and 4-mag bursts. The most massive cores generate the shortest and least accreting bursts, while the lightest cores produce longest bursts. Fig. 4(d) demonstrates that models with lower β accrete more mass and generate more 3-mag and 4-mag burst than in the simulations with higher initial core spin.

In Fig. 5, we display how the burst duration (in yr) versus the peak luminosity of the bursts (in $L_\odot$) scatters (top panel) and the duration of the bursts (in yr) versus their maximum accretion rate (in $M_\odot\,yr^{-1}$) (bottom panel) for each individual bursts without distinguishing the models with changing M_c and changing β. The colours indicate the mass that has been transferred from the disc to the protostar through the bursts (in $M_\odot$) (top panel) and the peak luminosity reached during the bursts (in $M_\odot$) (bottom panel), respectively. The bursts almost populate the entire Fig. 5(a). The low-luminosity 1-mag bursts are typically in the 10^3–$10^6\,L_\odot$ region and they are characterized by a wide range of duration (1–10^2 yr). The bursts that accrete less mass are the 1-mag dimmer ones. The bursts accreting the larger amount of mass are mostly 3- and 4-mag bursts and they are distributed decreasing with the burst duration time in the upper region of the figure with respect to the fit of $L(t)$. A similar trend is visible in Fig. 5(b), in which the more luminous bursts of 3 mag and 4 mag accrete more mass than the bursts producing dimmer 1- and 2-mag accretion bursts. The luminous bursts are generally of shorter duration as compared to the fainter bursts which last longer. The bursts of similar magnitude and peak luminosity in Fig. 5(b) are distributed along diagonals (from bottom left to upper right), which reflects the fact that the accretion rate $\dot{M}$ varies slowly during a given burst. Therefore, if the burst duration augments, the accreted mass also increases linearly, and the bursts of similar luminosities appear as parallel diagonal lines in the mass-duration plane.

One can note that the bursts with the largest accreted mass and shortest duration are also not necessarily the very most luminous ones (top left part of Fig. 5b). The total luminosity that we plot here reflects the variations of both the photospheric luminosity and the accretion luminosity, the latter being function of the accretion rate on to the protostar and of the inverse of the stellar radius (Meyer et al. 2019b). The protostars accreting the largest amount of mass

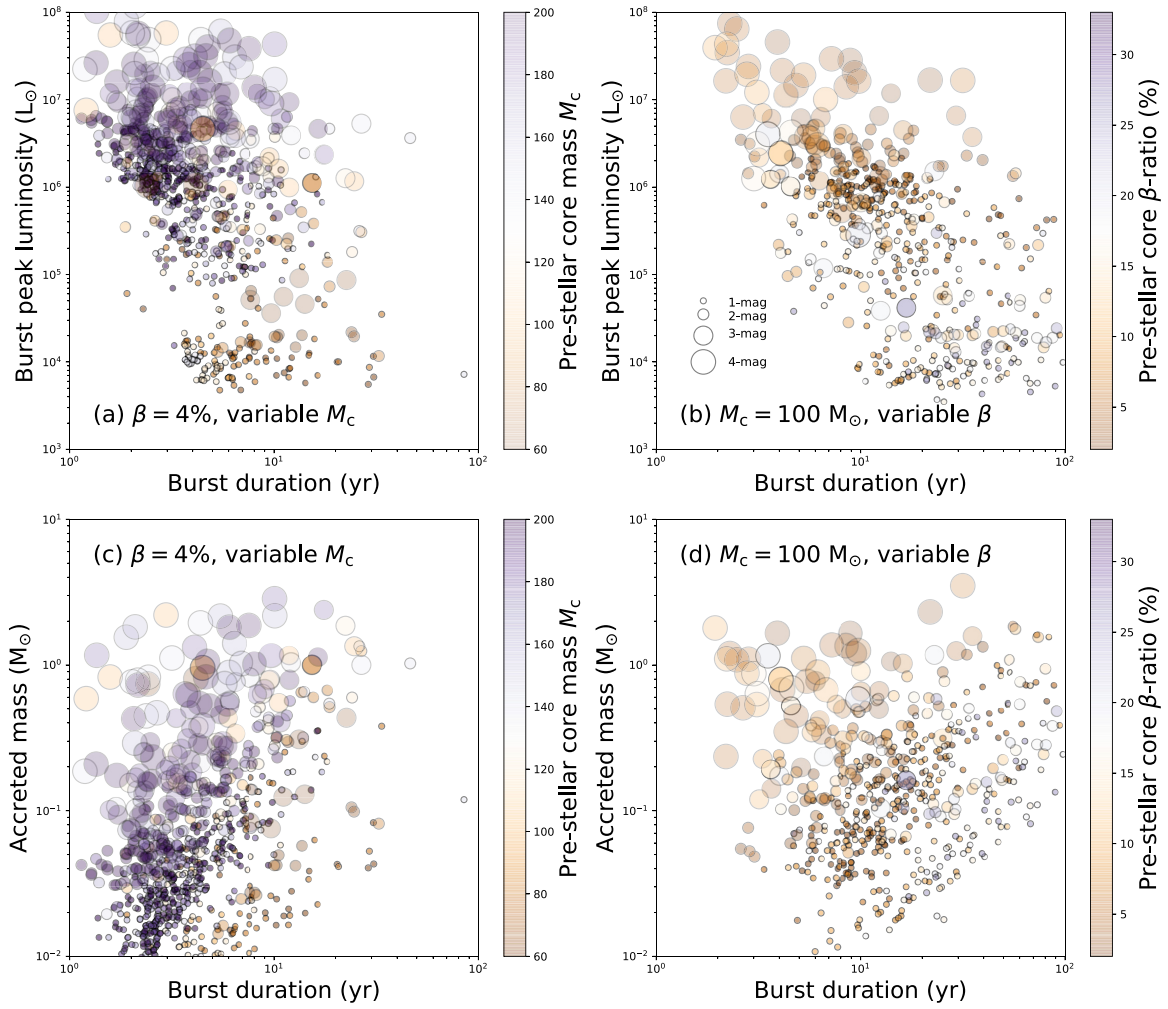

Figure 4. Scatter plots representing the burst peak luminosity versus duration of the bursts (top panels) and scatter plots displaying the accretion rate peak versus the duration of the bursts (bottom panels). Colour scales distinguish the models as a function of the pre-stellar core mass M_c (top panels) and the pre-stellar core β-ratio (bottom panels). The figures display the data for the line of increasing core mass M_c (left-hand panels) and the line of increasing β ratio (right-hand panels), respectively.

consequently see their radius bloating while going to the red part of the Hertzsprung–Russell diagram. Consequently, even tough they accrete the largest mass and generate 4-mag bursts, they are fainter than some other bursts. The energy in the bloated atmosphere is then radiated away while the protostar returns to the quiescent phase of accretion and continues its pre-ZAMS evolution towards the main sequence. It strongly impacts the nature of the ionizing flux released in the cavity that is normal to the disc plane (see also discussion Section 5). The proper time-scale of this phenomenon is difficult to predict without self-consistent stellar evolution calculations, which time-dependently account for the physics of accretion, such as the GENEC (Haemmerlé 2014; Haemmerlé et al. 2016, 2017) or the STELLAR (Yorke & Kruegel 1977; Hosokawa & Omukai 2009; Hosokawa, Yorke & Omukai 2010) codes. Only then the structure and upper layer thermodynamics of the MYSOs can be calculated. Our stellar evolution calculations previously performed with Run-100-4 per cent showed that when experiencing a 4-mag burst, MYSOs experience a sudden rise of their luminosity that is triggered by the brutal increase of the accretion rate at the moment of a disc clump accretion (Meyer et al. 2019b). This induces the formation of an upper convective layer, provoking a luminosity wave propagating outwards (Larson 1972), and causes the swelling of the protostellar radius (Hosokawa et al. 2010).

Our models for MYSOs show that this swelling lasts on the order of $100 - 1000$ yr, depending on how much mass is accreted during the burst, and the protostellar flare may appear as a longer, lower amplitude burst. Furthermore, the situation is even more complex as there is no one-to-one correspondence between the accretion rate and total luminosity, as the star can act as a capacitor and release part of the accreted energy in a delayed manner. This induces a rise in the photospheric luminosity, which might dominate the total luminosity in the late outburst stages when the MYSO returns to the quiescent phase. The protostellar flare may appear as a longer, lower amplitude burst. At least this can happen in the context of

Table 4. Same as Table 2 for the line of increasing M_c.

Model	N_{bst}	$L_{max}/L_{min}/L_{mean}$ (10^5 $L_\odot$)	$\dot{M}_{max}/\dot{M}_{min}/\dot{M}_{mean}$ ($M_\odot$ yr^{-1})	$t_{bst}^{max}/t_{bst}^{min}/t_{bst}^{mean}$ (yr)	t_{bst}^{tot} (yr)
		1-mag cutoff			
Run-60-4%	30	3.28 / 0.05 / 0.74	0.022 / 0.001 / 0.008	30.8 / 2.3 / 10.5	315
Run-80-4%	49	4.43 / 0.05 / 0.58	0.022 / 0.001 / 0.006	33.6 / 1.9 / 8.7	428
Run-120-4%	58	17.24 / 0.06 / 4.45	0.019 / 0.001 / 0.007	18.1 / 2.6 / 5.1	296
Run-140-4%	44	18.1 / 0.07 / 5.44	0.020 / 0.001 / 0.008	85 / 1.9 / 6.2	274
Run-160-4%	79	22.68 / 0.79 / 10.6	0.018 / 0.003 / 0.008	17.1 / 1.6 / 3.9	309
Run-180-4%	94	27.57 / 0.15 / 11.1	0.020 / 0.004 / 0.008	12.6 / 1.8 / 3.7	352
Run-200-4%	103	44.07 / 0.7 / 13.56	0.022 / 0.004 / 0.010	16.2 / 1.4 / 4.0	407
Total all models	59	44.07 / 0.05 / 5.97	0.022 / 0.001 / 0.007	85 / 1.4 / 6.0	309
		2-mag cutoff			
Run-60-4%	12	4.71 / 0.15 / 1.17	0.043 / 0.003 / 0.13	24.6 / 5.3 / 11.8	142
Run-80-4%	11	5.20 / 0.12 / 1.32	0.048 / 0.003 / 0.018	32.6 / 5.3 / 13.2	145
Run-120-4%	14	37.46 / 18.08 / 20.25	0.060 / 0.121 / 0.029	24.1 / 2.9 / 7.7	108
Run-140-4%	16	46.55 / 2.8 / 20.28	0.058 / 0.013 / 0.03	46.4 / 1.5 / 9.8	156
Run-160-4%	33	46.29 / 3.45 / 25.78	0.054 / 0.01 / 0.024	13.9 / 1.4 / 4.4	144
Run-180-4%	45	75.39 / 1.84 / 28.56	0.047 / 0.013 / 0.026	12.0 / 1.4 / 4.0	182
Run-200-4%	70	81.13 / 3.77 / 39.84	0.057 / 0.014 / 0.027	10.5 / 1.1 / 3.5	243
Total all models	53	81.13 / 0.12 / 18.17	0.060 / 0.003 / 0.067	46.4 / 1.1 / 7.6	149
		3-mag cutoff			
Run-60-4%	6	0.90 / 0.36 / 0.61	0.02 / 0.008 / 0.014	22.6 / 7.7 / 13.1	78
Run-80-4%	1	11.15	0.065	15.3	15
Run-120-4%	8	105 / 12.65 / 51.07	0.088 / 0.051 / 0.07	22.4 / 2.0 / 6.5	52
Run-140-4%	9	109.4 / 35.5 / 65.9	0.11 / 0.04 / 0.075	26.8 / 1.7 / 8.1	73
Run-160-4%	9	106.4 / 36.4 / 65.7	0.119 / 0.035 / 0.059	6.5 / 1.9 / 3.6	33
Run-180-4%	20	221.8 / 16.49 / 93.17	0.136 / 0.038 / 0.075	17.5 / 1.6 / 4.9	98
Run-200-4%	22	217.6 / 46.35 / 92.89	0.119 / 0.036 / 0.061	16.4 / 1.7 / 4.3	96
Total all models	10	221.8 / 0.36 / 50.5	0.136 / 0.008 / 0.06	26.8 / 1.6 / 8.3	65
		4-mag cutoff			
Run-60-4%	2	10.46 / 10.22 / 10.34	0.31 / 0.20 / 0.25	4.1 / 2.4 / 3.3	6.5
Run-80-4%	1	46.16	0.215	4.5	4.5
Run-120-4%	4	420.6 / 121.5 / 199.1	0.43 / 0.086 / 0.246	6.7 / 2.0 / 4.3	17
Run-140-4%	7	582.2 / 224.8 / 407.1	0.446 / 0.157 / 0.318	4.4 / 1.2 / 2.5	18
Run-160-4%	10	1171 / 55.49 / 394.3	0.87 / 0.13 / 0.33	10.1 / 1.9 / 4.9	49
Run-180-4%	6	1025 / 89.7 / 381.6	0.86 / 0.086 / 0.307	10.1 / 1.4 / 5.6	33
Run-200-4%	14	575 / 117.2 / 276.4	0.337 / 0.091 / 0.176	8 / 1.4 / 4.3	60
Total all models	6	1025/10.22/264.7	0.87/0.13/0.30	10.1/1.2/3.9	24

low-mass protostars; see Elbakyan et al. (2019). Recent observations show that some masers are very good tracers of the decrease of the radiation field, see Section 3.3 of Chen et al. (2020b) and Fig. 4 of Chen et al. (2020a), which can be interpreted as a clue of the burst duration. The flare of NGC 6334 I is going on still and that of S255 lasted for years (Szymczak et al. 2018), and stronger flares seem to be longer. This phenomenon is also probably influenced by the spatial resolution of the simulations, in the sense that higher resolution models will permit to better follow the collapse of the clump interiors, and by the size of the sink cell, inevitably introducing boundary effects. Indeed, our burst analysis of a higher resolution disc model in Meyer et al. (2019a) shows that the 4-mag bursts are less frequent than in those with lower resolution, although this calculation had been integrated over a more reduced time. Further simulations with a much higher spatial resolution are necessary to address this question in more detail.

The marginal histograms on the right and top sides of Figs 5(a) and (b) concern the bursts occurrence of the whole set of bursts experienced by all our protostars. The data are plotted with different colours depending on the burst magnitude, while the black lines show their cumulative occurrence. The top histograms are the same of both panels (a) and (b) as they equally represent the burst duration. Our conclusion confirms that the maximum burst duration is below 100 yr. We confirm that bursts with shorter duration induce stronger bursts, and hence it will be more unlikely to monitor these events in the context of MYSOs, questioning the observability of 4-mag, FU-Orionis-like accretion bursts. The mass gained during a burst extends from about 10 Jupiter masses to a solar mass, which is within the limits accreted during the outburst of, e.g. S255IR-NIRS 3 (Caratti o Garatti et al. 2017). As described in Meyer et al. (2019a), the distribution of accreted masses mirrors the variety of disc fragments, i.e. the clumps and dense spiral arm segments generated by gravitational instability in the disc.

We note that strongest accretion bursts may happen alongside with the formation of low-mass binary companions to MYSOs. We demonstrated in Meyer et al. (2018) that it is possible to form simultaneously both close/spectroscopic objects around a MYSO, while it simultaneously undergoes an outburst. This happens when migrating massive clumps get rid of their envelope while contracting into a dense nucleus, thus forming a secondary low-mass protostellar core. The burst luminosity distribution indicates that 1- and 2-mag bursts are more common than 3- and 4-mag bursts. Their luminosity peak is at $\approx 10^5$-10^6 $L_\odot$, while the other, higher luminosity bursts are much more uncommon. Still, there are 3-mag bursts with luminosities $\geq 10^6$ $L_\odot$, and a few rare 4-mag bursts peak at luminosities $\geq 10^7$ $L_\odot$; see also in Meyer et al. (2019a).

4.3 Quiescent versus burst phases of accretion

We calculate for each simulation model the proportion of final protostellar mass that is gained either in the quiescent or during the

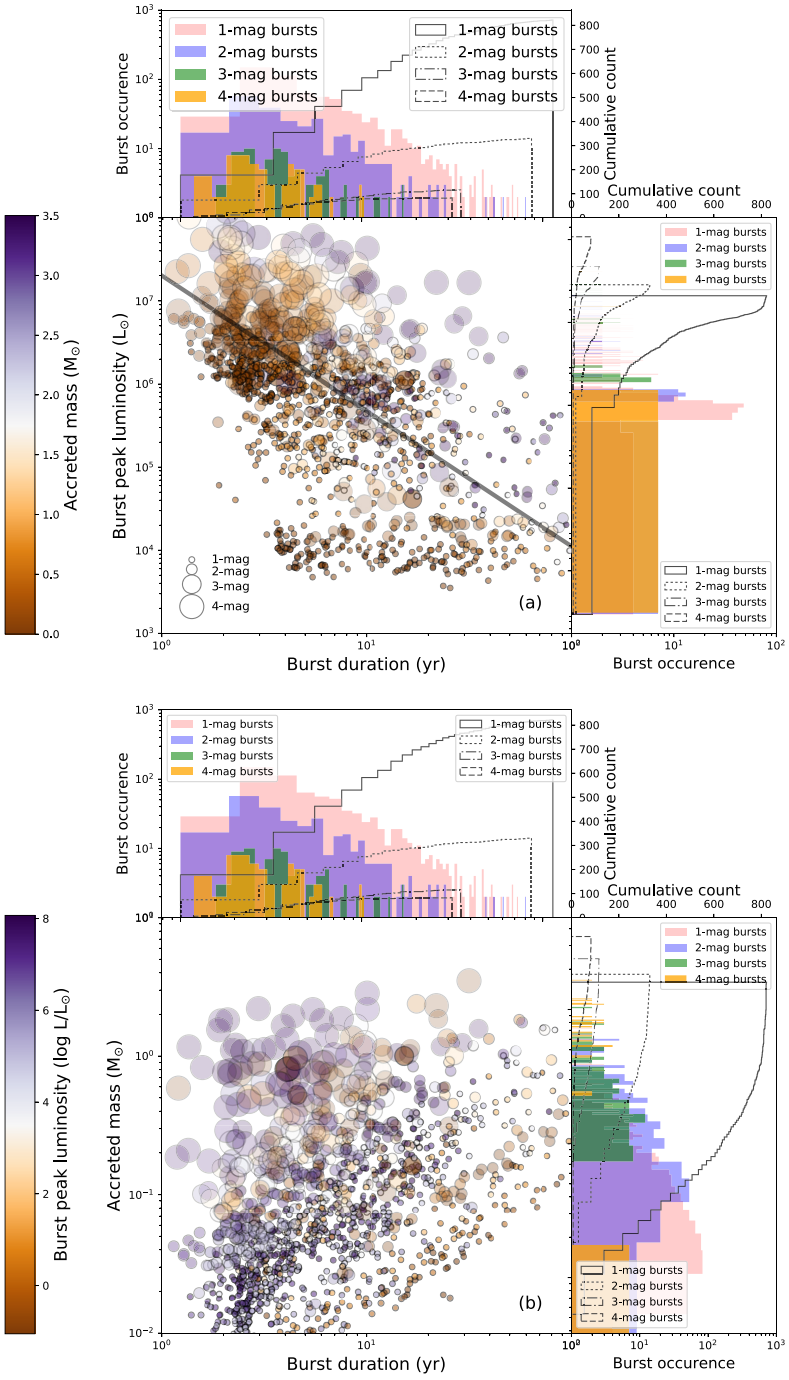

Figure 5. Scatter plots representing the burst peak luminosity as a function of the duration of the burst (top panel) and scatter plots displaying the accretion rate peak as a function of duration of the bursts (bottom panel) for all bursts in our parameter study. Colour scales distinguish the data as a function of the mass accreted by the protostar (top panel) and the bursts peak luminosity (bottom panel). The marginal histograms show the burst occurrence versus the duration of the bursts, peak luminosity, and mass accreted by the protostar during each individual bursts.

burst phases, respectively. The minimal, mean, and maximal values for the quiescent phase are reported in our Table 5 for the lines of increasing β and M_c, as well as for the other simulations' models. The models with different β-ratios indicate that the protostar acquires between 52.07 per cent and 77.71 per cent of their final mass during the quiescent phase, with a mean value of about 62.95 per cent. The rest of the mass is therefore accreted during the time spent in the burst mode ($L_{\rm tot} \geq 2.5 L_{\rm bg}$). The simulations with constant β-ratio

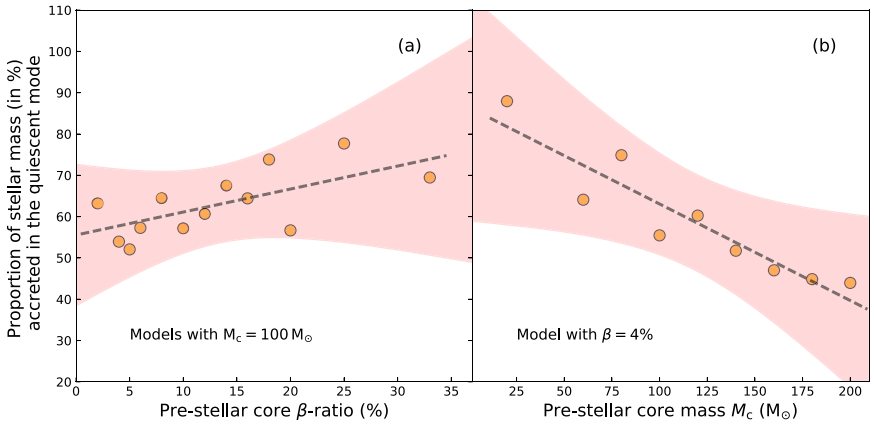

Figure 6. Proportion of final protostellar mass gained during the quiescent phases of accretion for our models along the line of increasing core mass M_c (a, left panel) and for the line of increasing β ratio (b, middle panel), respectively. Each orange dot represents a simulated protostar. The dashed black lines show the linear fits, respectively. The red zone represents the error interval to the fits.

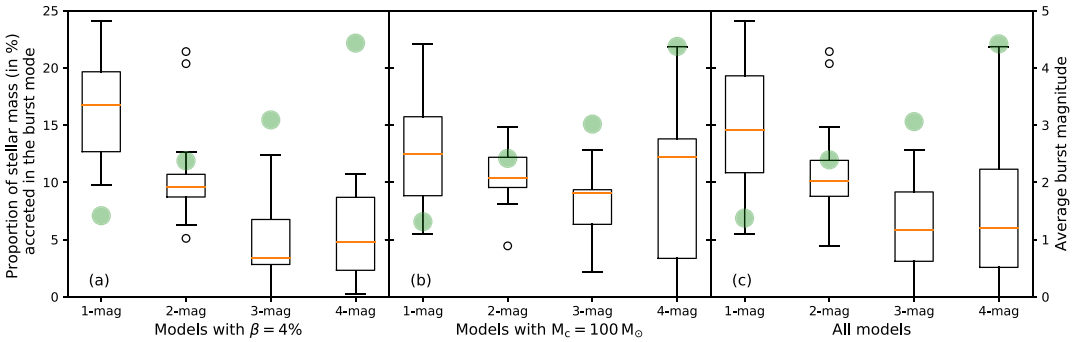

Figure 7. Box plot of the proportion of final protostellar mass accreted during the burst phases for our grid of simulated protostars. The results are displayed as a function of the burst magnitude, which can span from 2.5 (1 magnitude bursts) to 2.5^4 (4 magnitudes bursts) above the protostellar background luminosity. The orange line marks the mean value of a given series of bursts. The figures show the data for the line of increasing core mass M_c (a, left panel), the line of increasing β ratio (b, middle panel), and for all data (c, right panel), respectively. The green dots indicate the average burst magnitude for each model.

Table 5. Proportion of mass gained by the MYSOs in the quiescent phase of accretion (in %). The results are shown for the line of increasing β and M_c, respectively, as well as for all models together.

Models	Min (%)	Mean (%)	Max (%)
Lineofincreasingβ	52.07	62.95	77.71
LineofincreasingM$_c$	43.96	58.91	87.95
Allmodels	43.96	61.30	87.95

of 4 per cent but changing protostellar core mass M_c have a mean value of 58.91 per cent with extreme value of 43.96 per cent and 87.95 per cent, respectively.

Fig. 6 details the proportion of final protostellar mass gained during the quiescent phase of accretion, i.e. ignoring all burst phase, for all our models. One can see that it gradually increases with β from ≈ 55 per cent for the model with $\beta = 2$ per cent to ≈ 70 per cent for the models with $\beta = 33$ per cent (Fig. 6a), meaning that less mass is gained in the burst mode in the case of highly spinning cores. Inversely, the model with $M_c = 20\,M_\odot$ spends 87.95 per cent of its protostellar lifetime in the quiescent phase and such quantity monotonically decreases to the model with $M_c = 200\,M_\odot$ that spends half of its pre-main-sequence lifetime, namely 43.96 per cent, in the quiescent mode (see Fig. 6b). It indicates that our results are more sensitive to M_c than to its initial spin. The latter governs, for a given radius and core's structure, the duration of the free-fall gravitational collapse. Hence, the stars forming out of lightest pre-stellar cores are more prone to gain mass by quiescent disc accretion than by accretion-driven bursts, whereas the heaviest pre-stellar cores spend a larger fraction of their pre-zero-age-main sequence in the burst phase.

In Fig. 7, we show the box plots of the fraction of the final protostellar mass accreted during the burst phase for the 1-mag ($L_{tot} \geq 2.5L_{bg}$) to 4-mag bursts ($L_{tot} \geq 2.5^4 L_{bg}$). The figures display the data for the line of increasing core mass M_c (a, left panel), the line of increasing β ratio (b, middle panel), and for all data (c, right panel), respectively. For each burst sample, i.e. the lines of increasing M_c (a), increasing β (b), or both (c), we draw a box extending from the lower/first quartile Q_L (i.e. the data lower half's median) to upper quartile Q_U (i.e. the data upper half's median) of the considered sample, with an orange line at the median of all the data. With IQR $= Q_U - Q_L$ being the interquartile range, the box whiskers extend from the box to $1.5 \times Q_U$ and to $1.5 \times Q_L$, respectively. Flying points

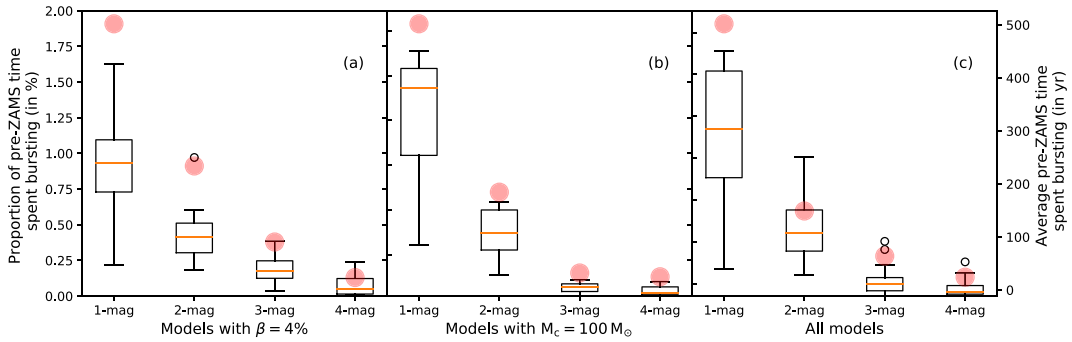

Figure 8. Box plot of the proportion of pre-zero-age-main-sequence-time (pre-ZAMS) the protostars spend in the burst mode of accretion. The results are displayed as a function of the burst magnitude, which can span from 2.5 (1 magnitude bursts) to 2.5^4 (4 magnitudes bursts) above the protostellar background luminosity. The orange line marks the mean value of a given series of bursts. The figure shows the data for the line of increasing core mass M_c (a, left panel), the line of increasing β ratio (b, middle panel), and for all data (c, right panel), respectively. The red dots indicate the average time the protostars spent in the burst phase (in yr).

marked as white circles are those past the range ($Q_L - 3IQR/2$, $Q_U + 3IQR/2$). Hence, the extend of the whiskers marks the dispersion of most bursts, except marginal ones represented as circles and lying outside of the whiskers. The green dots in the figure indicate the average magnitude of the bursts for all models. The burst magnitude is the exponent i defined as,

$$\frac{L_{\rm tot}}{L_{\rm bg}} = 2.5^i, \tag{44}$$

which corresponds to

$$i = \frac{1}{\log(2.5)} \log\left(\frac{L_{\rm tot}}{L_{\rm bg}}\right), \tag{45}$$

with $L_{\rm tot}$ and $L_{\rm bg}$ the total luminosity and the background luminosity, respectively. The arithmetic average is then performed for both the lines of the increasing β (Fig. 7a) and M_c (Fig. 7b) and for all models (Fig. 7c). Note that the average 1-mag burst can only be in the (1–2)-mag limit, the 2-mag burst can only be in the (2–3)-mag limit, and so forth. Interestingly, the data exhibit a significant homogeneity (Figs 7a and b) meaning that, on the average, the mean burst magnitude is independent of the pre-stellar core properties. Our approach is that modelling bursts can therefore be compared to observations; see Section 5.4.

Concerning the line of increasing M_c (Fig. 7a), most mass accreted during the burst phase is gained as 1-mag bursts, with a median amount of mass ≈ 17 per cent of the final protostellar mass. The amount of material accreted during the 2- and 3-mag bursts decreases with median values of 10 per cent and 4 per cent, respectively. Finally, for models at constant β-ratio, the mass accumulated during the 4-mag FU-Orionis-like bursts is slightly higher than that of the 3-mag burst, however, with a larger dispersion than, e.g. the 2-mag bursts. The situation is globally similar for the line of increasing β (Fig. 7b) as the median mass accreted by the protostar decreases from 13 per cent and 10 per cent for the 1-, 2-, and 3-mag bursts; nevertheless, the 4-mag bursts behave differently with a mean mass similar to that of the 1-mag bursts but with a huge dispersion spanning from < 5 per cent to > 20 per cent. This indicates that the β-ratio of the pre-stellar core affects much more the manner stars gain their mass than the initial core mass. Regarding the whole data set (Fig. 7c), a decreasing trend of the accreted mass during the accretion phases showing bursts versus the burst magnitude is found with 14 per cent, 10 per cent, and 6 per cent for the 1-, 2,- and 3-mag bursts, respectively, and another 6 per cent for the 4-mag burst, the latter being, however, attached to a huge dispersion of the values produced by differences in the models with changing β.

In Fig. 8, we display the statistics for the proportion of pre-ZAMS time the MYSOs spend in the burst mode of accretion (in per cent), together with the average time protostars experience accretion phases that are characterized by 1-mag, 2-mag, 3-mag, or 4-mag bursts, respectively (in yr). The models with $\beta = 4$ per cent have a rather large dispersion of the proportion of time they spend in 1-mag bursts, which spread between 0.25 per cent and 1.6 per cent of the calculated time, with a mean value around ≈ 1 per cent. These values gradually diminish as the burst magnitude augments and we find that our MYSOs spend very little (0.1 per cent) of their time experiencing 4-mag bursts (Fig. 8a). The same is true for the models with $M_c = 100\,M_\odot$, although the values are slightly larger for the 1-mag and 2-mag bursts (Fig. 8b), because our models with high initial β-ratio of their molecular pre-stellar core spend more time in the burst mode than those with lower β-ratio (Table 4). The statistics for all models (Fig. 8c) therefore indicates that MYSOs spend about 2 per cent of their pre-ZAMS time in the burst mode of accretion. The rare events are the fast 4-mag bursts responsible for the excursions in the cold regions of the Hertzsprung–Russell diagram (Meyer et al. 2019b). The findings in our parameter study therefore confirm the previously obtained results on the basis of a much smaller sample of massive protostars and which stated that MYOs spend about 1.7 per cent of their early formation phase in the burst mode of accretion (Meyer et al. 2019a).

5 DISCUSSION

This section presents different caveats in our method, further discusses the results in the light of known young high-mass stars that experienced an outburst, and compares them with their low-mass counterparts. Finally, we consider our outcomes by discussing them in the context of the temporal variabilities of massive protostellar jets.

5.1 Limitation of the model

Our parameter study is based on numerical models underlying assumptions regarding the numerical methods. The simplifications have already been thoroughly discussed in our pilot paper Meyer

et al. (2017). Particularly, we demonstrate therein that the discs in our simulations are adequately resolved by comparing the Truelove criterion, i.e. the minimal inverse Jeans number in the mid-plane of the accretion disc as a function of radius for three different grid resolutions. Note that the model Run-100-4 per cent in our study is the Run-1 of Meyer et al. (2018); see their figs 11 and 12. The limitations principally concern the spatial resolution of the computational grid and the consideration of additional physical processes such as magnetic fields and associated non-ideal effects in the numerical simulations. Photoionization is neglected in our scheme because we concentrate on studying the accretion disc, not the bipolar lobes filled with ionizing radiation, which develop perpendicular to it (Yorke, Bodenheimer & Tenorio-Tagle 1982; Rosen et al. 2016). That is why our computational mesh has a cosine-like grid along the polar direction, degrading the resolution of the protostellar cavity. Consequently, omitting photoionization in the scheme does not drastically change the outer disc physics ($\sim 100 - 1000$ au) that we concentrate on, while resulting in a substantial speed-up of the code.

Nevertheless, this physical mechanism not only governs the ionizing flux evacuated in the outflow lobes but also impacts the structure of accretion discs by photoevaporation (Hollenbach et al. 1994; McKee & Tan 2008). The stellar feedback (Lyman continuum, X-ray, and ultraviolet photons) irradiating the circumstellar medium can cause the ionization of the gas at the disc surface, thus leading to its evaporation as a steady flow into the interstellar medium (ISM). Without that, the accretion flow at the disc truncation radius stops shielding the neutral disc material. It launches so-called irradiated disc winds that host complex chemical reactions between enriched species and dust particles present in the disc. This particularly happens in the late phases of disc evolution, e.g. at the T-Tauri phases or even late, when giant planets have formed and orbit inside of it; see Ercolano & Owen (2016), Weber et al. (2020), Franz et al. (2020), and references therein. One should not expect photoionization to destroy the entire discs or even to affect the development of gravitational instability in the discs (Yorke & Welz 1996; Richling & Yorke 1997, 1998, 2000), and consequently it should not be a determinant factor in the burst mode of accretion in massive star formation. The flux of ionizing stellar radiation is a direct function of the protostellar properties, themselves depending on the accretion history. As stated above, high accretion rates induce bloating of the stellar radius and a decrease of its effective temperature and ionizing luminosity, released either in the polar lobes or towards the equatorial plane where the disc lies. Consequently, the H II region generated by the protostar becomes intermittent, with variations reflecting the episodic disc accretion history on to the protostellar surface (Hosokawa et al. 2016).

With the photon flux being switch-off towards the colder part of the Herztsprung–Russell diagram during the excursions of these stars undergoing a burst, one should expect the H II regions to disappear when $\dot{M}$ reaches its maximum peak. The ionized lobed region then gradually reappears as the star recovers pre-ZAMS surface properties corresponding to its quiescent phase of accretion, after radiating away the clump entropy during a phase of lower amplitude burst. Such a process has been revealed in the context of primordial, supermassive stars (Hosokawa et al. 2011; Hosokawa et al. 2012; Hosokawa et al. 2013). We postulated that this mechanism of blinking H II regions should also be at work in massive star formation and constitutes a major difference between present-day young low-mass and high-mass stars (Meyer et al. 2019b).

Future improvements might principally consist of changing the initial conditions in terms of internal structures of the pre-stellar core to make it more realistic and of increasing the spatial resolution of the grid simulation, so that we can further resolve disc fragmentation when circumstellar clumps migrate in the vicinity of the protostar. Indeed, the filamentary nature of the parent pre-stellar cores in which young massive star form should definitely affect the manner stars gain their mass; however, this will not support the midplane symmetry, which we impose in our simulations to divide the computational costs by a factor of 2. Similarly, a higher spatial resolution will permit to investigate trajectories of migrating clumps to the inner disc region. Nevertheless, circumventing the caveats of our current models would be at the cost of unaffordable computational resources, which will not permit a scan of the huge star formation parameter space. Longer simulations and a smaller sink cell radius $r_{\rm in}$ would also permit us to better simulate the fall, evolution, probable distortion, and/or segmentation of the clumps before they are accreted on to the star. Again, this would in its turn strongly modify the time-step controlling the time-marching algorithm of the calculations and therefore the overall cost of the calculations.

5.2 Time interval between bursts

Fig. 9 displays the normalized distribution $N/N_{\rm max}$ of the time intervals between two accretion-driven bursts in our simulations,

$$\Delta = t_{j+1}^{\{i-\rm mag\}} - t_{j}^{\{i-\rm mag\}}, \tag{46}$$

where the subscripts j and $j+1$ designate two consecutive bursts selected on the basis of their magnitude ($i-$ mag, with $1 \leq i \leq 4$) with respect to $L_{\rm bg}$. The distribution is calculated for each possible combination allowed by our 1-, 2-, 3-, and 4-mag bursts. We present the results for the 1- to 4-mag bursts in Figs 9(a)–(d); the panels in Figs 9(e)–(g) show the cumulative distribution of all bursts of magnitude 1 to 2 (1–2), 1 to 3 (1–3), and 1 to 4 (1–4), respectively. The other combinations are plotted in Figs 9(h)–(j). All time intervals are plotted in the logarithmic scale in yr. In each panel, we distinguish the results obtained for the models in the line of increasing $M_{\rm c}$ (green colour, $\beta = 4$ per cent) and for the line of increasing $\beta = 4$ per cent (red colour, $M_{\rm c} = 100\,{\rm M}_{\odot}$). The distribution including all bursts is shown with a thin black line in each panel. The number of bursts taken into account in the histograms decreases from panel (a) to panel (d) as a natural consequence of the occurrence of 1- to 4-mag bursts (Tables 2–3). Panel (g) is the plot in which all bursts in this study are considered.

Clearly, the inter-burst intervals span a wide range from several years to tens of thousands of years. When considering bursts of all durations, the short inter-burst intervals prevail. Bursts of higher amplitude (3-mag and 4-mag) have a bimodal distribution for the duration of quiescent phases between the bursts (Figs 9c–d). The inclusion of 1- and 2-mag bursts diminishes the bimodality in favour of the shorter inter-burst time intervals (Figs 9a–b). The differences between panels 9(a) and (f) and panels 9(h) and (j) highlight the fact that the bimodality is produced by the inter-burst time intervals between the lower magnitude bursts (1,2-mag bursts) on the one hand, and the higher magnitude bursts (3,4-mag bursts) on the other hand. The same is true for panel 9(i), while the disappearance of the bimodality is obvious in panels 9(e) and (f). This information may be used in future studies to compare the inter-burst time intervals with the jet spacings such as in Vorobyov et al. (2018).

Fig. 10 presents all the time intervals between the bursts calculated in our simulations during a period of 5 kyr (a), 10 kyr (b), and 30 kyr (c) once the disc has formed. The first three panels illustrate the development of the inter-burst time intervals as the disc evolves. The last panel (d) shows the histogram displaying the distribution of the

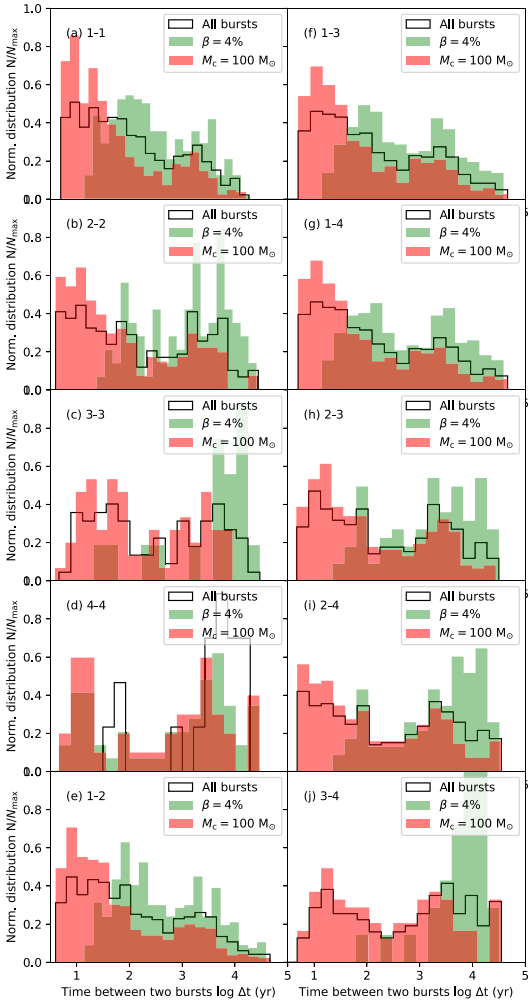

Figure 9. Normalized distribution N/N_{max} of the time intervals between two consecutive accretion-driven bursts in our simulations. It is calculated for each possible combination allowed by our 1-, 2-, 3-, and 4-mag bursts. We present the results for the 1- to 4-mag bursts exclusively (panels a–d) while the panels (e)–(g) concern the distribution of all consecutive bursts of magnitude 1 to 2 (1–2), 1 to 3 (1–3), and 1 to 4 (1–4), respectively. The other combinations are plotted in panels (h)–(j). All time intervals (in yr) are plotted in the logarithmic scale.

time intervals between the bursts for all bursts of all models and is the same distribution as in Fig. 9(g). The distribution is initially rather dispersed, especially along the line of increasing M_c (green bins); see Fig. 10(a). At this time, the disc begins to fragment and form gaseous clumps and the bursts are still mild. The models with higher β-ratios fragment faster and therefore the corresponding inter-burst intervals are shorter (green bins) than along the line of increasing M_c (red bins); see Figs 10(b) and (c). At later times, both series of model reach an equilibrium distribution that is made of two types of bursts separated by $\Delta t \sim 10^2$ yr and $\Delta t \geq 10^3$ yr, respectively. This bimodality is further illustrated for all bursts (black line in Fig. 10d). FU-Orionis-like bursts (and therefore close binary companions) should be observed in older, massive MYSOs, surrounded by rather extended and fragmented discs.

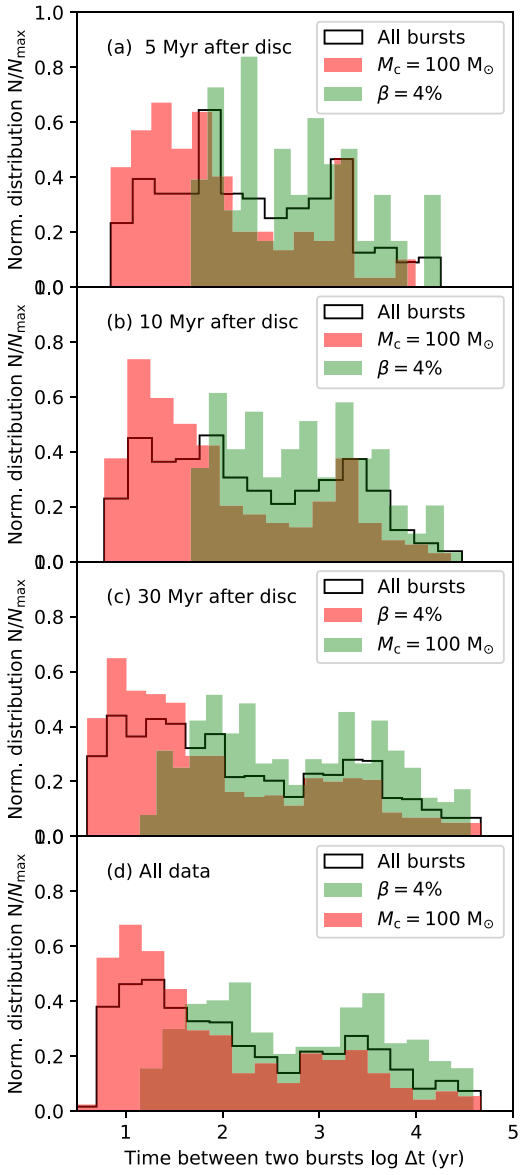

Figure 10. Time evolution of the normalized distribution N/N_{max} of the time intervals between two consecutive accretion-driven bursts in our simulations. It is calculated for each possible combination allowed by our 1-, 2-, 3-, and 4-mag bursts. The distribution is shown at times 5 kyr (a), 10 kyr (d), and 30 kyr (c) once the disc has formed and for all bursts of all models (d). All time intervals (in yr) are plotted in the logarithmic scale.

5.3 Protostellar jets as indicators of the burst history?

Protostellar outflows and jets are part of the accretion–ejection mechanism that carries angular momentum of the accreted matter away and thereby prevents the accreting protostar from spinning up to a break-up velocity. There are observational indications that the angles of the outflows from the high-mass young stellar object are wider for more evolved and luminous stars (Arce et al. 2007). In Meyer et al. (2019a), we already mentioned that tracing of the

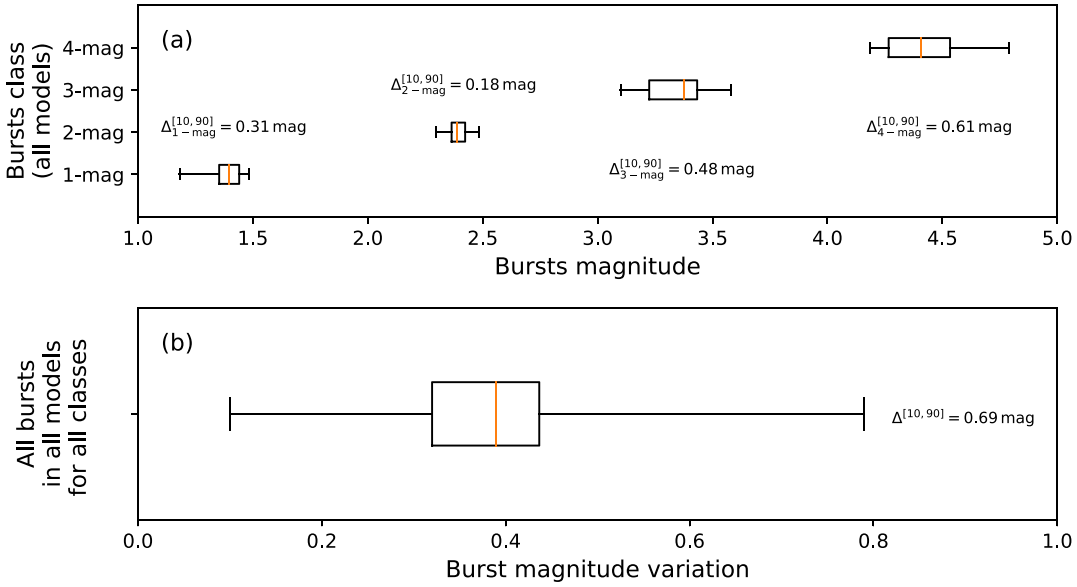

Figure 11. Box plot of the burst magnitude distribution as a function of the burst class for all models in this study. The bursts statistics are displayed per magnitude class (a) and for all bursts of all classes in all our simulations (b). The figure indicates the magnitude difference between the 10th and 90th percentiles of each burst class.

outflows allows to show that there are about four bursts in the luminous S255 NIRS3 during a time interval of ≈ 7000 yr before present-day observations (Wang et al. 2011; Zinchenko et al. 2015; Burns et al. 2016) and that the burst in NGC 6334I-MM1 was not a single event (Brogan et al. 2018).

Well pronounced jets are observed in the number of the younger massive stars in the infrared and radio ranges (see e.g. infrared survey by Caratti o Garatti et al. 2015 or radio surveys by Purser et al. 2018 and Obonyo et al. 2019). The jets manifest themselves as elongated structures in the close surroundings of the source and further knots sometimes organized in chains. So, they have potential to provide information on the history of eruptions. Protostellar jets are observed over a large source mass range (Frank et al. 2014), and recent studies show that the jets from the massive stars show similarity in physical parameters and origin with the jets from the low-mass stars (Caratti o Garatti et al. 2015; Fedriani et al. 2019).

Well accepted is the fact that the outflowing matter may not be constant in mass and velocity. Measurements of the shock velocities in the jets from the massive stars vary from hundreds to thousands $\mathrm{km\,s^{-1}}$ (McLeod et al. 2018; Purser et al. 2018). Therefore, faster material that is ejected at later times will catch up and run into slower material ahead of it, creating a new mini-bow shock. The knotty jets then are chains of these small bow-type structures. The proper motion measurements show that the dynamical times between the ejection of knots in the chains are on the order of a few decades (Eislöffel & Mundt 1992, 1998; Devine et al. 1997), whereas the times for the larger bow-type structure at their ends are on the order of centuries, and for the largest structures in the parsec-scale jets, they are even on the order of millennia (Eislöffel & Mundt 1997; Reipurth, Bally & Devine 1997). Moreover, it should be noted that the knot's brightness in the jets from the MYSOs is subject to time variability (Obonyo et al. 2019).

The interesting question arises that if these jets then are a frozen record of the accretion history of the source, and these jet knots could be used for a direct comparison with accretion events of the sources in model calculations, like the ones presented in this paper (see also Vorobyov et al. 2018). As described above, the chains of knots are not a one-to-one image of the source's accretion history, and this is principally because of possible merging of the shocks with different velocities and because the brightness of the shock knots sometimes varies with time. Little is known, however, also from a modelling point of view, whether all bursts lead to ejections of matter, how bursts can change the outflow speed, and if indeed stronger bursts are leading to faster outflowing material as well.

Keeping all the above-mentioned caveats in mind, we note that in most jets with regular chains of knots, the measured proper motions for each knot are not hugely different, so that one can assume that they are an indicator to a certain kind of similar burst events. At the mentioned time intervals of decades, these would then correspond to the first peak in the bi-modal burst distribution. The second peak in the bimodal burst distribution at 10^3–10^4 yr can correspond to the dynamical age of the bright knots of the jet observed in the distant source in the Large Magellanic Cloud – eight knots are detected in the 11-pc jet with the lifetime about $28 - 37$ kyr (McLeod et al. 2018). These knots probably represent the giant bow shocks seen at the end of the jets, or even multiple times in some parsec-scale jets.

5.4 What distinguishes massive star formation from its low-mass counterpart ?

5.4.1 Massive stars principally gain their mass through bursts

A series of differences between the formation processes in lower mass and higher mass star regimes arise from our study. First of all,

our accretion histories systematically exhibit accretion variability and accretion-driven outbursts along both the lines of increasing M_c and β and also for the models with the lowest M_c (Fig. 1). Although our results may be affected by physical mechanisms that are so far neglected, like the magnetization of the pre-stellar core or other non-ideal magneto-hydrodynamical effects, accretion bursts seem to be a systematic feature in the formation of massive protostars. When lower mass stellar objects form, on the contrary, accretion bursts caused by clump infall seem to exist only for cloud cores of sufficiently high mass and angular momentum (see fig. A1 in Elbakyan et al. 2019). A lower limit on the cloud core mass seems to exist also for accretion bursts triggered by the magnetorotational instability in the innermost parts of low-mass discs. Our study, based on a large sample of models, confirms the conclusions of Meyer et al. (2019a) stating that the MYSOs gain an important part of their final mass during the burst phase of accretion, sometimes amounting to 50 per cent or even more. On the contrary, the low-mass stars accrete on average about 5 per cent of their final mass with a peak value of 33 per cent (Dunham & Vorobyov 2012). The efficiency of gravitational instability in discs is consequently always at work in massive discs, which is consistent with the work of Kratter & Matzner (2006), Rafikov (2007), and Rafikov (2009), reporting that massive discs around high-mass protostars inevitably lead to fragmentation.

5.4.2 *Protostars in FU-Orionis-like burst phases evolve towards the red part of the Herztsprung–Russell diagram*

A series of similarities should also be underlined between the different mass regimes of star formation. Indeed, this picture of centrifugally balanced discs on to which inflowing material lands and competes with the disc thermodynamics and rotational shear equivalently applies to both regimes. Once disc fragmentation is triggered, the gaseous clumps migrate inwards, producing bursts once they are tidally destroyed near the star. Concurrently, the star migrates in the Herztsprung–Russell diagram (Elbakyan et al. 2019), irradiating the discs which should be noticed in infrared. Nevertheless, the low- and high-mass protostars show different types of excursions. The low-mass stars become bluer in the Herztsprung–Russell diagram, while the high-mass stars do it to redder, upper right part. Similar in both mass regimes is also the nearly linear relationship between the disc and protostellar masses, the respective effects of the initial M_c and β-ratio of the pre-stellar cores on to the disc properties, implying a comparable global evolution if accretion discs at all scales and masses are ruled by analogous physical mechanisms. The observational study on young low-mass protostars by Contreras Peña, Naylor & Morrell (2019) interestingly reports that 'Surprisingly many objects in this group show high-amplitude irregular variability over timescales shorter than 10 years, in contrast with the view that high-amplitude objects always have long outbursts'. This is consistent with our findings in the sense that our 3- and 4-mag bursts are characterized by a wide range of burst duration (see Fig. 5). All these correspondences strongly motivate further works on the detailed features of disc fragmentation in the context of massive protostars.

5.4.3 *The scatter in burst magnitudes is wider in massive star formation*

We show in Fig. 11 the scattering of the burst magnitude for all bursts in our data as a function of their burst class (from the 1-mag bursts to the 4-mag ones). The box plots present the data using whiskers extending from the 10th to the 90th percentile, which allows us to visualize the extent of the variation in magnitudes for all bursts encompassed within one burst class (e.g. between 1- and 2-mag, 2- and 3-mag, etc.). The variation reads

$$\Delta^{[10,90]}_{i-\mathrm{mag}} = |W^{90\mathrm{th}}_{i-\mathrm{mag}} - W^{10\mathrm{th}}_{i-\mathrm{mag}}|, \tag{47}$$

where $W^{90\mathrm{th}}_{i-\mathrm{mag}}$ and $W^{10\mathrm{th}}_{i-\mathrm{mag}}$ are the burst magnitude at the extent of the whiskers, respectively, and i denotes a considered burst class ($1 \leq i \leq 4$). The upper panel displays the bursts variation statistics for all burst in our parameter study as a function of the burst class (a) and for all the collection of bursts in our parameter study (b). We find variations of $\Delta^{[10,90]}_{1-\mathrm{mag}} = 0.31$ mag, $\Delta^{[10,90]}_{2-\mathrm{mag}} = 0.18$ mag, $\Delta^{[10,90]}_{3-\mathrm{mag}} = 0.48$ mag, and $\Delta^{[10,90]}_{4-\mathrm{mag}} = 0.61$ mag, respectively. The extend of the burst variation regardless of their magnitude class (Fig. 11b) gives $\Delta^{[10,90]}_{1-\mathrm{mag}} = 0.69$ mag. Particularly, one can compare the obtained burst variations with the value of 0.22 found for low-mass sources at 3.6 μm in the context of low-mass stellar objects in the Serpens South star formation region (Wolk et al. 2018). According to our study, the average luminosity variation in massive star formation is larger than that in low-mass star formation, which constitutes a remarkable difference between these two regimes.

6 CONCLUSION

This work explores the effects of both the initial mass ($M_c = 60$–$200\,\mathrm{M}_\odot$) and the rotational-to-gravitational energy ratio ($\beta = 0.5$–33 per cent) of a representative sample of molecular pre-stellar cores by means of three-dimensional gravito-radiation-hydrodynamics simulations. We utilize the method previously detailed in Meyer et al. (2019a). Our simulations model the evolution of molecular cores and how the collapsing material lands on to centrifugally balanced accretion discs surrounding young massive protostars. The efficient gravitational instability in the disc results in the aggregation of disc material in clumps within spiral structures. These blobs of gas can gravitationally fall towards the protostar and generate luminous accretion-driven outbursts (Meyer et al. 2017), affecting both the properties of the disc and its central MYSOs. We calculate in each model the accretion rate histories and light curves of the evolving massive protostars. As soon as a simulated protostar leaves the quiescent regime of accretion and enters the burst mode, we analyse the properties of the corresponding flare, such as its duration, peak luminosity, accreted mass, and intensity. These quantities are statistically analysed for the large sample of bursts that we extract from our grid of hydrodynamical simulations.

Under an assumption of negligible magnetic fields, which may have a major effect on accretion disc physics (Flock et al. 2011) and star formation processes (McKee, Stacy & Li 2020), we found that cores with higher mass M_c and/or β-ratio tend to produce circumstellar discs more susceptible to experience accretion bursts. All massive protostars in our sample have accretion bursts, even those with pre-stellar cores of low β-ratio ≤ 1 per cent. This constitutes, under our assumptions, a major difference between the mechanisms happening in the low-mass and massive regimes of star formation. All our disc masses scale as a power law with the mass of the protostars and disc-to-mass ratios $M_d/M_\star > 1$ are obtained in models with higher β or small M_c, as at equal age more massive discs are obtained from cores of greater M_c but larger β. Our results confirm that massive protostars accrete about 40–60 per cent of their mass in the burst mode and stronger bursts appear in the later phase of the disc evolution.

Our numerical experiments keep on indicating that present-day massive formation is a scaled up version of low-mass star formation, both being ruled by the burst mode of accretion. As for their low-mass counterparts, young massive stars experience a strong and sudden increase of their accretion rate, e.g. when a disc fragment falls on to the star. This results in large amplitude fluctuations of its total luminosity, a swelling of the stellar radius, and a decrease of the flux released in the protostar's associated H II region. Under our assumptions, we calculate within the 10 th and 90 th percentile of the collection of bursts in our simulations of forming massive stars, the extend of their luminosity variations is ≈0.69, which is much larger than that observed for low-mass protostars (Wolk et al. 2018). This constitutes a major difference between the high- and low-mass regimes of star formation to be verified by means of future observations. Lastly, we discuss the structure of massive protostellar jets as potential indicators of their driving star's burst history. We propose that the high-frequency component of the burst bimodal distribution would correspond to the regular chain of knots along the overall jet morphology, while the second, low-frequency component peaking at 10^3–10^4 yr would be associated with the giant bow shock at the top of these jets. Our results motivate further investigations of the burst mode of accretion in forming higher mass stars and its connection with the morphology of massive protostellar jets.

ACKNOWLEDGEMENTS

The authors thank the anonymous referee for comments that improved the quality of the paper. D. M.-A. Meyer thanks W. Kley for priceless advice on disc physics. The authors acknowledge the North-German Supercomputing Alliance (HLRN) for providing HPC resources that have contributed to the research results reported in this paper. The computational results presented have been partly achieved using the Vienna Scientific Cluster (VSC). E. I. Vorobyov and A. M. Sobolev acknowledge support by the Ministry of Science and Higher Education of the Russian Federation under the grant 075-15-2020-780 (E. I. Vorobyov was supported under contract 780-2 and A.M. Sobolev was supported under contract 780-10). V. G. Elbakyan acknowledges support from STFC grants ST/N000757/1 to the University of Leicester.

DATA AVAILABILITY

This research made use of the PLUTO code developed at the University of Torino by A. Mignone (http://plutocode.ph.unito.it/). The figures have been produced using the Matplotlib plotting library for the PYTHON programming language (https://matplotlib.org/). The data underlying this article will be shared on reasonable request to the corresponding author.

REFERENCES

Ahmadi A., Kuiper R., Beuther H., 2019, A&A, 632, A50
Ahmadi A. et al., 2018, A&A, 618, A46
André Oliva G., Kuiper R., 2020, A&A, 644, A41
Añez-López N. et al., 2020, ApJ, 888, 41
Arce H. G., Shepherd D., Gueth F., Lee C. F., Bachiller R., Rosen A., Beuther H., 2007, in Reipurth B., Jewitt D., Keil K., eds, Protostars and Planets V. University of Arizona Press, Tucson, p. 245
Beuther H. et al., 2019, A&A, 621, A122
Boley P. A. et al., 2019, preprint (arXiv:1912.08510)
Bonnell I. A., Bate M. R., Zinnecker H., 1998, MNRAS, 298, 93
Bosco F., Beuther H., Ahmadi A., Mottram J. C., Kuiper R., Linz H., Maud E. A., 2019, A&A, 629, A10
Breen S. L., Sobolev A. M., Kaczmarek J. F., Ellingsen S. P., McCarthy T. P., Voronkov M. A., 2019, ApJ, 876, L25
Brogan C. L. et al., 2018, ApJ, 866, 87
Burns R. A., 2018, in Tarchi A., Reid M. J., Castangia P., eds, Proc. IAU Symp., Vol. 336, Astrophysical Masers: Unlocking the Mysteries of the Universe. International Astronomical Union, p. 263
Burns R. A., Handa T., Nagayama T., Sunada K., Omodaka T., 2016, MNRAS, 460, 283
Burns R. A., Sugiyama K., Hirota T., Kim K.-T., Sobolev A. M., Stecklum B., MacLeod G. C., Yonekura Y. E. A., 2020, Nature Astron., 4, 506
Burns R. A. et al., 2017, MNRAS, 467, 2367
Caratti o Garatti A., Stecklum B., Linz H., Garcia Lopez R., Sanna A., 2015, A&A, 573, A82
Caratti o Garatti A. et al., 2017, Nature Phys., 13, 276
Carrasco-González C., Rodríguez L. F., Anglada G., Martí J., Torrelles J. M., Osorio M., 2010, Science, 330, 1209
Cesaroni R., Galli D., Lodato G., Walmsley M., Zhang Q., 2006, Nature, 444, 703
Cesaroni R., Hofner P., Araya E., Kurtz S., 2010, A&A, 509, A50
Chen X., Ren Z., Zhang Q., Shen Z., Qiu K., 2017, ApJ, 835, 227
Chen X., Sobolev A. M., Breen S. L., Shen Z.-Q., Ellingsen S. P., MacLeod G. C. E. A., 2020b, ApJ, 890, L22
Chen X. et al., 2020a, Nature Astron.
Chini R., Hoffmeister V. H., Nasseri A., Stahl O., Zinnecker H., 2012, MNRAS, 424, 1925
Contreras Peña C., Naylor T., Morrell S., 2019, MNRAS, 486, 4590
Cunningham N. J., Moeckel N., Bally J., 2009, ApJ, 692, 943
Devine D., Bally J., Reipurth B., Heathcote S., 1997, AJ, 114, 2095
Dunham M. M., Vorobyov E. I., 2012, ApJ, 747, 52
Durisen R. H., Boss A. P., Mayer L., Nelson A. F., Quinn T., Rice W. K. M., 2007, Protostars and Planets V. University of Arizona Press, Tucson, p. 607
Eislöffel J., Mundt R., 1992, A&A, 263, 292
Eislöffel J., Mundt R., 1997, AJ, 114, 280
Eislöffel J., Mundt R., 1998, AJ, 115, 1554
Elbakyan V. G., Vorobyov E. I., Rab C., Meyer D. M.-A., Güdel M., Hosokawa T., Yorke H., 2019, MNRAS, 484, 146
Ercolano B., Owen J. E., 2016, MNRAS, 460, 3472
Fedriani R. et al., 2019, Nature Commun., 10, 3630
Flock M., Dzyurkevich N., Klahr H., Turner N. J., Henning T., 2011, ApJ, 735, 122
Forgan D. H., Ilee J. D., Cyganowski C. J., Brogan C. L., Hunter T. R., 2016, MNRAS, 463, 957
Franz R., Picogna G., Ercolano B., Birnstiel T., 2020, A&A, 635, A53
Fuente A., Neri R., Martín-Pintado J., Bachiller R., Rodríguez-Franco A., Palla F., 2001, A&A, 366, 873
Gammie C. F., 2001, ApJ, 553, 174
Ginsburg A., Bally J., Goddi C., Plambeck R., Wright M., 2018, ApJ, 860, 119
Haemmerlé L., 2014, PhD thesis, Univ. Geneva
Haemmerlé L., Eggenberger P., Meynet G., Maeder A., Charbonnel C., 2016, A&A, 585, A65
Haemmerlé L., Eggenberger P., Meynet G., Maeder A., Charbonnel C., Klessen R. S., 2017, A&A, 602, A17
Harries T. J., 2015, MNRAS, 448, 3156
Harries T. J., Douglas T. A., Ali A., 2017, MNRAS, 471, 4111
Hollenbach D., Johnstone D., Lizano S., Shu F., 1994, ApJ, 428, 654
Hosokawa T., Hirano S., Kuiper R., Yorke H. W., Omukai K., Yoshida N., 2016, ApJ, 824, 119
Hosokawa T., Omukai K., 2009, ApJ, 691, 823
Hosokawa T., Omukai K., Yoshida N., Yorke H. W., 2011, Science, 334, 1250
Hosokawa T., Yorke H. W., Inayoshi K., Omukai K., Yoshida N., 2013, ApJ, 778, 178
Hosokawa T., Yorke H. W., Omukai K., 2010, ApJ, 721, 478
Hosokawa T., Yoshida N., Omukai K., Yorke H. W., 2012, ApJ, 760, L37
Hunter T., 2019, in Resolving the source of the massive protostellar accretion outburst in NGC6334I-MM1B, ALMA2019: Science Results and Cross-Facility Synergies, p. 91

Ilee J. D., Cyganowski C. J., Brogan C. L., Hunter T. R., Forgan D. H., Haworth T. J., Clarke C. J., Harries T. J., 2018, ApJ, 869, L24
Ilee J. D., Cyganowski C. J., Nazari P., Hunter T. R., Brogan C. L., Forgan D. H., Zhang Q., 2016, MNRAS, 462, 4386
Jankovic M. R. et al., 2019, MNRAS, 482, 4673
Johnston K. G. et al., 2015, ApJ, 813, L19
Johnston K. G. et al., 2019, A&A, 634, L11
Keto E., Wood K., 2006, ApJ, 637, 850
Klassen M., Pudritz R. E., Kuiper R., Peters T., Banerjee R., 2016, ApJ, 823, 28
Kobulnicky H. A. et al., 2014, ApJS, 213, 34
Kratter K. M., Matzner C. D., 2006, MNRAS, 373, 1563
Kraus S. et al., 2017, ApJ, 835, L5
Krumholz M. R., Klein R. I., McKee C. F., 2007, ApJ, 656, 959
Laor A., Draine B. T., 1993, ApJ, 402, 441
Larson R. B., 1969, MNRAS, 145, 271
Larson R. B., 1972, MNRAS, 157, 121
Liu S.-Y., Su Y.-N., Zinchenko I., Wang K.-S., Meyer D. M. A., Wang Y., Hsieh I.-T., 2020, ALMA View of the Infalling Envelope around a Massive Protostar in S255IR SMA1, preprint (arXiv:2010.09199)
MacLeod G. C. et al., 2018, MNRAS, 478, 1077
MacLeod G. C. et al., 2019, MNRAS, 489, 3981
Mahy L., Rauw G., De Becker M., Eenens P., Flores C. A., 2013, A&A, 550, A27
Maud L. T., Cesaroni R., Kumar M. S. N., Rivilla V. M., Ginsburg A., Klaassen P. D., Harsono D. E. A., 2019, A&A, 627, L6
Maud L. T., Hoare M. G., Galván-Madrid R., Zhang Q., de Wit W. J., Keto E., Johnston K. G., Pineda J. E., 2017, MNRAS, 467, L120
Maud L. T. et al., 2018, A&A, 620, A31
McKee C. F., Stacy A., Li P. S., 2020, MNRAS, 496, 5528
McKee C. F., Tan J. C., 2008, ApJ, 681, 771
McLeod A. F., Reiter M., Kuiper R., Klaassen P. D., Evans C. J., 2018, Nature, 554, 334
Meyer D. M.-A., Kuiper R., Kley W., Johnston K. G., Vorobyov E., 2018, MNRAS, 473, 3615
Meyer D. M.-A., Vorobyov E. I., Elbakyan V. G., Stecklum B., Eislöffel J., Sobolev A. M., 2019a, MNRAS, 482, 5459
Meyer D. M.-A., Vorobyov E. I., Kuiper R., Kley W., 2017, MNRAS, 464, L90
Meyer D. M. A., Haemmerlé L., Vorobyov E. I., 2019b, MNRAS, 484, 2482
Meyer D. M. A., Kreplin A., Kraus S., Vorobyov E. I., Haemmerle L., Eislöffel J., 2019c, MNRAS, 487, 4473
Mignone A., Bodo G., Massaglia S., Matsakos T., Tesileanu O., Zanni C., Ferrari A., 2007, ApJS, 170, 228
Mignone A., Zanni C., Tzeferacos P., van Straalen B., Colella P., Bodo G., 2012, ApJS, 198, 7
Motogi K., Hirota T., Machida M. N., Yonekura Y., Honma M., Takakuwa S., Matsushita S., 2019, ApJ, 877, L25
Nayakshin S., Lodato G., 2012, MNRAS, 426, 70
Obonyo W. O., Lumsden S. L., Hoare M. G., Purser S. J. D., Kurtz S. E., Johnston K. G., 2019, MNRAS, 486, 3664
Offner S. S. R., McKee C. F., 2011, ApJ, 736, 53
Padoan P., Haugbølle T., Nordlund Å., 2014, ApJ, 797, 32
Peters T., Banerjee R., Klessen R. S., Mac Low M.-M., Galván-Madrid R., Keto E. R., 2010, ApJ, 711, 1017
Purser S. J. D., Lumsden S. L., Hoare M. G., Cunningham N., 2018, MNRAS, 475, 2
Purser S. J. D. et al., 2016, MNRAS, 460, 1039
Rafikov R. R., 2007, ApJ, 662, 642
Rafikov R. R., 2009, ApJ, 704, 281
Reipurth B., Bally J., Devine D., 1997, AJ, 114, 2708
Reiter M., Kiminki M. M., Smith N., Bally J., 2017, MNRAS, 470, 4671
Richling S., Yorke H. W., 1997, A&A, 327, 317
Richling S., Yorke H. W., 1998, A&A, 340, 508
Richling S., Yorke H. W., 2000, ApJ, 539, 258
Rogers P. D., Wadsley J., 2012, MNRAS, 423, 1896
Rosen A. L., Krumholz M. R., McKee C. F., Klein R. I., 2016, MNRAS, 463, 2553
Rosen A. L., Li P. S., Zhang Q., Burkhart B., 2019, ApJ, 887, 108
Samal M. R., Chen W. P., Takami M., Jose J., Froebrich D., 2018, MNRAS, 477, 4577
Sanna A., Moscadelli L., Surcis G., van Langevelde H. J., Torstensson K. J. E., Sobolev A. M., 2017, A&A, 603, A94
Sanna A. et al., 2019, A&A, 623, A77
Seifried D., Banerjee R., Klessen R. S., Duffin D., Pudritz R. E., 2011, MNRAS, 417, 1054
Shchekinov Y. A., Sobolev A. M., 2004, A&A, 418, 1045
Shu F. H., 1977, ApJ, 214, 488
Szymczak M., Olech M., Wolak P., Gérard E., Bartkiewicz A., 2018, A&A, 617, A80
Testi L., 2003, in De Buizer J. M., van der Bliek N. S., eds, ASP Conf. Ser. Vol. 287, Galactic Star Formation Across the Stellar Mass Spectrum. Astron. Soc. Pac., San Francisco, p. 163
Toomre A., 1963, ApJ, 138, 385
Vorobyov E. I., 2009, ApJ, 704, 715
Vorobyov E. I., 2010, ApJ, 723, 1294
Vorobyov E. I., 2011a, ApJ, 728, L45
Vorobyov E. I., 2011b, ApJ, 729, 146
Vorobyov E. I., Basu S., 2006, ApJ, 650, 956
Vorobyov E. I., Basu S., 2010, ApJ, 719, 1896
Vorobyov E. I., Basu S., 2015, ApJ, 805, 115
Vorobyov E. I., Elbakyan V. G., Plunkett A. L., Dunham M. M., Audard M., Guedel M., Dionatos O., 2018, A&A, 613, A18
Wang Y. et al., 2011, A&A, 527, A32
Weber M. L., Ercolano B., Picogna G., Hartmann L., Rodenkirch P. J., 2020, MNRAS, 496, 223
Wolk S. J. et al., 2018, AJ, 155, 99
Wurster J., Bate M. R., 2019a, preprint (arXiv:1906.12276)
Wurster J., Bate M. R., 2019b, MNRAS, 486, 2587
Yorke H. W., Bodenheimer P., Tenorio-Tagle G., 1982, A&A, 108, 25
Yorke H. W., Kruegel E., 1977, A&A, 54, 183
Yorke H. W., Sonnhalter C., 2002, ApJ, 569, 846
Yorke H. W., Welz A., 1996, A&A, 315, 555
Zhao B., Caselli P., Li Z.-Y., Krasnopolsky R., 2018, MNRAS, 473, 4868
Zinchenko I. et al., 2015, ApJ, 810, 10
Zinchenko I. I., Liu S.-Y., Su Y.-N., Wang K.-S., Wang Y., 2019, ApJ, 889, 43

This paper has been typeset from a TEX/LATEX file prepared by the author.

The burst mode of accretion in massive star formation with stellar inertia

D. M.-A. Meyer[1⋆], E. I. Vorobyov[2,3], V. G. Elbakyan[4], S. Kraus[5], S.-Y. Liu[6], S. Nayakshin[4], A. M. Sobolev[7].

[1]*Institut für Physik und Astronomie, Universität Potsdam, Karl-Liebknecht-Strasse 24/25, 14476 Potsdam, Germany*
[2]*Institute of Astronomy, Russian Academy of Sciences, 48 Pyatnitskaya St., Moscow, 119017, Russia*
[3]*University of Vienna, Department of Astrophysics, Vienna, 1180, Austria*
[4]*School of Physics and Astronomy, University of Leicester, Leicester, LE1 7RH, UK*
[5]*University of Exeter, Department of Physics and Astronomy, Exeter, Devon EX4 4QL, UK*
[6]*Institute of Astronomy and Astrophysics, Academia Sinica, 11F of ASMAB, AS/NTU No.1, Sec. 4, Roosevelt Rd, Taipei 10617, Taiwan*
[7]*Ural Federal University, 19 Mira Str., 620002 Ekaterinburg, Russia*

Received; accepted

ABSTRACT

The burst mode of accretion in massive star formation is a scenario linking the initial gravitational collapse of parent pre-stellar cores to the properties of their gravitationally unstable discs and of their accretion-driven bursts. In this study, we present a series of high-resolution 3D radiation-hydrodynamics numerical simulations for young massive stars formed out of collapsing $100\,\mathrm{M}_\odot$ molecular cores spinning with several values of the ratio of rotational-to-gravitational energies $\beta = 5\%$–9%. The models include the indirect gravitational potential caused by disc asymmetries. We find that this modifies the barycenter of the disc, causing significant excursions of the central star position, which we term stellar wobbling. The stellar wobbling slows down and protracts the development of gravitational instability in the disc, reducing the number and magnitude of the accretion-driven bursts undergone by the young massive stars, whose properties are in good agreement with that of the burst monitored from the massive protostar M17 MIR. Including stellar wobbling is therefore important for accurate modeling disc structures. Synthetic ALMA interferometric images in the millimeter waveband show that the outcomes of efficient gravitational instability such as spiral arms and gaseous clumps can be detected for as long as the disc is old enough and has already entered the burst mode of accretion.

Key words: methods: numerical – radiative transfer – stars: circumstellar matter.

1 INTRODUCTION

The burst mode of accretion in star formation is a model proposed to explain the main accretion phase of low-mass stars. In this model, gaseous clumps formed via disk gravitational fragmentation migrate inwards and trigger accretion bursts when tidally destroyed in the vicinity of the star (Vorobyov & Basu 2006, 2010, 2015; Machida et al. 2011; Nayakshin & Lodato 2012; Zhao et al. 2018; Vorobyov et al. 2018). The burst mode of accretion links together several distinct phases experienced by young stars, starting from the initial free-fall collapse of cold pre-stellar cores, through the main accretion phase when a notable fraction of the final stellar mass is acquired during bursts, and finally to the T-Tauri phase, in which the characteristics of young stars may still be affected by the earlier burst phase (Baraffe et al. 2012; Vorobyov et al. 2017; Elbakyan et al. 2019). In this picture, the infall of gas from the collapsing protostellar core plays a key role, replenishing the material lost by the disc during accretion bursts, sustaining the disk in the gravitationally unstable stage and developing disc substructures such as spiral arms and fragments. The burst mode of accretion can resolve the so-called "luminosity problem" (Kenyon et al. 1990; Kenyon & Hartmann 1990, 1995; Dunham & Vorobyov 2012), and the burst characteristics are in accordance with the FU-Orionis-type stars (Vorobyov & Basu 2015).

A scaling relationship between star-forming mechanisms of low- and high-mass stars has been suspected for decades (Fuente et al. 2001; Testi 2003; Cesaroni et al. 2006; Johnston et al. 2013), Observations of bipolar H II regions and/or jets in the surroundings of young high-mass stars (Cunningham et al. 2009; Caratti o Garatti et al. 2015; Burns et al. 2017; Burns 2018; Reiter et al. 2017; Purser et al. 2018; Samal et al. 2018; Boley et al. 2019; Zinchenko et al. 2019; Goddi et al. 2020; Purser et al. 2021) pro-

⋆ E-mail: dmameyer.astro@gmail.com

vided clues and signatures in its favour. This has been strengthened by the detection of a first luminous flare from the high-mass protostar S255IR-NIRS3 (Caratti o Garatti et al. 2017), and by many others, both in the infrared and by maser emission, in the following years (Moscadelli et al. 2017; Szymczak et al. 2018; Brogan et al. 2018; MacLeod et al. 2018; Liu et al. 2018; Hunter et al. 2017; Proven-Adzri et al. 2019; Lucas et al. 2020; Chen et al. 2020; Olguin et al. 2020; Chen et al. 2020; Burns et al. 2020; Chen et al. 2021; Stecklum et al. 2021; Hunter et al. 2021). Additionally, the discovery, in radiation-hydrodynamics numerical simulations, of processes for the formation of high-mass stars such as accretion-driven outbursts, similar to that of their low-mass counterparts, suggested that the burst mode of accretion in star formation also applies to higher-mass objects (Meyer et al. 2017).

It has successively been found that gaseous clumps in accretion discs surrounding young high-mass stars have pressure and temperature ($> 2000\,\mathrm{K}$) consistent with the dissociation of molecular hydrogen, meaning that disc fragmentation is also at the origin of the formation of spectroscopic protobinaries (Meyer et al. 2018), see also Oliva & Kuiper (2020). The observability of these nascent binaries has been demonstrated by means of synthetic ALMA interferometric observations (Meyer et al. 2019). Further studies showed that massive young stellar objects accrete most of their mass within high-magnitude accretion-driven outbursts, taking place during a very short fraction of their pre-main-sequence life (Meyer et al. 2019). During the burst itself, the accretion rate sharply increases, generating a swelling of the protostellar radius, which, in its turn, provokes rapid excursions to the cold part of the Herzsprung-Russell diagram and triggers the intermittency of the irradiation fluxes filling the H II region of a young high-mass star (Meyer et al. 2019). Lastly, a parameter study exploring the properties and burst characteristics of a large collection of models for the formation of massive young stellar objects concluded that no massive protostars should form without bursts, which span over a bimodal distribution of short ($\sim 1 - 10\,\mathrm{yr}$) and long ($\sim 10^3 - 10^4\,\mathrm{yr}$) flares (Meyer et al. 2021), see also Elbakyan et al. (2021).

Gravitation-hydrodynamics naturally includes the gravitational interaction experienced by the substructures developed in the fragmenting accretion discs forming around young stars. Consequently, when the density field of an accretion disc is not described by a symmetric pattern because of the presence of irregular spiral arms and/or (migrating) gaseous clumps, the center of mass of the disc is not anymore coinciding with that of the location of the star. This is particularly true in the case of massive discs forming around high-mass protostars (Meyer et al. 2018). The gravitational interaction between the disc and the star consequently generates an acceleration and a displacement of the protostar as a result of total gravitational force of the disc operating onto the young star. While such a mechanism is intrinsically taken into account in grid-based simulations in Cartesian coordinates (Krumholz et al. 2007b; Seifried et al. 2011; Klassen et al. 2016; Rosen et al. 2019) and Lagrangian models (Springel 2010), it is often neglected in grid-based models using a spherical, cylindrical or polar coordinate system in which the star is fixed at the coordinate origin (Vorobyov & Basu 2006; Oliva & Kuiper 2020).

A number of studies on planet and low-mass star formation have not taken into account this gravitational backaction of the disc onto the star (Tanaka et al. 2002; Pickett et al. 2003; Tanaka & Ward 2004; Ou et al. 2007; Boley et al. 2007; Tsukamoto & Machida 2011; Fung & Artymowicz 2014; Szulágyi et al. 2014; Zhu & Stone 2014; Lin 2015) while some other studies did (Regály & Vorobyov 2017). There, the star-disc barycenter and the geometrical grid center are displaced with respect to each other, in response to the gravitational force of the disc mass exerted onto the protostar, and it provokes a motion of the central star through the disc. A solution to this problem, accounting for the intrinsic singularity present at the coordinate origin of curvelinear coordinate systems, consists in time-dependently displacing the whole disc in responce to an acceleration that the star experiences as a result of disc gravity force. This so-called non-inertial frame of reference, which considers the gravitational response to the disc of the stellar motion, has been introduced in Michael & Durisen (2010a).

We hereby continue our numerical investigation of the burst mode of accretion in massive star formation, by performing high spatial resolution simulations of radiation-hydrodynamical disc models for several initial rotation rates of the molecular pre-stellar core (Meyer et al. 2017). The numerical setup is augmented with the physics of stellar wobbling (Regály & Vorobyov 2017). We measure from our simulations, both the physical properties of the accretion discs, as well as the characteristics of the accretion-driven outbursts generated by the star-disc system (Meyer et al. 2017, 2018, 2021). We further discuss our results in the context of the observational appearance of the accretion discs, by performing synthetic interferometric images as seen by the *Atacama Large Millimeter/submillimeter Array* (ALMA) when operating at band 6 ($1.2\,\mathrm{mm}$). Beyond the confirmation of the observability of the disc of massive young stellar objects (Krumholz et al. 2007a; Jankovic et al. 2019; Meyer et al. 2019), these synthetic observables reveal how the outcomes of gravitational instability should look in realistic discs.

The outline of this study is organised as follows. In Section 2 we present the numerical methods for both the disc and the indirect potential that we use to model the circumstellar medium of young massive stars. In Section 3 we show the effects of the young star's motion onto the evolution of its circumstellar disc and on the properties of its pre-main-sequence accretion bursts. The caveats of our results are discussed in Section 4, together with the effect of stellar motion on interferometric emission. We conclude in Section 5.

2 METHOD

In this section we present the methodology used to perform our radiation-hydrodynamical simulations of accretion discs surrounding massive young stellar objects.

2.1 Initial conditions

The simulations in this study are initialised with a three-dimensional, rotating pre-stellar core of external radius R_c and radial density profile,

$$\rho(r) = \frac{(\beta_\rho + 3)}{4\pi} \frac{M_\mathrm{c}}{R_\mathrm{c}^{\beta_\rho+3}} r^{\beta_\rho}, \tag{1}$$

with r the radial coordinate, $M_\mathrm{c} = 100\,\mathrm{M}_\odot$ the mass of the molecular core and β_ρ a negative exponent taken to $\beta_\rho = -3/2$. The velocity field is set according to the following angular momentum distribution,

$$\Omega(R) = \Omega_0(\beta)\Big(\frac{R}{r_0}\Big)^{\beta_\Omega}, \tag{2}$$

with $\Omega_0(\beta)$ a normalization factor depending on the adopted β ratio, $r_0 = 20\,\mathrm{au}$ and $R = r\sin(\theta)$ the so-called cylindrical radius.

One can therefore calculate the ratio of kinetic-to-gravitational energy of the pre-stellar core, $\beta = E_{\rm rot}/E_{\rm grav}$, and determine its initial toroidal rotation profile $v_\phi(R) = R\Omega(R)$, while the other components of the velocity are set to $v_{\rm r} = v_\theta = 0$. The pre-stellar core's gravitational energy reads,

$$E_{\rm grav} = \frac{\beta_\rho + 3}{2\beta_\rho + 5}\frac{GM_{\rm c}^2}{R_{\rm c}}, \tag{3}$$

and its rotational kinetic energy is as follows,

$$E_{\rm rot} = \frac{(\beta_\rho + 3)}{4(\beta_\rho + 2\beta_\Omega + 5)}\frac{\Omega_0(\beta)^2 M_{\rm c} r_0^{-2\beta_\Omega}}{R_{\rm c}^{-2(\beta_\Omega+1)}}\int_0^\pi d\theta \sin(\theta)^{3+2\beta_\Omega}, \tag{4}$$

respectively. Our models explore a parameter space for several initial ratio β of the pre-stellar core, spanning from 0.05 to 0.09 (Meyer et al. 2021) and we assume that the core is in solid-body rotation ($\beta_\Omega = 0$). The list of models is reported in Table 1. For the sake of completeness and comparison, and to emphasize the importance of stellar wobbling, the high-resolution simulations are performed with and without stellar wobbling.

In this study, midplane-symmetric 3D numerical simulations using a a static grid are performed in spherical coordinates (r, θ, ϕ) with a grid $[r_{\rm in}, R_{\rm c}]\times[0, \pi/2]\times[0, 2\pi]$ that is spaced as a logarithm in the radial direction r, a cosine in the direction θ and uniform in ϕ. It is made of $256\times41\times256$ grid zones discretising the grid, that is taken to have $r_{\rm in} = 20\,{\rm au}$ and $R_{\rm c} = 0.1\,{\rm pc}$, respectively. The pre-stellar core is initialised with a constant temperature $T_{\rm c} = 10\,{\rm K}$, and the molecular material is treated as an ideal gas. As in Meyer et al. (2017) and Meyer et al. (2018), we impose outflow boundary conditions at the inner and outer part of the radial direction r. The mass accretion rate onto the protostar $\dot{M}$ is therefore measured as the gas flux crossing $r_{\rm in}$. The governing equations of these gravito-radiation-hydrodynamics simulations are solved using a scheme that is 2$^{\rm nd}$ order in space and time, using the PLUTO code (Mignone et al. 2007, 2012; Vaidya et al. 2018), within its version augmented for stellar evolution (Hosokawa & Omukai 2009), radiation transport (Kolb et al. 2013) and self-gravity. Hence, the method incorporates the protostellar radiation releasing photon from the photosphere of the young star and irradiating the inner disc region, before being subsequently diffused through the disk by flux-limited diffusion treated within the gray approximation (Kolb et al. 2013). We refer the reader further interested in the numerical method to Meyer et al. (2021).

2.2 Governing equations

The equations ruling the evolution of the modelled system read,

$$\frac{\partial\rho}{\partial t} + \boldsymbol{\nabla}\cdot(\rho\boldsymbol{v}) = 0, \tag{5}$$

$$\frac{\partial\rho\boldsymbol{v}}{\partial t} + \boldsymbol{\nabla}\cdot(\rho\boldsymbol{v}\otimes\boldsymbol{v}) + \boldsymbol{\nabla}p = \boldsymbol{f}, \tag{6}$$

$$\frac{\partial E}{\partial t} + \boldsymbol{\nabla}\cdot((E+p)\boldsymbol{v}) = \boldsymbol{v}\cdot\boldsymbol{f}, \tag{7}$$

standing for the conservation of mass, momentum and energy, where ρ is the gas density, $\boldsymbol{v}$ the gas velocity, $p = (\gamma-1)E_{\rm int}$ the thermal pressure and $\gamma = 5/3$ the adiabatic index. Additionally, the quantity,

$$\boldsymbol{f} = -\rho\boldsymbol{\nabla}\Phi_{\rm tot} - \lambda\boldsymbol{\nabla}E_{\rm R} - \boldsymbol{\nabla}\cdot\Big(\frac{\boldsymbol{F}_\star}{c}\Big)\boldsymbol{e}_{\rm r}, \tag{8}$$

is the force density vector, where λ is the flux limiter, and where $E_{\rm R}$, $\boldsymbol{e}_{\rm r}$ $\boldsymbol{F}_\star$, c are the thermal radiation energy density, radial unit vector, stellar radiation flux and the speed of light. Lastly, $E = E_{\rm int} + \rho\boldsymbol{v}^2/2$ represents the total, internal plus kinetic energy.

Radiation transfer is calculated by solving the equation of radiation transport for $E_{\rm R}$, the thermal radiation energy density,

$$\frac{\partial}{\partial t}\Big(\frac{E_{\rm R}}{f_{\rm c}}\Big) + \boldsymbol{\nabla}\cdot\boldsymbol{F} = -\boldsymbol{\nabla}\cdot\boldsymbol{F}_\star, \tag{9}$$

with $f_{\rm c} = 1/(c_{\rm v}\rho/4aT^3+1)$, and where $c_{\rm v}$ is the calorific capacity and a is the radiation constant, respectively. It is solved in the flux-limited diffusion approach, with $\boldsymbol{F}_\star(R_\star)$ the protostellar flux, i.e. the photospheric irradiation values are estimated using both the interpolated effective temperature $T_{\rm eff}$ and the stellar radius $R_\star$ from protostellar evolution models (Hosokawa & Omukai 2009). Similarly, the radiation flux reads $\boldsymbol{F} = -D\boldsymbol{\nabla}E_{\rm R}$, where D is the diffusion constant. The irradiating stellar flux is set at the inner boundary at a radius r as,

$$\boldsymbol{F}_\star(r) = \boldsymbol{F}_\star(R_\star)\Big(\frac{R_\star}{r}\Big)^2 e^{-\tau(r)}, \tag{10}$$

with $\tau(r)$ the optical depth of the medium, estimated with both constant gas opacity and dust opacities from Laor & Draine (1993). Self-gravity is included by solving the Poisson equation for the total gravitational potential and the stellar gravitational contribution, respectively.

2.3 Stellar inertia

The stellar motion has been implemented as an additional indirect potential $\Phi_{\rm wobbling}$, to which the force $\vec{F}_{\rm wobbling}$ is associated, following the prescription of Hirano et al. (2017). It is the opposite of the disc-to-star gravitational interaction $\vec{F}_{\rm wobbling} = \vec{F}_{\star/{\rm disc}} = -\vec{F}_{{\rm disc}/\star}$ The force is calculated in spherical coordinates, but the respective contributions from each individual grid cells of the computational domain are integrated in Cartesian coordinates. Hence, the force exerted by a given volume element δV of the disc reads,

$$\delta\vec{F}_{{\rm disc}/\star} = -GM_\star\frac{\delta M_{\rm disc}(r)}{r^2}\vec{e}_{\rm r}, \tag{11}$$

and the total force is therefore,

$$\vec{F}_{{\rm disc}/\star} = -GM_\star\int_{\rm disc}\frac{\rho(r)\delta V}{r^2}\vec{e}_{\rm r}, \tag{12}$$

with $M_\star$ the stellar mass, G the gravitational constant, $\vec{e}_{\rm r}$ the radial unit verctor and $\delta M_{\rm disc}(r) = \rho(r)\delta V$ the mass contained in the corresponding volume element.

Assuming the star to be fixed in the non-inertial frame of reference, the radial force can be expressed as a function of its projections in Cartesian coordinates. We obtain,

$$\vec{F}_{{\rm disc}/\star} = \sqrt{(F^x_{{\rm disc}/\star})^2 + (F^y_{{\rm disc}/\star})^2 + (F^z_{{\rm disc}/\star})^2}\vec{e}_{\rm r}, \tag{13}$$

with,

$$\vec{F}^x_{{\rm disc}/\star} = -GM_\star\Big[\int_{\rm disc}\frac{\rho\delta V}{r^2}\Big]\vec{e}_{\rm r}\cdot\vec{e}_{\rm x}, \tag{14}$$

$$\vec{F}^y_{{\rm disc}/\star} = -GM_\star\Big[\int_{\rm disc}\frac{\rho\delta V}{r^2}\Big]\vec{e}_{\rm r}\cdot\vec{e}_{\rm y}, \tag{15}$$

and

$$\vec{F}^z_{{\rm disc}/\star} = -GM_\star\Big[\int_{\rm disc}\frac{\rho\delta V}{r^2}\Big]\vec{e}_{\rm r}\cdot\vec{e}_{\rm z}, \tag{16}$$

Table 1. List of the simulation models performed in our study. The table provides the initial mass of the molecular pre-stellar core $M_{\rm c}$ (in $M_\odot$), its initial rotational-to-gravitational energy ratio β (in %), the final simulation time $t_{\rm end}$ and the final stellar mass $M_\star(t_{\rm end})$ in each simulation models, respectively. The last column indicates whether the simulation includes stellar wobbling.

Models	$M_{\rm c}$ ($\mathrm{M}_\odot$)	Grid resolution	β (%)	$t_{\rm end}$ (kyr)	$M_\star(t_{\rm end})$	Wobbling
Run-256-100$\mathrm{M}_\odot$-5%-wio	100	$256\times42\times256$	5	40.0	26.3	no
Run-256-100$\mathrm{M}_\odot$-5%-wi	100	$256\times42\times256$	5	40.0	25.9	yes
Run-256-100$\mathrm{M}_\odot$-7%-wio	100	$256\times42\times256$	7	40.0	24.3	no
Run-256-100$\mathrm{M}_\odot$-7%-wi	100	$256\times42\times256$	7	40.0	25.7	yes
Run-256-100$\mathrm{M}_\odot$-9%-wio	100	$256\times42\times256$	9	32.5	16.0	no
Run-256-100$\mathrm{M}_\odot$-9%-wi	100	$256\times42\times256$	9	32.5	18.5	yes

with $\vec{e}_{\rm x}$, $\vec{e}_{\rm y}$, $\vec{e}_{\rm z}$ the Cartesian unit vectors. In the disc midplane,

$$\vec{e}_{\rm r}\cdot\vec{e}_{\rm x} = C_\phi S_\theta, \quad (17)$$

$$\vec{e}_{\rm r}\cdot\vec{e}_{\rm y} = S_\phi S_\theta, \quad (18)$$

$$\vec{e}_{\rm r}\cdot\vec{e}_{\rm z} = C_\theta, \quad (19)$$

respectively, with ϕ and θ the azimuthal and polar angles of the spherical coordinate system, and where $C_\theta = \cos(\theta)$, $S_\theta = \sin(\theta)$, $C_\phi = \cos(\phi)$ and $S_\phi = \sin(\phi)$ respectively.

Finally, the effect of the indirect force is implemented as an acceleration term,

$$\vec{g}^{\,'} = \frac{\vec{F}_{\rm wobbling}}{M_\star} = -\frac{\vec{F}_{\rm disc/\star}}{M_\star}, \quad (20)$$

into the solver for gravitation of the code PLUTO. Explicitly, the components of $\vec{g}^{\,'}$ read,

$$g_r^{'} = \frac{1}{M_\star}\Big[F_{\rm disc/\star}S_\theta C_\phi + F_{\rm disc/\star}S_\theta S_\phi + F_{\rm disc/\star}C_\theta\Big], \quad (21)$$

$$\vec{g}_\phi^{\,'} = \frac{1}{M_\star}\Big[F_{\rm disc/\star}C_\theta C_\phi + F_{\rm disc/\star}C_\theta S_\phi - F_{\rm disc/\star}S_\theta\Big], \quad (22)$$

$$\vec{g}_\theta^{\,'} = \frac{1}{M_\star}\Big[-F_{\rm disc/\star}S_\phi + F_{\rm disc/\star}C_\phi\Big], \quad (23)$$

respectively. The stellar mass $M_\star$ is evaluated at each timesteps, as the time integral of the accretion rate $\dot{M}$ onto the sink cell.

3 RESULTS

This section explores the evolution of the protostellar disc properties such as the disc radius and mass, for both simulations without and with the inclusion of the stellar motion of the central high-mass star. Similarly, we present how the intensity and duration of the accretion-driven bursts change when the star is allowed to move, for several initial conditions of the pre-stellar core.

3.1 Discs

3.1.1 Structure and evolution

In Fig. 1 we plot the midplane density field of the accretion discs (in cm^{-3}) in our simulations with initial kinetic-to-gravitational energy $\beta = 5\%$ (top series of panels), $\beta = 7\%$ (middle series of panels) and $\beta = 9\%$ (bottom series of panels). For each model, the discs are shown at several time instances as well as a later time, both without and with stellar inertia. In the figures, we only represent the inner ($\leqslant 1000\,\mathrm{au}$) part of the computational domain, for time instances that are older than the end of the free-fall gravitational collapse of the pre-stellar cloud and the onset of the disc formation. The accretion discs without stellar wobbling qualitatively evolve as described in the previous papers of this series, by undergoing efficient gravitational instabilities responsible for the formation of spiral arms and other rotating, self-gravitating substructures such as gaseous clumps and disc fragments (Meyer et al. 2018, 2019). Notable differences in the models with stellar inertia compared to the simulations with fixed star appear at times $\geqslant 25\,\mathrm{kyr}$.

The models without and with stellar inertia initially do not reveal differences, regardless of the β-ratio of the collapsing molecular cloud. This is visible in the left column of each panels showing the discs at time 17 kyr. Their size increases as a function of the increasing β-ratio of the molecular cloud, because the timescale of the free-fall gravitational collapse is shorter for high β-ratio (see Fig. 2), hence at time 17 kyr the discs with $\beta = 9\%$ are slightly older and more developed than that with $\beta = 5\%$. The same is true at time 20.0 kyr. Even tough the discs are qualitatively similar in terms of overall structure, differences begin to appear in their morphology, such as the number and the geometry of the growing spiral arms, see Fig. 1-1b,1f.

In our model with $\beta = 5\%$, one can see at time 29.5 kyr, that the disc with stellar wobbling has a rather compact structure wrapped by a large spiral arm (Fig. 1-1g), while the simulation without stellar wobbling has a more complex inner structure and exhibit signs of fragmentation both at its center and in a spiral arm extending to distance $> 500\,\mathrm{au}$ from the protostar. The parent arm hosts a dense clump in the process of detaching from it, before migrating down to the protostar (Fig. 1-1c). At time 36.0 kyr, both discs exhibit signs of active gravitational instability. The disc model without wobbling is more extended and has a (northern) very massive and large clump $\sim 1000\,\mathrm{au}$ from the protostar as well as a (southern) dense spiral arm (Fig. 1-1d), while the model with wobbling has a rounder and more compact structure in which enrolled spiral arms host a few clumps at distances $< 500\,\mathrm{au}$ from the protostar (Fig. 1-1h). The discs are at different stages of internal reorganisation after it has experienced migrations of dense clumps onto the protostar, which generates an ejection of the clumps' gaseous tails that reshuffle the whole disc structure (Meyer et al. 2018).

Hence, stellar wobbling moderately delays the fragmentation of the disc and reduces its entire size. The explanation is that when stellar wobbling is not considered, the accretion disc alone contains all the angular momentum of the star-disc system. Permitting the protostar to move (i) redistributes this angular momentum between the star and the disk with a net effect that the disk angular momentum decreases. Without stellar inertia, the discs turn to be of larger radius, and, therefore, their more extended spiral arms

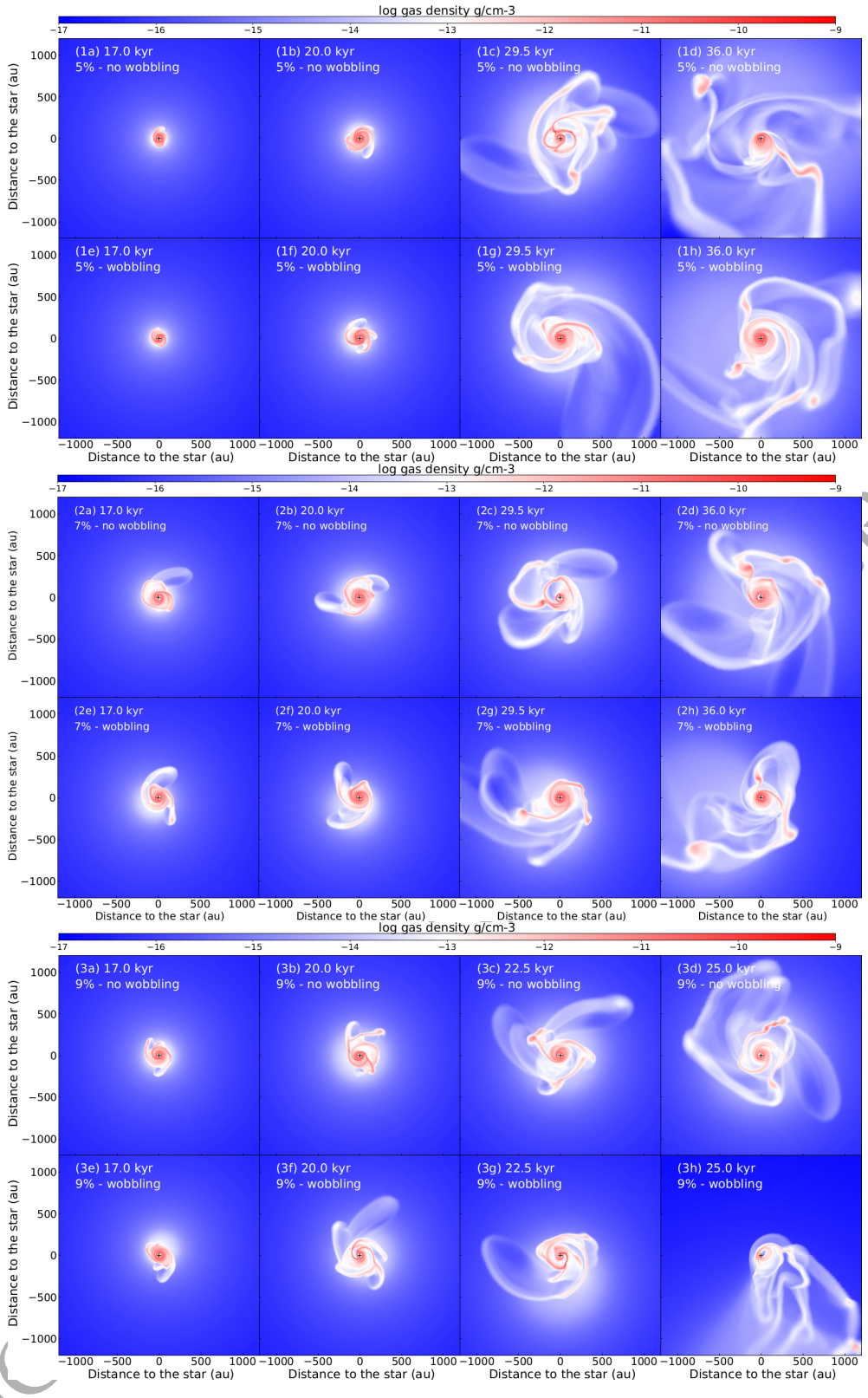

Figure 1. Density fields in the disc simulations with $\beta = 5\%$ (top), $\beta = 7\%$ (middle) and $\beta = 9\%$ (bottom). The figures display the disc midplane gas density (in g cm^{-3}), for several characteristics time instances of the accretion disc evolution, without (upper panels) and with (lower panels) stellar wobbling.

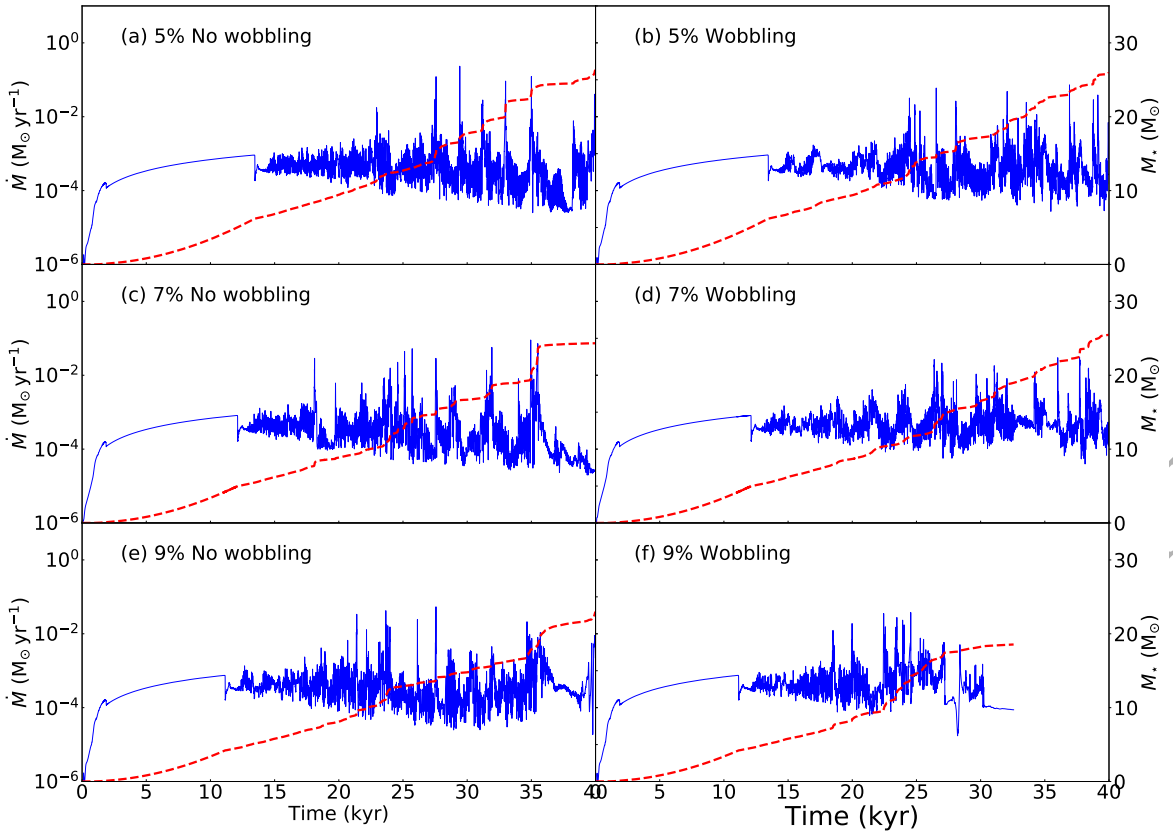

Figure 2. Accretion rate onto the protostar (in $\mathrm{M}_\odot\,\mathrm{yr}^{-1}$, solid blue line) and evolution of the mass of the young massive stellar objects (in $\mathrm{M}_\odot$) for our simulation models. The simulations are displayed for several β-ratio spanning from 5% (top) to 9% (bottom), without (left) and with (right) stellar motion.

are more prone to fragment because disk fragmentation occurs predomenantly at large radii (Johnson & Gammie 2003).

The above described effects of stellar wobbling in the disc evolution is equivalently found in the other simulation models with $\beta = 7\%$ and $\beta = 9\%$. The density field in the model with $\beta = 7\%$ indeed displays similar features, with a disc with stellar inertia that fragments quicker than in the model with $\beta = 5\%$, see Fig. 1-2c and Fig. 1-2g. Again, stellar inertia seems to make the circumstellar environment of the protostar more compact, with a smaller number of spiral arms. At time 36.0 kyr the disc with $\beta = 7\%$ without stellar wobbling carries a larger number of clumps than the model with stellar wobbling, although they exhibit a similar qualitative level of fragmentation. Lastly, the model with $\beta = 9\%$ slightly deviates from the simulations with $\beta \leqslant 7\%$. Because of its faster initial rotational velocity of the gas in the pre-stellar core, the development of gravitational instability in the disc takes more time than in the other models, see Fig. 1-3c and Fig. 1-3f. At later time (36.0 kyr), the effects of the indirect potential accounting for stellar inertia becomes so strong that the disc is strongly destroyed (see discussion on boundary effects in Section 4.1).

3.1.2 *Protostellar accretion rate*

Fig. 2 shows the accretion rate histories (thin solid blue line, in $\mathrm{M}_\odot\,\mathrm{yr}^{-1}$) and the stellar mass (thick dashed red line, in $\mathrm{M}_\odot$) of the young massive stellar objects forming in our simulations with kinetic-to-rotational energy radio $\beta = 5\%$ (a,b), 7% (c,d), 9% (e,f). The left panels show the accretion rates of the models without wobbling, while the right panels plot the models with wobbling, respectively. In the panels, one can see the initial increase of the accretion rate during the free-fall collapse of the pre-stellar material, up to the time of the onset of the disc formation, at time ≈ 12 kyr, when the accretion rate becomes variable because of azimuthal anisotropies in the accretion flow. At this time, the disc is small and of moderate size (Fig. 1-1a) and can be described to be in the so-called quiescent mode of accretion (Meyer et al. 2019).

At times $\approx$ 26 kyr, the accretion rate history displays several strong peaks corresponding to the transport of disc material through the sink cell at rates $\geqslant 10^{-2}\,\mathrm{M}_\odot\,\mathrm{yr}^{-1}$. Those features characterise the burst mode of accretion in which the protostar enters when accreting dense segments of spiral arms and/or migrating gaseous clumps, and, this translates into luminous accretion-driven flares (Meyer et al. 2017, 2019). Star-disc systems in the burst mode are associated with large discs of complex internal structures (Fig. 2b). The rest of the modelled disc evolution is constituted of a succession of episodic accretion bursts interspersed by quiescent phases of accretion, which is characteristic of young stars growing and gaining mass within the burst mode of accretion (Meyer et al. 2019, 2021). The evolution of the protostellar mass reflects this by displaying a series of step-like increases at the moment of the bursts (dotted red line of Fig. 2a), see also Meyer et al. (2018).

The accretion rate history of the model with $\beta = 5\%$ in-

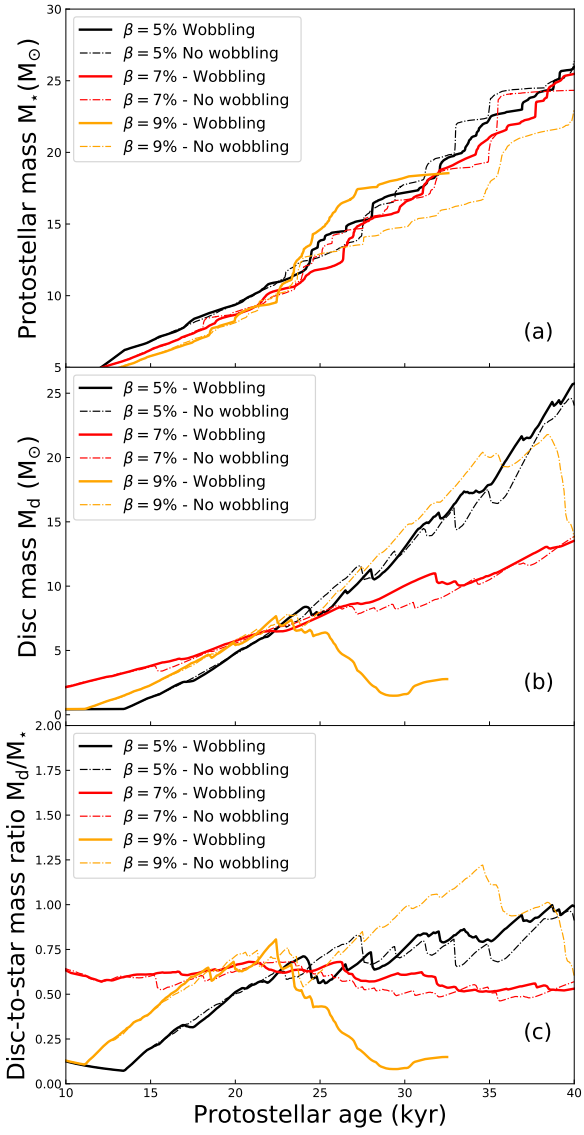

Figure 3. Protostellar mass (a), disc mass (b) and disc-to-star mass ratio (c) in our disc models with $\beta = 5\%$ (black), $\beta = 7\%$ (red) and $\beta = 9\%$ (orange). Data for both models with (solid lines) and without (dashed-dotted lines) stellar wobbling are shown in the figure.

cluding wobbling does not display strong qualitative differences in terms of accretion bursts compare to the models without stellar inertia, since the disc fragments (Fig. 1-1c,1g) and the protostar enters the burst mode of accretion at similar times ($\approx 24\,$Myr). The same is true in our simulation with $\beta = 7\%$. The accretion rate of the model with stellar wobbling and $\beta = 9\%$ is much more erratic as a consequence of the dramatic distortion of the disc by the stellar wobbling, see Fig. 1-3h. Because the accretion bursts of the models with wobbling are of reduced magnitude, the mass evolution does not exhibit the large step-like increase of the mass evolution in the models with wobbling. In all our models, the magnitude and the number of the strongest accretion events is reduced when wobbling is included, see our Table 2.

3.1.3 *Disc size, mass and disc-star mass ratio*

Fig. 3 plots the properties of the simulated star-disc systems, such as the protostellar mass (top panel, in $\mathrm{M}_\odot$), the disc mass (middle panel, in $\mathrm{M}_\odot$) and the disc-to-star mass ratio (bottom panel). On each panel, the quantities are shown for all 6 models of Table 1 represented in the figures by a color coding, with thick solid lines (models without wobbling) and thin dashed lines (models with wobbling) for the simulations with $\beta = 5\%$ (black), $\beta = 7\%$ (red), $\beta = 9\%$ (yellow). One can see that the protostellar mass histories are smoother in the simulations with wobbling than in those without, since, as discussed above, the onset of the gravitational instability happens sooner if no stellar inertia is included. However, in the models with $\beta = 5\%$ and $\beta = 7\%$, for the timescales of 40 kyr that we simulate, the final masses are similar, regardless of the physics taken into account in the simulation, as those simulations end with a final massive young protostellar object of $\approx 26\,\mathrm{M}_\odot$ and $\approx 25\,\mathrm{M}_\odot$, respectively. Inversely, for high β-ratio of 9%, it reveals a notable difference of a few solar mass between the stellar mass calculated without and with wobbling at times $\approx 32.5\,$kyr, as a direct consequence of gravitational instability boundary effects influencing the disc evolution in this fast-spinning system.

The middle panel of the figure (Fig. 3b) shows the evolution of the disc mass, calculated by integrating the gas density in a cylinder of dimensions 2000 au and height 500 au as in Klassen et al. (2016); Meyer et al. (2018). The disc mass evolution M_d (in $M_\odot$) is marked by abrupt decreases corresponding to the time instances when dense gaseous clumps disappear into the central sink cell of radius $r_\mathrm{in} = 20\,$au, also provoking step-like increase of the protostellar mass history (Fig. 3a). Indeed, when a clump is accreted and the mass and disc evolution have opposite variability, the first gains the amount of mass the latter loses. Note that the disc masses do not sensibly change whether wobbling is included or not, at least for the time that we simulate (40 kyr), except for the model with $\beta = 9\%$ that is affected by strong wobbling-related boundary issues (Section 4.2). The bottom panel shows the evolution of the disc-to-star mass ratio $M_\mathrm{d}/M_\star$ (Fig. 3c) which remains $\geqslant 0.5$ once the accretion discs form (Meyer et al. 2021), throughout all the simulations, except for the model with $\beta = 9\%$ and unfixed star, which deviates from this trend starting from time $\approx 25\,$kyr when the effects of the stellar wobbling are so strong that they induce a stretching of the circumstellar disc (see Fig. 1-3c, Fig. 1-3h and also Section 4.1).

3.1.4 *Disc thermodynamics*

In Fig. 4 the time-evolution of the disc midplane temperature is displayed as a function of the midplane gas density for the models with $\beta = 7\%$ without (left panels) and with wobbling (right panels), for times spanning from 17 kyr to 36 kyr. Color-coding shows the distance to the central protostar r/R_disc for each point in the figure, normalised to the disc size, with R_disc the maximum disc radius at a considered time, which we measure by tracking the region at which the infalling material lands onto the disc, using the azimuthaly-averaged midplane velocity profiles. The black line represents a fit to the whole dataset and the upper grayed region ($T \geqslant 2000\,$K) highlights the temperature above which molecular hydrogen dissociates. The diagonal branch along which both density and temperature increase as we go from larger to smaller distances, as typically protoplanetary discs do. The outer diluted and

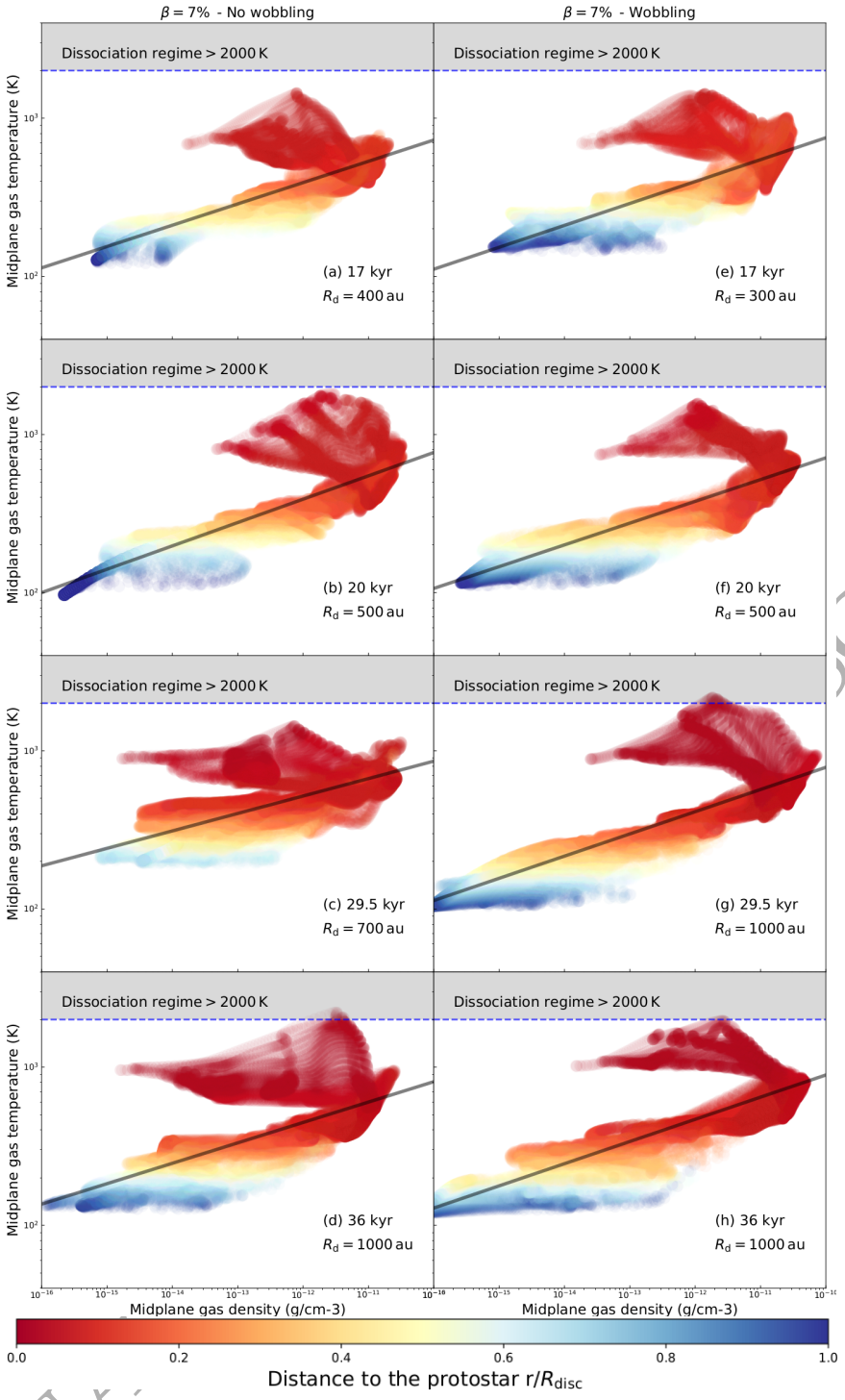

Figure 4. Evolution of the disc midplane in the density-temperature diagram for the model with $\beta = 7\%$, without (left panels a-d) and with stellar inertia (right panels e-h), for different time from 17 kyr to 36 kyr after the beginning of the simulation. The color indicate the distance of each midplane gas element to the central protostar, normalised to the size of the disc at the considered time instance. The gray zone highlight the region with $T \geqslant 2000$ K in which the gas is hotter than the molecular dissociation temperature. The black line is a fit to the entire dataset.

Table 2. Table displaying the main properties of the accretion bursts in our simulations series with $\beta = 5\%-9\%$. $N_{\rm bst}$ is the number of bursts undergone by the protostars at a given magnitude class. $L_{\rm max}/L_{\rm min}/L_{\rm mean}$ stands for the maximum, minimum, and mean burst luminosities. Equivalently, $\dot{M}_{\rm max}/\dot{M}_{\rm min}/\dot{M}_{\rm mean}$ correspond to the accretion rates onto the protostar, and $t_{\rm bst}^{\rm max}/t_{\rm bst}^{\rm min}/t_{\rm bst}^{\rm mean}$ relate to the accretion burst duration. $t_{\rm bst}^{\rm tot}$ is the total time a massive young stellar object spends bursting via a given burst magnitude class.

Model	$N_{\rm bst}$	$L_{\rm max}/L_{\rm min}/L_{\rm mean}$ (10^5 L$_\odot$)	$\dot{M}_{\rm max}/\dot{M}_{\rm min}/\dot{M}_{\rm mean}$ (M$_\odot$ yr^{-1})	$t_{\rm bst}^{\rm max}/t_{\rm bst}^{\rm min}/t_{\rm bst}^{\rm mean}$ (yr)	$t_{\rm bst}^{\rm tot}$ (yr)
		1-mag cutoff			
Run-256-100M$_\odot$-5%-wio	6	19.89 / 0.464 / 5.40	0.0397 / 0.0073 / 0.0170	15 / 4 / 9	51
Run-256-100M$_\odot$-5%-wi	10	3.65 / 0.494 / 2.05	0.0211 / 0.0065 / 0.0103	35 / 6 / 14	135
Run-256-100M$_\odot$-7%-wio	13	2.24 / 0.079 / 0.88	0.0224 / 0.0016 / 0.0087	33 / 8 / 14	182
Run-256-100M$_\odot$-7%-wi	14	6.2 / 0.067 / 1.79	0.0211 / 0.0015 / 0.0110	36 / 5 / 13	175
Run-256-100M$_\odot$-9%-wio	16	2.25 / 0.051 / 0.66	0.0239 / 0.0011 / 0.0088	74 / 5 / 19	304
Run-256-100M$_\odot$-9%-wi	11	1.06 / 0.052 / 0.32	0.0231 / 0.0011 / 0.0077	23 / 7 / 12	134
Total all models	**70**				**163**
		2-mag cutoff			
Run-256-100M$_\odot$-5%-wio	3	4.20 / 2.136 / 3.17	0.0295 / 0.0220 / 0.0265	14 / 5 / 10	30
Run-256-100M$_\odot$-5%-wi	7	17.03 / 1.338 / 7.02	0.0585 / 0.0245 / 0.0366	18 / 4 / 10	70
Run-256-100M$_\odot$-7%-wio	3	3.01 / 2.014 / 2.40	0.0523 / 0.0286 / 0.0414	9 / 4 / 8	23
Run-256-100M$_\odot$-7%-wi	3	9.13 / 1.248 / 5.84	0.0309 / 0.0262 / 0.0285	42 / 4 / 25	74
Run-256-100M$_\odot$-9%-wio	5	2.99 / 0.207 / 1.57	0.0531 / 0.0041 / 0.0308	11 / 5 / 8	41
Run-256-100M$_\odot$-9%-wi	4	2.29 / 0.243 / 1.09	0.0372 / 0.0049 / 0.0261	14 / 5 / 10	40
Total all models	**25**				**46**
		3-mag cutoff			
Run-256-100M$_\odot$-5%-wio	3	34.28 / 8.977 / 21.32	0.1207 / 0.0910 / 0.1083	12 / 3 / 6	18
Run-256-100M$_\odot$-5%-wi	1	21.66 / 21.661 / 21.66	0.0723 / 0.0723 / 0.0723	3 / 3 / 3	3
Run-256-100M$_\odot$-7%-wio	4	22.17 / 1.344 / 11.59	0.0888 / 0.0286 / 0.0610	15/4/7	28
Run-256-100M$_\odot$-7%-wi	-	-	-	-	-
Run-256-100M$_\odot$-9%-wio	-	-	-	-	-
Run-256-100M$_\odot$-9%-wi	2	0.83 / 0.608 / 0.72	0.0188 / 0.0122 / 0.0155	13 / 8 / 11	22
Total all models	**10**				**18**
		4-mag cutoff			
Run-256-100M$_\odot$-5%-wio	1	23.80 / 23.801 / 23.80	0.2313 / 0.2313 / 0.2313	2 / 2 / 2	2
Run-256-100M$_\odot$-5%-wi	-	-	-	-	-
Run-256-100M$_\odot$-7%-wio	-	-	-	-	-
Run-256-100M$_\odot$-7%-wi	-	-	-	-	-
Run-256-100M$_\odot$-9%-wio	-	-	-	-	-
Run-256-100M$_\odot$-9%-wi	-	-	-	-	-
Total all models	**1**				**2**

cold disc region (blue points) exhibit less horizontal deviation from the diagonal black line than the dense, hot inner part (red points), especially at after the beginning of the disc formation (Fig. 1-2a, Fig. 1-2e). There is a turn-over and a horizontal branch corresponding to the very inner disc regions that is warmer than the diagonal region, although density can vary in a wide range. Only in this region the gas temperature exceeds the molecular hydrogen dissociation threshold ($T \geqslant 2000\,\mathrm{K}$).

At later times, when the disc has begun to fragment, the horizontal deviations in the inner region is more pronounced as a result of the growth of the disc and scatter over a wider density range. The disc structure adopts a more complex morphology provoking additional branches in the high temperature part of the diagram, accounting for the many spiral arms forming by gravitational instability and enrolling around the sink cell (Fig. 4b). At time $29.5\,\mathrm{kyr}$ the disc strongly fragments (Fig. 4c). The gaseous clumps extend as a horizontal high temperature branch $\sim 500\,\mathrm{au}$ from the star. This upper region further evolves as the disc keeps on fragmenting, and more clumps form within the extended spiral arms, which translates into a scattering of the low-temperature region (blue dots of Fig. 4d).

The disc model with wobbling included is qualitatively similar to its fixed-star counterpart at time $17\,\mathrm{kyr}$ (Fig. 4a,e) in both structure and thermodynamical properties, except regarding the disc without stellar inertia is 25% larger since its radius reaches $400\,\mathrm{au}$ at that time whereas the other disc model extends up to $300\,\mathrm{au}$ only. At time $20\,\mathrm{kyr}$ the disc with wobbling does not exhibit the group of high temperature and high density point scattering close to the dissociation temperature regime (Fig. 4b,f), because the disc model with fixed protostar fragments more violently. The absence of early clumps in the model with wobbling results in a distribution of the disc midplane gas along the diagonal with much less scattering with respect to the black line (Fig. 4c,g), whereas the inner disc region is hotter and exceed the molecular hydrogen dissociation temperature. The disc, having fragments located in the inner region ($\leqslant 200\,\mathrm{au}$), is on the road to multiplicity (Meyer et al. 2018). Indeed, disc gas exceeding $2000\,\mathrm{K}$ implies second Larson collapse (Larson 1969, 1972) and formation of a protostar, which is not resolved in our simulations, and, therefore, multiplicity can only be inferred from this diagram. At this time, the disc without stellar inertia is more compact than that with wobbling. Finally, at time $36\,\mathrm{kyr}$ both discs are violently fragmenting and have the same overall size of $\approx 1000\,\mathrm{au}$.

3.2 Bursts

We perform an analysis of the variability in the accretion rate histories onto the young massive stellar objects. The stellar mass and

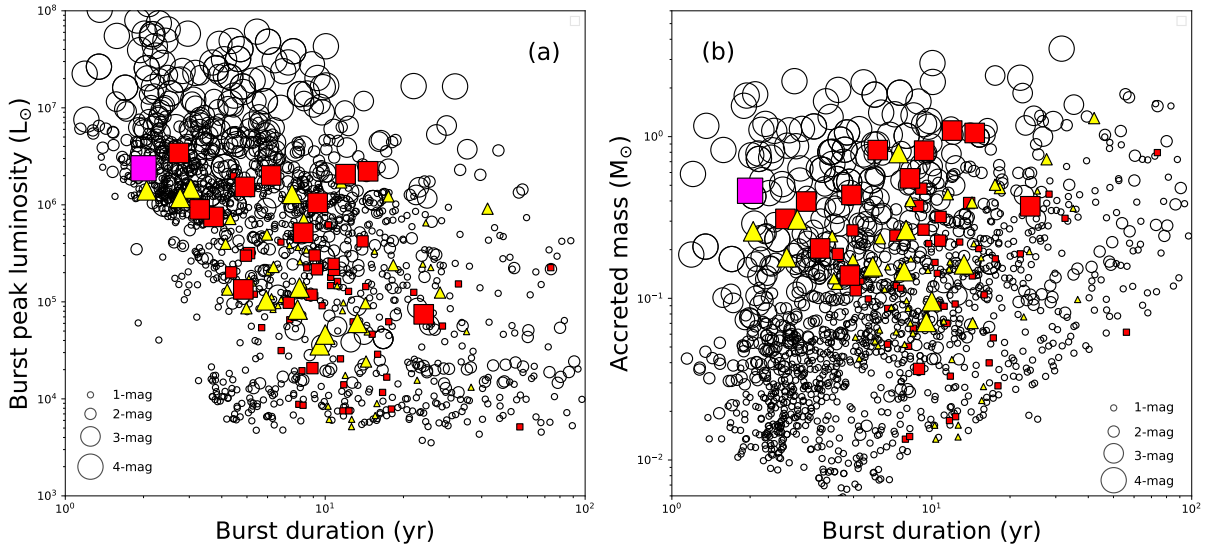

Figure 5. Distribution of the accretion-driven bursts in our series of simulation models in the burst duration-burst peak luminosity (a) and burst duration-burst accreted mass per burst (b) planes. The burst duration is in yr, the burst peak luminosity in $L_\odot$ and the accreted mass per burst in $M_\odot$, respectively. The burst are displayed for both the disc modelled without (red squares) and with (yellow triangles) stellar inertia. The figure indicates the burst modelled in the previous papers of this series as black circles (Meyer et al. 2021). The size of the symbols scale with the magnitude of the accretion-driven burst, from the smallest (1-mag bursts), to the largest (4-mag) bursts. Note that the single 4-mag burst of this high-resolution series of models is marked in magenta. Note that all except one single 4-mag bursts belong to the data in Meyer et al. (2021).

accretion rate measured in the radiation-hydrodynamics simulations are turned into a lightcurve via the estimate of the protostellar radius, interpolated from the evolutionary tracks of Hosokawa & Omukai (2009). Then, the total luminosity of the central massive young stellar objects is calculated for each model as $L_{\rm tot} = L_\star + L_{\rm acc}$, with $L_\star = L_\star(M_\star, \dot{M})$ the photospheric luminosity from Hosokawa & Omukai (2009) and $L_{\rm acc} = fGM_\star\dot{M}/R_\star$ the accretion luminosity, where G is the universal gravitational constant, $f = 3/4$ a factor accounting for the effective mass accreted onto the stellar surface, the rest being released into the a protostellar jet. Hence, the variability of the accretion rate reflects onto evolution of the total luminosity, see fig. 3. of Meyer et al. (2021). For each model, the lightcurves $L_{\rm tot}(t)$ are post-processed with the signal analysis method developed in Vorobyov et al. (2018), which filters out the accretion bursts from a synthetic quiescent background luminosity $L_{\rm bg}$. During each burst, the luminosity peak is compared to $L_{\rm bg}$ and the ongoing flare is classified as an i-magnitude (i-mag) burst, with i such that $L_{\rm tot} \geqslant 2.5^i L_{\rm bg}$. The method ensures that small variabilities of magnitude $\leqslant i = 1$, either from the vicinity of the sink cell or from the secular evolution of $L_{\rm bg}$, are not confused with true bursts (Elbakyan et al. 2019). The results for the bursts analysis are summarised in Table 2.

Models for the circumstellar medium of young massive stars show that the total number of bursts measured in the simulations decreases as their magnitude increases. In other words, there are more 1- and 2-mag bursts than 3- and 4-mag flares, and a similar tendency is found for the total time spent in the burst mode as a function of the burst magnitude, e.g. we count 70 1-mag bursts in total and only a single 4-mag burst in our entire series of simulations. This trend of declining burst activity of young massive stars is not modified when including wobbling in the simulations. The effect of disc wobbling on the burst properties can be summarised as follows. The number of 1-mag bursts varies at most by up to a factor of ≈ 2 when allowing the protostar to move. The number of 2-mag bursts only differs by $1-2$ bursts in the models with and without wobbling. Major differences appear with the 4-mag bursts, i.e. only a model without wobbling is able to produce such event, at least for the time interval that we simulate.

Additionally, higher-magnitude bursts are also much less common than their 1-mag counterparts. Only the model with $\beta = 5\%$ without wobbling exhibit a short 4-mag burst of duration 2 yr, suggesting that the realistic discs with stellar inertia do not undergo such mechanisms, at least during the early ≈ 40 kyr of their evolution. Higher-resolution simulations are required to further investigate the question of FU-Orionis-like bursts in massive star formation. The average luminosity of the 3-mag bursts is similar regardless of the physics included into the models, however, the models without wobbling can accreted slightly more mass per bursts.

In Fig. 5 the burst duration is plotted as a function of the maximum luminosity of each accretion-driven bursts (panel a), and as a function of the mass accreted throughout the burst (panel b). On the panels, the circles represent the data reported in the previous papers of this series which were computed at a lower spatial resolution (Meyer et al. 2021), and the circle size scales with the burst magnitude. The data for the current study are plotted as red squares (models without wobbling) and yellow triangles (models with wobbling). The bursts of lower magnitude (1-mag) are located in the $\leqslant 5 \times 10^5$ $L_\odot$ region of the plot, regardless of their duration, spanning from a few 1 yr to $\approx 10^2$ yr (Fig. 5a). The high magnitude bursts (3- and 4-mag bursts) are found in the rather short duration ($\leqslant 20$ yr) and higher luminosity ($> 10^5$ $L_\odot$) region of the figure, although a few bursts without wobbling do not follow this rule and are located in the long duration region of the figure. This is in accordance with simulations of lower spatial resolution (empty circles),

Table 3. Proportion (in %) of mass gain at the end of our simulation, as a function of the flare magnitude during the burst phase of accretion. The intensity of each individual burst is defined as in Meyer et al. (2019).

Models	β-ratio	Inertia	$L_{tot} \sim L_{bg}$	1−mag	2−mag	3−mag	4−mag
Run-256-100M$_\odot$-5%-wio	5 %	no	81.67	11.86	5.07	1.37	0.03
Run-256-100M$_\odot$-7%-wio	7 %	no	81.76	12.59	5.62	0.03	0.0
Run-256-100M$_\odot$-9%-wio	9 %	no	88.10	9.02	2.88	0.0	0.0
Mean	-	-	**83.84**	**11.16**	**4.53**	**0.46**	**0.01**
Run-256-100M$_\odot$-5%-wi	5 %	yes	77.54	11.17	4.61	6.65	0.0
Run-256-100M$_\odot$-7%-wi	7 %	yes	73.26	16.62	10.12	0.0	0.0
Run-256-100M$_\odot$-9%-wi	9 %	yes	84.20	10.98	4.18	0.64	0.0
Mean	-	-	**78.34**	**12.92**	**6.31**	**2.43**	**0.0**

however, the burst distribution in our simulations do not extend to the same upper limit in terms of the peak luminosity because of the absence of 4-mag bursts in our sample. The bursts are shorter and dimmer compared to a $128 \times 11 \times 128$ simulation. Importantly, the duration of the high-magnitude bursts in the model with wobbling is of slightly lower duration than those found in the simulation with fixed star. In the burst duration-accreted mass plane (Fig. 5b) we see that lower-magnitude bursts distribute along diagonals which indicate that the accreted mass scales linearly with the burst duration. Once again, as detailed in Meyer et al. (2021), some of the most mass-accreting bursts are amongst the faintest, since the total luminosity $L_{\rm tot}$ is dominated by the accretion luminosity $L_{\rm acc} \propto 1/R_\star$, with $R_\star$ increasing during the burst phase, when the protostar experiences excursions to the cold part of the Herzsprung-Russell diagram (Meyer et al. 2019).

In Table 3 we report the proportion of final mass accreted by our protostars during the quiescent and the burst phases, separated, for the latter, by the magnitude of the accretion-driven bursts. The mean proportion of final mass accreted during the burst phase of accretion amounts $\approx$ 17% for the models without wobbling and $\approx$ 22% when stellar inertia is included, respectively. Similarly, the average mass accreted during 1-mag bursts is $\approx 11-12\%$ with or without stellar wobbling, with a slight increase as a function of β-ratio. Differences mostly happen for the 2-mag bursts, with $\approx 4.5\%$ and $\approx 6.3\%$ of the total accreted mass with and without wobbling, respectively. Similarly, the protostars modelled with stellar inertia gain $\approx$ 2.4% of their mass experiencing 3-mag bursts. None of the models accrete mass via 4-mag bursts, since they are absent from the present simulations, except in the model without wobbling and $\beta = 5\%$ which produced a single occurrence of such a burst. In Meyer et al. (2019, 2021), we concluded that massive stars gain up to half of their zero-age-main-sequence mass by mass accretion in the burst mode, on the basis of models run up to $\sim$ 70 kyr. It is the later phase of the disc evolution that the strongest bursts appeared, while we stop our models sooner in the present study, because of the enormous computational costs of our higher-resolution calculations.

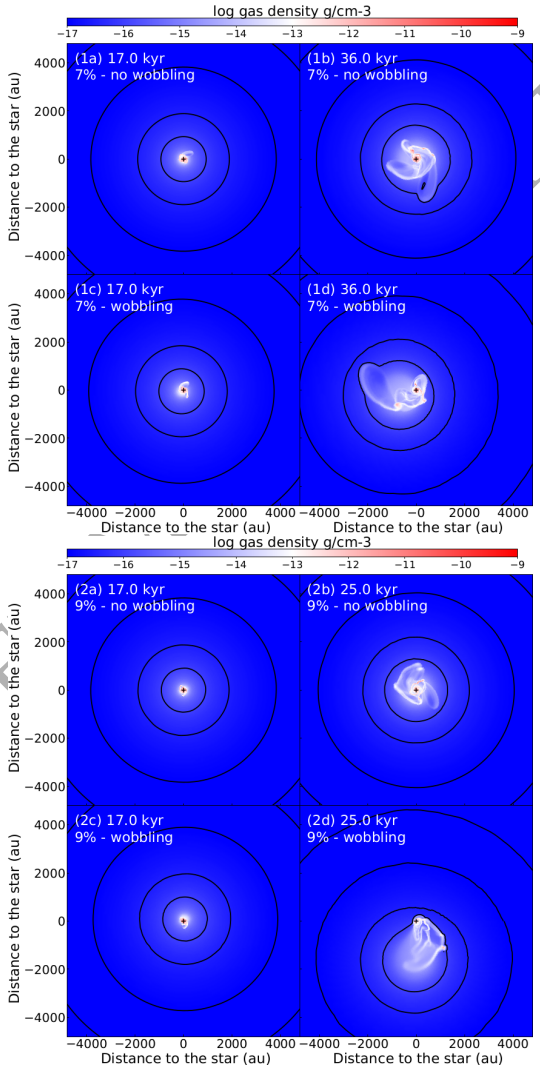

Figure 6. Disc midplane with $\beta = 7\%$ (upper series of panels) and $\beta = 9\%$ (lower series of panels), and, each of them displaying both models with (top) and without (bottom) wobbling. The figures show the disc midplane gas density, (in g cm^{-3}) for several selected characteristics time instances of the accretion disc evolution, and with solid black number density isocontours highlighting the effects of the stellar inertia onto the mass distribution in the computational domain.

4 DISCUSSION

This section reminds the reader the limitations of our simulation setup and discuss the observability of the accretion disc models if observed by means of the ALMA interferometer.

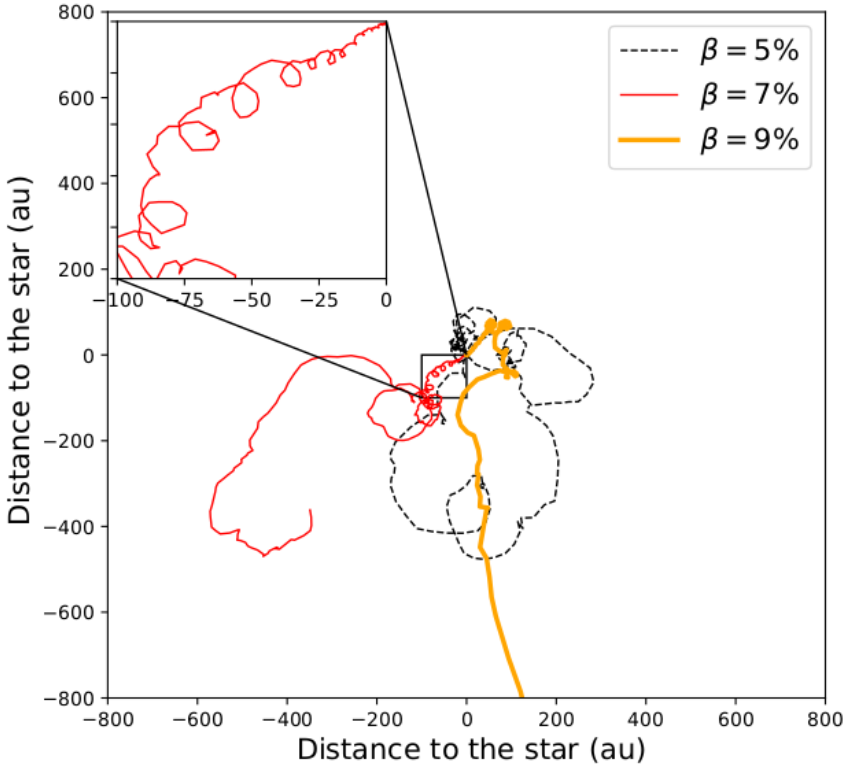

Figure 7. Time evolution of the position of the center of mass of the accretion discs modelled with stellar inertia (in au), for our simulation with $\beta = 5\%$ (black dashed line), $\beta = 7\%$ (red thin solid line) and $\beta = 9\%$ (orange thick solid line). Inset plot zooms on the wobbled motion induced by the stellar inertia.

4.1 Caveats

Most of the limitations in the numerical method utilised in this study have been presented in the parameter study (Meyer et al. 2021), particularly regarding the absence of magnetic fields, non-ideal magneto-hydrodynamics and photoionisation that mostly affect the bipolar jet filled with hot gas. While the magnetic feedback should be improved in future studies, not taking into account the protostellar ionization is acceptable since we concentrate onto the disc structure and its properties. Nevertheless, disc evaporation and disc wind are neglected in the simulations. This work explores the stellar motion induced by the disc in the fashion of Michael & Durisen (2010a); Regály & Vorobyov (2017) with moderate-resolution $256 \times 41 \times 256$ simulations, which is a major improvement relative to the models presented in Meyer et al. (2018) and Meyer et al. (2019) since our work is based on both high-resolution models performed with stellar inertia. Nevertheless, the midplane symmetry that we impose to our calculations intrinsically neglects any vertical motion of the massive protostar, although low-resolution tests suggested that this effect is not important (Meyer et al. 2018). In future studies we will consider higher-resolution models like those presented in Oliva & Kuiper (2020). The increased resolution of our simulations imposed to move the size of the inner radius of the sink cell $r_{\rm in}$ to 20 au instead of 10 au in Meyer et al. (2018, 2019). As the time-step restrictions are principally governed by the size of the innermost cell of the radial logarithmically expanding mesh, we had to keep the calculations affordable from the point of view of the computational costs.

As observed in Michael & Durisen (2010a) and (Regály & Vorobyov 2017) in the context of accretion discs of low-mass stars, stellar inertia delays the development of gravitational instabilities in the disc and modifies its overall appearance, in particular the spatial morphology of the structures growing in it. While the consideration of stellar inertia adds realism of the simulated models, it also introduces an additional boundary effect related to the displacement of the disc in the computational domain that mimics the stellar displacement in the non-inertial frame of reference. This particularly takes place when the mass of the disc is comparable to that of the protostar $M_{\rm d}/M_\star \approx 1$, as it is the case in the formation of our massive stars (Fig. 3b, see also our model with $\beta = 7\%$ in Fig. 1-3h). However, the timescales over which high-mass stars operate ($\sim$ kyr) is much shorter than that of their lower mass counterparts (Myr), and, therefore, the boundary effects are somehow less pronounced in our models except in the simulation with high β-ratio. An updated version of the code should handle moving boundaries and/or replenishing the void caused by means of the displacement of the density field by infalling pre-stellar core material that is initially out of the computational domain at radii $r \geqslant R_{\rm max}$.

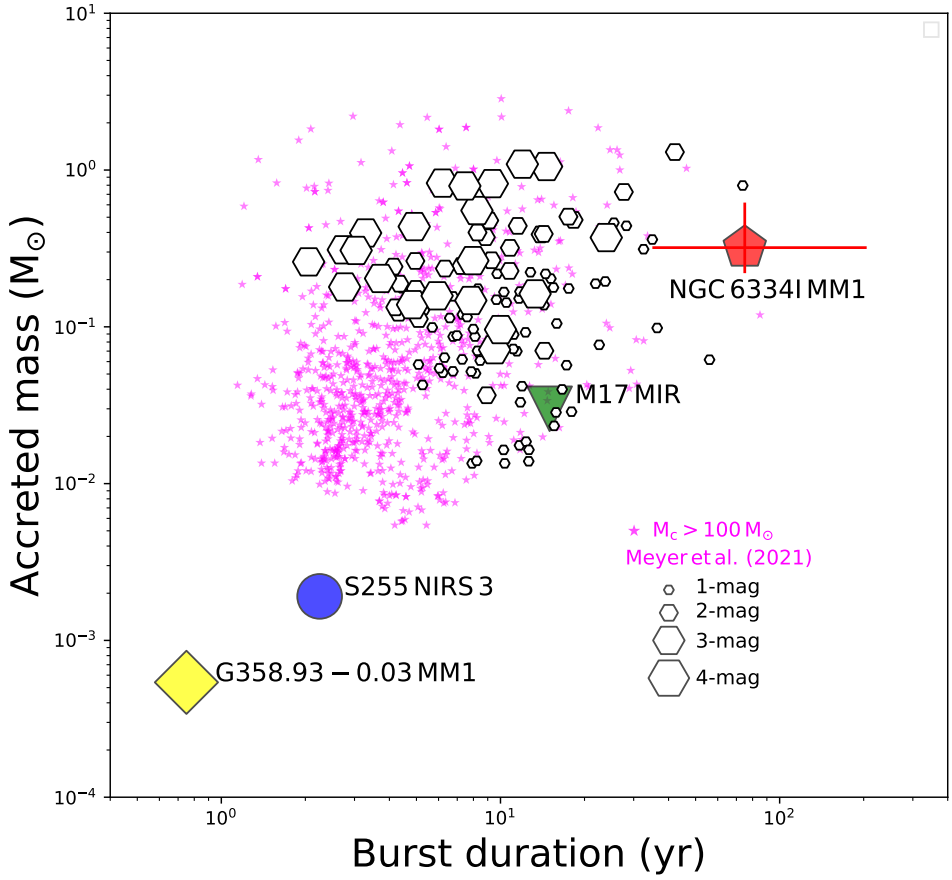

Figure 8. Comparison of our modelled bursts with the properties of observed bursts in the burst duration-accreted-mass diagram. The white hexagons are the burst from the simulated discs presented in this study, the coloured symbols stand for the burst observed so far from young high-mass stellar objects. The magenta stars represent the burst from the models with an initial molecular core model $M_c \geqslant 100\,\mathrm{M}_\odot$ in Meyer et al. (2021).

4.2 Effect of wobbling on disc structure

Fig. 6 shows a zoomed-out view of the midplane density field in ($\mathrm{g\,cm^{-3}}$) of the computational domain in our simulations with $\beta = 7\%$ (top panels) and $\beta = 9\%$ (bottom panels) for several selected time instances of the system evolution. The figures cover a region of 5000×5000 au including both the accretion disc in the inner $\leqslant 1000$ au and the still-collapsing pre-stellar core. Density isocontours as solid black lines highlight the structure of the density field of the molecular envelope and the disc. At 17 kyr, the midplane density in the collapsing envelope is axisymmetric as were the initial conditions for the pre-stellar core (Eq. 1), in both simulation with and without wobbling, see also Fig. 6 1a-1c (top). Almost at the end of the simulation (at time $\geqslant 36$ kyr) the deviation from the axisymmetry of the initial density structure is pronounced in the case with stellar inertia (Fig. 6 1d), as the stellar motion affects not only the accretion disc located in the inner region of the computational domain, but also the whole envelope. For fast initial rotation of the pre-stellar core ($\beta \geqslant 9\%$), the deviations from axisymmetry are magnified and happen quicker, at time 25 kyr, see Fig. 6 2d (bottom). The catastrophic effects of stellar wobbling on the envelope and disc evolution are caused by the fact that the acceleration caused by the non-inertial frame of reference shifts the material in the entire computational domain. As a result, a distortion in the gas density near the outer fixed boundary develops, which gradually feeds back and modifies through gravity the entire evolution of the inner structure.

We display the evolution of the position of the barycenter of the star-disc-envelope system in Fig. 7. The center of mass is calculated as,

$$x_{\mathrm{bar}}(t) = \frac{1}{M}\sum_{\mathrm{ijk}} x_{\mathrm{ijk}}\rho_{\mathrm{ijk}}dV_{\mathrm{ijk}}, \tag{24}$$

$$y_{\mathrm{bar}}(t) = \frac{1}{M}\sum_{\mathrm{ijk}} y_{\mathrm{ijk}}\rho_{\mathrm{ijk}}dV_{\mathrm{ijk}}, \tag{25}$$

and,

$$z_{\mathrm{bar}}(t) = \frac{1}{M}\sum_{\mathrm{ijk}} z_{\mathrm{ijk}}\rho_{\mathrm{ijk}}dV_{\mathrm{ijk}}, \tag{26}$$

where,

$$x_{\mathrm{ijk}} = r_{\mathrm{ijk}}\cos(\phi_{\mathrm{ijk}})\sin(\theta_{\mathrm{ijk}}) \tag{27}$$

$$y_{\mathrm{ijk}} = r_{\mathrm{ijk}}\cos(\phi_{\mathrm{ijk}})\sin(\theta_{\mathrm{ijk}}) \tag{28}$$

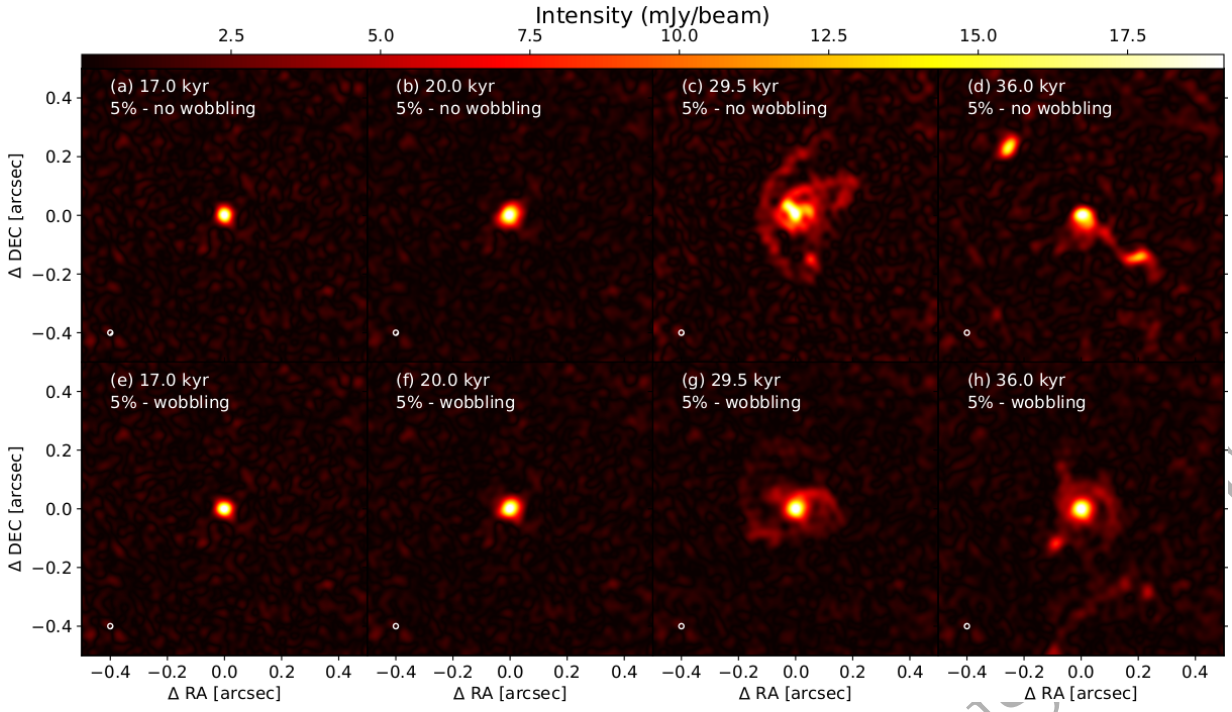

Figure 9. Synthetic emission maps of the models with $\beta = 5\%$, without (top panels) and with (bottom panels) stellar inertia, as seen by the ALMA interferometer in its antenna configuration 10. The disc are shown at the same characteristic times as for the upper series panels in Fig. 1. The distance to the source is assumed to be 1 kpc.

and,

$$z_{\rm ijk} = r_{\rm ijk}\cos(\theta_{\rm ijk}) \tag{29}$$

are the Cartesian coordinates of a disc volume element ijk, respectively. The midplane symmetry of the computational domain imposes $z_{\rm bar} = 0$ and the whole mass M included into it reads,

$$M = \iiint \rho dV = \sum_{\rm ijk} \rho_{\rm ijk} dV_{\rm ijk}, \tag{30}$$

where $dV_{\rm ijk}$ is the volume element of the grid zone ijk in the computational domain, with $1 \leqslant i \leqslant 256$, $1 \leqslant j \leqslant 41$ and $1 \leqslant k \leqslant 256$. The barycenter exhibits large excursions from the origin of the computational domain ($x = 0, y = 0, z = 0$) as well as smaller-scale periodic deviations from the path of the excursions. The large-scale motion is a direct consequence of the non-axisymmetric shape adopted by the infalling molecular material of the envelope and, as the β-ratio of the model increases, the excursions of the star away from the origin are more important (see yellow line of Fig. 7). The small amplitude displacement of the barycenter is caused by of the development of substructures in the disc, such as dense spiral arms and gaseous clumps, which are of much milder effects.

4.3 Comparison with monitored bursts

Fig. 8 compares our modelled bursts with the properties of observed flares, in the burst duration-accreted mass diagram. The white hexagons are the burst measures from the lightcurves calculated on the basis of the accretion rate histories of our simulated protostars and the coloured symbols stand for real bursts of high-mass stars. The red pentagon represents the burst of NGC 6334I MM1, which duration has been constrained to $t_{\rm bst} \approx 40-130$ yr (Hunter et al. 2021) and the correspondingly accreted mass estimated to $M_{\rm bst} \approx 0.1-0.3\,{\rm M}_\odot$ (Hunter et al. 2021; Elbakyan et al. 2021). Similarly, the yellow diamond marks the burst of G358.93-0.003 MM1, which properties are $t_{\rm bst} \approx 0.75$ yr and $M_{\rm bst} \approx 0.566\,{\rm M_J}$ (Stecklum et al. 2021; Elbakyan et al. 2021). The blue circle and the green triangle stand for the bursts monitored from the young massive stellar object S255 NIRS 3 ($t_{\rm bst} \approx 2.25$ yr, $M_{\rm bst} \approx 2\,{\rm M_J}$), see Caratti o Garatti et al. (2017); Elbakyan et al. (2021), and that of the recently-discovered outbursts of M17 MIR ($t_{bst} \approx 15$ yr, $M_{\rm bst} \approx 31.43\,{\rm M_J}$), see Chen et al. (2021); Elbakyan et al. (2021) and references therein.

The bursts observed from S255 NIRS 3 and G358.93-0.003 MM1 have a smaller amount of accreted mass compared to that found in our simulations, while their duration is consistent with our data, although G358.93-0.003 MM1 is shorter by an order of magnitude than the shortest burst duration measured from our models. This, however, can be explained by our too big inner sink cell radii. The use of a smaller sink would give the infalling gaseous clumps more time to lose their outer envelope via tidal stripping when migrating closer to the star, as studied in the so-called tidal downsizing model (Nayakshin 2015a,b; Nayakshin & Fletcher 2015; Nayakshin 2016). Consequently, the actual mass of the clump would become smaller as it approaches the star and only the core would survive. The accreted mass value observed for the burst of NGC 6334I MM1 is consistent with our modelled burst. This burst being classified as a 3-mag burst in the parlance of our simulations for the burst mode of accretion in massive star formation (Hunter et al. 2021), however, our models predict that such burst should be of slightly shorter duration. Such discrepancy could

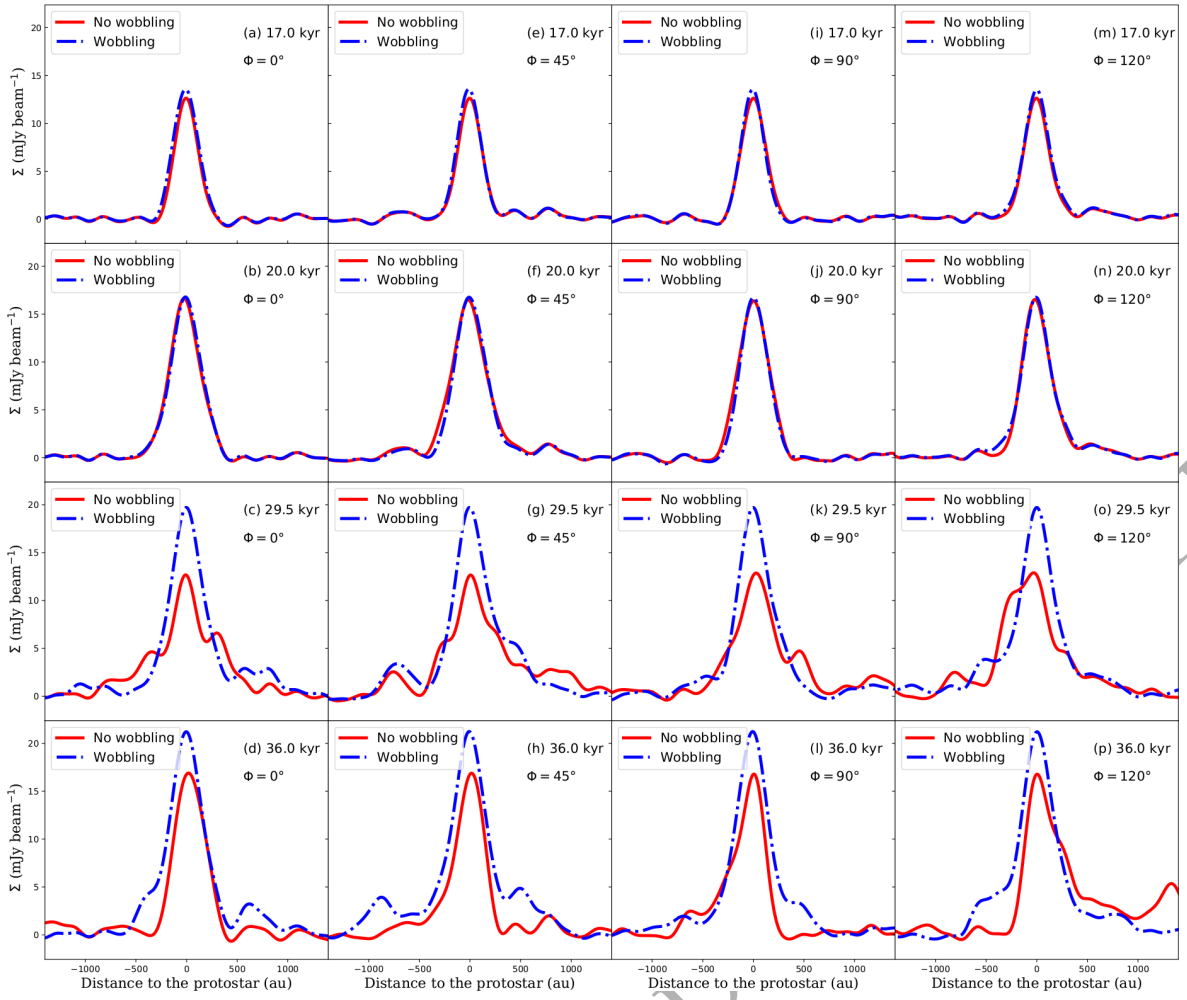

Figure 10. Cuts through the synthetic emission maps of our accretion disc model with $\beta = 5\%$ (in $\mathrm{mJy\,beam^{-1}}$) for the inner disc region. Each panel show the surface brightness without (solid red line) and with stellar inertia (dashed blue line). The horizontal lines of panels display the data for a same time instance, and each column correspond to a different cut through the emission maps, measured clock-wise, and characterised by the angle ϕ of the cut with respect to its vertical north-south direction.

be explained by the fact that the initial properties of the molecular cloud in which NGC 6334I MM1 forms might probably be different than that assumed in our simulations. The outburst of M17 MIR shows much more consistencies with our predictions, both in terms of duration and accreted mass (green triangle). The magenta stars of Fig. 8 are the bursts from the models with initial molecular cores $M_c \geqslant 100\,\mathrm{M}_\odot$ (Meyer et al. 2021), which have smaller accreted mass than the bursts of the present study which all assume $M_c = 100\,\mathrm{M}_\odot$. We speculate that the initial core of M17 MIR is perhaps of smaller mass than that responsible for the formation of the other protostars, i.e. S255 NIRS 3 and G358.93-0.003 MM1. Future studies tailored to particular bursts should take this into account.

Last, let's also underline that the observational measures of the burst properties are affected by a certain number of uncertainties. The burst properties are principally derived by measuring the variability in brightness temperature of the object, assumed to be equal to that of the dust temperature, from which the luminosity is calculated. This relies on geometrical effects potentially scattering radiation out of the observer's light-of-sight, and therefore decreasing the monitored brightness temperature and radiation intensity (Hunter et al. 2017). Additionally, absorption effects are at work, reducing the observed dust continuum flux and drastically reducing the observed accretion luminosity from which the accreted mass is derived (Johnston et al. 2013). Consequently, the real data in the burst duration-accreted mass diagram, represented by coloured symbols in Fig. 8 are not firm numbers, but high uncertainties estimates. Future observational work on the finer characterisation of burst properties would be highly desirable.

4.4 Emission maps and observability

We repeat the exercise of calculating predictive ALMA images for the simulated discs as done in Meyer et al. (2019), see also MacFarlane et al. (2019a,b); Skliarevskii et al. (2021). The dust density field calculated with the PLUTO code, taking into account the information about dust-sublimated regions, is imported into the radiative

transfert code RADMC-3D[1] (Dullemond 2012) for the characteristic simulation snapshots of the model with $\beta = 5\%$ in Fig. 1. It first calculates the dust temperature by Monte-Carlo simulation using the method of Bjorkman & Wood (2001) before ray-tracing 10^8 photons packages from the stellar surface to the disc. Then, it performs radiative transfer calculations against dust opacity assuming that the dust in the disc is the silicate mixture of Laor & Draine (1993). The source of photons is considered to be a black body of effective temperature $T_{\rm eff}$ determined for each disc snapshots using the stellar evolutionary tracks of Hosokawa et al. (2010).

Synthetic images of the disc are produced for a field of view covering a radius of $1000\,{\rm au}$ around the central protostar and made of 2000×2000 grid zones onto which the emissivity is projected. Images are calculated at $249.827\,{\rm Ghz}$ ($1.2\,{\rm mm}$) with a channel-width of $50.0\,{\rm Mhz}$ which corresponds to the ALMA band 6, assuming no inclination angle for the accretion disc with respect to the plane of the sky. Last, the simulated emission maps are treated with the Common Astronomy Software Applications CASA[2] (McMullin et al. 2007). We obtain simulated interferometric images which can be directly compared to the data acquired by the ALMA facility. The antennae are assumed to be in the most extended, long-baseline spatial configuration C43-10 using 43 $12\,{\rm m}$ antennae permitting to reach a maximal spatial resolution of $0.015"$. The distance to the source is assumed to be $1\,{\rm kpc}$. We refer the reader interested in further details on our method for simulating the synthetic images (Meyer et al. 2019).

Fig. 9 plots the $1.2\,{\rm mm}$ synthetic ALMA emission maps of the disc model with the rotation-to-gravitational ratio $\beta = 5\%$, without (top panels) and with stellar inertia (bottom panels), for the characteristic time instances of the disc evolution presented in Fig. 1-1. The images at time $17\,{\rm kyr}$ consist of a bright circle representing the nascent disc, right after the end of the free-fall gravitational collapse of the cloud material (Fig. 9a). This remains unchanged up to time $20\,{\rm kyr}$, since the star has not yet entered the burst mode and keeps on gaining mass by quiescent accretion from a stable and unfragmented disc (Fig. 1-1b). The model with stellar inertia does not exhibit identifiable substructures either at a similar time of evolution (Fig. 1-1e-f). At time $29.5\,{\rm kyr}$ the circumstellar medium of the massive protostar is made of a bright central stellar region, accompanied by a visible infalling gaseous clump in the close stellar surroundings. The entire structure is surrounded by a large-scale spiral arm wrapped around the inner disc (Fig. 9c). Note that the very extension of the spiral arm is not visible, hence, the observed disc does not fully reflect the entire size and composition of the whole object, see midplane density field in Fig. 1-1c. Fragmentation further modifies the disc millimeter appearance which takes the typical morphology of a massive double protosystem, see image Fig. 9d.

The simulation model including stellar inertia displays a typical two-armed structure at $29.5\,{\rm kyr}$ (Fig. 9g) and a more complex pattern at the end of the simulation, including an inner enrolled spiral arms, gaseous clumps and more extended arms with fainter clumps in the southern region (Fig. 9h). The spiral arms reveal a certain level of granulosity arising from the interferometric measures, not originating from the disc structure itself (Fig. 9c), and this can be misinterpreted as additional disc fragments as of the same brightness as the faintest gaseous clumps. These models take their importance in the context of the recently observed bursting young massive protostars and their circumstellar environments (Johnston et al. 2015; Chen et al. 2016; Ilee et al. 2016; Forgan et al. 2016; Maud et al. 2017; Chen et al. 2017; Maud et al. 2018; Ahmadi et al. 2018; Ilee et al. 2018; Maud et al. 2018; Sanna et al. 2019; Motogi et al. 2019; Maud et al. 2019; Liu et al. 2020; Sanna et al. 2021; Suri et al. 2021; Humphries et al. 2021; Vorster et al. 2021; Williams et al. 2022; McCarthy et al. 2022).

Fig. 10 displays cross-sections through the simulated images of the disc models without (solid red line) and with (dashed blue line) stellar wobbling plotted in Fig. 9 for several angles $\phi = 0°$, $45°$, $90°$ and $\phi = 120°$ with respect to the north-south axis. No notable differences happen at time $17.0\,{\rm kyr}$ between the simulation models without and with stellar inertia (Fig. 10a,e,i,m). This persists up to time $20.0\,{\rm kyr}$ in the sense that the two accretion discs models remain undistinguishable in terms of emission properties (Fig. 10b,f,j,n). The differences begin to be evident at times $\geqslant 29.5\,{\rm kyr}$. The models with stellar inertia are brighter at the center of the disc simulated without wobbling, see blue line in Fig. 10c. However, the discs without stellar wobbling display higher surface brightnesses in the inner $\leqslant 800\,{\rm au}$ region, see Fig. 10c,g,k,o, whereas this trend is inverted at later time ($36.0\,{\rm kyr}$), i.e. the disc with stellar inertia emits more than that modelled without wobbling, see Fig. 10d,h,l,p. Consequently, the disc model without wobbling underestimates the observability of the circumstellar medium of massive stars and produces massive binary/multiple systems easily (Fig. 10p). It is therefore necessary to include stellar wobbling in high-resolution simulations in order to reduce this over-fragmentation generated by the simulations presented in Meyer et al. (2019).

5 CONCLUSION

In this paper, we investigate the formation of young high-mass stars by means of high-resolution simulations. We perform three-dimensional gravito-radiation-hydrodynamical simulations with the PLUTO code (Mignone et al. 2007, 2012; Vaidya et al. 2018) of several collapsing pre-stellar cores of different kinetic-to-gravitational energy ratio $\beta = 5\%-9\%$. The performed numerical models are of spatial resolution equivalent to the highest resolution model presented in Meyer et al. (2018), hence, they are better resolved than in the parameter study (Meyer et al. 2021). Stellar motion is included in the simulation models via the introduction of an additional gravitational acceleration felt by the disc and envelope in the non-inertial frame of reference centered on the star (Michael & Durisen 2010b; Hosokawa et al. 2016; Regály & Vorobyov 2017). We analyse the various disc and pre-main-sequence accretion bursts properties, and, by means of radiative transfer calculations against dust opacity in the millimeter waveband, we explore the effect of the stellar motion onto the observability of the disc by the ALMA interferometer.

The growing non-axisymmetric disc substructures formed by gravitational instability such as spiral arms and gaseous clumps (Meyer et al. 2018) exert onto the protostar a force sufficient to off-set the barycenter of the star-disc system from the geometrical center of the computational domain. The morphology of the accretion discs is affected by the inclusion of stellar inertia into the simulations. The angular momentum of the disk decreases because part of it is transferred to the star, and, consequently, the discs fragment later, retain a rounder and more compact shape, and, form fewer gaseous clumps. The discs with wobbling eventually develop spiral arms from which migrating gaseous clumps form

[1] http://www.ita.uni-heidelberg.de/dullemond/software/radmc-3d/
[2] https://casa.nrao.edu/

and undergo the mechanism depicted in Meyer et al. (2017). Our models with stellar inertia experience fewer high-magnitude accretion bursts for fast initial pre-stellar core rotation ($\beta \geqslant 7\%$), than the models without stellar inertia. The properties of these bursts in our models with stellar inertia are in good agreements with that monitored from the young high-mass star M17 MIR (Chen et al. 2021).

Prediction for the interferometric observability of the disc models is calculated with radiative transfer calculations using the code RADMC-3D (Dullemond 2012) and the synthetic imaging code CASA (McMullin et al. 2007), in order to obtain $1.2\,\mathrm{mm}$ simulated ALMA observations. Disc fragments are visible for a Cycle 10 ALMA observation with the C-43 antenna configuration, as long as the disc is old enough to have experienced efficient gravitational fragmentation, and that the star entered the burst mode of accretion. Circumstellar clumps and other substructures should be searched in the inner $\approx 500 - 600\,\mathrm{au}$ of the disc of massive protostars.

The presented models should be improved in the future, both in terms of realism of the disc by including additional physical mechanisms and accurately treating the boundary effects in the non-inertial frame of reference, but also by extending the radiative transfer calculations to other wavebands of the electromagnetic spectrum in order to investigate the spectral evolution of the circumstellar medium of massive protostars (Frost et al. 2021).

ACKNOWLEDGEMENTS

The authors thank the anonymous referee for comments which improved the quality of the paper. DMA Meyer thanks T. Hosokawa for technical advice on stellar inertia. The authors acknowledge the North-German Supercomputing Alliance (HLRN) for providing HPC resources that have contributed to the research results reported in this paper. V.G. Elbakyan acknowledges support from STFC grants ST/N000757/1 to the University of Leicester. E. I. V. and A. M. S. acknowledge support of Ministry of Science and Higher Education of the Russian Federation under the grant 075-15-2020-780. S. Kraus acknowledges support from the European Research Council through an Consolidator Grant (Grant Agreement ID 101003096), and an STFC Consolidated Grant (ST/V000721/1). SY Liu acknowledges support from the grant MOST 108-2923-M-001-006-MY3.

DATA AVAILABILITY

This research made use of the PLUTO code developed at the University of Torino by A. Mignone (http://plutocode.ph.unito.it/). The figures have been produced using the Matplotlib plotting library for the Python programming language (https://matplotlib.org/). The data underlying this article will be shared on reasonable request to the corresponding author.

REFERENCES

Ahmadi A., Beuther H., Mottram J. C., Bosco F., Linz H., Henning T., Winters J. M., Kuiper R., Pudritz R., Sánchez-Monge Á., Keto E., Beltran M., Bontemps S., Cesaroni R., Csengeri T., Feng S., Galvan-Madrid R. e. a., 2018, A&A, 618, A46
Baraffe I., Vorobyov E., Chabrier G., 2012, ApJ, 756, 118
Bjorkman J. E., Wood K., 2001, ApJ, 554, 615
Boley A. C., Hartquist T. W., Durisen R. H., Michael S., 2007, ApJ, 656, L89
Boley P. A., Linz H., Dmitrienko N., Georgiev I. Y., Rabien S., Busoni L., Gässler W., Bonaglia M., Orban de Xivry G., 2019, arXiv e-prints, p. arXiv:1912.08510
Brogan C. L., Hunter T. R., Cyganowski C. J., Chibueze J. O., Friesen R. K., Hirota T., MacLeod G. C., McGuire B. A., Sobolev A. M., 2018, ApJ, 866, 87
Burns R. A., 2018, in Tarchi A., Reid M. J., Castangia P., eds, Astrophysical Masers: Unlocking the Mysteries of the Universe Vol. 336 of IAU Symposium, Water masers in bowshocks: Addressing the radiation pressure problem of massive star formation. pp 263–266
Burns R. A., Handa T., Imai H., Nagayama T., Omodaka T., Hirota T., Motogi K., van Langevelde H. J., Baan W. A., 2017, MNRAS, 467, 2367
Burns R. A., Sugiyama K., Hirota T., Kim K.-T., Sobolev A. M., Stecklum B., MacLeod G. C., Yonekura Y. e. a., 2020, Nature Astronomy, 4, 506
Caratti o Garatti A., Stecklum B., Garcia Lopez R., Eisloffel J., Ray T. P., Sanna A., Cesaroni R., Walmsley C. M., Oudmaijer R. D., de Wit W. J., Moscadelli L., Greiner J., Krabbe A., Fischer C., Klein R., Ibanez J. M., 2017, Nature Physics, 13, 276
Caratti o Garatti A., Stecklum B., Linz H., Garcia Lopez R., Sanna A., 2015, A&A, 573, A82
Cesaroni R., Galli D., Lodato G., Walmsley M., Zhang Q., 2006, Nature, 444, 703
Chen H.-R. V., Keto E., Zhang Q., Sridharan T. K., Liu S.-Y., Su Y.-N., 2016, ApJ, 823, 125
Chen X., Ren Z., Zhang Q., Shen Z., Qiu K., 2017, ApJ, 835, 227
Chen X., Sobolev A. M., Breen S. L., Shen Z.-Q., Ellingsen S. P., MacLeod G. C. e. a., 2020, ApJ, 890, L22
Chen X., Sobolev A. M., Ren Z.-Y., Parfenov S., Breen S. L., Ellingsen S. P., Shen Z.-Q., Li B., MacLeod G. C., Baan W., Brogan C., Hirota T., Hunter T. R., Linz H., Menten K., Sugiyama K., Stecklum B., Gong Y., Zheng X., 2020, Nature Astronomy
Chen Z., Sun W., Chini R., Haas M., Jiang Z., Chen X., 2021, ApJ, 922, 90
Cunningham N. J., Moeckel N., Bally J., 2009, ApJ, 692, 943
Dullemond C. P., , 2012, RADMC-3D: A multi-purpose radiative transfer tool, Astrophysics Source Code Library
Dunham M. M., Vorobyov E. I., 2012, ApJ, 747, 52
Elbakyan V. G., Nayakshin S., Vorobyov E. I., Caratti o Garatti A., Eislöffel J., 2021, A&A, 651, L3
Elbakyan V. G., Vorobyov E. I., Rab C., Meyer D. M.-A., Güdel M., Hosokawa T., Yorke H., 2019, MNRAS, 484, 146
Forgan D. H., Ilee J. D., Cyganowski C. J., Brogan C. L., Hunter T. R., 2016, MNRAS, 463, 957
Frost A. J., Oudmaijer R. D., Lumsden S. L., de Wit W. J., 2021, ApJ, 920, 48
Fuente A., Neri R., Martín-Pintado J., Bachiller R., Rodríguez-Franco A., Palla F., 2001, A&A, 366, 873
Fung J., Artymowicz P., 2014, ApJ, 790, 78
Goddi C., Ginsburg A., Maud L. T., Zhang Q., Zapata L. A., 2020, ApJ, 905, 25
Hirano S., Hosokawa T., Yoshida N., Kuiper R., 2017, Science, 357, 1375
Hosokawa T., Hirano S., Kuiper R., Yorke H. W., Omukai K., Yoshida N., 2016, ApJ, 824, 119
Hosokawa T., Omukai K., 2009, ApJ, 691, 823
Hosokawa T., Yorke H. W., Omukai K., 2010, ApJ, 721, 478
Humphries J., Hall C., Haworth T. J., Nayakshin S., 2021, MNRAS, 502, 953
Hunter T. R., Brogan C. L., De Buizer J. M., Towner A. P. M., Dowell C. D., MacLeod G. C., Stecklum B., Cyganowski C. J., El-Abd S. J., McGuire B. A., 2021, ApJ, 912, L17
Hunter T. R., Brogan C. L., MacLeod G., Cyganowski C. J., Chandler C. J., Chibueze J. O., Friesen R., Indebetouw R., Thesner C., Young K. H., 2017, ApJ, 837, L29
Ilee J. D., Cyganowski C. J., Brogan C. L., Hunter T. R., Forgan D. H., Haworth T. J., Clarke C. J., Harries T. J., 2018, ApJ, 869, L24

Ilee J. D., Cyganowski C. J., Nazari P., Hunter T. R., Brogan C. L., Forgan D. H., Zhang Q., 2016, MNRAS, 462, 4386
Jankovic M. R., Haworth T. J., Ilee J. D., Forgan D. H., Cyganowski C. J., Walsh C., Brogan C. L., Hunter T. R., Mohanty S., 2019, MNRAS, 482, 4673
Johnson B. M., Gammie C. F., 2003, ApJ, 597, 131
Johnston K. G., Robitaille T. P., Beuther H., Linz H., Boley P., Kuiper R., Keto E., Hoare M. G., van Boekel R., 2015, ApJ, 813, L19
Johnston K. G., Shepherd D. S., Robitaille T. P., Wood K., 2013, A&A, 551, A43
Kenyon S. J., Hartmann L., 1995, ApJS, 101, 117
Kenyon S. J., Hartmann L. W., 1990, ApJ, 349, 197
Kenyon S. J., Hartmann L. W., Strom K. M., Strom S. E., 1990, AJ, 99, 869
Klassen M., Pudritz R. E., Kuiper R., Peters T., Banerjee R., 2016, ApJ, 823, 28
Kolb S. M., Stute M., Kley W., Mignone A., 2013, A&A, 559, A80
Krumholz M. R., Klein R. I., McKee C. F., 2007a, ApJ, 665, 478
Krumholz M. R., Klein R. I., McKee C. F., 2007b, ApJ, 656, 959
Laor A., Draine B. T., 1993, ApJ, 402, 441
Larson R. B., 1969, MNRAS, 145, 271
Larson R. B., 1972, MNRAS, 157, 121
Lin M.-K., 2015, MNRAS, 448, 3806
Liu S.-Y., Su Y.-N., Zinchenko I., Wang K.-S., Meyer D. M. A., Wang Y., Hsieh I. T., 2020, ApJ, 904, 181
Liu S.-Y., Su Y.-N., Zinchenko I., Wang K.-S., Wang Y., 2018, ApJ, 863, L12
Lucas P. W., Elias J., Points S., Guo Z., Smith L. C., Stecklum B., Vorobyov E., Morris C., Borissova J., Kurtev R., Contreras Peña C., Medina N., Minniti D., Ivanov V. D., Saito R. K., 2020, MNRAS, 499, 1805
MacFarlane B., Stamatellos D., Johnstone D., Herczeg G., Baek G., Chen H.-R. V., Kang S.-J., Lee J.-E., 2019a, MNRAS, 487, 5106
MacFarlane B., Stamatellos D., Johnstone D., Herczeg G., Baek G., Chen H.-R. V., Kang S.-J., Lee J.-E., 2019b, MNRAS, 487, 4465
Machida M. N., Inutsuka S.-i., Matsumoto T., 2011, ApJ, 729, 42
MacLeod G. C., Smits D. P., Goedhart S., Hunter T. R., Brogan C. L., Chibueze J. O., van den Heever S. P., Thesner C. J., Banda P. J., Paulsen J. D., 2018, MNRAS, 478, 1077
Maud L. T., Cesaroni R., Kumar M. S. N., Rivilla V. M., Ginsburg A., Klaassen P. D., Harsono D. e. a., 2019, A&A, 627, L6
Maud L. T., Cesaroni R., Kumar M. S. N., van der Tak F. F. S., Allen V., Hoare M. G., Klaassen P. D., Harsono D., Hogerheijde M. R. e. a., 2018, A&A, 620, A31
Maud L. T., Hoare M. G., Galván-Madrid R., Zhang Q., de Wit W. J., Keto E., Johnston K. G., Pineda J. E., 2017, MNRAS, 467, L120
McCarthy T. P., Orosz G., Ellingsen S. P., Breen S. L., Voronkov M. A., Burns R. A., Olech M., Yonekura Y., Hirota T., Hyland L. J., Wolak P., 2022, MNRAS, 509, 1681
McMullin J. P., Waters B., Schiebel D., Young W., Golap K., 2007, in Shaw R. A., Hill F., Bell D. J., eds, Astronomical Data Analysis Software and Systems XVI Vol. 376 of Astronomical Society of the Pacific Conference Series, CASA Architecture and Applications. p. 127
Meyer D. M. A., Haemmerlé L., Vorobyov E. I., 2019, MNRAS, 484, 2482
Meyer D. M. A., Kreplin A., Kraus S., Vorobyov E. I., Haemmerle L., Eislöffel J., 2019, MNRAS, 487, 4473
Meyer D. M.-A., Kuiper R., Kley W., Johnston K. G., Vorobyov E., 2018, MNRAS, 473, 3615
Meyer D. M. A., Vorobyov E. I., Elbakyan V. G., Eislöffel J., Sobolev A. M., Stöhr M., 2021, MNRAS, 500, 4448
Meyer D. M.-A., Vorobyov E. I., Elbakyan V. G., Stecklum B., Eislöffel J., Sobolev A. M., 2019, MNRAS, 482, 5459
Meyer D. M.-A., Vorobyov E. I., Kuiper R., Kley W., 2017, MNRAS, 464, L90
Michael S., Durisen R. H., 2010a, MNRAS, 406, 279
Michael S., Durisen R. H., 2010b, MNRAS, 406, 279
Mignone A., Bodo G., Massaglia S., Matsakos T., Tesileanu O., Zanni C., Ferrari A., 2007, ApJS, 170, 228
Mignone A., Zanni C., Tzeferacos P., van Straalen B., Colella P., Bodo G., 2012, ApJS, 198, 7
Moscadelli L., Sanna A., Goddi C., Walmsley M. C., Cesaroni R., Caratti o Garatti A., Stecklum B., Menten K. M., Kraus A., 2017, A&A, 600, L8
Motogi K., Hirota T., Machida M. N., Yonekura Y., Honma M., Takakuwa S., Matsushita S., 2019, ApJ, 877, L25
Nayakshin S., 2015a, MNRAS, 454, 64
Nayakshin S., 2015b, arXiv e-prints, p. arXiv:1502.07585
Nayakshin S., 2016, MNRAS, 461, 3194
Nayakshin S., Fletcher M., 2015, MNRAS, 452, 1654
Nayakshin S., Lodato G., 2012, MNRAS, 426, 70
Olguin F. A., Hoare M. G., Johnston K. G., Motte F., Chen H. R. V., Beuther H., Mottram J. C., Ahmadi A., Gieser C., Semenov D., Peters T., Palau A., Klaassen P. D., Kuiper R., Sánchez-Monge Á., Henning T., 2020, MNRAS, 498, 4721
Oliva G. A., Kuiper R., 2020, A&A, 644, A41
Ou S., Ji J., Liu L., Peng X., 2007, ApJ, 667, 1220
Pickett B. K., Mejía A. C., Durisen R. H., Cassen P. M., Berry D. K., Link R. P., 2003, ApJ, 590, 1060
Proven-Adzri E., MacLeod G. C., Heever S. P. v. d., Hoare M. G., Kuditcher A., Goedhart S., 2019, MNRAS, 487, 2407
Purser S. J. D., Lumsden S. L., Hoare M. G., Cunningham N., 2018, MNRAS, 475, 2
Purser S. J. D., Lumsden S. L., Hoare M. G., Kurtz S., 2021, MNRAS, 504, 338
Regály Z., Vorobyov E., 2017, A&A, 601, A24
Reiter M., Kiminki M. M., Smith N., Bally J., 2017, MNRAS, 470, 4671
Rosen A. L., Li P. S., Zhang Q., Burkhart B., 2019, ApJ, 887, 108
Samal M. R., Chen W. P., Takami M., Jose J., Froebrich D., 2018, MNRAS, 477, 4577
Sanna A., Giannetti A., Bonfand M., Moscadelli L., Kuiper R., Brand J., Cesaroni R., Caratti o Garatti A., Pillai T., Menten K. M., 2021, A&A, 655, A72
Sanna A., Kölligan A., Moscadelli L., Kuiper R., Cesaroni R., Pillai T., Menten K. M., Zhang Q., Caratti o Garatti A., Goddi C., Leurini S., Carrasco-González C., 2019, A&A, 623, A77
Seifried D., Banerjee R., Klessen R. S., Duffin D., Pudritz R. E., 2011, MNRAS, 417, 1054
Skliarevskii A. M., Pavlyuchenkov Y. N., Vorobyov E. I., 2021, Astronomy Reports, 65, 170
Springel V., 2010, ARA&A, 48, 391
Stecklum B., Wolf V., Linz H., Caratti o Garatti A. e. a., 2021, A&A, 646, A161
Suri S., Beuther H., Gieser C., Ahmadi A., Sánchez-Monge Á., Winters J. M., Linz H., Henning T., Beltrán M. T., Bosco F., Cesaroni R., Csengeri T., Feng S., Hoare M. G., Johnston K. G., Klaassen P., Kuiper R., Leurini S., Longmore S., Lumsden S., Maud L., Moscadelli L., Möller T., Palau A., Peters T., Pudritz R. E., Ragan S. E., Semenov D., Schilke P., Urquhart J. S., Wyrowski F., Zinnecker H., 2021, A&A, 655, A84
Szulágyi J., Morbidelli A., Crida A., Masset F., 2014, ApJ, 782, 65
Szymczak M., Olech M., Wolak P., Gérard E., Bartkiewicz A., 2018, A&A, 617, A80
Tanaka H., Takeuchi T., Ward W. R., 2002, ApJ, 565, 1257
Tanaka H., Ward W. R., 2004, ApJ, 602, 388
Testi L., 2003, in De Buizer J. M., van der Bliek N. S., eds, Galactic Star Formation Across the Stellar Mass Spectrum Vol. 287 of Astronomical Society of the Pacific Conference Series, Intermediate Mass Stars (Invited Review). pp 163–173
Tsukamoto Y., Machida M. N., 2011, MNRAS, 416, 591
Vaidya B., Mignone A., Bodo G., Rossi P., Massaglia S., 2018, ApJ, 865, 144
Vorobyov E. I., Basu S., 2006, ApJ, 650, 956
Vorobyov E. I., Basu S., 2010, ApJ, 719, 1896
Vorobyov E. I., Basu S., 2015, ApJ, 805, 115

Vorobyov E. I., Elbakyan V., Hosokawa T., Sakurai Y., Guedel M., Yorke H., 2017, A&A, 605, A77
Vorobyov E. I., Elbakyan V. G., Plunkett A. L., Dunham M. M., Audard M., Guedel M., Dionatos O., 2018, A&A, 613, A18
Vorster J. M., Okwe Chibueze J., Hirota T., 2021, in South African Institute of Physics Conference at Potchefstroom Spatio-kinematics of the massive star forming region NGC6334I during an episodic accretion event. p. E1
Williams G. M., Cyganowski C. J., Brogan C. L., Hunter T. R., Ilee J. D., Nazari P., Kruijssen J. M. D., Smith R. J., Bonnell I. A., 2022, MNRAS, 509, 748
Zhao B., Caselli P., Li Z.-Y., Krasnopolsky R., 2018, MNRAS, 473, 4868
Zhu Z., Stone J. M., 2014, ApJ, 795, 53
Zinchenko I. I., Liu S.-Y., Su Y.-N., Wang K.-S., Wang Y., 2019, arXiv e-prints, p. arXiv:1911.11447

Evolved massive stars nebulae

Monthly Notices
of the
ROYAL ASTRONOMICAL SOCIETY

MNRAS **459,** 1146–1158 (2016)
Advance Access publication 2016 March 17

doi:10.1093/mnras/stw651

On the observability of bow shocks of Galactic runaway OB stars

D. M.-A. Meyer,[1]★ A.-J. van Marle,[2,3] R. Kuiper[1] and W. Kley[1]

[1] *Institut für Astronomie und Astrophysik, Universität Tübingen, Auf der Morgenstelle 10, D-72076 Tübingen, Germany*
[2] *KU Leuven, Centre for mathematical Plasma Astrophysics, Celestijnenlaan 200B, B-3001 Leuven, Belgium*
[3] *Laboratoire AstroParticule et Cosmologie – Universite Paris 7 Diderot – 10 rue Alice Domon et Leonie Duquet, Paris F-75013, France*

Accepted 2016 March 15. Received 2016 March 15; in original form 2015 December 8

ABSTRACT

Massive stars that have been ejected from their parent cluster and supersonically sailing away through the interstellar medium (ISM) are classified as exiled. They generate circumstellar bow-shock nebulae that can be observed. We present two-dimensional, axisymmetric hydrodynamical simulations of a representative sample of stellar wind bow shocks from Galactic OB stars in an ambient medium of densities ranging from $n_{\rm ISM} = 0.01$ up to $10.0\,{\rm cm}^{-3}$. Independently of their location in the Galaxy, we confirm that the infrared is the most appropriated waveband to search for bow shocks from massive stars. Their spectral energy distribution is the convenient tool to analyse them since their emission does not depend on the temporary effects which could affect unstable, thin-shelled bow shocks. Our numerical models of Galactic bow shocks generated by high-mass ($\approx 40\,{\rm M}_\odot$) runaway stars yield H α fluxes which could be observed by facilities such as the SuperCOSMOS H-Alpha Survey. The brightest bow-shock nebulae are produced in the denser regions of the ISM. We predict that bow shocks *in the field* observed at H α by means of Rayleigh-sensitive facilities are formed around stars of initial mass larger than about $20\,{\rm M}_\odot$. Our models of bow shocks from OB stars have the emission maximum in the wavelength range $3 \leq \lambda \leq 50\,\mu{\rm m}$ which can be up to several orders of magnitude brighter than the runaway stars themselves, particularly for stars of initial mass larger than $20\,{\rm M}_\odot$.

Key words: methods: numerical – circumstellar matter – stars: massive.

1 INTRODUCTION

The estimate of massive star feedback is a crucial question in the understanding of the Galaxy's functioning (Langer 2012). Throughout their short lives, they release strong winds (Holzer & Axford 1970) and ionizing radiation (Diaz-Miller, Franco & Shore 1998) which modify their ambient medium. This results in diaphanous H II regions (Dyson 1975), parsec-scale bubbles of stellar wind (Weaver et al. 1977), inflated (Petrovic, Pols & Langer 2006) or shed (Garcia-Segura, Mac Low & Langer 1996; Woosley, Heger & Weaver 2002) stellar envelopes that impact their close surroundings and which can alter the propagation of their subsequent supernova shock wave (van Veelen 2010; Meyer et al. 2015). Understanding the formation processes of these circumstellar structures allows us to constrain the impact of massive stars, e.g. on the energetics or the chemical evolution of the interstellar medium (ISM). Moreover, it links studies devoted to the dynamical evolution of supernova remnants expanding into the perturbed ISM (Rozyczka et al. 1993) with works focusing on the physics of the star-forming ISM (Peters et al. 2010).

While bow-shock-like structures can develop around any astrophysical object that moves supersonically with respect to its ambient medium (see e.g. Thun et al. 2016), it particularly affects the surroundings of bright stars running through the ISM (Blaauw 1961). These arc-like structures of swept-up stellar wind material and ISM gas are the result of the distortion of their stellar wind bubble by the bulk motion of their central star (Weaver et al. 1977). Their size and their morphology are governed by their stellar wind mass-loss, the wind velocity, the bulk motion of the runaway star, and their local ambient medium properties (Comerón & Kaper 1998). These distorted wind bubbles have been first noticed in optical [O III] λ 5007 spectral emission line around the Earth's closest runaway star, the OB star ζ Ophiuchi (Gull & Sofia 1979). Other noticeable fast-moving massive stars producing a stellar wind bow shock are, e.g. the blue supergiant Vela-X1 (Kaper et al. 1997), the red supergiant Betelgeuse (Noriega-Crespo et al. 1997b), and the very massive star BD+43°365 running away from Cygnus OB2 (Comerón & Pasquali 2007).

Analysis of data from the *Infrared Astronomical Satellite* facility (Neugebauer et al. 1984) later extended to measures taken with the

★ E-mail: dominique.meyer@uni-tuebingen.de

Wide-Field Infrared Satellite Explorer (Wright et al. 2010) led to the compilation of bow-shock records, see e.g. (van Buren & McCray 1988). Soon arose the speculation that those isolated nebulae can serve as a tool independent on assumptions regarding the internal physics of these stars, to constrain the still highly debated mass-loss of massive stars (Gull & Sofia 1979) and/or their ambient medium density (Huthoff & Kaper 2002). This also raised questions related to the ejection mechanisms of OB stars from young stellar clusters (Hoogerwerf, de Bruijne & de Zeeuw 2001). More recently, multi-wavelengths data led to the publication of the E-BOSS catalogue of stellar wind bow shocks (Peri et al. 2012; Peri, Benaglia & Isequilla 2015).

Early simulations discussed the general morphology of the bow shocks around OB stars (Brighenti & D'Ercole 1995, and references therein), their (in)stability (Blondin & Koerwer 1998) and the general incompatibility of the shape of stellar wind bow shocks with analytical approximations such as the one of Wilkin (1996), see in Comerón & Kaper (1998). However, observing massive star bow shocks remains difficult and they are mostly serendipitously noticed in infrared observations of the neighbourhood of stellar clusters (Gvaramadze & Bomans 2008). Moreover, their optical emission may be screened by the H II region which surrounds the driving star and this may affect their H α observations (Brown & Bomans 2005). We are particularly interested in the prediction of the easiest bow shocks to observe, their optical emission properties and their location in the Galaxy.

In this study, we extend our numerical investigation of the circumstellar medium of runaway massive stars (Meyer et al. 2014b, hereafter Paper I). Note that our approach is primarily focused on exploring the parameter space, rather than a series of simulations tailored to a specific bow-shock nebula. Our parameter study explores the effects of the ambient medium density on the emission properties of the bow-like nebulae around the most common runaway stars, in the spirit of works on bow shocks generated by low-mass stars (Villaver, Manchado & García-Segura 2012, and references therein). The underlying assumptions are the same as in our previous purely hydrodynamical models, i.e. we neglect the magnetization of the ISM, ignore any intrinsic inhomogeneity in the ISM density field and consider that both the wind and the ISM gas are a perfect gas.

Our paper is organized as follows. In Section 2, we present the numerical methods and the microphysics that is included in our models. The resulting numerical simulations are presented and discussed in Section 3. We then analyse and discuss the emission properties of our bow-shock models in Section 4. Finally, we formulate our conclusions in Section 5.

2 METHOD

2.1 Governing equations

The bow-shock problem is described in our work by the Euler equations of hydrodynamics. It is a set of equations for mass conservation,

$$\frac{\partial \rho}{\partial t} + \nabla \cdot (\rho \boldsymbol{v}) = 0, \tag{1}$$

conservation of linear momentum,

$$\frac{\partial \rho \boldsymbol{v}}{\partial t} + \nabla \cdot (\boldsymbol{v} \otimes \rho \boldsymbol{v}) + \nabla p = \boldsymbol{0}, \tag{2}$$

and conservation of energy,

$$\frac{\partial E}{\partial t} + \nabla \cdot (E \boldsymbol{v}) + \nabla \cdot (p \boldsymbol{v}) = \Phi(T, \rho) + \nabla \cdot \boldsymbol{F}_{\rm c}, \tag{3}$$

where,

$$E = \frac{p}{(\gamma - 1)} + \frac{\rho v^2}{2}, \tag{4}$$

and where ρ is the mass density of the gas, p its pressure, $\boldsymbol{v}$ the vector velocity. The temperature of the gas is given by,

$$T = \mu \frac{m_{\rm H}}{k_{\rm B}} \frac{p}{\rho}, \tag{5}$$

where $k_{\rm B}$ is the Boltzmann constant and μ is the mean molecular weight, such that $\rho = \mu n m_{\rm H}$ with n the total number density of the fluid and $m_{\rm H}$ the mass of a hydrogen atom. The adiabatic index of the gas is $\gamma = 5/3$. The equation (3) includes (i) the effects of both the cooling and the heating of the gas by optically thin radiative processes and (ii) the transport of heat by electronic thermal conduction (see Section 2.3).

2.2 Hydrodynamical simulations

We run two-dimensional, axisymmetric, hydrodynamical numerical simulations using the PLUTO code (Mignone et al. 2007, 2012) in axisymmetric, cylindrical coordinates on a uniform grid $[z_{\rm min}, z_{\rm max}] \times [O, R_{\rm max}]$ of spatial resolution $\Delta = 2.25 \times 10^{-4}$ pc cell^{-1} minimum. The stellar wind is injected into the computational domain filling a circle of radius 20 cells centred on to the origin O (see e.g. Comerón & Kaper 1998; Meyer et al. 2014a, and references therein). The interaction with the ISM is calculated in the reference frame of the moving star (van Marle, Langer & García-Segura 2007; van Marle et al. 2011; van Marle, Decin & Meliani 2014). Inflowing ISM gas mimicking the stellar motion is set at the $z = z_{\rm max}$ boundary whereas semipermeable boundary conditions are set at $z = z_{\rm min}$ and at $R = R_{\rm max}$. Wind material is distinguished from the ISM using a passive tracer Q that is advected with the gas and initially set to $Q = 1$ in the stellar wind and to $Q = 0$ in the ISM. The ISM composition is assumed to be solar (Asplund et al. 2009).

The stellar models are calculated using the stellar evolution code of Heger, Woosley & Spruit (2005), Yoon & Langer (2005), and Petrovic et al. (2005) also described in Brott et al. (2011). It includes the mass-loss recipe of Kudritzki et al. (1989) for the main-sequence phase and of de Jager, Nieuwenhuijzen & van der Hucht (1988) for the red supergiant phase. The stellar properties are displayed in fig. 3 of Paper I while we summarize the wind properties at the beginning of our simulations in our Table 1.

2.3 Microphysics

In order to proceed on our previous bow-shock studies (Paper I; Meyer et al. 2015), we include the same microphysics in our simulations of the circumstellar medium of runaway, massive stars, i.e. we take into account losses and gain of internal energy by optically thin cooling and heating together with electronic thermal conduction. Optically thin radiative processes are included into the model using the cooling and heating laws established for a fully ionized medium in Paper I. They are the right-hand term $\Phi(T, \rho)$ of equation (3) which is given by,

$$\Phi(T, \rho) = n_{\rm H} \Gamma(T) - n_{\rm H}^2 \Lambda(T), \tag{6}$$

where $\Gamma(T)$ and $\Lambda(T)$ are the heating and cooling laws, respectively, and $n_{\rm H}$ is the hydrogen number density. It mainly consist of

Table 1. Mass $M_\star$ (in $M_\odot$), luminosity $L_\star$ (in $L_\odot$), mass-loss $\dot{M}$ (in $M_\odot$ yr^{-1}), and wind velocity v_w (in km s^{-1}) of our runaway stars at the beginning of the simulations, at a time t_{start} (Myr) after the zero-age main sequence time. T_{eff} (in K) is the effective temperature of the star at t_{start}. The number of ionizing photons released per unit time $S_\star$ (in photon s^{-1}) is taken from Diaz-Miller et al. (1998). Finally, t_{MS} is the main-sequence time-scale of the star (in Myr).

$M_\star$ ($M_\odot$)	t_{start} (Myr)	$\log(L_\star/L_\odot)$	$\log(\dot{M}/M_\odot$ yr$^{-1})$	v_w (km s^{-1})	T_{eff} (K)	$S_\star$(photon s^{-1})	t_{MS}(Myr)
10	5.0	3.80	−9.52	1082	25 200	10^{45}	22.5
20	3.0	4.74	−7.38	1167	33 900	10^{48}	8.0
40	0.0	5.34	−6.29	1451	42 500	10^{49}	4.0

cooling contributions from hydrogen and helium for temperatures $T < 10^6$ K whereas it is principally due to metals for temperatures $T \geq 10^6$ K (Wiersma, Schaye & Smith 2009). A term representing the cooling from collisionally excited forbidden lines (Henney et al. 2009) incorporates the effects of, among other, the [O III] λ 5007 line emission. The heating contribution includes the reionization of recombining hydrogen atoms by the starlight (Osterbrock & Bochkarev 1989; Hummer 1994). All our models include electronic thermal conduction (Cowie & McKee 1977). The divergence term in equation (3) represents the flux of heat,

$$\boldsymbol{F}_c = \kappa \nabla T, \tag{7}$$

where κ is the heat conduction coefficient (Spitzer 1962). More details about thermal conduction are also given in Paper I.

2.4 Parameter range

This work consists of a parameter study extending our previous investigation of stellar wind bow shock (Paper I) to regions of the Galaxy where the ISM has either lower or higher densities. We perform re-runs of the models in Paper I that correspond to the main-sequence phase of our stars, but assume a different ISM background density and only consider the cases where the main-sequence lifetime of the stars is larger than the four crossing times of the gas $|z_{max} - z_{min}|/v_\star$ through the whole computational domain which are necessary to model steady state bow shocks. The boundary conditions are unchanged, i.e. we consider runaway stars of 10, 20, and 40 $M_\odot$ zero-age main-sequence (ZAMS) star moving with velocity $v_\star = 20$, 40, and 70 km s^{-1}, respectively. Differences come from the chosen ISM number density that ranges from $n_{ISM} = 0.01$ to 10.0 cm^{-3} whereas our preceding work exclusively focused on bow-shocks models with $n_{ISM} = 0.79$ cm^{-3}. The simulation labels are summarized in Table 2. The analysis of our simulations include the main-sequence models with $n_{ISM} = 0.79$ cm^{-3} of Paper I and we refer to them using their original labels.

3 BOW-SHOCKS MORPHOLOGY

3.1 Bow-shocks structure

In Fig. 1, we show the density fields in our hydrodynamical simulations of our 20 $M_\odot$ ZAMS star moving with velocity $v_\star = 70$ km s^{-1} in a medium of number density $n_{ISM} = 0.01$ (panel a, model MS2070n0.01), 0.1 (panel b, model MS2070n0.1), 0.79 (panel c, model MS2070), and 10.0 cm^{-3} (panel d, model MS2070n10), respectively. The figures correspond to times about 4.14, 3.29, 3.08, and 3.03 Myr after the beginning of the main-sequence phase. Our bow shocks have the typical structure of a circumstellar nebulae generated by a fast-moving OB star undergoing the conjugated effects of both cooling and heating by optically thin radiative processes and thermal conduction and the thickness of the shock layer depends on whether the shocks are adiabatic or radiative, which in their turn depends on the shock conditions, see Comerón & Kaper (1998), Paper I and the references therein. All our bow-shock simulations have such a structure.

Table 2. The hydrodynamical models. Parameters $M_\star$ (in $M_\odot$), $v_\star$ (in km s^{-1}), and n_{ISM} (in cm^{-3}) are the initial mass of the considered moving star, its space velocity and its local ISM density, respectively.

Model	$M_\star$ ($M_\odot$)	$v_\star$ (km s^{-1})	n_{ISM} (cm^{-3})
MS1020n0.01	10	20	0.01
MS1040n0.01	10	40	0.01
MS1070n0.01	10	70	0.01
MS2040n0.01	20	40	0.01
MS2070n0.01	20	70	0.01
MS1020n0.1	10	20	0.10
MS1040n0.1	10	40	0.10
MS1070n0.1	10	70	0.10
MS2020n0.1	20	20	0.10
MS2040n0.1	20	40	0.10
MS2070n0.1	20	70	0.10
MS4070n0.1	40	70	0.10
MS1020n10	10	20	10.0
MS1040n10	10	40	10.0
MS1070n10	10	70	10.0
MS2020n10	20	20	10.0
MS2040n10	20	40	10.0
MS2070n10	20	70	10.0
MS4020n10	40	20	10.0
MS4040n10	40	40	10.0
MS4070n10	40	70	10.0

3.2 Bow-shocks size

The bow shocks have a stand-off distance $R(0)$, i.e. the distance separating them from the star along the direction of motion predicted by Wilkin (1996). It decreases as a function of (i) $v_\star$, (ii) $\dot{M}$ (cf. Paper I), and (iii) n_{ISM} since $R(0) \propto n_{ISM}^{-1/2}$. A dense ambient medium produces a large ISM ram pressure $n_{ISM} v_\star^2$ which results in a compression of the whole bow shock and consequently in a reduction of $R(0)$. As an example, our simulations involving a 20 $M_\odot$ ZAMS star with $v_\star = 70$ km s^{-1} has $R(0) \approx 3.80$, 1.14, 0.38, and 0.07pc when the driving star moves in $n_{ISM} = 0.01$, 0.1, 0.79, and 10 cm^{-3}, respectively (Fig. 1a–d), which is reasonably in accordance with Wilkin (1996). All our measures of $R(0)$ are taken at the contact discontinuity, because it is appropriate measure to compare models with Wilkin's analytical solution (Mohamed, Mackey & Langer 2012).

In Fig. 2, we plot the ratio $R(0)/R(90)$ as a function of the stand-off distance of the bow shocks, where $R(90)$ is the distance between the star and the bow shock measured along the direction perpendicular to the direction of motion. The internal structure of the bow shocks depends on the stellar wind and the bulk motion of the star (Paper I) but are also sensible to the ISM density. Important

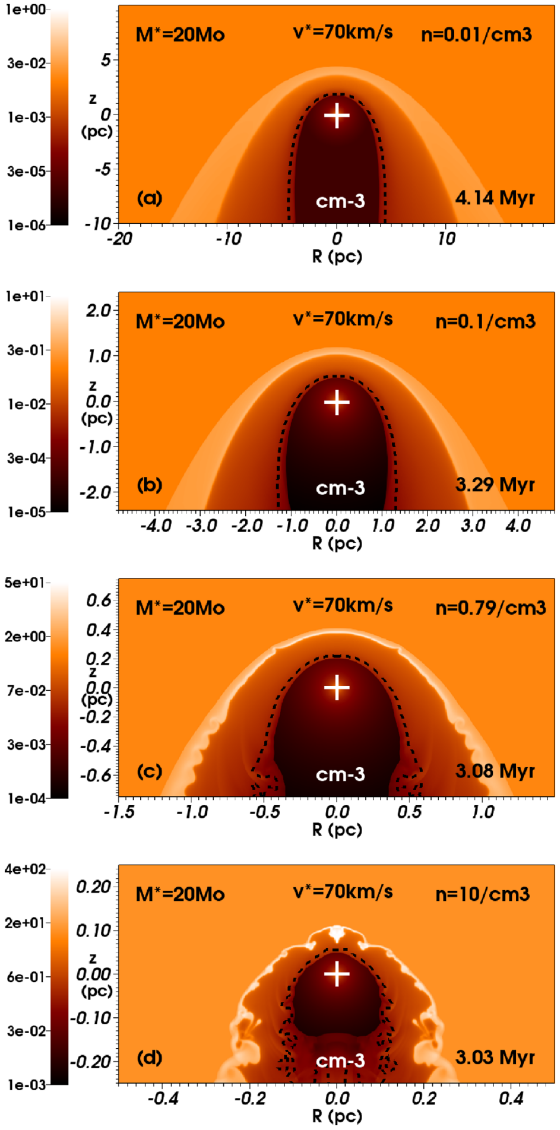

Figure 1. Stellar wind bow shocks from the main-sequence phase of the 20 $M_\odot$ ZAMS star moving with velocity 70 km s^{-1} as a function of the ISM density, with $n_{\rm ISM} = 0.01$ (a), 0.1 (b), 0.79 (c), and 10.0 cm^{-3} (d). The gas number density (in cm^{-3}) is shown in the logarithmic scale. The dashed black contour traces the boundary between wind and ISM material. The cross indicates the position of the runaway star. The R-axis represents the radial direction and the z-axis the direction of stellar motion (in pc). Only part of the computational domain is shown.

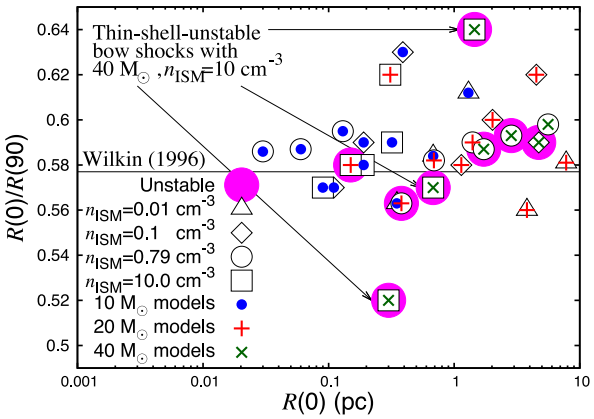

Figure 2. Axis ratio $R(0)/R(90)$ of our bow-shock models. The figure shows the ratio $R(0)/R(90)$ measured in the density field of our models measured at their contact discontinuity, as a function of their stand-off distance $R(0)$ (in pc). Symbols distinguish models as a function of (i) the ISM ambient medium with $n_{\rm ISM} = 0.01$ (triangles), 0.1 (diamonds), 0.79 (circles), and 10.0 cm^{-3} (squares) and (ii) of the initial mass of the star with 10 $M_\odot$ (blue dots), 20 $M_\odot$ (blue plus signs), and 40 $M_\odot$ (dark green crosses), respectively. The thin horizontal black line corresponds to the analytic solution $R(0)/R(90) = 1/\sqrt{3} \approx 0.58$ of Wilkin (1996). The large purple dots highlight the unstable bow shocks.

variations in the stars' ambient local medium can produce large compression of the region of shocked ISM gas, which in its turn decreases up to form a thin layer of cold shocked ISM gas (see Fig. 1b and fig. 1 of Comerón & Kaper 1998). This phenomenon typically arises in simulations combining moving stars with strong mass-loss such as our 40 $M_\odot$ ZAMS star, together with velocity $v_\star \geq 40$ km s^{-1} and/or $n_{\rm ISM} \geq 1$ cm^{-3} (see large magenta dots in Fig. 2). Those thin-shells are more prone to develop non-linear instabilities (Vishniac 1994; Garcia-Segura et al. 1996).

Interestingly, analytic approximations of the overall shape of a bow shock often assume such an infinitely thin structure (Wilkin 1996) and predict that $R(0)/R(90) = 1/\sqrt{3} \approx 0.58$. Thin shells are very unstable and experience periodical large distortions which can make the shape of the bow shock inconsistent with Wilkin's prediction of $R(0)/R(90)$ (see black arrows in Fig. 2). Most of the models are within 20 per cent of Wilkin's solution (see horizontal black line at $R(0)/R(90) \approx 1/\sqrt{3}$). Only a few models have $R(0)/R(90) \leq 1/\sqrt{3}$ because their opening is smaller than predicted. However, some simulations with $v_\star = 20$ km s^{-1} have large and spread bow shocks in which $R(0)/R(90) \geq 0.62$, see e.g. our simulation MS2020n0.1 with $R(90) \approx 4.51$ pc.

3.3 Non-linear instabilities and mixing of material

In Fig. 3, we show a time-sequence evolution of the density field in hydrodynamical simulations of 40 $M_\odot$ ZAMS star moving with velocity $v_\star = 70$ km s^{-1} in a medium of number density $n = 10.0$ cm^{-3} (model MS4070n10). The figures are shown at times 0.02 (a), 0.05 (b), 0.11 (c), and 0.12 Myr (d), respectively. After 0.02 Myr, the whole shell is sparsed with small-size clumps which are the seeds of non-linear instabilities (Fig. 3b). The fast stellar motion ($v_\star = 70$ km s^{-1}) provokes a distortion of the bubble into an ovoid shape (see fig. 7 of Weaver et al. 1977) and the high ambient medium density ($n = 10.0$ cm^{-3}) induces rapidly a thin shell after only about 0.01 Myr.

The bow shock then experiences a series of cycles in which small-scaled eddies grow in the shell (Fig. 3b) and further distort its apex into wing-like structures (Fig. 3c), which are pushed sidewards because of the transverse component of the stellar wind acceleration (Fig. 3d). Our model MS4070n10 has both characteristics from the models E 'High ambient density' and G 'Instantaneous cooling' of Comerón & Kaper (1998). Thin-shelled stellar wind bow shocks develop non-linear instabilities, in addition to the Kelvin–Helmholtz instabilities that typically affect interfaces between shearing flows

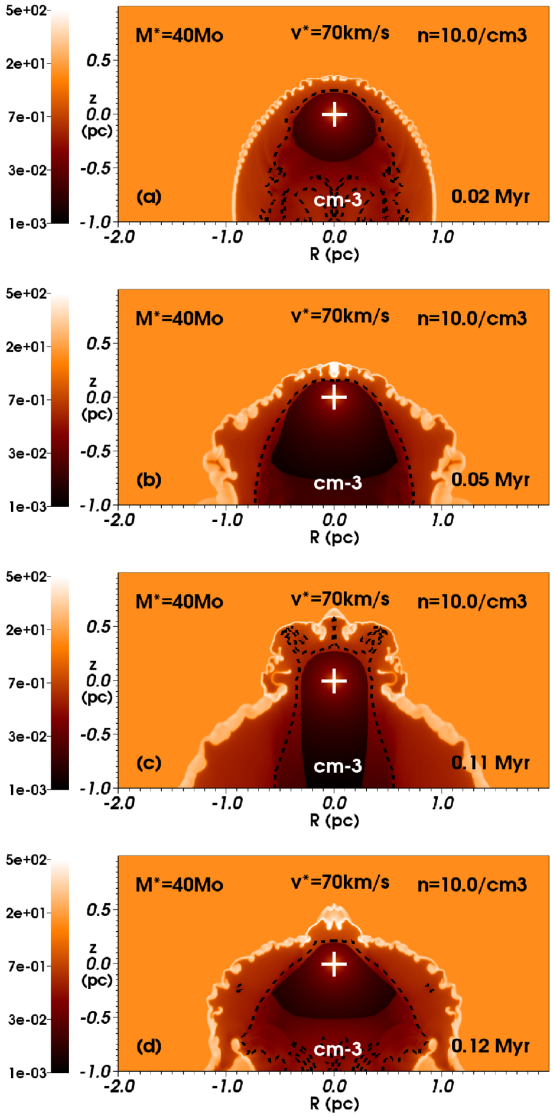

Figure 3. Same as Fig. 1 for our 40 $M_\odot$ ZAMS star moving through an ISM of density $n_{\rm ISM} = 10.0\,{\rm cm}^{-3}$ with velocity 70 km s^{-1} (model MS4070n10). Figures are shown at times 0.02 (a), 0.05 (b), 0.11 (c), and 0.12 Myr (d) after the beginning of the main-sequence phase of the star, respectively. It illustrates the development of the non-linear thin-shell instability in the bow shock.

of opposite directions, i.e. the outflowing stellar wind and the ISM gas penetrating the bow shocks (Vishniac 1994; Garcia-Segura et al. 1996; van Marle et al. 2007). A detailed discussion of the development of such non-linearities affecting bow shocks generated by OB runaway stars is in Comerón & Kaper (1998).

In Fig. 4, we plot the evolution of the volume of the bow shock in our model MS4070n10 (thick solid blue line), separating the volume of shocked ISM gas (thin dotted red line) from the volume of shocked stellar wind (thick dotted orange line) in the apex ($z \geq 0$) of the bow shock. Such a discrimination of the volume of wind and ISM gas is possible because a passive scalar tracer is numerically advected simultaneously with the flow. The figure further illustrates the preponderance of the volume of shocked ISM in the bow shock

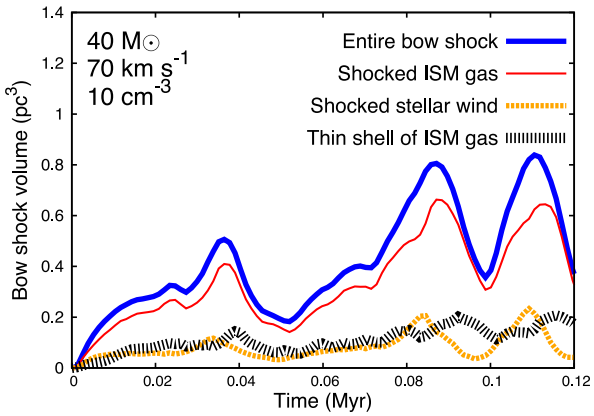

Figure 4. Bow-shock volume ($z \geq 0$) in our model MS4070n10 (see Fig. 3 a–e). The figure shows the volume of perturbed material (in pc^3) in the computational domain (thick solid blue line), together with the volume of shocked ISM gas (thin solid red line) and shocked stellar wind (thick dotted orange line), respectively, as function of time (in Myr). The large dotted black line represents the volume of the thin shell of shocked ISM.

compared to the stellar wind material, regardless the growth of eddies. Interestingly, the volume of dense shocked ISM gas (large dotted black line) does not have large time variations (see Section 4).

4 BOW-SHOCK ENERGETICS AND EMISSION SIGNATURES

4.1 Methods

In Fig. 5, the total bow-shock luminosity $L_{\rm total}$ (pale green diamonds) is calculated integrating the losses by optically thin radiation in the $z \geq 0$ region of the computational domain (Mohamed et al. 2012; Paper I). Shocked wind emission $L_{\rm wind}$ (orange dots) is discriminated from $L_{\rm total}$ with the help of the passive scalar Q that is advected with the gas, such that,

$$L_{\rm total} = 2\pi \iint_{z\geq 0} \Lambda(T) n_{\rm H}^2 R {\rm d}R{\rm d}z, \quad (8)$$

and,

$$L_{\rm wind} = 2\pi \iint_{z\geq 0} \Lambda(T) n_{\rm H}^2 Q R {\rm d}R{\rm d}z, \quad (9)$$

respectively. This allows us to isolate the stellar wind material in the bow shock. Additionally, we compute $L_{{\rm H}\,\alpha}$ (blue crosses) and $L_{[{\rm O\,III}]}$ (dark green triangles) which stand for the bow-shock luminosities at H α and at [O III] λ 5007 spectral line emission using the prescriptions for the emission coefficients in Dopita (1973) and Osterbrock & Bochkarev (1989), respectively. The overall X-ray luminosity $L_{\rm X}$ (black right crosses) is computed with emission coefficients generated with the XSPEC program (Arnaud 1996) with solar metallicity and chemical abundances from Asplund et al. (2009). The total infrared emission $L_{\rm IR}$ (red squares) is estimated as a re-emission of a fraction of the starlight bolometric flux on dust grains of gas-to-dust mass ratio 200, which are assumed to be present in the bow shocks. We assume that all dust grains are spherical silicates particles of radius $a = 5.0$ nm only, which are mixed with the gas and continuously penetrate the bow shock as we assume that the star moves with a constant velocity. More details on the dust model and the

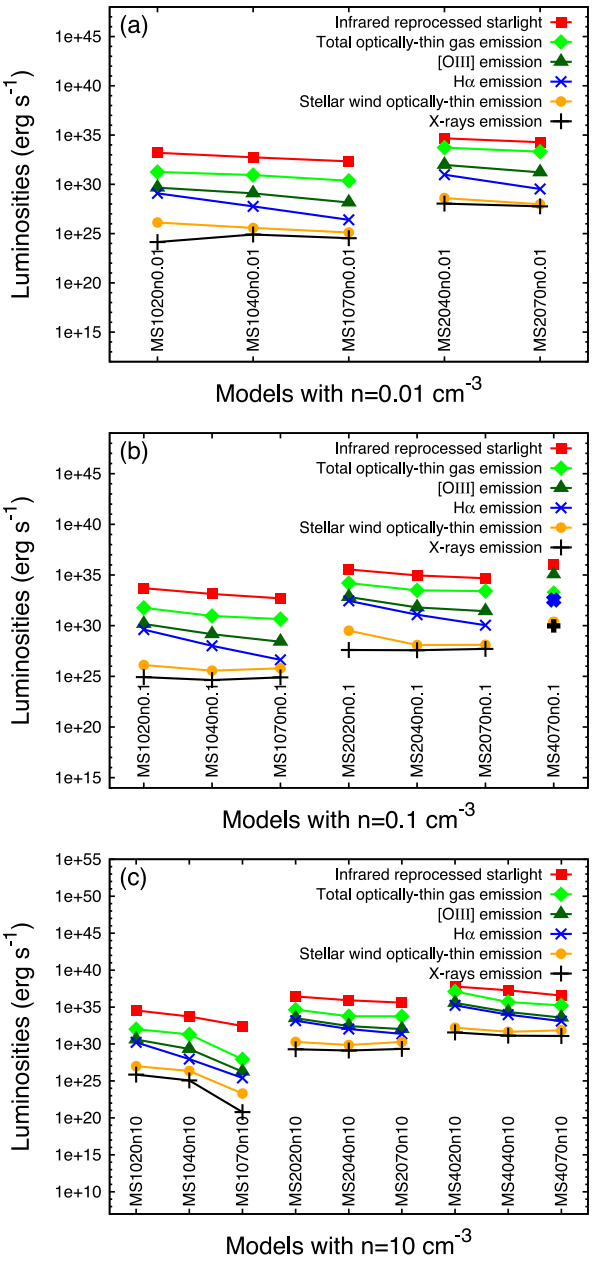

Figure 5. Bow-shocks luminosities. The panels correspond to models with an ISM density $n_{\rm ISM} = 0.01$ (a), 0.1 (b), and 10.0 cm^{-3} (c). The simulations labels are indicated under the corresponding values.

infrared estimate of the bow-shock emission is given in Appendix B of Paper I.

4.2 Results

4.2.1 Optical luminosities

In Fig. 5, we display the bow-shocks luminosities as a function of the initial mass of the runaway star, its space velocity $v_\star$ and its ambient medium density $n_{\rm ISM}$. At a given density of the ISM, all of our models have luminosities from optically thin gas radiation which varies with respect to the stellar mass-loss are as described in Paper I for the simulations with $n_{\rm ISM} \approx 0.79\,{\rm cm}^{-3}$. We can identify three major trends for the behaviour of the luminosity as follows.

(i) The total luminosity $L_{\rm total}$ decreases by at least an order of magnitude between the simulations with $v_\star = 20$ to 70 km s^{-1}. For example, our 10 M$_\odot$ ZAMS star, moving with velocity $v_\star = 20\,{\rm km\,s}^{-1}$ in an ISM of $n_{\rm ISM} \approx 0.01\,{\rm cm}^{-3}$, has $L_{\rm total} \approx 1.82 \times 10^{31}$ erg s^{-1} whereas the same star, moving through the same ISM but with velocity $v_\star = 70\,{\rm km\,s}^{-1}$, has $L_{\rm total} \approx 2.29 \times 10^{30}$ erg s^{-1} (see models MS1020n0.01 and MS1070n0.01 in Fig 5a). This arises because if the space motion of the star increases the compression factor of the shell of shocked ISM gas in the bow shock, it also reduces its volume which decreases the emission by optical-thin radiative processes (Meyer et al. 2014a).

(ii) The total bow-shock luminosity by optically thin processes increases by several orders of magnitude with $\dot{M}$. For example, the bow shock produced by our 10 M$_\odot$ ZAMS star moving with velocity $v_\star = 40\,{\rm km\,s}^{-1}$ in an ISM of $n_{\rm ISM} \approx 0.01\,{\rm cm}^{-3}$ has $L_{\rm total} \approx 8.68 \times 10^{30}$ erg s^{-1} whereas our 20 M$_\odot$ ZAMS star moving with the same speed through an identical medium has $L_{\rm total} \approx 5.38 \times 10^{33}$ erg s^{-1} (see models MS1040n0.01 and MS2040n0.01 in Fig 5a). In that sense, our results confirm that the bow-shock volume which increases with $\dot{M}$ and decreases with $v_\star$ governs their luminosity by optically thin cooling.

(iii) Finally, the bow-shock luminosity decreases if the ambient medium density $n_{\rm ISM}$ increases. This happens because a larger $n_{\rm ISM}$ decreases the volume of the bow shock $\propto R(90)^3$ since $R(90) \propto 1/\sqrt{n_{\rm ISM}}$, which has a stronger influence over the luminosity than the fact that the density in the post-shock region at the forward shock $\propto n_{\rm ISM}/4$ increases. For example, the bow shocks generated by our 20 M$_\odot$ ZAMS star moving with velocity $v_\star = 70\,{\rm km\,s}^{-1}$ in an ISM of density $n_{\rm ISM} = 0.01$, 0.1, 0.79, and 10.0 cm^{-3} have a bow-shock luminosity $L_{\rm total} \approx 2.04 \times 10^{33}$, 2.59×10^{33}, 3.72×10^{33}, and 5.62×10^{33} erg s^{-1} respectively, see models MS2070n0.01, MS2070n0.1, MS2070, and MS2070n10 (Fig. 1a–d). This further illustrates the dominant role of the bow-shock volume on $L_{\rm total}$, which is governed by the compression of the shell and by the strength of its stellar wind momentum, i.e. $\dot{M}$ and $v_{\rm w}$.

The behaviour of the optically thin emission originating from the shocked stellar wind $L_{\rm wind}$, the [O III] λ 5007 spectral line emission and the H α emission at fixed $n_{\rm ISM}$ are similar as described in Meyer et al. (2014a). The contribution of $L_{\rm wind}$ is smaller than $L_{\rm total}$ by several orders of magnitude for all models, e.g. our model MS1020n0.1 has $L_{\rm wind}/L_{\rm total} \approx 10^{-5}$. All our models have $L_{{\rm H}\,\alpha} < L_{[{\rm O\,III}]} < L_{\rm total}$ and the H α emission, the [O III] spectral line emission and $L_{\rm wind}$ have variations which are similar to $L_{\rm ISM}$ with respect to $M_\star$, $v_\star$, and $n_{\rm ISM}$.

Fig. 6, shows the light curve of our model MS4070n10 computed over the whole simulation and plotted as a function of time with the colour-coding from Fig. 5. Very little variations of the emission are present at the beginning of the calculation up to a time of about 0.004 Myr and it remains almost constant at larger times. We infer that in the case of a bow shock producing a thin shell of density larger than about 10 cm^{-3}, the distortions of the global structure are largely irrelevant to the luminosity, which is dominated by the dense, shocked, cold ISM gas (see discussion in 4.3). This is in accordance with the volume of the dense ISM gas trapped into the nebula (see large dotted black line in Fig. 4). The independence of $L_{\rm IR}$ with respect to the strong volume fluctuations of thin-shelled nebulae (Fig. 6) indicates that their spectral energy distributions is

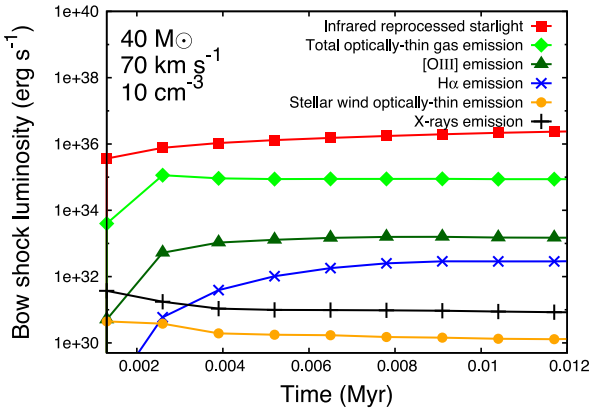

Figure 6. Luminosities of our bow-shock simulation of a 40 $M_\odot$ ZAMS star moving with velocity $v_\star = 70\,\mathrm{km\,s^{-1}}$ through a medium with $n_{\rm ISM} = 10\,\mathrm{cm^{-3}}$ (see corresponding time-sequence evolution of its density field in Fig. 3 a–e). Plotted quantities and colour-coding are similar to Fig. 5 and are shown as function of time (in Myr).

likely to be the appropriate tool to analyse them since it constitutes an observable which is not reliable to temporary effects.

4.2.2 *Infrared and X-rays luminosities*

Not surprisingly, the infrared luminosity, which originates from re-processed starlight on dust grains penetrating the bow shocks, $L_{\rm IR}$, is larger than $L_{\rm total}$ by about one–two orders of magnitude. This is possible because the re-emission of starlight by dust grains is not taken into account in our simulations. Unlike the optical luminosity, the infrared luminosity increases with $n_{\rm ISM}$, e.g. our models with $M_\star = 10\,M_\odot$ and $v_\star = 20\,\mathrm{km\,s^{-1}}$ have $L_{\rm IR} \approx 1.6 \times 10^{33}$, 5.0×10^{33}, 9.92×10^{33}, and $3.43 \times 10^{34}\,\mathrm{erg\,s^{-1}}$ if $n_{\rm ISM} = 0.01$, 0.1, 0.79, and $10.0\,\mathrm{cm^{-3}}$, respectively. Moreover, the ratio between $L_{\rm IR}$ and $L_{\rm total}$ increases with $n_{\rm ISM}$, e.g. $L_{\rm IR}/L_{\rm total} \approx 8.6$ and 144.1 for the models MS2040n0.01 and MS2040n10, respectively. $L_{\rm IR}$ increases with $M_\star$ (Figs. 5a–d). Particularly, we find that $L_{\rm IR} \gg L_{\rm H\alpha}$ and $L_{\rm IR} \gg L_{\rm [O\,III]}$, and therefore we conclude that the infrared waveband is the best way to detect and observe bow shocks from massive main-sequence runaway stars regardless of $n_{\rm ISM}$ (see Section 4.3.1).

Note that, according to the prescription for the dust temperature,

$$T_{\rm d}(r) = T_{\rm eff}\left(\frac{R_\star}{2r}\right)^{\frac{2}{4+s}}, \qquad (10)$$

where $T_{\rm eff}$ is the effective temperature of the moving star, $R_\star$ its radius, and s a parameter giving the slope of the opacity in the infrared regime (Spitzer 1978; Kuiper et al. 2012, and references therein). With $s = 1$ (Decin et al. 2006), it follows that the dust temperature of, e.g. our models with $n_{\rm ISM} = 0.79\,\mathrm{cm^{-3}}$ is about $T_{\rm d} \leq 100\,\mathrm{K}$ in the bow shock. The Planck distribution of such temperatures would peak in the mid-infrared and therefore one can expect that the dust continuum emission of the bow shocks lies in the wavelength range $3 \leq \lambda \leq 50\,\mu\mathrm{m}$. In Fig. 7(a), we compare the bow shocks and the stellar luminosities in this wavelength range, assuming that the 10, 20, and 40 $M_\odot$ ZAMS runaway stars are black bodies. Most of the bow shocks generated by a star of initial mass $\geq 20\,M_\odot$ are brighter in infrared than their central runaway star. This indicates that bow shocks can dominate the emission up to several orders of magnitudes for wavelengths $3 \leq \lambda \leq 50\,\mu\mathrm{m}$ and that saturation effects of the observations are improbable for those stars.

Several current and/or planned facilities are designed to observe at these wavelengths and may be able to detect bow shocks from runaway stars:

(i) First, the *James Webb Space Telescope* which Mid-Infrared Instrument (Swinyard et al. 2004) observes in the infrared (5–28 μm) that roughly corresponds to our predicted waveband of dust continuum emission from stellar wind bow shocks of runaway OB stars.

(ii) Secondly, the *Stratospheric Observatory for Infrared Astronomy* (*SOFIA*) airborne facility which Faint Object infraRed CAmera for the SOFIA Telescope (Adams et al. 2008) instrument detects photons in the 5.4–37 μm waveband.

(iii) Then, the proposed *Space Infrared Telescope for Cosmology and Astrophysics* (Kaneda et al. 2004) satellite would be the ideal tool to observe stellar wind bow shock, since it is planned to be mounted with (i) a far-infrared imaging spectrometer (30–210 μm), (ii) a mid-infrared coronagraph (3.5/5–27 μm), and (iii) a mid-infrared camera/spectrometer (5–38 μm).

(iv) Finally, we should mention the proposed The Mid-infrared E-ELT Imager and Spectrograph on the planned European Extremely Large Telescope (Brandl et al. 2006), that will be able to scan the sky in the 3–19 μm waveband.

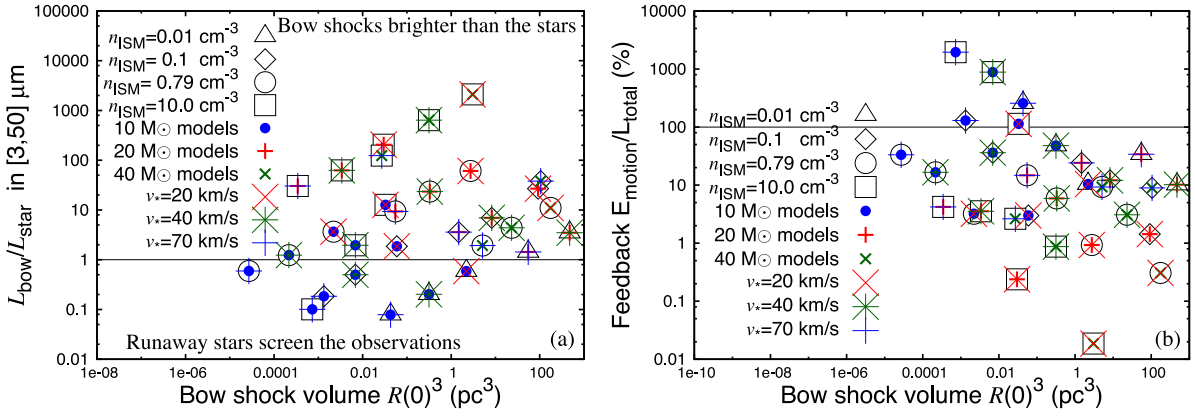

Figure 7. Comparison between the bow-shock luminosity of reprocessed starlight $L_{\rm bow} = L_{\rm IR}$ and the infrared stellar emission $L_\star$, both in the wavelength range [3; 50] μm (a). Ratio (in per cent) of the energy deposited per unit time due to the motion of the bow shock with its losses per unit time because of optically thin cooling (b).

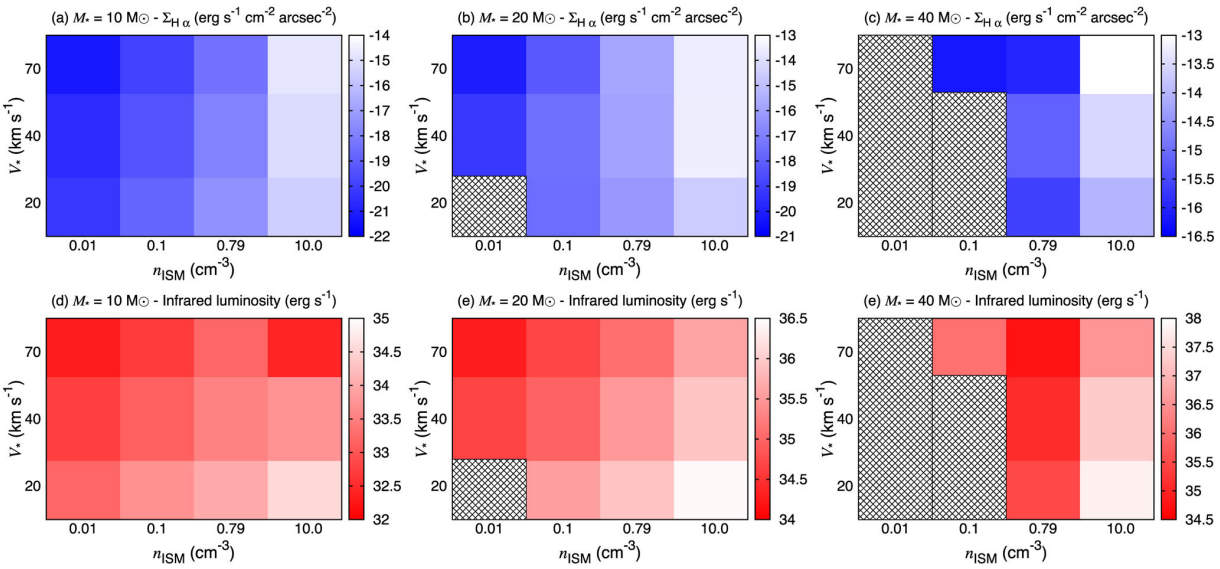

Figure 8. Bow-shock H α surface brightness (in erg s^{-1} cm^{-2} arcsec^{-2}, top blue panels) and infrared reprocessed starlight (in erg s^{-1}, bottom red panels) in the logarithmic scale. We display these quantities for our models with $M_\star = 10\,M_\odot$ (left-hand panels), $20\,M_\odot$ (middle panels), and $40\,M_\odot$ (right-hand panels). The hatched regions indicate that the corresponding bow-shock models are not included in our grid of simulations, since the duration of the main-sequence phase of these stars does not allow us to generate bow shocks in a steady state at these ambient medium density. On each plot, the horizontal axis is the ambient medium density n_{ISM} (in cm^{-3}) and the vertical axis is the space velocity $v_\star$ (in km s^{-1}) of our runaway stars.

Exploitation of the associated archives of these instruments in regions surroundings young stellar clusters and/or at the locations of previously detected bow-like nebulae (van Buren & McCray 1988; van Buren, Noriega-Crespo & Dgani 1995; Noriega-Crespo, van Buren & Dgani 1997a; Peri et al. 2012; Peri et al. 2015) are research avenues to be explored.

Finally, we notice that the X-rays emission are much smaller than any other emission lines or bands, e.g. the model MS2070 has $L_X/L_{H\,\alpha} \approx 10^{-5}$, and it is consequently not a relevant waveband to observe our bow shocks.

4.2.3 Feedback

We compute the energy rate $\dot{E}_{motion}$ deposited to the ISM by the stellar motion. It is estimated by multiplying the rate of volume of ISM swept-up with the bow shock per unit time $\dot{V} \approx \pi R(90)^2 v_\star$ by the ISM kinetic energy density defined as $\epsilon_{ISM} = \rho_{ISM}\Delta v^2/2$, with Δv is the changes in velocity across the shock. In the frame of reference of the moving star $\Delta v = ||v_\star - v_{gas}||$, and,

$$\epsilon_{ISM} = \frac{1}{2}\rho_{ISM}||v_\star - v_{gas}||^2, \quad (11)$$

where v_{gas} is the gas velocity at the post-shock region at the forward shock. Since the Rankine–Hugoniot relation indicates that $v_{gas} \approx v_\star/4$, then the relation $\dot{E}_{motion} = \dot{V}\epsilon_{ISM}$ reduces to,

$$\dot{E}_{motion} = \frac{9}{32}\rho_{ISM} v_\star^3 \pi R(90)^2, \quad (12)$$

where ρ_{ISM} is the ISM gas mass density.

The ratio $\dot{E}_{motion}/L_{total}$ is shown as a function of the bow-shock volume in Fig. 7(b). The simulations with $M_\star \geq 20\,M_\odot$ have a bow shock with $\dot{E}_{motion}/L_{total} \leq 100$ per cent which indicates that their associated nebulae have energy losses by optically thin radiative processes more important than the energy deposition by the stellar motion itself to the replenishing of the ISM. Our $10\,M_\odot$ ZAMS star can produce bow shocks having $\dot{E}_{motion}/L_{total} \gg 100$ per cent. However, since fast-moving $10\,M_\odot$ stars are the most common Galactic runaway stars of our sample (Eldridge, Langer & Tout 2011), it is difficult to estimate which sub-population of runaway massive stars, and by which process, contributes the most to the Galactic feedback. A population synthesis study, beyond the scope of this work, is therefore necessary to assess this question.

4.3 Discussion

4.3.1 The appropriated waveband to observe stellar wind bow shocks in the Galaxy

In Fig. 8, we show the H α surface brightness (in erg s^{-1} cm^{-2} arcsec^{-2}, panels a–c) and the infrared luminosity (in erg s^{-1}, panels d–f) for models with $M_\star = 10\,M_\odot$ (left-hand panels), $20\,M_\odot$ (middle panels), and $40\,M_\odot$ (right-hand panels). The surface brightness $\Sigma^{max}_{H\alpha}$ scales with n^2, see Appendix A of Paper I, therefore the lower the ISM background density of the star, i.e. the higher its Galactic latitude, the fainter the projected emission of the bow shocks and the lower the probability to observe them. The brightest bow shocks are generated both in infrared and H α by our most massive stars running in the denser regions of the ISM ($n_{ISM} = 10.0\,cm^{-3}$). The estimate of the infrared luminosity confirms our earlier result relative to bow-shock models with $n_{ISM} = 0.79\,cm^{-3}$ in the sense that the brightest bow shocks are produced by high-mass stars (Paper I) moving in a relatively dense ambient medium, i.e. within the Galactic plane (Fig. 8 d–f). At H α, these bow shocks are associated to fast-moving stars ($v_\star = 70\,km\,s^{-1}$) producing the strongest shocks, whereas in infrared they are associated to slowly moving stars ($v_\star = 20\,km\,s^{-1}$) generating the largest nebulae.

4.3.2 Synthetic optical emission maps

In Fig. 9, we plot synthetic H α and [O III] λ 5007 emission maps of the bow shocks generated by our 20 $M_\odot$ ZAMS star moving with velocity 70 km s^{-1} moving through a medium with $n_{\rm ISM} = 0.1$ (left column of panels), 0.79 (middle column of panels), and 10.0 cm^{-3} (right column of panels). The region of maximum H α emission of the gas is located close to the apex of the bow shock and extended to its trail ($z \leq 0$). This broadening of the emitting region is due to the high space velocity of the star, see Paper I. Neither the shocked stellar wind nor the hot shocked ISM of the bow shock contributes significantly to these emission since the H α emission coefficient $j_{\rm H\,\alpha} \propto T^{-0.9}$ and the contact discontinuity is the brightest part of the whole structure (Fig. 9a). The [O III] λ 5007 emission is maximum at the same location but, however, slightly different dependence on the temperature of the corresponding emission coefficient $j_{\rm [OIII]} \propto \exp(-1/T)/T^{1/2}$ (Dopita 1973) induces a weaker extension of the emission to the tail of the structure (Fig. 9a). The unstable simulations with $v_\star \geq 40$ km s^{-1} and $n_{\rm ISM} \simeq 10$ cm^{-3} have ring-like artefacts which dominate the emission (see Fig. 9e–h and Fig. 9i–l). They are artificially generated by the overdense regions of the shell that are rotated and mapped on to the Cartesian grid. A tridimensional unstable bow shock would have brighter clumps of matters sparsed around its layer of cold shocked ISM rather than regular rings (Mohamed et al. 2012). Regardless of the properties of their driving star, our bow shocks are brighter in large ambient medium, e.g. the model MS2070n0.1 has $\Sigma^{\rm max}_{\rm [H\,\alpha]} \approx 10^{-18}$ erg s^{-1} cm^{-2} arcsec^{-2} whereas the model MS2070n10 has $\Sigma^{\rm max}_{\rm [H\,\alpha]} \approx 3 \times 10^{-15}$ erg s^{-1} cm^{-2} arcsec^{-2}. The projected [O III] λ 5007 emission behaves similarly.

In Fig. 10, we show cross-sections of the H α surface brightness of the model MS2070n0.1. The cuts are taken along the symmetry axis of the figures and plotted as a function of the inclination angle ϕ with respect to the plane of the sky. The emission rises slightly as ϕ increases from for $\phi = 30^\circ$ (thin red solid line) to $\phi = 60^\circ$ (thick solid orange line) since $\Sigma^{\rm max}_{\rm [H\,\alpha]}$ peaks at about 6×10^{-19} and about 10^{-18} erg s^{-1} cm^{-2} arcsec^{-2}, respectively. The case with $\phi = 90^\circ$ is different since the emission decreases to about $\approx 2 \times 10^{-19}$ erg s^{-1} cm^{-2} arcsec^{-2} (see thick dotted green line in Fig. 10). The same is true for the [O III] emission since its dependence on the post-shock density is similar. These differences arise because a line-of-sight corresponding to $\phi = 60^\circ$ intercepts a larger amount of dense, emitting material in the layer of shocked ISM than a line-of-sight corresponding to $\phi \leq 30^\circ$ or $\phi = 90^\circ$. Large angles of inclination make the opening of the bow shocks larger (Fig. 10a–c, e–g, i–k) and the stand-off distance appears smaller (Fig. 10a–c). Note that bow shocks observed with a viewing angle of $\phi = 90^\circ$ do not resemble an arc-like shape but rather an overlapping of iso-emitting concentric circles (Fig. 10d, h, l).

4.3.3 Bow shocks observability at H α and comparison with observations

In Fig. 11, we show our bow shocks' H α surface brightness (a) and their $\Sigma^{\rm max}_{\rm [O\,III]}/\Sigma^{\rm max}_{\rm [H\,\alpha]}$ ratio (b), both as a function of the volume of emitting gas ($z \geq 0$). The colour coding of both panels takes over the definitions adopted in Fig. 2. The models with a 10 $M_\odot$ ZAMS star have a volume smaller than about a few pc^3 and have emission smaller than about 10^{-15} erg s^{-1} cm^{-2} arcsec^{-2}. The models with $M_\star = 20\,M_\odot$ have larger volume at equal $n_{\rm ISM}$ and can reach surface brightness of about a few 10^{-14} erg s^{-1} cm^{-2} arcsec^{-2} if $n_{\rm ISM} = 10$ cm^{-3}. Note that all models with $n_{\rm ISM} \geq 10.0$ cm^{-3} produce emission larger than the diffuse emission sensitivity threshold of the SuperCOSMOS H-Alpha Survey (SHS) of $\Sigma_{\rm SHS} \approx 1.1$–$2.8 \times 10^{17}$ erg s^{-1} cm^{-2} arcsec^{-2} (Parker et al. 2005) and such bow shocks should consequently be observed by this survey (see horizontal black line in Fig. 11a).

As discussed above, a significant fraction of our sample of bow-shocks models have an H α surface brightness larger than the sensitivity limit of the SHS survey (Parker et al. 2005). This remark can be extended to other (all-sky) H α observations campaigns, especially if their detection threshold is lower than the SHS. This is the case of, e.g. the Virginia Tech Spectral-Line Survey (Dennison, Simonetti & Topasna 1999) and the Wisconsin H-Alpha Mapper (Reynolds et al. 1998) which provide us with images of diffuse sensitivity detection limit that allow the revelation of structures associated with sub-Rayleigh intensity. Consequently, one can expect to find optical traces of stellar wind bow shocks from OB stars in these data. According to our study, their driving stars are more likely to be of initial mass $M_\star \geq 20\,M_\odot$ (Fig. 11a). This also implies that bow shocks *in the field* that are observed with such facilities are necessary produced by runaway stars of initial mass larger than $M_\star \geq 20\,M_\odot$. Moreover, we find that the models involving a 10 $M_\odot$ star and with $v_\star \geq 40$ km s^{-1} have $\Sigma^{\rm max}_{\rm [O\,III]}/\Sigma^{\rm max}_{\rm [H\,\alpha]} > 10$, whereas almost all of the other simulations do not satisfy this criterion (Fig. 11b).

Furthermore, we find a similarity between some of the cross-sections taken along the symmetry axis of the H α surface brightness of our bow-shock models (Fig. 10) and the measure of the radial brightness in emission measure of the bow shock generated by the runaway O star HD 57061 (see fig. 5 of Brown & Bomans 2005). This observable and our model authorize a comparison since H α emission and emission measures have the same quadratic dependence on the gas number density. The emission measure profile of HD 57061 slightly increases from the star to the bow shock and steeply peaks in the region close to the contact discontinuity, before to decrease close to the forward shock of the bow shock and reach the ISM background emission. Our H α profile with $\phi = 60^\circ$ is consistent with (i) the above described variations and (ii) with the estimate of the inclination of the symmetry axis of HD 57061 with respect to the plane of the sky of about 75°, see table 3 of Brown & Bomans (2005). Note that according to our simulations, the emission peaks in the region separating the hot from the cold shocked ISM gas.

Brown & Bomans (2005) extracted a subset of eight bow shocks at H α from the catalogue compiled by van Buren et al. (1995). The bow shocks of the stars HD149757 and HD158186 do not match any of our models. The O6.5V star HD17505 moving in a medium with $n_{\rm ISM} \approx 21$ cm^{-3} is also incompatible with the space of parameter covered by our study. The circumstellar nebulae of HD92206 [$R(0) \approx 3.67$ pc, $n_{\rm ISM} \approx 0.007$ cm^{-3}, $v_\star \approx 40.5$ km s^{-1}] and HD135240 [$R(0) \approx 3.50$ pc, $n_{\rm ISM} \approx 0.21$ cm^{-3}, $v_\star \approx 32.5$ km s^{-1}] have some of their properties similar to our models MS2040n0.01/MS2070n0.01 [$R(0) \approx 7.80$–3.80 pc, $n_{\rm ISM} = 0.01$ cm^{-3}, $v_\star = 40$–70 km s^{-1}] and MS2020n0.1/MS2040n0.1 [$R(0) \approx 3.51$–2.02 pc, $n_{\rm ISM} = 0.1$ cm^{-3}, $v_\star = 20$–40 km s^{-1}] but do not properly fit them. The bow shock of HD57061 [$R(0) \approx 7.56$ pc, $n_{\rm ISM} \approx 0.07$ cm^{-3}, $v_\star \approx 55.8$ km s^{-1}] matches particularly our model MS2040 with $R(0) \approx 7.8$ pc, $n_{\rm ISM} = 0.01$ cm^{-3} and $v_\star = 40$ km s^{-1}, and therefore constitute a good candidate for future tailored numerical simulations. More detailed simulations and subsequent post-processing of the corresponding data, e.g. including the effects of the extinction of the ISM on the infrared emission are necessary for a more detailed discussion of these results.

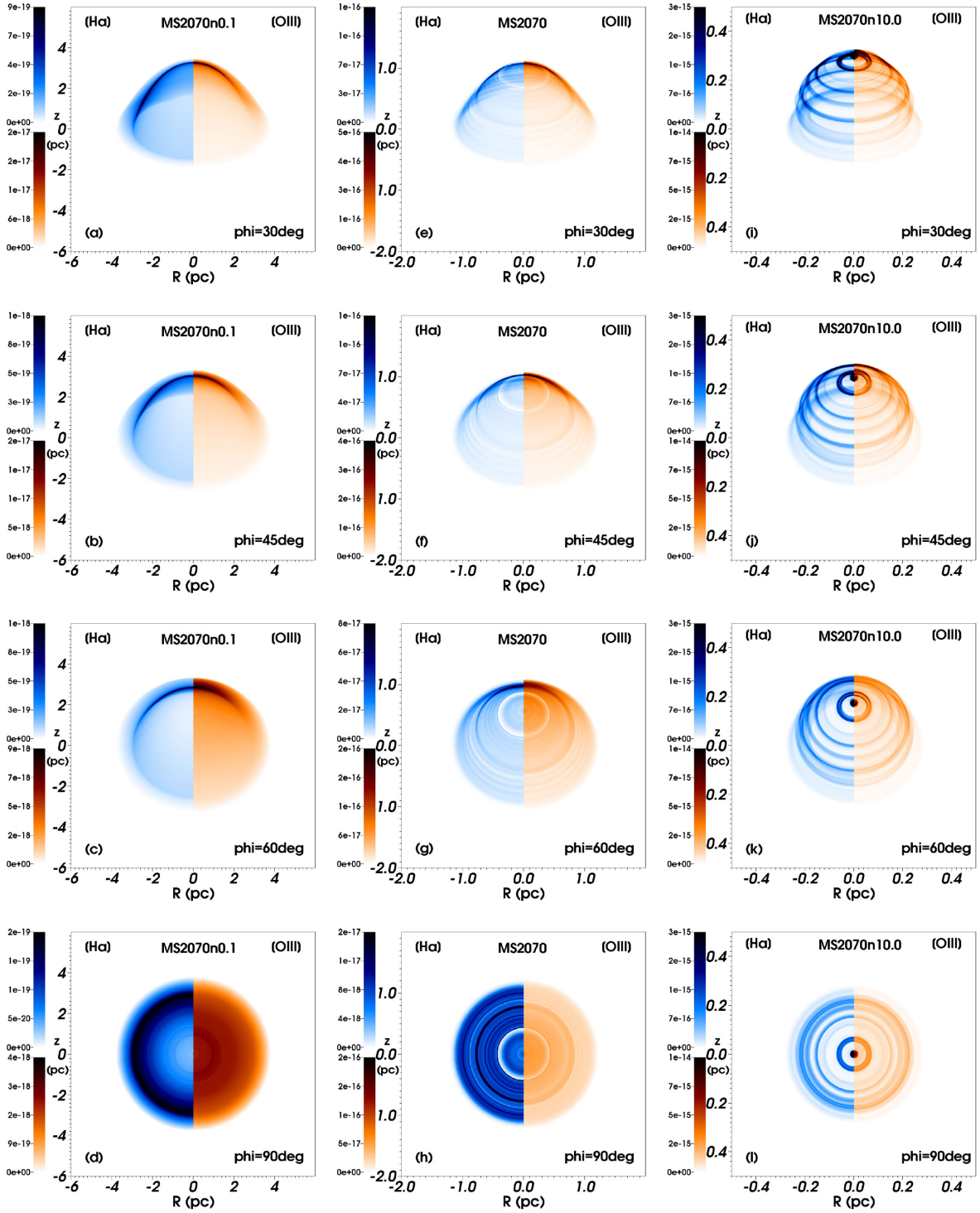

Figure 9. H α surface brightness (left, in erg s^{-1} cm^{-2} arcsec^{-2}) and projected [O III] λ 5007 spectral line emission (right, in erg s^{-1} cm^{-2} arcsec^{-2}) of the bow shocks generated by a 20 M$_\odot$ ZAMS star moving with velocity $v_\star = 70$ km s^{-1} through in a medium with $n_{\rm ISM} = 0.1$ (left column of panels a–d), 0.79 (middle column of panels e–h) and 10 cm^{-3} (right column of panels i–l). The figures correspond to an inclination angle $\phi = 30^\circ$ (top line of panels a,e,i), $\phi = 45^\circ$ (second line of panels b,f,j), $\phi = 60^\circ$ (third line of panels c,g,k), and $\phi = 90^\circ$ (bottom line of panels d,h,l) with respect to the plane of the sky. Quantities are calculated excluding the undisturbed ISM and plotted in the linear scale, as a function of the inclination angle and the ambient medium density.

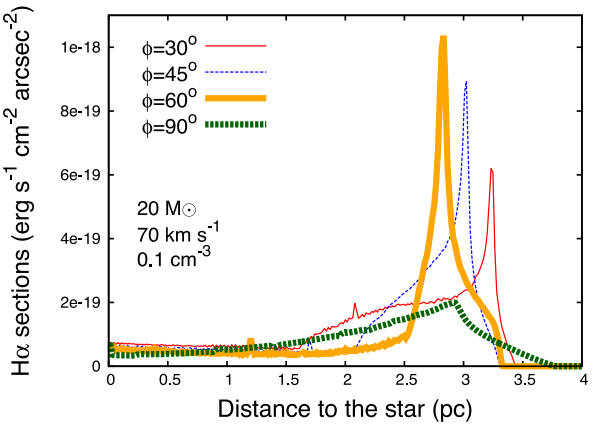

Figure 10. Cross-sections taken along the direction of motion of our 20 $M_\odot$ ZAMS star moving with velocity 70 km s^{-1} in an ambient medium of number density $n_{\rm ISM} = 0.1$ cm^{-3}. The data are plotted for inclination angles $\phi = 30°$ (thin solid red line), $\phi = 45°$ (thin dotted blue line), $\phi = 60°$ (thick solid orange line), and $\phi = 90°$ (thick dotted dark green line) through their H α surface brightness (see Fig. 9 a–d). The position of the star is located at the origin.

4.3.4 *Implication for the evolution of supernova remnants generated by massive runaway stars*

Massive stars evolve and die as supernovae, a sudden and strong release of matter, energy, and momentum taking place inside the ISM pre-shaped by their past stellar evolution (Langer 2012). In the case of a runaway progenitor, the circumstellar medium at the pre-supernova phase can be a bow-shock nebula with which the shock wave interacts before expanding further into the unperturbed ISM (Brighenti & D'Ercole 1994). The subsequent growing supernova remnant develops asymmetries since it is braked by the mass at the apex of the bow shock but expands freely in the cavity driven by the star in the opposite direction (Borkowski, Blondin & Sarazin 1992). If the progenitor is slightly supersonic, the bow shock is mainly shaped during the main-sequence phase of the star; whereas if the progenitor is a fast-moving star then the bow shock is essentially made of material from the last pre-supernova evolutionary phase. In the Galactic plane ($n_{\rm ISM} = 0.79$ cm^{-3}), such asymmetries arise if the apex of the bow shock accumulates at least 1.5 $M_\odot$ of shocked material (Meyer et al. 2015).

In Fig. 12, we present the mass trapped into the $z \geq 0$ region of our bow-shock models as a function of their volume. As in Fig. 11, the figure distinguishes the initial mass and the ambient medium density of each models. Amongst our bow-shock simulations, nine models have $M_{\rm bow} \gtrsim 1.5\,M_\odot$ and four of them are generated by the runaway stars which asymmetric supernova remnant studied in detail in Meyer et al. (2015). The other models with $v_\star \leq 40$ km s^{-1} may produce asymmetric remnants because they will explode inside their main-sequence wind bubble. The model MS4070n0.1 has $v_\star = 70$ km s^{-1} which indicates that the main-sequence bow shock will be advected downstream by the rapid stellar motion and the surroundings of the progenitor at the pre-supernova phase is made of, e.g. red supergiant material. Consequently, its shock wave may be unaffected by the presence of the circumstellar medium. We leave the examination via hydrodynamical simulations of this conjecture for future works. Interestingly, we notice that most of the potential progenitors of asymmetric supernova remnants are moving in a

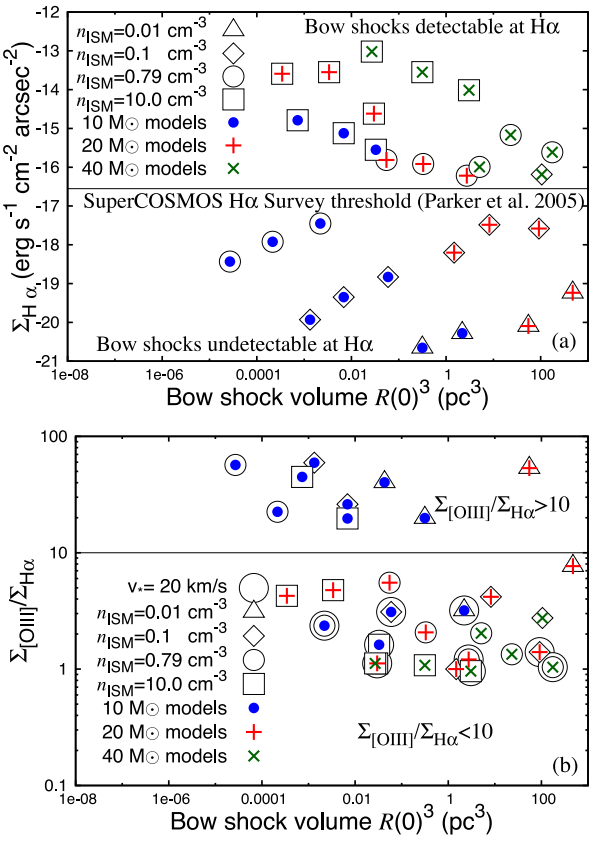

Figure 11. Bow-shock H α surface brightness (a) and ratio $\Sigma^{\rm max}_{[\rm O\,III]}/\Sigma^{\rm max}_{[\rm H\alpha]}$ (b) as a function of its volume $R(0)^3$ (in pc^3). Upper panel shows the H α surface brightness as a function of the detection threshold of the SHS of $\Sigma_{\rm SHS} \approx 1.1{-}2.8 \times 10^{-17}$ erg s^{-1} cm^{-2} arcsec^{-2} (Parker et al. 2005). Lower panel plots the ratio $\Sigma^{\rm max}_{[\rm O\,III]}/\Sigma^{\rm max}_{[\rm H\alpha]}$ of the same models.

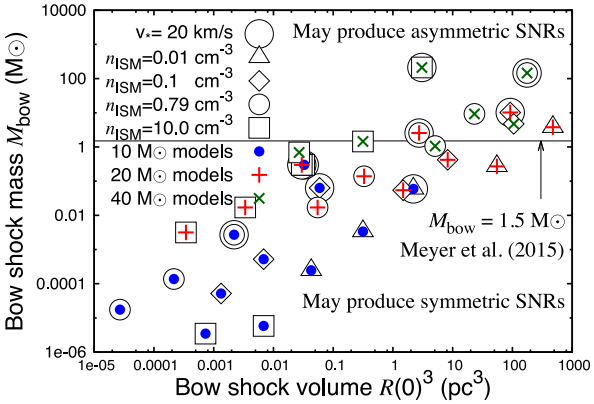

Figure 12. Bow-shocks mass as a function of the bow-shock volume. The figure shows the mass $M_{\rm bow}$ (in $M_\odot$) trapped in the $z \geq 0$ region of the bow shock as a function of its volume $R(0)^3$ (in pc^3). The dots distinguish between models (i) as a function of the ISM ambient medium with $n_{\rm ISM} = 0.01$ (triangles), 0.1 (diamonds), 0.79 (circles), and 10 cm^{-3} (squares), and (ii) as a function of the initial mass of the star with 10 (blue dots), 20 (red plus signs), and 40 $M_\odot$ (green crosses). The thin horizontal black line corresponds to $M_{\rm bow} = 1.5\,M_\odot$, i.e. the condition to produce an asymmetric supernova remnant if $n_{\rm ISM} = 0.79$ cm^{-3} (Meyer et al. 2015).

low-density medium $n_{\rm ISM} \leq 0.1\,{\rm cm}^{-3}$, i. e. in the rather high-latitude regions of the Milky Way. This is consistent with the interpretation of the elongated shape of, e.g. Kepler's supernova remnant as the consequence of the presence of a massive bow shock at the time of the explosion (Velázquez et al. 2006; Toledo-Roy et al. 2014).

4.3.5 The influence of the interstellar magnetic field on the shape of supernovae remnants

An alternative explanation for the asymmetrical shape of supernova remnants can be found in the influence of the interstellar magnetic field. Although the interstellar magnetic field does not influence the shape of an expanding supernova blast wave directly (Manchester 1987), it can influence the shape and size of the wind-blown bubble, as suggested by Arnal (1992) and shown numerically by van Marle, Meliani & Marcowith (2015). Such magnetic fields slow the expansion of the wind-blown bubble in the direction perpendicular to the direction of the field and, depending on the field strength can stop the expansion in that direction completely. The end result is an elongated, ellipsoid bubble, which in turn, would influence the expansion of the supernova remnant.

As shown by van Marle et al. (2015), the interstellar magnetic field would have to be fairly strong (beyond about 20 μG) to enable it to constrain the wind-bubble sufficiently that the scale of the bubble would be reduced to that of a bow shock. However, such field strengths are not unreasonable as field strengths of up to 60 μG, have been observed in the galactic core (Rand & Kulkarni 1989; Ohno & Shibata 1993; Frick et al. 2001; Opher et al. 2009; Shabala, Mead & Alexander 2010; Fletcher et al. 2011; Heerikhuisen & Pogorelov 2011; Vallée 2011) and fields that are stronger than that by an order of magnitude can be found inside molecular clouds (Crutcher et al. 1999).

There are two tests that can be used to distinguish whether the bubble into which a supernova remnant expands has been constrained by stellar motion, or by an interstellar magnetic field. One: the magnetic field in the galaxy tends to be aligned with the spiral arms. Gaensler (1998) showed that supernova remnants tend to be aligned with the galactic disc. This would seem to support the theory that it is the magnetic field, rather than a bow shock, that constrained the wind expansion. However, the correlation is not very strong. Two: the shape of the supernova remnant itself. van Marle et al. (2015) showed that a supernova remnant, expanding inside a magnetically constrained bubble, first collides with the outer edge along the minor axis of the ellipsoid bubble, while, in the direction along the major axis the expansion can continue uninterrupted. This produces a barrel-like supernova remnant. When expanding inside a bow shock, the collision would first occur at the front of the bow shock, creating a parabolic shape with free expansion only possible along the tail of the bow shock.

5 CONCLUSION

Our bow-shock simulations indicate that no structural difference arise when changing the density of the background ISM in which the stars move, i.e. their internal organization is similar as described in Comerón & Kaper (1998) and Paper I. The same is true for their radiative properties, governed by line cooling such as the [O III] λ 5007 line and showing faint H α emission, both principally originating from outer region of shocked ISM gas. We also find that their X-rays signature is fainter by several orders of magnitude than their H α emission, and, consequently, it is not a good waveband to search for such structures.

The best way to observe bow shocks remains their infrared emission of starlight reprocessed by shocked ISM dust (Meyer et al. 2014a). We find that the brightest infrared bow shocks, i.e. the most easily observable ones, are produced by high-mass ($M_\star \approx 40\,{\rm M}_\odot$) stars moving with a slow velocity ($v_\star \approx 20\,{\rm km\,s}^{-1}$) in the relatively dense regions ($n_{\rm ISM} \approx 10\,{\rm cm}^{-3}$) of the ISM, whereas the brightest H α structures are produced by these stars when moving rapidly ($v_\star \approx 70\,{\rm km\,s}^{-1}$). Thin-shelled bow shocks have mid-infrared luminosities which does not report the time-variations of their unstable structures. This indicates that spectral energy distributions of stellar wind bow shocks are the appropriate tool to analyse them since they do not depend on the temporary effects that affect their density field. We find that bow shocks from Galactic runaway stars have emission peaking in the wavelength range $3 \leq \lambda \leq 50\,\mu{\rm m}$. Interestingly, the circumstellar material can be up to several orders of magnitude brighter than the star and dominates the emission, especially if $M_\star \geq 20\,{\rm M}_\odot$.

A detailed analysis of our grid of simulations indicates that the H α surface brightness of Galactic stellar wind bow shocks increases if their angle of inclination with respect to the plane of the sky increases up to $\phi = 60^\circ$, however, edge-on viewed bow shocks are particularly faint. We find that all bow shocks generated by a $40\,{\rm M}_\odot$ ZAMS runaway star could be observed with Rayleigh-sensitive H α facilities and that bow shocks observed *in the field* by means of these facilities should have an initial mass larger than about $20\,{\rm M}_\odot$. Furthermore, all of our bow shocks generated by a $10\,{\rm M}_\odot$ ZAMS star moving with $v_\star \geq 40\,{\rm km\,s}^{-1}$ have a line ratio $\Sigma^{\rm max}_{\rm [O\,III]}/\Sigma^{\rm max}_{\rm [H\alpha]} > 10$. Our study suggests that slowly moving stars of ZAMS mass $M_\star \geq 20\,{\rm M}_\odot$ moving in a medium of $n_{\rm ISM} \geq 0.1\,{\rm cm}^{-3}$ generate massive bow shocks, i.e. are susceptible to induce asymmetries in their subsequent supernova shock wave. This study will be enlarged, e.g. estimating observability of red supergiant stars.

ACKNOWLEDGEMENTS

We thank the anonymous referee for numerous comments which greatly improved both the quality and the presentation of the paper. DMAM thanks P. F. Velazquez, F. Brighenti and L. Kaper for their advices, and F. P. Wilkin for useful comments on stellar wind bow shocks which partly motivated this work. This study was conducted within the Emmy Noether research group on 'Accretion Flows and Feedback in Realistic Models of Massive Star Formation' funded by the German Research Foundation under grant no. KU 2849/3-1. AJVM acknowledges support from FWO, grant G.0227.08, KU Leuven GOA/2008, 04 and GOA/2009/09. The authors gratefully acknowledge the computing time granted by the John von Neumann Institute for Computing (NIC) and provided on the supercomputer JUROPA at Jülich Supercomputing Centre (JSC).

REFERENCES

Adams J. D., Dekker H., 2008, in McLean I. S., Casali M. M., eds, Proc. SPIE Conf. Ser. Vol. 7014, Ground-based and Airborne Instrumentation for Astronomy II. SPIE, Bellingham, p. 70141R
Arnal E. M., 1992, A&A, 254, 305
Arnaud K. A., 1996, in Jacoby G. H., Barnes J., eds, ASP Conf. Ser. Vol. 101, Astronomical Data Analysis Software and Systems V. Astron. Soc. Pac., San Francisco, p. 17
Asplund M., Grevesse N., Sauval A. J., Scott P., 2009, ARA&A, 47, 481
Blaauw A., 1961, Bull. Astron. Inst. Neth., 15, 265

Blondin J. M., Koerwer J. F., 1998, New Astron., 3, 571
Borkowski K. J., Blondin J. M., Sarazin C. L., 1992, ApJ, 400, 222
Brandl B., Lenzen R., Venema L., Käufl H.-U., Finger G., Glasse A., Brandner W., Stuik R., 2006, in McLean I. S., Iye M., eds, Proc. SPIE Conf. Ser. Vol. 6269, Ground-based and Airborne Instrumentation for Astronomy. SPIE, Bellingham, p. 626920
Brighenti F., D'Ercole A., 1994, MNRAS, 270, 65
Brighenti F., D'Ercole A., 1995, MNRAS, 277, 53
Brott I. et al., 2011, A&A, 530, A115
Brown D., Bomans D. J., 2005, A&A, 439, 183
Comerón F., Kaper L., 1998, A&A, 338, 273
Comerón F., Pasquali A., 2007, A&A, 467, L23
Cowie L. L., McKee C. F., 1977, ApJ, 211, 135
Crutcher R. M., Roberts D. A., Troland T. H., Goss W. M., 1999, ApJ, 515, 275
de Jager C., Nieuwenhuijzen H., van der Hucht K. A., 1988, A&AS, 72, 259
Decin L., Hony S., de Koter A., Justtanont K., Tielens A. G. G. M., Waters L. B. F. M., 2006, A&A, 456, 549
Dennison B., Simonetti J. H., Topasna G. A., 1999, Bull. Am. Astron. Soc., 31, 1455
Diaz-Miller R. I., Franco J., Shore S. N., 1998, ApJ, 501, 192
Dopita M. A., 1973, A&A, 29, 387
Dyson J. E., 1975, Ap&SS, 35, 299
Eldridge J. J., Langer N., Tout C. A., 2011, MNRAS, 414, 3501
Fletcher A., Beck R., Shukurov A., Berkhuijsen E. M., Horellou C., 2011, MNRAS, 412, 2396
Frick P., Stepanov R., Shukurov A., Sokoloff D., 2001, MNRAS, 325, 649
Gaensler B. M., 1998, ApJ, 493, 781
Garcia-Segura G., Mac Low M.-M., Langer N., 1996, A&A, 305, 229
Gull T. R., Sofia S., 1979, ApJ, 230, 782
Gvaramadze V. V., Bomans D. J., 2008, A&A, 490, 1071
Heerikhuisen J., Pogorelov N. V., 2011, ApJ, 738, 29
Heger A., Woosley S. E., Spruit H. C., 2005, ApJ, 626, 350
Henney W. J., Arthur S. J., de Colle F., Mellema G., 2009, MNRAS, 398, 157
Holzer T. E., Axford W. I., 1970, ARA&A, 8, 31
Hoogerwerf R., de Bruijne J. H. J., de Zeeuw P. T., 2001, A&A, 365, 49
Hummer D. G., 1994, MNRAS, 268, 109
Huthoff F., Kaper L., 2002, A&A, 383, 999
Kaneda H. et al., 2004, in Mather J. C., ed., Proc. SPIE Conf. Ser. Vol. 5487, Optical, Infrared, and Millimeter Space Telescopes. SPIE, Bellingham, p. 991
Kaper L., van Loon J. T., Augusteijn T., Goudfrooij P., Patat F., Waters L. B. F. M., Zijlstra A. A., 1997, ApJ, 475, L37
Kudritzki R. P., Pauldrach A., Puls J., Abbott D. C., 1989, A&A, 219, 205
Kuiper R., Klahr H., Beuther H., Henning T., 2012, A&A, 537, A122
Langer N., 2012, ARA&A, 50, 107
Manchester R. N., 1987, A&A, 171, 205
Meyer D. M.-A., Gvaramadze V. V., Langer N., Mackey J., Boumis P., Mohamed S., 2014a, MNRAS, 439, L41
Meyer D. M.-A., Mackey J., Langer N., Gvaramadze V. V., Mignone A., Izzard R. G., Kaper L., 2014b, MNRAS, 444, 2754 (Paper I)
Meyer D. M.-A., Langer N., Mackey J., Velázquez P. F., Gusdorf A., 2015, MNRAS, 450, 3080
Mignone A., Bodo G., Massaglia S., Matsakos T., Tesileanu O., Zanni C., Ferrari A., 2007, ApJS, 170, 228
Mignone A., Zanni C., Tzeferacos P., van Straalen B., Colella P., Bodo G., 2012, ApJS, 198, 7
Mohamed S., Mackey J., Langer N., 2012, A&A, 541, A1
Neugebauer G. et al., 1984, ApJ, 278, L1
Noriega-Crespo A., van Buren D., Dgani R., 1997a, AJ, 113, 780
Noriega-Crespo A., van Buren D., Cao Y., Dgani R., 1997b, AJ, 114, 837
Ohno H., Shibata S., 1993, MNRAS, 262, 953
Opher M., Bibi F. A., Toth G., Richardson J. D., Izmodenov V. V., Gombosi T. I., 2009, Nature, 462, 1036
Osterbrock D. E., Bochkarev N. G., 1989, Sov. Astron., 33, 694
MacGillivrayParker Q. A., Phillipps S., Pierce M. J., Hartley M., Hambly N. C., Read M. A., 2005, MNRAS, 362, 689
Peri C. S., Benaglia P., Brookes D. P., Stevens I. R., Isequilla N. L., 2012, A&A, 538, A108
Peri C. S., Benaglia P., Isequilla N. L., 2015, A&A, 578, A45
Peters T., Banerjee R., Klessen R. S., Mac Low M.-M., Galván-Madrid R., Keto E. R., 2010, ApJ, 711, 1017
Petrovic J., Langer N., Yoon S.-C., Heger A., 2005, A&A, 435, 247
Petrovic J., Pols O., Langer N., 2006, A&A, 450, 219
Rand R. J., Kulkarni S. R., 1989, ApJ, 343, 760
Reynolds R. J., Tufte S. L., Haffner L. M., Jaehnig K., Percival J. W., 1998, PASA, 15, 14
Rozyczka M., Tenorio-Tagle G., Franco J., Bodenheimer P., 1993, MNRAS, 261, 674
Shabala S. S., Mead J. M. G., Alexander P., 2010, MNRAS, 405, 1960
Spitzer L., 1962, Physics of Fully Ionized Gases, 2nd edn. Interscience, New York
Spitzer L., 1978, Physical processes in the interstellar medium. Wiley-Interscience, New York
Swinyard B. M., Rieke G. H., Ressler M., Glasse A., Wright G. S., Ferlet M., Wells M., 2004, in Mather J. C., ed., Proc. SPIE Conf. Ser. Vol. 5487, Optical, Infrared, and Millimeter Space Telescopes. SPIE, Bellingham, p. 785
Thun D., Kuiper R., Schmidt F., Kley W., 2016, preprint (arXiv:1601.07799)
Toledo-Roy J. C., Esquivel A., Velázquez P. F., Reynoso E. M., 2014, MNRAS, 442, 229
Vallée J. P., 2011, New Astron. Rev., 55, 23
van Buren D., McCray R., 1988, ApJ, 329, L93
van Buren D., Noriega-Crespo A., Dgani R., 1995, AJ, 110, 2914
van Marle A. J., Langer N., García-Segura G., 2007, A&A, 469, 941
van Marle A. J., Meliani Z., Keppens R., Decin L., 2011, ApJ, 734, L26
van Marle A. J., Decin L., Meliani Z., 2014, A&A, 561, A152
van Marle A. J., Meliani Z., Marcowith A., 2015, A&A, 584, A49
van Veelen B., 2010, PhD thesis, Utrecht University, Netherland
Velázquez P. F., Vigh C. D., Reynoso E. M., Gómez D. O., Schneiter E. M., 2006, ApJ, 649, 779
Villaver E., Manchado A., García-Segura G., 2012, ApJ, 748, 94
Vishniac E. T., 1994, ApJ, 428, 186
Weaver R., McCray R., Castor J., Shapiro P., Moore R., 1977, ApJ, 218, 377
Wiersma R. P. C., Schaye J., Smith B. D., 2009, MNRAS, 393, 99
Wilkin F. P., 1996, ApJ, 459, L31
Woosley S. E., Heger A., Weaver T. A., 2002, Rev. Mod. Phys., 74, 1015
Wright E. L. et al., 2010, AJ, 140, 1868
Yoon S.-C., Langer N., 2005, A&A, 443, 643

This paper has been typeset from a TEX/LATEX file prepared by the author.

Monthly Notices
of the
ROYAL ASTRONOMICAL SOCIETY

MNRAS **464,** 3229–3248 (2017)
Advance Access publication 2016 October 5

doi:10.1093/mnras/stw2537

Bow shock nebulae of hot massive stars in a magnetized medium

D. M.-A. Meyer,[1]★ A. Mignone,[2] R. Kuiper,[1] A. C. Raga[3] and W. Kley[1]

[1]*Institut für Astronomie und Astrophysik, Universität Tübingen, Auf der Morgenstelle 10, D-72076 Tübingen, Germany*
[2]*Dipartimento di Fisica Generale Facoltà di Scienze M.F.N., Università degli Studi di Torino, Via Pietro Giuria 1, I-10125 Torino, Italy*
[3]*Instituto de Ciencias Nucleares, Universidad Nacional Autónoma de México, Ap. 70-543, 04510 D.F., México*

Accepted 2016 October 2. Received 2016 October 2; in original form 2015 September 30

ABSTRACT

A significant fraction of OB-type, main-sequence massive stars are classified as *runaway* and move supersonically through the interstellar medium (ISM). Their strong stellar winds interact with their surroundings, where the typical strength of the local ISM magnetic field is about 3.5–7 μG, which can result in the formation of bow shock nebulae. We investigate the effects of such magnetic fields, aligned with the motion of the flow, on the formation and emission properties of these circumstellar structures. Our axisymmetric, magneto-hydrodynamical simulations with optically thin radiative cooling, heating and anisotropic thermal conduction show that the presence of the background ISM magnetic field affects the projected optical emission of our bow shocks at Hα and [O III] λ 5007 which become fainter by about 1–2 orders of magnitude, respectively. Radiative transfer calculations against dust opacity indicate that the magnetic field slightly diminishes their projected infrared emission and that our bow shocks emit brightly at 60 μm. This may explain why the bow shocks generated by ionizing runaway massive stars are often difficult to identify. Finally, we discuss our results in the context of the bow shock of ζ Ophiuchi and we support the interpretation of its imperfect morphology as an evidence of the presence of an ISM magnetic field not aligned with the motion of its driving star.

Key words: MHD – methods: numerical – circumstellar matter – stars: massive.

1 INTRODUCTION

Massive star formation is a rare event that strongly impacts the whole Galactic machinery. These stars can release strong winds and ionizing radiation which shape their close surroundings into beautiful billows of swept-up and irradiated interstellar gas, which , in the case of a static or a slowly moving star, can produce structures such as the Bubble Nebula (NGC 7635) in the constellation of Orion (Moore et al. 2002). The detailed study of the circumstellar medium of these massive stars provides us an insight into their internal physics (Langer 2012); it provides information on their intrinsic rotation (Langer, García-Segura & Mac Low 1999), their envelope's (in)stability (Yoon & Cantiello 2010) and allows us to understand the properties of their close surroundings throughout their evolution (van Marle et al. 2006; Chita et al. 2008) and after their death (Orlando et al. 2008; Chiotellis, Schure & Vink 2012). This information is relevant for evaluating their feedback, i.e. the amount of energy, momentum and metals that massive stars inject into the interstellar medium (ISM) of the Galaxy (Vink 2006).

In particular, the bow shocks that develop around some fast-moving massive stars ejected from their parent stellar clusters provide an opportunity to constrain both their wind and local ISM properties (Huthoff & Kaper 2002; Meyer et al. 2014a). Over the past decades, stellar wind bow shocks have first been serendipitously noticed as bright [O III] λ 5007 spectral line arc-like shapes and/or distorted bubbles surrounding some massive stars having a particularly large space velocity with respect to their ambient medium. As a textbook example of such a bow shock, we refer the reader, e.g. to ζ Ophiuchi (Gull & Sofia 1979, see Fig. 13 below). Further infrared observations, e.g. with the *Infrared Astronomical Satellite* (*IRAS*; Neugebauer et al. 1984) and the *Wide-Field Infrared Satellite Explorer* (*WISE*; Wright et al. 2010) facilities have made possible the compilation of catalogues of dozens of these bow shock nebulae (van Buren & McCray 1988a; van Buren, Noriega-Crespo & Dgani 1995; Noriega-Crespo, van Buren & Dgani 1997a) and have motivated early numerical simulations devoted to the parsec-scale circumstellar medium of moving stars (Brighenti & D'Ercole 1995a,b). Recently, modern facilities led to the construction of multi-wavelengths data bases, see e.g. the E-BOSS catalogue (Peri et al. 2012; Peri, Benaglia & Isequilla 2015) or the recent study of Kobulnicky et al. (2016). Moreover, a connection with high-energy astrophysics has been established, showing that stellar wind bow shocks produce cosmic rays in the same way as the expanding shock waves of growing supernova remnants do (del Valle, Romero & Santos-Lima 2015).

★ E-mail: dominique.meyer@uni-tuebingen.de

It is the discovery of bow shocks around the historical stars Betelgeuse (Noriega-Crespo et al. 1997b) and Vela-X1 (Kaper et al. 1997) that revived the interest of the scientific community regarding such circumstellar structures generated by massive stars. The fundamental study of Comerón & Kaper (1998) demonstrates that complex morphologies can arise from massive stars' wind–ISM interactions. Bow shocks are subject to a wide range of shear-like and non-linear instabilities (Blondin & Koerwer 1998) producing severe distortions of their overall forms, which can only be analytically approximated (Wilkin 1996) in the particular situations of either a star moving in a relatively dense ISM (Comerón & Kaper 1998) or a high-mass star hypersonically moving through the Galactic plane (Meyer et al. 2014b, hereafter Paper I). Tailoring numerical models to runaway red supergiant stars allows us to constrain the mass loss and local ISM properties of Betelgeuse (van Marle et al. 2011; Cox et al. 2012; Mackey et al. 2012) or IRC-10414 (Gvaramadze et al. 2014; Meyer et al. 2014a). For the sake of simplicity, these models neglect the magnetization of the ISM.

However, magnetic fields are an essential component of the ISM of the Galaxy, e.g. its large-scale component has a tendency to be aligned with the galactic spiral arms (Gaensler 1998). If the strength of the ISM magnetic field can reach up to several tenths of Gauss in the centre of our Galaxy (see Rand & Kulkarni 1989; Ohno & Shibata 1993; Opher et al. 2009; Shabala, Mead & Alexander 2010), it can be even stronger in the cold phase of the ISM (Crutcher et al. 1999). In particular, radio polarization measures of the magnetic field in the context of Galactic ionized supershells are reported to be 2–6 μG in Harvey-Smith, Madsen & Gaensler (2011). This value is in accordance with previous estimates of the field strength in the warm phase of the ISM (Troland & Heiles 1986) and was supported by hydrodynamical (HD) simulations (Fiedler & Mouschovias 1993). Such a background magnetic field should therefore be included in realistic models of circumstellar nebulae around massive stars.

Numerical studies of magneto-hydrodynamical (MHD) flows around an obstacle are approximated in the plane-parallel approach in de Sterck, Low & Poedts (1998) and de Sterck & Poedts (1999). A significant number of circumstellar structures, such as the vicinity of our Sun (Pogorelov & Semenov 1997), planetary nebulae developing in the vicinity of intermediate-mass stars (Heiligman 1980) or supernova remnants (Rozyczka & Tenorio-Tagle 1995), have been studied in such a two-dimensional approach (see also Soker & Dgani 1997; Pogorelov & Matsuda 2000). The presence of a weak magnetic field can inhibit the growth rate of shear instabilities in the bow shocks around cool stars such as the runaway red supergiant Betelgeuse in the constellation of Orion (van Marle, Decin & Meliani 2014). We place our work in this context, focusing on bow shocks generated by hot, fast winds of main-sequence massive stars.

In this study, we continue our investigation of the circumstellar medium of runaway massive stars moving within the plane of the Milky Way (Paper I; Meyer et al. 2015, 2016). As a logical extension of them, we present MHD models of a sample of some of the most common main-sequence, runaway massive stars (Kroupa 2001) moving at the most probable space velocities (Eldridge, Langer & Tout 2011). We ignore any intrinsic inhomogeneity or turbulence in the ISM. Particularly, we assume an axisymmetric magnetization of the ISM surrounding the bow shocks in the spirit of van Marle et al. (2014). We concentrate our efforts on an initially 20 $M_\odot$ star; however, we also consider bow shocks generated by lower and higher initial mass stars. This project principally differs from Paper I because (i) the inclusion of an ISM background magnetic field leads to anisotropic heat conduction (HC; see e.g. Balsara, Tilley & Howk 2008) and (ii) our study does not concentrate on the secular stellar wind evolution of our bow-shock-producing stars. Note that our study introduces a reduced number of representative models due to the high numerical cost of the MHD simulations. Following Acreman, Stevens & Harries (2016), we additionally appreciate the effects of the ISM magnetic field on the bow shocks with the help of radiative transfer calculations of dust continuum emission.

This paper is organized as follows. We start in Section 2 with a review of the physics included in our models for both the stellar wind and the ISM. We also recall the adopted numerical methods. Our models of bow shocks generated by main-sequence, runaway massive stars moving in a magnetized medium are presented together with a discussion of their morphology and internal structure in Section 3. We detail the emission properties of our bow shocks and discuss their observational implications in Section 4. Finally, we formulate our conclusions in Section 5.

2 METHOD

In the present section, we briefly summarize the numerical methods and microphysics utilized to produce MHD bow shock models of the circumstellar medium surrounding hot, runaway massive stars.

2.1 Governing equations

We consider a magnetized flow past a source of hot, ionized and magnetized stellar wind. The dynamics are described by the ideal equations of magneto-hydrodynamics and the dissipative character of the thermodynamics originates from the treatment of the gas with heating and losses by optically thin radiation together with electronic HC. These equations are

$$\frac{\partial \rho}{\partial t} + \nabla \cdot (\rho \boldsymbol{v}) = 0, \tag{1}$$

$$\frac{\partial \boldsymbol{m}}{\partial t} + \nabla \cdot (\boldsymbol{m} \otimes \boldsymbol{v} + \boldsymbol{B} \otimes \boldsymbol{B} + \hat{\boldsymbol{I}}\, p_{\rm t}) = \boldsymbol{0}, \tag{2}$$

$$\frac{\partial E}{\partial t} + \nabla \cdot ((E + p_{\rm t})\boldsymbol{v} - \boldsymbol{B}(\boldsymbol{v} \cdot \boldsymbol{B})) = \zeta(T, \rho, \mu), \tag{3}$$

and,

$$\frac{\partial \boldsymbol{B}}{\partial t} + \nabla \cdot (\boldsymbol{v} \otimes \boldsymbol{B} - \boldsymbol{B} \otimes \boldsymbol{v}) = \boldsymbol{0}, \tag{4}$$

where ρ and $\boldsymbol{v}$ are the mass density and the velocity of the plasma. In the relation of momentum conservation equation (2), the quantity $\boldsymbol{m} = \rho \boldsymbol{v}$ is the linear momentum of a gas element, $\boldsymbol{B}$ is the magnetic field, $\hat{\boldsymbol{I}}$ is the identity matrix, and

$$p_{\rm t} = p + \frac{\boldsymbol{B} \cdot \boldsymbol{B}}{2} \tag{5}$$

is the total pressure of the gas, i.e. the sum of its thermal component p and its magnetic contribution $(\boldsymbol{B} \cdot \boldsymbol{B})/2$, respectively. Equation (3) describes the conservation of the total energy of the gas,

$$E = \frac{p}{(\gamma - 1)} + \frac{\boldsymbol{m} \cdot \boldsymbol{m}}{2\rho} + \frac{\boldsymbol{B} \cdot \boldsymbol{B}}{2}, \tag{6}$$

where γ is the adiabatic index, which is taken to be 5/3, i.e. we assume an ideal gas. The right-hand source term $\zeta(T, \rho, \mu)$ in equation (3) represents (i) the heating and the losses by optically thin radiative processes and (ii) the heat transfers by anisotropic

electronic thermal conduction (see Section 2.3). Finally, equation (4) is the induction equation and governs the time evolution of the vector magnetic field $\boldsymbol{B}$. The relation

$$c_{\rm s} = \sqrt{\frac{\gamma p}{\rho}} \tag{7}$$

closes the system (equations 1−4), where $c_{\rm s}$ denotes the adiabatic speed of sound.

2.2 Boundary conditions and numerical scheme

We solve the above described system of equations (equations 1−7) using the open-source PLUTO code[1] (Mignone et al. 2007, 2012) on a uniform two-dimensional grid covering a rectangular computational domain in a cylindrical frame of reference $(O; R, z)$ of origin O and symmetry axis about $R = 0$. The grid $[O; R_{\rm max}] \times [-z_{\rm min}; z_{\rm max}]$ where $R_{\rm max}$, $-z_{\rm min}$ and $z_{\rm max}$ are the upper and lower limits of the OR and Oz directions, respectively, which are discretized with $N_{\rm R} = 2N_{\rm z} = 1000$ cells such that the grid resolution is $\Delta_R = \Delta_z = R_{\rm max}/N_{\rm R}$. Learning from previous bow shock models (Comerón & Kaper 1998; van Marle et al. 2006), we impose inflow boundary conditions corresponding to the stellar motion at $z = z_{\rm max}$ whereas outflow boundaries are set at $R = R_{\rm max}$ and $z = -z_{\rm min}$. Moreover, the stellar wind is modelled setting inflow boundary conditions centred around the origin (see Section 2.4).

We integrate the system of partial differential equations within the eight-wave formulation of the MHD equations (1)−(7), using a cell-centred representation consisting in evaluating ρ, $\boldsymbol{m}$, E and $\boldsymbol{B}$ using the barycentre of the cells (see section 2 of Paper I). This formulation, used together with the Harten–Lax–van Leer approximate Riemann solver (Harten, Lax & van Leer 1983), conserves the divergence-free condition $\nabla \cdot \boldsymbol{B} = \boldsymbol{0}$. The method is a second-order, unsplit, time-marching algorithm scheme controlled by the Courant–Friedrich–Levy parameter initially set to $C_{\rm cfl} = 0.1$. The gas cooling and heating rates are linearly interpolated from tabulated cooling curves (see Section 2.3) and the corresponding rate of change is subtracted from the total energy E. The parabolic term of HC is integrated with the Super-Time-Stepping algorithm (Alexiades, Amiez & Gremaud 1996).

2.3 Gas microphysics

The source term $\zeta(T, \rho, \mu)$ in equation (3) represents the non-ideal thermodynamics processes that we take into account, and reads

$$\zeta(T, \rho, \mu) = \Phi(T, \rho) + \nabla \cdot \boldsymbol{F}_{\rm c} \tag{8}$$

where $\Phi(T, \rho)$ is a function that stands for the processes by optically thin radiation where

$$T = \mu \frac{m_{\rm H}}{k_{\rm B}} \frac{p}{\rho} \tag{9}$$

is the gas temperature, with $\mu = 0.61$ the mean molecular weight of the gas, $k_{\rm B}$ the Boltzmann constant and $m_{\rm H}$ the proton mass, respectively. The gain and losses by optically thin radiative processes are taken into account via the following law:

$$\Phi(T, \rho) = n_{\rm H}\Gamma(T) - n_{\rm H}^2\Lambda(T), \tag{10}$$

where $\Lambda(T)$ and $\Gamma(T)$ are the rate of change of the gas internal energy induced by heating and cooling as a function of T, respectively, and where $n_{\rm H} = \rho/\mu(1 + \chi_{\rm He,Z})m_{\rm H}$ is the hydrogen number density with $\chi_{\rm He,Z}$ the mass fraction of the coolants heavier than hydrogen. Details about the processes included into the cooling $\Lambda(T)$ and heating $\Gamma(T)$ laws are given in section 2 of Paper I.

The divergence term in the source function in equation (8) represents the anisotropic heat flux,

$$\boldsymbol{F}_{\rm c} = \kappa_{||}\hat{\boldsymbol{b}}(\hat{\boldsymbol{b}} \cdot \nabla T) + \kappa_{\perp}(\nabla T - \hat{\boldsymbol{b}} \cdot \nabla T), \tag{11}$$

where $\hat{\boldsymbol{b}} = \boldsymbol{B}/||\boldsymbol{B}||$ is the magnetic field unit vector. It is calculated through the interface of the nearest neighbouring cells in the whole computational domain according to the temperature difference ΔT and the local field orientation $\hat{\boldsymbol{b}}$ (see appendix of Mignone et al. 2012). The coefficients $\kappa_{||}$ and $\kappa_{\perp}$ are the heat coefficients along the directions parallel and normal to the local magnetic field streamline, respectively. Along the direction of the local magnetic field,

$$\kappa_{||} = K_{||}T^{5/2}, \tag{12}$$

with

$$K_{||} = \frac{1.84 \times 10^{-5}}{\ln(\mathcal{L})}\ {\rm erg\ s^{-1}\ K^{-1}\ cm^{-1}}, \tag{13}$$

where $\ln(\mathcal{L}) = 29.7 + \ln(T/10^6\sqrt{n})$ is the Coulomb logarithm, with n the gas total number density (Spitzer 1962). The HC coefficients satisfy $\kappa_{\perp}/\kappa_{||} \approx 10^{-16} \ll 1$ for the densities that we consider (Parker 1963; Velázquez et al. 2004; Balsara et al. 2008; Orlando et al. 2008). The value of $\boldsymbol{F}_{\rm c}$ varies between the classical flux in equation (11) and the saturated conduction regime (Balsara et al. 2008) which limits the heat flux to

$$F_{\rm sat} = 5\phi\rho c_{\rm iso}^3, \tag{14}$$

for very large temperature gradients ($\geq 10^6\ {\rm K\ pc^{-1}}$), with $c_{\rm iso} = p/\rho$ the isothermal speed of sound and $\phi < 1$ a free parameter that we set to the typical value of 0.3 (Cowie & McKee 1977).

2.4 Setting up the stellar wind

We impose the stellar wind at the surface of a sphere of radius $20\Delta z$ pc centred into the origin O with wind material. Its density is

$$\rho_{\rm w} = \frac{\dot{M}}{4\pi r^2 v_{\rm w}}, \tag{15}$$

where $\dot{M}$ is the star's mass-loss rate and r is the distance to the origin O. We interpolate the wind parameters from stellar evolution models of non-rotating massive stars with solar metallicity that we used for previous studies (see Paper I). Our stellar wind models are have been generated with the stellar evolution code described in Heger, Woosley & Spruit (2005) and subsequently updated by Yoon & Langer (2005), Petrovic et al. (2005) and Brott et al. (2011). It utilizes the mass-loss prescriptions of Kudritzki et al. (1989) for the main-sequence phase of our massive stars and of de Jager, Nieuwenhuijzen & van der Hucht (1988) for the red supergiant phase. Despite the fact that our wind models report the marginal evolution of main-sequence winds (see Paper I), they remain quasi-constant during the part of the stellar evolution that we follow. We refer the reader interested in a graphical representation of the utilized wind models to fig. 3 of Paper I, while we report the wind properties at the beginning of our simulations in our Table 1. Note that our adopted values for the stellar wind velocity belong to the lower limit of the range of validity for stellar winds of OB stars (see below in Section 3.1.3).

[1] http://plutocode.ph.unito.it/

Table 1. Stellar wind parameters at the beginning of the simulations, at a time $t_{\rm start}$ after the beginning of the zero-age main-sequences of the star. Parameter $M_\star$ (in $M_\odot$) is the initial mass of the star, $L_\star$ the stellar luminosity (in $L_\odot$), $\dot{M}$ its mass loss and $v_{\rm w}$ the wind velocity (see also table 1 of Meyer et al. 2016).

$M_\star$ ($M_\odot$)	$t_{\rm start}$ (Myr)	$\log(L_\star/L_\odot)$	$\log(\dot{M}/M_\odot\,{\rm yr}^{-1})$	$v_{\rm w}$ (km s^{-1})	$T_{\rm eff}$ (K)
10	5.0	3.80	−9.52	1082	25 200
20	3.0	4.74	−7.38	1167	33 900
40	0.0	5.34	−6.29	1451	42 500

Since we assume a spherically symmetric stellar wind density, thermal pressure and velocity profiles, we use the Parker prescription (Parker 1958) to model the magnetic field in the stellar wind. It consists of a radial component of the field

$$B_{\rm r} = B_\star \left(\frac{R_\star}{r}\right)^2, \tag{16}$$

where $B_\star$ and $R_\star$ are the stellar surface magnetic field and the stellar radius, respectively, and of a toroidal component, which, in the case of a non-rotating star, this reduces to $B_\phi = 0$. The $\propto 1/r^2$ radial dependence of equation (16) makes the strength of the stellar magnetic field almost negligible at the wind termination shock that is typically about a few tenths of pc from the star that we study (Paper I). However, imposing a null magnetic field in the stellar wind region would let the direction of the heat flux $\boldsymbol{F}_{\rm c}$ undetermined in the region of (un)shocked wind material of the bow shock (see magnetic field unit vector $\hat{\boldsymbol{b}}$ in the right-hand side of equation 11). Note that, given their analogous radial dependence on r, stellar wind and stellar magnetic field are similarly implemented into our axisymmetric simulations. In these simulations, the stellar surface magnetic field is set to $B_\star \simeq 1.0$ kG (Donati et al. 2002) at $R_\star = 3.66\,R_\odot$ (Brott et al. 2011) where $R_\odot$ is the solar radius.

2.5 Setting up the ISM

Our runaway stars are moving through the warm ionized phase of the ISM, i.e. we assume that they run in their own H II region inside which the gas is considered as homogeneous, laminar and fully ionized fluid. The ISM composition assumes solar metallicity (Lodders 2003), with $n_{\rm H} = 0.57\,{\rm cm}^{-3}$ (Wolfire et al. 2003) and with $T_{\rm ISM} \approx 8000$ K, initially. The model is a moving star within an ISM at rest. We solve the equations of motion in the frame in which the star is at rest and, hence, the ISM moves with $v_{\rm ISM} = -v_\star$, where $v_\star$ is the bulk motion of the star. The gas in the computational domain is evaluated with the cooling curve for photoionized gas described in fig. 4(a) of Paper I. In particular, our initial conditions neglect the possibility that a bow shock might trap the ionizing front of the H II region (see section 2.4 of Paper I for an extended discussion of the assumptions underlying our method for modelling bow shocks from hot massive stars). Additionally, an axisymmetric magnetic field $\boldsymbol{B} = -B_{\rm ISM}\,\hat{\boldsymbol{z}}$ field is imposed over the whole computational domain, with $B_{\rm ISM} > 0$ its strength and $\hat{\boldsymbol{z}}$ the unit vector along the Oz direction. Finally, our simulations trace the respective proportions of ISM gas with respect to the wind material using a passive scalar tracer according to the advection equation,

$$\frac{\partial(\rho Q)}{\partial t} + \nabla\cdot(\boldsymbol{v}\rho Q) = 0, \tag{17}$$

where Q is a passive tracer with initial value $Q(\boldsymbol{r}) = 1$ for the wind material and $Q(\boldsymbol{r}) = 0$ for the ISM gas, respectively.

2.6 Simulation ranges

We first focus on a baseline bow shock generated by an initially $20\,M_\odot$ star moving with a velocity $v_\star = 40\,{\rm km\,s}^{-1}$ in the Galactic plane of the Milky Way whose magnetic field is assumed to be $B_{\rm ISM} = 7\,\mu$G (Draine 2011). Then, we consider models with velocity $v_\star = 20$ to $70\,{\rm km\,s}^{-1}$, explore the effects of a magnetization of $B_{\rm ISM} = 3.5\,\mu$G, and carry out simulations of initially 10 and $40\,M_\odot$ stars moving at velocities $v_\star = 40$ and $70\,{\rm km\,s}^{-1}$, respectively. We investigate the effects of the ISM magnetic field carrying out a couple of additional purely HD simulations, as comparison runs. All our simulations are started at a time about 4.5 Myr after the zero-age main-sequence phase of our stars and are run at least four crossing times $|z_{\rm max} - z_{\rm min}|/v_\star$ of the gas through the computational domain, such that the system reaches a steady or quasi-stationary state in the case of a stable or unstable bow shock, respectively.

We label our MHD simulations concatenating the values of the initial mass $M_\star$ of the moving star (in $M_\odot$), its bulk motion $v_\star$ (in km s^{-1}) and the included physics 'Ideal' for dissipativeless simulations, 'Cool' if the model includes heating and losses by optically thin radiative processes, 'Heat' for HC and 'All' if cooling, heating and HC are taken into account together. Finally, the labels inform about the strength of the ISM magnetic field. We distinguish our MHD runs from our previously published HD studies (Paper I) adding the prefix 'HD' and 'MHD' to the simulation labels of our HD and MHD simulations, respectively. All the information relative to our models is summarized in Table 2.

3 RESULTS AND DISCUSSION

This section presents the MHD simulations carried out in the context of our Galactic, ionizing, runaway massive stars. We detail the effects of the included microphysics on a baseline bow shock model, discuss the morphological differences between our HD and MHD simulations and consider the effects of the adopted stellar wind models. Finally, we review the limitations of the model.

3.1 Bow shock thermodynamics

3.1.1 Effects of the included physics: hydrodynamics

In Fig. 1, we show the gas density field in a series of bow shock models of our initially $20\,M_\odot$ star moving with velocity $40\,{\rm km\,s}^{-1}$ through a medium of ISM background density $n_{\rm H} = 0.59\,{\rm cm}^{-3}$ and of magnetic field strength $B_{\rm ISM} = 7\,\mu$G. The crosses indicate the position of the moving star. The figures correspond to a time about 5 Myr after the beginning of the main-sequence phase of the star. The stellar wind and ISM properties are the same for all figures, only the included physics is different for each model (our Table 2). Left-hand panels are HD simulations whereas right-hand panels are MHD simulations, respectively. From top to bottom, the included thermodynamic processes are adiabatic (a), take into account optically thin radiative processes of the gas (b), heat transfers (c) or both (d). The black dotted lines are the contours $Q(\boldsymbol{r}) = 1/2$, which trace the discontinuity between the stellar wind and the ISM gas. The streamlines (a–c) and vector velocity field (d) highlight the penetration of the ISM gas into the different layers of the bow shock.

The internal structure of the bow shocks can be understood by comparing the time-scales associated with the different physical processes at work. The dynamical time-scale represents the time interval it takes the gas to advect through a given layer of our bow

Table 2. Nomenclature and grid parameters used in our (magneto-)hydrodynamical simulations. The quantities $M_\star$ (in $M_\odot$) and $v_\star$ (in $km\,s^{-1}$) are the initial mass of the stars and their space velocity, respectively, whereas B_{ISM} (in μG) is the strength of the ISM magnetic field. Parameters Δ, z_{min} and R_{max} are the resolution of the uniform grid (in $pc\,cell^{-1}$) and the lower and upper limits of the domain along the R-axis and z-axis (in pc), respectively. The last column contains the physics included in each simulation. HC refers to isotropic thermal conduction in the case of a HD simulation and to anisotropic thermal conduction in the case of a MHD simulation, respectively.

Model	$M_\star$ ($M_\odot$)	$v_\star$ ($km\,s^{-1}$)	B_{ISM} (μG)	Δ (10^{-3} $pc\,cell^{-1}$)	z_{min} (pc)	R_{max} (pc)	Included microphysics
HD2040Ideal	20	40	–	8.0	−2.0	8.0	HD, adiabatic
HD2040Cool	20	40	–	8.0	−2.0	8.0	HD, cooling, heating
HD2040Heat	20	40	–	8.0	−2.0	8.0	HD, HC
HD2040All	20	40	–	8.0	−2.0	8.0	HD, cooling, heating, HC
MHD2040IdealB7	20	40	7.0	8.0	−2.0	8.0	MHD
MHD2040CoolB7	20	40	7.0	8.0	−2.0	8.0	MHD, cooling, heating
MHD2040HeatB7	20	40	7.0	8.0	−2.0	8.0	MHD, HC
MHD2040AllB7	20	40	7.0	8.0	−2.0	8.0	MHD, cooling, heating, HC
MHD1040AllB7	10	40	7.0	3.0	−2.0	6.0	MHD, cooling, heating, HC
MHD2020AllB7	20	20	7.0	6.0	−3.0	12.0	MHD, cooling, heating, HC
MHD2040AllB3.5	20	40	3.5	8.0	−2.0	8.0	MHD, cooling, heating, HC
MHD2070AllB7	20	70	7.0	1.2	−1.0	3.0	MHD, cooling, heating, HC
MHD4070AllB7	40	70	7.0	1.6	−4.0	16.0	MHD, cooling, heating, HC

shocks, i.e. the region of shocked ISM or the layer of shocked wind. It is defined as

$$t_{dyn} = \frac{\Delta l}{v}, \tag{18}$$

where Δl is the characteristic lengthscale of the region of the bow shock measured along the Oz direction and where v is the gas velocity in the post-shock region of the considered layers. According to the Rankine–Hugoniot relations and taking into account the non-ideal character of our model, we should have $v \simeq v_\star/4$ in the shocked ISM and $v \simeq v_w/4$ in the post-region at the forward shock (FS) and at the reverse shock (RS), respectively.

The cooling time-scale is defined as

$$t_{cool} = \frac{E_{int}}{\dot{E_{int}}} = \frac{p}{(\gamma-1)\Lambda(T)n_H^2}, \tag{19}$$

where $\dot{E_{int}}$ is the rate of change of internal energy E_{int} (Orlando et al. 2005). The HC time-scale measures the rapidity of heat transfer into the bow shock, and is given by

$$t_{heat} = \frac{7pl^2}{2(\gamma-1)\kappa(T)T}, \tag{20}$$

where l is a characteristic length of the bow shock along which heat transfers take place. Measuring the density, pressure and velocity fields in our simulations, we evaluate and compare those quantities defined in equations (18)–(20) at both the post-shock regions at the forward and RSs. Results for both the layers of shocked wind and shocked ISM material are given in Table 3.

Our HD, dissipation-free bow shock model HD2040Ideal has a morphology governed by the gas dynamics only (Fig. 1a). It has a contact discontinuity separating the outer region of cold shocked ISM from the inner region of hot shocked stellar wind, which are themselves bordered by the forward and RSs, respectively. There is no advection of ISM material into the wind region (see the ISM gas streamlines in Fig. 1a). The model HD2040Cool including cooling by optically thin radiation has a considerably reduced layer of dense, shocked ISM gas caused by the rapid losses of internal energy ($t_{dyn} \gg t_{cool}$; see time-scales in our Table 3). Its thinness favours the growth of Kelvin–Helmholtz instabilities and allows large eddies to develop in the shocked regions (Fig. 1b). The layer of hot gas is isothermal because the regular wind momentum input at the RS prevents it from cooling and it therefore conserves its hot temperature ($t_{cool} \gg t_{dyn}$) whereas the distance between the star and the contact discontinuity,

$$R(0) = \sqrt{\frac{\dot{M}v_w}{4\pi\rho_{ISM}v_\star^2}}, \tag{21}$$

does not evolve (Wilkin 1996).

The model HD2040Heat takes into account thermal conduction which is isotropic in the case of the absence of magnetic field. The heat flux reads

$$\boldsymbol{F_c} = \kappa\nabla T, \tag{22}$$

and transports internal energy from the RS to the contact discontinuity ($t_{dyn} \gg t_{heat}$) which in its turn splits the dense region into a hot ($t_{dyn} \gg t_{heat}$) and a cold layer of shocked ISM gas ($t_{dyn} \ll t_{heat}$), respectively. This modifies the penetration of ISM gas into the bow shock and causes the region of shocked wind to shrink to a narrow layer of material close to the RS (Fig. 1c). Not surprisingly, the model with both cooling and conduction HD2040All (Fig. 1d) presents both the thermally split region of shocked ISM ($t_{dyn} \ll t_{heat}$, $t_{dyn} \gg t_{cool}$, $t_{cool} \ll t_{heat}$) and a reduced layer of shocked wind material ($t_{dyn} \gg t_{heat}$, $t_{dyn} \ll t_{cool}$, $t_{cool} \gg t_{heat}$) that reorganizes the internal structure of the bow shock together with a dense shell of cool ISM gas (see also discussion in Paper I). For the sake of clarity, Fig. 1(d) overplots the gas velocity fields as white arrows which illustrate the penetration of ISM gas into the hot layer of the bow shock.

3.1.2 *Effects of the included physics: magneto-hydrodynamics*

We plot in the right-hand panels of Fig. 1 the ideal MHD simulation of our initially $20\,M_\odot$ star moving with $v_\star = 40\,km\,s^{-1}$ through a medium where the strength of the magnetic field is $B_{ISM} = 7\,\mu G$ (e) together with models including cooling and heating by optically thin radiation (f), anisotropic HC (g) and both (h). Despite the fact that the overall morphology of our MHD bow shock models is globally similar to the models with $B_{ISM} = 0\,\mu G$, a given number of significant changes relative to both their shape and internal structure arise. Note that in the context of our MHD models, t_{heat} represents the heat transfer time-scale normal to the fields lines.

Our ideal MHD model has the typical structure of a stellar wind bow shock, with a region of shocked ISM gas surrounding

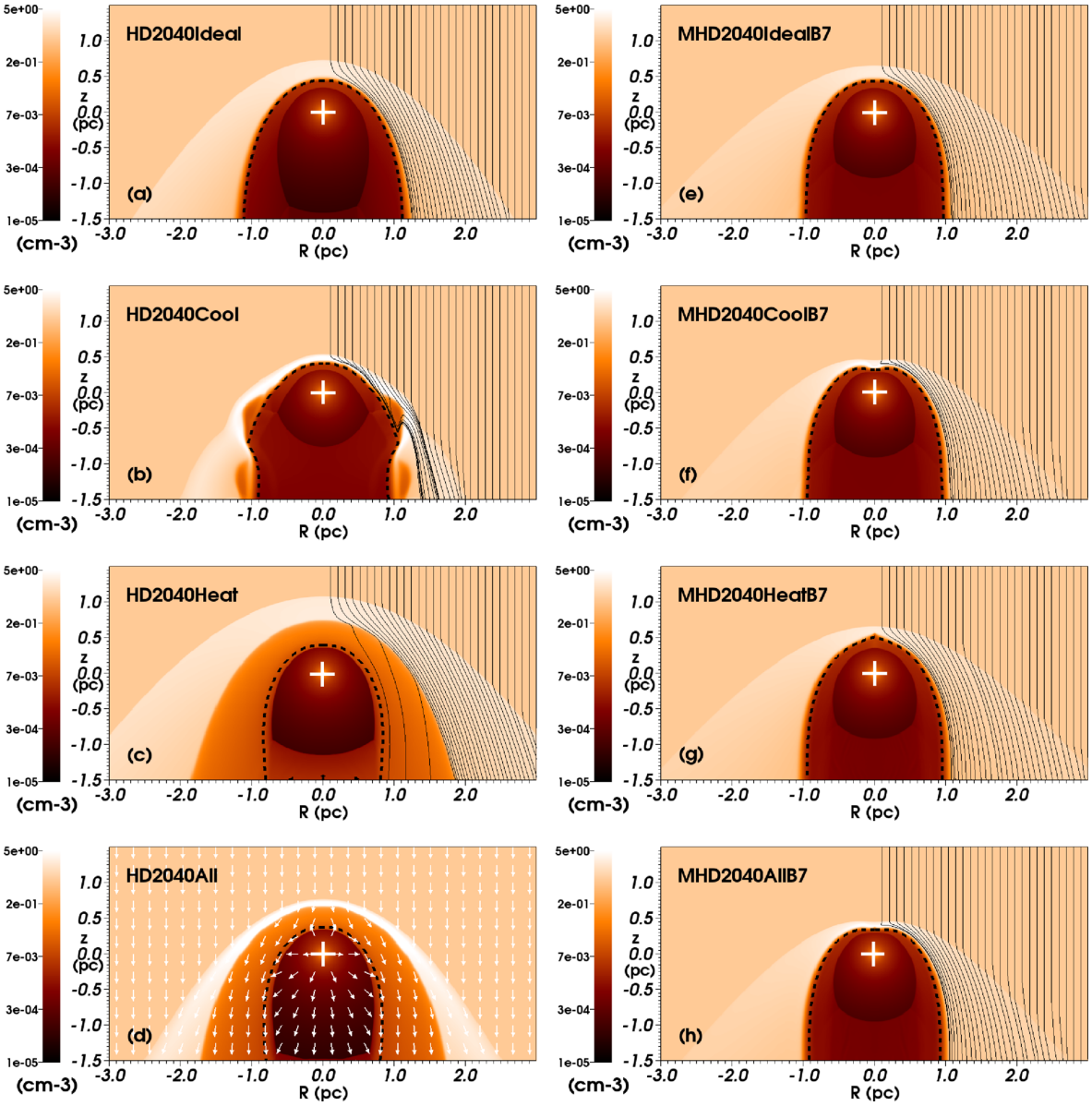

Figure 1. Changes in the morphology of a stellar wind bow shock with variation of the included physics. Figures show gas number density plotted with a density range from 10^{-5} to 5 cm^{-3} in the logarithmic scale for an initially 20 $M_\odot$ star moving with velocity 40 km s^{-1}. Left-hand panels are the HD models whereas right-hand panels are the MHD models with $B_{\rm ISM} = 7$ μG. The first line of panels shows adiabatic (a) and ideal MHD (e) models, respectively. The second line of panels plots models with optically thin radiative processes (b,f); the third line shows models including thermal (an-)isotropic conduction (c,g) and the last line plots models including cooling, heating and (an-)isotropic thermal conduction (d,h). The nomenclature of the models follows our Table 2. For each figure, the dotted thick line traces the material discontinuity, i.e. the interface of the wind/ISM regions, $Q(\boldsymbol{r}) = 1/2$. The right part of each figure overplots ISM flow streamlines, except panel (d), which explicitly plots the velocity field as white arrows over the whole computational domain. The crosses mark the position of the star. The R-axis represents the radial direction and the z-axis the direction of stellar motion (in pc). Only a fraction of the computational domain is shown.

the one of shocked wind gas. The contact discontinuity acts as a border between the two kinds of material (Fig. 1e). The model with cooling MHD2040CoolB7 has smaller but denser layer of ISM gas (Fig. 1f) due to the rapid cooling time ($t_{\rm cool} \ll t_{\rm dyn}$). The MHD model with thermal conduction is similar to our model MHD2040IdealB7 since, due to its anisotropic character, heat transport is cancelled across the magnetic field lines ($t_{\rm heat} \ggg t_{\rm dyn}$). Note the boundary effect close to the apex along the Oz direction as a result of the HC along the direction of the ISM magnetic field lines (Fig. 1g). Finally, our model with both processes has its dynamics governed by the cooling in the region of shocked ISM ($t_{\rm heat} \ggg t_{\rm dyn}$, $t_{\rm heat} \ggg t_{\rm cool}$, $t_{\rm cool} \ll t_{\rm dyn}$) and by the wind momentum in the region of shocked wind ($t_{\rm heat} \ggg t_{\rm dyn}$, $t_{\rm heat} \ggg t_{\rm cool}$, $t_{\rm dyn} \ll t_{\rm cool}$).

Table 3. Characteristics dynamical time-scale $t_{\rm dyn}$, cooling time-scale $t_{\rm cool}$ and thermal conduction time-scale $t_{\rm heat}$ (in Myr) measured along the Oz direction from our simulations of our initially 20 $M_\odot$ star moving velocity 40 km s^{-1} (see Figs 1a–h). We estimate the various time-scales in both the post-shock region at the FS and the RS of our bow shocks. The black hyphen indicates that the corresponding physical process is not included in the models (our Table 2).

Model	$t_{\rm dyn}$ (Myr)	$t_{\rm cool}$ (Myr)	$t_{\rm heat}$ (Myr)
HD2040Ideal (FS)	2.5×10^{-2}	–	–
HD2040Ideal (RS)	4.7×10^{-3}	–	–
HD2040Cool (FS)	1.0×10^{-2}	4.5×10^{-3}	–
HD2040Cool (RS)	3.7×10^{-3}	$3.5 \times 10^{+3}$	–
HD2040Heat (FS)	6.5×10^{-2}	–	$1.2 \times 10^{+3}$
HD2040Heat (RS)	1.3×10^{-2}	–	1.2×10^{-4}
HD2020All (FS)	9.0×10^{-3}	5.1×10^{-3}	$8.7 \times 10^{+5}$
HD2020All (RS)	1.1×10^{-2}	$2.5 \times 10^{+1}$	4.0×10^{-3}
MHD2040IdealB7 (FS)	1.8×10^{-2}	–	–
MHD2040IdealB7 (RS)	4.3×10^{-3}	–	–
MHD2040CoolB7 (FS)	1.1×10^{-1}	4.3×10^{-2}	–
MHD2040CoolB7 (RS)	2.0×10^{-3}	$1.0 \times 10^{+3}$	–
MHD2040HeatB7 (FS)	1.0×10^{-2}	–	$1.1 \times 10^{+25}$
MHD2040HeatB7 (RS)	6.7×10^{-3}	–	$5.5 \times 10^{+9}$
MHD2040AllB7 (FS)	3.0×10^{-1}	3.4×10^{-3}	$1.4 \times 10^{+18}$
MHD2040AllB7 (RS)	2.3×10^{-3}	$3.0 \times 10^{+4}$	$5.4 \times 10^{+7}$

3.1.3 Effects of the boundary conditions: stellar wind models

The shape of the bow shock generated around a runaway massive star in the warm phase of the ISM is a function of the respective strength of both the ISM ram pressure $\rho_{\rm ISM} v_\star^2$ and the stellar wind ram pressure $\rho_{\rm w} v_{\rm w}^2$, as seen in the frame of reference of the moving object (see explanations in Mohamed, Mackey & Langer 2012). According to equation (15), $\rho_{\rm w} = \dot{M}/4\pi r^2 v_{\rm w}$ which implies that $\rho_{\rm w} v_{\rm w}^2 \propto \dot{M} v_{\rm w}$. In other words, in a given ambient medium and at a given peculiar velocity, the governing quantity in the shaping of such bow shock is $\dot{M} v_{\rm w}$ and its stand-off distance $R(0)$ goes as $\sqrt{\dot{M} v_{\rm w}}$ (see equation 21). Nevertheless, if the production of stellar evolution models depends on specific prescriptions relative to $\dot{M}$ that are consistently used through the calculations (in our case the recipe of Kudritzki et al. 1989), the estimate of the wind velocity is posterior to the calculation of the stellar structure and it does not influence $\dot{M}$, $T_{\rm eff}$ or $L_\star$.

The manner to calculate $v_{\rm w}$ is not unique (Castor, Abbott & Klein 1975; Kudritzki et al. 1989; Kudritzki & Puls 2000; Eldridge et al. 2006) and it can also be assumed to characteristic values for the concerned stars (Comerón & Kaper 1998; van Marle, Decin & Meliani 2014; van Marle, Meliani & Marcowith 2015; Acreman et al. 2016). In our study, the wind velocities are in the lower limit of the range of validity for the main-sequence massive stars that we consider; nonetheless, they still remain within the order of magnitude of, e.g. late O stars (Martins et al. 2007) or weak-winded stars (Comerón & Kaper 1998). Furthermore, the evolution of massive stars is governed by physical mechanisms strongly influencing their feedback such as the presence of low-mass companions (Sana et al. 2012), which are neglected in our stellar evolution models. Produced before their zero-age main-sequence phase, e.g. by fragmentation of the accretion disc that surrounds massive protostars (Meyer et al. 2017), those dwarf stars entirely modify the evolution of massive stars and consequently affect their wind properties (de Mink, Pols & Hilditch 2007; de Mink et al. 2009; Paxton et al. 2011; Marchant et al. 2016).

Using wind velocities faster by a factor of α would enlarge the bow shocks by a factor of $\sqrt{\alpha}$ and, eventually, in the HD case, favour the growth of instabilities (cf. Fig. 1b). However, the results of our numerical study would be similar in the sense that the presence of the field essentially stabilizes the nebulae and inhibits the effects of HC (cf. Figs 1a and h), reduces their size (Section 3.2.1) and modifies, e.g. their infrared emission accordingly (see Section 4.3). In Fig. 2, we compare our values of $\dot{M} v_{\rm w}$ (Table 1) with the non-rotating stellar evolutionary models published in Brott et al. (2011). We conclude that the bow shocks generated with our initially 10, 20 and 40 $M_\odot$ weak-winded stellar models correspond to nebulae produced by initially ≈10, ≈18 and ≈32 $M_\odot$ standard massive stars at Galactic metallicity, respectively. Therefore, our models have full validity for this study of magnetized bow shock nebulae, albeit of lower zero-age main-sequence mass in the case of our heaviest runaway star.

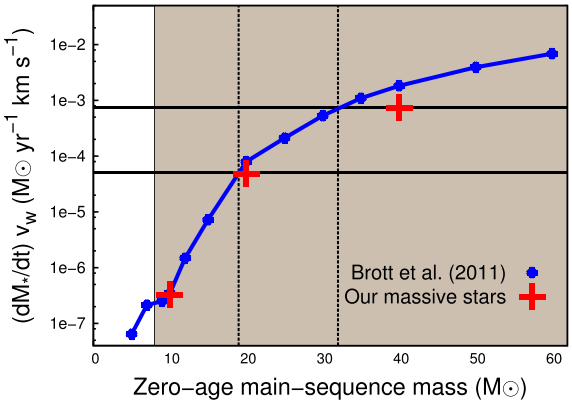

Figure 2. Comparison of the quantity $\dot{M} v_{\rm w}$ between our weak-winded stars and the non-rotating Galactic models of Brott et al. (2011). The grey zone of the plot corresponds to the mass regime of massive stars ($M_\star \geq 8\,M_\odot$). Solid and dotted lines are lines of constant $\dot{M} v_{\rm w}$ and $M_\star$, respectively.

3.2 Hydrodynamics versus magneto-hydrodynamics

3.2.1 The effects of the magnetic pressure

The ISM magnetic pressure, proportional to $\boldsymbol{B}_{\rm ISM}^2$, dynamically compresses the region of shocked ISM gas such that the density in the post-shock region at the FS slightly increases. Similarly, the shape of the bow shock's wings of shocked ISM is displaced sidewards compared to our model with $B_{\rm ISM} = 0$ μG (Figs 1a and e). The size of the layer of ISM gas diminishes along the direction of motion of the moving star and the position of the termination shock sets at a distance from the star where the wind ram pressure equals the ISM total pressure decreases as measured along the Oz axis. The effects of the cooling are standard in the sense that it makes the region of shocked ISM thinner and denser, i.e. the position of the FS decreases, together with the bow shock volume. The effects of HC are cancelled ($t_{\rm dyn} \ll t_{\rm heat}$) in the direction perpendicular to the field lines, i.e. in the direction perpendicular to the streamline collinear to both the RS and the contact discontinuity.

3.2.2 Stagnation point morphology and discussion in the context of plasma physics studies

The topology at the apex of our MHD bow shock (Fig. 1h) is different from the traditional single-front bow shock morphology (Fig. 1d). This can be discussed at the light of plasma physics

studies (de Sterck et al. 1998; de Sterck & Poedts 1999). These works explore the formation of exotic shocks and discontinuities that affect the particularly dimpled apex of bow shocks generated by field-aligned flows around a conducting cylinder (de Sterck et al. 1998). They extended this result to bow shocks produced around a conducting sphere and showed that the inflow parameter space leading to such structures is similar to plasma β and Alfvénic Mach number values allowing the formation of so-called switch-on shocks (de Sterck & Poedts 1999).

Switch-on shocks are allowed when plasma β of the inflowing material, i.e. the ratio of the gas and magnetic pressures, which read

$$\beta = \frac{8\pi n k_{\rm B} T}{\boldsymbol{B}_{\rm ISM} \cdot \boldsymbol{B}_{\rm ISM}}, \tag{23}$$

and its Alfvénic Mach number

$$M_{\rm A} = \frac{v}{v_{\rm A}}, \tag{24}$$

where

$$v_{\rm A} = \frac{|\boldsymbol{B}_{\rm ISM}|}{\sqrt{4\pi n m_{\rm H}}} \tag{25}$$

is the Alfvénic velocity, satisfy some particular conditions. Note that in equation (24) the velocities are taken along the shock normal. On the one hand, the plasma beta must be such that

$$\beta < \frac{2}{\gamma}, \tag{26}$$

whereas, on the other hand, the Alfvénic Mach number verifies the following order relation,

$$1 < M_{\rm A} < \sqrt{\frac{\gamma(1-\beta)+1}{\gamma-1}}, \tag{27}$$

where γ is the adiabatic index (see equation 1 in Pogorelov & Matsuda 2000). Numbers from our simulations indicate that the ISM thermal pressure $n_{\rm ISM} k_{\rm B} T_{\rm ISM} \approx 8.62 \times 10^{-13}$ dyne s^{-2}, therefore we find $\beta > 2/\gamma \approx 1.2$ for $B_{\rm ISM} \leq 3.5$ μG (see bow shocks with normal morphologies in Figs 3a and b) but $\beta \approx 0.44 < 2/\gamma \approx 1.2$ for $B_{\rm ISM} = 7$ μG (see dimpled bow shock in Fig. 3c). The Alfvénic Mach number $M_{\rm A} = v/v_{\rm A} \approx 40.0\,{\rm km\,s^{-1}}/17.2\,{\rm km\,s^{-1}} \approx 2.33$ which is outside the range $1 < M_{\rm A} < ((\gamma(1-\beta)+1)/(\gamma-1))^{1/2} \approx 1.70$. Similarly, the model with $v_\star = 70\,{\rm km\,s^{-1}}$ is such that $M_{\rm A} > ((\gamma(1-\beta)+1)/(\gamma-1))^{1/2}$ whereas our slower model with $v_\star = 20\,{\rm km\,s^{-1}}$ gives $1 < M_{\rm A} \approx 1.16 < ((\gamma(1-\beta)+1)/(\gamma-1))^{1/2}$, which is inside the range in equation (27). We conclude that the upstream ISM conditions in our MHD simulations producing dimpled bow shocks have values consistent with the existence of switch-on shocks [see also sketch of the (β, $M_{\rm A}$) plane in fig. 3 of de Sterck & Poedts (1999)].

However, we cannot affirm that the dimpled apex topology of our MHD bow shock models is of similar origin to the ones in de Sterck et al. (1998) and de Sterck & Poedts (1999). Only their particular concave-inward form that differs from the classical shape of HD bow shocks (Fig. 1e) authorizes a comparison between the two studies. Nevertheless, we notice that our bow shocks are also generated in an ambient medium in which the plasma beta and the Alfvénic Mach number have parameter values consistent with the formation of switch-on shocks, which has been showed to be similar to the parameter values producing dimpled bow shocks around charged obstacles (see de Sterck et al. 1998; de Sterck & Poedts 1999, and references therein). Additional investigations, left for future studies, are required to assess the question of the exact nature the various discontinuities affecting MHD bow shocks of OB stars.

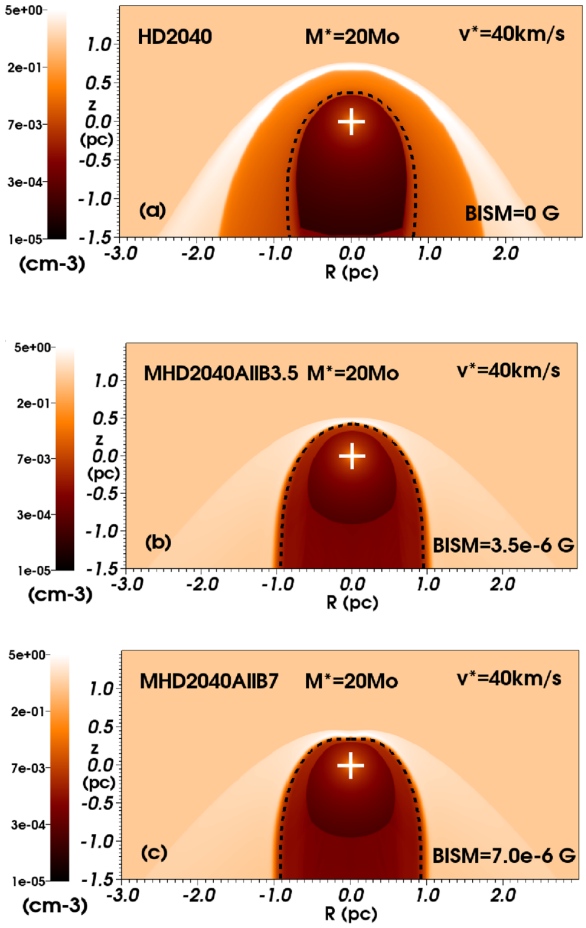

Figure 3. Models of stellar wind bow shocks of our initially 20 $M_\odot$ star moving with velocity $v_\star = 40\,{\rm km\,s^{-1}}$ represented as a function of its ISM magnetic field strength, with $B_{\rm ISM} = 0$ (a), 3.5 (b) and 7.0 μG (c).

3.2.3 *Effects of the magnetic field strength*

Fig. 3 is similar to Fig. 1 and displays the effects of the ISM magnetic field strength $B_{\rm ISM} = 0$ (a), 3.5 (b) and 7.0 μG (c) on the shape of the bow shocks produced by our initially 20 $M_\odot$ star moving with velocity $v_\star = 40\,{\rm km\,s^{-1}}$. In Fig. 4 we show density (solid lines) and temperature (dotted lines) profiles from our HD simulation (thick blue lines) and MHD model (thin red lines) of the bow shocks in Fig. 3. The profiles are taken along the symmetry axis of the computational domain. The global structure of the bow shock is similar for both simulations, i.e. it consists of a hot bubble ($T \approx 10^7$ K) surrounded by a shell of dense ($n \approx 10\,{\rm cm^{-3}}$) shocked ISM gas. The profiles in Fig. 4 highlight the progressive compression of the bow shocks by the ISM total pressure which magnetic component increases as $B_{\rm ISM}$ is larger. Several mechanisms at work might be responsible for such discrepancy:

(i) The magnetic pressure in the ISM. If one neglects the thermal pressures $nk_{\rm B}T$ in both the supersonic stellar wind and the inflowing ISM, and omits the magnetic pressure $\propto B_\star^2 \propto r^{-4}$ at the wind

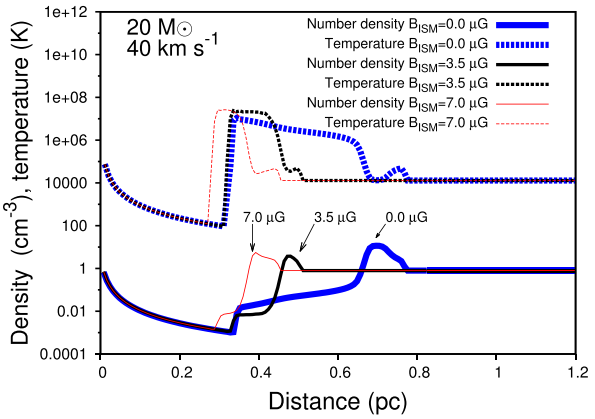

Figure 4. Number density (solid lines, in cm^{-3}) and temperature (dotted lines, in K) profiles in our HD (thick blue lines) and MHD (thin red lines) bow shock models of an initial $20\,\mathrm{M}_{\odot}$ star moving with velocity $v_{\star} = 40\,\mathrm{km\,s}^{-1}$. The profiles are measured along the symmetry axis Oz.

termination shock, then the pressure balance between ISM and stellar wind gas reads

$$\rho_{\mathrm{w}} v_{\mathrm{w}}^2 = \rho_{\mathrm{ISM}} v_{\star}^2 + \frac{B_{\mathrm{ISM}}^2}{8\pi}, \tag{28}$$

from which one can derive the bow shock stand-off distance in a planar-aligned field bow shock,

$$R(0) = \left(\frac{2\dot{M} v_{\mathrm{w}}}{B_{\mathrm{ISM}}^2 + 8\pi \rho_{\mathrm{ISM}} v_{\star}^2} \right)^{1/2}, \tag{29}$$

which is slightly smaller from the one derived in a purely HD context (Wilkin 1996).

(ii) The cooling by optically thin radiative processes. Changes in the density at the post-shock region at the FS influence the temperature in the shocked ISM gas, which in their turn modify the cooling rate of the gas, itself affecting its thermal pressure. This results in not only an increase of the density of the shell of ISM gas but also a decrease of the temperature in the hot region of shocked stellar wind material that shrinks in order to maintain its total pressure equal to $\rho_{\mathrm{ISM}} v_{\star}^2 + B_{\mathrm{ISM}}^2/8\pi$.

(iii) The magnetic field lines inside the bow shock. The compression of the layer of shocked ISM gas modifies the arrangement of the field lines in the post-shock region at the FS. Thus, the term $B_{\mathrm{ISM}}^2/8\pi$ corresponding to the magnetic pressure increases and modifies the effects of radiative cooling in the simulations (see above).

(iv) Symmetry effects. The solution may also be affected by the intrinsic two-dimensional nature of our simulations, which may develop numerical artifices close to the symmetry axis. In the case of MHD simulations of objects moving supersonically along the direction of the ISM magnetic field, such effects are more complex than a simple accumulation of material at the apex of the nebula, but might present artificial shocks (see also Section 3.4).

Appreciating in detail which of the above cited processes dominates the solution would require three-dimensional numerical simulations which are beyond the scope of this work. Moreover, establishing an analytic theory of the position of the contact discontinuity of a magnetized bow shock is a non-trivial task since the thin-shell limit (Wilkin 1996) is not applicable. In particular, the hot bubble loses about three quarter of its size along the Oz direction when the ISM magnetic field strength increases up to $B_{\mathrm{ISM}} = 7\,\mu\mathrm{G}$ (Figs 3a and c). This modifies the volume of hot shocked ISM gas advected thanks to heat transfers towards the inner part of the bow shock of our model HD2040All, reducing it to a narrow layer made of shocked wind material since anisotropic thermal conduction forbids the penetration of ISM gas in the hot region. The effects of the ISM magnetization on our optical and infrared bow shocks' emission properties are further discussed in Section 4.

All of our MHD simulations have a stable density field (Figs 1e–h). The simulations with cooling but without heat transfer (Fig. 1b) show that the presence of the magnetic field inhibits the growth of Kelvin–Helmholtz instabilities (Fig. 1f) that typically develops within the contact discontinuity of the bow shocks because they are the interface of two plasma moving in opposite directions (Comerón & Kaper 1998; van Marle, Langer & García-Segura 2007, Paper I). The solution does not change performing the simulation MHD2040AllB7 at double and quadruple spatial resolution, and conclude that our results are consistent with both numerical studies devoted to the growth and saturation of these instabilities in the presence of a planar magnetic field (see e.g. Keppens et al. 1999) and with results obtained for slow-winded, cool runaway stars moving in a planar-aligned magnetic field (van Marle et al. 2014). Note that detailed numerical studies demonstrating the suppression of shear instabilities by the presence of a background magnetic field also exist in the context of jets from protostars (Viallet & Baty 2007).

3.3 Effects of the star's bulk motion

Fig. 5 is similar to Fig. 3 and plots a grid of density field of our initially $20\,\mathrm{M}_{\odot}$ star moving with velocity $v_{\star} = 20$ (a), 40 (b) and $70\,\mathrm{km\,s}^{-1}$ (c). The scaling effect of the bulk motion of the star on the bow shocks morphology is similar to our HD study (Paper I). At a given strength of the ISM magnetic field, the compression of the FS increases as the spatial motion of the star increases because the ambient medium ram pressure is larger. The relative thickness of the layers of ISM and wind behaves similarly as described in Paper I. Our model with $v_{\star} = 20\,\mathrm{km\,s}^{-1}$ has a layer of shocked ISM larger than the layer of shocked wind because the relatively small ISM ram pressure induces a weak FS (Fig. 5a). The shell of shocked ISM is thinner in our simulation with $v_{\star} = 70\,\mathrm{km\,s}^{-1}$ because the strong FS has a high post-shock temperature which allows an efficient cooling of the plasma (Fig. 5c).

The density field in our models with ISM inflow velocity similar to the Alfvénic speed ($v_{\star} = 20 \simeq v_{\mathrm{A}} \approx 17.2\,\mathrm{km\,s}^{-1}$) has the dimpled shape of its apex of the bow shock (Fig. 5a). The model with $v_{\star} = 70\,\mathrm{km\,s}^{-1}$ has inflow ISM velocity larger than the Alfvénic speed and presents the classical single-front morphology (Fig. 5c) typically produced by stellar wind bow shocks (Brighenti & D'Ercole 1995a,b; Comerón & Kaper 1998; Meyer et al. 2016). A similar effect of the Alfvénic speed is discussed in, e.g. fig. 4 of de Sterck & Poedts (1999). Again, exploring in detail whether the formation mechanisms of our dimpled bow shocks are identical to the ones obtained in calculations of bow shock flow over a conducting sphere is far beyond the scope of this work. Note the absence of instabilities in our MHD bow shock simulations compared to our HD models.

3.4 Model limitation

First and above, our models suffer from their two-dimensional nature. If carrying out axisymmetric models is advantageous in order to decrease the amount of computational resources necessary to

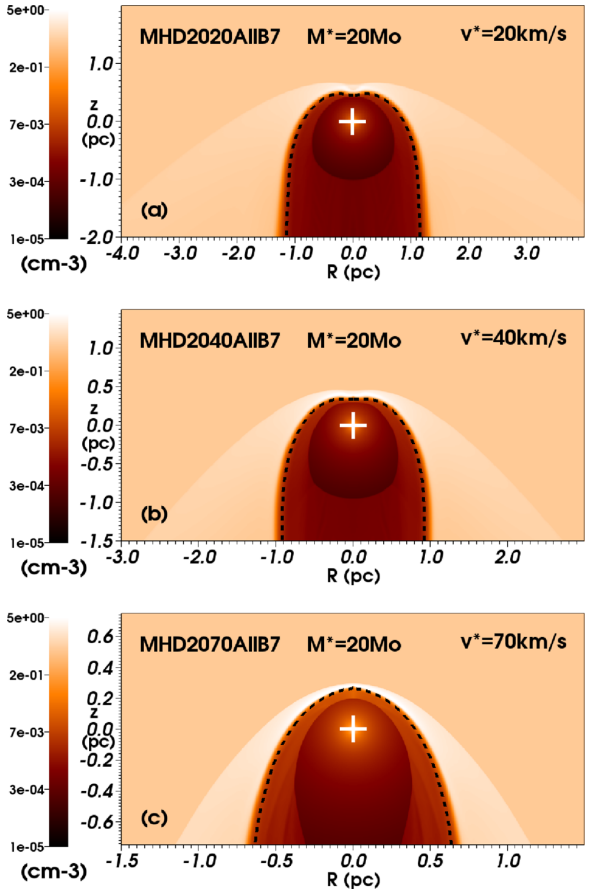

Figure 5. Grid of stellar wind bow shocks from our initially 20 $M_\odot$ star represented as a function of its space velocity with respect to the ISM, with velocity $v_\star = 20$ (a), 40 (b) and 70 km s^{-1} (c). The nomenclature of the models follows Table 2. The bow shocks are shown at about 5 Myr after the beginning of the main-sequence phase of the central star's evolution. All our MHD models assume a strength of the ISM magnetic field $B_{\rm ISM} = 7$ μG. The gas number density is shown with a density range from 10^{-5} to 5.0 cm^{-3} in the logarithmic scale. The crosses mark the position of the star. The solid black contour traces the boundary between wind and ISM material $Q_1(r) = 1/2$. The R-axis represents the radial direction and the z-axis the direction of stellar motion (in pc). Only part of the computational domain is shown in the figures.

perform the simulations, however, it forbids the bow shocks from generating a structure which apex would be totally unaffected by symmetry-axis-related phenomena, common in this case of calculations (Meyer et al. 2016). This prevents our simulations from being able to assess, e.g. the question of the relation between the seeds of the non-linear thin-shell instability at the tip of the structure and the growth of Kelvin–Helmholtz instabilities occurring later in the wings of the bow shocks. Only full 3D models of the same bow shocks could fix such problems and allow us to further discuss in detail the instability of bow shocks from OB stars. We refer the reader to van Marle et al. (2015) for a discussion of the dimension dependence of numerical solutions concerning the interaction of magnetic fields with HD instabilities.

In particular, the selection of admissible shocks, which is generally treated using artificial viscosity in purely HD simulations, is more complex in our MHD context (see discussion in Pogorelov & Matsuda 2000). This can lead to additional fragilities of the solution, especially close to the symmetry axis of our cylindrically symmetric models. Although the stability of these kinds of shocks is still under debate (de Sterck & Poedts 2000, 2001), we will try to address these issues in future three-dimensional simulations. Moreover, such models would (i) allow us to explore the effects of a non-aligned ISM magnetic field on the morphology of the bow shocks and (ii) will make subsequent radiative transfer calculations meaningful, e.g. considering polarization maps using full anisotropic scattering of the photons on the dust particles in the bow shocks. The space of parameters investigated in our study is also limited, especially in terms of the explored range of space velocity $v_\star$ and ISM density $n_{\rm ISM}$ and will be extended in a follow-up project. Finally, other physical processes such as the presence of a surrounding H II region or the intrinsic viscous, granulous and turbulent character of the ISM are also neglected and deserve additional investigations.

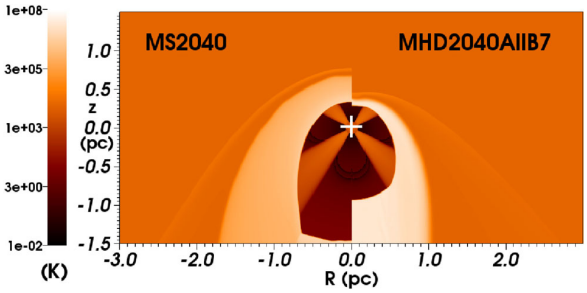

Figure 6. Temperature field (in K) in the models MS2040 and MHD2040AllB7. The cross-like structure in the central region of freely expanding stellar wind is a boundary effect caused by the pressure.

4 COMPARISON WITH OBSERVATIONS AND IMPLICATIONS OF OUR RESULTS

In this section, we extract observables from our simulations, compare them to observations and discuss their astrophysical implications. We first recall the used post-processing methods and then compare the emission by optically thin radiation of our MHD bow shocks with HD models of the same star moving at the same velocity. Given the high temperature generated by collisional heating (Fig. 6), we particularly focus on the Hα and [O III] λ 5007 optical emission. Moreover, stellar wind bow shocks from massive stars have been first detected at these spectral lines and hence constitute a natural observable. We complete our analysis with infrared radiative transfer calculations and comment on the observability of our bow shock nebulae. Finally, we discuss our findings in the context of the runaway massive star ζ Ophiuchi.

4.1 Post-processing methods

Fig. 7 plots the projected optical emission of our model of an initially 20 $M_\odot$ star moving at 40 km s^{-1} in Hα (a) and [O III] λ 5007 (b) in erg s^{-1} cm^{-2} arcsec^{-2}. The left-hand part of the panels corresponds to the star moving into an ISM with no background magnetic field (HD model MS2040, Paper I) whereas right-hand parts correspond to $B_{\rm ISM} = 7$ μG (MHD model MHD2040AllB7). We take into account the rotational symmetry about $R = 0$ of our models and integrate the emission rate assuming that our bow shocks lay in the plane of the sky, i.e. the star moves perpendicular to the

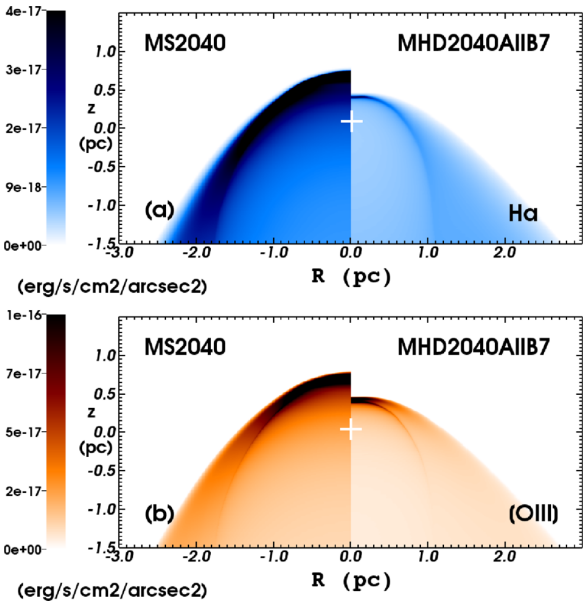

Figure 7. Surface brightness maps of Hα (a), [O III] (b) surface brightness (in erg s^{-1} cm^{-2} arcsec^{-2}), respectively, of our bow shock model generated by our initially 20 M$_\odot$ star moving with velocity $v_\star = 40$ km s^{-1}. Quantities are calculated excluding the undisturbed ISM and plotted in the linear scale. The left-hand part of the panels refers to the HD model MS2040, and the right-hand part to the MHD model MHD2040AllB7. The crosses mark the position of the star. For the sake of comparison, these optical maps are presented as in Paper I.

observers' line-of-sight. The spectral line emission coefficients are evaluated using the prescriptions for optical spectral line emission from Dopita (1973) and Osterbrock & Bochkarev (1989), which read

$$j_{[\mathrm{H}\alpha]}(T) \approx 1.21 \times 10^{-22} T^{-0.9} n_\mathrm{p}^2 \,\mathrm{erg\,s^{-1}\,cm^{-3}\,sr^{-1}}, \tag{30}$$

where n_p is the number of proton in the plasma, and,

$$j_{[\mathrm{O\,III}]}(T) \approx 3.23 \times 10^{-21} \frac{\mathrm{e}^{-\frac{28737}{T}}}{4\pi\sqrt{T}} n_\mathrm{p}^2 \,\mathrm{erg\,s^{-1}\,cm^{-3}\,sr^{-1}}, \tag{31}$$

for the Hα and [O III] λ 5007 spectral lines, respectively. Additionally, we assume solar oxygen abundances (Lodders 2003) and cease to consider the oxygen as triply ionized at temperatures larger than 10^6 K (cf. Cox, Gull & Green 1991).

The bow shock luminosities L are estimated integrating the emission rate,

$$L = 2\pi \iint_{\mathcal{D}} \Lambda(T) n_\mathrm{H}^2 R\,dR\,dz, \tag{32}$$

where $\mathcal{D}$ represents its volume in the $z > 0$ part of the computational domain (Mohamed et al. 2012, Paper I). Similarly, we calculate the momentum deposited by the bow shock by subtracting the stellar motion from the ISM gas velocity field. We compute $L_{\mathrm{H}\alpha}$ and $L_{[\mathrm{O\,III}]}$, the bow shock luminosity in [O III] λ 5007 and Hα, respectively. Furthermore, we discriminate the total bow shock luminosity L_total from the shocked wind emission L_wind. For distinguishing the two kinds of material, we make use of a passive scalar Q that is advected with the gas. We estimate the overall X-ray luminosity L_X with emission coefficients generated with the XSPEC program (Arnaud 1996) with solar metallicity and chemical abundances from Asplund et al. (2009). Moreover, the total infrared emission L_IR is estimated as a fraction of the starlight bolometric flux $L_\star$ (Brott et al. 2011) intercepted by the ISM silicate dust grains in the bow shock,

$$\Gamma_\star^\mathrm{dust} = \frac{L_\star}{4\pi d^2} n_\mathrm{d} \sigma_\mathrm{d} (1 - A) \,\mathrm{erg\,s^{-1}\,cm^{-3}}, \tag{33}$$

plus the collisional heating,

$$\Gamma_\mathrm{coll,photo}^\mathrm{dust}(T) = \frac{2^{5/2} f Q n n_\mathrm{d} \sigma_\mathrm{d}}{\sqrt{\pi m_\mathrm{p}}} (k_\mathrm{B} T)^{3/2} \,\mathrm{erg\,s^{-1}\,cm^{-3}}, \tag{34}$$

where $a = 5.0$ nm is the dust grains radius,

$$\sigma_\mathrm{d} = \pi a^2 \,\mathrm{cm}^2 \tag{35}$$

is their geometrical cross-section, d their distance from the star and $A = 1/2$ their albedo. Additionally, n_d is the dust number density whereas $Q \simeq 1$ represents the grains electrical properties. More details regarding to the estimate of the bow shock infrared luminosity are given in appendix B of Paper I.

Last, infrared images are computed performing dust continuum calculations against dust opacity for the bow shock generated by our 20 M$_\odot$ star moving with velocity 40 km s^{-1}, using the radiative transfer code RADMC-3D[2] (Dullemond 2012). We map the dust mass density fields in our models on to a uniform spherical grid [0; R_sph] $\times$ [0; θ_max], where $R_\mathrm{sph} = (R_\mathrm{max}^2 + z_\mathrm{max}^2)^{1/2}$ and $\theta_\mathrm{max} = 180^\circ$. We assume a dust-to-gas mass ratio of 1/200. The dust density field is computed with the help of the passive scalar tracer Q that allows us to separate the dust-free stellar wind of our hot OB stars with respect to the dust-enriched regions of the bow shock, made of shocked ISM gas. Additionally, we exclude the regions of ISM material that are strongly heated by the shocks or by electronic thermal conduction (Paper I), and which are defined as much hotter than about a few 10^4 K. RADMC-3D then self-consistently determines the dust temperature using the Monte Carlo method of Bjorkman & Wood (2001) and Lucy (1999) that we use as input to the calculations of our synthetic observations.

The code solves the transfer equation by ray-tracing photons packages from the stellar atmosphere that we model as a blackbody point source of temperature T_eff (see our Table 1) that is located at the origin of the spherical grid. The dust is assumed to be composed of silicates (Draine & Lee 1984) of mass density 3.3 g cm^{-3} that follow the canonical power-law distribution $n(a) \propto a^{-q}$ with $q = -3.3$ (Mathis, Rumpl & Nordsieck 1977) and where $a_\mathrm{min} = 0.005$ µm and $a_\mathrm{max} = 0.25$ µm, the minimal and maximal dust sizes (van Marle et al. 2011). We generate the corresponding RADMC-3D input files containing the dust scattering κ_scat and absorption κ_abs opacities such that the total opacity $\kappa_\mathrm{tot} = \kappa_\mathrm{scat} + \kappa_\mathrm{abs}$ (see Fig. 9a) on the basis of a run of the Mie code of Bohren and Huffman (Bohren & Huffman 1983), which is available as a module of the HYPERION[3] package (Robitaille 2011). Our radiative transfer calculations produce spectral energy distributions (SEDs) and isophotal images of the bow shocks at a desired wavelength, which we choose to be $\lambda =$ 24 and 60 µm because they correspond to the wavelengths at which stellar wind bow shocks are typically observed [see Sexton et al. (2015) and van Buren & McCray (1988a), van Buren et al. (1995), Noriega-Crespo et al. (1997a), respectively]. Our SEDs and images are calibrated as such that we consider that the objects are located at a distance 1 pc from the observer.

[2] http://www.ita.uni-heidelberg.de/dullemond/software/radmc-3d/
[3] http://www.hyperion-rt.org/

Table 4. Maximum optical surface brightness of our MHD simulations with $B_{\rm ISM} = 7$ μG. The second and third columns are the quantities $\Sigma^{\rm max}_{\rm [H\alpha]}$ and $\Sigma^{\rm max}_{\rm [O\,III]}$ representing the maximum projected emission in [O III] λ 5007 and Hα (in erg cm^{-2} s^{-1} arcsec^{-2}), respectively. Models consisting of the HD counterpart of our bow shock models have their labels in italic in the first column (see description in table 1 in Paper I). The surface brightnesses are measured along the direction of motion of the star at the apex of our bow shocks, close to the symmetry axis Oz.

Model	$\Sigma^{\rm max}_{\rm [H\alpha]}$ (erg cm^{-2} s^{-1} arcsec^{-2})	$\Sigma^{\rm max}_{\rm [O\,III]}$ (erg cm^{-2} s^{-1} arcsec^{-2})	$\Sigma^{\rm max}_{\rm [H\alpha]}/\Sigma^{\rm max}_{\rm [H\alpha]}$
MHD1040AllB7	2.5×10^{-19}	7.0×10^{-18}	28.0
MS1040	1.0×10^{-18}	2.5×10^{-17}	25.0
MHD2020AllB7	1.7×10^{-17}	6.8×10^{-17}	4.0
MS2020	6.0×10^{-17}	7.2×10^{-17}	1.2
MHD2040AllB7	2.9×10^{-17}	1.6×10^{-16}	5.5
MHD2040AllB3.5	1.0×10^{-16}	3.2×10^{-16}	3.2
MS2040	1.2×10^{-16}	2.5×10^{-16}	2.1
MHD2070AllB7	8.0×10^{-18}	2.0×10^{-16}	25.0
MS2070	1.5×10^{-16}	8.5×10^{-16}	5.7
MHD4070AllB7	1.2×10^{-17}	5.5×10^{-16}	45.8
MS4070	4.0×10^{-16}	1.0×10^{-15}	2.5

4.2 Results: optically thin emission

In Table 4 we report the maximum surface brightness measured along the direction of motion of the stars in the synthetic emission maps build from our models at both the Hα and [O III] λ 5007 spectral line emission. We find that the presence of an ISM magnetic field makes the Hα signatures fainter by about 1–2 orders of magnitudes whereas the [O III] λ 5007 emission maps are about 1 order of magnitude fainter, respectively. The luminosity of stellar wind bow shocks is a volume integral (Paper I) and this volume decreases when a large ISM magnetic pressure compresses the nebula (Figs 1d and h). Thus, their surface brightness is fainter despite the fact that the density and temperature of their shocked regions are similar (Fig. 4).

The ratio of our bow shock models' maximum [O III] and Hα maximum surface brightness increases in the presence of the magnetic field, e.g. the HD model MS2040 has $\Sigma^{\rm max}_{\rm [O\,III]}/\Sigma^{\rm max}_{\rm [H\alpha]} \approx 2.1$ whereas our model MHD2040AllB7 has $\Sigma^{\rm max}_{\rm [O\,III]}/\Sigma^{\rm max}_{\rm [H\alpha]} \approx 5.5$ if $B_{\rm ISM} = 7$ μG. We notice that the spectral line ratio $\Sigma^{\rm max}_{\rm [O\,III]}/\Sigma^{\rm max}_{\rm [H\alpha]}$ augments with the increasing space velocity of the star, e.g. our models MHD2020B7, MHD2040AllB7 and MHD2070B7 have $\Sigma^{\rm max}_{\rm [O\,III]}/\Sigma^{\rm max}_{\rm [H\alpha]} \approx 4.0$, 5.5 and 25.0, respectively. This difference between [O III] λ 5007 and Hα emission is more pronounced in our MHD simulations. As for our HD study, the region of maximum emission peaks close to the contact discontinuity in the layer of shocked ISM material, in the region of the stagnation shock (Paper I, see also Figs 7a and b).

The ISM magnetic field does not change the order relations we previously established with HD bow shocks generated by main-sequence stars (fig. 13 a in Paper I), i.e. $L_{\rm wind} < L_{\rm H\alpha} < L_{\rm total} < L_{\rm IR}$ (see orange dots, blue crosses of Saint-Andrew, dark green triangles and black squares in Fig. 8a, respectively). Additionally, as discussed above in the context of projected emission maps, we find that the optical spectral line emission that we consider is such that $L_{\rm [O\,III]} > L_{\rm H\alpha}$. This confirms and extends to MHD bow shocks, a result previously obtained by integrating the optically thin emission in the range $8000 \leq T \leq 10^6$ K (Paper I). Our MHD bow shock models have Hα and [O III] emission originating from the shocked ISM gas and their emission from the wind material is negligible ($L_{\rm total}/L_{\rm wind} \approx 10^{-6}$). Moreover, we find that the bow shock X-rays

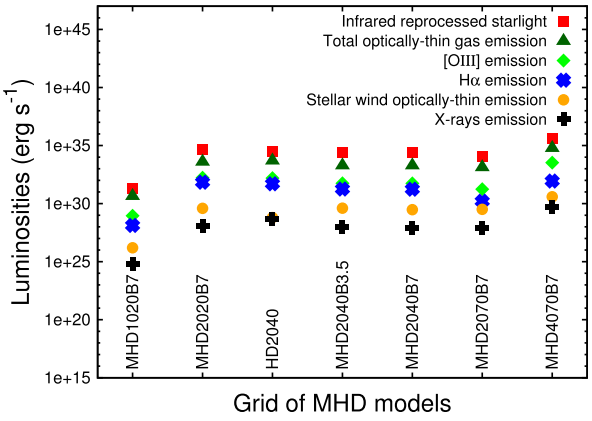

Figure 8. Bow shock luminosities and feedback of our MHD models. We separate the infrared reprocessed starlight (red squares, in erg s^{-1}) and distinguish the total emission by optically thin radiation from the bow shock (dark-green triangles, in erg s^{-1}) from the emission from the shocked wind material only (orange dots, in erg s^{-1}). Additionally, we show the luminosity from [O III] λ 5007 emission (green losanges, in erg s^{-1}), the luminosity from Hα emission (blue crosses, in erg s^{-1}) and the X-rays luminosity in both the soft and hard energy bands $E > 0.5$ eV ($T > 5.8 \times 10^6$ K). For the sake of comparison, we add the feedback of the HD model HD2040 corresponding to $B_{\rm ISM} = 0$ μG (originally published in Paper I). The simulation labels are indicated under the corresponding values.

emission is very small in all our simulations ($L_{\rm X}/L_{\rm wind} \approx 10^{-1}$, see black crosses in Fig. 8a).

4.3 Results: dust continuum infrared emission

4.3.1 Spectral energy distribution

Fig. 9(b) plots a comparison between the SEDs of two bow shock models generated by our 20 $M_\odot$ star moving with velocity 40 km s^{-1}, either through an unmagnetized ISM (model MS2040, solid blue line) or in a medium with $B_{\rm ISM} = 7$ μG (model MHD2040AllB7, dotted red line) for a viewing angle of the nebulae of $\phi = 0°$. The figure represents the flux density F_λ (in Jy) as a function of the wavelength λ (in μm) for the waveband including the $0.01 \leq \lambda \leq 2000$ μm. The star is responsible for the component in the range $0.01 \leq \lambda \leq 10$ μm that corresponds to a blackbody spectrum of temperature $T_{\rm eff} = 33\,900$ K (see Table 1) while the circumstellar dust produces the feature in the waveband $10 \leq \lambda \leq 2000$ μm. The bow shock's component is in the waveband including the wavelengths at which stellar wind bow shock are typically recorded, e.g. at 60 μm (van Buren & McCray 1988a; van Buren et al. 1995; Noriega-Crespo et al. 1997a).

The SED of the magnetized bow shock has a slightly larger flux than the SED of the HD bow shock in the waveband $10 \leq \lambda \leq 30$ μm, because its smaller size makes the shell of dense ISM gas closer to the star, increasing therefore the dust temperature (Fig. 9b). At $\lambda \approx 30$ μm, the HD bow shock emits by slightly more than half an order of magnitude than the magnetized nebula, e.g. at $\lambda \approx 60$ μm our model MS2040 has a density flux $F_\lambda \approx 3 \times 10^{-1}$ Jy whereas our model MHD2040AllB7 shows $F_\lambda \approx 1 \times 10^{-1}$ Jy, respectively. This is consistent with the previously discussed reduction of the projected optical emission of our bow shocks. This relates to the changes in size of the nebulae induced by the inclusion of the magnetic field in our simulations, which reduces the mass of dust in the structure responsible for the reprocessing of the starlight, e.g. our models

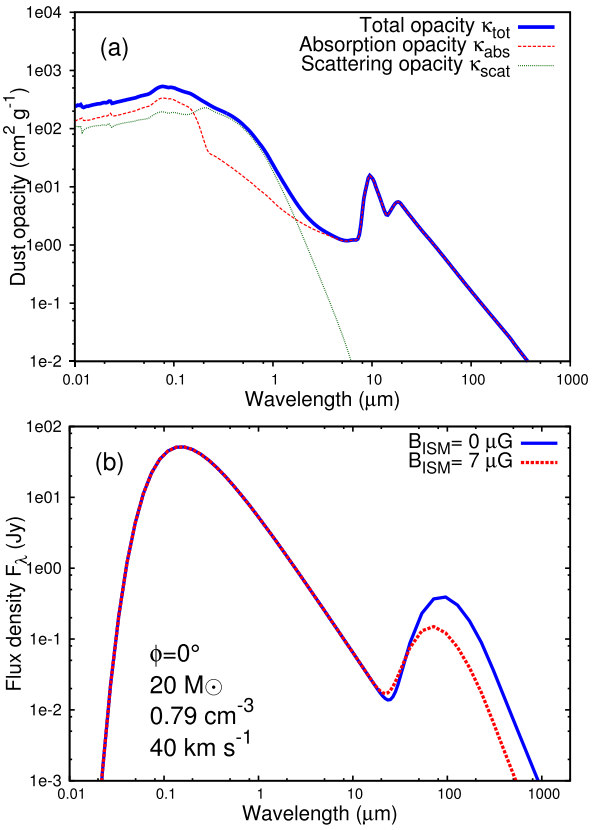

Figure 9. Top panel: dust opacities used in this study, inspired from Acreman et al. (2016). The figure shows the total opacity κ_{tot} (blue solid thick line), the absorption opacity κ_{abs} (red dotted thin line) and the scattering opacity κ_{scat} (green dashed thin line). Bottom panel: SEDs of our model involving a 20 $M_\odot$ star moving with a velocity of 40 km s^{-1}, considered in the HD (model MS2040 with $B_{ISM} = 0$ μG, solid blue line) and in the MHD contexts (model MHD2040AllB7 with $B_{ISM} = 7$ μG, dotted red line). The plot shows the flux density F_λ (in Jy) as a function of the wavelength λ (in μm) for an inclination angle $\phi = 0°$ of the bow shock.

MS2040 and MHD2040AllB7 contain about $M_d \approx 3 \times 10^{-2}\,M_\odot$ and $M_d \approx 2 \times 10^{-3}\,M_\odot$, respectively, where M_d is the dust mass trapped into the nebulae. The reduced mass of dust into the magnetized bow shock absorbs a lesser amount of the stellar radiation and therefore re-emits a smaller quantity of energy, reducing F_λ in the waveband $\lambda \geq 30$ μm (Fig. 9b). Note that the infrared surface brightness of a bow shock is also sensible to the density of its ambient medium, i.e. F_λ is much larger in the situation of a runaway star moving in a medium with $n_{ISM} \simeq 1000$ cm^{-3} (Acreman et al. 2016).

4.3.2 Synthetic infrared emission maps

Our Fig. 10 plots a series of synthetic infrared emission maps of our bow shock models produced by an initially 20 $M_\odot$ star moving with velocity 40 km s^{-1} in its purely HD (MS2040) or MHD configuration (MHD2040AllB7) at the wavelengths corresponding to the central wavelengths of the *IRAS* facility's main broad-band images (van Buren & McCray 1988b), i.e. $\lambda = 25$ μm (left column of panels), 60 μm (middle column of panels) and 100 μm (right column of panels). The maps are represented with an inclination angle of $\phi = 30°$ (Figs 10a, e and i), 45° (Figs 10b, f and j), 60° (Figs 10c, g and k) and 90° (Figs 10d, h and l) with respect to the plane of the sky and the projected flux is plotted in units of erg s^{-1} cm^{-2} arcsec^{-2}. As in the context of their optical emission (Fig. 7), the overall size of the infrared magnetized bow shocks is smaller than in the HD case because of the reduction of their stand-off distance $R(0)$ (see e.g. Figs 10a, e and j). The global morphology of our infrared bow shock nebulae does not change significantly. It remains a single, bright arc at the front of an ovoid structure that is symmetric with respect to the direction of motion of the runaway star and extended to the trail ($z \leq 0$) of the bow shocks due to the supersonic motion of the star (Acreman et al. 2016). In the HD case, the region of maximum emission is the region containing the ISM dust, the temperature of which is less than a few 10^4 K, i.e. between the contact discontinuity and the FS of the bow shock (Paper I; Acreman et al. 2016) whereas in the magnetized case, the maximum emission is reduced to a thin region close to the discontinuity between hot stellar wind and colder ISM. Both the shocked stellar wind and the shocked ISM of the bow shock do not contribute to these emission because the material is too hot.

Fig. 11 reports cross-sections taken along the direction of motion of the bow shock and comparing their surface brightnesses at several wavebands λ and viewing angles ϕ. It illustrates that, as in the case of the optical emission, the presence of the ISM magnetic field makes the bow shocks slightly dimmer, e.g. for $\phi = 45°$ our model has a maximal surface brightness of $\Sigma^{max}_{100\,\mu m} \approx 4.3 \times 10^{-17}$ erg s^{-1} cm^{-2} arcsec^{-2} whereas $\Sigma^{max}_{100\,\mu m} \approx 2.6 \times 10^{-17}$ erg s^{-1} cm^{-2} arcsec^{-2} for $B_{ISM} = 0$ and 7 μG, respectively. Fig. 12 shows different cross-sections of the projected infrared emission of the magnetized bow shock of our initially 20 $M_\odot$ star moving with velocity $v_\star = 40$ km s^{-1}. The emission at $\lambda = 60$ μm is more important that at $\lambda = 25$ μm and at $\lambda = 100$ μm, e.g. it peaks at $\Sigma^{max}_{60\,\mu m} \approx 8.2 \times 10^{-17}$ erg s^{-1} cm^{-2} arcsec^{-2} whereas $\Sigma^{max}_{25\,\mu m} \approx 2.6 \times 10^{-17}$ erg s^{-1} cm^{-2} arcsec^{-2} and $\Sigma^{max}_{100\,\mu m} \approx 3.0 \times 10^{-17}$ erg s^{-1} cm^{-2} arcsec^{-2}, respectively, at a distance of 0.55 pc from the star and assuming an inclination angle of the bow shock of $\phi = 45°$ (Fig. 12a). All our models have similar behaviour of their infrared surface brightness as a function of λ and ϕ. Note also that the evolution of the position of the stand-off distance of the bow shock is consistent with the study of Acreman et al. (2016) in the sense that it increases at larger ϕ (Fig. 12b).

4.4 Implications of our results and discussion

4.4.1 Bow shocks Hα and [OIII] observability

The surface brightnesses at Hα and [O III] λ 5007 spectral line emission of our stellar wind bow shocks reported in Section 4.4.4 indicate that (i) the presence of the ISM magnetic field makes their projected emission $\Sigma_{H\alpha}$ and $\Sigma_{[O\,III]}$ fainter by 2 and 1–2 orders of magnitude and (ii) that this reduction of the nebulae's emission is more important as the strength of the B field is larger. Consequently, the emission signature of a purely HD bow shock model that is above the diffuse emission sensitivity threshold of, e.g. the SuperCOSMOS H-Alpha Survey (SHS) of $\Sigma_{SHS} \approx 1.1$-2.8×10^{-17} erg s^{-1} cm^{-2} arcsec^{-2} can drop down below it once the ISM magnetic field is switched-on. As an example, our HD model of a 20 $M_\odot$ star moving with velocity $v_\star = 70$ km s^{-1} (Paper I) could be observed since it has $\Sigma_{H\alpha} \approx 1.5 \times 10^{-16} \geq \Sigma_{SHS}$ whereas

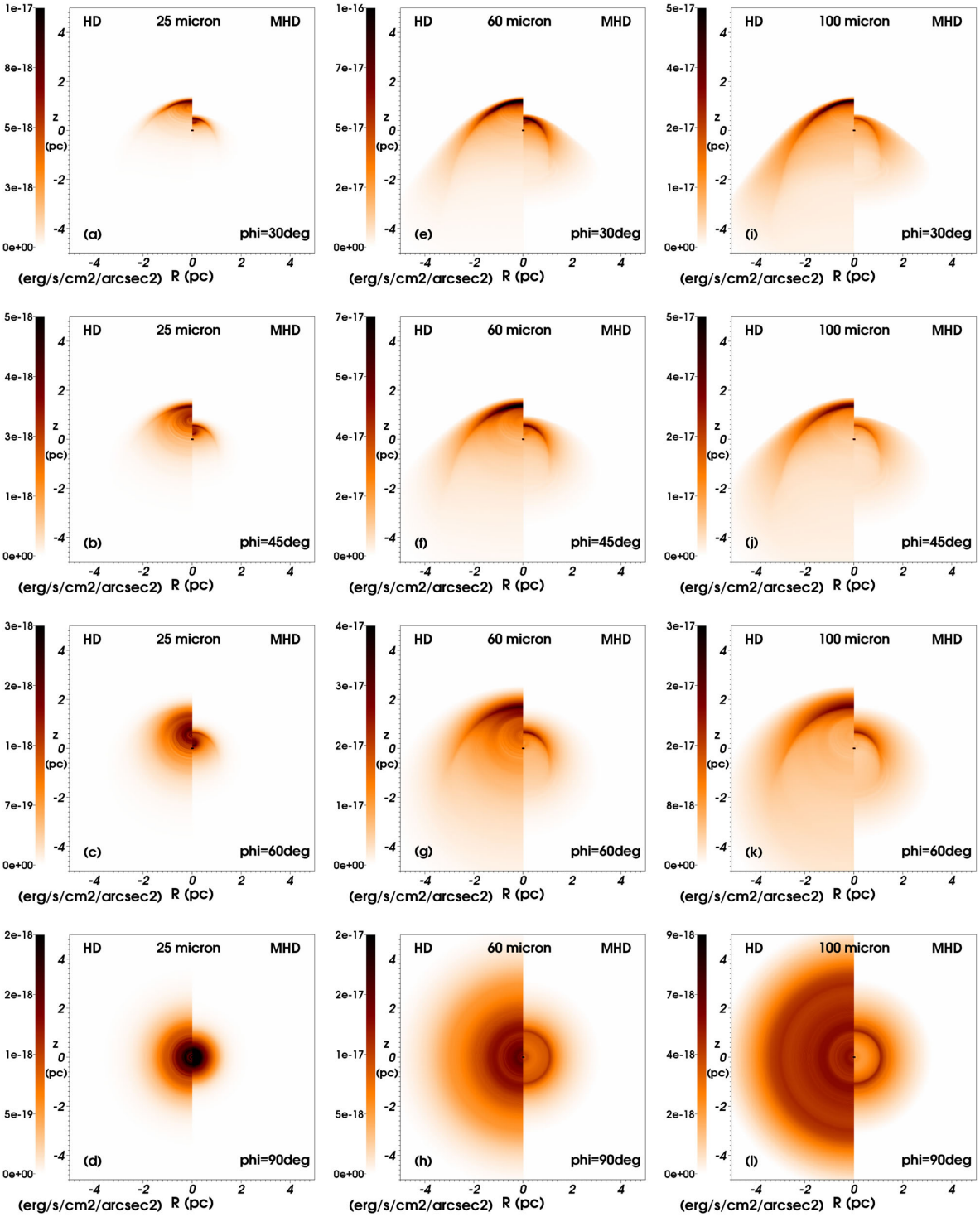

Figure 10. Isophotal infrared emission maps of our bow shock models MS2040 and MHD2040AllB7. It represents our initially 20 $M_\odot$ star moving with velocity 40 km s^{-1} as seen at wavelengths $\lambda = 25$ (a–d), 60 μm (e–h) and 100 μm (i–l). The projected flux is in units of erg s^{-1} cm^{-2} arcsec^{-2}. The maps are generated with an inclination angle of $\phi = 30$ (a,e,i), 45 (b,f,j), 60 (c,g,k) and 90° (d,h,l) with respect to the plane of the sky. For each panel, the surface brightness is plotted in the linear scale and its maximum corresponds to the maximum of the HD (left) and MHD bow shock models (right).

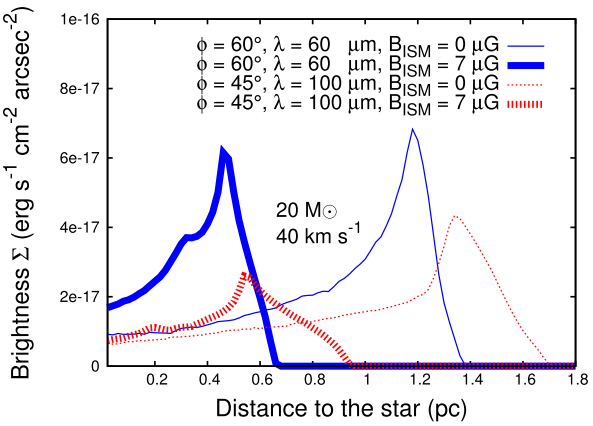

Figure 11. Cross-sections taken through the direction of motion of the bow shock of our initially 20 $M_\odot$ star moving in a medium with velocity $v_\star = 40\,\mathrm{km\,s^{-1}}$, both in a medium with $B_{\rm ISM} = 0$ and 7 μG. The emission are shown for a viewing angle of $\phi = 45^\circ$ and at the waveband $\lambda = 60$ μm (dotted red curves) and for $\phi = 60^\circ$ at $\lambda = 100$ μm (solid blue curves). The surface brightness (in $\mathrm{erg\,s^{-1}\,cm^{-2}\,arcsec^{-2}}$) is plotted as a function of the distance to the star (in pc). The position of the star is located at the origin.

our MHD model of the same runaway star has $\Sigma_{\rm H\alpha} \approx 8.0 \times 10^{-18} \ll \Sigma_{\rm SHS}$ and would be invisible with regard to the SHS facility (our Table 4).

This may explain why not so many stellar wind bow shocks are discovered at Hα around isolated, hot massive stars, despite the fact the ionization of their circumstellar medium must produce such emission (Brown & Bomans 2005). Since $\Sigma_{\rm H\alpha} \propto n^2$ (see appendix A of Paper I), it implies that the more diluted the ISM constituting the surrounding of an exiled star, i.e. the higher the runaway star's Galactic latitude, the smaller the probability to observe its bow shock at Hα. In other words, the search for bow shocks at this wavelength may work well within the Galactic plane or in relatively dense regions of the ISM. Note also that in the presence of the magnetic field, all models have $\Sigma_{\rm [OIII]}/\Sigma_{\rm H\alpha} > 1$, which is consistent with the discovery of the first bow-shock-producing massive stars ζ Ophiuchi in [O III] λ 5007 emission.

4.4.2 *Surrounding H II region and dust composition*

Massive stars release huge amount of ultraviolet photons (Diaz-Miller, Franco & Shore 1998) that ionize the hydrogen constituting their surroundings (Dyson 1975), giving birth to an H II region overwhelming the stellar wind bubble of the star (Weaver et al. 1977; van Marle 2006). In the case of a runaway star, the stellar motion produces a bow shock surrounded by a cometary H II region (Raga 1986; Mac Low et al. 1991; Raga et al. 1997; Arthur & Hoare 2006; Zhu et al. 2015), the presence of which in our study is simply taken into account assuming that the ambient medium of the star is fully ionized; however, we neglect its turbulent internal structure. The gas that is between the FS of the bow shock and the outer part of the H II region is filled by ISM dust that emits infrared thermal emission by efficiently reprocessing the stellar radiation, i.e. it is brighter than the emission by gas cooling (Paper I).

While our study shows that our nebulae are brighter at 60 μm (Fig. 12), i.e. at the waveband at which catalogues of bow shocks from OB stars have been compiled (van Buren & McCray 1988a; van Buren et al. 1995; Noriega-Crespo et al. 1997a), the study of Mackey et al. (2016) compared the respective brightnesses of the front of a distorted circumstellar bubble with the outer edge of its surrounding H II region and find the 24 μm waveband to be ideal to observe the structure generated by the stellar wind. However, the presence of the ISM background magnetic field makes our infrared arc smaller and slightly dimmer, i.e. more difficult to detect in the case of a distant runaway star which could explain why a large proportion of observed H II regions do not contain dust-free cavities encircled with bright mid-infrared arcs (Sharpless 1959; Churchwell et al. 2006; Wachter et al. 2010; Simpson et al. 2012). Further radiation magneto-hydrodynamic simulations are required to fully assess the question of the infrared screening of stellar wind bow shocks by their own H II regions, particularly for an ambient medium corresponding to the Galactic plane ($n_{\rm ISM} \simeq 1\,\mathrm{cm^{-3}}$).

Following Pavlyuchenkov, Kirsanova & Wiebe (2013), we consider that the dust filling the H II region and penetrating into the bow shock is similar to that of the ISM. Our radiative transfer calculations nevertheless suffer from uncertainties regarding to the composition of this ISM dust. Our mixture is made of silicates (Draine & Lee 1984), which could be modified, e.g. changing the

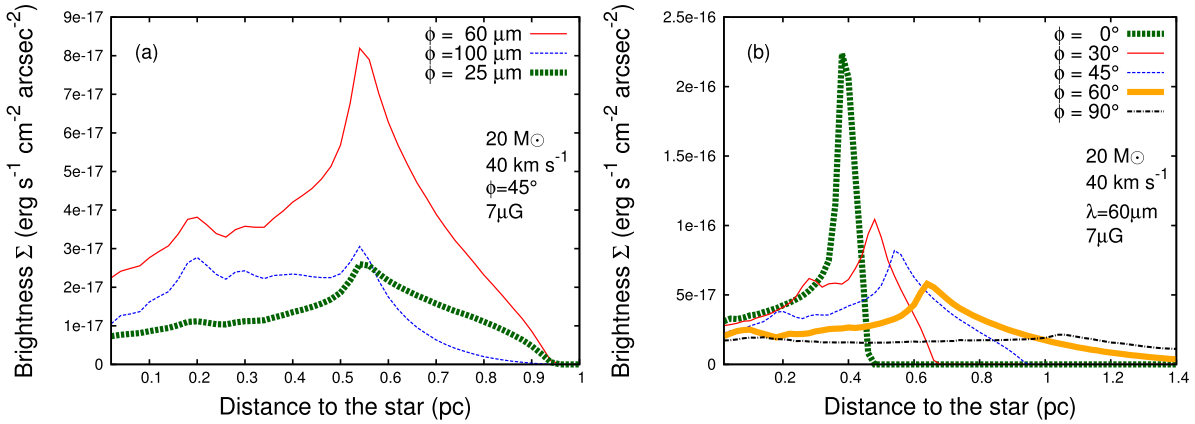

Figure 12. Cross-sections taken through the direction of motion of the bow shock of our initially 20 $M_\odot$ star moving in a medium with $B_{\rm ISM} = 7$ μG with velocity $v_\star = 40\,\mathrm{km\,s^{-1}}$. The emission is shown for the principal broad-band images of the *IRAS* telescope for a viewing angle $\phi = 45^\circ$ (a) and for the wavelength $\lambda = 60$ μm as a function of different viewing angle ϕ (b). The surface brightness (in $\mathrm{erg\,s^{-1}\,cm^{-2}\,arcsec^{-2}}$) is plotted as a function of the distance to the star (in pc). The position of the star is located at the origin.

Figure 13. *WISE* 3.4 μm (band *W1*, Wright et al. 2010) of the stellar wind bow shock surrounding the massive runaway O9.5 V star ζ Ophiuchi. The image represents about 35 arcmin in the horizontal direction, which at a distance of 112 pc corresponds to about 1.12 pc.

slope of the dust size distribution. Particularly, the inclusion of very small grains such as polycyclic aromatic hydrocarbon (PAHs; see Wood et al. 2008) may be an appropriate update of the dust mixture, as it has been shown to be necessary to fit observations of mid-infrared bow shocks around O stars in dense medium in M17 and RCW 49 (Povich et al. 2008). Enlarging our work in a wider study, e.g. scanning the parameter space of the quantities governing the formation of Galactic stellar wind bow shocks ($v_\star$, $n_{\rm ISM}$, $M_\star$) in order to discuss both their SEDs and infrared images, will be considered in a follow-up paper, e.g. performing a systematic post-processing of the grid of bow shock simulations of Meyer et al. (2016) with RADMC-3D. Then, thorough comparison of numerical simulations with, e.g. the *IRAS* observations of van Buren & McCray (1988a), van Buren et al. (1995), Noriega-Crespo et al. (1997a) would be achievable.

4.4.3 Shaping of the circumstellar medium of runaway massive stars at the pre-supernova phase

It has been shown in the context of Galactic, high-mass runaway stars that the pre-shaped circumstellar medium in which these stars die and explode as a Type II supernova is principally constituted of its own main-sequence wind bubble, distorted by the stellar motion. Further evolutionary phase(s) produces additional bubble(s) and/or shell(s) whose evolution is contained inside the initial bow shock (Brighenti & D'Ercole 1994, 1995a). The expansion of the subsequent supernova shock wave is strongly impacted by the progenitor's pre-shaped circumstellar medium inside which it develops initially (see e.g. Cox et al. 1991). Particularly, the more well-defined and stable the walls of the tunnel formed by the RS of the bow shock are, the easier the channelling the supernovae ejecta inside it (see in particular appendix A of Meyer et al. 2015, and references therein).

Our study shows that the presence of background ISM magnetic field aligned with the direction of motion of a main-sequence runaway star inhibits the growth of both shear instabilities that typically affect these circumstellar structures (Fig. 1). Consequently, a planar-aligned magnetic field would further shape the RS of moving stars' bow shocks as a smooth tube in which shocks waves could be channelled as a jet-like extension, e.g. as in Cox et al. (1991). Additionally, the shock wave colliding with the FS of circumstellar structures of runaway stars that are sufficiently dense to make their subsequent supernova remnant asymmetric (Meyer et al. 2015) would be more collimated along the direction of motion of its progenitor and/or ambient magnetic field. This may produce additional asymmetries to the elongated shape of supernova remnants exploding in a magnetized ISM (Rozyczka & Tenorio-Tagle 1995).

4.4.4 The case of the hot runaway star ζ Ophiuchi

The O9.5 V star ζ Ophiuchi is the Earth's closest massive, main-sequence runaway star. Infrared observations, e.g. with the *WISE* 3.4 μm facility (band *W1*, Wright et al. 2010, see Fig. 13[4]) highlighted the complex topology of its stellar wind bow shock, originally discovered in [O III] λ 5007 spectral line (Gull & Sofia 1979) and further observed in the infrared waveband (van Buren & McCray 1988b). The properties of the particular, non-axisymmetric shape of its circumstellar nebula which moves in the H II region Sh 2-27 (Sharpless 1959) are studied in a relatively large literature (see Mackey, Langer & Gvaramadze 2014a,

[4] http://wise2.ipac.caltech.edu/docs/release/allsky/

and references therein). The mass loss of ζ Ophiuchi has been estimated in the range $\dot{M}_\zeta \approx 1.58 \times 10^{-9}$–$1.43 \times 10^{-7}\,\mathrm{M_\odot\,yr^{-1}}$ (Gvaramadze, Langer & Mackey 2012), which, according to equation (21), taking $R(0) \approx 0.16$ pc (Gvaramadze et al. 2012), adopting $v_\star \approx 26.5\,\mathrm{km\,s^{-1}}$ and considering a typical OB star wind velocity of $v_\mathrm{w} \approx 1500\,\mathrm{km\,s^{-1}}$, constrains its ambient medium density to $n_\zeta \approx 3$-$4\,\mathrm{cm^{-3}}$ (cf. Gull & Sofia 1979).

Assuming (i) the magnetization of the close surrounding of ζ Ophiuchi to be $B_\mathrm{ISM} = 7\,\mu$G (Mackey et al. 2014a), (ii) that the conditions for switch-on shocks to be permitted are fulfilled, i.e. plasma and Alfvénic velocities are normal to the shock, and (iii) considering that its ISM properties are, in addition to the above presented quantities, such that $\gamma = 1.67$, $T_\mathrm{ISM} = 8000$ K, it comes that $\beta \geq 2/\gamma$ and $M_\mathrm{A} < 1$. This indicates that, under our hypotheses, the ambient medium of ζ Ophiuchi does not allow the existence of switch-on shocks. Consequently, the imperfect shape of its bow shock (Fig. 13) may not be explained invoking the particular double-front topology of bow shocks that can be produced in such regime, but rather by the presence of a background ISM magnetic field whose direction is not aligned with respect to the motion of the star. Further tri-dimensional MHD models are needed in order to assess the question of ζ Ophiuchi's background ISM magnetic field direction, the position of its contact discontinuity and a more precise estimate of its stellar wind mass loss.

4.4.5 *The case of runaway cool stars*

Our results apply to bow shocks generated by hot, main-sequence OB stars that move through the hot ionized gas of their own H II region (Raga et al. 1997) and archetype of which is the nebulae surrounding ζ Ophiuchi (see above discussion). Externally photoionized cool runaway stars that move rapidly in the H II region produced by an other source of ionizing radiation have particularly bright optical emission [see e.g. the cases of the red supergiant Betelgeuse (Mohamed et al. 2012; Mackey et al. 2014b) and IRC-10414 (Meyer et al. 2014a)]. These circumstellar structures are themselves sensitive to the presence of even a weak ISM background magnetic field of a few μG (van Marle et al. 2014). Consequently, one can expect that the inclusion of such a field in numerical models tailored to these objects would affect their associated synthetic emission maps and update the current estimate of their driving star's mass loss and/or ambient medium density (Meyer et al. 2016).

According to the fact that the warm phase of the ISM is typically magnetized, the reduction of both optical and infrared surface brightnesses of circumstellar structures generated by massive stars should be a rather common phenomenon. In particular, it should also concern bow shocks of OB runaway stars once they have evolved through the red supergiant phase (Paper I). However, the proportion of red supergiant stars amongst the population of all runaway massive stars should be similar to the proportion of red supergiant with respect to the population of static OB stars, which is, to the best of our knowledge, contradicted by observations. The recent study of van Marle et al. (2014) shows that a background ISM magnetic field can inhibit the growth of shear instabilities, i.e. forbids the development of potentially bright infrared knots, in the bow shock of Betelgeuse, and this may help in explaining why the scientific literature only reports four known runaway red supergiant stars, amongst which only three have a detected bow shock, i.e. Betelgeuse (Noriega-Crespo et al. 1997b), IRC-10414 (Meyer et al. 2014a) and μ Cep (Cox et al. 2012). The extragalactic, hyperveloce red supergiant star J004330.06+405258.4 in M31 has all kinematic characteristics to generate a bow shock but it has not been observed so far (Evans & Massey 2015). This remark is also valid for bow shocks generated by runaway massive stars experiencing other evolutionary stages such as the so-called blue supergiant phase (see e.g. Kaper et al. 1997).

4.4.6 *Comparison with the bow shock around the Sun*

The Sun is moving into the warm phase of the ISM (McComas et al. 2015) and the properties of its ambient surrounding, the so-called local interstellar medium (LISM) are similar to the ISM in which our runaway stars move, especially in terms of Alfvénic Mach number and plasma β (Florinski et al. 2004; Burlaga, Florinski & Ness 2015). The study of the interaction between our Sun and the LISM led to a large literature, including, amongst other, numerical investigations of the bow shock formed by the solar wind (see e.g. Baranov & Malama 1993; Pogorelov & Matsuda 1998; Zank 2015, and references therein). If obvious similitudes between the bow shock of the Sun and those of our massive stars indicate that the physical processes governing the formation of circumstellar nebulae around OB stars such as electronic thermal conduction or the influence of the background local magnetic field have to be included in the modelling of those structures (Zank et al. 2009), nevertheless, the bow shock of the Sun is, partly due to the differences in terms of effective temperature and wind velocity, on a totally different scale. Further resemblances with bow-like nebulae from massive stars are therefore mostly morphological.

As a low-mass star ($< 8\,\mathrm{M_\odot}$), the Sun is much cooler ($T_\mathrm{eff} \approx 6000$ K) than the runaway OB stars considered in the present work ($T_\mathrm{eff} > 20\,000$ K) and its mass loss ($\dot{M}_\odot \approx 10^{-14}\,\mathrm{M_\odot\,yr^{-1}}$) is much smaller than that of a main-sequence star with $M_\star \geq 20\,\mathrm{M_\odot}$ (our Table 1), which makes its stellar luminosity fainter by several orders of magnitude ($L_\star/\mathrm{L_\odot} \geq 10^3$). Moreover, the solar wind velocity at 1 au is about $350\,\mathrm{km\,s^{-1}}$ (Golub & Pasachoff 1997) whereas our OB stars have larger wind velocities ($> 1000\,\mathrm{km\,s^{-1}}$; see Table 1). Stellar winds from solar-like stars consequently develop a smaller ram pressure and expel less linear momentum than massive stars such as our $20\,\mathrm{M_\odot}$ star and their associated corresponding circumstellar structures, i.e. wind bubbles or bow shocks are scaled down to a few tens or hundreds of au. Note also that the Sun is too cool to produce ionizing radiations and generated an H II region that is susceptible screen its optical/infrared wind bubble. In other words, if the numerical methods developed to study the bow shock surrounding the Sun are similar to the ones utilized in our study, the solar solutions are more appropriated to investigate the surroundings of cool, low-mass stars such as asymptotic giant stars (AGB) (see Wareing, Zijlstra & O'Brien 2007b,a; Raga et al. 2008; Esquivel et al. 2010; Villaver, Manchado & García-Segura 2012; Chiotellis et al. 2016), or the trails let by planetesimals moving in stellar systems presenting a common envelope (see Thun et al. 2016, and references therein).

Early two-dimensional numerical models of the solar neighbourhood were carried out assuming that the respective directions of both the Sun's motion and the LISM magnetic field are considered as parallel, as we hereby do with our massive stars (Pogorelov & Matsuda 1998). More sophisticated simulations have produced three-dimensional models in which the Sun moves obliquely through the LISM (see e.g. Baranov, Barmin & Pushkar' 1996; Boley, Morris & Desch 2013). Such investigation is observationally motivated by the perturbated and non-uniform appearance of the heliopause, e.g. the boundary between the interplanetary and ISM

(Kawamura, Heerikhuisen & Pogorelov 2010) which revealed the need for 3D calculations, able to report the non-stationary character of the trail of the bow shock of the Sun (Washimi & Tanaka 1996; Linde et al. 1998; Ratkiewicz et al. 1998). Those models are more complex than our simplistic two-dimensional simulations and investigate, e.g. the charge exchanges arising between the stellar wind and the LISM (Fitzenreiter, Scudder & Klimas 1990). These studies also highlighted the complexity and fragility of such models, e.g. regarding the variety of instable MHD discontinuities that affect shock waves propagating through a magnetized flow and differentiating the shocks from purely HD discontinuities described by the Rankine–Hugoniot (see also de Sterck et al. 1998; de Sterck & Poedts 1999). Additionally, those solutions are affected by the spatial resolution of the calculations and the inclusion of numerical viscosity in the models (Lopez, Merkin & Lyon 2011; Wang et al. 2014, and references therein).

Finally, let us mention an other obvious difference between bow shock of the Sun and the nebulae generated by the runaway OB stars that we model. The proximity of the Earth with the Sun makes it easier to be studied and analysed by means of, e.g. radio observations (Baranov, Krasnobaev & Onishchenko 1975) while its innermost substructures are directly reachable with spacecrafts such as *Voyager 1* and *Voyager 2*.[5] Their missions partly consisted in leaving the neighbourhood of our Sun in order to explore the heliosheath, i.e. the layer corresponding to the region of shocked solar wind that is between the contact discontinuity (the heliopause) and the RS of the solar bow shock (the wind termination shock). The *Voyager* engines crossed the outermost edge of the Solar system between 2004 and 2007 at the expected distance of 94 and 84 au from the Earth (Linde et al. 1998), giving the first experimental data on the physics of the ISM (Chalov et al. 2016). Those measures proved the existence of the solar bow shock, and also highlighted the particular conditions of the outer space in terms of magnetic phenomenon (Richardson 2016) and effects of cosmic rays (Webber 2016). In order to make our models more realistic, those physical processes should be taken into account in future simulations of bow shocks from runaway high-mass stars.

5 CONCLUSION

In this study, we presented MHD models of the circumstellar medium of runaway, main-sequence, massive stars moving supersonically through the plane of the Galaxy. Our two-dimensional simulations first investigated the conjugated effects of optically thin radiative cooling and heating together with anisotropic thermal transfers on a field-aligned, MHD bow shock flow around an OB-type, fast-moving star. We then explored the effects of the stellar motion with respect to the bow shocks, focusing on an initially $20\,\mathrm{M}_\odot$ star moving with velocities $v_\star = 20$, 40 and $70\,\mathrm{km\,s^{-1}}$. We presented additional models of an initially $10\,\mathrm{M}_\odot$ star moving with velocities $v_\star = 40\,\mathrm{km\,s^{-1}}$ and of an initially $40\,\mathrm{M}_\odot$ star moving with velocities $v_\star = 70\,\mathrm{km\,s^{-1}}$. The ISM magnetic field strength is set to $B_{\rm ISM} = 7\,\mu$G. We also considered bow shock nebulae produced within a weaker ISM magnetic field ($B_{\rm ISM} = 3.5\,\mu$G). The other ISM properties are unchanged for each models.

Our models show that although the magnetization of the ISM does not radically change the global aspect of our bow shock nebulae, it slightly modifies their internal organization. Anisotropic thermal transfers do not split the region of shocked ISM gas as in our HD models (Paper I), since the presence of the magnetic field in the regions of shocked material forbids HC perpendicular to the magnetic field lines. The field lines, initially parallel to the direction of stellar motion, are bent round by the bow shock into a sheath around the fast stellar wind bubble. As shown in Heitsch et al. (2007), the presence of the magnetic field stabilizes the contact discontinuities inhibiting the growth of the Kelvin–Helmholtz instabilities that typically occur in pure HD models at the interface between shocked ISM and shocked stellar wind.

As in our previous HD study (Paper I), bow shocks are brighter in infrared reprocessed starlight. Their emission by optically thin radiation mostly originates from the shocked ISM and their [O III] λ 5007 spectral line emission is higher than their Hα emission. Notably, their X-rays emission is negligible compared to their optical luminosity and therefore it does not constitute the best waveband to search for hot massive stars' stellar wind bow shocks. We find that the presence of an ISM background magnetic field has the effect of reducing the optical synthetic emission maps of our models, making them fainter by one and two orders of magnitude at [O III] λ 5007 and Hα, respectively. This may explain why not so many of them are observed at these spectral lines. We confirm that, under our assumptions and even in the presence of a magnetic field, circumstellar structures produced by high-mass, slowly moving stars are the easiest observable bow shock nebulae in the warm neutral phase of the Milky Way.

We performed dust continuum radiative transfer calculations of our bow shock models (cf. Acreman et al. 2016) and generated SEDs and isophotal emission maps for different wavelengths $25 \leq \lambda \leq 100\,\mu$m and viewing angles $0^\circ \leq \phi \leq 90^\circ$. Consistently with the observation of van Buren & McCray (1988a), van Buren et al. (1995), Noriega-Crespo et al. (1997a), the calculations show that our bow shocks are brighter at 60 μm. The projected infrared emission can also be diminished in the presence of the ISM magnetic field, in particular at wavelengths $\lambda \geq 60\,\mu$m, since the amount of dust trapped into the bow shock is smaller. We also notice that the change in surface brightness of our emission maps as a function of the viewing angle of the bow shock is similar as in the optical waveband, i.e. it is brighter if $\phi = 0^\circ$ and fainter if $\phi = 90^\circ$ (see Meyer et al. 2016).

In future models, we would like to extend this pioneering study of massive stars' bow shocks within the magnetized ISM towards three-dimensional models in which the ISM magnetic field is unaligned with respect to the motion of the star, as it has been done in order to appreciate its influence on the morphology of the global heliopause (Pogorelov & Matsuda 1998). Such simulations will help to better understand the structure of the circumstellar nebulae forming around hot, ionizing, massive runaway stars and allow us to predict more accurately, e.g. the optical emission signatures of these bow shocks. Thorough comparison with particular hot, bow-shock-producing massive stars, e.g. ζ Ophiuchi, might then be feasible.

ACKNOWLEDGEMENTS

The authors thank Tom Hartquist for his kind help and very helpful advices when reviewing this paper and Richard Stancliffe for numerous grammatical comments when carefully reading the manuscript. DM-A Meyer gratefully thanks T. Robitaille and C. Dullemond for their support with the HYPERION and the RADMC-3D radiative transfer codes, respectively, as well as D. Thun for fruitful discussion concerning his master thesis. Are also acknowledged Professor R. Jalabert and G. Weick from the Institute of Physics and Chemistry

[5] http://voyager.jpl.nasa.gov/mission/interstellar.html

of Materials of Strasbourg (IPCMS) for their kind help concerning the Mie theory. This study was in parts conducted within the Emmy Noether research group on 'Accretion Flows and Feedback in Realistic Models of Massive Star Formation' funded by the German Research Foundation under grant no. KU 2849/3-1. The authors gratefully acknowledge the computing time provided on the supercomputer JUROPA at Jülich Supercomputing Centre (JSC) and on the bwGrid cluster Tübingen. This research has made use of 'Aladin sky atlas' and 'VizieR catalogue access tool' both developed at CDS, Strasbourg Observatory, France.

REFERENCES

Acreman D. M., Stevens I. R., Harries T. J., 2016, MNRAS, 456, 136
Alexiades V., Amiez G., Gremaud P.-A., 1996, Commun. Numer. Methods Eng., 12, 31
Arnaud K. A., 1996, in Jacoby G. H., Barnes J., eds, Astronomical Society of the Pacific Conference Series Vol. 101, Astronomical Data Analysis Software and Systems V. XSPEC: The First Ten Years. Astron. Soc. Pac., San Francisco, p. 17
Arthur S. J., Hoare M. G., 2006, ApJS, 165, 283
Asplund M., Grevesse N., Sauval A. J., Scott P., 2009, ARA&A, 47, 481
Balsara D. S., Tilley D. A., Howk J. C., 2008, MNRAS, 386, 627
Baranov V. B., Malama Y. G., 1993, J. Geophys. Res., 98, 15157
Baranov V. B., Krasnobaev K. V., Onishchenko O. G., 1975, Sov. Astron. Lett., 1, 81
Baranov V. B., Barmin A. A., Pushkar' E. A., 1996, Astron. Lett., 22, 555
Bjorkman J. E., Wood K., 2001, ApJ, 554, 615
Blondin J. M., Koerwer J. F., 1998, New Astron., 3, 571
Bohren C. F., Huffman D. R., 1983, Absorption and Scattering of Light by Small Particles. Wiley, New York
Boley A. C., Morris M. A., Desch S. J., 2013, ApJ, 776, 101
Brighenti F., D'Ercole A., 1994, MNRAS, 270, 65
Brighenti F., D'Ercole A., 1995a, MNRAS, 277, 53
Brighenti F., D'Ercole A., 1995b, MNRAS, 273, 443
Brott I. et al., 2011, A&A, 530, A115
Brown D., Bomans D. J., 2005, A&A, 439, 183
Burlaga L. F., Florinski V., Ness N. F., 2015, ApJ, 804, L31
Castor J. I., Abbott D. C., Klein R. I., 1975, ApJ, 195, 157
Chalov S. V., Malama Y. G., Alexashov D. B., Izmodenov V. V., 2016, MNRAS, 455, 431
Chiotellis A., Schure K. M., Vink J., 2012, A&A, 537, A139
Chiotellis A., Boumis P., Nanouris N., Meaburn J., Dimitriadis G., 2016, MNRAS, 457, 9
Chita S. M., Langer N., van Marle A. J., García-Segura G., Heger A., 2008, A&A, 488, L37
Churchwell E. et al., 2006, ApJ, 649, 759
Comerón F., Kaper L., 1998, A&A, 338, 273
Cowie L. L., McKee C. F., 1977, ApJ, 211, 135
Cox C. I., Gull S. F., Green D. A., 1991, MNRAS, 250, 750
Cox N. L. J., Kerschbaum F., van Marle A. J., Decin L., Ladjal D., Mayer A., 2012, A&A, 543, C1
Crutcher R. M., Roberts D. A., Troland T. H., Goss W. M., 1999, ApJ, 515, 275
de Jager C., Nieuwenhuijzen H., van der Hucht K. A., 1988, A&AS, 72, 259
de Mink S. E., Pols O. R., Hilditch R. W., 2007, A&A, 467, 1181
de Mink S. E., Cantiello M., Langer N., Pols O. R., Brott I., Yoon S.-C., 2009, A&A, 497, 243
de Sterck H., Poedts S., 1999, A&A, 343, 641
de Sterck H., Poedts S., 2000, in Verheest F., Goossens M., Hellberg M. A., Bharuthram R., eds, AIP Conf. Ser. Vol. 537. Waves in Dusty, Solar, and Space Plasmas. Disintegration and Reformation of Intermediate Shock Segments in 3D MHD Bow Shock Flows. Am. Inst. Phys., New York, p. 232
de Sterck H., Poedts S., 2001, in Freistühler H., Warnecke G. m.. f. p, eds, Waves in Dusty, Solar, and Space Plasmas. International Series of Numerical Mathematics, Vol. 141, Overcompressive Shocks and Compound Shocks in 2D and 3D Magnetohydrodynamic Flows. Birkhäuser
de Sterck H., Low B. C., Poedts S., 1998, Phys. Plasmas, 5, 4015
del Valle M. V., Romero G. E., Santos-Lima R., 2015, MNRAS, 448, 207
Diaz-Miller R. I., Franco J., Shore S. N., 1998, ApJ, 501, 192
Donati J.-F., Babel J., Harries T. J., Howarth I. D., Petit P., Semel M., 2002, MNRAS, 333, 55
Dopita M. A., 1973, A&A, 29, 387
Draine B. T., 2011, Physics of the Interstellar and Intergalactic Medium. Princeton Univ. Press
Draine B. T., Lee H. M., 1984, ApJ, 285, 89
Dullemond C. P., 2012, RADMC-3D: A Multi-purpose Radiative Transfer Tool. Astrophysics Source Code Library
Dyson J. E., 1975, Ap&SS, 35, 299
Eldridge J. J., Genet F., Daigne F., Mochkovitch R., 2006, MNRAS, 367, 186
Eldridge J. J., Langer N., Tout C. A., 2011, MNRAS, 414, 3501
Esquivel A., Raga A. C., Cantó J., Rodríguez-González A., López-Cámara D., Velázquez P. F., De Colle F., 2010, ApJ, 725, 1466
Evans K. A., Massey P., 2015, AJ, 150, 149
Fiedler R. A., Mouschovias T. C., 1993, ApJ, 415, 680
Fitzenreiter R. J., Scudder J. D., Klimas A. J., 1990, J. Geophys. Res., 95, 4155
Florinski V., Pogorelov N. V., Zank G. P., Wood B. E., Cox D. P., 2004, ApJ, 604, 700
Gaensler B. M., 1998, ApJ, 493, 781
Golub L., Pasachoff J. M., 1997, The Solar Corona. Cambridge University Press, Cambridge
Gull T. R., Sofia S., 1979, ApJ, 230, 782
Gvaramadze V. V., Langer N., Mackey J., 2012, MNRAS, 427, L50
Gvaramadze V. V., Menten K. M., Kniazev A. Y., Langer N., Mackey J., Kraus A., Meyer D. M.-A., Kamiński T., 2014, MNRAS, 437, 843
Harten A., Lax P. D., van Leer B., 1983, SIAM Rev., 25, 35
Harvey-Smith L., Madsen G. J., Gaensler B. M., 2011, ApJ, 736, 83
Heger A., Woosley S. E., Spruit H. C., 2005, ApJ, 626, 350
Heiligman G. M., 1980, MNRAS, 191, 761
Heitsch F., Slyz A. D., Devriendt J. E. G., Hartmann L. W., Burkert A., 2007, ApJ, 665, 445
Huthoff F., Kaper L., 2002, A&A, 383, 999
Kaper L., van Loon J. T., Augusteijn T., Goudfrooij P., Patat F., Waters L. B. F. M., Zijlstra A. A., 1997, ApJ, 475, L37
Kawamura A. D., Heerikhuisen J., Pogorelov N. V., 2010, AGU Fall Meeting Abstracts
Keppens R., Tóth G., Westermann R. H. J., Goedbloed J. P., 1999, J. Plasma Phys., 61, 1
Kobulnicky H. A. et al., 2016, ApJ, preprint (arXiv:1609.02204)
Kroupa P., 2001, MNRAS, 322, 231
Kudritzki R.-P., Puls J., 2000, ARA&A, 38, 613
Kudritzki R. P., Pauldrach A., Puls J., Abbott D. C., 1989, A&A, 219, 205
Langer N., 2012, ARA&A, 50, 107
Langer N., García-Segura G., Mac Low M.-M., 1999, ApJ, 520, L49
Linde T. J., Gombosi T. I., Roe P. L., Powell K. G., Dezeeuw D. L., 1998, J. Geophys. Res., 103, 1889
Lodders K., 2003, ApJ, 591, 1220
Lopez R. E., Merkin V. G., Lyon J. G., 2011, Ann. Geophys., 29, 1129
Lucy L. B., 1999, A&A, 344, 282
McComas D. J. et al., 2015, ApJ, 801, 28
Mac Low M.-M., van Buren D., Wood D. O. S., Churchwell E., 1991, ApJ, 369, 395
Mackey J., Mohamed S., Neilson H. R., Langer N., Meyer D. M.-A., 2012, ApJ, 751, L10
Mackey J., Langer N., Gvaramadze V. V., 2014a, MNRAS, 444, 2754
Mackey J., Mohamed S., Gvaramadze V. V., Kotak R., Langer N., Meyer D. M.-A., Moriya T. J., Neilson H. R., 2014b, Nature, 512, 282
Mackey J., Haworth T. J., Gvaramadze V. V., Mohamed S., Langer N., Harries T. J., 2016, A&A, 586, A114

Marchant P., Langer N., Podsiadlowski P., Tauris T. M., Moriya T. J., 2016, A&A, 588, A50
Martins F., Genzel R., Hillier D. J., Eisenhauer F., Paumard T., Gillessen S., Ott T., Trippe S., 2007, A&A, 468, 233
Mathis J. S., Rumpl W., Nordsieck K. H., 1977, ApJ, 217, 425
Meyer D. M.-A., Gvaramadze V. V., Langer N., Mackey J., Boumis P., Mohamed S., 2014a, MNRAS, 439, L41
Meyer D. M.-A., Mackey J., Langer N., Gvaramadze V. V., Mignone A., Izzard R. G., Kaper L., 2014b, MNRAS, 444, 2754 (Paper I)
Meyer D. M.-A., Langer N., Mackey J., Velázquez P. F., Gusdorf A., 2015, MNRAS, 450, 3080
Meyer D. M.-A., Vorobyov E. I., Kuiper R., Kley W., 2017, MNRAS, 464, L90
Meyer D. M.-A., van Marle A.-J., Kuiper R., Kley W., 2016, MNRAS, 459, 1146
Mignone A., Bodo G., Massaglia S., Matsakos T., Tesileanu O., Zanni C., Ferrari A., 2007, ApJS, 170, 228
Mignone A., Zanni C., Tzeferacos P., van Straalen B., Colella P., Bodo G., 2012, ApJS, 198, 7
Mohamed S., Mackey J., Langer N., 2012, A&A, 541, A1
Moore B. D., Walter D. K., Hester J. J., Scowen P. A., Dufour R. J., Buckalew B. A., 2002, AJ, 124, 3313
Neugebauer G. et al., 1984, ApJ, 278, L1
Noriega-Crespo A., van Buren D., Dgani R., 1997a, AJ, 113, 780
Noriega-Crespo A., van Buren D., Cao Y., Dgani R., 1997b, AJ, 114, 837
Ohno H., Shibata S., 1993, MNRAS, 262, 953
Opher M., Bibi F. A., Toth G., Richardson J. D., Izmodenov V. V., Gombosi T. I., 2009, Nature, 462, 1036
Orlando S., Peres G., Reale F., Bocchino F., Rosner R., Plewa T., Siegel A., 2005, A&A, 444, 505
Orlando S., Bocchino F., Reale F., Peres G., Pagano P., 2008, ApJ, 678, 274
Osterbrock D. E., Bochkarev N. G., 1989, Sov. Astron., 33, 694
Parker E. N., 1958, ApJ, 128, 664
Parker E. N., 1963, Interplanetary Dynamical Processes. Interscience Publishers, New York
Pavlyuchenkov Y. N., Kirsanova M. S., Wiebe D. S., 2013, Astron. Rep., 57, 573
Paxton B., Bildsten L., Dotter A., Herwig F., Lesaffre P., Timmes F., 2011, ApJS, 192, 3
Peri C. S., Benaglia P., Brookes D. P., Stevens I. R., Isequilla N. L., 2012, A&A, 538, A108
Peri C. S., Benaglia P., Isequilla N. L., 2015, A&A, 578, A45
Petrovic J., Langer N., Yoon S.-C., Heger A., 2005, A&A, 435, 247
Pogorelov N. V., Matsuda T., 1998, J. Geophys. Res., 103, 237
Pogorelov N. V., Matsuda T., 2000, A&A, 354, 697
Pogorelov N. V., Semenov A. Y., 1997, A&A, 321, 330
Povich M. S., Benjamin R. A., Whitney B. A., Babler B. L., Indebetouw R., Meade M. R., Churchwell E., 2008, ApJ, 689, 242
Raga A. C., 1986, ApJ, 300, 745
Raga A. C., Noriega-Crespo A., Cantó J., Steffen W., van Buren D., Mellema G., Lundqvist P., 1997, Rev. Mex. Astron., 33, 73
Raga A. C., Cantó J., De Colle F., Esquivel A., Kajdic P., Rodríguez-González A., Velázquez P. F., 2008, ApJ, 680, L45
Rand R. J., Kulkarni S. R., 1989, ApJ, 343, 760
Ratkiewicz R., Barnes A., Molvik G. A., Spreiter J. R., Stahara S. S., Vinokur M., Venkateswaran S., 1998, A&A, 335, 363
Richardson I. G., 2016, preprint (arXiv:1603.06137)
Robitaille T. P., 2011, A&A, 536, A79
Rozyczka M., Tenorio-Tagle G., 1995, MNRAS, 274, 1157
Sana H. et al., 2012, Science, 337, 444
Sexton R. O., Povich M. S., Smith N., Babler B. L., Meade M. R., Rudolph A. L., 2015, MNRAS, 446, 1047
Shabala S. S., Mead J. M. G., Alexander P., 2010, MNRAS, 405, 1960
Sharpless S., 1959, ApJS, 4, 257
Simpson R. J. et al., 2012, MNRAS, 424, 2442
Soker N., Dgani R., 1997, ApJ, 484, 277
Spitzer L., 1962, Physics of Fully Ionized Gases. Intersci. Publ.
Thun D., Kuiper R., Schmidt F., Kley W., 2016, A&A, 589, A10
Troland T. H., Heiles C., 1986, ApJ, 301, 339
van Buren D., McCray R., 1988a, ApJ, 329, L93
van Buren D., McCray R., 1988b, ApJ, 329, L93
van Buren D., Noriega-Crespo A., Dgani R., 1995, AJ, 110, 2914
van Marle A. J., 2006, PhD thesis, Utrecht University
van Marle A. J., Langer N., Achterberg A., García-Segura G., 2006, A&A, 460, 105
van Marle A. J., Langer N., García-Segura G., 2007, A&A, 469, 941
van Marle A. J., Meliani Z., Keppens R., Decin L., 2011, ApJ, 734, L26
van Marle A. J., Decin L., Meliani Z., 2014, A&A, 561, A152
van Marle A. J., Meliani Z., Marcowith A., 2015, A&A, 584, A49
Velázquez P. F., Martinell J. J., Raga A. C., Giacani E. B., 2004, ApJ, 601, 885
Viallet M., Baty H., 2007, A&A, 473, 1
Villaver E., Manchado A., García-Segura G., 2012, ApJ, 748, 94
Vink J. S., 2006, in Lamers H. J. G. L. M., Langer N., Nugis T., Annuk K., eds, Astronomical Society of the Pacific Conference Series 353. Stellar Evolution at Low Metallicity: Mass Loss, Explosions, Cosmology. Massive Star Feedback – From the First Stars to the Present. Astron. Soc. Pac., San Francisco, p. 113
Wachter S., Mauerhan J. C., Van Dyk S. D., Hoard D. W., Kafka S., Morris P. W., 2010, AJ, 139, 2330
Wang C., Han J. P., Li H., Peng Z., Richardson J. D., 2014, J. Geophys. Res. (Space Phys.), 119, 6199
Wareing C. J., Zijlstra A. A., O'Brien T. J., 2007a, MNRAS, 382, 1233
Wareing C. J., Zijlstra A. A., O'Brien T. J., 2007b, ApJ, 660, L129
Washimi H., Tanaka T., 1996, Space Sci. Rev., 78, 85
Weaver R., McCray R., Castor J., Shapiro P., Moore R., 1977, ApJ, 218, 377
Webber W. R., 2016, preprint (arXiv:1604.06477)
Wilkin F. P., 1996, ApJ, 459, L31
Wolfire M. G., McKee C. F., Hollenbach D., Tielens A. G. G. M., 2003, ApJ, 587, 278
Wood K., Whitney B. A., Robitaille T., Draine B. T., 2008, ApJ, 688, 1118
Wright E. L. et al., 2010, AJ, 140, 1868
Yoon S.-C., Cantiello M., 2010, ApJ, 717, L62
Yoon S.-C., Langer N., 2005, A&A, 443, 643
Zank G. P., 2015, ARA&A, 53, 449
Zank G. P., Pogorelov N. V., Heerikhuisen J., Washimi H., Florinski V., Borovikov S., Kryukov I., Müller H. R., 2009, Space Sci. Rev., 146, 295
Zhu F.-Y., Zhu Q.-F., Li J., Zhang J.-S., Wang J.-Z., 2015, ApJ, 812, 87

This paper has been typeset from a TEX/LATEX file prepared by the author.

Monthly Notices
of the
ROYAL ASTRONOMICAL SOCIETY

MNRAS **506,** 5170–5189 (2021)
Advance Access publication 2021 July 19

https://doi.org/10.1093/mnras/stab2026

3D MHD astrospheres: applications to IRC-10414 and Betelgeuse

D. M.-A. Meyer [1]★ A. Mignone [2] M. Petrov,[3] K. Scherer [4,5] P. F. Velázquez[6] and P. Boumis [7]

[1]*Institut für Physik und Astronomie, Universität Potsdam,, Karl-Liebknecht-Strasse 24/25, D-14476 Potsdam, Germany*
[2]*Dipartimento di Fisica Generale Facoltà di Scienze M.F.N., Università degli Studi di Torino, Via Pietro Giuria 1, I-10125 Torino, Italy*
[3]*Max Planck Computing and Data Facility (MPCDF), Gießenbachstrasse 2, D-85748 Garching, Germany*
[4]*Institut für Theoretische Physik, Lehrstuhl IV: Plasma-Astroteilchenphysik, Ruhr-Universitäat Bochum, D-44780 Bochum, Germany*
[5]*Research Department, Plasmas with Complex Interactions, Ruhr-Universitäat Bochum, D-44780 Bochum, Germany*
[6]*Instituto de Ciencias Nucleares, Universidad Nacional Autónoma de México, CP 04510, Mexico City, Mexico*
[7]*Institute for Astronomy, Astrophysics, Space Applications and Remote Sensing, National Observatory of Athens, 15236, Penteli, Greece*

Accepted 2021 July 12. Received 2021 July 10; in original form 2021 June 23

ABSTRACT

A significative fraction of all massive stars in the Milky Way move supersonically through their local interstellar medium (ISM), producing bow shock nebulae by wind-ISM interaction. The stability of these observed astrospheres around cool massive stars challenges precedent 2D (magneto-)hydrodynamical (MHD) simulations of their surroundings. We present 3D MHD simulations of the circumstellar medium of runaway M-type red supergiant stars moving with velocity $v_\star = 50\,\mathrm{km\,s^{-1}}$. We treat the stellar wind with a Parker spiral and assume a 7 μG magnetization of the ISM. Our free parameter is the angle θ_{mag} between ISM flow and magnetization, taken to 0°, 45°, and 90°. It is found that simulation dimension, coordinate systems, and grid effects can greatly affect the development of the modelled astrospheres. Nevertheless, as soon as the ISM flow and magnetization directions differs by more than a few degrees ($\theta_{\mathrm{mag}} \geq 5°$), the bow shock is stabilized, most clumpiness and ragged structures vanishing. The complex shape of the bow shocks induce important projection effects, e.g. at optical H α line, producing complex of astrospheric morphologies. We speculate that those effects are also at work around earlier-type massive stars, which would explain their diversity of their observed arc-like nebula around runaway OB stars. Our 3D MHD models are fitting well observations of the astrospheres of several runaway red supergiant stars. The results interpret the smoothed astrosphere of IRC-10414 and Betelgeuse (αOri) are stabilized by an organized non-parallel ambient magnetic field. Our findings suggest that IRC-10414 is currently in a steady state of its evolution, and that Betelgeuse's bar is of interstellar origin.

Key words: radiative transfer – circumstellar matter – stars: massive.

1 INTRODUCTION

Massive stars ($M_\star \geq 8\,\mathrm{M}_\odot$) are preponderant engines in the cycle of matter of the interstellar medium (ISM) of galaxies (Maeder 2009). They blow strong stellar winds, and, by synthetizing heavy chemical elements in their interiors, massive stars typically evolve from a long hot main-sequence phase to a short cold red supergiant phase (Ekström et al. 2012). They may also experience series of eruptive luminous blue mass-losing events and/or finally finish their lives as hot Wolf–Rayet stars, respectively (Vink 2006). The number, duration, and stellar surface properties of these successive evolutionary phases are mostly determined by their initial mass, rotation rate (Brott et al. 2011; Szécsi et al. 2020), but also chemical composition (Sander, Vink & Hamann 2020), which uniquely characterize the evolution and fate of massive stars (Woosley, Heger & Weaver 2002). Throughout their lives, they lose mass and radiate strong ionizing photons, which both shape their surroundings as circumstellar bubble nebulae made of stellar wind and ISM material (Weaver et al. 1977).

The internal structures of wind-blown bubbles reflect the past stellar evolution of massive stars (Garcia-Segura, Langer & Mac Low 1996; Freyer, Hensler & Yorke 2003, 2006; Dwarkadas 2007; Gvaramadze, Kniazev & Fabrika 2010; van Marle, Meliani & Marcowith 2015; Meyer, Petrov & Pohl 2020a). These circumstellar nebulae are punctual valves located in the ISM which release energy, momentum, and heavy elements that considerably enrich their local ambient medium (Langer 2012). Some massive stars ($\lesssim 40\,\mathrm{M}_\odot$) eventually die as core-collapse supernova, a final explosive event marking their evolution (Woosley & Bloom 2006; Smartt 2009). It engenders a propagating blastwave, first going through their circumstellar medium, before further expanding into the pristine ISM (Chevalier 1977; Weiler & Sramek 1988). When the ejecta material of the defunct star shocks its surroundings, it produces nebulae of complex morphologies called supernova remnants, displaying unusual patterns of enriched gas emitting light throughout the whole electromagnetic spectrum, by means of both thermal and non-thermal emission (Weiler & Sramek 1988).

About 4−10 per cent of all massive main-sequence stars are moving supersonically though the ISM (Renzo et al. 2019). This happens when (i) the stars are ejected by gravitational swing from their parent stellar clusters (Lada & Lada 2003), (ii) by the explosive dissociation of binary systems (Blaauw 1961; Gies 1987; Hoogerwerf, de Bruijne & de Zeeuw 2001; Dinçel et al. 2015) or (iii) when massive binary system captures a third star, producing an unstable triple

★ E-mail: dmameyer.astro@gmail.com

binary system from which one of the original binary component is ejected (Gvaramadze & Gualandris 2011). Hence, massive stars can move with high space velocities (from tens to hundreds of km s^{-1}), and therefore the wind-blown bubble of a runaway massive star is distorted as a bow shock nebula (Wilkin 1996). Such a circumstellar structures can mainly be observed in the context of hot massive runaway stars at various wavelengths (Gull & Sofia 1979; Kaper et al. 1997; Brown & Bomans 2005; De Becker et al. 2017). However, they are mostly visible in the infrared waveband (van Buren & McCray 1988; van Buren, Noriega-Crespo & Dgani 1995; Noriega-Crespo, van Buren & Dgani 1997a; Povich et al. 2008; Peri et al. 2012; Peri, Benaglia & Isequilla 2015; Kobulnicky et al. 2016, 2017) whose emission are governed by dust physics (Henney & Arthur 2019a,b,c; Henney et al. 2019). Stellar wind bow shocks also exhibit polarized emission (Shrestha et al. 2018, 2021) and they are suspected to be cosmic ray accelerators (del Valle & Pohl 2018; Benaglia et al. 2021). While massive stars run away, stellar evolution keeps going, and, consequently, a significant fraction of all core-collapse supernova remnants involve a runaway progenitor (Eldridge, Langer & Tout 2011). The wind bubble and stellar wind bow shocks forming around runaway stars, ending their lives as red a supergiant, constitute the pre-supernova circumstellar medium inside of which the blastwave will subsequently expand (van Marle, Langer & García-Segura 2005; Gvaramadze 2006; van Marle et al. 2008; Chiotellis, Schure & Vink 2012; van Marle, Meliani & Marcowith 2012; Broersen et al. 2014; Meyer et al. 2015; Chiotellis, Boumis & Spetsieri 2021; Meyer et al. 2021).

Bow shocks form when the stellar wind of evolved red supergiant massive stars interact with their ambient medium (Meyer et al. 2014b). Because of their minimal terminal wind velocities ($\sim$20 km s^{-1}), the bow shocks of red supergiant stars are much smaller than those forming around moving hot OB stars, and, because of the low effective temperature of the star, the physics taking place inside of them is also more complex (Teyssier et al. 2012; Matsuura et al. 2014). Their winds are the site of rich chemical reactions (Cannon et al. 2021), and the clumps aggregating therein lead to the formation of large molecules (O'Gorman et al. 2015; Montargès et al. 2019). The dusty, neutral winds of red supergiant stars eventually interact with the hot, ionized gas of either the remaining H II region of the OB star they descent from or of a neighbouring stellar cluster including, e.g. hot Wolf–Rayet star(s) (Meyer et al. 2014a; Mackey et al. 2016). The neutral-ionized interface generates a photoionized-confined shell separating molecular gas from its ionized surroundings, which can be observed (Mackey et al. 2014). Note that similar features based of enhanced neutral walls also exist in the heliosheath and in the astrosheaths of the Sun (Izmodenov et al. 2003; Scherer et al. 2014). Three known bow-shock-producing red supergiant stars have been observed so far, namely that of Betelgeuse (Noriega-Crespo et al. 1997b), μCep (Cox et al. 2012a), and IRC-10414 (Gvaramadze et al. 2014), raising the question of their apparent smooth shape despite the instabilities predicted to be at work therein (Dgani, van Buren & Noriega-Crespo 1996a,b). The active role of the external ionization and magnetic fields has been shown to be a potential stabilizer in several numerical simulations (Meyer et al. 2014a; van Marle et al. 2015).

Stellar wind bow shocks from intermediate-mass and massive stars have been studied in many previous works. Several numerical models were produced to understand the functioning and emission properties of bow shock surroundings hot (Blondin & Koerwer 1998; Comerón & Kaper 1998; Meyer et al. 2014b, 2016, 2017; Green et al. 2019; Meyer et al. 2020b) and cold (Brighenti & D'Ercole 1995; Wareing, Zijlstra & O'Brien 2007a,b; van Marle et al. 2011; Cox et al. 2012b; Villaver, Manchado & García-Segura 2012; van Marle, Decin & Meliani 2014; Acreman, Stevens & Harries 2016) runaway massive stars. The runaway red supergiant stars Betelgeuse (Cox et al. 2012a; Mackey et al. 2012; Mohamed, Mackey & Langer 2012) and IRC-10414 (Meyer et al. 2014a) motivated dedicated studies tailored to their environment. Until recently, most simulations, except very few, were 2D hydrodynamical models. Over the past few years, several 3D hydrodynamical (Blondin & Koerwer 1998; Mohamed et al. 2012) and 3D (magneto-)hydrodynamical (3D MHD) models have been performed (Gvaramadze et al. 2018; Katushkina et al. 2018; Scherer et al. 2020; Baalmann et al. 2021). However, no one so far has investigated the appearance of bow shocks from moving red supergiant stars using 3D MHD simulations. Therefore, the question is, which differences exist between two- and 3D simulations of bow shocks around cool stars? How does a 3D MHD Eulerian bow shock model compare to that of its 2D hydrodynamical counterpart? Does it affect the optical emission properties of the astrosphere? Can one directly compare 3D MHD models to observed bow shocks and pronounce on the stability and the surroundings of, e.g. IRC-10414 or Betelgeuse? In this paper, we investigate employing 3D MHD numerical simulations the effects of an ISM magnetic field that is not aligned with the direction of motion of a red supergiant star on to the structure and emission properties of its associated stellar wind bow shock.

Our study is organized as follows. We introduce the reader to the numerical methods used to perform our 3D MHD simulations of stellar wind bow shocks around runaway red supergiant stars in Section 2. We describe the results and analyse therein the effects of the presence of the ISM magnetic field on to the organization, stabilization, and emission properties of the bow shock nebulae in Section 3. Our results are further discussed in Section 4, and we conclude in Section 5.

2 METHOD

This section presents both the governing equations that we solve to simulate the circumstellar medium of evolved, cool runaway massive stars, together with the initial conditions used in our study.

2.1 Governing equations

We consider the problem of a circumstellar nebulae generated by stellar wind-ISM interaction around an evolved massive stellar object supersonically moving through a magnetized ISM. The evolution of the gas constituting the so-produced stellar wind bow shock is described by the following non-ideal MHD equations,

$$\frac{\partial \rho}{\partial t} + \nabla \cdot (\rho \boldsymbol{v}) = 0, \tag{1}$$

$$\frac{\partial \boldsymbol{m}}{\partial t} + \nabla \cdot (\boldsymbol{m} \otimes \boldsymbol{v} + \boldsymbol{B} \otimes \boldsymbol{B} + \hat{\boldsymbol{I}}\, p) = \boldsymbol{0}, \tag{2}$$

$$\frac{\partial E}{\partial t} + \nabla \cdot ((E + p)\boldsymbol{v} - \boldsymbol{B}(\boldsymbol{v} \cdot \boldsymbol{B})) = \Phi(T, \rho), \tag{3}$$

and,

$$\frac{\partial \boldsymbol{B}}{\partial t} + \nabla \cdot (\boldsymbol{v} \otimes \boldsymbol{B} - \boldsymbol{B} \otimes \boldsymbol{v}) = \boldsymbol{0}, \tag{4}$$

where $\boldsymbol{B}$ is the magnetic field vector. Additionally, ρ is the mass density, $\boldsymbol{m} = \rho \boldsymbol{v}$ stands for the linear momentum vector, $\hat{\boldsymbol{I}}$ is the identity matrix, the quantity p stands for the thermal pressure, v is

the gas velocity and,

$$E = \frac{p}{(\gamma - 1)} + \frac{\boldsymbol{m} \cdot \boldsymbol{m}}{2\rho} + \frac{\boldsymbol{B} \cdot \boldsymbol{B}}{2}, \tag{5}$$

if the total energy of the system, respectively. In the above relations, $\gamma = 5/3$ is the adiabatic index. Optically thin radiative cooling and heating of the gas are represented by the source term $\Phi(T, \rho) = n_{\rm H}\Gamma(T) - n_{\rm H}^2\Lambda(T)$, where $\Lambda(T)$ and $\Gamma(T)$ stand for the gas energy losses and photoheating, and where $T = \mu m_{\rm H} p/k_{\rm B}\rho$ is the gas temperature. These cooling laws of photoionized gas is described in great detail in Meyer et al. (2014b).

The MHD equations are solved with the PLUTO code (Mignone et al. 2007, 2012; Vaidya et al. 2018) using a second-order dimensionally unsplit scheme with linear reconstruction and the HLL Riemann solver (Harten, Lax & van Leer 1983). The divergence-free condition is controlled using the eight-wave formulation by Powell (1997). The simulations timesteps are controlled by the Courant–Friedrich–Levy condition that is initially set to $C_{\rm cfl} = 0.1$.

2.2 Initial conditions

We adopt a Cartesian coordinate system and a $[-0.8; 0.8] \times [-0.8; 0.8] \times [-0.2; 0.4]\,{\rm pc}^3$ computational domain that is mapped with a uniform grid made of $512 \times 512 \times 192$ grid zones.[1] The stellar wind is launched in spherical wind zone of radius $r_{\rm in} = 20$ cells centred on to the origin of the domain (0,0,0), where the wind properties are imposed. Particularly, the stellar wind density reads

$$\rho_w(r) = \frac{\dot{M}}{4\pi r^2 v_{\rm w}}, \tag{6}$$

with $\dot{M}$ the mass-loss rate of the star, r the radial distance to the origin, and $v_{\rm w}$ the terminal wind velocity. The simulations are conducted in the reference frame of the star, and our method is therefore the 3D Cartesian equivalent of the standard cylindrically symmetric manner of modelling the wind–ISM interaction of massive stars (Comerón & Kaper 1998; van Marle et al. 2011; van Marle et al. 2014; Green et al. 2019).

We adopt as initial conditions the stellar properties of the runaway red supergiant IRC-14414, which mass-loss rate $\dot{M} \approx 10^{-6}\,{\rm M}_\odot\,{\rm yr}^{-1}$, wind velocity $v_{\rm w} \approx 21\,{\rm km\,s}^{-1}$, ISM gas of number density $n_{\rm ISM} \approx 3.3\,{\rm cm}^{-3}$, and stellar bulk motion $v_\star = 50\,{\rm km\,s}^{-1}$ have been measured and constrained in Gvaramadze et al. (2014) and in Meyer et al. (2014a), respectively. Our stellar wind boundary conditions constrained by observations are motivated (i) the availability of real data to compare our simulations to, and (ii) the uncertainty existing regarding to the theoretical estimate of mass-loss rates of red supergiant stars (Farrell et al. 2020). The star is considered as moving into a fully ionized ambient medium, produced either by the H II region of its previous OB main-sequence phase, or by a neighbouring stellar cluster (Gvaramadze et al. 2014; Meyer et al. 2014a). Consequently, although red supergiant stars are cool objects, the ISM temperature is taken to $T_{\rm ISM} \approx 8000\,{\rm K}$ and gas obeys the heating and cooling rules for photoionized plasma detailed in Meyer et al. (2014a). Inflow and outflow boundary conditions are imposed at the faces of our Cartesian computational domain.

For the sake of completeness, a stellar magnetic field $B_\star$ is imposed at the inner wind boundary, in addition to the wind, as a Parker spiral (Parker 1958; Weber & Davis 1967). It is made of a radial component,

$$B_{\rm r}(r) = B_\star \left(\frac{R_\star}{r}\right)^2, \tag{7}$$

and of a toroidal component,

$$B_\phi(r) = B_{\rm r}(r) \left(\frac{v_\phi(\theta)}{v_{\rm w}}\right) \left(\frac{r}{R_\star} - 1\right), \tag{8}$$

with,

$$v_\phi(\theta) = v_{\rm rot} \sin(\theta), \tag{9}$$

respectively, where $R_\star = 1000\,{\rm R}_\odot$ is the stellar radius (Dolan et al. 2016), $v_{\rm rot} = 5\,{\rm km\,s}^{-1}$ is the angular velocity at the stellar equator of the runaway supergiant star Betelgeuse (Kervella et al. 2018) and $B_\star = 0.2\,{\rm G}$ is its stellar surface magnetic field (Vlemmings, van Langevelde & Diamond 2005), respectively. The poloidal component of the stellar magnetic field is initially set to $B_\theta = 0\,{\rm G}$. The rotation axis of the star is, for the sake of simplicity, taken to be the Oz axis. Hence, our problem possesses three characteristic direction: the rotation axis (Oz), the direction of stellar motion arbitrarily shifted along the Ox and Oy directions by $\leq 10^\circ$ each (see Section 4.2) and the direction of the large-scale ISM magnetic field, shifted from that of stellar motion by $\theta_{\rm mag}$ (Table 1). Considering the lack of observational data regarding the magnetic field of IRC-10414, the rotation and magnetic properties in our models have been taken to that of the well-studied evolved cool stars Betelgeuse (Kervella et al. 2018) and other late-type giant stars such as Mira (Vlemmings, Diamond & van Langevelde 2002; Vlemmings et al. 2005), respectively. Following studies tailored to the M-typed star V374 Peg, Proxima Centauri and LHS 1140, we scale the toroidal component of the stellar magnetic field to that of the Sun (Herbst et al. 2020; Baalmann et al. 2021). We refer the reader further interested on our magnetized stellar wind boundaries to the works of Chevalier & Luo (1994), Rozyczka & Franco (1996), García-Segura, Ricker & Taam (2018), and García-Segura, Taam & Ricker (2020).

The organized large-scale magnetization of the ISM is modelled by $\vec{B}_{\rm ISM}$ and chosen to lay in a plane described by its inclination with respect to the direction of stellar motion. We perform several simulations with changing inclination angle $\theta_{\rm mag}$ of the local vector magnetic field $\vec{B}_{\rm ISM}$ with respect to the direction of stellar motion $-\vec{v}_\star$. In most simulations that we run, the inflow is not parallel to the Oz axis (see Section 4.2). The strength of the ISM magnetic field is taken to the standard value of $B_{\rm ISM} = 7\,\mu{\rm G}$ for the warm phase of the ISM (van Marle et al. 2014, 2015; Meyer et al. 2017). Finally, the advection equation,

$$\frac{\partial(\rho Q)}{\partial t} + \boldsymbol{\nabla} \cdot (\boldsymbol{v}\rho Q) = 0, \tag{10}$$

allows us to differentiate stellar wind from ISM materials and to trace the mixing of those stellar wind material into the forming gas nebula. The tracer Q is initially set to $Q(r \leq r_{\rm in}) = 1$ in the wind and to $Q(r > r_{\rm in}) = 0$ in the ISM, respectively. Table 1 summarizes the simulation models in our study.

3 RESULTS

In this section, we describe and analyse the structure of MHD bow shocks forming around a runaway red supergiant star. We pay a particular attention to the study of the bow shock stability as a function of the angle $\theta_{\rm mag}$ between the direction of motion of the star and that of the local magnetic field.

[1] Our spatial resolution of $3.125 \times 10^{-3}\,{\rm pc\,zone}^{-1}$ is therefore coarser by an order of magnitude than that of Meyer et al. (2014a) and van Marle et al. (2014), which are $2.25 \times 10^{-4}\,{\rm pc\,zone}^{-1}$ and $7.8125 \times 10^{-4}\,{\rm pc\,zone}^{-1}$, respectively.

Table 1. List of models in our study. The columns inform on the simulation labels, the angle $\theta_{\rm mag}$ (in degrees) between the direction of the ISM magnetic field and the direction of stellar motion, the strength of the ISM magnetic field $B_{\rm ISM}$ (in μG), whether the star moves along the axis Oz of the Cartesian computational domain, the name of the red supergiant star to which the model is tailored to, whether optically thin radiative cooling and heating is included, and, finally, the general purpose of each runs.

Model	$\theta_{\rm mag}(^\circ)$	$B_{\rm ISM}(\mu{\rm G})$	$\vec{v}_\star \parallel Oz$	Star	Heating and radiative cooling	Purpose
Run-test-1	0	0	Yes	IRC-10414[a]	No	Test grid effects
Run-test-2	0	0	No	IRC-10414[a]	No	Test grid effects
Run-$\theta_{\rm mag}$-0	0	7	No	IRC-10414[a]	Heating/cooling for ionized gas	Bow shock stability study
Run-$\theta_{\rm mag}$-45	45	7	No	IRC-10414[a]	Heating/cooling for ionized gas	Bow shock stability study
Run-$\theta_{\rm mag}$-90	90	7	No	IRC-10414[a]	Heating/cooling for ionized gas	Bow shock stability study
Run-αOri	90	7	No	Betelgeuse[b]	Heating/cooling for ionized gas	Comparison with observations

Stellar wind properties are taken from (a) Meyer et al. (2014a) and (b) van Marle et al. (2014), respectively.

3.1 Bow shock stability as a result of the ISM magnetic field direction

In Fig. 1 we display the number density field (in cm^{-3}) in the $z = 0$ plane for models Run-$\theta_{\rm mag}$-0, Run-$\theta_{\rm mag}$-45, and Run-$\theta_{\rm mag}$-90, assuming different angles between the direction of motion of the star and that of the local magnetic field $\theta_{\rm mag} = 0^\circ$ (a), $\theta_{\rm mag} = 45^\circ$ (b), and $\theta_{\rm mag} = 90^\circ$ (c), respectively. In each panel, the black contour marks the region in the astrosphere at which the mass contribution of stellar and ISM balance, respectively (Meyer et al. 2017). The black cross marks the position of the star. The model Run-$\theta_{\rm mag}$-0 with ISM magnetic field direction parallel to that of the stellar motion recovers the hydrodynamical limit and produces an unstable bow shock exhibiting a very distorted, ragged, and clumpy layer of shocked ISM material, consistent with the previous 3D hydrodynamical simulations of stellar wind bow shocks of Blondin & Koerwer (1998). The astropause, i.e. a tangential discontinuity[2] (black line), is no more path-connected as a result of the turbulent velocity and magnetic fields in it, producing regions of ISM gas engulfed into the layer of stellar wind (Fig. 1a).

The stand-off distance of the bow shock (Baranov, Krasnobaev & Kulikovskii 1971) is defined as

$$R(0) = \sqrt{\frac{\dot{M} v_{\rm w}}{4\pi \rho_{\rm ISM} v_\star^2}}, \tag{11}$$

where $\rho_{\rm ISM} = \mu n_{\rm ISM} m_{\rm H}$, $n_{\rm ISM}$ standing for the gas density of the ambient medium, μ the ISM mean molecular weight, and $m_{\rm H}$ the proton mass. It is measured from the simulation data as $R(0) \approx 0.14$ pc (Fig. 1a–c). The stand-off distance lies on the inflow line, as Baranov et al. (1971) determined it using an incompressible irrotational fluid model, as does implicitly Wilkin (1996) who also assumes a thin-shell approach to the overall bow shock structure. The models with $\theta_{\rm mag} = 45^\circ$ (Fig. 1b) and $\theta_{\rm mag} = 90^\circ$ (Fig. 1c) have smoother and stable bow shock structures. Because of the extra stress and pressure provided by the ISM magnetic field, the layers of astropause and the forward shock are stabilized (see also van Marle et al. 2014), although the nebula still reveals traces of large-scale eddies, repetitively advected from the apex to the tail of the bow shock (black line in Fig. 1c). The layer of shocked ISM material is enlarged and the post-shock density at the forward shock is dimmer Meyer et al. (2017).

In Fig. 2 we plot the number density field (in cm^{-3}) in the $y = 0$ (left) and $x = 0$ (right) planes in our models Run-$\theta_{\rm mag}$-0 (top), Run-$\theta_{\rm mag}$-45 (middle), and Run-$\theta_{\rm mag}$-90 (bottom), assuming different angle between the direction of motion of the star and that of the local magnetic field $\theta_{\rm mag} = 0^\circ$ (a,d), $\theta_{\rm mag} = 45^\circ$ (b,e), and $\theta_{\rm mag} = 90^\circ$ (c,f), respectively. As described above, the model with $\theta_{\rm mag} = 0$ is clearly unstable and turbulent, with several knots and clumps overpassing the stand-off distance. This has been revealed in the 3D hydrodynamical simulations of the Rayleigh–Taylor and Vishiniac-unstable stellar wind bow shock modelled of Blondin & Koerwer (1998). The figures corresponding to the model with $\theta_{\rm mag} = 90^\circ$ highlight that the astropause can have different stability properties and can be different along distinct cross-sections such as the Oxz and Oyz planes. This induces projection effects of the nebula's emission on to the plane of the sky, according to the viewing angle it is observed from (our Section 3.3).

Fig. 3 further illustrates the density fields in the plane Oxy of models Run-$\theta_{\rm mag}$-0 (left) and Run-$\theta_{\rm mag}$-90 (right). The overplotted vectors fields highlight the gas velocity (blue) and the magnetization (red) of the plasma. One sees the isotropic stellar wind flowing from the central black cross marking the position of the star, to the tangential discontinuity (thin black line). The size of the vectors scale with the magnitude of the field they represent. Hence, the Parker magnetic field in the stellar wind, several orders of magnitude smaller than that of the ambient ISM, are not visible at the naked eye in these figures. The velocity field is reduced in the post-shock region at the forward shock, as testifies the smaller blue arrows, which re-accelerate in the winged region of shocked ISM behind the apex of the astrosphere (see also our discussion on the Mach number in Section 3.2). Similarly, the ISM magnetic field is compressed in the wings of the bow shock, filled with shocked ISM material (right-hand panels of Fig. 3).

Fig. 4 compares the analytic solution of Wilkin (1996) with the density field (in cm^{-3}) of the bow shock in our simulation model Run-$\theta_{\rm mag}$-90. The figure displays a cross-section through the plane Oxy and Wilkin's solution is added as coloured coutours representing the approximation for the morphology of an infinitely thin bow shock. It reads

$$R(\theta) = R(0)\csc(\theta)\sqrt{3(1-\theta)\cot(\theta)}, \tag{12}$$

with θ is the angle between the direction of stellar motion in degrees and $R(0)$ the stand-off distance (equation 11). The black contour corresponds to the stand-off distance derived from the observations of surroundings of IRC-10414 (Gvaramadze et al. 2014), while the green contour fits the astropause (marked with blue thin contour). A couple of remarks naturally arise from this comparison. First, the analytic approximation for bow shocks around red supergiant stars matches well the overall circumstellar structure. It is therefore suitable, e.g. for observers constraining the geometry of observed nebulae. However, it does not corresponds to a characteristic layer of the bow shock, such as the tangential discontinuity, for angles $\theta \geq$

[2]Also called astropause, tangential discontinuity, wind-ISM interface, or pressure equilibrium surface

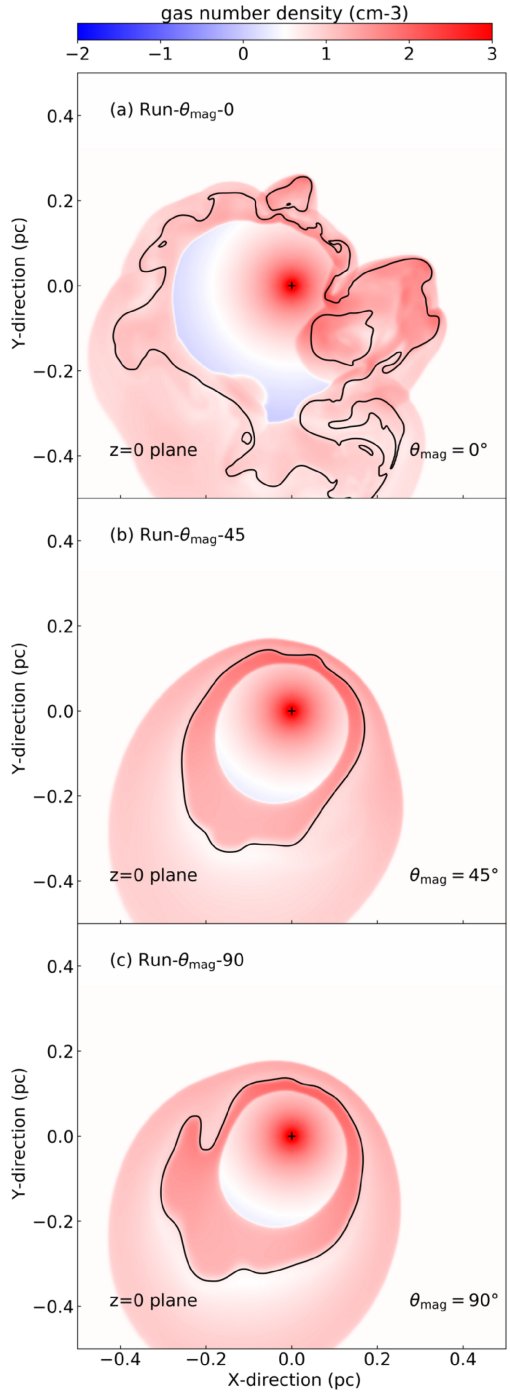

Figure 1. Density fields in the $z = 0$ plane of models Run-$\theta_{\rm mag}$-0, Run-$\theta_{\rm mag}$-45, and Run-$\theta_{\rm mag}$-90. The simulations assume different angles between the direction of motion of the star and that of the local magnetic field, with $\theta_{\rm mag} = 0^\circ$ (a), $\theta_{\rm mag} = 45^\circ$ (b), and $\theta_{\rm mag} = 90^\circ$ (c), respectively. The black contour is the location in the bow shock where the gas is made of equal proportion of stellar wind and ISM material ($Q = 0.5$). The black cross marks the position of the star.

20–30°. Its applicability is therefore limited to the apex of the bow shock (Blondin & Koerwer 1998; Mohamed et al. 2012).

3.2 Bow shock internal properties

Fig. 5 shows the distribution of the gas density (right) and gas velocity (left), for both all gas in the bow shock nebulae (yellow) and for the shocked ISM gas component (blue), respectively. Figures are displayed for different angles, namely, $\theta_{\rm mag} = 0^\circ$ (top), $\theta_{\rm mag} = 45^\circ$ (middle), and $\theta_{\rm mag} = 90^\circ$ (bottom). Gas number density (in cm^{-3}) and velocity (in km s^{-1}) are plotted in log-scale, while the distribution represents the number of grid zones that is a measure of the volume. Inspection of the left-hand panels reveals that the inclination of the ISM magnetic field $\theta_{\rm mag}$ induces notable differences in the bow shock density distribution between the models; see e.g. models with $\theta_{\rm mag} = 0^\circ$ (Fig. 5a) and with $\theta_{\rm mag} = 45^\circ$ (Fig. 5b). Indeed, the unstable model in the hydrodynamical limit (Fig. 5a) has a density distribution which is globally larger than in the other models (Fig. 5b and c). This illustrates the well-known effect of magnetic fields in dimming the gas density in post-shock region at the forward shock (Meyer et al. 2017). Note that density distribution peaks are similar in all three models (Fig. 5a–c) as each bow shock model is driven by the same star. Not much difference is noticeable between the models with $\theta_{\rm mag} = 45^\circ$ and $\theta_{\rm mag} = 90^\circ$, suggesting also that their respective maximal emissivity $\propto n^2$ might not greatly differ compared to the case with $\theta_{\rm mag} = 0^\circ$ (see Section 3.3).

The right-hand panels display histogram for the gas velocity distributions in the astrospheres. The similar upper part of all distributions (Fig. 5d–f) in each panels comes from the fact that all simulations have the same central star expelling the same winds, moving at the same space velocity $v_\star = 50\,{\rm km\,s^{-1}}$ through the same ISM. Only mild differences are found in the low-velocity region of the two distributions, because of the changes in the velocity field in the post-shock region at the forward (bow) shock and at the reverse (termination) shock, respectively The more the flow is laminar in the shocked ISM (the less the tangential discontinuity is unstable) the lower will be the minimum gas velocity (Fig. 5e). This may have observational consequences, e.g. on atomic and molecular line emissions of the nebula, which is much beyond the scope of this study.

In Fig. 6 we further illustrate the internal structure of the stable bow shock in our model Run-$\theta_{\rm mag}$-45. The plot is a 3D rendering of the astrophere around the runaway red supergiant star IRC-10414. Transparent clipped number density surfaces render the bow shock structure and streamlines mark the magnetic field (yellow) and velocity fields (red), respectively. It shows how the stellar magnetic field, initially made of a Parker spiral transported with the stellar wind in the equatorial plane of the star, fills the entire region of freely-expanding accelerated unshocked stellar wind. These field lines do not reconnect with the ISM magnetic field lines that penetrate the forward shock and stabilize the astropause, but rather expand as a wider spiral in the tail of the bow shock. The gas streamlines also highlight the isotropically-outflowing stellar wind from the inner stellar boundary, which enters the region of shocked wind and bends towards the tail of the astrosphere. The ISM gas enters the bow shock in its turn and flow along the wind-ISM discontinuity.

Fig. 7 displays the temperature field (top panels), sonic Mach number field (middle top panels), Alfévnic Mach number field (middle top panels) and fast magnetosonic Mach number field (middle bottom panels) in the $z = 0$ plane of our bow shock models, displayed as a function of $\theta_{\rm mag} = 0^\circ$ (left), $\theta_{\rm mag} = 45^\circ$ (middle), and $\theta_{\rm mag} = 90^\circ$ (right). The black contour is astropause interface of the

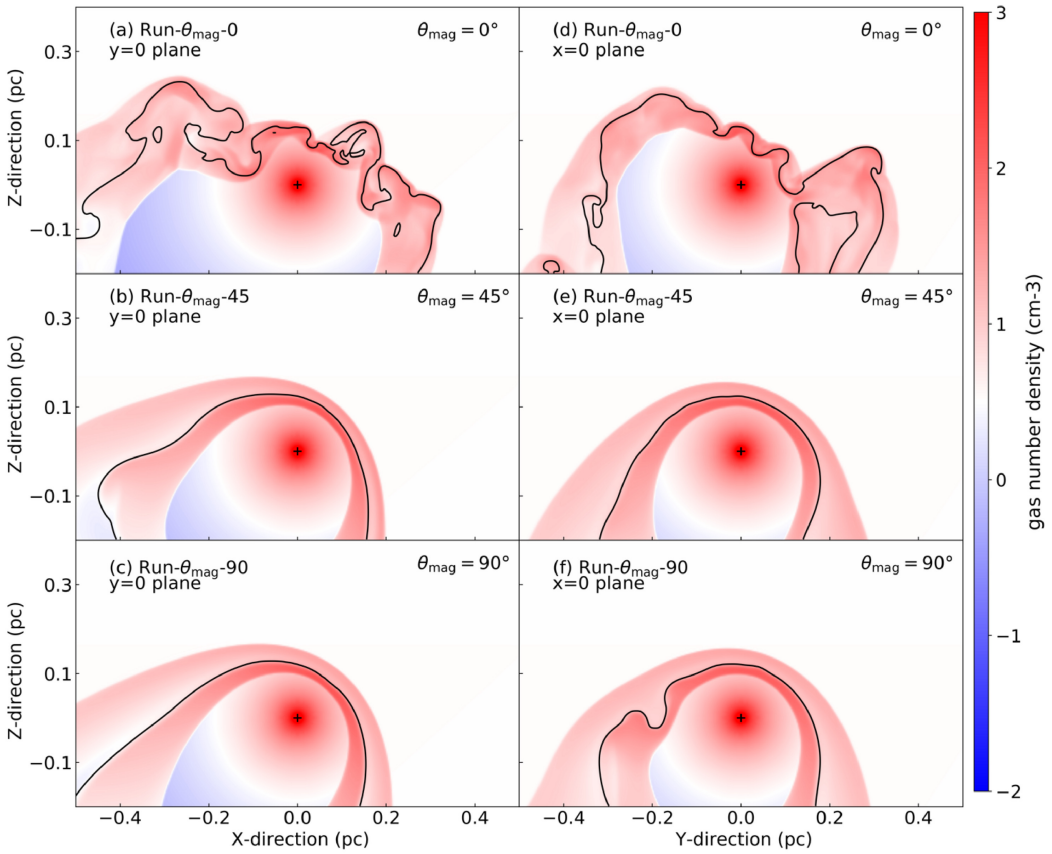

Figure 2. Density fields in the $x = 0$ (left) and $y = 0$ (right) planes of models Run-θ_{mag}-0, Run-θ_{mag}-45, and Run-θ_{mag}-90, assuming different angle between the direction of motion of the star and that of the local magnetic field, $\theta_{mag} = 0°$ (top), $\theta_{mag} = 45°$ (middle), and $\theta_{mag} = 90°$ (bottom), respectively. The black contour is the location of the tangential discontinuity (where we have equal proportion of stellar wind and ISM material, i.e. $Q = 0.5$). The black cross marks the position of the star.

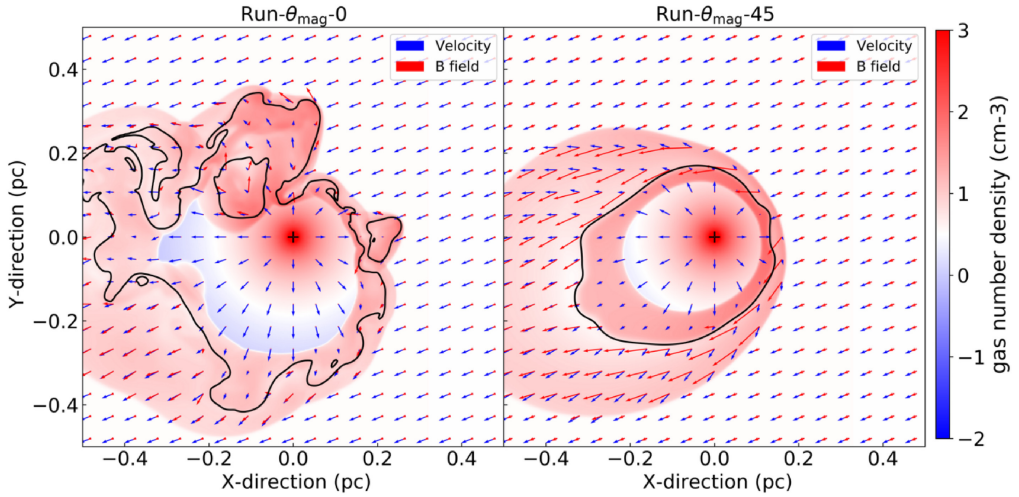

Figure 3. Distribution of the gas density in the $z = 0$ plane of our bow shock models Run-θ_{mag}-0 (left) and Run-θ_{mag}-45 (right). The velocity and magnetic field vector fields are represented with blue and red arrows, respectively. Differences between the vector directions are in the plane normal to the figures. The black contour is the location of the tangential discontinuity ($Q = 0.5$). Gas number density is plotted in the logarithmic scale.

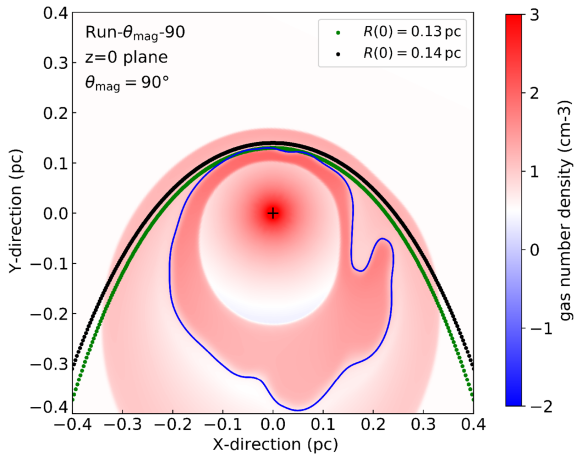

Figure 4. Comparison between Wilkin's analytic solution (Wilkin 1996) for the overall shape of the bow shock model Run-θ_{mag}-90. Wilkin's solution is given for two stand-off distances, the observed one (black) and that fitting the astropause of the bow shock nebula (green).

bow shock, i.e. the location of the nebula made of equal proportion of stellar wind and ISM material ($Q = 0.5$). On each panel the cross marks the position of the star. The temperature maps illustrate that the maximum temperature is at the bow shock, where it exceeds that at the termination shock (Fig. 7a–c) (see also Meyer et al. 2017).

The series of panels on the Mach number,

$$M = \frac{v}{c_s}, \tag{13}$$

shows that the gas is supersonic in the free-streaming wind and in the unshocked ISM gas, respectively. Indeed, the accelerated stellar wind v_w is larger than the radially-decreasing temperature by adiabatic cooling c_s, and $v_\star = 50\,\mathrm{km^{-1}} > c_s \approx 10\,\mathrm{km^{-1}}$ everywhere in the unperturbed ISM. The gas is sub-sonic in the shocked regions, both located downstream the termination shock and the bow shock, as a result of the changes in both the post-shock temperature and velocity ($M < 1$). This permits us to clearly classify the astrosphere of IRC-10414 as a bow shock, instead of other circumstellar structures such as bow wave or dust waves that can be produced around moving stars (Pogorelov et al. 2017; Henney & Arthur 2019c). Note also that the sonic Mach number increases in the region of shocked stellar wind gas in the in wings of the bow shock (Fig. 3e and f).

The Alfénic Mach number is defined as

$$M_A = \frac{v}{v_A} = \frac{v}{|\vec{B}|/\sqrt{\rho}}, \tag{14}$$

and the fast-magnetosonic Mach number reads as

$$M_f = \frac{v}{v_f} \tag{15}$$

with the fast-magnetosonic speed,

$$v_f = \sqrt{\frac{1}{2}\left(\left(c_s^2 + v_A^2\right) + \sqrt{\left|\left(c_s^2 + v_A^2\right)^2 - 4c_s^2 v_A^2 \cos(\Theta)^2\right|}\right)}, \tag{16}$$

where Θ is the angle between the gas velocity $\vec{v}$ and magnetic field $\vec{B}$ vector fields. Note that the sound speed is the characteristic dynamical quantity of an hydrodynamical simulation, whereas the fast-magnetosonic speed is the relevant dynamical quantity of an magneto-hydrodynamical model, respectively. Expanding stellar wind and unperturbed ISM are supersonic, super-Alfénic, and super-fast magnetosonic. The values of the sonic Mach number M is lower in the shocked wind region than in that of the shocked ISM gas because the post-shock gas velocity at the termination shock is smaller than at the forward shock, and because the sound speed is larger in that dense region of shocked wind (Fig. 7a–c). Similarly, the Alfénic Mach number M_A is smaller in the shocked ISM region at the apex of the bow shock than in the layer of shocked stellar wind, because of both the changes in compressed magnetic field lines and gas number density (Fig. 7h and i). The fast-magnetosonic Mach number M_f is below unity in all shocked regions of the stable bow shocks but larger than unity in the freely streaming stellar wind and in the ambient medium, as described in Scherer et al. (2020).

Fig. 8 shows cross-sections in the number density and Mach number fields taken through the maps displayed in Fig. 7, measured along the $y = 0$ directions. The stellar wind density profile is clearly visible at the origin of the domain, which decreases $\propto 1/r^2$ to values that are lower in the $y < 0$ part of the figure than in the $y > 0$, in the region of the bow shock opposite of the direction of stellar motion. The sonic Mach number M profile reflects the decrease of the temperature in the stellar wind under the effect of adiabatic cooling while the the external photo-heating accelerates the stellar wind (Fig. 8d; see also Meyer et al. 2014a; Mackey et al. 2014) from the inner stellar wind region that is excluded from the computational domain, to the termination shock of the bow shock. As expected and above described, the fast magnetosonic Mach number M_f diminishes and is $M_f < 1$ in the post-shock layers of materials located between the termination shock and the bow shock (Fig. 8c).

3.3 Emission maps

We produce emission maps using the RADMC-3D code (Dullemond 2012) that permits calculating radiative transfer for analytic prescription of emission coefficients such as optical Hα optical emission. In Fig. 9, we plot Hα emission maps of our bow shock model Run-θ_{mag}-0. The figure displays the surface brightness Σ (in erg cm^2 s^{-1} arcsec^{-2}) of a nebula located at a distance of 2 kpc, corresponding to the IRC-10414 distance (Gvaramadze et al. 2014). The projected emissivity is shown under several considered rotation of the polar ϕ and azimuthal θ viewing angles, respectively. The white cross marks the position of the runaway star. The bow shock of the model Run-θ_{mag}-0 results turbulent. Its exhibits a diffuse nebula morphology, showing several filaments and knots dispersed around the central object. The star is much brighter than its surroundings, which raises the question of the saturation of observed fluxes and of the screening of red supergiant bow shocks.

A series of two arcs is visible ahead of the star, roughly in the direction of stellar motion (Fig. 9a). However, the star is not at the geometrical centre of the arc and some clumps are much beyond the bow shock (Fig. 9a–c). Note that this structures are very different from the circular ones obtained with 2D hydrodynamical simulations in Meyer et al. (2014b). The images with $\phi = 45°$ are brighter than that with $\phi = 0°$ by a factor $2 - 3$, as expected from previous 2D simulations. This behaviour is because the line-of-sight intercepts more dense material and consequently produces brighter surface brightness (Fig. 9d–f). The observed star-arc distance (called stand-off distance in the observational literature) varies significantly between models, some of them revealing distorted and clumpy arcs close to the star (Fig. 9d). The changes in the bow shock morphology are important for mild changes in the viewing angle (Fig. 9e). In these conditions, it is very difficult to distinguish a circumstellar structure, and even more uneasy to identify bow shocks, if at all, although the nebula has formed and exist (Fig. 9).

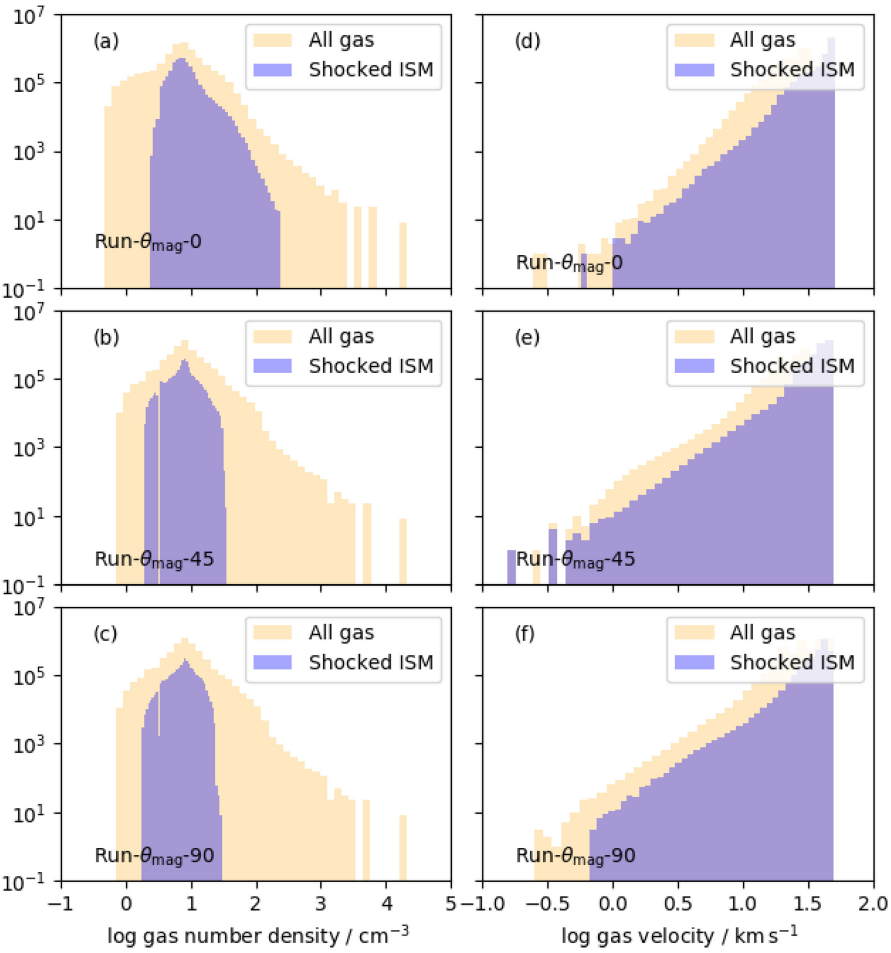

Figure 5. Distribution of the gas density (left-hand panels) and gas velocity (right-hand panels) in our bow shock models Run-θ_{mag}-0 (top, a and d), Run-θ_{mag}-45 (middle, b and e), and Run-θ_{mag}-90 (bottom, c and f). The histograms distinguish between the all gas in the bow shock nebulae (yellow) and the shocked ISM material (blue). Gas number density and velocity are plotted in the logarithmic scale.

In Fig. 10, we display Hα emission maps of our astrosphere model Run-θ_{mag}-45. The projected emissivity morphology is very different than in the case with $\theta_{mag} = 0°$, as evident bow shock morphologies are visible in each panel of the figure. The maximum emission originates from the sub-sonic and super-Alfénic region of shocked stellar wind, much denser than the compressed magnetized ISM material, plus a lighter overarching arc tracing the forward shock of the bow shock. Bright clumps appear in the shocked wind close to the region of maximum emission (Fig. 10a–c). This fact reflects the instabilities at the interface between wind and ISM material visible in the *Oxy* plane (black line in Fig. 2b). These infrared bow shocks are not strictly symmetric with respect to the direction of motion of the star, as a consequence of the inclined magnetic field direction inducing extended wing-like regions of shocked ISM gas of different size (Fig. 2b). By projection effects, these regions can produce brighter zones wrongly suggesting, from a purely observational point of view, the presence of filaments, while it relies large-scale instabilities in the astropause interface. High-resolution simulations would result in qualitatively different patterns, and this should be explored in future works. This structure can also appear as stripes normal to the direction of motion of the runaway star (Fig. 9e and f) difficult to interpret from the observational point of view. As in Fig. 9 the surface brightness of the astrosphere is more significant with $\theta = 45°$ than with $\theta = 0°$. Finally, note that some models are also very smooth (Fig. 9h) and fit well with the 2D predictions of Meyer et al. (2014b; see Section 4.3).

In Fig. 11, we show Hα emission maps for our bow shock model Run-θ_{mag}-90. The situation is similar to that in our model Run-θ_{mag}-45. Several shapes arise from projection effects, with differences in the maximum emission of the circumstellar material (Fig. 11a). Very smooth shells (Fig. 11h) or irregular (Fig. 11d, g, and i) patterns of dense shocked stellar wind are mostly consequences of the unstable tangential discontinuity. Interestingly, the perpendicular orientation of the ISM magnetic field can result in series of multiple arcs normal to the direction of motion of the star (Fig. 11f) as modelled in the context of hot OB stars in Katushkina et al. (2017, 2018; see also Baalmann et al. 2021). Furthermore, the opening of the bow shock can significantly differ from a projection model to another, with rounder termination shocks (Fig. 11f) and wider arcs (Fig. 11d). Overall, our emission maps reveal the importance of projection effects in the appearance of stellar wind bow shocks from runaway red supergiant stars at Hα. It supports the use of astrometric

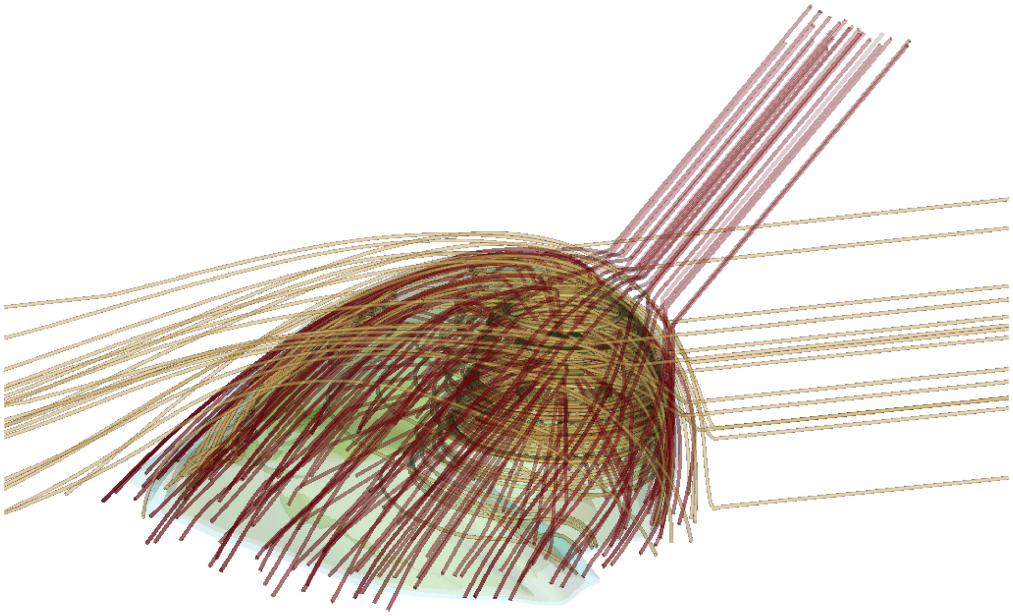

Figure 6. Rendering of the structure of the 3D MHD bow shock in our model Run-$\theta_{\rm mag}$-45, forming around a runaway red supergiant star moving into an constant ambient medium in which the direction of stellar motion and local magnetic field direction make an angle of $\theta_{\rm mag} = 45^\circ$. The transparent clipped surfaces are number density isocontours. The yellow and red lines are gas velocity and magnetic field streamlines, respectively.

measures, such as GAIA in order to determine the direction of proper motion of runaway stars instead of their circumstellar bow shocks, the latter being a source of errors resulting from the random orientation of projected astrospheres (see Peri et al. 2015).

4 DISCUSSION

In this section, we discuss the limitations of our simulation method. As application, we reproduce the bow shocks of two runaway red supergiant stars, IRC-10414 and Betelgeuse (see below), respectively. Last, we discuss our findings in the context of nebulae around other massive stars and core-collapse supernova remnants.

4.1 Model limitation

Our 3D MHD simulations are a leap forward in studying the circumstellar medium of runaway late-type (super)giant stars, as it includes both stellar and ISM magnetic fields within a 3D framework, completed with radiative transfer calculations. Therefore, the simulations are intrinsically more realistic, for example in terms of development and damping of instabilities in the bow shock structure, compare to that previously conducted in, e.g. Meyer et al. (2014b). Mainly, it is possible to explore and study the effects of an ISM magnetic field that is not aligned with the direction of stellar motion, which latter configuration was imposed by the 2D cylindrical coordinate system used in the other studies of that series and in van Marle et al. (2014). We study this effect by varying the angle $\theta_{\rm mag}$ between the direction of stellar motion and the direction of the ISM magnetic field. Our results stress the stabilizing role of the ISM magnetic field already noticed in 2D precedent works with $\theta_{\rm mag} = 0^\circ$ (van Marle et al. 2014; Meyer et al. 2017).

Nevertheless, within the stellar wind properties of IRC-10414, the damping of instabilities in stellar wind bow shocks is very efficient in 3D only if $\theta_{\rm mag} \geq$ a few degrees, while simulations with $\theta_{\rm mag} = 0^\circ$ recovers the hydrodynamical unmagnetized limit (Fig. 12). These latter results have different stability properties than the 2D models of Meyer et al. (2014b). This effect is a noteworthy difference between our 3D simulations and precedent 2D works in the context of the surroundings of IRC-10414. We interpret this difference as originating from the dissimilar coordinate systems used in these two works. The first one employs a cylindrical 2D coordinate system that possesses a symmetry axis affecting the development of instabilities and leading to the complex topology of the bow shock apex (Comerón & Kaper 1998; Meyer et al. 2017). The second one considers a 3D Cartesian coordinate system that permits circumventing that issue (Mignone 2014).

The spatial resolution of the simulations has become an essential parameter regarding the development of bow shock instabilities (van Marle et al. 2014). In that sense, future simulations should consider simulation models with even higher spatial resolution. However, one should keep in mind that fully resolving Rayleigh–Taylor-based instabilities can not be achieved numerically using Eulerian codes (Blondin & Koerwer 1998; Mohamed et al. 2012), and that tending to such result would be at prohibitive numerical costs. Furthermore, our models does not include all microphysical mechanisms at work in the circumstellar medium of late-type giant stars, such non-ideal MHD processes like Ohmic diffusion and Hall effect, known to affect the density of magnetized plasmas, chemical reactions at work in the shocked enriched stellar winds or acceleration of stellar wind electrons and protons at the termination shock of bow shock nebulae (del Valle & Pohl 2018). Apart from lacking physical processes, our choices regarding boundary and initial conditions for stellar wind and the ISM will be studied in a future parameter study.

Indeed, the present study is tailored to the runaway red supergiant IRC-10414 whose surface properties have been constrained by means of observations (Gvaramadze et al. 2014) completed with numerical simulations (Meyer et al. 2014a). Our models therefore do not include stellar evolution as wind boundary conditions, e.g. time-dependently

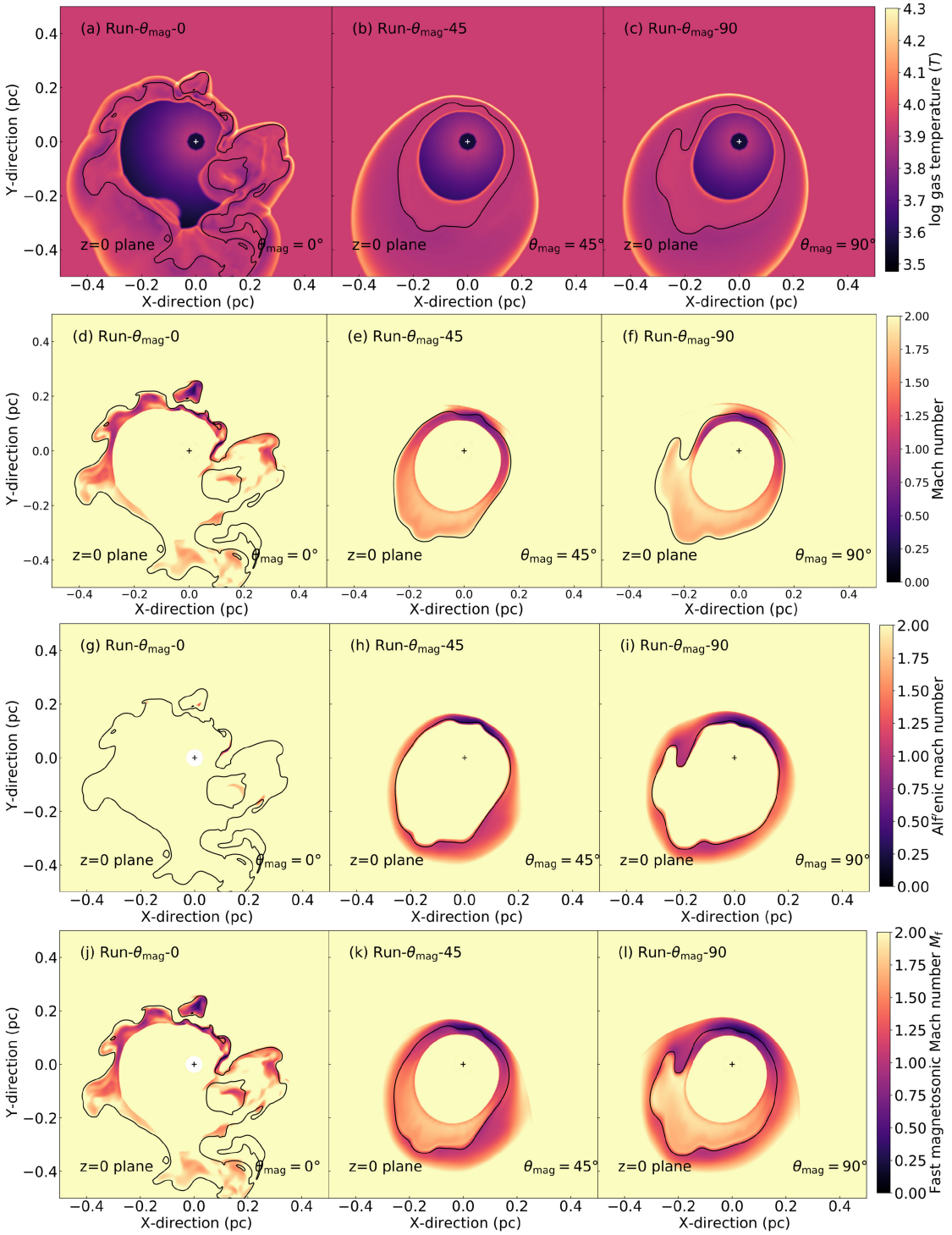

Figure 7. Temperature T (top panels), sonic Mach number M (middle top panels), Alfévnic Mach M_A number (middle top panels), and fast magnetosonic Mach number M_f (middle bottom panels) in the $z = 0$ plane of our bow shock models. Bow shock models are displayed as a function of the angle between the direction of stellar motion and ISM magnetic field, which spans from $\theta_{mag} = 0°$ (left) to $\theta_{mag} = 90°$ (right). The black contour is astropause interface into the bow shock, and on each panel the central black and white crosses marks the position of the star.

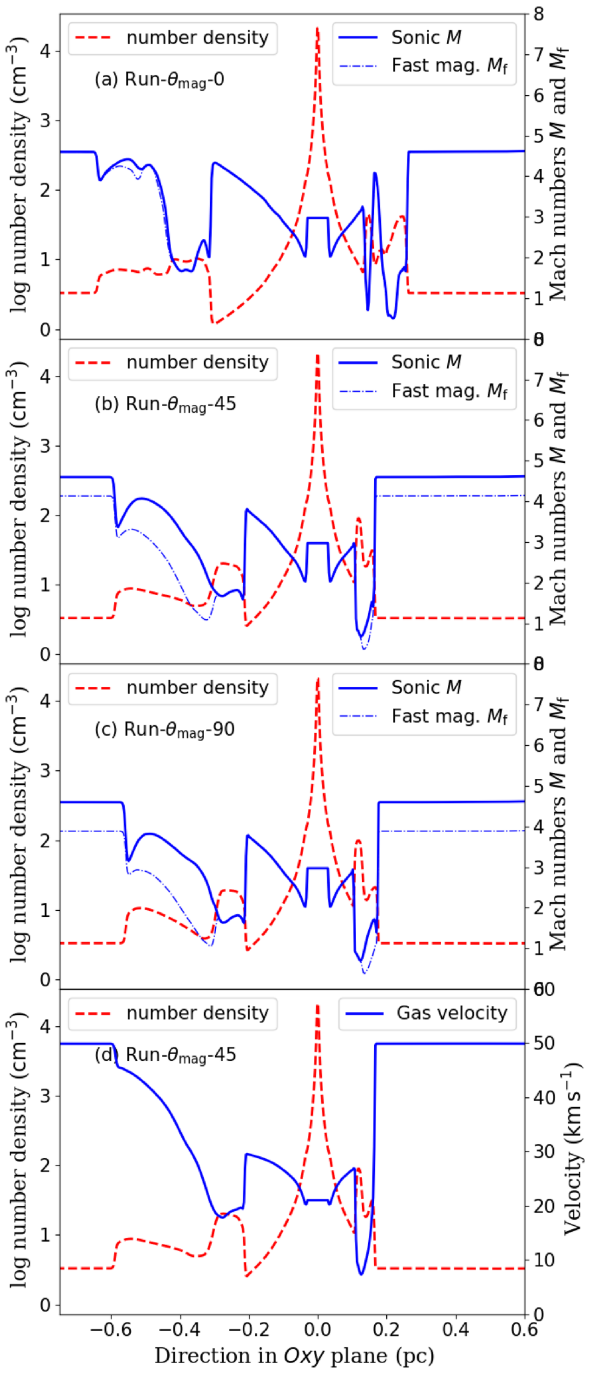

Figure 8. Cuts along the Oy axis in our Run-θ_{mag}-0 (a), Run-θ_{mag}-45 (b), and Run-θ_{mag}-90 (c), showing the gas number density, the sonic Mach number M, and the fast-magnetosonic Mach number M_f profiles. The last panel shows the acceleration of the stellar wind in Run-θ_{mag}-45 (d). Gas number density is plotted in the logarithmic scale, Mach numbers, and gas velocity in the linear scale.

interpolating evolutionary tracks (Brott et al. 2011; Szécsi et al. 2020) that would permit better treatment of the surroundings of red supergiant stars (Mackey et al. 2012; Meyer et al. 2014b). On the other hand, the stellar evolution can be useful to model core-collapse supernova remnants from 10–20 $M_\odot$ massive runaway progenitor stars (Katsuda et al. 2018). Additionally, the manner of the surrounding medium remains rather simplistic in our study as we assume a uniform, warm and ionized ISM. A natural improvement will assume a more realistic turbulent, inhomogeneous (Walch et al. 2011), and clumpy (Baalmann et al. 2021) medium. This would account for the intrinsic turbulence driven by the stellar winds of neighbouring massive stars and/or travelling shock wave from supernova remnants (Peters et al. 2017; Seifried et al. 2018).

4.2 Grid-induced effects on bow shock instability

Previous 3D Eulerian numerical works on stellar wind bow shock showed that instabilities develop along the Ox and Oy axis when the star moves along the Oz axis (Blondin & Koerwer 1998). In order to avoid such an effect, our simulations impose on the star a trajectory that does no coincide with a preferential direction of the 3D Cartesian coordinate system (Ox, Oy, and Oz). Our direction of stellar motion makes arbitrary angles $\leq 10^\circ$ with the planes Oxy and Oxz, respectively. In Fig. 13, we plot a series of two models labelled Run-test-1 and Run-test-2 (Table 1) that compare the above discussed grid effects. We carry out these tests within the hydrodynamical limit ($B_\star = B_{ISM} = 0$). The difference lies in the direction of the stellar motion imposed by the outer boundary conditions at the planes $x = 0.8$, $y = 0.8$, and $z = 0.4$, respectively. In Run-test-1 the star moves along the Oz axis while in Run-test-2 it moves along an arbitrary direction as described above.

The most important differences are the changes in the topology of the different discontinuities present in these cross-sections. The termination shock, astropause interface, and forward shock are spherically symmetric in Run-test-1 (Fig. 13a) while absent in Run-test-2 (Fig. 13b). This fact reflects different faster-growing modes at work in the two simulation tests, confirms the findings of Blondin & Koerwer (1998), and illustrates the necessity to impose the star a direction of motion that does not coincide with any Cartesian axis unless grid-induced regular patterns such as the $m = 4$ mode of Fig. 13(a) will develop in the shocked stellar wind. Although both are physical, Run-test-2 is closer to what would happen in nature. The isothermal stellar wind bow shock of Blondin & Koerwer (1998) concerns a slow-winded and dense-winded star, moving with velocity $\approx$60 km s^{-1} that develops a ragged, unstable, and clumpy circumstellar structure. Their figs 9 and 10 show the bow shock structure strongly influenced by the grid during many crossing-time of the ISM flow through the computational domain before becoming turbulent. Our method permits us to eliminate these grid effects without waiting for many flow times and reduce computational costs.

4.3 Comparison with observations

4.3.1 The case of IRC-10414

For the sake of completeness, we perform a comparison with observations between our modelled bow shock, which stellar wind properties are tailored to that of IRC-10414, and observational data of that particular circumstellar nebula. In Fig. 14, we plot a synthetic image of the simulation model Run-θ_{mag}-45 generating a stable nebula, as seen at the optical Hα emission line with a viewing angle characterized by $\theta = 90^\circ$ and $\phi = 120^\circ$ and whose emission maps

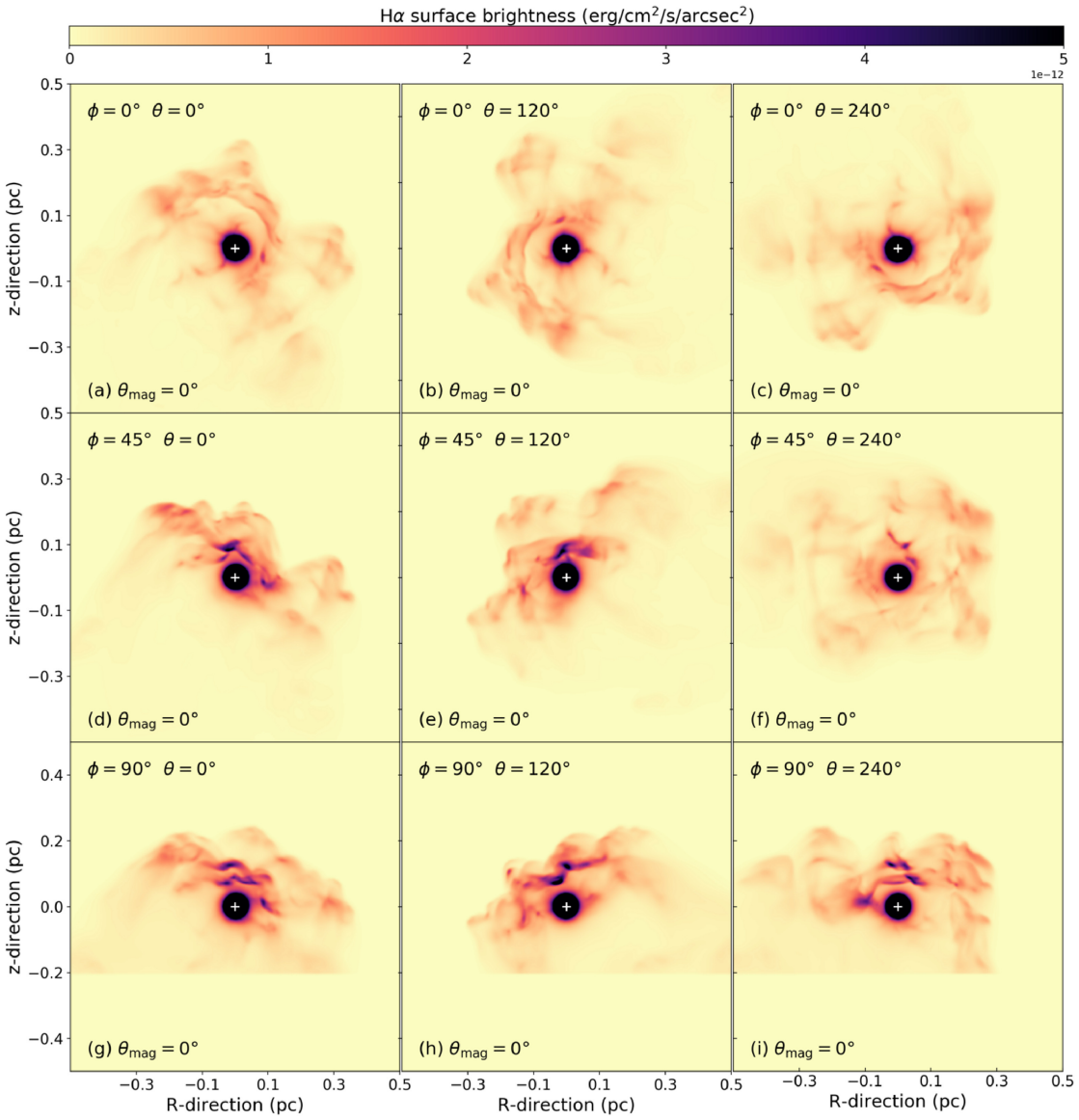

Figure 9. Emission maps of our bow shock model Run-$\theta_{\rm mag}$-0. The figure plots the H α surface brightness (in erg cm^2 s^{-1} arcsec^{-2}). Quantities are calculated excluding the undisturbed ISM and plotted in the linear scale, under several viewing angles ϕ and θ, respectively. The white cross marks the position of the star.

has been rotated so that the symmetry axis of the bow shock fits with the vertical axis of the plot. The figure additionally shows several contours from the observations taken by the *Aristarchos* telescope from the National Observatory of Athene (NOA) located at Mt Helmos, Greece (2326 m above sea level). The data have been acquired via a single 30 min exposure, on 2013 August 9. The thin black lines are several H α+[N II] surface brightness isocontours highlighting the image background sky, and two thick black isocontours trace the arced circumstellar nebulae of IRC-10414. Last, the blue contour marks the analytic solution derived by Wilkin (1996). The data do not extend under $z = 0$ as the telescope aperture was chosen to screen part of the star.

The observed bow shock is stable in the sense that no large-scale instabilities have developed. However, overplotted isocontours indicate that the flux in some region of the nebula is somewhat diffused. Perhaps this is caused by contamination from the starlight or background field sources, e.g. in the $R < 0$ and $z > 0$ part of the image. Despite good qualitative agreements between our predictions and observations, the curvature of the bow shock is not the same in the $R < 0$ and $R > 0$ regions of the figure. This difference may rely on projection effects that our models do not reproduce, and better fine-tuning of our simulations would be necessary to address this question beyond the scope of our study [see Baalmann et al. (2021) for a first attempt]. Therefore, even more complex 3D MHD models are necessary to fit the data better, e.g. considering local variations in the ambient medium density and/or the turbulent character of the medium the star moves in. We chose to fit the data by matching the region at the left part ahead of the apex of the bow shock. However, we could have

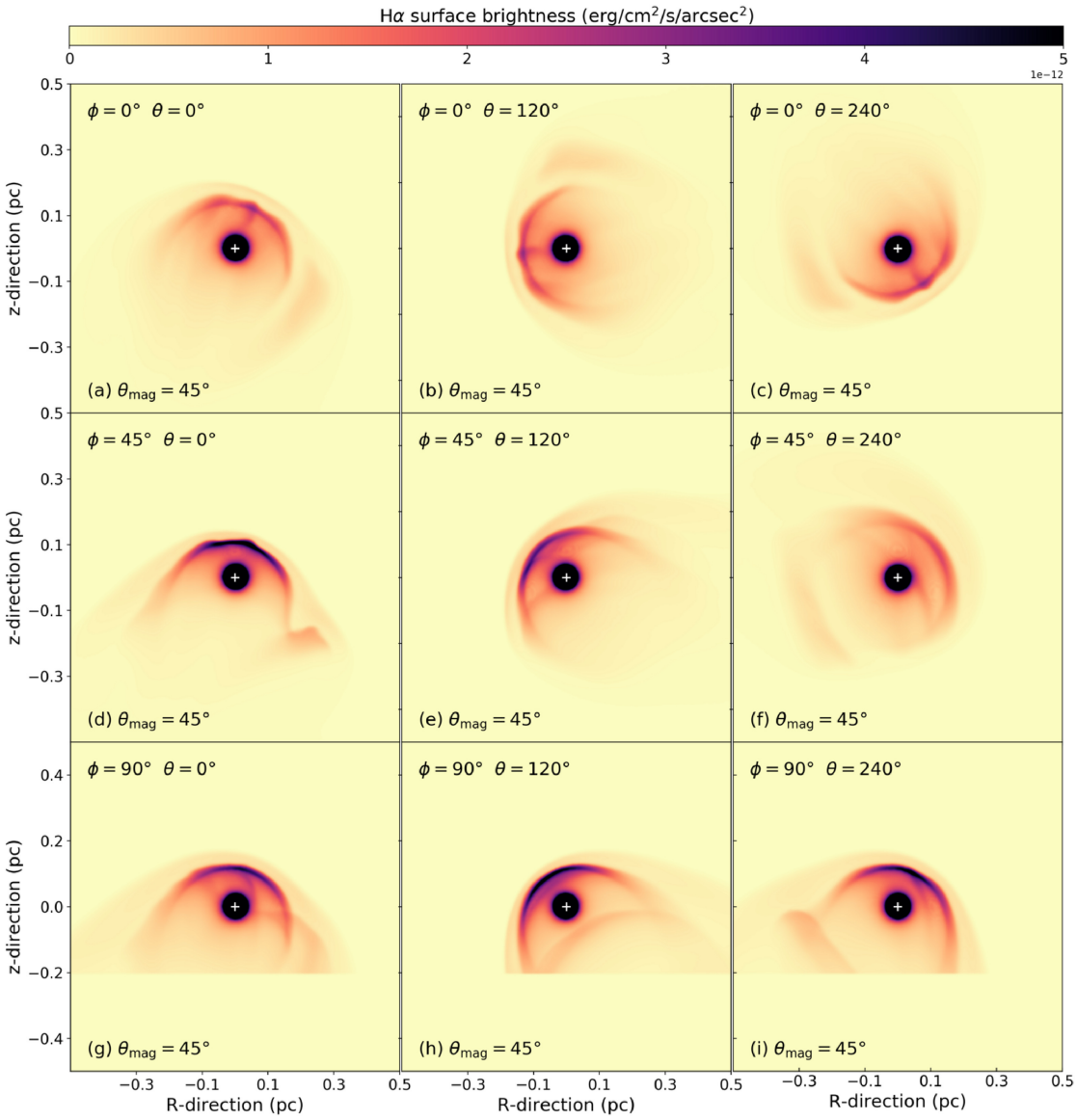

Figure 10. Same as Fig. 9 for our model Run-θ_{mag}-45.

chosen to further rotate the nebula and fit one of our radiative transfer model with the region at the right of the apex of the bow shock, which would have engendered simulation/observations discrepancies in the left-hand part of the structure. This argument is strengthened by the blue contour representing Wilkin's solution and consistent with only a part of the observed bow shock. Overall, our relatively good comparison with observations stresses that the bow shock of IRC-10414 is probably in a steady state. In other words, the star might have probably entered the red supergiant phase more than ∼0.1 Myr ago, which corresponds to the crossing-time of the simulation.

4.3.2 The case of Betelgeuse

Betelgeuse (αOrioniz) is the Earth-closet red supergiant star located in Orion's neighbouring massive star-forming region. It is a runaway stellar object that displays a parsec-scale bow shock (Noriega-Crespo et al. 1997b). This object is a laboratory to study the physics of cool stellar winds such as dust and test stellar pulsations models of these variable stars. Betelgeuse is the priority target of active researches on photometric variability of cool stars such as red supergiant and asymptotic giant branch stars. These works permitted the monitoring of Betelgeuse's light curve and its Great optical Dimming (Dupree et al. 2020; Levesque 2021) together with measures of its magnetic field (Mathias et al. 2018; Montargès et al. 2021). Its intriguing circumstellar medium constituted of a stellar wind bow shock, a bright inner ring, and a more extended unexplained bar makes it an interesting target for hydrodynamical modelling. Previous studies on the surrounding of Betelgeuse taught us that it is a runaway star that probably experienced a blue loop. It was recently returned to the red supergiant phase (Mackey et al. 2012), leaving

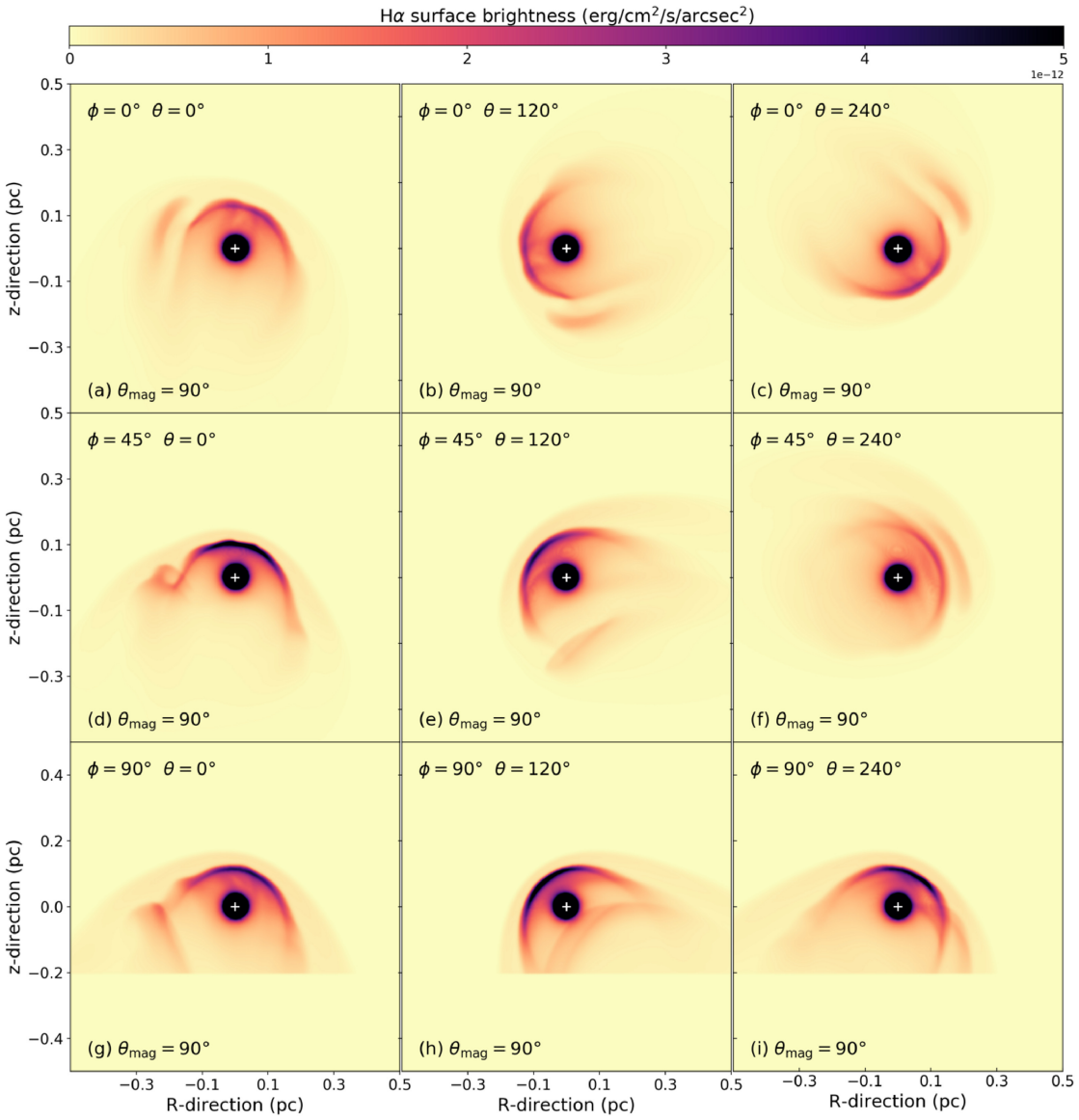

Figure 11. Same as Fig. 9 for our model Run-θ_{mag}-90.

behind its precedent blue supergiant bow shock after briefly forming Napoleon's hat (Wang, Dyson & Kahn 1993). The youngness of its stellar wind bow shock is also the main conclusion of the work of Mohamed et al. (2012), presenting 3D hydrodynamical Lagrangian simulations tailored to the surroundings of αOrioniz. The smooth appearance of the astrosphere of Betelgeuse contradicts some simulation model of Mohamed et al. (2012). The inhibition of Rayleigh–Taylor instabilities growing at the dense tangential discontinuity interface has been studied with 2.5D MHD simulations in van Marle et al. (2014), showing that the ambient magnetic field of Orion's arm is sufficiently strong to reduce and damp the instabilities in the bow shock around Betelgeuse and modify its appearance. As for the astrosphere of IRC-10414, Betelgeuse is externally photoionized. The radiation pressure from the ionized ISM confines each of the H II region of Betelgeuse, where the cool wind meets its hot accelerating wind within a neutral shell, and is therefore located inside of the termination shock of the bow shock (Mackey et al. 2014).

To further validate our method, we perform an additional 3D MHD simulation of Betelgeuse's astrosphere by adopting the parameters of van Marle et al. (2014). In our simulation Run-αOri, the mass-loss rate of the star is $\dot{M} \approx 3 \times 10^{-6}\,\mathrm{M_\odot\,yr^{-1}}$, the stellar wind velocity is $v_w = 15\,\mathrm{km\,s^{-1}}$, and its space velocity $v_\star = 28.3\,\mathrm{km\,s^{-1}}$, respectively. The ISM ambient medium has a density $n_{ISM} = 1.89\,\mathrm{cm^{-3}}$, and we consider, as for IRC-10414, that its circumstellar medium is externally ionized. Apart from the stellar wind and ISM properties, the numerical setup is the same as for IRC-10414. We adopt $\theta_{mag} = 90°$, i.e. we assume that the ambient medium magnetic field lines are nearly parallel to Betelgeuse's bar. The surroundings of Betelgeuse is more complex than that of IRC-10414. Hence, we proceed differently

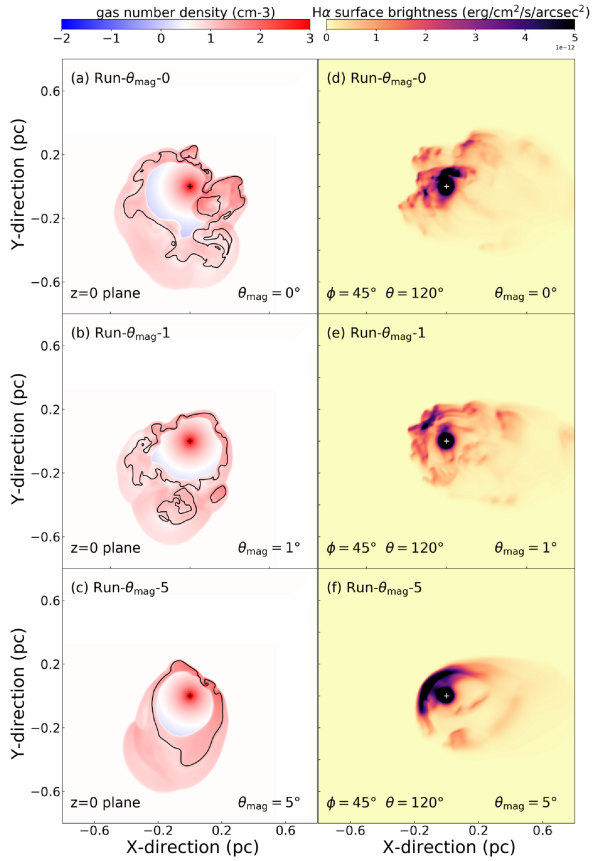

Figure 12. Density fields in the $z = 0$ plane of models Run-$\theta_{\rm mag}$-0, Run-$\theta_{\rm mag}$-1, and Run-$\theta_{\rm mag}$-5, assuming different angle between the direction of motion of the star and that of the local magnetic field $\theta_{\rm mag} = 0^\circ$ (a), $\theta_{\rm mag} = 1^\circ$ (b), and $\theta_{\rm mag} = 5^\circ$ (c), respectively. The right part of the figure plots the corresponding surface brightness (in erg cm^2 s^{-1} arcsec^{-2}) assuming a viewing angle $\phi = 45^\circ$ and $\theta = 180^\circ$, respectively. The black contour is the location of the bow shock made of equal proportion of stellar wind and ISM material. The black (left) and white (right) crosses mark the position of the star.

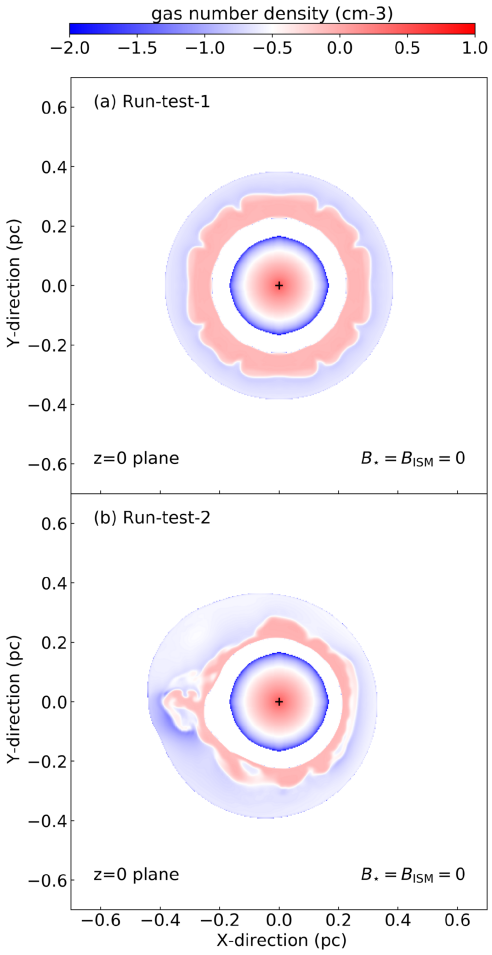

Figure 13. Density fields in the $z = 0$ plane of models Run-test-1 and Run-test-2, with $B_\star = B_{\rm ISM} = 0$ G. Difference between the two simulations is the direction along which the star moves, i.e. along Oz (a) and along an arbitrary direction slightly deviating from Oz (b). When the star runs parallel to the vertical direction, instabilities develop symmetrically in the bow shock (see also Blondin & Koerwer 1998). The black cross marks the position of the star.

as in Fig. 14. Betelgeuse's bow shock is not visible in Hα because the star is too bright and its young nebulae too small; we mask the material that is inside of the photoionized-confined shell (also not modelled) extending up to radius $\sim$ pc. The bar is added as a denser region of Gaussian density profile peaking at 70 cm^{-3} and inclined with the direction of stellar motion with an angle that we adjust so that projected emission fits infrared observations. Fig. 15 compares an Hα emission map of the bow shock of Betelgeuse and its bar with overlaid PACSHERSCHEL[3] infrared data (black contours). The blue contour is Wilkin's solution for the bow shock morphology calculated with the observed stand-off distance of Betelgeuse's astrosphere, whereas the red circle marks the location of the neutral shell forming at the neutral-ionized wind interface (Mackey et al. 2014). The projected bow shock structure matches well the infrared emission and we conclude that our simulation model for Betelgeuse as a $\simeq$ 15 kyr old red supergiant star whose astrosphere is magnetically stabilized and that is a probable explanation for the circumstellar medium of that star. We do not need any stellar argument to explain the bar that we treat as independent from the astropause interaction region, without any stellar evolution argument at the origin of the formation of, e.g. a double bow shock structure of Mackey et al. (2012). The concavity of the bar, slightly opposite of that of the astrosphere (see Noriega-Crespo et al. 1997b; van Marle et al. 2014), leads us to interpret the bar as of circumstellar origin, which supports the conclusions of Decin et al. (2012). The bow shock and Betelgeuse's bar result on a serendipitous disposition and projection effects from both components.

Last, this radiative transfer modelling for the surroundings of Betelgeuse calls a few comments, the first concerning the selected simulated snapshot that we decided to produce Fig. 15. We took the youngest bow shock whose aspect ratio is consistent with Betelgeuse's observed one and is measured to $R(0) = 0.275$ pc and $R(0)/R(90) \approx 0.76$ (Mohamed et al. 2012; van Marle et al. 2014). It consists to the time instance 0.015 Myr after the onset of Run-αOri, when the physical size of the astropshere corresponds to that derived in Noriega-Crespo et al. (1997b). The aspect ratio $R(0)/R(90)$ persists

[3]ESA Herschel Science Archive Observation ID: 1342242656.

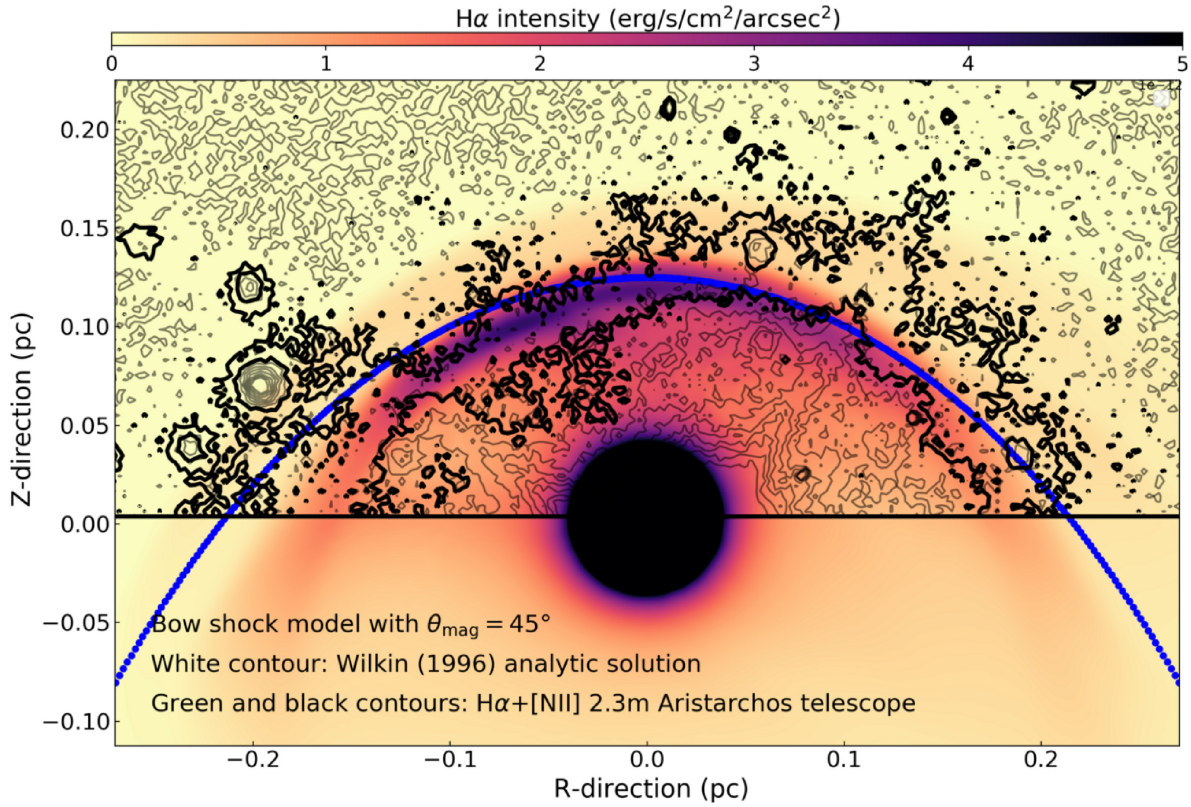

Figure 14. Comparison between our bow shock model Run-$\theta_{\rm mag}$-45 and observational data of the circumstellar medium of IRC-10414. The image plots the surface Hα brightness calculated from our model with $\theta_{\rm mag} = 45^\circ$ (in erg cm^2 s^{-1} arcsec^{-2}) and the Hα+[N II] data taken by the 2.3 m *Aristarchos* telescope, as black contours. Thin contours are the background data and thick contours trace the bow shock nebula. The blue contour represents the analytic solution of Wilkin (1996).

up to 0.4 Myr. At the same time, the nebula grows, i.e. bow shocks at a later time will still reasonably match the HERSCHEL observations, however, at the cost of reevaluating the distance to the star. Secondly, the adopted inclination angle of the Betelgeuse bow shock with respect to the plane of the sky. For the sake of simplicity, when generating the initial conditions for the radiative transfer calculation, we have assumed an inclination angle of 0°. Further modelling with the RADMC-3D code indicates that no noticeable differences appear for inclination angles $\leq$30°. However, for angles $>$45° the Hα bow shock experiences significant projection effects, as already noted using column densities by Mohamed et al. (2012; see also Fig. 16).

4.4 Implication for other astrophysical objects

4.4.1 Implication for bow shocks around OB stars

The many projection effects at work in our optical Hα emission maps of bow shocks around runaway red supergiant stars (Figs 9–11) can be discussed in the context of earlier-type massive stars. Various catalogues of arc-like nebulae have been established, principally in the infrared waveband of the electromagnetic spectrum (van Buren & McCray 1988; van Buren et al. 1995; Noriega-Crespo et al. 1997a; Kobulnicky, Gilbert & Kiminki 2010; Peri et al. 2012, 2015; Kobulnicky et al. 2016, 2017). Many astrospheres around those main-sequence massive OB stars display partly irregular shapes, making their detailed classification difficult, redundant, and uneasy. At the light of the emission maps of our 3D MHD simulations, we propose that other bow shocks are affected by similar projection effects, and that the peculiar morphology of some bow shocks around earlier-type massive stars are hence produced. This would greatly reduce the taxonomy of different physical morphologies of astrospheres.

4.4.2 Implication for core-collapse supernova remnants

Besides constraining stellar evolutionary parameters, the prime importance for the study of the surroundings of evolved massive stars is their role as the pre-supernova circumstellar medium of core-collapse supernova progenitors (Borkowski, Blondin & Sarazin 1992; Velázquez et al. 2006; Broersen et al. 2014; Toledo-Roy et al. 2014; Chiotellis et al. 2019; Chiotellis et al. 2021). After the explosive death of a massive star, the supernova shock wave will inevitably interact with its pre-shaped surroundings, which, according to the mass that is trapped into it (Meyer et al. 2015), first potentially feels its presence from the dynamical point of view, generates an asymmetric supernova remnant, and eventually further expands into the ambient medium (Meyer et al. 2020a). Inversely, the morphologies of core-collapse supernovae remnants permit to constrain the properties of its circumstellar medium, itself function of the past evolution of the progenitor star. A significant fraction of massive stars being runaway stellar objects, a similar fraction of core-collapse supernova

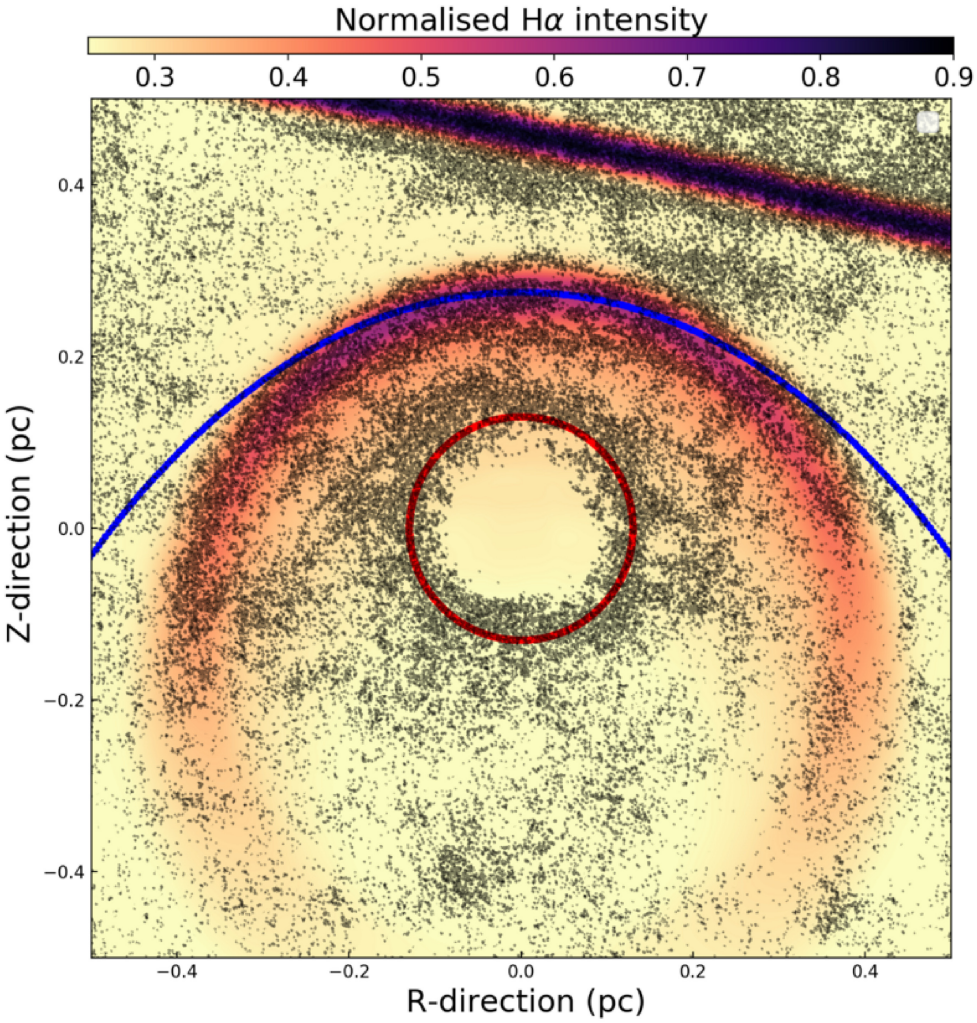

Figure 15. Comparison between our bow shock model Run-αOri and observational data of the circumstellar medium of Betelgeuse. The image plots the normalized Hα surface brightness calculated from our model Run-αOri tailored to Betelgeuse, assuming with $\theta_{\rm mag} = 90^\circ$ (in erg cm^2 s^{-1} arcsec^{-2}) and the infrared 170 μm taken by the space-borne telescope HERSCHEL as black contours. The upper structure is the bar accompanying Betelgeuse's bow shock (Noriega-Crespo et al. 1997b). The blue line represents the analytic solution of Wilkin (1996), the red circle marks the photo-ionizing confined shell interpreted and modelled in Mackey et al. (2014).

remnants must have been shaped, or at least must have at some time beard imprints of their progenitor's bow shock, driven either by a red supergiant or a Wolf–Rayet star (Katsuda et al. 2018). Therefore, the expanding supernova shock wave properties will be completely different once it has passed through its circumstellar medium, and this will affect, e.g. particle acceleration mechanisms therein. Carefully understanding cosmic ray acceleration in core-collapse supernovae requires an accurate treatment of its ambient medium prior to the explosion, and our work shows that this should be performed by means of 3D MHD simulations.

5 CONCLUSION

In this study, we explore the morphology and emission properties of the astrosphere generated around a runaway evolved cool massive star. We present the first 3D MHD simulations of bow shocks forming in the vicinity of a runaway supergiant star, tailoring our simulations devoted to the surroundings of the M-type star IRC-10414 (Gvaramadze et al. 2014; Meyer et al. 2014a). Our numerical simulations are 3D Cartesian models performed with the PLUTO code (Mignone et al. 2007, 2012; Vaidya et al. 2018), a well-tested tool for modelling astropause interactions (Meyer et al. 2017). Constant adopted stellar wind properties are that of IRC-10414, constrained in Gvaramadze et al. (2014) and Meyer et al. (2014a), and we assume that the ISM in which the star moves is supported by a typical magnetic field of strength 7 μG. Our free parameter is the orientation of the ISM magnetic field with respect to the direction of stellar motion. We run a simulation for 0.4 Myr, which corresponds to a few dynamical crossing-time of the gas throughout the computational domain. For the sake of completeness, stellar rotation and magnetic field are included into the numerical setup as a Parker spiral. This 3D MHD study therefore permits exploring the effects of a non-aligned magnetic field on the structure and emission properties of the resulting stellar wind bow shock.

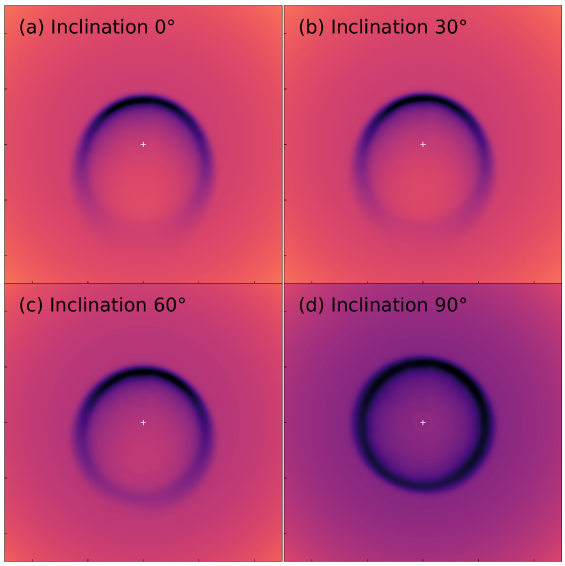

Figure 16. Series of rendered emission maps highlighting the effects of the inclination angles with respect to the plan of the sky, for our best-fitting model from Run-αOri to Betelgeuse's bow shock. We refer the reader to fig. 12 of Mohamed et al. (2012) for a similar exercise. The images are non-background subtracted and convolved with a Gaussian filter. The position of the star is marked by a white cross.

Magnetic fields stabilize astrospheres (van Marle et al. 2014; Meyer et al. 2017; Scherer et al. 2020). Mainly, when the local ISM magnetic field is aligned with less than a few degrees with that of the stellar motion, the bow shock is ragged, clumpy, and strongly unstable, while previous 2D simulations produced stable structures (Meyer et al. 2014a). Axisymmetric patterns are broken, principally because of large-scale 3D eddies developing at the astropause interface and affecting the overall morphology of the bow shock wings. Grid-induced effects are at work when the star moves along a characteristic axis of the 3D Cartesian coordinate system, while they vanish when the stellar motion is directed along an arbitrary direction. Such results stress the need for 3D MHD simulations, further tackling the problem of the circumstellar medium of massive stars (van Marle et al. 2015). We find that the stellar magnetic field is dynamically unimportant in shaping the astrosphere of evolved red supergiant massive stars, which is consistent with other studies devoted to, e.g. the heliosphere (Pogorelov et al. 2017) and the study on λ Cephei of Scherer et al. (2020).

Synthetic optical Hα emission maps of 3D MHD astrospheres around cool stars show that projection effects are important in the observed shape of the nebulae, and we speculate that this must also affect the astrospheres of earlier-type massive stars. This study shows that the problem of the smooth appearance of red supergiant bow shock can be solved with a simple, mild magnetization of its ambient medium, and that the previously proposed external ionization and/or youth of the structure might not be enough to explain the unique appearance of both IRC-10414 and Betelgeuse, although it participates to it (van Marle et al. 2014). We conclude that IRC-10414 is a star in a steady state and that Betelgeuse's bar is of interstellar origin. Our work is therefore in accordance with the bow shock models for Betelgeuse of Mohamed et al. (2012) and van Marle et al. (2014), but it is in clear disfavour regarding what was proposed in Mackey et al. (2012). Our results will serve for future modelling of the circumstellar medium of runaway red supergiant stars and to realistically simulate the early supernova-blastwave interaction happening in core-collapse supernova remnants.

ACKNOWLEDGEMENTS

DMAM thanks L. Decin and A.-J. van Marle for advice on observational data. The authors acknowledge the North-German Supercomputing Alliance (HLRN) for providing HPC resources that have contributed to the research results reported in this paper. MP acknowledges the Max Planck Computing and Data Facility (MPCDF) for providing data storage resources and HPC resources which contributed to test and optimize the PLUTO code. PFV acknowledges the financial support for PAPIIT-UNAM grant IA103121. This work is based on observations made with the '*Aristarchos*' telescope operated on the Helmos Observatory by the Institute of Astronomy, Astrophysics, Space Applications and Remote Sensing of the National Observatory of Athens.

DATA AVAILABILITY

This research made use of the PLUTO code developed at the University of Torino by A. Mignone and collaborators (http://plutocode.ph.unito.it/) and of the RADMC-3D code developed by C. Dullemond and collaborators at the University of Heidelberg (https://www.ita.uni-heidelberg.de/~dullemond/software/radmc-3d/), respectively. The figures have been produced using the MATPLOTLIB plotting library for the PYTHON programming language (https://matplotlib.org/). The 3D renderings have been generated using the VISIT software https://visit-dav.github.io/visit-website/. Observational data of the circumstellar medium of Betelgeuse have been obtained via the Herschel data Schearch of the NASA/IPAC Infrared Science Archive (https://irsa.ipac.caltech.edu/applications/Herschel/). The data underlying this article will be shared on reasonable request to the corresponding author.

REFERENCES

Acreman D. M., Stevens I. R., Harries T. J., 2016, MNRAS, 456, 136
Baalmann L. R., Scherer K., Kleimann J., Fichtner H., Bomans D. J., Weis K., 2021, A&A, 650, A36
Baranov V. B., Krasnobaev K. V., Kulikovskii A. G., 1971, Sov. Phys. Doklady, 15, 791
Benaglia P., del Palacio S., Hales C., Colazo M. E., 2021, MNRAS, 503, 2514
Blaauw A., 1961, Bull. Astron. Inst. Netherlands, 15, 265
Blondin J. M., Koerwer J. F., 1998, New Astron., 3, 571
Borkowski K. J., Blondin J. M., Sarazin C. L., 1992, ApJ, 400, 222
Brighenti F., D'Ercole A., 1995, MNRAS, 277, 53
Broersen S., Chiotellis A., Vink J., Bamba A., 2014, MNRAS, 441, 3040
Brott I. et al., 2011, A&A, 530, A115
Brown D., Bomans D. J., 2005, A&A, 439, 183
Cannon E. et al., 2021, MNRAS, 502, 369
Chevalier R. A., 1977, ARA&A, 15, 175
Chevalier R. A., Luo D., 1994, ApJ, 421, 225
Chiotellis A., Schure K. M., Vink J., 2012, A&A, 537, A139
Chiotellis A., Boumis P., Derlopa S., Steffen W., 2019, preprint (arXiv:1909.08947)
Chiotellis A., Boumis P., Spetsieri Z. T., 2021, MNRAS, 502, 176
Comerón F., Kaper L., 1998, A&A, 338, 273
Cox N. L. J. et al., 2012a, A&A, 537, A35
Cox N. L. J., Kerschbaum F., van Marle A.-J., Decin L., Ladjal D., Mayer A., 2012b, A&A, 543, C1
De Becker M., del Valle M. V., Romero G. E., Peri C. S., Benaglia P., 2017, MNRAS, 471, 4452

Decin L. et al., 2012, A&A, 548, A113
del Valle M. V., Pohl M., 2018, ApJ, 864, 19
Dgani R., van Buren D., Noriega-Crespo A., 1996a, ApJ, 461, 372
Dgani R., van Buren D., Noriega-Crespo A., 1996b, ApJ, 461, 927
Dinçel B., Neuhäuser R., Yerli S. K., Ankay A., Tetzlaff N., Torres G., Mugrauer M., 2015, MNRAS, 448, 3196
Dolan M. M., Mathews G. J., Lam D. D., Quynh Lan N., Herczeg G. J., Dearborn D. S. P., 2016, ApJ, 819, 7
Dullemond C. P., 2012, RADMC-3D: A Multi-Purpose Radiative Transfer Tool, Astrophysics Source Code Library. preprint (ascl:1202.015)
Dupree A. K. et al., 2020, ApJ, 899, 68
Dwarkadas V. V., 2007, ApJ, 667, 226
Ekström S. et al., 2012, A&A, 537, A146
Eldridge J. J., Langer N., Tout C. A., 2011, MNRAS, 414, 3501
Farrell E. J., Groh J. H., Meynet G., Eldridge J. J., 2020, MNRAS, 494, L53
Freyer T., Hensler G., Yorke H. W., 2003, ApJ, 594, 888
Freyer T., Hensler G., Yorke H. W., 2006, ApJ, 638, 262
Garcia-Segura G., Langer N., Mac Low M.-M., 1996, A&A, 316, 133
García-Segura G., Ricker P. M., Taam R. E., 2018, ApJ, 860, 19
García-Segura G., Taam R. E., Ricker P. M., 2020, ApJ, 893, 150
Gies D. R., 1987, ApJS, 64, 545
Green S., Mackey J., Haworth T. J., Gvaramadze V. V., Duffy P., 2019, A&A, 625, A4
Gull T. R., Sofia S., 1979, ApJ, 230, 782
Gvaramadze V. V., 2006, A&A, 454, 239
Gvaramadze V. V., Gualandris A., 2011, MNRAS, 410, 304
Gvaramadze V. V., Kniazev A. Y., Fabrika S., 2010, MNRAS, 405, 1047
Gvaramadze V. V., Menten K. M., Kniazev A. Y., Langer N., Mackey J., Kraus A., Meyer D. M.-A., Kamiński T., 2014, MNRAS, 437, 843
Gvaramadze V. V., Alexashov D. B., Katushkina O. A., Kniazev A. Y., 2018, MNRAS, 474, 4421
Harten A., Lax P. D., van Leer B., 1983, SIAM Rev., 25, 35
Henney W. J., Arthur S. J., 2019a, MNRAS, 486, 3423
Henney W. J., Arthur S. J., 2019b, MNRAS, 486, 4423
Henney W. J., Arthur S. J., 2019c, MNRAS, 489, 2142
Henney W. J., Tarango-Yong J. A., Ángel Gutiérrez-Soto L., Arthur S. J., 2019, preprint (arXiv:1907.00122)
Herbst K. et al., 2020, ApJ, 897, L27
Hoogerwerf R., de Bruijne J. H. J., de Zeeuw P. T., 2001, A&A, 365, 49
Izmodenov V., Malama Y. G., Gloeckler G., Geiss J., 2003, ApJ, 594, L59
Kaper L., van Loon J. T., Augusteijn T., Goudfrooij P., Patat F., Waters L. B. F. M., Zijlstra A. A., 1997, ApJ, 475, L37
Katsuda S., Takiwaki T., Tominaga N., Moriya T. J., Nakamura K., 2018, ApJ, 863, 127
Katushkina O. A., Alexashov D. B., Izmodenov V. V., Gvaramadze V. V., 2017, MNRAS, 465, 1573
Katushkina O. A., Alexashov D. B., Gvaramadze V. V., Izmodenov V. V., 2018, MNRAS, 473, 1576
Kervella P. et al., 2018, A&A, 609, A67
Kobulnicky H. A., Gilbert I. J., Kiminki D. C., 2010, ApJ, 710, 549
Kobulnicky H. A. et al., 2016, ApJS, 227, 18
Kobulnicky H. A., Schurhammer D. P., Baldwin D. J., Chick W. T., Dixon D. M., Lee D., Povich M. S., 2017, AJ, 154, 201
Lada C. J., Lada E. A., 2003, ARA&A, 41, 57
Langer N., 2012, ARA&A, 50, 107
Levesque E. M., 2021, Nature, 594, 343
Mackey J., Mohamed S., Neilson H. R., Langer N., Meyer D. M.-A., 2012, ApJ, 751, L10
Mackey J., Mohamed S., Gvaramadze V. V., Kotak R., Langer N., Meyer D. M.-A., Moriya T. J., Neilson H. R., 2014, Nature, 512, 282
Mackey J., Haworth T. J., Gvaramadze V. V., Mohamed S., Langer N., Harries T. J., 2016, A&A, 586, A114
Maeder A., 2009, Physics, Formation and Evolution of Rotating Stars. Astronomy and Astrophysics Library, Springer, Berlin Heidelberg, ISBN 978-3-540-76948-4
Mathias P., Auriere M., Lopez Ariste A., Petit P., Tessore B., Josselin E., et al., 2018, A&A, 615, A116
Matsuura M. et al., 2014, MNRAS, 437, 532
Meyer D. M. A., Mignone A., Kuiper R., Raga A. C., Kley W., 2017, MNRAS, 464, 3229
Meyer D. M. A., Petrov M., Pohl M., 2020a, MNRAS, 493, 3548
Meyer D. M. A., Oskinova L. M., Pohl M., Petrov M., 2020b, MNRAS, 496, 3906
Meyer D. M. A., Pohl M., Petrov M., Oskinova L., 2021, MNRAS, 502, 5340
Meyer D. M.-A., Gvaramadze V. V., Langer N., Mackey J., Boumis P., Mohamed S., 2014a, MNRAS, 439, L41
Meyer D. M.-A., Mackey J., Langer N., Gvaramadze V. V., Mignone A., Izzard R. G., Kaper L., 2014b, MNRAS, 444, 2754
Meyer D. M.-A., Langer N., Mackey J., Velázquez P. F., Gusdorf A., 2015, MNRAS, 450, 3080
Meyer D. M.-A., van Marle A.-J., Kuiper R., Kley W., 2016, MNRAS, 459, 1146
Mignone A., 2014, J. Comput. Phys., 270, 784
Mignone A., Bodo G., Massaglia S., Matsakos T., Tesileanu O., Zanni C., Ferrari A., 2007, ApJS, 170, 228
Mignone A., Zanni C., Tzeferacos P., van Straalen B., Colella P., Bodo G., 2012, ApJS, 198, 7
Mohamed S., Mackey J., Langer N., 2012, A&A, 541, A1
Montargès M. et al., 2019, MNRAS, 485, 2417
Montargès M., Cannon E., Lagadec E., de Koter A., P. Kervella, J. Sanchez-Bermudez, et al., 2021, Nature, 594, 365
Noriega-Crespo A., van Buren D., Dgani R., 1997a, AJ, 113, 780
Noriega-Crespo A., van Buren D., Cao Y., Dgani R., 1997b, AJ, 114, 837
O'Gorman E. et al., 2015, A&A, 573, L1
Parker E. N., 1958, ApJ, 128, 664
Peri C. S., Benaglia P., Brookes D. P., Stevens I. R., Isequilla N. L., 2012, A&A, 538, A108
Peri C. S., Benaglia P., Isequilla N. L., 2015, A&A, 578, A45
Peters T. et al., 2017, MNRAS, 467, 4322
Pogorelov N. V., Heerikhuisen J., Roytershteyn V., Burlaga L. F., Gurnett D. A., Kurth W. S., 2017, ApJ, 845, 9
Povich M. S., Benjamin R. A., Whitney B. A., Babler B. L., Indebetouw R., Meade M. R., Churchwell E., 2008, ApJ, 689, 242
Powell K. G., 1997, An Approximate Riemann Solver for Magnetohydrodynamics. Springer Berlin Heidelberg, Berlin, Heidelberg, p. 570
Renzo M. et al., 2019, A&A, 624, A66
Rozyczka M., Franco J., 1996, ApJ, 469, L127
Sander A. A. C., Vink J. S., Hamann W. R., 2020, MNRAS, 491, 4406
Scherer K., Fichtner H., Fahr H. J., Bzowski M., Ferreira S. E. S., 2014, A&A, 563, A69
Scherer K., Baalmann L. R., Fichtner H., Kleimann J., Bomans D. J., Weis K., Ferreira S. E. S., Herbst K., 2020, MNRAS, 493, 4172
Seifried D., Walch S., Haid S., Girichidis P., Naab T., 2018, ApJ, 855, 81
Shrestha M., Neilson H. R., Hoffman J. L., Ignace R., 2018, MNRAS, 477, 1365
Shrestha M., Neilson H. R., Hoffman J. L., Ignace R., Fullard A. G., 2021, MNRAS, 500, 4319
Smartt S. J., 2009, ARA&A, 47, 63
Szécsi D., Wünsch R., Agrawal P., Langer N., 2020, preprint (arXiv:2004.08203)
Teyssier D. et al., 2012, A&A, 545, A99
Toledo-Roy J. C., Esquivel A., Velázquez P. F., Reynoso E. M., 2014, MNRAS, 442, 229
Vaidya B., Mignone A., Bodo G., Rossi P., Massaglia S., 2018, ApJ, 865, 144
van Buren D., McCray R., 1988, ApJ, 329, L93
van Buren D., Noriega-Crespo A., Dgani R., 1995, AJ, 110, 2914
van Marle A. J., Langer N., García-Segura G., 2005, A&A, 444, 837
van Marle A. J., Langer N., Yoon S.-C., García-Segura G., 2008, A&A, 478, 769
van Marle A. J., Meliani Z., Keppens R., Decin L., 2011, ApJ, 734, L26
van Marle A. J., Meliani Z., Marcowith A., 2012, A&A, 541, L8
van Marle A. J., Decin L., Meliani Z., 2014, A&A, 561, A152
van Marle A. J., Meliani Z., Marcowith A., 2015, A&A, 584, A49
Velázquez P. F., Vigh C. D., Reynoso E. M., Gómez D. O., Schneiter E. M., 2006, ApJ, 649, 779
Villaver E., Manchado A., García-Segura G., 2012, ApJ, 748, 94

Vink J. S., 2006, in Lamers H. J. G. L. M., Langer N., Nugis T., Annuk K., eds, ASP Conf. Ser. Vol. 353, Stellar Evolution at Low Metallicity: Mass Loss, Explosions, Cosmology, Astron. Soc. Pac., San Francisco. p. 113
Vlemmings W. H. T., Diamond P. J., van Langevelde H. J., 2002, A&A, 394, 589
Vlemmings W. H. T., van Langevelde H. J., Diamond P. J., 2005, A&A, 434, 1029
Walch S., Wünsch R., Burkert A., Glover S., Whitworth A., 2011, ApJ, 733, 47
Wang L., Dyson J. E., Kahn F. D., 1993, MNRAS, 261, 391
Wareing C. J., Zijlstra A. A., O'Brien T. J., 2007a, MNRAS, 382, 1233
Wareing C. J., Zijlstra A. A., O'Brien T. J., 2007b, ApJ, 660, L129
Weaver R., McCray R., Castor J., Shapiro P., Moore R., 1977, ApJ, 218, 377
Weber E. J., Davis Leverett J., 1967, ApJ, 148, 217
Weiler K. W., Sramek R. A., 1988, ARA&A, 26, 295
Wilkin F. P., 1996, ApJ, 459, L31
Woosley S. E., Bloom J. S., 2006, ARA&A, 44, 507
Woosley S. E., Heger A., Weaver T. A., 2002, Rev. Mod. Phys., 74, 1015

This paper has been typeset from a TEX/LATEX file prepared by the author.

Monthly Notices
of the
ROYAL ASTRONOMICAL SOCIETY

MNRAS **496,** 3906–3911 (2020) doi:10.1093/mnras/staa1700

On the ring nebulae around runaway Wolf–Rayet stars

D. M.-A. Meyer [1]★ L. M. Oskinova,[1,2] M. Pohl[1,3] and M. Petrov[4]

[1] *Universität Potsdam, Institut für Physik und Astronomie, Karl-Liebknecht-Strasse 24/25, 14476 Potsdam, Germany*
[2] *Department of Astronomy, Kazan Federal University, Kremlevskaya Str 18, Kazan, Russia*
[3] *DESY, Platanenallee 6, 15738 Zeuthen, Germany*
[4] *Max Planck Computing and Data Facility (MPCDF), Gießenbachstrasse 2, D-85748 Garching, Germany*

Accepted 2020 June 9. Received 2020 June 6; in original form 2020 May 12

ABSTRACT

Wolf–Rayet stars are advanced evolutionary stages of massive stars. Despite their large mass-loss rates and high wind velocities, none of them displays a bow shock, although a fraction of them are classified as runaway. Our 2.5-D numerical simulations of circumstellar matter around a 60-$M_\odot$ runaway star show that the fast Wolf–Rayet stellar wind is released into a wind-blown cavity filled with various shocks and discontinuities generated throughout the preceding evolutionary phases. The resulting fast-wind–slow-wind interaction leads to the formation of spherical shells of swept-up dusty material similar to those observed in the near-infrared at 24 μm with *Spitzer*, which appear to be comoving with the runaway massive stars, regardless of their proper motion and/or the properties of the local ambient medium. We interpret bright infrared rings around runaway Wolf–Rayet stars in the Galactic plane as an indication of their very high initial masses and complex evolutionary history. Stellar-wind bow shocks become faint as stars run in diluted media, therefore our results explain the absence of bow shocks detected around Galactic Wolf–Rayet stars, such as the high-latitude, very fast-moving objects WR71, WR124 and WR148. Our results show that the absence of a bow shock is consistent with the runaway nature of some Wolf–Rayet stars. This questions the in situ star formation scenario of high-latitude Wolf–Rayet stars in favour of dynamical ejection from birth sites in the Galactic plane.

Key words: MHD – radiative transfer – methods: numerical – stars: circumstellar matter.

1 INTRODUCTION

The evolution of massive stars is poorly understood. It is characterized by the release of forceful winds, the intensity of which increases as the stars evolve. Strong winds interact with the local interstellar medium (ISM), leading to the formation of circumstellar wind bubbles structured by several shocks and discontinuities (Weaver et al. 1977). These pc-scale shells reflect both wind and ISM properties. They constitute the imprint of the past stellar evolution of massive stars on their ambient medium (Meyer et al. 2014). In particular, high-mass stars are expected to evolve through the so-called Wolf–Rayet (WR) phase. Despite the growing consensus on Galactic WR stars as the last pre-supernova evolutionary phase of $\geq 20\,M_\odot$ stars, the precise evolutionary channels leading to such stellar objects remain uncertain (Crowther 2007). This stage is characterized by very strong winds enriched in C, N or O that are blown from the stellar surface with velocities up to 3000–5000 km s^{-1} and large mass-loss rates reaching $10^{-5}\,M_\odot\,yr^{-1}$ (Hamann, Gräfener & Liermann 2006; Sander, Hamann & Todt 2012; Bestenlehner et al. 2014).

WR stars often live in binary systems or have a binary evolutionary history. These evolved stars have most likely travelled away from their birthplace in the Galactic plane, either after many-body gravitational interaction within stellar groups or under the influence of the kick given by the shock wave of a defunct binary companion, which ended its life as a supernova explosion (Moffat & Seggewiss 1979; Dinçel et al. 2015). However, only a handful of runaway WR stars are known in the Galaxy. This could be because measurement of radial velocity is complicated for WR optical spectra dominated by broad emission lines. Therefore, the position of a WR star in the high-latitude region of the Milky Way often serves as the primary indication of its runaway nature. The three most-studied high Galactic latitude WR stars are the binary WR 148 (WN8+B3IV: Munoz et al. 2017), WR 124 together with its suspected relativistic companion (WN8h: Toalá et al. 2018 and references therein) and WR 71 (WN6: Moffat et al. 1998).

The traditional method to discover runaway stars involves observations of bow shocks. Indeed, one could expect that fast-moving WR stars are prone to producing bow-shock nebulae (Wilkin 1996) under the conjugated influence of both their fast, dense stellar winds and their rapid bulk motion. This picture has been supported by several numerical hydrodynamical investigations of

★ E-mail: dmameyer.astro@gmail.com

WR wind–ISM interaction, predicting the formation of either unstable bow shocks (van Marle, Langer & García-Segura 2005) or unstable ring-like shells (Brighenti & D'Ercole 1995a). However, no observational evidence of a bow shock around a WR star has been reported so far. On the other hand, WR stars are commonly surrounded by nebulae with a variety of morphologies, including ring nebulae (Miller & Chu 1993; Marston 1997; Toalá et al. 2015), which have been observed in optical Hα and [O III] lines as well as in the mid-infrared (Barniske, Oskinova & Hamann 2008). Recently, WR nebulae have been observed in the mm range (Fenech et al. 2018). Gräfener et al. (2012) pointed out the prevalence of nebulae around WR stars that only recently entered this evolutionary stage.

Interestingly, even fast-moving WR stars (with velocities up to $v_\star \simeq 200\,\mathrm{km\,s^{-1}}$ relative to the ISM) are located at the centre of compact spherical shells (Gvaramadze, Kniazev & Fabrika 2010). The question is therefore: why do fast-moving WR stars not produce bow shock nebulae at all? How can their surroundings be shaped as a stable, circular shell? And why are those stars centred systematically on those ring-like shells, which appear to be comoving with the star?

To answer these questions, we investigate the morphology of the circumstellar medium around evolving runaway WR stars by means of two-dimensional magnetohydrodynamical and radiative transfer simulations. This study is organized as follows. We review the numerical models in Section 2, present the ring nebulae models in Section 3, discuss their significance in Section 4 and draw conclusions in Section 5.

2 NUMERICAL SIMULATIONS

We perform a series of two-and-a-half dimensional (2.5D) magneto-hydrodynamical (MHD) simulations with the PLUTO code (Mignone et al. 2012). The simulations have been carried out using a cylindrical coordinate system (R, z) mapped with a uniform grid $[z_{\rm min}; z_{\rm max}] \times [0; R_{\rm max}]$ of minimum resolution $\Delta = 0.08\,\mathrm{pc\,cell^{-1}}$. A stellar wind is injected in the computational domain as a half sphere of radius 20 cells centred on the origin and a continuous inflow is set at the $z = z_{\rm max}$ boundary, so that the wind–ISM interaction is modelled in the frame of reference of the moving star (Meyer et al. 2016). We consider the ISM material to be at solar metallicity (Asplund et al. 2009). Energy loss/gain by optically thin radiative cooling and heating are taken into account using a cooling law for a fully ionized medium (Meyer et al. 2014). Its equilibrium temperature is about 8000 K, i.e. we assume that the ambient medium is ionized by a strong stellar radiation field (Mackey et al. 2015). We assume the stars move parallel to the local ISM magnetic field of strength, 7 μG (van Marle, Decin & Meliani 2014; Meyer et al. 2017).

We performed a series of three numerical simulations. Two ionized ISM are considered, with densities corresponding to either the Galactic plane ($n_{\rm ISM} = 0.79\,\mathrm{cm^{-3}}$) or high Galactic latitudes ($n_{\rm ISM} = 0.01\,\mathrm{cm^{-3}}$). Stars move therein with a typical space velocity of 30–100 km s^{-1} (Renzo et al. 2019) or 200 km s^{-1}, respectively. We use the stellar evolution model for a non-rotating 60-M$_\odot$ star of Groh et al. (2014). The track follows the stellar evolution from the zero-age main sequence through a B supergiant stage, a luminous blue variable (LBV) stage, characterized by a few eruptions, and finally the WR phase (Fig. 1). Our simulation parameters are summarized in Table 1.

We post-process our MHD models further with the code RADMC-3D (Dullemond 2012), which calculates the radiative transfer against dust opacity. The dust density field is constructed from the MHD models assuming a standard dust-to-gas mass ratio of 1/200 and

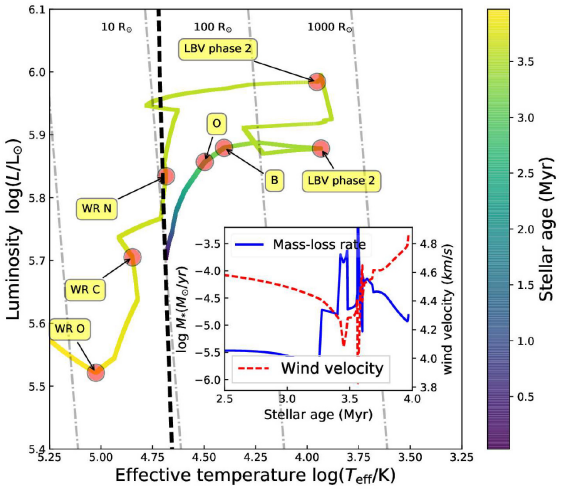

Figure 1. Evolutionary track of a star with an initial mass of 60 M$_\odot$ (Groh et al. 2014). Inset: mass-loss rate and wind velocity for the post-main-sequence phases.

Table 1. Simulation models. Listed are the space velocity of the star, $v_\star$, and its ambient-medium number density, $n_{\rm ISM}$.

Model	$v_\star$ (km s^{-1})	$n_{\rm ISM}$ (cm^{-3})
Run-v30-n0.79	50	0.79
Run-v100-n0.79	100	0.79
Run-v200-n0.01	200	0.01

the dust temperatures are calculated by Monte Carlo simulations. Following Green et al. (2019), the ionized stellar winds and gas hotter than 10^6 K are considered dust-free. Synthetic infrared images are then produced by ray-tracing stellar photons from the stellar atmosphere through the stellar surroundings. The star is assumed to be a spherical blackbody of effective temperature $T_{\rm eff}$, bolometric luminosity $L_\star$ and radius $R_\star$ interpolated from the stellar evolution track of Groh et al. (2014). We use opacities for a dust mixture based on silicate crystals (Laor & Draine 1993).

3 RESULTS

Figs 2–7 illustrate the results of our numerical models. Fig. 2 displays the gas number density (in cm^{-3}) of our model Run-v30-n0.79 plotted on a logarithmic scale (left-hand panels) and the corresponding *Spitzer* 24-μm infrared emission maps (right-hand panels). Note from the figure that the wind–ISM interaction generates a steady-state MHD bow-shock system composed of an inner termination shock and an outer forward shock engulfing two regions of hot, low-density stellar wind and cold, dense shocked ISM (Meyer et al. 2017). In Fig. 2(b), one sees that the wind material of the B-type phase passes through the main-sequence bow shock and produces the appearance of a Napoleon's Hat surrounding a cavity of low-density stellar wind.

Density profiles along the symmetry axis of model Run-v30-n0.79 taken at selected times are shown in Fig. 3. The solid thin lines illustrates the stellar surroundings at the WR time, with the expanding wind (0–2 pc), the WR shell (2–2.5 pc), the successive cold/hot/cold LBV phases engendering two shells (5.5–7.5 pc) and

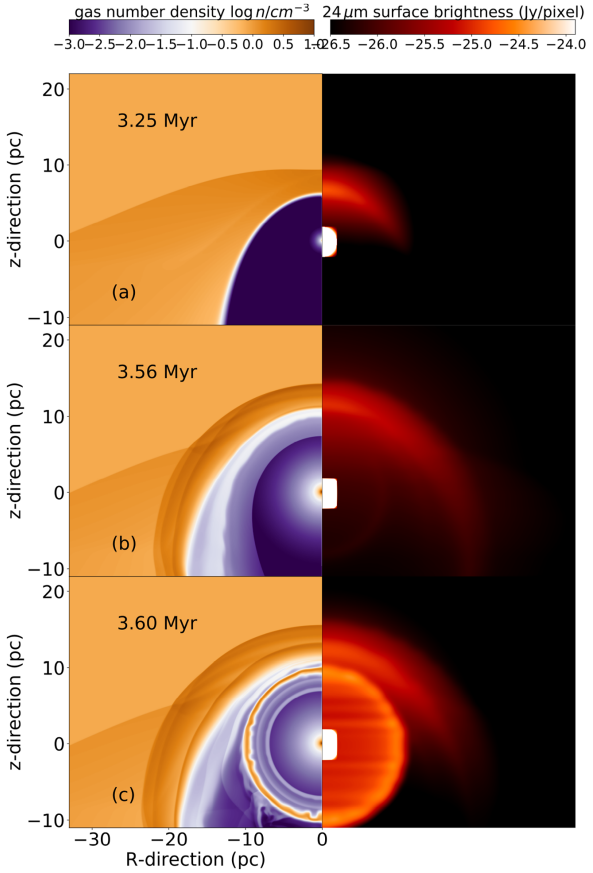

Figure 2. Density (left) and infrared 24-μm emission maps (right) of the circumstellar medium around a star with initial mass 60 $M_\odot$ and evolving along the evolutionary track shown in Fig. 1. We plot the results for the model Run-v30-n0.79, in which the star moves with velocity 30 km s^{-1} in a medium of number density 0.79 cm^{-3}, which corresponds to the warm phase of the Galactic plane. From top to bottom, selected snapshots are displayed, with (a) the steady-state bow shock of the runaway star's main-sequence phase, (b) the 'Napoleon's hat' developing during the B-type phase of stellar evolution and making room for slow LBV materials to expand inside it and (c) the LBV material swept up as a mid-infrared ring nebula by the fast WR wind. The spherical ring is brighter than the bow shock generated by the pre-WR winds.

the shock front of B spectral type, which has reached and pushed outwards the former main-sequence stellar wind bubble (10–12.5 pc). From time 3.579 Myr, the WR shell keeps on expanding (Figs 2b and c), reaching (3.609 Myr) and merging (3.614 Myr) with the shocked layers of O- and B-type wind material. At later times (thick dotted line), the WR material has merged with the main-sequence bow shock.

Fig. 4 is like Fig. 2 but for our model Run-v100-n0.79, i.e. a star with velocity $v_\star = 100$ km s^{-1}. The shaping of the circumstellar medium happens in a similar way, with a WR ring nebula developing inside the cavity of slow LBV gas (Fig. 4a). As an effect of the faster stellar motion, no Napoleon's Hat forms and the ring interacts sooner with the bow shock, since its stand-off distance is smaller (Wilkin 1996). Such a ring does not behave like regular bow-shock-producing material, and a bright arc-like nebula does not form, as is evident in the infrared emission maps in Figs 2–6,

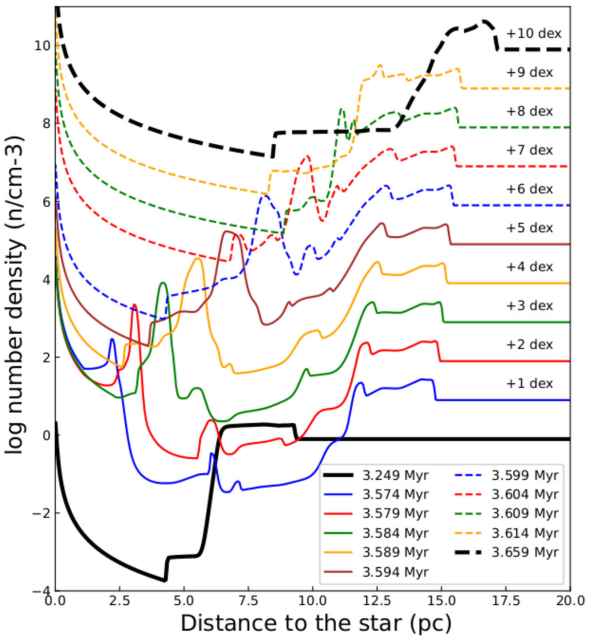

Figure 3. Number density profiles (in cm^{-3}) taken along the direction of motion of the runaway star, at selected times (in Myr) before, during and after the release of the WR WN shell. Each profile is offset by 1 dex.

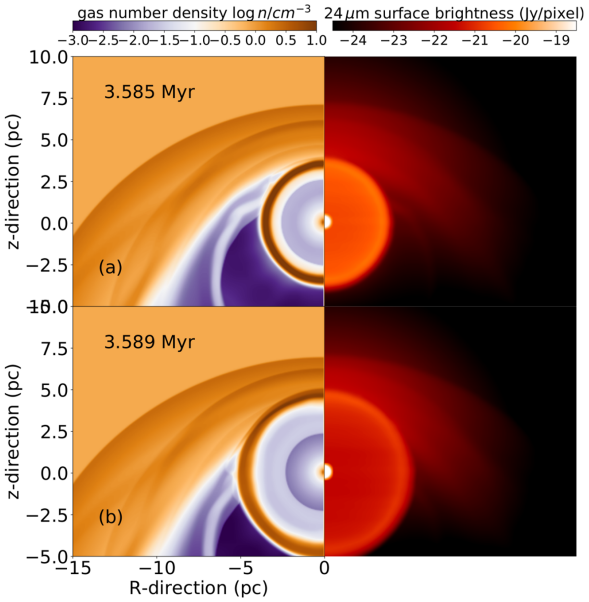

Figure 4. Same as Fig. 2 for the model Run-v100-n0.79. The 60-$M_\odot$ star moves with velocity 100 km s^{-1} in a medium of number density 0.79 cm^{-3}, corresponding to the warm phase of the Galactic plane. From top to bottom, the images (a) show that the fast wind–slow wind interaction generates a ring nebula around the fast-moving WR star in the Galactic plane and (b) illustrate how the pre-WR evolution of the runaway star engenders series of arcs and filaments in the main-sequence bow shock. This compares well with the Hα surroundings of WR 16 (left panel of fig. 1 in Toalá & Guerrero 2013).

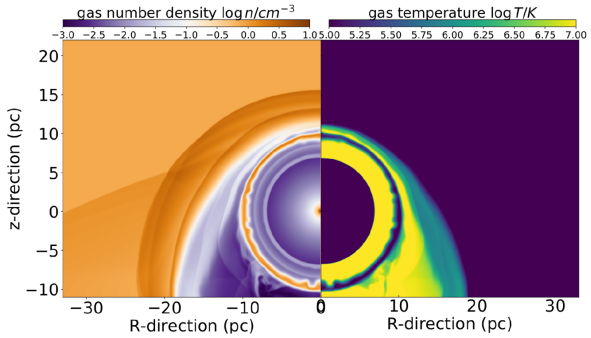

Figure 5. Density field (left) and temperature map of the shocked pre-WR wind and ISM materials (right) in our model Run-v30-n0.79 at time 3.6 Myr. The right-hand image shows the temperature map of the shock materials (inner shocked pre-WR stellar winds and outer shocked main-sequence and ISM gas). For clarity, the hot WR freely expanding wind and the unperturbed ISM have been substracted from the image. The swept-up LBV material is colder than its direct surroundings. Only the ring nebula, together with the stellar wind bow shock, has $T \leq 10^6$ K and can contain unsublimated dust particles. The other regions are therefore excluded from the radiative transfer calculations.

as a consequence of the dust spatial distribution. Fig. 5 illustrates the location of the dust in the nebulae. It plots the gas density field (left, in g cm^{-3}) and the corresponding shocked material distribution (right, in K). The portion of the ring that collides with the termination shock upstream of the stellar motion becomes denser, although its overall circular shape is conserved.

Fig. 6 is the same as Fig. 2 but for our model Run-v200-n0.01. The star moves at very high speed in a diluted medium taken to be 0.01 cm^{-3}, which is typical of the low density found in and above the Galactic plane. Consequently, the stand-off distance of the pre-WR bow shock is huge, about 20 pc, and so is the cavity of low-density stellar wind embedded inside it. The shell of the fast WR wind expands into it and assumes the shape of a ring-like nebula. Due to the very extended shape of the bow shock, the ring has lots of space and time to expand, and consequently Rayleigh–Taylor instability develops. The curvature of the unstable WR ring is modified once it interacts with the contact discontinuity produced during the previous evolutionary phase; it adopts a somewhat oblate morphology with higher density upstream of the stellar motion. This mechanism naturally holds for high latitudes above the Galactic plane where the ISM density is dilute, which makes the bow shock fainter and emphasizes the process of ring formation.

Note that the 2.5D nature of the MHD simulations implies a rotation of the solution around the Oz axis of the computational domain when interfacing the MHD bow shock model with the radiative transfer code. Consequently, the projection of Rayleigh–Taylor-unstable ring nebulae induces a series of stripe-like features in the infrared emission map (right-hand part of Figs 6b and c); see also Meyer et al. (2016). The detailed structure of the apex of the MHD bow shocks might also be affected by the axis of symmetry, as it can induce a concave-inward form that differs from the classical shape of stellar-wind bow shocks; see Fig. 6(b) and fig. 1 of Meyer et al. (2017). Similarly, artefacts can develop in the trail of bow-shock nebulae when gas accumulates and accumulates along the symmetry axis; see fig. 5 of Meyer, Petrov & Pohl (2020). However, the latter does not affect our results. Circumventing those 2.5D-induced artefacts would require computationally intensive full 3D MHD models.

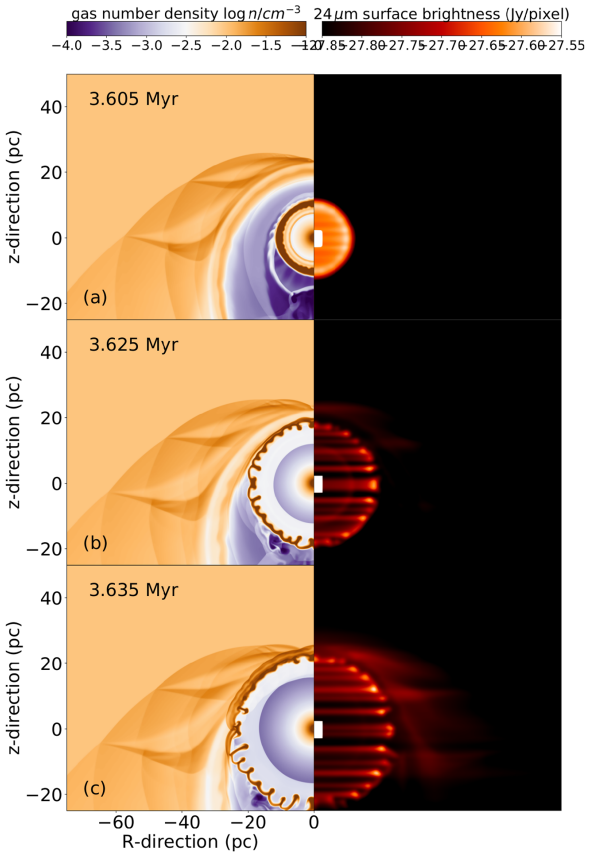

Figure 6. Same as Fig. 2 but for our model Run-v200-n0.01. The star moves with velocity 200 km s^{-1} in a medium of number density 0.01 cm^{-3}, corresponding to the dilute phase of the Galactic plane and/or the higher latitude region above the Galactic disc. As the medium is diluted, the bow shock generated by the runaway star is huge and its infrared signature is faint, respectively (b). The region filled by slow LBV material is large, which permits the ring swept-up by the fast WR wind to expand spherically despite the driving star's huge bulk velocity. This simulation model has qualitative properties in accordance with WR 124 and its surrounding nebular structure M1-67 (van der Sluys & Lamers 2003).

In Fig. 7 we show the velocity profile along the direction of motion of the star at an early time of ring expansion in our model Run-v30-n0.79. The successive wind phases carve the main-sequence bow shock, making room for the *fast* WR wind to expand into a *slower* medium harbouring multiple shocks and discontinuities of the cold/hot LBV and earlier-type wind, hence producing a ring nebula. As the speed of the slow gas in the cavity is still larger than the stellar bulk motion, the ring seems to be comoving with the runaway star.

4 DISCUSSION

In this article, we presented numerical models for the circumstellar medium of very massive runaway stars. For a star with initial mass of 60 $M_\odot$ that follows an evolutionary path characterized successively by phases with O and B spectral type, multiple cold/hot LBV eruptions and several final WR phases (Groh et al. 2014), we investigate the formation of ring-like nebulae. Our simulations show that the stellar wind remains confined inside its main-sequence wind

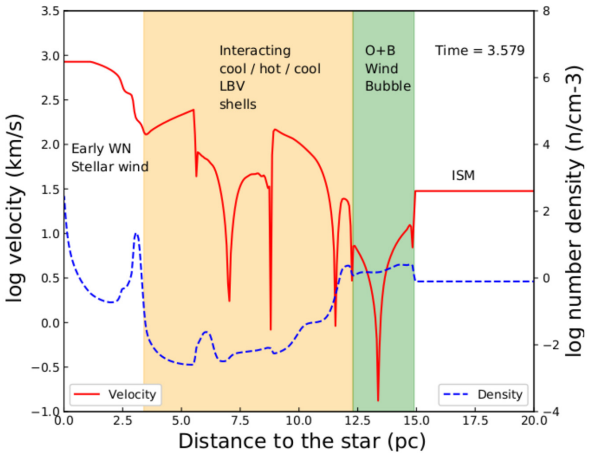

Figure 7. Profiles of gas velocity (in km s^{-1}) and number density taken along the direction of motion of the runaway star at time 3.579 Myr in our model Run-v30-n0.79, which involves a star moving at 30 km s^{-1} (see also Fig. 3). The orange and green regions highlight regions made mostly of LBV or O/B material. Note that additional mixing may happen.

bubble. We calculate the radiative transfer against dust opacity in the stellar environment and demonstrate that the ring-formation mechanism discussed above explains the systematic centring of circumstellar shells surrounding many evolved massive stars such as WR stars, which are observed as mid-infrared circular circumstellar nebulae (Gvaramadze et al. 2010).

Previous models of 20–30 $M_\odot$ runaway WR stars assumed simpler evolution through a red supergiant phase. They indicated that the early WR wind expands spherically before eventually interacting directly with the ISM, once the WR ring has passed through the relatively compact red supergiant bow shock (Brighenti & D'Ercole 1995b; van Marle et al. 2005). The shells of WR wind are distorted rapidly once they interact with the ISM. For very massive stars, the rings develop in much larger cavities, and therefore the observation of a ring comoving with very fast runaway WR stars is the consequence of complex stellar evolution involving a series of LBV eruptions. This constrains the star's initial mass to $> 40\,M_\odot$, i.e. to the mass range of stars that do not evolve directly to the WR stage via a single red supergiant phase.

Inside the wind-blown bubble, the post-main-sequence winds generate a pattern of various shocks and unstable discontinuities separating slow, dense and cold gas from hot and fast material that collide with each other, creating a cavity of slow stellar wind inside which the fast WR material is released. Star-centred rings such as the nebula surrounding WR71 are far denser and closer to the star than the bow shock, and consequently they appear brighter in dust-scattered starlight than the bow shock itself (Faherty et al. 2014; Flagey et al. 2014). LBV winds are often anisotropic. Older rings may therefore lose their early sphericity on account of propagation in an anisotropic wind zone, which explains the variety of observed shells (Gvaramadze et al. 2010; Stock & Barlow 2010).

For slower stars moving in the Galactic plane, a Napoleon's Hat forms on account of multiple arced structures arising from the succession of different phases (Fig. 2). Another trace of complex pre-WR evolution is the series of arcs produced in the main-sequence bow shock when the various winds interact with the termination shock (Figs 4 and 6). The aftermath of the succession of mass-loss events is visible at Hα in the vicinity of WR 16's shell; see the left panel of fig. 1 in Toalá & Guerrero (2013).

Our simulations compare well with high-latitude runaway WR stars. The properties of the early WN-type star WR 124 with its nebular structure M1-67 and the star WR 148, both moving at velocities $v_\star \approx 200\,\mathrm{km\,s^{-1}}$, resemble our Run-v200-n0.001. WR 124 is not surrounded by a circular ring but a series of clumps, filaments and arcs, suggesting that the star just entered the WN phase and that no swept-up dust material has formed yet. Associating the arcs with LBV ejections, van der Sluys & Lamers (2003) derived the presence of a large-scale bow at 1.3 pc from the star. Such a small stand-off distance is in conflict with our model, as we obtain ≈ 20 pc, however we use an ISM density of $n_{\rm ISM} \approx 0.01\,\mathrm{cm^{-3}}$, while van der Sluys & Lamers assumed $n_{\rm ISM} \approx 1.0\,\mathrm{cm^{-3}}$, which we deem too large for a high-latitude star. WR 124's bow shock is located at a larger distance and it is therefore much fainter compared with the nebular shell M1-67.

WR 148 has similar altitude and proper motion to WR124, but displays neither a bow shock nor a detected nebula. Our models suggest that the existing ring nebula is too young to be seen at such a distance (> 8 kpc) and that a large, faint bow shock should surround it. Our model Run-v200-n0.01 assumes the highest known stellar velocity of a WR star, but a very dilute medium. Any star located higher above the Galactic disc will naturally produce an even larger cavity of slow stellar wind and rings of swept-up hot material (Rate & Crowther 2020). This explains the systematic absence of observed bow shocks around high-latitude runaway WR stars. They are too large, diluted and faint to be detected, despite their huge proper motion and significant mass-loss rate (Toalá et al. 2015). Finally, our models explain the circumstellar structures around high-latitude WR stars without assuming their in situ formation.

Lastly, the duration of the LBV phase might affect the development of the ring nebula. The stellar evolution model of Groh et al. (2014) assumes a rather long LBV phase of 2.35×10^5 yr, while much shorter LBV phases exist., e.g. in the case of lower-mass (20–25 $M_\odot$) progenitors (Chita et al. 2008; Groh, Meynet & Ekström 2013) or at lower metallicity, such as in the Large Magellanic Cloud (Bohannan 1997). Shorter LBV eruptions will supply the interior of the bow shock with less material and consequently diminish the amount of material accumulated in the ring, which will become thinner as it expands outwards. This might affect our results, as long as the star is at rest or moves slowly (Meyer et al. 2020), whereas if it moves fast and/or in a dense medium the stand-off distance of the bow shock is short and less LBV material is required to generate a ring nebula that will last less time. The length of the WR phase does not matter in ring production, as it acts as a source of momentum that sweeps up the LBV material. All these elements are consistent with the conclusions of Gräfener et al. (2012), who found that ring nebulae are mostly observed around early-type WR stars.

The models presented in this article are computed from one particular stellar-evolution model (Groh et al. 2014). The formation of ring nebulae around runaway WR stars should remain qualitatively the same regardless of the details of the evolution history, as long as the star undergoes episodes of faster and slower winds and ejects a considerable amount of mass after its main-sequence phase (such as a LBV mass ejection).

5 CONCLUSION

Our simulations change the paradigm of the surroundings of WR stars and reveal a complex picture of the formation of WR ring nebulae. In the Galactic plane, the same fast wind–slow wind

interaction mechanism is responsible for the formation of the observed near-infrared ring nebulae that appear to be comoving with some runaway WR stars (Gvaramadze et al. 2010), as long as sufficiently complex evolution, via e.g. a B spectral-type phase and LBV eruptions, happens and enlarges the wind cavity. The presence of infrared rings, which are brighter than the bow shock, therefore reflects the very large ($> 40\,M_{\odot}$) initial mass of these WR stars.

The absence of detected bow shocks and the presence of diffuse ring nebulae around high-Galactic-latitude WR stars does not imply the nonexistence of supersonic stellar motion through the ISM, because that would produce a distant and very faint bow shock. Our study motivates further high-resolution, multi-wavelength observational campaigns of the circumstellar medium of Galactic WR stars, such as the 3-mm interferometric ALMA (Atacama Large Millimeter/submillimeter Array) observations of Westerlund 1 (Fenech et al. 2018) or the observations of non-thermal radio emission of WR wind bubble G2.4+1.4 (Prajapati et al. 2019), in order to unveil their detailed structures and to constrain the late evolution of their driving star.

ACKNOWLEDGEMENTS

The authors thank G. Koenigsberger (Universidad Nacional Autónoma de México) for her kind and useful comments on the nomenclature of Wolf-Rayet stars which improved the consistency of this study.

The authors acknowledge the North-German Supercomputing Alliance (HLRN) and the Max Planck Computing and Data Facility (MPCDF) for providing HPC resources. LMO acknowledges financial support from the Deutsches Zentrum für Luft und Raumfahrt (DLR) grant FKZ 50 OR 1809 and partial support from the Russian Government Program of Competitive Growth of Kazan Federal University.

DATA AVAILABILITY

This research made use of the PLUTO code developed by A. Mignone at the University of Torino (http://plutocode.ph.unito.it/), the radiative transfer code RADMC-3D developed by C. P. Dullemond at the University of Heidelberg (http://www.ita.uni-heidelberg.de/dullemond/software/radmc-3d/) and the MATPLOTLIB plotting library for the PYTHON programming language (https://matplotlib.org/). The data underlying this article will be shared on reasonable request to the corresponding author.

REFERENCES

Asplund M., Grevesse N., Sauval A. J., Scott P., 2009, ARA&A, 47, 481
Barniske A., Oskinova L. M., Hamann W. R., 2008, A&A, 486, 971
Bestenlehner J. M. et al., 2014, A&A, 570, A38
Bohannan B., 1997, in Nota A., Lamers H., eds, ASP Conf Ser. Vol. 120. Luminous Blue Variables: Massive Stars in Transition, Astron. Soc. Pac., San Francisco, p. 3
Brighenti F., D'Ercole A., 1995a, MNRAS, 277, 53
Brighenti F., D'Ercole A., 1995b, MNRAS, 273, 443
Chita S. M., Langer N., van Marle A. J., García-Segura G., Heger A., 2008, A&A, 488, L37
Crowther P. A., 2007, ARA&A, 45, 177
Dinçel B., Neuhäuser R., Yerli S. K., Ankay A., Tetzlaff N., Torres G., Mugrauer M., 2015, MNRAS, 448, 3196
Dullemond C. P., 2012, RADMC-3D: A multi-purpose radiative transfer tool, Astrophysics Source Code Library, record ascl:1108.016.
Faherty J. K., Shara M. M., Zurek D., Kanarek G., Moffat A. F. J., 2014, AJ, 147, 115
Fenech D. M. et al., 2018, A&A, 617, A137
Flagey N., Noriega-Crespo A., Petric A., Geballe T. R., 2014, AJ, 148, 34
Gräfener G., Vink J. S., Harries T. J., Langer N., 2012, A&A, 547, A83
Green S., Mackey J., Haworth T. J., Gvaramadze V. V., Duffy P., 2019, A&A, 625, A4
Groh J. H., Meynet G., Ekström S., 2013, A&A, 550, L7
Groh J. H., Meynet G., Ekström S., Georgy C., 2014, A&A, 564, A30
Gvaramadze V. V., Kniazev A. Y., Fabrika S., 2010, MNRAS, 405, 1047
Hamann W. R., Gräfener G., Liermann A., 2006, A&A, 457, 1015
Laor A., Draine B. T., 1993, ApJ, 402, 441
Mackey J., Gvaramadze V. V., Mohamed S., Langer N., 2015, A&A, 573, A10
Marston A. P., 1997, ApJ, 475, 188
Meyer D. M. A., Mignone A., Kuiper R., Raga A. C., Kley W., 2017, MNRAS, 464, 3229
Meyer D. M. A., Petrov M., Pohl M., 2020, MNRAS, 493, 3548
Meyer D. M.-A., Gvaramadze V. V., Langer N., Mackey J., Boumis P., Mohamed S., 2014, MNRAS, 439, L41
Meyer D. M.-A., Mackey J., Langer N., Gvaramadze V. V., Mignone A., Izzard R. G., Kaper L., 2014, MNRAS, 444, 2754
Meyer D. M.-A., van Marle A.-J., Kuiper R., Kley W., 2016, MNRAS, 459, 1146
Mignone A., Zanni C., Tzeferacos P., van Straalen B., Colella P., Bodo G., 2012, ApJS, 198, 7
Miller G. J., Chu Y.-H., 1993, ApJS, 85, 137
Moffat A. F. J., Seggewiss W., 1979, A&A, 77, 128
Moffat A. F. J. et al., 1998, A&A, 331, 949
Munoz M., Moffat A. F. J., Hill G. M., Shenar T., Richardson N. D., Pablo H., St-Louis N., Ramiaramanantsoa T., 2017, MNRAS, 467, 3105
Prajapati P., Tej A., del Palacio S., Benaglia P. CH I.-C., Vig S., Mand al S., Kanti Ghosh S., 2019, ApJ, 884, L49
Rate G., Crowther P. A., 2020, MNRAS, 493, 1512
Renzo M. et al., 2019, A&A, 624, A66
Sander A., Hamann W. R., Todt H., 2012, A&A, 540, A144
Stock D. J., Barlow M. J., 2010, MNRAS, 409, 1429
Toalá J. A., Guerrero M. A., 2013, A&A, 559, A52
Toalá J. A., Guerrero M. A., Ramos-Larios G., Guzmán V., 2015, A&A, 578, A66
Toalá J. A. et al., 2018, ApJ, 869, L11
van der Sluys M. V., Lamers H. J. G. L. M., 2003, A&A, 398, 181
van Marle A. J., Langer N., García-Segura G., 2005, A&A, 444, 837
van Marle A. J., Decin L., Meliani Z., 2014, A&A, 561, A152
Weaver R., McCray R., Castor J., Shapiro P., Moore R., 1977, ApJ, 218, 377
Wilkin F. P., 1996, ApJ, 459, L31

This paper has been typeset from a TEX/LATEX file prepared by the author.

Monthly Notices
of the
ROYAL ASTRONOMICAL SOCIETY

MNRAS **507,** 4697–4714 (2021)
Advance Access publication 2021 August 28

https://doi.org/10.1093/mnras/stab2426

On the bipolarity of Wolf–Rayet nebulae

D. M.-A. Meyer ★

Institut für Physik und Astronomie, Universität Potsdam, Karl-Liebknecht-Strasse 24/25, D-14476 Potsdam, Germany

Accepted 2021 August 20. Received 2021 August 19; in original form 2021 July 27

ABSTRACT

Wolf–Rayet stars are amongst the rarest but also most intriguing massive stars. Their extreme stellar winds induce famous multiwavelength circumstellar gas nebulae of various morphologies, spanning from circles and rings to bipolar shapes. This study is devoted to the investigation of the formation of young, asymmetric Wolf–Rayet gas nebulae and we present a 2.5-dimensional magneto-hydrodynamical toy model for the simulation of Wolf–Rayet gas nebulae generated by wind–wind interaction. Our method accounts for stellar wind asymmetries, rotation, magnetization, evolution, and mixing of materials. It is found that the morphology of the Wolf–Rayet nebulae of blue supergiant ancestors is tightly related to the wind geometry and to the stellar phase transition time interval, generating either a broadened peanut-like or a collimated jet-like gas nebula. Radiative transfer calculations of our Wolf–Rayet nebulae for dust infrared emission at 24 μm show that the projected diffuse emission can appear as oblate, bipolar, ellipsoidal, or ring structures. Important projection effects are at work in shaping observed Wolf–Rayet nebulae. This might call a revision of the various classifications of Wolf–Rayet shells, which are mostly based on their observed shape. Particularly, our models question the possibility of producing pre-Wolf–Rayet wind asymmetries, responsible for bipolar nebulae like NGC 6888, within the single red supergiant evolution channel scenario. We propose that bipolar Wolf–Rayet nebulae can only be formed within the red supergiant scenario by multiple/merged massive stellar systems, or by single high-mass stars undergoing additional, e.g. blue supergiant, evolutionary stages prior to the Wolf–Rayet phase.

Key words: MHD – radiative transfer – circumstellar matter – stars: massive – stars: Wolf–Rayet.

1 INTRODUCTION

Formed out of the gravitational collapse of opaque pre-stellar cores, high-mass stellar objects, i.e. with mass $\geq 8\,M_\odot$, are cosmic regulators of the cycle of matter at work in the interstellar medium (ISM) of galaxies (Maeder 2009; Langer 2012). One of their characteristic features is the fast and strong wind blown out from their surface and powered by the complex nuclear reactions at work in their interior. Throughout their lives, massive stars first experience a rather long, main-sequence phase corresponding to the burning of hydrogen in their cores (Ekström et al. 2012). It is characterized by the release of diluted, hot, and supersonic winds from the stellar surface, and, once their hydrogen is exhausted, stellar evolution is triggered. The entire evolution of massive stars is fixed by their zero-age main-sequence properties, such as their mass, angular velocity, and chemical composition, which uniquely determines their evolution and ultimate fate (Woosley, Heger & Weaver 2002; Vink 2006; Brott et al. 2011; Szécsi et al. 2020). These initial stellar characteristics rule the time dependence of the stellar surface properties, as well as the number and duration of the various evolutionary phases, up to their death, either as a core-collapse supernova leaving behind a plerionic supernova remnant or directly collapsing as a black hole (Chevalier 1977; Weiler & Sramek 1988; Woosley et al. 2002; Woosley & Bloom 2006; Smartt 2009; Müller & Janka 2015; Gabler, Wongwathanarat & Janka 2021).

Amongst the many possible evolutionary histories massive stars can undergo, high-mass stellar objects can evolve to the so-called Wolf–Rayet stage. This phase is characterized by fast ($\sim$1000–5000 km s^{-1}) and dense stellar winds expelled at mass-loss rates $\geq 10^{-5}\,M_\odot\,\mathrm{yr}^{-1}$ and enriched in C, N, and O elements (Hamann, Gräfener & Liermann 2006; Sander, Hamann & Todt 2012; Bestenlehner et al. 2014). The precise manner a massive stellar object acquires the spectroscopic properties of a Wolf–Rayet star is not completely understood; however, a few typical evolutionary paths have been identified (Crowther 2007). The most common channel reposes in an evolution from the main-sequence to the Wolf–Rayet phase through a red supergiant phase, and it mostly concerns Galactic stars with masses $\geq 20\,M_\odot$. Heavier zero-age main-sequence stars (up to $\sim 60\,M_\odot$) have been shown theoretically to experience a much more complex evolution, including several successive luminous blue variable phases, during which the star blows, sometimes eruptively, blue supergiant material (Groh et al. 2014).

The interaction of the stellar wind of massive stars with the ISM produces gas nebulae witnessing the release of energy, momentum, and heavy chemical elements that enriched their local ambient medium (Langer 2012). The classical picture for stellar wind-ISM interaction is that of Weaver et al. (1977) and it consists of several parsec-scale structured circumstellar bubbles surrounding massive stars. The circumstellar medium of Wolf–Rayet stars is different, as many of them display unusual smaller-scale ring-like gas nebulae detected in Hα and infrared, both in the Milky Way, see Chu & Treffers (1981) and Treffers & Chu (1982), and in the Magellanic Clouds (Chu 1982b, 1983; Dopita et al. 1994; Weis et al. 1997; Hung

★ E-mail: dmameyer.astro@gmail.com

et al. 2021), respectively. A classification of circumstellar structures around Wolf–Rayet stars arose from those studies (Chu 1981, 1982a,b; Treffers & Chu 1982; Chu, Treffers & Kwitter 1983; Toalá et al. 2015). Several follow-up surveys deepened and completed these observations in the Southern hemisphere, see Marston, Chu & Garcia-Segura (1994) and Marston et al. (1994). Wolf–Rayet nebulae entered the X-rays domain with *ASCA* (Wrigge et al. 2005) *ROSAT* and *Chandra* (Guerrero & Chu 2008), *XMM–Newton* (Toalá et al. 2012) observations from their (shocked) stellar winds witnessing emission of optically thin high-temperature plasma. More recently, a radio non-thermal synchrotron counterpart of the stellar wind bubble of a Wolf–Rayet ring nebula indicated that these circumstellar nebulae are the site of particles acceleration (Prajapati et al. 2019). This accumulation of observations motivates the present numerical efforts aiming at understanding the peculiar vicinity of young Wolf–Rayet stars.

Numerical simulations rapidly became an efficient tool to understand the different physical processes at work in the circumstellar medium of massive stars (Comerón & Kaper 1998; Freyer, Hensler & Yorke 2003; Dwarkadas 2005; Freyer, Hensler & Yorke 2006; Toalá & Arthur 2011; van Marle et al. 2011; van Marle, Meliani & Marcowith 2015), to constrain stellar evolution models/probe local ISM conditions (Mackey et al. 2012, 2014), and to understand the pre-supernova surroundings of dying massive stars, with which supernovae shock waves subsequently interact (Chevalier & Liang 1989; Ciotti & D'Ercole 1989; van Marle, Langer & García-Segura 2005; van Marle et al. 2006; Meyer et al. 2021b). Particularly, the gas nebulae formed around Wolf–Rayet stars have been studied numerically as evolved winds, colliding with the material of a larger-scale main-sequence wind-blown bubble (Brighenti & D'Ercole 1997; Dwarkadas 2007; van Marle, Langer & García-Segura 2007; van Marle, Keppens & Meliani 2011).

It has recently been shown in Meyer et al. (2020a), on the basis of magneto-hydrodynamical (MHD) simulations, that (i) the circumstellar rings appearing to be comoving with the fastest-moving Wolf–Rayet stars are a trace of their very high initial masses ($\gtrsim$35 to $\sim$60 $M_\odot$) inducing complex evolutionary histories and that (ii) their large-scale surroundings are main-sequence stellar wind bow shocks fainter than the inner rings which became unobservable as the driving star runs into diluted media (Gvaramadze, Kniazev & Fabrika 2010). This solved the apparent missing bow shock problem around some high-latitude, Galactic, very fast-moving Wolf–Rayet stars like WR124, surrounded by its compact gas nebula M1–67 (Chu 1981; van der Sluys & Lamers 2003; Marchenko, Moffat & Crowther 2010; Toalá et al. 2018) or WR71 (Faherty et al. 2014; Flagey et al. 2014). If we can now qualitatively explain the formation of quasi-spherical rings around very fast-moving Wolf–Rayet stars, detailed observations of these gas nebulae reveal much more complex structures whose formation are far from being understood. Which mechanisms distinguish between the production of ring-like shells from ovoidal and/or other complex shapes? What can we learn regarding the past evolution of massive stars with nebulae of such morphologies?

In this study, we continue our investigations of the shaping of circumstellar Wolf–Rayet nebulae started in Meyer et al. (2020a). We concentrate on the production of bipolar asymmetries and non-spherical morphologies observed in the vicinity of some young Wolf–Rayet stars (Toalá et al. 2015). The starting point of this study is the work of Brighenti & D'Ercole (1997), in which the development of young aspherical Wolf–Rayet nebulae is examined using a hydrodynamical wind–wind interaction model. Their simulations focus on the particular scenario of a red supergiant star, with asymmetric stellar wind properties, evolving to a Wolf–Rayet stage of symmetric stellar wind properties. In the same spirit, we build a magneto-hydrodynamical toy model for rotating blue supergiant stars with asymmetric stellar winds and evolving to the Wolf–Rayet phase. The effects of asymmetries in the blue supergiant wind are investigated using the recipe of Raga et al. (2008). We perform near-infrared synthetic observables of the corresponding bipolar stellar wind nebulae, in order to discuss their respective emission properties and facilitate qualitative comparison to observations available in the literature.

Our study is organized as follows. First, we present the numerical methods utilized for the MHD simulations of Wolf–Rayet gas nebulae evolving after having undergone a previous blue supergiant phase in Section 2. We show our results regarding the dynamical evolution of bipolar MHD Wolf–Rayet nebulae generated by wind–wind interaction in Section 3. The results are further discussed in Section 4, and finally, we present our conclusions in Section 5.

2 METHOD

This section presents the numerical methods used in this project, together with the initial conditions and parametrized boundary conditions of the simulations. Last, we introduce the reader to the models performed in this study.

2.1 Governing equations

We set our problem in the frame of non-ideal magneto-hydrodynamics, described by the following series of equations,

$$\frac{\partial \rho}{\partial t} + \nabla \cdot (\rho \boldsymbol{v}) = 0, \tag{1}$$

$$\frac{\partial \boldsymbol{m}}{\partial t} + \nabla \cdot (\boldsymbol{m}\otimes\boldsymbol{v} - \boldsymbol{B}\otimes\boldsymbol{B} + \hat{\mathbf{I}} p_{\rm t}) = \boldsymbol{0}, \tag{2}$$

$$\frac{\partial E}{\partial t} + \nabla \cdot ((E + p_{\rm t})\boldsymbol{v} - \boldsymbol{B}(\boldsymbol{v} \cdot \boldsymbol{B})) = \Phi(T, \rho), \tag{3}$$

and

$$\frac{\partial \boldsymbol{B}}{\partial t} + \nabla \cdot (\boldsymbol{v}\otimes\boldsymbol{B} - \boldsymbol{B}\otimes\boldsymbol{v}) = \boldsymbol{0}, \tag{4}$$

where $\boldsymbol{B}$ represents the magnetic field vector, ρ stands for the mass density,

$$\boldsymbol{m} = \rho \boldsymbol{v} \tag{5}$$

is the linear momentum vector, $\hat{\mathbf{I}}$ the identity matrix, $p_{\rm t}$ is the total pressure, and is v the gas velocity, respectively. The total energy of the system reads

$$E = \frac{p}{(\gamma - 1)} + \frac{\boldsymbol{m} \cdot \boldsymbol{m}}{2\rho} + \frac{\boldsymbol{B} \cdot \boldsymbol{B}}{2}, \tag{6}$$

and the sound speed is defined as

$$c_{\rm s} = \sqrt{\frac{\gamma p}{\rho}}, \tag{7}$$

which closes the above system of equations, and where $\gamma = 5/3$ is the adiabatic index.

Radiative cooling and heating of the gas,

$$\Phi(T, \rho) = n_{\rm H}\Gamma(T) - n_{\rm H}^2\Lambda(T), \tag{8}$$

are explicitly included via optically thin processes for loss $\Lambda(T)$ and gain $\Gamma(T)$ in the source term, where

$$T = \mu \frac{m_{\rm H}}{k_{\rm B}} \frac{p}{\rho} \tag{9}$$

is the gas temperature, and using the laws of photoionized gas is described in great detail in Meyer et al. (2021a). Hence, our method ignores any explicit treatment of the radiation pressure from the photon field of the central star. This is correct for cool blue supergiant stars, while we neglect the detailed position of the ionization front generated by the young Wolf–Rayet stars, as well as its effects on the shell instabilities (Toalá & Arthur 2011).

A passive scalar tracer is included in the stellar wind,

$$\frac{\partial(\rho Q)}{\partial t} + \nabla \cdot (\boldsymbol{v}\rho Q) = 0, \tag{10}$$

to follow the advection of the new-born Wolf–Rayet circumstellar nebula, as compared to the previous blue supergiant wind. This system of equations is solved by use of the eight-wave algorithm (Powell 1997), within a second-order Runge–Kutta with parabolic reconstruction of the variables between neighbouring cells together with the HLL Riemann solver (Harten, Lax & van Leer 1983). This unsplit scheme ensures that the magnetic field is divergence free everywhere in the computational domain. The simulations time-steps are controlled by the Courant–Friedrich–Levi condition that we set to $C_{\rm cfl} = 0.1$.

2.2 Initial conditions

We carry out MHD simulations with the PLUTO code (Mignone et al. 2007, 2012; Vaidya et al. 2018). The calculations are performed using a 2.5-dimensional spherical coordinate system (O;r, θ, ϕ) of origin O, with r the radial direction, θ the poloidal coordinate, and ϕ the toroidal component. The coordinate system $[r_{\rm in}, r_{\rm out}] \times [0, \pi] \times [0, 2\pi]$ is mapped with a mesh that is uniform along the polar and toroidal directions, while it expands logarithmically along the radial direction. It permits to reach high spatial resolutions close to the stellar wind boundary $r_{\rm in} = 0.02$ pc, while reducing the total number of grid zones in the simulation domain and reducing the computational costs. In total, we use $200 \times 200 \times 1$ grid zones. Outflow boundary conditions are assigned at the outer boundary $r_{\rm out} = 10$ pc, reflective boundary conditions are imposed along the symmetry axis $\theta = 0$ and $\theta = \pi$, while periodic boundary conditions are used at the borders $\phi = 0$ and $\phi = 2\pi$. Since the inner boundary is much larger than the radius of the photosphere ($r_{\rm in} \gg R_\star$), stellar gravity and wind acceleration mechanisms such as coronal heating and radiation pressure are neglected in the computational domain. Therefore, the acceleration of the stellar wind to the terminal velocity is not modelled in the simulations.

The simulations are initialized with the asymmetric stellar wind of a blue supergiant star. The adopted latitude dependence of the wind density is that developed in the context of the astrosphere of the runaway asymptotic giant branch star Mira (Raga et al. 2008). It reads

$$\rho_w(r, \theta) = \frac{\dot{M}}{4\pi r^2 v_{\rm w}} \rightarrow \frac{A}{r^2} f(\theta), \tag{11}$$

with $\dot{M}$ the stellar mass-loss rate, $v_{\rm w}$ the stellar wind velocity, and r the radial distance to the central star. The function

$$f(\theta) = \xi - (\xi - 1)|\cos(\theta)|^p \tag{12}$$

measures the wind anisotropy, with p a parameter determining the flattening degree of the density towards the equator and ξ is the equator-to-pole density ratio, respectively. The scaling factor A ensures that the latitude dependence in the stellar wind conserves the amount of mass lost by the star per unit time. It is evaluated by writing the mass conservation at the stellar surface,

$$\dot{M} = 4\pi r^2 \int_0^{\pi/2} \rho_w(r, \theta) v_w(r, \theta) \sin(\theta) {\rm d}\theta, \tag{13}$$

yielding

$$\dot{M} = 4\pi A v_{\rm w} \int_0^{\pi/2} |f(\theta)|^p \sin(\theta) {\rm d}\theta, \tag{14}$$

where $v_{\rm w}$ is the stellar wind terminal velocity, and, finally, one obtains,

$$A = \frac{\dot{M}}{4\pi v_{\rm w}} \frac{(\xi - 1)^2}{8\xi^{5/2} - 20\xi + 12}, \tag{15}$$

using $p = 1/2$. We chose this prescription for stellar wind asymmetries since it has already been used in the context of massive stars (Fang, Yu & Zhang 2017), although other recipes exist (Frank, Balick & Davidson 1995; Blondin, Lundqvist & Chevalier 1996).

Additionally, Raga et al. (2008) prescribe stellar wind flow assigned at the wind boundary $r_{\rm in}$ to account for the asymmetry function as

$$v(r_{\rm in}, \theta) = \frac{v_{\rm w}}{\sqrt{f(\theta)}}, \tag{16}$$

so that the ram pressure of the wind of the inner boundary,

$$\rho_{\rm w}(r_{\rm in}, \theta) v(r_{\rm in}, \theta)^2 = \frac{A}{r_{\rm in}^2} f(\theta) \left(\frac{v_{\rm w}}{\sqrt{f(\theta)}}\right)^2 \propto \left(\frac{v_{\rm w}}{r_{\rm in}}\right)^2, \tag{17}$$

remains isotropic. Stellar rotation is included in the model by considering the following latitude-dependent equatorial rotation velocity,

$$v_\phi(\theta) = v_{\rm rot} \sin(\theta), \tag{18}$$

where $v_{\rm rot}$ is the star's equatorial rotation speed. Last, the magnetization of the stellar winds is treated as a Parker spiral. It is a split monopole,

$$B_{\rm r}(r) = B_\star \left(\frac{R_\star}{r}\right)^2, \tag{19}$$

where $R_\star$ is the stellar radius, $B_\star$ the stellar surface magnetic field, plus a toroidal component,

$$B_\phi(r) = B_{\rm r}(r) \left(\frac{v_\phi(\theta)}{v_{\rm w}}\right) \left(\frac{r}{R_\star} - 1\right), \tag{20}$$

which relies on both the stellar surface magnetic field strength and on the stellar rotation velocity $v_{\rm rot}$. This so-called Parker stellar wind is a parametrization for magnetized low-mass stars that have been developed and widely used in studies devoted to the heliosphere (Parker 1958; Pogorelov & Semenov 1997; Pogorelov & Matsuda 2000; Pogorelov, Zank & Ogino 2004). It has been adapted to the intermediate stellar mass regime in works investigating the shaping of planetary nebula (Chevalier & Luo 1994; Rozyczka & Franco 1996; García-Segura, Ricker & Taam 2018; García-Segura, Taam & Ricker 2020) and stellar wind bow shocks (Herbst et al. 2020; Scherer et al. 2020; Meyer et al. 2021a), respectively.

2.3 Time-dependent stellar boundary conditions

At time $t_{\rm wr} - \Delta t$ the blue supergiant to Wolf–Rayet phase begins to take place, controlled by several quantities, namely its duration Δt and the manner the surface stellar properties evolve, determined by the quintuplet ($\dot{M}$, $v_{\rm w}$, $v_{\rm rot}$, $B_\star$, $R_\star$). The stellar wind velocity is

modulated following (Brighenti & D'Ercole 1997)

$$v_{\rm w}(r_{\rm in},t)=\begin{cases} v_{\rm w}^{\rm bsg}/\sqrt{f(\theta)} & \text{if } t\leq t_{\rm wr}-\Delta t,\\ v_{\rm w}^{\rm bsg}/\sqrt{f(\theta)}+\Delta v F & \text{if } t_{\rm wr}-\Delta t<t \text{ and } t\leq t_{\rm wr},\\ v_{\rm w}^{\rm wr} & \text{if } t_{\rm wr}<t,\end{cases} \tag{21}$$

with $\Delta v=|v_\star^{\rm wr}-v_\star^{\rm bsg}|$. In the above and following relations, the superscript 'bsg' and 'wr' stand for the blue supergiant and Wolf–Rayet winds, respectively. The manner the wind velocity changes over Δt is controlled by

$$F=F(t,t_{\rm wr},\Delta t)=\left(\frac{t-(t_{\rm wr}-\Delta t)}{\Delta t}\right)^{\beta/2}, \tag{22}$$

that is a function invoked when $t_{\rm wr}-\Delta t<t$ and $t\leq t_{\rm wr}$, defined such that $F(t=t_{\rm wr}-\Delta t)=0$ and $F(t=t_{\rm wr})=1$. For $\beta=2$, the transition is linear, while it is a power law for $\beta\neq 2$. The changes in wind density are as follows:

$$\dot{M}(r_{\rm in},t)=\begin{cases}\dot{M}^{\rm bsg} & \text{if } t\leq t_{\rm wr},\\ \dot{M}^{\rm wr} & \text{if } t_{\rm wr}<t,\end{cases} \tag{23}$$

with a sharp transition at $t_{\rm wr}$ (Brighenti & D'Ercole 1997). These relations imply that only the Wolf–Rayet wind is launched isotropically while the previous winds are affected by the isotropy function $f(\theta)$.

Our MHD set-up requires additional, similar prescriptions for the other quantities necessary to fully fix both the Parker spiral and the passive tracers tracking the mixing of material into the gas nebula. We introduce, in the same fashion as done for the hydrodynamical case of Brighenti & D'Ercole (1997), prescriptions for the toroidal and poloidal components of the stellar surface magnetic field. They read,

$$B_\star(r_{\rm in},t)=\begin{cases}B_\star^{\rm bsg} & \text{if } t\leq t_{\rm wr}-\Delta t,\\ B_\star^{\rm bsg}+\Delta B_\star F & \text{if } t_{\rm wr}-\Delta t<t \text{ and } t\leq t_{\rm wr},\\ B_\star^{\rm wr} & \text{if } t_{\rm wr}<t,\end{cases} \tag{24}$$

with $\Delta B_\star=|B_\star^{\rm wr}-B_\star^{\rm bsg}|$. Equivalently, the stellar radius evolves as,

$$R_\star(r_{\rm in},t)=\begin{cases}R_\star^{\rm bsg} & \text{if } t\leq t_{\rm wr}-\Delta t,\\ \Delta R_\star(1-F)+R_\star^{\rm wr} & \text{if } t_{\rm wr}-\Delta t<t \text{ and} t\leq t_{\rm wr},\\ R_\star^{\rm wr} & \text{if } t_{\rm wr}<t,\end{cases} \tag{25}$$

with $\Delta R_\star=|R_\star^{\rm bsg}-R_\star^{\rm wr}|$. Finally, the time-dependent evolution of the equatorial angular velocity reads,

$$v_{\rm rot}(r_{\rm in},t)=\begin{cases}v_{\rm rot}^{\rm bsg} & \text{if } t\leq t_{\rm wr}-\Delta t,\\ \Delta v_{\rm rot}(1-F)+v_{\rm rot}^{\rm wr} & \text{if } t_{\rm wr}-\Delta t<t \text{ and } t\leq t_{\rm wr},\\ v_{\rm rot}^{\rm wr} & \text{if } t_{\rm wr}<t,\end{cases} \tag{26}$$

with $\Delta v_{\rm rot}=|v_{\rm rot}^{\rm bsg}-v_{\rm rot}^{\rm wr}|$. Last, the evolution of the passive scalar tracer at the stellar wind boundary obeys the relation

$$Q(r_{\rm in},t)=\begin{cases}0 & \text{if } t\leq t_{\rm wr}-\Delta t,\\ F & \text{if } t_{\rm wr}-\Delta t<t \text{ and } t\leq t_{\rm wr},\\ 1 & \text{if } t_{\rm wr}<t,\end{cases} \tag{27}$$

which permits to separate the cold, dusty, blue supergiant gas ($Q\leq 1/2$) from the Wolf–Rayet material ($Q>1/2$).

Table 1. Stellar surface parameters used in our two-wind models.

Quantities	Symbol	Supergiant	Wolf–Rayet
Accretion rate	$\dot{M}$ ($\mathrm{M_\odot\,yr^{-1}}$)	10^{-6}	$10^{-4.3}$
Wind velocity	$v_{\rm w}$ ($\mathrm{km\,s^{-1}}$)	500	1900
Angular velocity	$v_{\rm rot}$ ($\mathrm{km\,s^{-1}}$)	60	10
Surface field	$B_\star$ (G)	1	100
Stellar radius	$R_\star$ ($\mathrm{R_\odot}$)	20	2.3

2.4 Simulation models

The simulations are initialized with stellar wind properties corresponding to a blue supergiant star. We let the system evolved to a few 10^4 yr up to a time $t_{\rm wr}-\Delta t$. This time interval corresponds to the typical time-scale of a luminous blue variable phase (Smith 2017) and it permits to have potential magneto-hydrodynamical boundary effects provoked by the onset of stellar rotation at $t=0$ to be transported out of the computational domain under the effects of the constant wind inflow. The blue supergiant stellar properties are as follows. We use $\dot{M}^{\rm bsg}=10^{-6}\,\mathrm{M_\odot\,yr^{-1}}$, which is of the order of magnitude of that of Sher 25 (Smartt et al. 2002), $v_{\rm w}^{\rm bsg}=500\,\mathrm{km\,s^{-1}}$, that is consistent with the values for HD 168625 ($350\pm 100\,\mathrm{km\,s^{-1}}$; Mahy et al. 2016) and for $Sk-69^\circ 279$ ($800\pm 100\,\mathrm{km\,s^{-1}}$; Gvaramadze et al. 2018). The stellar radius is $R_\star^{\rm bsg}=20\,\mathrm{R_\odot}$, which is that of $Sk-69^\circ 279$ ($800\pm 100\,\mathrm{km\,s^{-1}}$; Gvaramadze et al. 2018), and $v_{\rm rot}^{\rm bsg}=60\,\mathrm{km\,s^{-1}}$ (Mahy et al. 2016). The surface magnetic field of the blue supergiant ancestor star is taken to be $B_\star^{\rm bsg}=1\,\mathrm{G}$, which is of the order of the magnetic fields observed in other cool stars (Vlemmings, Diamond & van Langevelde 2002; Vlemmings, van Langevelde & Diamond 2005; Kervella et al. 2018)

The toroidal component of the stellar magnetic field is scaled with the value for the solar wind measured at 1 au (Herbst et al. 2020; Scherer et al. 2020). The Wolf–Rayet stellar properties are as follows. We use $\dot{M}^{\rm wr}=10^{-4.3}\,\mathrm{M_\odot\,yr^{-1}}$, $v_{\rm w}^{\rm wr}=1900\,\mathrm{km\,s^{-1}}$, $R_\star^{\rm wr}=2.3\,\mathrm{R_\odot}$, and $v_{\rm rot}^{\rm wr}=10\,\mathrm{km\,s^{-1}}$, respectively. These quantities are the values of the Wolf–Rayet star WR1 (WN4). Our stellar parameters are summarized in Table 1. The stellar surface magnetic field is rather unconstrained, and we decided to take $B_\star^{\rm wr}=100\,\mathrm{G}$. Similarly, we assume that the toroidal component of the magnetic field scales with the magnetic field in the solar wind (Herbst et al. 2020; Scherer et al. 2020).

In this work, we use our toy model to explore the effects of the progenitor stellar wind and phase transition properties on the shaping of the Wolf–Rayet nebulae. The simulation models are summarized in Table 2.

2.5 Radiative transfer calculations

As most circumstellar nebulae around evolved massive stars have been observed in the (near)-infrared waveband, we consequently desire, in order to discuss our models in the context of real data, to know how our simulated objects would look like if observed at that particular waveband. We perform radiative transfer calculations of our MHD simulation outputs against dust opacity using the RADMC-3D code (Dullemond 2012). Dust density fields are constructed by assuming a standard gas-to-dust ratio of 1/200 and it is imported into RADMC-3D. The dust temperature is simulated by Monte Carlo calculation using the algorithm of Bjorkman & Wood (2001) and photon packages are ray-traced from the stellar atmosphere to the stellar wind nebulae. The 24 μm near-infrared emissivity is estimated using the Silicates dust opacity of Laor & Draine (1993) and it is projected on to the plane of the sky according to a particular selected

Table 2. List of models in our study. The table informs on the simulation labels, whether the blue supergiant wind is symmetric or not, the blue supergiant to Wolf–Rayet phase transition time-scale Δt (in yr), and the exponent β controlling the variations of the different quantities during the phase transition, the flattening degree of the blue supergiant wind towards the equator p, and the equator-to-pole density ratio ξ, respectively. The last column gives the general purpose of each simulation models.

Model	Asymmetric wind	Δt (yr)	β	p	ξ	Purpose
Run-Base	Yes	0	4	1/4	20	Baseline model
Run-Sym	No	0	–	–	–	Model with isotropic progenitor wind
Run-Δt 10 kyr	Yes	10^4	4	1/4	20	Model with Δt10kyr phase transition
Run-ξ20	Yes	10^4	4	1/4	20	Model with phase transition and lower pole-to-equator density contrast
Run-ξ100	Yes	10^4	4	3/4	100	Model with phase transition and higher pole-to-equator density contrast
Run-β4	Yes	5×10^4	4	1/4	20	Model with quadratic interpolation between winds during the phase transition
Run-β2	Yes	5×10^4	4	1/4	20	Model with linear interpolation between winds during the phase transition

viewing angle. The irradiating central massive star is assumed to be a spherical blackbody radiator of effective temperature $T_{\rm eff}$ that is taken as

$$T_{\rm eff}(t) = \begin{cases} T_{\rm eff}^{\rm bsg} & \text{if } t \leq t_{\rm wr} - \Delta t, \\ \Delta T_{\rm eff}(1-F) + T_{\rm eff}^{\rm wr} & \text{if } t_{\rm wr} - \Delta t < t \text{ and } t \leq t_{\rm wr}, \\ T_{\rm eff}^{\rm wr} & \text{if } t_{\rm wr} < t, \end{cases} \tag{28}$$

where $\Delta T_{\rm eff} = |T_{\rm eff}^{\rm wr} - T_{\rm eff}^{\rm bsg}|$. The stellar radius $R_\star(t)$ is determined from equation (25). The hot, Wolf–Rayet material is distinguished from the cold blue supergiant gas using the passive scalar tracer of equation (27). We produce emission maps for a distance to the stellar source of 1 kpc, that is typical for massive star-forming regions.

3 RESULTS

This section presents the results from the modelling of Wolf–Rayet gas nebulae of blue supergiant ancestors. We compare the effects of the asymmetries and evolutionary phases of various pre-Wolf–Rayet stellar winds on the geometry of the gas nebulae.

3.1 Wolf–Rayet nebulae of asymmetric versus spherical blue supergiant wind

In Fig. 1, we plot the number density field in our baseline simulation Run-Base (left-hand column of panels) and our model Run-Sym (right-hand column of panels), which assume asymmetric and isotropic blue supergiant progenitor stellar winds, respectively. The dashed green contour is the tangential discontinuity, where blue supergiant and Wolf–Rayet stellar winds are in equal proportions ($Q = 0.5$). Solid black and dashed–dotted red contours trace v_ϕ and B_ϕ, respectively, and the white cross marks the position of the star. The model Run-Sym obviously generates a spherical nebula (Figs 1d and f) by fast-wind–slow-wind collision, as modelled in the work of Meyer et al. (2020a). In model Run-Base, the asymmetric blue wind is expelled as a torus of outflowing material, see the studies of Raga et al. (2008) and Fang et al. (2017), respectively, on to which stellar rotation and a Parker wind is superposed (Fig. 1a). Both models have no phase transition, therefore, the Wolf–Rayet stellar wind directly interacts with the luminous blue supergiant stellar wind. The initial spherically symmetric stellar wind of Run-Base is channelled by its surroundings and adopts a bipolar morphology (Figs 1c and e). One clearly sees magnetic dipoles in both the old slow and new fast winds, whose field lines are compressed in the shell region. Given the size of the nebula ($\leq$10 pc), the asymmetric nebulae can develop inside of the region bordered by the termination shock of the main-sequence stellar wind bubble (Meyer et al. 2020a). These rings should therefore form even in the context of the supersonic bulk motion of the driving blue supergiant star (Figs 1b, d, and f). This mechanism is therefore the MHD equivalent of the young aspherical Wolf–Rayet nebulae of red supergiant stars of Brighenti & D'Ercole (1997), this time in the context of a blue supergiant ancestor.

Fig. 2 shows cross-sections taken through the number density field of the Wolf–Rayet nebulae. The figure plots the cross-sections, taken at intervals of 0.1 kyr through several characteristic simulation snapshots of the blue supergiant to Wolf–Rayet phase transition event. The left-hand part of each panel corresponds to the polar direction, whereas the right-hand part of the panels corresponds to the equatorial plane of the nebulae. The spherical nebula in Run-Sym (Fig. 2b) is obviously similar along both the polar and equatorial directions. The shell of swept-up blue wind grows under the effect of the expelled Wolf–Rayet momentum and the contrast in density along both direction decreases, i.e. the post-shock density of the Wolf–Rayet nebulae diminishes with time and so does the corresponding emission (see Section 4.2). At time 40.1 kyr, the cross-sections of the asymmetric model Run-Base exhibit clear differences between the polar and equatorial directions (Fig. 2a), as a result of the wind asymmetry. When the Wolf–Rayet material begins to blow, the shell of swept-up supergiant gas is denser in the equatorial plane than in the direction perpendicular to the equator, see thick blue and thin lines of Fig. 2(a). This latitude-dependent density contrast is at the origin of the asymmetric character of some observed Wolf–Rayet nebulae.

3.2 Effects of the phase transition time-scale

Fig. 3 compares the density fields in our simulation models Run-Base (left-hand panels) and Run-Δt10kyr (right-hand panels), which differ by the blue supergiant to Wolf–Rayet phase transition interval. Such transition period is non-existent in model Run-Base while it is $\Delta t = 0.1$ kyr in model Run-Δt10kyr. Our phase transition time-scale is in accordance with both the typical duration of luminous blue phases $\sim 10^4$ yr and with the time-scale of blue-to-red phase transition (Mackey et al. 2012; Groh et al. 2014). The Wolf–Rayet nebula in Run-Base is generated by the simultaneous changes of the wind velocity and density, engendering a peanut-like morphology, which shocked layer accumulates compressed magnetic field lines, as described in Section 3.1. In Run-Δt10kyr, the stellar wind velocity increases first, provoking a more elongated jet-like nebula; before that the sudden changes in wind density fill it with denser, isotropic Wolf–Rayet material (see equations 21–23). In the latter case, Rayleigh–Taylor instabilities form in the equatorial plane, as a consequence of the wind–wind collision at work therein, see the discussion

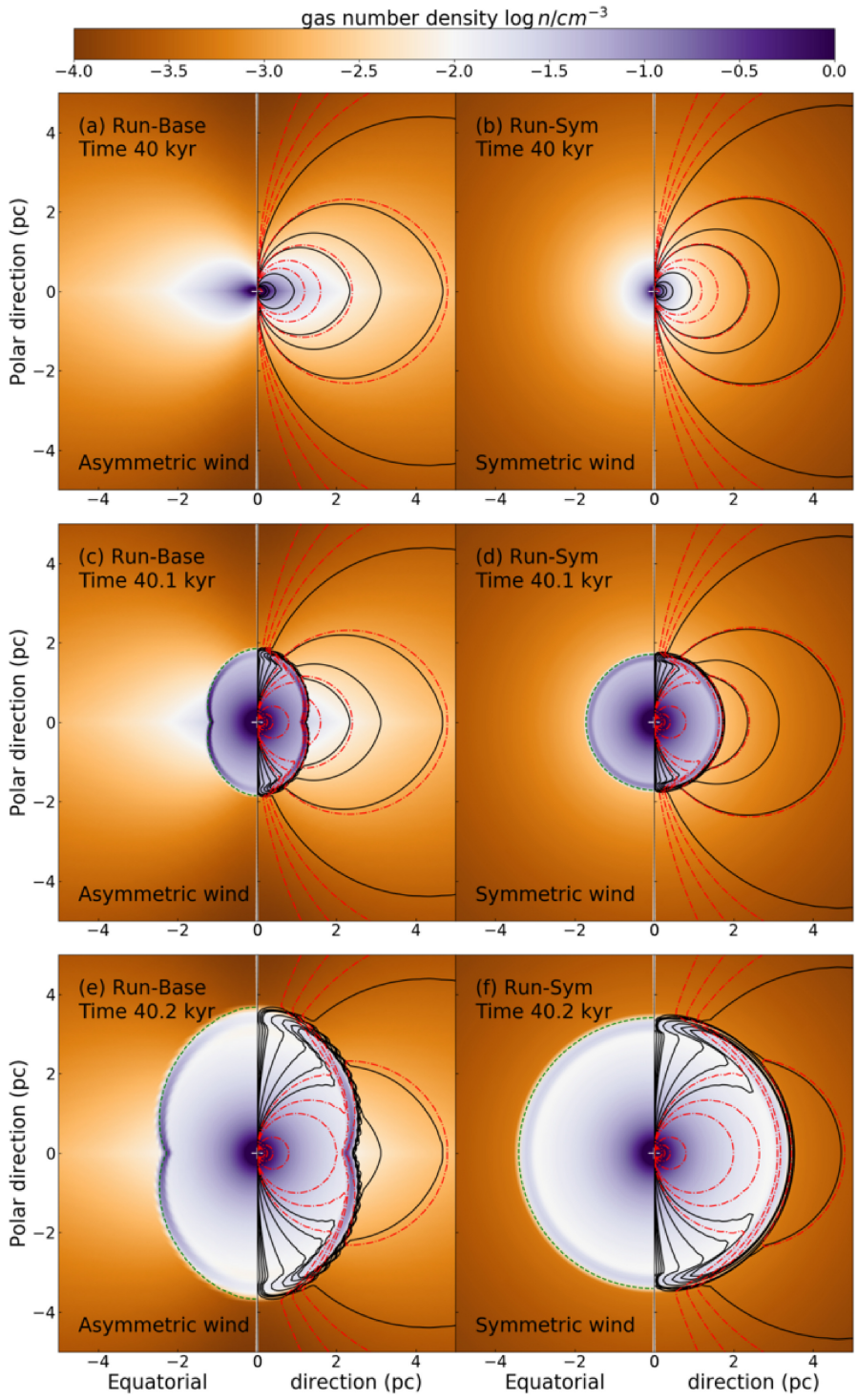

Figure 1. Number density field in our simulation models Run-Base (a) and Run-Sym (b). The dashed green contour is the tangential discontinuity of the Wolf–Rayet nebula, i.e. the location of the nebula made of equal proportion of blue supergiant and Wolf–Rayet stellar winds, where the passive scalar $Q = 0.5$. The solid black and dashed–dotted red contours on the right-hand part of each panels represent isovalues of the toroidal component of the velocity v_ϕ and magnetic field B_ϕ, respectively. The white cross marks the position of the star.

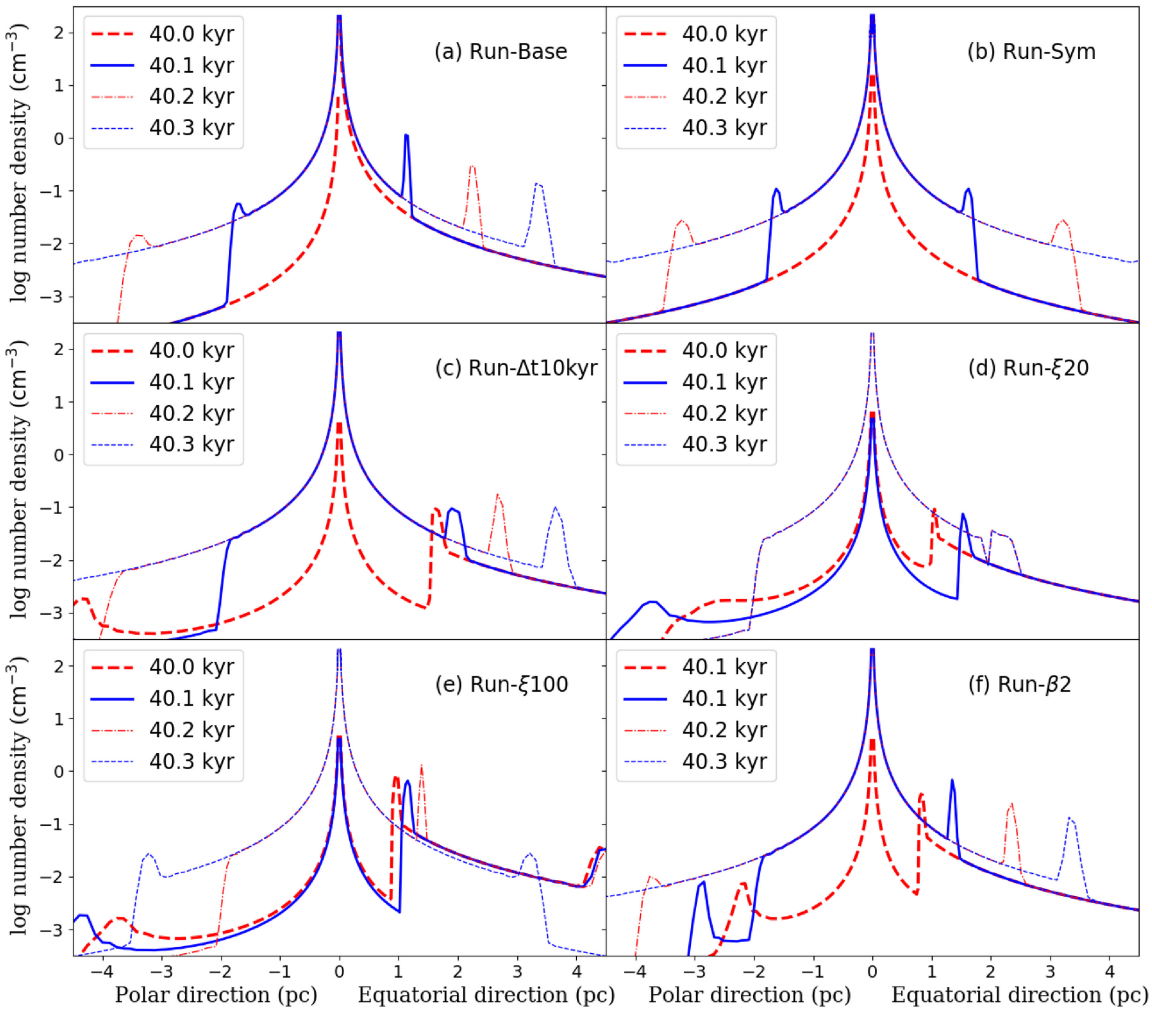

Figure 2. Cross-sections in the density field and toroidal magnetic field of the evolving Wolf–Rayet nebula. The panels correspond to different simulations, and in each panel the cross-section are plotted for both directions along the polar (left) and equatorial (right) directions of the domain.

in Brighenti & D'Ercole (1997). This comparison shows that the properties of the time windows during which the wind properties evolve have a little influence on the overall appearance of Wolf–Rayet nebulae. Our simplistic set-up uses analytic prescriptions that mimic the evolution of the central massive star; hence, the detailed shape of the nebula might be slightly different with more realistic, time-dependent stellar wind prescriptions, e.g. using pre-computed evolutionary tracks (Brott et al. 2011).

In model Run-Δt10kyr, the accelerating stellar wind has already interacted with the dense equatorial blue supergiant wind, resulting in a bipolar shell (Figs 3a and b) that is later filled by the Wolf–Rayet wind. The wind–wind interaction is stronger for a reduced phase transition interval Δt (Figs 3a and c), while the density of the shocked material in Run-Δt10kyr is reduced, as a consequence of the diminished wind momentum at the moment just before the sudden changes in mass-loss rate at $t_{\rm wr}$. Nevertheless, in both models, the Wolf–Rayet wind eventually melts with the shell of swept-up blue supergiant material, and comparable equatorial densities are reached (Fig. 3a) as it expands outwards (Fig. 3c). Finally, once the hot gas filled the bipolar cavity, both nebulae have similar overall dimensions except at the poles, where the magnetic field lines are collimated (Fig. 3d). This further illustrates that the morphology of older asymmetric Wolf–Rayet nebulae is governed by the surface characteristics and stellar wind properties, such as terminal velocity and mass-loss rate of the ancestor stars, as well as the manner in which the evolutionary phase transition happens, but not by the ambient medium properties.

3.3 Effects of the blue supergiant stellar wind asymmetries

Fig. 4 compares two simulation models, Run-ξ20 and Run-ξ100, both with the same phase transition time-scale $\Delta t = 10$ kyr, but different density flattening degrees towards the equator p and density equator-to-pole ratios ξ, namely, $p = 1/4$ and $\xi = 20$ (Run-ξ20) and $p = 3/4$ and $\xi = 100$ (Run-ξ100), respectively. The different pre-Wolf–Rayet morphologies of the circumstellar medium profoundly impact the development of the shell generated by wind–wind interaction between blue supergiant to the Wolf–Rayet winds. The denser the material in the equator, the more

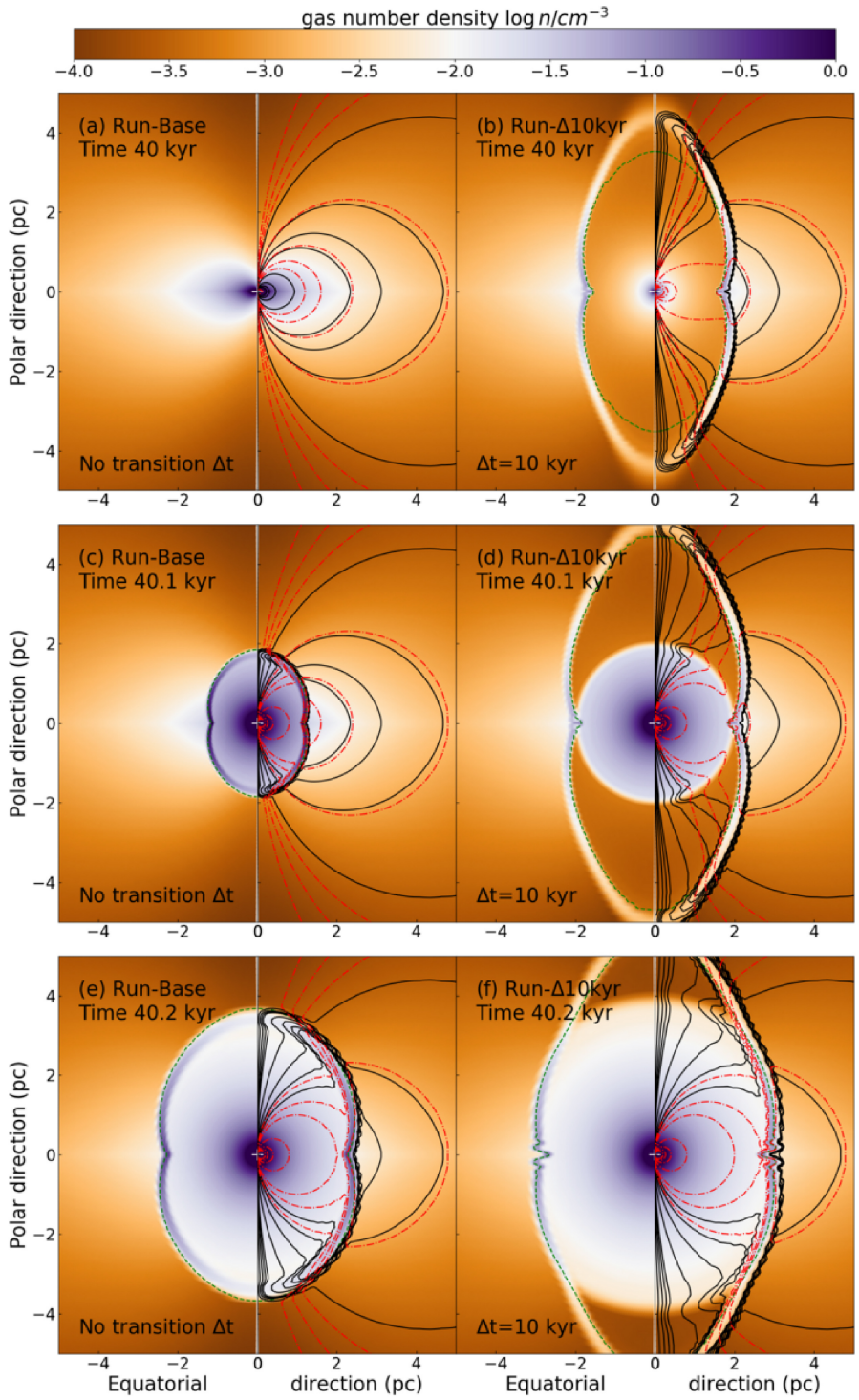

Figure 3. Same as Fig. 1 with our models Run-Base and Run-Δt10kyr, exploring the effect of a phase transition time-scale $\Delta t \neq 0$.

collimated the Wolf–Rayet stellar wind (Fig. 4b), as a result of the thicker disc-like blue supergiant distribution (Fig. 4a). On the other hand, the simulation with a thinner equatorial plane produces a peanut-like nebula, recalling the mechanisms for the shaping of the homunculus of η-Carina (Langer, García-Segura & Mac Low 1999; González et al. 2004; Hirai et al. 2021). Note the gradual opening of the magnetic field lines as the wind speed accelerates (Figs 3a, c, e and b, d, f). Again, this is mostly shaped by the

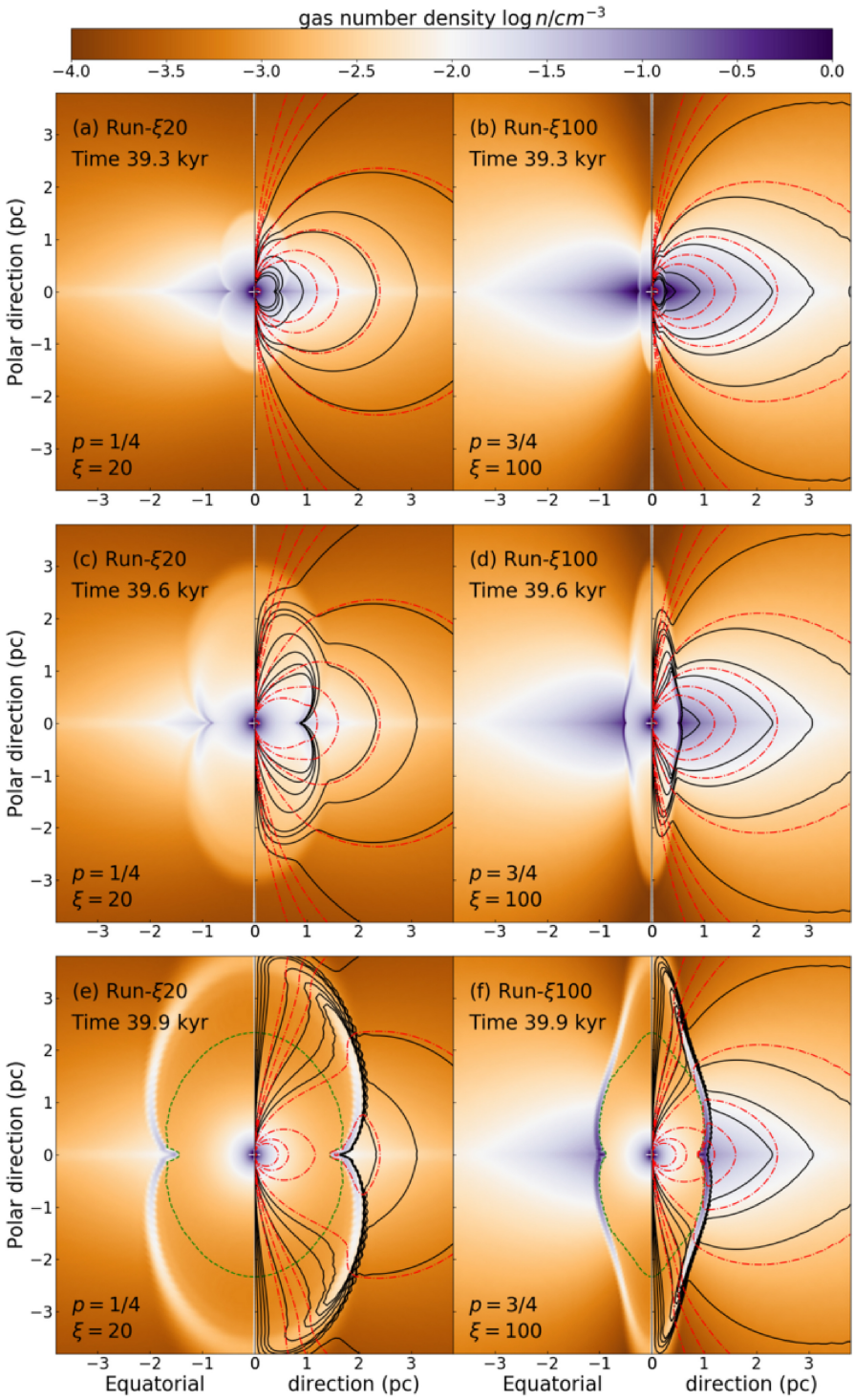

Figure 4. Same as Fig. 1 with our models Run-ξ20 and Run-ξ100, exploring the effect of the flattening degree p and density ratio ξ of the progenitor wind.

blue supergiant wind whose velocity gradually increases during the phase transition up to reaching the fast values of the Wolf–Rayet star (black dotted line in Figs 4c and d). The discrepancy between peanut-like and jet-like Wolf–Rayet nebulae persists at later times, when the stellar phase transition keeps going (Figs 4e and f).

As soon the Wolf–Rayet stellar wind interacts with the walls of the nebula, the wind–wind interface becomes naturally much

denser in the model with $\xi = 100$ than in the case with $\xi = 20$ (Figs 4c and d). This reflects in the cross-sections taken through the density fields of the simulations (Figs 4d and e). Indeed, the model with $\xi = 20$ produces a larger shell in the equatorial plane, whereas that with $\xi = 100$ is more compact, thinner and also much denser. The density jump at the expanding front is larger at time 40.1 kyr in our model Run-ξ100, than in our simulation Run-p1/2 and it stalls at $\approx$1 pc from the star, whereas the other nebula in Run-p1/2 is more enlarged in the equatorial plane. The flattening degree of the density towards the equator and the equator-to-pole density ratio turns to be a major parameter in the shaping of Wolf–Rayet nebulae, as it controls their final aspect ratio and therefore their overall morphology. Within the explored parameter space, we therefore produce either peanut-like or jet-like shapes.

3.4 Effects of phase transition properties

Our last series of comparison tests consist in changing the interpolation between the blue supergiant and Wolf–Rayet stellar surface properties during the phase transition. It is governed by the exponent parameter β in equation (22), set to $\beta = 2$ in our model Run-β2 (linear interpolation) and to $\beta = 4$ in our Run-β4 (squared polynomial interpolation). The transition phase time-scale is set to $\Delta t = 5$ kyr. In Figs 5 (a) and (b), the pre-shaped circumstellar medium in which the Wolf–Rayet star blows its material is similar, and how the blue supergiant stellar wind gradually adopts a faster speed is the only effect responsible for differences in the nebula's morphologies. This keeps on going for another 0.1 kyr, until the tangential discontinuity between the two colliding winds reaches the cavity. Nevertheless, when the full Wolf–Rayet wind blows through and fully fills the cavity, morphological differences are rather small (Figs 5e and f). The field lines are opened under the effect of the faster equatorial rotation of the Wolf–Rayet star. Instabilities developing in the equatorial plane, as in model Run-Δt10kyr, appear in both runs, despite of the different, longer phase transition. The apex of the polar lobes remains the only trace of the different stellar evolution history of the final Wolf–Rayet stars.

3.5 Magnetic properties of the Wolf–Rayet nebulae

In Fig. 6(a), we plot a time evolution series of cross-sections taken through the number density field (top panel) in our simulation model assuming an aspherical blue supergiant stellar wind (Run-Base). The selected times correspond to the moment the Wolf–Rayet wind begins blowing into the blue supergiant material. Fig. 6(b) displays cross-sections taken at the same time instances and location, through the toroidal density field B_ϕ (in μG) and plotted in the logarithmic scale. One sees that the magnetic field in the Wolf–Rayet nebula, governed by its toroidal component is maximum in the region of the expanding shell. The compression factor of the magnetic stellar wind field reflects that of the expanding shell density (Figs 6a and b), and, inversely, the toroidal field B_ϕ is weaker along the polar direction. Fig. 6(c) (bottom panels) plots the Alfénic Mach number in the circumstellar nebula. The gas is super-Alfénic everywhere, with lower values $M_{\rm A} \sim 1.5$ in the region of the equatorial plane, in the compressed shell, and it peaks at $M_{\rm A} \approx 4$ along the polar direction.

In Fig. 7, we display scatter plots for the distribution of gas in the computational domain, representing the number density (in cm^{-3}) of the wind as a function of its velocity (in km s^{-1}), coloured by the value of the toroidal magnetic field B_ϕ (in μG). The different panels of the figure correspond to several time instances of the simulations, from the younger (top panels) to the older times (bottom panels), and each column represents a simulation model. The constant, isotropically freely streaming stellar wind of the blue supergiant progenitor is represented by an horizontal line of decreasing toroidal magnetic field from the high to the lower densities (Figs 7a and b). When the star evolves to the Wolf–Rayet phase, the horizontal line is split into two horizontal lines of different velocities, a fast velocity, high-density one (the Wolf–Rayet component), and a slow, low-density one (the blue component), see Fig. 7(c). The model Run-Base with anisotropic stellar wind vertically spreads the horizontal line of Fig. 7(a) as a broadened band, whose height is a function of the degree of flattening of the wind and of the equator-to-pole density ratio, see Figs 7(d) and (e). The phase transition, with spherical Wolf–Rayet wind blown into an asymmetric blue supergiant wind, shifts the high-density part of the bar-like distribution to a higher velocity, higher number density horizontal line (Fig. 7f). The region between the two winds exhibits variations of the toroidal magnetic field from the density compression during the wind–wind interaction, which results in more scattering of the data in the velocity–density plane (Fig. 7f).

The model with both anisotropic pre-Wolf–Rayet stellar wind and long phase transition time-scale, Run-Δt10kyr, exhibits a distribution in the ρ-v diagram both reporting the initial freely expanding, high-density stellar wind as a high-density horizontal bar, plus a low-density region broadened in velocity, as a result of the blue supergiant asymmetries, already at work at that time (Fig. 7g). At later times, the transition region greatly affects the gas properties in the equatorial plane and this results in a larger toroidal magnetic field (Figs 7h and i). At even later times, the development of instabilities at the wind–wind interface in the equatorial plane strongly disperses the high-velocity gas in the ρ-v diagram (Fig. 7i). Similarly, the simulation with Run-ξ100 exhibits a more important scattering of the magnetized blue supergiant and expanding Wolf–Rayet stellar winds. The velocity broadening is strong, as a result of the large equator-to-pole density ratio ξ. The jet-like nebula has a dispersion of the material therein that contains highly magnetized, swept-up, slow diluted blue supergiant stellar wind in the equatorial plane (Figs 7k and l). The different velocity distributions in peanut-like ($\xi = 20$) and jet-like ($\xi = 100$) Wolf–Rayet nebulae clearly appear as a consequence of the aspect ratio of the wind bubble, see Figs 7(i) and (l).

Fig. 8 shows our models Run-β4 and Run-β2, respectively, which differ by the manner the various quantities of the stellar wind are interpolated during the phase transition. At time 40 kyr both nebulae have already grown when the new-born Wolf–Rayet wind is blown into the accelerated blue supergiant wind, as testifies the S-shape in the density–velocity plane. The distribution of the gas therein presents both the broadened low-velocity component from an equatorially asymmetric blue supergiant stellar wind and the horizontally distributed component of a rapid Wolf–Rayet wind. Both distributions with changing β are qualitatively similar (Figs 8a and b), while differences at the transition between the two components appear, as the wind–wind interaction region at the equatorial plane is not the same. The model with nonlinear interpolation ($\beta = 4$) reveals compressed gas with a stronger magnetization B_ϕ. The phase transition continues modifying the curved, S-shaped region of scattered dots between the two components of the ancestor and evolved stellar winds. Such curvature is more pronounced in the case

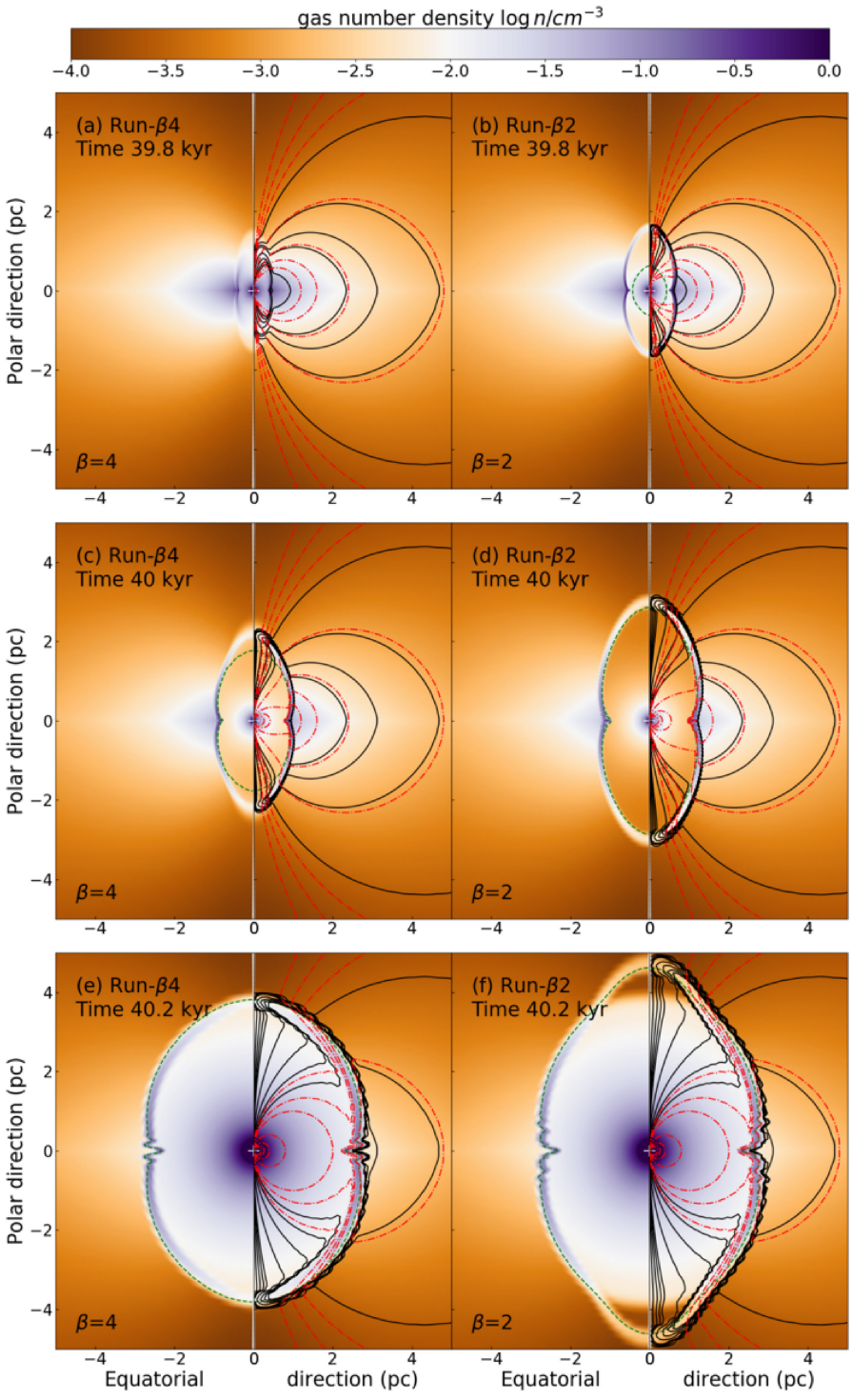

Figure 5. Same as Fig. 1 with our models Run-β4 and Run-β2, exploring the effects of the interpolation exponent β during the phase transition.

with $\beta = 4$ because the wind momentum increases faster with the polynomial interpolation than in the linear case with $\beta = 2$, which results in an accumulation of dense, magnetized and fast material in the equatorial plane (Figs 8c and d). The high-velocity component turns into a thin horizontal line once the Wolf–Rayet wind is fully established. The instabilities developing in those peanut-like Wolf–Rayet nebulae are responsible for the scattering of points in the high-density, high-velocity parts of the diagram.

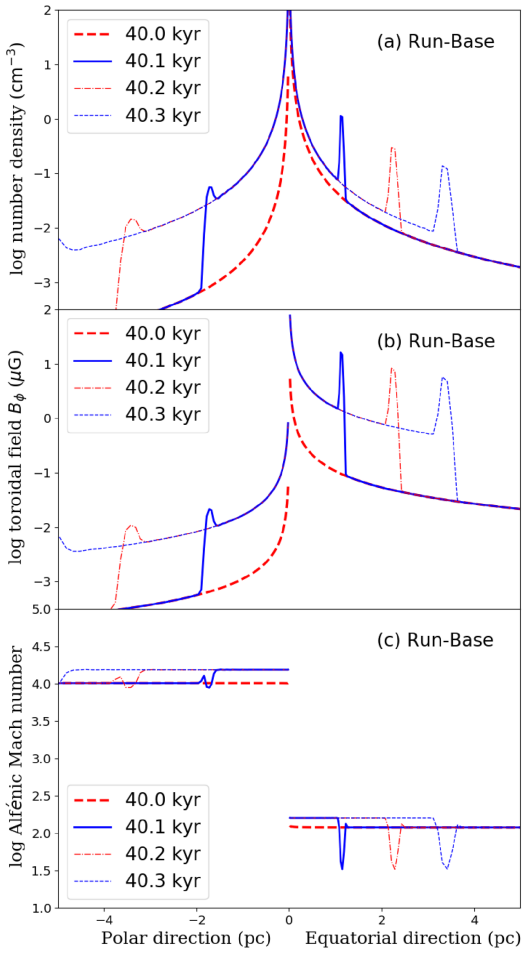

Figure 6. Cross-sections in the density field (top panel), toroidal magnetic field (middle panel), and Alfénic Mach number (bottom panel) of the evolving Wolf–Rayet nebula in our simulation Run-Base. In each panel, the cross-sections are plotted for both the polar (left) and the equatorial (right) directions of the computational domain.

4 DISCUSSION

This section discusses the caveats of our method and compares our study to results in precedent works. We also discuss the infrared emission properties of the young Wolf–Rayet wind nebulae, and, finally, we compare our results with observations.

4.1 Model limitations

The very first caveat of our simulations is their 2.5-dimensional nature, as our method naturally imposes axisymmetry to the Wolf–Rayet nebulae (Heiligman 1980; García-Segura et al. 1999). While this is acceptable in our pilot study, performing full 3D MHD models better resolving the detailed formation of, e.g. instabilities during the wind–wind interaction mechanisms (Brighenti & D'Ercole 1997; Meyer et al. 2020a) should be considered in the future. Secondly, we neglected several microphysical processes, such as radiation transport in the close surroundings of the massive star. The high temperatures of the Wolf–Rayet star ($\sim 10^5$ K) must affect the local thermodynamical properties and the energy budget of the stellar wind, and, as radiation pressure is at work therein, this should change the gas dynamics (Moens et al. 2021). Any chemical and/or non-ideal MHD mechanisms are also totally neglected in our simulations. Their consideration, much beyond the scope of our simplistic work, will be treated in follow-up studies. Last, our study, which continues the work of Brighenti & D'Ercole (1997), utilizes analytic prescriptions for the evolution of the stellar wind properties. It has the advantage to directly use stellar properties derived from e.g. observations of blue supergiant stars (Smartt et al. 2002; Mahy et al. 2016; Smith 2017; Gvaramadze et al. 2018), however, at the cost of the introduction of free parameters such as the time-scale Δt of the corresponding phase transition. This can be circumvented by using self-consistently calculated theoretical stellar evolution models (Brott et al. 2011; Szécsi et al. 2020).

4.2 Infrared emission maps

In Fig. 9, we display 24 µm emission maps calculated on the basis of our Wolf–Rayet nebula model Run-Base, using the RADMC-3D code. The surface brightness is plotted in the linear scale in erg cm^2 s^{-1} arcsec^{-2} for several viewing angles and the images are calculated excluding the hot dust-free Wolf–Rayet gas, see Meyer et al. (2020a). On each panel, the central white cross marks the position of the star. The first column of panels displays the time-dependent edge-view evolution of the close circumstellar medium of the massive stars. Before the evolution of the blue supergiant star, the asymmetric wind generates a bright oblate disc-like shape extending in the equatorial plane of the star (Fig. 9a). This model does not have a long phase transition interval Δt, and the hot Wolf–Rayet wind directly interacts with the dense equatorial colder gas. This interaction region emits in the mid-infrared, which produces the bipolar morphology (Fig. 9d). As the phase transition ends, the nebula further extends and become fainter at the poles, while conserving its overall bipolar bubbly shape. The second column of panels plots the same sequence of images considered with an inclination angle $\theta = 45^\circ$ with respect to the plane of the sky. The situation is qualitatively the same as for $\theta = 0^\circ$, except that the bright infrared equatorial ring appears as an ellipse (Figs 9e and h). The last column of panels displays top-viewed nebulae, which, as a consequence of the 2.5D nature of the simulations, look like rings extending away from the evolving central star (Figs 9f and i). The maximum emission region is the interaction layer where the Wolf–Rayet wind reaches the termination shock of the blue supergiant nebula (Figs 9d–f).

Fig. 10 is as Fig. 9 for the other simulations models listed in Table. 1. The left-hand column of panels shows the nebula when the wind–wind collision begins, while the right-hand column of panels shows the circumstellar nebula around the Wolf–Rayet stars at a later time. Both series of images are displayed with a viewing angle of $\theta = 45^\circ$ with respect to the plane of sky. The model Run-Δt10kyr has a phase transition $\Delta t = 10$ kyr extending the time interval during which the Wolf–Rayet wind merges with the previous blue supergiant material. This results in a denser region of wind–wind interaction and a brighter bipolar nebula (Fig. 10a) materialized as an ellipsoid in the projected equatorial plane (Fig. 10b). Our model Run-ξ20 has a different density flattening degree towards the equator. It emphasizes the bipolar aspect of the nebula, which is less bubbly and more elongated (Figs 10c and d). Our model Run-ξ100 with a larger equator-to-pole density ratio $\xi = 100$ generates a tubular nebula as during the phase transition the wind material is channelled into the direction perpendicular to the equator, resulting in a less compressed and 24 µm-fainter expanding shell. The model Run-β4

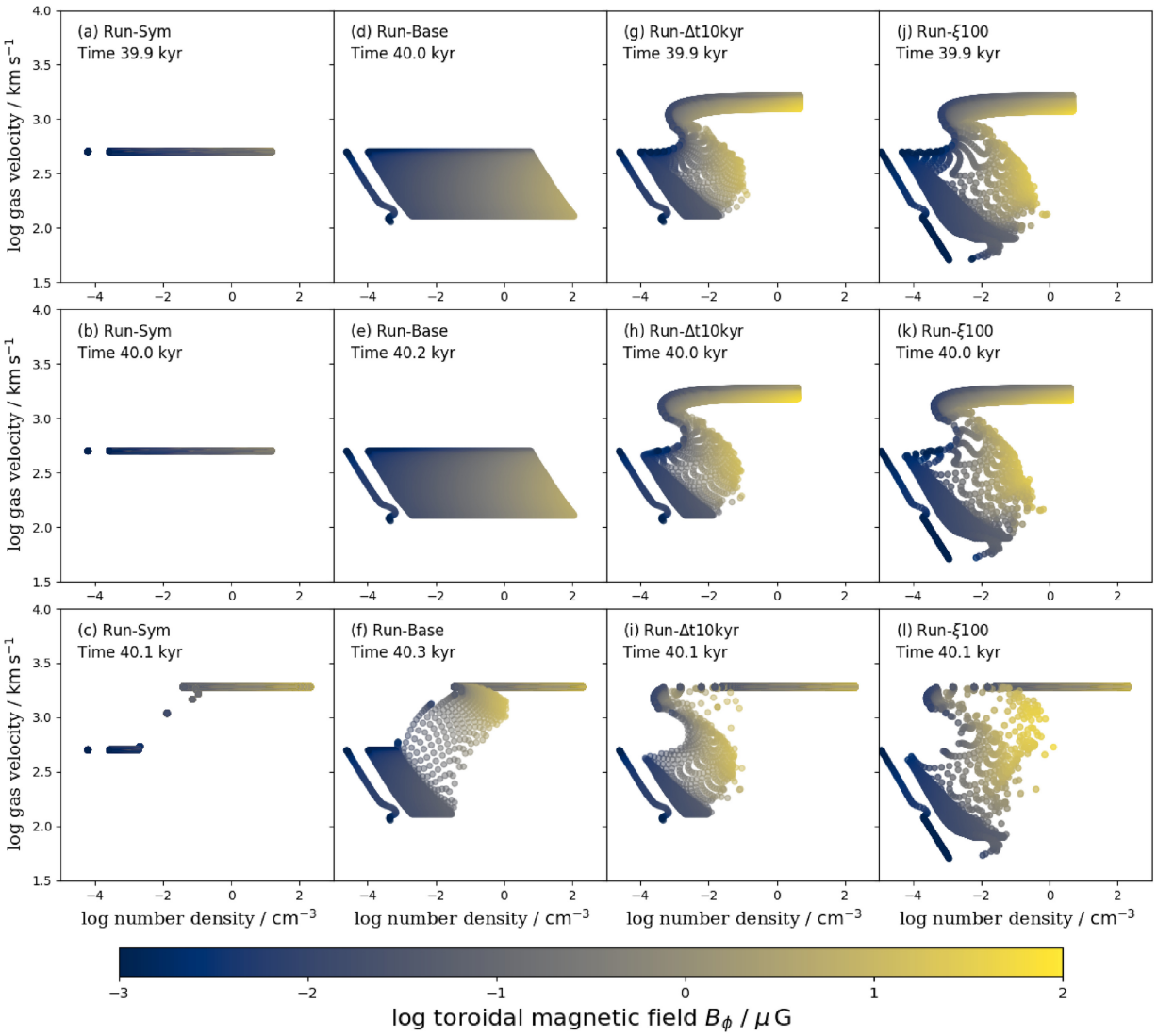

Figure 7. Correlation between the number density and the velocity of the gas in the inner 5 pc of the computational domain, for several simulations of the stellar wind nebulae generated during blue supergiant to Wolf–Rayet phase transitions, with colours representing the strength of the toroidal of the magnetic field B_ϕ.

with a nonlinear interpolation of the stellar wind quantities during the phase transition produces a quicker and more violent wind–wind collision and a brighter interaction region (Figs 10g and h). Our model Run-β2 with a linear interpolation induces a more important compression of the shell of stellar wind, and also a more pronounced bipolar morphology (Figs 10i and j).

4.3 Comparison with observations

4.3.1 Generalities

The geometry of Wolf–Rayet nebulae is a long-standing problem and still rather unexplored mystery. All except one simulation performed to date predict their appearance to be both spherical and affected by hydrodynamical instabilities originating from the evolved Wolf–Rayet stellar wind, blown into the interior of its own main-sequence stellar wind bubble and interacting with the shell generated during its previous, e.g. red supergiant, evolutionary stage (Freyer et al. 2003, 2006; Toalá & Arthur 2011; Meyer, Petrov & Pohl 2020b). All these models assume a static massive star undergoing a succession of isotropically launched stellar winds. As discussed above, a cool, dense stellar wind launched along the equator of the star can make the Wolf–Rayet nebula strongly anisotropic, shaping the outflow as a bipolar structure. The physical origin of the equatorial stellar wind is so-far included as subgrid models in the few simulations run so far, see Brighenti & D'Ercole (1997). Our study is therefore the first work continuing that on asymmetric Wolf–Rayet nebulae of Brighenti & D'Ercole (1997).

The previous paper of our series explored the effects of the stellar bulk motion on the formation of Wolf–Rayet stars. Indeed, the fastest runaway massive stars of the Milky Way are strong-winded and bow-shock-free Wolf–Rayet stars carrying circular rings, which challenged our understanding of the formation of Wolf–Rayet nebulae (Meyer et al. 2020a). A typical example is

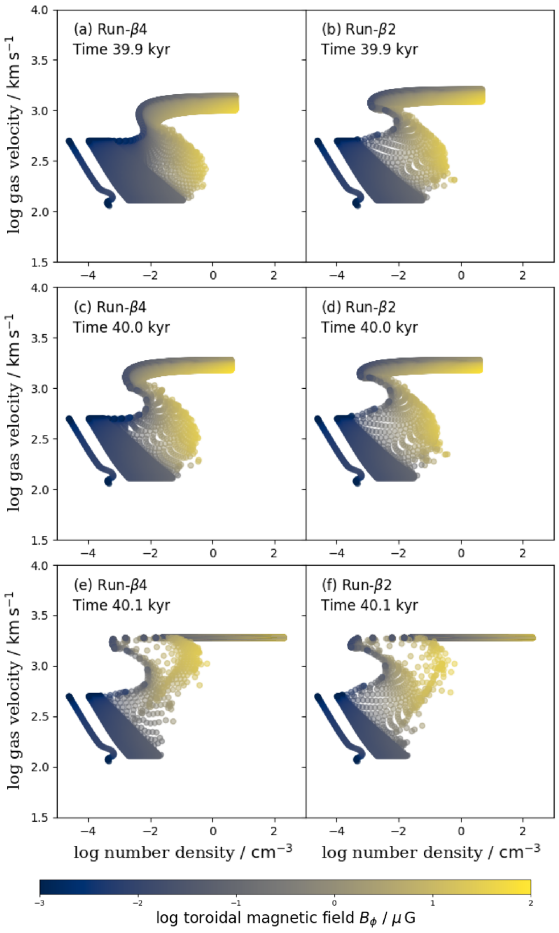

Figure 8. Same as Fig. 7 for our models Run-β4 and Run-β2.

the nebula M1-67 around the star WR124 (van der Sluys & Lamers 2003). The proposed simple solution for their formation scenario teaches us that the stellar motion of the driving star does not influence the growth of Wolf–Rayet nebulae, since the region of free-streaming between stellar surface and main-sequence wind bubble's termination shock is sufficiently extended. This is largely the case for high-latitude objects, as the diluted medium therein favours the production of huge and extended bow shocks, making room for wind–wind shell collision to happen without being affected by the ISM material. Importantly, the absence of observed ISM material in Wolf–Rayet nebulae (Fernández-Martín et al. 2012; Esteban et al. 2016) indicates that most Wolf–Rayet shells, including bipolar Wolf–Rayet nebulae, are probably produced this way, and, this further implies that the large-scale wind-blown bubble can be ignored when numerically modelling them.

However, the very complex shape of many observed Wolf–Rayet nebulae challenges this picture (Toalá et al. 2015). When exactly bipolarity happens and which factors are in control of this? Which progenitors are responsible for which kind of circumstellar nebulae? The well-studied bipolar Wolf–Rayet nebulae NGC 6888, of probable red supergiant ancestor, and RCW58, seemingly coming from a blue supergiant, are the ideal cases to test numerical models like ours against observations, see the discussion in Garcia-Segura, Mac Low & Langer (1996) and Garcia-Segura, Langer & Mac Low (1996). Bipolarity of single blue supergiant origin is the situation that we simulate in the present study, and it is in accordance with the interpretation of Garcia-Segura et al. (1996) in the context of RCW58. However, what can our result teach us regarding the other, red supergiant-based scenario?

4.3.2 What makes NGC 6888 asymmetric?

The gaseous nebula NGC 6888, also called the veil nebula, the crescent nebula, Caldwell 27, Sharpless 105, is an asymmetric wind bubble found around the evolved massive Wolf–Rayet WN66(h)-type star WR 136. Its particular shape is made of two bipolar lobes and of an equatorial ring of denser material. It has long been studied in great detail (Parker 1978; Treffers & Chu 1982; Garcia-Segura et al. 1996; Fernández-Martín et al. 2012; Mesa-Delgado et al. 2014; Toalá et al. 2014; Esteban et al. 2016; Rubio et al. 2020). Early observations of the surroundings of NGC 6888 revealed a variation of the level ionization, traced by the optical line ratios [N II]/Hα in the many clumps along the surface of the shell, witnessing an efficient mixing of materials preceding the formation of the Wolf–Rayet shell (Parker 1978; Fernández-Martín et al. 2012). The presence of dust and enriched elements around Wolf–Rayet nebulae indicate that (i) they result from wind–wind interaction of evolved material, (ii) one of the evolved winds is that of a cold, dust-producing, supergiant phase of stellar evolution, and (iii) the kind of detected dust tells us that the wind from a main-sequence star does not contribute to the shaping of the nebula. NGC 6888 has been the site of the first observation of the aftermath of the CNO cycle of nuclear reactions into the stellar core (Mesa-Delgado et al. 2014), and its progenitor star has been constrained to be a single, red-supergiant-evolving star of 25–40 $M_\odot$ (Stock & Barlow 2014; Mesa-Delgado et al. 2014). Hence, these Wolf–Rayet stars must probably have undergone a red supergiant evolutionary phase, and, such scenario has been modelled using 1D and 2D spherically symmetric hydrodynamical simulations in Garcia-Segura et al. (1996). However, if it is clear that WR136 has been a cold star prior to the Wolf–Rayet phase (Stock & Barlow 2014), the origins of the progenitor's asymmetries are still not understood.

Our results show that a non-eruptive single blue supergiant star cannot spin sufficiently fast to produce an asymmetric pre-Wolf–Rayet circumstellar medium (our Fig. 1). Since red supergiants and other late-type stars do not rotate fast (Kervella et al. 2018; Vlemmings et al. 2002, 2005), their shells cannot be greatly affected by rotational and/or magnetic effects either. Therefore, the question is how NGC 6888 can produce a bipolar Wolf–Rayet nebula with an equatorial ring, obviously witnessing the existence of an equatorial structure produced during a post-main-sequence evolutionary phase prior to the Wolf–Rayet phase? The most accepted picture, supported by CNO yields measured in the nebula, made of a main-sequence, red supergiant and Wolf–Rayet single star evolutionary channel, is therefore challenged by our results, as explanations for the polar asymmetries of the pre-Wolf–Rayet wind are still missing.

We speculate that a mechanism, similar to that revealed for asymptotic giant stars, see particularly Decin et al. (2020) and Decin (2020), in which multiplicity generates a latitude dependence of the stellar wind, should be at work in the context of red supergiant stars as well, and in particular to the central star(s) of NGC 6888 before it adopted a Wolf–Rayet spectral type. Other possibility could be alternative evolution scenario involving an (eruptive) luminous blue

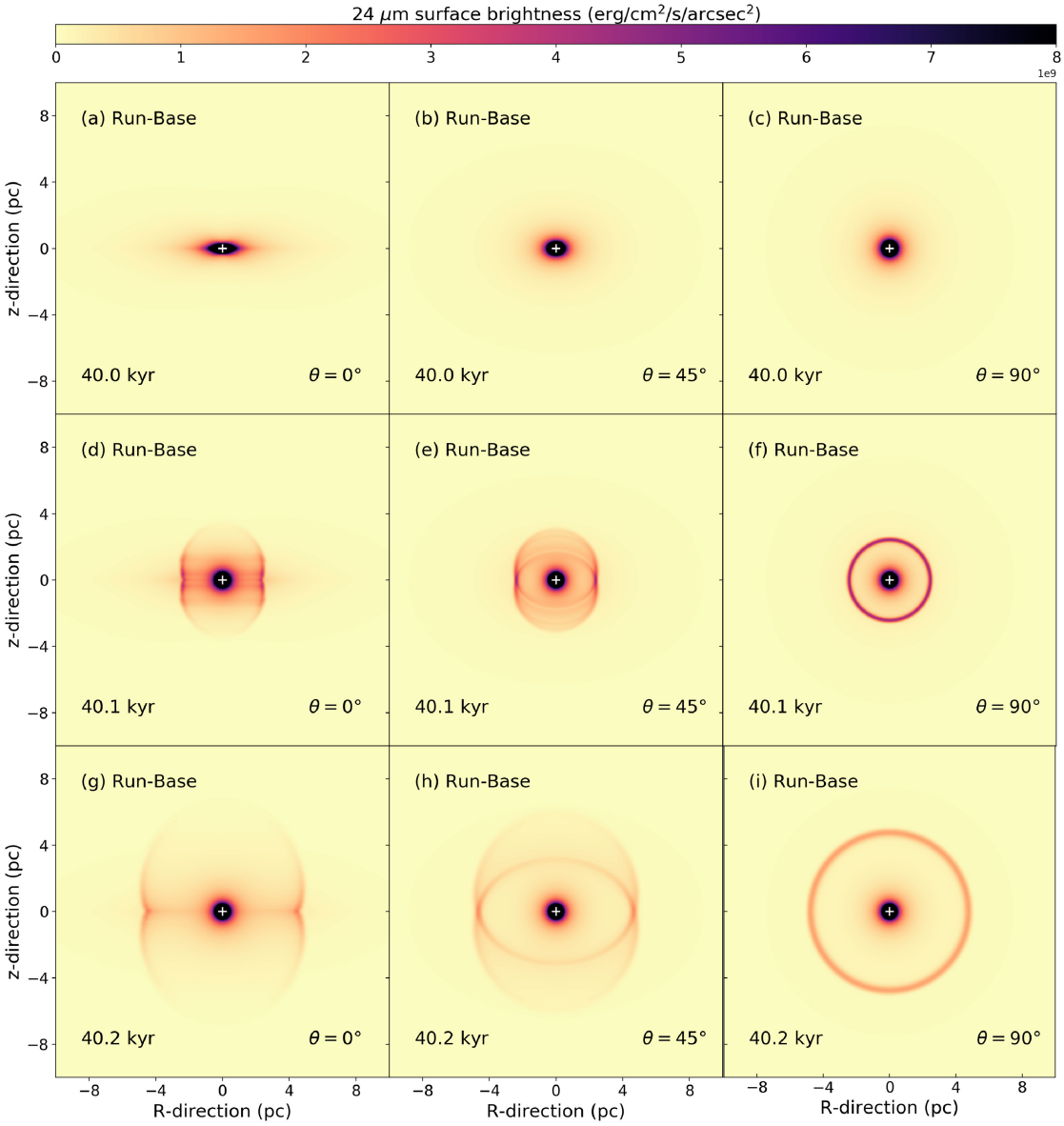

Figure 9. Emission maps calculated from the Wolf–Rayet circumstellar nebulae model Run-Base. The figure plots the 24 μm surface brightness (in erg cm^2 s^{-1} arcsec^{-2}) of our Wolf–Rayet nebulae. Quantities are calculated excluding the non-dusty Wolf–Rayet material plotted with the linear scale, under several viewing angles θ. The white cross marks the position of the star.

variable event, e.g. within a blue loop (Chita et al. 2008; Mackey et al. 2012), however less in accordance with the dust size measures of Rubio et al. (2020) shown to be typical for red supergiants. Their constraint of the initial mass of WR136 to ≈50–60 $M_\odot$ might reconcile both arguments, dust and asymmetries being generated at different phases of the complex evolution of a (potentially multiple) stellar system. Our allegation that the driving stellar object of NGC 6888 is not, despite the findings of Stock & Barlow (2014), Rubio et al. (2020), a single star, is supported by the detection of periodical modulation in line emission from the Wolf–Rayet star WR 134, interpretable as an inhomogeneous outflow (Morel et al. 1998) or as a trace of a so far undetected close companion (Meyer et al. 2018). The close companions to evolved massive stars (Koenigsberger & Schmutz 2020) and the circumstellar nebulae of extragalactic Wolf–Rayet stars such as GR290 in the Galaxy M33 (Maryeva et al. 2018, 2020) also support our arguments. All this motivates further investigations of that problem.

5 CONCLUSION

In this paper, we study the possibility of forming asymmetric Wolf–Rayet nebulae as a direct result of equatorial anisotropies in the blue supergiant stellar wind preceding the Wolf–Rayet phase. We present a two-wind toy model for the investigation of circumstellar medium generated from the evolutionary phase transition of different latitude-dependent distributions. Our MHD simulations are

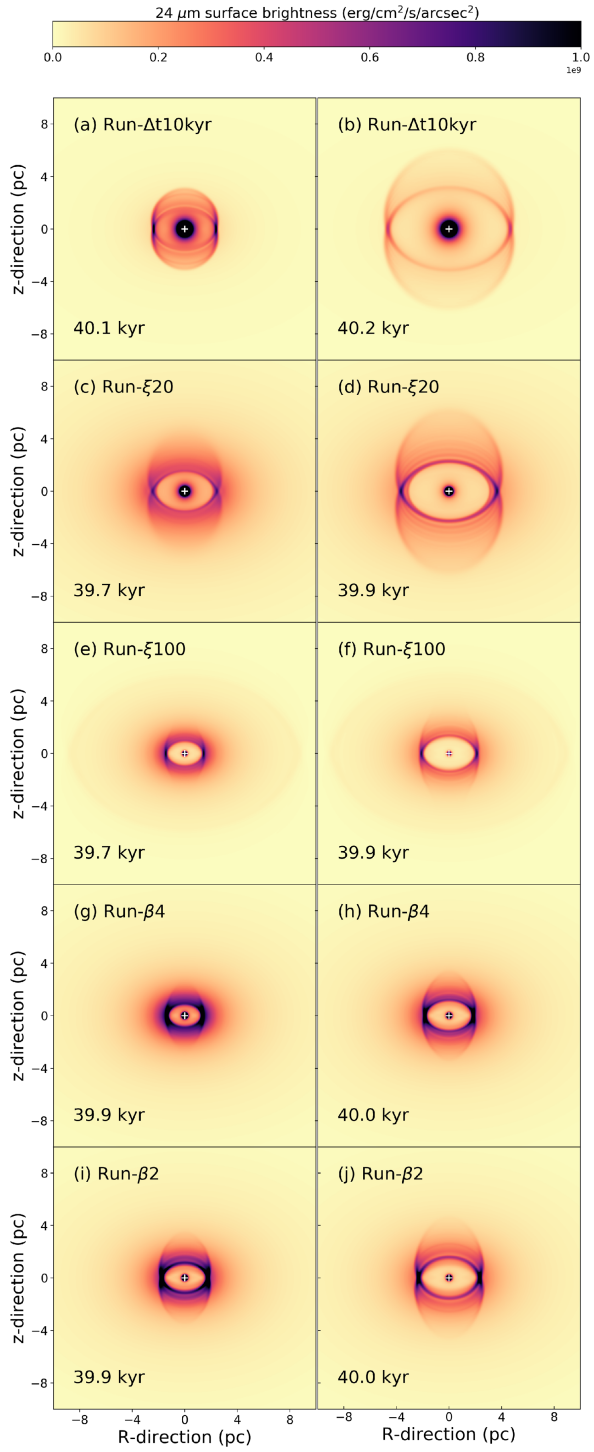

Figure 10. Same as Fig. 9 for our other models. Images assume an inclination angle of $\theta = 45°$.

performed with a spherically symmetric grid in the 2.5D fashion, using the PLUTO code (Mignone et al. 2007, 2012; Vaidya et al. 2018). We concentrate on the ∼10 pc surrounding the star, and treat both stellar magnetic field and stellar rotation, using a combination of the recipe for asymmetric winds of Raga et al. (2008) and magnetized astrospheres (Parker 1958). This study updates the pioneering work of Brighenti & D'Ercole (1997) on the early aspherical evolution of young Wolf–Rayet nebulae from red supergiant stars. Particularly, our toy model permits to change the rotation, mass-loss, magnetic properties of the evolving stars, while simultaneously exploring the phase transition interval between the two evolutionary stages. It allows us to explore at reduced computational costs, the wind–wind interaction of typical magnetized stellar outflows responsible for the shaping of circumstellar nebulae. We also explore, by means of radiative transfer calculations, the emission properties of those gas nebulae.

The density distribution in the pre-Wolf–Rayet surroundings is directly responsible for the shaping of our Wolf–Rayet nebulae and the stellar magnetic field seems to be dynamically unimportant in the process of producing the bipolarities, in the sense that only evolving MHD flows in rotation produce spherical nebulae, at least in the corner of the parameter space of blue supergiant and subsequent Wolf–Rayet stars that we explore. An equatorially compressed circumstellar distribution gives the Wolf–Rayet stellar wind a peanut-like morphology, which is further elongated along the polar direction as a jet-like shape if the polar-to-equatorial density distribution ratio increases, or in case a substantially long phase transition period (∼kyr) between the two winds. The topology of the magnetic field lines is greatly modified when the Wolf–Rayet wind starts blowing into the previous cold material. The rotating blue supergiant dipole B_ϕ sees its magnetic field lines opened and channelled to the poles of the structure. Interestingly, all our nebulae are shaped by wind–wind interaction taking place in the free-streaming stellar wind of the ancestor star, i.e. inside of the termination shock of its main-sequence stellar wind bubble (Weaver et al. 1977). This implies that the nebulae will appear the same regardless of their driving star's bulk motion (Meyer et al. 2020a) and that the nebulae are free of ISM material. We propose to characterize the evolution of MHD asymmetric Wolf–Rayet nebulae in the ρ-v-B_ϕ diagram, which we show to concisely report the main feature of our MHD Wolf–Rayet nebulae as a characteristic S-shape.

Radiative transfer calculations against dust opacity of the Wolf–Rayet nebulae provided us with mid-infrared 24 μm synthetic emission maps, showing that their projected emission reflects the anisotropies of the blue pre-Wolf–Rayet wind. We demonstrate that projection effects play a non-negligible role in the shaping of observed Wolf–Rayet nebulae. According to the observer's viewing angle, these transient objects can appear as a oblate form, a bipolar structure, an ellipse, or a ring. Last, we discuss the potential origins of the pre-Wolf–Rayet circumstellar anisotropies. Two main scenarios have been identified so far, involving either a red or a blue supergiant star. However, we show that solely the blue supergiant one can, within the single star scenario, generate density distributions sufficiently asymmetric to channel the Wolf–Rayet stellar wind and to produce Wolf–Rayet nebulae's bipolarity. This leads us to question the well-accepted past evolution of the famous asymmetric bubble nebula NGC 6888 around the Wolf–Rayet WR 136, believed to be the archetypal resulting nebulae of a single red supergiant-to-Wolf–Rayet-evolving star. We propose that NGC 6888 might be driven by a multiple system, or underwent additional evolutionary phases.

ACKNOWLEDGEMENTS

The author thanks the referee A. Raga from the University of Mexico for his numerous comments which greatly improved the quality of the paper. The author thanks L. Oskinova from the University of Potsdam for discussions regarding evolved massive stars. The author acknowledges the North-German Supercomputing Alliance (HLRN) for providing HPC resources that have contributed to the research results reported in this paper.

DATA AVAILABILITY

This research made use of the PLUTO code developed at the University of Torino by A. Mignone and collaborators (http://plutocode.ph.unito.it/) and of the RADMC-3D code developed by C. Dullemond and collaborators at the University of Heidelberg (https://www.ita.uni-heidelberg.de/~dullemond/software/radmc-3d/), respectively. The figures have been produced using the Matplotlib plotting library for the PYTHON programming language (https://matplotlib.org/). The data underlying this article will be shared on reasonable request to the corresponding author.

REFERENCES

Bestenlehner J. M. et al., 2014, A&A, 570, A38
Bjorkman J. E., Wood K., 2001, ApJ, 554, 615
Blondin J. M., Lundqvist P., Chevalier R. A., 1996, ApJ, 472, 257
Brighenti F., D'Ercole A., 1997, MNRAS, 285, 387
Brott I. et al., 2011, A&A, 530, A115
Chevalier R. A., 1977, ARA&A, 15, 175
Chevalier R. A., Liang E. P., 1989, ApJ, 344, 332
Chevalier R. A., Luo D., 1994, ApJ, 421, 225
Chita S. M., Langer N., van Marle A. J., García-Segura G., Heger A., 2008, A&A, 488, L37
Chu Y.-H., 1981, ApJ, 249, 195
Chu Y.-H., 1982a, ApJ, 254, 578
Chu Y.-H., 1982b, ApJ, 255, 79
Chu Y.-H., 1983, ApJ, 269, 202
Chu Y.-H., Treffers R. R., 1981, ApJ, 250, 615
Chu Y.-H., Treffers R. R., Kwitter K. B., 1983, ApJS, 53, 937
Ciotti L., D'Ercole A., 1989, A&A, 215, 347
Comerón F., Kaper L., 1998, A&A, 338, 273
Crowther P. A., 2007, ARA&A, 45, 177
Decin L. et al., 2020, Science, 369, 1497
Decin L. et al., 2020, Science, 369, 1497
Dopita M. A., Bell J. F., Chu Y.-H., Lozinskaya T. A., 1994, ApJS, 93, 455
Dullemond C. P., Juhasz A., Pohl A., Sereshti F., Shetty R., Peters T., Commercon B., Flock M., 2012, RADMC-3D: a multi-purpose radiative transfer tool, Astrophysics Source Code Library, record ascl:1202.015
Dwarkadas V. V., 2005, ApJ, 630, 892
Dwarkadas V. V., 2007, ApJ, 667, 226
Ekström S. et al., 2012, A&A, 537, A146
Esteban C., Mesa-Delgado A., Morisset C., García-Rojas J., 2016, MNRAS, 460, 4038
Faherty J. K., Shara M. M., Zurek D., Kanarek G., Moffat A. F. J., 2014, AJ, 147, 115
Fang J., Yu H., Zhang L., 2017, MNRAS, 464, 940
Fernández-Martín A., Martín-Gordón D., Vílchez J. M., Pérez Montero E., Riera A., Sánchez S. F., 2012, A&A, 541, A119
Flagey N., Noriega-Crespo A., Petric A., Geballe T. R., 2014, AJ, 148, 34
Frank A., Balick B., Davidson K., 1995, ApJ, 441, L77
Freyer T., Hensler G., Yorke H. W., 2003, ApJ, 594, 888
Freyer T., Hensler G., Yorke H. W., 2006, ApJ, 638, 262
Gabler M., Wongwathanarat A., Janka H.-T., 2021, MNRAS, 502, 3264
Garcia-Segura G., Langer N., Mac Low M.-M., 1996, A&A, 316, 133
Garcia-Segura G., Mac Low M.-M., Langer N., 1996, A&A, 305, 229
García-Segura G., Langer N., Różyczka M., Franco J., 1999, ApJ, 517, 767
García-Segura G., Ricker P. M., Taam R. E., 2018, ApJ, 860, 19
García-Segura G., Taam R. E., Ricker P. M., 2020, ApJ, 893, 150
González R. F., de Gouveia Dal Pino E. M., Raga A. C., Velázquez P. F., 2004, ApJ, 616, 976
Groh J. H., Meynet G., Ekström S., Georgy C., 2014, A&A, 564, A30
Guerrero M. A., Chu Y.-H., 2008, ApJS, 177, 216
Gvaramadze V. V., Kniazev A. Y., Fabrika S., 2010, MNRAS, 405, 1047
Gvaramadze V. V., Kniazev A. Y., Maryeva O. V., Berdnikov L. N., 2018, MNRAS, 474, 1412
Hamann W. R., Gräfener G., Liermann A., 2006, A&A, 457, 1015
Harten A., Lax P. D., van Leer B., 1983, SIAM Rev., 25, 35
Heiligman G. M., 1980, MNRAS, 191, 761
Herbst K. et al., 2020, ApJ, 897, L27
Hirai R., Podsiadlowski P., Owocki S. P., Schneider F. R. N., Smith N., 2021, MNRAS, 503, 4276
Hung C. S., Ou P.-S., Chu Y.-H., Gruendl R. A., Li C.-J., 2021, ApJS, 252, 21
Kervella P. et al., 2018, A&A, 609, A67
Koenigsberger G., Schmutz W., 2020, A&A, 639, A18
Langer N., 2012, ARA&A, 50, 107
Langer N., García-Segura G., Mac Low M.-M., 1999, ApJ, 520, L49
Laor A., Draine B. T., 1993, ApJ, 402, 441
Mackey J., Mohamed S., Neilson H. R., Langer N., Meyer D. M.-A., 2012, ApJ, 751, L10
Mackey J., Mohamed S., Gvaramadze V. V., Kotak R., Langer N., Meyer D. M.-A., Moriya T. J., Neilson H. R., 2014, Nature, 512, 282
Maeder A., 2009, Physics, Formation and Evolution of Rotating Stars. Springer, Berlin
Mahy L., Hutsemékers D., Royer P., Waelkens C., 2016, A&A, 594, A94
Marchenko S. V., Moffat A. F. J., Crowther P. A., 2010, ApJ, 724, L90
Marston A. P., Yocum D. R., Garcia-Segura G., Chu Y.-H., 1994, ApJS, 95, 151
Marston A. P., Chu Y.-H., Garcia-Segura G., 1994, ApJS, 93, 229
Maryeva O., Koenigsberger G., Egorov O., Rossi C., Polcaro V. F., Calabresi M., Viotti R. F., 2018, A&A, 617, A51
Maryeva O. V., Koenigsberger G., Karpov S. V., Lozinskaya T. A., Egorov O. V., Rossi C., Calabresi M., Viotti R. F., 2020, A&A, 635, A201
Mesa-Delgado A., Esteban C., García-Rojas J., Reyes-Pérez J., Morisset C., Bresolin F., 2014, ApJ, 785, 100
Meyer D. M.-A., Kuiper R., Kley W., Johnston K. G., Vorobyov E., 2018, MNRAS, 473, 3615
Meyer D. M.-A., Oskinova L. M., Pohl M., Petrov M., 2020a, MNRAS, 496, 3906
Meyer D. M.-A., Petrov M., Pohl M., 2020b, MNRAS, 493, 3548
Meyer D. M.-A., Mignone A., Petrov M., Scherer K., Velázquez P. F., Boumis P., 2021a, MNRAS, 506, 5170
Meyer D. M.-A., Pohl M., Petrov M., Oskinova L., 2021b, MNRAS, 502, 5340
Mignone A., Bodo G., Massaglia S., Matsakos T., Tesileanu O., Zanni C., Ferrari A., 2007, ApJS, 170, 228
Mignone A., Zanni C., Tzeferacos P., van Straalen B., Colella P., Bodo G., 2012, ApJS, 198, 7
Moens N., Sundqvist J. O., El Mellah I., Poniatowski L., Teunissen J., Keppens R., 2021, preprint (arXiv:2104.03968)
Morel T. et al., 1998, Ap&SS, 260, 173
Müller B., Janka H.-T., 2015, MNRAS, 448, 2141
Parker E. N., 1958, ApJ, 128, 664
Parker R. A. R., 1978, ApJ, 224, 873
Pogorelov N. V., Matsuda T., 2000, A&A, 354, 697
Pogorelov N. V., Semenov A. Y., 1997, A&A, 321, 330
Pogorelov N. V., Zank G. P., Ogino T., 2004, ApJ, 614, 1007
Powell K. G., 1997, An Approximate Riemann Solver for Magnetohydrodynamics. Springer, Berlin, p. 570
Prajapati P., Tej A., del Palacio S., Benaglia P., CH I.-C., Vig S., Mandal S., Kanti Ghosh S., 2019, ApJ, 884, L49
Raga A. C., Cantó J., De Colle F., Esquivel A., Kajdic P., Rodríguez-González A., Velázquez P. F., 2008, ApJ, 680, L45

Rozyczka M., Franco J., 1996, ApJ, 469, L127
Rubio G., Toalá J. A., Jiménez-Hernández P., Ramos-Larios G., Guerrero M. A., Gómez-González V. M. A., Santamaría E., Quino-Mendoza J. A., 2020, MNRAS, 499, 415
Sander A., Hamann W.-R., Todt H., 2012, A&A, 540, A144
Scherer K., Baalmann L. R., Fichtner H., Kleimann J., Bomans D. J., Weis K., Ferreira S. E. S., Herbst K., 2020, MNRAS, 493, 4172
Smartt S. J., 2009, ARA&A, 47, 63
Smartt S. J., Lennon D. J., Kudritzki R. P., Rosales F., Ryans R. S. I., Wright N., 2002, A&A, 391, 979
Smith N., 2017, Phil. Trans. R. Soc. A, 375, 20160268
Stock D. J., Barlow M. J., 2014, MNRAS, 441, 3065
Szécsi D., Wünsch R., Agrawal P., Langer N., 2020, preprint (arXiv:2004.08203)
Toalá J. A., Arthur S. J., 2011, ApJ, 737, 100
Toalá J. A., Guerrero M. A., Chu Y.-H., Gruendl R. A., Arthur S. J., Smith R. C., Snowden S. L., 2012, ApJ, 755, 77
Toalá J. A., Guerrero M. A., Gruendl R. A., Chu Y.-H., 2014, AJ, 147, 30
Toalá J. A., Guerrero M. A., Ramos-Larios G., Guzmán V., 2015, A&A, 578, A66
Toalá J. A. et al., 2018, ApJ, 869, L11
Treffers R. R., Chu Y.-H., 1982, ApJ, 254, 569
Vaidya B., Mignone A., Bodo G., Rossi P., Massaglia S., 2018, ApJ, 865, 144
van der Sluys M. V., Lamers H. J. G. L. M., 2003, A&A, 398, 181
van Marle A. J., Langer N., García-Segura G., 2005, A&A, 444, 837
van Marle A. J., Langer N., Achterberg A., García-Segura G., 2006, A&A, 460, 105
van Marle A. J., Langer N., García-Segura G., 2007, A&A, 469, 941
van Marle A. J., Meliani Z., Keppens R., Decin L., 2011, ApJ, 734, L26
van Marle A. J., Keppens R., Meliani Z., 2011, Bull. Soc. R. Sci. Liege, 80, 310
van Marle A. J., Meliani Z., Marcowith A., 2015, A&A, 584, A49
Vink J. S., 2006, in Lamers H. J. G. L. M., Langer N., Nugis T., Annuk K., eds, ASP Conf. Ser. Vol. 353, Stellar Evolution at Low Metallicity: Mass Loss, Explosions, Cosmology. Astron. Soc. Pac., San Francisco, p. 113
Vlemmings W. H. T., Diamond P. J., van Langevelde H. J., 2002, A&A, 394, 589
Vlemmings W. H. T., van Langevelde H. J., Diamond P. J., 2005, A&A, 434, 1029
Weaver R., McCray R., Castor J., Shapiro P., Moore R., 1977, ApJ, 218, 377
Weiler K. W., Sramek R. A., 1988, ARA&A, 26, 295
Weis K., Chu Y.-H., Duschl W. J., Bomans D. J., 1997, A&A, 325, 1157
Woosley S. E., Bloom J. S., 2006, ARA&A, 44, 507
Woosley S. E., Heger A., Weaver T. A., 2002, Rev. Mod. Phys., 74, 1015
Wrigge M., Chu Y.-H., Magnier E. A., Wendker H. J., 2005, ApJ, 633, 248

This paper has been typeset from a TEX/LATEX file prepared by the author.

Core-collapse supernova remnants

Monthly Notices
of the
ROYAL ASTRONOMICAL SOCIETY

MNRAS **493,** 3548–3564 (2020)
Advance Access publication 2020 February 26

doi:10.1093/mnras/staa554

Wind nebulae and supernova remnants of very massive stars

D. M.-A. Meyer [1]★ M. Petrov[2] and M. Pohl[1,3]

[1]*Institut für Physik und Astronomie, Universität Potsdam, Karl-Liebknecht-Strasse 24/25, D-14476 Potsdam, Germany*
[2]*Max Planck Computing and Data Facility (MPCDF), Gieenbachstrasse 2, D-85748 Garching, Germany*
[3]*DESY, Platanenallee 6, D-15738 Zeuthen, Germany*

Accepted 2020 February 19. Received 2020 February 19; in original form 2019 December 20

ABSTRACT

A very small fraction of (runaway) massive stars have masses exceeding 60–70 $M_\odot$ and are predicted to evolve as luminous blue variable and Wolf–Rayet stars before ending their lives as core-collapse supernovae. Our 2D axisymmetric hydrodynamical simulations explore how a fast wind (2000 km s^{-1}) and high mass-loss rate (10^{-5} $M_\odot$ yr^{-1}) can impact the morphology of the circumstellar medium. It is shaped as 100 pc-scale wind nebula that can be pierced by the driving star when it supersonically moves with velocity 20–40 km s^{-1} through the interstellar medium (ISM) in the Galactic plane. The motion of such runaway stars displaces the position of the supernova explosion out of their bow shock nebula, imposing asymmetries to the eventual shock wave expansion and engendering Cygnus-loop-like supernova remnants. We conclude that the size (up to more than 200 pc) of the filamentary wind cavity in which the chemically enriched supernova ejecta expand, mixing efficiently the wind and ISM materials by at least 10 per cent in number density, can be used as a tracer of the runaway nature of the very massive progenitors of such 0.1 Myr old remnants. Our results motivate further observational campaigns devoted to the bow shock of the very massive stars BD+43°3654 and to the close surroundings of the synchrotron-emitting Wolf–Rayet shell G2.4+1.4.

Key words: shock waves – methods: numerical – circumstellar matter – stars: massive.

1 INTRODUCTION

Massive stars ($M_\star \geq 8\,M_\odot$) are objects whose formation is an uncommon but crucial event in the interstellar medium (ISM) of our Galaxy (Langer 2012). Their strong winds release a large amount of momentum and energy into their surrounding ISM and form bubbly circumstellar structures that chemically enrich their local environment (Weaver et al. 1977). Wind bubbles of main-sequence, OB-type massive stars are predicted to expand up to $\simeq$ 100 pc away from the star. The shocked photoionized stellar wind material and the ISM gas are separated by an unstable contact discontinuity segregating the inner hot, diluted shocked wind gas from the outer layer of cold, dense shocked ISM gas. These nebulae grow inside the huge H II regions generated by the ionizing radiation field of early-type hot massive stars (Dyson 1975; Dyson & Gulliford 1975), however, sufficiently massive stellar wind bubbles can trap the ionization front of their own central star (Dwarkadas & Rosenberg 2013). Wind bubbles mainly radiate by means of optical forbidden-line emission (Schneps et al. 1981; Smith et al. 1984), in the X-ray energy band via thermal photons emitted by the inner hot region (Zhekov 2014), and in the infrared waveband by reprocessing of starlight by ISM dust that is trapped into the outer layer of the bubble (van Buren & McCray 1988). Stellar wind bubbles of static massive stars conserve their spherical shape regardless of the central star's evolution, see Garcia-Segura, Mac Low & Langer (1996a), Freyer, Hensler & Yorke (2003, 2006), Dwarkadas (2007).

The spherical symmetry of stellar wind nebulae is broken if their central star moves with respect to their local ambient medium, and they eventually turn into a similarly organized but arc-like shape (Baranov, Krasnobaev & Kulikovskii 1971; Wilkin 1996). The resulting so-called stellar wind bow shocks form around the 4–10 per cent of all main-sequence stars that move supersonically through the ISM (see Gies 1987; Blaauw 1993; Huthoff & Kaper 2002). The physics of bow shocks around OB stars partly relies on the (in)efficiency of heat conduction (Meyer et al. 2017; Green et al. 2019), while their detailed internal structure depends on the coupling between dust and gas (Henney & Arthur 2019a,b,c). Their morphology is a function of the stellar mass-loss rate (Gull & Sofia 1979; Gvaramadze et al. 2014; Meyer et al. 2014a), ambient medium density (Kaper et al. 1997), and stellar bulk motion (Meyer et al. 2014a), respectively. The evolution of massive stars induces brutal changes in the stellar wind properties (Langer 2012). The dense but slow wind of evolved red supergiant stars makes bow shocks prone to develop thin-shell instabilities (Dgani, van Buren & Noriega-Crespo 1996; Blondin & Koerwer 1998; Mackey et al. 2012; Meyer et al. 2014b), which can be inhibited either by an external ionizing radiation field (Meyer et al. 2014a) or by the

★ E-mail: dmameyer.astro@gmail.com

ambient magnetization of the ISM (van Marle, Decin & Meliani 2014). These dusty nebulae are mainly observable in the infrared waveband (van Buren 1993; van Buren, Noriega-Crespo & Dgani 1995; van Marle et al. 2011; Cox et al. 2012; Peri et al. 2012; Mackey et al. 2014; Peri, Benaglia & Isequilla 2015; Kobulnicky et al. 2016, 2017; Kobulnicky, Chick & Povich 2018) although they thermally emit in the other wavebands, see Kaper et al. (1997), Jorissen et al. (2011). Interestingly, such bow shocks are suspected to accelerate protons and electrons in the stellar wind to high energies and to act as cosmic ray injectors (del Valle, Romero & De Becker 2013; del Valle, Romero & Santos-Lima 2015; del Valle & Pohl 2018), producing variable high-energy and gamma-ray emission (del Valle & Romero 2014), however at much lower luminosity than, e.g. pulsars or supernova remnants (SNRs; De Becker et al. 2017; Toalá, Oskinova & Ignace 2017; Binder, Behr & Povich 2019). Recent measures have reported synchrotron emission from the Wolf–Rayet ring bubble G2.4+1.4 (Prajapati et al. 2019).

When bow shock-driving massive stars cease to evolve, the distorted bubble nebula shaped throughout the post-ZAMS (zero-age main sequence) star life constitutes the environment in which the moving high-mass star dies, e.g. as a core-collapse supernova (Franco et al. 1991; Rozyczka et al. 1993; Ekström et al. 2012). The deviations from the spherically symmetric expansion of the shock wave depend on the density and mass accumulated in the circumstellar medium of the progenitor. The blastwave first expands in a cavity of unshocked stellar wind, before interacting with the reverse shock of the bow shock, whose presence slows down the progression of the shock wave in the direction of motion of the progenitor, while it facilitates its rapid expansion in the opposite direction, inducing characteristic asymmetries in the SNR. Typical examples among young SNRs are Kepler's SNR (Borkowski, Blondin & Sarazin 1992; Velázquez et al. 2006; Chiotellis, Schure & Vink 2012), Tycho (Vigh et al. 2011; Williams et al. 2013), or the Cygnus Loop (Meyer et al. 2015; Fang, Yu & Zhang 2017). Note that asymmetries can be caused by the geometry of the explosion itself (Toledo-Roy et al. 2014). Having established that the morphology of SNRs from massive progenitors is a function of their past stellar evolution, the question arises, which massive stars are most prone to generate a dense asymmetric circumstellar medium and hence the most aspherical remnants?

The accumulation of mass in the surroundings of an evolving star can arise from the brutal release of dense shells of material during the post-main-sequence phase. As additional effect to that of the progenitor's stellar motion, this naturally leads to asymmetric and inhomogeneous cavities in which the supernova blastwave will expand. This particularly affects high-mass stars evolving through eruptive stellar evolutionary stages such as so-called luminous blue variable or Wolf–Rayet phases (González & Koenigsberger 2014; Humphreys et al. 2017), characterized by the sudden inflation of the star together with an increase of the star's mass-loss rate and wind velocity. This results in the ejection of dense shells of envelope material into the stellar surroundings (Gräfener et al. 2017; Sanyal et al. 2017; Grassitelli et al. 2018). Such evolving high-mass stars that are rare and predicted to end their life as a core-collapse supernova (Meynet & Maeder 2005; Ekström et al. 2012) have been observed both in the Milky Way (van der Hucht 2001) and in the Large Magellanic Cloud (Hainich et al. 2014). Moreover, a significant fraction of them have fast proper motion, which can be explained by many-body gravitational interaction leading to their escape from their parent cluster (Gvaramadze & Gualandris 2011; Gvaramadze et al. 2013). Particularly, this mechanism is able to produce very massive ($\simeq$ 55–85 $M_\odot$) fast-moving stars such as the

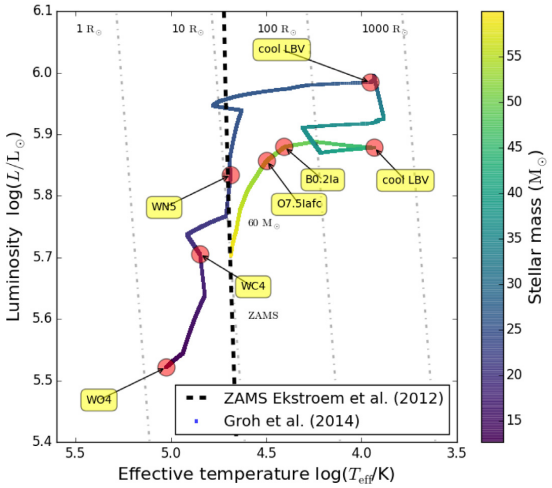

Figure 1. Herzsprung–Russel diagram of the non-rotating 60 $M_\odot$ ZAMS star considered in this study, based on Groh et al. (2014).

main-sequence star BD+43°3654 that runs away from the Cygnus OB2 region (Comerón & Pasquali 2007). Hence, these moving stellar objects that are inclined to provoke morphological distortions of their wind nebulae (O'Hara et al. 2003) are also good candidates for the production of strongly asymmetric SNRs. In this study, we explore the effects of consecutive luminous blue variable and Wolf–Rayet winds on to the shaping of nebulae around a 60 $M_\odot$ star (Freyer et al. 2003; van Marle, Langer & García-Segura 2007; Toalá & Arthur 2011; Wareing, Pittard & Falle 2017) (see Fig. 1), and we investigate how its bulk motion can affect the development of asymmetries in their subsequent SNR in the spirit of the first paper of this series devoted to runaway red supergiant progenitors (Meyer et al. 2015).

Our study is divided as follows. First, we present in Section 2 the methods for the numerical modelling of the circumstellar medium of a moving, massive Wolf–Rayet-evolving star. We present our results for the dynamics of the stellar surroundings from the ZAMS to the SNR phase in Section 3. Particularly, we concentrate on the mixing of material induced in the remnants and on their associated thermal X-ray emission properties. Our outcomes are further discussed in Section 4. Finally, we conclude in Section 5.

2 METHOD

This section introduces the reader to the methods used to perform hydrodynamical simulations of the surroundings of a massive star undergoing both luminous blue variable and Wolf–Rayet phases. The evolution of the circumstellar medium is simulated from the ZAMS of the progenitor to the late phase of SNR evolution, for several proper motion speeds of the driving star.

2.1 Simulation method for the pre-supernova phase

The structure of the pre-supernova circumstellar medium arises from stellar wind–ISM interaction. We model it with the same method as was used for studying bow shocks of runaway massive stars, summarized in Meyer et al. (2016). The stellar surroundings are simulated with axisymmetric, two-dimensional nu-

merical hydrodynamics simulations performed with the PLUTO[1] code (Mignone et al. 2007, 2012). We use cylindrical coordinates with a uniform grid $[O; R_{\rm max}] \times [z_{\rm min}; z_{\rm max}]$ that is discretized with $N_{\rm R} \times N_z$ grid zones. The uniform spatial mesh resolution is $\Delta = R_{\rm max}/N_{\rm R} = (z_{\rm max} - z_{\rm min})/N_z$. The supersonic stellar wind is injected into the computational domain via a sphere of 20 cells in radius centred at the origin of the grid and filled with the wind density profile

$$\rho_w = \frac{\dot{M}}{4\pi r^2 v_{\rm w}}, \tag{1}$$

where $\dot{M}$ denotes the time-dependent mass-loss rate of the massive star, r is the distance to the origin of the domain, O, and $v_{\rm w}$ is the wind velocity. The same method has been used in Comerón & Kaper (1998) and van Marle et al. (2007, 2011, 2014). The stellar wind parameters ρ_w and $v_{\rm w}$ are time-dependently interpolated from the tabulated stellar evolution model of a non-rotating 60 $M_\odot$ star presented in Groh et al. (2014). The wind-blown bubble resulting from the wind–ISM interaction is computed in the rest frame of the central star, and its proper stellar motion $v_\star$ is taken into account by setting an inflowing medium at the $z = z_{\rm max}$ boundary. Outflow boundary conditions are assigned at $z = z_{\rm min}$ and $R = R_{\rm max}$, respectively. The stellar wind material injected into the domain is distinguished from the ambient medium using a passive tracer, Q_1, that is initially set to $Q_1(\boldsymbol{r}) = 1$ in the wind material and to $Q_1(\boldsymbol{r}) = 0$ in the ISM gas, respectively. We follow the mixing of materials in the circumstellar structure using the advection equation

$$\frac{\partial(\rho Q_1)}{\partial t} + \nabla \cdot (\boldsymbol{v} \rho Q_1) = 0. \tag{2}$$

The computationally intensive calculations were performed on the HPC systems Cobra using Intel Skylake processors and Draco using Intel Haswell, Broadwell processors at the Max Planck Computing and Data Facility (MPCDF)[2] in Garching, and on the North-German Supercomputing Alliance (HLRN)[3] using the HPC compute system in Berlin operating with Cray XC40/30 processors, respectively.

2.2 Setting up the supernova explosion

Once the pre-supernova circumstellar medium has been modelled, we insert a spherically symmetric explosion into a spherically symmetric stellar wind in order to separately calculate in 1D fashion the initial expansion of the supernova shock wave into the progenitor's last freely expanding wind, whose solution is used as initial condition for the 2D SNRs (Meyer et al. 2015). The expanding blastwave is characterized by its energy, taken to be $E_{\rm ej} = 10^{51}$ erg, and by the mass of the ejecta released at the time of the explosion, $M_{\rm ej}$, estimated as

$$M_{\rm ej} = M_\star - \int_{t_{\rm ZAMS}}^{t_{\rm SN}} \dot{M}(t)\,{\rm d}t - M_{\rm NS} = 11.1\,{\rm M}_\odot, \tag{3}$$

where $t_{\rm ZAMS}$ and $t_{\rm SN}$ are the ZAMS and supernova times, respectively, and where $M_{\rm NS} = 1.4\,{\rm M}_\odot$ is the mass of the remnant neutron star.

The expansion of the supernova shock wave is launched using the method of Whalen et al. (2008) and van Veelen et al. (2009), in which a blastwave density profile, $\rho(r)$, is deposited on the top of the progenitor's wind profile taken from the modelled nebulae, at the pre-supernova time. We ensure that the outer boundary of this 1D computational domain is smaller than the value of the wind termination shock of the pre-shaped circumstellar medium. The ejecta profile is defined by two characteristic lengths corresponding to the radius of the progenitor's core at the moment of the explosion, $r_{\rm core}$, and the position of the forward shock of the blastwave, $r_{\rm max}$. The simulation is initialized at time $t_{\rm max} = r_{\rm max}/v_{\rm max}$, with $v_{\rm max} = 30\,000\,{\rm km\,s^{-1}}$ the ejecta top speed (van Veelen et al. 2009). The quantity $r_{\rm max}$ is a free parameter determined according to the numerical procedure described in Whalen et al. (2008). The density profile of the ejecta follows a piece-wise function

$$\rho(r) = \begin{cases} \rho_{\rm core}(r) & \text{if } r \le r_{\rm core}, \\ \rho_{\rm max}(r) & \text{if } r_{\rm core} < r < r_{\rm max}, \\ \rho_{\rm csm}(r) & \text{if } r \ge r_{\rm max}, \end{cases} \tag{4}$$

with a constant density

$$\rho_{\rm core}(r) = \frac{1}{4\pi n} \frac{\left(10 E_{\rm ej}^{n-5}\right)^{-3/2}}{\left(3 M_{\rm ej}^{n-3}\right)^{-5/2}} \frac{1}{t_{\rm max}^3}, \tag{5}$$

imposed for the plateau of the ejecta in the $[O; r_{\rm core}]$ region of the domain. The quantity

$$\rho_{\rm max}(r) = \frac{1}{4\pi n} \frac{\left(10 E_{\rm ej}^{n-5}\right)^{(n-3)/2}}{\left(3 M_{\rm ej}^{n-3}\right)^{(n-5)/2}} \left(\frac{r}{t_{\rm max}}\right)^{-n}, \tag{6}$$

is a function of $r_{\rm core}$ and $r_{\rm max}$ (Truelove & McKee 1999), where the index, n, is set to $n = 11$ that is typical for core-collapse supernova explosions (Chevalier 1982). In equation (4), $\rho_{\rm cms}$ is the freely expanding wind profile measured from the pre-supernova simulations of the circumstellar medium. The ejecta speed follows a homologous-expansion profile

$$v(r) = \frac{r}{t}, \tag{7}$$

for times $t > t_{\rm max}$, where t is the time after the supernova explosion. The velocity of the ejecta at the location of $r_{\rm core}$ reads

$$v_{\rm core} = \left(\frac{10(n-5)E_{\rm ej}}{3(n-3)M_{\rm ej}}\right)^{1/2}, \tag{8}$$

see Truelove & McKee (1999). The 1D solution for the ejecta–wind interaction is mapped on to the 2D domain when the forward shock of the expanding supernova blastwave reaches 8 pc. With the grid resolution that we consider, the mapped ejecta profiles are hence resolved with ∼160 grid zones.

Last, a second passive scalar $Q_2(\boldsymbol{r})$ is introduced, obeying the advection equation

$$\frac{\partial(\rho Q_2)}{\partial t} + \nabla \cdot (\boldsymbol{v} \rho Q_2) = 0, \tag{9}$$

which distinguishes the ejecta from the stellar wind and the ambient medium materials. It is initially set to $Q_2(\boldsymbol{r}) = 1$ for the region made of supernova ejecta material and to $Q_2(\boldsymbol{r}) = 0$ in the other part of the computational domain, respectively.

2.3 Governing equations

We model the stellar wind–ISM interaction and the SNR within the framework of the non-ideal hydrodynamics, i.e. by solving the Euler equations and by accounting for energy losses by optically

[1] http://plutocode.ph.unito.it/
[2] https://www.mpcdf.mpg.de/
[3] https://www.hlrn.de/

thin radiative cooling. We solve the set of equations composed of the equation for the conservation of mass

$$\frac{\partial \rho}{\partial t} + \nabla \cdot (\rho \boldsymbol{v}) = 0, \tag{10}$$

of linear momentum

$$\frac{\partial \rho \boldsymbol{v}}{\partial t} + \nabla \cdot (\boldsymbol{v} \otimes \rho \boldsymbol{v}) + \nabla p = \boldsymbol{0}, \tag{11}$$

and of the total energy

$$\frac{\partial E}{\partial t} + \nabla \cdot (E \boldsymbol{v}) + \nabla \cdot (p \boldsymbol{v}) = \Phi(T, \rho), \tag{12}$$

where

$$E = \frac{p}{(\gamma - 1)} + \frac{\rho v^2}{2}, \tag{13}$$

and ρ is the mass density of the gas, p its pressure, $\boldsymbol{v}$ the vector velocity, respectively. The gas temperature reads

$$T = \mu \frac{m_{\rm H}}{k_{\rm B}} \frac{p}{\rho}, \tag{14}$$

where $k_{\rm B}$ is the Boltzmann constant and μ is the mean molecular weight, so that the gas mass density reads

$$\rho = \mu \, n \, m_{\rm H}, \tag{15}$$

with n the total number density of the plasma and $m_{\rm H}$ the mass of a hydrogen atom. The adiabatic index of the gas is set to $\gamma = 5/3$. As in Meyer et al. (2015), we use a finite-volume method with the Harten–Lax–van Leer approximate Riemann solver, and integrate the Euler equations with a second-order, unsplit, time-marching algorithm.

Our simulations take into account internal energy losses and gains by optically thin cooling and heating, respectively. These mechanisms are represented with the right-hand term of equation (12)

$$\Phi(T, \rho) = n_{\rm H} \Gamma(T) - n_{\rm H}^2 \Lambda(T), \tag{16}$$

where $\Gamma(T)$ and $\Lambda(T)$ are the heating and cooling components of the expression, respectively, and where $n_{\rm H}$ is the hydrogen number density. The contribution for heating, Γ, mimics the reionization of recombining hydrogen atoms by the photon field of the hot star (Osterbrock & Bochkarev 1989; Hummer 1994). The cooling term is based on the prescriptions by optically thin cooling derived by Wiersma, Schaye & Smith (2009), accounting for the radiation losses for hydrogen and helium at $T < 10^6$ K and for metals at $T \geq 10^6$ K (Wiersma et al. 2009). The cooling curve has been updated with collisionally excited forbidden lines such as [OIII] λ 5007 line emission (Henney et al. 2009).

2.4 Simulation parameters

Fig. 2 plots the stellar surface properties that are used as boundary conditions in our hydrodynamical simulations. The star's post-main-sequence mass history (panel a, in $M_\odot$), mass-loss rate evolution (panel b, in $M_\odot\,yr^{-1}$), and wind velocity (panel c, in $km\,s^{-1}$) are plotted as a function of time (in Myr) starting from 3 Myr. Earlier times correspond to the O-type main-sequence phase of the star during which the stellar wind properties do not evolve much. The red dots on the figures denote the principal evolutionary phases and the yellow labels on the figures indicate the corresponding spectral type. The stellar evolution model of this ZAMS non-rotating 60 $M_\odot$ star has been computed up to the Si burning phase with the GENEC code (Ekström et al. 2012).

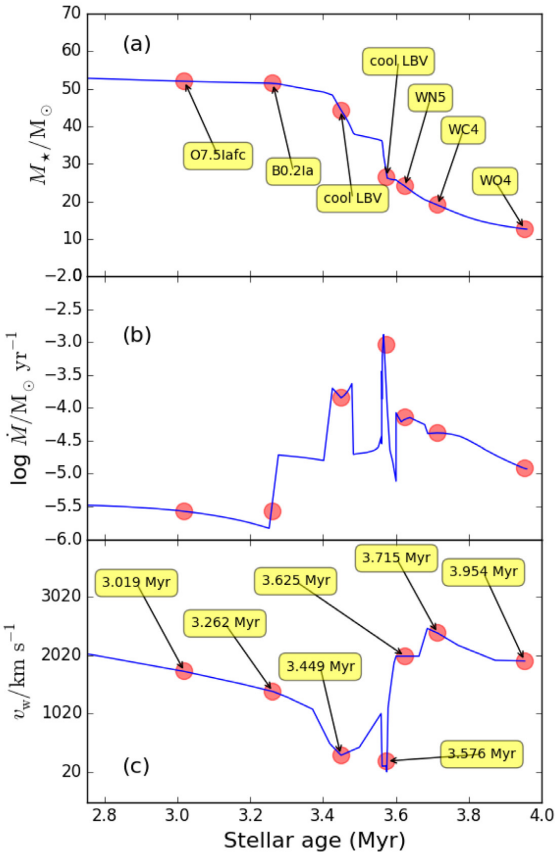

Figure 2. Post-main-sequence evolution of the stellar mass (top, panel a), mass-loss rate (middle, panel b), and wind velocity (bottom, panel c) as a function of time (in Myr) that we used as initial condition in our hydrodynamical simulations.

The effective temperature and the terminal wind velocity have been estimated using atmospheric radiative transfer modelling and prescriptions derived from observations of stellar populations (Groh et al. 2014). They are characterized by a long main-sequence phase lasting approximately 3 Myr during which the star blows winds of $\dot{M} \approx 10^{-6}$–$10^{-5.5}\,M_\odot\,yr^{-1}$, $v_\infty \approx 3500$–$2000\,km\,s^{-1}$ and loses roughly 8 $M_\odot$ of material. Beginning of the last Myr, the mass-loss increases to $\dot{M} \approx 10^{-5}\,M_\odot\,yr^{-1}$, while $v_\infty \approx 1300\,km\,s^{-1}$, and the star adopts a B spectral type. This is followed by two consecutive luminous blue variable eruptions with $\dot{M} \approx 10^{-3.5}$–$10^{-3}\,M_\odot\,yr^{-1}$ with wind velocity decreasing down to nearly $200\,km\,s^{-1}$. The star then evolves to the so-called Wolf–Rayet phase of both high mass-loss rate and a large wind velocity. We do not consider the last pre-supernova increase of the stellar wind velocity up to $\approx 5000\,km\,s^{-1}$ in this study, as very few examples of such strong-winded Wolf–Rayet stars have been so far monitored (Nugis & Lamers 2000; Toalá et al. 2015).

The free parameter in our series of 2D computationally intensive simulations is the space velocity of the star, $v_\star$, which spans from the static case producing a spherical wind-blown bubble ($v_\star = 0\,km\,s^{-1}$) to the runaway case generating a bow shock ($v_\star = 40\,km\,s^{-1}$). In all our models, as in the series of papers devoted to a grid of bow shocks models of Meyer et al. (2014b, 2016), the massive star is assumed to be located in the warm phase

Table 1. Simulation models in this study. The table gives the space velocity of the moving star, $v_\star$. The runs are labelled as 'CSM' for the pre-supernova modelling of the circumstellar medium and as 'SNR' for the simulations of their subsequent remnants, respectively.

Model	$v_\star$ (km s^{-1})	Grid size	Grid mesh	Description
Run-0-CSM	0	[0; 150] × [−150; 150]	3000 × 6000 cells	Static wind bubble
Run-10-CSM	10	[0; 150] × [−200; 100]	2000 × 4000 cells	Wind bubble with off-centred slowly moving star
Run-20-CSM	20	[0; 175] × [−250; 100]	2000 × 4000 cells	Bow shock of runaway star moving with Mach number $M = 1^a$
Run-40-CSM	40	[0; 150] × [−300; 100]	1500 × 4000 cells	Bow shock of runaway star moving with Mach number $M = 2^a$
Run-0-SNR	0	[0; 200] × [−200; 200]	3500 × 7000 cells	SNR of static progenitor
Run-10-SNR	10	[0; 200] × [−230; 170]	4000 × 8000 cells	SNR of slowly moving progenitor
Run-20-SNR	20	[0; 200] × [−275; 175]	3200 × 7000 cells	SNR of progenitor moving with Mach number $M = 1^a$
Run-40-SNR	40	[0; 200] × [−330; 170]	3200 × 8000 cells	SNR of progenitor moving with Mach number $M = 2^a$

[a]The stellar motion is supersonic with respect to the unperturbed ISM sound speed.

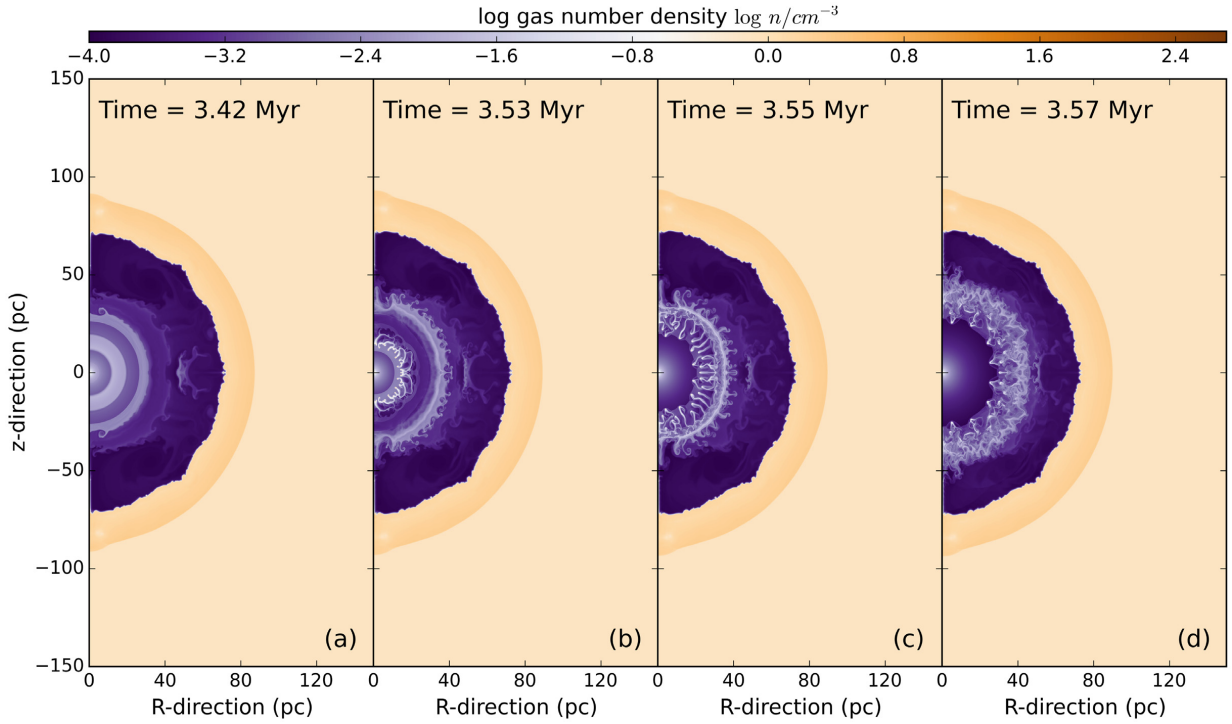

Figure 3. Time sequence of density maps (in cm^{-3}) with circumstellar shells released inside the stellar wind bubble generated by our massive star at rest ($v_\star = 0$ km s^{-1}), while it passes through two successive luminous blue variable phases before the Wolf–Rayet wind blows. The panels are shown at times 3.42 (a), 3.53 (b), 3.55 (c), and 3.57 Myr (d), respectively. On each panel the star is located at the origin.

of the ISM, characterized by a temperature of 8000 K and a number density of 0.79 cm^{-3}. After the modelling of the circumstellar medium of the evolving massive star up the pre-supernova phase, the solution is mapped on to a larger computational domain that is filled with unperturbed ambient ISM material. The supernova explosion is setup according to the method developed in Meyer et al. (2015) and described in the paragraphs above. Our simulation runs and their characteristics are summarized in Table 1.

3 RESULTS

In this section, we describe the pre-supernova circumstellar evolution of our 60 $M_\odot$ star and how the expanding supernova blast wave interacts with it. We present the thermal X-ray signatures of the SNRs and analyse the mixing of stellar wind, ISM material, and supernova ejecta.

3.1 The pre-supernova circumstellar medium

Our model Run-0-CSM for a static massive star develops a spherical wind bubble of swept-up wind and ISM gas. As the wind properties do not evolve much during the main-sequence phase (Groh et al. 2014), the bubble nebula grows according to the picture described in Weaver et al. (1977). When the OB-type star further evolves, the successive changes in the stellar properties produce several shells that expand at different velocities and eventually collide. Fig. 3 presents the bubble density field of Run-0-CSM for different time instances: at time 3.42 Myr the main-sequence bubble is constituted of an outer dense cold shell of radius around 60 pc surrounding a hot diluted region at radii 25–50 pc, inside of which the post-main-sequence shells are released (Fig. 3a). The dense shells collide with each other (Fig. 3b) and then develop instabilities (Figs 3c and d) as described in Garcia-Segura et al. (1996a), van Marle et al. (2007),

and van Marle & Keppens (2012). At the pre-supernova time, the circumstellar medium has adopted the shape of a spherically symmetric structure in which the expanding shells have reached the contact discontinuity of the main-sequence bubble separating hot shocked wind and cold shocked ISM (Fig. 4a). The slow stellar motion of $10\,\mathrm{km\,s^{-1}}$ in Run-10-CSM is not sufficient to break this spherical symmetry (Fig. 4b). When the star moves into its own wind bubble, the post-main-sequence shells are released from an off-centre location in the bubble. The shell of colliding winds interacts first with the bubble in the direction of motion of the star. This rapidly destabilizes the contact discontinuity of the nebula ahead of the star's direction of motion, whereas in the opposite direction the post-main-sequence material interacts later, as a natural consequence of the off-centred position of the star in the nebula (Fig. 4b).

Fig. 4(c) reports the pre-supernova circumstellar medium in our model Run-20-CSM in which the star moves through the ISM with Mach number $M = v_\star/c_\mathrm{s} = 1$. The main-sequence stellar wind bubble is still spherical, and of size similar to that in Run-10-CSM. The star has travelled $3\,\mathrm{Myr} \times 20\,\mathrm{km\,s^{-1}} \simeq 60\,\mathrm{pc}$ during its main-sequence phase, which is approximately the final radius of its own wind bubble. The shells of luminous blue variable and Wolf–Rayet material are hence released directly in the dense cold shocked ISM gas, not in the stellar wind cavity (Figs 4a and b). The shells expand freely in the unperturbed ISM ahead of the direction of stellar motion and develop Rayleigh–Taylor instabilities, whereas they fill the interior of the main-sequence wind bubble in the opposite direction. The overall shape of the circumstellar medium therefore becomes strongly asymmetric, i.e. it is shaped as a bubble of cold OB gas with embedded enriched post-main-sequence material, ahead of which a bow shock of thin, instable but dense material forms into the ambient medium, as a consequence of the high Wolf–Rayet wind density ($\dot{M} \approx 10^{-5}\,\mathrm{M_\odot\,yr^{-1}}$). When the star moves even faster, e.g. with velocity $v_\star = 40\,\mathrm{km\,s^{-1}}$, the luminous blue variable and Wolf–Rayet shells are expelled out of the main-sequence nebula and expand quasi-spherically into the ISM, see model Run-40-CSM (Fig. 5). The pre-supernova circumstellar medium is completely asymmetric, and only a narrow region of the post-main-sequence ring is connected to the drop-like nebula that reflects the distortion of the wind bubble by the stellar motion. Note that a boundary effect develops as material accumulates close to the symmetry axis (Figs 4 and 5). This well-known problem (Mackey et al. 2015) is unavoidable in two-dimensional axisymmetric simulations of this kind using uniform grids. It can be circumvented by means of three-dimensional calculations, however, at the cost of losses in spatial resolution (Rodríguez-González et al. 2019).

3.2 Dynamics of asymmetric supernova remnants

If one neglects asymmetries potentially developing in the supernova explosion itself (Toledo-Roy et al. 2014), the remnant of a massive progenitor star at rest conserves its sphericity as the forward shock wave expands symmetrically into the wind cavity. At time 10 kyr it interacts with the dense region of the progenitor's wind bubble (Fig. 6a) and is reverberated towards the centre of the explosion. Subsequent multiple internal reflections of the shock wave generate a large turbulent region (Fig. 6b). In Fig. 7, we show time sequences of the density field (rows) of an SNR produced by a $60\,\mathrm{M_\odot}$ star moving with different space velocities (columns). The bulk motion of the star spans from $v_\star = 10$ (left column) to $40\,\mathrm{km\,s^{-1}}$ (right column), and the remnants are displayed from 10 (top row) up to 100 kyr (bottom row) after the explosion.

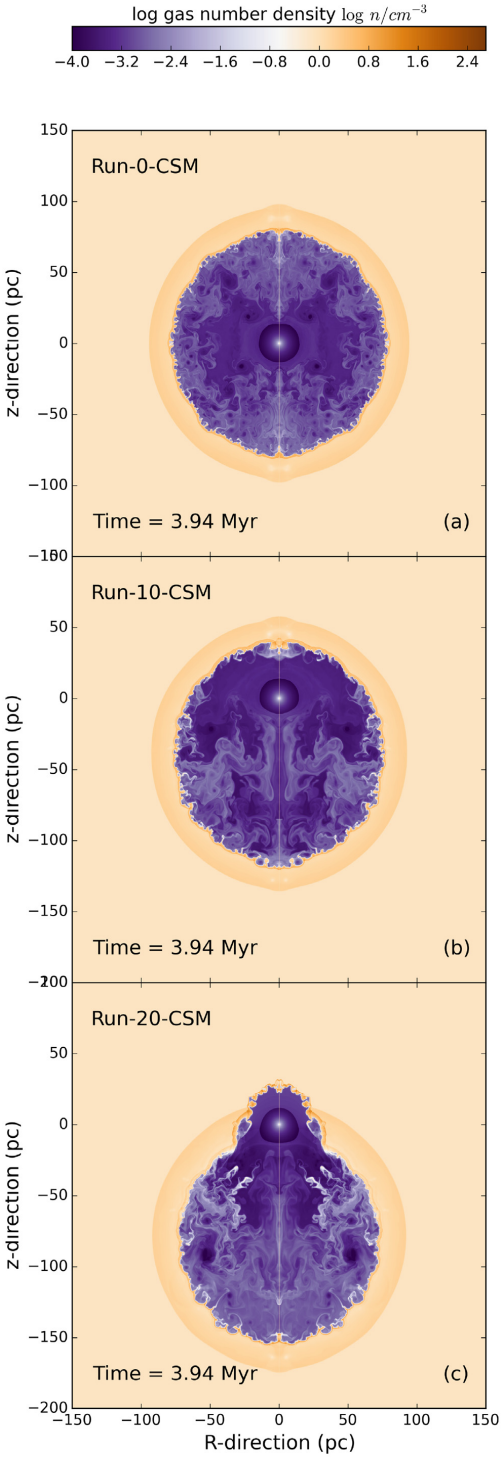

Figure 4. Density field (in $\mathrm{cm^{-3}}$) of the circumstellar medium of a massive star moving with $v_\star = 0$ (a), 10 (b), and $20\,\mathrm{km\,s^{-1}}$ (c) at the pre-supernova time. On each panel the star is located at the origin.

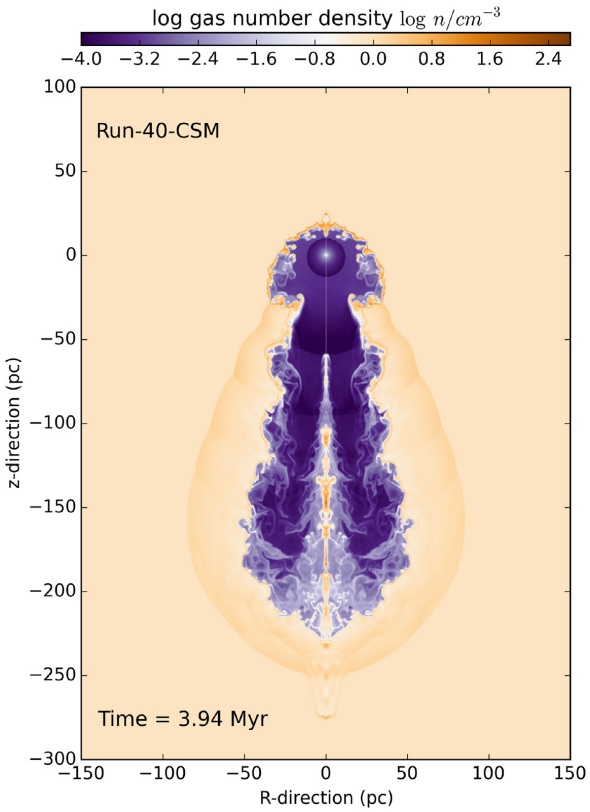

Figure 5. Same as Fig. 4 for a star moving with $v_\star = 40\,\mathrm{km\,s^{-1}}$. The star is located at the origin.

Our model Run-10-SNR with a slowly moving star is plotted in the first column of panels of Fig. 7. The shock wave is clearly identifiable in Fig. 7(a) as it has not yet interacted with the termination shock of the wind bubble. Reflected shocks form when the shock wave collides with termination shock of the wind bubble and with the dense main-sequence shell, respectively, making interior of the bubble asymmetric (Fig. 7d). At later times (50–100 kyr), the part of the shock wave which propagates along the stellar direction of motion through the bubble, penetrates the dense layer of shock ISM gas and makes it slightly denser as it had more time to interact with it, while the interior of the remnant is filled with a mixture of low-density, high-temperature ejecta and filamentary shocked wind material which keeps on melting with each other (Figs 7g and j).

In our model Run-20-SNR, the ejecta first fill the protuberance generated by the evolved Wolf–Rayet wind (Fig. 7b). As for a slower supernova progenitor, the shock wave progressively penetrates and expands into the entire upper cavity of the remnant which turns into a hot region of mixed wind and ISM material. The shock wave moves back and forth inside the post-main-sequence mushroom as it experiences multiple reflections between the centre of the explosion and the walls of the protuberance (Figs 7e and h). Once it goes through, a transmitted shock front freely expands into the unperturbed ISM and begins to locally recover a global spherical aspect, albeit affected by Rayleigh–Taylor instabilities (Fig. 7k). Simultaneously, the unstable shock wave expands downstream the progenitor star's direction inside the cavity and eventually reaches the bottom of the wind bubble (Fig. 7k).

In our fast-moving model Run-40-SNR, the supernova shock first fills the Wolf–Rayet bubble, which gets heated by reverberations against the unstable post-main-sequence ring (Figs 7c, f, and i). It is then channelled as a jet-like extension to the spherical region of shocked ejecta into the tubular cavity formed by the tail of the progenitor's bow shock with the mechanism described in Blandford

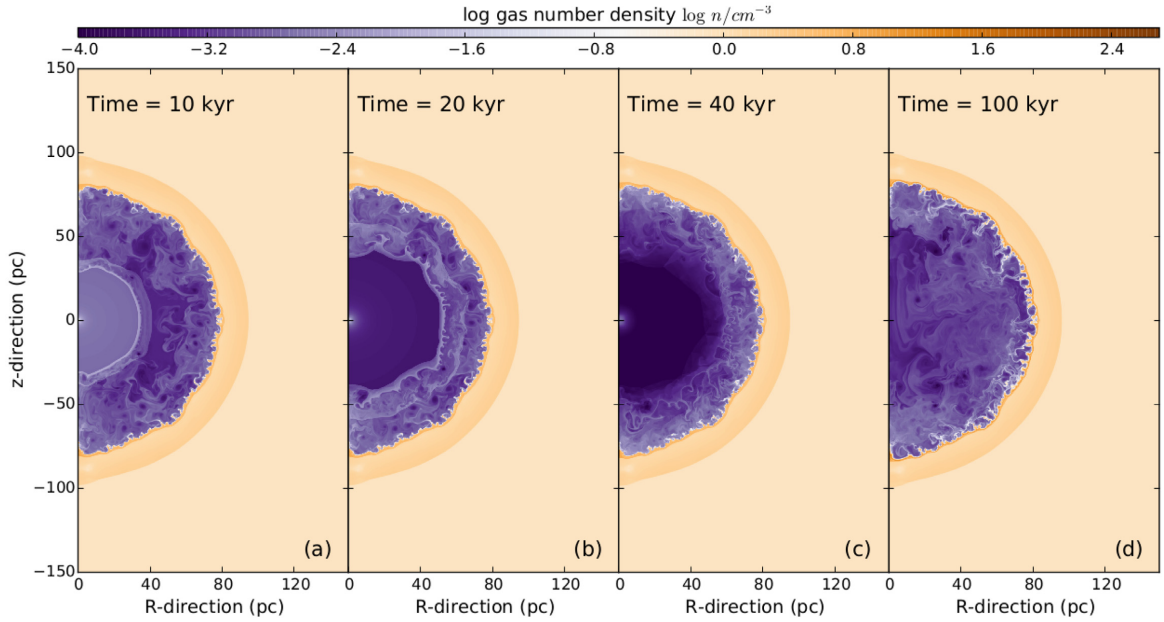

Figure 6. Density fields (in $\mathrm{cm^{-3}}$) in the SNR of a $60\,\mathrm{M_\odot}$ star at rest throughout its entire pre-supernova evolution. Panel (a, left) shows the reflection of the shock wave off the perimeter of the wind bubble at time 10 kyr, and panel (b, right) displays the end state after internal reflection at time 100 kyr.

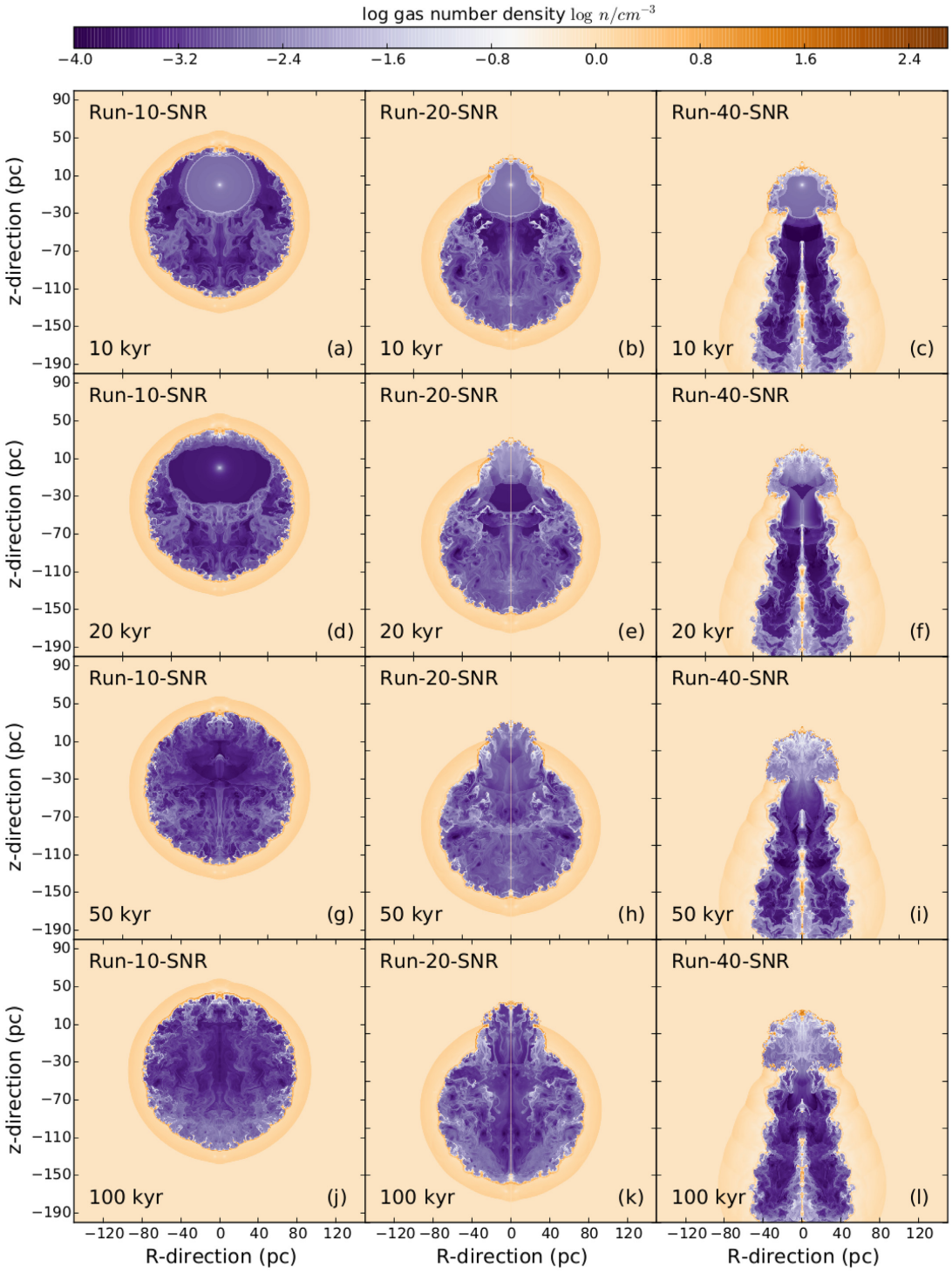

Figure 7. Density fields (in cm^{-3}) of the SNRs generated by a moving $60\,M_{\odot}$ stars. The columns display the models Run-10-SNR (left, $v_{\star} = 10\,km\,s^{-1}$), Run-20-SNR (middle, $v_{\star} = 20\,km\,s^{-1}$), and Run-40-SNR (right, $v_{\star} = 40\,km\,s^{-1}$). Each remnant is shown at times 10 (top row, panels a–c), 20 (second row, panels d–f), 50 (third row, panels g–i), and 100 kyr (bottom row, panels j–l), respectively.

et al. (1983) and Cox, Gull & Green (1991). Last, the reflection of the shock wave that also happens inside the tail of the bow shock fills the main-sequence nebula with hot gas as described in Meyer et al. (2015), see Fig. 7(l).

3.3 X-ray signature

The thermal X-ray luminosity for the circumstellar nebulae and the SNRs of our massive star is plotted as a function of time in Fig. 8.

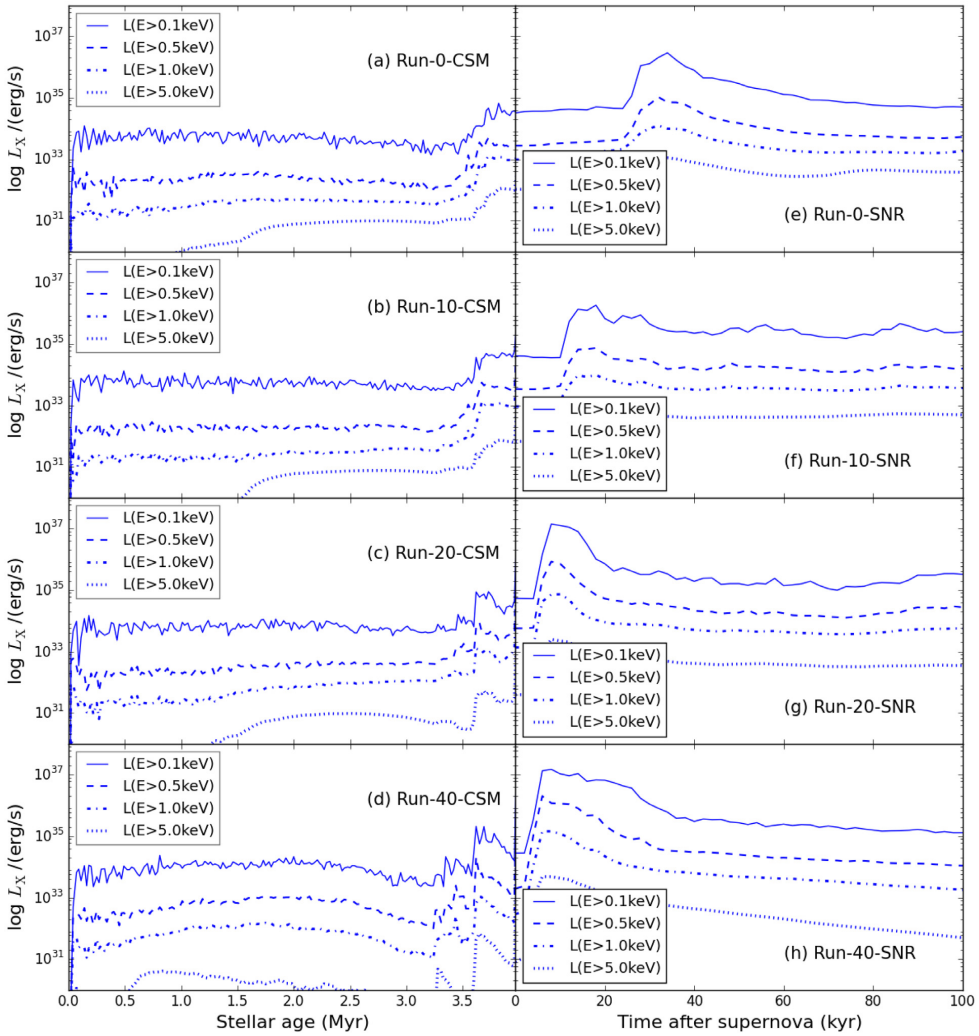

Figure 8. Light curves of thermal X-ray before (left-hand panels) and after the supernova explosion (right-hand panels). The integrated luminosity is plotted as a function of time, for different energy bands (in erg s^{-1}, blue lines) and for several space velocities of the progenitor, spanning from $v_\star = 0\,\mathrm{km\,s^{-1}}$ (top panels) to $v_\star = 40\,\mathrm{km\,s^{-1}}$ (bottom panels), respectively.

To predict the emission properties of our old ($10 - 100$ kyr) SNRs, we generate X-ray light curves (cf. Meyer et al. 2015). For each simulation snapshot, the X-ray emission coefficient, $j_\mathrm{X}^{E\geq\alpha}$ for the $E \geq \alpha$ energy band, is calculated and integrated over the whole nebula

$$L_X^{E\geq\alpha} = \iint_{\mathrm{SNR}} j_\mathrm{X}^{E\geq\alpha}(T) n_\mathrm{H}^2 \mathrm{dV}, \quad (17)$$

where n_H is the hydrogen number density in the SNR. The thermal X-ray emission coefficient of the diffuse ISM is tabulated as a function of temperature with the XSPEC[4] software (Arnaud 1996) which uses the solar abundances of Asplund et al. (2009).

The pre-supernova evolution of the thermal X-ray luminosity in our model Run-0-CSM, in which the star is at rest, begins by a rapid increase up to $L_\mathrm{X}^{E\geq0.1\,\mathrm{keV}} \approx 10^{34}\,\mathrm{erg\,s^{-1}}$ during the initial expansion of the wind bubble, followed by a nearly constant brightness throughout the entire main-sequence phase of the star (up to ≈ 3.2 Myr). The small luminosity variations during this phase are caused by the instabilities in the shocked ISM. When the star moves quickly, an important mechanism is vortex shedding, described in Wareing, Zijlstra & O'Brien (2007) and Green et al. (2019). A slight increase of the luminosity $L_\mathrm{X}^{E\geq0.1\,\mathrm{keV}}$ coincides with the post-main-sequence evolutionary phases of the star, when the nebula reaches $L_\mathrm{X}^{E\geq0.1\,\mathrm{keV}} \approx 10^{35}\,\mathrm{erg\,s^{-1}}$. This represents the fraction of the stellar wind mechanical luminosity that is not lost by, e.g. forbidden-line emission of the hot diluted gas in the shock wind region and/or by the ISM gas heated by thermal transfer (Mackey et al. 2015; Green et al. 2019). The light curves in the other energy bands exhibit similar behaviour, albeit offset by 1, 2, and 4 order of magnitude for the luminosities $L_\mathrm{X}^{E\geq0.5\,\mathrm{keV}}$, $L_\mathrm{X}^{E\geq1.0\,\mathrm{keV}}$, and $L_\mathrm{X}^{E\geq5.0\,\mathrm{keV}}$, respectively. The low level of $L_\mathrm{X}^{E\geq5.0\,\mathrm{keV}}$ illustrates that the hot gas ($T \geq 10^7$ K) emitting by free–free emission negligibly contributes to cooling in the nebula. The soft X-ray luminosity that we obtain from our model is consistent with predictions for nebulae around Wolf–Rayet stars, i.e. of the order of $10^{33}\,\mathrm{erg\,s^{-1}}$ (Dwarkadas &

[4] https://heasarc.gsfc.nasa.gov/xanadu/xspec/

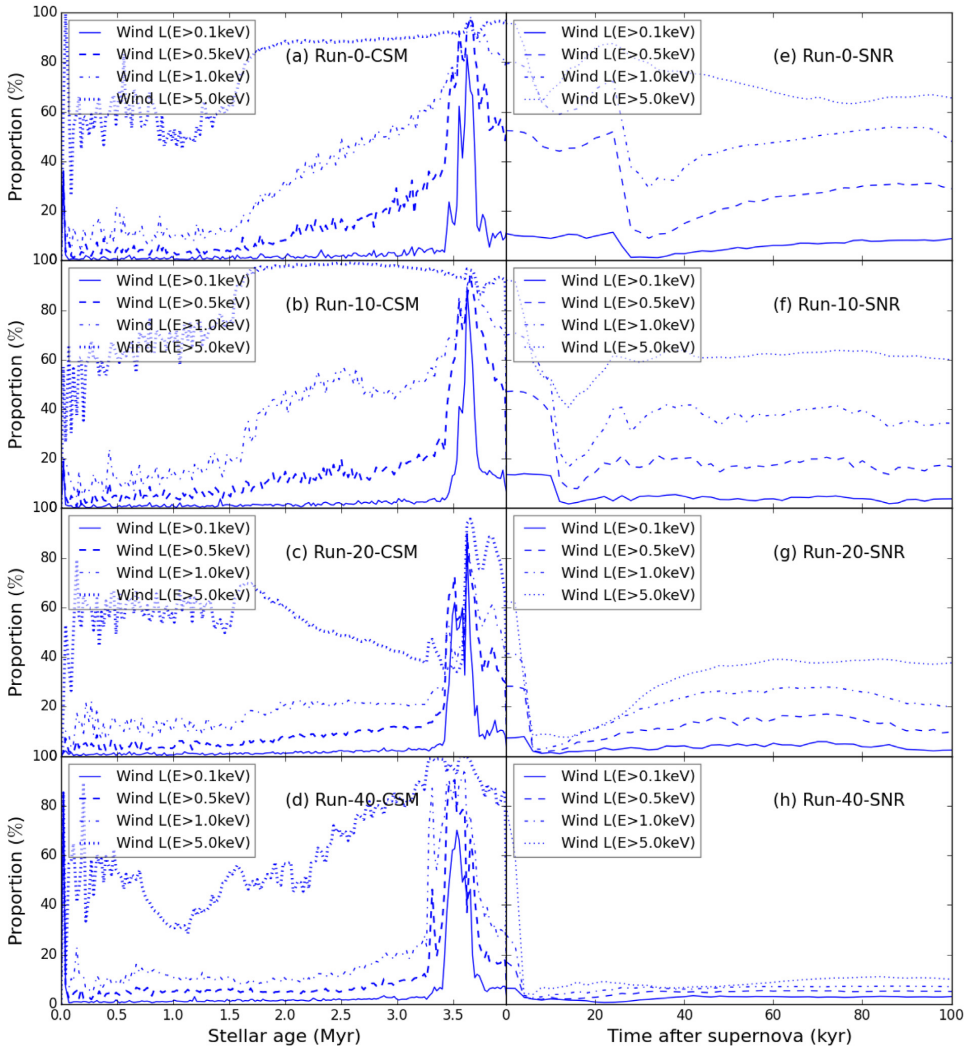

Figure 9. Stellar wind contributions to the thermal X-ray luminosity (in per cent) as a function of time for the pre-supernova epoch (left-hand panels) and the SNR phase (right-hand panels). Each panel covers several energy bands, and each row shows results for different space velocities of the progenitor, spanning from $v_\star = 0\,\mathrm{km\,s^{-1}}$ (top panels) to $v_\star = 40\,\mathrm{km\,s^{-1}}$ (bottom panels), respectively.

Rosenberg 2013; Toalá & Guerrero 2013; Toalá et al. 2014), and the hard component from hot gas is dimmer (Chu et al. 2003). This trend is not greatly affected by the stellar motion of the high-mass star, see Figs 8(b)–(d), except during the post-main-sequence evolutionary phases during which the highest energy emission, $L_\mathrm{X}^{E\geq5.0\,\mathrm{keV}}$, exhibits stronger variations as $v_\star$ increases, reflecting the fact that the wind material released by the star interacts differently with the main-sequence bubble and/or the ISM material, see our model Run-40-CSM at times 3.2–3.7 Myr (Fig. 8d).

The post-supernova evolution of the thermal X-ray luminosities begins with $L_\mathrm{X}^{E\geq0.1\,\mathrm{keV}} \approx 10^{34}\,\mathrm{erg\,s^{-1}}$ in the static star case (Fig. 8e) and slightly more for a runaway progenitor (Fig. 8h). A sudden rise of the light curves happens when the forward shock collides with the wind termination shock. In the static case this happens around 25 kyr after the explosion (see Figs 8e, 7a and d) and sooner if the bulk motion of the progenitor is larger (Figs 8f–h) since the stand-off distance of the corresponding bow shock is smaller (Wilkin 1996). The luminosities then decrease, none the less, they are interspersed with additional peaks and/or variations provoked by the reflections of the reverberated shock wave on to the cavity's wall. As before the time of the explosion, the luminosities in the more energetic bands are about 1, 2, and 3 order of magnitude lower for $L_\mathrm{X}^{E\geq0.5\,\mathrm{keV}}$, $L_\mathrm{X}^{E\geq1.0\,\mathrm{keV}}$, and $L_\mathrm{X}^{E\geq5.0\,\mathrm{keV}}$, respectively, i.e. the remnants of runaway progenitors are easier to observe in the soft X-ray band than in the hard X-ray band. This order relation persists throughout the expansion of the SNR in the ISM (Figs 8f–h). However, the hard X-ray emission decreases faster as function of time because the SNR expands into the ISM and cools so that the hot gas contribution to the emission is less and less important (Meyer et al. 2015).

Fig. 9 plots the evolution of the stellar wind contribution to the thermal X-ray luminosity, calculated for each energy band as

$$L_\mathrm{X}^{E\geq\alpha} = \iint_\mathrm{SNR} j_\mathrm{X}^{E\geq\alpha}(T) n_\mathrm{H}^2 Q_1 \mathrm{dV}, \tag{18}$$

where Q_1 is the passive scalar discriminating stellar wind from other kinds of material. The $E \geq 5.0\,\mathrm{keV}$ luminosity mostly originates

from the stellar wind while the emission at $E \geq 1.0$ keV largely comes from the shocked ISM gas. The stellar wind contribution to the latter is about a few per cent when the bubble grows at times $\leq$ 1.5 Myr and increases up to $\geq$ 80 per cent when the star has evolved to the post-main-sequence phases, see our models Run-0-CSM and Run-10-CSM (Figs 9a and b). In the runaway progenitor cases, this contribution reaches only about 60 per cent (Fig. 9d) which means that the expelled luminous blue variable and Wolf–Rayet shells emit more by thermal bremsstrahlung than the ISM material. In the other energy bands, the stellar wind contribution of their emission is negligible during the main-sequence phase, as it represents $\leq$ 10–15 per cent of the overall emission, but it progressively increases when the bubble is formed at time 1.5 Myr. This changes during the luminous blue variable and the Wolf–Rayet phases when the wind contribution to $L_{\rm X}^{E\geq 0.5\,{\rm keV}}$ rises up to 90 per cent. Note that for a static star $L_{\rm X}^{E\geq 0.1\,{\rm keV}}$ exhibits variations reflecting the successive mass-loss rate variations happening during the luminous blue variable eruptions and Wolf–Rayet events (Fig. 9a). These variations of the stellar wind contribution to $L_{\rm X}^{E\geq 0.1\,{\rm keV}}$ are independent of the speed of the progenitor star (Figs 9b–d).

The proportion of thermal X-ray-emitting wind material in the SNRs is a function of the bulk motion of the progenitor star, and, consequently, relates on the distribution of circumstellar material at the supernova time. Its largest contribution, about 10 per cent, arises in the $E \geq 5.0$ keV energy band (Figs 9e–h). This further illustrates how the contribution of stellar wind to the soft X-ray emission in the remnant decreases with gas temperature. Once the expansion of the supernova shock wave in the unperturbed stellar wind ceases ($<$ 5–10 kyr), the wind contribution to the hard X-ray emission decreases from about 80 per cent in the static case to below 10 per cent for our fastest-moving progenitor. Our results highlight that thermal X-ray emission of remnants from fast-moving progenitors originates from ISM material, as most of the wind gas has been advected far from the location of the explosion and had time to cool before the moment of the blastwave–circumstellar medium interaction. Note that the figure represents the proportion of wind material exclusively, the rest originating from the sum of the shocked ISM gas plus the ejecta melting into the SNR (see Section 3.4). The ejecta contribution to the thermal X-ray emission is not important compared to that of the wind and ISM because its mass is much smaller than the overall remnant mass.

3.4 Mixing of material

Fig. 10 illustrates the temporal evolution of the mixing of ejecta/wind/ISM material in our SNR model Run-20-SNR for a progenitor star moving with speed $v_\star = 20\,{\rm km\,s^{-1}}$. The panels correspond to the remnant at times 10 (a), 20 (b) 40 (c), and 100 kyr (d) after the explosion, respectively. On each plot, the left-hand side shows the value of $1 - Q_1$, i.e. the proportion of ISM gas in the computational domain and the right-hand side shows the value of the tracer Q_1 for the stellar wind material, respectively, both spanning from 0 to 1, with 0 standing for the complete absence of a given species while 1 stands for a medium exclusively made of this kind of species, respectively. The black contours indicate the locations where the remnant temperature is $T = 10^5$, 10^6, and 10^7 K, while the white lines are isocontours for the gas density with levels $n = 1.0$, 10^1, 10^2, and $10^3\,{\rm cm^{-3}}$. Additionally, the overplotted blue contours trace the regions at which ejecta contribute 10 per cent of the gas.

After 10 kyr, the supernova blastwave bounces against the ring opened by the final Wolf–Rayet wind of the defunct star, where it is partially reverberated towards the centre of the explosion and partially transmitted to the ISM through the bow shock according to the mechanism described in Borkowski et al. (1992) and Meyer et al. (2015). The SNR is mostly filled with hot stellar wind gas surrounded by a main-sequence shell of dense, cold ISM material. The interface between wind and ISM is the former unstable contact discontinuity of the pre-supernova bubble with which the various post-main-sequence shells collided (Fig. 10a). After 20–40 kyr, the supernova shock wave that passed through the Wolf–Rayet wind keeps on expanding into the unperturbed ISM, and the reflection of its forward shock to the centre of the explosion begins, enhancing the mixing of stellar wind and ISM material. This is the process that is responsible for the formation of Cygnus-loop SNR, although that particular objects concern a lower mass, red supergiant progenitor (Meyer et al. 2015; Fang et al. 2017).

Simultaneously, the reverberated shock wave develops instabilities at the interface between ejecta and mixed wind/ISM material (Figs 10b and c), while the region occupied by the ejecta further expands into the interior of the wind blown cavity (Fig. 10c). After 40 kyr, the SNR assumes an asymmetric morphology made of the large, spherical, former main-sequence bubble (lower part) and the Wolf–Rayet-produced cocoon (upper part). The bubble concentrates the stellar wind material surrounded by a layer of shocked ISM mixed with ejecta material while the almost ejecta-free upper mushroom is filled with a mixture of wind and ISM gas. The ejecta material lies in a tubular zone located at the inside of the bottom region of the remnant, directed towards to the direction of motion of the supernova progenitor, as well as in the region to the former centre of the explosion (Fig. 10d).

Fig. 11 is similar to Fig. 10 for our model Run-40-SNR with a runaway progenitor star moving at $v_\star = 40\,{\rm km\,s^{-1}}$. As the progenitor rapidly moves, the main-sequence bubble is elongated. The blastwave bounces against the stellar wind bow shock of the progenitor which is separated from the nebula that was produced during its main-sequence phase of evolution. This advects the ejecta all across the Wolf–Rayet shell-like region generated during the progenitor's ultimate evolutionary stage, which is centred on to the location of the explosion (Figs 11a and b). Between 20 kyr and 40 kyr, the shockwave/Wolf–Rayet shell interaction continues, and so does the mixing of material, as part of the supernova shock wave expands into the low-density cavity of unperturbed wind material, along the direction opposite of the motion of the progenitor. Pushed downward by the ejecta, the former unperturbed shocked stellar wind develops instabilities at its interface with the shocked ISM (Figs 11b and c).

At time 40 kyr, the SNR has an internal structure different from that of Run-20-SNR (with $v_\star = 20\,{\rm km\,s^{-1}}$). It is made of an upper quasi-circular region and a longer, tail-like structure. Both regions have efficiently mixed stellar wind and ISM gas. The ejecta are both located in the upper cocoon and in the main-sequence wind bubble (Fig. 11d). Models Run-20-SNR and Run-40-SNR reveal the importance of progenitor motion in the mixing of different materials in remnants of massive runaway progenitors. The degree of wind/ISM mixing and the distances from the centre of the explosion at which it happens increases with $v_\star$ (Figs 10d and 11d) as a consequence of the elongation of the stellar wind bubble. It channels the supernova shock wave when the Mach number of the progenitor moving through the ambient medium is $v_\star/c_{\rm s} \sim 2$, with $c_{\rm s}$ the unperturbed ISM sound speed, while the ejecta distribution remains is spherical only if the progenitor is either at rest or slowly moving and explode inside and/or off-centred in its main-sequence circumstellar bubble, at least in the ambient medium that we consider.

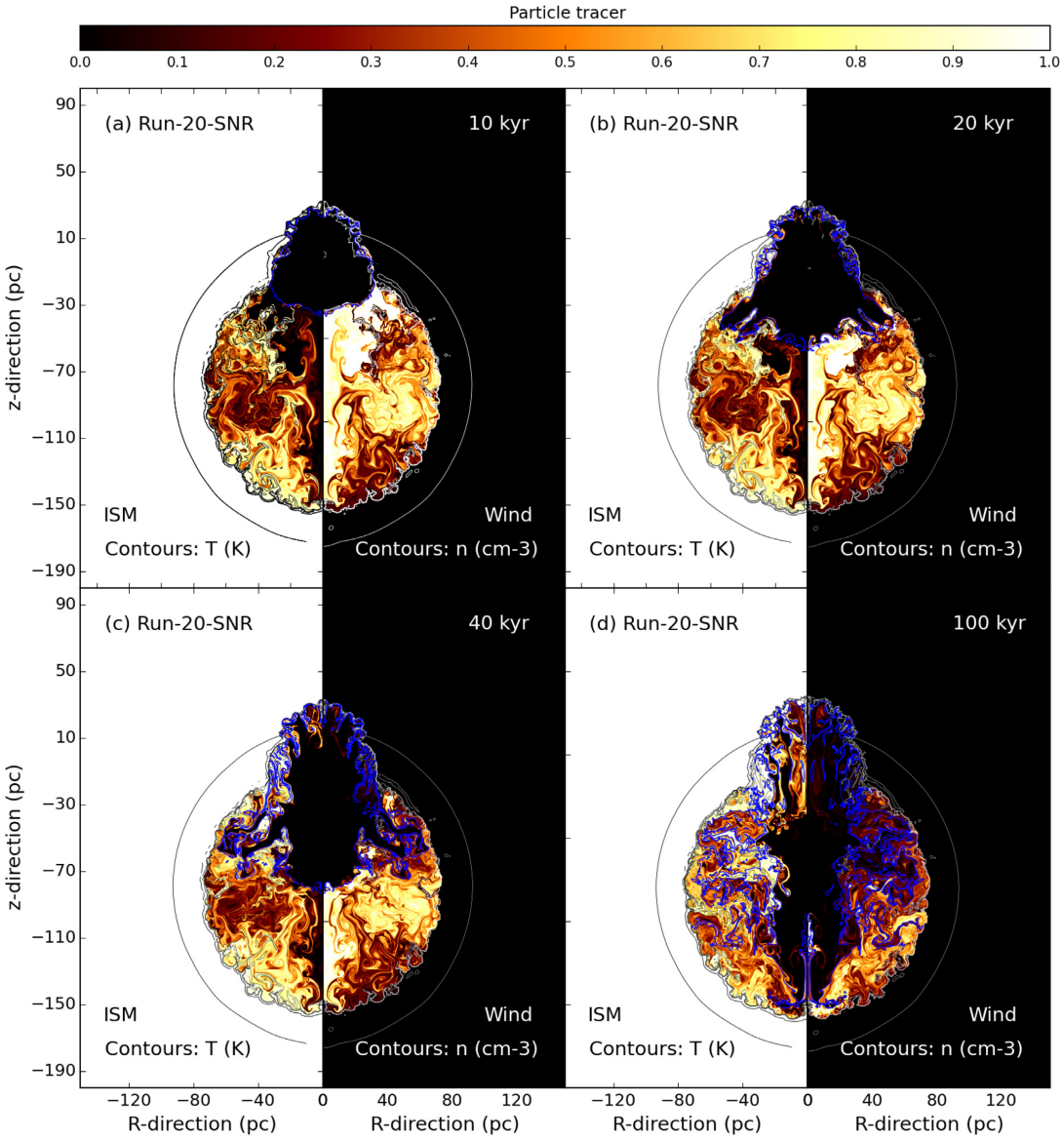

Figure 10. Mixing of material in the SNR generated by a progenitor moving with velocity 20 km s^{-1}, shown at times 10 (a), 20 (b), 50 (c), and 100 kyr (d). The figures plot the value of the quantity $1 - Q_1$ representing the proportion of ISM material (left part of the panels) and the value of the passive scalar tracer Q_1 standing for the proportion of stellar wind gas (right part of the panels), respectively. The overplotted black contours indicate the temperature ($T = 10^5$, 10^6, and 10^7 K, left part of the panels), while the white contours stands for the gas number density ($n = 1.0$, 10^1, 10^2, and 10^3 cm^{-3}, right part of the panels). The blue contours of the passive scalar field Q_2 indicate a 10 per cent contribution of ejecta in number density.

4 DISCUSSION

This section presents the limitations of our method, discusses our results in the context of previous studies, compares our results with observations of asymmetric SNRs, and further discusses the potential role of stellar wind nebula as cosmic ray accelerators.

4.1 Caveats of the models

The first limitation of our method is the two-dimensional nature of the hydrodynamical simulations, which restricts the realism of the modelled wind bubbles and SNRs. Axisymmetry in particular prevents us from investigating the effects of, e.g. the angles between the direction of motion of the progenitor star, the local interstellar magnetic field, and the axis of stellar rotation. Three-dimensional simulations such as in Katushkina et al. (2017, 2018) would be highly desirable for a more realistic depiction of the surroundings of massive stars, however, their huge computational costs would inhibit scanning the parameter space. The treatment of the intrinsic nature of the ISM is simplified by assuming a uniform medium of number density 1 cm^{-3} and temperature 8000 K (Meyer et al. 2014b). Any intrinsic native turbulence in the velocity field of the medium,

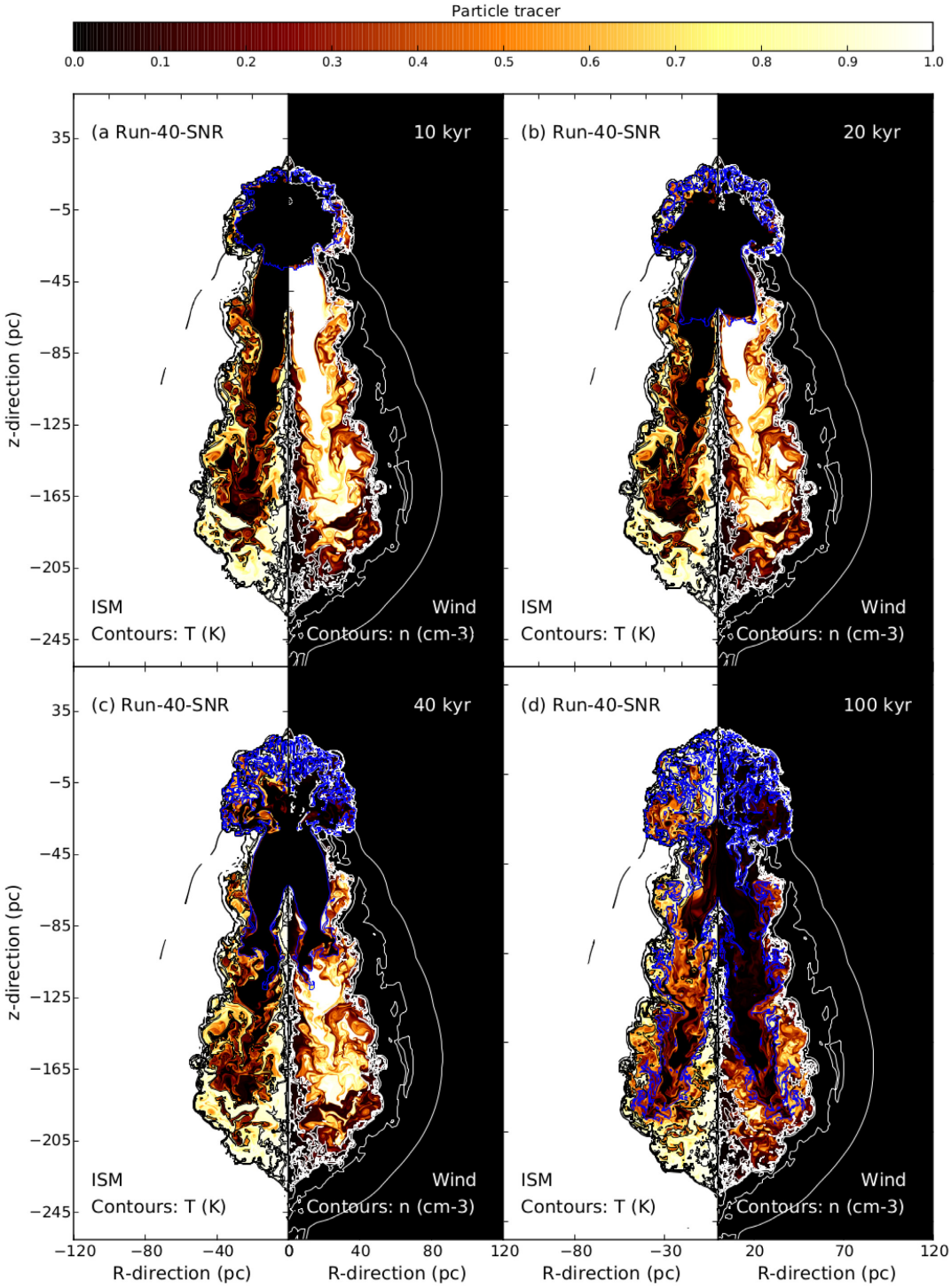

Figure 11. Same as Fig. 10 but here for a progenitor moving with velocity 40 km s^{-1}. The figures plot the value of the quantity $1 - Q_1$ representing the proportion of ISM material (left part of the panels) and the value of the passive scalar tracer Q_1 standing for the proportion of stellar wind gas (right part of the panels), respectively. The blue contours of the passive scalar field Q_2 indicate a 10 per cent contribution of ejecta in number density.

clumps, or filamentary structures that could potentially influence the development of shocks wave are also neglected, see Gvaramadze et al. (2018). The stellar wind history used as boundary conditions is also not unique, and other evolutionary tracks and alternative stellar rotation rates can change the luminous blue variable or the Wolf–Rayet phase of massive stars (Ekström et al. 2012). They would produce a different wind bubble and consequently result in dissimilar SNRs.

4.2 Comparison with previous studies

Our method uses a self-consistently calculated stellar evolution history as boundary for the stellar wind, and the hydrodynamical simulations are performed for a different corner of the parameter space and on a higher spatial grid resolution than in other studies. Previous works tackled the problem of the circumstellar medium of Wolf–Rayet-evolving stars either considering static stars (Garcia-Segura & Mac Low 1995; Garcia-Segura, Langer & Mac Low 1996b) or using lower resolution calculations of moving stars in the context of the formation of dense circumstellar regions eventually leading to GRBs (Eldridge et al. 2006; van Marle et al. 2006, 2007; Eldridge, Langer & Tout 2011). The series of work of Brighenti & D'Ercole (1994, 1995a,b) is the closest to our approach in the sense that it explores the morphology of wind bubbles blown by massive stars by first calculating the evolution of their surroundings before launching a blastwave in it.

Only one study of this series investigates the shape of SNRs from moving Wolf–Rayet progenitors, although not priorily undergoing luminous blue variable eruptions (Brighenti & D'Ercole 1994). Their model 1 has ISM properties and a stellar motion similar to our run Run-20-SNR, however, assuming a different stellar wind history as it includes a cool red supergiant phase while we here simulate luminous blue variable and Wolf–Rayet stars. A slowly moving progenitor (our calculations Run-10-CSM and Run-10-SNR) is also not considered in that work. Last, a couple of works have been tailored to the study of specific young SNRs, whose shape might be explained by the presence of a bow shock around the progenitor prior to its explosion. These studies mainly concern the Crab nebula (Cox et al. 1991) and the Kepler SNR (Borkowski et al. 1992; Velázquez et al. 2006; Chiotellis et al. 2012; Toledo-Roy et al. 2014). These models apply to much younger ($\sim 1000\,\mathrm{yr}$) SNRs than ours and cover a different corner of the problem's parameter space.

4.3 Comparison with observations

4.3.1 Comparison with existing wind nebulae: the case of BD+43°3654

The most obvious object permitting a comparison with our models for the pre-supernova circumstellar medium of the $60\,\mathrm{M}_\odot$ of Groh et al. (2014) is the very massive $\simeq 55$–$85\,\mathrm{M}_\odot$ runaway star BD+43°3654, which probably escaped from the Cygnus OB2 region (Comerón & Pasquali 2007). BD+43°3654 is an $\approx 1.6\,\mathrm{Myr}$-old, O4If-typed main-sequence stellar object stellar whose properties have been constrained to be $\dot{M} \approx 10^{-5}\,\mathrm{M}_\odot\,\mathrm{yr}^{-1}$ and $v_\mathrm{w} \approx 2300\,\mathrm{km\,s}^{-1}$, respectively. Its surrounding is shaped as a well-defined, axisymmetric bow shock nebula visible in the infrared. Using the observed geometry of the bow shock, its proper motion has been estimated to be $\approx 40\,\mathrm{km\,s}^{-1}$ and its ambient medium density to be $n_\mathrm{ISM} = 6\,\mathrm{cm}^{-3}$ (Comerón & Pasquali 2007).

Nevertheless, the formula for the stand-off distance of a bow shock measured along the direction of motion of its driving star

$$R_\mathrm{SO} = \sqrt{\frac{\dot{M} v_\mathrm{w}}{4 n_\mathrm{ISM} v_\star^2}}, \tag{19}$$

informs that n_ISM is a function of $\dot{M}$ (Baranov et al. 1971; Wilkin 1996) and the discoverers of BD+43°3654's bow shock discussed in Comerón & Pasquali (2007) that any overestimate of the wind properties $\dot{M}$ or v_w will translate into a overestimate of its background ISM density, which may therefore be smaller than $n_\mathrm{ISM} = 6\,\mathrm{cm}^{-3}$ by a factor of $\approx$3. This is comparable with the value of $\simeq 0.79\,\mathrm{cm}^{-3}$ used in our study. By interpolating our stellar evolutionary track, we find $\dot{M} \approx 10^{-5}\,\mathrm{M}_\odot\,\mathrm{yr}^{-1}$ and $v_\mathrm{w} \approx 2865\,\mathrm{km\,s}^{-1}$ for the stellar age of BD+43°3654 $\approx 1.6\,\mathrm{Myr}$, that is rather consistent with the derivations of Comerón & Pasquali (2007). Hence, our model Run-40-CSM fits well the case of BD+43°3654 and our simulation can be considered as a prediction of the future evolution of its pre- and eventual post-supernova circumstellar medium.

4.3.2 Comparison with existing supernova remnants

We note that Brighenti & D'Ercole (1994, 1995b) proposed that barrel-shaped SNRs such as G296.5+10.0 (Storey et al. 1992; Harvey-Smith et al. 2010) and other bipolar remnants of similar morphology (Bisnovatyi-Kogan, Lozinskaia & Silich 1990) have been generated by the interaction between a supernova shock wave with the walls of a low-density wind cavity produced by the stellar motion of its own progenitor, into which the forward shock has been channelled (Cox et al. 1991). This idea has been supported by Meyer et al. (2015) with optical H α and [OIII] synthetic emission maps derived from hydrodynamical simulations of red supergiant-evolving runaway progenitor stars. However, most such SNRs have been shown to be aligned with the galactic magnetic field and directed towards the Galactic centre. This observational evidence suggests that their formation is better explained as effect of the interstellar magnetic field in Galactic spiral arms (Gaensler 1998). This hypothesis has been supported with both magnetohydrodynamical simulations and non-thermal synchrotron and radio emission maps (Orlando et al. 2007).

We can also see noticeable differences between our SNRs models generated by runaway luminous blue variable/Wolf–Rayet progenitors and those for runaway red supergiant progenitors (see Meyer et al. 2015). In the case of a red supergiant progenitor, the ejecta blow out beyond the last wind bow shock and freely expands into the ISM, if the progenitor moves sufficiently fast and/or if the stellar wind is not too dense. A heavier ZAMS stars and/or a slower progenitor generate a denser bow shock of swept-up ISM which will trap the new-born cold red supergiant shell and the subsequent shock wave. This feature is present in all of our runaway ($v_\star \geq 20\,\mathrm{km\,s}^{-1}$) Wolf–Rayet progenitor runs. One should therefore expect to observe remnant from runaway Wolf–Rayet progenitor with Cygnus Loop nebula-like morphology, which would resemble a remnant of a runaway red supergiant-evolving star (Tenorio-Tagle, Rozyczka & Yorke 1985; Aschenbach & Leahy 1999; Meyer et al. 2015; Fang et al. 2017), although of different size and chemical composition. Inversely, our results argue against a $60\,\mathrm{M}_\odot$ ZAMS star as progenitor of historical SNRs such as Kepler's or Tycho and support solutions involving symbiotic binary systems of a runaway AGB star together with an type Ia explosive companion (Borkowski et al. 1992; Velázquez et al. 2006; Vigh et al. 2011; Chiotellis et al. 2012; Williams et al. 2013; Toledo-Roy et al. 2014).

The SNR G109.1−1.0 (CTB 109) has for long been suspected to be an isolated SNR whose progenitor may have moved quickly (Brighenti & D'Ercole 1994, 1995b). However, evidence of dense molecular material aside of the remnant (Sánchez-Cruces et al. 2018) suggests it being produced by a shock wave evolving into a rather low-density medium that is sparsed with higher density cloudlets (Coe et al. 1989; Sasaki et al. 2006), see also the numerical simulations of Bolte, Sasaki & Breitschwerdt (2015). The remnant VRO 42.05.01 (Arias et al. 2019) may be the archetypal example of an SNR interacting with an ISM cavity. The low-density region inducing the asymmetries may have been formed

by a previous supernova (Rho & Petre 1997) or by the motion of the progenitor star itself (Derlopa et al. 2019). Recent observations of molecular emission and numerical studies tailored to VRO 42.05.01 suggest that the progenitor could have been a massive runaway star interacting with a hot diluted ISM tunnel (Derlopa et al. 2019), but indicated also that an asymmetric Wolf–Rayet wind is sufficient to produce its overall morphology (Chiotellis et al. 2019). The influence of the anisotropy of post-main-sequence stellar winds should be investigated in future studies. The SNR S147 has been suggested to result from a Wolf–Rayet progenitor (Gvaramadze 2006) in a multiple system (Dinçel et al. 2015).

4.4 Are Wolf–Rayet nebulae efficient cosmic rays accelerators?

There is a growing interest in the non-thermal surroundings of massive stars. The strong winds of OB and Wolf–Rayet stars generate magnetized termination shocks such that a proportion of the stellar mechanical luminosity could power high-energy cosmic rays (Webb, Axford & Forman 1985; Seo, Kang & Ryu 2018). A number of numerical simulations calculating the acceleration and diffusion of cosmic rays in static stellar wind/bow shock environments of massive stars have been performed (del Valle et al. 2013, 2015; del Valle & Pohl 2018), and speculative predictions were announced for the Bubble nebula, a runaway OB star moving through dense molecular gas (Green et al. 2019). Particle acceleration and the production of non-thermal emission in the surroundings of pre-supernova (runaway) massive stars are expected to arise from processes similar to those operating in young SNRs (Reynolds 2011), albeit with smaller efficiency (Voelk & Forman 1982; Zirakashvili & Ptuskin 2018).

Per object, circumstellar cosmic ray feedback of high-mass stars is of lower importance in the Galactic energy budget compare to other non-thermal-emitting objects such as SNRs (Seo et al. 2018; Rangelov et al. 2019) or colliding winds in binaries (Benaglia & Romero 2003; De Becker et al. 2006; Reimer, Pohl & Reimer 2006; De Becker & Raucq 2013). Accordingly non-thermal X-rays from stellar wind bow shocks surrounding OB stars have not been detected to date (Toalá et al. 2016; De Becker et al. 2017; Toalá et al. 2017; Binder et al. 2019). Prajapati et al. (2019) recently claimed the detection of synchrotron emission from a series of shells and arc around the Wolf–Rayet nebula G2.4+1.4. Our results further explore the circumstellar medium of evolved massive stars and provide the background on which we shall investigate the synchrotron, inverse Compton and gamma-ray emission, e.g. using the RATPAC code (Telezhinsky, Dwarkadas & Pohl 2012a,b, 2013).

5 CONCLUSION

Motivated by the existence of stars, whose mass exceeds $\sim 60\,M_\odot$ and which can either be affected by high proper motion and/or generate circumstellar nebulae by stellar wind–ISM interaction (Tatischeff, Duprat & de Séréville 2010; Gvaramadze & Gualandris 2011; Gvaramadze et al. 2013), we investigate the shaping of circumstellar nebulae around a non-rotating $60\,M_\odot$ stars (Groh et al. 2014) and we explore how they can influence the development of asymmetries in their SNRs. These stars are characterized by a violent evolution history including several successive luminous blue variable and Wolf–Rayet phases. Using high-resolution 2D hydrodynamical simulations performed with the PLUTO code (Mignone et al. 2007, 2012), we investigate how the ejection of the dense shells associated with these evolutionary phases can couple to the stellar proper motion and carve aspherical low-density cavities of wind material, inside of which the star dies as a core-collapse supernova. The resulting remnant therefore adopts anisotropies reflecting the imprint of star's past evolution history on to its close surroundings (Meyer et al. 2015). We consider several static, slowly moving, and fast stars evolving in the warm phase of the ISM, and we predict the thermal X-ray signature of both their stellar wind nebulae and SNRs up to 100 kyr after the explosion.

We show that, as long as such a massive ($\sim 60\,M_\odot$) progenitor star moves supersonically through the ISM, its subsequent SNR will display similarity to that of the Cygnus-loop nebulae. The role of the strong luminous blue variable and Wolf–Rayet shells winds predicted by the Geneva stellar evolutionary tracks (Groh et al. 2014) add to the asymmetries produced by the stellar motion as they induce outflows that can pierce the main-sequence wind bubble of the progenitor star, opening a route for the later supernova shock wave. A rather modest bulk motion ($10\,km\,s^{-1}$) of our $60\,M_\odot$ star is not sufficient to break the sphericity of the overall remnant as the expanding supernova shock wave is trapped into the defunct, quasi-spherical stellar wind bubble (Weaver et al. 1977).

However, as the progenitor star moves faster, the explosion is off-set with respect to the geometrical centre of the wind nebula and, in the runaway limit of the stellar motion, happens outside of the bubble, in a ring of Wolf–Rayet and ISM material. The shock wave blows out of the wind nebula, resulting in an homogeneous mixing of material throughout the elongated remnant, while ejecta are reverberated around the centre of the explosion. This leads to the formation of two-lobe structures ahead and behind the centre of the explosion, inside of which the degree of mixing of ejecta with wind and ISM materials is correlated to the progenitor's motion. Our pre-supernova nebulae and SNRs are bright in soft thermal X-rays from shocked ISM gas, except during the luminous blue variable eruptions of the progenitor when it comes from the stellar wind. Additionally, such remnants of low-velocity progenitors exhibit a hard X-rays component of shocked stellar wind.

Our results stress that a single runaway high-mass star can affect the chemical composition of an entire local region of the ISM, see e.g. Tatischeff et al. (2010). Consequently, we highlight the importance of chemically investigating the large-scale surroundings (~ 100 pc) of SNRs, as it is a trace of the possible runaway nature of the defunct star(s), but also since the distribution of enriched material that has mixed in it with the ISM informs on the past stellar evolution of supernova progenitor(s). Furthermore, our simulated remnants indicate that luminous blue variable/Wolf–Rayet-type progenitors cannot be the origin of SNRs with morphologies such as those of Cas A, RCW86, Kepler or Tycho. Their young age (≤ 2500 yr) and compact size are not in accordance with our results, which either support scenarios involvingType Ia supernova and/or suggest a non-Wolf–Rayet-evolving core-collapse progenitor. Stellar wind–ISM interaction should therefore be further investigated by scanning the parameter study of the problem and by modelling such remnants with, e.g. global 3D magnetohydrodynamical simulations. Particularly, the large termination shocks that form around luminous blue variable and Wolf–Rayet stars suggest that these wind nebulae might accelerate particles as high-energy cosmic rays. This is consistent with the recent monitoring of synchrotron emission from the Wolf–Rayet shell nebula G2.4+1.4 (Prajapati et al. 2019) and motivates future observational and theoretical studies on the non-thermal emission of circumstellar structures such as synchrotron and inverse Compton radiation.

ACKNOWLEDGEMENTS

The authors thank the anonymous referee for comments which improved the quality of the paper. DMAM and MP acknowledge B. Hnatyk for constructive discussion. The authors acknowledge the North-German Supercomputing Alliance (HLRN) for providing HPC resources that have contributed to the research results reported in this paper. MP acknowledges the Max Planck Computing and Data Facility (MPCDF) for providing data storage resources and HPC resources which contributed to test and optimize the PLUTO code. This research made use of the PLUTO code developed at the University of Torino by A. Mignone and collaborators, the MATPLOTLIB plotting library for the PYTHON programming language, and the XSPEC X-ray spectral fitting package developed by K. Arnaud and collaborators at the University of Maryland. DMAM thanks the Lorentz Center at the University of Leiden for organizing and hosting the workshop 'Historical Supernovae, Novae and Other Transient Events' in October 2019, where many insightful discussions which participated to the completion of this paper took place.

REFERENCES

Arias M. et al., 2019, A&A, 622, A6
Arnaud K. A., 1996, in Jacoby G. H., Barnes J., eds, ASP Conf. Ser. Vol. 101, Astronomical Data Analysis Software and Systems V. Astron. Soc. Pac., San Francisco, p. 17
Aschenbach B., Leahy D. A., 1999, A&A, 341, 602
Asplund M., Grevesse N., Sauval A. J., Scott P., 2009, ARA&A, 47, 481
Baranov V. B., Krasnobaev K. V., Kulikovskii A. G., 1971, Sov. Phys. Dokl., 15, 791
Benaglia P., Romero G. E., 2003, A&A, 399, 1121
Binder B. A., Behr P., Povich M. S., 2019, AJ, 157, 176
Bisnovatyi-Kogan G. S., Lozinskaia T. A., Silich S. A., 1990, Ap&SS, 166, 277
Blaauw A., 1993, in Cassinelli J. P., Churchwell E. B., eds, ASP Conf. Ser. Vol. 35, Massive Stars: Their Lives in the Interstellar Medium. Astron. Soc. Pac., San Francisco, p. 207
Blandford R. D., Kennel C. F., McKee C. F., Ostriker J. P., 1983, Nature, 301, 586
Blondin J. M., Koerwer J. F., 1998, New Astron., 3, 571
Bolte J., Sasaki M., Breitschwerdt D., 2015, A&A, 582, A47
Borkowski K. J., Blondin J. M., Sarazin C. L., 1992, ApJ, 400, 222
Brighenti F., D'Ercole A., 1994, MNRAS, 270, 65
Brighenti F., D'Ercole A., 1995a, MNRAS, 273, 443
Brighenti F., D'Ercole A., 1995b, MNRAS, 277, 53
Chevalier R. A., 1982, ApJ, 258, 790
Chiotellis A., Schure K. M., Vink J., 2012, A&A, 537, A139
Chiotellis A., Boumis P., Derlopa S., Steffen W., 2019, preprints (arXiv:1909.08947)
Chu Y.-H., Guerrero M. A., Gruendl R. A., García-Segura G., Wendker H. J., 2003, ApJ, 599, 1189
Coe M. J., Davies S. R., Fahlman G. G., Gregory P. C., 1989, MNRAS, 238, 649
Comerón F., Kaper L., 1998, A&A, 338, 273
Comerón F., Pasquali A., 2007, A&A, 467, L23
Cox C. I., Gull S. F., Green D. A., 1991, MNRAS, 250, 750
Cox N. L. J. et al., 2012, A&A, 537, A35
De Becker M., Raucq F., 2013, A&A, 558, A28
De Becker M., Rauw G., Sana H., Pollock A. M. T., Pittard J. M., Blomme R., Stevens I. R., van Loo S., 2006, MNRAS, 371, 1280
De Becker M., del Valle M. V., Romero G. E., Peri C. S., Benaglia P., 2017, MNRAS, 471, 4452
del Valle M. V., Pohl M., 2018, ApJ, 864, 19
del Valle M. V., Romero G. E., 2014, A&A, 563, A96
del Valle M. V., Romero G. E., De Becker M., 2013, A&A, 550, A112
del Valle M. V., Romero G. E., Santos-Lima R., 2015, MNRAS, 448, 207
Derlopa S., Boumis P., Chiotellis A., Steffen W., Akras S., 2019, preprint (arXiv:1909.06131)
Dgani R., van Buren D., Noriega-Crespo A., 1996, ApJ, 461, 372
Dinçel B., Neuhäuser R., Yerli S. K., Ankay A., Tetzlaff N., Torres G., Mugrauer M., 2015, MNRAS, 448, 3196
Dwarkadas V. V., 2007, ApJ, 667, 226
Dwarkadas V. V., Rosenberg D. L., 2013, High Energy Density Phys., 9, 226
Dyson J. E., 1975, Ap&SS, 35, 299
Dyson J. E., Gulliford P., 1975, Ap&SS, 37, 477
Ekström S. et al., 2012, A&A, 537, A146
Eldridge J. J., Genet F., Daigne F., Mochkovitch R., 2006, MNRAS, 367, 186
Eldridge J. J., Langer N., Tout C. A., 2011, MNRAS, 414, 3501
Fang J., Yu H., Zhang L., 2017, MNRAS, 464, 940
Franco J., Tenorio-Tagle G., Bodenheimer P., Rozyczka M., 1991, PASP, 103, 803
Freyer T., Hensler G., Yorke H. W., 2003, ApJ, 594, 888
Freyer T., Hensler G., Yorke H. W., 2006, ApJ, 638, 262
Gaensler B. M., 1998, ApJ, 493, 781
Garcia-Segura G., Mac Low M.-M., 1995, ApJ, 455, 145
Garcia-Segura G., Mac Low M.-M., Langer N., 1996a, A&A, 305, 229
Garcia-Segura G., Langer N., Mac Low M.-M., 1996b, A&A, 316, 133
Gies D. R., 1987, ApJS, 64, 545
González R. F., Koenigsberger G., 2014, A&A, 561, A105
Gräfener G., Owocki S. P., Grassitelli L., Langer N., 2017, A&A, 608, A34
Grassitelli L., Langer N., Grin N. J., Mackey J., Bestenlehner J. M., Gräfener G., 2018, A&A, 614, A86
Green S., Mackey J., Haworth T. J., Gvaramadze V. V., Duffy P., 2019, A&A, 625, A4
Groh J. H., Meynet G., Ekström S., Georgy C., 2014, A&A, 564, A30
Gull T. R., Sofia S., 1979, ApJ, 230, 782
Gvaramadze V. V., 2006, A&A, 454, 239
Gvaramadze V. V., Gualandris A., 2011, MNRAS, 410, 304
Gvaramadze V. V., Kniazev A. Y., Chene A.-N., Schnurr O., 2013, MNRAS, 430, L20
Gvaramadze V. V., Menten K. M., Kniazev A. Y., Langer N., Mackey J., Kraus A., Meyer D. M.-A., Kamiński T., 2014, MNRAS, 437, 843
Gvaramadze V. V., Alexashov D. B., Katushkina O. A., Kniazev A. Y., 2018, MNRAS, 474, 4421
Hainich R. et al., 2014, A&A, 565, A27
Harvey-Smith L., Gaensler B. M., Kothes R., Townsend R., Heald G. H., Ng C.-Y., Green A. J., 2010, ApJ, 712, 1157
Henney W. J., Arthur S. J., 2019a, MNRAS, 486, 3423
Henney W. J., Arthur S. J., 2019b, MNRAS, 486, 4423
Henney W. J., Arthur S. J., 2019c, MNRAS, 489, 2142
Henney W. J., Arthur S. J., de Colle F., Mellema G., 2009, MNRAS, 398, 157
Hummer D. G., 1994, MNRAS, 268, 109
Humphreys R. M., Davidson K., Hahn D., Martin J. C., Weis K., 2017, ApJ, 844, 40
Huthoff F., Kaper L., 2002, A&A, 383, 999
Jorissen A. et al., 2011, A&A, 532, A135
Kaper L., van Loon J. T., Augusteijn T., Goudfrooij P., Patat F., Waters L. B. F. M., Zijlstra A. A., 1997, ApJ, 475, L37
Katushkina O. A., Alexashov D. B., Izmodenov V. V., Gvaramadze V. V., 2017, MNRAS, 465, 1573
Katushkina O. A., Alexashov D. B., Gvaramadze V. V., Izmodenov V. V., 2018, MNRAS, 473, 1576
Kobulnicky H. A. et al., 2016, ApJS, 227, 18
Kobulnicky H. A., Schurhammer D. P., Baldwin D. J., Chick W. T., Dixon D. M., Lee D., Povich M. S., 2017, AJ, 154, 201
Kobulnicky H. A., Chick W. T., Povich M. S., 2018, ApJ, 856, 74
Langer N., 2012, ARA&A, 50, 107
Mackey J., Mohamed S., Neilson H. R., Langer N., Meyer D. M.-A., 2012, ApJ, 751, L10

Mackey J., Mohamed S., Gvaramadze V. V., Kotak R., Langer N., Meyer D. M.-A., Moriya T. J., Neilson H. R., 2014, Nature, 512, 282
Mackey J., Gvaramadze V. V., Mohamed S., Langer N., 2015, A&A, 573, A10
Meyer D. M.-A., Gvaramadze V. V., Langer N., Mackey J., Boumis P., Mohamed S., 2014a, MNRAS, 439, L41
Meyer D. M.-A., Mackey J., Langer N., Gvaramadze V. V., Mignone A., Izzard R. G., Kaper L., 2014b, MNRAS, 444, 2754
Meyer D. M.-A., Langer N., Mackey J., Velázquez P. F., Gusdorf A., 2015, MNRAS, 450, 3080
Meyer D. M.-A., van Marle A.-J., Kuiper R., Kley W., 2016, MNRAS, 459, 1146
Meyer D. M.-A., Mignone A., Kuiper R., Raga A. C., Kley W., 2017, MNRAS, 464, 3229
Meynet G., Maeder A., 2005, A&A, 429, 581
Mignone A., Bodo G., Massaglia S., Matsakos T., Tesileanu O., Zanni C., Ferrari A., 2007, ApJS, 170, 228
Mignone A., Zanni C., Tzeferacos P., van Straalen B., Colella P., Bodo G., 2012, ApJS, 198, 7
Nugis T., Lamers H. J. G. L. M., 2000, A&A, 360, 227
O'Hara T. B., Meixner M., Speck A. K., Ueta T., Bobrowsky M., 2003, ApJ, 598, 1255
Orlando S., Bocchino F., Reale F., Peres G., Petruk O., 2007, A&A, 470, 927
Osterbrock D. E., Bochkarev N. G., 1989, SvA, 33, 694
Peri C. S., Benaglia P., Brookes D. P., Stevens I. R., Isequilla N. L., 2012, A&A, 538, A108
Peri C. S., Benaglia P., Isequilla N. L., 2015, A&A, 578, A45
Prajapati P., Tej A., del Palacio S., Benaglia P., CH I.-C., Vig S., Mand al S., Kanti Ghosh S., 2019, ApJ, 884, L49,
Rangelov B., Montmerle T., Federman S. R., Boissé P., Gabici S., 2019, ApJ, 885, 105
Reimer A., Pohl M., Reimer O., 2006, ApJ, 644, 1118
Reynolds S. P., 2011, Ap&SS, 336, 257
Rho J., Petre R., 1997, ApJ, 484, 828
Rodríguez-González A., Meliani Z., Sánchez-Cruces M., Rivera-Ortiz P. R., Castellanos-Ramírez A., 2019, A&A, 631, A170
Rozyczka M., Tenorio-Tagle G., Franco J., Bodenheimer P., 1993, MNRAS, 261, 674
Sánchez-Cruces M., Rosado M., Fuentes-Carrera I., Ambrocio-Cruz P., 2018, MNRAS, 473, 1705
Sanyal D., Langer N., Szécsi D., -C Yoon S., Grassitelli L., 2017, A&A, 597, A71
Sasaki M., Kothes R., Plucinsky P. P., Gaetz T. J., Brunt C. M., 2006, ApJ, 642, L149
Schneps M. H., Haschick A. D., Wright E. L., Barrett A. H., 1981, ApJ, 243, 184
Seo J., Kang H., Ryu D., 2018, J. Korean Astron. Soc., 51, 37
Smith L. J., Pettini M., Dyson J. E., Hartquist T. W., 1984, MNRAS, 211, 679
Storey M. C., Staveley-Smith L., Manchester R. N., Kesteven M. J., 1992, A&A, 265, 752
Tatischeff V., Duprat J., de Séréville N., 2010, ApJ, 714, L26
Telezhinsky I., Dwarkadas V. V., Pohl M., 2012a, Astropart. Phys., 35, 300
Telezhinsky I., Dwarkadas V. V., Pohl M., 2012b, A&A, 541, A153
Telezhinsky I., Dwarkadas V. V., Pohl M., 2013, A&A, 552, A102
Tenorio-Tagle G., Rozyczka M., Yorke H. W., 1985, A&A, 148, 52
Toalá J. A., Arthur S. J., 2011, ApJ, 737, 100
Toalá J. A., Guerrero M. A., 2013, A&A, 559, A52
Toalá J. A., Guerrero M. A., Gruendl R. A., Chu Y.-H., 2014, AJ, 147, 30
Toalá J. A., Guerrero M. A., Ramos-Larios G., Guzmán V., 2015, A&A, 578, A66
Toalá J. A., Oskinova L. M., González-Galán A., Guerrero M. A., Ignace R., Pohl M., 2016, ApJ, 821, 79
Toalá J. A., Oskinova L. M., Ignace R., 2017, ApJ, 838, L19
Toledo-Roy J. C., Esquivel A., Velázquez P. F., Reynoso E. M., 2014, MNRAS, 442, 229
Truelove J. K., McKee C. F., 1999, ApJS, 120, 299
van Buren D., 1993, in Cassinelli J. P., Churchwell E. B., eds, ASP Conf. Ser. Vol. 35, Massive Stars: Their Lives in the Interstellar Medium. Astron. Soc. Pac., San Francisco, p. 315
van Buren D., McCray R., 1988, ApJ, 329, L93
van Buren D., Noriega-Crespo A., Dgani R., 1995, AJ, 110, 2914
van der Hucht K. A., 2001, New Astron. Rev., 45, 135
van Marle A. J., Keppens R., 2012, A&A, 547, A3
van Marle A. J., Langer N., Achterberg A., García-Segura G., 2006, A&A, 460, 105
van Marle A. J., Langer N., García-Segura G., 2007, A&A, 469, 941
van Marle A. J., Meliani Z., Keppens R., Decin L., 2011, ApJ, 734, L26
van Marle A. J., Decin L., Meliani Z., 2014, A&A, 561, A152
van Veelen B., Langer N., Vink J., García-Segura G., van Marle A. J., 2009, A&A, 503, 495
Velázquez P. F., Vigh C. D., Reynoso E. M., Gómez D. O., Schneiter E. M., 2006, ApJ, 649, 779
Vigh C. D., Velázquez P. F., Gómez D. O., Reynoso E. M., Esquivel A., Matias Schneiter E., 2011, ApJ, 727, 32
Voelk H. J., Forman M., 1982, ApJ, 253, 188
Wareing C. J., Zijlstra A. A., O'Brien T. J., 2007, ApJ, 660, L129
Wareing C. J., Pittard J. M., Falle S. A. E. G., 2017, MNRAS, 470, 2283
Weaver R., McCray R., Castor J., Shapiro P., Moore R., 1977, ApJ, 218, 377
Webb G. M., Axford W. I., Forman M. A., 1985, ApJ, 298, 684
Whalen D., van Veelen B., O'Shea B. W., Norman M. L., 2008, ApJ, 682, 49
Wiersma R. P. C., Schaye J., Smith B. D., 2009, MNRAS, 393, 99
Wilkin F. P., 1996, ApJ, 459, L31
Williams B. J., Borkowski K. J., Ghavamian P., Hewitt J. W., Mao S. A., Petre R., Reynolds S. P., Blondin J. M., 2013, ApJ, 770, 129
Zhekov S. A., 2014, MNRAS, 443, 12
Zirakashvili V. N., Ptuskin V. S., 2018, Astropart. Phys., 98, 21

This paper has been typeset from a TEX/LATEX file prepared by the author.

Monthly Notices
of the
ROYAL ASTRONOMICAL SOCIETY

MNRAS **502,** 5340–5355 (2021)
Advance Access publication 2021 February 17

doi:10.1093/mnras/stab452

Non-thermal radio supernova remnants of exiled Wolf–Rayet stars

D. M.-A. Meyer[1]★, M. Pohl,[1,2] M. Petrov[3] and L. Oskinova[1,4]

[1]*Institut für Physik und Astronomie, Universität Potsdam, Karl-Liebknecht-Strasse 24/25, D-14476 Potsdam, Germany*
[2]*DESY Platanenallee 6, D-15738 Zeuthen, Germany*
[3]*Max Planck Computing and Data Facility (MPCDF), Gießenbachstrasse 2, D-85748 Garching, Germany*
[4]*Department of Astronomy, Kazan Federal University, Kremlevskaya Str 18, Kazan, Russia*

Accepted 2021 February 10. Received 2021 February 10; in original form 2020 December 15

ABSTRACT

A signification fraction of Galactic massive stars ($\geq$8 $M_\odot$) are ejected from their parent cluster and supersonically sail away through the interstellar medium (ISM). The winds of these fast-moving stars blow asymmetric bubbles thus creating a circumstellar environment in which stars eventually die with a supernova explosion. The morphology of the resulting remnant is largely governed by the circumstellar medium of the defunct progenitor star. In this paper, we present 2D magneto-hydrodynamical simulations investigating the effect of the ISM magnetic field on the shape of the supernova remnants of a 35 $M_\odot$ star evolving through a Wolf–Rayet phase and running with velocity 20 and 40 km s^{-1}, respectively. A 7 μG ambient magnetic field is sufficient to modify the properties of the expanding supernova shock front and in particular to prevent the formation of filamentary structures. Prior to the supernova explosion, the compressed magnetic field in the circumstellar medium stabilizes the wind/ISM contact discontinuity in the tail of the wind bubble. A consequence is a reduced mixing efficiency of ejecta and wind materials in the inner region of the remnant, where the supernova shock wave propagates. Radiative transfer calculations for synchrotron emission reveal that the non-thermal radio emission has characteristic features reflecting the asymmetry of exiled core-collapse supernova remnants from Wolf–Rayet progenitors. Our models are qualitatively consistent with the radio appearance of several remnants of high-mass progenitors, namely the bilateral G296.5+10.0 and the shell-type remnants CTB109 and Kes 17, respectively.

Key words: radiation mechanisms: non-thermal – stars: massive – ISM: supernova remnants.

1 INTRODUCTION

Massive stars are born with masses $M_\star \geq 8\,M_\odot$. Despite their rareness, they are of prime importance in the cycle of matter in the interstellar medium (ISM) of our Galaxy (Langer 2012). After a relatively long hydrogen-burning main-sequence phase, they experience a series of evolutionary phases characterized by abrupt changes in their surface properties (radius, effective temperature, mass-loss rate, and wind velocity). Those evolutionary phases alternate between hot, possibly eruptive phases of dilute supersonic winds (Brott et al. 2011) and colder periods of inflated radius with a dense, slow stellar wind (Ekström et al. 2012). The number and characteristics of the post-main-sequence phases are, amongst other, a function of the initial mass, the intrinsic rotation (Yoon & Langer 2005), and the chemical composition of the star (Sanyal et al. 2017). These various winds produce shells in the circumstellar medium that develop instabilities and eventually collide together (Garcia-Segura, Mac Low & Langer 1996; Freyer, Hensler & Yorke 2003, 2006). They chemically enrich the ISM and drive turbulence in it, on account of the large amount of momentum and energy the winds deposit in the stellar surroundings. Finally, the majority of massive stars end their life as core-collapse supernova, whose shock wave expands into their circumstellar medium (Woosley, Heger & Weaver 2002), shaped by stellar winds and radiation.

Wolf–Rayet stars are an advance evolutionary stage of stars with initial mass $\geq$20 $M_\odot$, generally following a supergiant phase. Their stellar winds are fast, dense, and chemically enriched in C, N, and O elements (Hamann, Gräfener & Liermann 2006; Sander, Hamann & Todt 2012; Bestenlehner et al. 2014). The interaction of fast Wolf–Rayet wind with slower wind material expelled at previous evolutionary stage results in complex stellar surroundings such as ring nebulae (Stock & Barlow 2010; Gvaramadze, Kniazev & Fabrika 2010a; Meyer et al. 2020) or bipolar bubbles (Gvaramadze, Kniazev & Fabrika 2010b). A fraction of Wolf–Rayet star is ocated at high Galactic latitude (Moffat et al. 1998; Munoz et al. 2017; Toalá et al. 2018). These fast-moving Wolf–Rayet stars that left their parent stellar clusters and reached low-density regions of the ISM. There, they eventually explode as a core-collapse supernova inside the cavity carved by the stellar wind (Franco et al. 1991; Rozyczka et al. 1993; Dwarkadas 2007). Wolf–Rayet-evolving stars are therefore ideal progenitor candidates for core-collapse supernova remnants (Katsuda et al. 2018).

Several mechanisms determine the morphology of the supernova remnants of massive progenitors. Clumpiness affecting the shock-wave propagation can arise from wind–wind interaction as observed in the supernova remnant Cas A (van Veelen et al. 2009). In addition to instabilities directly developing in the supernova

★ E-mail: dmameyer.astro@gmail.com

explosion itself (Janka, Melson & Summa 2016), asymmetries in supernova remnants may be a direct consequence of interactions between the expanding shock wave and an anisotropic circumstellar medium. Of prime importance for the shaping of supernova remnants is the peculiar motion of very high-mass progenitors moving through the ISM (Meyer, Petrov & Pohl 2020). As an example, RWC 86 (Broersen et al. 2014; Gvaramadze et al. 2017) or the Cygnus Loop (Aschenbach & Leahy 1999; Fang, Yu & Zhang 2017) reveal features consistent with the typical characteristics of off-centre explosions in massive stellar wind bubbles, suggesting that they might have been produced by a fast-moving progenitor, see also Toledo-Roy et al. (2014). All the numerous mechanisms, which induce deviations from sphericity in supernova shock waves, can operate in parallel, providing a huge parameter space governing the evolution of core-collapse supernova remnants. Explanations of their observed morphologies are subject to degeneracies and alternative scenarios. Runaway Wolf–Rayet stars constitute therefore the ideal candidates for the production of isolated, *asymmetric* core-collapse supernova remnants (Meyer et al. 2015).

The structure and properties of the ISM are also involved in the shaping of supernova remnants (Ferreira & de Jager 2008). The ISM has an intrinsic filamentary, turbulent, and magnetized nature. Its gravito-turbulent evolution, powered by the formation of massive pre-stellar cores, stellar wind outflows, and supernova feedback enriching the ISM, drives turbulence in it and participates in the formation of the next generation of stars. Native ISM magnetic field is an important player in the evolution of the circumstellar medium around massive stars. As an example, the internal physics of bow shock nebulae around runaway stars (Gvaramadze et al. 2014; Meyer et al. 2014; van Marle, Decin & Meliani 2014; Meyer et al. 2017), as well as the organization of supernova remnants (Orlando et al. 2007; Ferreira & de Jager 2008; Orlando et al. 2008; Schneiter et al. 2010; Orlando et al. 2012) are partially determined by the local ambient magnetic field. Furthermore, the local direction of magnetic field makes thermal conduction anisotropic (Balsara, Tilley & Howk 2008; Meyer et al. 2017) and can suppress (magneto-)hydrodynamical instabilities (Viallet & Baty 2007; van Marle et al. 2014). Importantly, it has been shown that the magnetization of the ISM strongly elongates stellar wind bubbles around static massive stars along the direction of the local field lines (van Marle, Meliani & Marcowith 2015). The question is therefore how important for the shaping of the supernova remnants are the effects of the ISM magnetization as compared to those of the motion of runaway Wolf–Rayet progenitors?

In this work, we investigate, by means of numerical magneto-hydrodynamical (MHD) simulations, the effects of a background ISM magnetic field on the morphological evolution of supernova remnants generated by runaway massive progenitors. We adopt the standard two-dimensional axisymmetric approach developed by many authors (Comerón & Kaper 1998; Mackey et al. 2012; Meyer et al. 2016). It consists of first modelling the pre-supernova circumstellar medium of massive progenitors before launching a supernova blastwave in it (Velázquez et al. 2006; Chiotellis, Schure & Vink 2012; van Marle, Meliani & Marcowith 2012; Meyer et al. 2015). We examine the remnant morphologies and perform radiative transfer calculations for their non-thermal radio synchrotron emission maps. The mixing of supernova ejecta, stellar winds, and ISM material is also discussed, comparing models with and without ISM magnetic field. Last, we discuss these remnants in the context of cosmic ray acceleration before comparing them to Galactic supernova remnants from massive progenitors.

Our study is organized as follows. First, we present the numerical methods used for the MHD simulations of supernova remnants of 35 $M_\odot$ runaway massive stars in Section 2. We describe our results for the dynamical evolution of both the stellar surroundings and the supernova remnant, together with predictive non-thermal radio synchrotron emission maps of these objects in Section 3. We analyse therein the effects of the presence of the ISM magnetic field on to the remnants evolution. Our results are further discussed in Section 4, and finally, we present our conclusions in Section 5.

2 NUMERICAL SIMULATIONS

This section describes the methods used to perform simulations of the circumstellar medium of a 35 $M_\odot$ massive star evolving up to the Wolf–Rayet phase and ending its life in a supernova explosion. We simulate the stellar surroundings from the zero-age phase of the progenitor to the late phase of supernova remnant evolution, varying the velocity of the star relative to the ISM and investigating the role of the ISM magnetic field. The simulations are used for further radiative transfer calculations of non-thermal radio synchrotron emission.

2.1 Simulation method for the pre-supernova phase

The pre-supernova circumstellar medium around the progenitor star is the wind-blown bubble generated by interaction between the stellar wind and the local ISM. We simulate it as described in Meyer et al. (2020). We first perform 2D cylindrical, axisymmetric, magneto-hydrodynamics numerical models with a coordinate system $[z_{\rm min}; z_{\rm max}] \times [O; R_{\rm max}]$ that is mapped with a uniform grid of spatial resolution $R_{\rm max}/N_{\rm R}$. The stellar wind of the 35 $M_\odot$ star is released at the centre of the domain into a uniformly distributed ISM. A circular wind zone of radius 20 cells is filled with the wind density profiles,

$$\rho_w(r) = \frac{\dot{M}}{4\pi r^2 v_{\rm w}}, \tag{1}$$

where $\dot{M}$ is the wind mass-loss rate at different evolutionary phases interpolated from a stellar evolutionary track, r is the distance to the origin of the domain, O, and $v_{\rm w}$ is the velocity of the stellar wind (Comerón & Kaper 1998; van Marle et al. 2011, 2014).

In Fig. 1, we show the evolutionary path of the star and its wind, which we use in the simulations. The stellar mass (panel a, in $M_\odot$), the mass-loss rate (panel b, in $M_\odot\,{\rm yr}^{-1}$), and the terminal wind velocity (panel c, in $\mathrm{km\,s^{-1}}$) are displayed beginning at the age 3 Myr. The wind properties of this zero-age-main-sequence, non-rotating 35-$M_\odot$ star at Galactic metallicity has been interpolated from the Geneva library of stellar models calculated with the GENEC code (Ekström et al. 2012) by means of the online interface SYCLIST.[1] The terminal speed, $v_{\rm w}$, is modified for high effective temperatures and massive stars using the approximation of Eldridge et al. (2006):

$$v_{\rm w} = \sqrt{\beta(T)}v_{\rm esc} = \sqrt{\beta(T)\frac{2GM_\star}{R_\star}}, \tag{2}$$

where $v_{\rm esc}$ is the escape speed of the star, $R_\star$ the stellar radius, and

$$\beta_{\rm w}(T) = \begin{cases} 1.0 & \text{if } T \leq 10000\,\mathrm{K}, \\ 1.4 & \text{if } T \leq 21000\,\mathrm{K}, \\ 2.65 & \text{if } T > 21000\,\mathrm{K}, \end{cases} \tag{3}$$

a corrective function depending on the temperature T.

[1] https://www.unige.ch/sciences/astro/evolution/en/database/syclist/

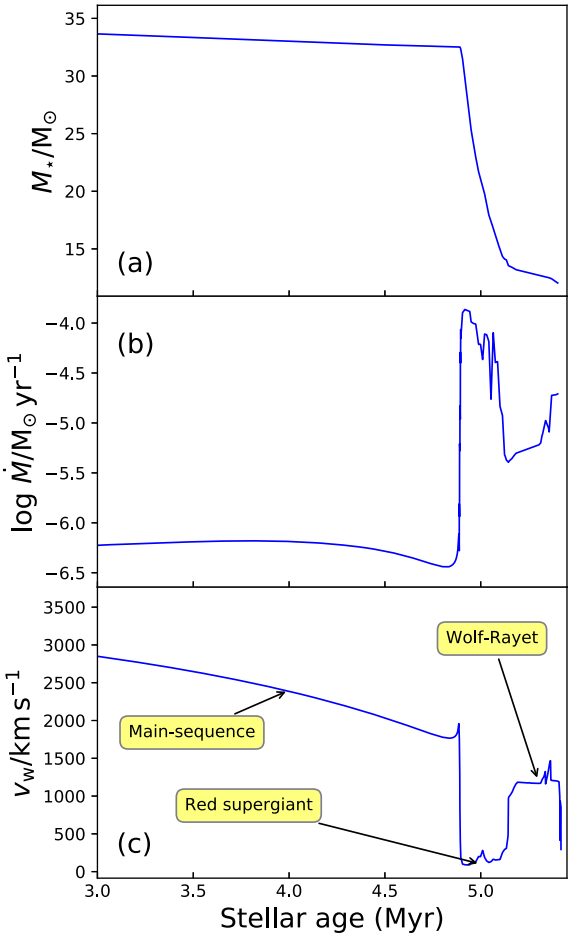

Figure 1. Stellar properties at the end of the main-sequence and during the post-main-sequence evolution of the 35 $\mathrm{M}_\odot$ star. The panels show the stellar mass (top, panel a), mass-loss rate (middle, panel b), and wind velocity (bottom, panel c) as a function of time (in Myr).

The star first experiences a rather long main-sequence phase lasting about 4.8 Myr, blowing winds with $\dot{M} \approx 10^{-6.2}\,\mathrm{M}_\odot\,\mathrm{yr}^{-1}$ and $v_\mathrm{w} \approx 3000\,\mathrm{km\,s}^{-1}$. After the long main-sequence phase, the star becomes cooler and inflates to become a red supergiant with mass-loss rate $\dot{M} \approx 10^{-4}\,\mathrm{M}_\odot\,\mathrm{yr}^{-1}$ and wind speed $v_\mathrm{w} \approx 50\,\mathrm{km\,s}^{-1}$. It finally evolves to the Wolf–Rayet phase, characterized by both a high mass-loss rate ($\dot{M} \approx 10^{-5.0}\,\mathrm{M}_\odot\,\mathrm{yr}^{-1}$) and a large wind speed ($v_\mathrm{w} \approx 1500\,\mathrm{km\,s}^{-1}$).

To study the circumstellar medium around runaway Wolf–Rayet stars, we conducted a series of simulations with varying stellar velocities spanning from $v_\star = 10$ to $v_\star = 40\,\mathrm{km\,s}^{-1}$. The star moves in z-direction, and we simulate in the frame of the star, ISM gas of number density $n_\mathrm{ISM} \approx 0.79\,\mathrm{cm}^{-3}$ and temperature $T_\mathrm{ISM} \approx 8000\,\mathrm{K}$ as in the H II regions around hot stars. The ISM material flows in with speed $v_\star$ at the boundary $z = z_\mathrm{max}$. Outflow boundaries conditions are set at $z = z_\mathrm{min}$ and $R = R_\mathrm{max}$, respectively. Each value of $v_\star$ is explored with and without magnetization of the ISM. The ISM magnetic field direction is parallel to the Oz axis, as a direct consequence of the simulation geometry, and it is set to $B_\mathrm{ISM} = 7\,\mu\mathrm{G}$ that is typical value for the warm phase of the ISM (van Marle et al. 2014, 2015; Meyer et al. 2017). The flow of material past the stellar wind is characterized by the Alfvén speed:

$$v_\mathrm{A} = \sqrt{\frac{\boldsymbol{B}_\mathrm{ISM}\cdot\boldsymbol{B}_\mathrm{ISM}}{4\pi n m_\mathrm{H}}}, \tag{4}$$

which together with the sound speed (equation 18) determines the Alfvénic and sonic Mach number of the stellar wind bubble in the ISM. We list both for each model in Table 1.

A continuity equation,

$$\frac{\partial(\rho Q_1)}{\partial t} + \nabla\cdot(\boldsymbol{v}\rho Q_1) = 0, \tag{5}$$

is used to trace the mixing of stellar wind material into the ISM, with ρ the mass density, respectively. Initially, the tracer Q_1 is set to $Q_1(\boldsymbol{r}) = 1$ in the wind and to $Q_1(\boldsymbol{r}) = 0$ in the ISM.

2.2 Supernova explosion

After establishing the circumstellar medium around the pre-supernova massive star, we simulate the supernova explosion as a spherically symmetric shock wave expanding into the freely expanding stellar wind of the progenitor. The supernova–wind interaction then serves as initial condition of a subsequent two-dimensional calculation of the corresponding remnant (Meyer et al. 2015, 2020). The properties of the blastwave are parametrized by the explosion energy, $E_\mathrm{ej} = 10^{51}$ erg, and the ejecta mass,

$$M_\mathrm{ej} = M_\star - \int_{t_\mathrm{ZAMS}}^{t_\mathrm{SN}} \dot{M}(t)dt - M_\mathrm{NS} = 11.64\,\mathrm{M}_\odot, \tag{6}$$

where t_ZAMS and t_SN denote the times of zero age and supernova, respectively, and $M_\mathrm{NS} = 1.4\,\mathrm{M}_\odot$ is the mass of the remnant neutron star left behind the supernova explosion. Note that we use the canonical explosion energy typically taken in hydrodynamical simulations of supernova remnants (van Veelen et al. 2009; van Marle et al. 2010, 2012). However, detailed dedicated studies estimate the energy released throughout the explosion of a core-collapse progenitor to be rather in the range $E_\mathrm{ej} = 1\text{–}5 \times 10^{50}$ erg (Smartt 2009; Janka 2012; Moriya et al. 2018). A passive scalar, $Q_2(\boldsymbol{r})$, obeying the continuity equation,

$$\frac{\partial(\rho Q_2)}{\partial t} + \nabla\cdot(\boldsymbol{v}\rho Q_2) = 0, \tag{7}$$

is used to distinguish supernova ejecta from stellar wind or ISM material, by setting $Q_2(\boldsymbol{r}) = 1$ in the supernova-ejecta region and $Q_2(\boldsymbol{r}) = 0$ otherwise.

The supernova shock wave is released into the progenitor's stellar wind bubble (Whalen et al. 2008; Zirakashvili & Ptuskin 2018) by superposing a 1D blastwave density profile, $\rho(r)$, on to the pre-supernova wind distribution. We used a typical ejecta profile for the early expansion of a core-collapse supernovae. It involves a homologuous expansion, $v = r/t$, the radius of the progenitor star's core at the time of the supernova, r_core, and the outermost extension r_max of the blastwave. We start the calculations at

$$t_\mathrm{max} = \frac{r_\mathrm{max}}{v_\mathrm{max}}, \tag{8}$$

where $v_\mathrm{max} = 30000\,\mathrm{km\,s}^{-1}$ is the ejecta velocity at r_max (van Veelen et al. 2009). The value of r_max is determined by the explosion energy and ejecta mass (Whalen et al. 2008). The density profile of the ejecta is set as

$$\rho(r) = \begin{cases} \rho_\mathrm{core}(r) & \text{if } r \le r_\mathrm{core}, \\ \rho_\mathrm{max}(r) & \text{if } r_\mathrm{core} < r < r_\mathrm{max}, \end{cases} \tag{9}$$

Table 1. List of models. The columns indicate the velocity of the star, $v_\star$, the grid resolution and size in pc, and the sonic and Alfénic Mach number of the moving star with respect to the ISM. The runs are labelled 'CSM' for the pre-supernova modelling and 'SNR' for the remnant simulations, and likewise 'HD' for hydrodynamics and 'MHD' for magneto-hydrodynamics.

Model	$v_\star$ (km s^{-1})	Grid size	Grid mesh	M	M_A
Run-35-MHD-20-CSM	20	[0; 175] × [−250; 100]	2000 × 4000 cells	1.0	1.16
Run-35-HD-20-CSM	20	[0; 175] × [−250; 100]	2000 × 4000 cells	1.0	1.16
Run-35-MHD-40-CSM	40	[0; 150] × [−300; 100]	1500 × 4000 cells	2.0	2.32
Run-35-HD-40-CSM	40	[0; 150] × [−300; 100]	1500 × 4000 cells	2.0	2.32
Run-35-MHD-20-SNR	20	[0; 200] × [−275; 175]	4000 × 9000 cells	1.0	1.16
Run-35-HD-20-SNR	20	[0; 200] × [−275; 175]	4000 × 9000 cells	1.0	1.16
Run-35-MHD-40-SNR	40	[0; 200] × [−330; 170]	4000 × 10000 cells	2.0	2.32
Run-35-HD-40-SNR	40	[0; 200] × [−330; 170]	4000 × 10000 cells	2.0	2.32

where

$$\rho_\mathrm{core}(r) = \frac{1}{4\pi n}\frac{\left(10E_\mathrm{ej}^{n-5}\right)^{-3/2}}{\left(3M_\mathrm{ej}^{n-3}\right)^{-5/2}}\frac{1}{t_\mathrm{max}^3}, \tag{10}$$

is constant, whereas the ejecta density further out follows a power law,

$$\rho_\mathrm{max}(r) = \frac{1}{4\pi n}\frac{\left(10E_\mathrm{ej}^{n-5}\right)^{(n-3)/2}}{\left(3M_\mathrm{ej}^{n-3}\right)^{(n-5)/2}}\left(\frac{r}{t_\mathrm{max}}\right)^{-n}, \tag{11}$$

with $n = 11$ (Chevalier 1982; Truelove & McKee 1999).

Beyond r_max, the density profile is that of the freely expanding wind as found in the pre-supernova wind bubble simulations. The ejecta speed at the distance r_core from the centre of the explosion is (Truelove & McKee 1999)

$$v_\mathrm{core} = \left(\frac{10(n-5)E_\mathrm{ej}}{3(n-3)M_\mathrm{ej}}\right)^{1/2}. \tag{12}$$

This 1D ejecta-wind interaction solution is mapped on to the 2D domain of the subsequent simulation. We integrate the equations up to 150 kyr after the supernova.

2.3 Governing equations

The dynamics of a magnetized flow is described by the equations of ideal magneto-hydrodynamics plus losses and heating by optically thin radiation,

$$\frac{\partial\rho}{\partial t} + \nabla\cdot(\rho\boldsymbol{v}) = 0, \tag{13}$$

$$\frac{\partial\boldsymbol{m}}{\partial t} + \nabla\cdot(\boldsymbol{m}\otimes\boldsymbol{v} + \boldsymbol{B}\otimes\boldsymbol{B} + \hat{\mathbf{I}}p_\mathrm{t}) = \mathbf{0}, \tag{14}$$

$$\frac{\partial E}{\partial t} + \nabla\cdot((E + p_\mathrm{t})\boldsymbol{v} - \boldsymbol{B}(\boldsymbol{v}\cdot\boldsymbol{B})) = \Phi(T,\rho), \tag{15}$$

and

$$\frac{\partial\boldsymbol{B}}{\partial t} + \nabla\cdot(\boldsymbol{v}\otimes\boldsymbol{B} - \boldsymbol{B}\otimes\boldsymbol{v}) = \mathbf{0}, \tag{16}$$

with the linear momentum vector, $\boldsymbol{m} = \rho\boldsymbol{v}$, and the magnetic field vector, $\boldsymbol{B}$. The total energy of the system reads

$$E = \frac{p}{(\gamma-1)} + \frac{\boldsymbol{m}\cdot\boldsymbol{m}}{2\rho} + \frac{\boldsymbol{B}\cdot\boldsymbol{B}}{2}, \tag{17}$$

where $\gamma = 5/3$ is the adiabatic index for ideal gas and p is the thermal pressure. The definition of the adiabatic sound speed,

$$c_\mathrm{s} = \sqrt{\frac{\gamma p}{\rho}}, \tag{18}$$

closes the system, which we integrate using the so-called eight-wave algorithm. This second-order unsplit scheme satisfies $\nabla\cdot\boldsymbol{B} = \mathbf{0}$. The time-march of the algorithm obeys the standard Courant–Friedrich–Levy condition that is set to $C_\mathrm{cfl} = 0.1$ at the beginning of the simulations.

The source term,

$$\Phi(T,\rho) = n_\mathrm{H}\Gamma(T) - n_\mathrm{H}^2\Lambda(T), \tag{19}$$

accounts for optically thin radiative cooling, $\Lambda(T)$, and heating, $\Gamma(T)$. The gas temperature is

$$T = \mu\frac{m_\mathrm{H}}{k_\mathrm{B}}\frac{p}{\rho}, \tag{20}$$

where $\mu = 0.61$ is the mean molecular weight, k_B the Boltzmann constant, and m_H the proton mass. The hydrogen number density is computed as

$$n_\mathrm{H} = \frac{\rho}{\mu(1+\chi_\mathrm{He,Z})m_\mathrm{H}}, \tag{21}$$

with $\chi_\mathrm{He,Z}$ the mass fraction of all coolants heavier than H. The functions $\Gamma(T)$ and $\Lambda(T)$ are described in details in Meyer et al. (2017).

2.4 Non-thermal synchrotron radio emission

The forward shock of the supernova remnant in particular will accelerate charged particles, such as electrons, to high energy. In the presence of magnetic field relativistic electrons produce synchrotron emission that is an excellent diagnostic (Reynolds 2008). To permit a comparison with the vast observational data of non-thermal radio synchrotron emission from supernova remnants, we produce synthetic emission maps on the basis of our MHD simulations.

Energy losses of GeV-scale electrons are likely negligible, and so we assume the electron spectrum,

$$N(E) = KE^{-s}, \tag{22}$$

where E denotes the electron energy and the index, $s = 2$, is expected for a strong shock. Diffusive transport is typically slower than advection in the GeV band, and so the accelerated electron density follows the gas density and is in fact proportional to it, if the injection efficiency at the forward shock is a constant (Drury 1983a,b). Amongst the several prescriptions for the non-thermal synchrotron emission coefficient of a magnetized gas available in the literature, we choose to use that of Jun & Norman (1996). We refer the reader interested in details regarding to our choice of emission coefficient within this core-collapse supernova remnant problem in our Appendix A. Therefore, at a given frequency, ν, the

radio synchrotron emission coefficient reads

$$j_{\rm sync}(\nu) \propto K^{2-s}\, p^{s-1}\, B_{\perp}^{(s+1)/2} \nu^{-(s-1)/2}, \tag{23}$$

which reduces to

$$j_{\rm sync}(\nu) \propto n^{2-s}\, p^{s-1}\, B_{\perp}^{(s+1)/2} \nu^{-(s-1)/2}, \tag{24}$$

where p is the gas thermal pressure and $B_{\perp}$ is the magnetic-field component perpendicular to the line of sight.

Let $\vec{l}$ be the unit vector of the observer's line of sight. Defining the viewing angle of the observer as $\theta_{\rm obs} = \angle(\vec{l}, \vec{B})$, the total strength of the magnetic field and its perpendicular component are obtained as

$$B_{\perp} = |\vec{B}| \sin(\theta_{\rm obs}) \tag{25}$$

and

$$|\vec{B}| = \sqrt{B_{\rm R}^2 + B_{\rm z}^2}. \tag{26}$$

Then, at a given frequency the emission coefficient finally reads

$$j_{\rm sync}(\theta_{\rm obs}) \propto n^{2-s}\, p^{s-1} \left(|\vec{B}| \sqrt{1 - \left(\frac{\vec{B}\cdot\vec{l}}{|\vec{B}|} \right)^2} \right)^{(s+1)/2}, \tag{27}$$

which we use in our radiative transfer calculations.

For each simulation, we selected snapshots that are representative of the phases of the supernova remnant evolution, namely at times 6, 20, and 40 kyr after the explosion, respectively. The corresponding density, temperature, and magnetic-field distributions are first translated from the two-dimensional cylindrical coordinates system to a three-dimensional spherical coordinate system (r, θ, ϕ) with 512^3 cells and the same origin, for which we rotate the cylindrical solution around the symmetry axis. On each grid zone, we pre-calculate the local component of the magnetic field that is normal to line of sight of the observer. Finally, we use a modified version of the radiative transfer code RADMC-3D[2] to perform ray-tracing integration of the radio synchrotron emission coefficient along a given line of sight with aspect angle $\theta_{\rm obs}$. The non-thermal radio intensity,

$$I = \int_{\rm SNR} j_{\rm sync}(\theta_{\rm obs}) {\rm d}l, \tag{28}$$

is then used to synthesize normalized emission maps.

3 RESULTS

We present in this section the results for the pre- and post-supernova circumstellar medium of a runaway Galactic 35 $M_{\odot}$ progenitor star, investigate how the stellar motion and the magnetization of the ISM affect the mixing of materials, and present the evolution of their projected radio synchrotron emission.

3.1 Pre-supernova circumstellar medium of runaway stars

Fig. 2 presents our results for a star moving with $v_{\star} = 20\,{\rm km\,s^{-1}}$, comparing the hydrodynamical picture (top) with the MHD description (bottom). The red isocontours trace $Q_1 = 0.5$, which marks the places in the remnant with a 50/50 proportion of ISM and stellar wind. The wind of the massive star generated an ovoid bubble of size ∼100 pc (Fig. 2a) in which the star is off-centred on account of stellar motion (cf. Weaver et al. 1977; Meyer et al. 2020). The large-scale stellar-wind bow shock is organized according to the classical picture of Weaver et al. (1977), made of an inner termination shock, a contact discontinuity, and an outer forward shock. They distinguish the expanding stellar wind, the hot low-density shocked wind, the cold dense ISM gas, and the ambient medium, respectively. The post-main-sequence wind, i.e. the red supergiant and Wolf–Rayet materials, are released inside expanding stellar wind and develop instabilities at the interface separating the cold and hot gas (Fig. 2).

For a larger speed of the star, $v_{\star} = 40\,{\rm km\,s^{-1}}$, the spherical symmetry is broken, and the star reaches the forward shock of its own wind bubble, itself distorted under the effects of stellar motion (Fig. 3a,b). A chimney of unperturbed stellar wind is carved into the layer of shocked ISM, and the post-main-sequence wind is blown through the tube (red isocontours). This phenomenon is even more pronounced in the case of a very fast progenitor star with $v_{\star} = 70\,{\rm km\,s^{-1}}$ (Meyer et al. 2015). Interestingly, once the star has left its wind bubble, direct wind–ISM interaction resumes at the distance

$$R_{\rm SO} = \sqrt{\frac{\dot{M} v_{\rm w}}{4\pi n_{\rm ISM} v_{\star}^2}}, \tag{29}$$

and a new bow shock forms (Baranov, Krasnobaev & Kulikovskii 1971). An analytic estimate for the location of the contact discontinuity of bow shocks reads

$$\frac{R(\theta)}{R_{\rm SO}} = \frac{\sqrt{3(1-\theta){\rm cotan}(\theta)}}{\sin(\theta)}, \tag{30}$$

where θ is the angle to the direction of stellar motion (Wilkin 1996). This bow shock is in its turn subject to instabilities (Brighenti & D'Ercole 1995a,b) and constitutes the location in which the supernova explosion takes place (Brighenti & D'Ercole 1994; Chiotellis et al. 2012; Meyer et al. 2015).

The interstellar magnetic field has strong impact on the distribution of shocked ISM, as demonstrated in van Marle et al. (2015). As an example, in Figs 2(b) and 3(b) one clearly sees that the layer of shocked ISM is puffed up along the local magnetic field as a result of the damping of Alfvén waves (van Marle et al. 2015). The effect is weaker for a fast-moving progenitor on account of the lower ratio of magnetic and ram pressure (Fig. 3b). The entire interior structure of the wind bubble is elongated when the star moves quickly. The magnetic field lines are aligned with the termination shock and discontinuities, providing additional pressure that modifies the circumstellar gas dynamics (Figs 2b). It can also damp instabilities at the contact discontinuity between hot shocked wind and cold shocked ISM gas, primarily in the tail of the wind bubble. Our models combine the asymmetry in the stellar wind bubbles of moving stars (Meyer et al. 2015) with the magnetic-pressure effect that were previously explored for static stars (van Marle et al. 2015).

3.2 Supernova remnants

Fig. 4 displays the structure of the supernova remnant at time 40 kyr after the explosion. Each panel corresponds to a different simulation, with density plotted on the left-hand part of the panel and the temperature on the right-hand part of the panel, respectively. The blue isocontour marks the regions with 10 per cent abundance of ejecta in number density. The left-hand panels are derived from hydrodynamical simulations, to be compared with MHD results on the right. The stellar velocities are $v_{\star} = 20\,{\rm km\,s^{-1}}$ (top) and $v_{\star} = 40\,{\rm km\,s^{-1}}$ (bottom), respectively.

The shape of the supernova remnants is governed by the distribution of the pre-supernova circumstellar medium (Meyer et al. 2015,

[2] https://www.ita.uni-heidelberg.de/~dullemond/software/radmc-3d/

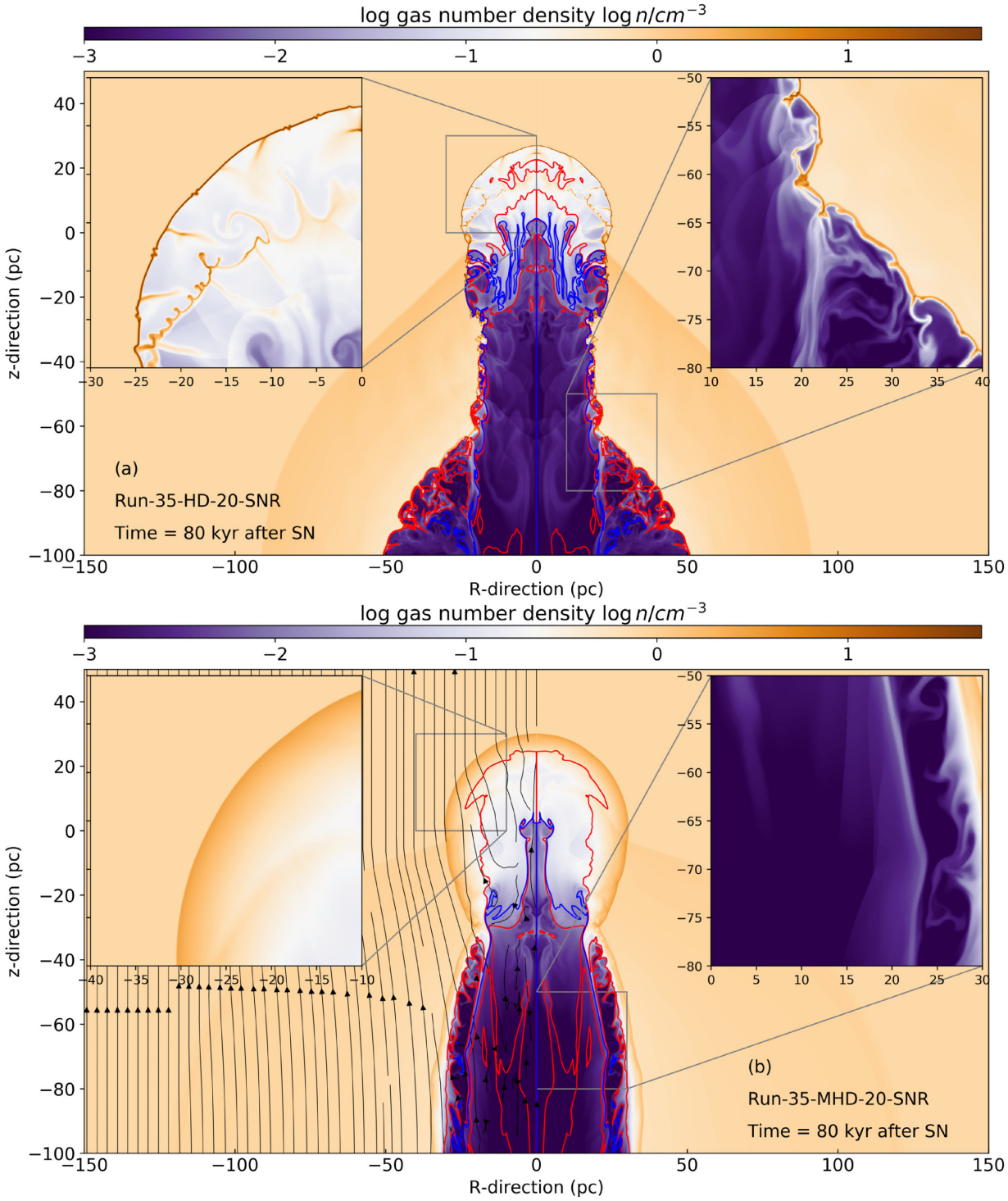

Figure 2. Density rendering of the supernova remnant of a 35-$M_\odot$ progenitor moving with $v_\star = 20\,\mathrm{km\,s^{-1}}$ through uniform ISM of number density $n_{\mathrm{ISM}} = 0.78\,\mathrm{cm^{-3}}$. Before exploding, the remnant passed through main-sequence, red supergiant, and Wolf–Rayet phases (Ekström et al. 2012). The top panel displays the hydrodynamical model, whereas the bottom one shows the magneto-hydrodynamical picture for a 7-μG ambient magnetic field oriented parallel to the stellar motion in z-direction. Inset boxes highlight the dynamic filamentary structures developing from ejecta-wind-ISM interactions (left inset) and the structure of the stellar wind cavity produced by the progenitor's motion and located behind the centre of the explosion (right inset). The red lines are iso-temperature contours ($T = 10^6$ and 10^7 K), and the blue contours trace the region with a 10 per cent contribution of supernova ejecta in number density.

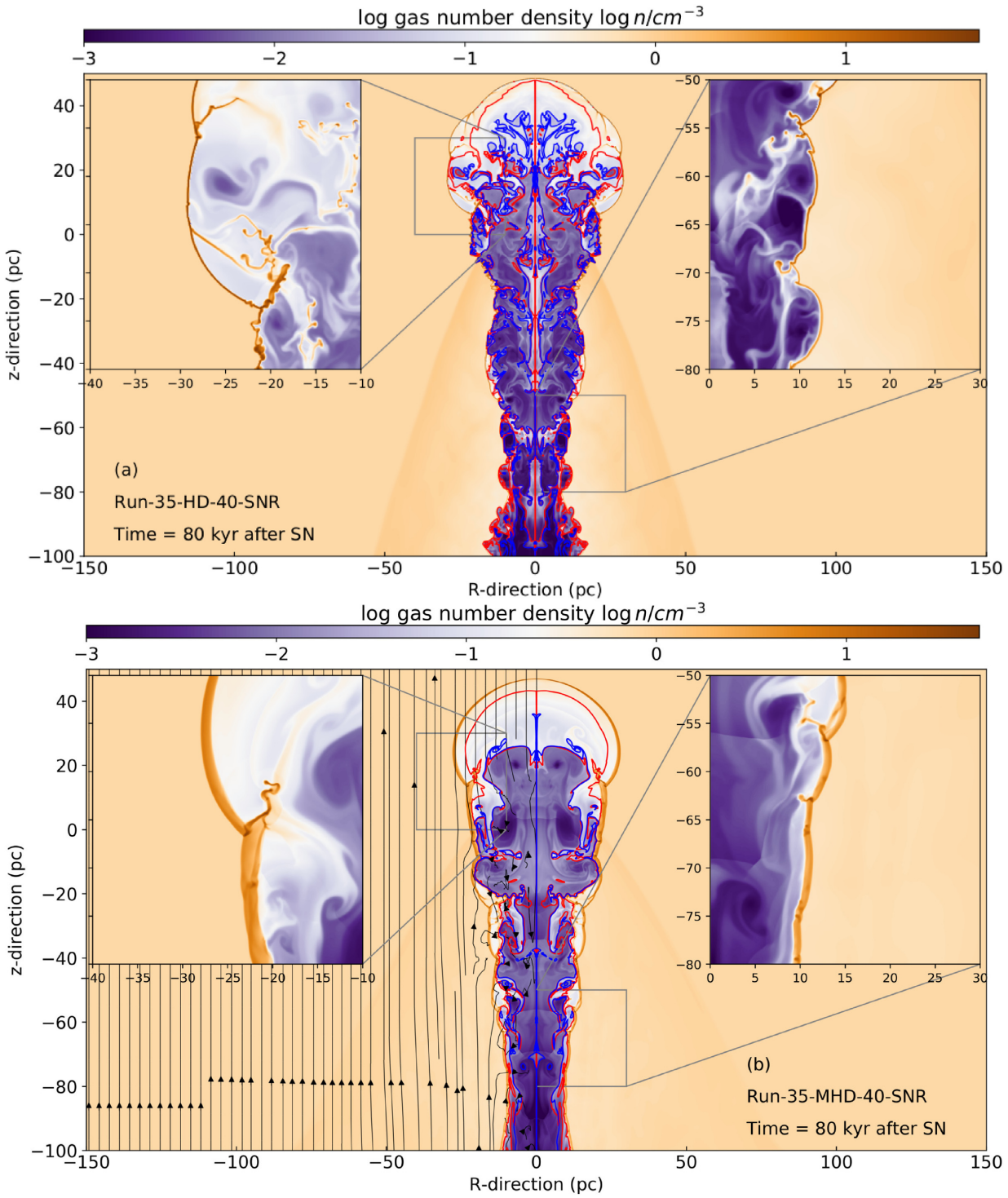

Figure 3. As Fig. 2, but for the supernova remnant of a progenitor moving with 40 km s^{-1}.

2020). Fig. 4(b,d) show that the faster the progenitor moves through the ISM, the sooner the supernova shock wave interacts with the termination shock of the progenitor's wind bubble. For smaller $v_\star$, the elongated shape of the MHD wind bubble permits the Wolf–Rayet wind to expand freely into the unperturbed red supergiant stellar wind and to generate by wind–wind collision a ring of dense swept-up material (Meyer et al. 2020), inside which the blastwave is subsequently released and expands spherically. A similar situation has been explored for static progenitor in the context of Cas A (van Veelen et al. 2009). This phenomenon is particularly prominent for

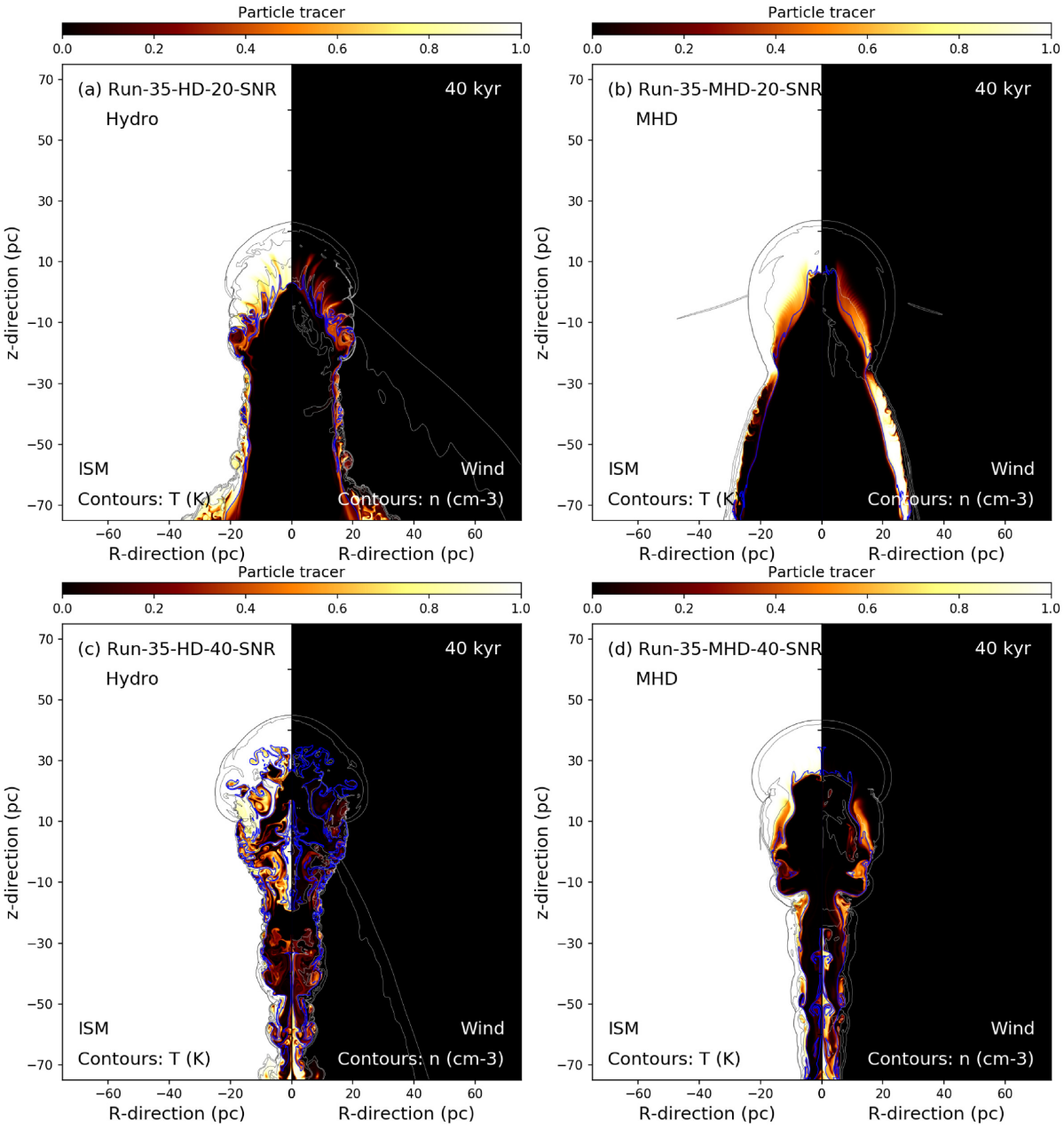

Figure 4. Mixing of material in supernova remnants from massive runaway progenitors. The top row displays results for $v_\star = 20\,\mathrm{km\,s^{-1}}$ and the bottom panels are for $v_\star = 40\,\mathrm{km\,s^{-1}}$. The left column shows purely hydrodynamical models, while the right column is for MHD runs. Each remnant is shown at time 40 kyr after the supernova explosion. Each image gives the ISM fraction $(1 - Q_1)$ and the fraction of stellar-wind material (Q_1) in the left and right part, respectively. The black temperature contours have the levels $T = 10^5$, 10^6 , 10^7 K, and the white number density contours stand for $n = 1.0$, 10^1, 10^2, $10^3\,\mathrm{cm^{-3}}$. The blue contours make the locations with 10 per cent ejecta fraction by number.

small ISM density, $n_{\mathrm{ISM}} \ll 1$, since the radius of the main-sequence wind termination shock is much larger (van Marle et al. 2015), and so is the region filled by the last free-streaming wind.

The effects of the ISM magnetic field are also more pronounced for low progenitor speed, $v_\star = 20\,\mathrm{km\,s^{-1}}$. The supernova remnant shock wave rapidly interacts with the wind bubble in the progenitor's direction of motion, and it is first reverberated towards the centre of the explosion and subsequently channelled into the wind cavity carved during the main-sequence phase, inducing a hot region hosting a lot of mixing of wind, ejecta, and shocked ISM gas (Fig. 4a). The reflections are different in the MHD case, where they occur both parallel and normal to the progenitor's motion, on account of the tubular shape of the shocked-wind region (Fig. 4b,d). A different morphology arises for fast-moving progenitors, with a rather unmixed lobe of shocked ISM ahead of the stellar motion, and a channelled region of mixed ejecta and wind material in the tail (Fig. 4c,d).

3.3 Effect of ISM magnetic field on the remnant's properties

Magnetic field changes the morphology of the pre-supernova stellar wind bubble, which will eventually influence the structure of the remnant and the mixing of material in it. At a magnetized shock, the component of the magnetic field along the shock normal remains unchanged, and that in the shock plane is compressed (Shu 1992). This results in an increased magnetic pressure in the shocked ISM and, consequently, in an enlargement of the bubble perpendicular to the direction of motion, which for static wind bubbles has been demonstrated by van Marle et al. (2015). Further effects are a reduced compression ratio of the forward shock and a puffing-up of the shocked ISM gas layer. Although the MHD jump conditions imply that the ISM field is not compressed ahead of the star, since the cylindrical coordinate system imposes a parallel field, we cannot exclude that this is an artefact. We refer the reader to the thorough discussion in Meyer et al. (2017). Full three-dimensional simulations of both the pre-supernova and remnant phase of moving massive progenitor star are necessary to address this question in appropriate detail.

3.4 Radio synchrotron emission maps

3.4.1 Basic consideration

We perform a back-of-the-envelope estimate of the validity of our assumptions regarding the radio synchrotron emission. We select one-dimensional cross-section of the flow variables ρ, p, and T originating from the centre of the explosion and following the direction of stellar motion, along the axis of symmetry, Oz, in the models, respectively. We then measure the time-dependent position, $R_{\rm FS}(t)$, and speed, $v_{\rm FS}(t)$, of the forward shock, using the shock-finder algorithm of the RATPAC code (Telezhinsky, Dwarkadas & Pohl 2012, 2013; Bhatt et al. 2020). The radiation synthesis is based on the assumption that the forward shock accelerates a certain fraction of particles passing through it, and that the subsequent transport of radio-emitting electrons in the downstream region is entirely advective.

In our radiation transfer model, diffusion is neglected and we shall now verify this assumption. Upstream of the forward shock the density of electrons re-accelerated as cosmic rays exponentially decreases, $N(E,x) \propto e^{-x/x_{\rm c}(t)}$ with length-scale:

$$x_{\rm c}(t) = \frac{D(E)}{v_{\rm FS}(t)}, \tag{31}$$

where $D(E)$ is the diffusion coefficient and E is the energy of the electrons. For simplicity, we shall assume that the diffusion coefficient is a multiple of the Bohm limit, $D(E) \approx \eta D_{\rm Bohm}(E) = \eta\, c/3\, r_{\rm L}(E)$, where $r_{\rm L}$ denotes the Larmor radius of the electrons and η is a scalar controlling the . Using the characteristic frequency of synchrotron radiation, equation (31) can be rewritten as

$$\frac{x_{\rm c}(t)}{\rm pc} \simeq \frac{\eta}{3000}\sqrt{\frac{\nu_{\rm syn}}{10\,{\rm GHz}}}\left(\frac{v_{\rm FS}(t)}{3000\,{\rm km\,s^{-1}}}\right)^{-1}\left(\frac{B(t)}{10\,\mu{\rm G}}\right)^{-1.5}. \tag{32}$$

It is evident that for reasonably well-developed cosmic ray scattering ($\eta \ll 1000$), the precursor of radio-emitting electrons is tiny compared to the size of the system and produces a negligible contribution of synchrotron emission. Note that a significant abundance of magnetic field perpendicular the shock surface will slow down diffusive transport away from the shock and hence reduces η.

Diffusion in the downstream region may transport electrons beyond the discontinuity to the ejecta region. Within time t, advective transport displaces electrons from the shock by the distance $\Delta_{\rm adv} \simeq t\, v_{\rm FS}(t)/4$. Diffusive transport displaces by $\Delta_{\rm dif} \simeq \sqrt{D(E)t}$,

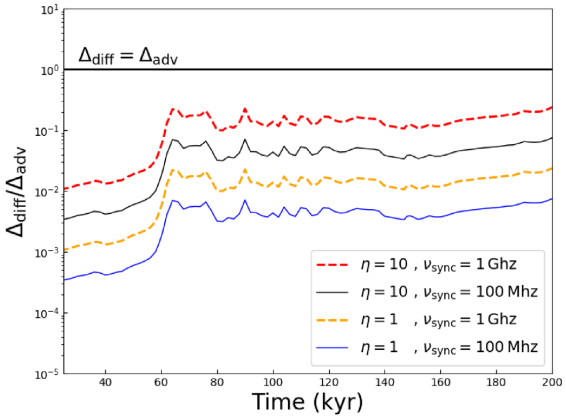

Figure 5. Comparison between the diffusion time-scale, $\Delta_{\rm diff}$, and the advection time-scale, $\Delta_{\rm adv}$, of a particle accelerated at the forward shock of the supernova remnant in our simulation Run-35-MHD-40-SNR of a 35-$M_\odot$ progenitor moving with $v_\star = 40\,{\rm km\,s^{-1}}$. The quantity $\Delta_{\rm diff}/\Delta_{\rm adv}$ is plotted as a function of remnant age for several values of η and synchrotron frequency $\nu_{\rm sync}$, respectively. Values well below unity imply that diffusion can be neglected in the estimate of radio emission maps.

and so ignorability of diffusion requires

$$t\, v_{\rm FS}(t)/4 \gg \sqrt{D(E)t} \quad \Rightarrow\ t\, v_{\rm FS}(t) \gg 16 x_{\rm c}(t). \tag{33}$$

With x_c as given in equation (32), we find that the condition is likely met. Fig. 5 plots $\Delta_{\rm diff}/\Delta_{\rm adv}$ as a function of time for our simulation model Run-35-MHD-40-SNR and several values of $\eta \leq 10$ and $\nu_{\rm sync \leq 1\,Ghz}$. To be noted from the figure is that $\Delta_{\rm diff}/\Delta_{\rm adv} \ll 1$ for times ≤ 200 kyr, and consequently we can ignore cosmic ray diffusion in the production of radio emission maps.

3.4.2 Non-thermal emission maps

We generate non-thermal radio emission maps from our MHD models of supernova remnants at representative points of time in the evolution of the supernova remnants. Using the procedure described in Section 2.4, we pre-compute for each viewing angle, $\theta_{\rm obs}$, the distribution of magnetic field normal to the line of sight, $B_\perp$. An illustrative example based on model Run-35-MHD-40 at time 80 kyr is given in Fig. 6. Then, we compute the radio intensity with our modified version of the RADMC3D code. In Fig. 7, we show intensity maps for supernova remnant ages 6 kyr (top), 20 kyr (middle), and 80 kyr (bottom) for a progenitor moving with $v_\star = 20\,{\rm km\,s^{-1}}$. We selected three viewing angles to the equatorial plane, $\theta_{\rm obs} = 0^\circ$ (left), $\theta_{\rm obs} = 45^\circ$ (middle), and $\theta_{\rm obs} = 90^\circ$ (right) and normalized the background-substracted maps. Fig. 8 displays corresponding radio maps for $v_\star = 40\,{\rm km\,s^{-1}}$.

Model Run-35-MHD-20 with progenitor moving at $v_\star = 20\,{\rm km\,s^{-1}}$ traces the expanding supernova blastwave that is distorbed by its interaction with the circumstellar medium. Later, 40 kyr after the explosion, the expanding shock wave has reached the unperturbed ISM and is fairly bright there. The radio arcs are now larger than at time 20 kyr and the brightest region on the sides have a bilateral morphology. Note that the maps are background-subtracted, and the region of shocked stellar wind may be dimmer than the galactic radio background, leaving only the filamentary arcs prominently visible. For an inclination angle $\theta_{\rm obs} = 45^\circ$ the remnants look rounder and more bubbly. One and the same remnant can appear with bilateral or arced structures depending on $\theta_{\rm obs}$. For $\theta_{\rm obs} = 90^\circ$ the observer's

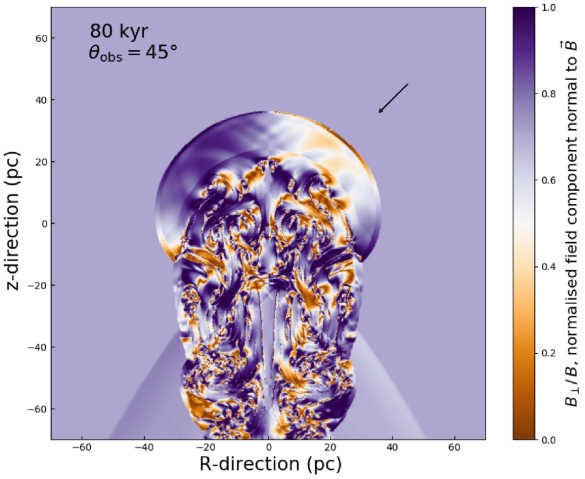

Figure 6. Normalized projection of the magnetic field perpendicular to the line of sight, $B_\perp/B$, for model Run-35-MHD-40 model with progenitor speed $v_\star = 40\,\mathrm{km\,s^{-1}}$ at time 80 kyr after the supernova explosion. The black arrow marks the direction of the observer's line of sight, making an angle $\theta_{obs} = 45^\circ$ with the z-axis.

line of sight is aligned with the direction of stellar motion, and the projected remnant appears as a ring-like structure in the sky, on account of the two-dimensional nature of the simulations. Since the magnetic field is parallel to the stellar motion, $B_\perp \simeq 0$ in the shocked ISM, and the brightest emission originates from the regions of mixing, primarily in the reflected shock wave.

The radio intensity maps of our simulation Run-35-MHD-40 with progenitor speed $v_\star = 40\,\mathrm{km\,s^{-1}}$ are shown in Fig. 8. The emission is brighter than in model Run-35-MHD-20 as a result of the faster progenitor star producing stronger shocks in its supernova remnant. At time 6 kyr after the explosion, the shock wave has already been greatly distorted by the Wolf–Rayet circumstellar material and has lost sphericity to become as ovoid-like structure. Later in time, the shock wave adopts a hour-glass-like shape that appears spherical in the radio map for $\theta_{obs} = 45^\circ$ and to a lesser degree at $\theta_{obs} = 0^\circ$. After 40 kyr, the remnant has a bulb-like morphology that arises from both the shock wave expansion into the ISM and the channeling of the shock wave into the low-density cavity of unshocked stellar wind in the tail. The radio intensity peak shifts to the location where the shock wave intercepts the trail of stellar wind (Fig. 8d,e). The density in the region of wind–ISM interaction is more important than in the case of a progenitor moving with $v_\star = 20\,\mathrm{km\,s^{-1}}$, and so the stabilizing effect of the magnetic field inside of the remnant is reduced. Hence, more ring-like structures appear in the emission maps, for example in Fig. 8(h). We would observe a series of concentric rings for $\theta_{obs} = 90^\circ$, each of them corresponding to a ring in the trail of shocked stellar wind interacting with the channelled supernova shock wave. There is more variety and complexity in the radio appearance for fast-moving progenitors.

4 DISCUSSION

This section discusses the limitations of our method, compares our results to earlier results, and further examines our findings in the context of particle acceleration. Finally, we compare our results with observational data.

4.1 Model limitations

As any numerical study, our method suffers from simplifications that limit the realism of our results. The most obvious one is the cylindrical coordinate system with rotational invariance, which intrinsically imposes a symmetry axis to the models. This approach is convenient in the modelling of the circumstellar medium of massive stars and their subsequent supernova remnants (Franco et al. 1991; Rozyczka & Tenorio-Tagle 1995; Comerón 1997; Comerón & Kaper 1998; van Marle, Langer & García-Segura 2005, 2007; Ferreira & de Jager 2008; van Marle et al. 2014; Green et al. 2019), at the expense of forcing an directional alignment of the motion of the progenitor, the local ISM magnetic field, and progenitor's axis of rotation. Only fully three-dimensional simulations permit flexibility in the directional arrangement (e.g. Katushkina et al. 2017, 2018), but they are far too expensive to permit scanning the parameter space of remnants from massive progenitors.

Supernova remnants from massive progenitors are multiphase regions composed of a warm, magnetized ISM through which the progenitor star moves, the evolving stellar wind, and a hot component produced by the interaction between the supernova shock wave and the material of the wind bubble and the shocked ISM gas. Supernova remnants may be located close to dense, cold molecular clouds that can further affect their evolution and modify the gas chemistry. The pressure of the cosmic rays accelerated in the supernova remnant (Ferrand, Decourchelle & Safi-Harb 2014), anisotropic heat transfer (Orlando et al. 2005), photoionizing progenitor radiation, or the turbulence in the ISM should also be included in the models (Moranchel-Basurto et al. 2017; Villagran et al. 2020), but that is far beyond the scope of the current study and may be considered in future work. Last, note that intrinsic dense molecular (Zhou & Chen 2011; Zhou et al. 2014, 2016) or low-density components (Arias et al. 2019a,b) of the ambient medium are an additional, in some context an even preponderant element to take into account in the shaping of core-collapse supernova remnants.

4.2 Comparison with previous works

This study extends earlier work beginning with Meyer et al. (2015) on hydrodynamical models of supernova remnants of runaway stars with initial 10, 20, and 40 $M_\odot$, which end their lives as red supergiants and generate Cygnus-Loop-like nebulae. The second study of this series explored the appearance of wind nebulae and remnants of a 60 $M_\odot$ progenitor star going through luminous-blue-variable and Wolf–Rayet phases, with emphasis on the mixing of material inside the remnant Meyer et al. (2020). What is new and different in the present study is the inclusion of the ISM magnetic field during both the pre- and the post-supernova phase, together with the post-processing of radio synchrotron intensity maps. The effect of ISM magnetization on the environment of massive stars has been investigated by van Marle et al. (2015), albeit without distinguishing ejecta from wind and ISM gas as we do by means of passive scalar tracers. Moreover, our models include a state-of-art stellar evolutionary model for the wind history of the 35 $M_\odot$ star that we concentrate on.

4.3 Comparison with observations

4.3.1 Remnants of core-collapse supernovae

Katsuda et al. (2018) determined several properties, such as the distance and the progenitor mass, of core-collapse supernova

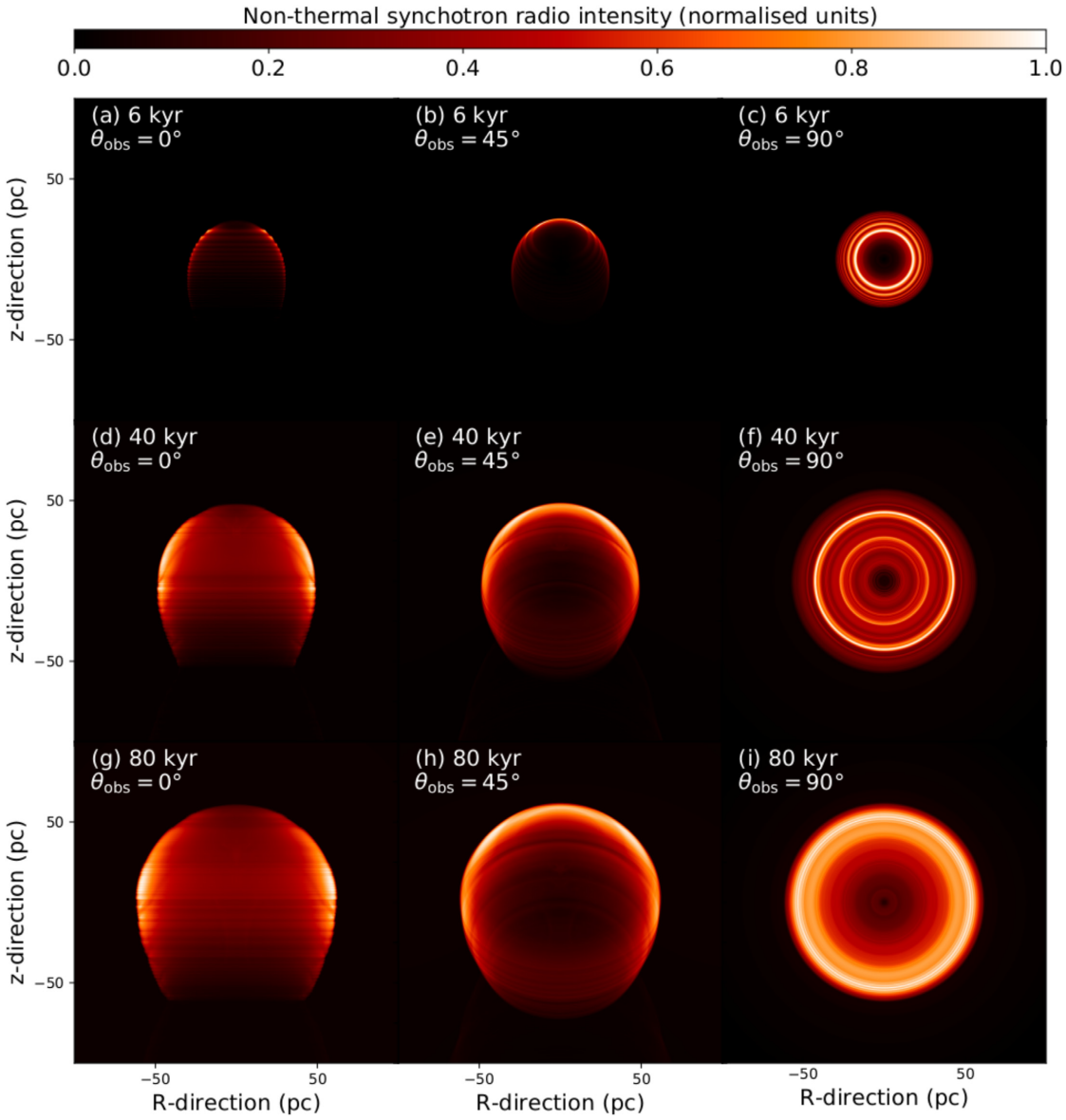

Figure 7. Normalized maps of radio synchrotron intensity of supernova remnants with progenitor speed $v_\star = 20\,\mathrm{km\,s^{-1}}$ at times 6 kyr (top), 40 kyr (middle), and 80 kyr (bottom) after the supernova explosion, respectively. The viewing angle between the equatorial plane and the line of sight is $\theta_{obs} = 0°$ (left), $\theta_{obs} = 45°$ (middle), and $\theta_{obs} = 90°$ (right).

remnants in the Milky Way and in low-metallicity dwarf galaxies such as the Large and Small Magellanic Clouds. They found that most of the identified remnants of massive progenitors in the Galaxy have a zero-age main-sequence mass $\geq$22.5 $M_\odot$. There is a general agreement between predictive stellar evolution models that the progenitor exploded with such mass, either as a red supergiant or as a Wolf–Rayet star, although more exotic situations such as blue supergiant progenitor star exist (Hillebrandt et al. 1987). Note that, in the context of massive binary systems, the explosion of the component can kick the companion, producing runaway stars (Lux et al. 2021). Our models explore the Wolf–Rayet possibility using a zero-age main-sequence 35 $M_\odot$ star. As we concentrate on the evolution of rather older remnants, about 6–80 kyr after the explosion, our predictions are applicable to the objects listed between Kes 79 and W51C in table 1 of Katsuda et al. (2018).

Our models constitute baseline models to be further tailored to specific supernova remnants, in particular Kes 79, G350.1-0.3, G292.0+1.8, RX J1713.7-3946, Kes 79, G290.1-0.8, 3C 391, W44, G284.3-1.8, or CTB109. Note that C-, N-, and O-enriched material, witness of post-main-sequence winds from massive stars, has been directly observed in the remnant G296.1-0.5 (Castro et al. 2011), making it an evident candidate of a supernova remnant with Wolf–Rayet progenitor that is worth exploring numerically with simulations like ours. As underlined by Katsuda et al. (2018), the distribution of core-collapse supernovae in the Galaxy does not fit

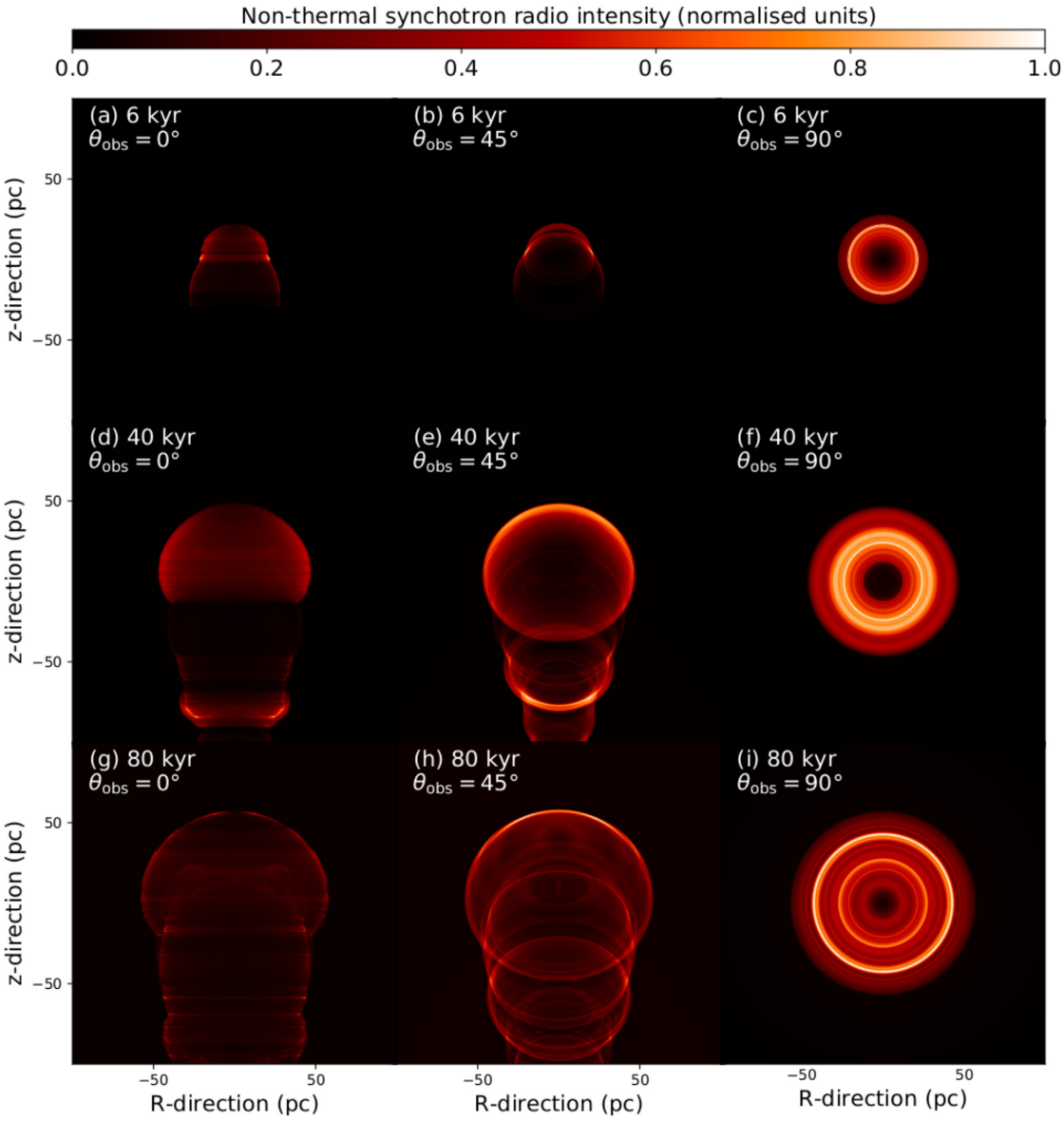

Figure 8. As Fig. 7 but here for model Run-35-MHD-40-SNR with progenitor moving with 40 km s^{-1}.

any initial mass function, which suggest that there should be many more unidentified remnants our simulations would be applicable to. Note also that models for core-collapse remnants do not generally apply to the so-called historical supernova remnants since these are mostly of Type Ia (Green & Stephenson 2003), except for Cas A (van Veelen et al. 2009; Zhou et al. 2018) and RWC 86 (Gvaramadze et al. 2017), respectively.

The space motion of the progenitor is the other fundamental ingredient of our simulations, together with the zero-age main-sequence mass. If the massive progenitor is at rest, then its circumstellar wind bubble remains spherical (Weaver et al. 1977). The star and the centre of its subsequent explosion are located at its centre (Freyer et al. 2006; Dwarkadas 2007). A sub-sonic motion of the progenitor will off-centre the remnant with respect to the wind bubble without changing its overall appearance (Meyer et al. 2020). Hence, remnants from slowly moving progenitor star should reflect the spherical symmetry of their circumstellar medium. However, as *in situ* star formation does not seem to be an obvious route to explain isolated Wolf–Rayet stars (Gvaramadze et al. 2012; Meyer et al. 2020), static massive stars should live and die inside their parent star formation region, where they would participate in the regulation of subsequent star formation (Paron et al. 2009). The feedback from stellar winds and/or jets of other (young) stellar objects (Bally, Reipurth & Davis 2007; Fendt 2009; Fendt & Sheikhnezami 2013) will affect the medium in which massive stars form (Murray, Goyal & Chang 2018), evolve, and die. This should result in a very complex morphology, possibly further complicated by ISM cavities and enhanced levels of turbulence, in the ambient medium hosting a huge mix of material in a super bubble in which the supernova subsequently explodes (van Marle et al. 2012).

4.3.2 Comparison with specific objects

Most supernova remnants in the Milky Way lie within 5° of the galactic plane. The dilute ISM at high galactic latitudes makes (circumstellar) shocks weaker, resulting in fainter supernova remnants such as, for example, the rather evolved radio source G181.1+9.5 (Kothes et al. 2017). This latitude-dependence of the radio surface brightness of supernova remnants is known as the Σ–D relation (Caswell & Lerche 1979). The modelled 35 $M_\odot$ runaway star moving with $v_\star = 40\,\mathrm{km\,s^{-1}}$ travels about 220 pc before exploding, about the same as the height of G181.1+9.5 above the galactic plane (≈250 pc). Dedicated simulations would be highly desirable to explore the differences in the radio properties between supernova remnants of runaway progenitors in the Galactic place and those at higher galactic latitudes, as well as the effects of metallicities. Our non-thermal radio emission maps authorize a couple of further, direct comparisons with supernova remnants of massive, evolved progenitors, namely G296.5+10.0, the shell-type remnants CTB 109, and Kes 17.

First, G296.5+10.0 is a supernova remnant of core-collapse origin, confirmed by the trace of magnetized wind in which the supernova shock wave expands, and the presence of a neutron star therein (Harvey-Smith et al. 2010). Radio observations with the Australia Telescope Compact Arrary at 1.4 GHz reveal a bipolar shape, which qualitatively similar to those in our model with velocity $v_\star = 20\,\mathrm{km\,s^{-1}}$, Run-35-MHD-20-SNR, at time 6 kyr, when the shock wave interacts with the stellar-wind bow shock and accelerates electrons (Fig. 7a). Similarly, Fig. 8(a) also resembles greatly the 7 kyr old bilateral supernova remnant G296.5+10.0, implying that its progenitor might have been a rather fast-moving star of mass 20–40 $M_\odot$. Secondly, the shell-type remnant CTB 109 is the remnant of a core-collapse supernova remnant of a 30–40$M_\odot$ progenitor, which matches the mass range of the 35-$M_\odot$ stellar model used in this study. Its age is around 14 000 yr, see Katsuda et al. (2018).

According to our results, CTB 109 should be surrounded by a circumstellar structure, i.e. a red-supergiant wind bubble engulfing a Wolf–Rayet ring, with which the supernova shock wave interacts, although its overall shape has been reproduced in the context of a type Ia explosion, i.e. without the presence of a dense circumstellar wind bubble generated by a massive progenitor (Bolte, Sasaki & Breitschwerdt 2015). Its opened shell appearance, e.g. as seen with the Canadian Galactic Plane Survey at 1420 MHz (Kothes & Foster 2012), is similar to our model Run-35-MHD-SNR at times 6–40 kyr (Fig. 8b,e). Note also that CTB 109 is a hadronic gamma-ray emitter (Castro et al. 2012). The last example is the supernova remnant Kes 17 that is less than 40000 yr old and with a progenitor mass 25–30$M_\odot$ consistent with the Wolf–Rayet scenario (Katsuda et al. 2018). Its double-arced morphology observed with the Australian Telescope Array at 20 cm resembles our model Run-35-MHD-40-SNR at times 40 kyr (Fig. 8c).

5 CONCLUSIONS

We explore the formation, structure, and radio signatures of supernova remnants of massive, Wolf–Rayet-evolving supernova progenitors ejected from their parent cluster and moving through the ISM of the Milky Way. Our study concentrates on the coupled impact of stellar motion and the magnetization of the ISM. We perform MHD simulations over the entire stellar lifetime, as they successively evolve through a long main-sequence phase, a red supergiant, and a Wolf–Rayet phase, and eventually spawn a core-collapse supernova remnant. Numerical models are performed with the PLUTO code (Mignone et al. 2007, 2012) by simulating the circumstellar medium of massive stars, into which we launch a core-collapse supernova shock wave. We follow its interaction with the stellar surroundings and the local ambient ISM supported by an organized 7 μG magnetic field. Considering two speeds of the runaway progenitors and running the simulations up to the oldest evolutionary phase of the supernova remnants, 150 kyr after the explosion, their morphologies, their structures, the mixing of material happening in them are explored.

The presence of an ISM magnetic field profoundly affects the gas properties. Prior to the supernova explosion, the compressed magnetic field in the circumstellar medium stabilizes the wind/ISM contact discontinuity in the tail of the bubble. Indeed, compressed magnetic field in the outer remnant stabilizes and elongates the wind/ISM contact discontinuity of the cavity of unshocked stellar wind, in which the ejecta is channelled. A consequence is a reduced mixing efficiency of ejecta and evolved stellar-wind material enriched in C, N, and O elements in the inner region of the remnant, where the supernova shock wave propagates. Moreover, after the supernova explosion, the density downstream of the supernova shock front is reduced in our MHD simulations when it propagates into the pristine ambient medium, on account of the damping of turbulence. This must influence the acceleration processes of cosmic ray electrons and protons in supernova remnants from massive progenitors and will be investigated in future works (Bhatt et al. 2020). We emphasize the need for a careful treatment of the gas microphysics to properly simulate young supernova remnants interacting with circumstellar structures. This particularly applies to runaway massive progenitors whose supernova shock front is reverberated towards the centre of the explosion, generating a complex region made of shocks, discontinuities, and filamentary structures, in which non-thermal particles can be accelerated.

Last, using our modified version of the radiative transfer code RADMC/3D (Dullemond 2012) we produced synthetic radio-intensity maps showing projected arcs and filaments that we interpret as a morphological characteristic of supernova remnants of fast-moving Wolf–Rayet stars. Our radio predictions are qualitatively in accordance with the morphology of several core-collapse remnants, such as the bilateral G296.5+10.0, as well as the shell-type supernova remnants CTB 109 and Kes 17, identified as originating from 25–40 $M_\odot$ progenitors (Katsuda et al. 2018) that might have undergone a Wolf–Rayet phase. Our simulations and predictions regarding the non-thermal emission of supernova remnants from massive progenitors are relevant for and may be applied to the various galactic and extragalactic core-collapse remnants (Katsuda et al. 2018).

ACKNOWLEDGEMENTS

Authors are grateful to the referee, P. Velazquez, for comments on synchrotron emission that greatly improved the quality of the manuscript. The authors thank Allard Jan van Marle from Ulsan National Institute of Science and Technology for his kind advices on MHD simulations of the surroundings of massive stars. The authors acknowledge the North-German Supercomputing Alliance (HLRN) for providing HPC resources that have contributed to the research results reported in this paper. MP acknowledges the Max Planck Computing and Data Facility (MPCDF) for providing data storage resources and HPC resources that contributed to test and optimized the PLUTO code. LMO acknowledges partial support by the Russian Government Program of Competitive Growth of Kazan Federal University.

DATA AVAILABILITY

This research used the PLUTO code developed at the University of Torino by A. Mignone (http://plutocode.ph.unito.it/) and of the RADMC-3D code developed at the University of Heidelberg by C. Dullemond (https://www.ita.uni-heidelberg.de/~dullemond/software/radmc-3d/). The figures have been produced using the Matplotlib plotting library for the Python programming language (https://matplotlib.org/). The data underlying this article will be shared on reasonable request to the corresponding author.

REFERENCES

Arias M., Domček V., Zhou P., Vink J., 2019a, A&A, 627, A75
Arias M. et al., 2019b, A&A, 622, A6
Aschenbach B., Leahy D. A., 1999, A&A, 341, 602
Ávila-Aroche A., Velázquez P. F., Camps-Fariña A., Toledo-Roy J. C., Esquivel A., 2020, MNRAS, 495, 2112
Bally J., Reipurth B., Davis C. J., 2007, in Reipurth B., Jewitt D., Keil K., eds, Protostars and Planets V, Observations of Jets and Outflows from Young Stars, University of Arizona Press, Tucson. p. 215
Balsara D. S., Tilley D. A., Howk J. C., 2008, MNRAS, 386, 627
Baranov V. B., Krasnobaev K. V., Kulikovskii A. G., 1971, Sov. Phys. Dokl., 15, 791
Bestenlehner J. M. et al., 2014, A&A, 570, A38
Bhatt M., Sushch I., Pohl M., Fedynitch A., Das S., Brose R., Plotko P., Meyer D. M.-A., 2020, Astropart. Phys., 123, 102490
Bolte J., Sasaki M., Breitschwerdt D., 2015, A&A, 582, A47
Brighenti F., D'Ercole A., 1994, MNRAS, 270, 65
Brighenti F., D'Ercole A., 1995a, MNRAS, 277, 53
Brighenti F., D'Ercole A., 1995b, MNRAS, 273, 443
Broersen S., Chiotellis A., Vink J., Bamba A., 2014, MNRAS, 441, 3040
Brott I. et al., 2011, A&A, 530, A115
Castro D., Slane P. O., Gaensler B. M., Hughes J. P., Patnaude D. J., 2011, ApJ, 734, 86
Castro D., Slane P., Ellison D. C., Patnaude D. J., 2012, ApJ, 756, 88
Caswell J. L., Lerche I., 1979, MNRAS, 187, 201
Chevalier R. A., 1982, ApJ, 258, 790
Chiotellis A., Schure K. M., Vink J., 2012, A&A, 537, A139
Comerón F., 1997, A&A, 326, 1195
Comerón F., Kaper L., 1998, A&A, 338, 273
Drury L., 1983a, Space Sci. Rev., 36, 57
Drury L. O., 1983b, Rep. Prog. Phys., 46, 973
Dullemond C. P., 2012, Astrophysics Source Code Library, record ascl:1202.015, RADMC-3D: A multi-purpose radiative transfer tool
Dwarkadas V. V., 2007, ApJ, 667, 226
Ekström S. et al., 2012, A&A, 537, A146
Eldridge J. J., Genet F., Daigne F., Mochkovitch R., 2006, MNRAS, 367, 186
Fang J., Yu H., Zhang L., 2017, MNRAS, 464, 940
Fendt C., 2009, ApJ, 692, 346
Fendt C., Sheikhnezami S., 2013, ApJ, 774, 12
Ferrand G., Decourchelle A., Safi-Harb S., 2014, ApJ, 789, 49
Ferreira S. E. S., de Jager O. C., 2008, A&A, 478, 17
Franco J., Tenorio-Tagle G., Bodenheimer P., Rozyczka M., 1991, PASP, 103, 803
Freyer T., Hensler G., Yorke H. W., 2003, ApJ, 594, 888
Freyer T., Hensler G., Yorke H. W., 2006, ApJ, 638, 262
Garcia-Segura G., Mac Low M.-M., Langer N., 1996, A&A, 305, 229
Green D. A., Stephenson F. R., 2003, in Weiler K., ed., Lecture Notes in Physics, Vol. 598 , Supernovae and Gamma-Ray Bursters of Historical Supernovae. Springer-Verlag, Berlin, p. 7
Green S., Mackey J., Haworth T. J., Gvaramadze V. V., Duffy P., 2019, A&A, 625, A4
Gvaramadze V. V., Kniazev A. Y., Fabrika S., 2010a, MNRAS, 405, 1047
Gvaramadze V. V., Kniazev A. Y., Fabrika S., 2010b, MNRAS, 405, 1047
Gvaramadze V. V., Weidner C., Kroupa P., Pflamm-Altenburg J., 2012, MNRAS, 424, 3037
Gvaramadze V. V., Menten K. M., Kniazev A. Y., Langer N., Mackey J., Kraus A., Meyer D. M.-A., Kamiński T., 2014, MNRAS, 437, 843
Gvaramadze V. V. et al., 2017, Nat. Astron., 1, 0116
Hamann W. R., Gräfener G., Liermann A., 2006, A&A, 457, 1015
Harvey-Smith L., Gaensler B. M., Kothes R., Townsend R., Heald G. H., Ng C. Y., Green A. J., 2010, ApJ, 712, 1157
Hillebrandt W., Hoeflich P., Weiss A., Truran J. W., 1987, Nature, 327, 597
Janka H.-T., 2012, Annu. Rev. Nucl. Part. Sci., 62, 407
Janka H.-T., Melson T., Summa A., 2016, Annu. Rev. Nucl. Part. Sci., 66, 341
Jun B.-I., Norman M. L., 1996, ApJ, 472, 245
Katsuda S., Takiwaki T., Tominaga N., Moriya T. J., Nakamura K., 2018, ApJ, 863, 127
Katushkina O. A., Alexashov D. B., Izmodenov V. V., Gvaramadze V. V., 2017, MNRAS, 465, 1573
Katushkina O. A., Alexashov D. B., Gvaramadze V. V., Izmodenov V. V., 2018, MNRAS, 473, 1576
Kothes R., Foster T., 2012, ApJ, 746, L4
Kothes R., Reich P., Foster T. J., Reich W., 2017, A&A, 597, A116
Langer N., 2012, ARA&A, 50, 107
Lux O., Neuhäuser R., Mugrauer M., Bischoff R., 2021, preprint (arXiv:2101.05771)
Mackey J., Mohamed S., Neilson H. R., Langer N., Meyer D. M.-A., 2012, ApJ, 751, L10
Meyer D. M.-A., Gvaramadze V. V., Langer N., Mackey J., Boumis P., Mohamed S., 2014, MNRAS, 439, L41
Meyer D. M.-A., Langer N., Mackey J., Velázquez P. F., Gusdorf A., 2015, MNRAS, 450, 3080
Meyer D. M.-A., van Marle A.-J., Kuiper R., Kley W., 2016, MNRAS, 459, 1146
Meyer D. M.-A., Mignone A., Kuiper R., Raga A. C., Kley W., 2017, MNRAS, 464, 3229
Meyer D. M.-A., Petrov M., Pohl M., 2020, MNRAS, 493, 3548
Meyer D. M.-A., Oskinova L. M., Pohl M., Petrov M., 2020, MNRAS, 496, 3906
Mignone A., Bodo G., Massaglia S., Matsakos T., Tesileanu O., Zanni C., Ferrari A., 2007, ApJS, 170, 228
Mignone A., Zanni C., Tzeferacos P., van Straalen B., Colella P., Bodo G., 2012, ApJS, 198, 7
Moffat A. F. J. et al., 1998, A&A, 331, 949
Moranchel-Basurto A., Velázquez P. F., Giacani E., Toledo-Roy J. C., Schneiter E. M., De Colle F., Esquivel A., 2017, MNRAS, 472, 2117
Moranchel-Basurto A., Velázquez P. F., Ares de Parga G., Reynoso E. M., Schneiter E. M., Esquivel A., 2020, MNRAS, 494, 1531
Moriya T. J., Förster F., Yoon S.-C., Gräfener G., Blinnikov S. I., 2018, MNRAS, 476, 2840
Munoz M., Moffat A. F. J., Hill G. M., Shenar T., Richardson N. D., Pablo H., St-Louis N., Ramiaramanantsoa T., 2017, MNRAS, 467, 3105
Murray D., Goyal S., Chang P., 2018, MNRAS, 475, 1023
Orlando S., Peres G., Reale F., Bocchino F., Rosner R., Plewa T., Siegel A., 2005, A&A, 444, 505
Orlando S., Bocchino F., Reale F., Peres G., Petruk O., 2007, A&A, 470, 927
Orlando S., Bocchino F., Reale F., Peres G., Pagano P., 2008, ApJ, 678, 274
Orlando S., Bocchino F., Miceli M., Petruk O., Pumo M. L., 2012, ApJ, 749, 156
Paron S., Ortega M. E., Rubio M., Dubner G., 2009, A&A, 498, 445
Reynolds S. P., 2008, ARA&A, 46, 89
Rozyczka M., Tenorio-Tagle G., 1995, MNRAS, 274, 1157
Rozyczka M., Tenorio-Tagle G., Franco J., Bodenheimer P., 1993, MNRAS, 261, 674
Sander A., Hamann W. R., Todt H., 2012, A&A, 540, A144
Sanyal D., Langer N., Szécsi D., -C Yoon S., Grassitelli L., 2017, A&A, 597, A71
Schneiter E. M., Velázquez P. F., Reynoso E. M., de Colle F., 2010, MNRAS, 408, 430
Schneiter E. M., Velázquez P. F., Reynoso E. M., Esquivel A., De Colle F., 2015, MNRAS, 449, 88

Shu F. H., 1992, The Physics of Astrophysics. Volume II: Gas Dynamics, University Science Books, Mill Valley
Smartt S. J., 2009, ARA&A, 47, 63
Stock D. J., Barlow M. J., 2010, MNRAS, 409, 1429
Telezhinsky I., Dwarkadas V. V., Pohl M., 2012, Astropart. Phys., 35, 300
Telezhinsky I., Dwarkadas V. V., Pohl M., 2013, A&A, 552, A102
Toalá J. A. et al., 2018, ApJ, 869, L11
Toledo-Roy J. C., Esquivel A., Velázquez P. F., Reynoso E. M., 2014, MNRAS, 442, 229
Truelove J. K., McKee C. F., 1999, ApJS, 120, 299
van Marle A. J., Langer N., García-Segura G., 2005, A&A, 444, 837
van Marle A. J., Langer N., García-Segura G., 2007, A&A, 469, 941
van Marle A. J., Smith N., Owocki S. P., van Veelen B., 2010, MNRAS, 407, 2305
van Marle A. J., Meliani Z., Keppens R., Decin L., 2011, ApJ, 734, L26
van Marle A. J., Meliani Z., Marcowith A., 2012, A&A, 541, L8
van Marle A. J., Decin L., Meliani Z., 2014, A&A, 561, A152
van Marle A. J., Meliani Z., Marcowith A., 2015, A&A, 584, A49
van Veelen B., Langer N., Vink J., García-Segura G., van Marle A. J., 2009, A&A, 503, 495
Velázquez P. F., Vigh C. D., Reynoso E. M., Gómez D. O., Schneiter E. M., 2006, ApJ, 649, 779
Velázquez P. F. et al., 2017, MNRAS, 466, 4851
Viallet M., Baty H., 2007, A&A, 473, 1
Villagran M. A., Velázquez P. F., Gómez D. O., Giacani E. B., 2020, MNRAS, 491, 2855
Weaver R., McCray R., Castor J., Shapiro P., Moore R., 1977, ApJ, 218, 377
Whalen D., van Veelen B., O'Shea B. W., Norman M. L., 2008, ApJ, 682, 49
Wilkin F. P., 1996, ApJ, 459, L31
Woosley S. E., Heger A., Weaver T. A., 2002, Rev. Mod. Phys., 74, 1015
Yoon S.-C., Langer N., 2005, A&A, 443, 643
Zhou P., Chen Y., 2011, ApJ, 743, 4
Zhou P., Safi-Harb S., Chen Y., Zhang X., Jiang B., Ferrand G., 2014, ApJ, 791, 87
Zhou P., Chen Y., Safi-Harb S., Zhou X., Sun M., Zhang Z.-Y., Zhang G.-Y., 2016, ApJ, 831, 192
Zhou P., Li J.-T., Zhang Z.-Y., Vink J., Chen Y., Arias M., Patnaude D., Bregman J. N., 2018, ApJ, 865, 6
Zirakashvili V. N., Ptuskin V. S., 2018, Astropart. Phys., 98, 21

APPENDIX A: EMISSION COEFFICIENTS FOR NON-THERMAL SYNCHROTRON EMISSION

To the best of our knowledge, three main recipes are available for the emission coefficient of non-thermal radio synchrotron emission in the context of supernova remnants (Jun & Norman 1996; Orlando et al. 2007; Ávila-Aroche et al. 2020). Considering the electron spectrum in the vicinity of the shocks,

$$N(E) = K E^{-s}, \tag{A1}$$

where E is the electron energy and $s = 2$ the index and $K \propto n$. They read as,

$$j_{\rm sync}^{\rm Orlando}(\nu) \propto K B_{\perp}^{(s+1)/2} \nu^{-(s-1)/2}, \tag{A2}$$

with $\theta_{\rm obs}$ the viewing angle of the observer, $B_{\perp}$ the magnetic field component perpendicular to the line of sight and ν the emission frequency:

$$j_{\rm sync}^{\rm Jun}(\nu) \propto K^{2-s} p^{s-1} B_{\perp}^{(s+1)/2} \nu^{-(s-1)/2}, \tag{A3}$$

where p is the gas thermal pressure, and

$$j_{\rm sync}^{\rm Avila}(\nu) \propto K v'^{2(s-1)} B_{\perp}^{(s+1)/2} \nu^{-(s-1)/2}, \tag{A4}$$

where v' is the gas velocity in the rest frame of the explosion, respectively. This diagnostics has been widely used in, e.g. the context of the core-collapse but also Type Ia progenitors such as the historical supernova remnants Tycho (Moranchel-Basurto et al. 2020) and SN 1006 (Schneiter et al. 2015; Velázquez et al. 2017).

We generate comparative normalized non-thermal radio emission maps from two selected models of supernova remnants. First, one with a progenitor star moving rather slowly with velocity 20 km s^{-1}, and in which the thermal pressure compares with the ram and magnetic pressures (Fig. A1). Secondly, a model with a fast-moving progenitor is moving with velocity 40 km s^{-1} and in which the ISM magnetic pressure is dynamically unimportant (Fig. A2). Fig. A1 a reveals the bright radio synchrotron circumstellar medium of the progenitor, produced by wind–ISM interaction before the explosion of the massive star, while Fig. A1(b,c) do not. The recipe used in Fig. A1(a) clearly overestimates particle acceleration from the forward shock of the stellar wind bubble, which is much weaker than the forward shock of the expanding supernova blastwave. Hence, the emission coefficient in Orlando et al. (2007) is not the most suitable to our core-collapse remnant problem. The models calculated with the other emission coefficients do not permit to select an optimal one for our study (Fig. A1b,c). The emission coefficient in equation (A3) of Jun & Norman (1996) has a dependence on the thermal pressure p, implying that it is sensitive to cooling and heating by optically thin radiative cooling processes and therefore traces the fast shocks well. Similarly, the recipe of emission coefficient in equation (A4) of Ávila-Aroche et al. (2020) goes as $j_{\rm sync}^{\rm Avila}(\nu) \propto v^2$, which imposes a strong dependence of the chosen frame in which we simulate the stellar wind bubble and the supernova explosion. Consequently, we decide in our study to use the recipe of Jun & Norman (1996).

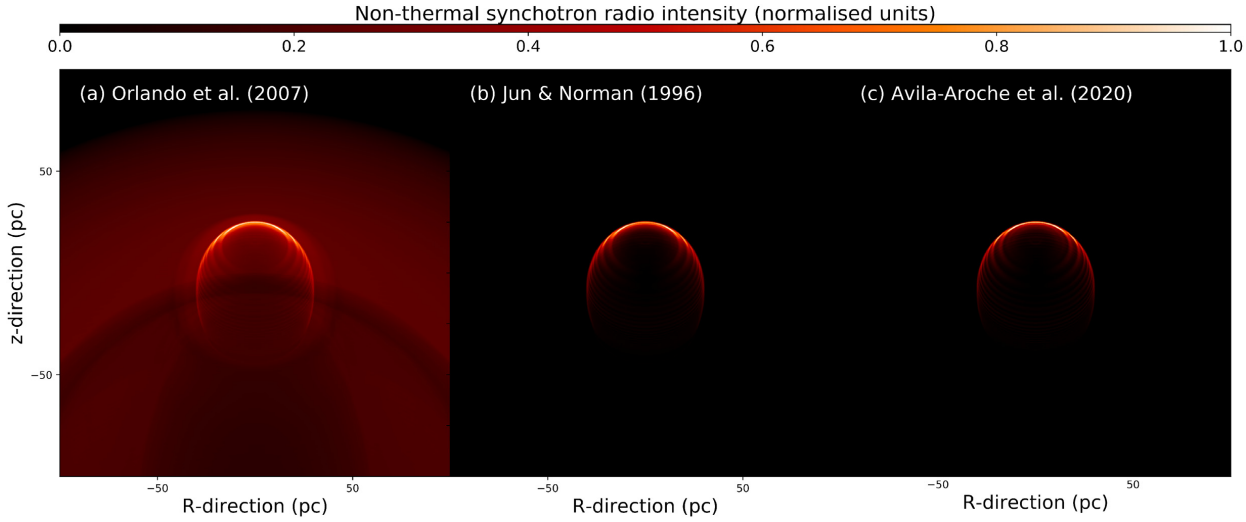

Figure A1. Normalized maps of radio synchrotron intensity of supernova remnants with progenitor speed $v_\star = 20\,\mathrm{km\,s^{-1}}$ at time 6 kyr, and calculated using several prescriptions for the non-thermal emission coefficient. The viewing angle between the equatorial plane and the line of sight is $\theta_{\rm obs} = 45^\circ$ (middle).

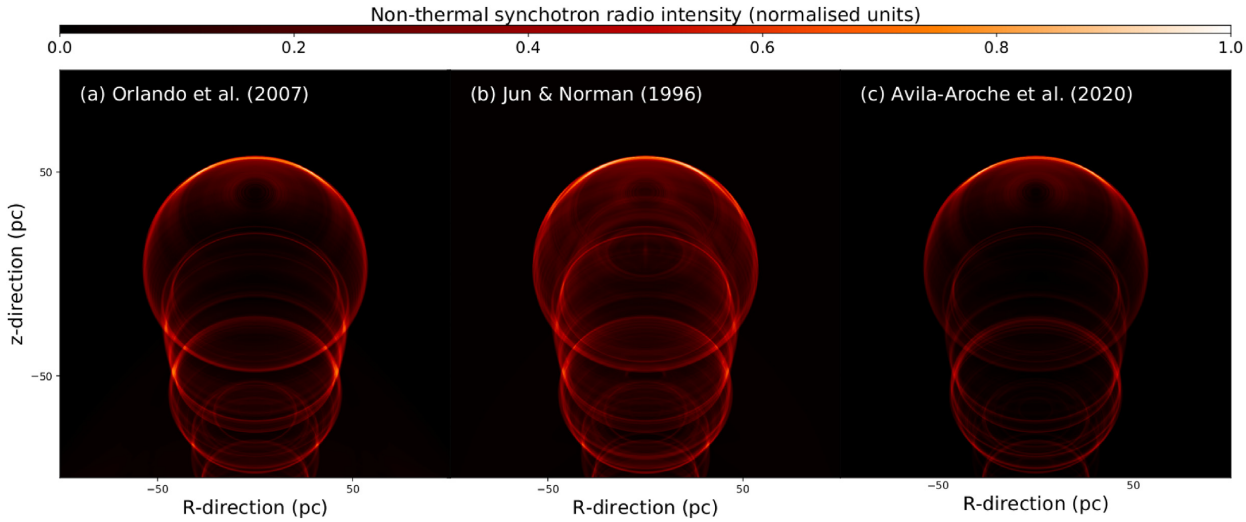

Figure A2. Same as Fig. A1 with progenitor speed $v_\star = 40\,\mathrm{km\,s^{-1}}$ at time 80 kyr.

This paper has been typeset from a TEX/LATEX file prepared by the author.

Monthly Notices of the ROYAL ASTRONOMICAL SOCIETY

MNRAS **515,** 594–605 (2022) https://doi.org/10.1093/mnras/stac1832
Advance Access publication 2022 July 4

Rectangular core-collapse supernova remnants: application to Puppis A

D. M.-A. Meyer [1]★ P. F. Velázquez,[2] O. Petruk [3,4] A. Chiotellis,[5] M. Pohl,[1,6] A. Camps-Fariña,[2,7] M. Petrov,[8] E. M. Reynoso,[9] J. C. Toledo-Roy,[2] E. M. Schneiter [9,10] A. Castellanos-Ramírez [11] and A. Esquivel [2]

[1]*Institut für Physik und Astronomie, Universität Potsdam, Karl-Liebknecht-Strasse 24/25, D-14476 Potsdam, Germany*
[2]*Instituto de Ciencias Nucleares, Universidad Nacional Autónoma de México, CP 04510 Mexico City, Mexico*
[3]*Institute for Applied Problems in Mechanics and Mathematics, NAS of Ukraine, Naukova 3-b, UA-79060 Lviv, Ukraine*
[4]*Astronomical Observatory of Taras Shevchenko National University of Kyiv, 3 Observatorna str Kyiv, UA-04053 Kyiv, Ukraine*
[5]*Institute for Astronomy, Astrophysics, Space Applications and Remote Sensing, National Observatory of Athens, 15236 Penteli, Greece*
[6]*DESY Platanenallee 6, D-15738 Zeuthen, Germany*
[7]*Departamento de Física de la Tierra y Astrofísica, Universidad Complutense de Madrid, E-28040 Madrid, Spain*
[8]*Max Planck Computing and Data Facility (MPCDF), Gießenbachstrasse 2, D-85748 Garching, Germany*
[9]*Instituto de Astronomía y Física del Espacio (IAFE), Av. Int. Güiraldes 2620, Pabellón IAFE, Ciudad Universitaria, 1428 Buenos Aires, Argentina*
[10]*Departamento de Materiales y Tecnología, FCEFyN-UNC, Av. Vélez Sarsfield 1611, Córdoba, Argentina*
[11]*Instituto de Astronomía, Universidad Nacional Autónoma de México, Ap. 70-264, CDMX 04510, México*

Accepted 2022 June 29. Received 2022 June 20; in original form 2022 May 16

ABSTRACT

Core-collapse supernova remnants are the gaseous nebulae of galactic interstellar media (ISM) formed after the explosive death of massive stars. Their morphology and emission properties depend both on the surrounding circumstellar structure shaped by the stellar wind–ISM interaction of the progenitor star and on the local conditions of the ambient medium. In the warm phase of the Galactic plane ($n \approx 1\,\mathrm{cm}^{-3}$, $T \approx 8000\,\mathrm{K}$), an organized magnetic field of strength 7 μG has profound consequences on the morphology of the wind bubble of massive stars at rest. In this paper, we show through 2.5D magnetohydrodynamical simulations, in the context of a Wolf–Rayet-evolving $35\,\mathrm{M}_\odot$ star, that it affects the development of its supernova remnant. When the supernova remnant reaches its middle age (15–20 kyr), it adopts a tubular shape that results from the interaction between the isotropic supernova ejecta and the anisotropic, magnetized, shocked stellar progenitor bubble into which the supernova blast wave expands. Our calculations for non-thermal emission, i.e. radio synchrotron and inverse-Compton radiation, reveal that such supernova remnants can, due to projection effects, appear as rectangular objects in certain cases. This mechanism for shaping a supernova remnant is similar to the bipolar and elliptical planetary nebula production by wind–wind interaction in the low-mass regime of stellar evolution. If such a rectangular core-collapse supernova remnant is created, the progenitor star must not have been a runaway star. We propose that such a mechanism is at work in the shaping of the asymmetric core-collapse supernova remnant Puppis A.

Key words: stars: evolution – stars: massive – ISM: supernova remnants – methods: MHD.

1 INTRODUCTION

Core-collapse supernova remnants are the result of the explosive death of massive stars ($\geq 8\,\mathrm{M}_\odot$). These astrophysical events are rare. However, the mass and energy release in supernova explosions triggers a feedback process of substantial importance in the behaviour and evolution of the interstellar medium (ISM). This feedback enriches the ISM with heavy elements and drives turbulence, regulating future star formation processes (Hopkins, Quataert & Murray 2011). Core-collapse supernova remnants result from the propagation of the energetic blastwave produced by supernova explosions into the surroundings of a high-mass star, which prior to the explosion shaped its environment as structured, concentric layers of hot and cold gas, either from the stellar wind or from the ISM, separated by shocks (Woosley & Weaver 1986; Smartt 2009). Hence, the morphology of supernova remnants is a function of both the density distribution of the circumstellar medium (partly reflecting the past evolution of the progenitor star) and the local condition of the ISM. Therefore, studying the morphology of supernova remnants is key to understand stellar evolution, to constrain local properties of the ISM, and to examine the physics of particle acceleration at shocks (Langer 2012). The classic picture for core-collapse supernova remnants can be found in Chevalier (1982), Chevalier & Liang (1989), and Truelove & McKee (1999).

The vast variety of morphologies found in core-collapse supernova remnants is a mystery. Most of them substantially deviate from the spherically symmetric solution (Aschenbach & Leahy 1999; Arias et al. 2019a, b; Domček et al. 2022; Zhou et al. 2022). Many reasons can be invoked to explain this observational trend, like

★ E-mail: dmameyer.astro@gmail.com

asymmetric stellar winds, or the presence of inhomogeneities in the surrounding medium. Both cases can induce a non-spherical expansion of the supernova shock wave. Indeed, the life span of the progenitor star, the successive stellar evolutionary phases, and the properties of the corresponding stellar winds depend on the star's initial mass (Maeder & Meynet 2000). The stellar rotation (Szécsi et al. 2022) and the existence of one or more companions (Sana et al. 2012) are additional factors that strongly modify the structure of the stellar wind bubble and, consequently, that of the supernova remnant. The density distribution of the local, primeval ISM, such as the presence of a dense molecular component close to the site of the explosion, is another source of anisotropy prone to affect the propagation of the supernova blastwave (Fesen et al. 2018; Boumis et al. 2022).

Over the past decades, the wind bubble problem has spurred the interest of the numerical astrophysical community (Garcia-Segura, Mac Low & Langer 1996a; Garcia-Segura, Langer & Mac Low 1996b; Freyer, Hensler & Yorke 2003, 2006; Dwarkadas 2005; Eldridge et al. 2006). Moreover, the large morphological variety of supernova remnants provided a natural continuation of that computational effort, both in the high-mass (Dwarkadas 2007; van Veelen et al. 2009) and low-mass (Chiotellis, Schure & Vink 2012; Chiotellis et al. 2013; Broersen et al. 2014; Chiotellis, Boumis & Spetsieri 2020, 2021) regime of the progenitors. Many processes have been identified as sources of asymmetry in the circumstellar medium of massive stars, and consequently in their subsequent supernova remnants. Amongst others, the role of radiation in shaping the surroundings of massive stars is investigated in Toalá & Arthur (2011) and Geen et al. (2015). The runaway motion of a fraction of massive stars (Blaauw 1961; Gies 1987; Moffat et al. 1998) distorts wind bubbles into bow shocks (Gull & Sofia 1979; Wilkin 1996; Baalmann et al. 2020, 2021, 2022; Scherer et al. 2020; Herbst et al. 2022), naturally providing an asymmetric environment to the expanding shock wave and generating asymmetric supernova remnants (Franco et al. 1991; Rozyczka et al. 1993; Brighenti & D'Ercole 1995a, b; Fang et al. 2013; Fang, Yu & Zhang 2017; Zhang, Tian & Wu 2018; Meyer et al. 2020b; Yang, Bao & Liu 2020; Meyer 2021), themselves able to govern the morphology of pulsar wind nebulae (Meyer & Meliani 2022). Recently, Das et al. (2022) noted a softening of the non-thermal particle spectra when the shock wave goes through shocked circumstellar material. Similarly, the role of material expelled throughout pulsating mass-loss events occurring during the last century of the progenitor's life has been highlighted in the context of the asymmetries in the expanding shock wave of Cassiopea A (Orlando et al. 2021, 2022). More generally, the lengthening effects of an organized magnetic field on the morphology of stellar wind bubble was analysed by van Marle, Meliani & Marcowith (2015).

This study is a first step in tackling the problem of the particular appearance of the core-collapse supernova remnant Puppis A, which exhibits a rhomboid shape, inside of which several filaments are arranged orthogonal to each other, providing the overall appearance of nested squares and rectangles. This specific arrangement is observable at many wavebands, spanning from the infrared (Arendt et al. 2010) and the optical/X-rays regimes (Hwang, Flanagan & Petre 2005) to non-thermal radio emission (Hewitt et al. 2012). We employ magnetohydrodynamical (MHD) simulations to explore the single O-type progenitor scenario for Puppis A proposed in Reynoso, Cichowolski & Walsh (2017). In our chosen sequence of events, the supernova explosion takes place within a circumstellar medium that has been self-consistently pre-shaped by the previous release of mass and energy along the successive stellar evolutionary phases (main-sequence, red supergiant, and Wolf–Rayet) into the ISM.

Our work is organized as follows. In Section 2, we review the numerical methods and the initial conditions employed to perform numerical MHD simulations for the circumstellar medium and subsequent supernova remnant of a massive progenitor at rest in a magnetized ISM. The asymmetries in the supernova remnant are directly obtained as a result of the interaction of the supernova shock wave with the pre-shaped magnetized circumstellar medium of the progenitor star (van Marle et al. 2015). The evolution of the remnant is presented in Section 3. We investigate the non-thermal and thermal appearance of our supernova remnant in Section 4, and further discuss our findings in the context of the core-collapse supernova remnant Puppis A. Finally, we summarize our conclusions in Section 5.

2 METHOD

In this section, we provide the reader with a description of the numerical methods utilized to perform simulations of asymmetric core-collapse supernova remnants of rectangular appearance. We also briefly summarize the radiative transfer recipes for non-thermal emission used in the analysis of our simulated models.

2.1 Circumstellar medium

First, the circumstellar medium of a massive star is simulated. The 2.5D models are carried out in cylindrical coordinates (R, z, θ) with a static grid, under the simplifying assumption of z-axis symmetry. The dimensions of the grid is $[O, R_{\rm max}] \times [z_{\rm min}, z_{\rm max}] \times [0, 2\pi]$, with a mesh that is uniform along the R- and z-directions. It is constructed of $N_{\rm R} = 2500$ and $N_{\rm z} = 5000$ grid zones and it extends to $R_{\rm max} = z_{\rm max} = 150\,{\rm pc}$ and $z_{\rm min} = -150\,{\rm pc}$. The uniform resolution of the mesh is therefore $\Delta = |z_{\rm max} - z_{\rm min}|/N_{\rm z} = R_{\rm max}/N_{\rm R}$. Reflective conditions are assigned along the z-axis (i.e. at the boundary $R = 0$) and outflow conditions at the other boundaries, respectively. The computational domain is initially filled with gas having the properties of the warm phase of the ISM in the Galactic plane of the Milky Way, with number density $n_{\rm ISM} \approx 0.79\,{\rm cm}^{-3}$ and $T_{\rm ISM} \approx 8000\,{\rm K}$. The magnetization of the ISM is imposed by the geometry of the domain with magnetic field parallel to the symmetry axis Oz.

Our choice of an organized, parallel magnetic field is justified, since even though the typical description of the ISM is that of a turbulent plasma (Passot, Vazquez-Semadeni & Pouquet 1995; Zank, Nakanotani & Webb 2019), a large-scale coherent magnetic field is present in the spiral disc galaxies (see models and observations of Baryshnikova et al. 1987; Yusef-Zadeh & Morris 1987; Beck 2007; Brown et al. 2007; Jansson & Farrar 2012a). This large-scale field is responsible for, e.g. the alignment of supernova remnants with the enrolled arms of the Milky Way (Gaensler 1998) and affects the development of stellar wind bubbles of massive stars (van Marle et al. 2015). The turbulent component of the magnetic field has a significant strength overall (Jansson & Farrar 2012b), but it includes fluctuations with wavelength up to about 100 pc with an energy density that falls off with wavenumber, k. Radiation modelling of young supernova remnants suggests that the coherence length of the magnetic field can indeed be large compare to the size scale of our simulations (Pais et al. 2020). Then the random magnetic field on small scales acts as an additional isotropic, negligible pressure to the ambient medium in which circumstellar shocks propagate.

The stellar wind is imposed in a sphere of radius $r_{\rm in} = 20$ grid zones, following the method of Comerón & Kaper (1998) (see also Mackey et al. 2012; Meyer et al. 2014). The stellar wind density is

Table 1. List of models in this study. All simulations assume a non-rotating static 35 $M_\odot$ star at solar metallicity. The table indicates for each simulation their label, the number of grid points used, and the strength of the ISM magnetic field (in μG).

Model	Grid mesh	$B_{\rm ISM}$ (μG)	Description
Run-35-HD-0-CSM	2500 × 5000	0	Circumstellar medium in unmagnetized ISM
Run-35-MHD-0-CSM	2500 × 5000	7	Circumstellar medium in magnetized ISM
Run-35-HD-0-SNR	3000 × 6000	0	Supernova remnant in unmagnetized ISM
Run-35-MHD-0-SNR	3000 × 6000	7	Supernova remnant in magnetized ISM

imposed assuming the profile

$$\rho_w = \frac{\dot{M}}{4\pi r^2 v_{\rm w}}, \tag{1}$$

where $r = \sqrt{R^2 + z^2}$ is the radial distance from the pre-supernova location, $\dot{M}$ the mass-loss rate, and $v_{\rm w}$ the wind terminal velocity. The mass-loss rate $\dot{M}$ is time-dependently interpolated from the stellar evolutionary track of Ekström et al. (2012); the wind velocity is obtained from the escape velocity using the law of Eldridge et al. (2006). This star successfully evolves through a long hot main-sequence phase, a short cold red supergiant phase and finishes its life via a hot Wolf–Rayet phase. The main properties of the star are presented in great details in Meyer et al. (2021a). The evolution of the wind–ISM interaction is followed throughout the entire star life, from the onset of the main-sequence phase at $t = 0$ to the pre-supernova time at $t = 5.41$ Myr.

We perform two simulation models of similar ISM and stellar wind properties, the difference being the strength of the ISM magnetic field, taken to be $B_{\rm ISM} = 0$ μG (hydrodynamical model) and $B_{\rm ISM} = 7$ μG (MHD model), see Table 1.

2.2 Supernova remnant

Once we know the structure of the circumstellar medium at the pre-supernova time, we calculate the initial ejecta–wind interaction in spherical symmetry in the radial range $[O; r_{\rm out}]$. The ejecta material fills the inner $r \leq r_{\rm max} < r_{\rm out}$ region of the domain. The corresponding density field is defined as a constant density,

$$\rho_{\rm core} = \frac{1}{4\pi n} \frac{\left(10 E_{\rm ej}^{n-5}\right)^{-3/2}}{\left(3 M_{\rm ej}^{n-3}\right)^{-5/2}} \frac{1}{t_{\rm max}^3}, \tag{2}$$

within $r \leq r_{\rm core}$, and a power-law density profile

$$\rho_{\rm max}(r) = \frac{1}{4\pi n} \frac{\left(10 E_{\rm ej}^{n-5}\right)^{(n-3)/2}}{\left(3 M_{\rm ej}^{n-3}\right)^{(n-5)/2}} \frac{1}{t_{\rm max}^3} \left(\frac{r}{t_{\rm max}}\right)^{-n}, \tag{3}$$

in the $r_{\rm core} < r \leq r_{\rm max}$ region, respectively, with $n = 11$ (see Chevalier 1982; Truelove & McKee 1999).

The ejecta speed follows homologous expansion, $v(r) = r/t$, and

$$v_{\rm core}(r_{\rm core}) = \left(\frac{10(n-5)E_{\rm ej}}{3(n-3)M_{\rm ej}}\right)^{1/2}. \tag{4}$$

The forward shock of the supernova blastwave at $r_{\rm max}$ has a flow speed of $v_{\rm max} = 30\,000$ km s^{-1}, which constrains the time of the simulation start $t_{\rm max} = r_{\rm max}/v_{\rm max}$. The value of $r_{\rm max}$ is calculated using the method described in van Veelen et al. (2009). The value of $r_{\rm max}$ is arbitrary as long as the mass it embeds is smaller than that of the ejecta, and $t_{\rm max}$ is determined assuming $v_{\rm max} = 30\,000$ km s^{-1}. In equations (2)–(4), $E_{\rm ej} = 5 \times 10^{50}$ erg is the total energy released by the supernova explosion, and $M_{\rm ej} = 10.12\,M_\odot$ is the ejecta mass, calculated as the pre-supernova stellar mass minus a neutron star mass of $M_{\rm NS} = 1.4\,M_\odot$. Finally, the 1D ejecta–wind interaction is mapped on to a 2.5D computational domain before the forward shock of the blastwave runs into the termination shock of the stellar wind bubble, see method in Meyer, Petrov & Pohl (2020a) and Meyer et al. (2021a). We assume that supernova ejecta and stellar wind are not magnetized.

2.3 Governing equations

The time evolution of the gas is calculated within the frame of ideal magnetohydrodynamics (Meyer et al. 2020b), described by

$$\frac{\partial \rho}{\partial t} + \nabla \cdot (\rho \boldsymbol{v}) = 0, \tag{5}$$

$$\frac{\partial \boldsymbol{m}}{\partial t} + \nabla \cdot \left(\boldsymbol{m} \otimes \boldsymbol{v} - \boldsymbol{B} \otimes \boldsymbol{B} + \hat{\boldsymbol{I}}\, p_{\rm t}\right) \boldsymbol{0}, \tag{6}$$

$$\frac{\partial E}{\partial t} + \nabla \cdot \left((E + p_{\rm t})\boldsymbol{v} - \boldsymbol{B}(\boldsymbol{v} \cdot \boldsymbol{B})\right) = \Phi(T, \rho), \tag{7}$$

and

$$\frac{\partial \boldsymbol{B}}{\partial t} + \nabla \cdot \left(\boldsymbol{v} \otimes \boldsymbol{B} - \boldsymbol{B} \otimes \boldsymbol{v}\right) = \boldsymbol{0}, \tag{8}$$

which stand for the mass continuity, momentum conservation, energy conservation equations, and for the evolution of the magnetic field, respectively. In the above relations, $\boldsymbol{m} = \rho \boldsymbol{v}$ is the vector momentum, ρ the gas density, v the gas velocity, p_t the total pressure, and

$$E = \frac{p}{(\gamma - 1)} + \frac{\boldsymbol{m} \cdot \boldsymbol{m}}{2\rho} + \frac{\boldsymbol{B} \cdot \boldsymbol{B}}{2}, \tag{9}$$

the total energy of the gas. The definition of the sound speed $c_{\rm s} = \sqrt{\gamma\, p/\rho}$ closes the system of equations, with $\gamma = 5/3$ the adiabatic index. Optically thin radiative cooling and photoheating $\Phi(T, \rho)$ are included into the equations via the prescriptions of Meyer et al. (2014), where T is the gas temperature.

The equations are solved using the PLUTO code[1] (Mignone et al. 2007, 2012; Vaidya et al. 2018). This study uses the Godunov-type solver utilized in Meyer et al. (2021b), made of the shock-capturing HLL Rieman solver (Harten, Lax & van Leer 1983) and the eight-wave finite-volume algorithm (Powell 1997) which ensures that the magnetic field remains divergence-free. The numerical method is made of a third-order Runge–Kutta time integrator, used together with the minmod flux limiter and the WENO3 interpolation scheme. The time-step is controlled by the Courant–Friedrich–Levy, initialized to $C_{\rm cfl} = 0.1$ (Meyer 2021).

2.4 Non-thermal emission maps

For further comparison between our MHD models and available observational data, we perform radiative transfer calculations of

[1] http://plutocode.ph.unito.it/

selected time instances of the supernova remnant evolution, for non-thermal emission such as synchrotron and inverse-Compton emission. Regarding the synchrotron radio emission, we use the method detailed in Meyer et al. (2021a). It first assumes a spectrum of the non-thermal electrons present in the post-shock region of the propagating supernova blastwave,

$$N(E) = K E^{-s}, \tag{10}$$

where $s = 2$, $K \propto n$ with n the gas number density, and with E the electron energy. The emission coefficient at frequency ν then reads

$$j_{\rm sync}(\nu) \propto n B_{\perp}^{(s+1)/2} \nu^{-(s-1)/2}, \tag{11}$$

where $B_{\perp}$ stands for the magnetic field component perpendicular to the observer's line of sight, l. The viewing angle $\theta_{\rm obs}$ is the inclination angle of the supernova remnant with respect to the plane of the sky. The emission maps are calculated using the radiative transfer code RADMC-3D[2] which permits ray-tracing integration of arbitrary emission coefficients, providing non-thermal emission maps of synchrotron intensity,

$$I = \int_{\rm SNR} j_{\rm sync}\,(\theta_{\rm obs})\,{\rm d}l. \tag{12}$$

Similarly, we calculate emission maps for inverse-Compton emission by assuming that the electron spectrum (equation 10) extends to a sharp cut-off at a very high energy $E_{\rm max}$. We make use of the emission coefficient at a given photon energy ϵ,

$$j_{\rm IC} = \int_0^{E_{\rm max}} N(E)\Lambda(E){\rm d}E \propto n\epsilon^{-(s-1)/2}, \tag{13}$$

with $\Lambda(E)$ an integral that is a function of the target photon field assumed to be the cosmic microwave background, as established in Petruk (2009). This method has been shown to be accurate from the Thomson to the Klein–Nishina regimes. We further assume that the maximum accelerated energy, $E_{\rm max}$, is the same everywhere in the supernova remnant. The normalized emission maps are obtained by performing the integral,

$$I = \int_{\rm shocks} j_{\rm IC}{\rm d}l, \tag{14}$$

for the shocked material in the vicinity of the forward and reverse shocks of the supernova remnant.

These simple recipes permit the calculation of predictive non-thermal emission from supernova remnant simulations (e.g. Castellanos-Ramírez, Velázquez & Cantó 2021). A more careful determination of synchrotron and inverse-Compton fluxes of our supernovae remnants models would require the explicit knowledge of the accelerated particle distribution as done in Brose, Telezhinsky & Pohl (2016), Brose et al. (2019), Sushch et al. (2022), and Das et al. (2022).

2.5 Thermal emission maps

Last, maps of optical Hα and soft X-rays emission from the core-collapse supernova remnants are calculated. The procedure is similar as for the non-thermal emission and uses different emission coefficients. The optical Hα intensity reads

$$I = \int_{\rm SNR} j_{\rm H\alpha}{\rm d}l, \tag{15}$$

[2]https://www.ita.uni-heidelberg.de/~dullemond/software/radmc-3d/

with

$$j_{\rm H\alpha} = \left(1.21 \times 10^{-22} T^{-0.9}\right) n_{\rm H}^2, \tag{16}$$

where $n_{\rm H}$ is the gas hydrogen number density (Meyer et al. 2015). The soft X-ray emission is calculated as

$$I = \int_{\rm SNR} j_{\rm XR}{\rm d}l, \tag{17}$$

with

$$j_{\rm XR} = \Lambda(T) n_{\rm H}^2, \tag{18}$$

with $\Lambda(T)$ the 0.1–1.0 keV emissivity for diffuse ISM obtained with the XSPEC software (Arnaud 1996).

3 RESULTS

In this section, we present our (non-)magnetized models for the pre-supernova circumstellar medium of static massive stars and for the evolution of their subsequent supernova remnant, together with predictions by radiative transfer calculation of their thermal and non-thermal appearance.

3.1 Asymmetric circumstellar medium

In Fig. 1, we show the density field (in cm^{-3}) in the simulations for the circumstellar medium of a static 35 M$_\odot$ star without (panel a, Run-35-HD-0-CSM) and with an ISM magnetic field (panel b, Run-35-MHD-0-CSM), see Table 1 for the models properties. The hydrodynamical simulation (Fig. 1a) exhibits the typical morphology of a stellar wind bubble generated by a massive static star. From the star to the outermost part of the bubble, we have: (1) the freely expanding Wolf–Rayet stellar wind, (2) the unstable shell of shocked Wolf–Rayet wind sweeping the hot diluted cavity of RSG material, (3) the contact discontinuity separating the main-sequence material and the ISM gas, (4) the large layer of cold, dense shocked ISM material, and (5) the forward shock sweeping the unperturbed ambient medium. The overall structure is globally spherically symmetric (Weaver et al. 1977), although the instabilities in the last Wolf–Rayet wind break this symmetry (Garcia-Segura et al. 1996a, b). We refer the reader interested in further details on the physics of stellar wind bubbles around massive stars to the literature devoted to this problem (Freyer et al. 2003, 2006; Dwarkadas 2005).

Fig. 1(b) displays the pre-supernova circumstellar medium of the massive star in a magnetized ISM. Only the strength of the magnetic field differs from Run-35-HD-0-CSM, in which it was set to $B_{\rm ISM} = 0\,\mu$G. The evolution of the contact discontinuity during the main-sequence phase of the stellar evolution is asymmetric and elongated as a consequence of being inhibited along the direction normal to the vertical ISM field lines (van Marle et al. 2015). Note that the density at the forward shock of the wind bubble is smaller in the magnetized case, since the magnetic pressure reduces the compression ratios of shocks (Figs 1a and b). The distribution of the RSG stellar wind is strongly affected by the shape of the contact discontinuity and it adopts the same oblong configuration. Similarly, the expansion of the Wolf–Rayet stellar wind, initially spherical, is modified by the morphology of the distribution of the termination shock of the stellar wind bubble, see also Meyer et al. (2020b).

3.2 Asymmetric supernova remnant

In Fig. 2, we show as a time sequence the evolution of the supernova blastwave into the circumstellar medium of a 35 M$_\odot$ star in a

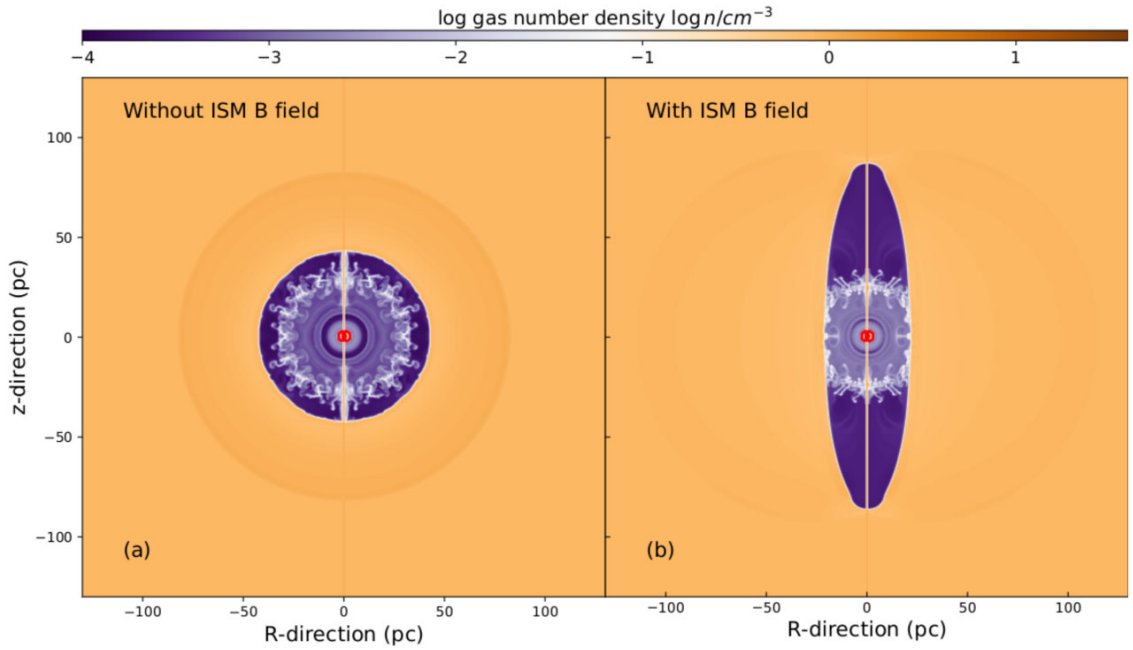

Figure 1. Number density field (in cm^{-3}) in our models for the circumstellar medium of a static 35 $M_\odot$ star, shown at the supernova time, without (a) and with (b) ISM magnetic field. The red contour marks the region of the circumstellar medium where supernova material and energy is injected.

magnetized ISM (model Run-35-MHD-0-CSM). The figures display the number density field of the supernova remnant between 6.25 kyr, (a), and 35.0 kyr, (i), after the explosion. The thin black contour marks the location where 50 per cent of the number density is contributed by ejecta. The supernova shock wave first expands into the freely expanding Wolf–Rayet wind and approaches the unstable shell of shocked Wolf–Rayet gas (Fig. 2a). The shell has begun to interact with the contact discontinuity of the main-sequence wind bubble and loses its spherical shape (van Marle et al. 2015). As the blastwave continues expanding, the shock wave loses sphericity (Fig. 2b) and adopts an elongated morphology mirroring that of the cavity of the stellar wind bubble previously shaped by the progenitor star (Fig. 2c). This is precisely the mechanism that our study aims at highlighting, within the context of the core-collapse supernova remnant Puppis A.

Partial reflection of the blastwave at the shell of Wolf–Rayet material sends gas back towards the centre of the explosion. Shock reflection is at work at the walls of the stellar wind cavity and, to a lesser degree, at the basis of the cylinder of Wolf–Rayet wind, which still expand and interact with the unperturbed wind material (Fig. 2d). A similar mechanism is at play at a stellar wind bow shock (Meyer et al. 2015) or a cold ISM region (Ferreira & de Jager 2008; Castellanos-Ramírez et al. 2021). The tubular morphology of the wind cavity consequently imposes the reflected shocks of supernova ejecta a cylindrical shape, which persists as it propagates towards the centre of the supernova remnant (Fig. 2e). Simultaneously, the forward shock of the supernova is transmitted through the Wolf–Rayet shell and keeps on expanding in the vertical direction of the cavity, as well as in the region of shocked ISM gas (Fig. 2f). After the vertically reflected waves join near the axis of symmetry of the supernova remnant, the process of reflection and transmission of the shock front continues and the supernova ejecta, Wolf–Rayet, red supergiant, and main-sequence materials mix within a thin unstable zone encompassing a dense central region of ejecta (Figs 2g–i).

3.3 Non-thermal emission

Fig. 3 shows the normalized radio synchrotron maps for our simulation Run-35-MHD-0-CSM at the time 12.5 kyr (left-hand panels), 16.5 kyr (left middle panels), 17.5 kyr (right middle panels), and 25.0 kyr (right-hand panels) after the supernova explosion, respectively. The images are obtained using the emission coefficient described in Section 2 and assuming viewing angles of $\theta_{\rm obs} = 0^\circ$ (top panels) and $\theta_{\rm obs} = 45^\circ$ (bottom panels).

When the shock wave hits the cavity walls, the radio appearance of the supernova remnant is that of two parallel bright bars aligned with the direction of the ISM magnetic field (Fig. 3a). This loss of sphericity of the expanding blastwave is also clearly visible with a viewing angle of $\theta_{\rm obs} = 45^\circ$ (Fig. 3e). As the blastwave propagates further and is reflected, we would see an outer hexagon produced by the ejecta penetrating the shock ISM material, inside of which two reflected parallel waves demarcate a bright bilateral region (Figs 3b and f). When the supernova blastwave reflects on to the shell of Wolf–Rayet stellar wind, it converges towards to the centre of the explosion. The region of shocked ejecta consequently adopts the shape of a bright rectangle embedded in an hexagon, at least for a viewing angle slightly tilted with respect to the plane of the sky (Figs 3c and g). However, once the reflected waves join in the centre of the supernova remnant, a very bright elongated region of shocked ejecta forms, and the remnant loses its rectangular shape (Figs 3d and h).

Fig. 4 compares synchrotron and inverse-Compton emission for the viewing angles $\theta_{\rm obs} = 0^\circ$ (top) and $\theta_{\rm obs} = 45^\circ$ (bottom) (left columns, respectively) at an age of 17.5 kyr, when the rectangular synchrotron morphology is most pronounced. The ring-like

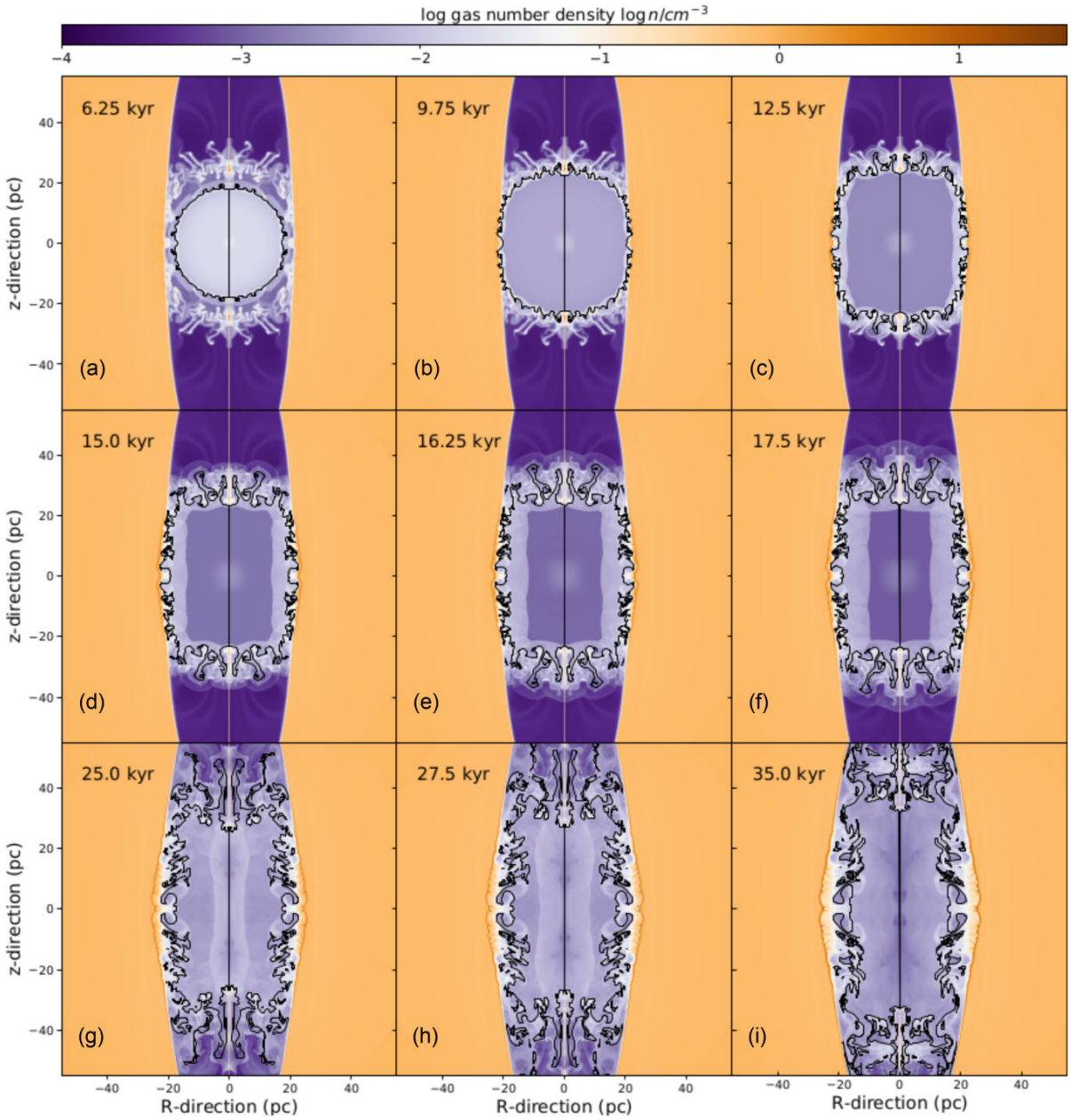

Figure 2. Number density field (in cm^{-3}) in our models for the supernova remnant of a static 35 $M_\odot$ star in a magnetized ISM. The black contour marks the region of the remnant made of 50 per cent of ejecta in number density.

features which appear for a viewing angle $\theta_{obs} = 45°$ are artefacts produced by the 2D nature of the simulations. The synchrotron map with $\theta_{obs} = 0°$ traces the compressed magnetic field in the reflected ejecta and in the ejecta penetrating the shocked ISM bubble (Fig. 4a). The inverse-Compton emission is faint within the central rectangle. In contrast, the brightest inverse-Compton emission originates from the dense material at the unstable ejecta/wind interface, perpendicular to the direction of the ISM magnetic field (Fig. 4b). For both non-thermal emission mechanisms the viewing angle is an important factor for the rectangular morphology (Figs 4e and f).

Fig. 5 displays a series of cross-sections taken vertically (left) and horizontally (right) through the intensity maps in Fig. 4 for a viewing angle of $\theta_{obs} = 0°$. The top panels of the figures display the cuts for synchrotron (thick dashed red line) and inverse-Compton (thin solid blue line) emission. Fig. 6 is as Fig. 5, but assuming a viewing angle of $\theta_{obs} = 45°$. The vertical slices show that the synchrotron cavity, extending from −20 to 20 pc, is centre-filled by bright rings produced by the axisymmetric character of our MHD simulation. This is not seen in the inverse-Compton intensity, regardless of the viewing angle θ_{obs} (Figs 5a and 6a). The horizontal cross-sections highlight the differential expansion of the supernova

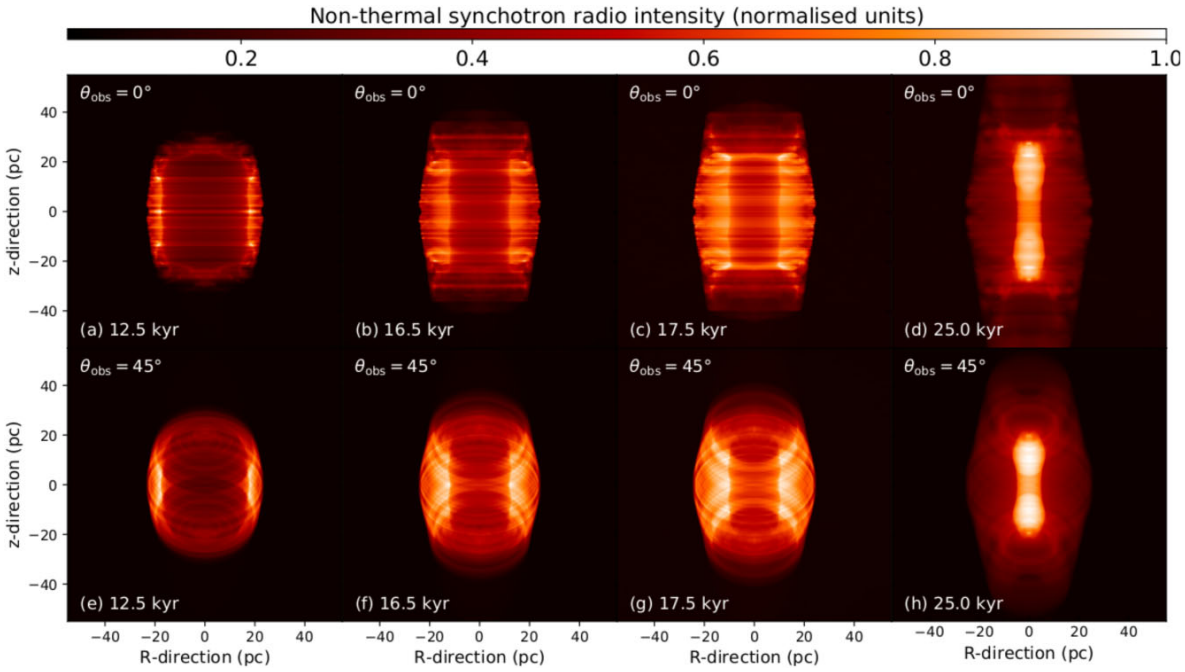

Figure 3. Normalized non-thermal radio synchrotron intensity maps of our supernova remnant model of a static 35 $M_\odot$ star, seen according viewing angles of $\theta_{\rm obs} = 0^\circ$ (top panels) and $\theta_{\rm obs} = 45^\circ$ (bottom panels). The images are displayed for time instances 12.5 kyr (left-hand panels) to 25.0 kyr (right-hand panels) after the supernova explosion. The images are centred on to the location of the supernova explosion.

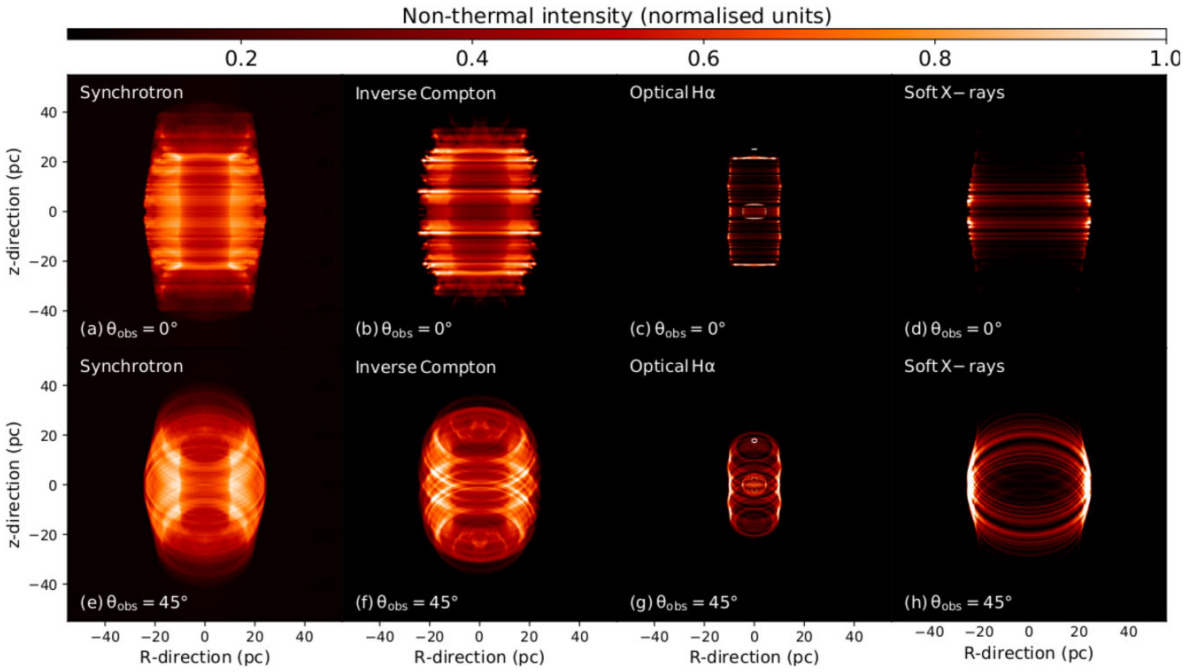

Figure 4. Normalized non-thermal radio synchrotron intensity (left) and inverse-Compton (middle left) as well as thermal optical Hα (middle right) and thermal X-rays (right) emission maps of our supernova remnant model of a static 35 $M_\odot$ star in a magnetized medium at time 17.5 kyr after the explosion, seen according to viewing angles of $\theta_{\rm obs} = 0^\circ$ (top) and $\theta_{\rm obs} = 45^\circ$ (bottom). The images are centre on to the location of the supernova explosion.

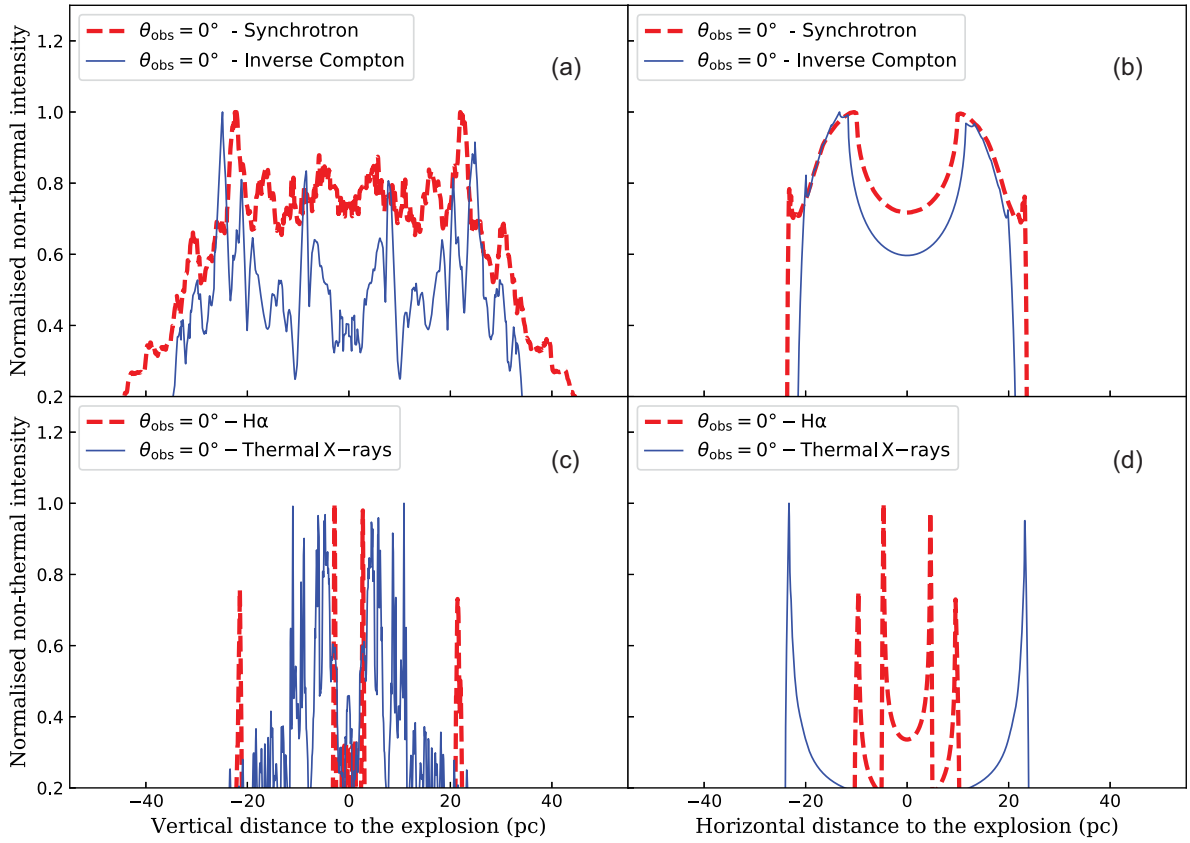

Figure 5. Cuts through the normalized synthetic non-thermal (a,b) and thermal (c,d) emission maps of our rectangular supernova remnant at time 17.5 kyr, taken through the centre of the explosion, along the vertical direction (left column) and the horizontal direction (right column), under a viewing angle of $\theta_{obs} = 0°$.

blastwave into the tubular magnetized circumstellar medium which induce the rectangular morphology, i.e. the brightest peaks of the horizontal slice sit about 20 pc from the centre of the explosion, while the vertical extent reaches up to 40 pc.

3.4 Thermal emission

The right-hand series of panels in Fig. 4 display optical Hα (panels c, g) and thermal X-ray (panels d, h) emission maps at the time of a prominent rectangular synchrotron morphology. The optical image traces the reverse shock of the blastwave being reverberated towards the centre of the explosion, giving the remnant its peculiar morphology, with a central dense ring that reflects the initial inner ejecta profile. The transmitted shock passing through the magnetized and elongated walls of the stellar wind cavity is not visible despite the high post-shock density, since the high temperature in this region forbids generous optical emission. The soft thermal X-ray emission basically originates from the supernova blastwave which penetrates into the walls of the cavity, where the gas is both dense and hot. The morphology of the projected emission is square, as is the overall shape of Puppis A.

The bottom panels of Figs 5 and 6 plot cross-sections taken vertically (panel c) and horizontally (panel d) through the optical (thick dashed red line) and thermal X-ray (thin solid blue line) emission maps, respectively. Both plots additionally highlight that the Hα photons are mostly emitted in the region limited by the reverberated forward shock of the supernova blastwave. Its vertical and horizontal extension away from the centre of the explosion differs greatly so that in projection the region looks like a rectangle. Conversely, the thermal X-ray emission finds its origin in the supernova shock wave penetrating into the shocked material of the stellar wind bubble. Both vertical and horizontal distributions of the emitted material extend to about 40 pc from the centre of the explosion, and in thermal X-rays the supernova remnant looks like a square surrounding the inner optical rectangle.

4 DISCUSSION

The caveats and limitations of our study are presented in this section and the results are discussed in the context of the rectangular supernova remnant Puppis A.

4.1 Limitation of the model

Two main caveats affect our simulation method. First of all, regarding our choice in terms of stellar wind boundaries, we neglect the magnetization of the progenitor stellar wind, as in the precedent papers of this series (Meyer et al. 2020a, 2021a), and as discussed in great details in van Marle et al. (2015). Nevertheless, this is a pre-requisite in the careful estimation of cosmic-rays propagation through core-collapse supernova remnants (Das et al. 2022; Sushch et al. 2022). The adopted scenario for the evolution of the progenitor

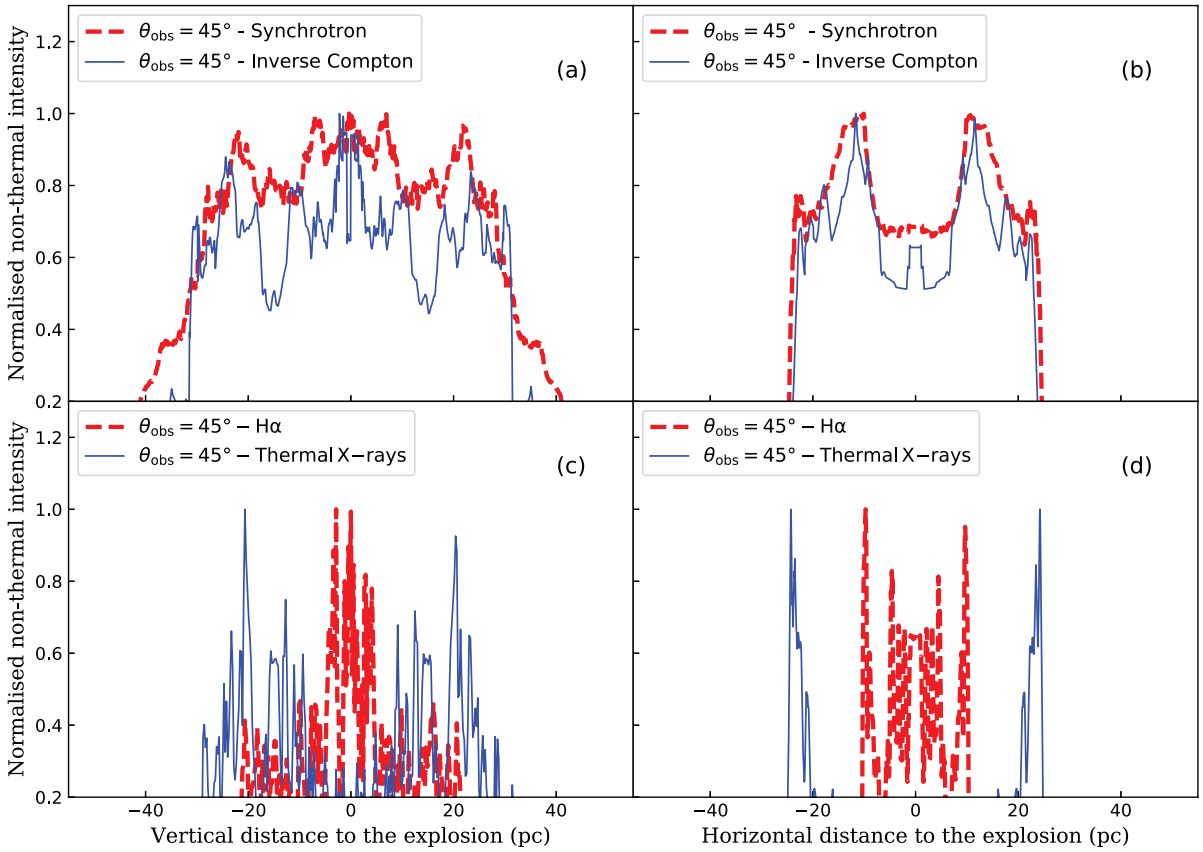

Figure 6. As Fig. 5, but with $\theta_{obs} = 45°$.

is arbitrarily taken to be that of a non-rotating 35 $M_\odot$ star with solar metallicity (Ekström et al. 2012). Hence, this first qualitative study for the formation of rectangular middle-age core-collapse supernova remnants is not fine-tuned to a particular object (see Section 4.2).

Secondly, we neglect any turbulence in the medium into which the star blows its wind. In reality, a surrounding H II region, potentially trapped into the dense layer of the growing stellar wind bubble (Weaver et al. 1977; van Marle, Langer & García-Segura 2004), develops velocity fluctuations when expanding into an inhomogeneous molecular cloud (Medina et al. 2014). Furthermore, the dense environment hosts star formation processes and typically is highly magnetized (Hennebelle & Falgarone 2012), influencing the development of circumstellar structures (Pardi et al. 2017) and supernova remnants (Korpi et al. 1999a, b), which in turn generate and maintain the level of turbulence of the ISM (Seifried et al. 2018). A more realistic depiction of the supernova–wind interaction in a magnetized ISM would require full 3D MHD simulations, better modelling of the circumstellar medium around the massive progenitor star (Meyer et al. 2021b), as well as the propagation of the supernova blastwave in it (Orlando et al. 2021, 2022).

4.2 Interpretation and comparison with observations

4.2.1 A new model for rectangular core-collapse remnants

Our study reveals how core-collapse supernova remnants can reveal a rectangular appearance, by a succession of shock reflections on the walls of the stellar wind cavity, provided their progenitor star blows its pre-supernova material in a medium that is uniformly magnetized (van Marle et al. 2015). This mechanism is the adapted version of the interacting-winds model employed for explaining the formation of bipolar and elliptical planetary nebulae, in a sense that the final outcome is attributed to the interaction of a rather spherical outflow with a pre-existing, non-spherical circumstellar structure.

In that mass regime, other models explain the formation of bipolar and multipolar planetary nebulae, characterized by showing point-symmetric features. These models consider a binary system inside (Bond, Liller & Mannery 1978; Livio, Salzman & Shaviv 1979; Soker & Livio 1994). One of the binary components launches a pair of precessing jets (Soker & Rappaport 2000) which interact with the AGB wind of the other star. This interaction produces point-symmetric planetary nebulae as observed in the Red Rectangle (Cohen et al. 2004; Velázquez et al. 2011), Hen 3-1475 (Riera et al. 2014), and IC 4634 nebulae (Guerrero et al. 2008). The interacting wind model considers the collision of an isotropic, fast, and low-density stellar wind (coming from a low-mass star) with a slow and high-density AGB wind, with a high-density equatorial region (shaped by stellar rotation). The wind–wind interaction induces an asymmetric flow and opens the stellar magnetic field lines (García-Segura & López 2000). Analogically, in our model involving a massive progenitor star, the spherical outflow is represented by the supernova ejecta, while the non-spherical circumstellar medium is sculptured by both the red supergiant and Wolf–Rayet stellar winds under the action of ISM magnetic fields.

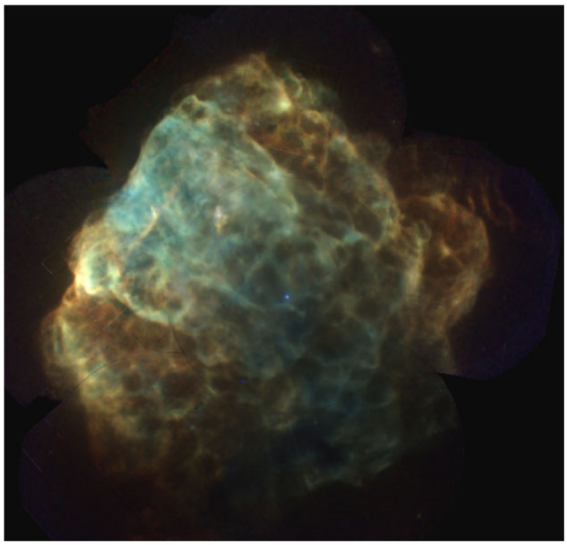

Figure 7. X-ray view of the supernova remnant Puppis A as a mosaic of *XMM–Newton* and Chandra data, taken from Dubner et al. (2013), where the red (0.3–0.7 keV), green (0.7–1.0 keV), and blue (1.0–8.0 keV) colours indicate each emission energy band. The supernova remnant exhibits a morphology strongly deviating from sphericity, appearing as an overall rectangular shape inside of which multiple square structures are imbricated.

We interpret the formation of such rectangular core-collapse supernova remnants as indication of slow or absent motion of the progenitor star. If the massive star were a fast-moving object, the cavity of stellar wind would be strongly asymmetric, and so would be the propagation of the shock wave (Meyer et al. 2015).

4.2.2 *Comparison with Puppis A*

Puppis A is the archetype of core-collapse supernova remnant with a rectangular morphology. It displays an unusual angular shape shown in a composite X-ray rendering (see Fig. 7) and a rectangular morphology in radio continuum (see fig. 1 in Reynoso et al. 2017), with an intensity enhancement towards the Eastern region. The massive nature of Puppis A's progenitor has been constrained due to (i) its O and Fe enriched interior (Charles, Culhane & Zarnecki 1978; Katsuda et al. 2013) and (ii) the runaway pulsar it hosts (Holland-Ashford et al. 2017; Vogt et al. 2018; Mayer et al. 2020). This supernova remnant has mainly been observed in the radio (Reynoso et al. 2017), infrared (Arendt et al. 1991, 2010; Arendt, Dwek & Petre 1991), optical (Goudis & Meaburn 1978), and X-Ray (Dwek et al. 1987; Dubner et al. 2013) band, providing a multiwavelength picture of the rectangular shape. Infrared emission from scattered light on dust trapped into the supernova remnant reveals that the supernova blastwave is not expanding into a stratified medium, except in the eastern region (Arendt et al. 1990), which is in accordance with our model.

High-energy data provided by the *Fermi-LAT* and *H.E.S.S.* facilities indicate that Puppis A is the site of particle acceleration up to the GeV band only, which supports the scenario of the supernova blastwave not yet massively interacting with the surrounding dense molecular clouds (Hewitt et al. 2012; H. E. S. S. Collaboration 2015; Xin et al. 2017). This fact favours the rectangular morphology being principally produced by the blastwave colliding with circumstellar material, as proposed our model. In particular, a blastwave passing through hot, shocked circumstellar material tends to produce soft cosmic ray spectra (Das et al. 2022), leading to much weaker emission in the TeV band than at GeV energies, as is observed. The sole signs of isolated cloud collision in the bright eastern knot of Puppis A (Paron et al. 2008), not included into our simulation, are therefore not responsible for its overall shaping.

Our numerical model is consistent with the observations of Puppis A, as it displays an overall squared X-ray shape (Figs 4d and h) with smaller imbricated optical rectangles (Figs 4c and g). This finding permits us to propose that the progenitor of Puppis A was a massive star which evolved in a background medium of organized magnetization in agreement with the scenario presented by Reynoso, Velázquez & Cichowolski (2018).

Throughout stellar evolution, the many stellar evolutionary phases released first main-sequence material that first shape an elongated cavity in which an evolved red supergiant wind is blown (Reynoso et al. 2017, 2018), and, depending on the mass of the progenitor, it might have further evolved up to the Wolf–Rayet phase. An extra numerical effort is necessary to fine-tune simulations to the case of Puppis A and its shaping.

5 CONCLUSION

This study investigates the possibility that core-collapse supernova remnants adopt a rectangular emission morphology. We perform 2.5D MHD simulations of the circumstellar medium of a 35 $M_\odot$ single massive star at rest (Ekström et al. 2012) evolving and dying in the warm phase of the Galactic plane of the Milky Way. The numerical models are performed with the PLUTO code (Mignone et al. 2007, 2012; Vaidya et al. 2018), which has been previously used to study the surroundings of massive stars and their associated supernova remnants (Meyer et al. 2014).

It is known that magnetic field of order of few μG is not effective to modify the shape of supernova remnant because the ratio of the magnetic pressure to the thermal pressure is small and magnetic field is not dynamically important in evolution of the remnant. However, it is very effective to determine the structure of the ambient density where this ratio is considerably larger than unity (van Marle et al. 2015). We demonstrate that such circumstellar medium of the progenitor star, profoundly pressure-supported by an organized background magnetic field, subsequently constrains the propagation of the supernova shock wave, inducing multiple shock reflections along the directions normal to the ISM magnetic fields. Eventually, in the middle age of its evolution (15–20 kyr), the remnant adopts the unusual rectangular morphology due to the isotropically expanding supernova ejecta interacting with the tubular structure of the progenitor surroundings.

We calculated intensity maps of radio synchrotron and inverse-Compton emission using radiative transfer calculations. At some viewing angles, these maps show a rectangular morphology for the age window between the reflection of the supernova shock wave off the circumstellar medium and the moment it reaches the centre of the remnant. This mechanism is the adapted version of the shaping of bipolar and elliptical planetary nebula by the interaction of two stellar winds (see García-Segura & López 2000). Our scenario for rectangular core-collapse supernova remnants requires that its progenitor was not a runaway star, for which the remnant will shape following the scenario of Meyer et al. (2021a). We suggest that the asymmetric supernova remnant Puppis A, depicting a rectangular morphology, is at least partly shaped by the mechanism described here.

Further investigations are necessary to validate our model for rectangular core-collapse supernova remnants, both on the observational and on the numerical side. The former to update our knowledge on the abundance of rectangular remnants from massive stars, the latter to understand the detailed morphology of Puppis A (Reynoso et al. 2017).

ACKNOWLEDGEMENTS

The authors thank the anonymous referee for comments which improved the quality of the paper. DMAM thanks L. Oskinova for discussion on X-ray observational data. The authors acknowledge the North-German Supercomputing Alliance (HLRN) for providing HPC resources that have contributed to the research results reported in this paper. MP acknowledges the Max Planck Computing and Data Facility (MPCDF) for providing data storage resources and HPC resources which contributed to test and optimize the PLUTO code. PFV, JCT-R, and AC-R acknowledge the financial support for PAPIIT-UNAM grants IA103121 and IG100422. AC-R acknowledges support from CONACYT postdoctoral fellowship. AC-F acknowledges financial support by the Spanish Ministry of Science and Innovation through the research grant PID2019-107427GB-C31. EMR is a member of the Carrera del Investigador Científico of CONICET, Argentina, and is partially funded by CONICET grant PIP 112-201701-00604CO.

DATA AVAILABILITY

This research made use of the PLUTO code developed at the University of Torino by A. Mignone (http://plutocode.ph.unito.it/) and of the RADMC-3D code developed at the University of Heidelberg by C. Dullemond (https://www.ita.uni-heidelberg.de/~dullemond/software/radmc-3d/). The figures have been produced using the MATPLOTLIB plotting library for the Python programming language (https://matplotlib.org/). The data underlying this article will be shared on reasonable request to the corresponding author.

REFERENCES

Arendt R. G., Dwek E., Petre R., Dickel J. R., Roger R. S., Milne D. K., Kesteven M. J., 1990, ApJ, 350, 266
Arendt R. G., Dwek E., Petre R., 1991, ApJ, 368, 474
Arendt R. G. et al., 2010, ApJ, 725, 585
Arias M. et al., 2019a, A&A, 622, A6
Arias M., Domček V., Zhou P., Vink J., 2019b, A&A, 627, A75
Arnaud K. A., 1996, in Jacoby G. H., Barnes J., eds, ASP Conf. Ser. Vol. 101, Astronomical Data Analysis Software and Systems V. Astron. Soc. Pac., San Francisco. p. 17
Aschenbach B., Leahy D. A., 1999, A&A, 341, 602
Baalmann L. R., Scherer K., Fichtner H., Kleimann J., Bomans D. J., Weis K., 2020, A&A, 634, A67
Baalmann L. R., Scherer K., Kleimann J., Fichtner H., Bomans D. J., Weis K., 2021, A&A, 650, A36
Baalmann L. R., Scherer K., Kleimann J., Fichtner H., Bomans D. J., Weis K., 2022, preprint (arXiv:2205.04823)
Baryshnikova I., Shukurov A., Ruzmaikin A., Sokoloff D. D., 1987, A&A, 177, 27
Beck R., 2007, A&A, 470, 539
Blaauw A., 1961, Bull. Astron. Inst. Neth., 15, 265
Bond H. E., Liller W., Mannery E. J., 1978, ApJ, 223, 252
Boumis P. et al., 2022, MNRAS, 512, 1658
Brighenti F., D'Ercole A., 1995a, MNRAS, 273, 443
Brighenti F., D'Ercole A., 1995b, MNRAS, 277, 53
Broersen S., Chiotellis A., Vink J., Bamba A., 2014, MNRAS, 441, 3040
Brose R., Telezhinsky I., Pohl M., 2016, A&A, 593, A20
Brose R., Sushch I., Pohl M., Luken K. J., Filipović M. D., Lin R., 2019, A&A, 627, A166
Brown J. C., Haverkorn M., Gaensler B. M., Taylor A. R., Bizunok N. S., McClure-Griffiths N. M., Dickey J. M., Green A. J., 2007, ApJ, 663, 258
Castellanos-Ramírez A., Velázquez P. F., Cantó J., 2021, MNRAS, 508, 5345
Charles P. A., Culhane J. L., Zarnecki J. C., 1978, MNRAS, 185, 15P
Chevalier R. A., 1982, ApJ, 258, 790
Chevalier R. A., Liang E. P., 1989, ApJ, 344, 332
Chiotellis A., Schure K. M., Vink J., 2012, A&A, 537, A139
Chiotellis A., Kosenko D., Schure K. M., Vink J., Kaastra J. S., 2013, MNRAS, 435, 1659
Chiotellis A., Boumis P., Spetsieri Z. T., 2020, Galaxies, 8, 38
Chiotellis A., Boumis P., Spetsieri Z. T., 2021, MNRAS, 502, 176
Cohen M., Van Winckel H., Bond H. E., Gull T. R., 2004, AJ, 127, 2362
Comerón F., Kaper L., 1998, A&A, 338, 273
Das S., Brose R., Meyer D. M. A., Pohl M., Sushch I., Plotko P., 2022, A&A, 661, A128
Domček V., Vink J., Zhou P., Sun L., Driessen L., 2022, A&A, 659, A63
Dubner G., Loiseau N., Rodríguez-Pascual P., Smith M. J. S., Giacani E., Castelletti G., 2013, A&A, 555, A9
Dwarkadas V. V., 2005, ApJ, 630, 892
Dwarkadas V. V., 2007, ApJ, 667, 226
Dwek E., Petre R., Szymkowiak A., Rice W. L., 1987, ApJ, 320, L27
Ekström S. et al., 2012, A&A, 537, A146
Eldridge J. J., Genet F., Daigne F., Mochkovitch R., 2006, MNRAS, 367, 186
Fang J., Yu H., Zhang L., 2017, MNRAS, 464, 940
Fang J., Yu H., Zhu B.-T., Zhang L., 2013, MNRAS, 435, 570
Ferreira S. E. S., de Jager O. C., 2008, A&A, 478, 17
Fesen R. A., Weil K. E., Cisneros I. A., Blair W. P., Raymond J. C., 2018, MNRAS, 481, 1786
Franco J., Tenorio-Tagle G., Bodenheimer P., Rozyczka M., 1991, PASP, 103, 803
Freyer T., Hensler G., Yorke H. W., 2003, ApJ, 594, 888
Freyer T., Hensler G., Yorke H. W., 2006, ApJ, 638, 262
Gaensler B. M., 1998, ApJ, 493, 781
García-Segura G., López J. A., 2000, ApJ, 544, 336
Garcia-Segura G., Mac Low M.-M., Langer N., 1996a, A&A, 305, 229
Garcia-Segura G., Langer N., Mac Low M.-M., 1996b, A&A, 316, 133
Geen S., Rosdahl J., Blaizot J., Devriendt J., Slyz A., 2015, MNRAS, 448, 3248
Gies D. R., 1987, ApJS, 64, 545
Goudis G., Meaburn J., 1978, A&A, 62, 283
Guerrero M. A. et al., 2008, ApJ, 683, 272
Gull T. R., Sofia S., 1979, ApJ, 230, 782
H. E. S. S. Collaboration, 2015, A&A, 575, A81
Harten A., Lax P. D., van Leer B., 1983, SIAM Rev., 25, 35
Hennebelle P., Falgarone E., 2012, A&AR, 20, 55
Herbst K. et al., 2022, Space Sci. Rev., 218, 29
Hewitt J. W., Grondin M. H., Lemoine-Goumard M., Reposeur T., Ballet J., Tanaka T., 2012, ApJ, 759, 89
Holland-Ashford T., Lopez L. A., Auchettl K., Temim T., Ramirez-Ruiz E., 2017, ApJ, 844, 84
Hopkins P. F., Quataert E., Murray N., 2011, MNRAS, 417, 950
Hwang U., Flanagan K. A., Petre R., 2005, ApJ, 635, 355
Jansson R., Farrar G. R., 2012a, ApJ, 757, 14
Jansson R., Farrar G. R., 2012b, ApJ, 761, L11
Katsuda S., Ohira Y., Mori K., Tsunemi H., Uchida H., Koyama K., Tamagawa T., 2013, ApJ, 768, 182
Korpi M. J., Brandenburg A., Shukurov A., Tuominen I., 1999a, A&A, 350, 230
Korpi M. J., Brandenburg A., Shukurov A., Tuominen I., Nordlund Å., 1999b, ApJ, 514, L99
Langer N., 2012, ARA&A, 50, 107
Livio M., Salzman J., Shaviv G., 1979, MNRAS, 188, 1
Mackey J., Mohamed S., Neilson H. R., Langer N., Meyer D. M.-A., 2012, ApJ, 751, L10
Maeder A., Meynet G., 2000, ARA&A, 38, 143

Mayer M., Becker W., Patnaude D., Winkler P. F., Kraft R., 2020, ApJ, 899, 138
Medina S. N. X., Arthur S. J., Henney W. J., Mellema G., Gazol A., 2014, MNRAS, 445, 1797
Meyer D. M. A., 2021, MNRAS, 507, 4697
Meyer D. M. A., Meliani Z., 2022, MNRAS, 515, L29
Meyer D. M.-A., Mackey J., Langer N., Gvaramadze V. V., Mignone A., Izzard R. G., Kaper L., 2014, MNRAS, 444, 2754
Meyer D. M.-A., Langer N., Mackey J., Velázquez P. F., Gusdorf A., 2015, MNRAS, 450, 3080
Meyer D. M. A., Petrov M., Pohl M., 2020a, MNRAS, 493, 3548
Meyer D. M. A., Oskinova L. M., Pohl M., Petrov M., 2020b, MNRAS, 496, 3906
Meyer D. M. A., Pohl M., Petrov M., Oskinova L., 2021a, MNRAS, 502, 5340
Meyer D. M. A., Mignone A., Petrov M., Scherer K., Velázquez P. F., Boumis P., 2021b, MNRAS, 506, 5170
Mignone A., Bodo G., Massaglia S., Matsakos T., Tesileanu O., Zanni C., Ferrari A., 2007, ApJS, 170, 228
Mignone A., Zanni C., Tzeferacos P., van Straalen B., Colella P., Bodo G., 2012, ApJS, 198, 7
Moffat A. F. J. et al., 1998, A&A, 331, 949
Orlando S., Wongwathanarat A., Janka H. T., Miceli M., Ono M., Nagataki S., Bocchino F., Peres G., 2021, A&A, 645, A66
Orlando S. et al., 2022, preprint (arXiv:2202.01643)
Pais M., Pfrommer C., Ehlert K., Werhahn M., Winner G., 2020, MNRAS, 496, 2448
Pardi A. et al., 2017, MNRAS, 465, 4611
Paron S., Dubner G., Reynoso E., Rubio M., 2008, A&A, 480, 439
Passot T., Vazquez-Semadeni E., Pouquet A., 1995, ApJ, 455, 536
Petruk O., 2009, A&A, 499, 643
Powell K. G., 1997, in Hussaini M. Y., van Leer B., Van Rosendale J., eds, An Approximate Riemann Solver for Magnetohydrodynamics. Springer, Berlin, Heidelberg, p. 570
Reynoso E. M., Cichowolski S., Walsh A. J., 2017, MNRAS, 464, 3029
Reynoso E. M., Velázquez P. F., Cichowolski S., 2018, MNRAS, 477, 2087
Riera A., Velázquez P. F., Raga A. C., Estalella R., Castrillón A., 2014, A&A, 561, A145
Rozyczka M., Tenorio-Tagle G., Franco J., Bodenheimer P., 1993, MNRAS, 261, 674
Sana H. et al., 2012, Science, 337, 444
Scherer K., Baalmann L. R., Fichtner H., Kleimann J., Bomans D. J., Weis K., Ferreira S. E. S., Herbst K., 2020, MNRAS, 493, 4172
Seifried D., Walch S., Haid S., Girichidis P., Naab T., 2018, ApJ, 855, 81
Smartt S. J., 2009, ARA&A, 47, 63
Soker N., Livio M., 1994, ApJ, 421, 219
Soker N., Rappaport S., 2000, ApJ, 538, 241
Sushch I., Brose R., Pohl M., Plotko P., Das S., 2022, ApJ, 926, 140
Szécsi D., Agrawal P., Wünsch R., Langer N., 2022, A&A, 658, A125
Toalá J. A., Arthur S. J., 2011, ApJ, 737, 100
Truelove J. K., McKee C. F., 1999, ApJS, 120, 299
Vaidya B., Mignone A., Bodo G., Rossi P., Massaglia S., 2018, ApJ, 865, 144
van Marle A. J., Langer N., García-Segura G., 2004, in Garcia-Segura G., Tenorio-Tagle G., Franco J., Yorke H. W., eds, Revista Mexicana de Astronomia y Astrofisica Conference Series, Vol. 22. p. 136
van Marle A. J., Meliani Z., Marcowith A., 2015, A&A, 584, A49
van Veelen B., Langer N., Vink J., García-Segura G., van Marle A. J., 2009, A&A, 503, 495
Velázquez P. F., Steffen W., Raga A. C., Haro-Corzo S., Esquivel A., Cantó J., Riera A., 2011, ApJ, 734, 57
Vogt F. P. A., Bartlett E. S., Seitenzahl I. R., Dopita M. A., Ghavamian P., Ruiter A. J., Terry J. P., 2018, Nat. Astron., 2, 465
Weaver R., McCray R., Castor J., Shapiro P., Moore R., 1977, ApJ, 218, 377
Wilkin F. P., 1996, ApJ, 459, L31
Woosley S. E., Weaver T. A., 1986, ARA&A, 24, 205
Xin Y.-L., Guo X.-L., Liao N.-H., Yuan Q., Liu S.-M., Wei D.-M., 2017, ApJ, 843, 90
Yang C.-Y., Bao B.-W., Liu S.-M., 2020, Res. Astron. Astrophys., 20, 048
Yusef-Zadeh F., Morris M., 1987, ApJ, 320, 545
Zank G. P., Nakanotani M., Webb G. M., 2019, ApJ, 887, 116
Zhang M. F., Tian W. W., Wu D., 2018, ApJ, 867, 61
Zhou P. et al., 2022, ApJ, 931, 144

This paper has been typeset from a TEX/LATEX file prepared by the author.

Monthly Notices
of the
ROYAL ASTRONOMICAL SOCIETY

MNRAS **515,** L29–L33 (2022) https://doi.org/10.1093/mnrasl/slac062

Pulsar wind nebulae of runaway massive stars

D. M.-A. Meyer [1]★ and Z. Meliani [2]

[1] *1Institut für Physik und Astronomie, Universität Potsdam, Karl-Liebknecht-Strasse 24/25, D-14476 Potsdam, Germany*
[2] *2Laboratoire Univers et Théories, Observatoire de Paris, Université PSL, Université de Paris, CNRS, F-92190 Meudon, France*

Accepted 2022 June 8. Received 2022 June 8; in original form 2022 May 10

ABSTRACT

A significant fraction of massive stars move at speed through the interstellar medium of galaxies. After their death as core-collapse supernovae, a possible final evolutionary state is that of a fast-rotating magnetized neutron star, shaping its circumstellar medium into a pulsar wind nebula. Understanding the properties of pulsar wind nebulae requires knowledge of the evolutionary history of their massive progenitors. Using two-dimensional magnetohydrodynamical simulations, we demonstrate that, in the context of a runaway high-mass red-supergiant supernova progenitor, the morphology of its subsequent pulsar wind nebula is strongly affected by the wind of the defunct progenitor star pre-shaping the stellar surroundings throughout its entire past life. In particular, pulsar wind nebulae of obscured runaway massive stars harbour asymmetries as a function of the morphology of the progenitor's wind-blown cavity, inducing projected asymmetric up–down synchrotron emission.

Key words: methods: MHD – stars: evolution – stars: massive – pulsars: general – ISM: supernova remnants.

1 INTRODUCTION

About 10 per cent to 25 per cent of OB-type massive stars are runaway objects (Blaauw 1961; Schoettler, Parker & de Bruijne 2022) with peculiar supersonic speeds with respect to their interstellar medium (ISM). Two main mechanisms are proposed to explain the production of such runaway stars, namely binary-supernova ejection and dynamical ejection from the stellar cluster (Hoogerwerf, de Bruijne & de Zeeuw 2000), and their trajectories can be traced back to their parent starburst regions (Schoettler et al. 2019). These massive stars die as core-collapse supernovae, releasing most of the remaining stellar mass at high speed into the surrounding circumstellar medium (CSM) before expanding into the ISM.

Often, at the location of the supernova explosion, there remains a highly magnetized and fast-rotating neutron star (a pulsar). The pulsar generates a powerful wind with a kinetic luminosity that can reach $\dot{E} \sim 10^{39}\,\mathrm{erg\,s^{-1}}$, inducing a growing pulsar wind nebula (PWN). This PWN evolves first into freely expanding supernova ejecta before reaching the supernova reverse shock (Blondin, Chevalier & Frierson 2001). After this, it interacts with the swept-up CSM and, at a later time, with the unshocked ISM.

Previous investigations on PWNe of moving pulsars have concentrated on the birth kick pulsar. This occurs when massive stars collapse (de Vries et al. 2021). The resulting pulsar propagates through the supernova ejecta (Slane et al. 2018). On time-scales of a few kyr, the fast-moving pulsar escapes the supernova remnant (SNR) and travels in the uniform and cold ISM (Barkov et al. 2019; Bucciantini, Olmi & Del Zanna 2020). The resulting PWN morphology is strongly deformed and develops an extended tail. Because of numerical and physical difficulties associated with the CSM modelling, the simulations of PWNe are mainly performed in classical hydrodynamics and deal only with moving pulsars inside supernova ejecta (Temim et al. 2015, 2022). Relativistic simulations have been performed for pulsars moving in the ISM (Barkov et al. 2019; Bucciantini et al. 2020), while others also deal with static pulsar winds expanding into the supernova ejecta in 1D and 2D (Blondin et al. 2001; van der Swaluw et al. 2003; van der Swaluw 2003; van der Swaluw, Downes & Keegan 2004; Slane et al. 2018). However, these works did not account for all the evolutionary phases of the stellar progenitor of the runaway pulsar.

For pulsars from massive runaway stars, their winds mainly expand in supernova remnant (SNRs) constituted of supernova ejecta and CSM materials. Thus, shocks and instabilities, as well as the overall PWN morphology, will be affected by these structures. Since SNRs are strongly affected by the CSM distribution (Cox et al. 2012), the PWNe and the properties of the various shocks therein should be, in turn, a function of the surrounding CSM. Most commonly, runaway massive stars shape the CSM with a large amount of red-supergiant material as dense asymmetric stellar-wind bow shocks (Cox et al. 2012; Henney & Arthur 2019a, b, c; Meyer, Petrov & Pohl 2020a; Herbst et al. 2022), so this should not be omitted in the modelling of their PWN.

Motivated by the above arguments, we numerically investigate the shaping of the PWN of a fast-moving massive core-collapse supernova progenitor. We focus on the particular effects of the CSM generated by the wind–ISM interaction of the progenitor star. This study is organized as follows. First, we present the numerical methods used to model the pulsar wind nebula of a runaway massive progenitor star in Section 2. The outcomes of the simulations are presented in Section 3. We discuss our results and draw our conclusions in Section 4.

2 METHOD

This study focuses on the entire evolution of the circumstellar medium of a runaway 20 $M_\odot$ star at Galactic metallicity. The stellar surface properties such as wind velocity and mass-loss rate histories

★ E-mail: dmameyer.astro@gmail.com

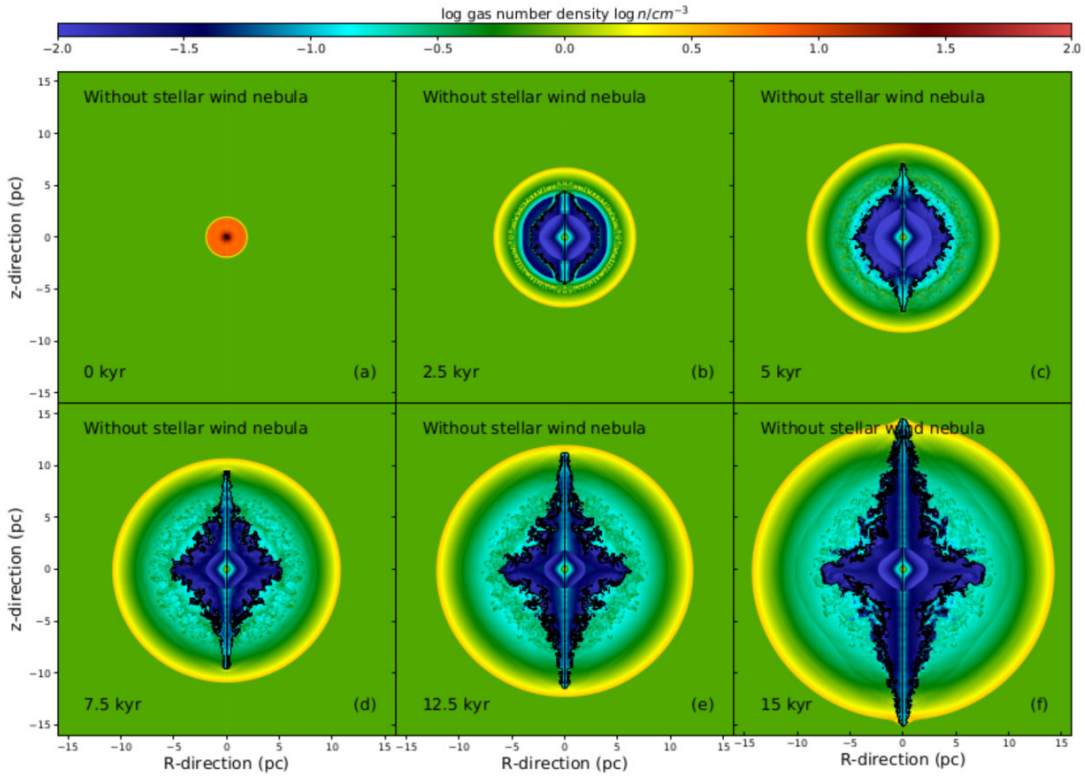

Figure 1. Time evolution of the number density field (in cm^{-3}) in the simulation of the nebula generated by a pulsar wind injected into the expanding ejecta of a core-collapse supernova. The black contour marks the region of the nebula made of 50 per cent of pulsar wind material in number density. Time is measured starting from the onset of the pulsar wind.

are taken from a model of the GENEVA evolutionary tracks library calculated without rotational mixing (Eldridge et al. 2006; Ekström et al. 2012).

We model the stellar surroundings from the zero-age main-sequence to the pre-supernova phase, through its red-supergiant phase. When the star achieves its evolution, we inject therein supernova core-collapse ejecta made of mass $M_{\rm ej} = 6.96\,\mathrm{M}_\odot$ and energy $E_{\rm ej} = 10^{51}$ erg, using a density power-law profile (Whalen et al. 2008; Meyer et al. 2020a). The pulsar wind is modelled according to Komissarov & Lyubarsky (2004), using a wind power $\dot{E}_{\rm o} = 10^{38}\,\mathrm{erg\,s}^{-1}$, a wind velocity $10^{-2}c$ with c the speed of light in vacuum, a pulsar spin $P_{\rm o} = 0.3$ s, a spin period variation $\dot{P}_{\rm o} = 10^{-17}\,\mathrm{s\,s}^{-1}$, and a wind magnetization parameter $\sigma = 10^{-3}$ (Slane 2017). The pulsar loses energy according to an initial spin-down time-scale $\tau_{\rm o} = P_{\rm o}/((N-1)\dot{P}_{\rm o})$, where the braking index $N = 3$ stands for magnetic dipole spin-down. The energy diminution equation therefore reads $\dot{E}(t) = \dot{E}_{\rm o}(1 + t/\tau_{\rm o})^{\alpha}$ with $\alpha = -(N+1)/(N-1)$; see Pacini & Salvati (1973). In this first paper, we run 2.5D simulations. Therefore, it is assumed that the spin axis and the direction of motion of the star coincide with the axis of symmetry of the cylindrical coordinate system.

The massive star moves through the ISM of the Milky Way's Galactic plane of initial gas density $0.79\,\mathrm{cm}^{-3}$ and temperature 8000 K (Wolfire et al. 2003; Meyer et al. 2014). We adopt an undisturbed ISM magnetic field parallel to the direction of motion of the star with a strength of 7 μG, which corresponds to an Alfvén speed of $v_{\rm A} = 17.2\,\mathrm{km\,s}^{-1}$ (Meyer et al. 2017).

The 2.5D numerical magnetohydrodynamical simulations are performed with the code PLUTO (Mignone et al. 2007, 2012). We make use of the Godunov-type numerical scheme HLL Riemann solver combined with the PPM limiter, together with a third-order Runge–Kutta time-marching algorithm controlled by the Courant–Friedrich–Levi number. As in van der Swaluw et al. (2003), we set the polytropic index to 5/3 and optically thin radiative cooling physics is used for all circumstellar evolutionary phases except when starting from the onset of the pulsar wind. More precisely, we make use of the optically thin cooling and heating curves for a fully ionized medium (Wiersma, Schaye & Smith 2009) of solar abundance (Asplund et al. 2009) presented in Meyer et al. (2014). Calculations are conducted following a mapping strategy (van Marle, Meliani & Marcowith 2015; Meyer et al. 2020a, 2021) in which the progenitor's CSM is first calculated, before supernova ejecta and eventually pulsar wind are injected into it. The models are conducted using a cylindrical coordinate system (R, z) that is mapped with a uniform mesh [0, 150] × [−50, 50] of spatial resolution $1.2 \times 10^{-2}\,\mathrm{pc\,cell}^{-1}$ for the CSM and a mesh [0, 20] × [−20, −20] of resolution $6.7 \times 10^{-3}\,\mathrm{pc\,cell}^{-1}$ for the PWN. The central sphere in which winds are imposed is of radius 20 cells (0.24 pc during the stellar-wind phase and 0.134 pc throughout the pulsar phase).

Two simulations are performed with a runaway star of space velocity $v_\star = 40\,\mathrm{km\,s}^{-1}$ (Mach number $\mathcal{M} \sim 4$). The first one considers the pulsar wind expanding into supernova ejecta only, while the second one also accounts for the progenitor's CSM.

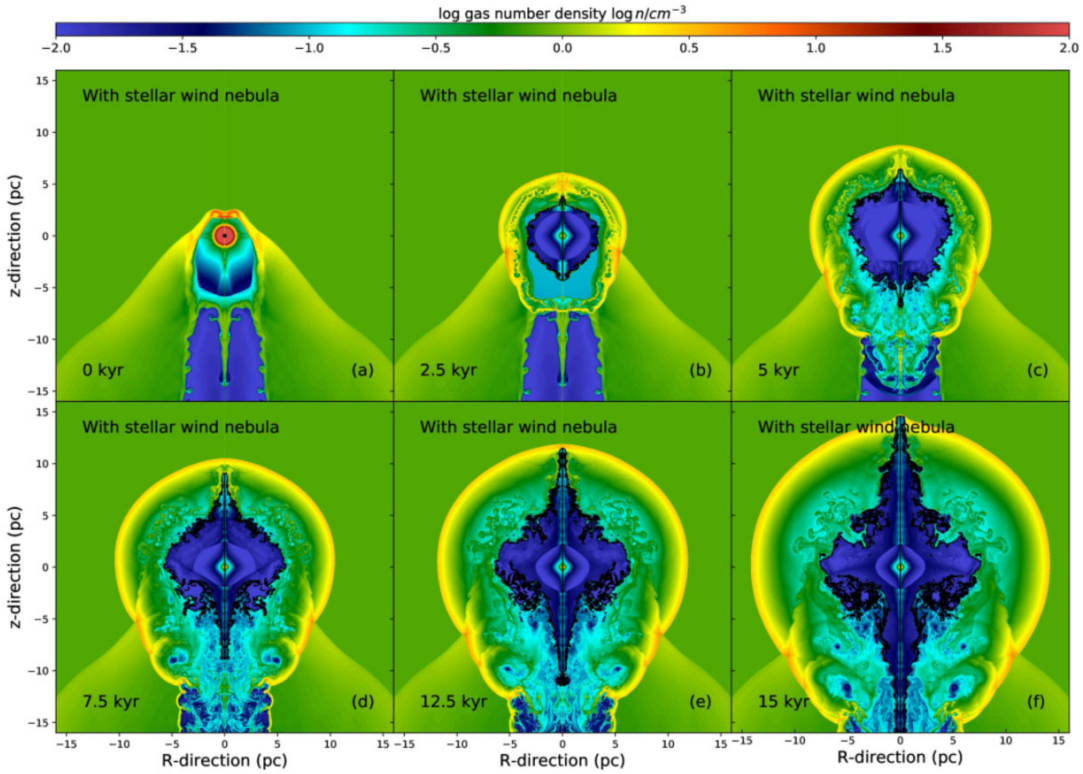

Figure 2. As for Fig. 1, with the presence of the circumstellar medium (CSM) generated by the wind–ISM interaction of the 20 $M_\odot$ massive runaway progenitor.

3 RESULTS

3.1 Model without wind–ISM interaction

For the sake of comparison, we first model a PWN accounting for core-collapse supernova ejecta but neglecting the CSM, the entire system being in supersonic motion in the ambient medium. The time sequence of the evolution of the number density field of such a system is displayed in Fig. 1.

The pulsar wind is set in the dense supernova ejecta that has expanded up to a few pc into the local ISM (Fig. 1a). About 2.5 kyr later, the PWN has adopted a structure made of the freely expanding pulsar wind, a PWN termination shock, a PWN/ejecta inner contact discontinuity (black contour), and a transmitted PWN forward shock propagating into the unshocked supernovae ejecta. The ejecta–ISM interaction leads to the formation of an outer ejecta–ISM contact discontinuity affected by strong Richtmyer–Meshkov instabilities (Kane, Drake & Remington 1999), while a reflected supernova termination shock forms and propagates inwards, heating the pulsar wind. Meanwhile, the supernova forward shock propagates through the ISM (Fig. 1b).

The system keeps on growing in size over the next few kyr, revealing an efficient mixing of pulsar and ejecta materials. The magnetized pulsar wind develops a bipolar jet along its rotation axis; see the black contours of Fig. 1(c). At time 7.5 kyr the PWN harbours an equatorial disc-like feature, normal to the bipolar jet, which has gone through the unstable region where the mixing of materials takes place and penetrates the outer layer of shocked ISM gas of the SNR (Fig. 1d). The magnetized PWN, at this point, displays the typical cross-like anisotropic morphology described in Komissarov & Lyubarsky (2004), embedded by an overall spherically symmetric expanding blastwave (Fig. 1e). Lastly, the jet of the pulsar catches up with the supernova remnant shock wave and begins to expand into the ISM, generating polar bow shocks (Fig. 1f).

During the evolution, the high speed of the supernova ejecta compensates the ISM ram pressure, allowing the SNR, and consequently the PWN morphology, to conserve an isotropic symmetry.

3.2 Effects of the progenitor's wind–ISM interaction

In the second model, all evolutionary stages of the massive progenitor are considered before the supernova explosion occurs and the pulsar starts blowing into the former stellar wind (Fig. 2). The gas distribution at the onset of the pulsar wind is complex, as the wind–ISM interaction has shaped it throughout the previous star's life. Its arc-like nebula is composed of a large-scale component produced by the main-sequence stellar wind plus the shell of the red-supergiant wind that has been subsequently released in it (Meyer et al. 2014). The pre-pulsar CSM is therefore a central region of expanding ejecta surrounded by a low-density cavity , with a high-density bow shock facing the direction of the progenitor's motion (Fig. 2a); see also Meyer et al. (2015, 2021). The asymmetric propagation of the supernova blastwave is strongly constrained by the walls of the cavity. It is channelled by the cavity in the direction opposite to that in which the stellar motion shock has gone through the CSM (Fig. 2b).

The global organization of the SNR and its central PWN exhibits qualitative dissimilarities to that of Fig. 1 as the gameof shock reflections generates a more complex object. The morphology of

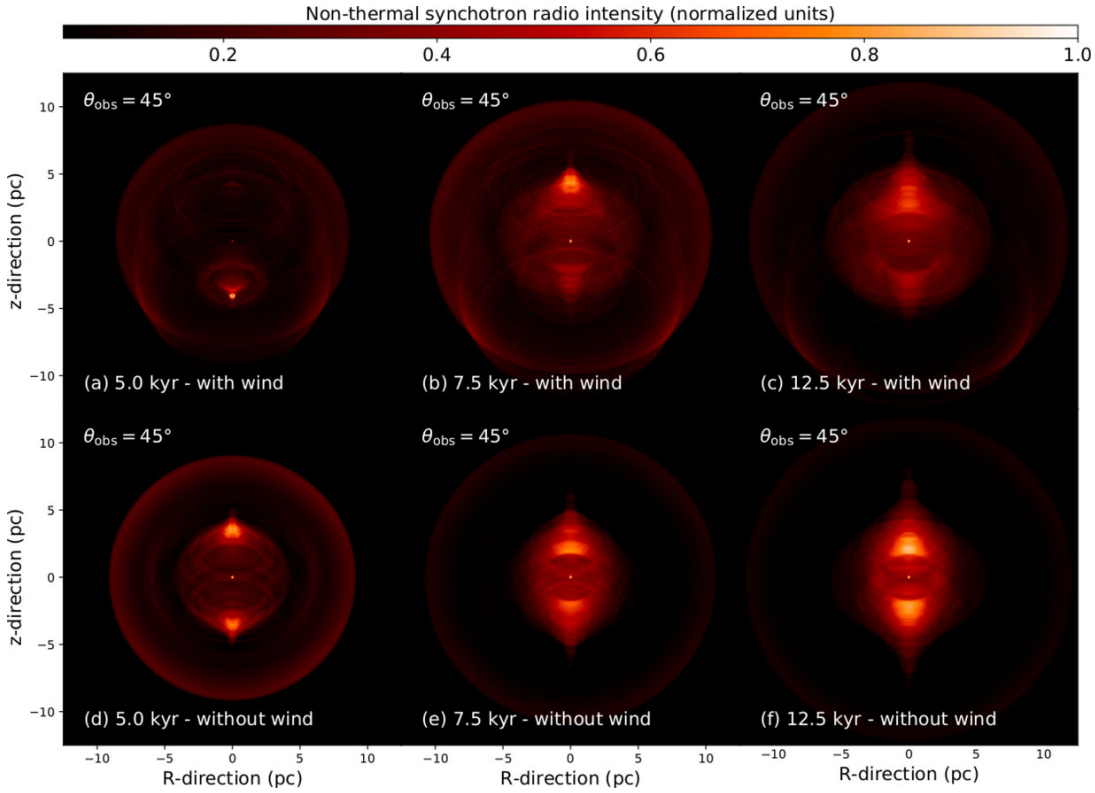

Figure 3. Selected time-sequence evolution of the synchrotron emission map assuming an angle $\theta_{obs} = 45°$ between the observer's line of sight and the axis of symmetry of the nebula. The images compare models with (top) and without (bottom) the stellar wind of the massive progenitor.

the pulsar wind–ejecta interface is governed by that of the ejecta region, adopting an ovoidal shape (Fig. 2c) different to that of the model without the progenitor's stellar wind (Fig. 1c). At the time 7.5 kyr, the supernova ejecta are channelled into the tubular region of shocked stellar wind generated by the progenitor's motion and the pulsar wind develops a bipolar jet, although the pulsar wind remains equatorially asymmetric (Fig. 2d). The nebula further evolves such that the inner contact discontinuity of the PWN is shaped as a function of (i) the pulsar magnetorotational properties and (ii) the supernova shock wave material that is reflected towards the centre of the explosion. Finally, the contact discontinuity recovers the overall morphology of a bipolar jet normal to an equatorial structure (Fig. 2e), with important persisting equatorial dissymmetries (Fig. 2f).

4 DISCUSSION AND CONCLUSION

In this paper, we numerically investigate, in the context of a runaway massive supernova progenitor and within the frame of the ideal magnetohydrodynamics, the influences of the CSM shape during all the progenitor's evolutionary stages on the long-term ($\sim$ kyr) morphological development of the PWN after the pulsar birth and on the instabilities growing at shocks. Other works concerning the release of pulsar winds in SNRs were set in the frame of ideal hydrodynamics (Blondin et al. 2001; van der Swaluw et al. 2003; van der Swaluw 2003; van der Swaluw et al. 2004; Slane et al. 2018) as well as magnetohydrodynamics; see Olmi & Torres (2020) and references therein. Nevertheless, although some studies have tackled the problem of runaway pulsars (Olmi & Bucciantini 2019), or even investigated the effects of a stratified ISM (Kolb et al. 2017), none of them include in detail the stellar-wind feedback of the core-collapse progenitor. In our scenario, the pulsar wind–supernova ejecta system is embedded into a dense CSM, where a large part of the progenitor mass lies, released as a pre-supernova stellar wind. Note that our models assume that the pulsar is static in the frame of reference of the runaway star, so we are neglecting the birth kick that many pulsars receive from the supernova explosion. Assuming a typical kick velocity of $\approx 400\,\mathrm{km\,s^{-1}}$ (Verbunt, Igoshev & Cator 2017), the pulsar would be displaced by about 6 pc over the 15 pc that we simulate. Therefore our results apply mainly to the low-velocity pulsar sub-population ($\leq 50\,\mathrm{km\,s^{-1}}$), which comprises $\approx$ 2–5 per cent of all pulsars (Igoshev 2020).

Our study shows, in the particular context of a fast-moving red-supergiant star in the Galactic plane, that the wind-blown bubble of a core-collapse supernova progenitor has a governing impact on the morphology of its subsequent PWN. As early as $\sim$ 2.5 kyr, the distribution of the contact discontinuity between a magnetized pulsar wind and the supernova ejecta adopts an oblong shape as a result of the anisotropic ejecta distribution. Since core-collapse SNRs are shaped according to their CSM, PWNe similarly take their morphology as a direct consequence of their progenitor's stellar evolution history. Because a significant fraction of massive stars are runaway objects, our findings imply that the stellar-wind history should not be neglected in the understanding of PWNe and that the CSM-induced asymmetries should account for up to 10 per cent to 25 per cent of all individual PWNe.

The stellar-wind history that we use is that of a $20\,M_\odot$ supergiant star, which is amongst the most common progenitors of core-collapse SNRs (Katsuda et al. 2018), although higher-mass evolutionary channels might exist, i.e. involving Wolf–Rayet progenitors. The bulk motion of the star is taken to be within that of the most common runaway stars (Blaauw 1993). However, a small fraction of high-mass stars move with very high velocities (Lennon et al. 2018) and might form PWNe, for which the influence of the CSM is milder. Given that the morphology of PWNe retains information from the stellar evolution history of massive stars, our model applies to objects in the Galactic disc region ($\sim 1\,\mathrm{cm}^{-3}$) rather than in the high-latitude parts of the Milky Way, where the low-density medium induces an extended CSM (Meyer et al. 2020b) with which supernova shock waves (and eventually pulsar winds) weakly interact. Conversely, massive stars running through dense molecular regions are more likely to form complex CSM and, therefore, to produce very asymmetric PWNe.

We generate predictive images for our asymmetric PWN from a runaway massive star. Fig. 3 plots non-thermal radio synchrotron emission maps using the emissivity $\propto p B_\perp^{(s+1)/2}$ with p the thermal pressure of the gas, $B_\perp$ the component of the magnetic field along the observer's line of sight, and $s = 2$ the power-law index of the non-thermal electron distribution (Jun & Norman 1996). The images are produced with the RADMC-3D code (Dullemond 2012), displayed with (top) and without (bottom) CSM, for selected time instances, and assuming an inclination angle of the pulsar of $\theta_{\rm obs} = 45^\circ$ to the plane of the sky. The pulsar wind is at first not visible in the region facing the progenitor's direction of motion, where the supernova shock wave interacting with the wind bubble dominates (Figs 3a, d). Once the pulsar polar jet grows and penetrates the dense region of stellar wind and ejecta, it becomes brighter than that in the cavity (Figs 3b, c). This projected up–down surface brightness asymmetry increases with time, as the front jet starts to interact with the shocked supernova material and the jet on the other side continues to propagate in the rarefied medium of the stellar-wind cavity.

Our results show that the effects of the progenitor's stellar wind impacts the global morphology of PWNe and consequently influences the properties of the shocks therein. This should significantly modify the injection and acceleration physics of the relativistic particle population, which, in turn, is responsible for the non-thermal emission properties of PWNe.

We intend to extend this work to a broader study, investigating the parameter space of various massive stellar progenitors, treating the pulsar wind relativistically, and including the kick received by a pulsar.

ACKNOWLEDGEMENTS

The authors thank the referee, W. Henney, for advice that improved the quality of the paper. The authors acknowledge the North-German Supercomputing Alliance (HLRN) for providing HPC resources that have contributed to the research results reported in this paper.

DATA AVAILABILITY

The data underlying this article will be shared on reasonable request to the corresponding author.

REFERENCES

Asplund M., Grevesse N., Sauval A. J., Scott P., 2009, ARA&A, 47, 481
Barkov M. V., Lyutikov M., Klingler N., Bordas P., 2019, MNRAS, 485, 2041
Blaauw A., 1961, Bull. Astron. Inst. Netherlands, 15, 265
Blaauw A., 1993, in Cassinelli J. P., Churchwell E. B., eds, ASP Conf. Ser. Vol. 35, Massive Stars: Their Lives in the Interstellar Medium. Astron. Soc. Pac., San Francisco, p. 207
Blondin J. M., Chevalier R. A., Frierson D. M., 2001, ApJ, 563, 806
Bucciantini N., Olmi B., Del Zanna L., 2020, J. Phys. Conf. Ser., 1623, 012002
Cox N. L. J., Kerschbaum F., van Marle A.-J., Decin L., Ladjal D., Mayer A., 2012, A&A, 537, A35
de Vries M. et al., 2021, ApJ, 908, 50
Dullemond C. P., 2012, Astrophysics Source Code Library, record ascl:1202.015
Ekström S. et al., 2012, A&A, 537, A146
Eldridge J. J., Genet F., Daigne F., Mochkovitch R., 2006, MNRAS, 367, 186
Henney W. J., Arthur S. J., 2019a, MNRAS, 486, 3423
Henney W. J., Arthur S. J., 2019b, MNRAS, 486, 4423
Henney W. J., Arthur S. J., 2019c, MNRAS, 489, 2142
Herbst K. et al., 2022, Space Sci. Rev., 218, 29
Hoogerwerf R., de Bruijne J. H. J., de Zeeuw P. T., 2000, ApJ, 544, L133
Igoshev A. P., 2020, MNRAS, 494, 3663
Jun B.-I., Norman M. L., 1996, ApJ, 472, 245
Kane J., Drake R. P., Remington B. A., 1999, ApJ, 511, 335
Katsuda S., Takiwaki T., Tominaga N., Moriya T. J., Nakamura K., 2018, ApJ, 863, 127
Kolb C., Blondin J., Slane P., Temim T., 2017, ApJ, 844, 1
Komissarov S. S., Lyubarsky Y. E., 2004, MNRAS, 349, 779
Lennon D. J. et al., 2018, A&A, 619, A78
Meyer D. M.-A., Mackey J., Langer N., Gvaramadze V. V., Mignone A., Izzard R. G., Kaper L., 2014, MNRAS, 444, 2754
Meyer D. M.-A., Langer N., Mackey J., Velázquez P. F., Gusdorf A., 2015, MNRAS, 450, 3080
Meyer D. M.-A., Vorobyov E. I., Kuiper R., Kley W., 2017, MNRAS, 464, L90
Meyer D. M. A., Petrov M., Pohl M., 2020a, MNRAS, 493, 3548
Meyer D. M. A., Oskinova L. M., Pohl M., Petrov M., 2020b, MNRAS, 496, 3906
Meyer D. M. A., Pohl M., Petrov M., Oskinova L., 2021, MNRAS, 502, 5340
Mignone A., Bodo G., Massaglia S., Matsakos T., Tesileanu O., Zanni C., Ferrari A., 2007, ApJS, 170, 228
Mignone A., Zanni C., Tzeferacos P., van Straalen B., Colella P., Bodo G., 2012, ApJS, 198, 7
Olmi B., Bucciantini N., 2019, MNRAS, 488, 5690
Olmi B., Torres D. F., 2020, MNRAS, 494, 4357
Pacini F., Salvati M., 1973, ApJ, 186, 249
Schoettler C., Parker R. J., Arnold B., Grimmett L. P., de Bruijne J., Wright N. J., 2019, MNRAS, 487, 4615
Schoettler C., Parker R. J., de Bruijne J., 2022, MNRAS, 510, 3178
Slane P., 2017, in Alsabti A. W., Murdin P., eds, Handbook of Supernovae, p. 2159
Slane P. et al., 2018, ApJ, 865, 86
Temim T., Slane P., Kolb C., Blondin J., Hughes J. P., Bucciantini N., 2015, ApJ, 808, 100
Temim T., Slane P., Raymond J. C., Patnaude D., Murray E., Ghavamian P., Renzo M., Jacovich T., 2022, ApJ, 932, 26
van der Swaluw E., 2003, A&A, 404, 939
van der Swaluw E., Achterberg A., Gallant Y. A., Downes T. P., Keppens R., 2003, A&A, 397, 913
van der Swaluw E., Downes T. P., Keegan R., 2004, A&A, 420, 937
van Marle A. J., Meliani Z., Marcowith A., 2015, A&A, 584, A49
Verbunt F., Igoshev A., Cator E., 2017, A&A, 608, A57
Whalen D., van Veelen B., O'Shea B. W., Norman M. L., 2008, ApJ, 682, 49
Wiersma R. P. C., Schaye J., Smith B. D., 2009, MNRAS, 393, 99
Wolfire M. G., McKee C. F., Hollenbach D., Tielens A. G. G. M., 2003, ApJ, 587, 278

This paper has been typeset from a TEX/LATEX file prepared by the author.